NOTICE

CERTAIN DATA CONTAINED IN THIS DOCUMENT MAY BE DIFFICULT TO READ IN MICROFICHE PRODUCTS.

CONF-910818--

LA-UR-91-3436

Issued: November 1991

Proceedings of the PILAC Optics Workshop

August 12 - 13, 1991

Los Alamos National Laboratory
Los Alamos, New Mexico 87545

LA-UR-91-3436

LA-UR--91-3436

DE92 004653

PILAC

PION LINAC AT LOS ALAMOS MESON PHYSICS FACILITY

Los Alamos National Laboratory is operated by the University of California for the United States Department of Energy under contract W-7405-ENG-36.

Proceedings of the PILAC Optics Workshop

August 12-13, 1991

LOS ALAMOS NATIONAL LABORATORY

Los Alamos National Laboratory, Los Alamos, NM 87545

This work was supported by the U.S. Department of Energy, Office of Energy Research.

These papers are printed as submitted by the authors.

An Affirmative Action/Equal Opportunity Employer

LA-UR-91-3436

Issued: November 1991

Proceedings of the PILAC Optics Workshop

August 12 - 13, 1991

Los Alamos

Los Alamos National Laboratory
Los Alamos, New Mexico 87545

CONTENTS - PROCEEDINGS OF THE PILAC OPTICS WORKSHOP

August 12 & 13, 1991

AGENDA

PILAC OPTICS WORKSHOP

LAMPF AUDITORIUM
MONDAY, AUGUST 12, 1991

8:30 - 9:10	Introduction	H.A.Thiessen
9:10 - 9:35	PILAC Injection Line Design	B. Blind
9:35 - 10:00	PILAC General-Purpose Line Design	N. Mao
10:00 - 10:30	**COFFEE BREAK**	
10:30 - 11:00	Program RAYTRACE	H. Enge
11:00 - 11:30	Design & Performance of MRS	R. Boudrie
11:30 - 11:45	Program MOTER	M. Klein
11:45 - 12:00	Recent Upgrades of MOTER	H. Butler
12:00 - 1:00	**LUNCH**	
1:00 - 1:15	Use of MOTER at Michigan State	J. Nolen
1:15 - 1:30	Spectrometer Design at Michigan State	A. Zeller
1:30 - 2:05	Use of MOTER at CEBAF & Related Topics	J. Napolitano
2:05 - 2:25	TOSCA Calculations at CEBAF	J. Lassiter
2:25 - 2:45	TOSCA Calculations for PILAC	B. Weintraub
2:45 - 3:00	Measurements of EPICS Quadrupoles	C. Morris
3:00 - 3:30	**COFFEE BREAK**	
3:30 - 3:45	Quadrupole Measurements and Analysis at Bates Laboratory	J. Zumbro
3:45 - 4:15	Analysis of 3D Quadrupole Data	J. Arrington
4:15 - 5:15	Quadrupole 3D Fringe Fields (Theoretical Lecture #1 of 2)	K. Halbach
6:30 - 10:00	Banquet and Discussion Session at Los Alamos Inn	Group

PILAC OPTICS WORKSHOP

LAMPF AUDITORIUM
TUESDAY, AUGUST 13, 1991

8 30 - 9 30	Quadrupole 3D Fringe Fields (Theoretical Lecture #2 of 2)	K Halbach
9:30 - 10:00	***COFFEE BREAK***	
10 00 - 10 30	Analysis of 3D Field Data	D Lobb
10 30 - 11 00	Analysis of Dipole Fringe Fields	F Neri
11 00 - 11:30	Quadrupoles with Perfect N=2 Symmetry	P Walstrom
11.30 - 12:00	CEBAF Superconducting Cos (2θ) Quadrupole	S. Nanda
12:00 - 1:00	***LUNCH***	
1.00 - 1.30	Upgrades to TRANSPORT and TURTLE	D Carey
1 30 - 2 00	GIOS	H Wollnik
2 00 - 2 30	MARYLIE	A Dragt
2 30 - 3:00	Optics Using Differential Algebra	M Berz
3:00 - 3:30	***COFFEE BREAK***	
3 30 - 3 45	A Possible Test of Quad Optics Using EPICS	H A. Thiessen
3 45 - 4 30	Group Discussion	
4 30 - 5 00	Rapporteur	K Brown

PILAC OVERVIEW

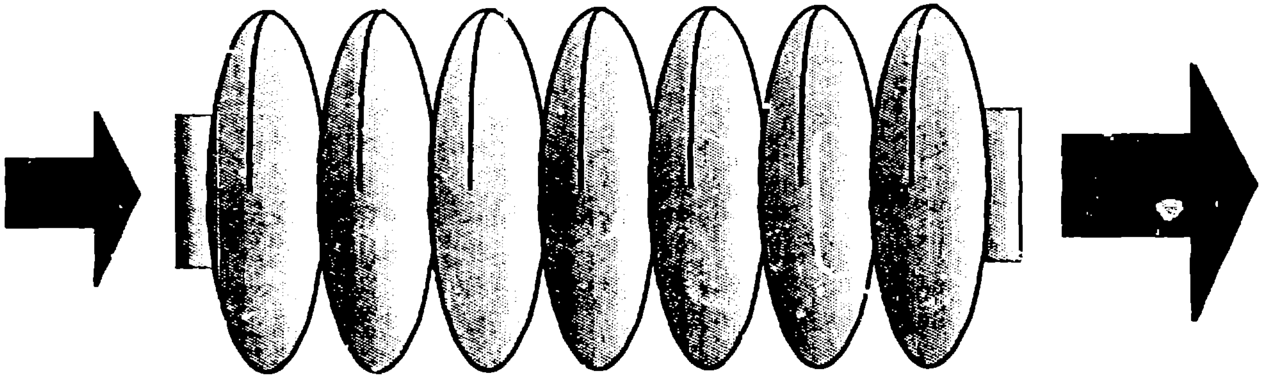

PILAC

Technical Summary and Recent Developments

• an Overview Talk for

• PILAC Optics Meeting

• by

• Arch Thiessen

• 12 August, 1991

Contents

Charge to Workshop !

- Review PILAC Optics Calculations !
  - Injection Line
  - High-Res Dispersed Line and Spectrometer
  - General-Purpose Line and MRS
- How Good Are Our Magnet Models ?
  - Optics is Only as Good as Field Models
  - Analyze 3-D Calculations and Measurements
  - Compare Available Codes with Emphasis on Field Models
- Can We Build Quads With Pure n=2 (including ends) ?
- Can We Use Entire Open Region of Quadrupoles ?
- What Do We Do When The System Is Constructed ?
  - Measurement Techniques
  - Analysis of Measurements
  - Shimming
  - Adjustable Elements

PILAC Design Study

Exec. Comm.
R.Chrien (Chair)
J. Rapaport (LUGI Chair)
J.McClelland (LANL)

Hypernuclear Reactions
E.Hungerford (Houston)
B.Gibson (LANL)

Barakat, M.
Barnes, P.
Chakravarti, S.
Chrien, R.
Dover, R.
Ejiri, H.
Hashimoto, O.
Hayes, A.
Johnson, M.
Leviatan, A.
Pile, P.

Fundamental Interactions
R.Ransome (Rutgers)
P.Herczeg (LANL)

Carlson, J.
Gibbs, W.
Gill, D.
Goldman, T.
Hoffman, C.
Holinde, K.
Meyer, B.
McClelland, J.
Nakai, K.
Nanda, S.
Nefkens, B.
Perdrisat, C.
Pocanic, D.
Rijken, Th.
Sistemich, K.
Strakovsky, I.
vanOers, Wm.

Baryon Resonances
M.Sadler (ACU)
W.Gibbs (LANL)

Carlson, J.
Chakravarti, S.
DeSwart, J.
Goldman, T.
Johnson, M.
Kyle, G.
Leviatan, A.
Liu, L.
Mukhopadhyay, N.
Rijken, Th.
Silbar, R.
Strakovsky, I.

High-Energy Pions
D.Ernst (TAMU)
D.Dehnhard (Minn.)

Burleson, G.
Chakravarti, S.
Dhuga, K.
Fortune, T.
Greene, S.
Hashimoto, O.
Hayes, A.
Johnson, M.
Liu, L.
Moore, C. F.
Peterson, R. J.
Sarafian, H.
Strottman, D.
Strakovsky, I.

Facilities
H.Thiessen (LANL)

Blind, B.
Butler, H.
Dehaven, R.
Gray, E.
Grand, P.
Green, A.
Li, Z.
Mao, N.
Piel, H.
Rusnak, B.
Smythe, R.
Spalek, G.
Swain, G.

Los Alamos

PILAC Team
Funded by LDRD

Technical Project Manager
Arch Thiessen

Design Study Team (MP)
Arch Thiessen, Team Leader

- Hal Butler, MOTER Software
- Barbara Blind, Injection Optics
- Naifeng Mao, Magnets & Extraction
- Myra Martinez, Group Secretary
- George Swain, LINAC Beam Dynamics
- Staff Member, Hi-Res Optics, tbd
- Karl Brown, SLAC, Collaborator
- Alex Dragt, Collaborator
- Harald Enge, MIT, Collaborator
- Pierre Grand, BNL, Collaborator
- Klaus Halbach, Collaborator

Cavity Team (AT)
George Spalek, Team Leader

- Brian Rusnak, Cavity Lab Operations
- Ed Gray, Couplers & Cavity Tuning
- Richard Maggs, Technician
- Alan Shapiro, Technician
- Postdoc, tbd
- Ernst Haebel, CERN, Collaborator
- Hasan Padamsee, Cornell, Collaborator
- Helmut Piel, Wuppertal, Collaborator

Los Alamos

Physics with Pions up to 1.1 GeV

- Λ-Hypernuclear Physics
  - Accessed thru (π,K) Reaction at 920 MeV
- Λ-Nucleon Scattering
  - Λ produced by (π,K) Reaction at 920 MeV
    - * Λ scattered in K production target
- Baryon Resonances
  - access to next 12 resonances above Δ
- Higher Energy Pion-Nucleus Scattering
  - longer mean-free-path of pion
  - role of π^+ and π^- reversed
  - single- and double-charge exchange
- Rare Decays - for example:
  - precision pion beta decay rate (0.1%)
    - * improved beam monitoring
      - *no e or p in PILAC beam !*
  - $\eta \rightarrow \mu\mu$ (CP violation)
    - * look for polarization of muons
- *Of These, (π,K) is the Most Demanding, hence Sets the Specifications for PILAC*

Los Alamos

What PILAC Will Do for Hypernuclear Physics

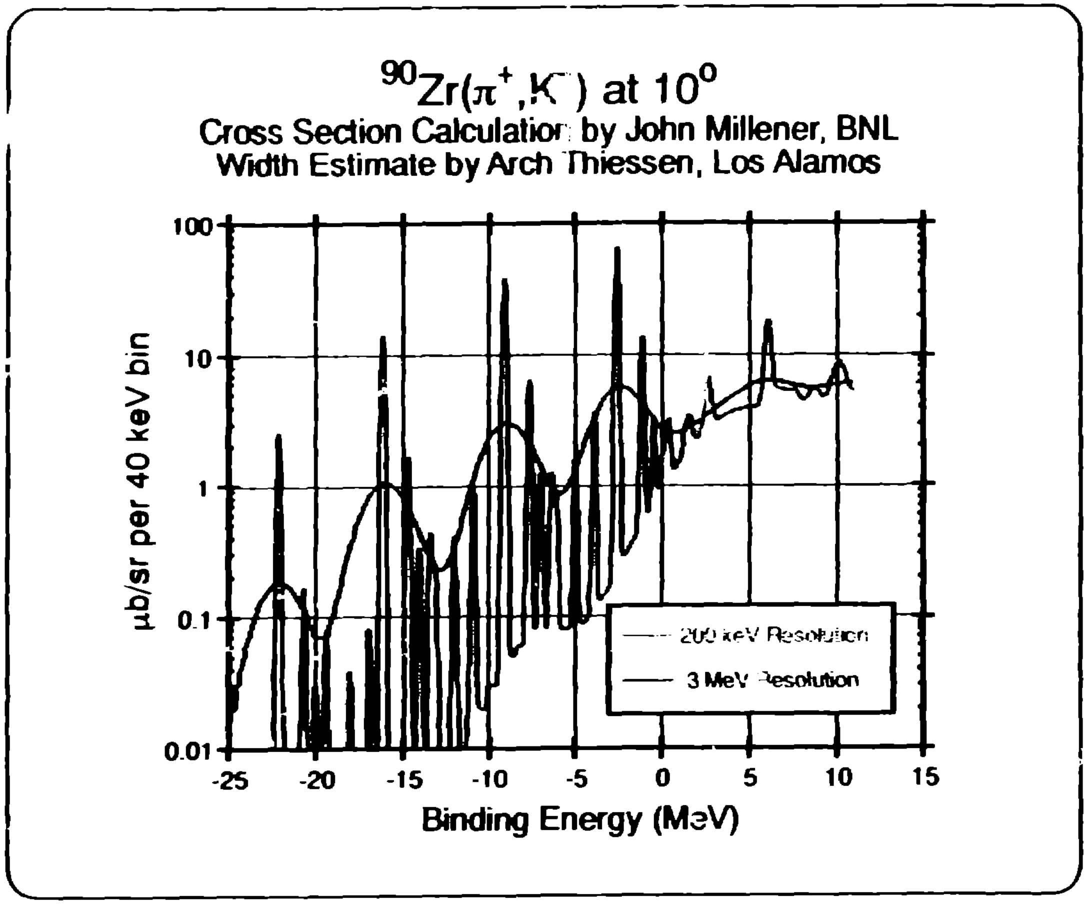

• 36 Counts in the Weakest State in a 1-Day Run

PILAC Concept

2 mA LAMPF Beam → Proton Buncher → High Intensity Pion Source → **High Gradient Pion Linac** → Beam Sharing System → User Facilities

PILAC Conceptual Layout

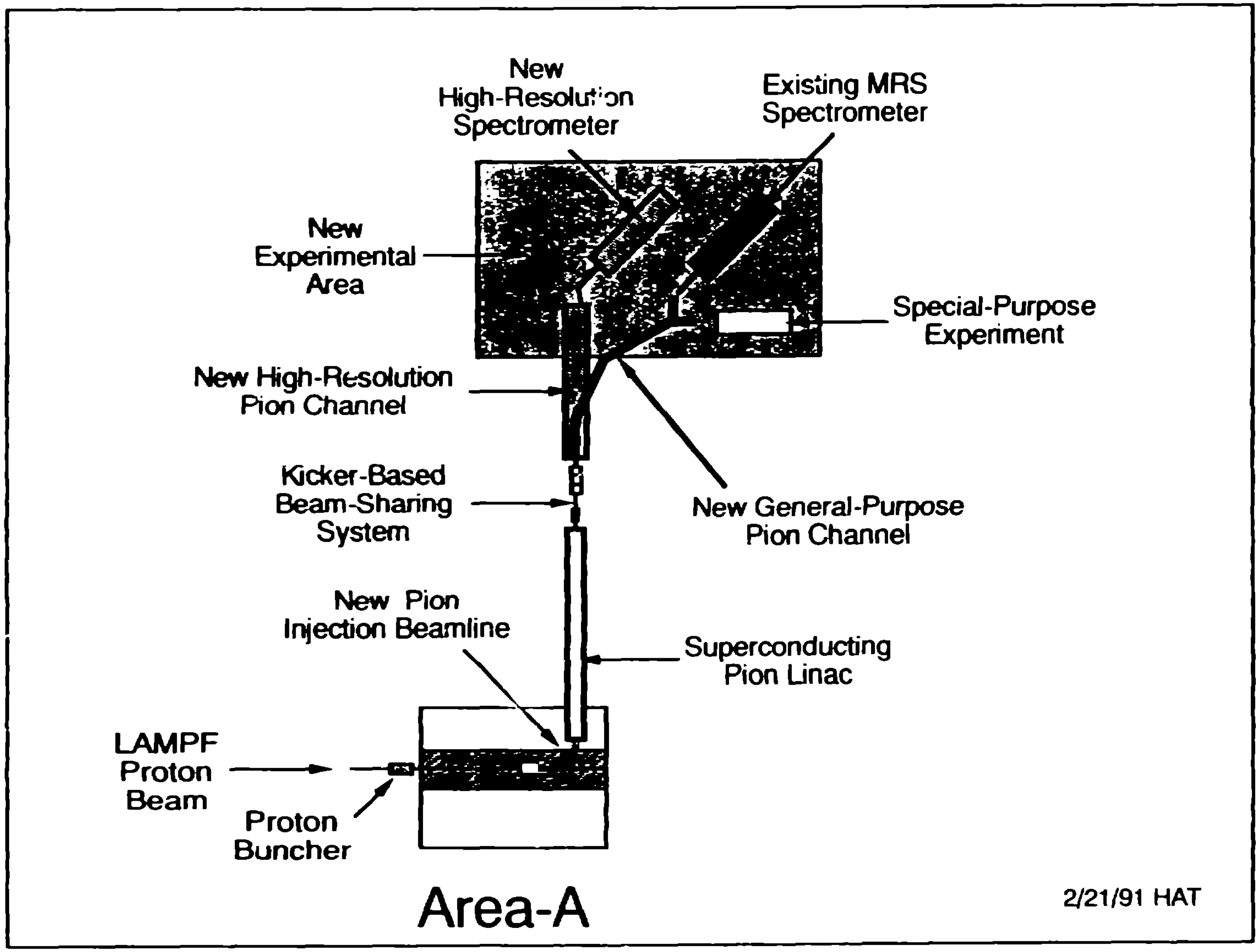

Los Alamos

PILAC Specifications

- Injection Line
  - 360 MeV (480 MeV/c) Fixed Energy
  - Acceptance - ±62mrad x ±3.6mm x ±3.5%
    - * 225 π mm-mrad
    - * 15 msr
    - * 7% dp/p
- Linac
  - 360-1070 MeV (480-1200 MeV/c) Injection
  - 225 π mm-mrad x 7%dp/p input @ 360 MeV
  - 113 π mm-mrad x 1.5% dp/p output @ 920 MeV
- High Resolution Dispersed Line - for VHV Configuration
  - 360-1070 MeV (480-1200 MeV/c)
  - Acceptance 113 π mm-mrad x ±0.75%
  - 10^{-4} Momentum Resolution
  - 5 mrad angular resolution
  - 10^9 π^+/sec at 920 MeV
- General-Purpose Line - for MRS in HHH Configuration
  - 200-1200 MeV/c
  - Acceptance 225 pi mm-mrad x ±1%
  - Adj Dispersion 2-4 cm/% to match MRS
  - 3 MeV fwhm at 920 MeV Including MRS
  - Broad Range of Tuning in Achromatic Mode
  - 10^9 π^+/sec at 920 MeV
- **Most Difficult Specification to Meet is Intensity Specification**

Los Alamos

How to Achieve High Yield ?

- Optimize Acceptance of Everything
- Every Element as Short as Possible
    - to Minimize Decay Losses
- Use Best Available Techology for Everything

Estimate of PILAC Yield

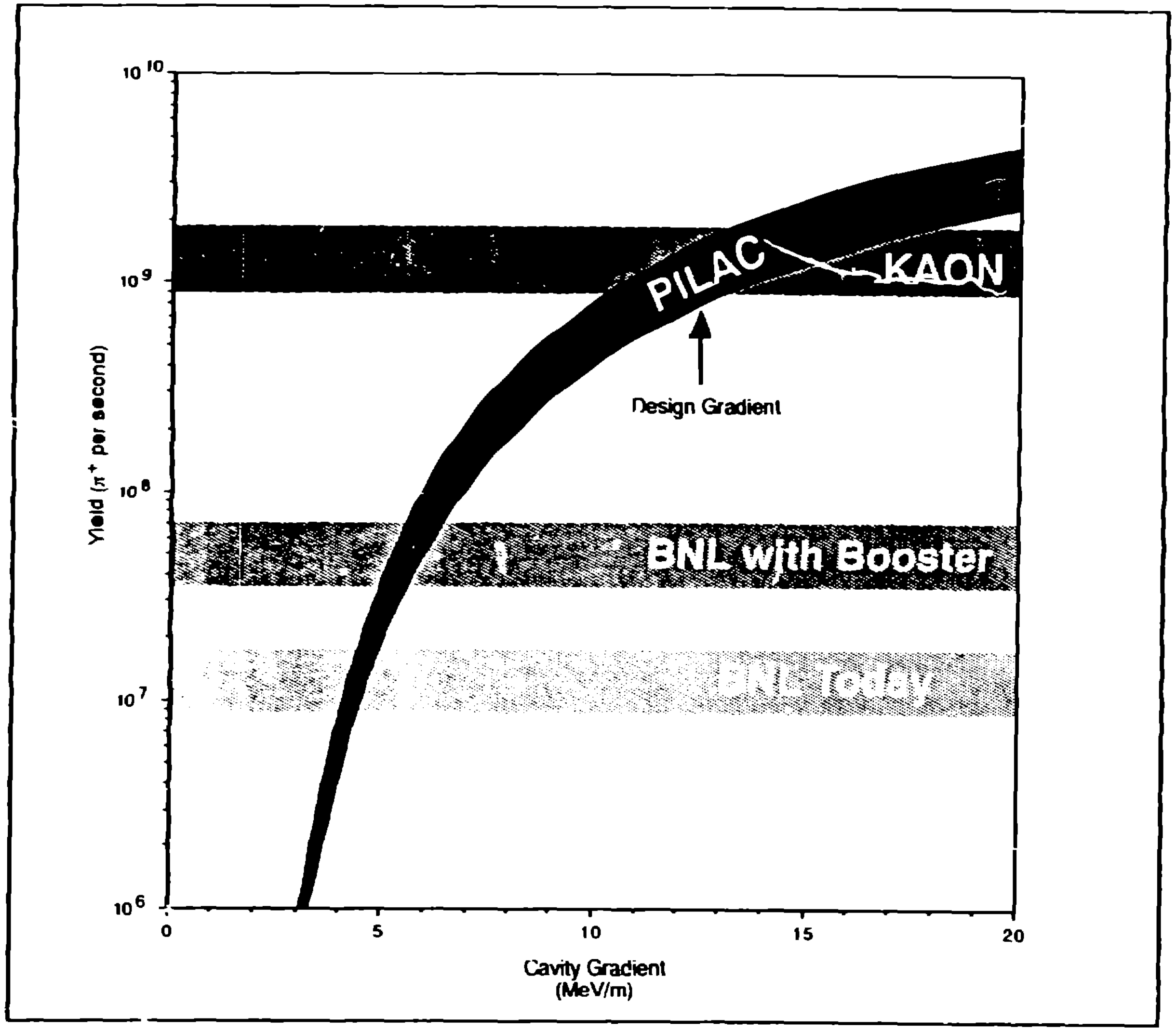

Los Alamos

PILAC Linac Design

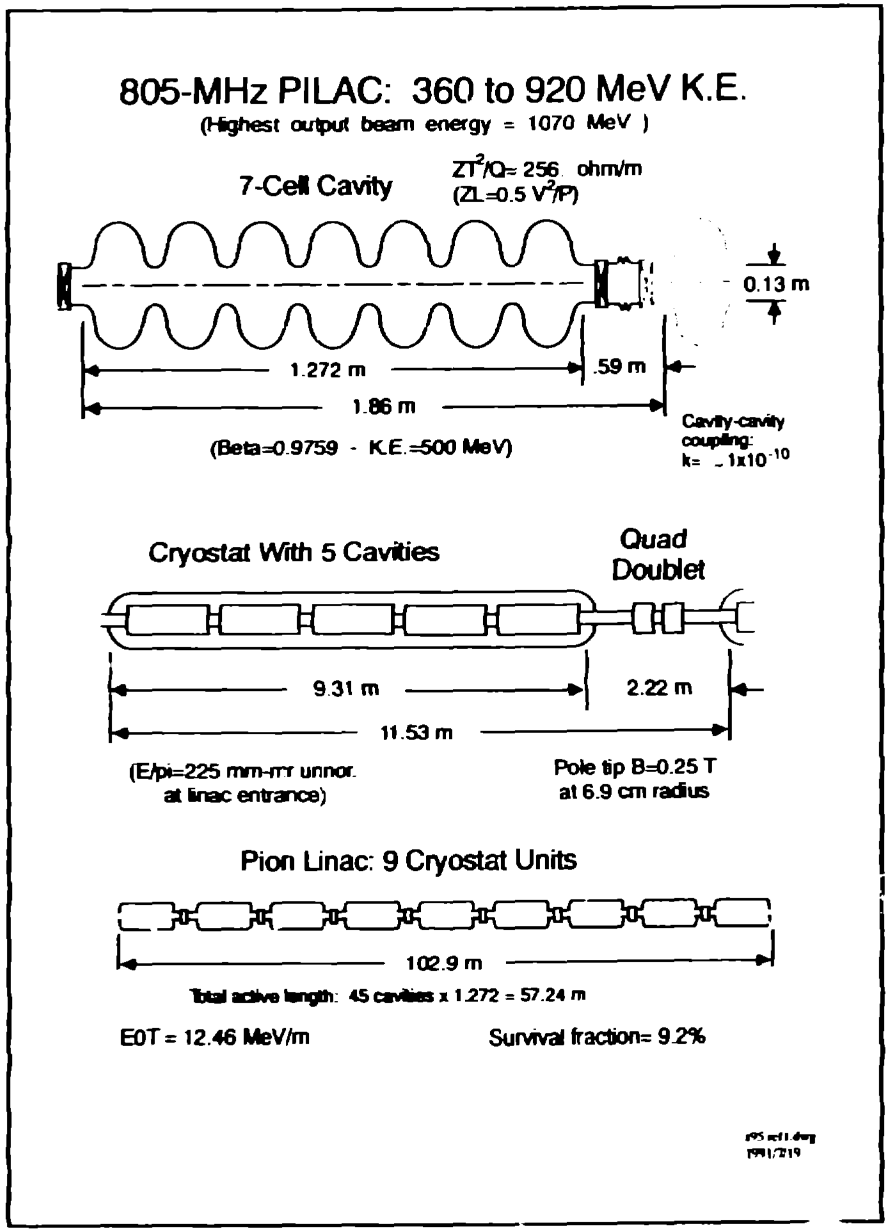

- Note:
  Negligible Beam Loading
- Linac Changes 7/91
  - 360 MeV Injection
  - ° Fixed Injection Energy
  - 45 Cavities
  - 83 ps x 7% Acceptance
  - * 9.2% Pion Survival

Scaling Up Cornell Technology

- Our Specification is
  - 12.5 MeV/m
  - Q_o=5 x10^9
- Present Limit is Field Emission
- Heat Treatment Dramatically Reduces Field Emission

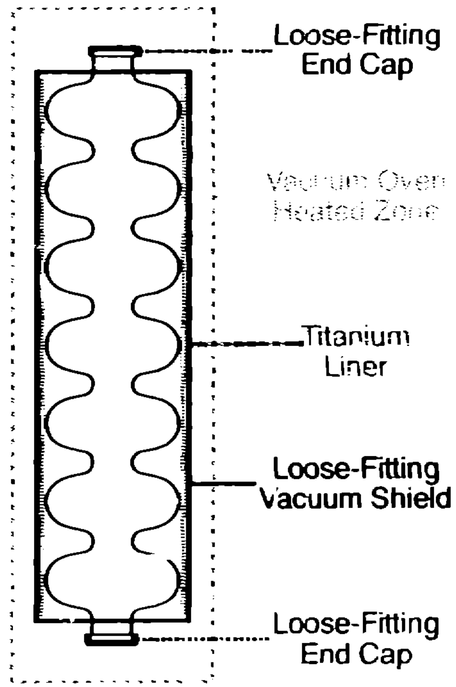

Heat Treatment Apparatus

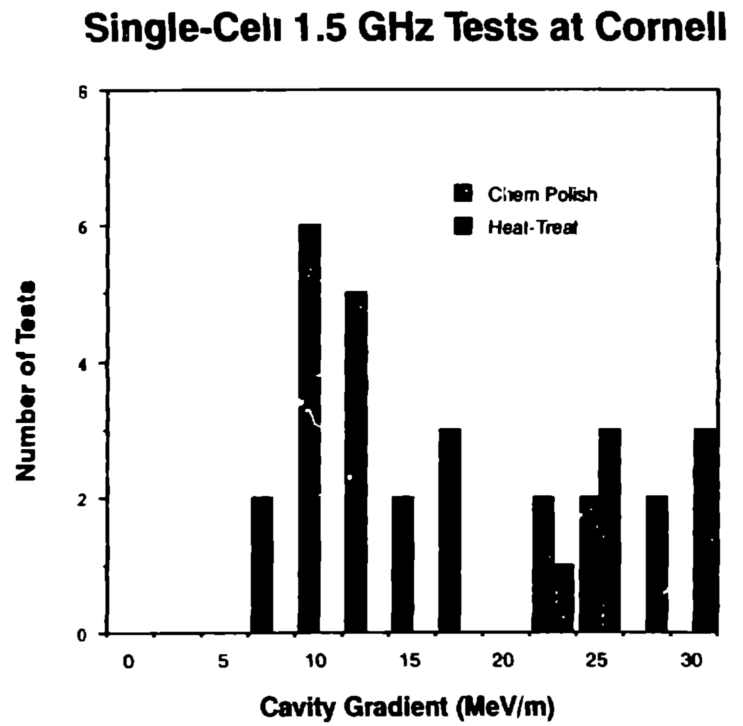

Zero-Degree Pion Channel Layout

- Input/Output Phase Space 225 π mm-mrad

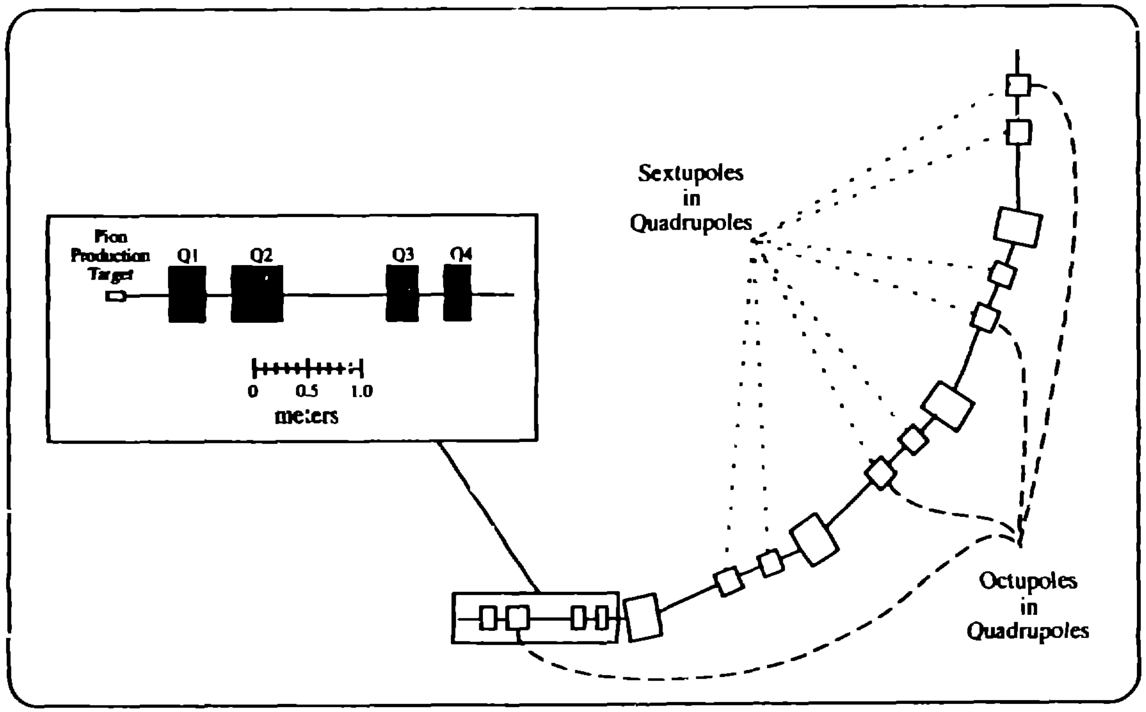

- 0° Production - 13 cm ATJ Graphite Target
- Acceptance - 10 Millisteradians x 6.5 % dp/p
- Third-Order Geometric and Chromatic Aberrations Corrected
- 82% Transmission into 225 π mm-mrad
- Designed by Barbara Blind

Possible Simultaneous π^+ and π^- Injection Line

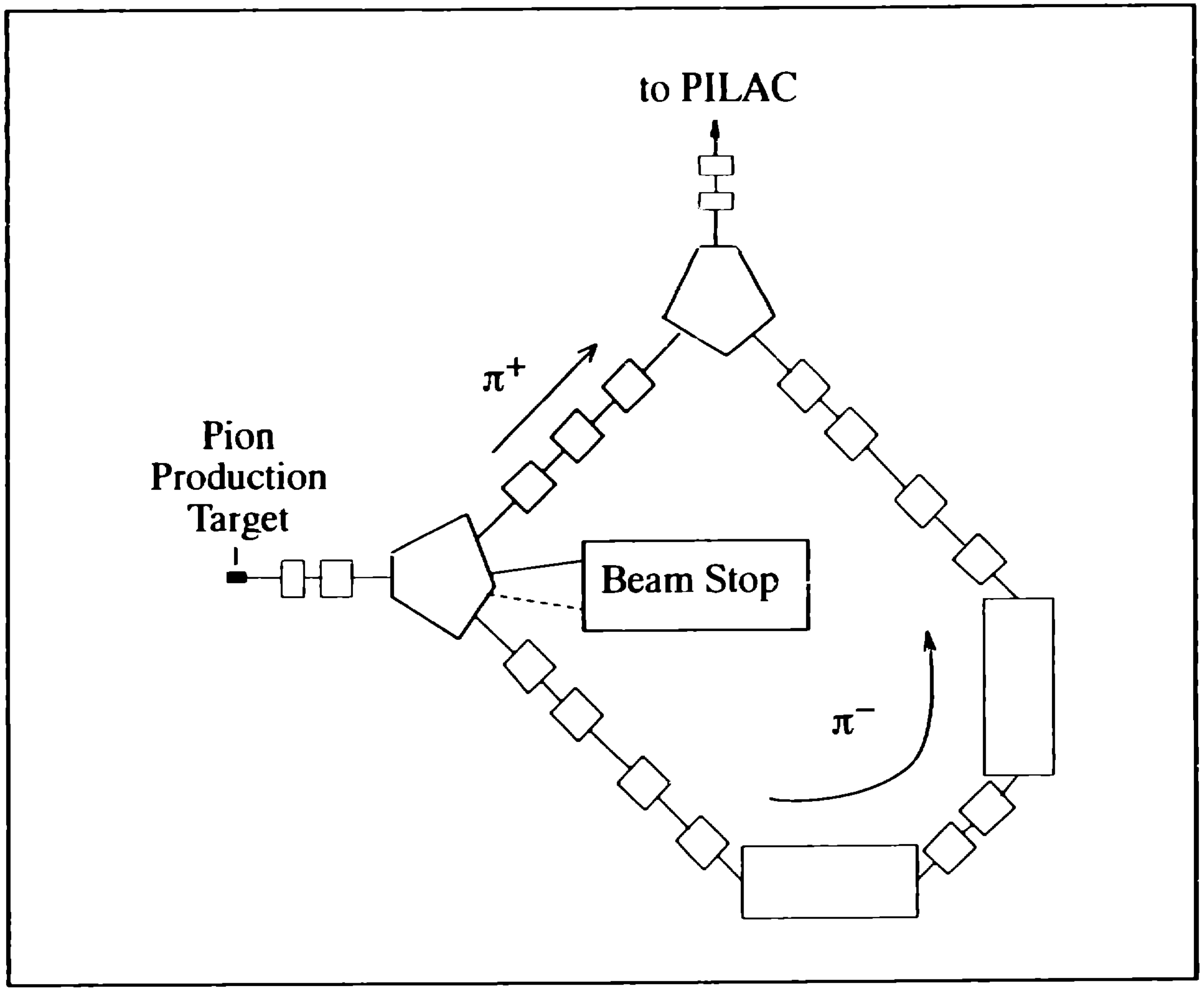

PILAC High Resolution Dispersed Pion Channel and Spectrometer

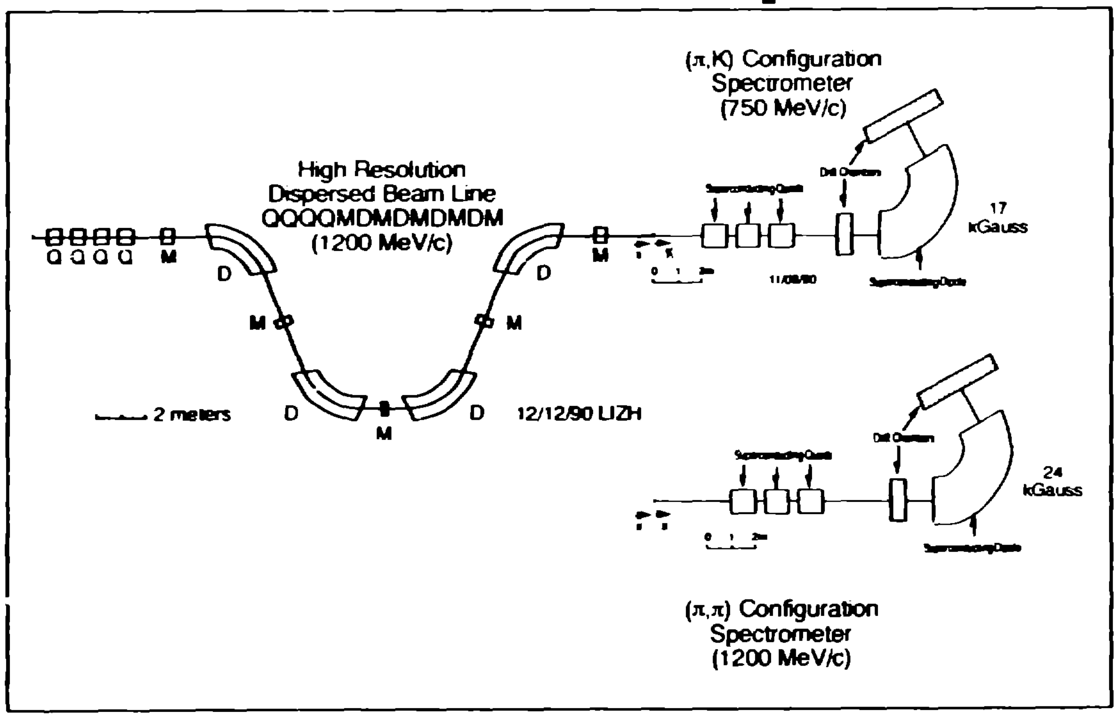

- 10^{-4} Beam Line and Spectrometer
- Meets 200 keV Resolution Requirement at 1 GeV
- Target Size - 40 cm high by 10 cm wide
- Spectrometer Solid Angle 27 msr
- Scattering angle Resolution - 5 mrad fwhm
    - 20 keV per mrad for (π,K) on Carbon at 12 Degrees

General-Purpose Pion Beam Line

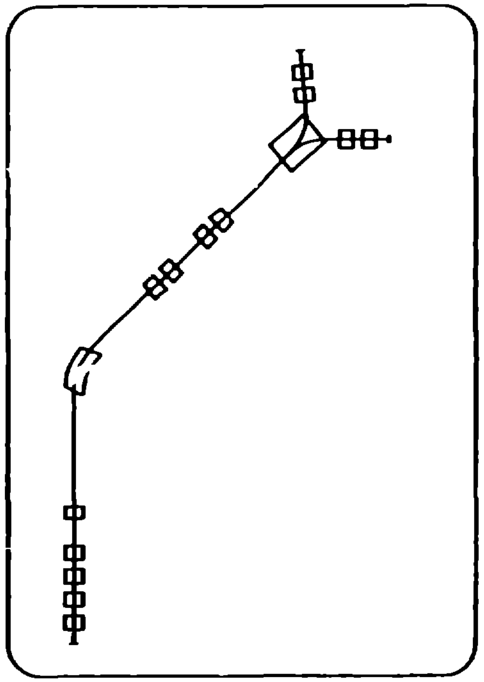

- Achromatic Mode for Experiments *and Future Energy Upgrade*
  - ~1 cm diameter Beam Spot
- Horizontal Dispersed Mode
  - 2 MeV Resolution with MRS
  - & Coincidence Experiments
- Naifeng Mao Responsible for Design

Beam Sharing in PILAC

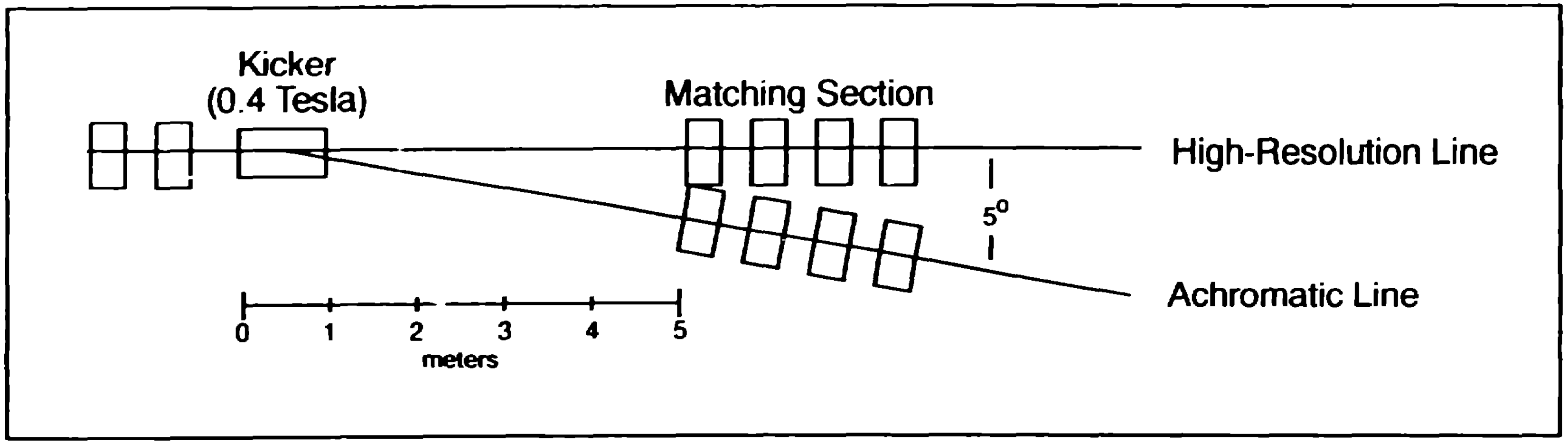

- Kicker-Based Beam-Sharing System
  - Full-Aperture Slow Laminated-Iron Kicker
    - * Synchronized with Linac Energy & Sign Change
      - by Rephasing of Cavities
    - * Switching Time 0.01 Sec
  - Shares Available Beam and Duty Factor
    - * on ~ 0.1 sec time scale
  - Compatible with Simultaneous π^+ and π^- Injection

LAMPF in 1991

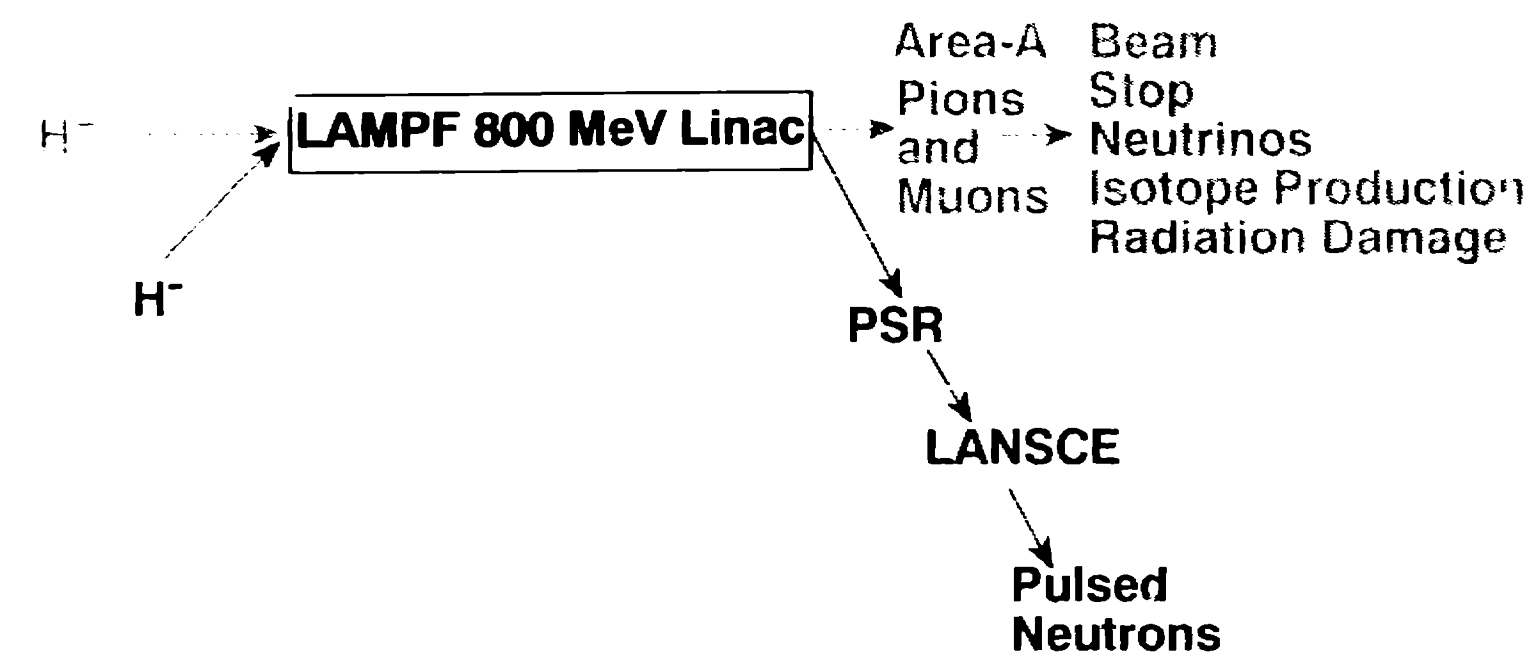

LAMPF in 2001 ?

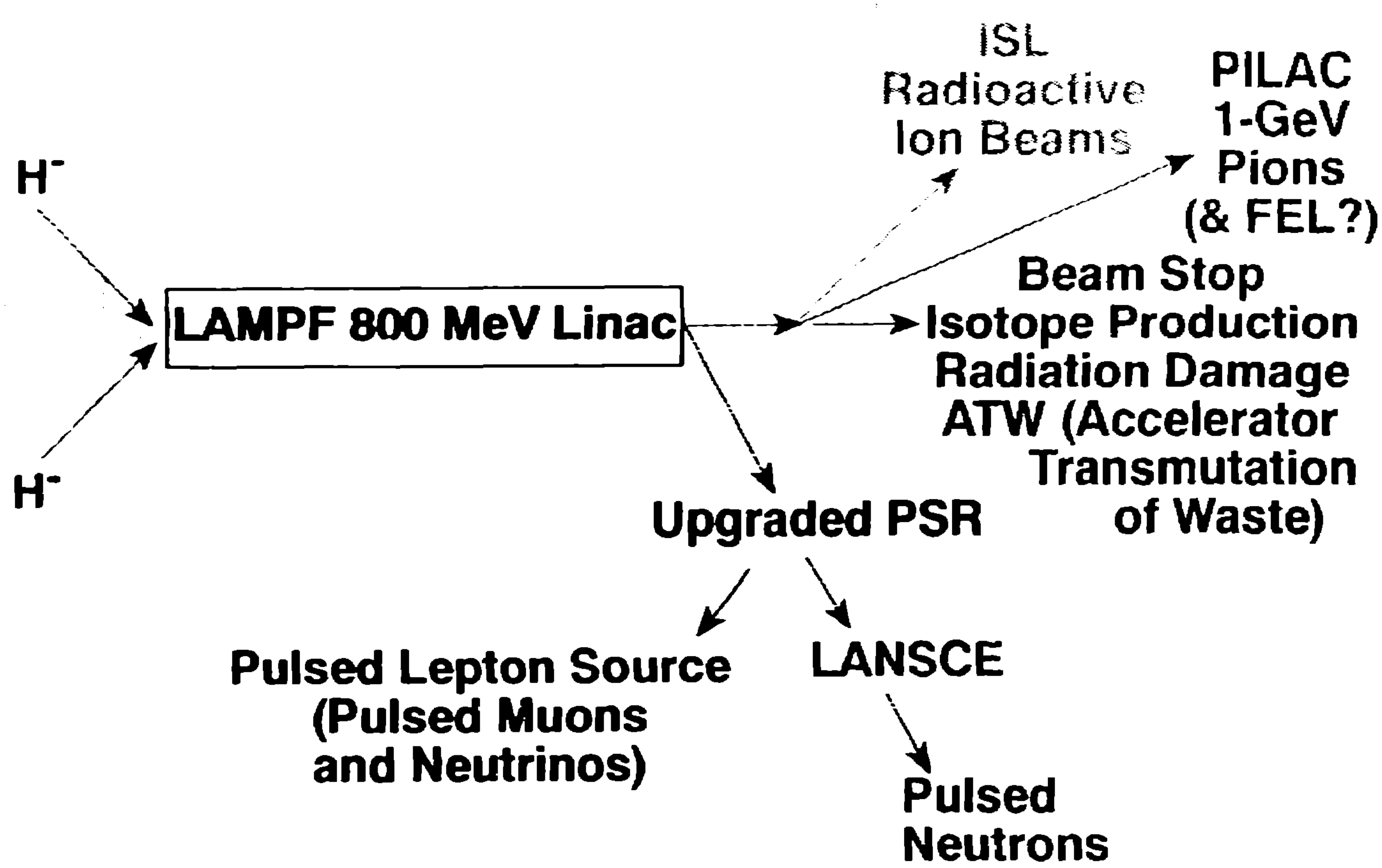

Possible Area-A Upgrade?

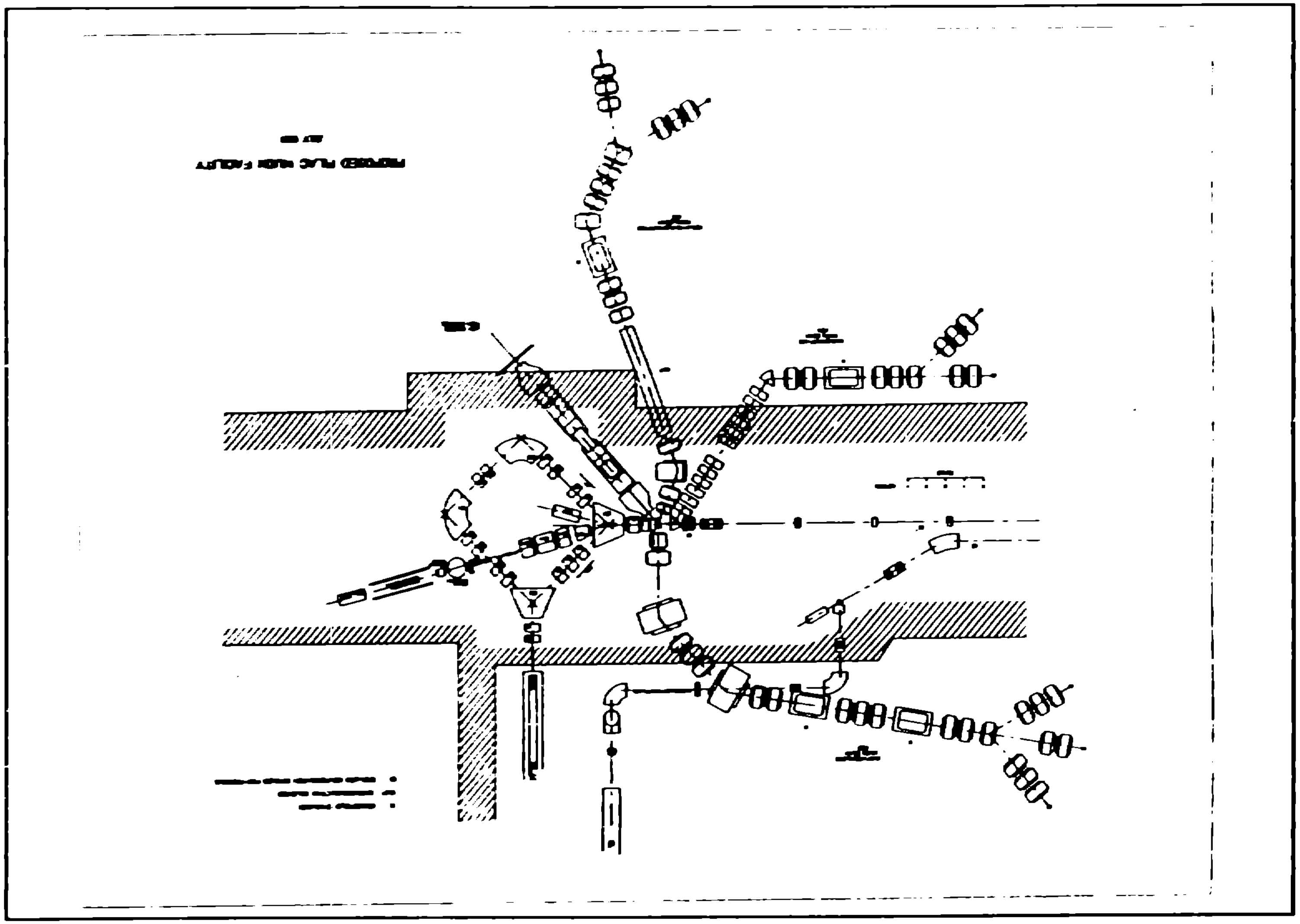

Summary: PILAC vs. Competition

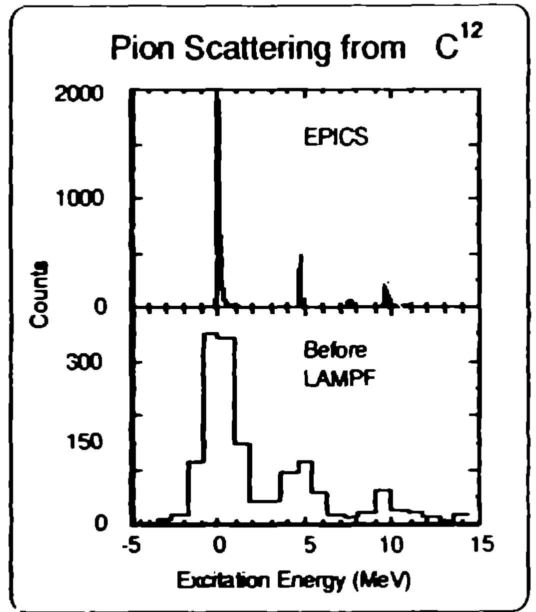

- **<u>High Energy</u>** (920 MeV)
  - Optimizes (π^+,K^+) Yield
- **<u>High Resolution</u>** (~200 keV)
  - 10x Better than Today
- **<u>High Intensity</u>** (~10^9 π^+/sec)
  - 100x Better than Today
- **<u>Broad Range of Nuclear Physics</u>**
  - Using Same Facility
  - in Simultaneous Operation
-
- **<u>Cost Effective</u>** - Minimum Cost Access to (π^+,K^+)
- **<u>PILAC Is RF Separator</u>** - Pion Beams of Unprecedented Purity
- **<u>Unique</u>** - PILAC is Possible Only at LAMPF
- **<u>High Technology in All Elements</u>**
  - High-Gradient Superconducting Linac
  - Large-Aperture Superconducting Quads
  - High-Field Superconducting Dipole
  - High-Acceptance π^+/π^- Injection Line

MOTER:

Morris Klein's Optimized Tracing of Enge's Rays

- RAYTRACE with Optimizer
- Very General Demand Definition
  - Including Software Corrections
    - * and Measuring Errors
- MAPPOLE Element (ray trace from field map)
- Random Ray Generator and Apertures
  - Human Cannot Bias Design by Incorrect Ray Pattern
  - MOTER is Equivalent to TRANSPORT plus TURTLE
- Adding Cavity Element and Longitudinal Dynamics
  - To Include Linac in Calculation

Limitation on PILAC Acceptance: Aperture of First Injection Line Magnet

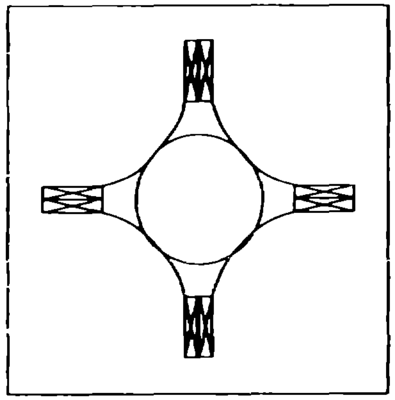

- Entire Magnet will be in Vacuum System
  - No Beam Pipe !
- Can We Use Entire Open Region?
  - Not Just Circular Region !
- Warning: We Must Go Outside of
  - Circle of Convergence !

Compare EPICS and PILAC

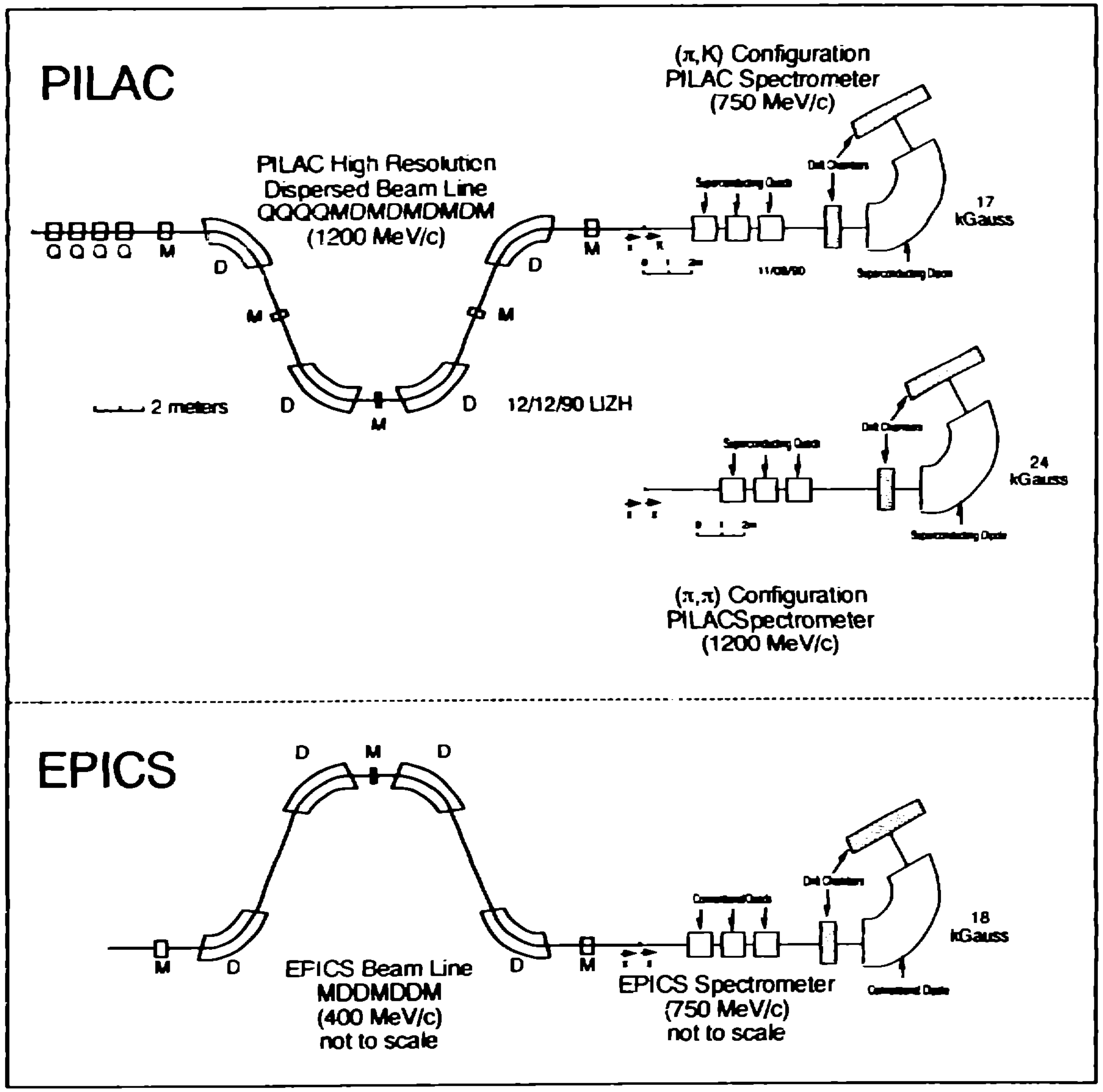

Recent Results on Hi-Res Beam Line Optics

- Calculations of Li & Thiessen Used 6-D Ellipsoid
- Changed to 4-D Ellipsoid
  - Uniform Distribution for x' & y'
- Re-Optimized Beam Line (without Match Section)
  - Required Use of 4th Order Corrections
  - Resolution Worsened ~20%

Problems of PILAC Beam Line and Spectrometer

- Spectrometer Dipole Must Go To 24 kiloGauss
    - Put in 2-D Calulation of Field with large 4^{th} Order
        * Resolution OK with 4^{th} Order Software Corrections
- Spectrometer Quads are Very Short
    - Effective Length 70 cm
    - Aperture Diameter 76 cm
    - Distance Between Effective Edges 40 cm
        * End Fields are Very Important
- Beam Line Requires 4^{th} Order Corrections in Multipoles
- Accuracy of Field Representation in Multipoles
    - Using "H. Enge" Rectangular Multipole Formulae
- Need to Design "Zero-Degree" System

Estimate of Effect of n=6 in Quad Fringe Field

Take Results from Napolitano and Hunter

at $r = 30\text{cm}$

0.1 Tesla x 12 cm in each of 2 bumps

separated by 15 cm

Assume Field is pure $n = 6$, $m = 0$, hence

$B_x \propto y^5$

Assume ray leaves center of target and arrives at $r = 30$ cm

Focussing such that ray is bent parallel to axis in 40 cm

Then kick projected back to target is

$$\Delta y = 300\,\text{mm} \times \frac{0.1\ \text{Tesla} \times 12\ \text{cm}}{0.8\ \text{Tesla} \times 40\ \text{cm}} \times 5 \times \frac{0.18 \times 20\ \text{cm}}{30\ \text{cm}} = 6.75\,\text{mm}$$

There are 4 fringe fields acting coherently

$\therefore$ total $\Delta y = 4 \times 6.75 = 27\text{mm}$

MAPPOLE

- Rectangular Grid of Measurements on Midplane
- Contains All Harmonic Polynomials in x,y,z up to 5th order
    - Each Polynomial is Solution of Laplace's Equation
- Can Use as Interpolating Polynomial or Least Squares Fit
    - Depending on Number of Nearest Points Used
- Has Function To Cut Off Field
    - To Simulate Shim on Field Clamp
- Checked by Generating Map Identical to RAYTRACE
    - With Enge's Field Formula on Midplane
- External Version Used Three Planes of Maps
    - Near Midplane and Near Poles
- PILAC Requires 10^{-4}
    - EPICS was $3x10^{-4}$

The Disappointments of MAPPOLE

- Computed Field Is Not Continuous In Plane of Pole Tip
- Cannot Reproduce Observed Bump in Field
  - 1" Grid Not Sufficient for 4" Gap
    - * "Rapid Mapper" Forced 1" Grid in Z
- Three Plane Version Did Not Help
  - Could Not Fit Midplane and Pole Plane Simultaneously
- Cutoff Function Poorly Represented Effect of Shim
  - Convergence of Shimming Process was Poor

Los Alamos

History of EPICS Beam Line Shimming

- Use 1st Dipole in MAPPOLE
  - Remaining Magnets as "DIPOLES"
- Shimmed Field Clamps
  - Using Maximum Field (15 kG) Map
  - Two Iterations on Shims
- Then Work on Shimming from Maps of 2nd Magnet
  - ... and 3rd and 4th Magnet
- Computational Results Not Very Satisfying
  - Could Not Estimate Accuracy of Procedure
- Final Trimming with Tuning of Multipoles
  - Using Elastic Scattering
- Shimming Procedure Probably Worked
  - Minimum Currents in Multipoles at 15 kG
  - Achieved Same Ballpark as Design Resolution
  - But No Precision Check of Off-Midplane Optics

History of EPICS Spectrometer Tuneup

- Calculated 2nd and 3rd Order Software Corrections
  - Using Available Dipole Map
  - Integral Harmonic Data for Quads
    - * No Use of Fringe Field Information
- Calculated Software Corrections Did Not Work !
  - Resolution Not Much Better Than 1st Order
- Determined Experimental Software Corrections
  - Using Elastic Scattering, Rods, & Slits, etc.
  - Achieved Same Ballpark as Design Resolution
- Problem May Have Been Unknown Chamber Offsets
  - Expansion Not Centered on Optic Axis

Los Alamos

What Must We Do Better the Next Time ?

- Use End Fields of Quads ?
- Use 3-D Field Map for 1st Injection Line Quad ?
  - and 3-D Calculation for Design Stage ?
- Use a Full 3-D Field Map of Dipoles ?
  - and 3-D Calculation for Design Stage ?

Summary: Charge to Workshop !

- Review PILAC Optics Calculations !
  - Injection Line
  - High-Res Dispersed Line and Spectrometer
  - General-Purpose Line and MRS
- How Good Are Our Magnet Models ?
  - Optics is Only as Good as Field Models
  - Analyze 3-D Calculations and Measurements
  - Compare Available Codes with Emphasis on Field Models
- Can We Build Quads With Pure n=2 (including ends) ?
- Can We Use Entire Open Region of Quadrupoles ?
- What Do We Do When The System Is Constructed ?
  - Measurement Techniques
  - Analysis of Measurements
  - Shimming
  - Adjustable Elements

Los Alamos

PILAC INJECTION LINE

PILAC INJECTION LINE:

EVOLUTION
AND
PRESENT STATUS

Barbara Blind

Accelerator Technology Division
Los Alamos National Laboratory
Los Alamos, NM 87545

August 12, 1991

EARLY DECISIONS

- 805 MHz linac
- focusing elements immediately downstream of the target

RECENT DESIGN PARAMETERS (TO JUNE 1991)

- 225 π-mm-mrad emittance
- $x = y = 4.5$ mm, $x' = y' = 50$ mrad   for the input beam
- $\pm 3.3\%$ momentum bite
- equivalent drift for the beamline of approximately 11 m
- transport of pions between 380 MeV and 530 MeV
- 0.5-m first drift

DEMONSTRATION OF A SUCCESSFUL π^+ LINE

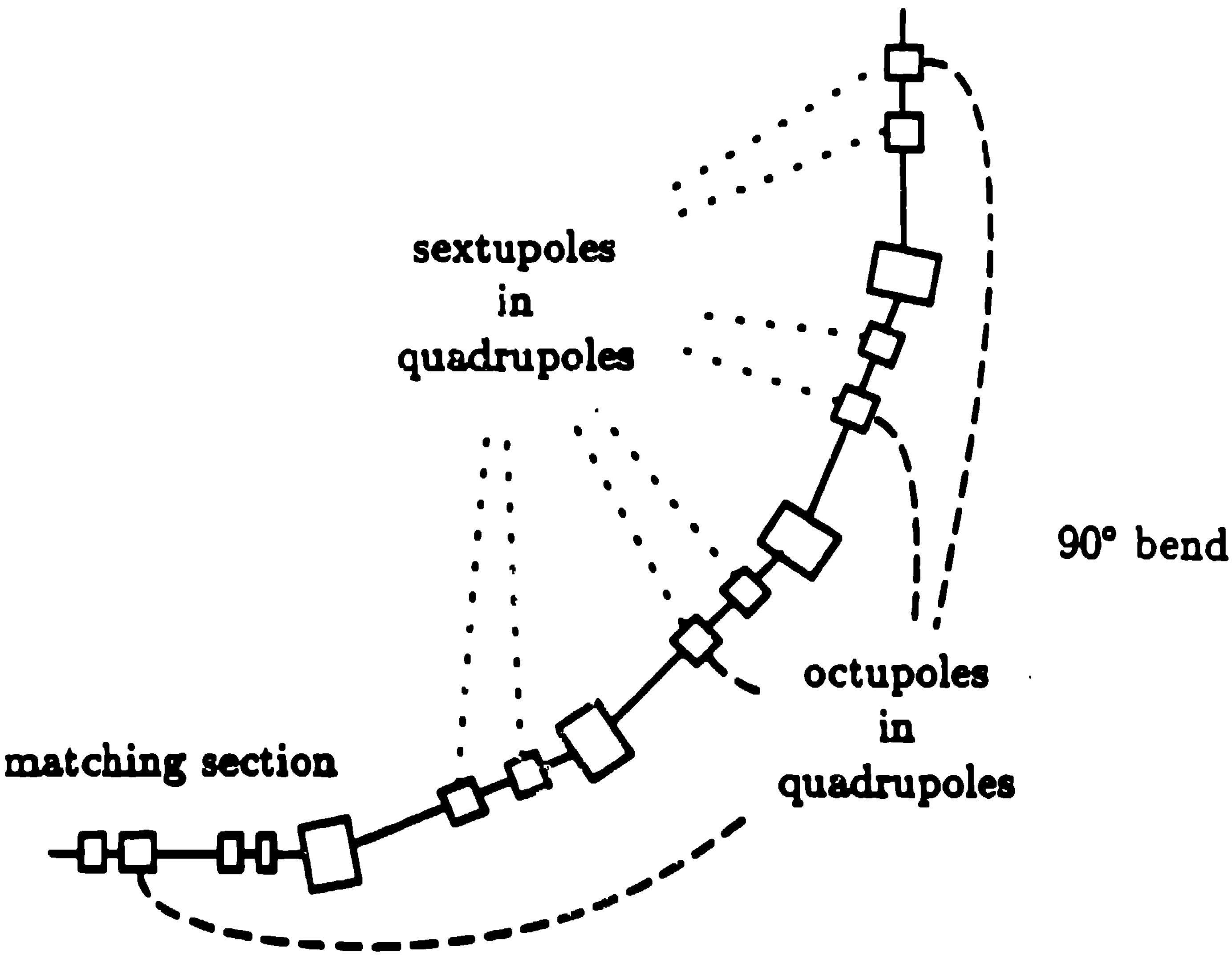

OUTPUT-BEAM PHASE-SPACE PROJECTIONS

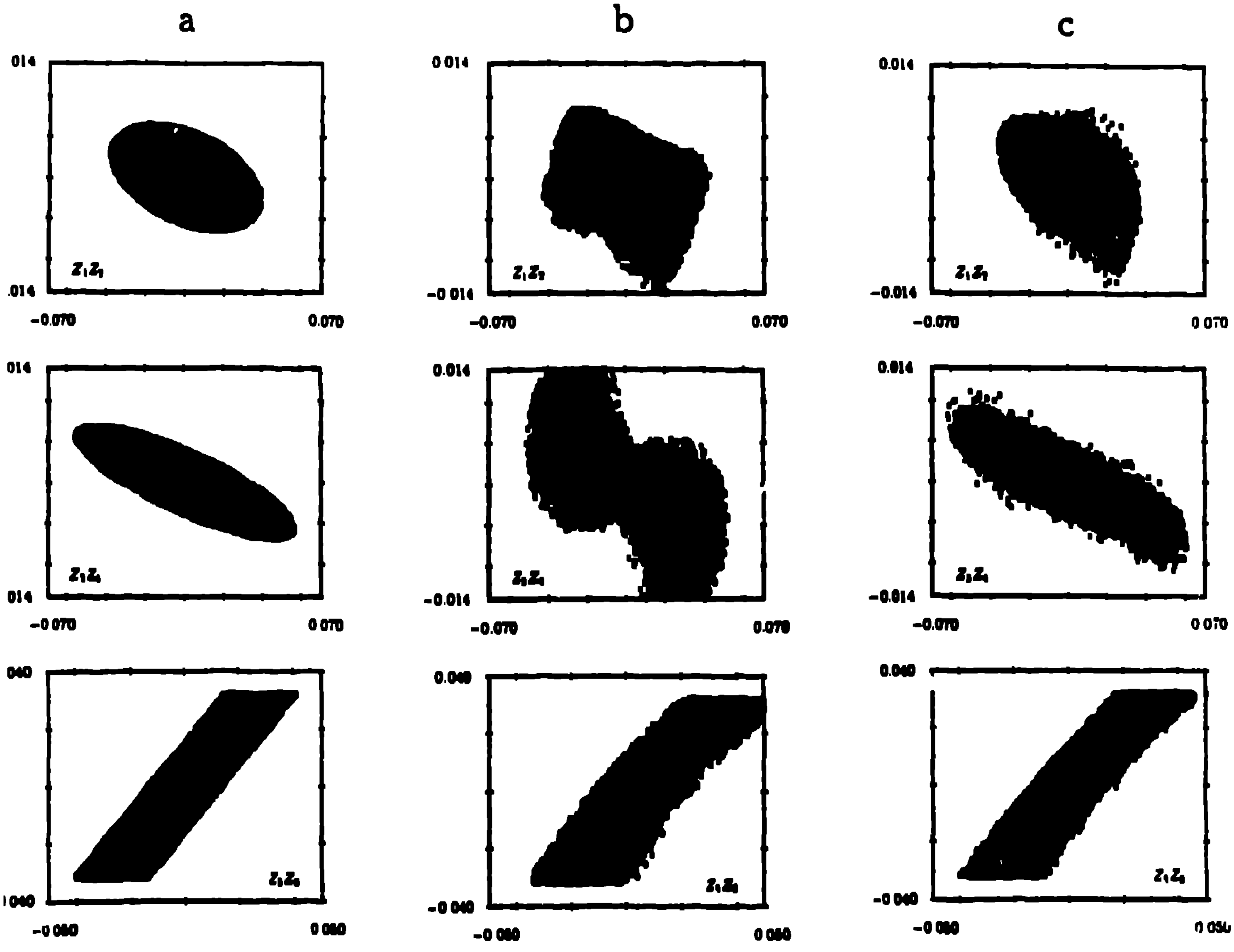

a) for beamline in linear approximation
b) for beamline without sextupoles and octupoles
c) for beamline with sextupoles and octupoles

PERFORMANCE

- with nonlinear correctors, 82.2% of pions are within transverse acceptance of accelerator
- without nonlinear correctors, 56.5% of pions are within transverse acceptance of accelerator
- beamline is 20.08 m long
- 50% of 380-MeV pions decay in transit
- thus: with (without) nonlinear elements, 41.1% (28.3%) of initial pions are captured
- equivalent drift of beamline is 11.06 m for 380-MeV pions, 5.10 m for 530-MeV pions

SIMULTANEOUS TRANSPORT OF π^+ AND π^-

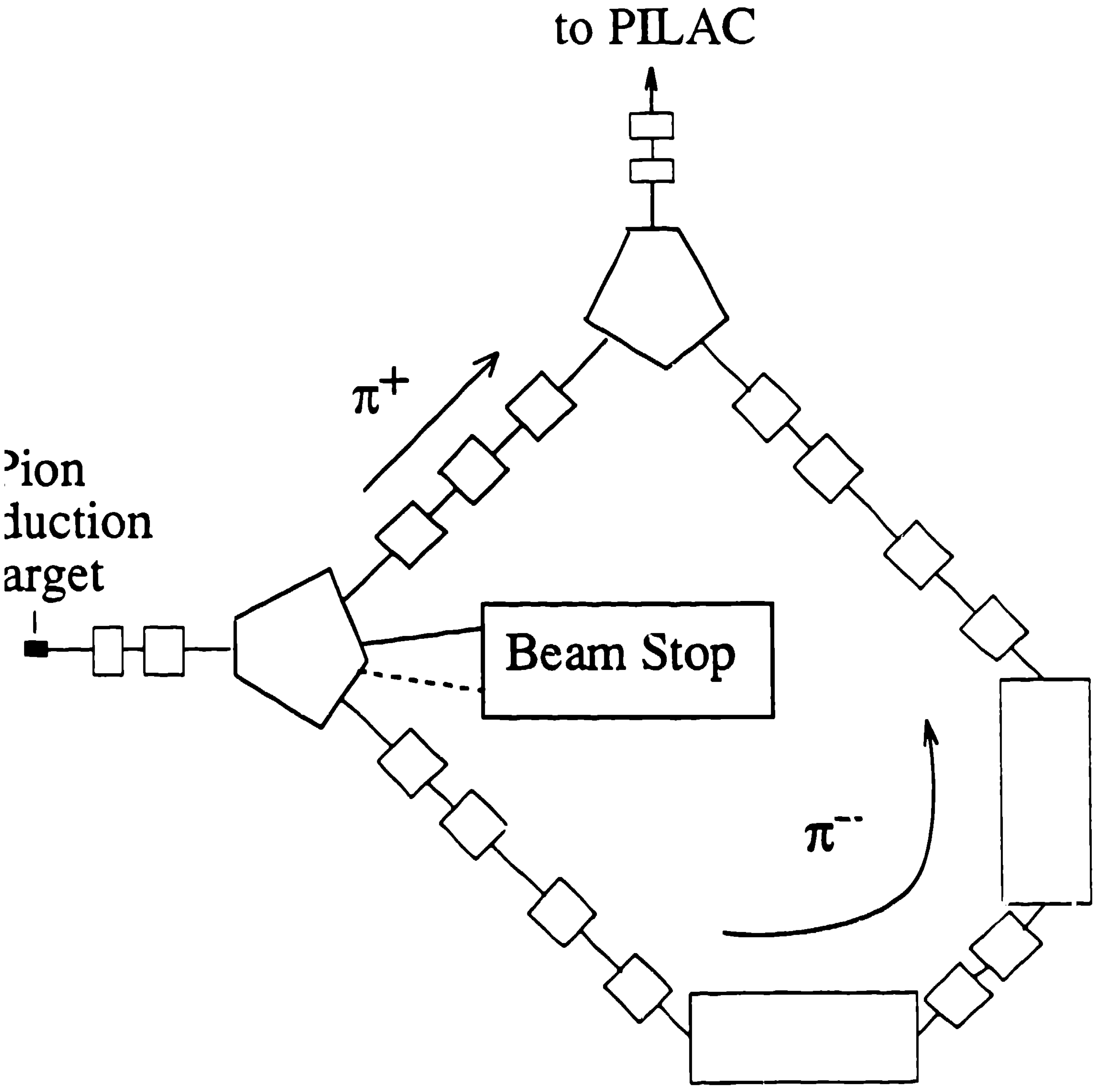

PERFORMANCE

left bend

- 64.3% of pions are within transverse acceptance of accelerator
- beamline is 10.53 m long
- 31% of 380-MeV pions decay in transit
- thus: 44.4% of initial pions are captured
- equivalent drift of beamline is 6.74 m for 380-MeV pions

right bend

- 37.7% of pions are within transverse acceptance of accelerator
- beamline is 24.47 m long
- 57% of 380-MeV pions decay in transit
- thus: 16.2% of initial pions are captured
- equivalent drift of beamline is −6.93 m for 380-MeV pions

OUTPUT-BEAM PHASE-SPACE PROJECTIONS

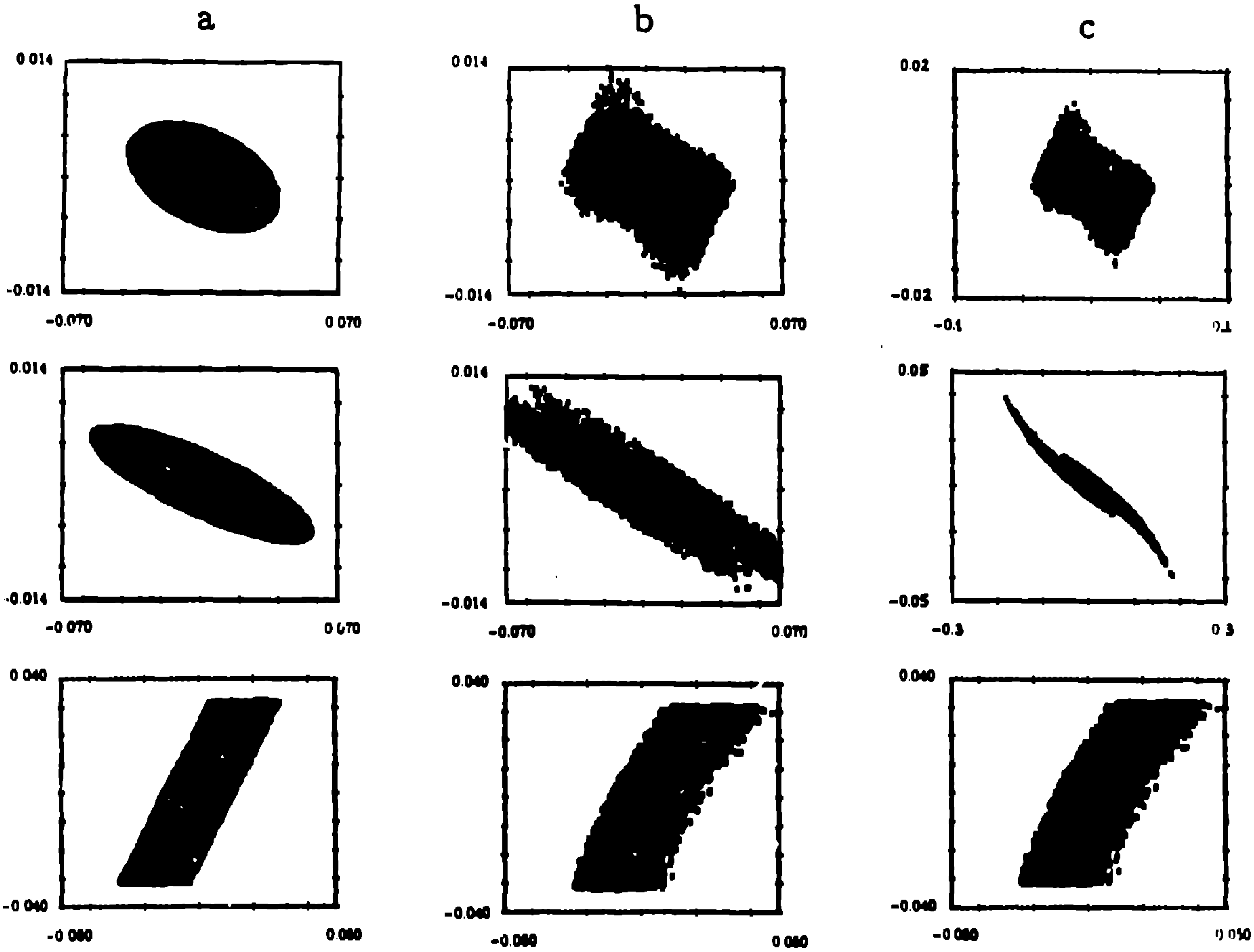

a) for left bend in linear approximation
b) for left bend with aberrations
c) for left bend with aberrations

OUTPUT-BEAM PHASE-SPACE PROJECTIONS

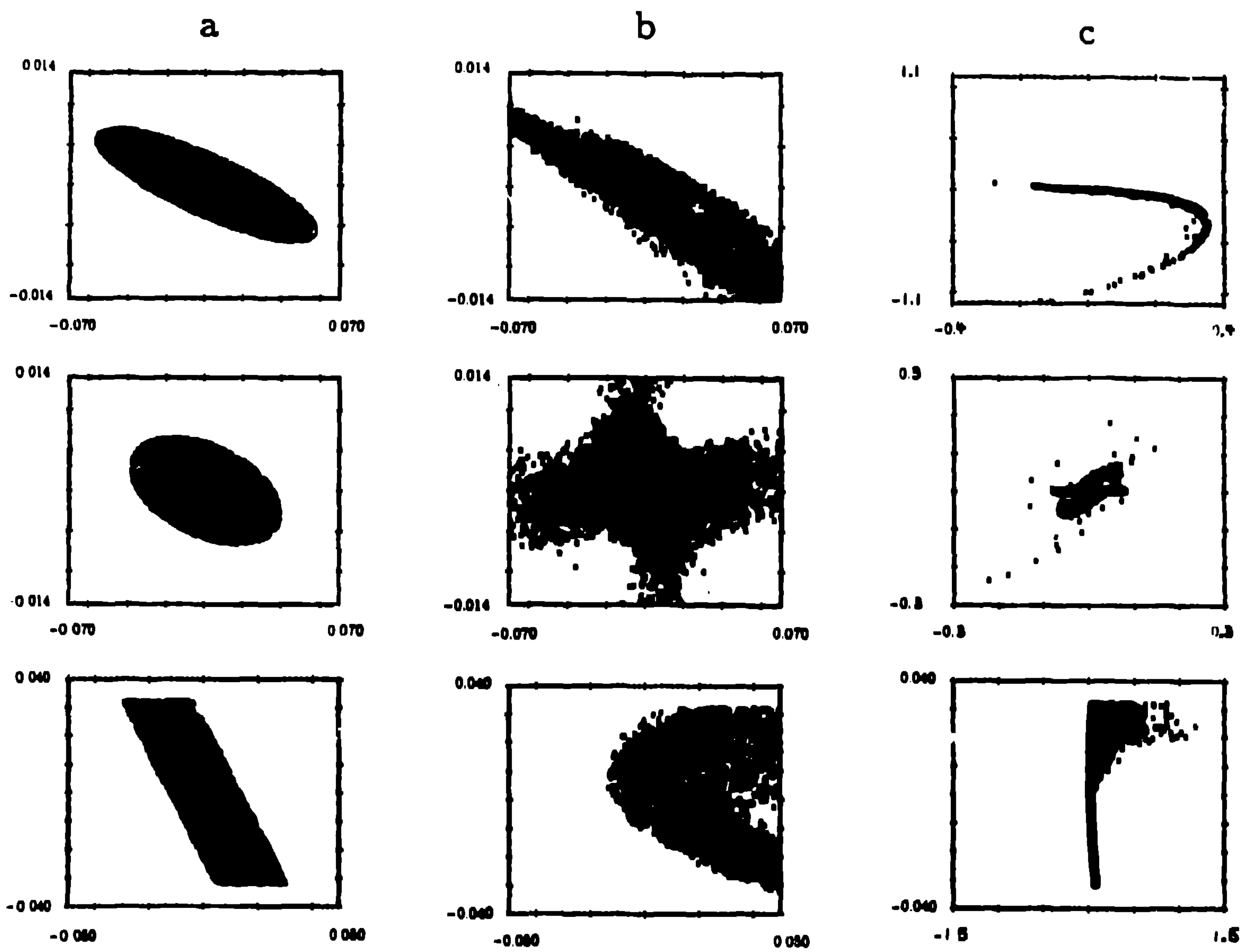

a) for right bend in linear approximation
b) for right bend with aberrations
c) for right bend with aberrations

PRESENT DESIGN PARAMETERS

- 225 π-mm-mrad emittance
- $x = y = 3.63$ mm, $x' = y' = 62$ mrad   for the input beam
- $\pm 3.5\%$ momentum bite
- transport of pions of 360 MeV
- 0.575-m first drift

PERFORMANCE WITH PRESENT DESIGN PARAMETERS

left bend

- 49.2% of pions are within transverse acceptance of accelerator
- beamline is 11.62 m long
- 33% of 360-MeV pions decay in transit
- thus: 33.0% of initial pions are captured
- equivalent drift of beamline is 8.12 m for 360-MeV pions

right bend

- 19.0% of pions are within transverse acceptance of accelerator
- beamline is 25.74 m long
- 59% of 360-MeV pions decay in transit
- thus: 7.8% of initial pions are captured
- equivalent drift of beamline is −3.29 m for 360-MeV pions

- path-length difference correct for simultaneous acceleration of 360-MeV π^+ and 360-MeV π^-

FEATURES OF PRESENT π^+/π^- TRANSPORT SYSTEM

many constraints on geometry

- proton beam transport/dumping
- switching of polarities
- shielding
- π^--beam matching

left bend

- simple
- easy to tune. in practise
- transversely matched
- equivalent drift approximately right
- pion transmission as good as can be expected for a system with the constraints imposed on this system

right bend

- complex
- hard to tune, in practise
- long
- transversely matched
- wrong equivalent drift
- very poor pion transmission

PROTON-BEAM HANDLING

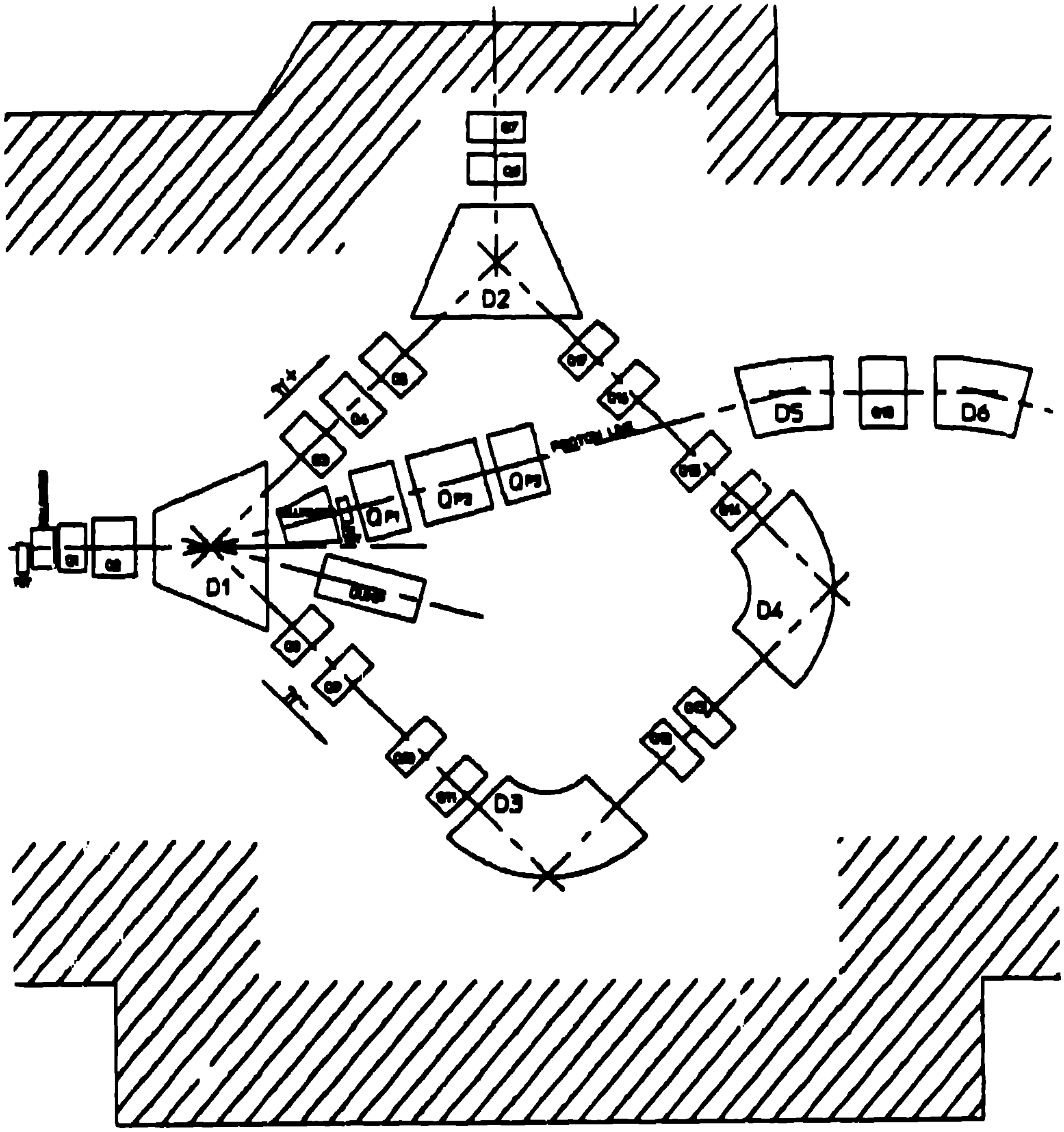

HOW TO REMEDY THE SITUATION – I

WITH SIMILAR BENDS?

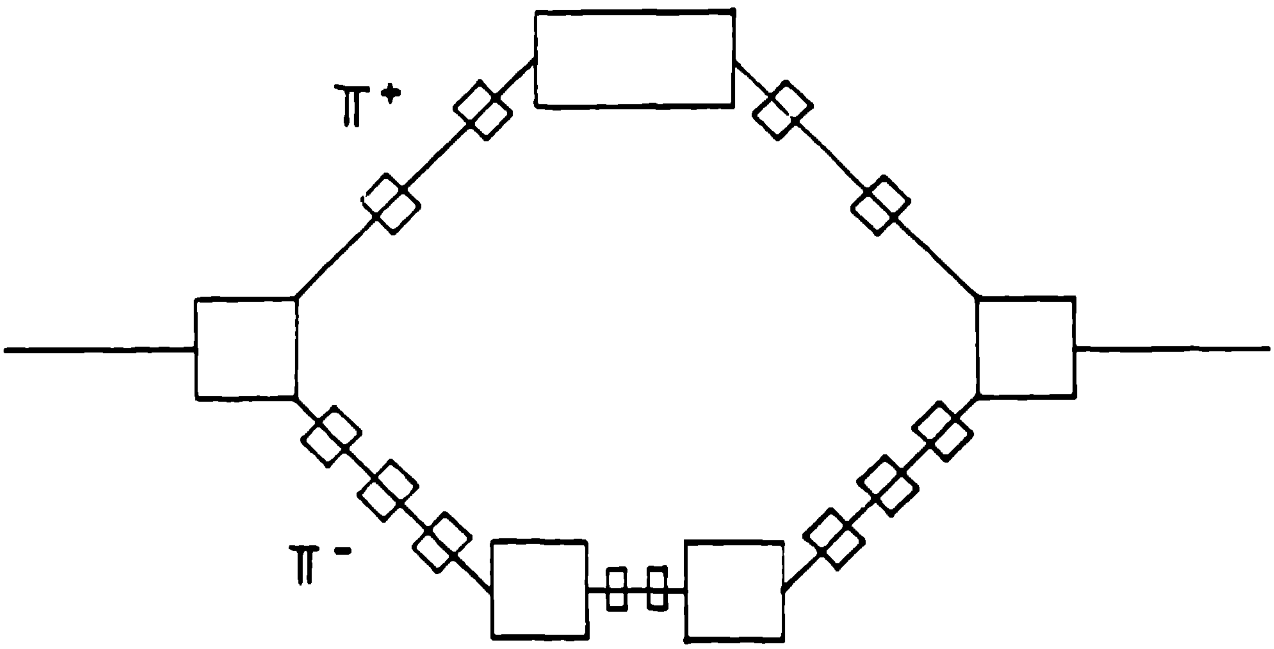

advantages

- both lines of similar quality
- no need to switch polarities
- approximately equal equivalent drifts for improved longitudinal match
- probably more π^- captured than with present system

disadvantages

- lines at least 16 m long, each
- probably fewer π^+ captured than with present system

PILAC GENERAL-PURPOSE LINE DESIGN

PILAC General-Purpose Beam Line

Naifeng Mao and Henry A. Thiessen

Los Alamos National Laboratory

MP-14, MS-H847

Los Alamos, NM 87545

August 12, 1991

PURPOSE

PILAC, a pion linac facility is being proposed to provide 1.07 GeV (1.20 GeV/c) pions at LAMPF (Los Alamos Meson Physics Facility)

The PILAC general-purpose beam line is being designed to deliver these pions to experiments that require either an achromatic beam on target or a dispersed beam while using the existing MRS (medium resolution spectrometer)

This beam line will also serve as a pion injector for a future linac extending the energy of PILAC to 1.6 GeV

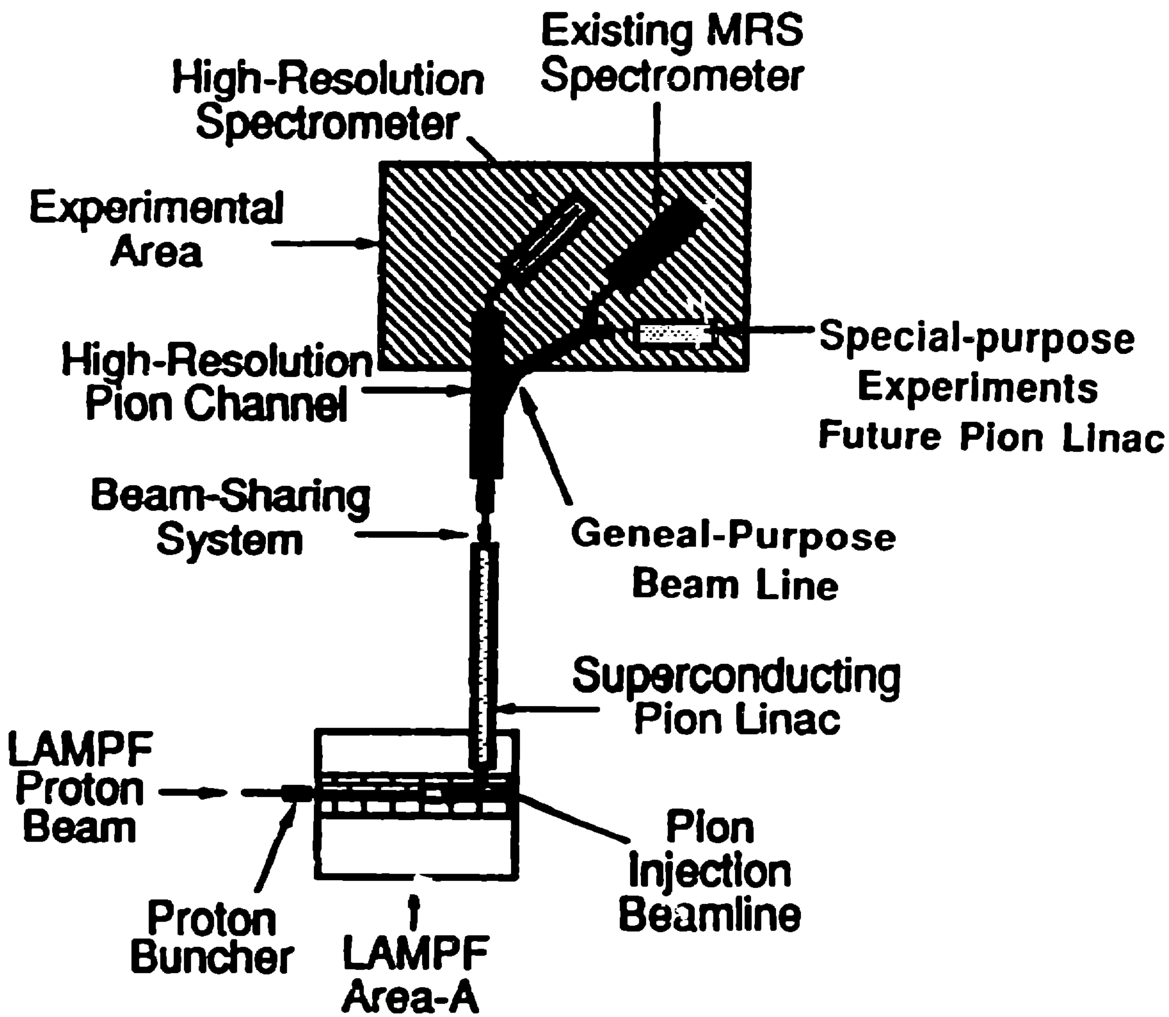

Concept for PILAC facility at LAMPF

LAYOUT

The beam line is downstream of the kicker-based beam sharing system, and unsymmetrical

It has two output ports: Port A (including A1 & A2) and Port B, to allow setup in one experimental cave while operating into a second cave

It consists of a matching section (four quadrupoles),
a main bending and focusing section
(two dipoles, four quadrupoles
and one sextupole),
two post-fousing sections
(four quadrupoles for each port)

It bends in horizontal plane, bending angles:
90 (5+40+45) deg. for Port A
0 (5+40-45) deg. for Port B

The distance (D) from the last quadrupole to
Port A1: 1.5m, Port A2: 3.5-4.5m, Port B: 1.5m

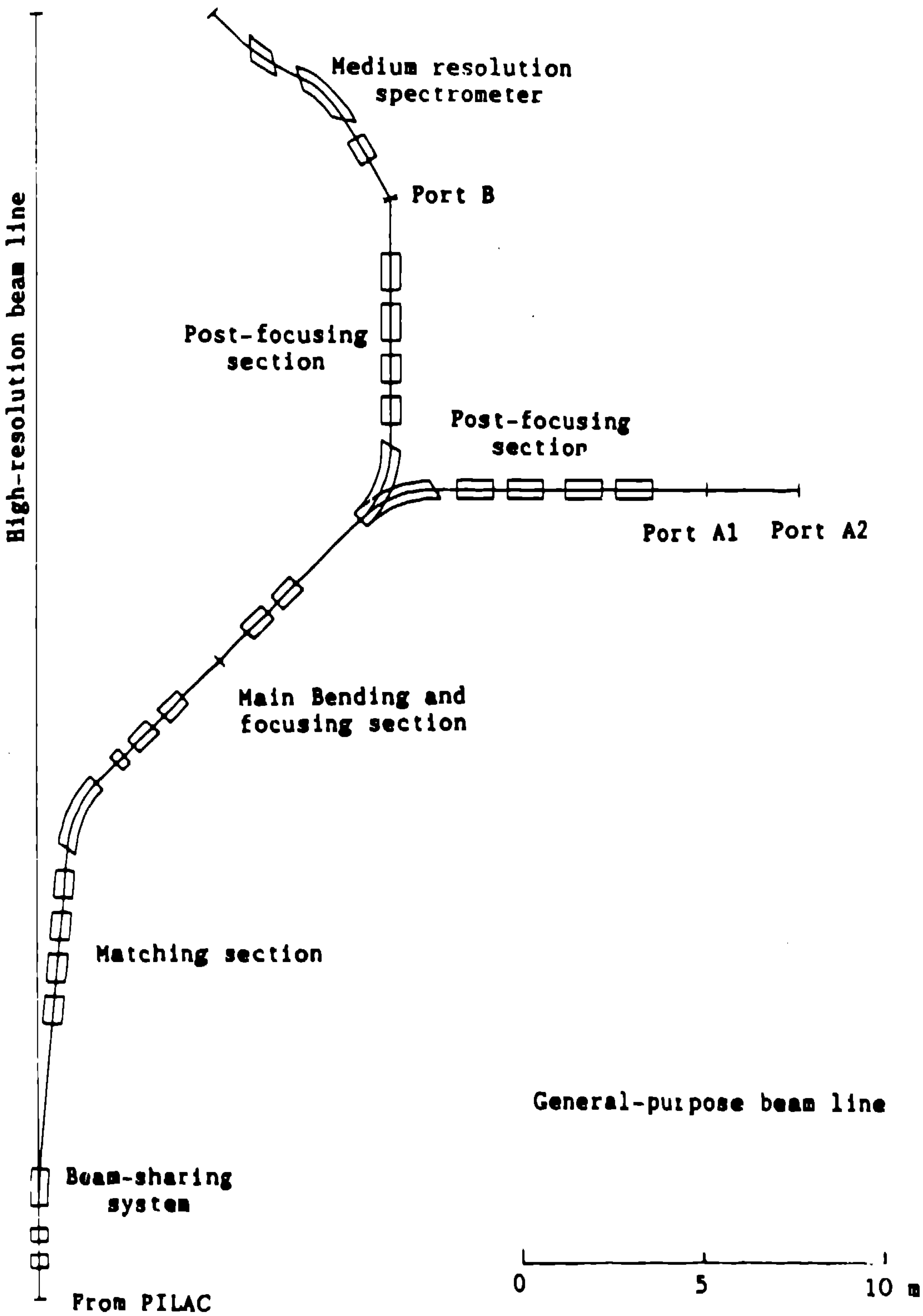
Medium resolution spectrometer
Port B
Post-focusing section
Post-focusing section
Port A1
Port A2
High-resolution beam line
Main Bending and focusing section
Matching section
General-purpose beam line
Beam-sharing system
From PILAC
0
5
10 m

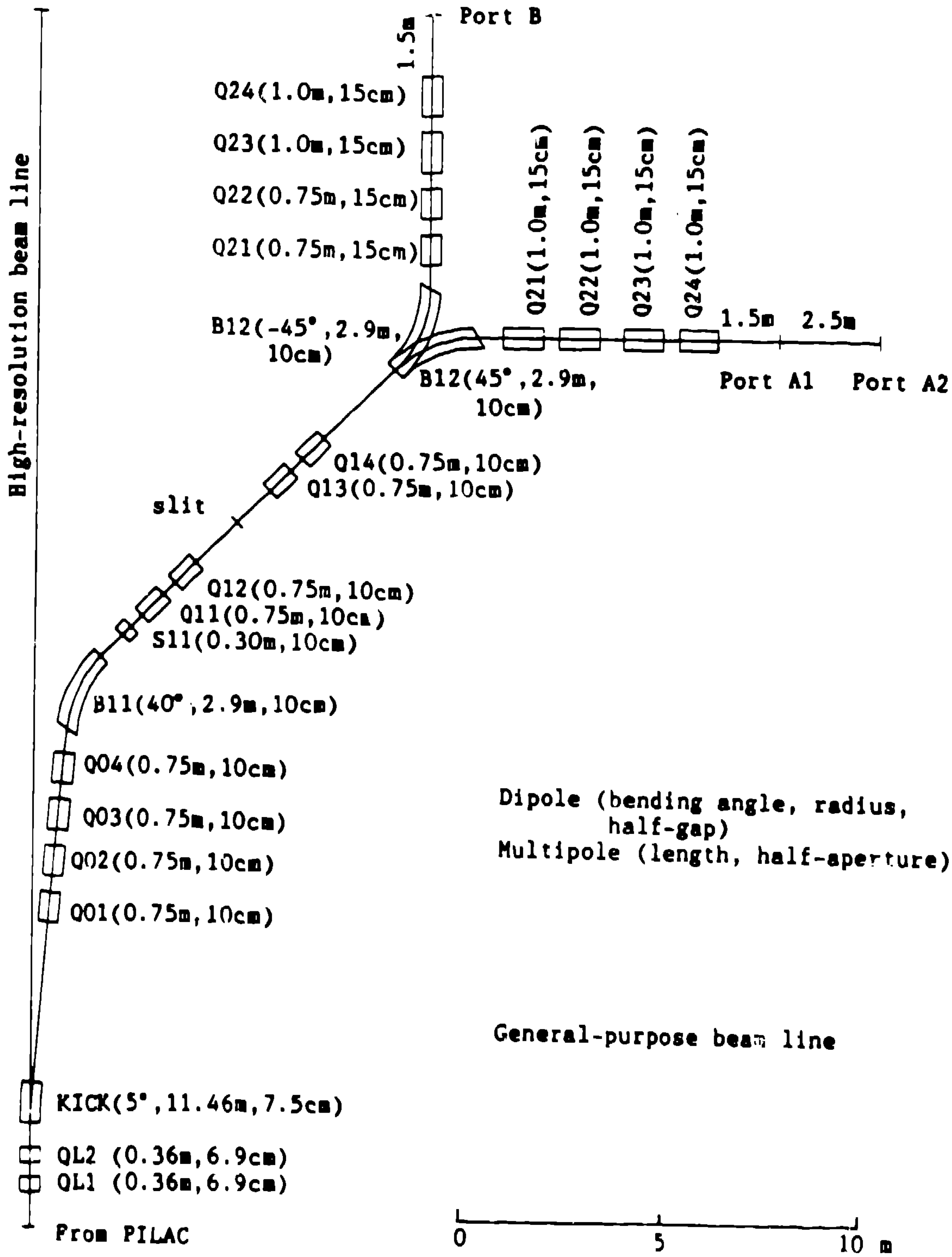
Port B
1.5m
Q24(1.0m,15cm)
Q23(1.0m,15cm)
Q22(0.75m,15cm)
Q21(0.75m,15cm)
Q21(1.0m,15cm)
Q22(1.0m,15cm)
Q23(1.0m,15cm)
Q24(1.0m,15cm)
1.5m
2.5m
B12(-45°,2.9m,
10cm)
B12(45°,2.9m,
10cm)
Port A1
Port A2
High-resolution beam line
Q14(0.75m,10cm)
Q13(0.75m,10cm)
slit
Q12(0.75m,10cm)
Q11(0.75m,10cm)
S11(0.30m,10cm)
B11(40°,2.9m,10cm)
Q04(0.75m,10cm)
Q03(0.75m,10cm)
Q02(0.75m,10cm)
Q01(0.75m,10cm)
Dipole (bending angle, radius,
half-gap)
Multipole (length, half-aperture)
General-purpose beam line
KICK(5°,11.46m,7.5cm)
QL2 (0.36m,6.9cm)
QL1 (0.36m,6.9cm)
From PILAC
0
5
10 m

TWO MODES OF OPERATION

ACHROMATIC MODE

for special-purpose experiments:
small beam spot, Port A1
tuneable beam spot, Port A1
large beam spot with small divergence, Port A2

for serving as a pion injector for a future pion
linac extending pion energy to 1.6 GeV, Port A1

DISPERSED MODE

for experiments with the existing medium resolution
spectrometer (HHH operation mode), Port B
HHH: Horizontal dispersion
Horizontal scattering
Horizontal analysis

INPUT BEAM

Central momentum	P=1.20 GeV/c (max.)	0.50 GeV/c (min.)
Momentum spread	$\delta=\pm0.75$ %	±1.06 %
Phase space	Axo=Ayo=112.5 π mm mrad	225 π mm mrad

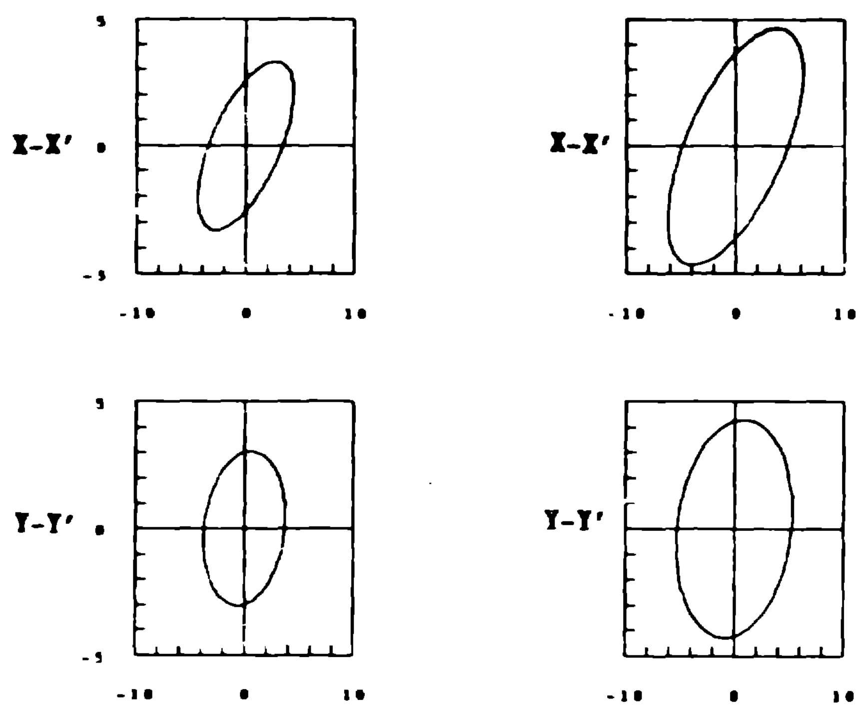

112.5 π mm mrad

225 π mm mrad

REQUIREMENTS FOR OUTPUT BEAM
Achromatic mode, Max. momentum beam

Momentum selection is needed at a slit to eliminate protons and electrons

Different output beam spots and phase space are required:

Small beam spot at Port A1: 0.6-0.7 cm radius by about 20 mrad half angular divergence

Tuneable beam spot at Port A1, spot radius over a wide range: 1.0, 1.5 and 2.0 cm

Large beam spot at Port A2, spot radius larger than 2.0 cm with less than 6 mrad half divergence

For min. momentum beam with double phase space, spot size by a factor of $\sqrt{2}$

As a pion injector for a future linac, output beam with a specified phase space

Area of phase space will not increase any more than necessary

REQUIREMENTS FOR OUTPUT BEAM
Dispersed mode, Max. momentum beam
(for use with the existing MRS)

Horizontal dispersion (R16) varies over a range of 2-4 cm/% for dispersion matching with MRS

Transfer matrix elements R26 and R12 adjustable for correction of kinematic line broadening
$-5 \leq R26 \leq 5$ mrad/% assumed in design

Narrow monochromatic beam spot: 0.2-0.4cm half width, to provide a beam line resolution of 0.2%
For min. momentum beam, by a factor of $\sqrt{2}$

Half height less than 1.5 cm (field of view of MRS: 1.57 cm)

CONSTRAINTS

Field at pole tips of quadrupoles not higher than 7.5 kG (half-aperture of quadrupole 10 or 15 cm)

Half gaps of dipoles not larger than 10 cm

Distance from the last quadrupole to the target not less than 1.5 m

METHOD AND PROCEDURE

Beam optics is calculated with program TRANSPORT in the first and second order

Design begins with the achromatic mode of operation at Port A1

When changing the beam output port or/and the mode of operation

the geometry of the beam line is unchangeable

only the field gradients of quadrupoles in the beam line can be readjusted

Design also begins with the maximum momentum beam, and then the minimum momentum beam with double phase space considered

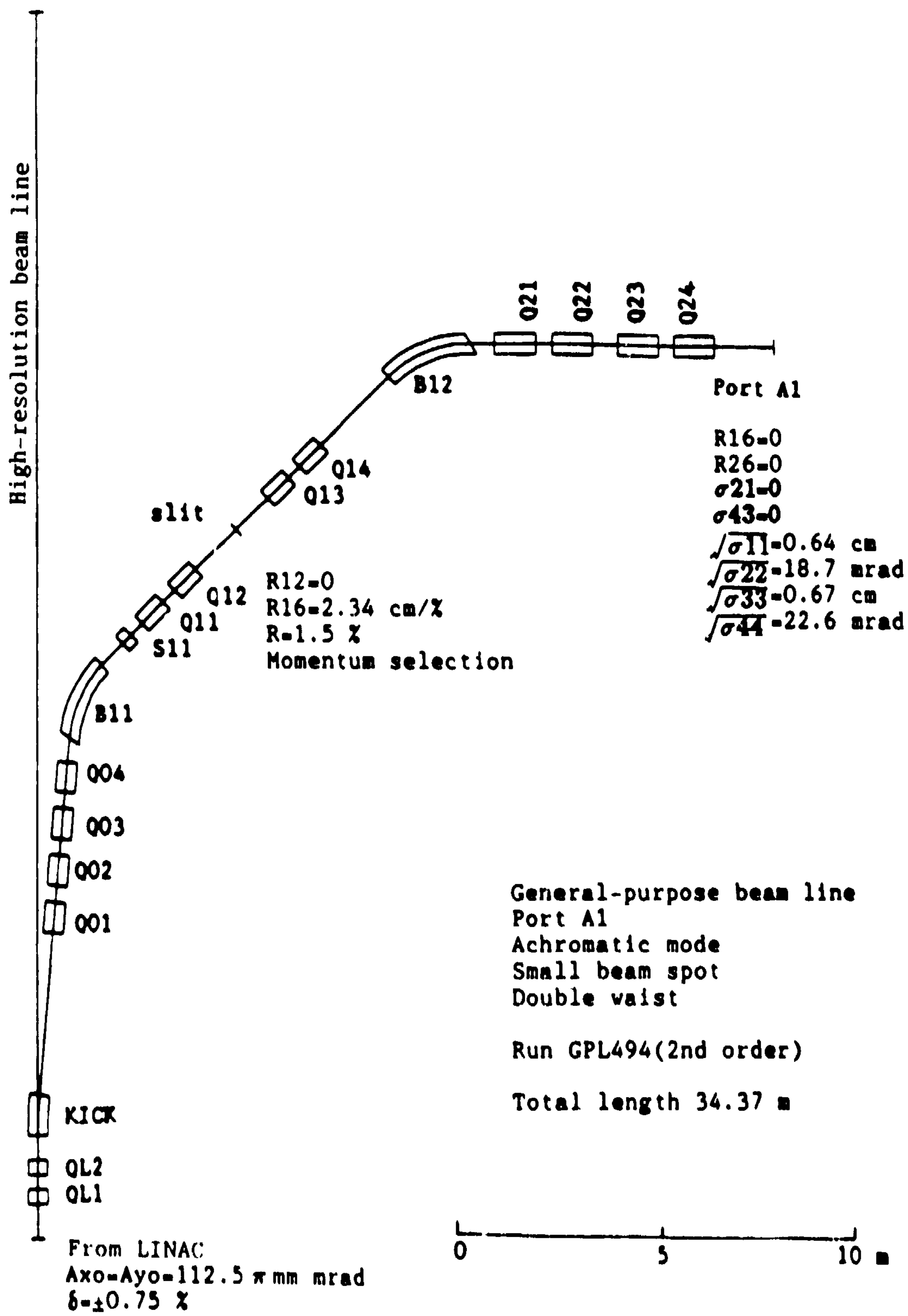
High-resolution beam line
Q21
Q22
Q23
Q24
B12
Port A1
R16=0
R26=0
σ21=0
σ43=0
$\sqrt{\sigma 11}$=0.64 cm
$\sqrt{\sigma 22}$=18.7 mrad
$\sqrt{\sigma 33}$=0.67 cm
$\sqrt{\sigma 44}$=22.6 mrad
Q14
Q13
slit
Q12
Q11
S11
R12=0
R16=2.34 cm/%
R=1.5 %
Momentum selection
B11
Q04
Q03
Q02
Q01
General-purpose beam line
Port A1
Achromatic mode
Small beam spot
Double waist
Run GPL494(2nd order)
Total length 34.37 m
KICK
QL2
QL1
From LINAC
Axo=Ayo=112.5 π mm mrad
δ=±0.75 %
0
5
10 m

GPL494(4),ACHROMATIC MODE,PORT A1,SMALL SPOT,2ND ORDER,AUG. 8,91
ROTATED TO ORIGINAL COORDINATE SYSTEM

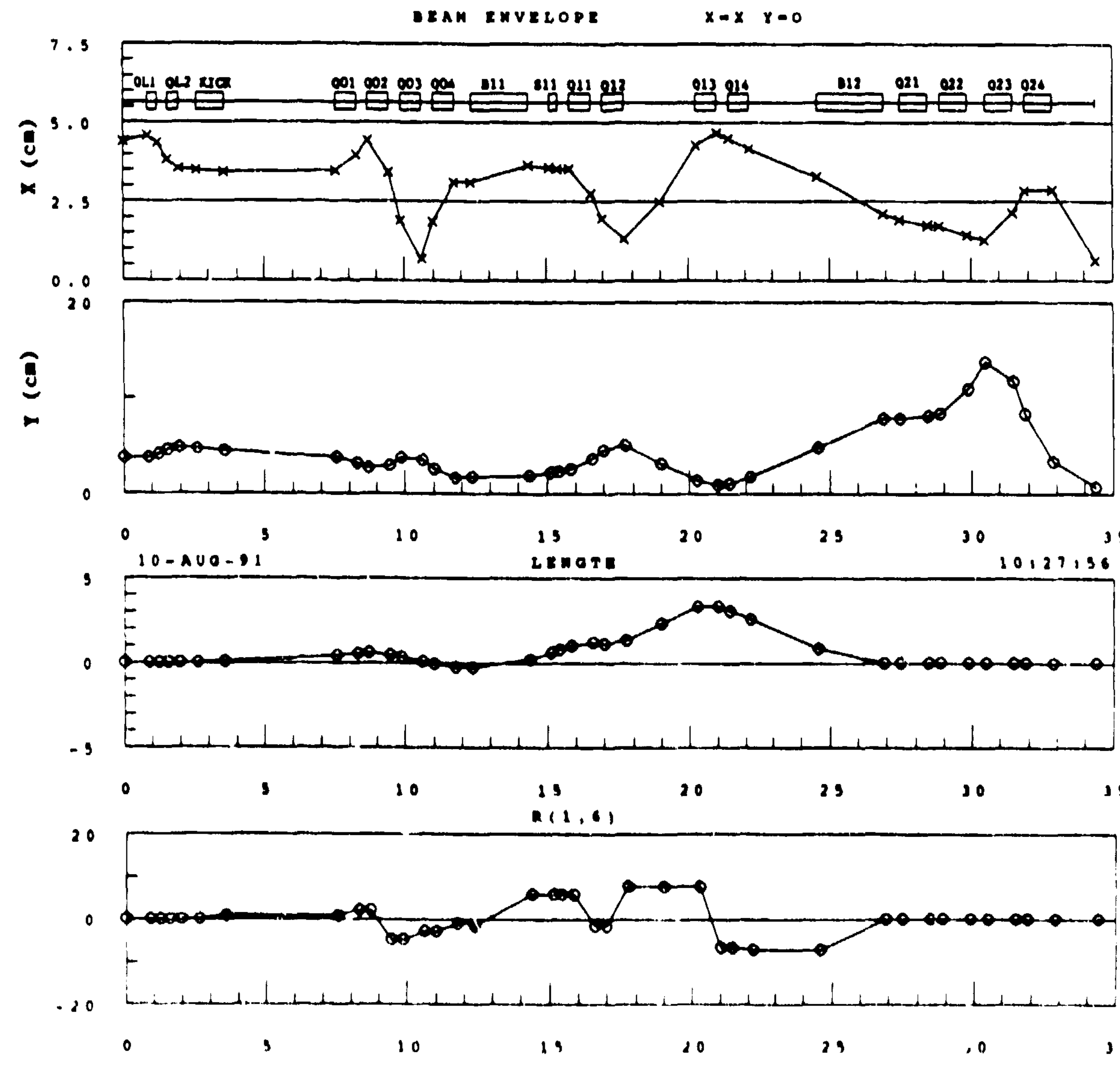

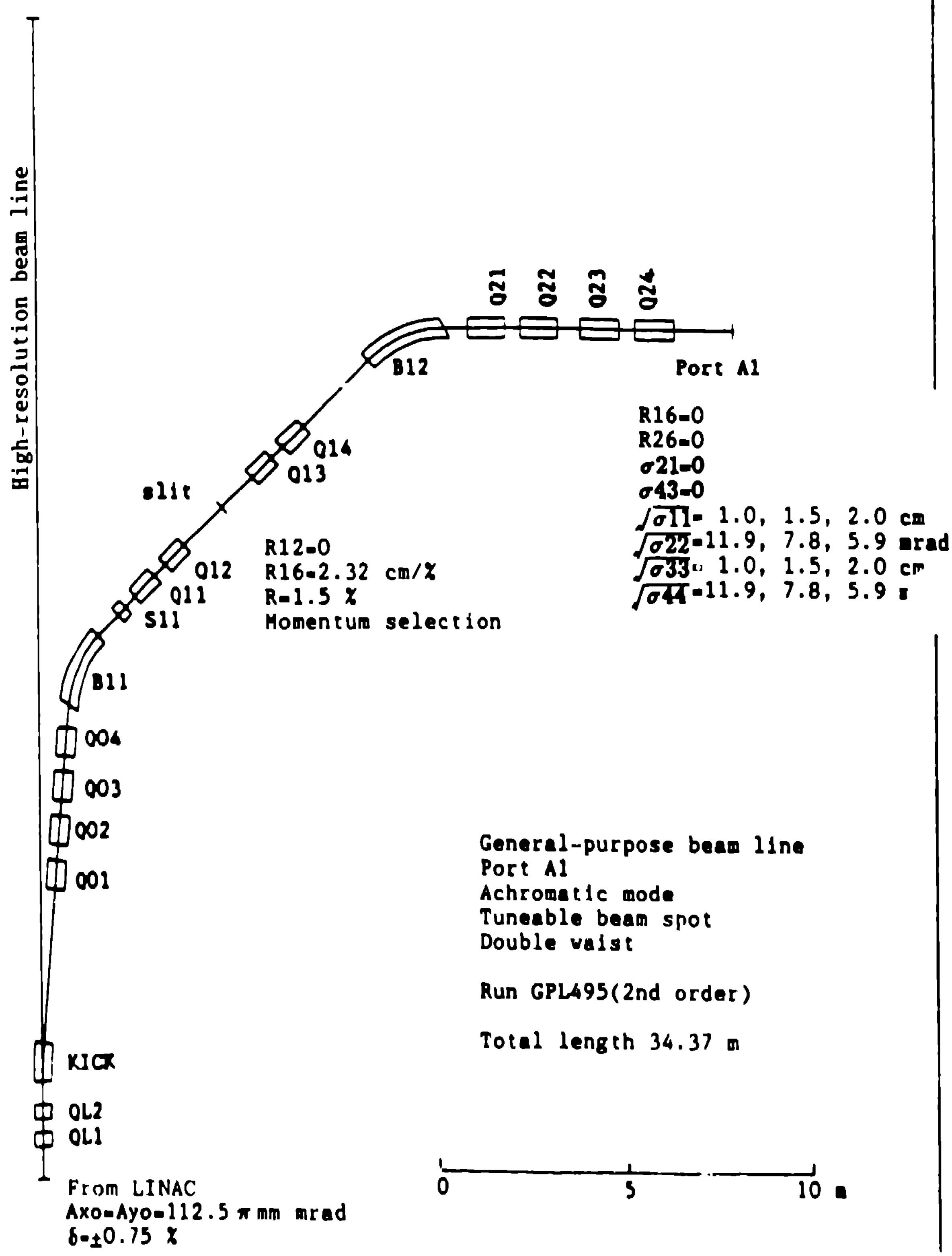
High-resolution beam line
Q21
Q22
Q23
Q24
B12
Port A1
R16=0
R26=0
σ21=0
σ43=0
√σ11= 1.0, 1.5, 2.0 cm
√σ22=11.9, 7.8, 5.9 mrad
√σ33= 1.0, 1.5, 2.0 cm
√σ44=11.9, 7.8, 5.9 m
Q14
Q13
slit
Q12
Q11
S11
R12=0
R16=2.32 cm/%
R=1.5 %
Momentum selection
B11
Q04
Q03
Q02
Q01
General-purpose beam line
Port A1
Achromatic mode
Tuneable beam spot
Double waist
Run GPL495(2nd order)
Total length 34.37 m
KICK
QL2
QL1
0
5
10 m
From LINAC
Axo=Ayo=112.5 π mm mrad
δ=±0.75 %

p.16

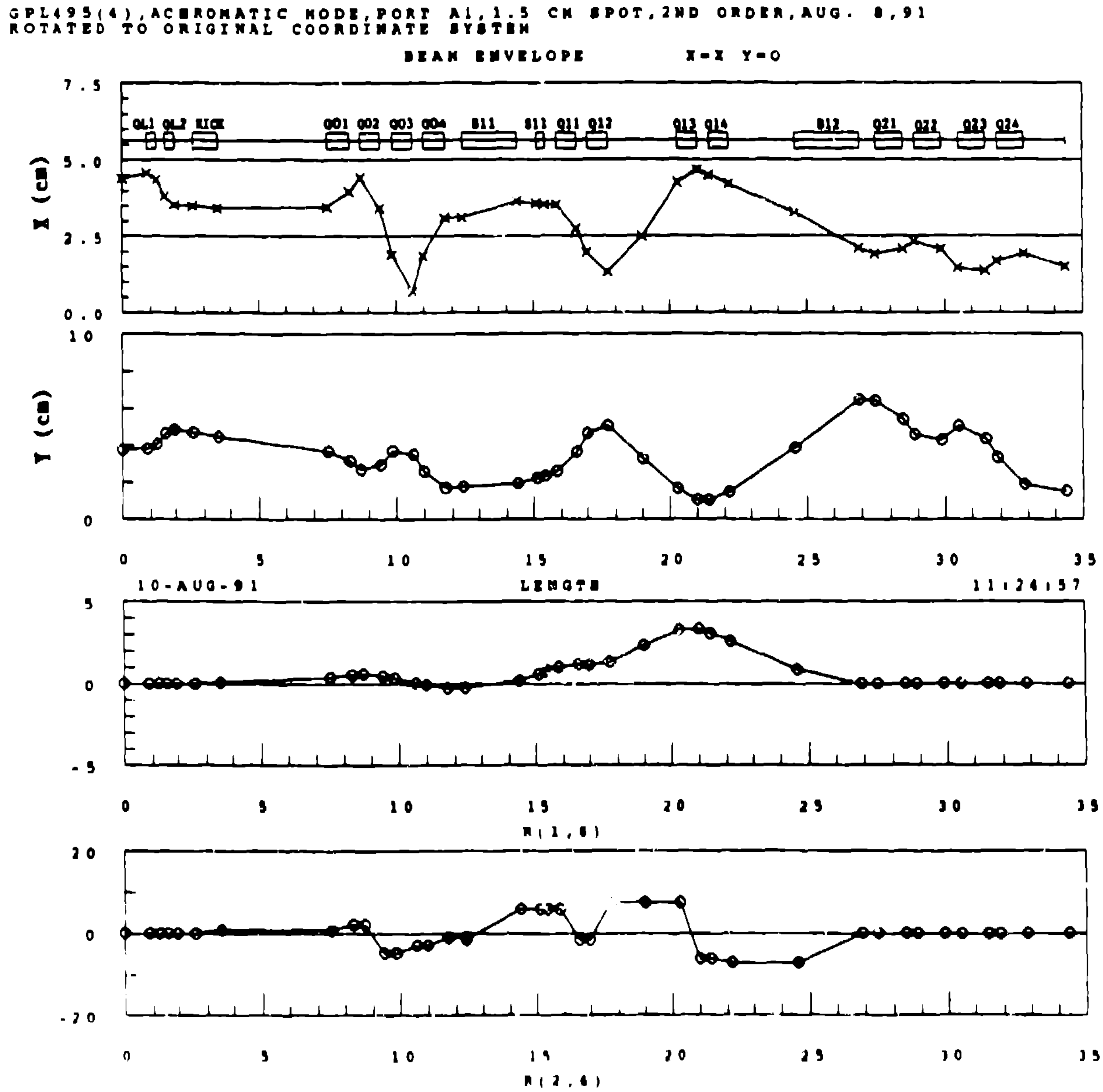
GPL495(4),ACHROMATIC MODE,PORT A1,1.5 CM SPOT,2ND ORDER,AUG. 8,91
ROTATED TO ORIGINAL COORDINATE SYSTEM
BEAM ENVELOPE X=X Y=O
X (cm)
Y (cm)
QL1 QL2 KICK QD1 QD2 QD3 QD4 B11 S11 Q11 Q12 Q13 Q14 B12 Q21 Q22 Q23 Q24
10-AUG-91
LENGTH
11:24:57
R(1,6)
R(2,6)

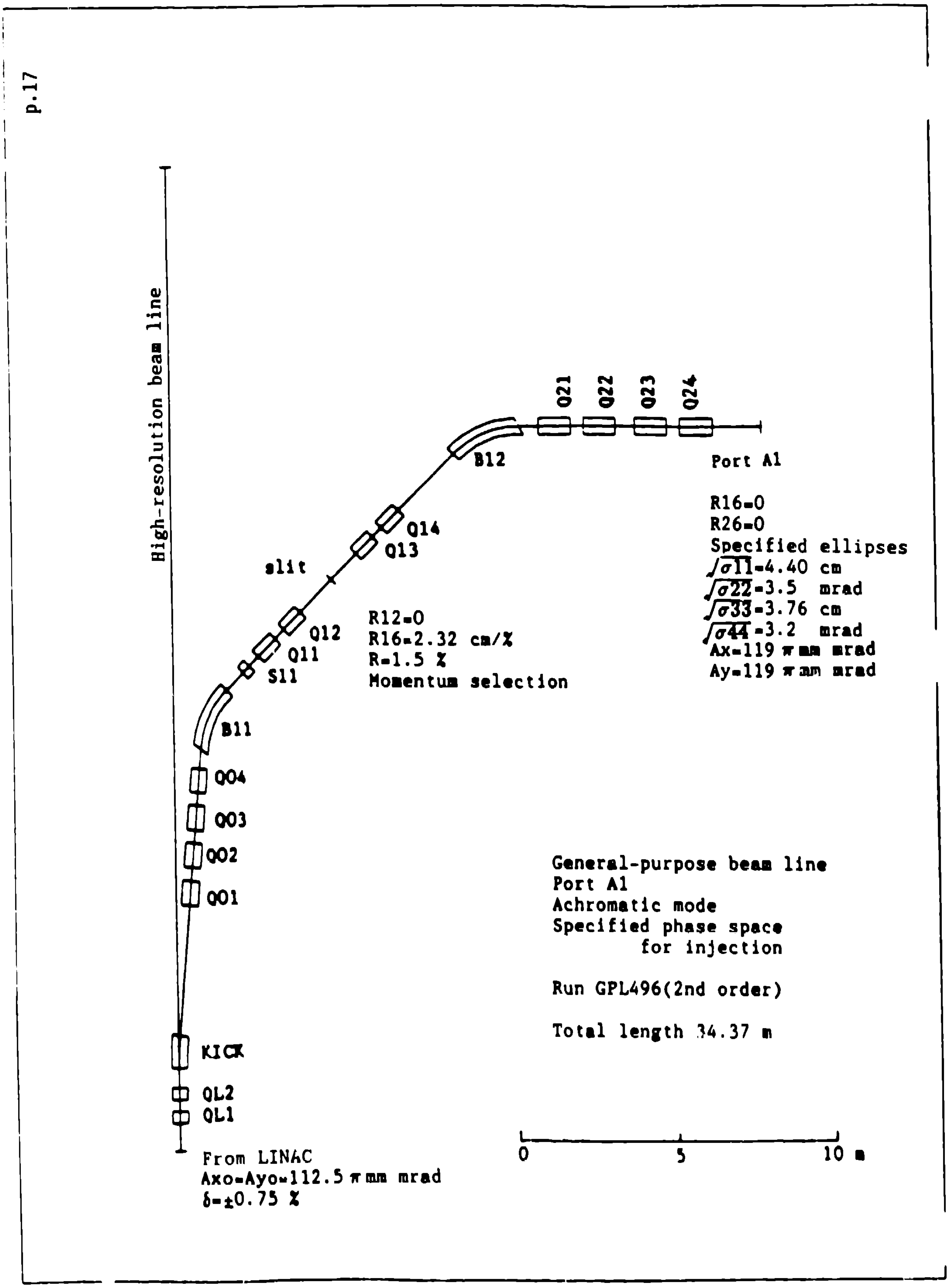
p.17
High-resolution beam line
Q21
Q22
Q23
Q24
B12
Port A1
R16=0
R26=0
Specified ellipses
$\sqrt{\sigma 11}$=4.40 cm
$\sqrt{\sigma 22}$=3.5 mrad
$\sqrt{\sigma 33}$=3.76 cm
$\sqrt{\sigma 44}$=3.2 mrad
Ax=119 π mm mrad
Ay=119 π mm mrad
Q14
Q13
slit
Q12
Q11
S11
R12=0
R16=2.32 cm/%
R=1.5 %
Momentum selection
B11
Q04
Q03
Q02
Q01
General-purpose beam line
Port A1
Achromatic mode
Specified phase space
for injection
Run GPL496(2nd order)
Total length 34.37 m
KICK
QL2
QL1
0
5
10 m
From LINAC
Axo=Ayo=112.5 π mm mrad
δ=$\pm$0.75 %

GPL496(4),ACHROMATIC MODE,PORT A1,FOR INJECTION,2ND ORDER,AUG. 8,91
ROTATED TO ORIGINAL COORDINATE SYSTEM

BEAM ENVELOPE X=X Y=0

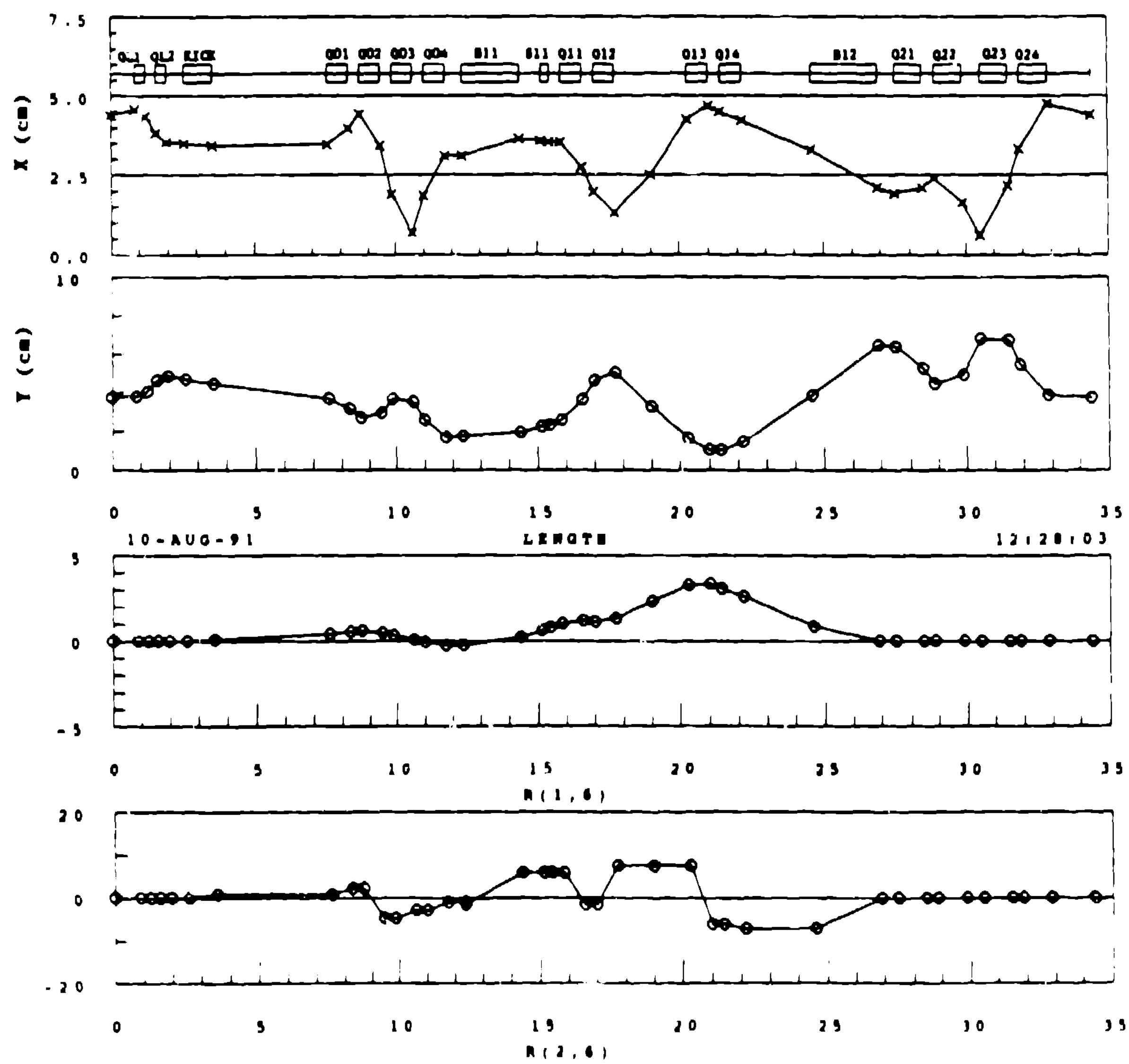

p.19

GPL496(4),ACHROMATIC MODE,PORT A1,FOR INJECTION,2ND ORDER,AUG. 8,91
PHASE ELLIPSES

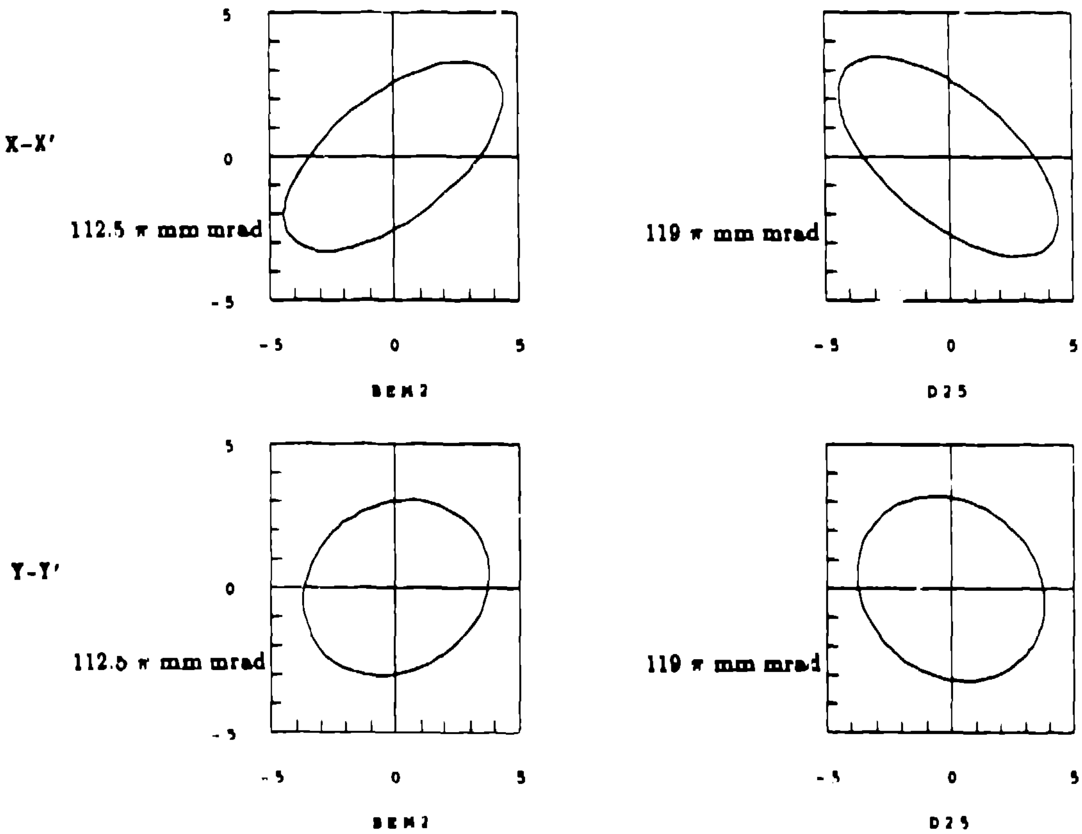

10-AUG-91 12:28:03

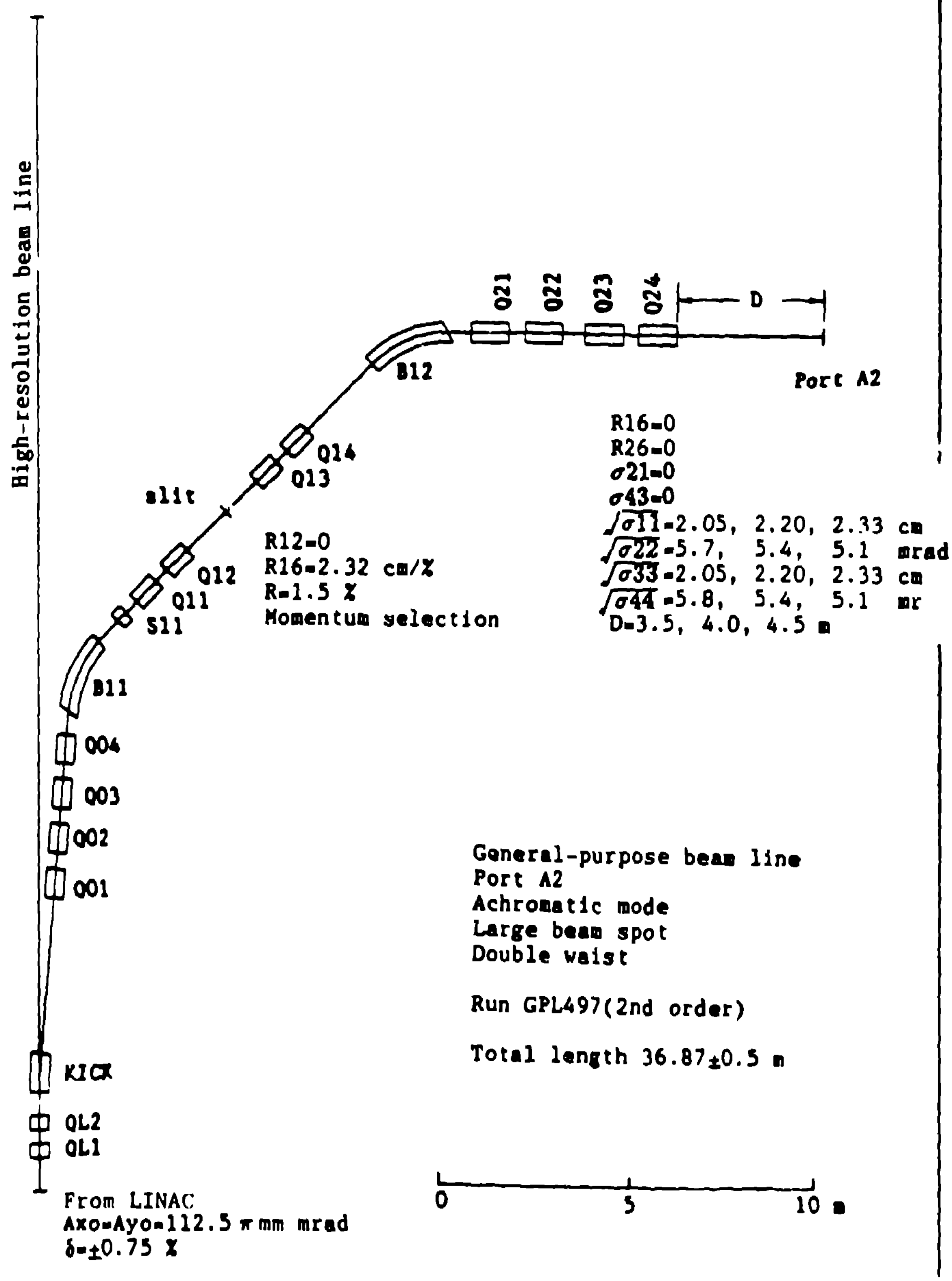
High-resolution beam line
Q21
Q22
Q23
Q24
D
B12
Port A2
R16=0
R26=0
σ21=0
σ43=0
√σ11=2.05, 2.20, 2.33 cm
√σ22=5.7, 5.4, 5.1 mrad
√σ33=2.05, 2.20, 2.33 cm
√σ44=5.8, 5.4, 5.1 mr
D=3.5, 4.0, 4.5 m
Q14
Q13
slit
R12=0
R16=2.32 cm/%
R=1.5 %
Momentum selection
Q12
Q11
S11
B11
Q04
Q03
Q02
Q01
General-purpose beam line
Port A2
Achromatic mode
Large beam spot
Double waist
Run GPL497(2nd order)
Total length 36.87±0.5 m
KICK
QL2
QL1
From LINAC
Axo=Ayo=112.5 π mm mrad
δ=±0.75 %
0
5
10 m

p.21

GPL497(4),ACHROMATIC MODE,PORT A2,D25=4.0M,2ND ORDER,AUG. 8,91
ROTATED TO ORIGINAL COORDINATE SYSTEM

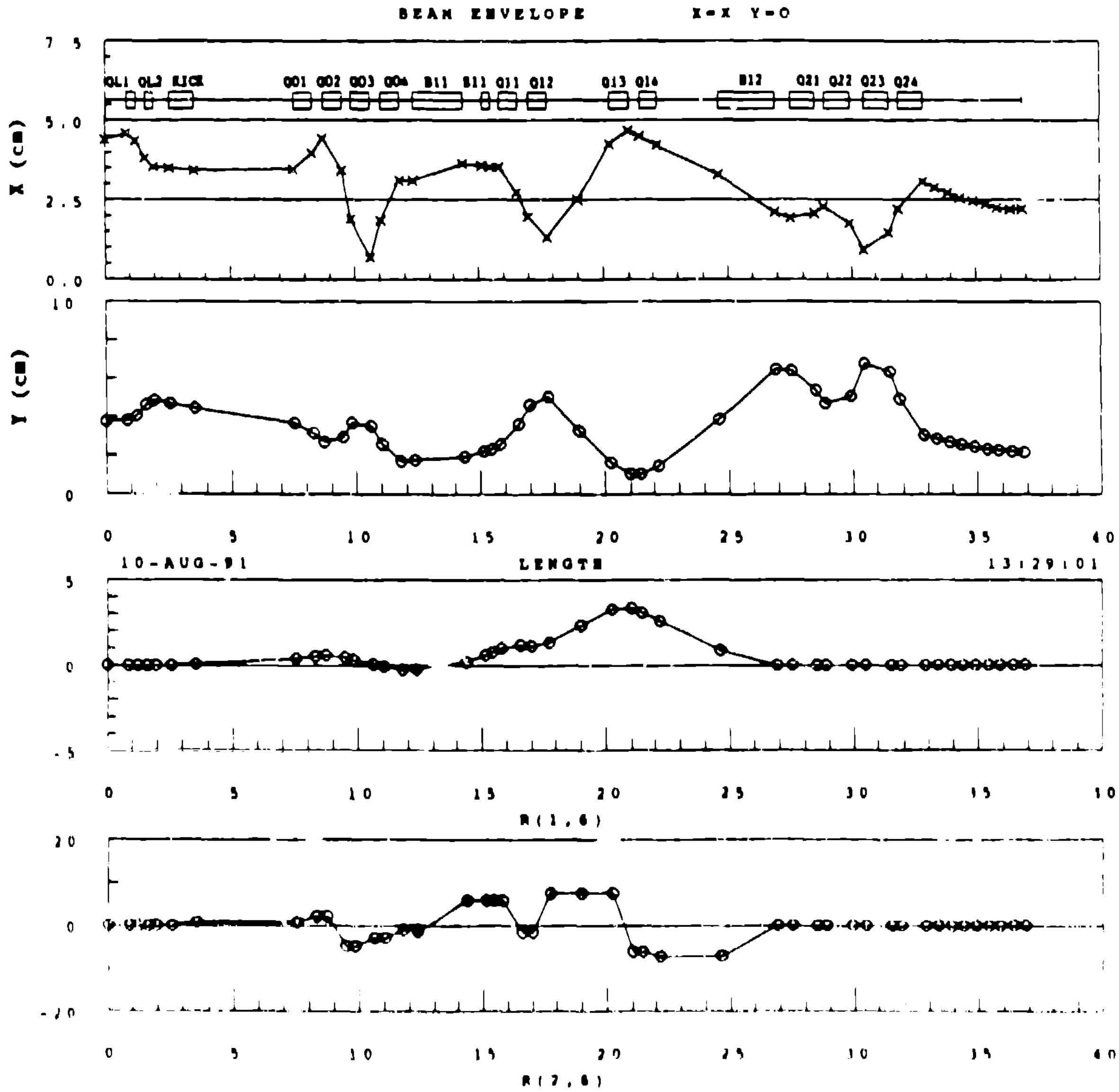

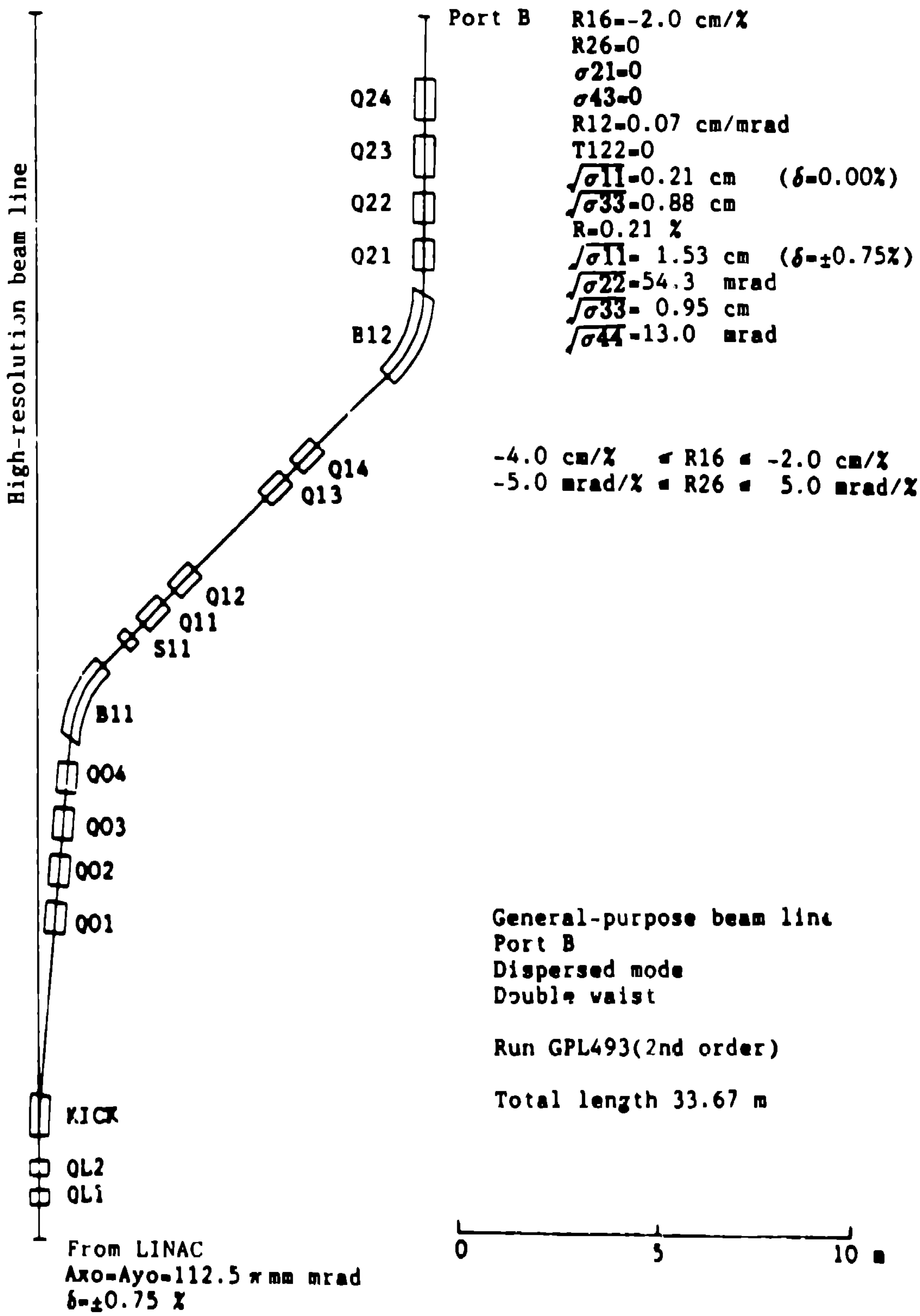

High-resolution beam line
Port B
R16=-2.0 cm/%
R26=0
σ21=0
σ43=0
R12=0.07 cm/mrad
T122=0
√σ11=0.21 cm (δ=0.00%)
√σ33=0.88 cm
R=0.21 %
√σ11= 1.53 cm (δ=±0.75%)
√σ22=54.3 mrad
√σ33= 0.95 cm
√σ44=13.0 mrad
Q24
Q23
Q22
Q21
B12
Q14
Q13
Q12
Q11
S11
B11
Q04
Q03
Q02
Q01
KICK
QL2
QL1
-4.0 cm/% ≤ R16 ≤ -2.0 cm/%
-5.0 mrad/% ≤ R26 ≤ 5.0 mrad/%
General-purpose beam line
Port B
Dispersed mode
Double waist
Run GPL493(2nd order)
Total length 33.67 m
0
5
10 m
From LINAC
Axo=Ayo=112.5 π mm mrad
δ=±0.75 %

GPL493(4),DISPERSED MODE,PORT B1,R16=-2.0,R26=0.0,DP/P=0.75,AUG. 7,91
ROTATED TO ORIGINAL COORDINATE SYSTEM

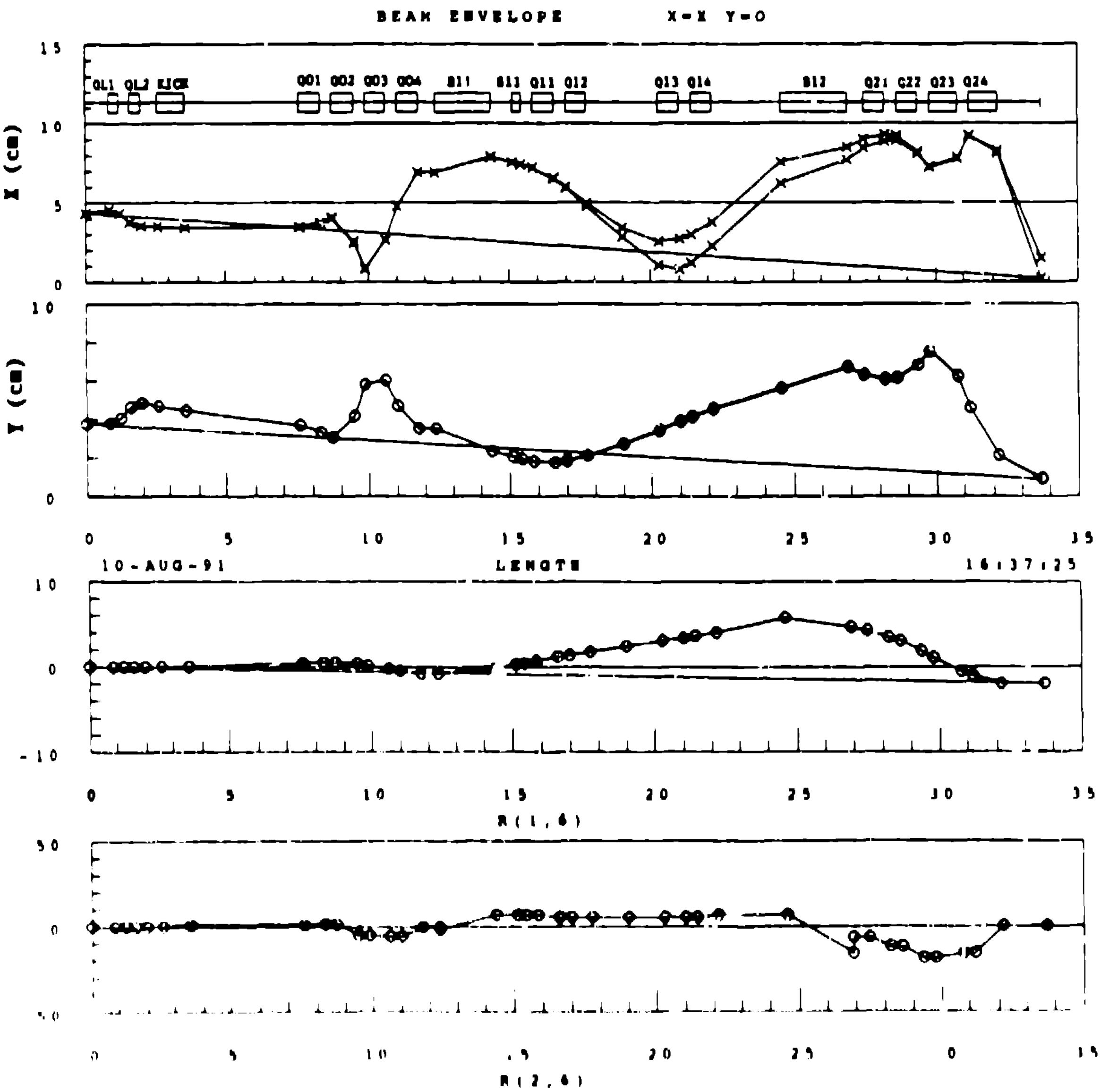

GENERAL-PURPOSE BEAM LINE

$A_{xo}=A_{yo}=112.5\ \pi$ mm mrad
$\delta=\pm 0.75\%$

Port (D)		A 1 (1.5m)	A 2 (3.5m-4.5m)	B (1.5m)
Achromatic Mode R16=R26=0 σ21=σ43=0 Momentum selection R=1.5%	small beam spot	0.64cm*18.7mr(H) 0.67cm*22.6mr(V)		
	tuneable beam spot	1.0,1.5,2.0cm 1.50cm*7.8mr(H) 1.50cm*7.8mr(V)		
	specified phase space (for injection)	4.40cm*3.5mr(H) 3.76cm*3.2mr(V) Ax=119 π mm mr Ay=119 π mm mr		
	large beam spot		D=4.0m 2.20cm*5.4mr(H) 2.20cm*5.4mr(V)	
Dispersed Mode	-4.0 ≤ R16 ≤ -2.0 cm/% -5.0 ≤ R26 ≤ 5.0 mr/% σ21=0 σ43=0			R16=-2.0 cm/% R26= 0.0 mr/% R12=0.07 cm/mr R=0.21 % 1.53cm*54.3mr(H) 0.95cm*13.0mr(V)

GENERAL-PURPOSE BEAM LINE

$A_x\varepsilon = A_y\varepsilon = 225\ \pi$ mm mrad
$\delta = \pm 1.06\%$

Port (D)		A 1 (1.5m)	A 2 (3.5m-4.5m)	B (1.5m)
Achromatic Mode R16=R26=0 σ21=σ43=0 Momentum selection R=2.2%	small beam spot	1.17cm*21.0mr(H) 1.23cm*23.3mr(V)		
	tuneable beam spot	1.4,2.0,2.5cm 2.00cm*12.1mr(H) 2.00cm*12.1mr(V)		
	specified phase space (for injection)			
	large beam spot		D=4.0m 3.11cm*7.9mr(H) 3.11cm*8.1mr(V)	
Dispersed Mode	-4.0 ≤ R16 ≤ -2.0 cm/% -5.0 ≤ R26 ≤ 5.0 mr/% σ21=0 σ43=0			R16=-2.0 cm/% R26= 0.0 mr/% R12=0.07 cm/mr R=0.29 % 2.18cm*76.8mr(H) 1.35cm*18.8mr(V)

GPL499(4),ACHROMATIC MODE,PORT A1,SMALL SPOT,2ND ORDER,AUG. 9,91
ROTATED TO ORIGINAL COORDINATE SYSTEM

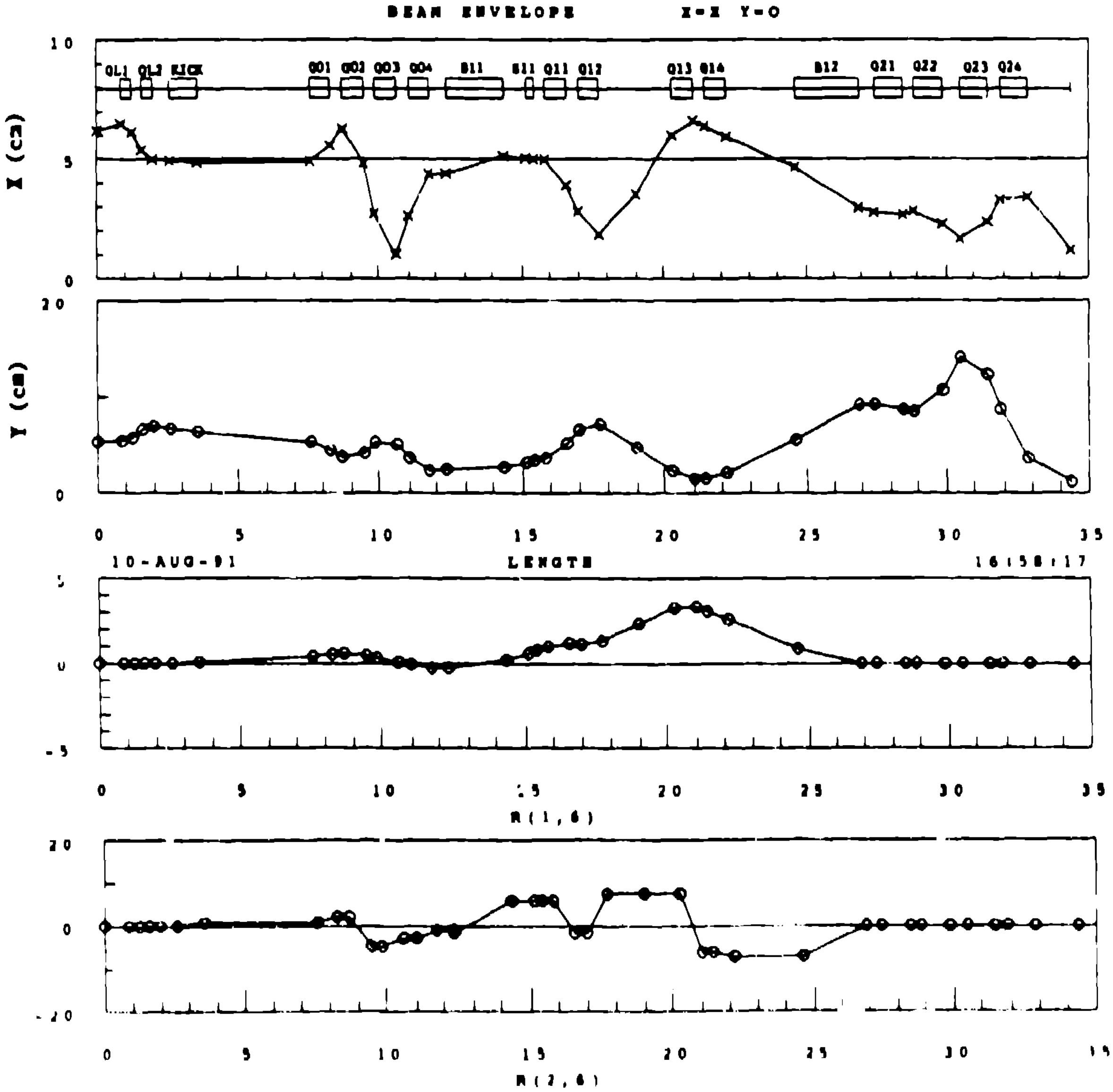

SUMMARY

A general-purpose pion beam line with two output ports and two operation modes designed

Meet the requirements in the first and second order

Correction of kinematic line broadening by ajusting transfer matrix elements R26 and R12 at Port B (for dispersed mode operation) needs to be studied in detail

PROGRAM RAYTRACE

August 6, 1991

RAYTRACE and the Real World

Harald A. Enge

These notes discuss some "loose ends" in RAYTRACE and some practical hints for the use of the program. A section of the RAYTRACE manual is included as an introduction.

1. Fringing field descriptions in MTYP2 dipoles.

Figure 7 in the manual and Eq. 19 explains how we determine a "representative" distance to the effective field boundary. There has not been much checking done to justify this particular formula. The only definite things that can be said for it is that it gives a) the correct answer for a straight boundary and b) the right trend for a curved one. Figure 1 of this report shows an example of iso-B lines calculated by use of the procedure. It illustrates at the same time the effect of the proximity of the pole corners, discussed next.

2. Finite width of poles.

The manual defines what we mean with the effective field boundary (EFB). Quote: "This problem has been resolved by redefining the EFB as a mechanical reference boundary - a curve following the mechanical shape of the pole piece. The position of the EFB relative to the pole piece is the position calculated on the assumption that the boundary is straight" This statement actually is not quite complete. We generally modify the EFB as defined above by curving it around the corners of the pole piece using even-order S-parameters. The order of these parameters depends upon the ratio of pole width W to air gap D, that is, a very narrow pole requires a second-order correction, a wide one requires an eight-order correction. The formulas we are using are, for Rogowski poles (with R=orbit radius):

$$n = W/D = 2(i+\delta) \quad \text{where } i = \text{integer}, \ \delta < 1$$

$$S_{2i} = \frac{0.5(1-\delta)D}{R}\left(\frac{2R}{W}\right)^{2i}$$

$$S_{2i+2} = \frac{0.5\delta D}{R}\left(\frac{2R}{W}\right)^{2i+2}$$

The width W is measured at the root of the pole piece.

For a magnet without pole tapering, change the factor 0.5 to 0.3.

3. How wide should the poles be?

For magnets operating in the range of 1.2 tesla and up the sides of the poles must be tapered to avoid saturation. Generally, a 60-degree taper with a width of one airgap is adequate (Fig. 2).

How close to the edge can the particle move before they experience a drop in field of a factor 10^{-4}? We are assuming flat poles, i.e. no "Rose shims". For x>0 we can express the scalar potential as:

$$\phi = -B_0 y + \sum_n A_n e^{-k_n x} \sin k_n y$$

This satisfies the requirement that the perturbing part of the scalar potential is zero at the pole surfaces and on the midplane provided

$$k_n D = 2\pi n \quad \text{with } n = \text{integer}$$

The lowest term (n=1) gives

$$k_1 = 2\pi/D$$

This term decays a factor 10 over a distance

$$\Delta x = (D/2\pi)\ln 10 = 0.367D$$

At the corner (x=0) the magnitude of the perturbation is $\Delta B/B \approx 0.2$. Assuming this is all from the lowest order term, we find the distance from the corner to the point where the term has been reduced by a factor 2000 (to $\Delta B/B = 10^{-4}$) given by

$$k_1 x = \ln 2000 = 7.6$$

which gives

$$x = 7.6\ D/2\pi = 1.21\ D$$

This analysis shows that for high-precision magnets without Rose shims the total widths of pole pieces (measured at the roots) should be at least 4.5 airgaps plus the width of the beam.

Figure 3 shows an example of a profile along the same idea as the Rose shim. The purpose of the Rose shim, or the corresponding bump used in this case, is to eliminate the lowest-order term in the expansion. The higher-order terms decay much faster with increasing x.

The profile in Fig. 3 produces a $\Delta B/B$ less than 10^{-4} in a region which is approximately one airgap wide. The total width of the root of the pole is 4.58 times the airgap.

4. Magnet dipoles with gradients.

In the subroutines MTYP3 and MTYP4 the fringing-field expressions are similar to the ones for MTYP2 except, of course, the n-value and higher-order terms of $\Delta R/R$ are included. Outside the EFB we are using x instead of ΔR in these expressions. This is because outside the pole pieces the field cannot "know about" the curvature of the magnet. Both n and the higher-order gradients should probably decay with increasing distance from the poles. This has not been written in to these programs.

5. Fitting the fringing-field expression to real data.

We either use measured fringing-field curves or data produced by POISSON calculations to fit the fringing-field expression (Eqs. 6,7 and 8 in the manual). We use a program called LASLFIT which also calculates the position of the EFB.

Be aware that the last coefficient in Eq. 7 must be odd and positive (C03 or C05) otherwise the expression (6) does not have the correct asymptotic behavior.

Details of the off-median-plane field are very sensitive to the value of the coefficients. Not so much so in a "Rogowski" magnet as in a sharp-cornered magnet. Fortunately, the field integral along a straight line in the z-direction is not influenced by these uncertainties.

We have experienced some difficulties with the corresponding expressions in quadrupoles in cases where the x-amplitudes in the fringing field exceeded the aperture radius. It probably would be better to fit the field of a quadrupole at the aperture radius rather than the gradient as measured at the axis. LASLFIT is not sophisticated enough for this, but it should be easy enough to write a program for the purpose.

6. Subroutine POLES.

The subroutine handles quadrupoles, sextupoles, octupoles, decapoles, dodecapoles and any combination thereof. There is a provision for adjusting the effective lengths of the various multipoles relative to the quadrupole if there is an admixture. The higher-order poles may also have a different rate of falloff of B vs. z in the fringing field. The corresponding constants (on the last line of the subroutine) have never been determined for any existing multipole. Other than this, the various multipoles are assumed to be proportional through the element. In other words, there is no provision for putting in a dodecapole, for instance in the fringing fields only.

It is possible, of course to introduce the dodecapoles (or other multipoles) as short ("deltafunction") elements before and after the quadrupole with proper backtracking to place the effects in the appropriate positions. These elements should either have no fringing field zones or fringing field zones of "regular" length. Very short fringing field zones (large coefficients) are likely to give trouble.

7. TRANSPORT to RAYTRACE conversion.

We practically always run TRANSPORT first on any ion-optical problem. In a few instances TRANSPORT does not have the required mechanism. One example comes to mind: a dc accelerator. We ran the element alone with RAYTRACE, constructed an appropriate matrix and plugged it into the TRANSPORT input. That does not give the correct answers for the magnetic strengths of the elements following the matrix, but that is easy to adjust afterwards by multiplying by the ratio of the momenta.

We generally find very good agreement between focal strengths of dipoles in TRANSPORT and RAYTRACE. Of course, TRANSPORT does not have the zeroth-order shift XCORR which we have to insert. If the boundaries have curvatures, we also need to have non-zero values for DELS (see below). Quadrupoles are more tricky. This is because TRANSPORT does not consider the reduced focusing strengths of the fringing fields (relative to the field integral).

In general the sum of the focusing strengths $1/f_x$ and $1/f_y$ for a dipole is proportional to the integral of B^2 along the path. The same holds approximately for a quadrupole <u>doublet</u> (or triplet), except it is the square of the <u>gradient</u> we are considering. So, just as for the dipole, we "lose" overall focusing power in the fringing field.

Our method for obtaining a better match between TRANSPORT and RAYTRACE is as follows. Our TRANSPORT input looks like this:

```
3. -R/2 ;             (Drift -R/2)
5.0A R B 2R ;         (Quad, length R, half gradient)
5.0A (L-R) B R ;      (Quad, length L-R, full gradient)
5.0A R B 2R ;         (Quad, length R, half gradient)
3. -R/2 ;             (Drift -R/2)
```

The first and last entry assures that the insertion length of the quadrupole is L meters. The two entries of lengths R have half gradients and represent the fringing fields. The reason for halving the gradient by using an artificial radius 2R rather than a field B/2 is to make it easier to optimize the strength by varying the three B's simultaneously and equally (variable A as shown here).

The quadrupole strengths calculated by the aid of TRANSPORT as described represent the first approximation for RAYTRACE. In some cases we need higher accuracy. In one example we required eight transfer coefficients to have certain values. Our procedure was:

a. Run TRANSPORT with qudrupoles represented as shown above.

b. Run RAYTRACE with the strength determined under a). Record the values of the coefficients which were: x/x, θ/x, θ/θ, y/y, ϕ/y, ϕ/ϕ, x/δ, and θ/δ. (The two coefficients x/θ and y/ϕ are not included since they can be determined from the others by use of Liouville's Theorem).

c. Run TRANSPORT varying seven quadrupole strengths, BQ's, and a drift length, l, to produce the same coefficients as RAYTRACE.

The changes ΔBQ and Δl required in the TRANSPORT parameters to produce the same output as RAYTRACE are recorded.

d. Change the RAYTRACE strengths by -ΔBQ and -Δl; and run RAYTRACE again. This now produces first-order transfer coefficient very similar to TRANSPORT, i.e. it produces the desired beam transfer.

8. Subroutine MULTIPOLE

As written, this subroutine describes an element that can contain any cominbation of multipoles up to dodecapole. In this respect it is similar to POLES, but the field descritpion as a function of z is bell-shaped and intended to be short. There are two variables in the field expression that can be used to fit measured or calculated values for B(z). Since the element is intended to be short, the effect on a stiff beam is almost that of a deltafunction, so an accurate description of B(z) is not critical. With the values $c_7 = 0.4$ and $c_8 = 0.1$, suggested in the manual, the "effective length" of the multipole is at least in one case studied about $1.2L_M$. The relationship of strengths between the MULTIPOLE and POLES is therefore given by:

$$1.2B_M L_M (W/2)^{-n} c_n = B_Q L_Q R_Q^{-n}$$

where n is the order of the desired effect (0 for dipole, etc.) The factor 1.2 should be taken with a grain of salt.

RAYTRACE ELEMENTS

1. DIPO - Six dipole versions
2. EDIP - Cylindrical electrostatic deflector
3. POLE - Quadrupole to dodecapole
4. MULT - Multipole correction element
5. SOLE - Single-layer solenoid
6. VELS - E×B velocity selector
7. LENS - Matrix plus spher., chrom. aberr.
8. SHRT - Coordinate shifts, rotation
9. DRIF - Straight drift
0. COLL - Rectangular or elliptic apertures
1. ACCE - DC accelerator
2. EINZ - Symmetric einzel lens

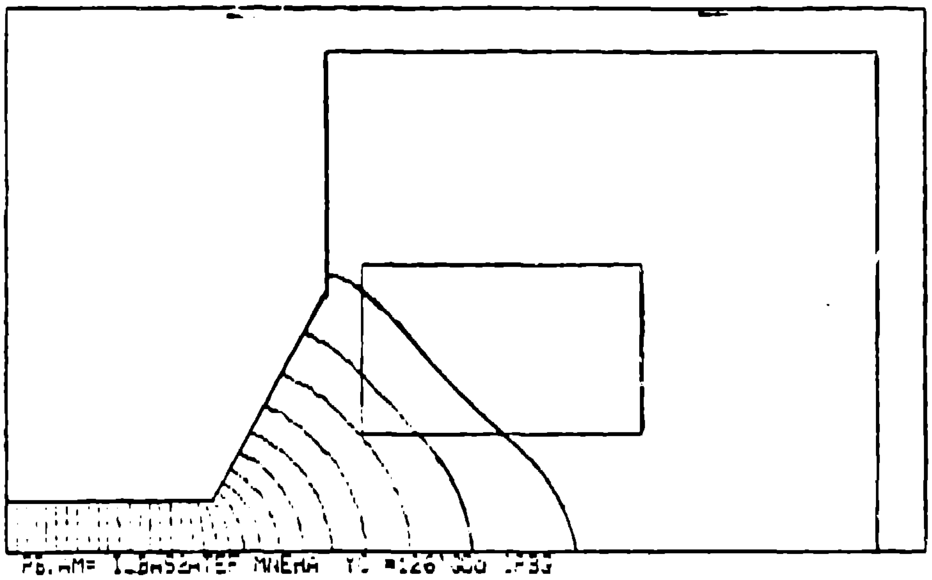

Fig. 1. Pole piece profile at entrance and exit

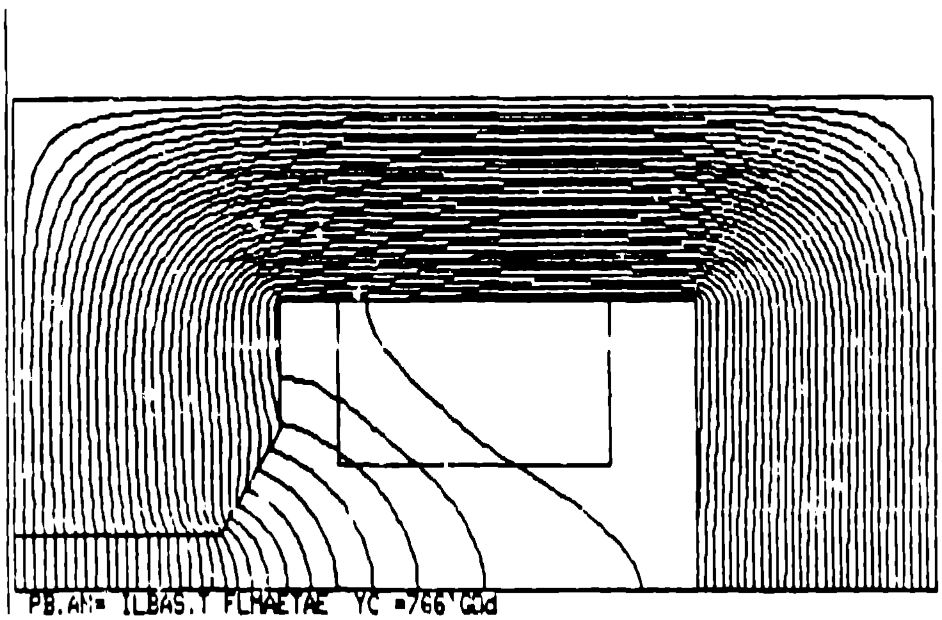

Fig. 2. Cross section of magnet (one half)

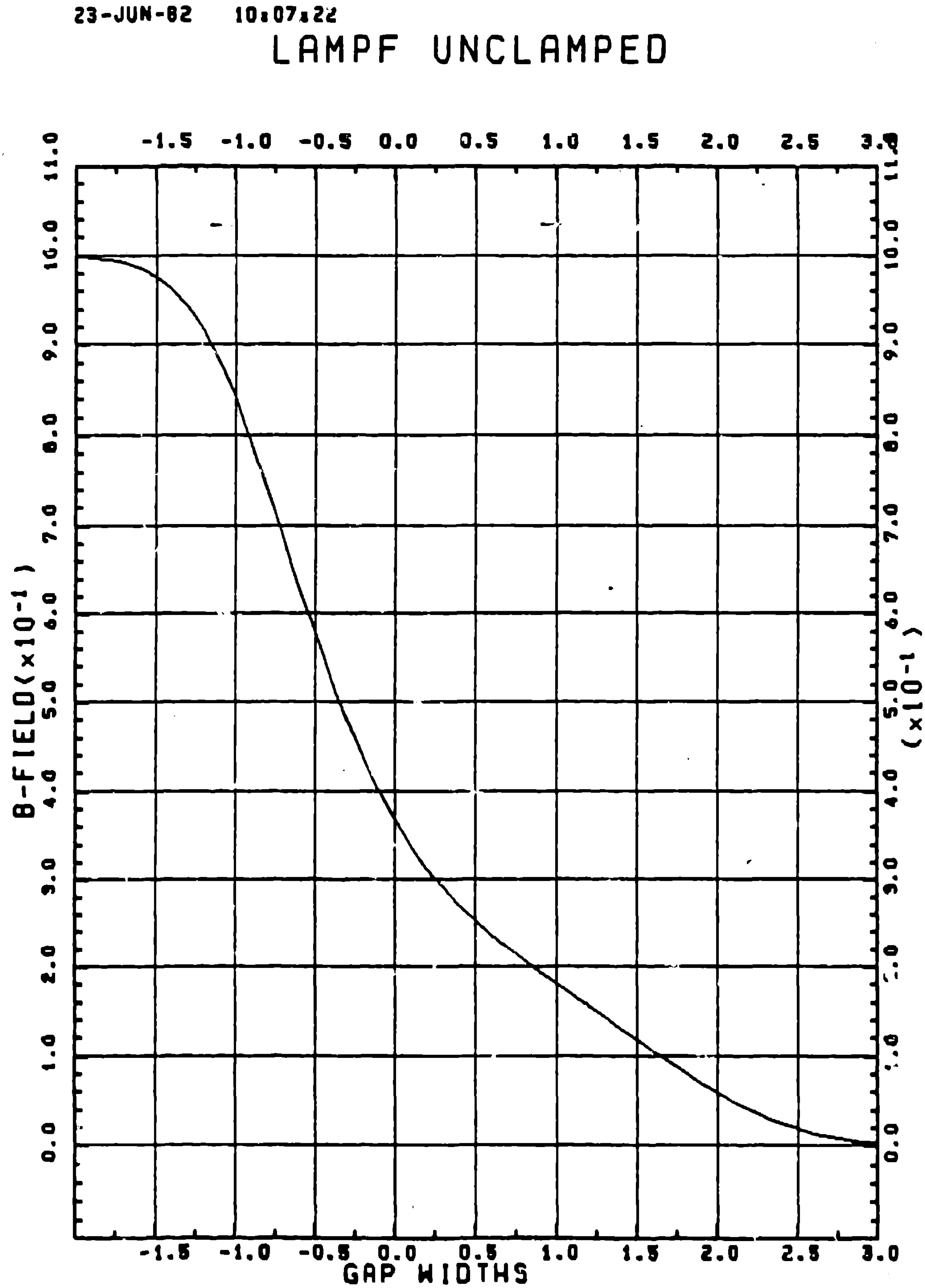
23-JUN-82 10:07:22
LAMPF UNCLAMPED
B-FIELD(×10-1)
(×10-1)
GAP WIDTHS
-1.5 -1.0 -0.5 0.0 0.5 1.0 1.5 2.0 2.5 3.0
0.0 1.0 2.0 3.0 4.0 5.0 6.0 7.0 8.0 9.0 10.0 11.0

Fringing field of dipole, Median plane

$$B_Y = B_0/(1+e^S)$$

$$S = C00 + C01s + C02s^2 + C03s^3 + C04s^4 + C05s^5$$

sD = modified shortest distance to EFB

The EFB described by:

$$\Delta z/R = -[S02(x/R)^2 + \ldots\ldots + S08(x/R)^8]$$

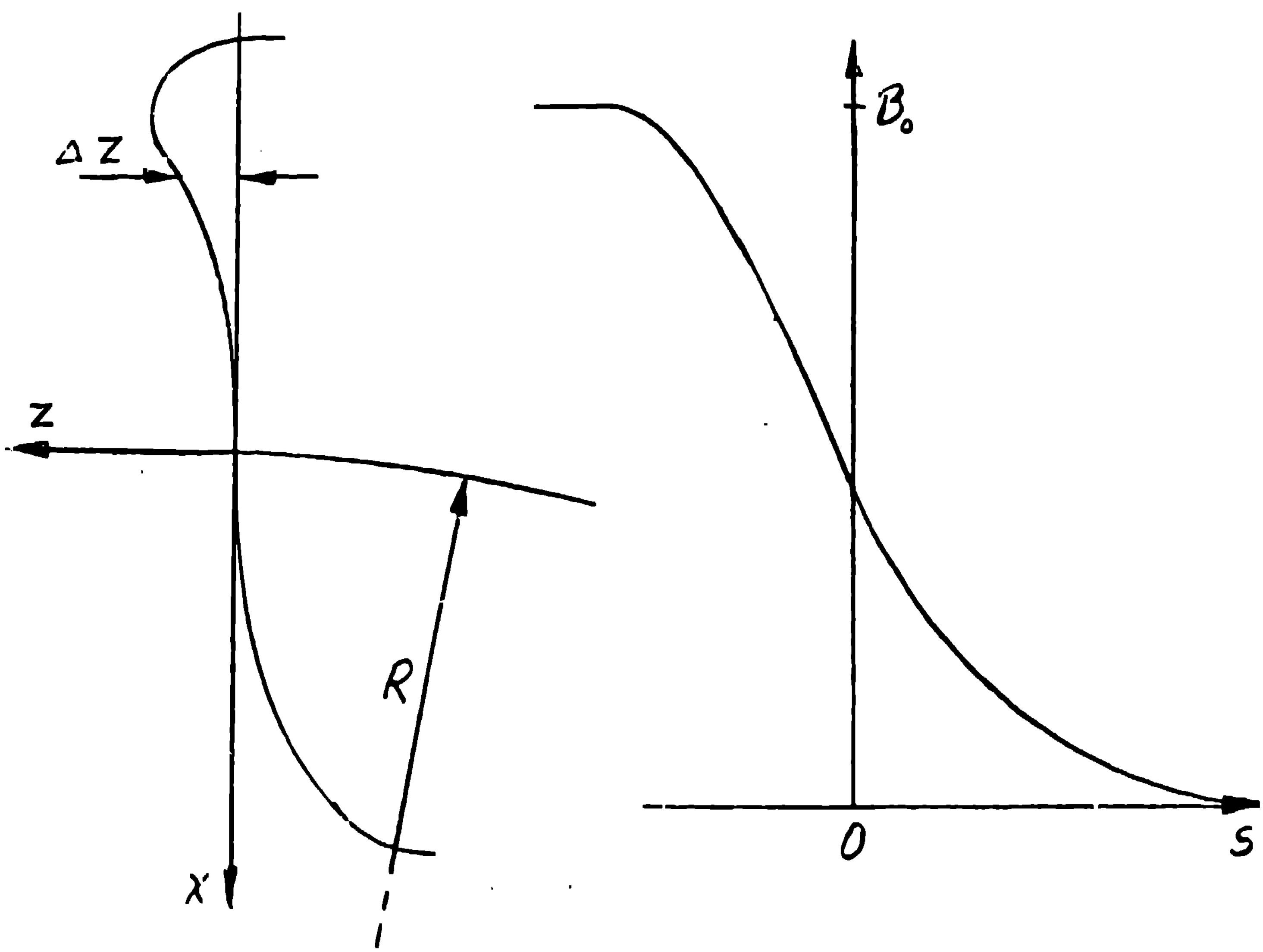

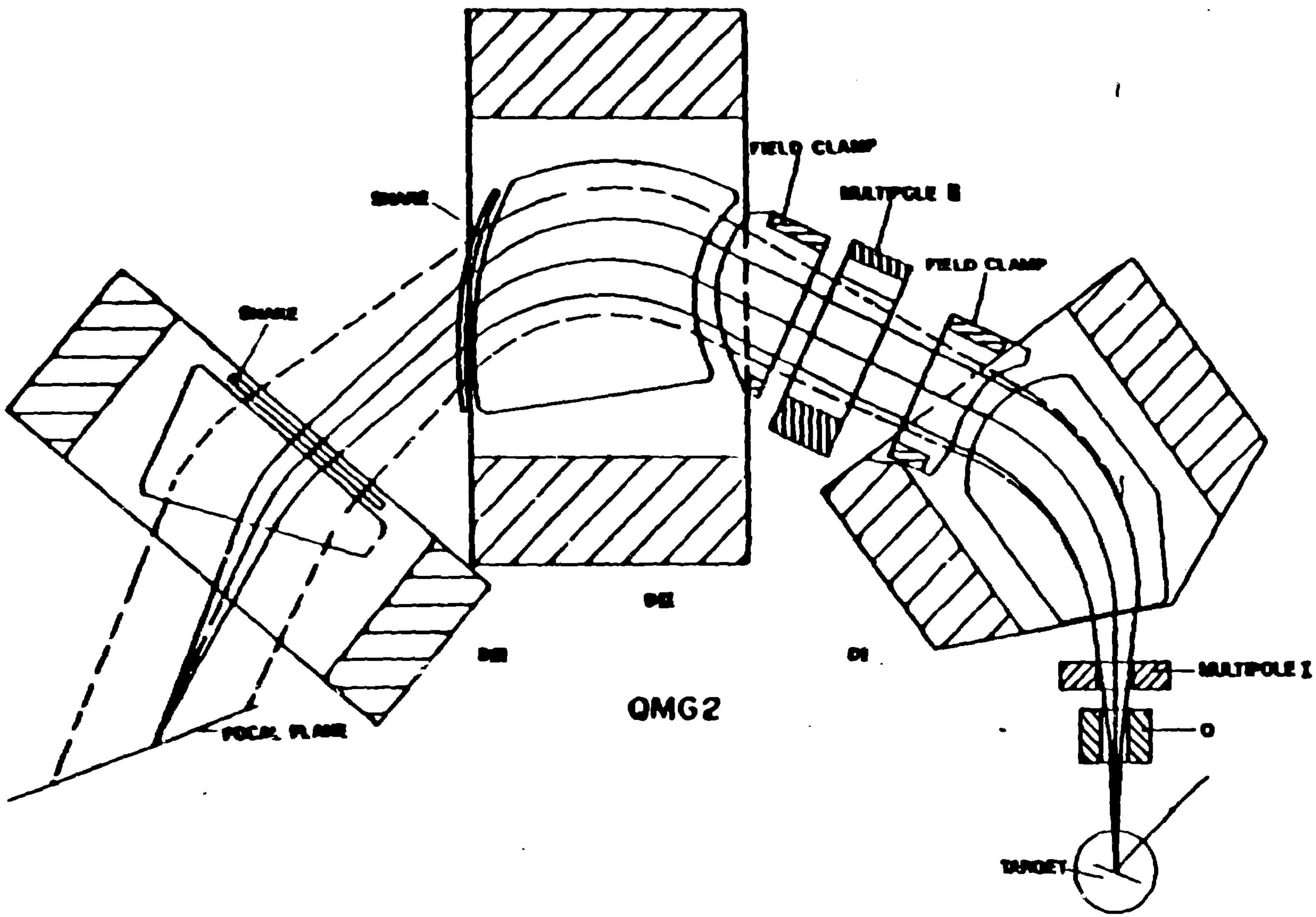
FIELD CLAMP
MULTIPOLE II
FIELD CLAMP
FOCAL PLANE
MULTIPOLE I
Q
TARGET
QMG2

$$n = W/D = 2(i+\delta) \text{ where } i = \text{integer}, \delta<1$$

$$S_{2i} = 0.5(1-\delta)(D/R)(2R/W)^{2i}$$

$$S_{2i+2} = 0.5\delta(D/R)(2R/W)^{2i+2}$$

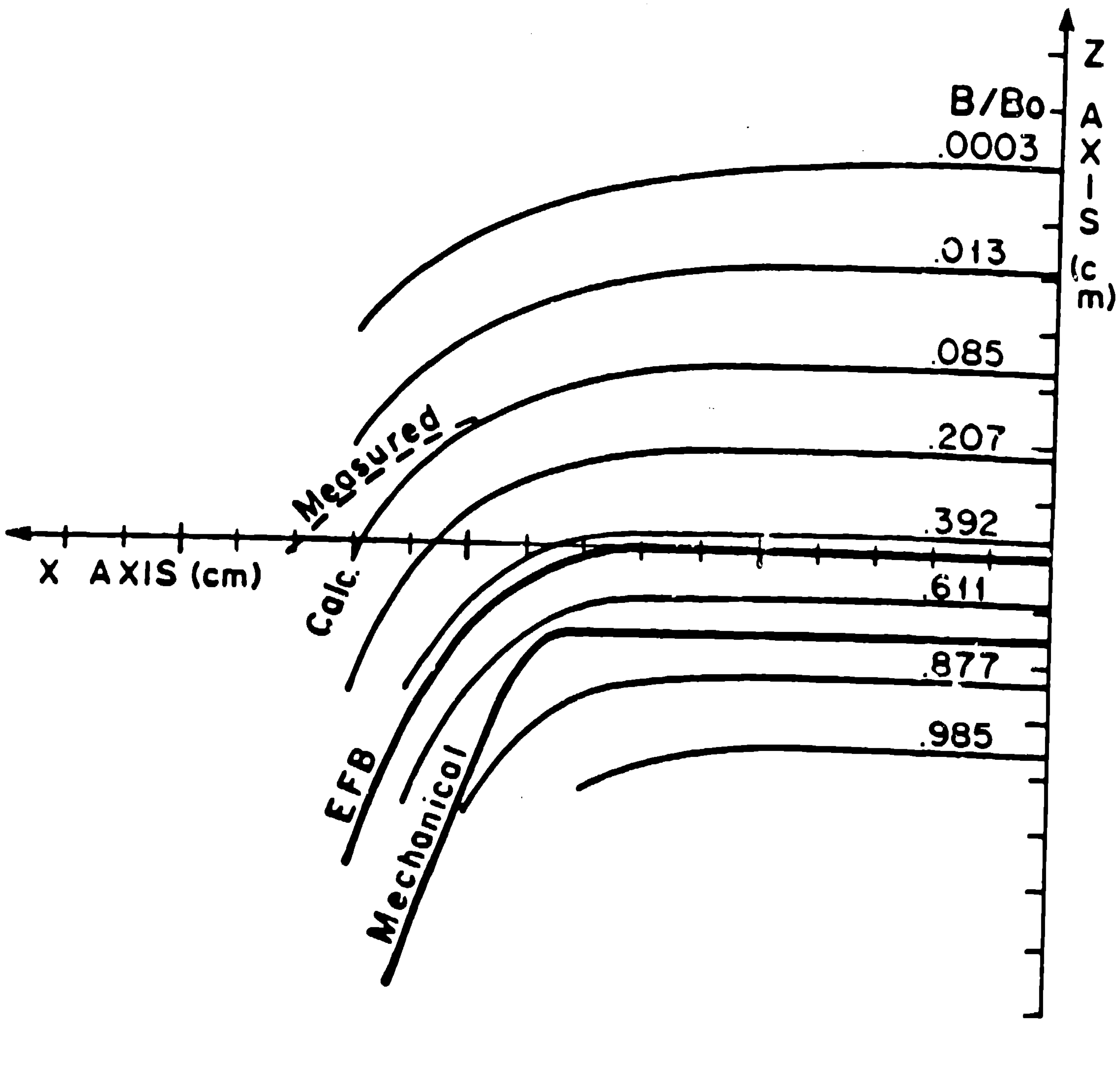

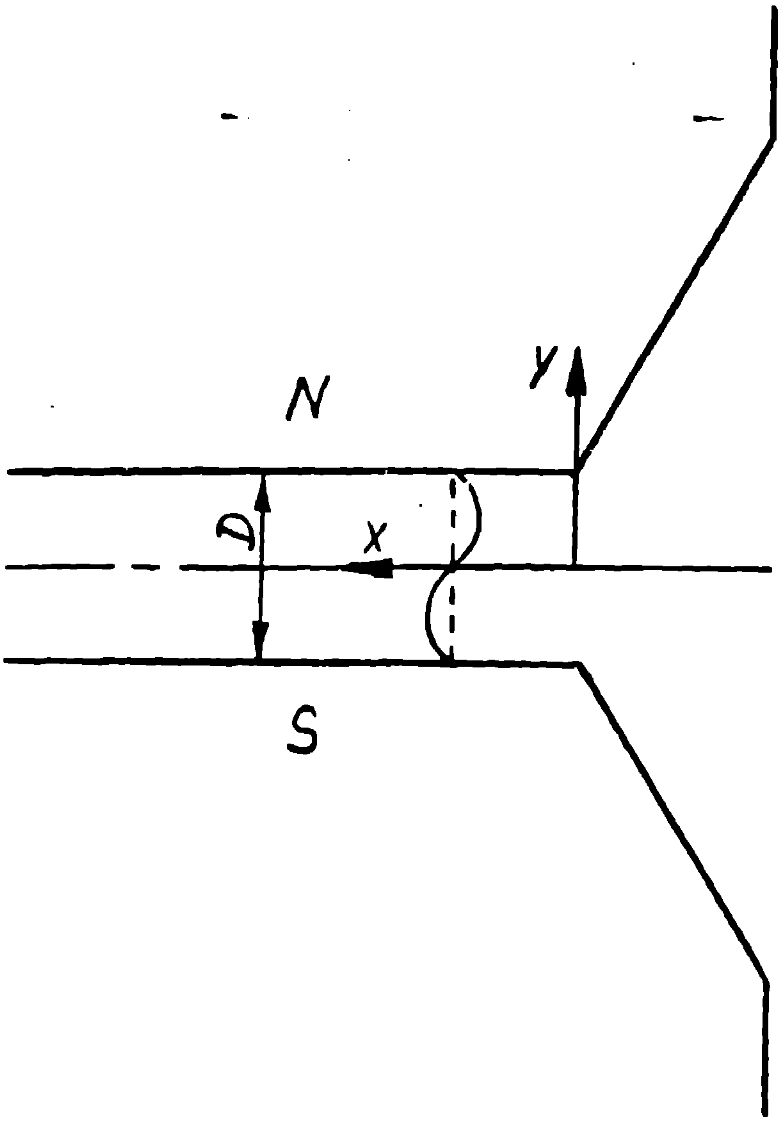

$$\phi = -B_0 y + \sum_n A_n e^{-k_n x} \sin k_n y$$

$$k_n D = 2\pi n$$

$$k_1 = 2\pi/D$$

A factor 10 reduction:

$$\Delta x = (D/2\pi) \ln 10 = 0.367 D$$

$$\Delta B/B_0 = 10^{-4} \text{ at } x = 1.21 D$$

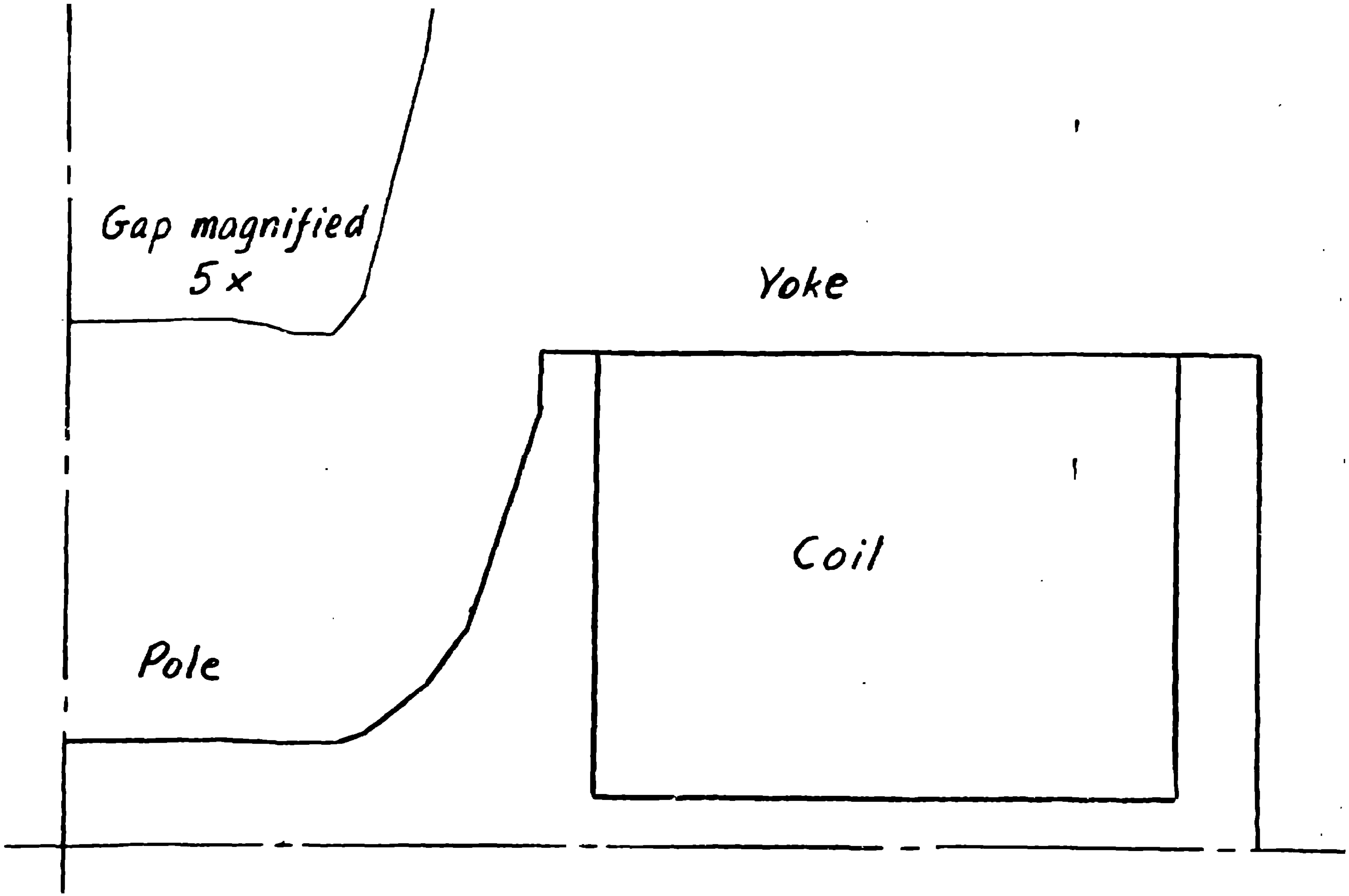
Gap magnified
5×
Yoke
Coil
Pole

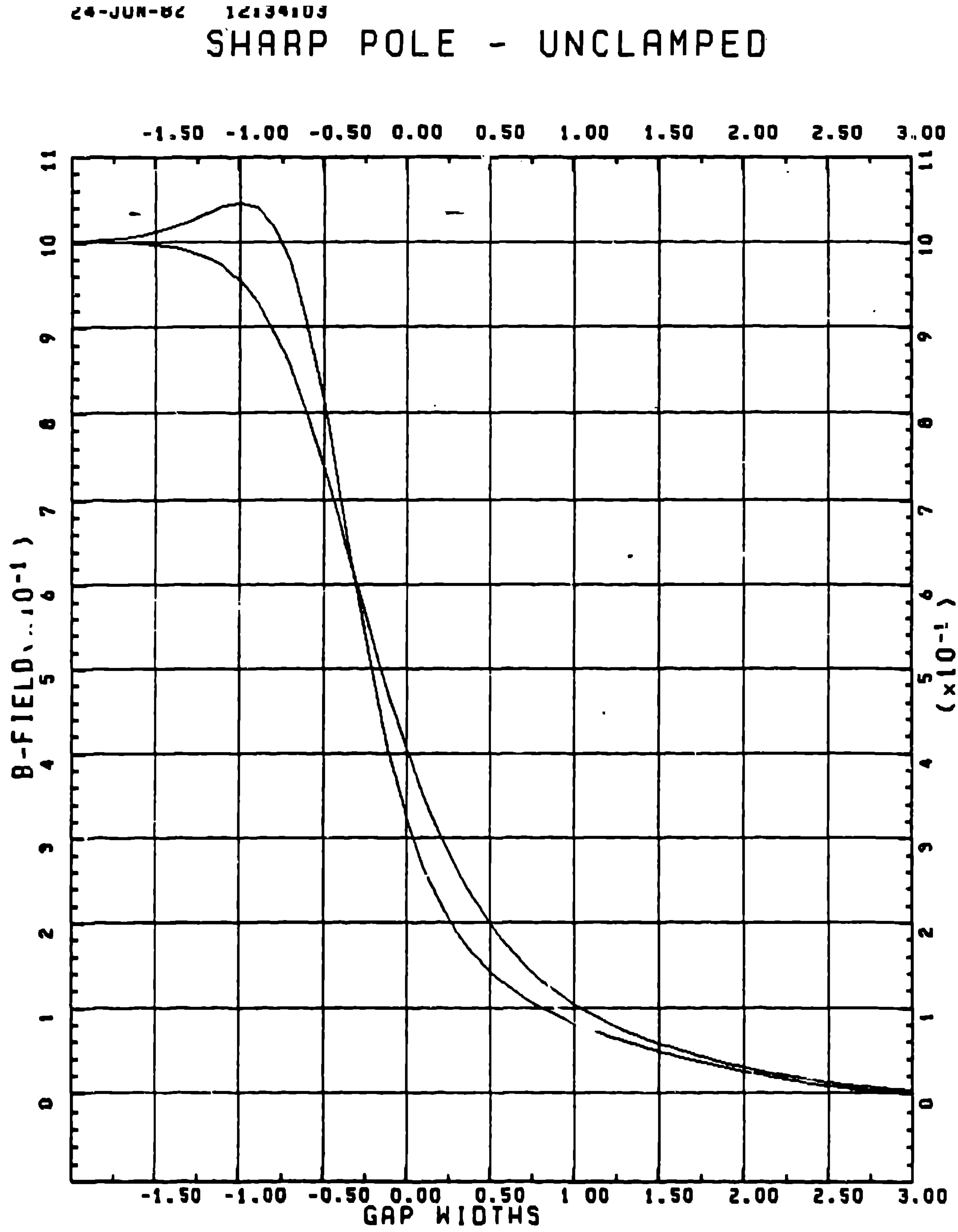

24-JUN-82 12:34:03
SHARP POLE - UNCLAMPED
B-FIELD (x10-1)
(x10-1)
GAP WIDTHS
-1.50 -1.00 -0.50 0.00 0.50 1.00 1.50 2.00 2.50 3.00
0 1 2 3 4 5 6 7 8 9 10 11

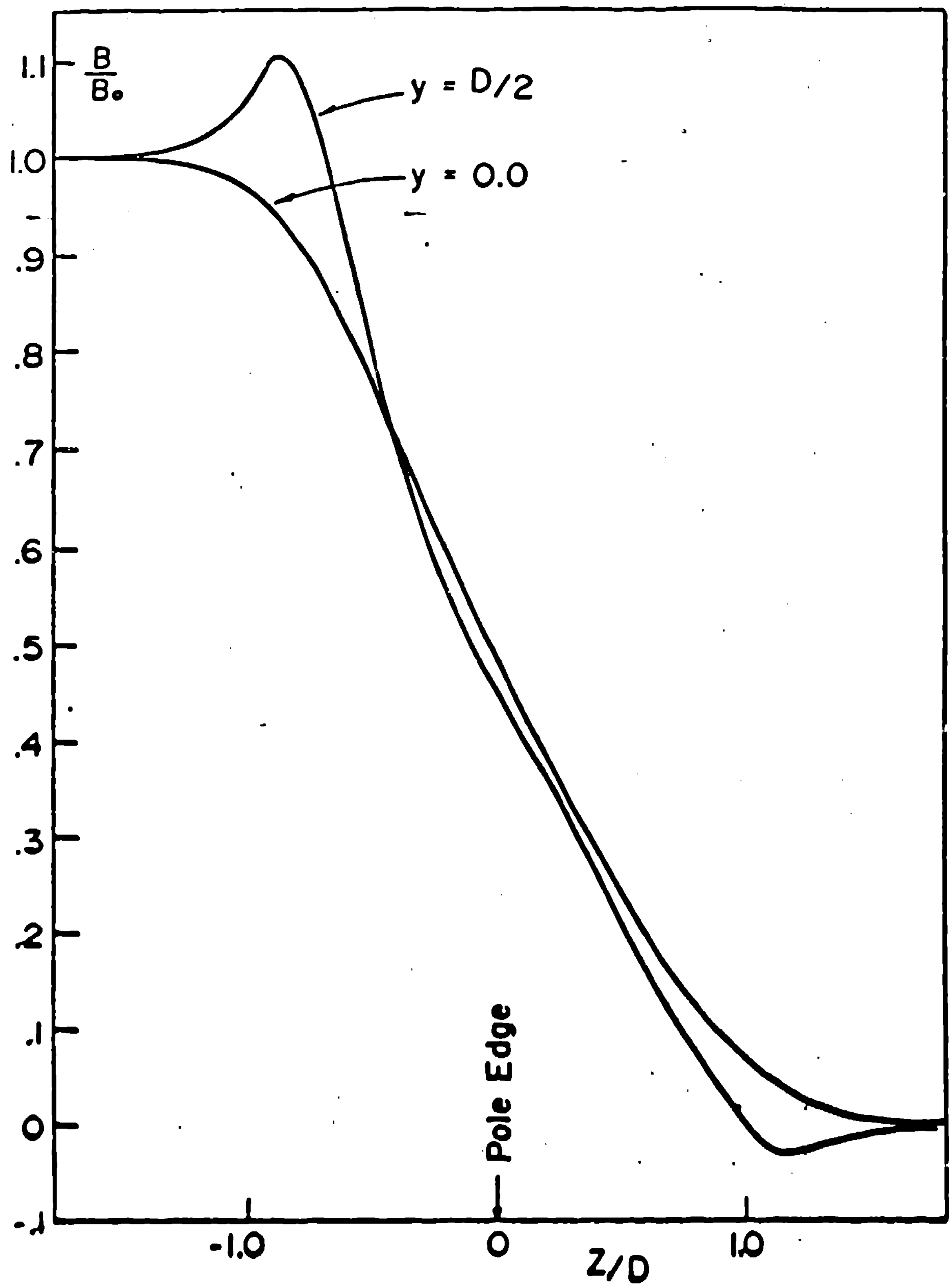

Fig.

3. -R/2 ; (Drift -R/2)
5.0A R B 2R ; (Quad, length R, half gradient)
5.0A (L-R) B R ; (Quad, length L-R, full gradient)
5.0A R B 2R ; (Quad, length R, half gradient)
3. -R/2 ; (Drift -R/2)

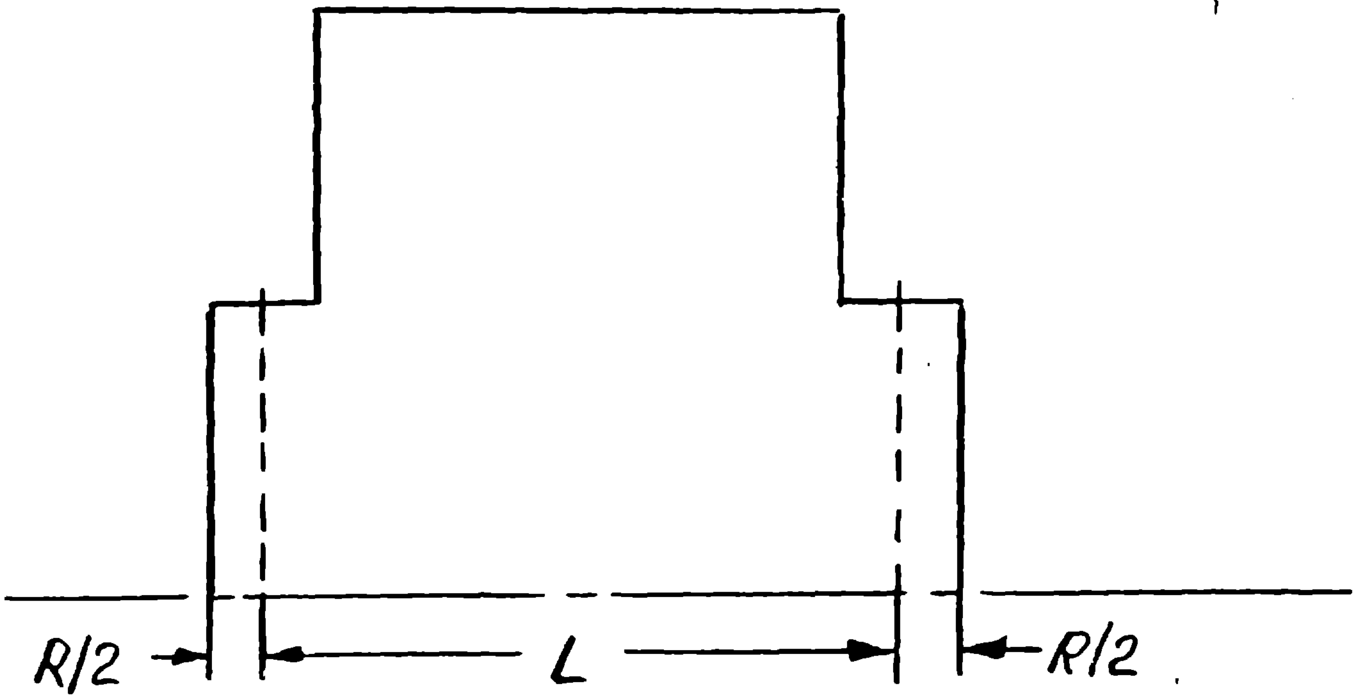

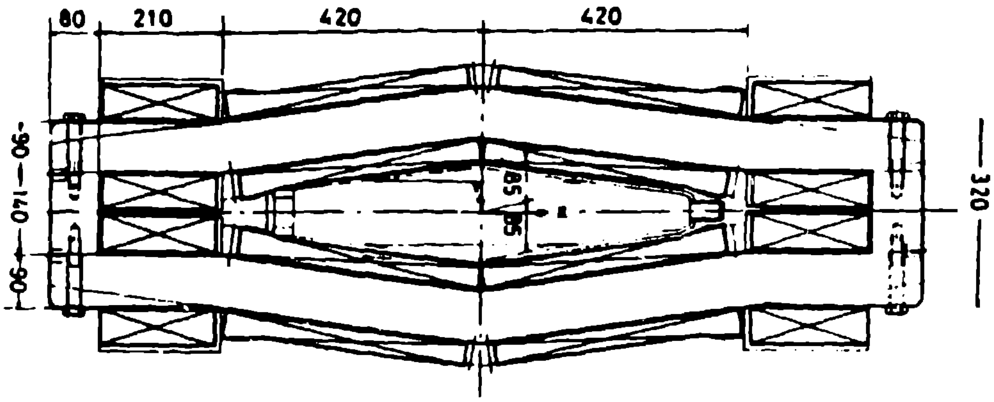

(a)

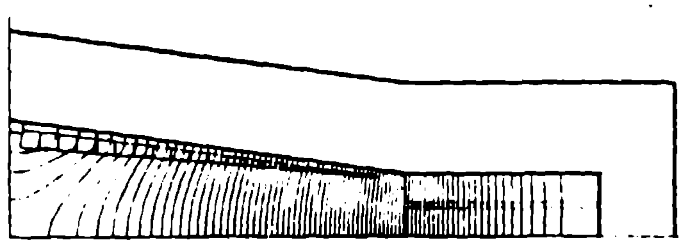

(b)

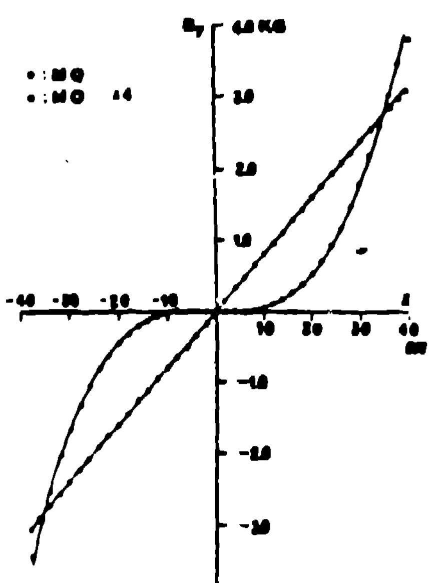

(a)

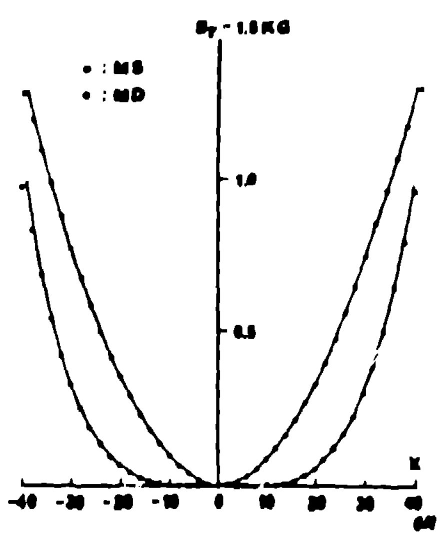

(b)

III. Ray Tracing

The motion of a particle carrying a charge Q is governed by the Lorentz force,

$$\vec{F} = Q[\vec{E} + \vec{v} \times \vec{B}], \tag{3}$$

where $\vec{E}$ is the electric field and $\vec{B}$ is the magnetic field. In a rectangular (x, y, z) coordinate system, the equations of motion along each of the axes may be written as

$$\begin{aligned} d(m\dot{x})/dt &= Q(E_x + v_y B_z - v_z B_y) \\ d(m\dot{y})/dt &= Q(E_y + v_z B_x - v_x B_z) \\ d(m\dot{z})/dt &= Q(E_z + v_x B_y - v_y B_x) \end{aligned} \tag{4}$$

In **RAYTRACE**, the equations of motion are solved by means of a step-by-step numerical integration with time as the independent variable. A fourth-order Runge-Kutta integration routine is used. When sufficiently small step sizes are taken, the accuracy is limited only by the uncertainties in our knowledge of the electric and magnetic fields. Round-off errors are negligible if the standard double-precision version of **RAYTRACE** is used. Various routines describe the field distribution in terms of a few simple parameters for each type of element. Most of these parameters are directly related to dimensions and specifications on an engineering drawing of the element. The modular nature of the code allows easy access for addition of new devices or modification of the "field" routines to correspond to specific needs.

In most of the elements, the particle typically moves through three distinct regions: the entrance fringing field, the "uniform" field and the exit fringing field. Fig. 2 shows, as an example, the layout for a dipole magnet. The different coordinate systems are related by a non-real geometrical ray ABCD which is a straight line from A to B, a circular arc from B to C, and a straight line from C to D. All calculations are made with reference to the four rectangular coordinate systems with origins at A, B, C and D. The rest of the dipole parameters are discussed in detail in Sec. V.

Each element has an input coordinate system and an output coordinate system such as A and D for the DIPOLE. The output coordinate system of one element coincides with the input coordinate system of the next element. As presently written, the code can handle 200 elements and trace 100 rays through them.

The program calculates the path of one particle at a time through all elements of the system. If desired, every step is printed out on a single line giving the independent variable, time (converted to path length into the system), position, velocity components, field components and the angles θ and ϕ indicating directions relative to the yz-plane and the xz-plane.

There are three options for a final coordinate system in which the positions and directions of the rays are given:

a) the D-axis system of the final element

b) z-axis along the projection of ray number 1 on the xz-plane, origin at $z_D = 0$

c) z-axis as for case b but with origin where the projections (on the xz-plane) of ray 1 and ray 2 intersect.

Fig. 3 shows the positions of three "focal axes" systems relative to the D coordinate system for the final element. The positions of the origins for different energies form a focal surface. For a spectrometer the detectors are placed on or near this focal surface.

A set of fourteen rays with specified initial angles θ and ϕ, and all originating from the same point (the source), can be used to calculate transfer coefficients depending upon θ and ϕ only, from first to fifth order (e.g., $x/\theta^2\phi^2$). If the fourteen rays are run for five different energies, the program will calculate the focal plane angle and chromatic aberration coefficients such as $x/\theta^2\delta^3$, etc. Another option is to use a specified set of 46 rays to calculate first, second and third order coefficients for x, θ, y, and ϕ at the exit in terms of x, θ, y, ϕ at the entrance and $\delta = \Delta p/p$.

The units used in **RAYTRACE** are:

lengths:	**cm**
angles, general:	**degrees**
beam direction:	**milliradians**
energy:	**MeV**
magnetic fields:	**Tesla**
electric fields:	**kV/cm**

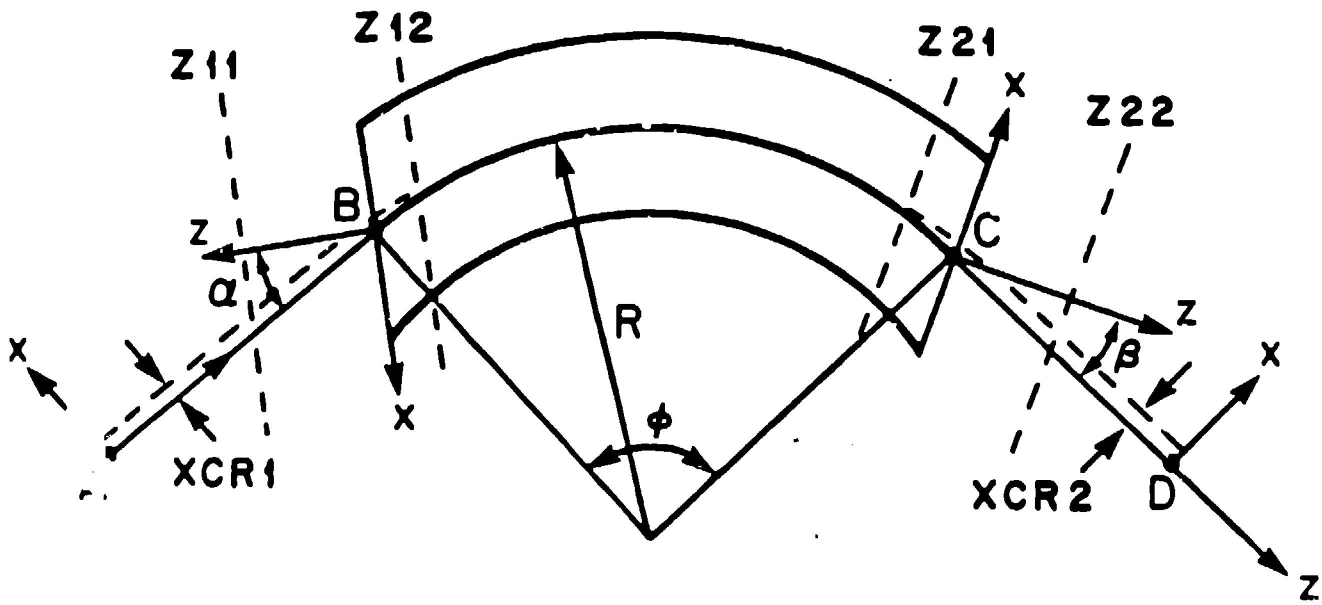

Figure 2. Definition of the most important parameters used in the DIPOLE subroutine.

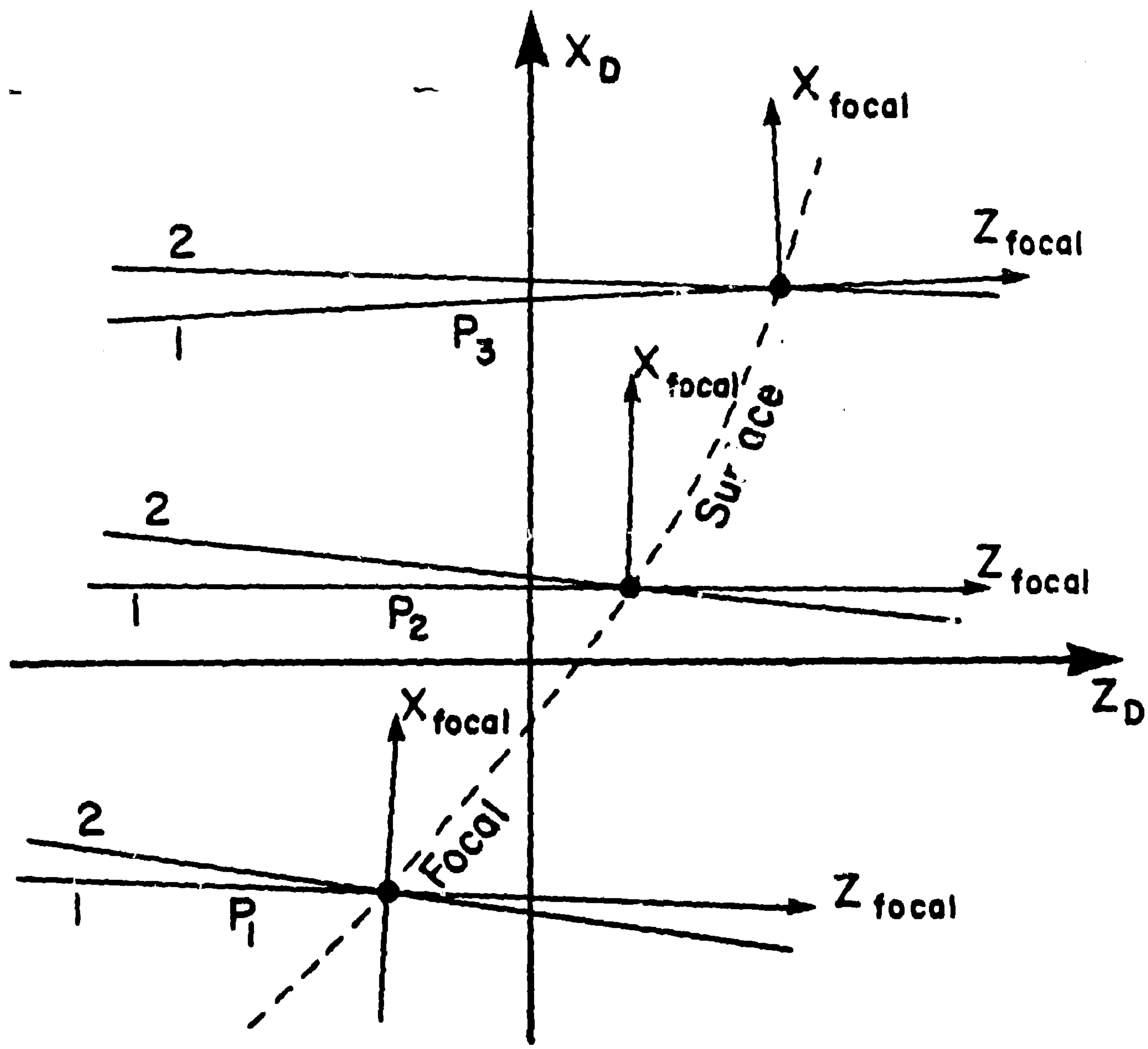

Figure 8. Output coordinate system formed at the intersection of Ray 1 and Ray 2 for three different momenta

9

V. Element Routines

A. DIPOLE. Magnetic Dipole.

The dipole subroutine requires 12 records in the input data file. A short description of these records is given in Appendix 1. A more detailed description of the subroutine is presented here. However, it is necessary first to discuss in some detail the meaning of the term "the effective field boundary" (EFB).

Fig. 4 shows a set of pole profiles with coil cross sections used in a modern dipole (for a spectrometer). The 30° and 75° cuts produce a crude approximation to a Rogowski profile.[5] The three examples show a "regular" profile, a profile with "field clamp" (magnetic short-circuit), and one with a removable insert used to adjust the position of the "Effective Field Boundary" (EFB). The dash-dotted lines indicate the positions of the EFB, defined as the position of sharp cutoff of the field with the same field integral as the real distribution assuming the integration is performed along a straight line. Two practical questions need to be discussed:

1. What is the meaning of the term Effective Field Boundary for a charged particle which moves along a curved path?

2. What is the position of the Effective Field Boundary if the mechanical boundary has a curvature?

As far as **RAYTRACE** is concerned, the first question can be dismissed immediately as irrelevant. The program needs a prescription for calculating the field at a given point in the fringing field region, given some pole profile and given some curvature of the mechanical pole boundary projected on the xz-plane.

The second question is more difficult to answer, especially if the curvature called for is not a simple circular one, concave or convex. This problem has been resolved by redefining the EFB as a mechanical reference boundary – a curve following the mechanical shape of the pole piece. The position of the EFB, relative to the pole piece is the position calculated on the assumption that the boundary is straight. With tapered poles such as shown in Fig. 4, the taper should preferably be of such a depth that the EFB coincides with the contour at the root of the pole. This makes the engineering design and installation much easier and less prone to errors.

1) MTYP=1 (Homogeneous Field): General Description

The DIPOLE subroutine has six options identified with a parameter called MTYP with values 1 through 6. The data records are very similar for all six, and the particle tracking through the magnet is similar for all. The difference lies in the field descriptions, both in the fringing and "uniform" fields. The following general description applies to a homogeneous field magnet (MTYP=1) with the simplest treatment of the fringing field. The differences between the MTYP's are then described in subsequent sections.

The general layout of a magnetic dipole is shown in Fig. 2, where the most important parameters are defined. The input coordinate and velocity components of a particle are given in coordinate system A. The first step is to make a transformation to system B.

$$
\begin{aligned}
x_B &= (A - z_A)\sin\alpha - (x_A + \mathrm{XCR1})\cos\alpha \\
y_B &= y_A \\
z_B &= (A - z_A)\cos\alpha + (x_A + \mathrm{XCR1})\sin\alpha \\
(v_x)_B &= -(v_z)_A \sin\alpha - (v_x)_A \cos\alpha \\
(v_y)_B &= +(v_y)_A \\
(v_z)_B &= -(v_z)_A \cos\alpha + (v_x)_A \sin\alpha
\end{aligned}
\tag{5}
$$

The constant XCR1 appears in Fig. 2. Its significance is discussed later. The particle is next carried along a straight line to the beginning of the entrance fringing field as defined by the parameter Z11. Note that the

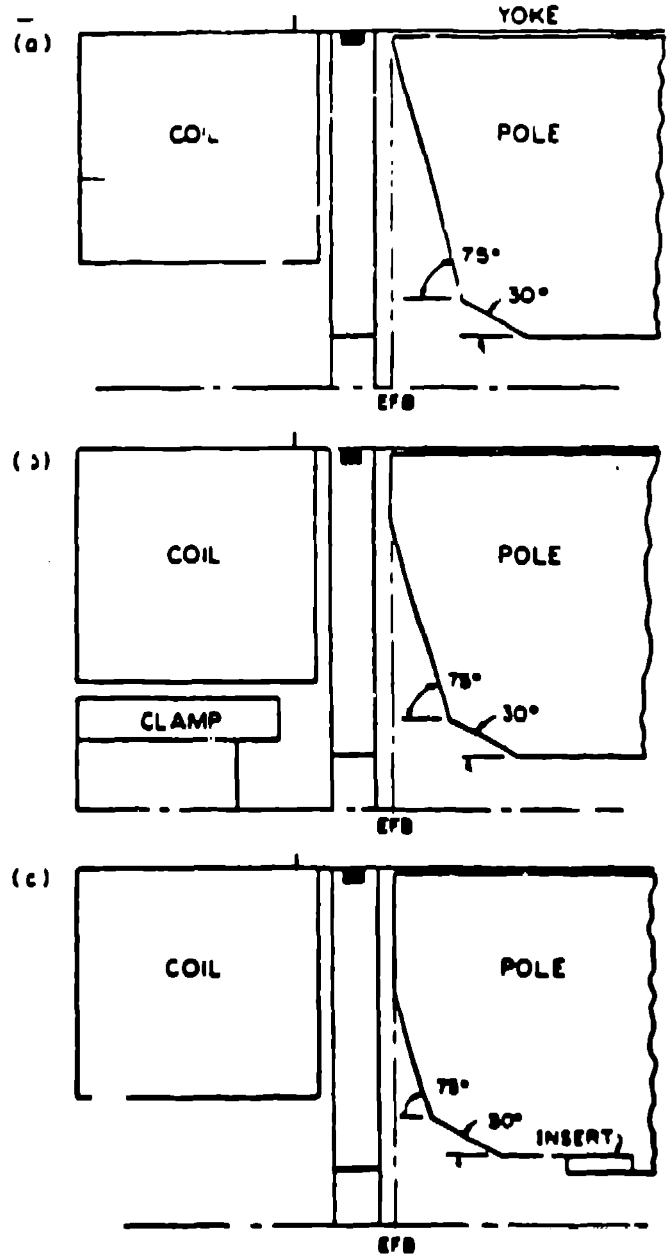

Figure 4. Rogowski pole profiles for three different cases. All are designed such that the Effective-Field Boundary (EFB) approximately coincides with the upper portion of the pole.

"object distance" A can be zero or even negative. The "image distance" B of one element and the "object distance" A for the next must, of course, add up to the physical distance between the elements. How this distance is divided is dictated by where the user wants to see an intermediate printout.

Consider first a particle moving in the median plane. The particle is carried through the entrance fringing field zone by numerical integration of the equations of motion with a magnetic field given by

$$B_y = \frac{B_0 - B_R}{1 + e^S} + B_R \tag{6}$$

in the median plane. B_0 is the uniform field (MTYP=1) inside the gap of the magnet, B_R is the asymptotic constant field outside the magnet (normally 0) and S is a parameter that increases monotonically with z (in the B-axis system). It is expressed as a power series in the parameter s:

$$S = C00 + C01s + C02s^2 + C03s^3 + C04s^4 + C05s^5. \tag{7}$$

For a straight-line effective field boundary (EFB), we have

$$s = z/D \tag{8}$$

where D is the magnet airgap. Equation (6) gives the correct asymptotic behavior of the field for $z \to \pm\infty$ provided C05 is positive. The basic integration step size in the entrance fringing field is LF1 which is an input parameter (Appendix 1). The recommended value is LF1= $0.3D$ or smaller.

The coefficients in Eq. (7) are generally determined by a least-square fit between the field given by Eqs. (6,7,8) and either a measured field or a field calculated by the aid of programs such as POISSON[7]. We generally find that the exact shape of the fringing field curve is not so important for the optical properties of a dipole, provided the coefficients used produce an effective-field boundary at $z = 0$ and approximately the correct slope for the curve B vs. z. For details see Ref. 8.

If the EFB is curved, a correction $\Delta s = \Delta z/D$ is made to Eq. (7) with Δz given by

$$\Delta z/R = -[\mathrm{S02}(x/R)^2 + \mathrm{S03}(x/R)^3 + \cdots + \mathrm{S08}(x/R)^8] \tag{9}$$

Here R is the layout radius for the dipole and the S0n's are coefficients describing curvatures of 2nd and 3rd orders, etc. This simple correction ($\Delta s = \Delta z/D$) applies to MTYP=1 only.

If the curvature of the EFB is circular, one can, instead of the S0n's, read in a parameter RAP1 (RAP2 for the exit) which is the inverse of the radius of curvature in cm^{-1}. The program will then convert RAP1 to a power series in (x/R) with even order terms up to eighth order. If the data also contains non-zero parameters S02, etc., these will be added to those calculated from RAP1 (RAP2). RAP1 and RAP2 are positive for convex boundaries.

The program continuously tests whether or not the particle has passed the plane z =-Z12. If the particle has passed the plane on a given step, it is brought back to the previous point and carried forward with a reduced step size such that it lands approximately on the plane. The coordinates are then transformed to system C at the exit effective edge.

$$\begin{aligned}
x_C &= -x_B \sin(\varphi - \alpha - \beta) - z_B \cos(\varphi - \alpha - \beta) - 2R \sin\frac{\varphi}{2} \sin(\frac{\varphi}{2} - \beta) \\
y_C &= y_B \\
z_C &= -x_B \cos(\varphi - \alpha - \beta) + z_B \cos(\varphi - \alpha - \beta) - 2R \sin\frac{\varphi}{2} \cos(\frac{\varphi}{2} - \beta) \\
(v_x)_C &= -(v_x)_B \sin(\varphi - \alpha - \beta) - (v_z)_B \cos(\varphi - \alpha - \beta) \\
(v_y)_C &= (v_y)_B \\
(v_z)_C &= -(v_x)_B \cos(\varphi - \alpha - \beta) + (v_z)_B \sin(\varphi - \alpha - \beta)
\end{aligned} \tag{10}$$

The integration through the uniform part of the field is straightforward with $B_y = B_0$. Again, the program continuously tests whether or not the particle has passed the plane z =Z21, and a correction is made such that it lands approximately on the plane. It is then carried through the exit fringing field where the field description is identical to that of the entrance fringing field with the appropriate parameters. After the particle has been deposited approximately on the plane z =Z22, a coordinate transformation is made to system D.

$$
\begin{aligned}
x_D &= z_C \sin\beta + x_C \cos\beta - \mathrm{XCR2} \\
y_D &= y_C \\
z_D &= z_C \cos\beta - x_C \sin\beta - B \\
(v_x)_D &= (v_z)_C \sin\beta + (v_x)_C \cos\beta \\
(v_y)_D &= (v_y)_C \\
(v_z)_D &= (v_z)_C \cos\beta - (v_x)_C \sin\beta
\end{aligned}
\tag{11}
$$

The particle is then translated along a straight line until it intersects the xy-plane ($z_D = 0$) of that system.

If the path length of a particle inside the dipole is relatively short, it may never be in anything close to a uniform field. The recommendation is then *not* to reduce the absolute values of Z12 and Z21 but to let the two fringing field zones overlap. The program then integrates the equations of motion *backwards* through the uniform field. Fig. 5 illustrates the effect of this procedure. The total field integral corresponds to the area under the partially dashed curve in Fig. 5 . The result is essentially that in the middle the deficiencies for both curves are added to produce a total deficiency as shown. This procedure simplifies the work for the designer. He does not have to worry about overlap, wholly or partially, by the fringing field zones. One warning is in order, though: the particle orbit must intersect the beginning of the exit fringing field zone either by moving forward or backwards; otherwise, it will start moving in circles in a uniform field. The program cuts off the integration after 200 steps in either zone and prints out the message: "Exceeded maximum number of steps in element i, zone j".

For particles moving off the median plane, the formula for the component B_y is modified and the components B_x and B_z are also evaluated. This is done by Taylor expansions in y through third order for B_x and B_z and through fourth order for B_y. Symmetry about the median plane insures that B_x and B_z contain only odd orders of y and B_y only even orders. The corresponding expressions are

$$
\begin{aligned}
B_x &= (y/1!)\partial B_x/\partial y + (y^3/3!)\partial^3 B_x/\partial y^3 \\
B_y &= B_y + (y^2/2!)\partial^2 B_y/\partial y^2 + (y^4/4!)\partial^4 B_y/\partial y^4 \\
B_z &= (y/1!)\partial B_z/\partial y + (y^3/3!)\partial^3 B_z/\partial y^3
\end{aligned}
\tag{12}
$$

where the fields and their derivatives on the right hand side are to be evaluated at $y = 0$.

The derivatives appearing in these equations are all computed by the use of Maxwell's equations converting derivatives of the kind $(\partial^{i+j} B_y/\partial x^i \partial z^j)_{y=0}$ into the desired forms. The derivatives of B_y in the median plane are determined numerically by calculating $(B_y)_{y=0}$ in a thirteen-point grid. Fig. 6 shows such a grid. The grid constant DG is an input parameter (see Appendix 1) which should be given a value of the order of $0.3D$. The results of the Taylor expansions (with $\Delta = DG$) are

$$
\begin{aligned}
B_y = B_{00} &- \frac{y^2}{\Delta^2}\left[\frac{2}{3}(B_{10} + B_{-10} + B_{01} + B_{0-1} - 4B_{00}) - \frac{1}{24}(B_{20} + B_{-20} + B_{02} + B_{0-2} - 4B_{00})\right] \\
&+ \frac{y^4}{\Delta^4}\left[-\frac{1}{6}(B_{10} + B_{-10} + B_{01} + B_{0-1} - 4B_{00}) + \frac{1}{24}(B_{20} + B_{-20} + B_{02} + B_{0-2} - 4B_{00})\right. \\
&\left. + \frac{1}{12}(B_{11} + B_{-11} + B_{1-1} + B_{-1-1} - 2B_{10} - 2B_{-10} - 2B_{01} - 2B_{0-1} + 4B_{00})\right]
\end{aligned}
\tag{13}
$$

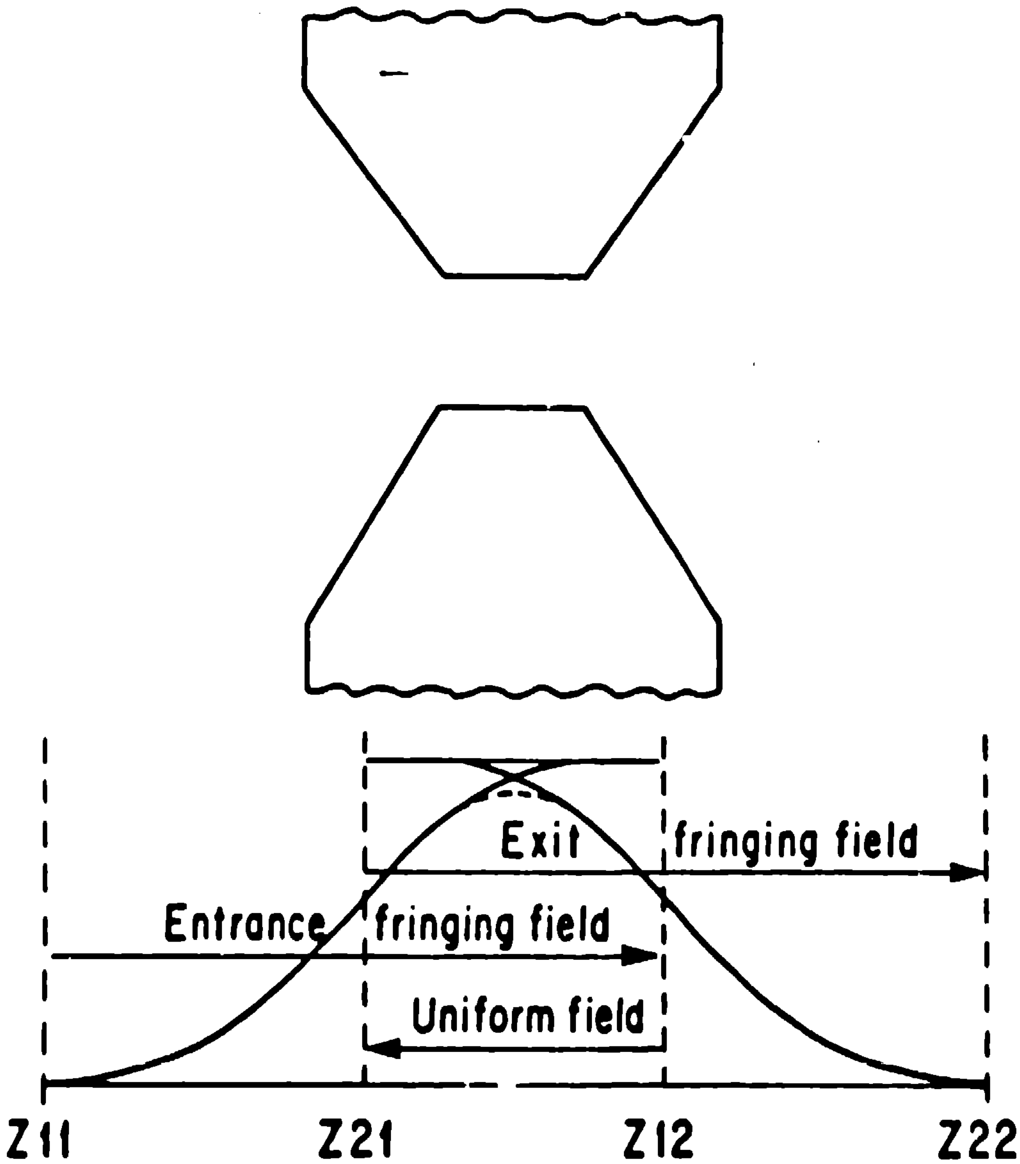

Figure 5. Overlapping fringing-field zones. The dashed curve indicates approximately what the net effect will be on the particle by the "backward" integration.

$$B_x = \frac{y}{\Delta}\left[\frac{2}{3}(B_{10} - B_{-10}) - \frac{1}{12}(B_{20} - B_{-20})\right] + \frac{y^3}{\Delta^3}\left[\frac{1}{6}(B_{10} - B_{-10}) - \frac{1}{12}(B_{20} - B_{-20}) - \frac{1}{12}(B_{11} + B_{1-1} - B_{-11} - B_{-1-1} - 2B_{10} + 2B_{-10})\right] \tag{14}$$

$$B_z = \frac{y}{\Delta}\left[\frac{2}{3}(B_{01} - B_{0-1}) - \frac{1}{12}(B_{02} - B_{0-2})\right] + \frac{y^3}{\Delta^3}\left[\frac{1}{6}(B_{01} - B_{0-1}) - \frac{1}{12}(B_{02} - B_{0-2}) - \frac{1}{12}(B_{11} + B_{-11} - B_{1-1} - B_{-1-1} - 2B_{01} + 2B_{0-1})\right] \tag{15}$$

where the subscripts refer to the index number of the points in Fig. 6.

For an MTYP=1 magnet, the coefficients describing the variation of B_y vs. radial position: n, BET1, GAMA and DELT (Appendix 1) are zero. If the data record for these constants has non-zero values, these values are ignored.

In the input data there appear four more constants that need explanation. The first two are XCR1 and XCR2, both of which are identified in Fig. 2. The layout ray for the dipole connecting the origins of the four coordinate systems is a non-real ray consisting of a straight line, a circular arc and another straight line. No real particle will follow this trajectory. If one, somewhat arbitrarily, insists that a ray defined as the central ray shall follow the layout circular arc inside the magnet – and therefore have a magnetic rigidity of $B_0 R$ – corrections must be made outside. That is, one must shift the magnet relative to the centerline of other optical elements by an amount[8]

$$\mathrm{XCR1} = D^2 I_1 / R \cos^2 \alpha \tag{16}$$

where I_1 is an integral that depends upon the shape of the fringing field. Its value varies from $I_1 = 0.3$ for a "short-tail" fringing field to about $I_1 = 0.7$ for a "long-tail" fringing field. The shift at the exit is similar with α replaced by β. For a symmetric magnet ($\alpha = \beta$), the shifts may not be necessary in practice. A particle moving along the z_A axis can be made to exit along the z_D axis by adjustment of the magnetic field. It will then move on an inside track relative to the layout arc inside the magnet. The corrections discussed here are a nuisance for the engineer who is laying out the system and should not be used unless they are important. Whether or not they are used, **RAYTRACE** will always predict the correct positions and angles of the rays traced.

The two remaining dipole parameters are DELS1 and DELS2. These can be used to shift the positions of the effective field boundaries at entrance and exit, respectively. For instance, if field mapping indicates that the EFB at entrance is off by an amount Z_{err} into the magnet from its intended position, **RAYTRACE** can be re-run with

$$\mathrm{DELS1} = Z_{err}/D \tag{17}$$

In general, Eq. (8) now becomes (for MTYP=1)

$$s = (z + \Delta z)/D + \mathrm{DELS1} \tag{8}$$

Of course, DELS2 serves a similar purpose at the exit of the dipole.

In the past, DELS1 has been used to correct for the position of the effective field boundary due to the curvature of the boundary. The effective field boundary for a magnet with convex curvature is closer to the magnet than when the boundary is straight - assuming the same pole piece profile. If the same coefficients C00-C05 are used to describe the fringing field for both cases, DELS can be used to correct the position of the EFB but, of course, not the shape of the $B_y(s)$ curve.[9] In the current version for MTYP=2, we attempt to make the correction due to curvature in a more direct way, applicable to a boundary of any shape (within reason) and without the use of DELS.

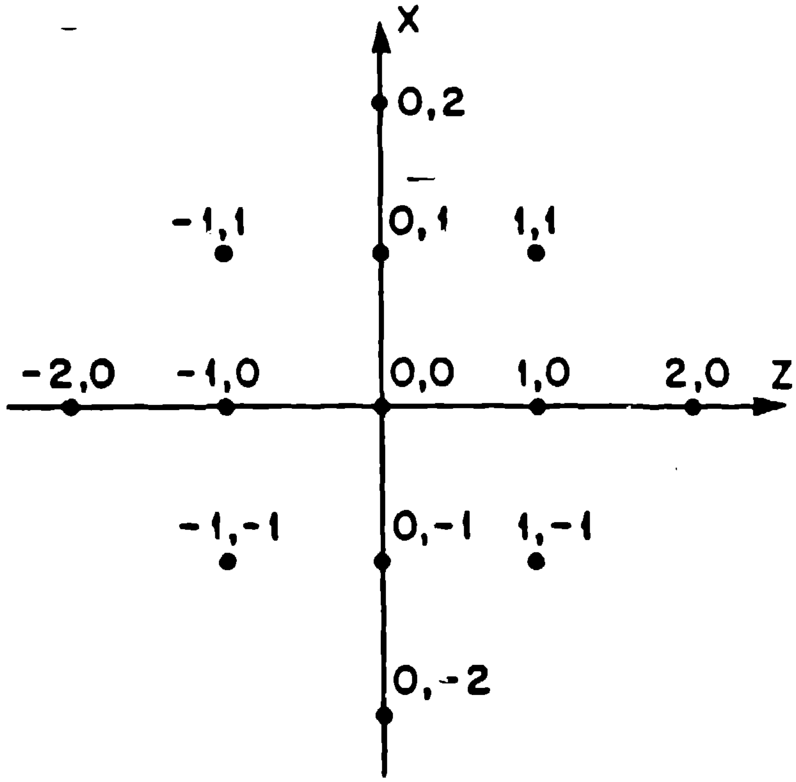

Figure 6. Thirteen-point grid used to determine numerical derivatives of B_y in the median plane.

A new feature has been added to the dipole routines, MTYP=1,...,5. The field distribution on the median plane of the fringing field can be calculated and stored in an array with a distance DG between neighbouring points. When a ray is traced through the fringing field zone, the field on the median plane for a given point is determined by interpolating between neighbouring grid points. If the particle is not in the median plane, the interpolation routine must be used thirteen times and the field components calculated as described earlier (Eqs. 13-15).

This new feature can result in a considerable saving in computer time when a large number of rays are to be traced or when the system contains a number of identical dipoles. The feature is activated by specifying an array number IMAP for the dipole (see Appendix 1). Identical dipoles would have the same value for IMAP≤5.

The array on the entrance side will have n_x n_z points where

$$n_x = (\mathrm{WDE} + 2\mathrm{Z11}\tan\alpha)/\mathrm{DG} + 6$$
$$n_z = (\mathrm{Z11} - \mathrm{Z12})/\mathrm{DG} + 6.$$

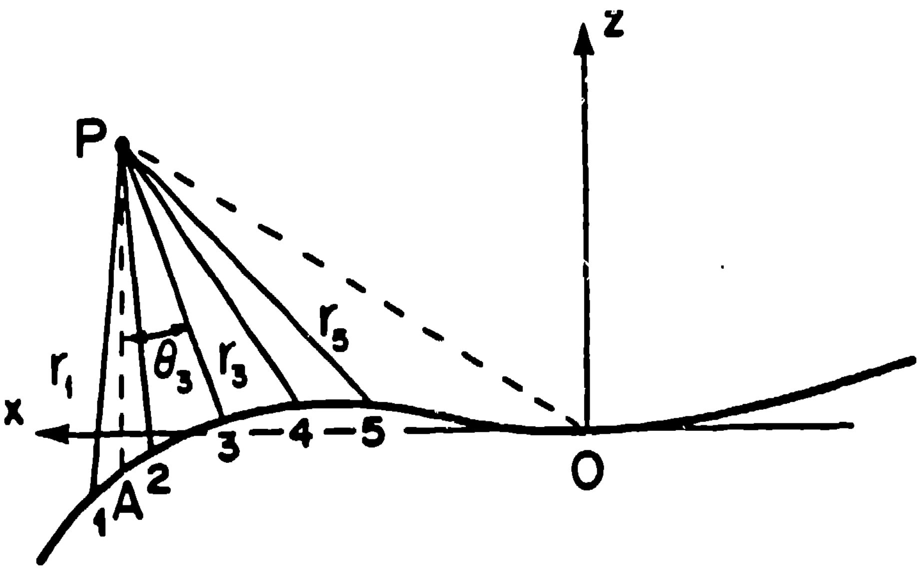

Figure 7. A spray of five "feeler rays" used to determine a represantative distance to the EFB and thereby the value of B_y.

Corresponding expressions apply to the exit side.

2) MTYP=2. Homogeneous-Field Dipole

The only difference between MTYP=1 and MTYP=2 is the way the parameter s is calculated. In both cases s represents distances to the effective field boundary. In MYTP=1 sD is simply the distance to the EFB measured in the z-direction, i.e. not generally the shortest distance. In MTYP=2 the shortest distance to the effective field boundary from a given point is determined. However, this is not simply used to calculate s as distance/D. Rather, the line representing the shortest distance is only the middle one of a spray of five lines from the point where the particle is. An average, strongly weighted towards the middle line, is then used to calculate a representative distance and thereby s. The average is weighted in such a way that if the boundary is straight, sD is exactly equal to the shortest distance.

Assume first that the shortest distance from point P to the EFB has been found. This distance, r_3 in Fig. 7, is divided by 4, and the distances to four other points 1,2,4, and 5 are determined with the relationship between the x-coordinates for the points being (see Fig. 7):

$$x_{i+1} = x_i + \frac{r_3}{4}\cos\theta_3. \tag{18}$$

The formula used to calculate s is

$$sD = 1.41875(\sum_{i=1}^{5} r_i^{-4})^{-1/4}. \tag{19}$$

The algorithm for finding the shortest distance is as follows:

a) The distance in the z-direction from point P to the EFB is determined as for MTYP=1.

b) This distance is compared to the distance from point P to the origin. The shortest of the two, call it a, is divided by 5.

c) The square of the distance from point P to 11 points on the EFB is calculated, five points on each side of point A (Fig. 7) in addition to $(z_P - z_A)^2$. Between two neighbouring points, the distance in the x-direction is $\Delta x = a/5$.

d) The 11 distances squared are compared and the smallest of these is selected.

e) The x-distance between the two points on either side of the selected shortest distance is further subdivided by 10 to $\Delta x = a/25$, and squares of distances are calculated between the field point P and the points on the field boundary.

f) Again the smallest of the 11 squares and its smallest neighbour are selected. Call the distance to the point with the lowest x-value r_1 and call the other r_2.

g) Another subdivision is now performed to find an even shorter distance, but this time by the use of some trigonometry (see Fig. 8). It is assumed that the EFB between the two points (with $\Delta x = a/25$) can be considered to be a straight line. This is line c, the length of which is grossly exaggerated compared to r_1 and r_2 in Fig. 8. Some elementary trigonometry applied to the triangles in Fig. 8 yields

$$x_3 = x_1 + \frac{c^2 + r_1^2 - r_2^2}{2c^2}(x_2 - x_1) \tag{20}$$

This then determines the central point on the EFB for the spray of five lines, discussed above.

As explained earlier for MTYP=1 when the particle is off the median plane, the field B_y in the median plane must be determined 13 times such that the appropriate derivatives can be calculated. The relative accuracy of these determinations of B_y-values has to be high, especially if y/DG is much larger than unity (see Eq. 13).

We call the representative distance for the central point s_0D. The corresponding values for the other twelve points are then determined as

$$sD = s_0D + \Delta sD \tag{21}$$

where ΔsD is given by (see Fig. 9)

$$\Delta sD = s_0D + \mathrm{DG}(i\cos\delta - j\sin\delta) - (z_{s_1} - z_P + A\sin\delta)\cos\delta \tag{22}$$

111

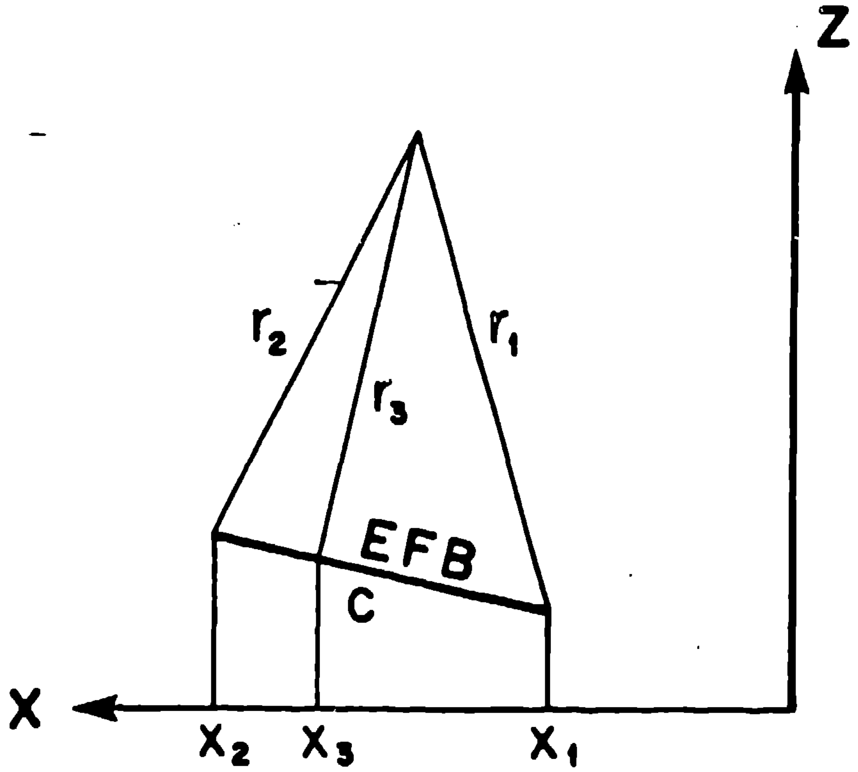

Figure 8. Trigonometry used to evaluate the shortest distance between the field point and the boundary.

with

$$A = DG(j\cos\delta + i\sin\delta), \tag{23}$$

$$x_1 = x_P + A\cos\delta$$

and

$$\delta = \arctan(dz/dx) \tag{24}$$

at the point P. The two indices i and j identify the grid point. They are the numbers appearing in Fig. 6.

Since the Runge-Kutta integration routine looks up the field components B_x, B_y, and B_z four times for each integration step, altogether 52 values of sD have to be determined for each integration step.

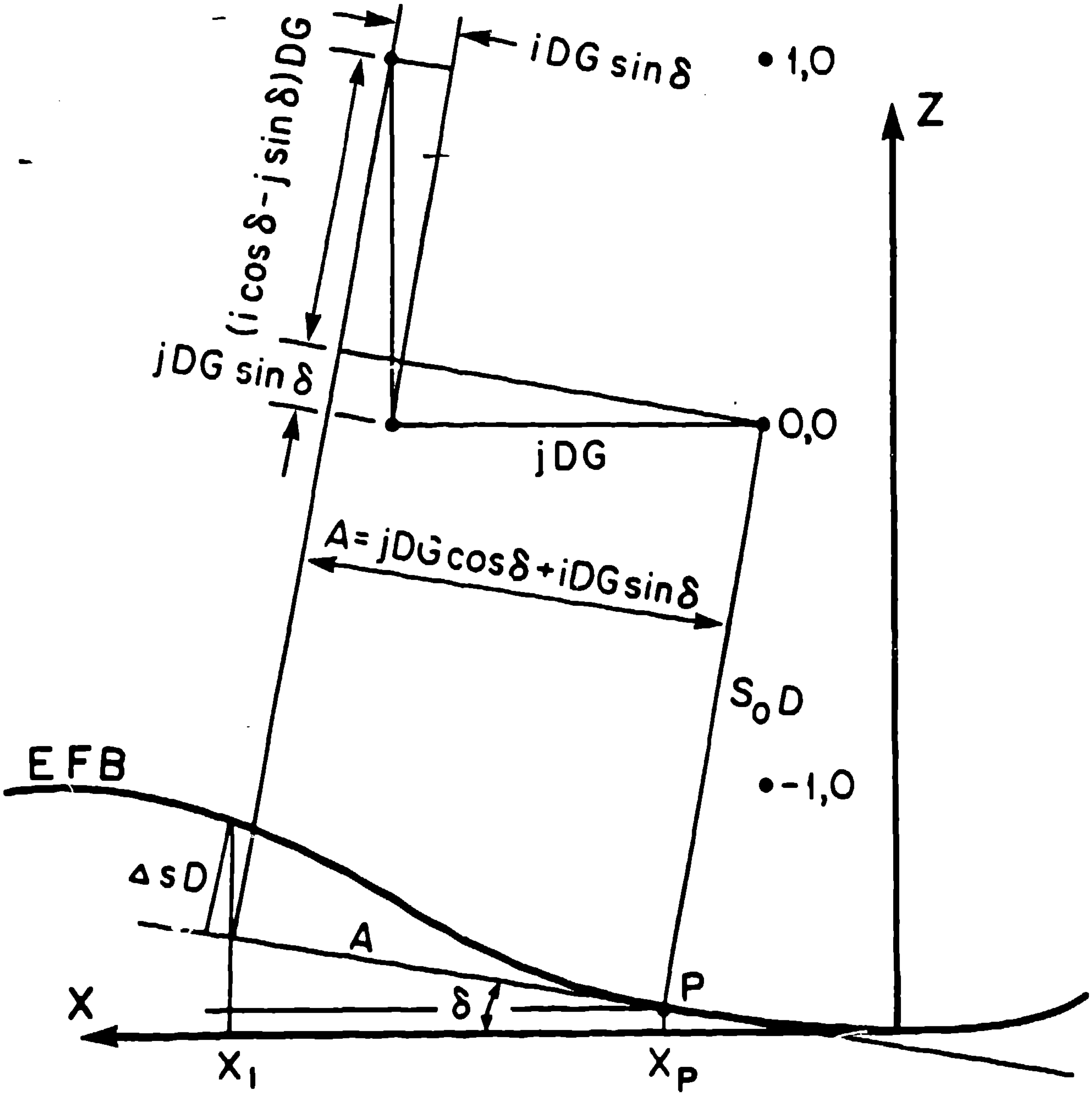

Figure 9. Geometry used for determining corrections to sD which are required for calculating off-midplane components of B.

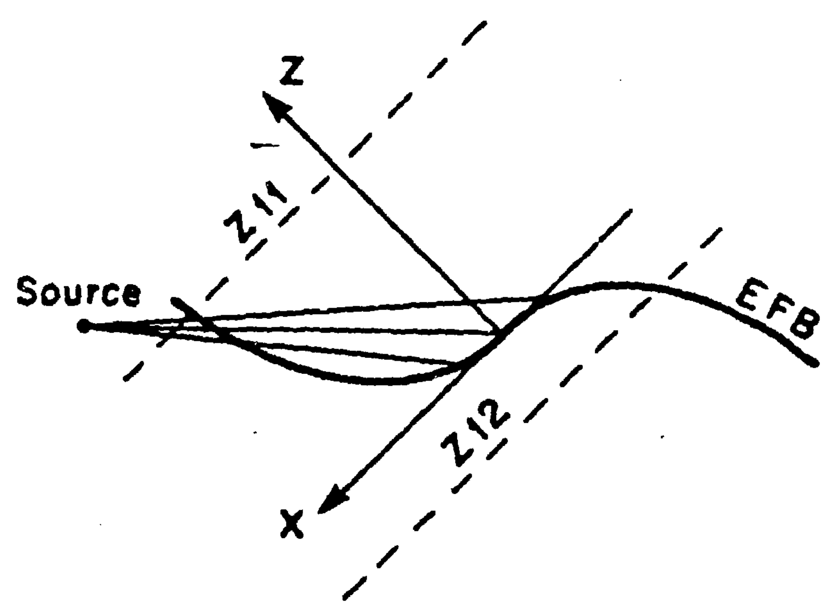

Figure 10. Possible result of an indiscriminate use of the parameters SO2, etc. that describe the shape of the EFB.

The program, of course, determines whether the integration point is inside or outside the EFB. With any reasonable boundary corresponding to a practical magnet, the computer should have no trouble in finding the shortest distance to the boundary. It is, however, possible for the ion-optical designer to confuse the computer with indiscriminate use of higher order corrections. Fig. 10 shows an example that speaks for itself. It is generally wise to use eighth order terms S08 and S18 to represent the limited width of the pole pieces. For instance, if the pole width is W as measured in the x-direction, an eighth-order correction term S08$=50DR^7/W^8$ will push the EFB towards the corner of the pole piece by an amount $-\Delta z = 0.2D$ at $x = \pm W/2$. This is the right order of magnitude.

3) MTYP=3. Dipole with Field Gradient.

MTYP=3 is used for a dipole with nonzero value for any of the parameters n, BET1, GAMA, or DELT. This includes otherwise uniform-field magnets for which one wishes to study the effect of limited pole face width. The fourth order term DELT is then probably the most appropriate term to use. The field description on the median plane in the "uniform" region for MTYP=3 is

$$B_y = B_0[1 - n\Delta r/R + \mathrm{BET1}(\Delta r/R)^2 + \mathrm{GAMA}(\Delta r/R)^3 + \mathrm{DELT}(\Delta r/R)^4] \quad (26)$$

and the field off the median plane is determined by a Taylor expansion in y using analytic derivatives.

B. Dipole (12 records)

Record	Variable		Format
1	DIPOLE		A4
2	LF1	- Entrance fringing field integration step size (cm)	6F10.5
	LU1	- Uniform field integration step size (cm)	
	LF2	- Exit fringing field integration step size (cm)	
	DG	- Differential step size used in determining off mid-plane components of B using numerical differential methods. Recommended for all four step sizes: 0.3D (D=Gap) although LU1 can be made larger to save computer time. For MTYP=6, DG serves another function. See Sec. V. A.	
	MTYP	- Magnetic dipole option MTYP=0,1 - Uniform field dipole. Fringing field determined by calculation of the distance to the effective field boundary in the z-direction. MTYP=2 - Uniform field dipole. Fringing field determined as described in Sec. V.A. MTYP=3 - Non-uniform field dipole with n-value and second-, third-, and fourth-order corrections. Fringing field determined as for MTYP=2, but including n-value, etc. MTYP=4 - Non-uniform field dipole - cylindrical geometry. Similar to MTYP=3 but better suited for purely conical pole pieces. This option is used to describe magnets with wedge-shaped gaps ("CLAMSHELL") by making R large, PHI small, and by setting BET1=GAMA=DELT=0 but n≠0, and normally large because R is artificially large. MTYP=5 - Uniform field dipole, circular pole option. MTYP=6 - Pretzel magnet option.	
	IMAP	- Array number for generating and identifying fringing field array maps. If IMAP=0, maps are not generated and the field components are calculated directly for each point, i.e. four times for each integration step. Two dipoles with identical values of IMAP will share a common array. IMAP≤5.	
3	A	- Distance (cm) from origin of system A (initial) to system B (situated at entrance edge EFB of magnetic element)	5F10.5

Record	Variable		Format
	B	- Distance (cm) from origin of system C (situated at exit edge EFB of magnetic element) to origin of output system D	
	D	- Gap width (cm)	
	R	- Radius of curvature (cm) used in geometrical construction of layout	
	BF	- Nominal value of the field on the central radius R (Tesla)	
4	PHI	- Angular extent between the EFB of system B and that of system C (degrees). Nominally equivalent to the bend angle	3F10.5
	ALPHA	- Angle between the central trajectory and the normal to the effective field boundary (EFB) at entrance (degrees)	
	BETA	- Angle between the central trajectory and the normal to the exit boundary (degrees). Both ALPHA and BETA are positive when the normals are outside the orbit for positive transverse plane focussing.	
5	NDX	- 'n-value', of field index for non-uniform field magnets (first-order term)	4F10.5
	BET1	- 'β-value', of field index for non-uniform field magnets (second-order term).	
	GAMA	- 'γ-value', of field index for non-uniform field magnets (third-order term).	
	DELT	- 'δ-value', of field index for non-uniform field magnets (fourth-order term).	
6	Z11	- Integration limit (cm) defining the start of the entrance fringing field zone in coordinate system B. Normally positive.	4F10.5
	Z12	- Integration limit (cm) defining the termination of the entrance fringing field zone in coordinate system B. Normally negative	
	Z21	- Integration limit (cm) defining the start of the exit fringing field zone in coordinate system C. Normally negative.	
	Z22	- Integration limit (cm) defining the termination of the exit fringing field zone in coordinate system C. Normally positive.	

B. Dipole (12 records) - Continued

Record	Variable		Format
7	C00 C01 C02 C03 C04 C05	- Coefficients used in the expansion of the fringing field fall-off at the entrance of the magnetic element.	6F10.5
8 -	C10 C11 C12 C13 C14 C15	- Coefficients used in the expansion of the fringing field fall-off at the exit of the magnetic element.	6F10.5
9	BR1	- Correction for presence of constant field in region of entrance fringe field (Tesla).	6F10.5
	BR2	- Correction for presence of constant field in region of exit fringe field (Tesla). In the Split-Pole Spectrometer, BR1 and BR2 describe the asymptotic field in the split.	
	XCR1	- Equivalent to a coordinate system shift (cm) at the entrance (element SHRT) with Δx=-XCR1. Used to correct for displacement of central ray caused by extended fringing field (see Fig. 2). Use XCR1=XCR2=0 unless the actual hardware element will be offset.	
	XCR2	- Equivalent to a coordinate system shift (cm) at the exit with Δx=XCR2. Used to correct for displacement of central ray caused by extended fringing field.	
	DELS1	- A correction to the location of the effective field boundary. The effective field boundary at entrance is moved towards the magnet (for positive Δs) by an amount Δs =DELS1$*D$.	
	DELS2	- A correction to the location of the effective field boundary. The effective field boundary at exit is moved towards the magnet (for positive Δs) by an amount Δs =DELS2$*D$.	

Record	Variable		Format
10	RAP1	- Inverse radius of curvature of entrance boundary (cm^{-1}). Convex surfaces are positive.	2F10.5
	RAP2	- Inverse radius of curvature of exit boundary (cm^{-1}). Convex surfaces are positive. In the program, except for MTYP=5, circles described by RAP1 and RAP2 are approximated with an eighth-order power series.	
–	WDE	- Mechanical width of the entrance pole boundary. Used only when IMAP is non-zero.	
	WDX	- Mechanical width of the exit pole boundary. Used only when IMAP is non-zero.	
11	S02 S03 S04 S05 S06 S07 S08	- Coefficients used in description of entrance boundary curvature. Contributions of RAP1 are added to those of S02, S04, S06, and S08.	7F10.5
12	S12 S13 S14 S15 S16 S17 S18	- Coefficients used in description of exit boundary curvature. Contributions of RAP2 are added to those of S12, S14, S16, and S18.	7F10.5

DESIGN & PERFORMANCE OF MRS

Medium-Resolution Spectrometer

Medium Energy Resolution (~ 1 MeV at 800 MeV) Identify discrete states
Good Solid Angle (~ 10 msr)
Large Momentum acceptance (± 20%)
Polarized proton and neutron beams
Net Bend Angle (18°) allows for detection of all spin projections from (300-800MeV)
Massive shielding and software traceback for good background suppression

(p,p') mode

Elastic/inelastic scattering on polarized/unpolarized light targets
Spin observables in the continuum
Coincidence experiments such as (p,p'π), (p,2p), (p,p'γ)

(n,p) mode

Third component of spin-isospin excitations (p,p), (p,n), (n,p)
Isovector spin transfer measurements to continuum
Identification of isovector resonances

Design Goals

		800 MeV p's
Momentum		
Central @17 kgauss	1500 MeV/c	
@ + 20% $\Delta p/p$	1800 MeV/c	
Full Acceptance		
Momentum Bite	± 20% $\Delta p/p$	± 250 MeV
Resolution	0.2% (FWHM) $\Delta p/p$	2.5 MeV
Solid Angle	7 msr	
Reduced Acceptance		
Momentum Bite	± 3%	± 37 MeV
Resolution	0.08% (FWHM) $\Delta p/p$	1.0 MeV
Solid Angle	9 msr	

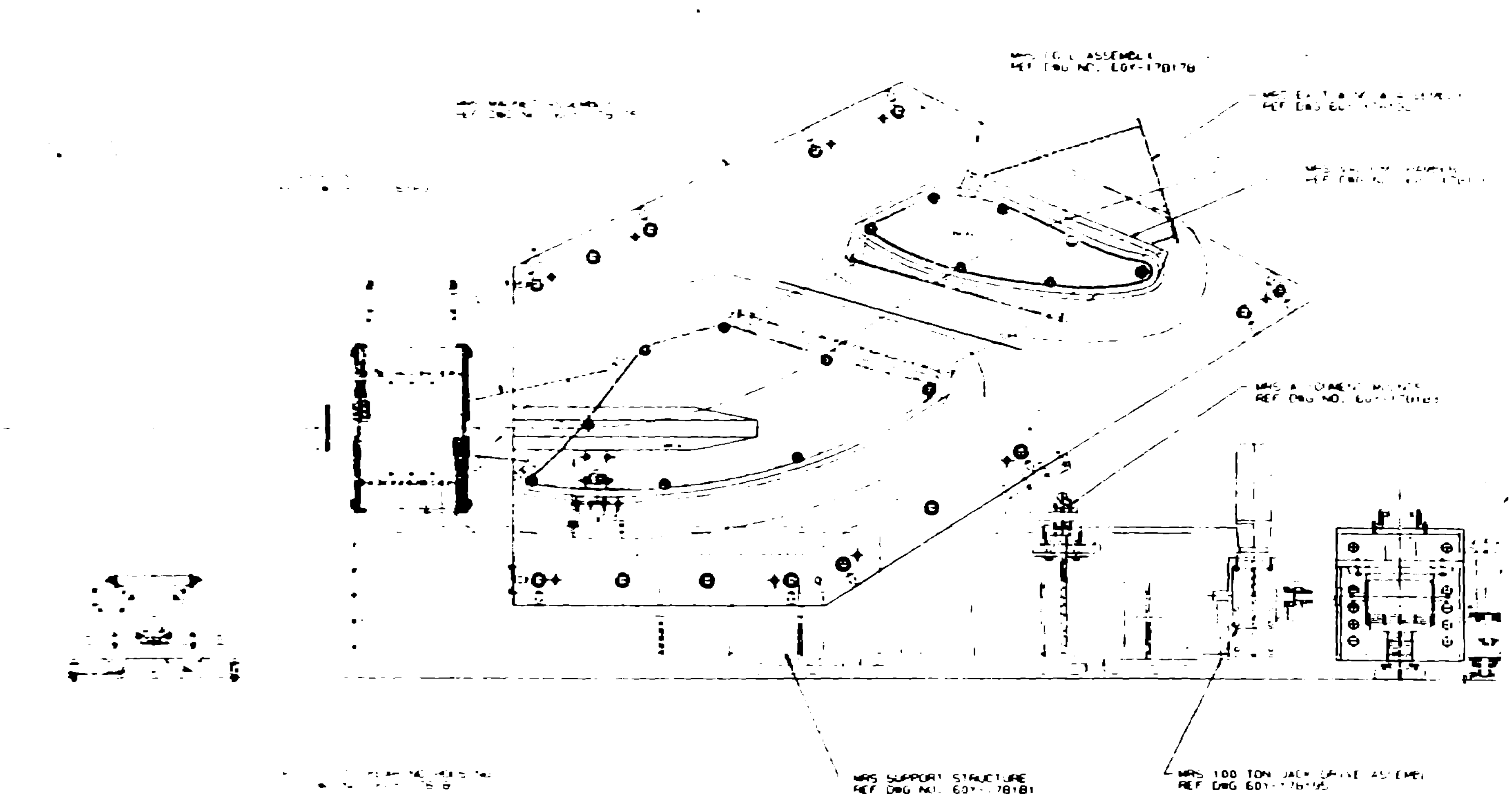

MEDIUM RESOLUTION SPECTROMETER
LAMPF

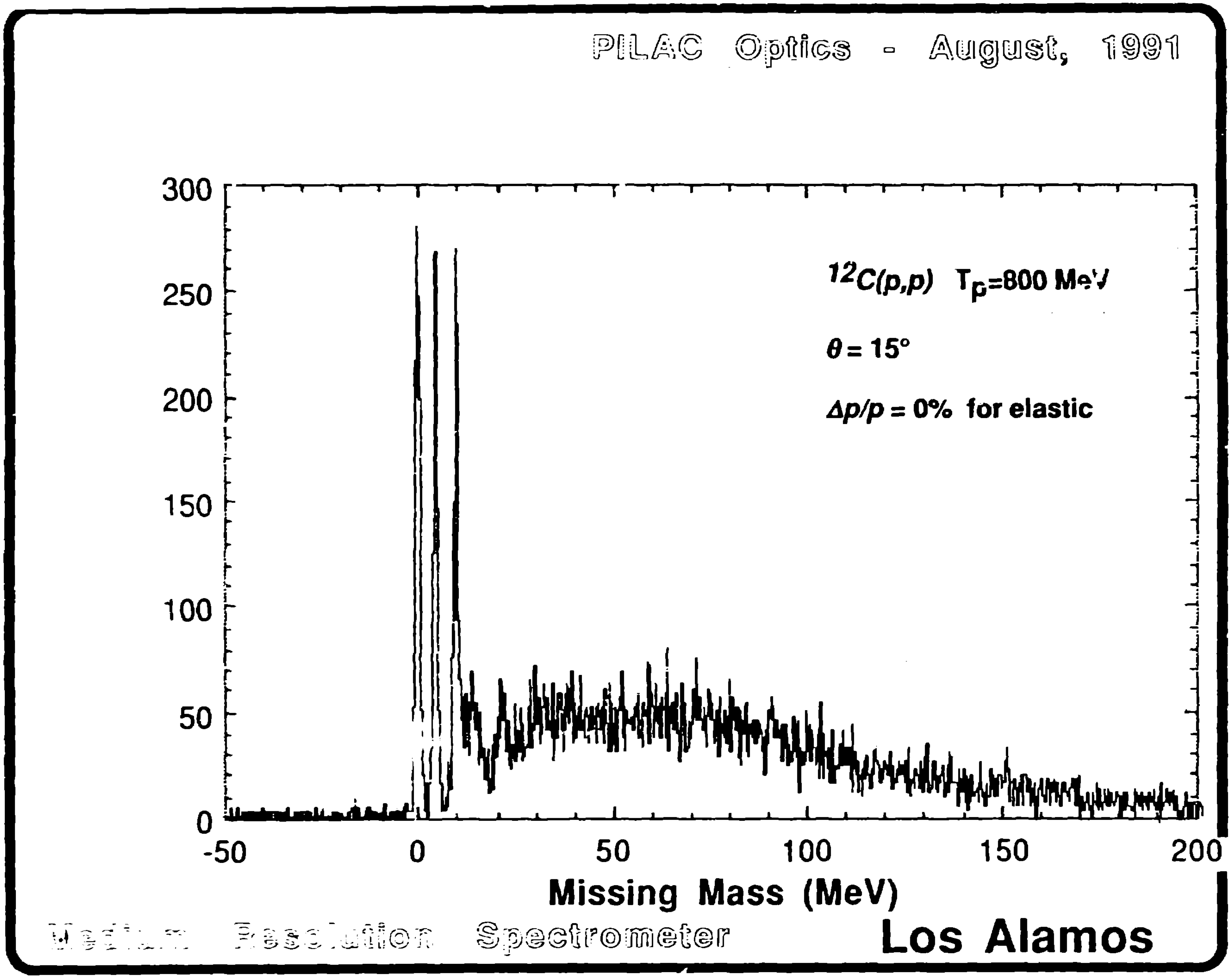
PILAC Optics - August, 1991
$^{12}C(p,p)$ T_p=800 MeV
$\theta = 15°$
$\Delta p/p$ = 0% for elastic
300
250
200
150
100
50
0
-50
0
50
100
150
200
Missing Mass (MeV)
Medium Resolution Spectrometer
Los Alamos

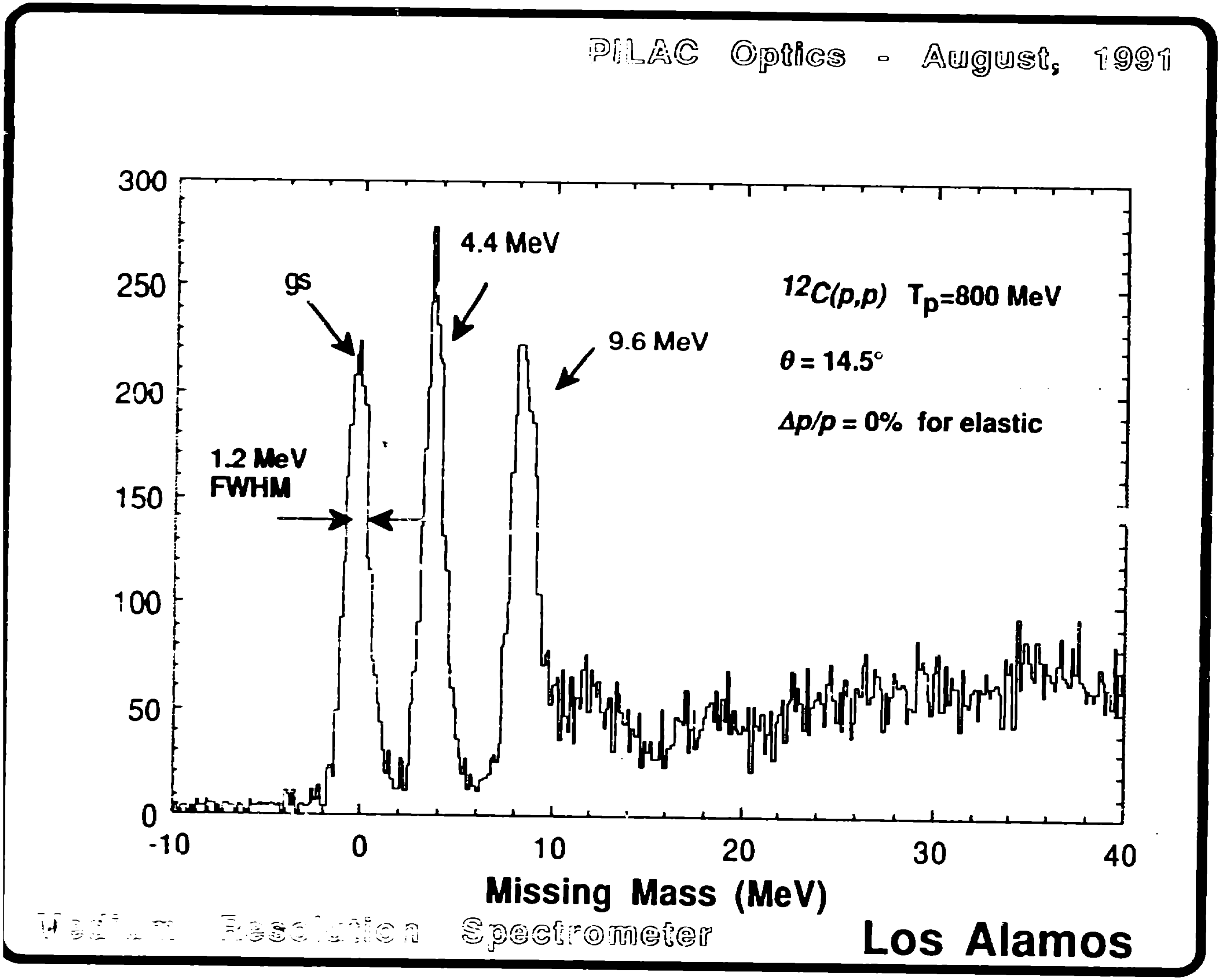
PILAC Optics - August, 1991
4.4 MeV
gs
9.6 MeV
12C(p,p) Tp=800 MeV
θ = 14.5°
Δp/p = 0% for elastic
1.2 MeV FWHM
300
250
200
150
100
50
0
-10
0
10
20
30
40
Missing Mass (MeV)
Medium Resolution Spectrometer
Los Alamos

PILAC Optics - August, 1991

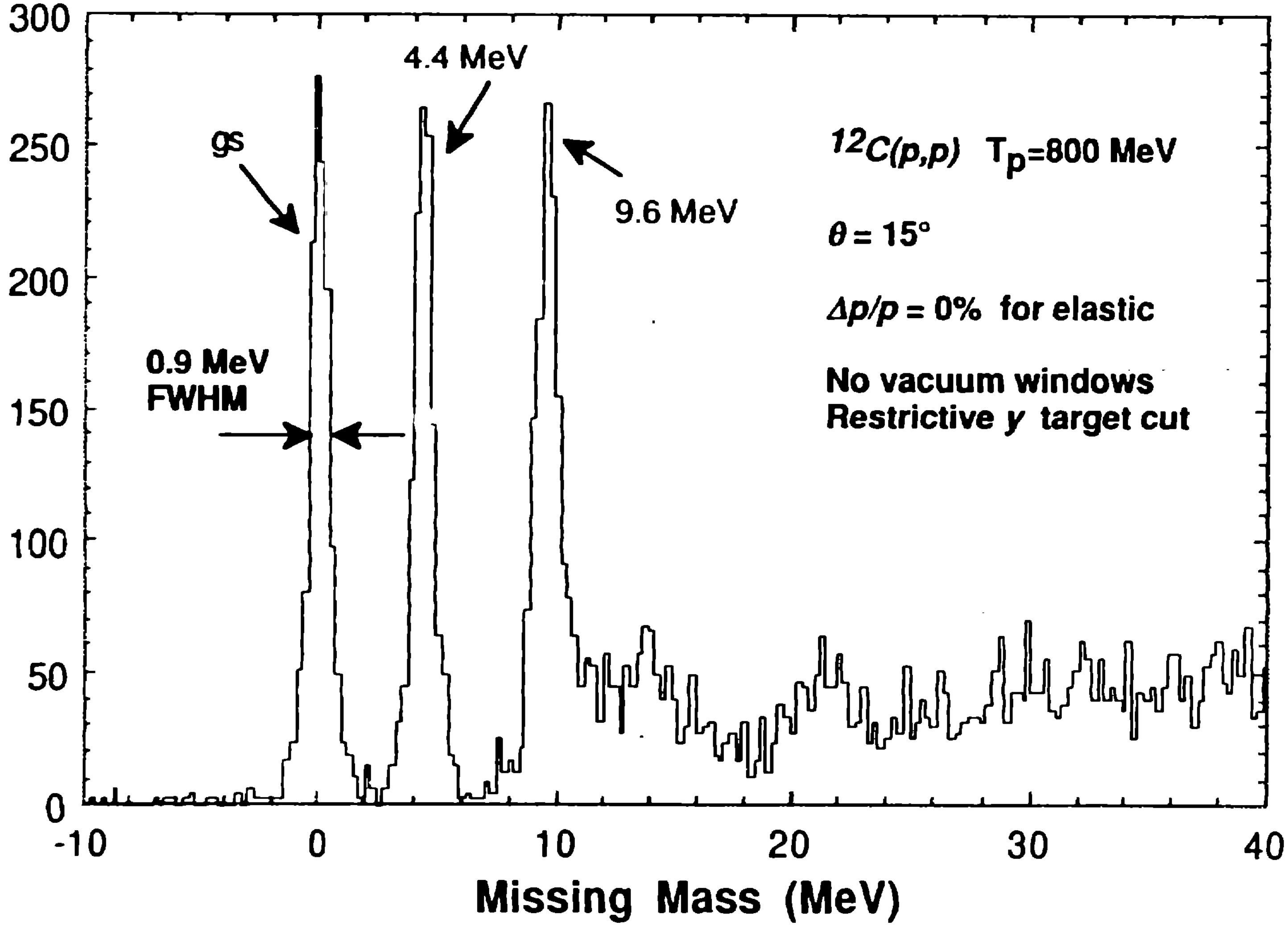

Medium Resolution Spectrometer **Los Alamos**

PILAC Optics - August, 1991

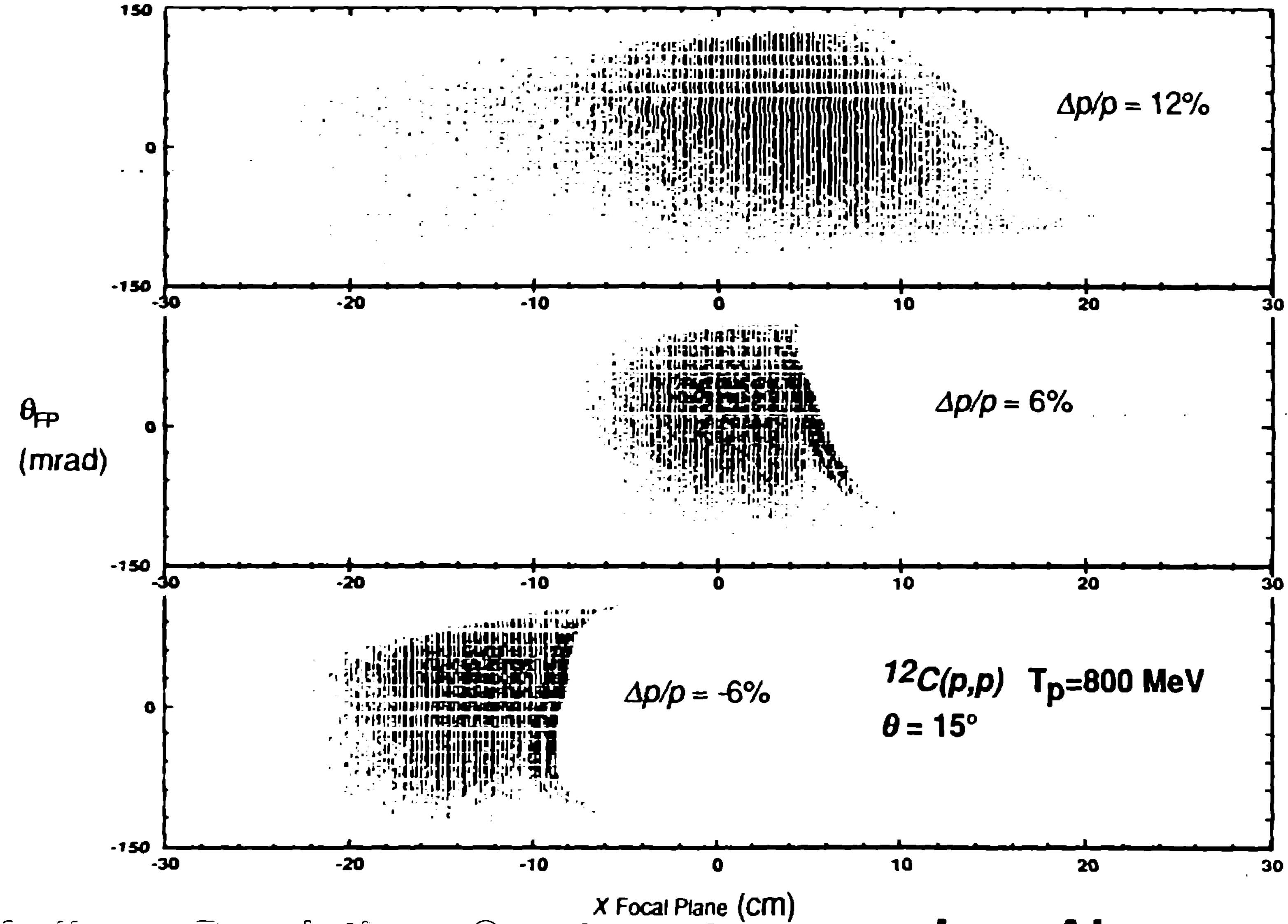

Medium Resolution Spectrometer

Los Alamos

Optical System

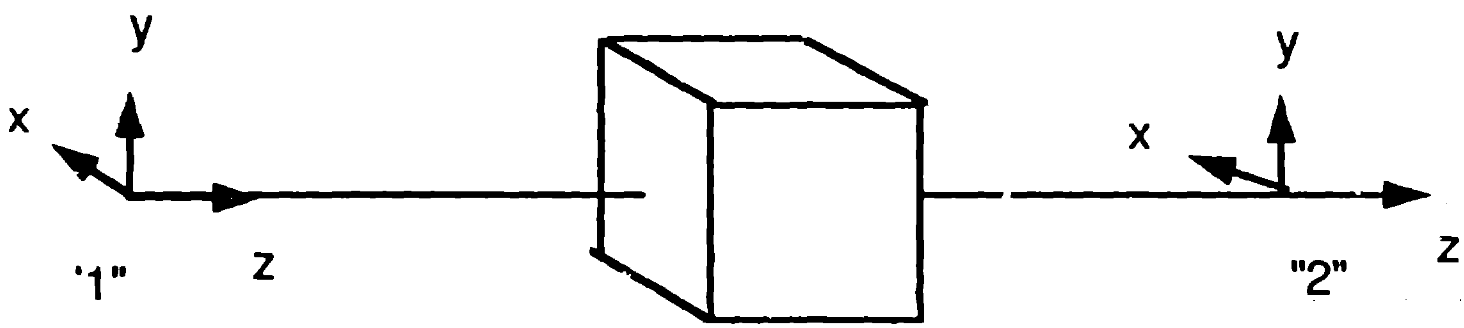

$$x_2 = F(x_1, \theta_1, y_1, \phi_1, \delta)$$

$$x_2 = (x/x)x_1 + (x/\theta)\theta_1 + (x/\delta)\delta + (x/x^2)x_1^2$$
$$+ (x/x\theta)x_1\theta_1 + (x/\theta^2)\theta_1^2 + (x/x\delta)x_1\delta$$
$$+ (x/\theta\delta)\theta_1\delta + (x/\delta^2)\delta^2 + (x/y^2)y_1^2 + (x/y\phi)y_1\phi_1$$
$$+ (x/\phi^2)\phi_1^2 + \textit{Higher order terms}$$

Polynomial Optimization

- Set Experimental Parameters
  Magnet settings - elastics, quasi's
  Position rods, slits ...
- Maximize background rejection
  Muon rejection ...
- For each "Good Event" write "Ray" to disk file
  Includes calculated quantities
  $x, \theta, y, \phi, \delta \ldots$
- Vary magnet parameters
- Again write "Rays" to disk file
- *Append ray files so that system is overdetermined*
- Solve linear least squares problem

Units:
θ,ϕ mrad
x,y cm
δ %

PILAC Optics - August, 1991

Polynomials

$\Delta p/p$ (δ) =		y (target) =		ϕ (target)		θ (target)	
-.233		-0.114		-16.3		0.0	
0.957	x	-0.015	x	10.1	y	0.911	$x0$
0.010	x^2	-0.207	y	-6.47	ϕ	-0.5	θ
0.889 E-2	θ	0.040	ϕ	0.380 E-2	$y\phi$		
-0.388 E-4	θ^2	0.718 E-2	xy	-0.467	x		
0.253 E-2	$x\theta$	-0.748 E-2	$x\phi$	0.310	xy		
0.632 E-5	$x\theta^2$	-0.826 E-3	x^2y	0.459 E-3	$x\phi$		
-0.440 E-7	$x\theta^3$	0.152 E-3	$x^2\phi$	0.215 E-2	xy^2		
0.308 E-2	y			0.316 E-2	$x\phi^2$		
0.162 E-2	xy			-0.404 E-2	$xy\phi$		
-0.292 E-2	y^2			0.120 E-2	x^2		
-0.988 E-2	ϕ			0.678 E-2	$x^2\phi$		
-0.454 E [illegible]	$x\phi$			-0.974 E-2	x^2y		
-0.758 E-5	$x\phi^2$			0.191 E-3	$x^2y\phi$		
0.730 E-4	ϕ^2						

Medium Resolution Spectrometer

Los Alamos

PROGRAM MOTER

Early MOTERing Days

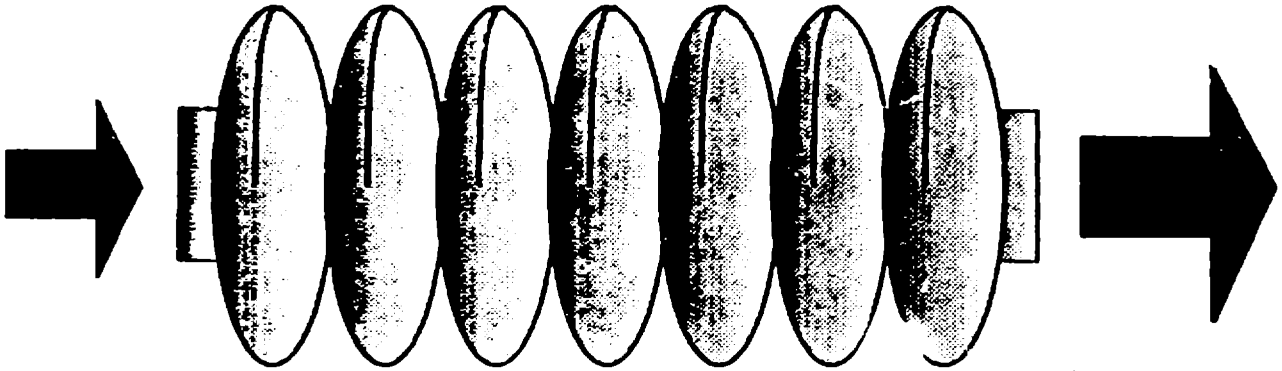

an historical presentation
to the PILAC Working Group
by
Morris M. Klein
12 August 1991

Los Alamos

Overview

- The environment at Los Alamos
  - Personnel
  - Computer
- How MOTER was conceived
- What we accomplished

Major Tasks 20 Years Ago

- Design a state-of-the-art spectrometer on a limited budget
- Extend data off axis within the magnets
- Model the fringe fields and their extent
- Develop a universal objective function
- Develop an effective optimization package

MOTER's Main Features

- H. Enge and S. Kowalski's ray-trace package
- M. Klein and T. Doyle Levenberg-Marquart least-squares optimization package
- Monte Carlo sampling of phase space
- Flexibly defined objective function

H. Enge and S. Kowalski's Ray-Trace Program

- Basic magnet elements with modification
  - Dipole, Quadrapole, Sextapole
- Additional elements
  - Separator, target simulation, ...
- Optimization-control elements
  - Srot, Drift, Hisgrm
  - Layout based on central ray or fixed position

Los Alamos

The Flexible Objective Function

$$\Phi(\vec{u}) = \sum_{i=1}^{M} \frac{D_i^2(\vec{u})}{\sigma_i^2} + \sum_{j=1}^{J} \frac{S_j^2}{\sigma_j^2}$$

The demand D_i is defined as

$$D_i = \left\langle \sum_{k=1}^{q} c_{ik} P_k(\vec{u}) \right\rangle$$

P_k denotes a term of the form $x_{comp_1}(loc_1) x_{comp_2}(loc_2) \cdots x_{comp_n}(loc_n)$

where $x_{comp_i}(loc_i)$ is x, x', y, y', l, or δ

example:

$$D_i = x_6 - c_1 x_0 + c_2 x_3 x_4$$

The Levenberg-Marquart Algorithm

Minimize $$\Phi(\vec{u}) = \sum_{k=1}^{M} D_k^2(\vec{u}) + p^2\left(u_1^2 + u_2^2 + \cdots + u_n^2\right)$$

Expand $\Phi(\vec{u}+\vec{z})$ **in a Taylor series through second order and retain first order partial derivatives after setting** $\frac{\partial \Phi}{\partial z_j} = 0$

Result $$D_{k,i}\left[D_{k,j} Z^j + D_k\right] + p^2 \delta_{ij} Z^j = 0$$

$$i = 1,2,\cdots,N$$

$$k = 1,2,\cdots,M$$

Where $$D_{k,i} = \frac{\partial D_k(\vec{u})}{\partial u^i}$$

Limiting Solutions

$p \approx 0$ $\quad z_j \approx -\left[D_{k,j} D_k\right]^{-1}\left[D_{k,j} D_k\right]$ **Normal Equations**

$p >> 1$ $\quad z_j \approx -\left[D_{k,j} D_k\right]^{-1} / p^2$ **Negative Gradient**

Los Alamos

The ETA search

One dimensional scaling of $\vec{z}$

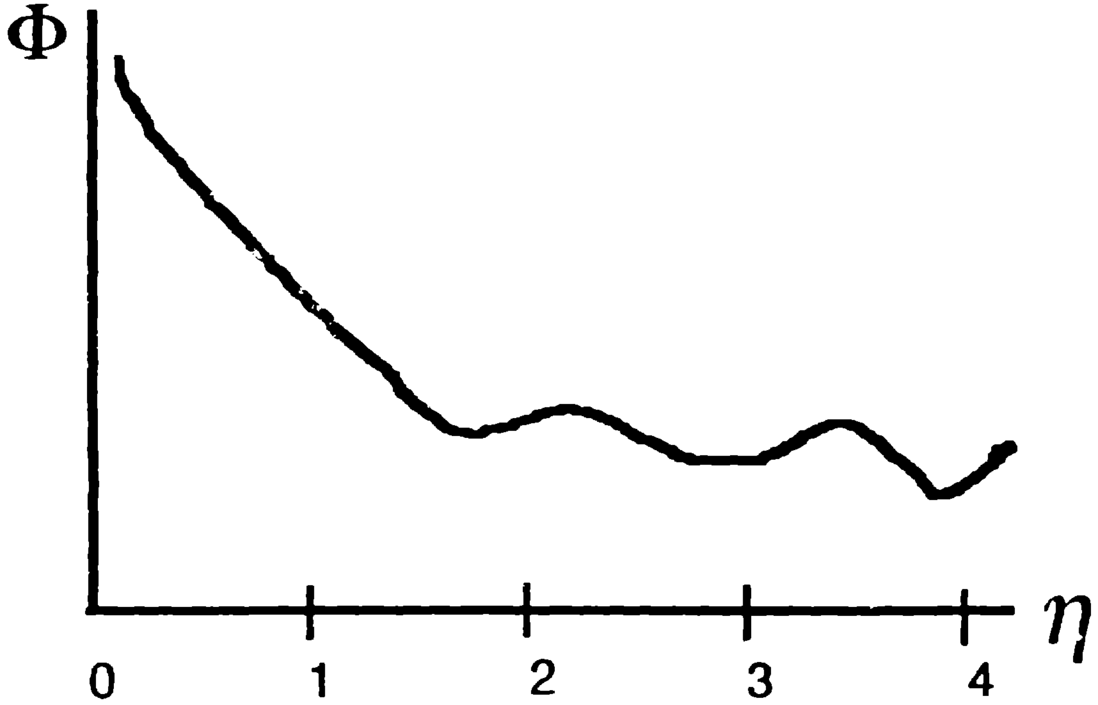

Optimization "Booby Traps"

- **Mathematical**
  - Vanishing Jacobian defines search region

    e.g.

$$D_1 = x^2 - y$$

$$D_2 = y^2 - 1$$

$$\Phi(x,y) = D_1^2 + D_2^2$$

$$|J| = |D_{i,j}| = 4xy$$

- **Physical System**
  - Unrealistic parameter values
  - Lost rays

Starting Point Defines Solution Region

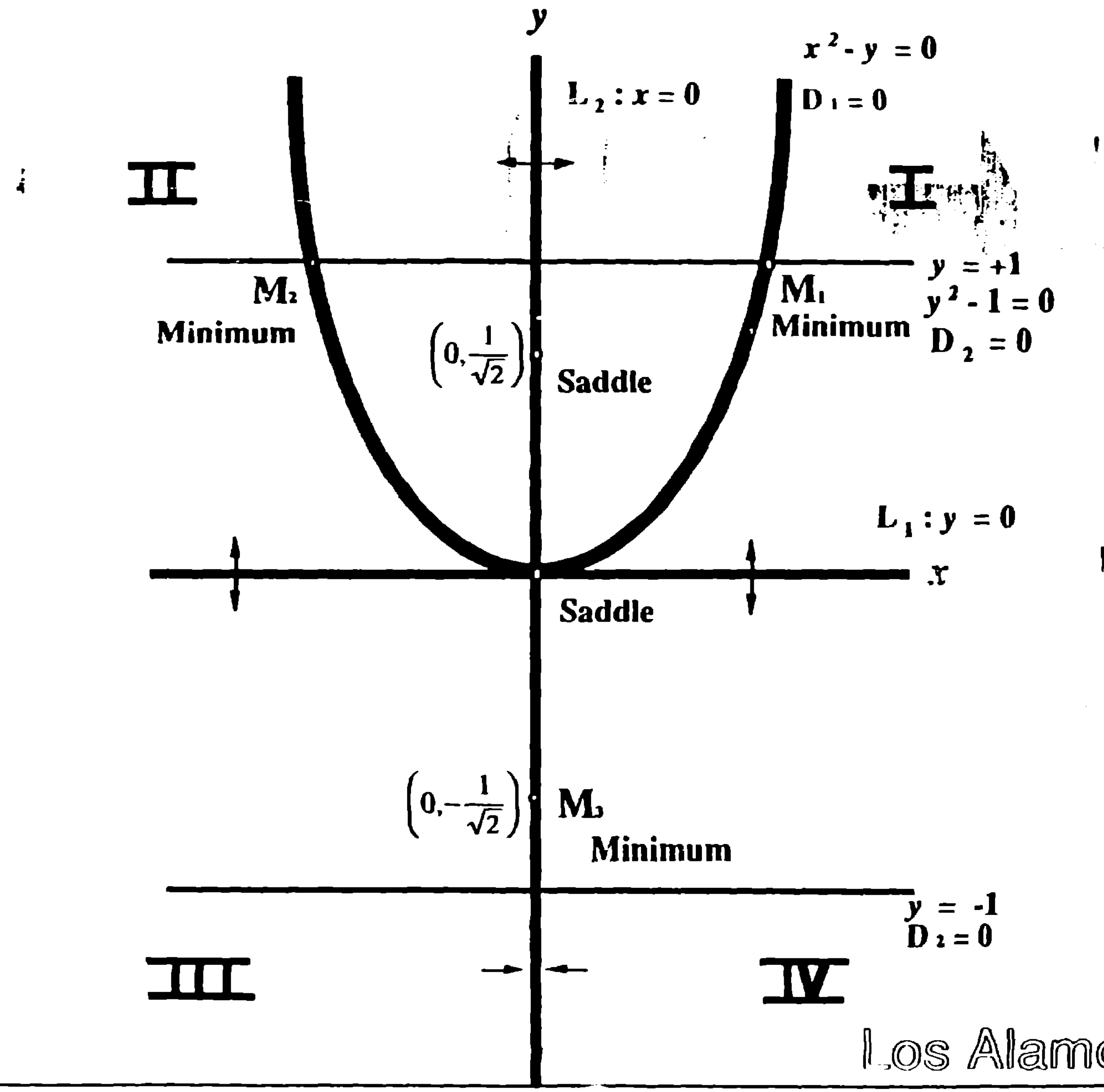

Monte Carlo Sampling of Phase Space

- Adequately sample the target and aperture
- Minimize designer's biases
- Model measurement precision
- Obtain representative resolution function

Accomplishments

- HRS Beam Line—TRANSPORT, MINIM, and MOTER
- QDD Spectrometer—Kowalski and Enge design using MOTER to define field clamps
- EPICS Beam Line—as HRS except for high-order terms
- EPICS Spectrometer—fourth-order 19-term resolution function

Conclusion

Twenty years ago our MOTER-based designs worked and resulted in the world's first software-corrected spectrometers.

Twenty years from now I can visualize us meeting to design the successor to PILAC.

RECENT UPGRADES OF MOTER

D R A F T
August 12, 1991

USER MANUAL FOR MOTER

Table of Contents

1. INTRODUCTION

Pending

Subroutines in **MOTER** as of 03/21/91

APCKD
APCKM
APCKQ
BDIP
BDMP
BDPP
BMPM
BMULT
BOUNDS
BPLS
BPOLES
BPRETZ
BQUAD
BRECP
CAVITY
DBESI0
DBESI1
DECPL
DEFFRR
DERIV
DERV
DIPOLE
DOTPRO
DRIFT
DZDX
ECRD
ECSGLSS
ECWR
ERDEF1
ETASRCH
FITMAT
FJMPM
FLAG
FMILNE2
FMIN1
FNMIRK
FOCL
GATAN
GLSS
GTAN
HATINT
HEX
HISGRM
HPOLY2
HQUAD
LABRT
LOADRN
MAPPOLE
MAPSET
MATINV
MATRIX
MAXINT
MAXR
MLTT
MOTR
MULT
NDIP
NDPP
OCTPL
OPTIMIZ
PHIGRAD
PLTOUT
POLES
PRESET
PRIM
PRNT
PRNT2
PRNT3
QUAD
RAN1
RANDOM
RANDRAY
RANSCAT
RAYPRNT
RAYS
READLCM
RECPOL2
RECPOLE
ROTATE
SAVRAN
SDIP
SECOND
SEPA
SEPAR
SHROT
SLIT
SOS
TRACE
VECPROD
VECSUM
WEDGE
WRITELCM
ZEFB
ZP1
ZP2

2. RUNNING MOTER

Pending

3. MAG INPUT FILE

MOTER requires three data files, named: MAG, DMD, and OPT. If optimization is not requested, then only the MAG file is required. Each of these data files is organized into records defining one or more parameters. The format of these records is field-free; i.e., leave one or more blanks between each parameter field. In the following table the start of each record is marked by a bullet (•).

3.1 MAG File Format

	Parameter	Description of Parameter
•	NTITLE	- Title or other identifier
•	NR	- Number of rays to be traced (400 maximum).
	NP	- Number of integration steps before next printing of intermediate results. NP=100 causes printing of ray coordinates at each transition in an element. NP>200 suppresses printing.
	IEORP	- If =1, DELP will be interpreted as $\Delta E/E$, the particle's fractional (in %) deviation from the nominal kinetic energy. Otherwise, DELP will be taken to be $\Delta p/p$.
	JRAND	- If positive, generate random rays.
	ICON	- If positive, determine the C-coefficients after each trace.
	NRAND	- Number of normal random measurements to be generated for each demand flagged to receive a measurement error.
	ITUNE	- If =1, generate new scatter random number set for each trace; if =0, generate only at start of iteration cycle.
•	JOPTIMIZE	- If =OPTI, optimize. If =NOOP, perform only a trace. If =ISNG perform only one iteration of optimization -- a trick to get histograms without optimizing.
•	IRANDUM	- If =0, then starting seed is arbitrarily =1776. If >0, initial seed is given by IRANSTA. If <0, reload status of the random number generator from a file named 'MOTER.RAN'
	IRANSTA	- Starting seed when IRANDUM > 0; otherwise, ignored.
•	PMOMO	- Momentum of design particle in MeV/c.
	PMASS	- Mass of design particle in amu.
•	*Beamline*	- Beamline element parameter list, terminated by a SENTINEL record. Appropriate keywords are: DRIFt, DIPOle, POLEs, MULTipole corrector, SHRT, and SENTinel. Other elements are available but have not been revalidated. See Section 6 for the appropriate format.

- NINDEP1 - Number of independent variables flagged in element parameter list above.

  ISET - =1 .

- DELTA() - Step size for optimization derivatives. Must be NINDEP1 values in same order as independent variables in beamline. If NINDEP1=0, omit this record from the data stream.

- LPRIMP() - Print out ray data after each element listed in LPRIMP. List 8 locations per line. A line with -1 terminates the reading. If first location =0, print ray data at start of 1st element.

- JRKSTMX - If >1, use Runge-Kutta in MAPPOLE.

  JHAMMNG - =0; not used.

  Note At this juncture the next record to be supplied depends on JRAND. If JRAND $\leq$ 0, omit the next four records from the data stream; otherwise, you must provide them.

- IBMTYPE - If =0, beam comes from a target; if =1, beam comes from an accelerator.

  NSIGMA - An integer from 1 to 6 specifying the number of parameters defining the beam. This can be any subset of the standard TRANSPORT beam parameter set: (X, θ, Y, ϕ, l, δ).

  ISIGMA(i) - Six integers (one for each dimension) from 0 to 3. If =0, the i-th term in the beam parameter set is not defined. If =1, use uniform distribution. If =2, use Gaussian distribution. If =3, use user-defined distribution.

- (SIGMA(i), (RSIGMA(i,j), j=1,6), i=1,6) Six records of 7 numbers each.

  - SIGMA(i) is the standard deviation of the distribution associated with the i-th term in the beam parameter set, i.e., sqrt(σ(i,i)). RSIGMA(i,j) is the σ(i,j) matrix as defined in TRANSPORT to describe the beam hyperellipsoid.

- KRAY - Number of input rays to be read in. If KRAY is 0 and NR is 20, then the program computes aberration coefficients. The R-matrix and four of the third-order aberration coefficients are computed (the ones important for telescope design).

  KOUT - If =0, do not output generated ray data. If =1, write output to file 7.

- FRAC - Fraction of particles that will be protons; (1-FRAC) will be pions. For now this option is disabled, i.e., FRAC = 0.

- (XI(i), VXI(i), YI(i), VYI(i), ZI(i), VZI(i), DELP(i), RMASS(i), i=1,nrays)

  If JRAND ≤ 0, supply nrays = NR records of 8 numbers each -- the starting coordinates of the i-th particle. Otherwise, supply nrays = KRAY records of starting coordinates. If KRAY = 0, skip these records as well as the offset records defined next. For now, RMASS(i) will be set to PMASS no matter what value the user specifies.

- OFFSET(i) - Increment all XI() by the amount OFFSET(1).
  Increment all VXI() by the amount OFFSET(2).
  Increment all YI() by the amount OFFSET(3).
  Increment all VYI() by the amount OFFSET(4).

Note If JRAND ≤ 0, the input data stream is complete at this point; the records below may be omitted.

- J - If J≤0, terminate reading of MAG file.
- IRANCMP(J) - If J is between 1 and 6, freeze the J-th input parameter, IRANCMP(J), to a fixed value, RANCMP(J), and read another value for J.

  RANCMP(J)

4. DMD INPUT FILE

The DMD file spells out the demands which as a sum of squares define the merit function or resolution of the system. Measurement errors can be introduced into the demand formulation. This is done by degrading the ray data through a suitable normal random number distribution at the time the demands are composed. Unlike multiple scattering the effect is not propagated to successive elements. The demands may be in the form of objectives or penalties, which prevent large high order dipole terms or large deviations from predetermined values. As in any valid merit function relative weights on each demand composing it must be defined. The merit function has been normalized so as to be insensitive to the number of rays traced or number of penalty functions.

4.1 DMD File Format

Parameter	Parameter Description
• TITLE	- Title or other identifier
• IOPT	- =0, not used.
ICNORM	- If =1, column max scaling of matrix defining coefficients is desired. (Permits observation of relative contributions of terms composing demand.) If =0, scaling is not desired.
	<u>Demand Component Record</u>. One or more of the following records terminated by one with I = 0, -1, or -2 and followed by a Relative Weight record constitute a Demand Group. If I=0, then one or more Demand Groups will follow the Relative Weight record. The final Demand Group will have I = -1 or -2 and will be followed by a Relative Weight record with WT = 0. A collection of Demand Groups forms the Merit Function.
• I	- If I = -1, demand definition process is complete; append a Relative Weight record (defined after this record) with WT = 0. Sextupole strengths to be treated as a group in each order. If I = -2, same as above but sextupole strengths treated individually. If I = 0, Demand Group is complete with this record; one or more Demand Groups will follow. If I = positive integer, components of Demand Group being defined, such definition continuing up to and including a 0, -1, or -2 record.

Restrictions:

- A maximum of 40 coefficients may appear in the definition of any one Demand Group.
- A maximum of 400 I's may be used to define the set of *all* demands.
- A maximum of 10 Demand Groups may appear in the definition of the merit function.

LOC - Location in magnet system where demand component is being defined. LOC=0 corresponds to the input side of the system. LOC="integer" refers to the output of the magnet element numbered "integer", all elements being counted. The magnet system was defined in the MAG input file.

NCOMP - A number in the range 1-7 designating X, θ, Y, ϕ, l, δ, and t, respectively. NCOMP=5 permits the introduction of a constant term (independent of ray data) into the demand definition.

COTIE - An integer designating possible ties within a Demand Group. For example, x at LOC 1 may be tied to δ at LOC 0 to form an $(x|\delta)$ term in the demand. Any number of LOC, NCOMP records may be tied. A maximum of 40 coefficients may be defined in any given demand with a total of 400 such coefficients defined for all demands. Integers used for COTIE should be equal for components to be paired, unequal for components not to be paired, and should form a monotone nondecreasing natural sequence (no integer skipped).

ISIDE - If =0, coefficient of demand component defined by present grouping of COTIE records is to be determined by program. If =1, coefficient defined by present grouping of COTIE records is preset and frozen; must appear at least once in each demand definition and appear in the record introducing (through COTIE) the terms corresponding to this coefficient.

CSTOR - Value of present coefficients; must appear in same record as ISIDE=1.

JRANTIE - Positive integer. Individual components which form terms in the demand may be tagged to receive a normally distributed measure error having mean zero and standard deviation SDEV. All components tagged with identical integers receive an identical measurement error independent of the demand grouping in which they reside. Each distinct ray receives NRAND (MAG file) distinct measurement errors. This increases the effective number of rays composing the demands to NR*NRAND rays. The distribution is redefined at the beginning of each iteration cycle of the optimization. JRANTIE =0 indicates no error is desired The integers need not appear in any particular order. However, to promote efficient use of computer space, all integers up to the maximum one should be defined. If the maximum integer times NRAND is >100, then NRAND will be reset to the largest integer such that MAX(JRANTIE*NRAND) ≤ 100.

SDEV - Standard deviation attached to measurement error; needs to be defined only once for each integer JRANTIE defined.

Relative Weight Record. This record is used to weight a Demand Group and, after I = -1 or -2, to terminate with WT = 0 the demand file; i.e., the defining of the Merit Function.

- WT - If positive number, it is interpreted at the relative weight for the preceding demand; it is not normalized.
  If =0, DMD file is complete; no more data follows.
  If negative number, sextupole strength demand being defined with weight equal to ABS(WT).
- IORD - If IORD = 2, 3, 4, 5 then RAP, CAT, CSVN, CNN terms are to be treated as penalty demands. If previous I = -1, then ignore LOCSEX, SEXTZRO and use all terms of given order from all dipoles as a group. If previous I = -2, use only the order term tagged by LOCSEX. If IORD = 0, no penalty is implied.
- LOCSEX - = FLOC integer. If integer is negative, then pick up order component from entrance fringe field; if positive, use component from exit fringe field. LOCSEX = 0 is treated as "do-nothing" signal.
- SEXTZERO - = number. Penalty demand is to be defined as a deviation from the value set in SEXTZERO. SEXTZERO = 0 is treated as "do-nothing" signal.

3.2 DMD File Examples

5. OPT INPUT FILE

This input file enables the user of MOTER to tune the optimizer package for its most efficient operation. The optimizer routines are based on the Levenberg algorithm for minimizing a sum of squares. The optimizer first determines a direction of descent lying between that given by first variational principles and the negative gradient. Given this direction, its length is then determined by a quadratic search procedure. The parameters which can be set in this file control the operational characteristics at the beginning of each pass, the exit criterion for each pass, and the optimizer print control. The reading of the OPT file is initiated in the subroutine OPTIMIZ.

5.1 OPT File Format

In what follows the underlined numbers are the default values.

	Parameter	Description of Parameter
•	NPROBS	- 1 Problem number.
2	ITERS	- 10 Number of iterations allowed per pass.
3	NPO	- 0 (1) To bypass (include) P=0 in the P-table.
4	NPRINT1	- 0 (1) To bypass (print) the P-table.
5	NPRINT2	- 0 (1) To bypass (print) the η search triplets.
6	NETASCH	- 0 (1) To omit (include) a Z(P) η search.
7	MONO	- 0 (1) To continue (halt) the P-table search at the first maxima.
8	NTABLE	- 3 Number of P-table entries.
9	NPIV	- 0 (1) When the maximum modified column vector -- the modified length divided by the original length -- determines the next pivot.
10	MXFCN	- 3 Maximum number of function evaluations permitted in the search for ETA.
11	ICROW	- 0 (1) Column followed by row maximum scaling not desired (desired).
12	KREAD	- 0 (1) OPTP groups will (will not) be defined for succeeding passes.
•	GRDZMIN	- 1.0E-20 Exit when the inner product of the newly chosen z-search direction and the negative gradient evaluated at the same point in parameter space lies between 0.0 and GRDZMIN.
2	PHIMIN	- 1.0E-25 Exit when the merit function, PHI, is less than the non-zero PHIMIN.
3	ZSQMIN	- 1.0E-24 Exit when Z^2 < ZSQMIN.
4	APZERO	- 1.0E-14 Approcimate value for zero used in the least squares rank determination.

5 CMIN - <u>1.0E-3</u> Starting value of P^2 which is equal to CMIN(DIAGMAX).

6 CMAX - <u>1.0</u> End value of P^2 which is equal to CMAX(DIAGMAX).

7

• RELPHI - <u>1.0E-13</u> Exit when the relative drop in the merit function, PHI, following an iteration cycle is less than the input value of RELPHI. Note: the maximum recommended value of RELPHI is 1.0E-3.

2 RELPPHI - <u>1.0</u> Exit from the P-table search when the relative PHI drop is greater than RELPPHI.

3 RELDGMX - <u>1.0E-25</u> Halt the differentiation and the P-table search when the relative change in the matrix diagonal maximum is less than RELDGMX.

4 ETAVREL - <u>1.5E-2</u> Exit from the η search when the parabolic vertex sequence relative change is less than ETAVREL.

5 ETAHALT - <u>1.0E-2</u> Halt the η search when the relative PHI drop is less than ETAHALT times the relative P-table PHI drop.

6 USQMX - <u>1.0E+6</u> Freeze a bounded variable when its unconstrained mapping exceeds USQMX in absolute magnitude.

To use the default value of a variable, enter -77 for the corresponding integer in the first record and -77. for the appropriate floating-point variable in the last two records.

5.2 OPT File Example

The following is an example of an OPT file.

```
-77  2  0  -77  -77  0  -77  0  -77  -77  1  1
-77.  -77.  -77.  -77.  1.E-5  1.
1.E-23  1.  1.E-20  1.E-25  1.5E-20  -77.
```

In this case the following variables in the OPT file do not use their default value:

ITERS	2	CMIN	1.E-5	RELPHI	1.E-23
NPO	0	CMAX	1.	RELPPHI	1.
NETASCH	0			RELDGMX	1.E-20
NTABLE	0			ETAVREL	1.E-25
ICROW	1			ETAHALT	1.5E-20
KREAD	1				

6. ELEMENT INPUT PARAMETERS

This section is devoted to a description of the parameters needed to define each type of element. The elements supported in this version of MOTER are given in Table 6.1. The coding for those elements above the dashed line was imported from the (02/19/89) version of RAYTRACE and revalidated on selected test cases. The elements below the dashed line are new or were carried over from an earlier version of MOTER and have not been validated.

TABLE 6.1

	Element Type	Keyword	Parameters
A.	Drift	DRIF(T)	1
B.	Dipole	DIPO(LE)	63
C.	Multipole	POLE(S)	40
D.	Multipole Corrector	MULT	23
E.	Shift-Rotate	SHRT	6
F.	End-of-System	SENT(INEL)	0
---	-------------------	-----------	----
G.	Cavity	CAVI(TY)	6
	Solenoid	SOLE	8
	ES Deflector	EDIP	30
	Velocity Selector	VELS	47
	Lens	LENS	11
	Collimator	COLL	5
	Accelerator	ACCE	24
	Einzel Lens	EINZ	15

6.1 Element Input Format

An effort has been made to present the user with as forgiving an input format as is possible. Each element is described by (1) an alphabetic keyword followed by (2) a list of parameter values. The keyword must appear by itself on the first line of the element input (although it can appear anywhere on the line.) Only the first four characters of the keyword are used; all other characters appearing on the line are ignored. A blank line preceding the keyword line will be ignored.

The list of parameter values is expected on the second and subsequent lines. The format is free-field, i.e., the only spacing requirement is that the numbers be separated by one or more blanks. The parameters can be grouped on the lines to suit the user's sense of organization, e.g., as they are grouped in the parameter definitions below. They will be read as a single record and the reading will continue until the proper number of parameters for a given element has been read. The only requirement is that the numbers be in the order specified below. The "Offset" column is meant to assist in the ordering.

6.2 Variable Parameters

In principle any parameter of an element may be denoted as a variable quantity that is to be optimized. Thus, following the records defining each element is a variable (zero or more) number of records, one for each parameter that is to be varied, up to a maximum of 30, followed by a terminating record. The format for these records is given below.

<u>Parameter</u>	<u>Description of Parameter</u>
• J1	Order number in the parameter list
J2	An integer to be assigned to this parameter. The integers should be assigned in the natural order (do not skip any). If two parameters are assigned the same integer, they become tied variables, i.e., the change calculated by the optimizer will be applied to all variables tied together by a particular integer. If J2 is negative, the change calculated by the optimizer is subtracted from the associated variable; this feature is used, e.g., to preserve the length of a drift. ABS(J2) must be ≤ 30.
J3	Defines the type of bounds to be applied to this variable parameter. J3 = 0: unbounded J3 = 1: bounded from below only J3 = 2: bounded from above and below J3 = 3: bounded from above only
BL	Value of the lower bound
BU	Value of the upper bound

The specifying of which parameters of an element (if any) are to be varied is terminated by a record with J1 = J2 = J3 = 0.

6.3 Element Types

The pages which follow describe the parameters needed to define each element type.

A. Drift

Keyword: **DRIF(T)**

Parameter	Description	Offset
DZ	- Field-free drift ~~le~~ngth (cm).	+ 0

B. Dipole

Keyword: **DIPO(LE)**

Parameter	Description	Offset
LF1	- Entrance fringing–field integration step size (cm).	+ 0
LU1	- Uniform field integration step size (cm).	+ 1
LF2	- Exit fringing field integration step size (cm).	+ 2
DG	- Differential step size used in determining off mid-plane components of B using numerical methods. Recommended for all four step sizes: 0.3D (D=Gap) although LU1 can be made larger to save computer time. For MTYP=6, DG serves another function -- see Sec. V. A. in the RAYTRACE manual.	+ 3
MYTP	- Magnetic dipole option MTYP=0,1 - Uniform field dipole. Fringing field determined by calculation of the distance to the effective field boundary in the z-direction. MTYP=2 - Uniform field dipole. Fringing field determined as described in Sec. V.A. in the RAYTRACE manual. MTYP=3 - Non-uniform field dipole with n-value and second-, third, and forth-order corrections Fringing field determined as for MTYP=2, but including n-value, etc. MTYP=4 - Non-uniform field dipole; cylindrical geometry. Similar to MTYP=3 but better suited for purely conical pole pieces. This option is used to describe magnets with wedge-shaped gaps ("CLAMSHELL") by making R large, PHI small, and by setting BET1=GAMA=DELT=0 but n=0, and normally large because R is artificially large. MTYP=5 - Uniform field dipole; circular pole option. MTYP=6 - Pretzel magnet option.	+ 4
IMAP	- Array number for generating and identifying fringing field array maps. If IMAP=0, maps are not generated and the field components are calculated directly for each point, i.e., four times for each integration step. Two dipoles with identical values of IMAP will share a common array. IMAP≤5.	+ 5
A	- Distance (cm) from the origin of system A (initial) to system B (situated at the entrance edge EFB of the magnetic element).	+ 6
B	- Distance (cm) from origin of system C (situated at the exit edge EFB of the magnetic element) to origin of output system D.	+ 7
D	- Gap width (cm).	+ 8
R	- Radius of curvature (cm) used in geometrical construction of layout.	+ 9
BF	- Nominal value of the field on the central radius R (Tesla).	+10
PHI	- Angular extent (degrees) between the EFB of system B and that of system C. Nominally equivalent to the bend angle.	+11
ALFA	- Angle (degrees) between the central trajectory and the normal to the entrance (EFB).	+12

BETA	- Angle (degrees) between the central trajectory and the normal to the exit boundary. Both ALFA and BETA are positive when the normals are outside the orbit for positive transverse plane focussing.	+13
NDX	- 'n-value' of field index for non-uniform field magnets (first-order term).	+14
BET1	- 'β-value' of field index for non-uniform field magnets (second-order term).	+15
GAMA	- 'γ-value' of field index for non-uniform field magnets (third-order term).	+16
DELT	- 'δ-value' of field index for non-uniform field magnets (forth-order term).	+17
Z11	- Integration limit (cm) defining the start of the entrance fringing field zone in coordinate system B. Normally positive	+18
Z12	- Integration limit (cm) defining the termination of the entrance fringing field zone in coordinate system B. Normally negative.	+19
Z21	- Integration limit (cm) defining the start of the exit fringing field zone in coordinate system C. Normally negative	+20
Z22	- Integration limit (cm) defining the termination of the exit fringing field zone in coordinate system C. Normally positive.	+21
C00	- Coefficients used in the expansion of the fringing field fall-off at the entrance of the magnetic element.	+22
C01		+23
C02		+24
C03		+25
C04		+26
C05		+27
C10	- Coefficients used in the expansion of the fringing field fall-off at the exit of the magnetic element.	+28
C11		+29
C12		+30
C13		+31
C14		+32
C15		+33
BR1	- Correction for presence of constant field in region of entrance fringe field (Tesla).	+34
BR2	- Correction for presence of constant field in region of exit fringe field (Tesla). In the Split-Pole Spectrometer, BR1 and BR2 describe the asymptotic field in the split.	+35
XCR1	- Equivalent to a coordinate system shift (cm) at the entrance (element SHRT) with Δx=-XRC1. Used to correct for displacement of central ray caused by extended fringing field (see Fig. 2 in RAYTRACE manual). Use XCR1=SCR2=0 unless the actual hardware element will be offset.	+36
XCR2	- Equivalent to a coordinate system shift (cm) at the exit with Δx=XCR2. Used to correct for displacement of central ray caused by extended fringing field.	+37
DELS1	A correction to the location of the effective field boundary. The effective field boundary at the entrance is moved towards the magnet (for positive Δz) by an amount Δz = DELS1*D.	+38

DELS2	- A correction to the location of the effective field boundary. The effective field boundary at the exit is moved towards the magnet (for positive Δz) by an amount Δz = DELS2*D.	+39
RAP1	- Inverse radius of curvature of entrance boundary (cm^{-1}). Convex surfaces are positive.	+40
RAP2	- Inverse radius of curvature of exit boundary (cm^{-1}). Convex surfaces are positive. In the program, except for MTYP=5, circles described by RAP1 and RAP2 are approximated with an eighth-order power series.	+41
WDE	- Mechanical width of the entrance pole boundary. Used only when IMAP is non-zero	+42
WDX	- Mechanical width of the exit pole boundary. Used only when IMAP is non-zero.	+43
S02	- Coefficients used in description of entrance boundary curvature.	+44
S03	Contributions of RAP1 are added to those of S02, S04, S06 and S08.	+45
S04		+46
S05		+47
S06		+48
S07		+49
S08		+50
S12	- Coefficients used in description of exit boundary curvature.	+51
S13	Contributions of RAP2 are added to those of S12, S14, S16, and S18.	+52
S14		+53
S15		+54
S16		+55
S17		+56
S18		+57
ZIN	- Aperture checking begins at a point ZIN (cm) inside the entrance	+58
ZOUT	fringing field (Z11> ZIN> Z12) measured in coordinate system B. It continues at each integration step through the uniform field zone and on to ZOUT in the exit fringing field (Z21< ZOUT< Z22) measured in coordinate system C.	+59
XMAX	- Half-aperture collimation limits (cm) set on a ray passing thru the	+60
YMAX	magnetic element. In the bending plane, the particle's (x,z) coordinates are converted to a radius, Rxy, measured from the center of the bend. If this radius exceeds RHO±XMAX, where RHO is the nominal bending radius, a message is issued, once only, indicating that an aperture was grazed and where. A similar message is issued if |Y|≥YMAX in the non-bending plane. A value of XMAX=0 suppresses aperture checking	+61
APMX	- The aperture constraints above are passive, i.e., the particle's 6-coordinate is not modified if the aperture condition is exceeded. APMX provides an active constraint in the bending plane. A typical value for APMX might be 1.1. If Rxy≥RHO±APMX*XMAX, then the transverse velocity in the bending plane is set to zero and the particle's radial position is set to that of the constraining aperture. A tattletale message is issued , once only in each zone, when this action occurs. A similar constraint is applied in the non-bend plane, i.e., |Y|≥APMX*YMAX. Setting APMX=0 disables this option.	+62

C. Multipole

Keyword: **POLE**

Parameter	Description	Offset
LF1	- Entrance fringing field integration step size (cm).	+ 0
LU1	- Uniform field integration step size (cm).	+ 1
LF2	- Exit fringing field integration step size (cm). Recommended for all three step sizes: 0.3R	+ 2
A	- Distance (cm) from the origin of system A (initial) to system B situated at the EFB of the entrance edge of magnetic element.	+ 3
B	- Distance (cm) from origin of system C (situated at the EFB of the magnetic element) to origin of output system D.	+ 4
L	- Effective length (cm) of magnetic element.	+ 5
R	- Aperture radius (cm) used to calculate field strength.	+ 6
BQ	- Quadrupole component of the pole tip field at r=R (Tesla).	+ 7
BH	- Hexapole component of the pole tip field at r=R (Tesla).	+ 8
BO	- Octapole component of the pole tip field at r=R (Tesla).	+ 9
BD	- Decapole component of the pole tip field at r=R (Tesla).	+10
BDD	- Dodecapole component of the pole tip field at r=R (Tesla).	+11
Z11	- Integration limit (cm) defining the start of the entrance fringing field zone in coordinate system B. Normally positive	+12
Z12	- Integration limit (cm) defining the termination of the entrance fringing field zone in coordinate system B. Normally negative.	+13
Z21	- Integration limit (cm) defining the start of the exit fringing field zone in coordinate system C. Normally negative	+14
Z22	- Integration limit (cm) defining the termination of the exit fringing field zone in coordinate system C. Normally positive.	+15
C00	- Coefficients used in the expansion of the fringing field fall-off at	+16
C01	the entrance of the magnetic element. (These are the coefficients	+17
C02	of a power series in s = z/2R in accordance with the 1 July 1987	+18
C03	RAYTRACE manual. Earlier versions of RAYTRACE used z/R.)	+19
C04		+20
C05		+21
C10	- Coefficients used in the expansion of the fringing field fall-off at	+22
C11	the exit of the magnetic element. (See comment above on s = z/2R).	+23
C12		+24
C13		+25
C14		+26
C15		+27
FRH	- Fractional radius of multipoles, in terms of quadrupole radius.	+28
FRO	Used in calculating fringing field fall-off, e.g.,FRH=0.9 makes the	+29
FRD	hexapole fall off 0.9^{-1} times faster with distance from the EFB than	+30
FRDD	the quadrupole field. A value of 0.0 given for any of these parameters is redefined to 1.0.	+31

)SH - A correction for the effective length of individual multipole +32
SO elements relative to the quadrupole. A positive DS represents a +33
)SD displacement inward of the EFB at the entrance and exit in units +34
)SDD of 2R. +35

:IN - Aperture checking begins at a point ZIN (cm) inside the entrance +36
:OUT fringing field (Z11> ZIN> Z12) measured in coordinate system B. It +37
continues at each integration step through the uniform field zone and on to ZOUT in the exit fringing field (Z21< ZOUT< Z22) measured in coordinate system C.

R1X - Half-aperture collimation limits (cm) set on a ray passing thru the +38
R2Y magnetic element. If R1X is positive, the aperture is taken to be +39
elliptical. A negative value for R1X (R2Y is always positive) specifies a hyperbolic aperture for which the limiting equations are: 2|XY| = R1X**2, |X| = R2Y and |Y| = R2Y. If the specified aperture condition is exceeded, a message is issued, once only in each zone, indicating that the aperture was grazed and where. A value of R1X=0 suppresses aperture checking.

D. Multipole Corrector

Keyword: MULT

Parameter	Description	Offset
LF	- Integration step size (cm).	+ 0
DG	- Differential step size (cm) used in determining off-midplane components of B using a numerical technique. Recommended for both step sizes: 0.3D.	+ 1
A	- Distance (cm) from origin of system A (initial) to coordinate system situated at center of multipole element.	+ 2
B	- Distance (cm) from coordinate system situated at center of multipole element to origin of output system D.	+ 3
L	- Length of the Multipole Corrector (cm).	+ 4
W	- Width (cm) of multipole element.	+ 5
D	- Gap (cm) of multipole element.	+ 6
BF	- Nominal value of field at x = W/2 and z = 0, i.e., the value the field at x = W/2 will attain if one of the coefficients C0-C5 is equal to unity and the others are zero.	+ 7
Z1	- Starting point of integration (cm) measured from coordinate system at center of multipole element. Normally negative	+ 8
Z2	- Termination point of integration (cm) measured from coordinate system at center of multipole element. Normally positive.	+ 9
C0	- Coefficients describing dipole, quadrupole, etc. content of the field. Normal range: -1.0 to 1.0.	+10
C1		+11
C2		+12
C3		+13
C4		+14
C5		+15
C6	- Not used.	+16
C7	- Coefficients used to define how the field varies with z/L, basically describing a bell-shaped curve. Typical values are C7 = 0.4 and C8 = 0.1.	+17
C8		+18
ZIN	- Aperture checking beings at a point ZIN (cm), ZIN ≥ Z1, inside the element and continues at each integration step to ZOUT (cm), ZOUT ≤ Z2. Both quantities are measured from the center of the element, which means that ZIN is normally negative while ZOUT is normally positive.	+19
ZOUT		+20
XMAX	- Half-aperture collimation limits (cm) set on a ray passing thru the magnetic element. If |X| > XMAX or |Y| > YMAX in the region being monitored, a message is issued, once only, indicating that the aperture was grazed. A value of XMAX=0 supresses aperture checking.	+21
YMAX		+22

E. Shift-Rotate

Keyword: **SHRT**

Parameter	Description	Offset
X0	- All following coordinate systems are displaced in the x-direction by an amount X0 (cm) as measured in the preceding system.	+ 0
Y0	- All following coordinate systems are displaced in the y-direction by an amount Y0 (cm) as measured in the preceding system.	+ 1
Z0	- All following coordinate systems are displaced in the z-direction by an amount Z0 (cm) as measured in the preceding system.	+ 2
ψ_x	- The rest of the optical system as a unit is rotated ψ_x (degrees) about the x-axis of the preceding system.	+ 3
ψ_y	- The rest of the optical system as a unit is rotated ψ_y (degrees) about the y-axis of the preceding system.	+ 4
ψ_z	- The rest of the optical system as a unit is rotated ψ_z (degrees) about the z-axis of the preceding system.	+ 5

F. End-of-System

Keyword: **SENT(INEL)**

Parameters: NONE

- This element is required to signal the end of the list of elements. It has no parameters associated with it.

USE OF MOTER AT MICHIGAN STATE

Use of MOTER at Michigan State

J. Nolen

Spectrometer Design at MSU/NSCL

Use of MOTER and future ideas:

1. Simple spectrograph: QQDOS 34°

2. Reaction Product Mass Separator "RPMS"
   QQWDQQ

3. Fragment separator "A1200"

4. Large spectrograph: "S800"
   QQDD software correction

5. Using DA technique for on-line corrections

QQD Spectrograph

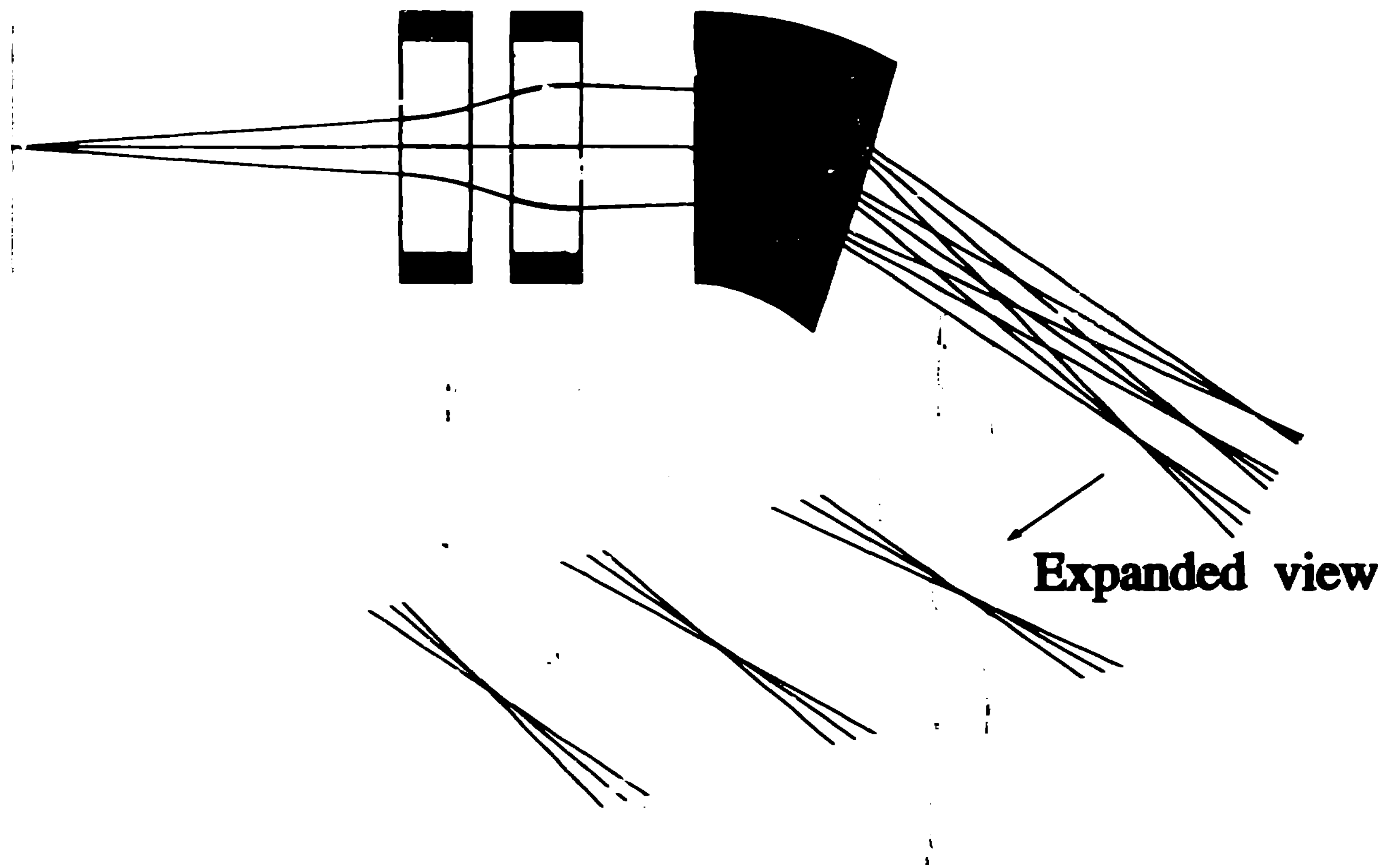

and the production target was 790 mg/cm^2 ^{9}Be.

MSU-89-010

First Order Beam Envelopes

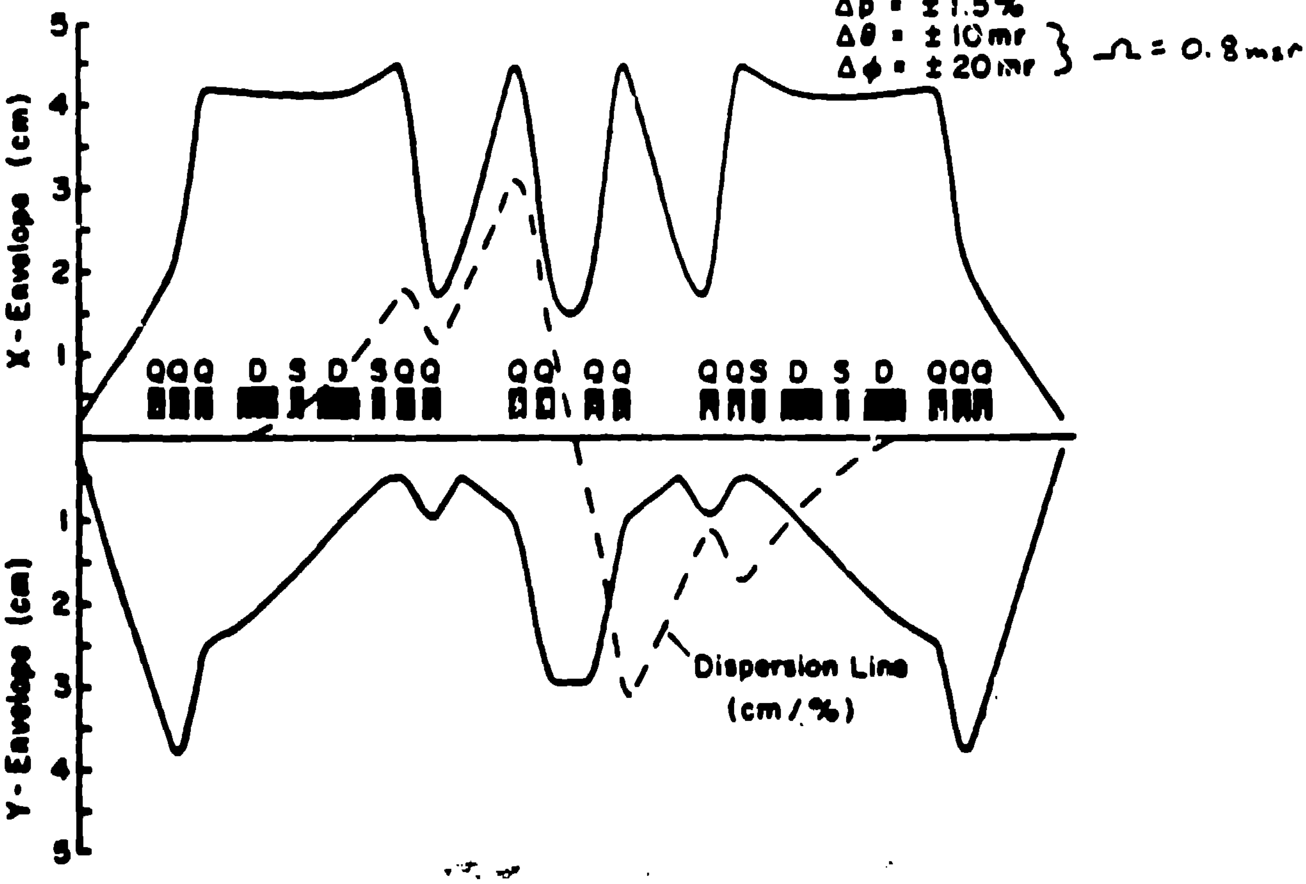

Schematic Layout

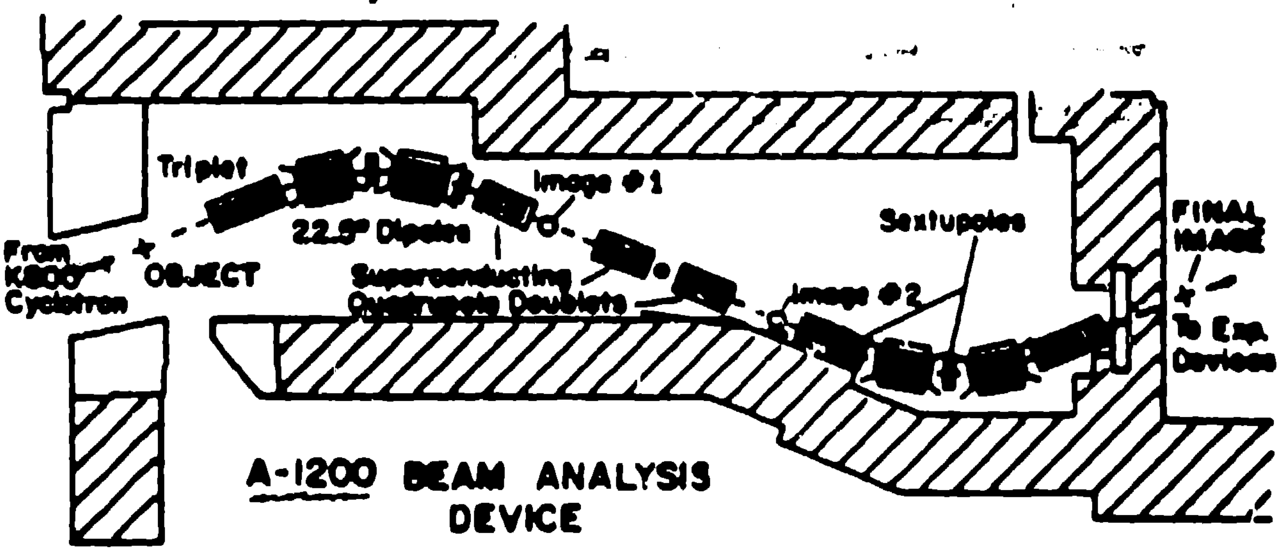

20 m long
16 [illegible]

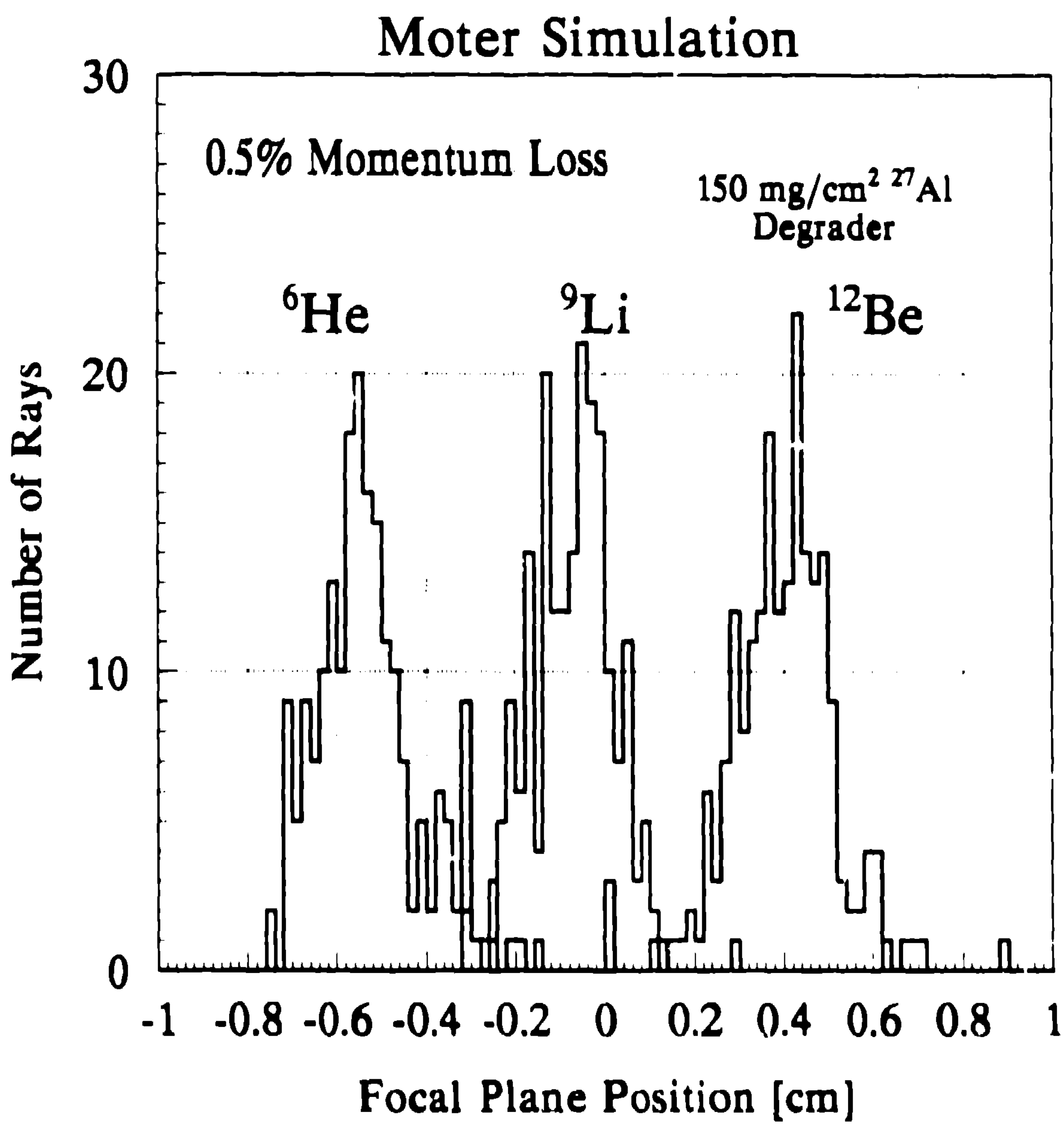
Moter Simulation
0.5% Momentum Loss
150 mg/cm² ²⁷Al
Degrader
⁶He
⁹Li
¹²Be
Number of Rays
Focal Plane Position [cm]
30
20
10
0
-1
-0.8
-0.6
-0.4
-0.2
0
0.2
0.4
0.6
0.8
1

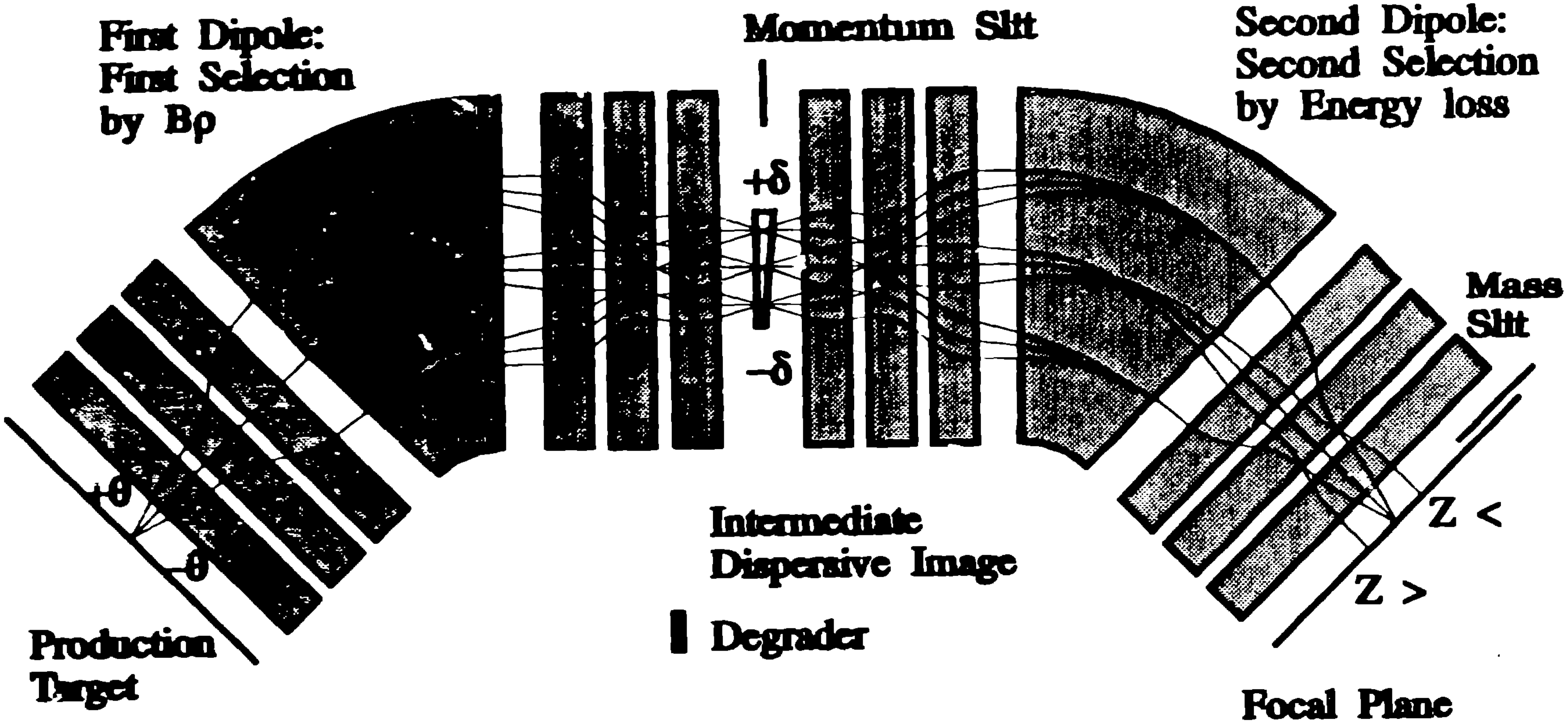

First Dipole:
First Selection
by Bρ
Momentum Slit
Second Dipole:
Second Selection
by Energy loss
+δ
−δ
+θ
−θ
Mass
Slit
Z <
Z >
Intermediate
Dispersive Image
Degrader
Production
Target
Focal Plane

MOTER

"Demands" - very flexible

e.g. Forward Maps
Inverse Maps
Measurement errors

Optimization Determine best compromise between hardware and software corrections.

Forward:

e.g. $$x_f = (x|\theta)\theta_0 + (x|x)x_0 + (x|\delta)\delta + (x|\theta^2)\theta_0^2 + (x|\delta^2)\delta^2 + (x|\theta\delta)\theta_0\delta + (x|\theta\delta^2)\theta_0\delta^2 + \cdots$$

$$\begin{pmatrix} x_f \\ \theta_f \\ y_f \\ \phi_f \\ \delta \end{pmatrix} = R_n \begin{pmatrix} x_0 \\ \theta_0 \\ y_0 \\ \phi_0 \\ \delta \end{pmatrix}$$

R matrix

MOTER fit:

Trace 100 or more rays / random.

Guess which higher order terms are important and let MOTER calculate their coef. by fitting random rays.

Plot "error" histogram and rerun to minimize errors

$$\Delta x_m \equiv (x_{traced} - x_{fit})_m$$

<u>Inverse</u> fit (omit x_0)

$$\delta = (\delta|x)\,x_f$$

$$+(\delta|\theta x)\,\theta_f x_f + (\delta|\theta^2)\,\theta_f^2 + (\delta|x^2)\,x_f^2$$

$$+(\delta|\theta x^2)\,\theta_f x_f^2 + \cdots$$

For every random ray distribute values of x_f, θ_f, etc randomly according to σ_f, ϵ_f, etc. (~10 values per ray.)

Use DA to determine inverse map:

Forward non-linear sub-map of system:

$$\begin{pmatrix} x_f \\ \theta_f \\ y_f \\ \phi_f \end{pmatrix} = A_n \begin{pmatrix} \theta_0 \\ y_0 \\ \phi_0 \\ \delta \end{pmatrix}$$

$$A_n \equiv A_1 + A_{n-1}$$

A_n to "necessary" order

- calculate with COSY-∞
  or MOTER / RAYTRACE

Want:
$$\begin{pmatrix} \theta_0 \\ y_0 \\ \phi_0 \\ \delta \end{pmatrix} = M_n \begin{pmatrix} x_f \\ \theta_f \\ y_f \\ \phi_f \end{pmatrix} \qquad M_n \equiv A_n^{-1}$$

non-linear inverse

A theorem & recursion relation:
Existance of $A_1^{-1} \Rightarrow A_n^{-1}$ exists.

Paper presented at 1991 Particle Accel. Conf.', San Francisc

On-line Correction of Aberrations in Particle Spectrographs

M. Berz, K. Joh, J. A. Nolen
Department of Physics and Astronomy and
National Superconducting Cyclotron Laboratory,

B. M. Sherrill and A. F. Zeller
National Superconducting Cyclotron Laboratory,
Michigan State University, East Lansing, Mi 48824

Abstract

A new method is presented that allows the reconstruction of trajectories and the on-line correction of residual aberrations that limit the resolution of particle spectrographs. Using a computed or fitted high order transfer map that describes the uncorrected aberrations of the spectrograph under consideration, it is possible to determine a pseudo transfer map that allows the computation of the corrected data of interest as well as the reconstructed trajectories in terms of position measurements in two planes near the focal plane.

The technique is only limited by the accuracy of the position measurements and the accuracy of the transfer map. In practice the method can be expressed as an inversion of a pseudo transfer map and implemented in the differential algebraic framework. The method will be used to correct residual high aberrations in the S800 spectrograph which is under construction at the National Superconducting Cyclotron Laboratory at Michigan State University.

1 Introduction

Efficient modern high-resolution mass spectrographs usually offer rather large phase space acceptances. One such spectrograph is the S800 currently under construction at Michigan State University's National Superconducting Cyclotron Laboratory [1, 2]. Such large acceptance high resolution spectrographs usually require a careful consideration and correction of aberrations. But because of the large phase space acceptance, effects of rather high orders contribute. This makes the correction process often considerably more difficult and complex, and sometimes even prevents a complete correction of aberrations in the conventional sense.

It is often possible to circumvent or at least alleviate these problems by using additional information about the particles. In particular, one often measures not only their final position but also their final angle by means of a second detector. With this additional information it is to some degree possible to retroactively construct the whole trajectory of the particle. This information can be used both for the numerical correction of the quantities of interest, but it also reveals additional properties like the initial angle, which is of course of interest in the study of many nuclear processes.

In the past such trajectory reconstruction techniques were quite involved, often requiring extensive ray tracing and the storage of large arrays of ray data and extensive interpolation. In this paper, we present a rather direct and efficient method based on differential algebraic (DA) techniques.

In recent years we have shown that maps of particle optical systems can be computed to much higher orders than previously possible using DA methods [3, 4, 5, 6]. Furthermore, the techniques also allow the accurate treatment of very complicated fields that can be treated only approximately otherwise. In our particular case, these include the fringe fields of the large aperture magnets required for such particle spectrographs. So for the first time there is now the possibility to really compute all the aberrations that comprise a modern high resolution spectrograph without having to rely on tedious ray tracing.

On the practical side this requires high order codes for the computation of highly accurate maps for realistic fields. The new code COSY INFINITY [7, 8, 9, 10] allows such computations in a very powerful language environment. It also has extensive and general optimization capabilities, supports interactive graphics and provides ample power for customised problems, and it provides all the necessary tools for efficient trajectory reconstruction.

In the next section, we will discuss an important algorithm for this task, the inversion of transfer maps. Section 3 outlines the use of map inversion techniques for the purposes of trajectory reconstruction. Section 4 provides an outlook for the practical application in connection with the S800 spectrograph.

2 Inversion of Transfer Maps

At the core of the operations that follow is the need to invert transfer maps in their DA representation. Though at first glance this appears like a very difficult problem, we will see that indeed there is a rather elegant and closed

*Supported in Part by the U.S. National Science Foundation, Grant Number PHY 89-13815

algorithm to perform this task.

We begin by splitting the map A_n into its linear and nonlinear parts:

$$A_n = A_{1n} + A_{2n}. \quad (1)$$

Furthermore, we write the sought for inverse as M_n.

$$A^{-1n} = M_n \quad (2)$$

Composing the functions, we obtain

$$\begin{aligned}(A_1 + A_{2n}) \circ M_n &= E_n \Rightarrow \\ A_1 \circ M_n &= E_n - A_{2n} \circ M_n \Rightarrow \\ M_n &= A_1^{-1} \circ (E_n - A_{2n} \circ M_{n-1}). \quad (3)\end{aligned}$$

Here "o" stands for the composition of maps. In the last step use has been made of the fact that knowing M_{n-1} allows us to compute $A_{2n} \circ M_{n-1}$. The necessary computation of A_1^{-1} is a linear matrix inversion.

Equation (3) can now be used in a recursive manner to compute the M_i order by order.

3 Trajectory Reconstruction

The result of the computation of the transfer map of the system allows us to relate final quantities to initial quantities and parameters. In our case, the relevant quantities are the positions in x and y directions as well as the measures of slopes p_x/p_0, p_y/p_0 and the energy of the particles under consideration. Usually the initial x, ~~which is determined by the target thickness or a subsequent slit,~~ is kept small, ~~to provide a minimal entrance width.~~ So the final positions and slopes are primarily determined by the energy, and to higher orders also by the initial y position and the initial slopes.

In the full transfer map we now set x_i to zero and consider the following submap:

$$\begin{pmatrix} x_f \\ a_f \\ y_f \\ b_f \end{pmatrix} = S \begin{pmatrix} a_i \\ y_i \\ b_i \\ d \end{pmatrix} \quad (4)$$

This map relates the quantities which can be measured in the two planes to the quantities of interest. The map S is not a regular transfer map, and in particular its linear part does not have to be a priori invertible. In a well designed particle spectrograph, the linear part has the following form:

$$\begin{pmatrix} x_f \\ a_f \\ y_f \\ b_f \end{pmatrix} = \begin{pmatrix} 0 & 0 & 0 & * \\ * & 0 & 0 & * \\ 0 & * & * & 0 \\ 0 & * & * & 0 \end{pmatrix} \cdot \begin{pmatrix} a_i \\ y_i \\ b_i \\ d_i \end{pmatrix} \quad (5)$$

where a star denotes an entry that is not zero. Since the system is imaging, clearly (x,a) vanishes, and all the other zero terms vanish because of midplane symmetry. (x,d) is maximized in spectrograph design, and (a,a) cannot vanish in an imaging system because of symplecticity. In fact, to reduce the effect of the finite size entrance slit, (x,x) is minimized within the constraints, and so (a,a) = 1/(x,x) is also maximized.

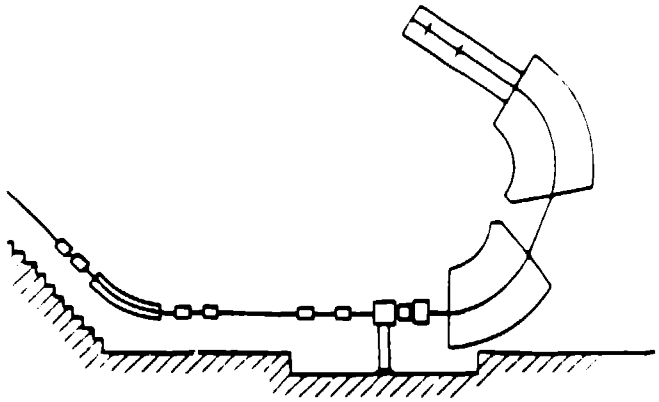

Figure 1: The vertical layout of the S800 spectrograph

Because of symplecticity, (y,y)(b,b)-(y,b)(b,y) = 1, and so we obtain for the total determinant of S:

$$|S| = (x,d) \cdot (a,a) \neq 0, \quad (6)$$

besides being nonzero, the size of the determinant is also a good measure of the quality of the spectrograph: the larger the better.

So certainly the linear matrix is invertible, and according to the last section, this entails that the whole nonlinear map S is invertible to arbitrary order, and thus it is possible to compute the initial quantities of interest to arbitrary order.

A closer inspection of the algorithm shows that in each iteration, the result is multiplied by the inverse of the linear matrix S. Since the determinant of this inverse is the inverse of the original determinant and is thus quite small, this entails that the originally large terms in the nonlinear part of the original map are more and more suppressed. So clearly even with trajectory construction, the original investment in the quality of the spectrograph, which is determined by its dispersion and its x demagnification, directly influences the quality of the trajectory reconstruction.

4 The Correction of Aberrations in Spectrographs

The proposed superconducting magnetic spectrograph, the S800 [1] shown in fig. 1, for the National Superconducting Cyclotron Laboratory will allow the study of heavy ion reactions with magnetic rigidities of up to 1.2 GeV/c. It will have an energy resolution of one part in 10000 with a

Table 1: The S800 Spectrograph

Drift	l = 60 cm
Quad	l = 40 cm, G_{max} = 21 T/m , ~~d~~ r = ~~.01~~ .1 m
Drift	l = 20 cm
Quad	l = 40 cm, G_{max} = 6.8 T/m, ~~d~~ r = ~~.02~~ .2 m
Drift	l = 50 cm
Dipole	r = 2.6667 m, $B_{max} = 1.5T$, ϕ = 75 deg, ϵ_1 = 0 deg, ϵ_2 = 30 deg
Drift	l = 140 cm
Dipole	r = 2.6667 m, $B_{max} = 1.5T$, ϕ = 75 deg, ϵ_1 = 30 deg, ϵ_2 = 0 deg
Drift	l = 257.5 cm

large solid angle of about 20 msr and an energy acceptance of about 10 percent.

The spectrograph will be used in connection with the new K1200 Superconducting Cyclotron for beams of protons up to Uranium with energies of 2 to 200 MeV/u. It will provide unique opportunities for research in various areas, including the study of giant resonances, charge exchange, direct reaction studies and fundamental investigations of nuclear structure [11].

The S800 consists of two superconducting quadrupoles and two 75 degree dipoles with y-focusing edge angles. Table 1 lists the parameters of the system. The settings of the quadrupoles shown here correspond to particles of 193.04 MeV, mass 100 and charge 50. Standard optics notation is used.

After a careful measurement of the crucial fringe fields of the dipoles, we will be using COSY to determine the high order properties of the map of the spectrograph. The computation of the map S from the resulting transfer map can be performed directly within the COSY environment, and so can the inversion of the map S. Altogether, a correction map S is found, the nonlinearity of which is determined by the nonlinearity of the original map and the quality in the spectrograph measured by (x,d)/(x,x). It is anticipated that the correction map can be used for an on line determination of the relevant data without having to store the raw two plane position measurements.

In closing we would like to note that the method can also be employed for spectrographs for which no sufficient field measurements are known. To this end, one has to perform experimental ray tracing and fit the resulting data with a polynomial type transfer map. Also in this case, the inversion can be done in the map picture resulting in a rather compact representation of the data necessary for correction.

References

[1] J. Nolen, A.F. Zeller, B. Sherrill, J. C. DeKamp, and J. Yurkon. A proposal for construction of the S800 spectrograph. Technical Report MSUCL-694, National Superconducting Cyclotron Laboratory, 1989.

[2] L. H. Harwood A. F. Zeller, J. A. Nolen and E. Kashy. The MSU 1.2 GeV/c spectrograph. In *Workshop on High Resolution, Large Acceptance Spectrometers, ANL/PHY-81-2*. Argonne National Laboratory, 1982.

[3] M. Berz. Arbitrary order description of arbitrary particle optical systems. *Nuclear Instruments and Methods*, A298:426, 1990.

[4] M. Berz. Differential Algebraic description of beam dynamics to very high orders. *Particle Accelerators*, 24:109, 1989.

[5] M. Berz. Differential Algebraic treatment of beam dynamics to very high orders including applications to spacecharge. *AIP Conference Proceedings*, 177:275, 1988.

[6] M. Berz. Differential Algebraic description and analysis of trajectories in vacuum electronic devices including spacecharge effects. *IEEE Transactions on Electron Devices*, 35-11:2002, 1988.

[7] M. Berz. COSY INFINITY Version 3 reference manual. Technical Report MSUCL-751, National Superconducting Cyclotron Laboratory, Michigan State University, East Lansing, MI 48824, 1990.

[8] M. Berz. Computational aspects of design and simulation: COSY INFINITY. *Nuclear Instruments and Methods*, A298:473, 1990.

[9] M. Berz. COSY INFINITY, an arbitrary order general purpose optics code. *Computer Codes and the Linear Accelerator Community*, Los Alamos LA-11857-C:137, 1990.

[10] M. Berz. COSY INFINITY. In *Proceedings 1991 Particle Accelerator Conference*, San Francisco, CA, 1991.

[11] N. Anantaraman and B. Sherrill, Editors. Proceedings of the international conference on heavy ion research with magnetic spectrographs. Technical Report MSUCL-685, National Superconducting Cyclotron Laboratory, 1989.

SPECTROMETER DESIGN AT MICHIGAN STATE

SPECTROMETER DESIGN AT NSCL/MSU

A. ZELLER

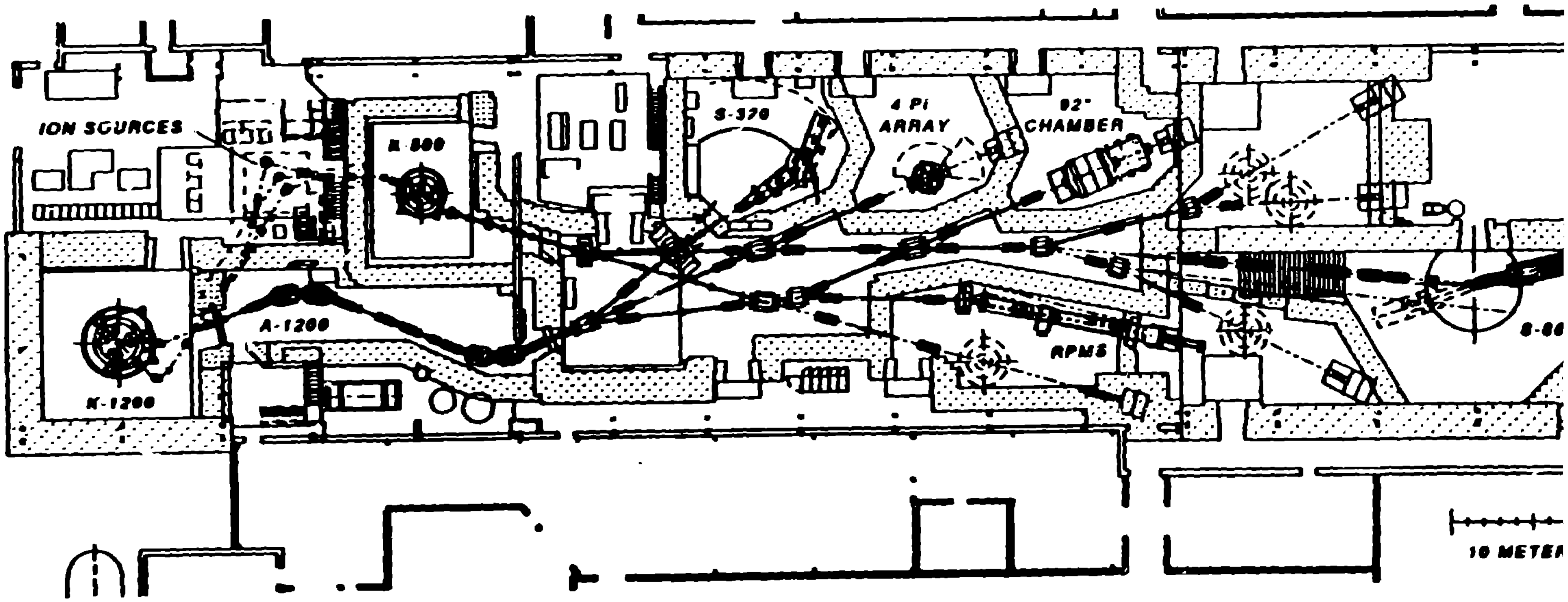

ION SOURCES
K-500
K-1200
A-1200
S-320
4 Pi
ARRAY
92"
CHAMBER
RPMS

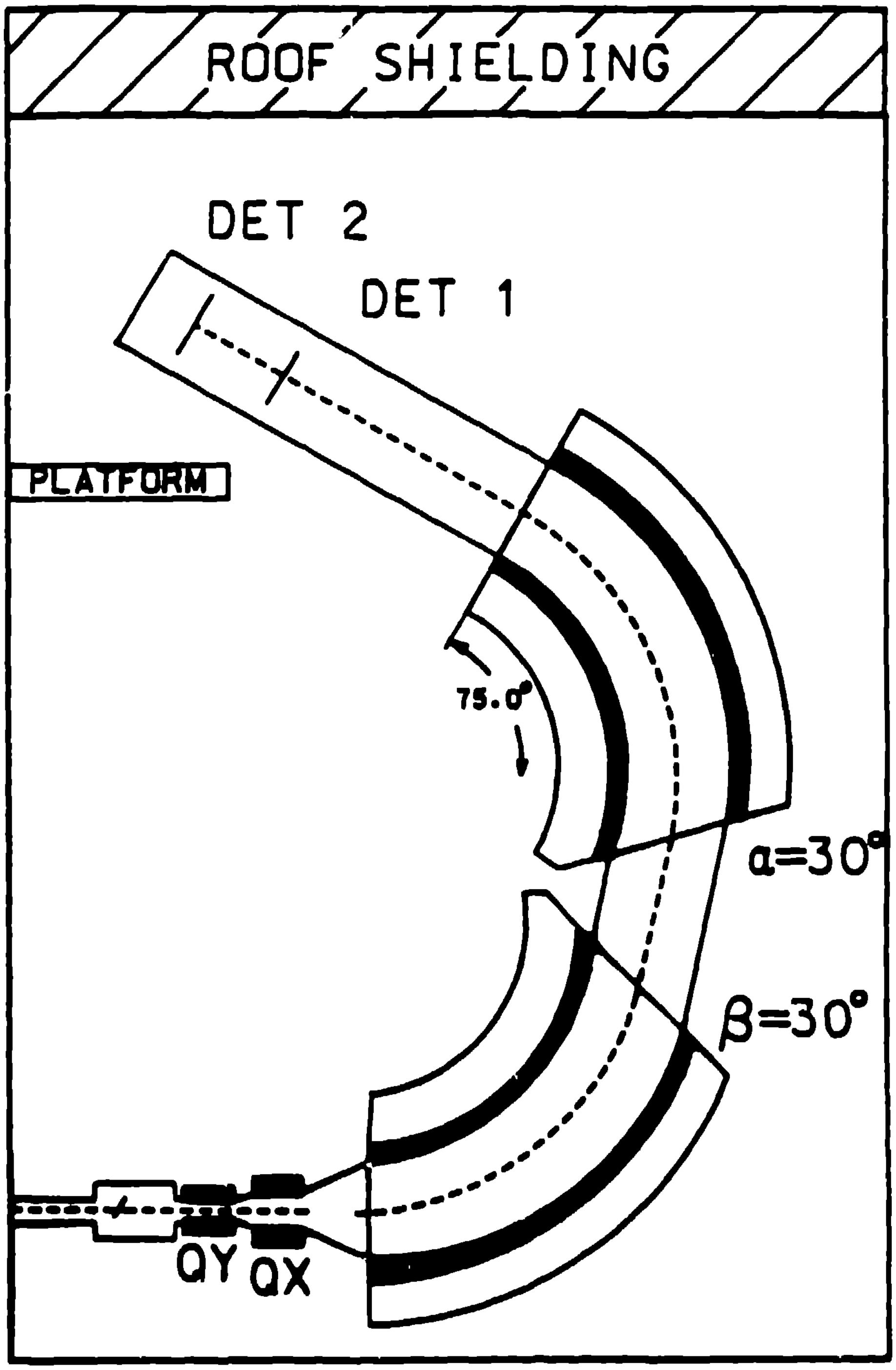
ROOF SHIELDING
DET 2
DET 1
PLATFORM
75.0°
α=30°
β=30°
QY
QX

PARAMETERS OF THE MSU 1.2 GeV/c SPECTROGRAPH

ENERGY RESOLUTION:	$\Delta E/E = 10^{-4}$ WITH 1mm RADIAL OBJECT SIZE FOR BEAM ANALYSIS SYSTEM
ENERGY RANGE:	$\Delta E/E$ = 10%
SOLID ANGLE:	Ω = 10-20 msr
RESOLVING POWER:	D/M = 11.7
RADIAL DISPERSION:	D = 9 cm/%
RADIAL MAGNIFICATION:	M = 0.78
AXIAL DISPERSION:	R_{34} = 0.74 mm/mr
ANGULAR RESOLUTION:	$\Delta\theta \leq 2$ mr (TOTAL OF BEAM PLUS SPECTROGRAPH CONTRIBUTIONS)
FOCAL PLANE SIZE:	50 cm (RADIAL) X 15 cm (AXIAL)
FOCAL PLANE TILT:	0°
MAGNETIC RIGIDITY:	$B\rho$ = 4T-m
DIPOLE FIELDS:	B = 1.5T(ρ = 2.7 m)
DIPOLE GAP:	D = 15 cm
DIPOLE SIZE:	3.5 m LONG X 100 cm WIDE (75° BEND) QTY OF 2
WEIGHT OF DIPOLES:	APPROX. 70 TONS EACH
QUAD SIZES:	*1) 20 cm ID X 40 cm LONG *2) 35 cm X 17 cm X 40 cm
DETECTOR REQUIREMENTS:	TWO 2-DIMENSIONAL DET., 1m SEPARATION *1) 50 cm X 15 cm *2) 62 cm X 16 cm RESOLUTION: RADIAL 0.2 mm AXIAL 0.4 mm

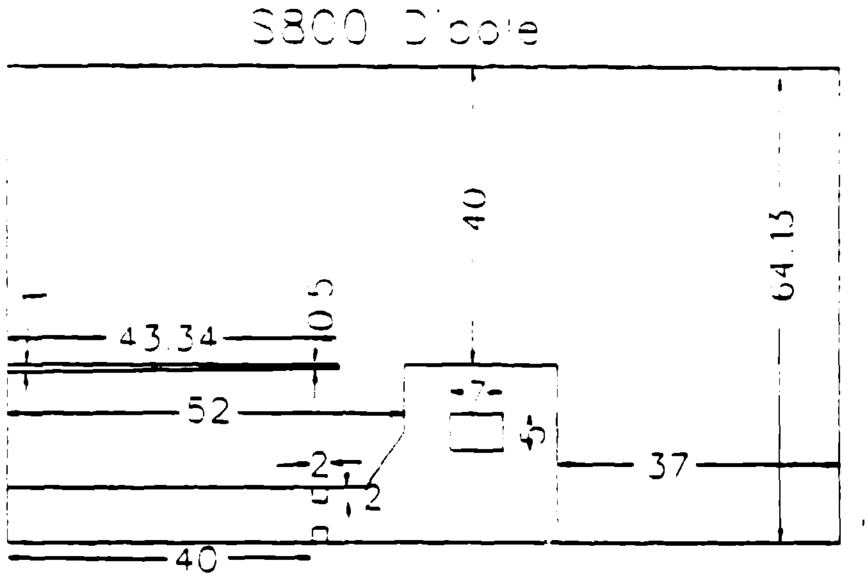

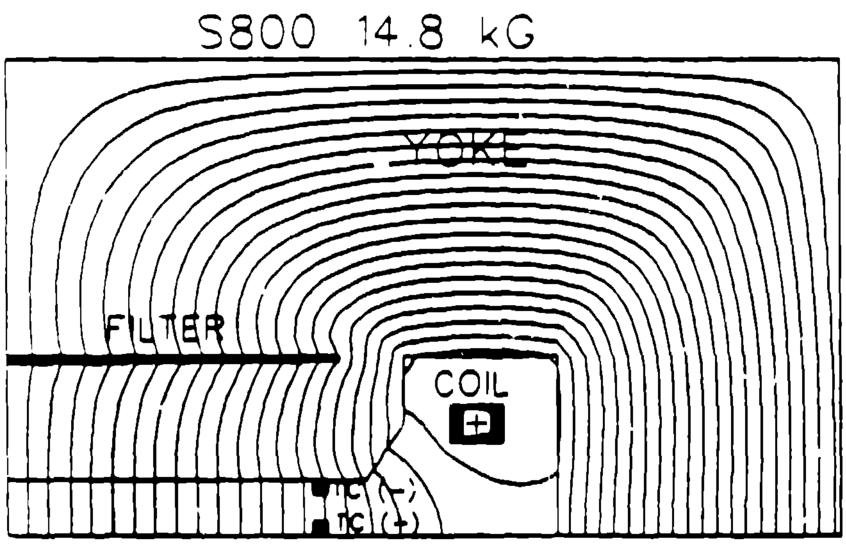

Software corrections $\longrightarrow$ $\frac{\Delta B}{B_0} \leq 5\times10^{-5}$

$\frac{dB}{dr} \leq 1$ G/cm to 35 cm

This Page is Blank

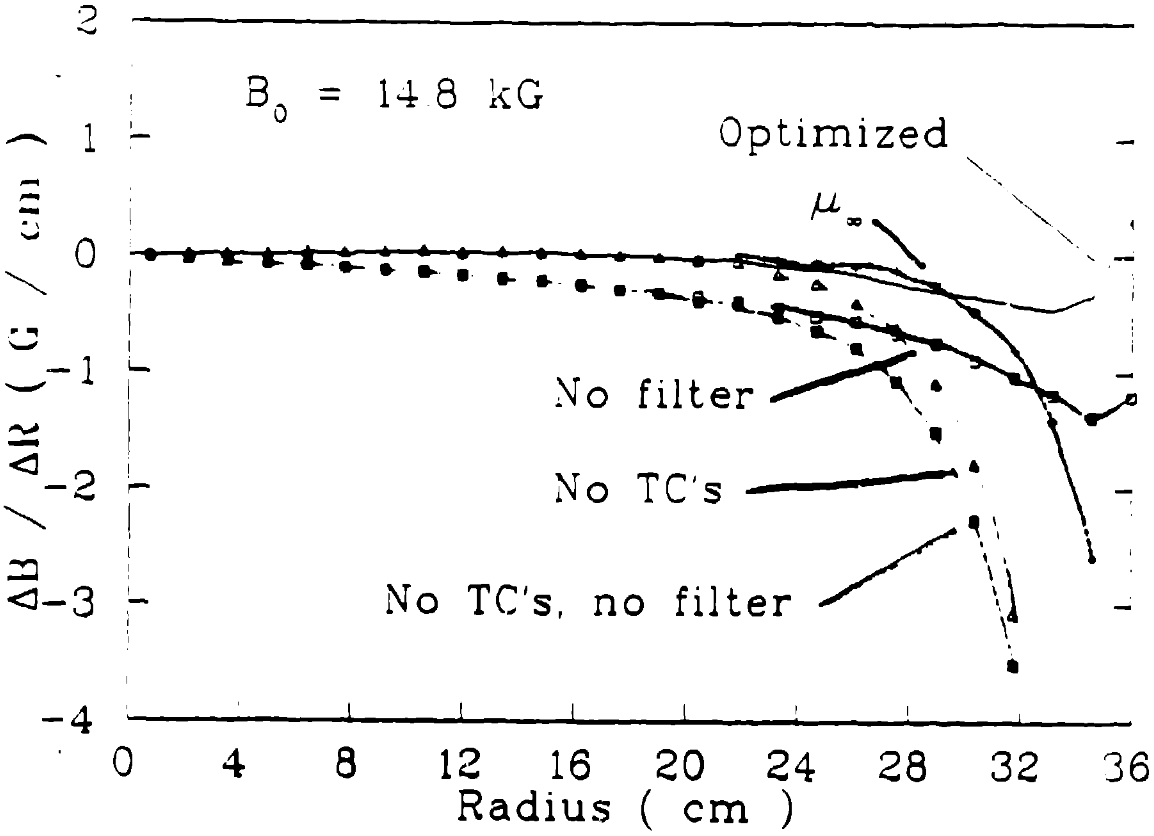

B_0 = 14.8 kG
Optimized
μ_∞
No filter
No TC's
No TC's, no filter
ΔB / ΔR (G / cm)
Radius (cm)
2
1
0
−1
−2
−3
−4
0
4
8
12
16
20
24
28
32
36

MSUCL 81-260

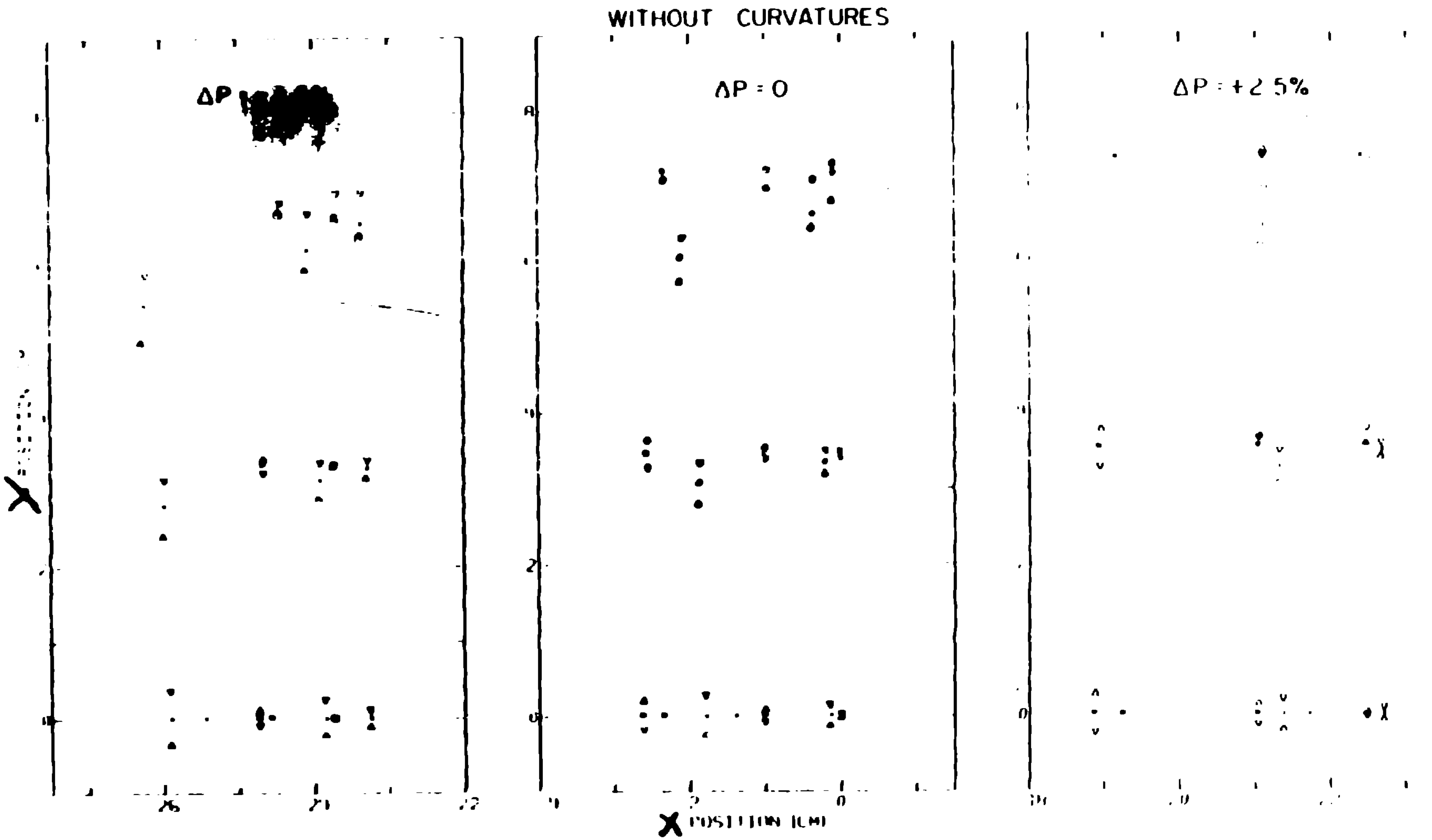

FOCAL PLANE

Table 1

trix elements" used in MOTER obtained by trial and error.

x (momentum)	y (scattering angle)
$\theta\delta(\theta x)$ *	θy *
θ^2 *	$\theta\phi$ *
$\delta^2(x^2)$ *	$\phi\delta$ *
ϕ^2 *	$y\delta$ *
ϕy *	$y\delta$ *
y^2 *	$\theta^2 y$ *
θ^3 *	ϕ^3 *
$\theta^2\delta(\theta^2 x)$ *	$\theta^2\phi$ *
$\theta\delta^2(x^2\theta)$ *	$y\theta\delta$ *
$\theta\phi^2$ *	$\theta\phi\delta$ *
$\delta^3(x^3, x\delta^2)$ *	$\theta\phi^2$ *
$\phi^2\delta(\phi^2 x)$ *	$y^2\phi$ *
θ^4 *	$\phi\delta^2$ *
$\theta^2\phi^2$	$y\delta^2$ *
y^4	$\theta y\phi^2$ *
$\theta^3\delta(\theta^3 x)$ *	$\theta\phi^3$ *
$\phi^2 y^2$	$\theta^3\phi$ *
θ^5	$\phi^3\delta$ *
$\theta^3\phi^2$	$y\phi^2\delta$ *
$\theta\phi^4$	$\theta^2\phi\delta$ *
	$\theta y\phi^2\delta$
	ϕ^5
	$y^3\phi^2$
	$y^{[illegible]}\phi^3$

* Common to both lists

Table 2
Matrix elements from COSY INFINITY

x	y
$\theta y \phi$	$x\theta^2\phi$
$x\theta^2\phi$	$\theta\phi\delta^2$
$\theta^2\delta^2$	
$\theta\delta^3$	
$\theta^3\delta^2$	

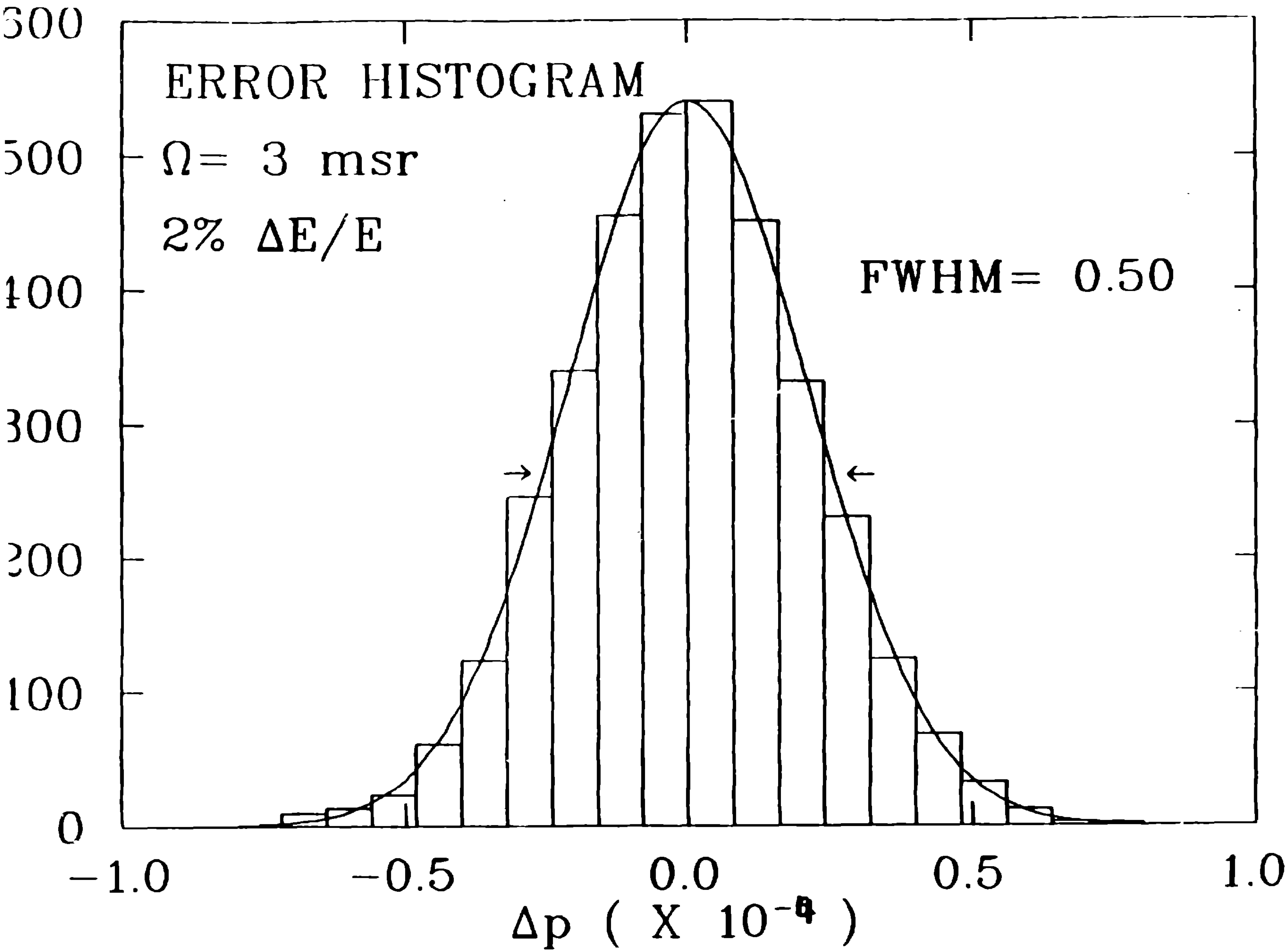
ERROR HISTOGRAM
Ω= 3 msr
2% ΔE/E
FWHM= 0.50
600
500
400
300
200
100
0
−1.0
−0.5
0.0
0.5
1.0
Δp (X 10^-4)

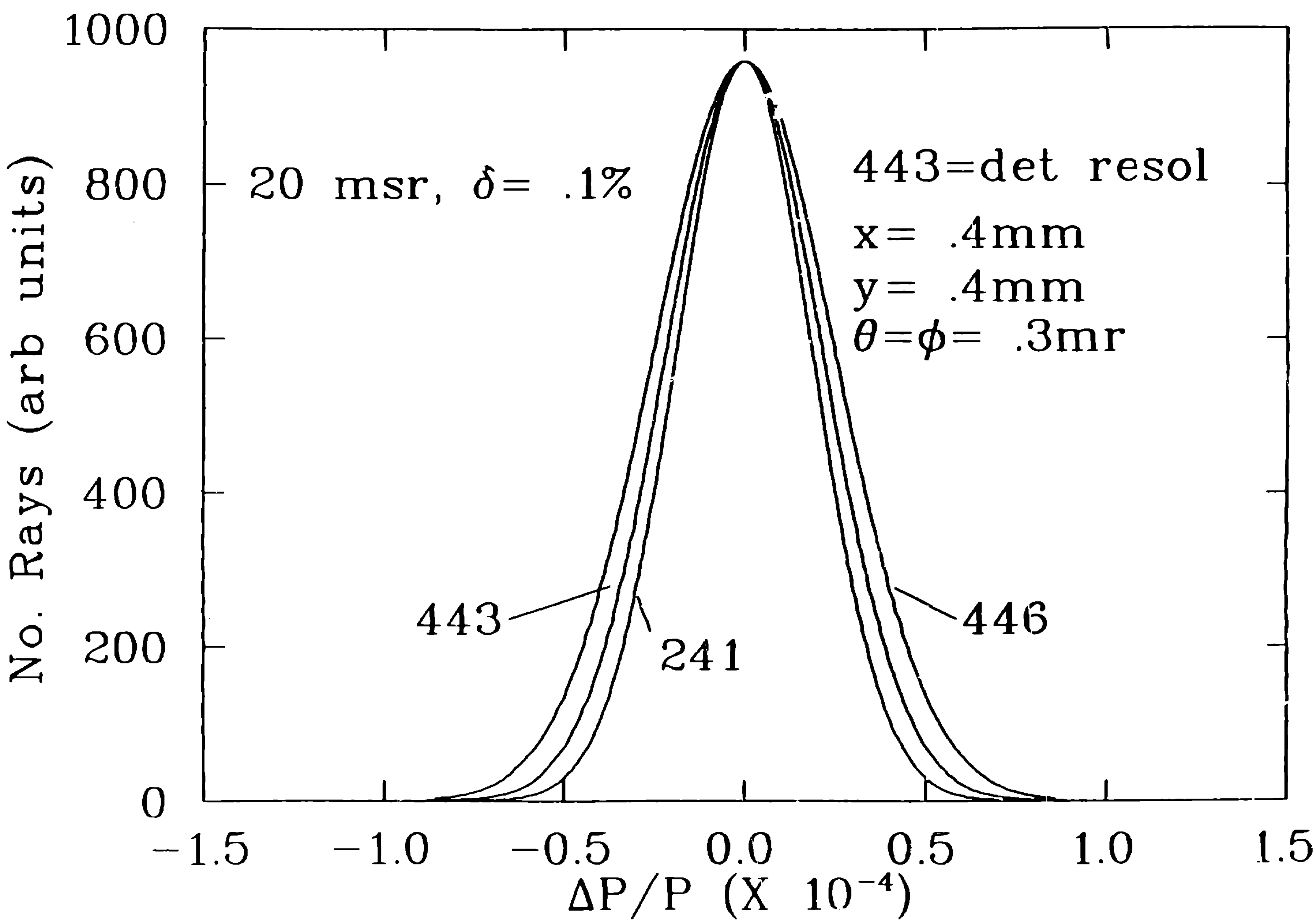

20 msr, δ= .1%
443=det resol
x= .4mm
y= .4mm
θ=φ= .3mr
443
241
446
No. Rays (arb units)
0
200
400
600
800
1000
−1.5
−1.0
−0.5
0.0
0.5
1.0
1.5
ΔP/P (X 10^-4)

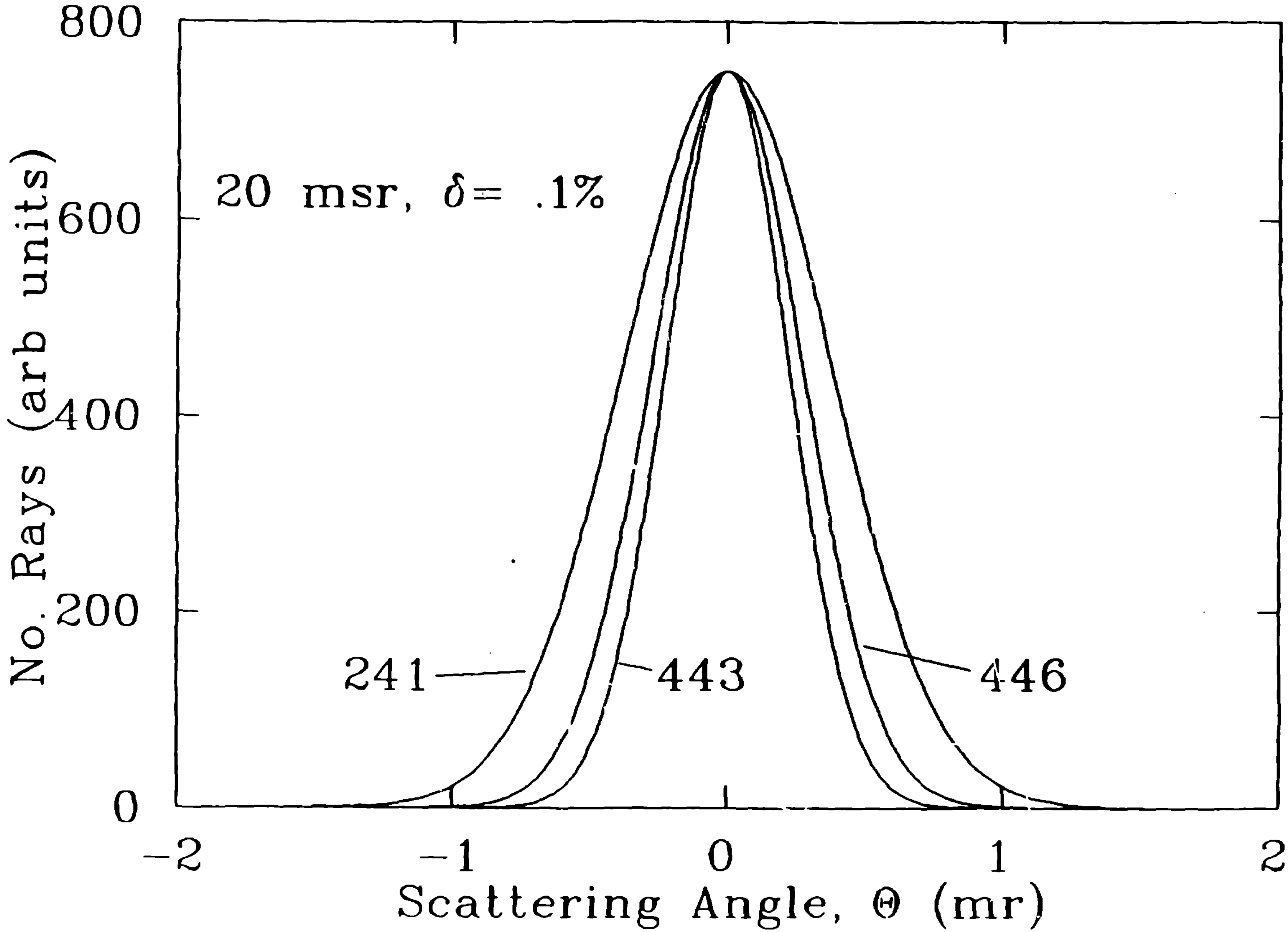

800
600
400
200
0
No. Rays (arb units)
20 msr, δ= .1%
241
443
446
−2
−1
0
1
2
Scattering Angle, Θ (mr)

196

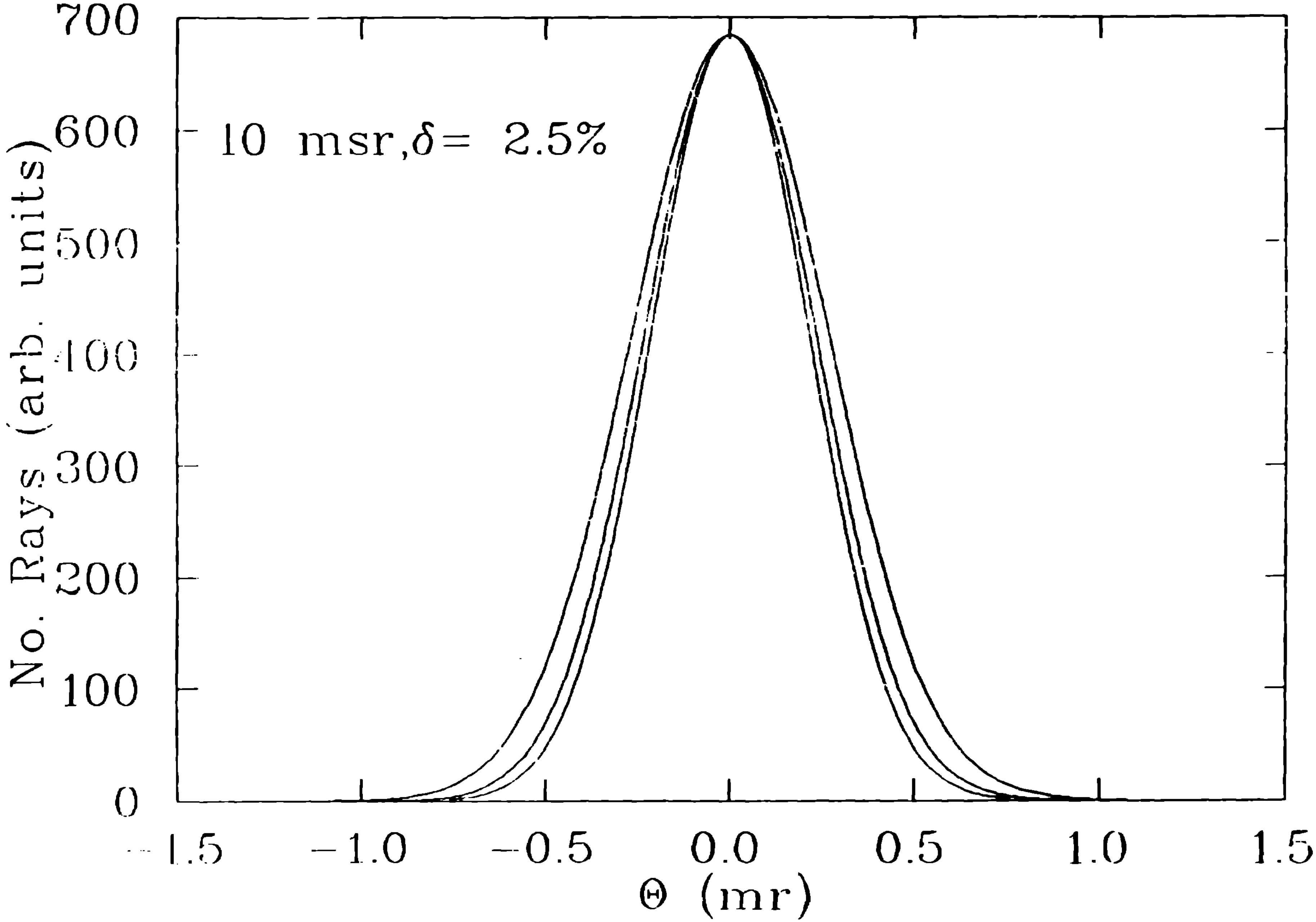

700
600
500
400
300
200
100
0
10 msr,δ= 2.5%
No. Rays (arb. units)
−1.5
−1.0
−0.5
0.0
0.5
1.0
1.5
Θ (mr)

197

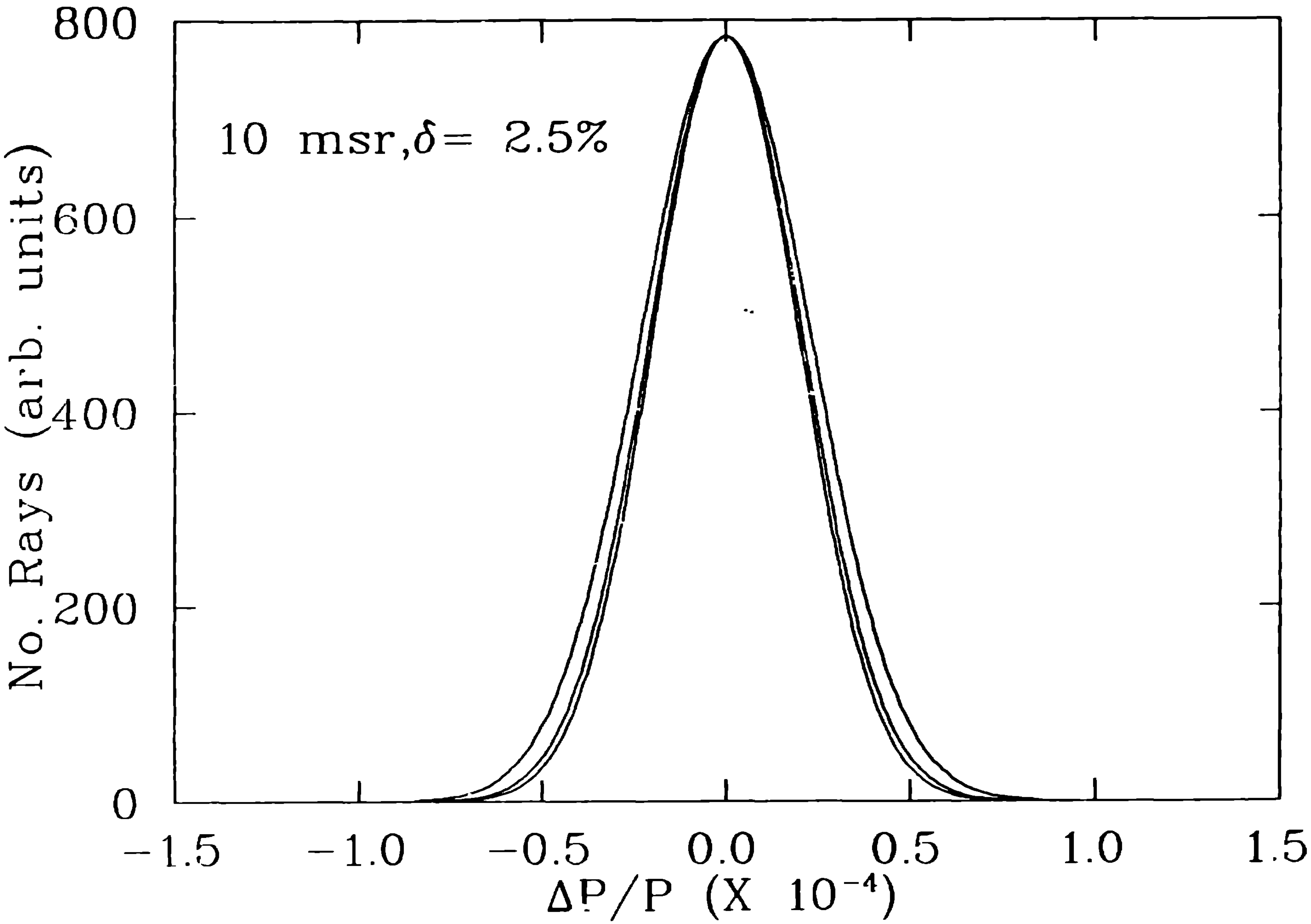

10 msr, δ= 2.5%
No. Rays (arb. units)
800
600
400
200
0
−1.5
−1.0
−0.5
0.0
0.5
1.0
1.5
$\Delta P/P$ (X 10^{-4})

198

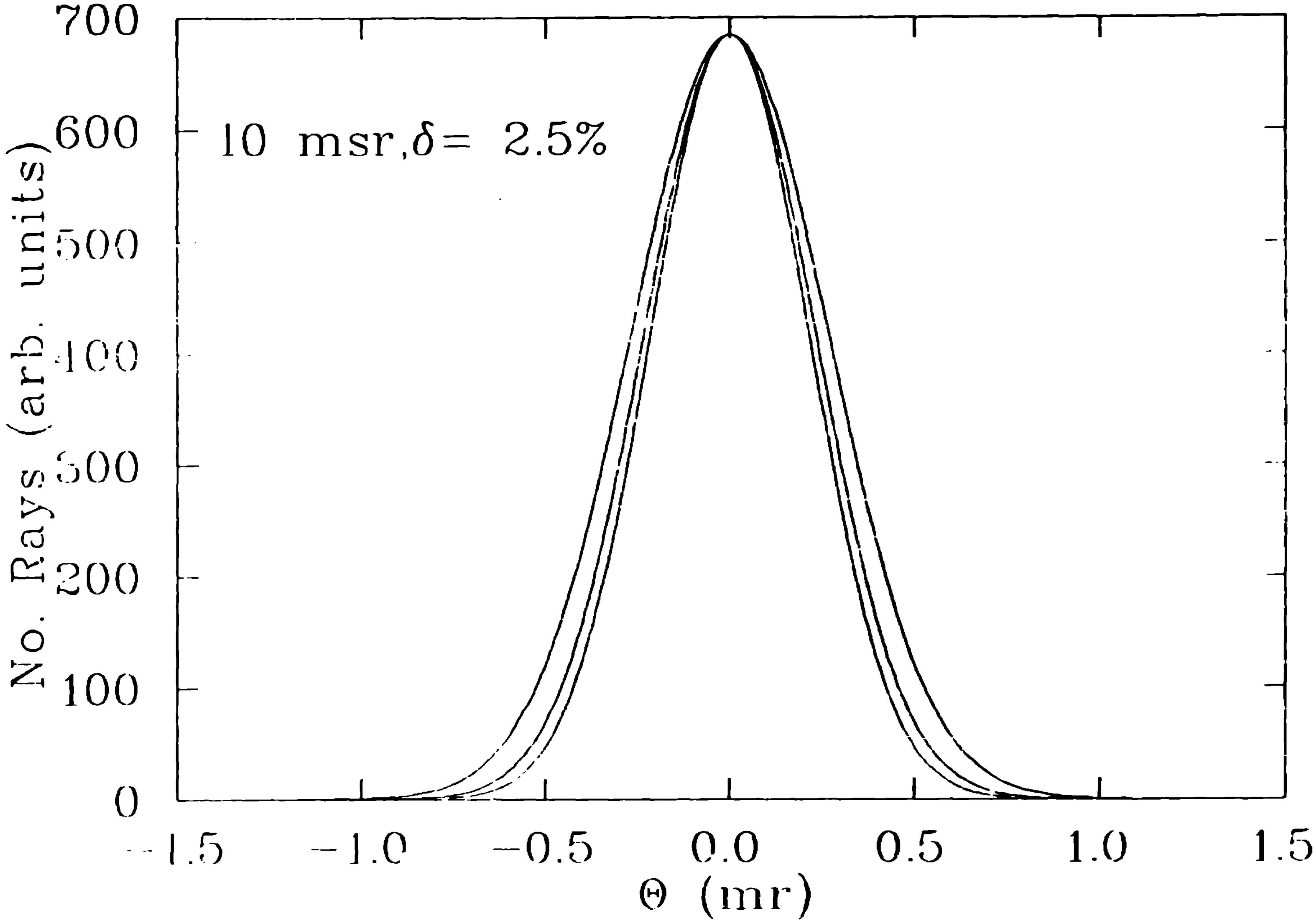

10 msr,δ= 2.5%
No. Rays (arb. units)
Θ (mr)
0
100
200
300
400
500
600
700
−1.5
−1.0
−0.5
0.0
0.5
1.0
1.5

Table 3
S800 spectrograph resolutions

	No gradients in dipoles				Gradients			
	Ω=20, δ=.1		Ω=10, δ=2.5		Ω=20, δ=.1		Ω=10, δ=2.5	
	$\Delta p/p$	$\Delta\theta$	$\Delta p/p$	$\Delta\theta$	$\Delta p/p$	$\Delta\theta$	$\Delta p/p$	$\Delta\theta$
ld	0.49	0.53	0.46	0.50	0.49	0.51	0.46	0.51
ld+COSY	0.49	0.53	0.45	0.50	0.49	0.51	0.45	0.50
OSY only	0.50	0.62	0.45	0.63	0.50	0.61	0.45	0.64

nits are $\Delta p/p = 1 \times 10^{-4}$, $\Delta\theta$= mr, Ω= msr, δ= ±%

USE OF MOTER AT CEBAF & RELATED TOPICS

J. NAPOLITANO, CEBAF
PILAC OPTICS WORKSH
AUGUST 12-13, 1991

FIELDS IN A "REAL" QUADRUPOLE MAGNET

W/ TED HUNTER
STEVE LASSITER
LEIGH HARWOOD

EFFECTS IN A "REAL" SPECTROMETER

THE CEBAF 6 GeV/c HIGH MOMENTUM SPECTROME

W/ STEVE WOOD
CHEN YAN
LEIGH HARWOOD

LARGE APERTURE QUADRUPOLE MAGNETS

Superconducting magnets with large apertures are useful for designing high momentum, large acceptance spectrometers.

EXAMPLES:

	MSU/NSCL S800	UNDER CONSTRUCTION
(x2)	CEBAF HRS 4 GeV	DESIGN COMPLETED
	CEBAF HMS 6 GeV	DESIGN COMPLETED

NOTE: NO (?) OPERATING FOCUSSING SPECTROMETERS WITH SUPERCONDUCTING LARGE APERTURE MAGNETS

HOWEVER, ...

Aberrations grow with large powers of the radius.

→ How bad are these aberrations and what is their effect on spectrometer performance?

ABERRATIONS IN QUADRUPOLE MAGNETS

THE PERFECT QUADRUPOLE :

$$\Phi(r,\theta,z) = \frac{r_0}{2} D_2 \left(\frac{r}{r_0}\right)^2 \cos 2\theta$$

FOR $-L/2 \le z \le L/2$; $= \emptyset$ OTHERWISE

i.e. $B_\theta \propto r \rightarrow$

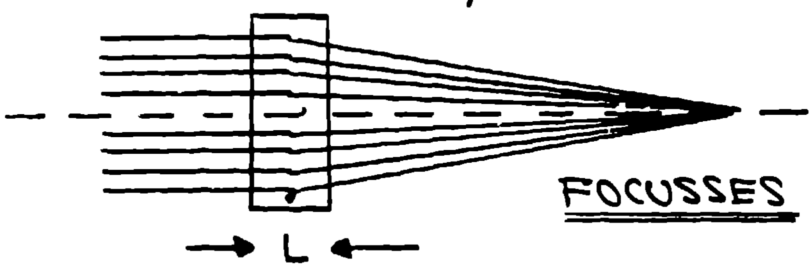

TWO SOURCES OF NON-r^2 DEPENDENCE :

- HIGHER ORDER MULTIPOLES (see P. Walstrom, tomorro

$$\Phi_n(r,\theta,z) = \frac{r_0}{n} D_n \left(\frac{r}{r_0}\right)^n \cos n\theta \qquad n > 2$$

— RESIDUALS OF 8-FOLD SYMMETRY ($n=6,10,14,\ldots$)
— RESULTS OF NOT 8-FOLD SYMMETRY ($n =$ anything

- FRINGE EFFECTS

$$\Phi_n(r,\theta,z) = \frac{r_0}{n} D_n(z) \left(\frac{r}{r_0}\right)^n \cos n\theta$$

INDUCES HIGHER ORDER r^{2m} ($m \ge 1$) TERMS THROUGH DERIVATIVES OF $D_n(z)$

A General Form for the 3D Solution to Laplace's Equation

See K. Halbach, Today & Tomorrow

$$\Phi(r,\theta,z) = \sum_{n=0}^{\infty} \left\{ \underbrace{\sum_{m=0}^{\infty} \frac{r_0}{2m+n}\, b_{m,n}(z) \left(\frac{r}{r_0}\right)^{2m}}_{m \geq 1 \text{ induced in fringe}} \right\} \left(\frac{r}{r_0}\right)^{n} \cos n\theta$$

For $m \geq 1$ find
$$b_{m,n}(z) = \frac{2m+n}{4m(m+n)(2m+n-2)}\, r_0^2\, \frac{d^2 b_{m-1,n}}{dz^2}$$

This leads to
$$\int_0^{\infty} B_{\theta,n}(r,z)\,dz = \left(\frac{r}{r_0}\right)^{n-1} \int_0^{\infty} b_{0,n}(z)\,dz$$

i.e. <u>the field integral at constant z is given solely by the leading order radial term for that multipole</u> (b_{0n})

In our work we use TOSCA & OPERA to determine $\Phi(r,\theta,z)$ including multipoles. Then we fit the output results to determine the $b_{m,n}(z)$.

AN EXAMPLE J.N. & T. HUNTER NIM A301 (1991) 46?

A SUPERCONDUCTING COLD IRON QUADRUPOLE:
L. HARWOOD, S. LASSITER, W. TUBEL IEEE TRANS. MAG.
25 (1989) 1910

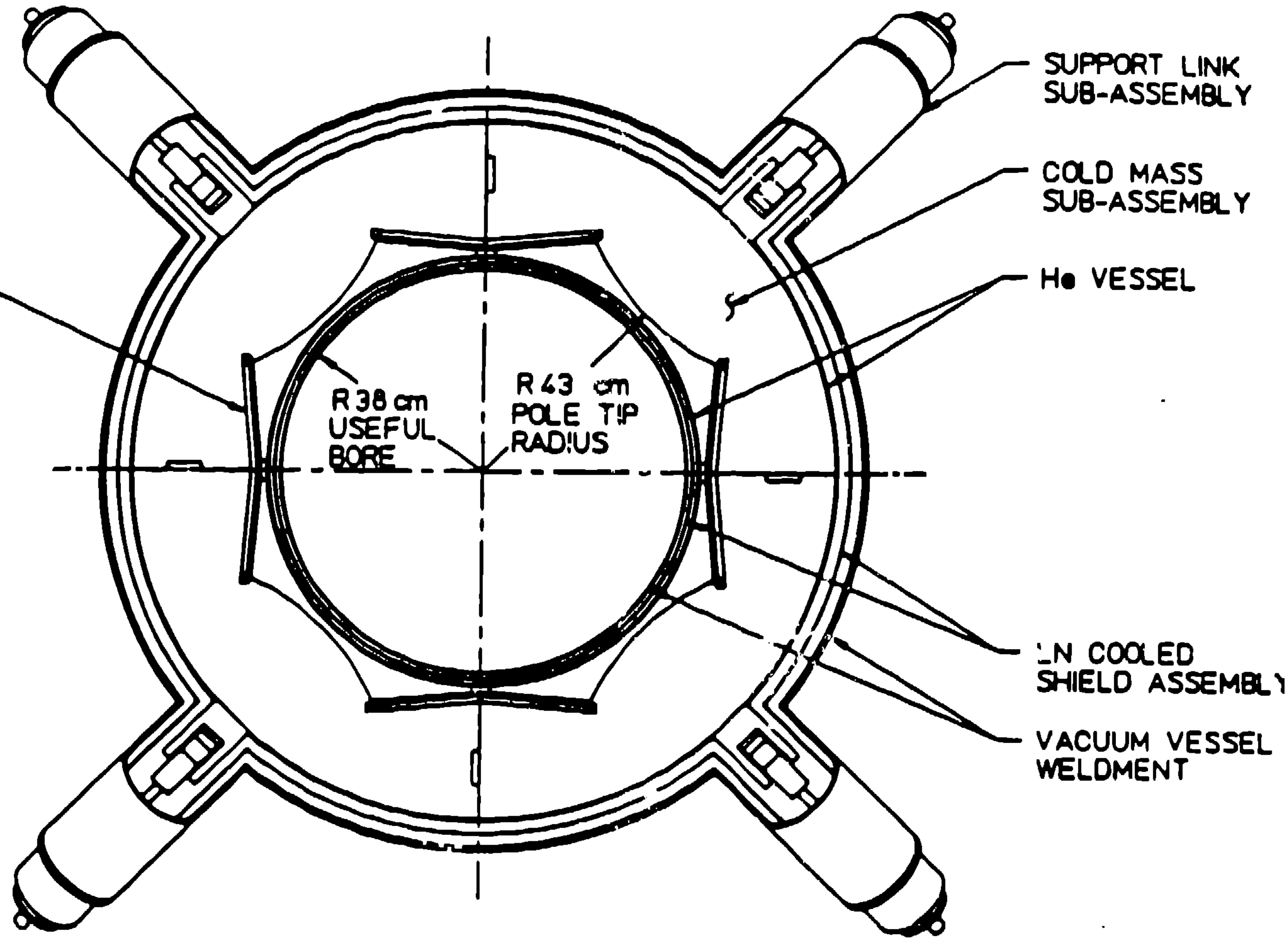

NOTE: STEVE LASSITER (THIS MEETING) WILL PRESENT DETAILS ON THE CURRENT DESIGN AND ANALYSIS STATUS OF THE MAGNETS TO BE USED IN THE HMS

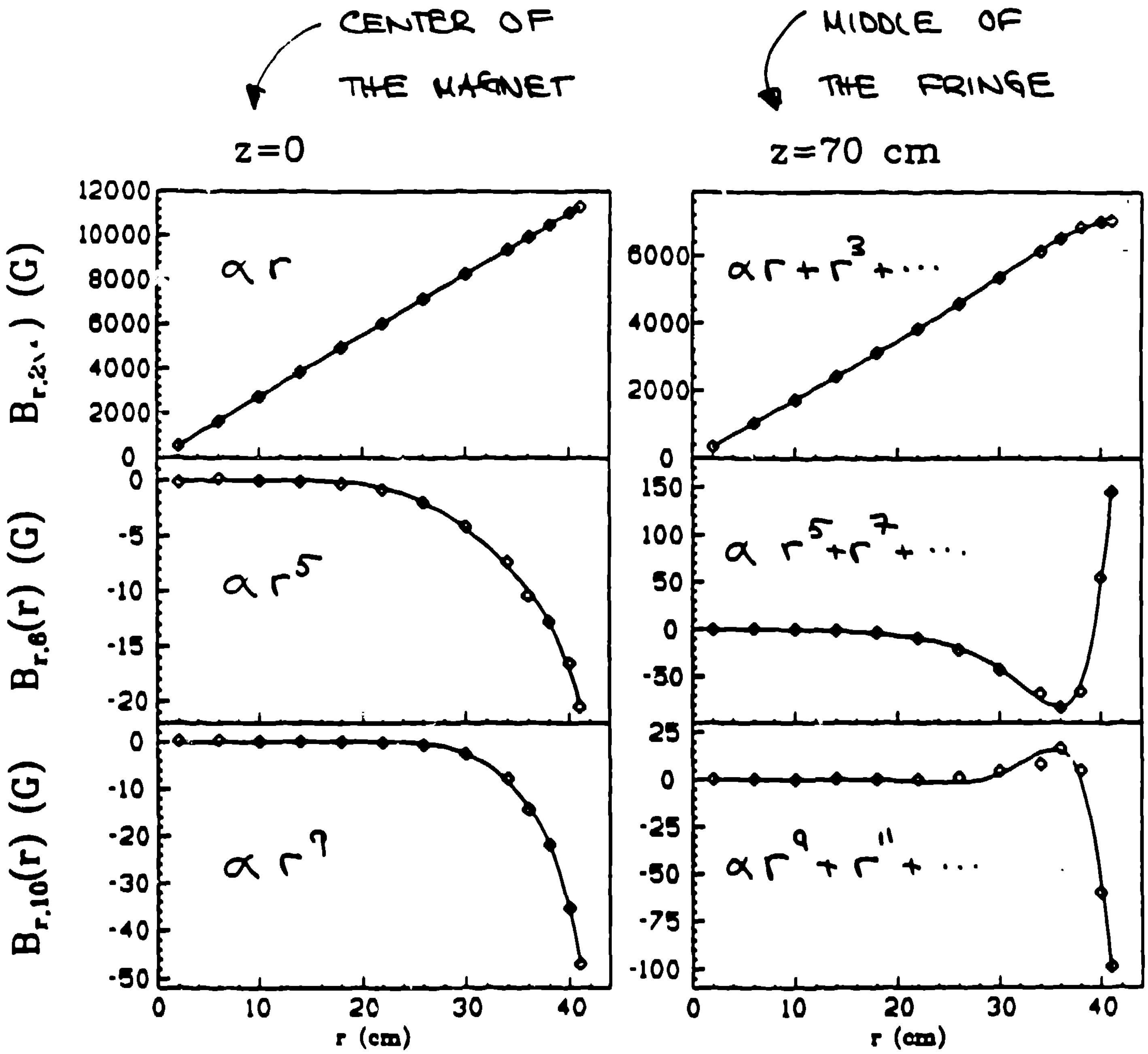

CENTER OF THE MAGNET
MIDDLE OF THE FRINGE
z=0
z=70 cm
$B_{r,2}(r)$ (G)
$B_{r,6}(r)$ (G)
$B_{r,10}(r)$ (G)
$\alpha\ r$
$\alpha\ r + r^3 + \cdots$
$\alpha\ r^5$
$\alpha\ r^5 + r^7 + \cdots$
$\alpha\ r^7$
$\alpha\ r^9 + r^{11} + \cdots$
r (cm)

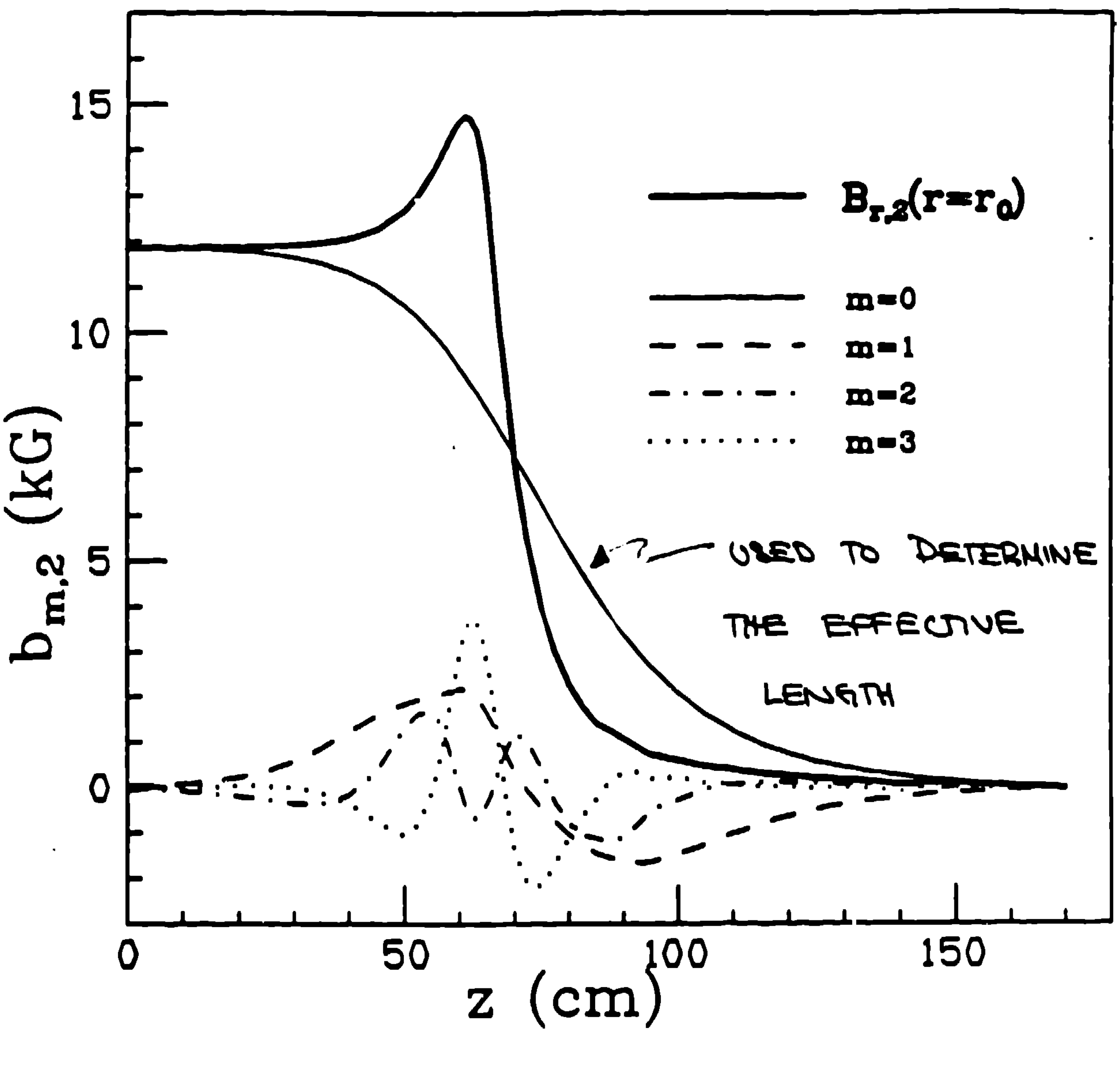
15
10
5
0
0
50
100
150
z (cm)
$b_{m,2}$ (kG)
$B_{r,2}(r=r_0)$
m=0
m=1
m=2
m=3
USED TO DETERMINE
THE EFFECTIVE
LENGTH

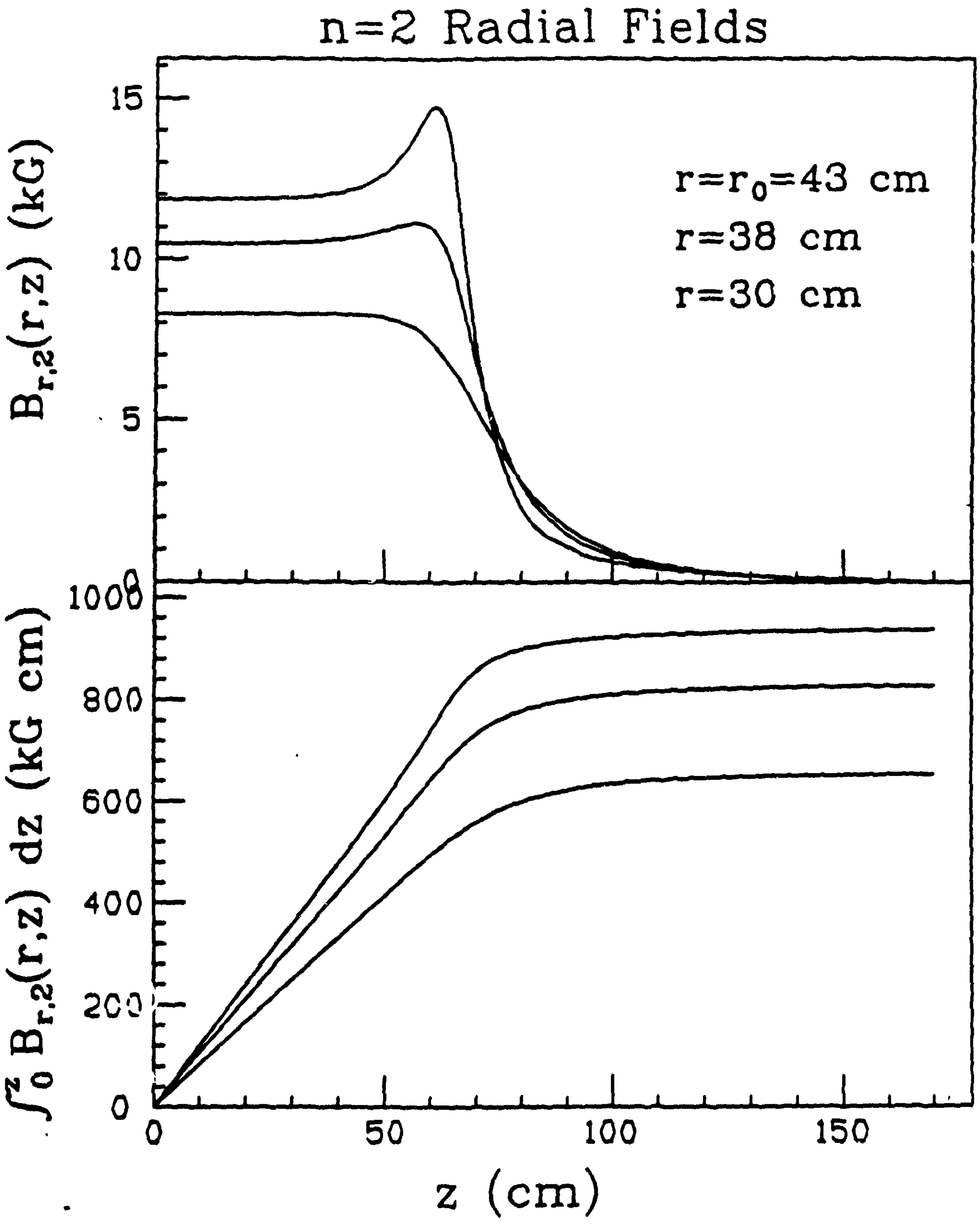
n=2 Radial Fields
15
10
5
0
r=r0=43 cm
r=38 cm
r=30 cm
Br,2(r,z) (kG)
1000
800
600
400
200
0
∫0z Br,2(r,z) dz (kG cm)
0
50
100
150
z (cm)

"DEMONSTRATION" OF THE RELATION

$$\int_0^\infty B_{n,r}(r,z)\,dz = \left(\frac{r}{r_0}\right)^{n-1}\int_0^\infty b_{0,n}(z)\,dz$$

Multipole Components Integrated From $z = 0$ to "∞"

	B.C.: $\Phi = constant$				B.C.: $\partial\Phi/\partial z = 0$			
	Fit $B_{r,n}(r)$		Fit $\Phi_n(r)$		Fit $B_{r,n}(r)$		Fit $\Phi_n(r)$	
Integrated Quantity	All Data	Only $r \leq 38$	All Data	Only $r \leq 38$	All Data	Only $r \leq 38$	All Data	Only $r \leq 38$
$n = 2$ ($T \cdot m$)								
$b_{0,2}$	0.935	0.935	0.935	0.935	0.940	0.940	0.940	0.940
$B_{r,2}(43\ cm)$	0.939		0.937		0.943		0.941	
$B_{r,2}(38\ cm)$	0.828	0.828	0.828	0.828	0.832	0.832	0.832	0.832
$B_{r,2}(30\ cm)$	0.653	0.653	0.653	0.653	0.656	0.656	0.656	0.656
$n = 6$ (% of $n = 2$)								
$b_{0,6}$	-1.84	-0.89	-1.12	-1.20	-1.77	-0.74	-1.03	-1.11
$B_{r,6}(43\ cm)$	-1.30		-1.24		-1.19		-1.15	
$B_{r,6}(38\ cm)$	-0.79	-0.78	-0.73	-0.73	-0.72	-0.72	-0.67	-0.67
$B_{r,6}(30\ cm)$	-0.28	-0.29	-0.28	-0.28	-0.25	-0.26	-0.26	-0.26
$n = 10$ (% of $n = 2$)								
$b_{0,10}$	8.09	-11.34	0.84	1.50	8.24	-10.15	0.75	1.44
$B_{r,10}(43\ cm)$	-0.130		0.238		-0.156		0.222	
$B_{r,10}(38\ cm)$	0.149	0.146	0.105	0.075	0.134	0.130	0.096	0.066
$B_{r,10}(30\ cm)$	0.018	0.025	0.015	0.014	0.017	0.023	0.014	0.013

THE HIGH MOMENTUM SPECTROMETER (HMS)

FOR ELECTRON AND HADRON DETECTION: HALL C @ CEBAF

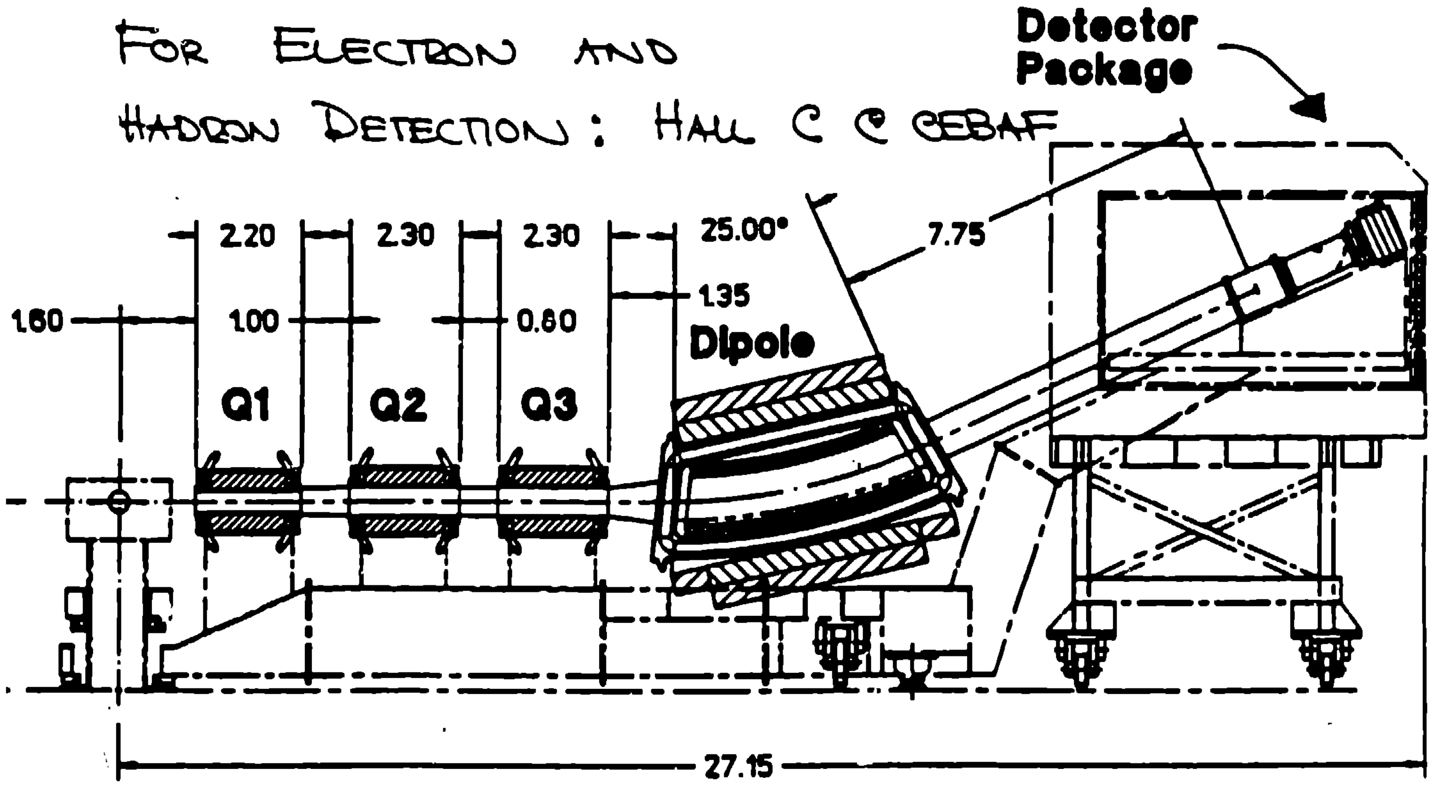

MAXIMUM CENTRAL MOMENTUM (NOM.) ____ 6 GeV/c

MOMENTUM ACCEPTANCE ________ ±5% → ±10%

SCATTERING ANGLE ACCEPTANCE ____ ± 25 mr

OUT-OF-PLANE ANGLE ACCEPTANCE ____ ± 82.5 mr

SOLID ANGLE (NOMINAL) ________ 6.5 msr

TARGET LENGTH ACCEPTANCE ____ ± 5 cm

MOMENTUM RESOLUTION ________ ≲ 0.1 %

SCATTERING ANGLE RESOLUTION ____ ≃ 0.4 mr

PARALLEL - TO - POINT

NO HARDWARE HIGHER ORDER CORRECTIONS!

SUPERCONDUCTING "COLD IRON" QUADRUPOLES FOR THE HMS

	Q1	Q2/Q3
Gradient (G/cm)	605	445
Pole Radius (cm)	25	35
"Good Field" Radius (cm)	22	30
Pole Tip Field (T)	1.512	1.56
Magnet Effective Length (cm)	189	210
Coil Cross Section Area (cm^2)	9.30	12.93
Current Density (A/cm^2)	16,178	16,800
Turns/pole	76	110
Operation current	2,171	1,976
Total Length (feet)	4,000	6,100
Stored Energy (10^6 J)	0.25	0.5

Ideal Design Criteria:

Deviation in Gradient $\leq 2.0 \times 10^{-3}$ out to warm radius

Error in Field $\leq 2.0 \times 10^{-4}$ out to warm radius

SEE TALK BY S. LASSITER FOR MORE DETAILS

FILE HMSPARAPT2: D/M=1.2 ; 6.75M TO FOCUS ; 215CM Q3

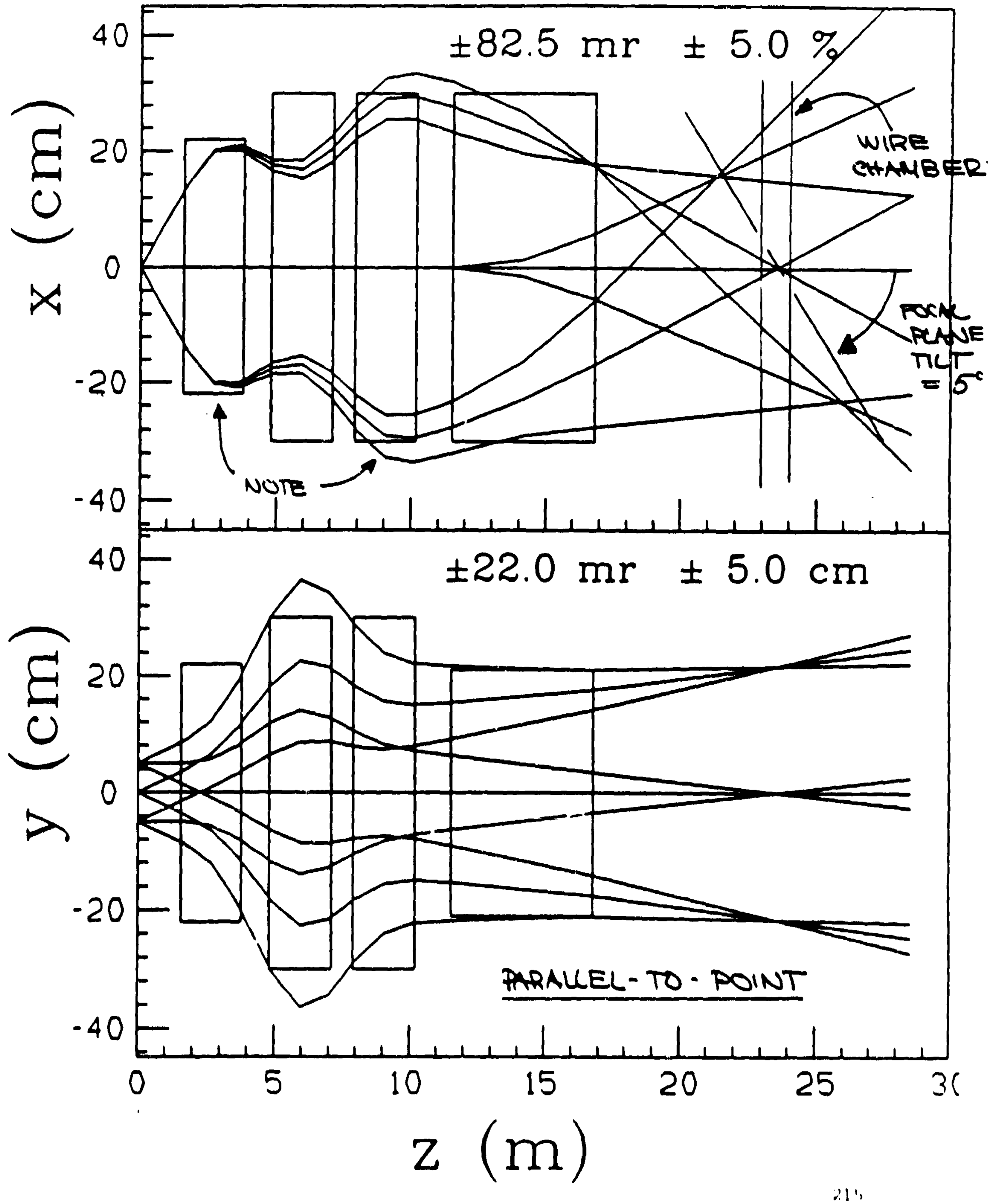

EVOLUTION OF TRANSPORT MATRIX ELEMENTS

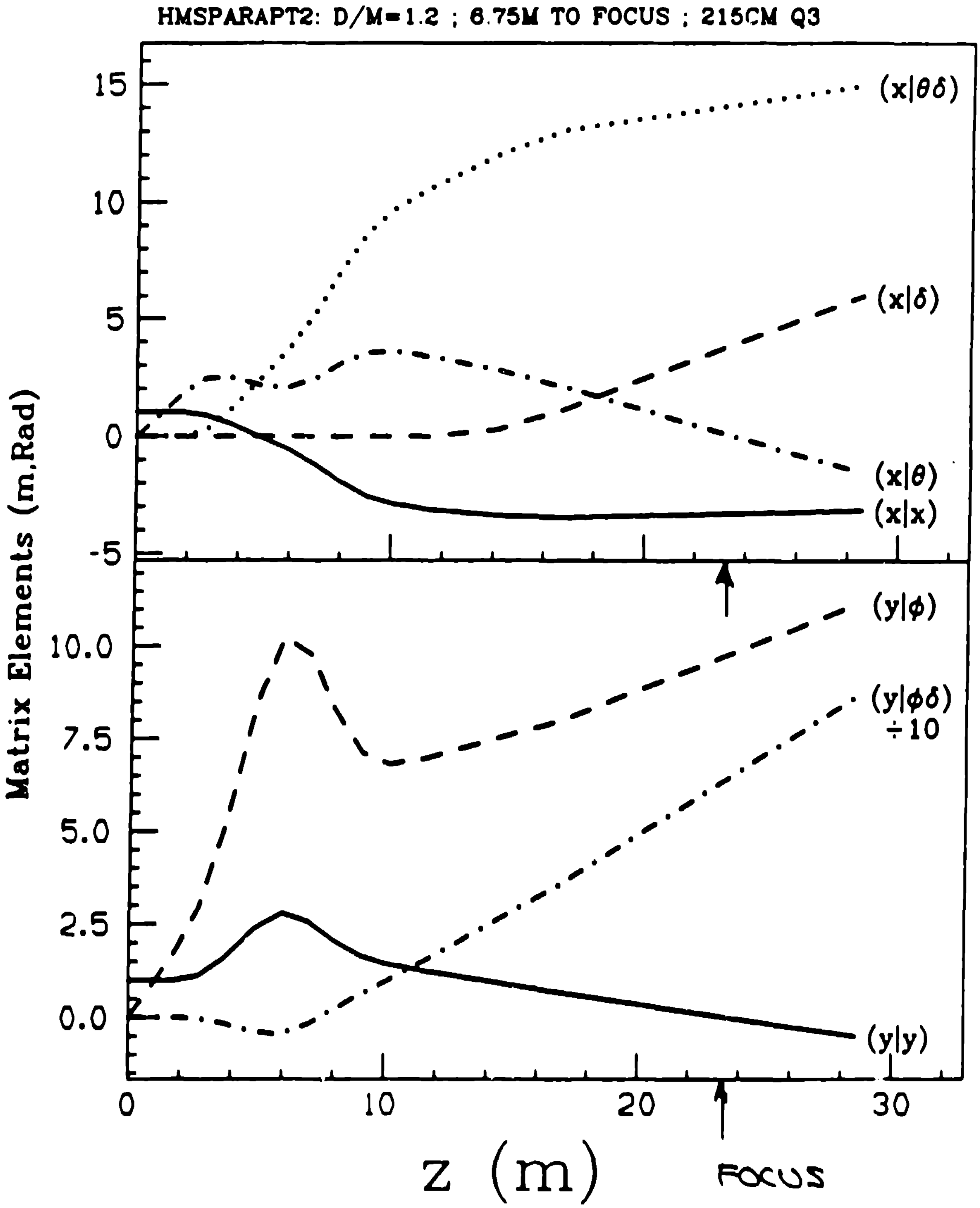

COMPARISON: SLAC 8 GEV SPECTROMETER

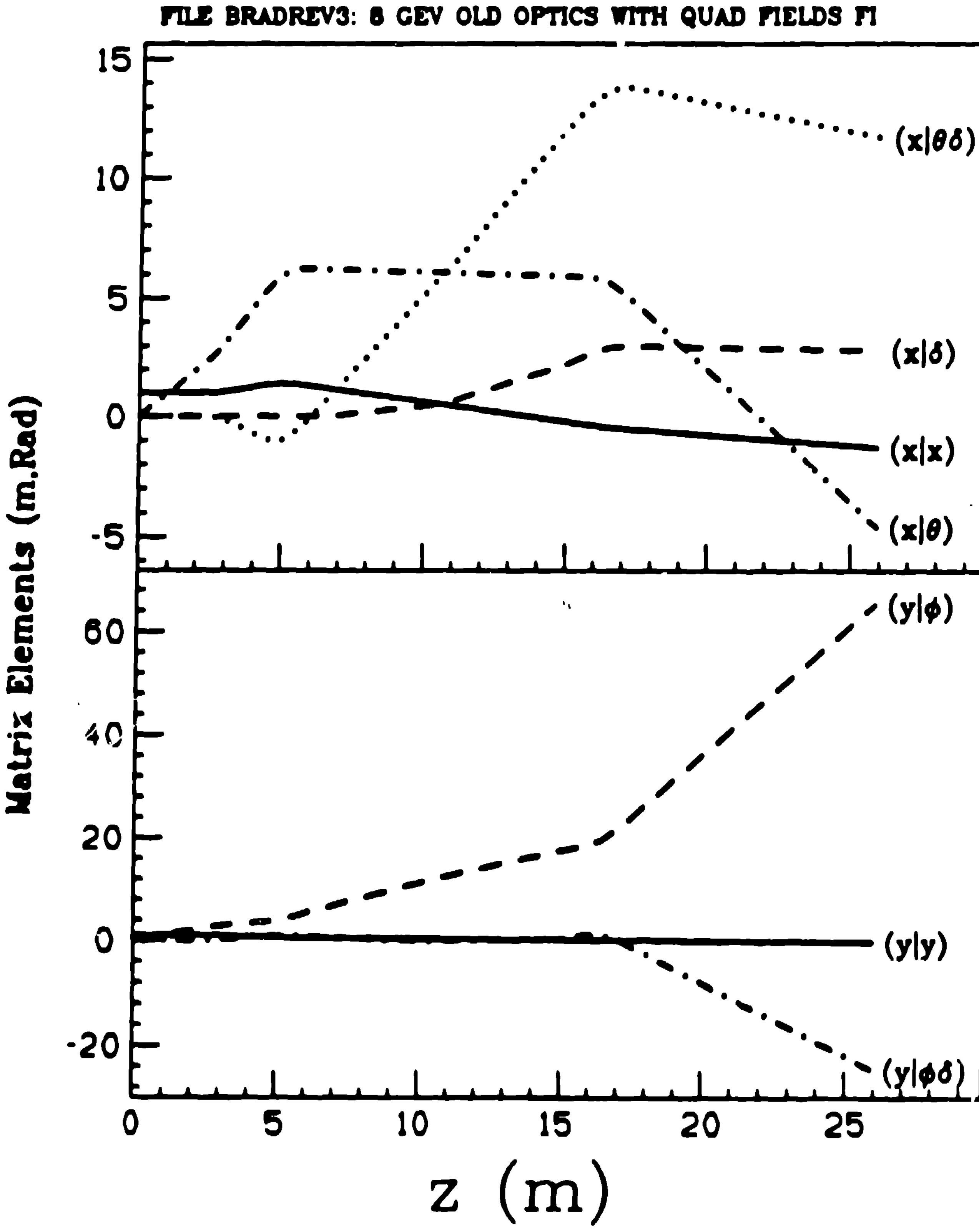

MATRIX ELEMENTS AT FOCUS

"FILE BMSPARAPT2: D/M=1.2 ; 6.75M TO FOCUS ; 215CM Q3 "

TRANSFORM 1* "PRNT"

-3.26268	0.00000	0.00000	0.00000	0.00000	3.91522
0.27371	-0.30650	0.00000	0.00000	0.00000	4.12724
0.00000	0.00000	0.00000	0.98268	0.00000	0.00000
0.00000	0.00000	-1.01762	0.27135	0.00000	0.00000
1.45375	-0.12000	0.00000	0.00000	1.00000	-0.16528
0.00000	0.00000	0.00000	0.00000	0.00000	1.00000

2ND ORDER TRANSFORM*

1 11	6.407E-04								
1 12	1.571E-04	1 22	-3.422E-05						
1 13	0.000E+00	1 23	0.000E+00	1 33	-7.285E-05				
1 14	0.000E+00	1 24	0.000E+00	1 34	7.351E-06	1 44	-1.680E-04		
1 15	0.000E+00	1 25	0.000E+00	1 35	0.000E+00	1 45	0.000E+00	1 55	0.000E+00
1 16	-2.968E-02	1 26	1.411E-02	1 36	0.000E+00	1 46	0.000E+00	1 56	0.000E+00
								1 66	-3.801E-02
2 11	-3.335E-04								
2 12	-1.335E-04	2 22	-4.507E-06						
2 13	0.000E+00	2 23	0.000E+00	2 33	-5.747E-04				
2 14	0.000E+00	2 24	0.000E+00	2 34	-2.890E-04	2 44	-1.102E-04		
2 15	0.000E+00	2 25	0.000E+00	2 35	0.000E+00	2 45	0.000E+00	2 55	0.000E+00
2 16	-6.512E-02	2 26	1.604E-03	2 36	0.000E+00	2 46	0.000E+00	2 56	0.000E+00
								2 66	-4.038E-02
3 11	0.000E+00								
3 12	0.000E+00	3 22	0.000E+00						
3 13	3.725E-03	3 23	-4.394E-05	3 33	0.000E+00				
3 14	9.248E-04	3 24	2.190E-06	3 34	0.000E+00	3 44	0.000E+00		
3 15	0.000E+00	3 25	0.000E+00	3 35	0.000E+00	3 45	0.000E+00	3 55	0.000E+00
3 16	0.000E+00	3 26	0.000E+00	3 36	1.651E-01	3 46	6.500E-02	3 56	0.000E+00
								3 66	0.000E+00
4 11	0.000E+00								
4 12	0.000E+00	4 22	0.000E+00						
4 13	1.986E-03	4 23	-9.865E-06	4 33	0.000E+00				
4 14	1.081E-03	4 24	-1.042E-04	4 34	0.000E+00	4 44	0.000E+00		
4 15	0.000E+00	4 25	0.000E+00	4 35	0.000E+00	4 45	0.000E+00	4 55	0.000E+00
4 16	0.000E+00	4 26	0.000E+00	4 36	1.129E-01	4 46	4.383E-02	4 56	0.000E+00
								4 66	0.000E+00
5 11	-1.098E-02								
5 12	7.925E-04	5 22	-2.039E-04						
5 13	0.000E+00	5 23	0.000E+00	5 33	-8.579E-03				
5 14	0.000E+00	5 24	0.000E+00	5 34	-5.709E-03	5 44	-1.370E-03		
5 15	0.000E+00	5 25	0.000E+00	5 35	0.000E+00	5 45	0.000E+00	5 55	0.000E+00
5 16	-1.367E-02	5 26	-4.066E-03	5 36	0.000E+00	5 46	0.000E+00	5 56	0.000E+00
								5 66	-5.749E-03

FILE PARAPT3C: FIVE ENERGY (+-5%) VERSION OF PARAPT3B RT90.1
FILE PARAPT3B: FROM PARAPT3A W/NEW Q FRINGES ; XQ FOR ZOR=0 ; NEW STEPS

					TRANSPORT		
ENERGY(MEV)	=	5700.000	5850.000	6000.000		6150.000	6300.000
XOR (CM)	=	-15.743	-8.836	-0.001		10.738	23.408
YOR (CM)	=	0.000	0.000	0.000		0.000	0.000
ZOR (CM)	=	-222.717	-112.979	0.017		117.557	240.864
TH (MR)	=	-21.696	-10.576	-0.001		10.069	19.671
PHI (MR)	=	0.000	0.000	0.000		0.000	0.000
|XMAX|(CM)	=	1.539	1.632	1.746		1.878	2.027
2|YMAX|(CM)	=	27.336	35.126	43.382		52.093	61.274
X/TH	=	0.000	0.000	0.000		0.000	0.000
T/TH	=	-0.309	-0.308	-0.305	-0.307	-0.300	-0.294
Y/PH	=	6.631	8.405	10.287	9.827	12.273	14.369
P/PH	=	0.062	0.186	0.298	0.271	0.400	0.493
X/TH**2	=	-0.318	-0.333	-0.339	-0.342	-0.335	-0.322
X/PH**2	=	-0.709	-1.262	-1.875	-1.680	-2.532	-3.218
T/TH**2	=	-0.008	-0.006	-0.004	-0.005	-0.003	-0.001
T/PH**2	=	-0.094	-0.105	-0.118	-0.110	-0.132	-0.146
Y/TH*PH	=	0.291	0.179	0.028	0.022	-0.158	-0.374
P/TH*PH	=	-0.063	-0.088	-0.110	-0.104	-0.129	-0.144
X/TH**3	=	-10.151	-10.866	-11.730		-12.735	-13.873
X/TH*PH**2	=	-202.674	-209.663	-217.528		-226.167	-235.527
T/TH**3	=	0.175	0.086	0.001		-0.080	-0.157
T/TH*PH**2	=	-1.483	-2.544	-3.457		-4.239	-4.909
Y/PH**3	=	-863.564	-871.884	-882.712		-896.925	-915.129
Y/TH**2*PH	=	-138.989	-155.346	-172.140		-189.393	-207.148
P/PH**3	=	-67.657	-63.712	-60.390		-57.582	-55.194
P/TH**2*PH	=	-10.703	-11.084	-11.411		-11.686	-11.910
X/TH**4	=	0.884	0.622	0.344		0.060	-0.220
X/TH**2*PH**2	=	44.470	52.211	59.988		67.797	75.639
X/PH**4	=	228.554	276.645	315.432		347.187	373.709
T/TH**4	=	-0.042	-0.047	-0.050		-0.051	-0.051
T/TH**2*PH**2	=	0.015	0.538	1.022		1.464	1.861
T/PH**4	=	7.157	9.470	11.039		12.072	12.720
Y/TH**3*PH	=	-1.989	-0.882	0.372		1.714	3.100
Y/TH*PH**3	=	33.113	34.387	34.554		33.514	31.122
P/TH**3*PH	=	2.038	2.090	2.108		2.096	2.061
P/TH*PH**3	=	19.464	18.240	16.915		15.537	14.133
X/TH**5	=	7.206	8.216	8.381		7.620	5.849
X/TH**3*PH**2	=	42.696	15.260	-35.395		-111.632	-216.275
X/TH*PH**4	=	119.642	-22.365	-193.057		-389.670	-610.586
T/TH**5	=	0.000	0.000	0.000		0.000	0.000
X/PH**2(Trunc.)	=	-0.598	-1.128	-1.723		-2.364	-3.037
X/TH*PH**2(Tr.)	=	-202.326	-209.570	-217.863		-227.115	-237.295
X/T**2 (Trunc.)	=	-0.312	-0.329	-0.337		-0.334	-0.324
X/T**3 (Trunc.)	=	-10.102	-10.810	-11.673		-12.683	-13.833

PSI	=	85.138				
N	=	1		2	3	4
X/D**N	=	3.915	3.915	15.192	0.156	56.163
X/T*D**N	=	0.000		-43.388	40.252	-221.899
X/T**2*D**N	=	-2.148E-02		7.576E+00	-1.003E+01	-1.316E+01
X/T**3*D**N	=	-3.744E+01		-1.116E+02	9.026E+01	-4.475E+02
X/T**4*D**N	=	-1.130E+01		-4.389E+00	1.048E+02	-1.236E+02
X/T**5*D**N	=	-1.139E+01		-7.414E+02	-8.704E+02	-1.017E+02

SOME WORDS ABOUT RAYTRACE (¿ NOTER)

FRINGE FIELD ABERRATIONS

RAYTRACE Correctly calculates higher order radial terms by taking (analytic) derivatives of the $D_{M,N}(z)$

FRINGE EXPANSION IN $z/2R$ NOT z/R !

Fringe field is expressed as an expansion around effective field boundary in terms of $s = z/2R$, not $s = z/R$ as implied by early manu

MINOR CHANGES FROM RT 82.0 → RT 90.1

- More significant figures on output
- Some change in DIPOLE parameter definitions
- Added "image size" output
- Runs a little slower now ($T_{CPU} \times \simeq 1.4$)
- More precise value of "c" = 2.9979... (!)

HIGHER MULTIPOLE FRINGE IS NON-REALISTIC

A. Thiessen, et.al., are working on this

RESOLUTION RECONSTRUCTION via RAYTRACE

THE QUESTION: How well does the spectrometer reconstruct momentum, scattering angle, etc... and how is it affected by aberrations due to the quadrupoles?

THE APPROACH: Write momentum, etc... as polynomials in x, x', y, y' at the detector and trace lots of rays to get resolution.

PROGRAMS:

- "OLD" MOTER (L. HARWOOD)
- "NEW" MOTER (S. WOOD)

  ★ OPTIMIZATION OF MAGNET PARAMETERS

  - LIMITED NUMBER OF RAYS; NOT TOO FLEXIBLE

- RAYTRACE + MINUIT (CERN Product) (JN)

  - CONFIRM MOTER RESULTS
  - TOWARDS EXPERIMENT MONTE CARLO

THE PROCEDURE

1) GENERATE RAYS

   — Phase space choices

   — Apertures in or out

   — which version of RAYTRACE or MOTER

2) PICK TERMS IN RECONSTRUCTION POLYNOMIAL

   this work uses (for momentum reconstruction

$$\delta = (\delta|x)x + (\delta|x^2)x^2 + (\delta|x\theta)\theta + (\delta|\theta^2)\theta^2$$
$$+ (\delta|x^3)x^3 + (\delta|x^2\theta)x^2\theta + (\delta|x\theta^2)x\theta^2 + (\delta|\theta^3)\theta^3$$

3) FIND TERMS BY MINIMIZING RESOLUTION

   that is, determine the values of $(\delta|x)$, etc... by minimizing $\langle(\delta-\delta_0)^2\rangle$ as a function of the values.

4) MOTER: OPTIMIZATION OF MAGNET PARAMETERS

   MOTER can automatically repeat the above procedure, minimizing the final result even further by varying the magnet parameters.

NOTE: SAME PROCEDURE FOR OTHER VARIABLE

   i.e. ϕ (Scattering Angle) y (Target position)

   θ (Out-of-plane Angle)

222

EXAMPLE OF RESULTS

RESOLUTION IN DELTA (RAYTRACE)

USER1:[JIMNAP.HMS.OPTICS.RECON]PARAPT3B_RT_CDR.RECON;1
LIMITS: 0.00010 0.0825 0.0500 0.0250 0.0000 0.0500 ← PHASE SPACE

RMS Resolution= 5.899E-04

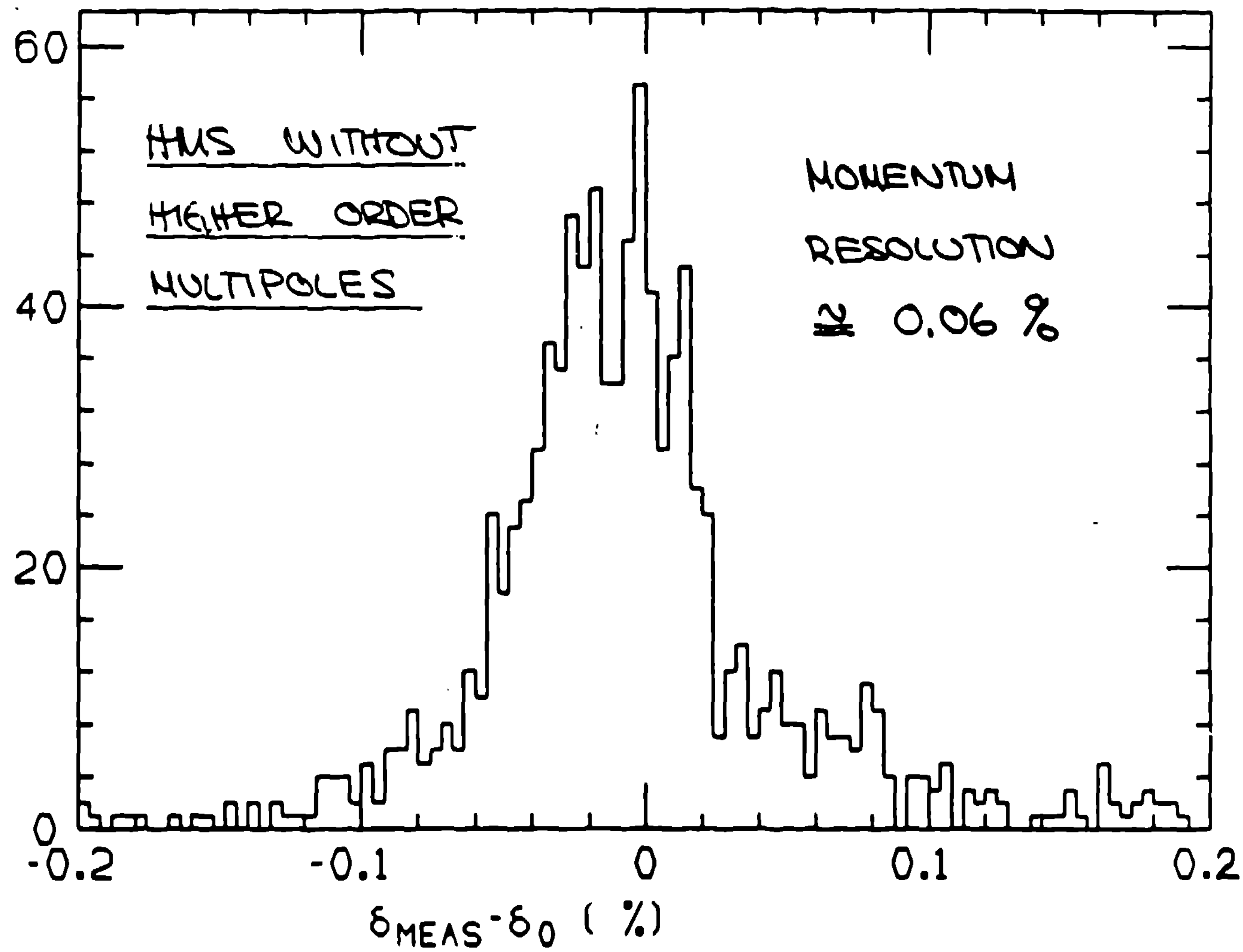

$(\delta|x)$= 2.564E-01
$(\delta|\theta)$= 0.000E+00
$(\delta|y)$= 0.000E+00
$(\delta|\phi)$= 0.000E+00

$(\delta|x^2)$= -2.927E-01
$(\delta|x\theta)$= 3.372E+00
$(\delta|xy)$= 0.000E+00
$(\delta|x\phi)$= 0.000E+00
$(\delta|\theta^2)$= -3.009E-01

$(\delta|\theta y)$= 0.000E+00
$(\delta|\theta\phi)$= 0.000E+00
$(\delta|y^2)$= 0.000E+00
$(\delta|y\phi)$= 0.000E+00
$(\delta|\phi^2)$= 0.000E+00

$(\delta|x^2\theta)$= -1.286E+01
$(\delta|x\theta^2)$= 7.514E+01
$(\delta|x^3)$= 6.884E-01
$(\delta|\theta^3)$= -1.358E+02

RESOLUTION IN PHI (RAYTRACE)

USER1:[JIMNAP.HMS.OPTICS.RECON]PARAPT3B_RT_CDR.RECON;1
LIMITS: 0.00010 0.0825 0.0500 0.0250 0.0000 0.0500

RMS Resolution= 5.373E-04

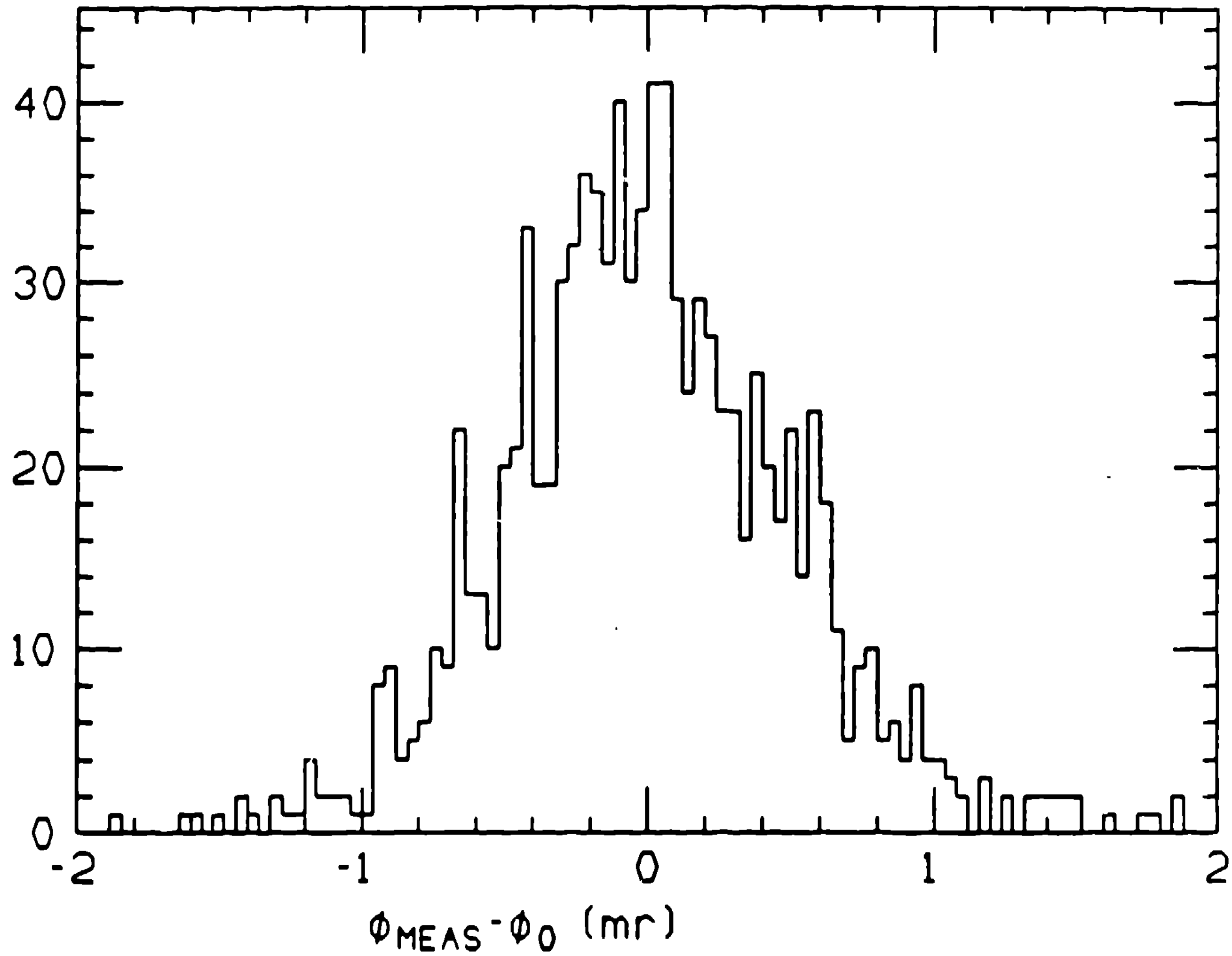

$(\phi\|x)$= 0.000E+00	$(\phi\|x^2)$= 0.000E+00	$(\phi\|\theta y)$= 0.000E+00
$(\phi\|\theta)$= 0.000E+00	$(\phi\|x\theta)$= 0.000E+00	$(\phi\|\theta\phi)$= 0.000E+00
$(\phi\|y)$= 1.077E-01	$(\phi\|xy)$=-2.850E-01	$(\phi\|y^2)$= 0.000E+00
$(\phi\|\phi)$=-1.178E-01	$(\phi\|x\phi)$= 4.325E+00	$(\phi\|y\phi)$= 0.000E+00
	$(\phi\|\theta^2)$= 0.000E+00	$(\phi\|\phi^2)$= 0.000E+00

$(\phi|\theta^2 y)$=-6.108E+00
$(\phi|\theta^2\phi)$= 1.112E+02

RESOLUTION IN Y (RAYTRACE)

USER1:[JIMNAP.HMS.OPTICS.RECON]PARAPT3B_RT_CDR.RECON;1

LIMITS: 0.00010 0.0825 0.0500 0.0250 0.0000 0.0500

RMS Resolution= 2.048E-03

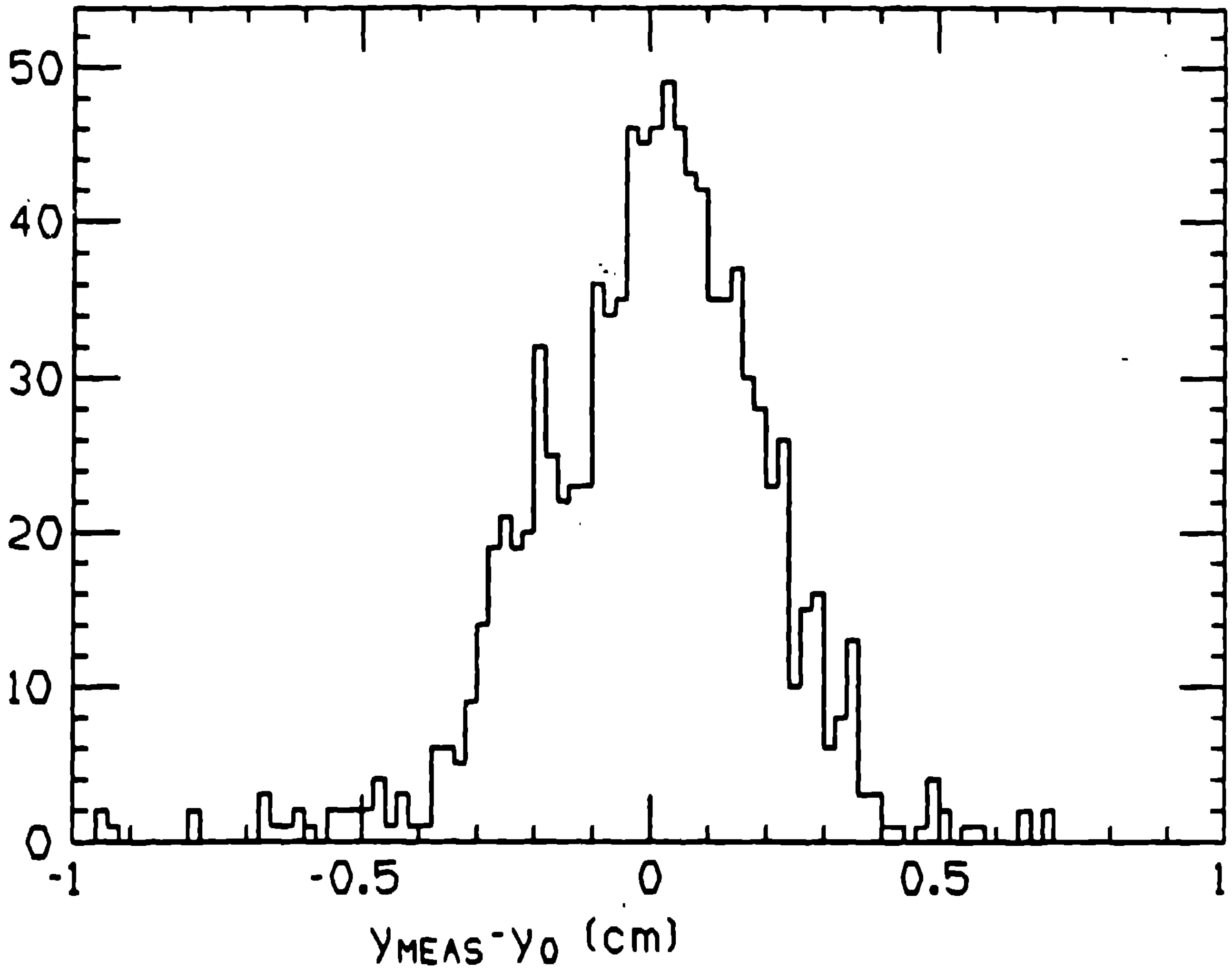

(y|x)= 0.000E+00	(y|x²)= 0.000E+00	(y|θy)= 8.560E-02
(y|θ)= 0.000E+00	(y|xθ)= 0.000E+00	(y|θφ)= 1.195E+01
(y|y)= 2.486E-01	(y|xy)= 1.080E+00	(y|y²)= 0.000E+00
(y|φ)=-9.418E+00	(y|xφ)=-1.777E+01	(y|yφ)= 0.000E+00
	(y|θ²)= 0.000E+00	(y|φ²)= 0.000E+00

RESOLUTION IN THETA (RAYTRACE)

USER1:[JIMNAP.HMS.OPTICS.RECON]PARAPT3B_RT_COR.RECON;1
LIMITS: 0.00010 0.08[illegible] 0.0500 0.0250 0.0000 0.0500

RMS Resolution= 6.514E-04

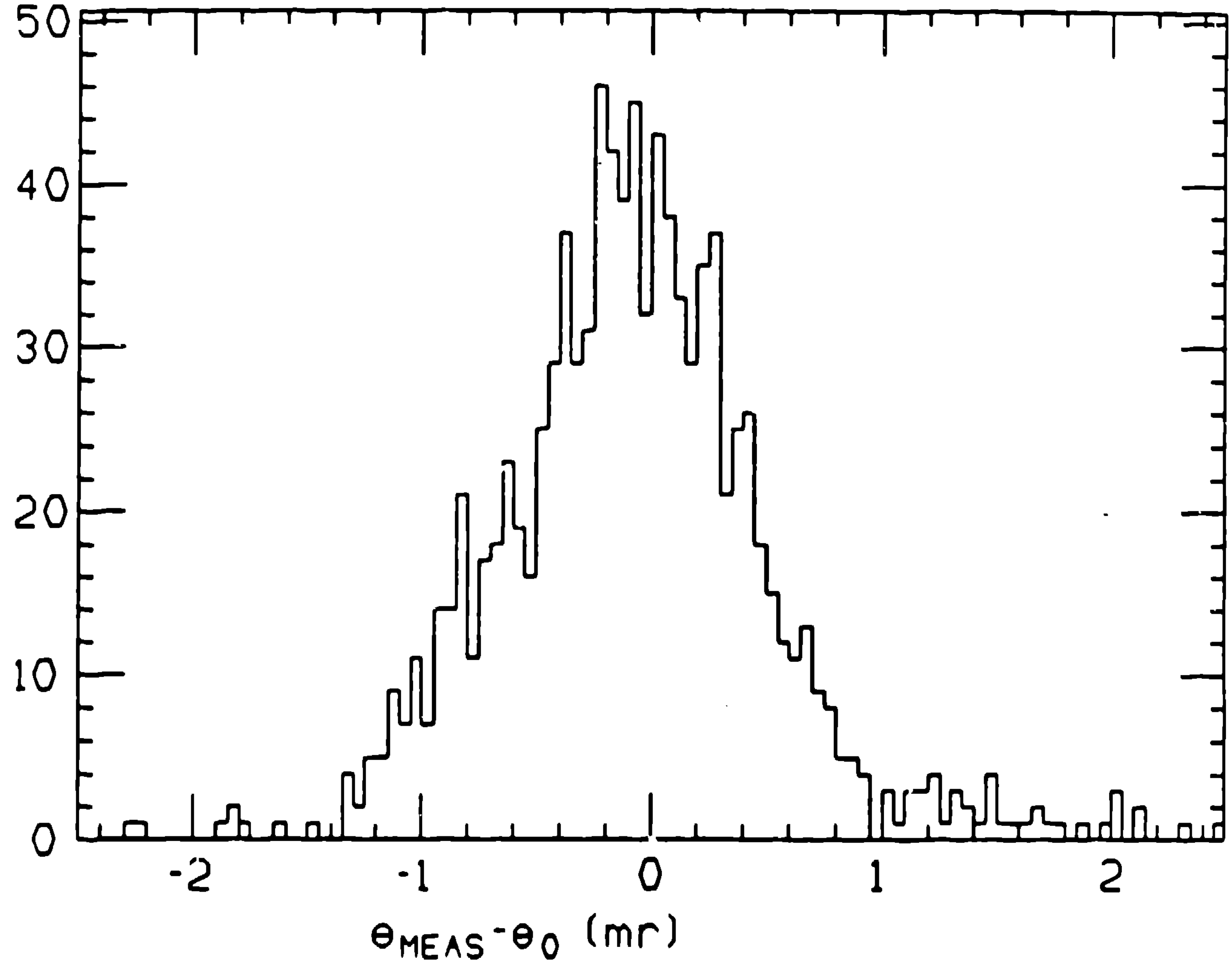

$(\theta\|x)$= 3.562E-01	$(\theta\|x^2)$=-4.427E-01	$(\theta\|y)$= 0.000E+00
$(\theta\|\theta)$=-3.364E+00	$(\theta\|x\theta)$= 4.173E+00	$(\theta\|\theta\phi)$= 0.000E+00
$(\theta\|y)$= 0.000E+00	$(\theta\|xy)$= 0.000E+00	$(\theta\|y^2)$= 0.000E+00
$(\theta\|\phi)$= 0.000E+00	$(\theta\|x\phi)$= 0.000E+00	$(\theta\|y\phi)$= 0.000E+00
	$(\theta\|\theta^2)$=-6.836E-01	$(\theta\|\phi^2)$= 0.000E+00

$(\theta|x^2\theta)$=-1.220E+01
$(\theta|x\theta^2)$= 4.097E+01
$(\theta|x^3)$= 7.976E-01

COMPARISON OF PROGRAMS

RESOLUTIONS AVERAGED OVER PHASE SPACE

	QUANTITY	RAYTRACE + MINUIT *	MOTER * **
QUADS ARE PURE $n=2$	MOMENTUM (0.1%)	0.59	0.56 – 0.68
	SCAT. ANGLE (mr)	0.54	0.52 – 0.62
	TARGET POSIT. (mm)	2.05	1.9 – 2.3
	OOP ANGLE (mr)	0.65	0.62 – 0.72
QUADS CONTAIN HIGHER ORDER MULTIPOLES	MOMENTUM (0.1%)	0.93	0.87 – 0.92
	SCAT. ANGLE (mr)	0.65	0.61 – 0.66
	TARGET POSIT. (mm)	2.37	2.2 – 2.3
	OOP ANGLE (mr)	0.99	0.92 – 0.97

Q1: −0.35% $n=4$ & −0.73% $n=6$

Q2: −0.29% $n=6$ Q3: −1.69% $n=6$

* NO DETECTOR RESOLUTION OR MULTIPLE SCATTERING

** NO OPTIMIZATION OF MAGNET PARAMETERS

RECONSTRUCTION PARAMETERS

(values for rays traced with pure n=2 quads)

PARAMETER	RAYTRACE + MINUIT	MOTER
$(\delta\|x)$	0.256	0.257
$(\delta\|x^2)$	−0.293	−0.291
$(\delta\|x\theta)$	3.372	3.360
$(\delta\|\theta^2)$	−0.301	−0.238
$(\delta\|x^3)$	0.688	0.708
$(\delta\|x^2\theta)$	−12.86	−12.44
$(\delta\|x\theta^2)$	75.14	66.95
$(\delta\|\theta^3)$	−135.8	−124.0
$(\phi\|y)$	0.108	0.107
$(\phi\|\phi)$	−0.118	−0.100
$(\phi\|xy)$	−0.285	−0.289
$(\phi\|x\phi)$	4.325	4.330
$(\phi\|\theta^2 y)$	−6.108	−7.192
$(\phi\|\theta^2\phi)$	111.2	106.1

ALL UNITS USE METERS AND RADIANS

Some Monte Carlo Results

The Effect of Quadrupole Aberrations

Run 10,000 Rays and look at resolution in slices

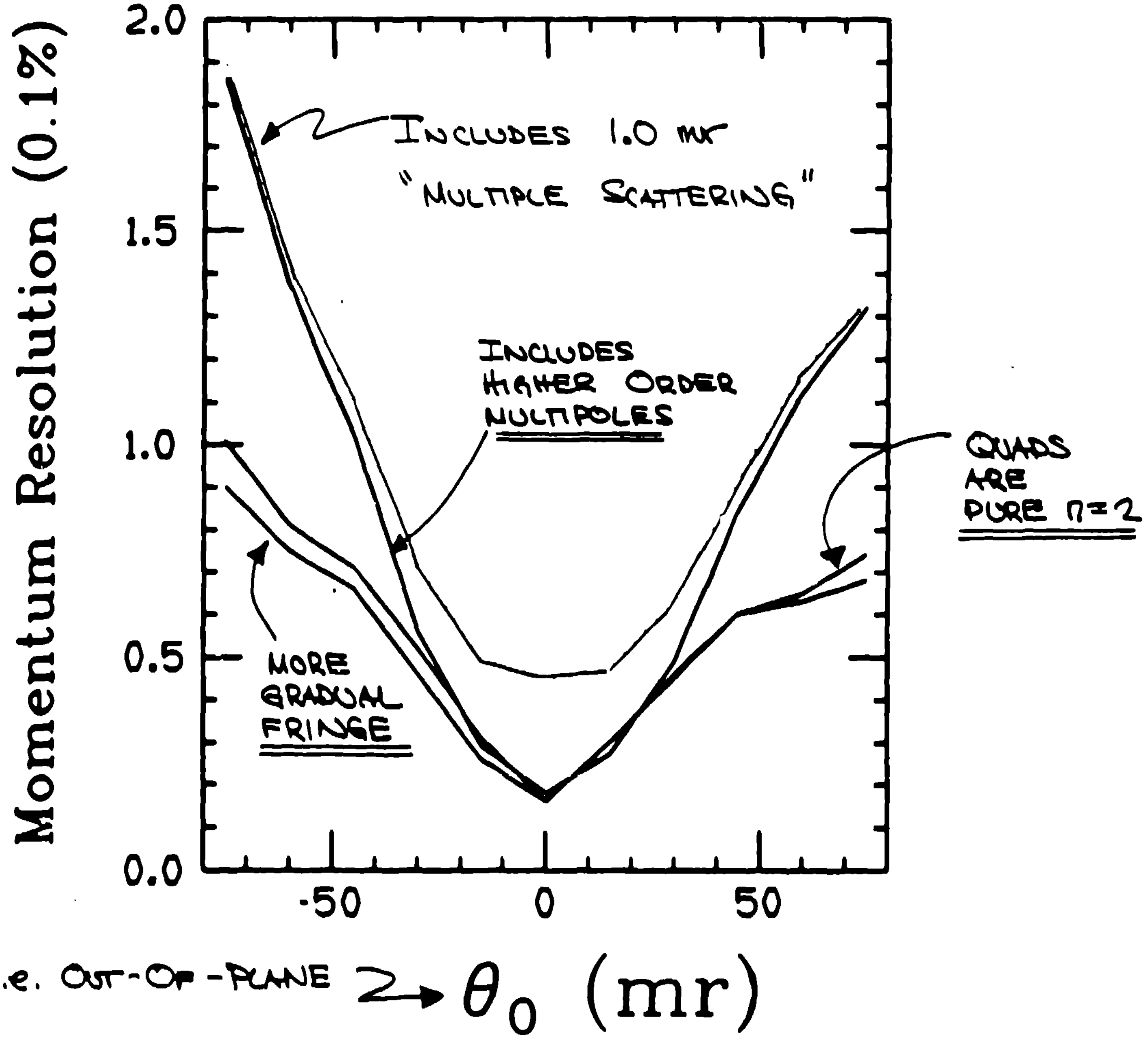

Recall: Large Θ_0 samples large radii in magnets Q1 and Q3

USING OPTIMIZATION FEATURE OF MOTER

Can we regain momentum resolution in the face of higher order multipoles?

Let MOTER vary Q1, Q2, Q3 field strengths keeping the fraction of higher order multipoles a constant. (Required a program modification!) Minimize momentum resolution.

FIND: δ: 0.90 $\longrightarrow$ 0.68 **IT WORKS!**

ϕ: 0.64 $\longrightarrow$ 0.57

y: 2.2 $\longrightarrow$ 2.0

θ: 0.95 $\longrightarrow$ 0.90

FOR: Q1: 1.487 $\longrightarrow$ 1.491

Q2: −1.457 $\longrightarrow$ −1.343

Q3: 0.748 $\longrightarrow$ 0.691

A LOOK AT THE EFFECT ON THE θ_0 - DEPENDENCE OF THE RESOLUTION

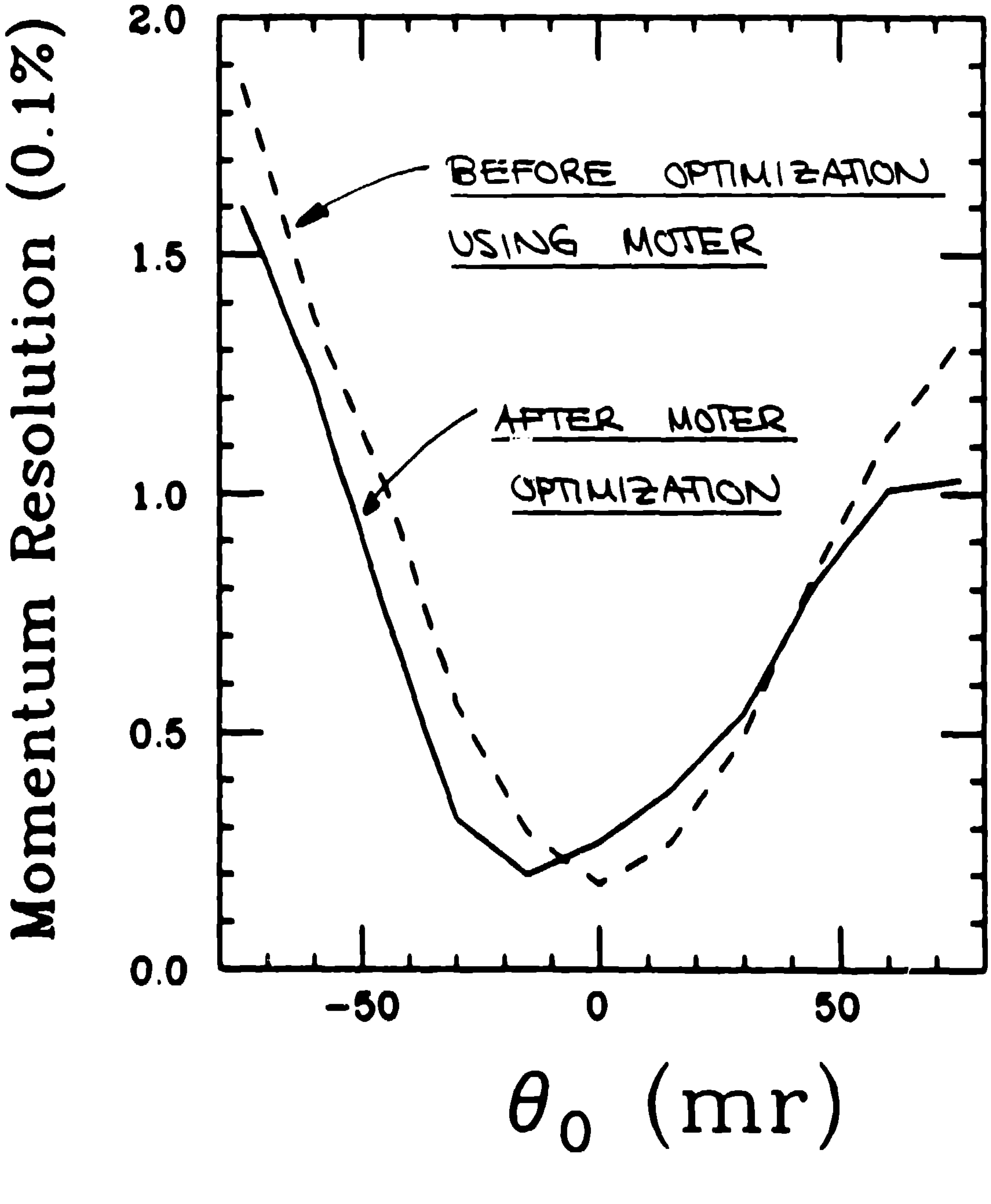

FILE PARAPT3D: FROM PARAPT3B W/ N=6 POLES ON QUADS, N=4 ON

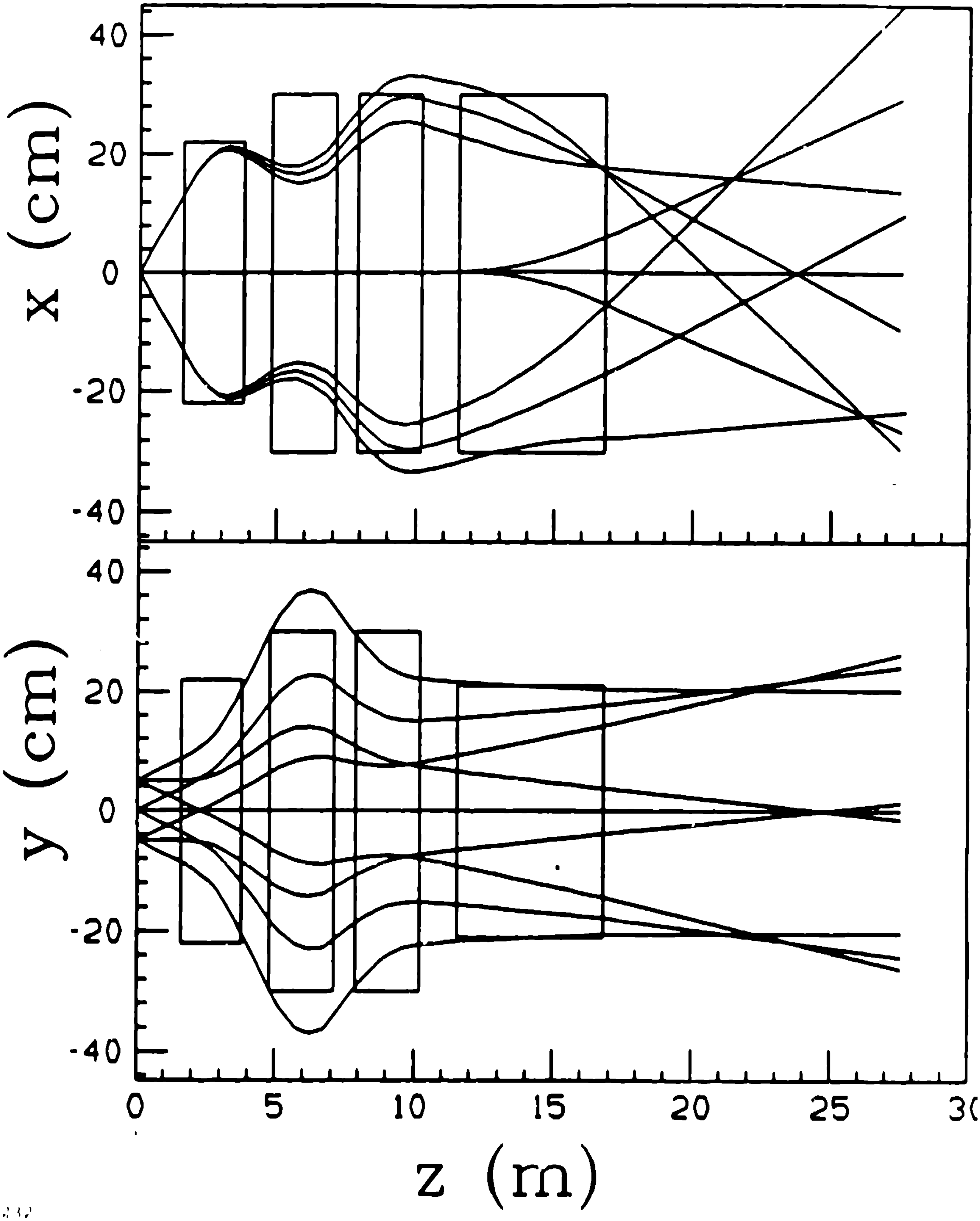

RAY PLOT AFTER MOTER OPTIMIZATION

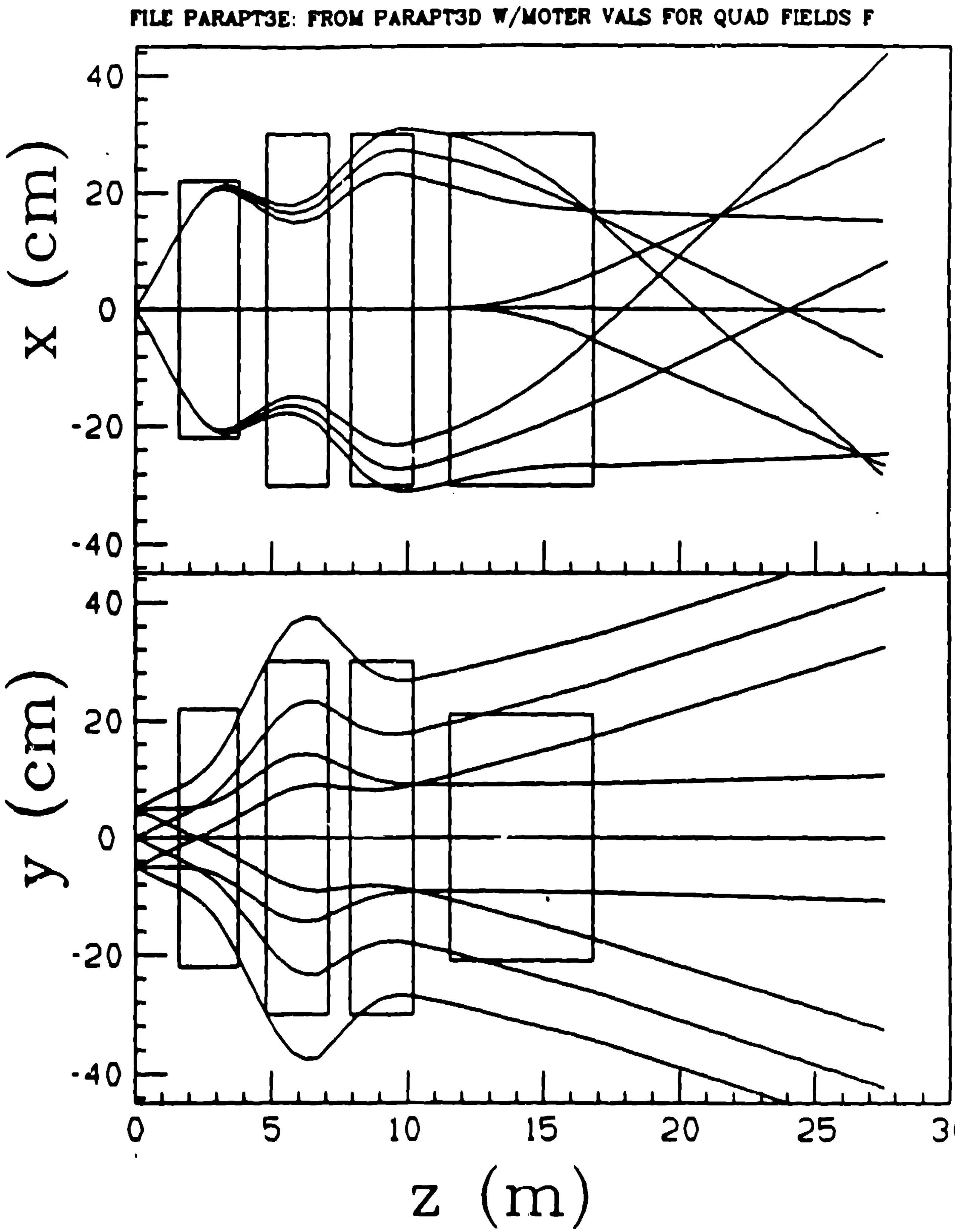

TOSCA CALCULATIONS AT CEBAF

LARGE APERTURE SUPERCONDUCTING CRYOSTABLE QUADRUPOLES FOR CEBAF'S HIGH MOMENTUM SPECTROMETER

STEVEN R. LASSITER

The Continuous Electron Beam Accelerator Facility
NEWPORT NEWS, VIRGINIA
UNITED STATES DEPARTMENT OF ENERGY

Q2/Q3 CROSS SECTION

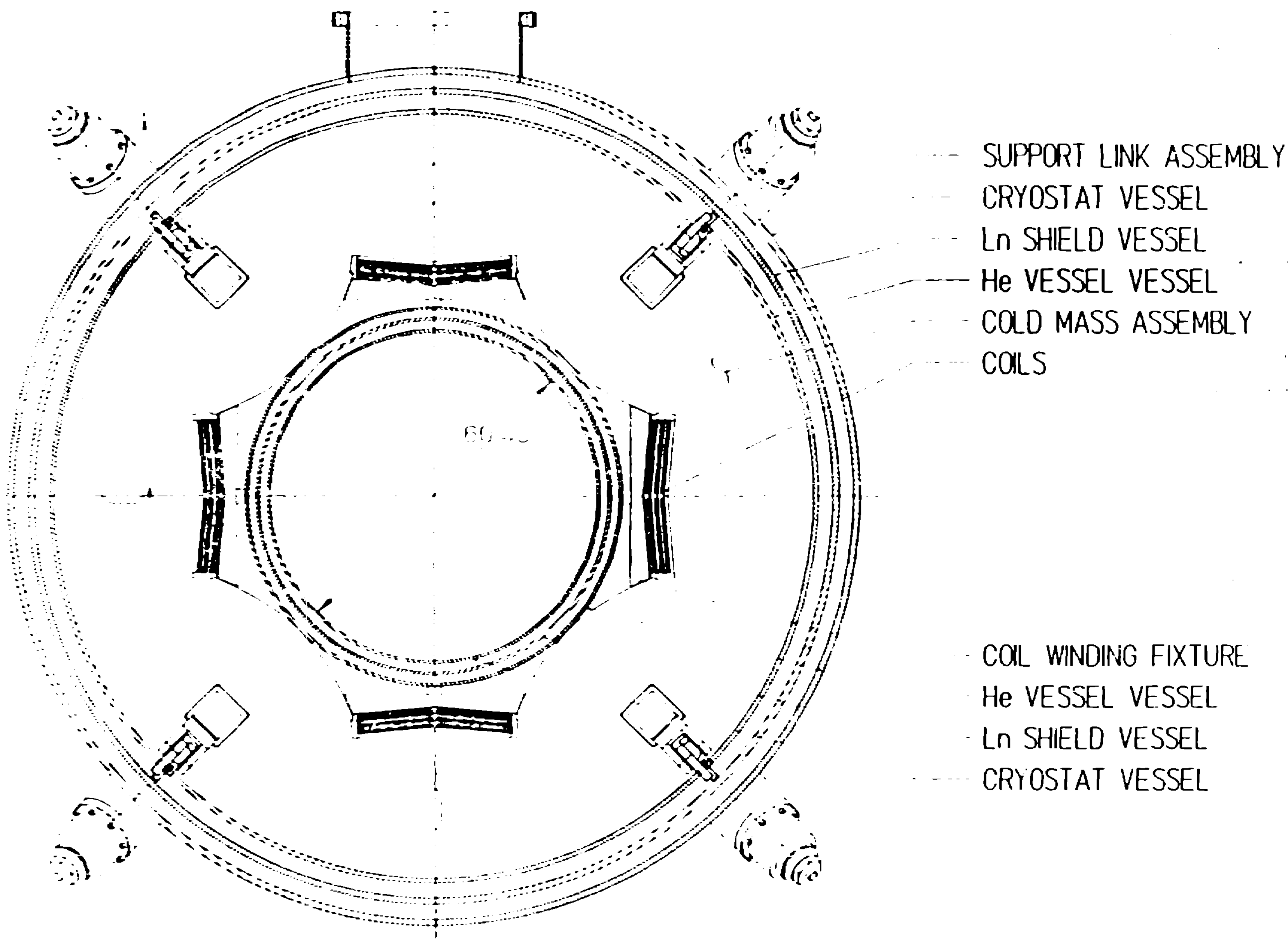

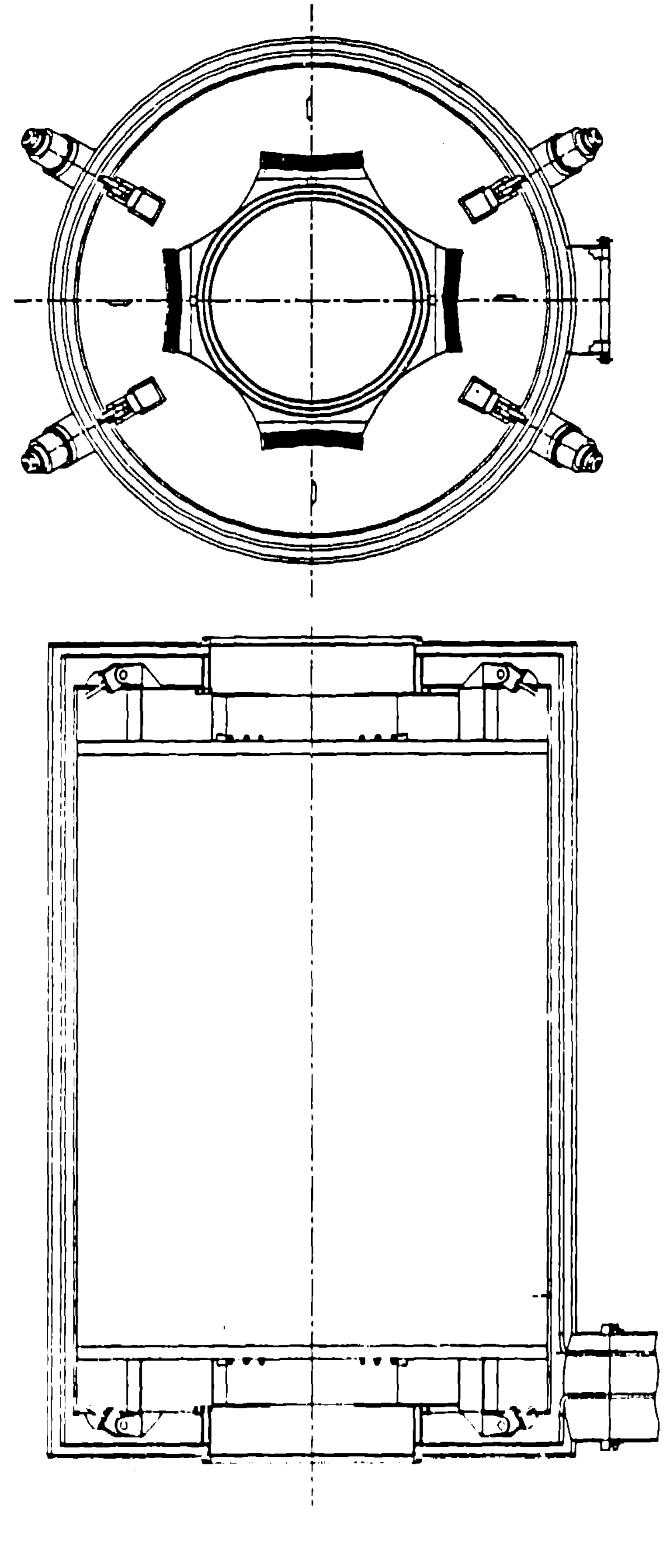

22B-R5.COND
8/Aug/91 08:33:47 Page 6 : DISP XEYE=0 0 SIZE=50

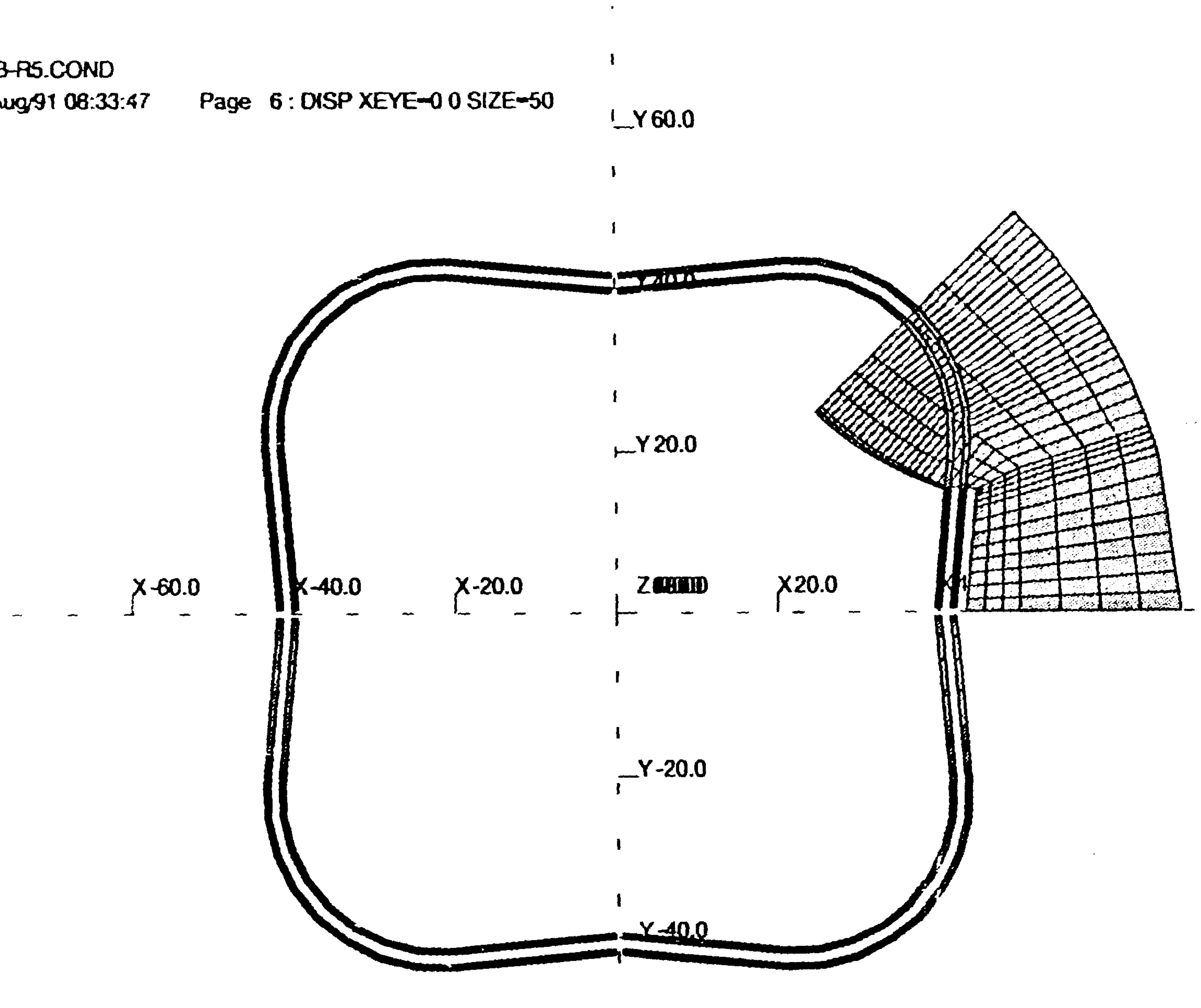

VF/OPER

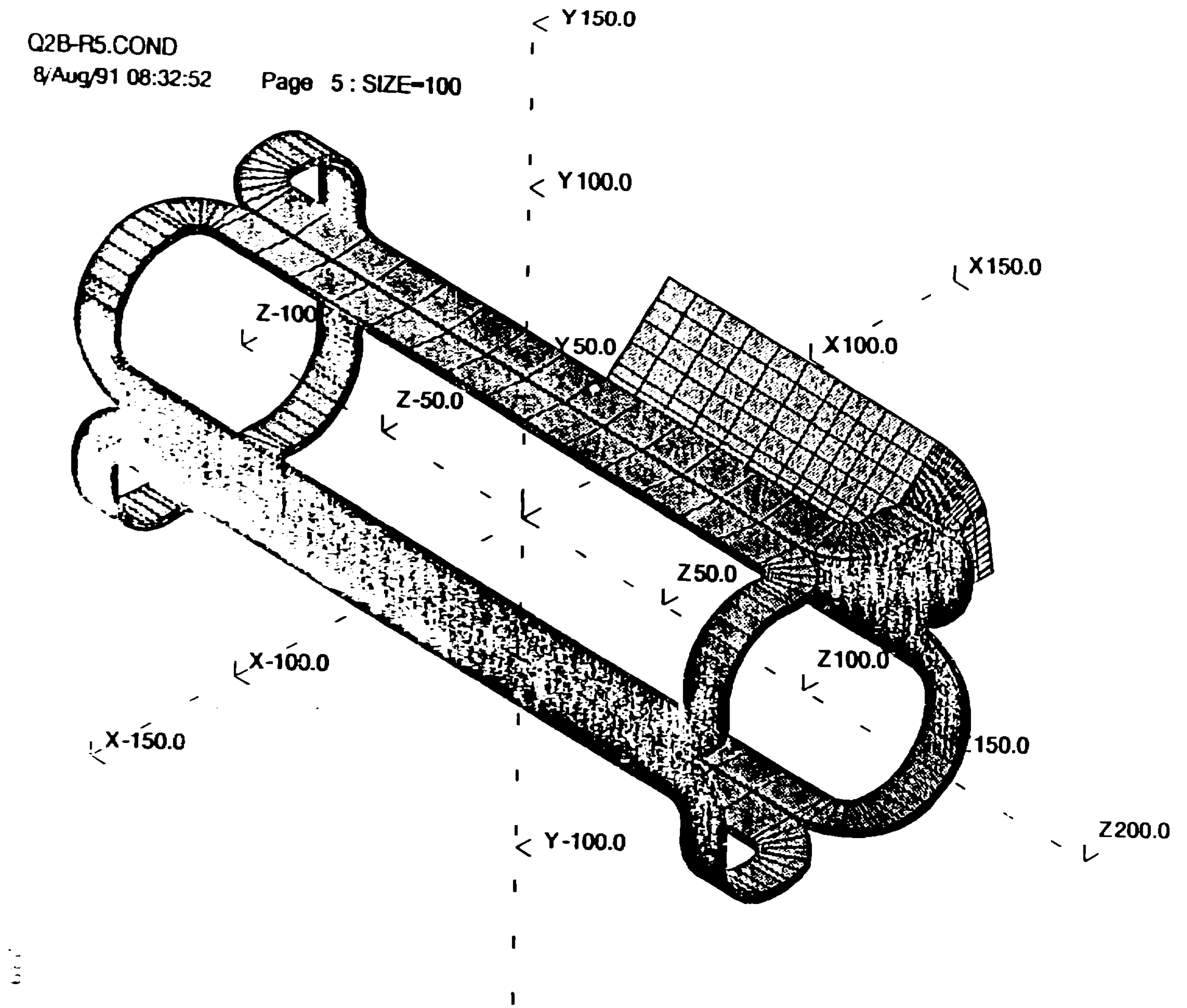
Q2B-R5.COND
8/Aug/91 08:32:52
Page 5 : SIZE=100
Y 150.0
Y 100.0
Y 50.0
Y -100.0
X 150.0
X 100.0
X -100.0
X -150.0
Z -100
Z -50.0
Z 50.0
Z 100.0
150.0
Z 200.0

VF/OPEI

Q2C-R5.TOSCAB

6 Aug/91 15:44:05 Page 10 : DISP XEYE=0 0

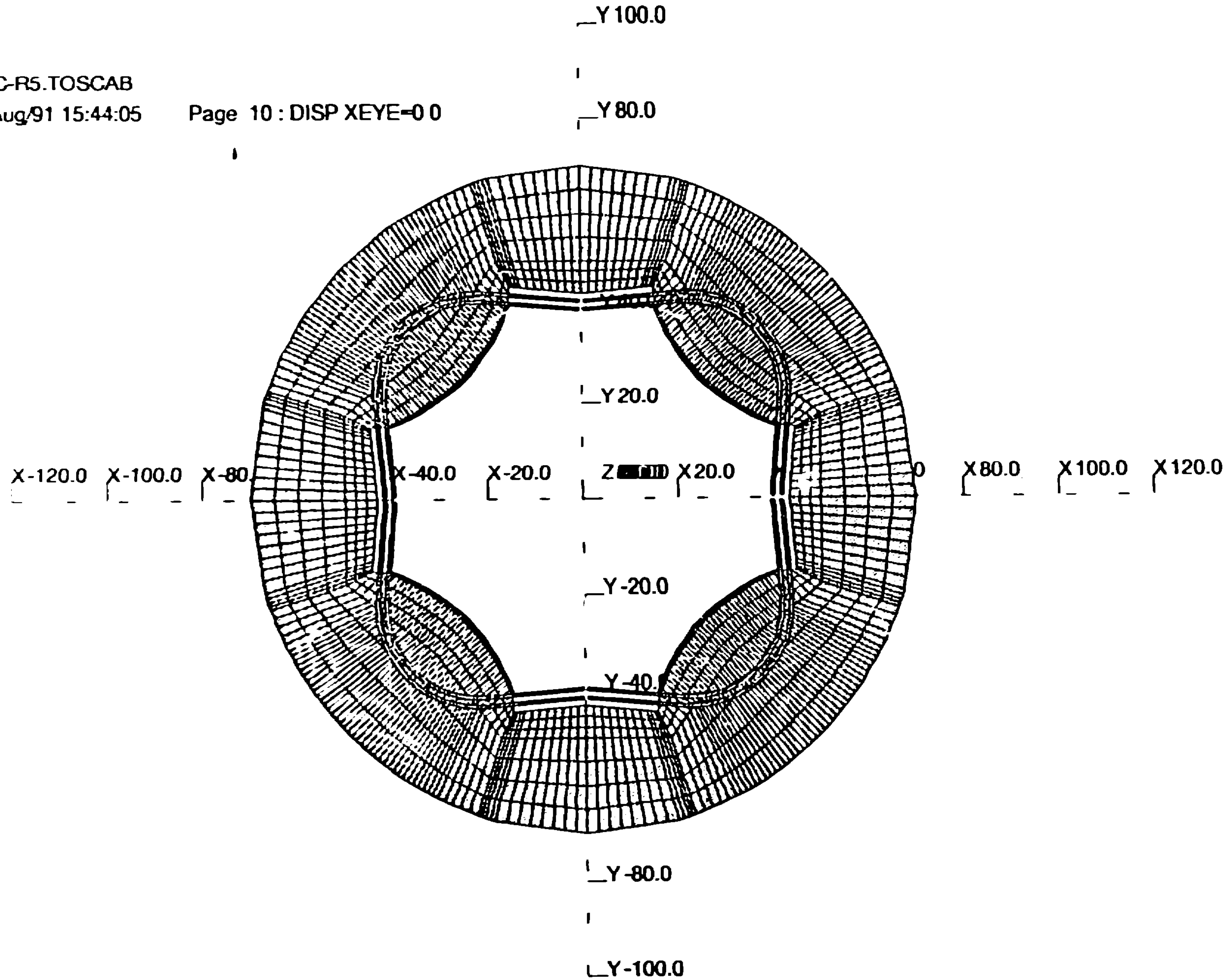

VF/OPE

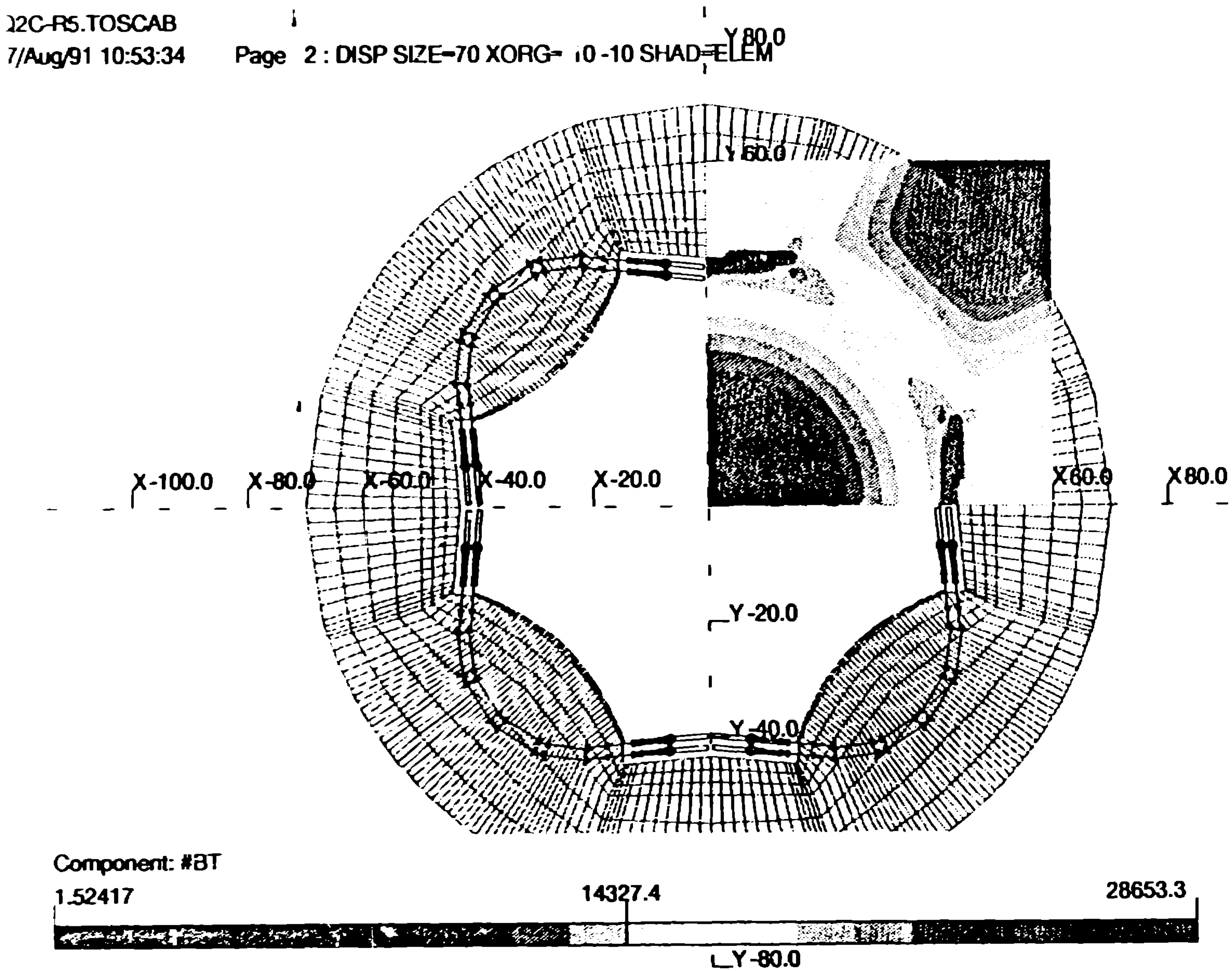

Q2C-R5.TOSCAB
7/Aug/91 10:53:34 Page 2 : DISP SIZE=70 XORG= 10 -10 SHAD=ELEM
Y 80.0
Y 60.0
X-100.0
X-80.0
X-60.0
X-40.0
X-20.0
X60.0
X80.0
Y -20.0
Y -40.0
Component: #BT
1.52417
14327.4
28653.3
Y -80.0

VF/OPERA

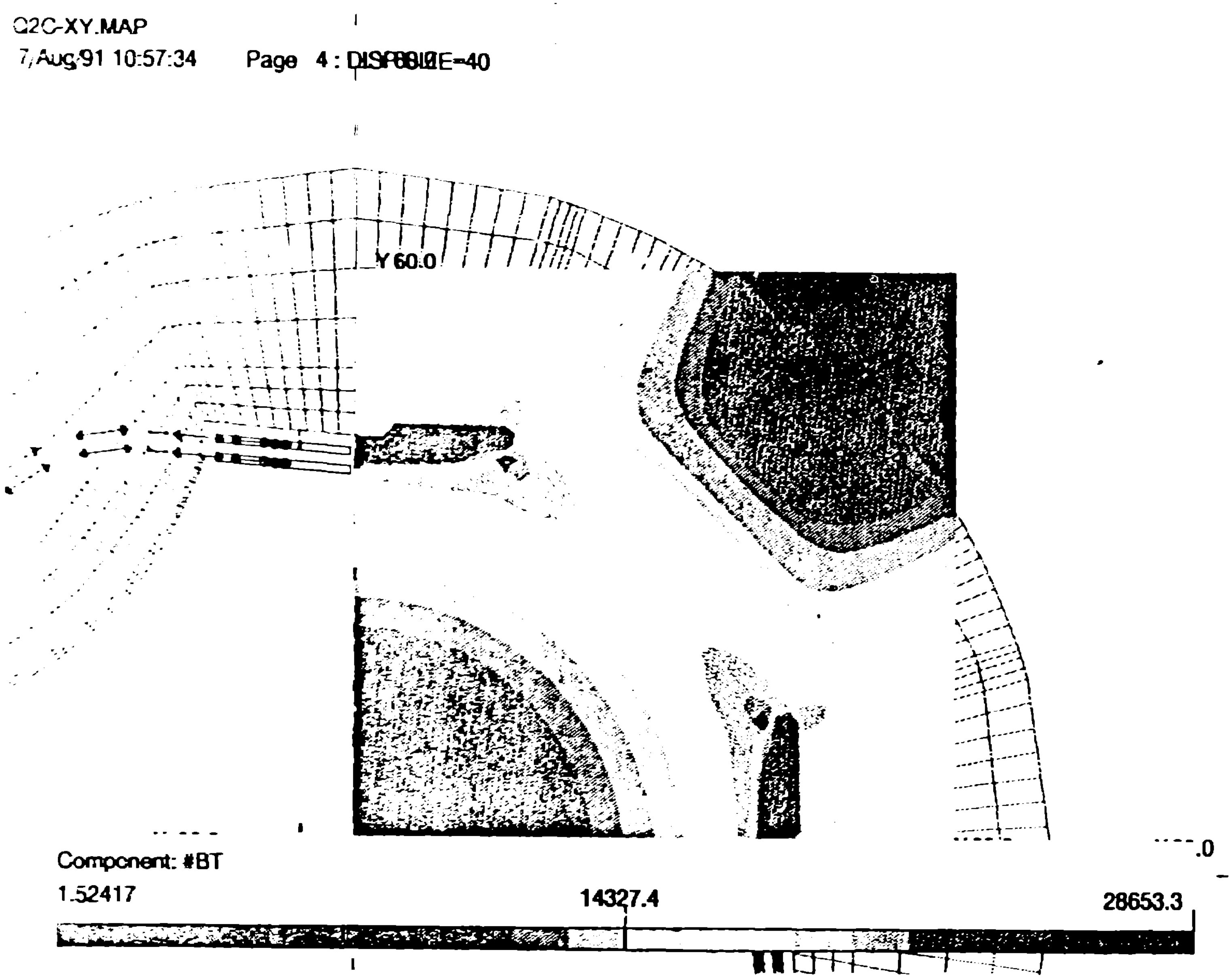
Q2C-XY.MAP
7/Aug/91 10:57:34
Page 4 : DISPSIZE=40
Y 60.0
.0
Component: #BT
1.52417
14327.4
28653.3

VF/OPEF

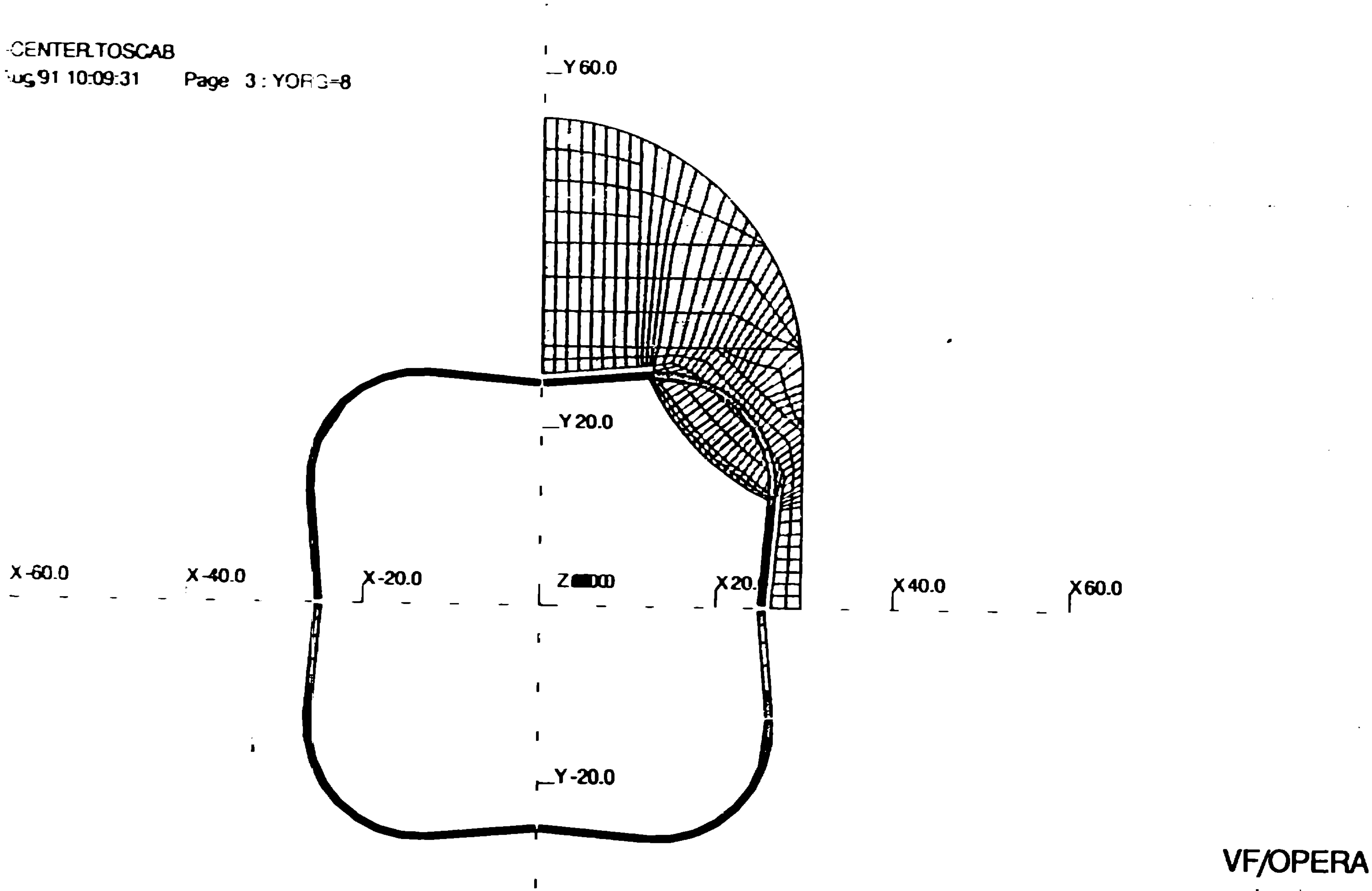

-CENTER.TOSCAB
ug 91 10:09:31 Page 3 : YORG=8
Y 60.0
Y 20.0
X -60.0
X -40.0
X -20.0
X 20.
X 40.0
X 60.0
Y -20.0
VF/OPERA

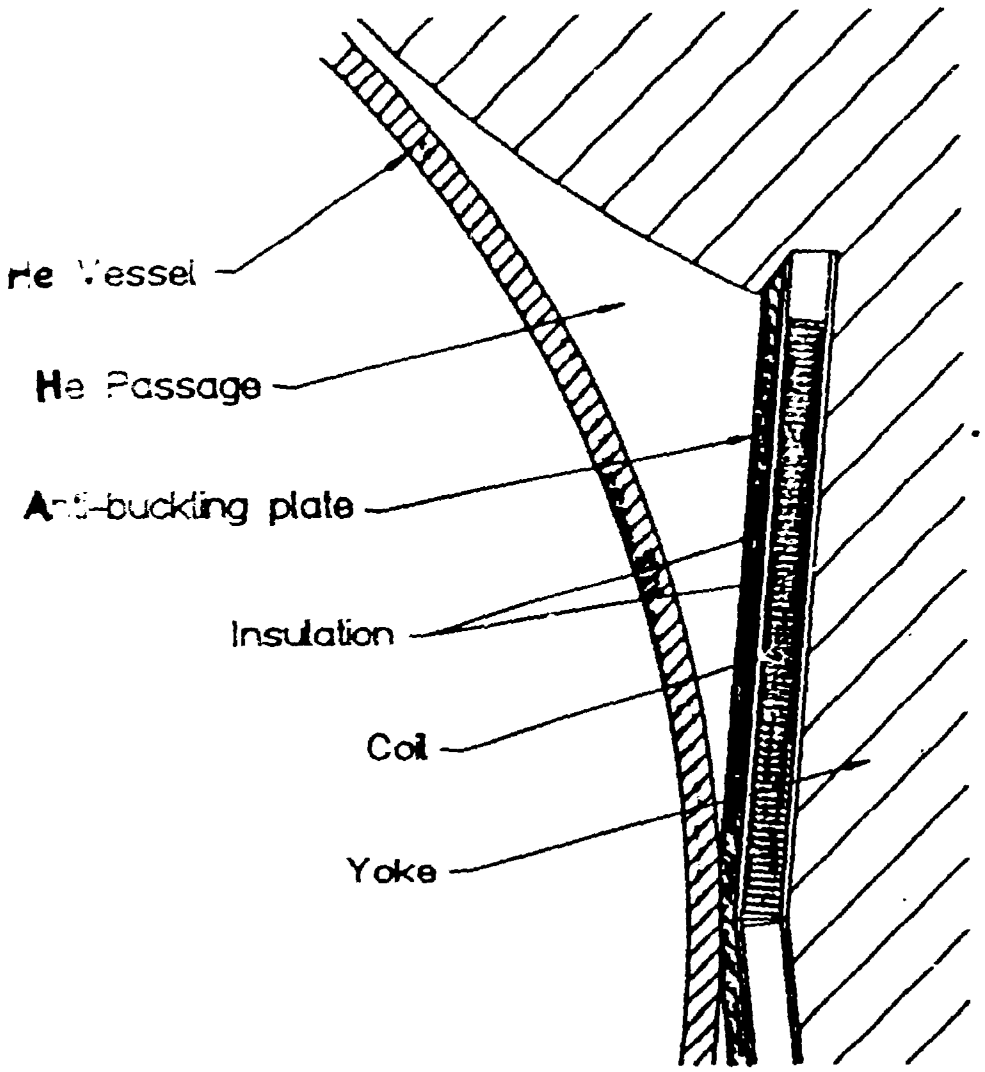

Close up of Q1 coil showing
the helium vessel,
anti-buckling plate, ground
insulation, yoke
and notch in the pole needed
for the anti-buckling plate.

The anti-buckling plate is
needed to support
the coil when the quadrants
are squeezed together.

Summary of TOSCA/OPERA Analysis for Q1

TOSCA Database File : Q1-V2.TOSCAB

Effective Length = 189.3 cm
Pole Radius = 25.0 cm

Radius of Fourier Analysis = 25.0 cm *
(extrapolated form R=22.0cm)

N	Integral [B(N) dz] (Tesla-meter)	% of Integral [B(2) dz]
2	1.4236	------
4	-5.58E-03	-0.392
6	1.07E-02	0.752
10	-3.02E-03	-0.212
14	-1.70E-02	-1.194

Radius of Fourier Analysis = 22.0 cm

N	Integral [B(N) dz] (Tesla-meter)	% of Integral [B(2) dz]
2	1.2527	------
4	-3.80E-03	-0.303
6	5.64E-03	-0.450
10	-9.55E-04	-0.076
14	-3.22E-03	-0.257

* B(N,25) = B(N,22) * (25./22.)^(N-1)

MAIN COILS ONLY NI = 150,000. AT/POLE
Radius of Fourier Analysis = 25.0 cm

N	Integral [B(N) dz] (Tesla-meter)	% of Integral [B(2) dz]
2	1.4236	------
4	-5.58E-03	-0.392
6	1.07E-02	0.752

Q1 WITH N=4 CORRECTION COILS TURNED ON

N	Integral [B(N) dz] (Tesla-meter)	% of Integral [B(2) dz]
2	1.4239	------
4	-5.18E-02	-3.638
6	1.09E-02	0.768

Q1 WITH N=6 CORRECTION COILS TURNED ON

N	Integral [B(N) dz] (Tesla-meter)	% of Integral [B(2) dz]
2	1.4214	------
4	-5.69E-03	-0.401
6	8.05E-02	5.666

Q1 WITH N=4 AND N=6 CORRECTION COILS TURNED ON

N	Integral [B(N) dz] (Tesla-meter)	% of Integral [B(2) dz]
2	1.4220	------
4	-5.18E-02	-3.643
6	8.09E-02	5.690

Q1 NI = 150,000 A.T./POLE

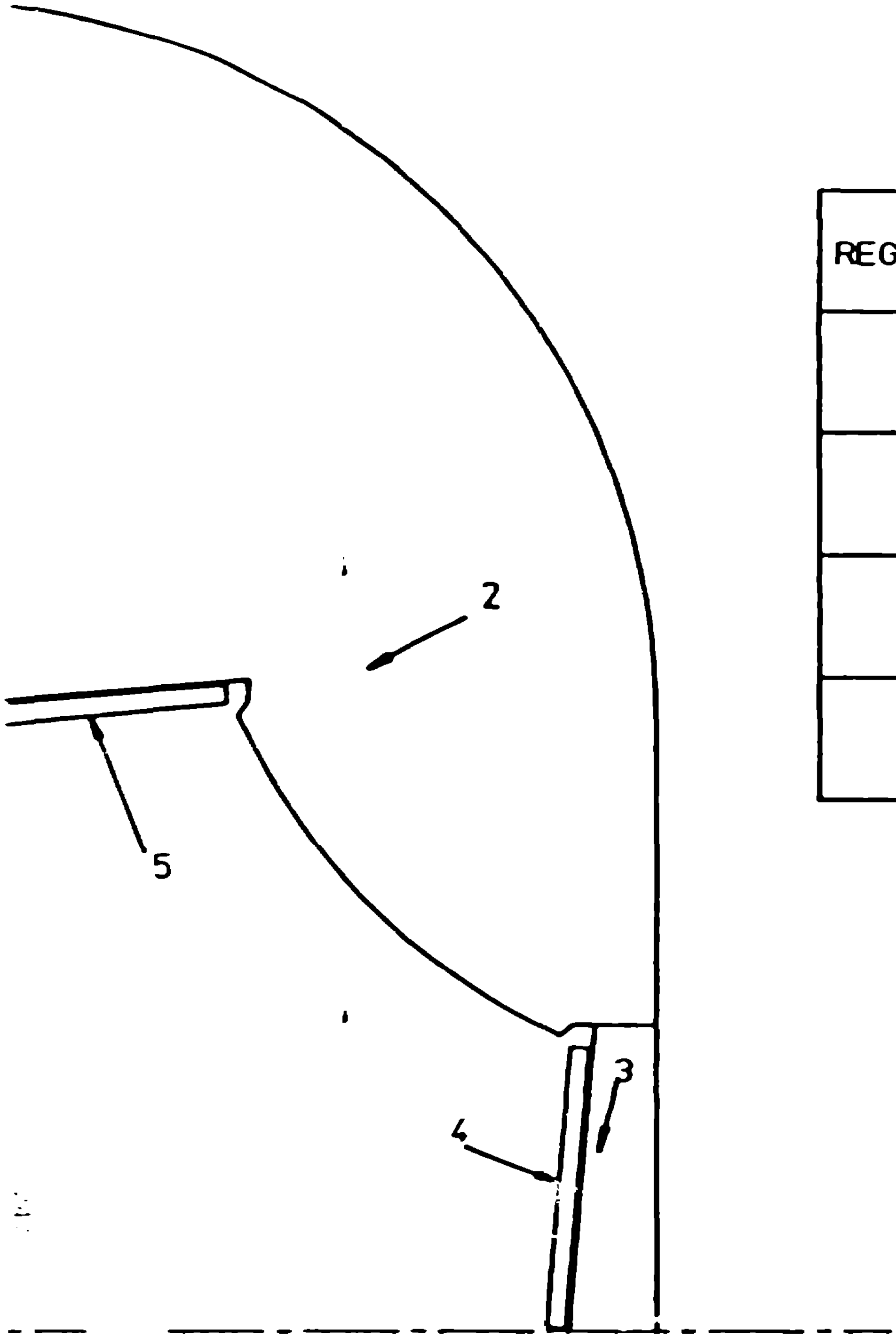

2-D MAGNETOSTATIC FORCES

REGION	F(X) (lbf/in)	F(Y) (lbf/in)	R (in)	Θ (deg)
2	-1581.0	-829.8	-6.360	-152.303
3	-34.7	-129.4	9.585	-105.013
4	621.4	-244.4	5.900	-21.466
5	-251.2	624.6	-5.961	111.911

3-D MAGNETOSTATIC FORCES

REGION	F(X) (lbf/in)	F(Y) (lbf/in)
4	632.83	-262.7
5	-280.8	641.05

3D COIL FORCES

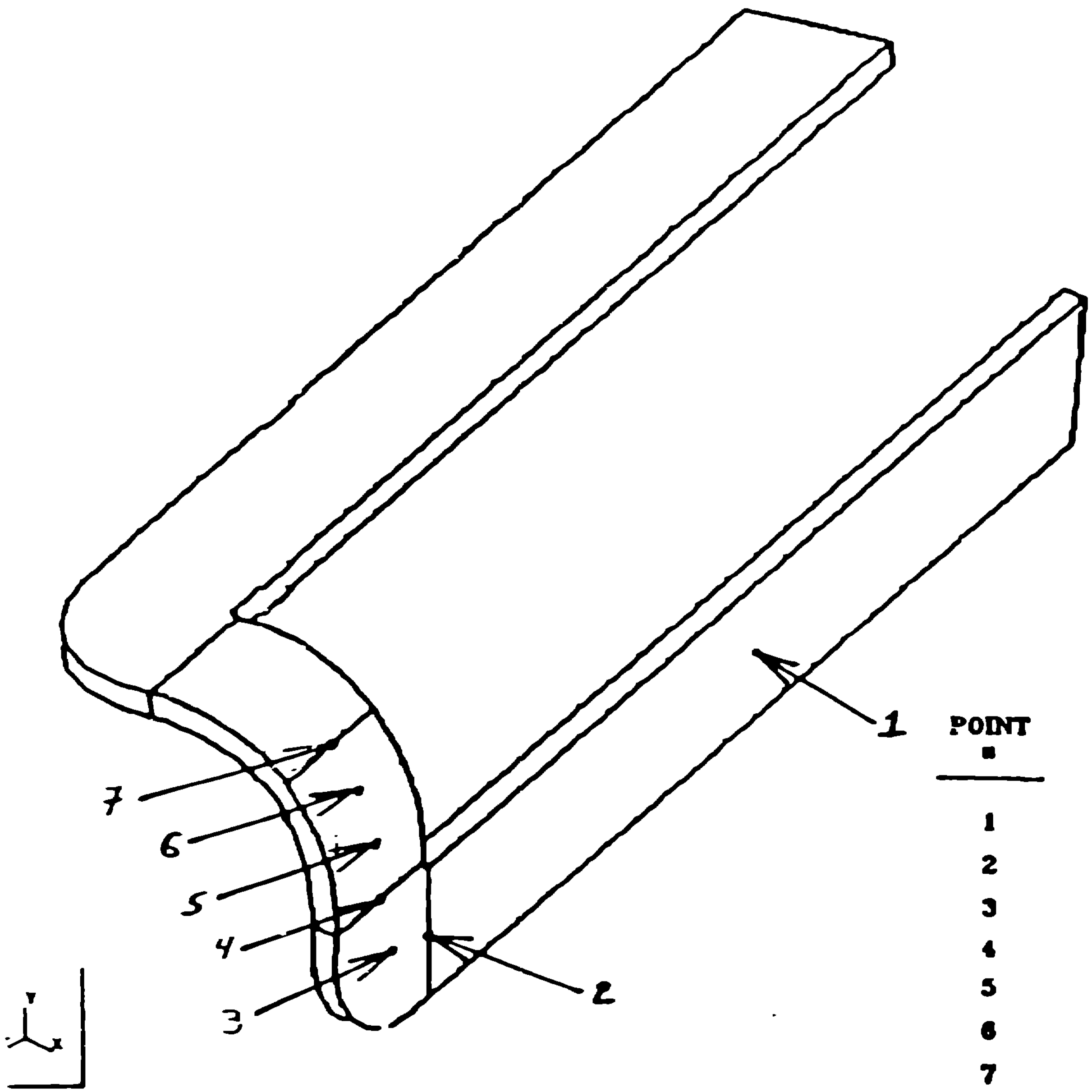

POINT #	FX (lbf)	FY (lbf)	FZ (lbf)
1	22050.0	−9163.2	0.0
2	570.8	−469.2	108.6
3	450.0	−301.7	258.7
4	463.1	−152.6	464.7
5	1041.2	135.6	444.1
6	819.0	518.7	171.9
7	516.0	810.1	169.[illegible]
8	126.2	135.6	444

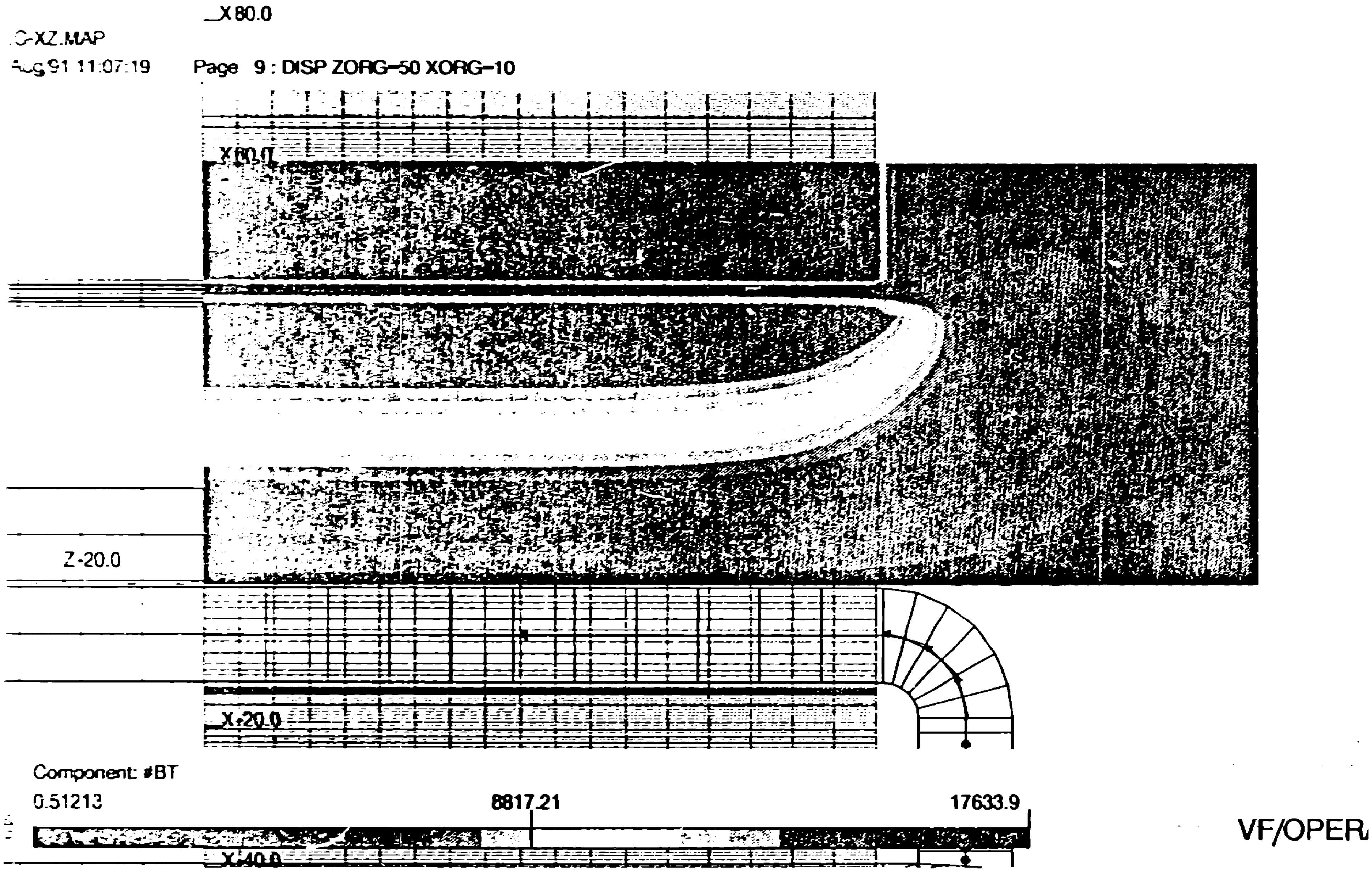
X 80.0
C-XZ.MAP
Aug 91 11:07:19
Page 9 : DISP ZORG=50 XORG=10
X 80.0
Z-20.0
X-20.0
Component: #BT
0.51213
8817.21
17633.9
X-40.0
VF/OPER

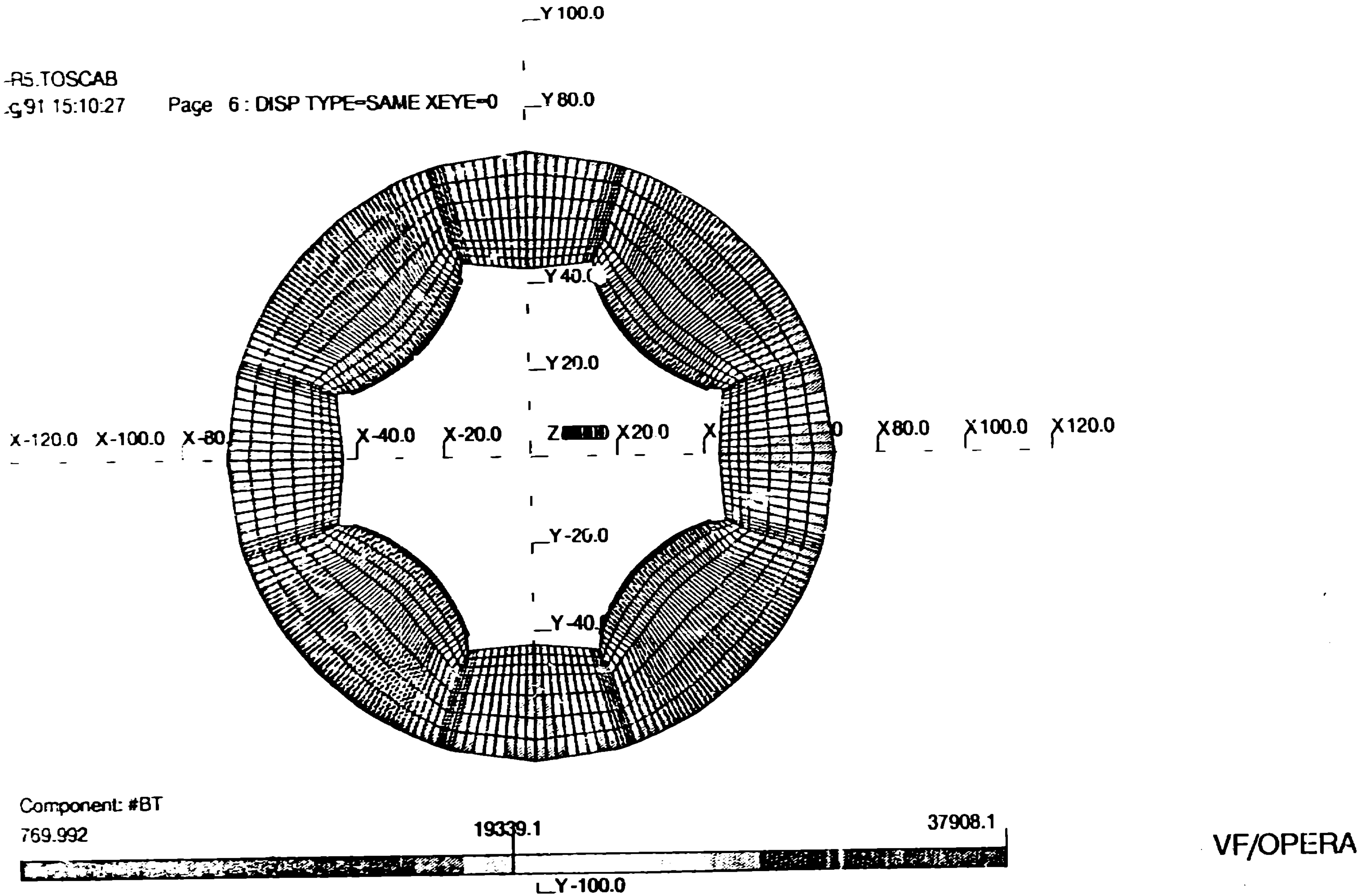
-R5.TOSCAB
.g 91 15:10:27 Page 6 : DISP TYPE=SAME XEYE=0
Y 100.0
Y 80.0
Y 40.0
Y 20.0
Y -20.0
Y -40.0
Y -100.0
X-120.0
X-100.0
X-80.0
X-40.0
X-20.0
X 20.0
X 80.0
X 100.0
X 120.0
Component: #BT
769.992
19339.1
37908.1
VF/OPERA

Q2C-R5.TOSCAB
6 Aug 91 15:42:00 Page 9 : DISP TYPE=SURF

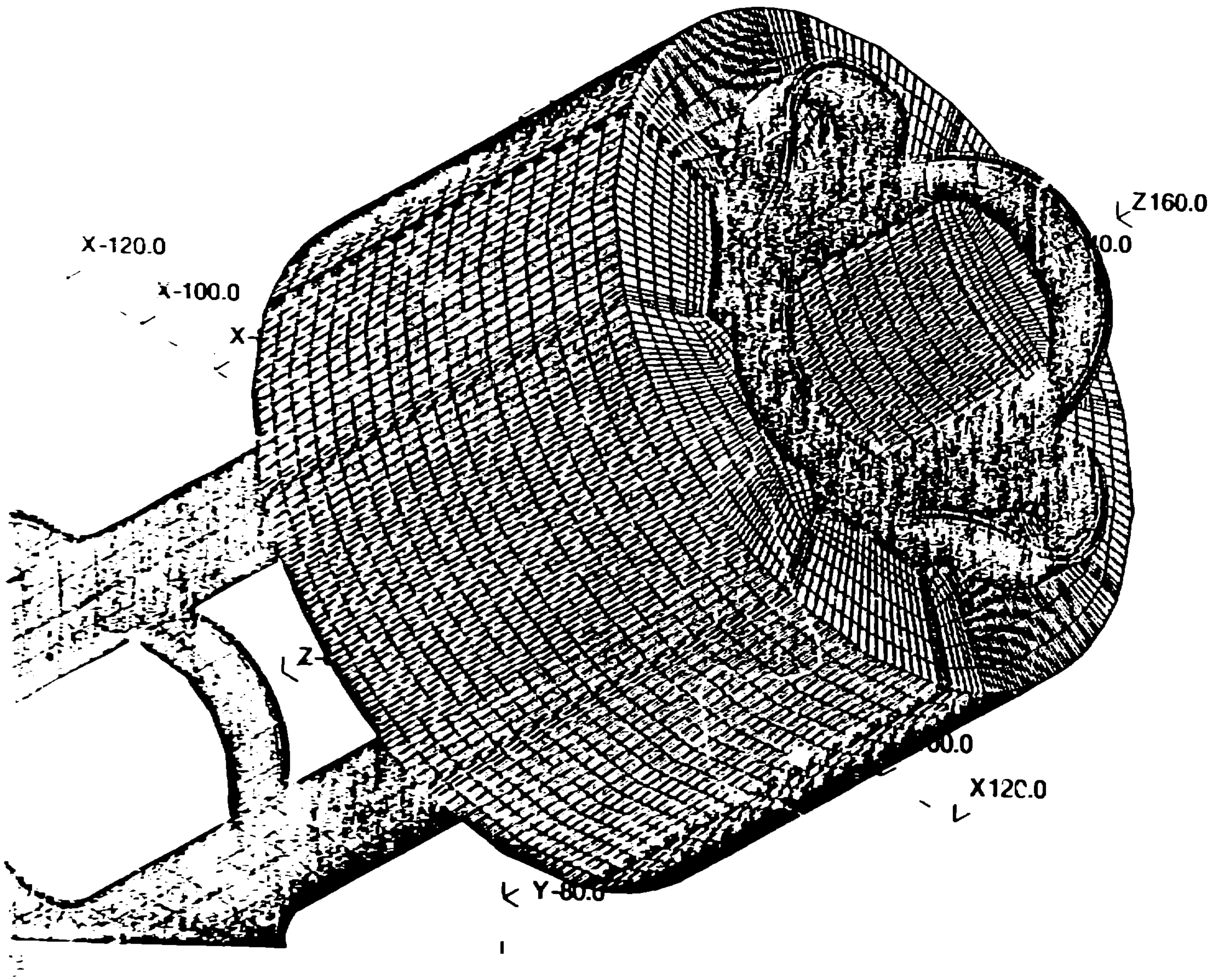

VF/OPER

Q2C-R5.TOSCAB

6 Aug 91 15:38:40 Page 7 : DISP XEYE=-100 YEYE=-100

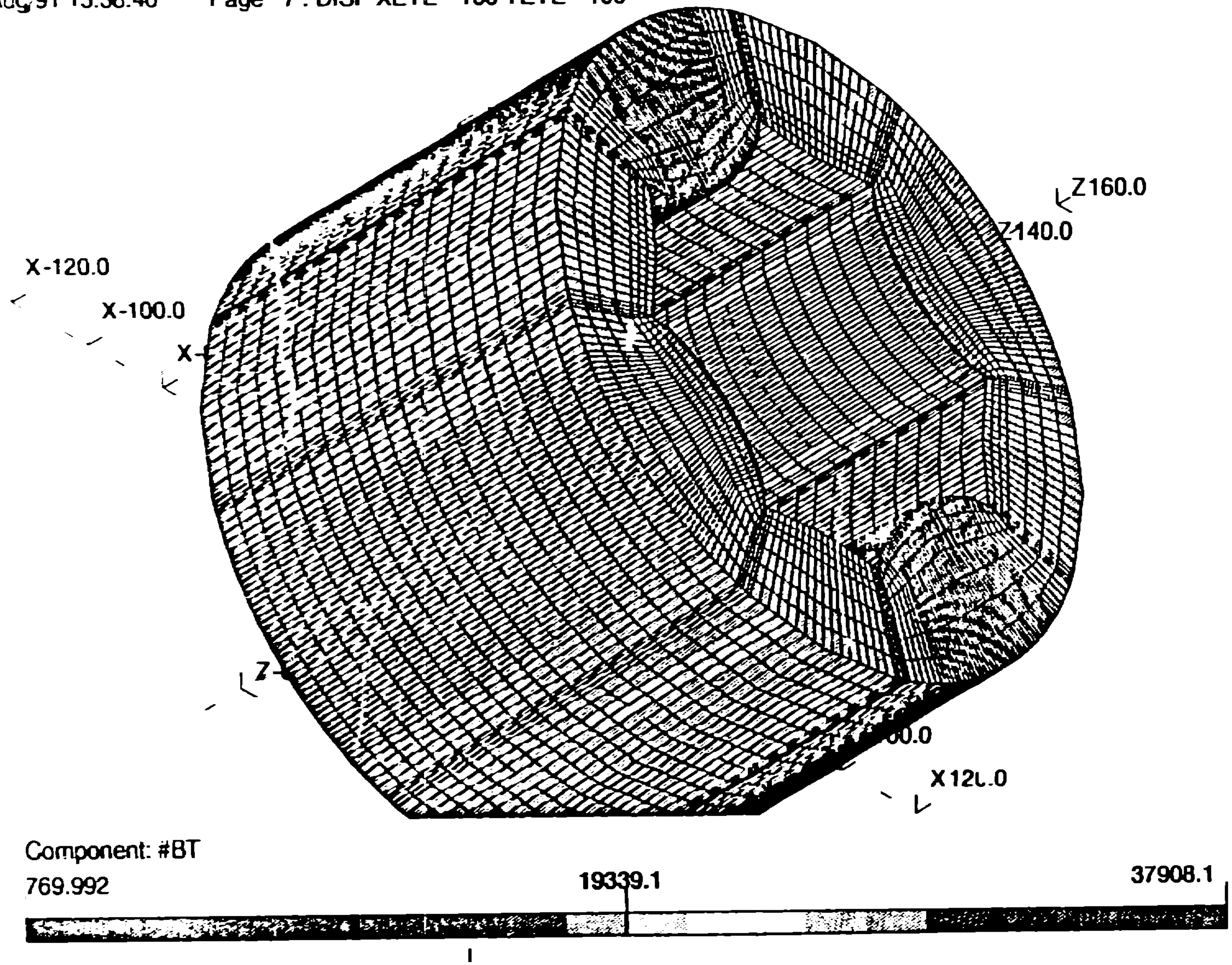

VF/OPE

:C-R5-CHAMF.TOSCAB

Aug/91 08:20:58 Page 5 : XEYE=-100 -100

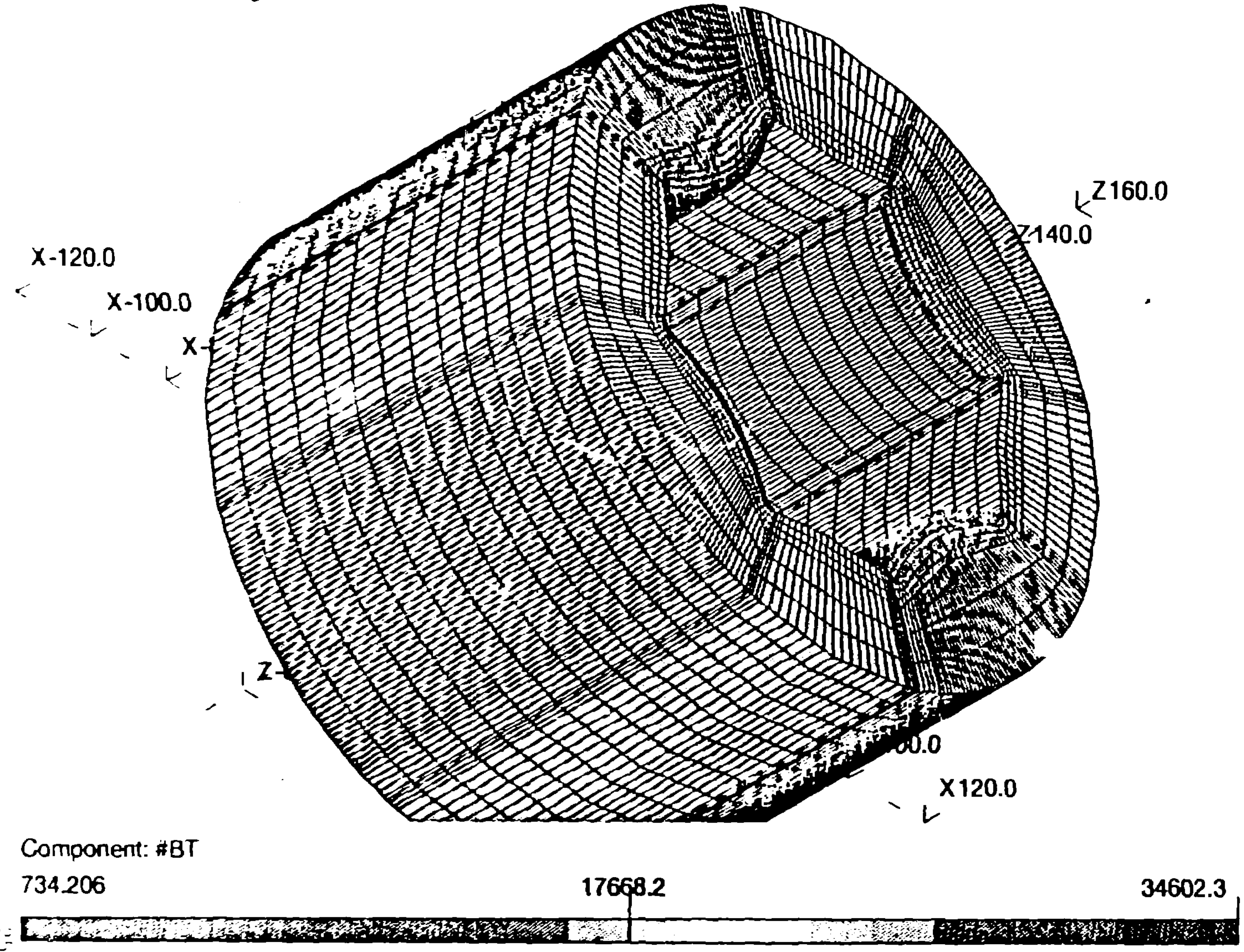

VF/OPERA

```
*****************************************************

is output created on  7-AUG-91 at 16:26:36

ERA output file used: q2c-r5-pot.har
SCA active file used:  Q2C-R5.TOSCAB     Component: POT

adrupole name Q2   with pole radius 35.0 fit up to r= 32.0

ing fitted values of b0,2(z) find:

        Effective length= 212.3 cm (2*106.1 cm)

        Fringe parameters     m             Cm
                              0          -0.0948
                              1          -2.8865
                              2           0.2589
                              3          -0.0611

ta Extracted for Quadrupole (n=2) Component
-------------------------------------------

tegral [b0            dz]=    1.7560 Tesla-m
tegral [B( 32.0 cm) dz]=    1.6037 Tesla-m
tegral [B( 28.3 cm) dz]=    1.4183 Tesla-m
tegral [B( 22.3 cm) dz]=    1.1200 Tesla-m

ta Extracted for n= 6 Component
-------------------------------

tegral [b0            dz]= 0.103E-01 Tesla-m   (  0.586% of n=2)
tegral [B( 32.0 cm) dz]= 0.920E-02 Tesla-m   (  0.573% of n=2)
tegral [B( 28.3 cm) dz]= 0.435E-02 Tesla-m   (  0.307% of n=2)
tegral [B( 22.3 cm) dz]= 0.131E-02 Tesla-m   (  0.117% of n=2)

ta Extracted for n=10 Component
-------------------------------

tegral [b0            dz]= 0.181E-01 Tesla-m   (  1.031% of n=2)
tegral [B( 32.0 cm) dz]= 0.102E-02 Tesla-m   (  0.064% of n=2)
tegral [B( 28.3 cm) dz]= 0.619E-03 Tesla-m   (  0.044% of n=2)
tegral [B( 22.3 cm) dz]= 0.702E-04 Tesla-m   (  0.006% of n=2)

ta Extracted for n=14 Component
-------------------------------

tegral [b0            dz]=-0.777E-01 Tesla-m   ( -4.425% of n=2)
tegral [B( 32.0 cm) dz]=-0.965E-03 Tesla-m   ( -0.060% of n=2)
tegral [B( 28.3 cm) dz]=-0.374E-03 Tesla-m   ( -0.026% of n=2)
tegral [B( 22.3 cm) dz]=-0.170E-04 Tesla-m   ( -0.002% of n=2)
```

Q2 SPEC SHEET

Effective Length	= 2.1m
Radius Pole	= .35m
Good Aperture Radius	= .30m
Field at Pole	= 1.56 Telsa
Gradient	= 4.457 Telsa/m
Field errors:	
at the Pole	$\frac{B(6)}{B(2)} < 3.0\ \%$
within Aperture	$\sum \frac{B(n)}{B(2)} < .3\ \%$
Physical weight	= 20.8 Tons
Physical length	= 2.6m
Physical Cross Section	= 1.56m Dia.
$\frac{\text{Length (yoke)}}{\text{Bore (pole)}}$	= 2.734

```
nary of TOSCA/OPERA analysis for Quadrupole Magnet
***************************************************

s output created on  7-AUG-91 at 16:23:32

RA output file used: q2c-r5-chamf-pot.har
CA active file used:  Q2C-R5-CHAMF.TOSCAB     Component: POT

drupole name Q2   with pole radius 35.0 fit up to r= 32.0

ng fitted values of b0,2(z) find:

       Effective length= 211.9 cm (2*105.9 cm)

       Fringe parameters     m          Cm
                             0        -0.0997
                             1        -2.8818
                             2         0.2757
                             3        -0.0703


a Extracted for Quadrupole (n=2) Component
-----------------------------------------

egral [b0            dz]=    1.7562 Tesla-m
egral [B( 32.0 cm) dz]=     1.6035 Tesla-m
egral [B( 28.3 cm) dz]=     1.4184 Tesla-m
egral [B( 22.3 cm) dz]=     1.1201 Tesla-m


a Extracted for n= 6 Component
------------------------------

egral [b0            dz]= 0.493E-02 Tesla-m  (  0.281% of n=2)
egral [B( 32.0 cm) dz]= 0.826E-02 Tesla-m  (  0.515% of n=2)
egral [B( 28.3 cm) dz]= 0.350E-02 Tesla-m  (  0.246% of n=2)
egral [B( 22.3 cm) dz]= 0.109E-02 Tesla-m  (  0.097% of n=2)


a Extracted for n=10 Component
------------------------------

egral [b0            dz]= 0.267E 01 Tesla-m  (  1.523% of n=2)
egral [B( 32.0 cm) dz]= 0.837E 03 Tesla-m  (  0.052% of n=2)
egral [B( 28.3 cm) dz]= 0.838E-03 Tesla-m  (  0.059% of n=2)
egral [B( 22.3 cm) dz]= 0.841E-04 Tesla-m  (  0.008% of n=2)


a Extracted for n=14 Component
------------------------------

egral [b0            dz]=-0.272E-01 Tesla-m  ( -1.549% of n=2)
egral [B( 32.0 cm) dz]=-0.387E-03 Tesla-m  ( -0.024% of n=2)
egral [B( 28.3 cm) dz]=-0.348E-03 Tesla-m  ( -0.025% of n=2)
egral [B( 22.3 cm) dz]=-0.114E-04 Tesla-m  ( -0.001% of n=2)
```

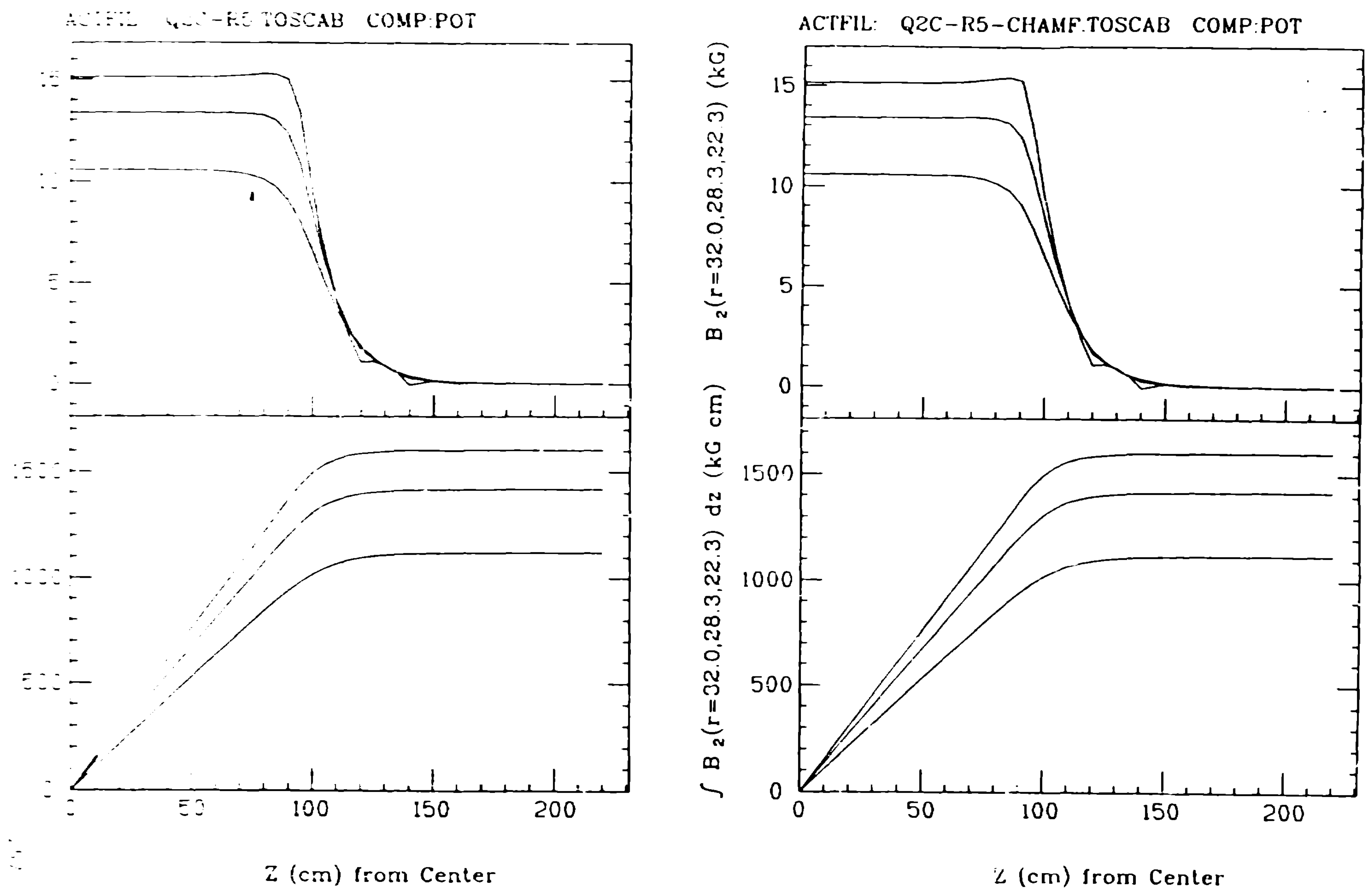
ACTFIL: Q2C-R5-CHAMF.TOSCAB COMP:POT
B_2(r=32.0,28.3,22.3) (kG)
$\int B_2$(r=32.0,28.3,22.3) dz (kG cm)
Z (cm) from Center
Z (cm) from Center

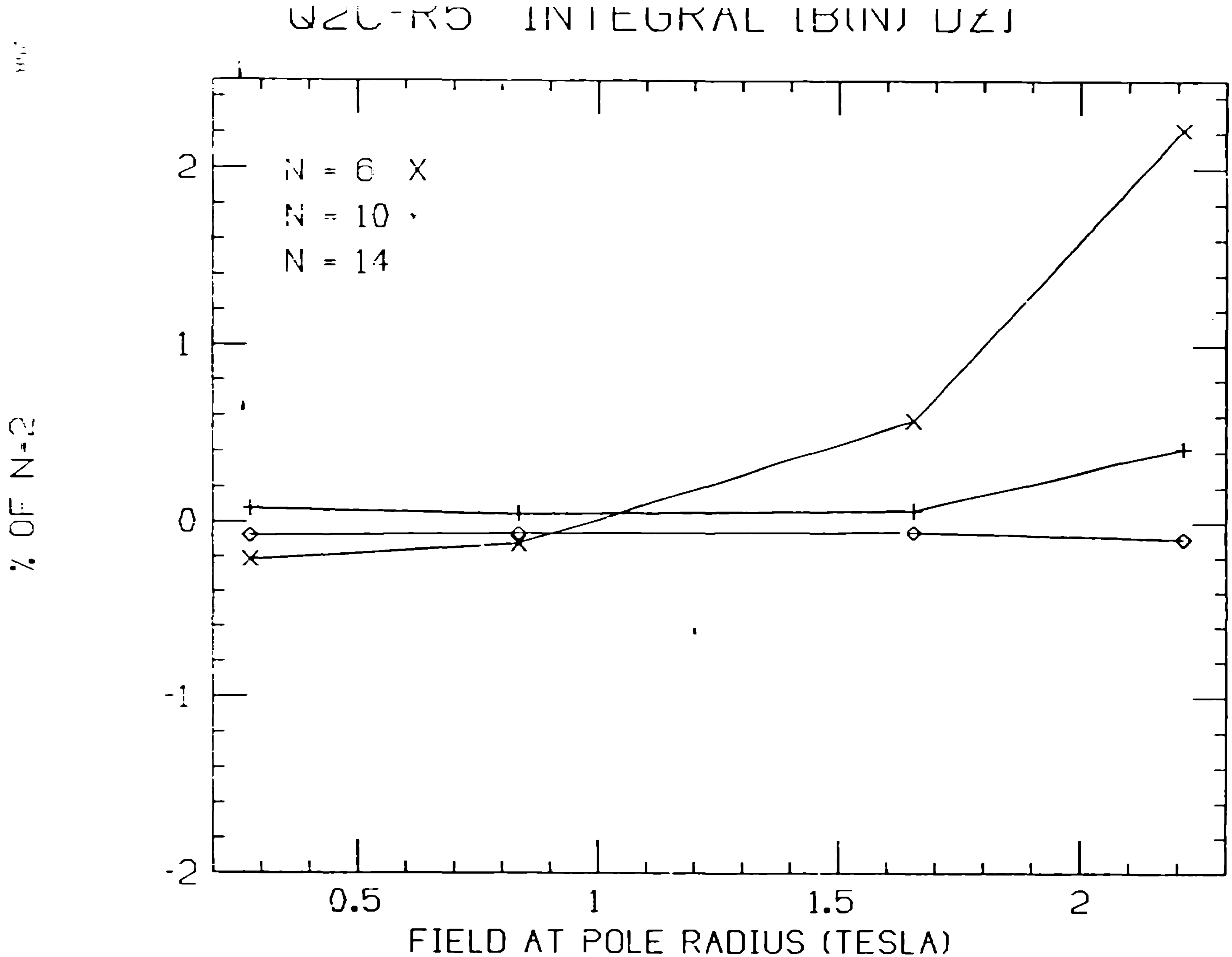
Q2C-R5 INTEGRAL (B(N) DZ)
N = 6 X
N = 10
N = 14
2
1
0
-1
-2
0.5
1
1.5
2
FIELD AT POLE RADIUS (TESLA)
% OF N=2

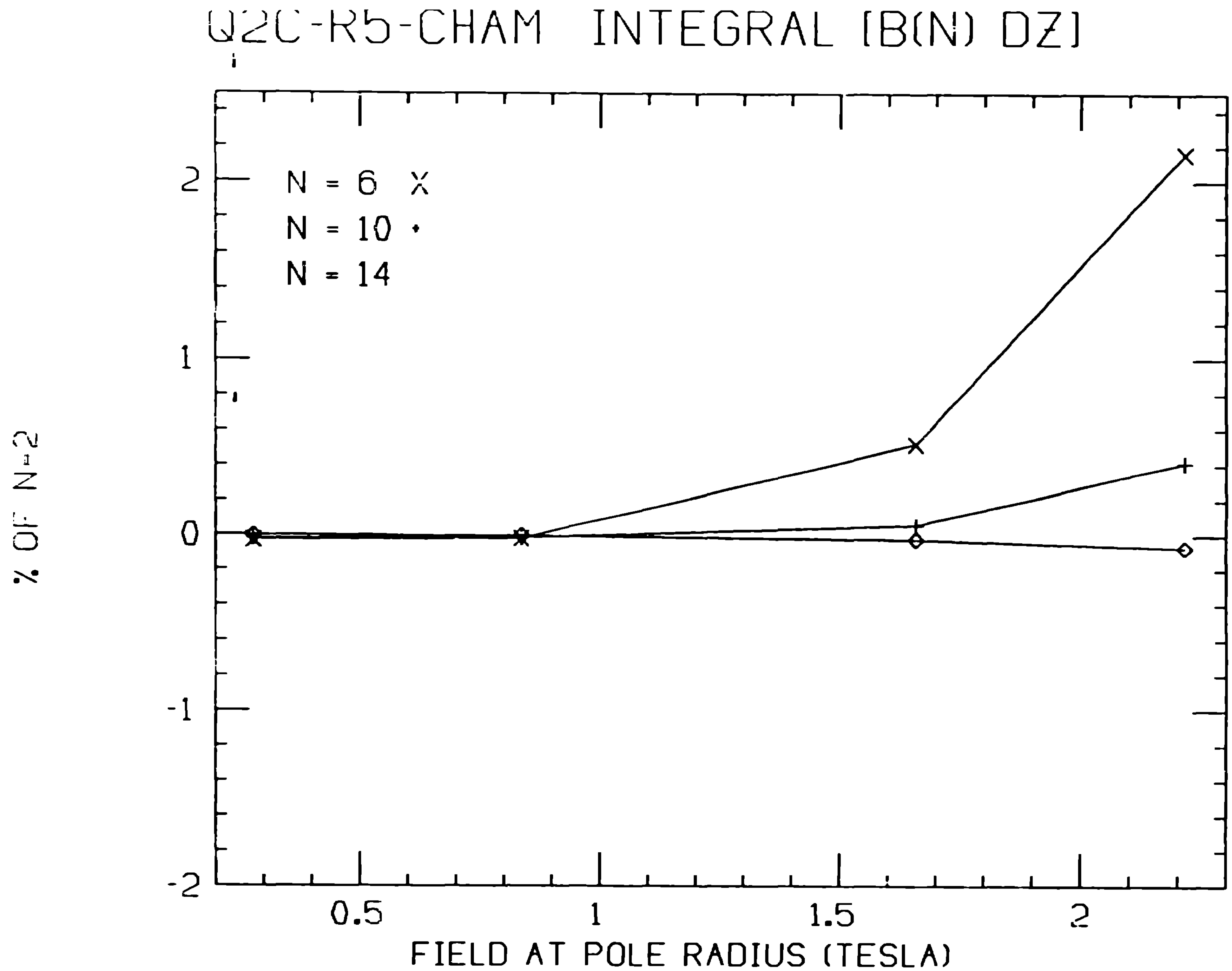
Q2C-R5-CHAM INTEGRAL [B(N) DZ]
N = 6 X
N = 10 +
N = 14
2
1
0
-1
-2
% OF N=2
0.5
1
1.5
2
FIELD AT POLE RADIUS (TESLA)

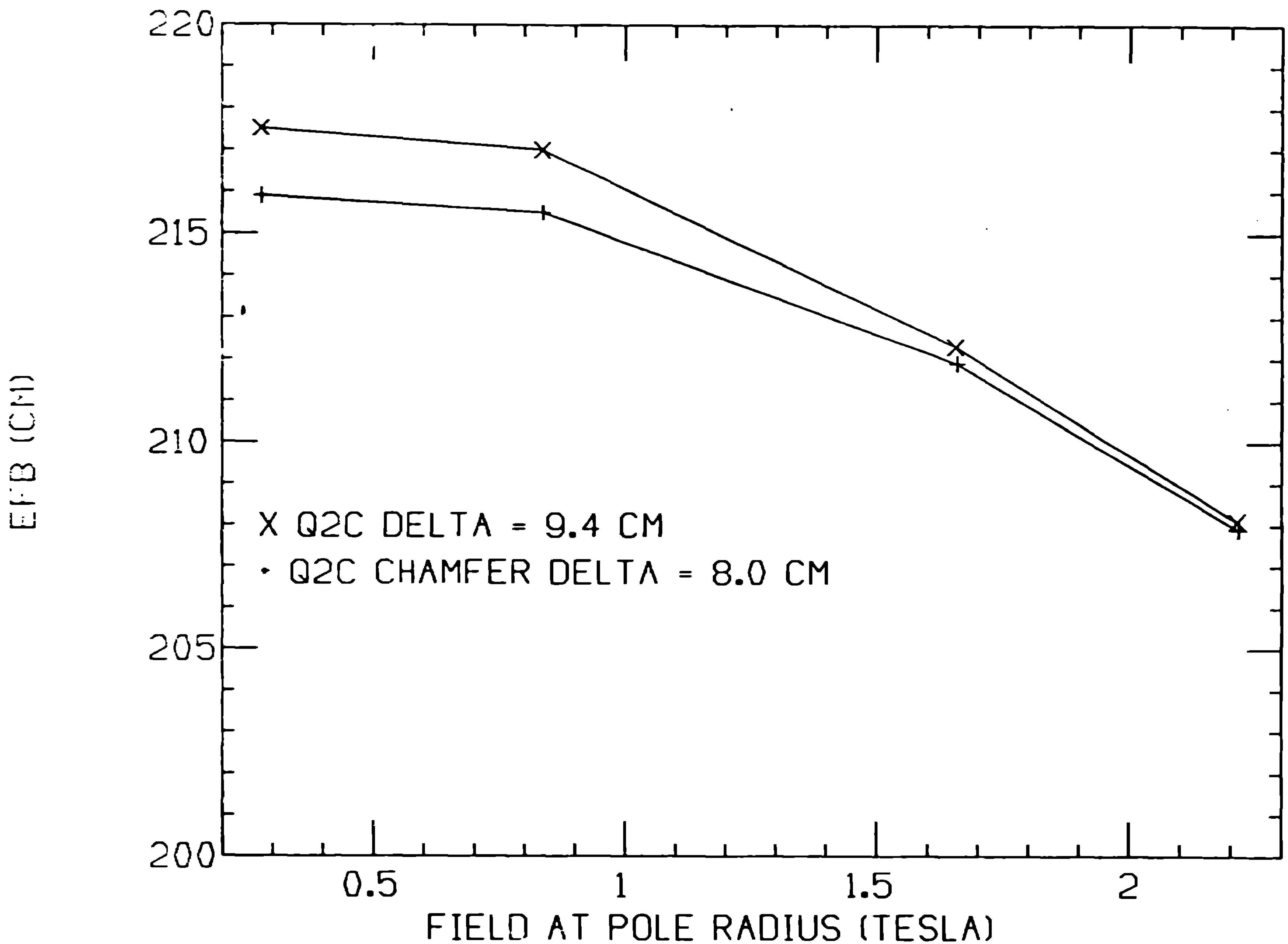
220
215
210
205
200
0.5
1
1.5
2
FIELD AT POLE RADIUS (TESLA)
EFB (CM)
X Q2C DELTA = 9.4 CM
+ Q2C CHAMFER DELTA = 8.0 CM

Q2C-POISSON HARMONICS

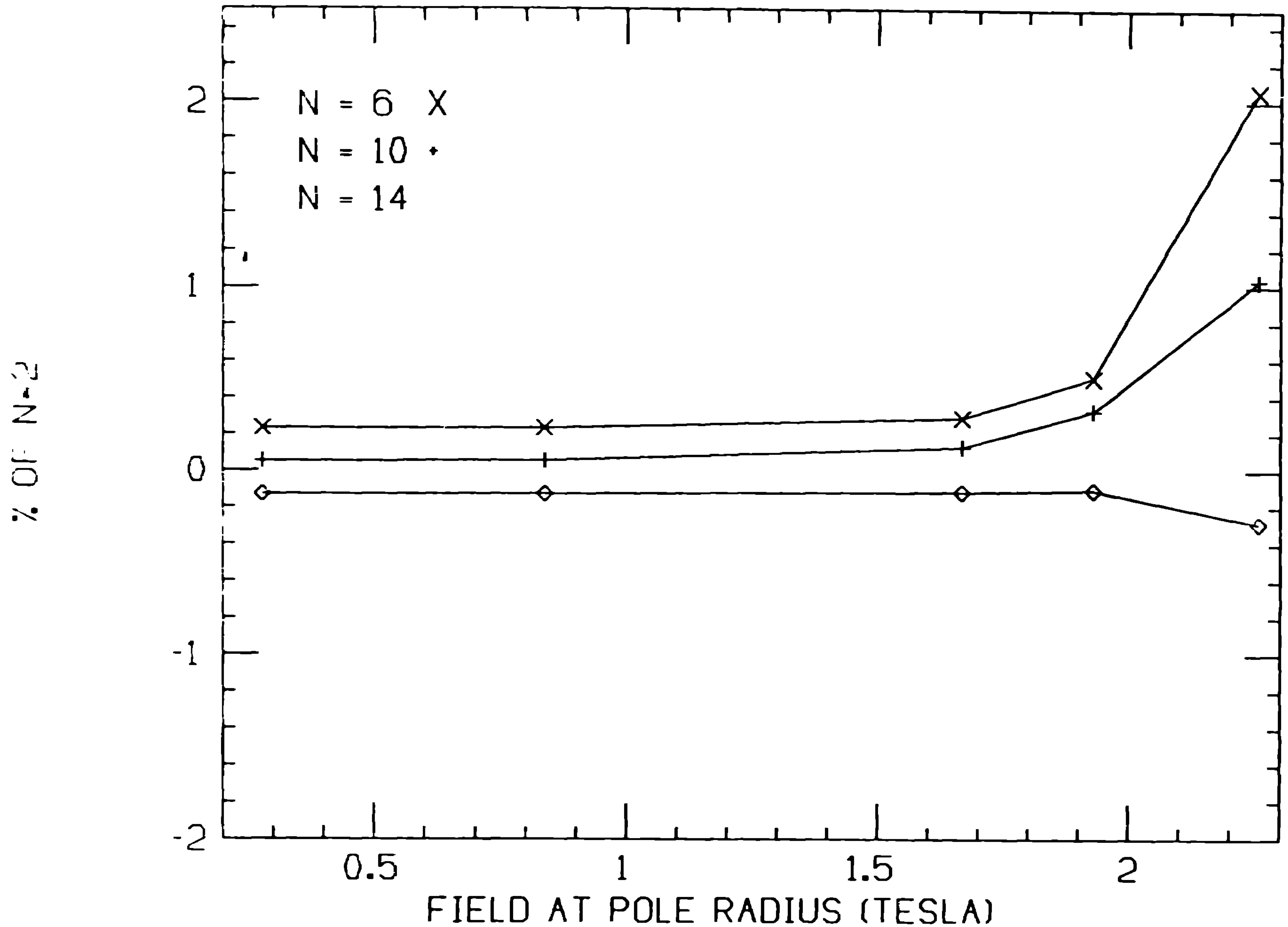

$$\frac{\int B(6)dz}{\int B(2)dz} < 3.0\ \%$$

$$\int B(6)dz = \int B(6)dl_{\text{CENTRAL}} + \int B(6)dz_{\text{ENDS}}$$

FOR COIL TOLERANCES WE CAN DO A TAYLOR SERIES EXPANSION

$$\frac{\int B(6)dz}{\int B(2)dz} = \underbrace{\left.\frac{\int B(6)dz}{\int B(2)dz}\right|_{\text{CENTRAL}} + \left.\frac{\int B(6)dz}{\int B(2)dz}\right|_{\text{ENDS}}}_{\text{FROM TOSCA}} + \frac{\delta \dfrac{\int B(6)dz}{\int B(2)dz}}{\delta E} \Delta E$$

WHERE $\dfrac{\delta \dfrac{\int B(6)dz}{\int B(2)dz}}{\delta E} = S$ IS THE INCREMENTAL CHANGE WITHIN THE MAGNET DUE TO COIL PLACEMENT ERRORS. THIS WAS CALCULATED IN 2-D ANALYSIS.

$$\frac{\int B(6)dz}{\int B(2)dz} < 3.0\ \% = \text{TOSCA RESULTS} + \text{COIL PLACEMENT}$$

$$= .011 + 3.68\frac{\%}{\text{in}^2} * 88\text{in} * \underline{.005''}$$

$$\frac{\int B(6)dz}{\int B(2)dz} = 1.63\%$$

SOURCES OF COIL PLACEMENT ERRORS

	S	ERROR
COIL HEIGHT	3.68%/in^2	1.62
) COIL - MEDIAN PLANE GAP SEPARATION	3.75%/in^2	1.65
) COIL THICKNESS	1.11%/in^2	.49
) COIL - Fe GAP SEPARATION	1.26%/in^2	.55
) FACE ANGLE	1.468%/deg-in	.25

OTAL $\frac{\int B(6)dz}{\int B(2)dz} = .011 + \sqrt{1.62^2 + 1.65^2 + .49^2 + .55^2 + .25^2)} = 2.45\%$

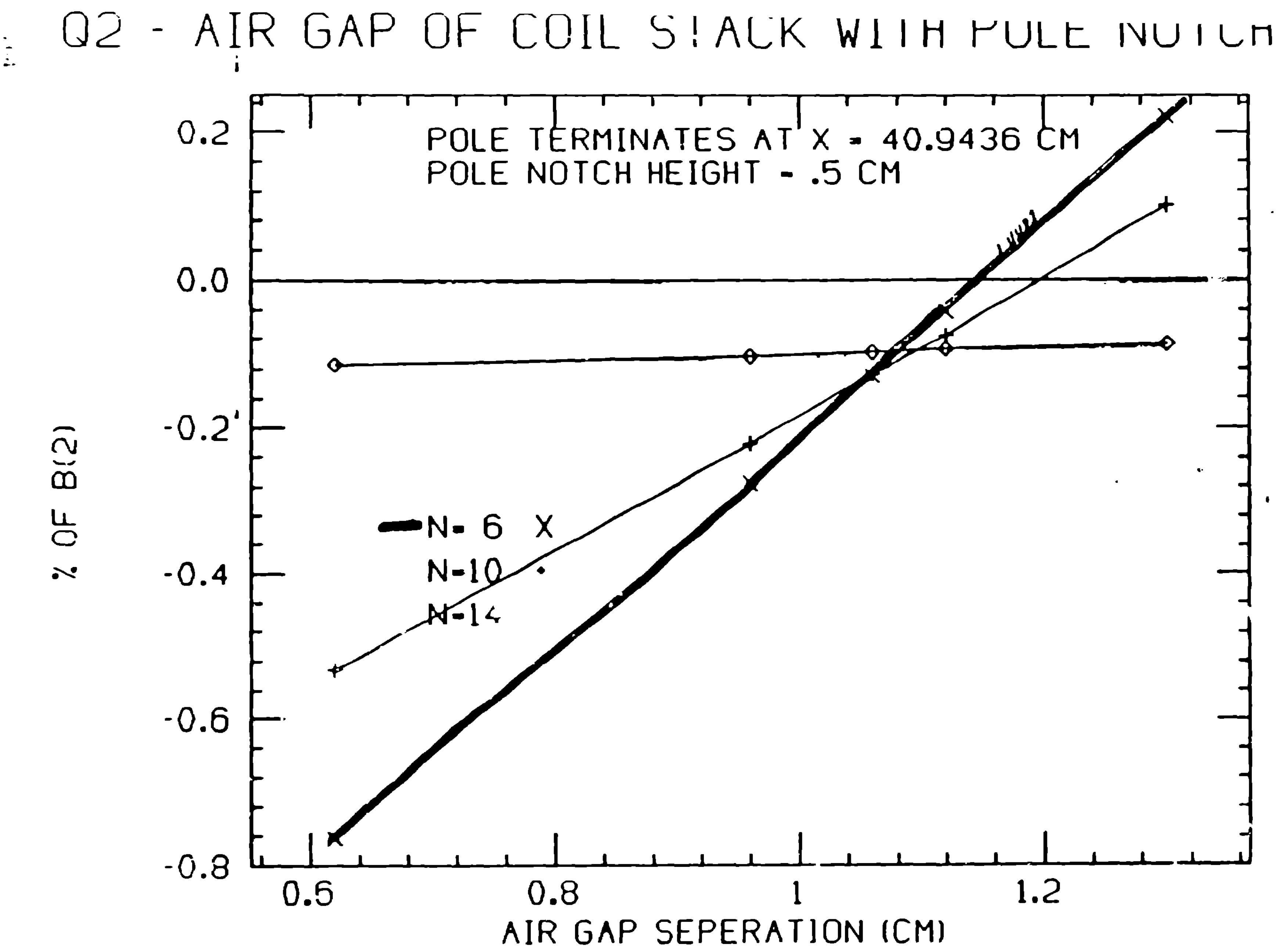
Q2 - AIR GAP OF COIL STACK WITH POLE NOTCH
POLE TERMINATES AT X = 40.9436 CM
POLE NOTCH HEIGHT = .5 CM
N= 6 X
N=10
N=14
% OF B(2)
0.2
0.0
-0.2
-0.4
-0.6
-0.8
0.6
0.8
1
1.2
AIR GAP SEPERATION (CM)

.2-N6.COND
?/Aug/91 08:48:06 Page 4 : DISP

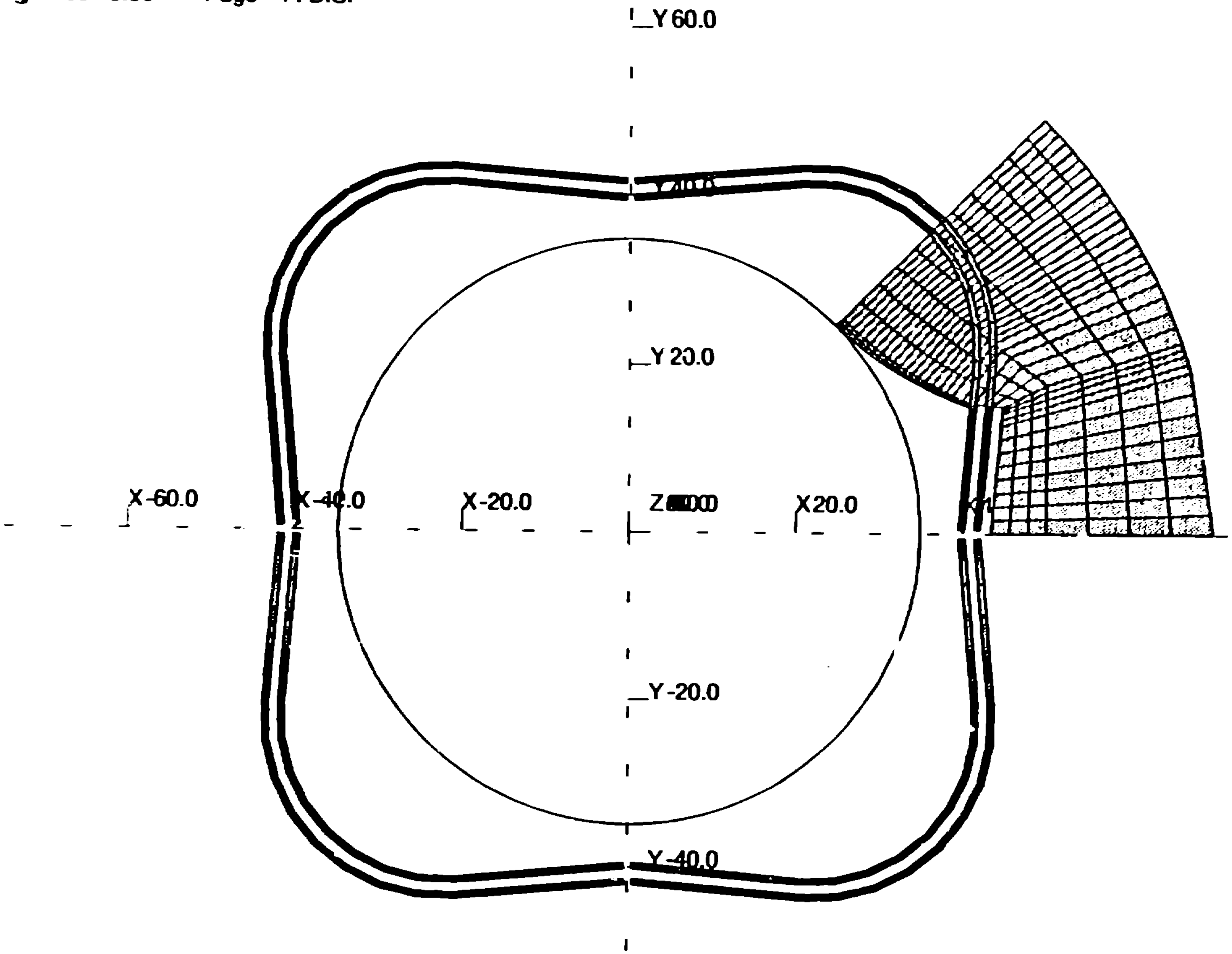

VF/OPER

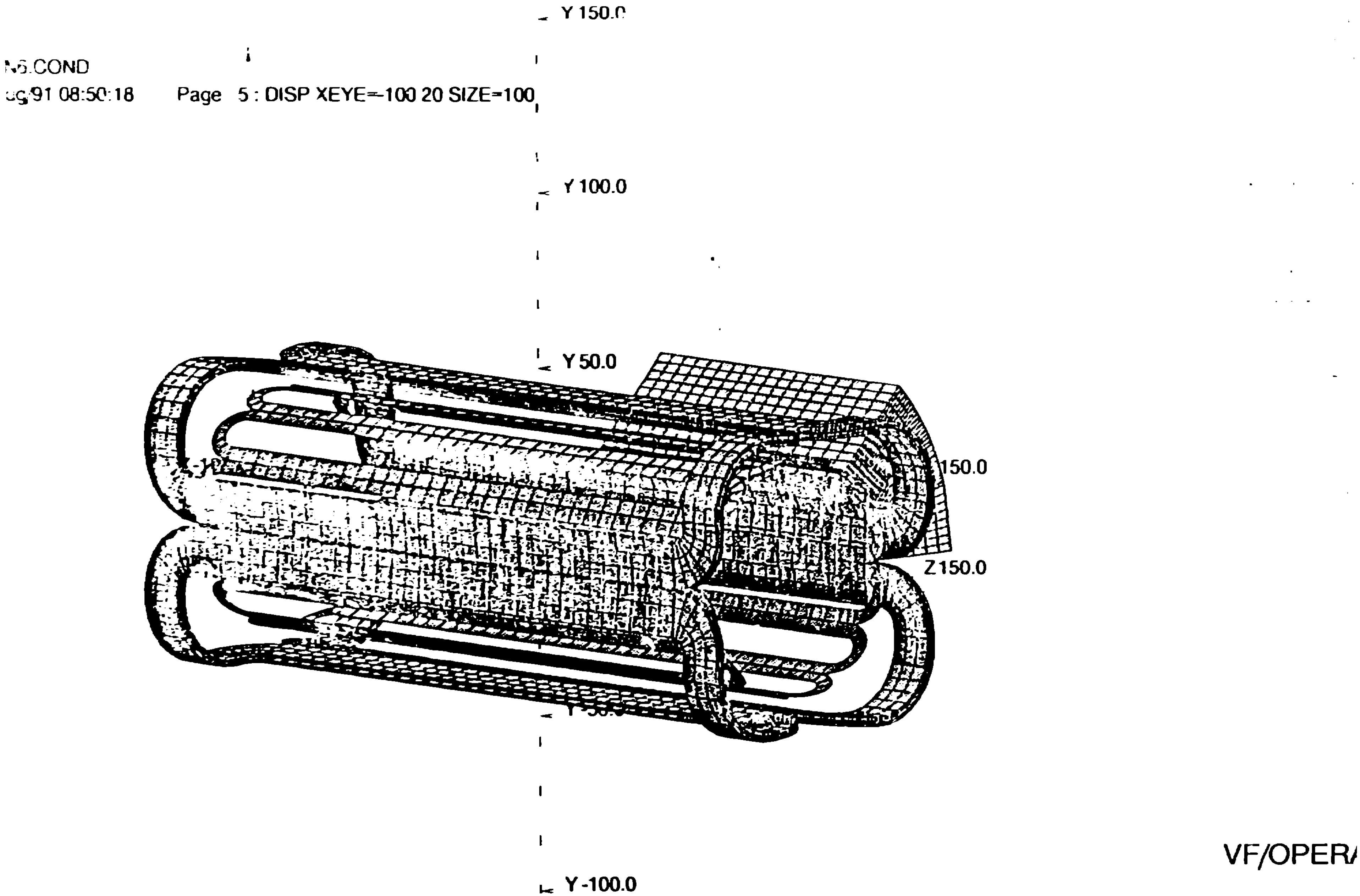

COND
91 08:50:18 Page 5 : DISP XEYE=-100 20 SIZE=100
Y 150.0
Y 100.0
Y 50.0
150.0
Z 150.0
Y -100.0
VF/OPER

Q1 CONDUCTOR SPEC. SHEET

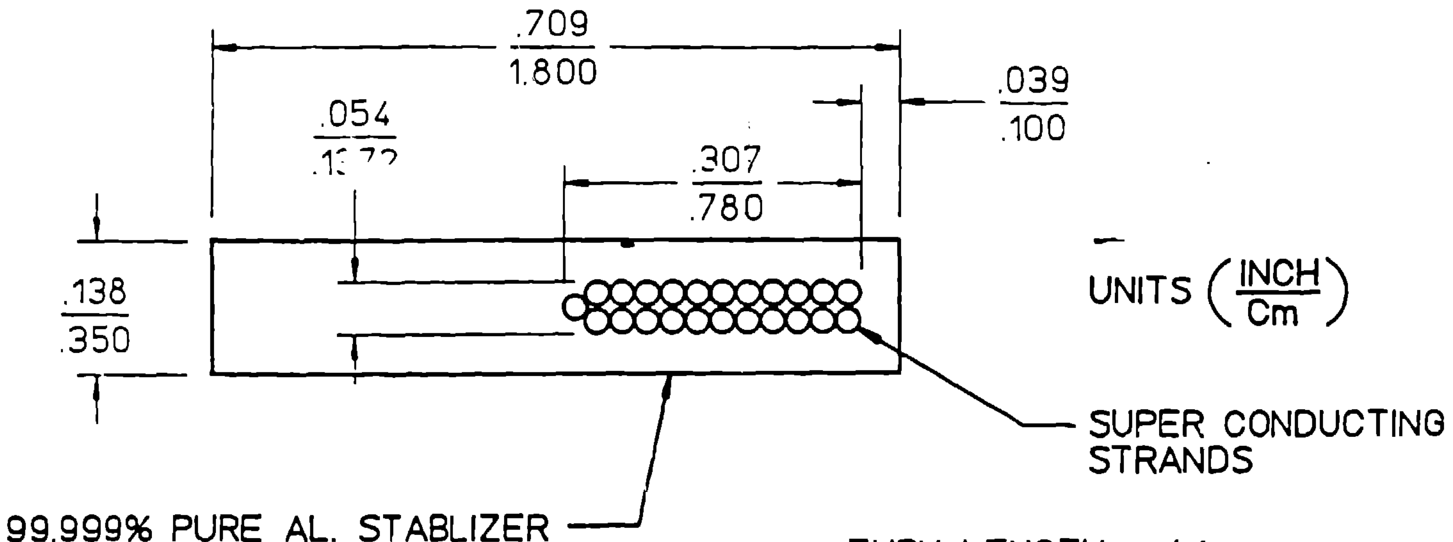

TURN LENGTH - 4.1m

Turns/Pole = 25

Layers/Coil = 1

Turns/Layer = 25

Current (Max)/Turn = 6800 Amps
(Cryostability)

NI (Total) = 680 KA-Turns (Max)

I(op) (6GeV/c) = 6000 Amps

α(op.) = .77

Super Conducting Filaments : 8 μm Diameter Nb-Ti Alloy, 2100 Filaments/Strand

Strand Diameter = 0.0268 ±0.0003 in.

Strands/Cable = 23

Strand Twist Pitch = 0.5 in

Cable Twist Pitch = 2.25 in

Strand Short-Sample Current (min) = 420A @ 20KG & 4.2K

Cable Short-Sample Current (min) = 9660A @ 20KG & 4.2K

Copper Resistivity Ratio = R(9.5K)/R(273K) = 0.023

AL Resistivity Ratio = R(4.2K)/R(273K) = 0.001

AL to CU to S.C. Ratio = 18.27/1.8/1.0

Q1 CROSS SECTION

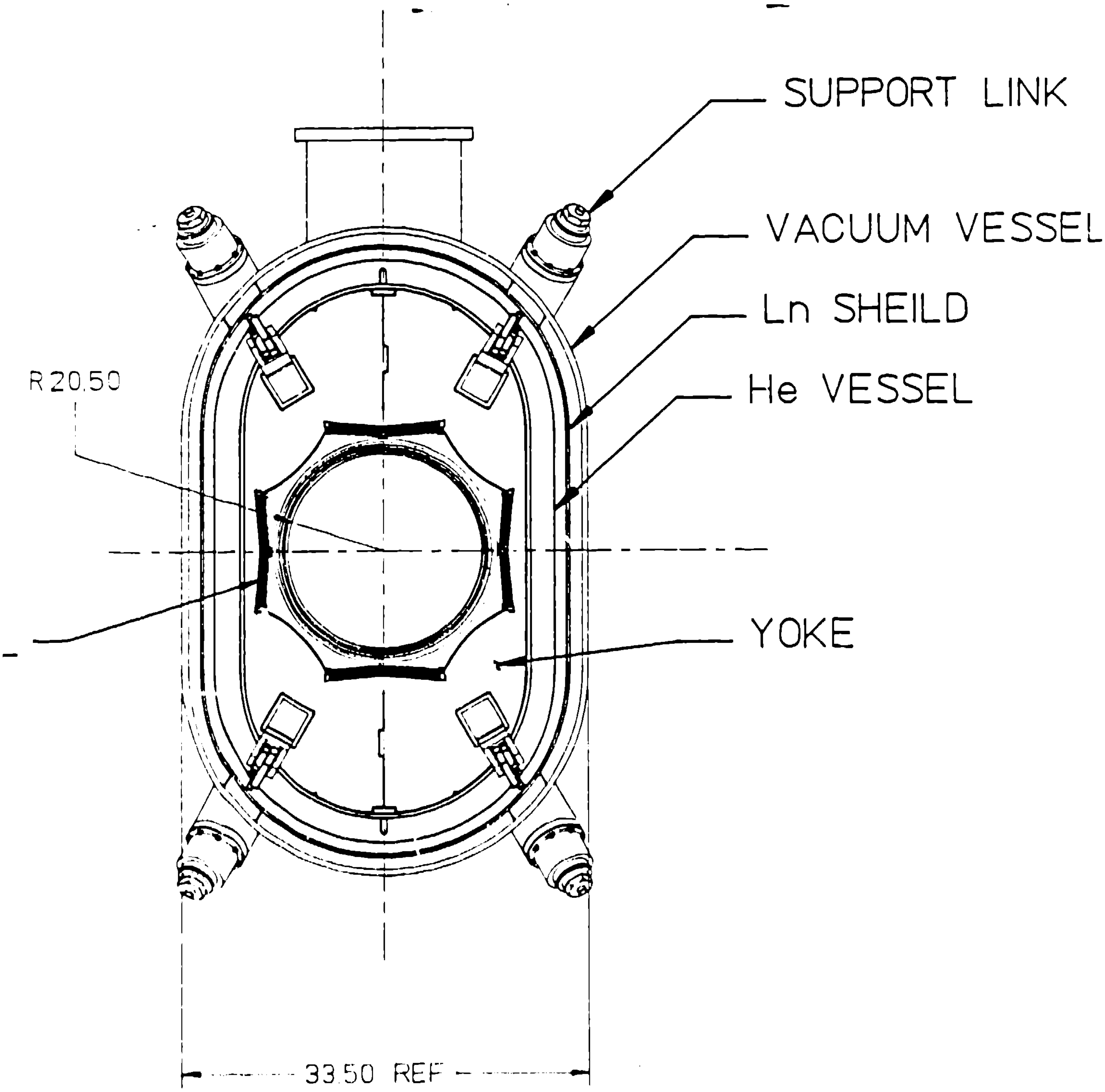

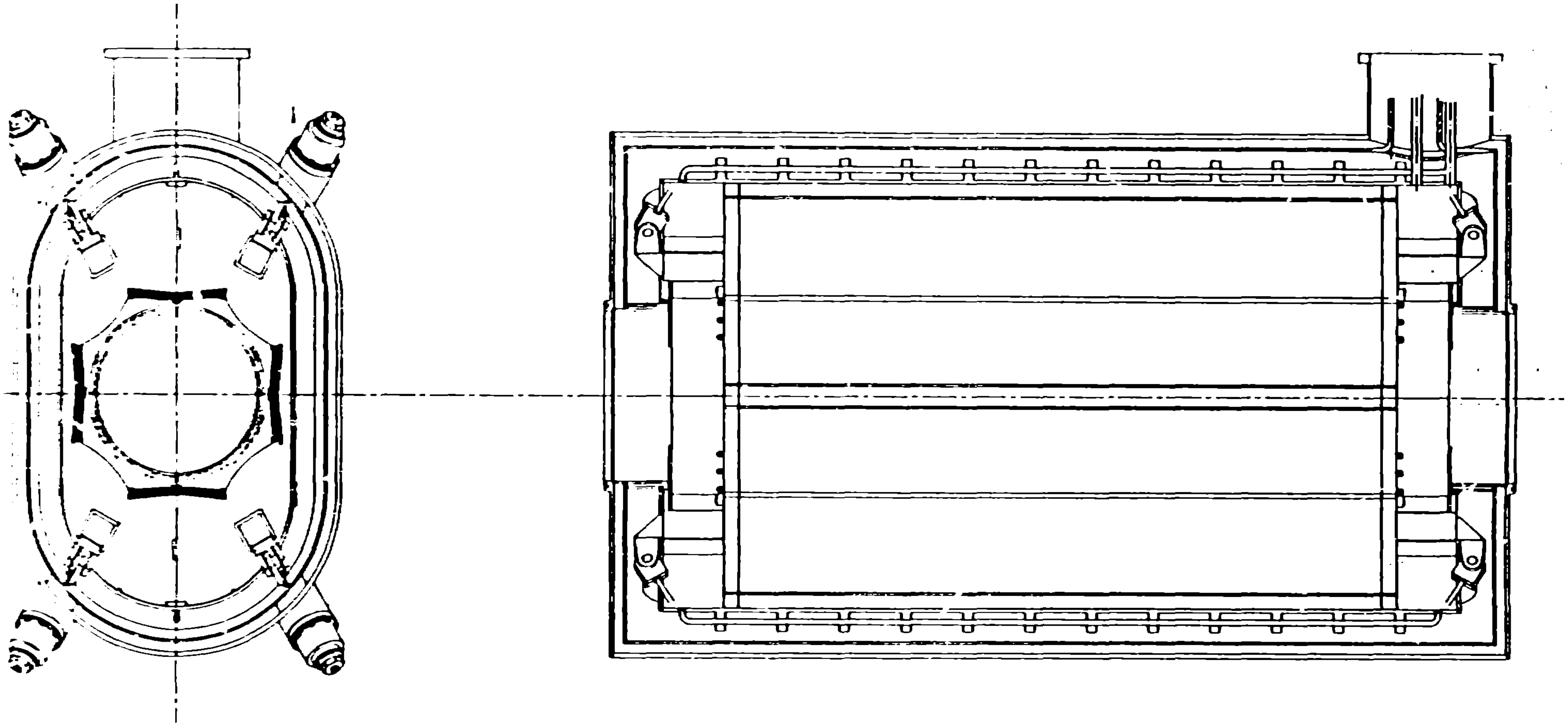

-CENTER TOSCAB
'ug 91 10:09:31 Page 3 : YORG=8

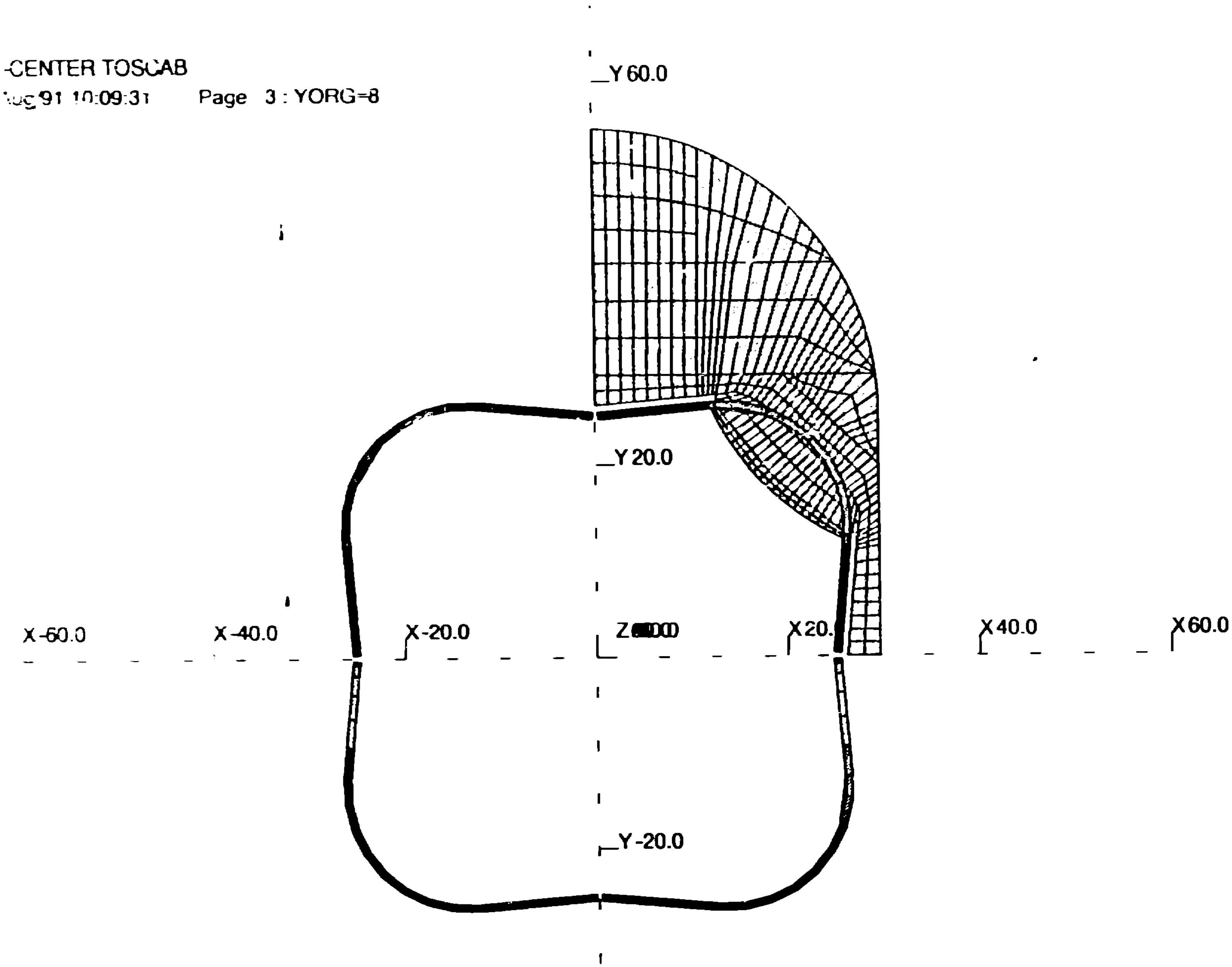

VF/OPERA

Q1-CENTER.TOSCAB

7 Aug/91 10:11:11 Page 4 : XEYE=-100 SIZE=70

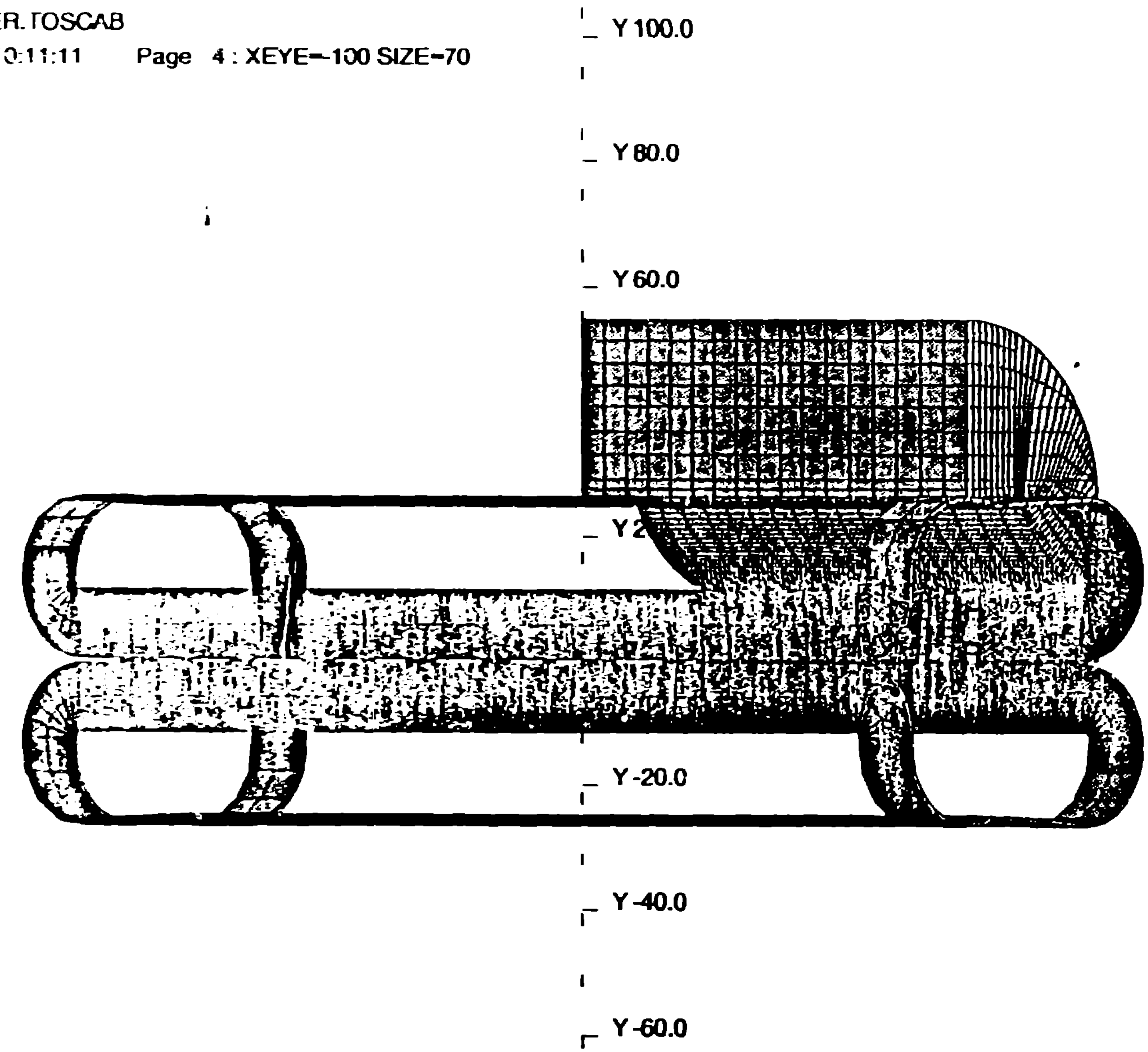

VF/OPEF

Summary of TOSCA/OPERA Analysis for Q1

TOSCA Database File : Q1-V2.TOSCAB

Effective Length = 189.3 cm
Pole Radius = 25.0 cm

Radius of Fourier Analysis = 25.0 cm *
(extrapolated form R=22.0cm)

N	Integral [B(N) dz] (Tesla-meter)	% of Integral [B(2) dz]
2	1.4236	------
4	-5.58E-03	-0.392
6	1.07E-02	0.752
0	-3.02E-03	-0.212
4	-1.70E-02	-1.194

Radius of Fourier Analysis = 22.0 cm

N	Integral [B(N) dz] (Tesla-meter)	% of Integral [B(2) dz]
2	1.2527	------
4	-3.80E-03	-0.303
6	5.64E-03	-0.450
0	-9.55E-04	-0.076
4	-3.22E-03	-0.257

* B(N,25) = B(N,22) * (25./22.)^(N-1)

Q1 CORRECTION COILS

MAIN COILS ONLY NI = 150,000. AT/POLE
Radius of Fourier Analysis = 25.0 cm

N	Integral [B(N) dz] (Tesla-meter)	% of Integral [B(2) dz]
2	1.4236	------
4	-5.58E-03	-0.392
6	1.07E-02	0.752

Q1 WITH N=4 CORRECTION COILS TURNED ON

N	Integral [B(N) dz] (Tesla-meter)	% of Integral [B(2) dz]
2	1.4239	------
4	-5.18E-02	-3.630
6	1.09E-02	0.768

Q1 WITH N=6 CORRECTION COILS TURNED ON

N	Integral [B(N) dz] (Tesla-meter)	% of Integral [B(2) dz]
2	1.4214	------
4	-5.69E-03	-0.401
6	8.05E-02	5.666

Q1 WITH N=4 AND N=6 CORRECTION COILS TURNED ON

N	Integral [B(N) dz] (Tesla-meter)	% of Integral [B(2) dz]
2	1.4220	------
4	-5.18E-02	-3.643
[illegible]	[illegible]	[illegible]

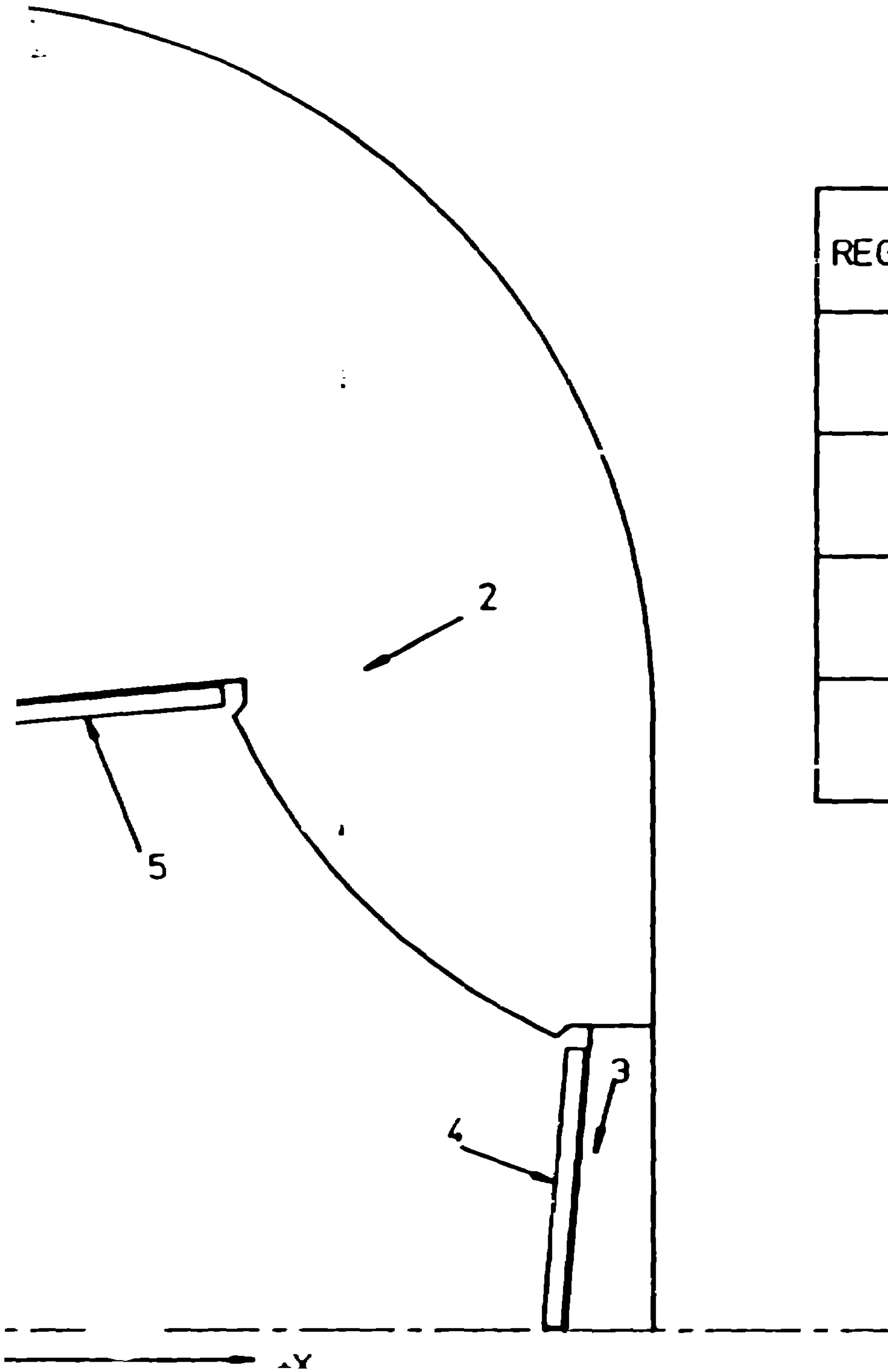

2-D MAGNETOSTATIC FORCES

REGION	F(X) (lbf/in)	F(Y) (lbf/in)	R (in)	Θ (deg)
2	-1581.0	-829.8	-6.360	-152.303
3	-34.7	-129.4	9.585	-105.013
4	621.4	-244.4	5.900	-21.466
5	-251.2	624.6	-5.961	111.911

3-D MAGNETOSTATIC FORCES

REGION	F(X) (lbf/in)	F(Y) (lbf/in)
4	632.83	-262.7
5	-280.8	641.05

3D COIL FORCES

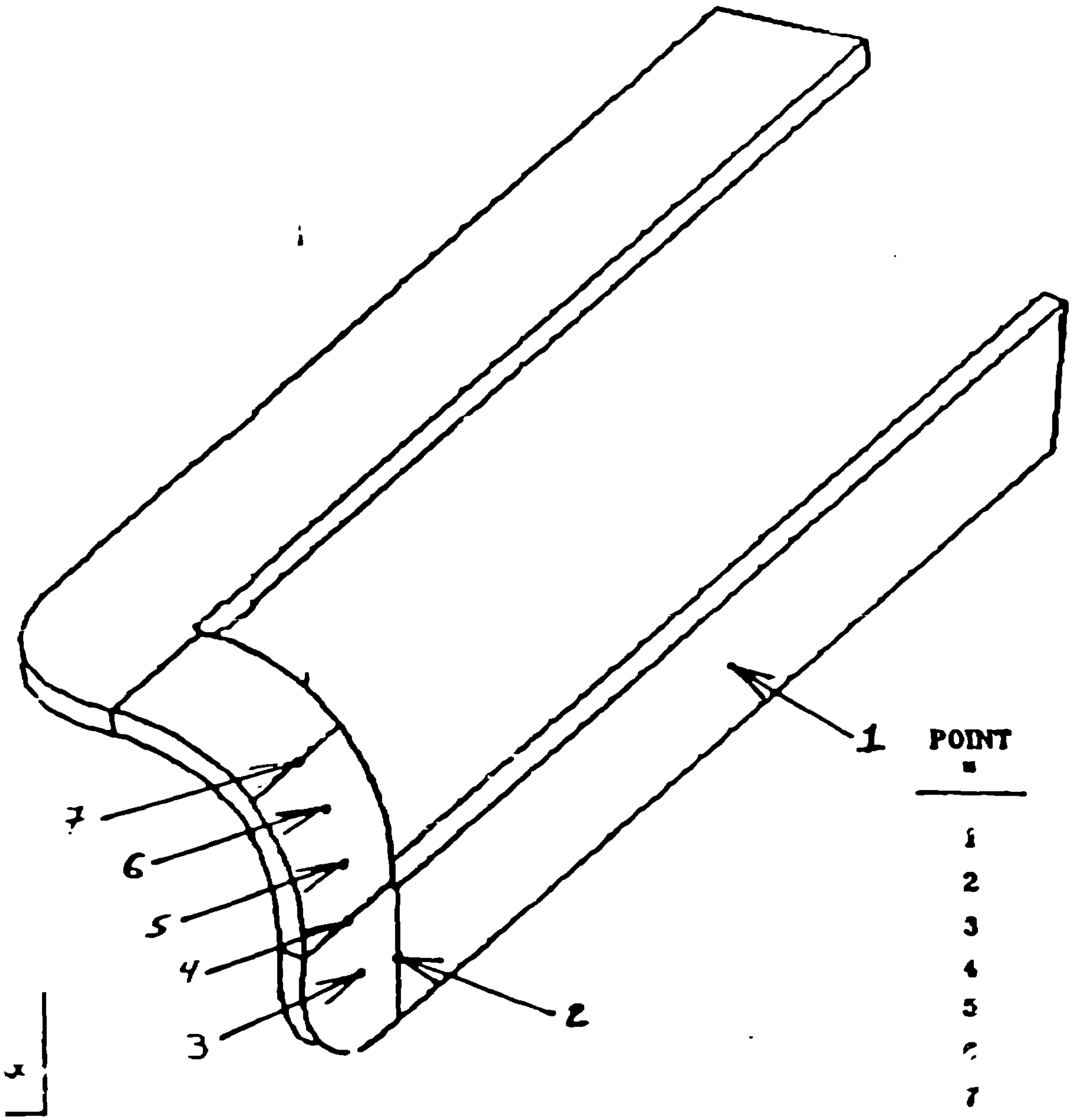

POINT #	FX (lbf)	FY (lbf)	FZ (lbf)
1	22050.0	-9163.2	0.0
2	570.8	-469.2	108.8
3	450.0	-301.7	258.7
4	463.1	-152.6	464.7
5	1041.2	135.6	444.1
6	819.0	518.7	171.9
7	516.0	810.1	169.[illegible]
8	126.2	135.6	444

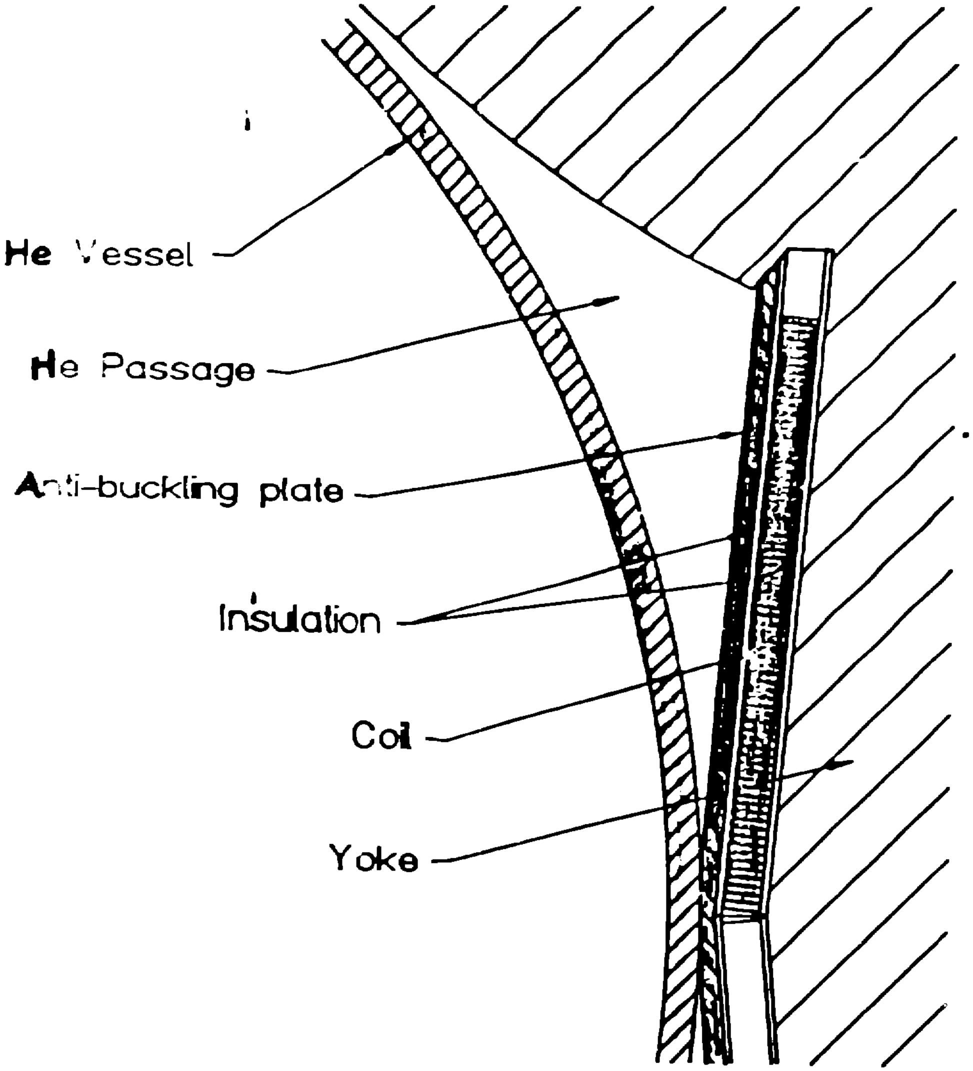

Close up of Q1 coil showing
the helium vessel,
anti-buckling plate, ground
insulation, yoke
and notch in the pole neede
for the anti-buckling plate.

The anti-buckling plate is
needed to support
the coil when the quadrants
are squeezed together.

LARGE APERTURE SUPERCONDUCTING CRYOSTABLE QUADRUPOLES FOR CEBAF'S HIGH MOMENTUM SPECTROMETER

S.R. Lassiter, P.D. Brindza, W.T. Hunter, R.R. Thorpe,
M.J. Fowler, J.A. Miller
Continuous Electron Beam Accelerator Facility
12000 Jefferson Avenue
Newport News, VA 23606

Abstract

The present design for CEBAF'S Hall C High Momentum Spectrometer[1,2] calls for two large aperture quadrupoles, each having the same physical characteristics but operating at different field gradients. A cold-iron, superconducting, laminated yoke magnet has been developed as the reference design. The results of the two and three dimensional magnetostatic studies will be presented here along with some details of the conductor and cryostat design.

Introduction

It is our intention here at CEBAF to purchase from industry, the magnets for the HMS spectrometer based upon magnetic performance specifications. This paper will present a reference design that we believe will meet the specifications listed in Table 1 below.

The design of Q2/Q3 was also constrained by other non-optical requirements such as size and weight of the magnet, cryostability, low current, and low power lead consumption. The magnetostatic analyses were performed for the requirements of the larger gradient Q2 magnet.

TABLE 1. Q2/Q3 Optical Requirements and Magnet Specifications

	Q2	Q3
Leff	= 210 cm	210 cm
Field Gradient	= 445.7 G/cm	194 G/cm
R(pole)	= 35 cm	35 cm
R(good field region)	= 30 cm	30 cm
Field @ Pole	= 1.56 Tesla	.68 Tesla
Dynamic Field range	= 10:1	
Integral Multipole Field errors (percent of quadrupole):		
Dodecapole(at pole)	< 3.0%	< 3.0%
Unknown Multipoles (within aperture)	< 0.3%	< 0.5%
Physical Length	= 3.0 m	
Iron Length	= 1.84 m	
Diameter of yoke	= 1.40 m	
Length/Bore ratio	= 5.5	
Weight of yoke	= 15 tons	

Geometry

The cold iron design of Q2/Q3 is based upon the conformal mapping of a window frame dipole into a quadrupole geometry. This method was used in the reference design of the smaller front end quadrupole Q1 of the HMS.[3] Figure 1 shows a cross section view of the Q2/Q3 quadrupole magnet.

Manuscript received September 24, 1990

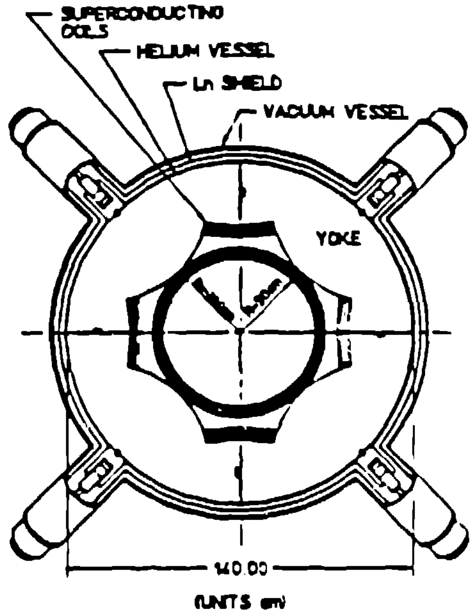

FIGURE 1 CROSS SECTIONAL VIEW OF Q2/Q3 SHOWING INNER AND OUTER CRYOSTAT. POLE RADIUS = 35cm

Yoke Design

Attention was given to the overall size of the yoke and to the field levels within the yoke. The field levels were controlled by sizing the width of the smallest flux path within the yoke to be equal to one half of the flux path length along the pole face for a field level of 1.6 Tesla, as shown in Figure 2. The magnetic properties of the yoke were taken from the internal table of POISSON[4]. This is listed as 1006 iron at 4.2 kelvin.

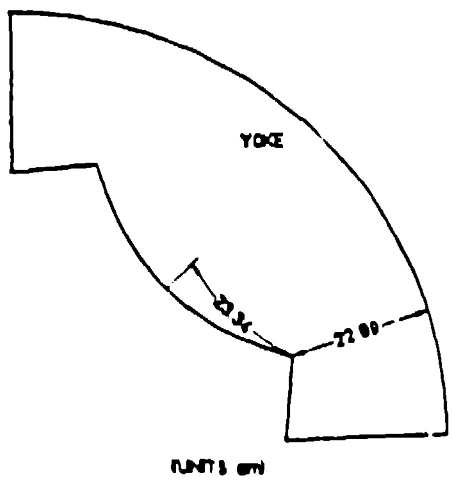

FIGURE 2 1/4 GEOMETRY OF Q2/Q3 SHOWING THE FLUX PATH LENGTH IN THE YOKE AND ALONG THE POLE FACE

We have investigated the process of numerically controlled laser cutting for the yoke/pole laminations as it relates to cost effectiveness and cutting precision. The tolerance control of the pole shape is of prime concern, as the field quality is determined as much by the pole shape as it is by the current distribution. Actual laser cut laminations were made for the Q1 geometry. Figure 3 gives the accuracy of this test fabrication. The machining tolerance of the laminations when modeled in POISSON were well within the magnetostatic specifications.

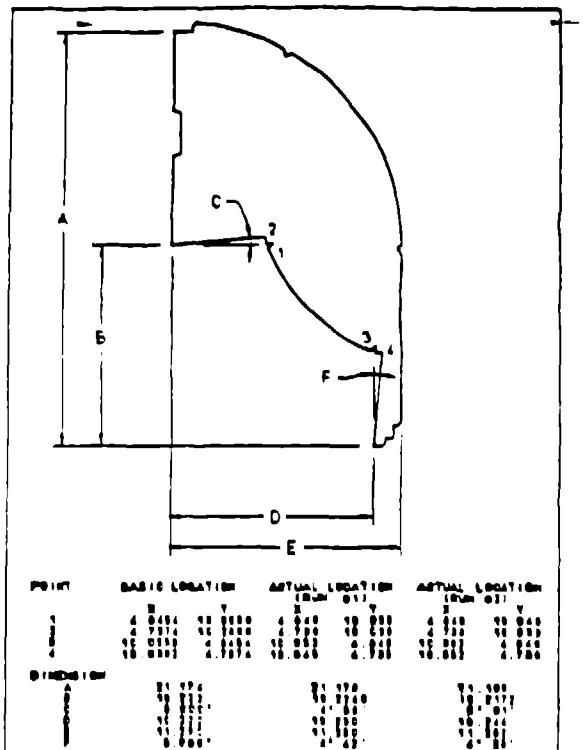

DIMENSIONS ARE IN INCHES

FIGURE 3 Q1 N.C. LASER-CUT LAMINATION TEST

Cryostat Design

The transition from warm to cold occurs over the spatial dimension of 5. cm inside the bore of the magnet. The inner warm bore will be a stainless steel cylinder wrapped in super- insulation to reduce the radiation heat load to the inflated stainless steel liquid nitrogen intercept panel. The helium stainless cylinder will also be wrapped with super insulation to reduce radiation heat loads. The cylinders will share a common vacuum between them to lower thermal conduction.

The magnet will be cooled by means of a natural thermal syphon supplied from a helium reservoir mounted above the magnet. The capacity of the reservoir is sized such that a 3 hour supply of liquid helium will be available in the event of short duration supply interruptions.

The cold iron yoke will be supported within the cryostat by eight constant tension support links that attach from the end of the laminations to standoffs attached to the outer vacuum vessel[1]. The link will be intercepted by a liquid nitrogen thermal shield to reduce heat conduction down the shaft.

Super Conductor Design

The Q2/Q3 quadrupole conductor is a multi-filament, .023 cm diameter, NbTi-copper, 11-strand Rutherford cable. This cable is then extruded into a high purity aluminum stabilizer (99.999 Al.) for cryostability. Figure 4 shows a cross sectional view of the conductor.

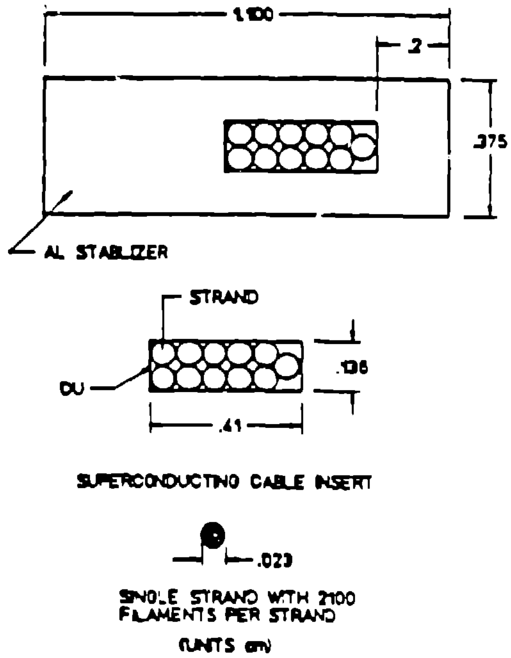

FIGURE 4 CROSS SECTIONAL VIEW OF CONDUCTOR

Table 2. Q2/Q3 cryostable conductor Parameters

Beam energy	= 6.0 Gev
NI/pole	= 217310 Amp Turns
# Turns/pole	= 71
Turn Length	= 465 cm
I/turn	= 3.061 KAmps
Ic/turn	= 4.62 KAmps
Al/Cu/NbTi	= 6.4/1.8/1
Stekly #	= .45
Stored Energy	= .31 MJ/m (Q2 at 1.56 Tesla)
Power Lead Consumption	= 9.1 L of helium/hour

For the Stekly calculation, no credit was taken for the copper present in the strands.

As increases in the beam energy for CEBAF look promising, the cryostability of the magnet is preserved up to the operating current of 4.6 KAmps, corresponding to a beam energy of 7.5 GeV/c.

Two Dimensional Quadrupole Field Calculations

The initial magnetostatic solutions were performed using the code POISSON to gain an understanding of the sensitivity of the 2-dimensional problem to coil and iron geometries. The need to allow for adequate helium flow passage channels in and around the coil stacks was used as a constraining parameter in minimizing the unwanted multipoles.

Three stacks of conductor were used to achieve the desired amp turns and lower the operating current. Gaps along the median plane for each coil stack were constrained to be equal in an attempt to reduce the number of individual parameters that could effect field quality. The heights of each coil stack were individually sized to reduce field errors. This results in an unequal number of turns per coil stack as well as the need for an additional spacer in the first two stacks. The turn to turn insulation consists of 2.2 mm thick G-10 spacers sized such that adequate helium flow would result as well as maximizing the current density. The spacing between the stacks of conductor was sized such that the width of the coils stacks would be kept to a minimum yet provided for sufficient helium flow along the stack heights. The superconducting cable is offset within the aluminum stabilizer as an aid in reducing the unwanted harmonics. The spacing between the coil stack and the iron yoke was also used to achieve a better field quality.

The current carrying portions of the conductor were modeled as uniform stacks in all of the magnetostatic analysis. Figure 5 shows the approximation to the current carrying portions of the conductor that were modeled in the magnetostatic problems.

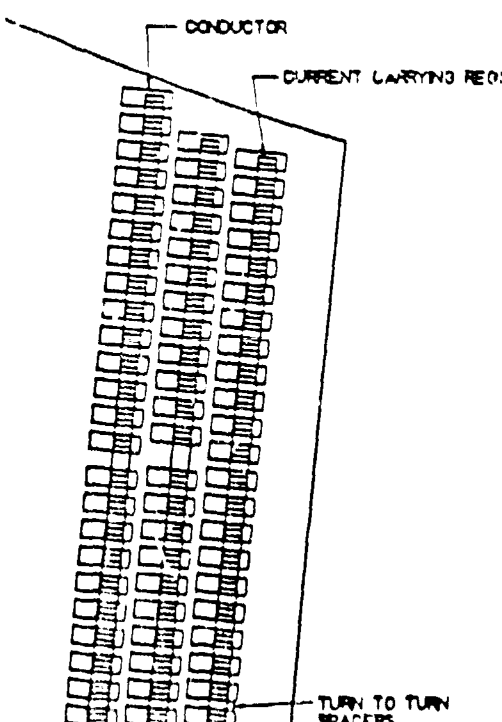

FIGURE 5 CURRENT CARRYING REGIONS AS MODELED IN POISSON AND TOSCA

Table 3 lists the coefficients of the field multipoles at a radius of 35 cm and a beam energy of 6.0 GeV/c.

Table 3. Poisson Harmonic Analysis

N	B(N)	B(N)/B(2) %
2	1.5540E+04	1.0000
6	6.8937E+00	0.0444
10	-1.0264E+01	-0.0776
14	-2.0747E+01	-0.1335

2 × N = multipole
Field is given by $B = \mathrm{Sum}\,[B(N)*(r/Rp)^{(N-1)}]$

The field within the iron yoke was 1.45 Tesla along the median axis and 1.6 Tesla at the pole. Flux leakage outside the iron was 6.5 Gauss next to the yoke and drops to 4.8 Gauss 30 cm away at the boundary. Figure 6 shows the 2-dimensional solution for one-eight of the geometry from POISSON.

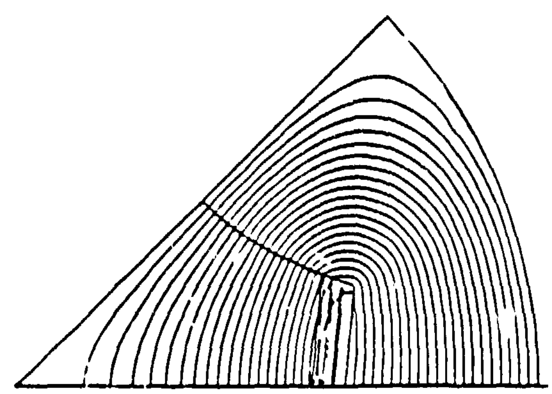

FIGURE 6. FIELD LINES AND GEOMETRY FROM POISSON

3-Dimensional Quadrupole Field Calculations

The three dimensional solution was done with the code TOSCA[6]. The effects of the shape of the end coil geometry and pole saturation were looked at since it is the integral multipole content that we must satisfy. As a starting point the magnet was modeled with no shaping of the poles at the end or use of field clamps to contain the field fall off. A well defined mesh was set up in the x,y plane using quadratic elements to obtain reasonable fits to the vector potential within the aperture of the magnet. This mesh was then extruded out along the z-axis with emphasis placed near the end of the magnet yoke and the region where the coils reside.

The post-processor OPERA[7] and the program EXTRACT[8] were used to analysis the integral multipole content of the magnet. The coefficients of a fourier fit to the total potential were integrated along the magnetic axis as a function of the radius The analytic derivative of the potential was then taken to derive the coefficients for the magnetic fields. Figure 7 shows the field fall off along the magnetic axis for a radius of 30 cm. Table 4 list the results of the three dimensional study.

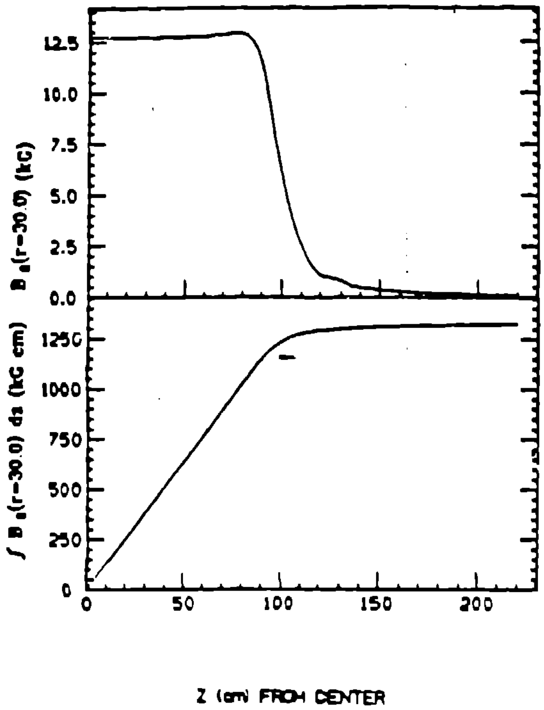

FIGURE 7. FIELD FALL OFF AND INTEGRAL OF QUADRUPOLE TERM

Table 4 Tosca Results and Parameters

ìective Length = 210 cm

N)	Integral (B(N) dz)	% of N=2
ır R=35 cm (Pole Radius)		
2)	1.545 Tesla-m	
6)	5.62E-03 Tesla-m	0.364
10)	9.66E-03 Tesla-m	0.625
14)	1.05E-02 Tesla-m	0.682
·r R=30 cm (Aperture Radius)		
2)	1.325 Tesla-m	
6)	2.77E-03 Tesla-m	0.209
10)	2.21E-03 Tesla-m	0.167
14)	9.23E-04 Tesla-m	0.070

The sum of the unknown multipoles (-ie- N=10 and 14) the aperture of the magnetic is .237% of the quadrupole d the dodecapole is only .364% of the quadrupole at the le. Studies will continue to investigate the effects of pole amfering, field clamps and coil end geometries in regards to eir contribution to the integral content.

Conclusion

A reference design has been modeled for the large aperture perconducting quadrupoles that meets the optical require-ents of the High Momentum Spectrometer. It is our aim to mplete the design work to allow a Request for Proposals to out by December 1990.

References

1. Conceptual Design Report Basic Experimental Equipment - Hall C. April 13, 1990.
2. P.D. Brindza et al., "CEBAF Superconducting Spectrometer Design", *IEEE Transaction on Magnets*, Mag-25, 1897, 1989.
3. L.H. Harwood, et al., "A Superconducting Iron-Dominated Quadrupole for CEBAF", *IEEE Transaction on Magnets*, Mag-25, 1910, 1989.
4. POISSON MANUAL
5. J.A. Miller, et al., "Cryostat Design And Magnetostatic Analysis of the 6 Gev Superconducting Dipole for the High Momentum Spectrometer", *Submitted to IEEE Transaction on Magnets.*
6. TOSCA, *Vectra Fields Limited*
7. OPERA, *Vectra Fields Limited*
8. J. Napolitano et al., "Calculations of Higher Multipole Components in a Large Superconducting Quadrupole Magnet", *Submitted to Nuclear Instruments and Methods.*

TOSCA CALCULATIONS FOR PILAC

Presentation not made.

MEASUREMENTS OF EPICS QUADRUPOLES

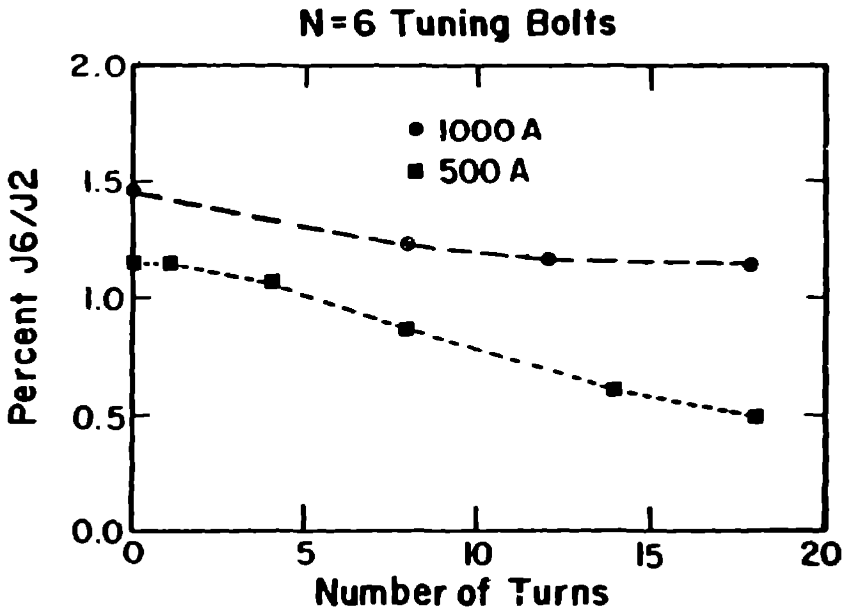
N=6 Tuning Bolts
1000 A
500 A
Percent J6/J2
2.0
1.5
1.0
0.5
0.0
0
5
10
15
20
Number of Turns

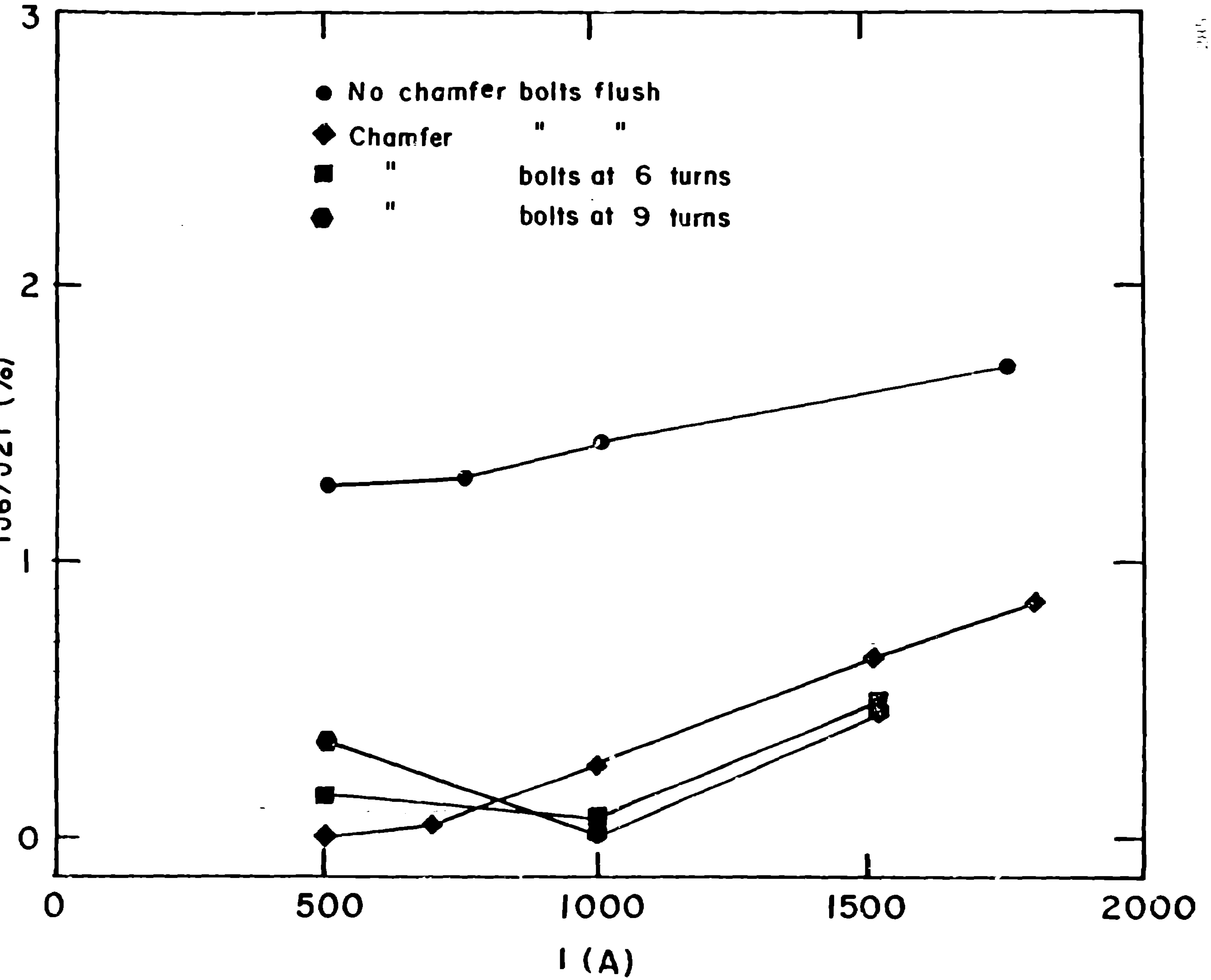

No chamfer bolts flush
Chamfer " "
" bolts at 6 turns
" bolts at 9 turns
IJ6/J21 (%)
I (A)
0
1
2
3
500
1000
1500
2000

$$\nabla^2 V = \left(\frac{\partial^2}{\partial r^2} + \frac{1}{r}\frac{\partial}{\partial r} + \frac{1}{r^2}\frac{\partial^2}{\partial \phi^2} + \frac{\partial^2}{\partial z^2} \right) V = 0$$ cylindrical laplacian

$$V = \sum_{n=0}^{\infty} \left(V_{n,1} \sin n\phi + V_{n,2} \cos n\phi \right)$$ fourier expansion

... equations

$$\left(\frac{\partial^2}{\partial r^2} + \frac{1}{r}\frac{\partial}{\partial r} - \frac{n^2}{r^2} + \frac{\partial^2}{\partial z^2} \right) V_n = 0$$ separate for $V_{n,1}$ + $V_{n,2}$

Fourier transform in z

$$\left(\frac{\partial^2}{\partial r^2} + \frac{1}{r}\frac{\partial}{\partial r} - \frac{n^2}{r^2} + p^2 \right) V_n = 0$$

$$v_n(r,p) = J_n(rp) \cdot f_n(p)$$ no second kind solution

$$J_n(x) = \frac{(x/2)^n}{n!} \Lambda_n(x)$$ Jahnke, Emde

$$\Lambda_n(x) = \sum_{k=0}^{\infty} \frac{n!}{(n+k)!} \frac{(-x^2/4)^k}{k!}$$

$x = r p$

$$v_n(r,p) = r^n \Lambda_n(rp) \cdot a_n(p)$$

inverse transform

$$V_n(r,z) = r^n \Lambda'\left(r \frac{\partial}{\partial z}\right) \cdot a_n(z)$$

Special cases

10/31/74 Quadrupole mapper allignment procedures

1) set axis of rotation parallel to z-axis

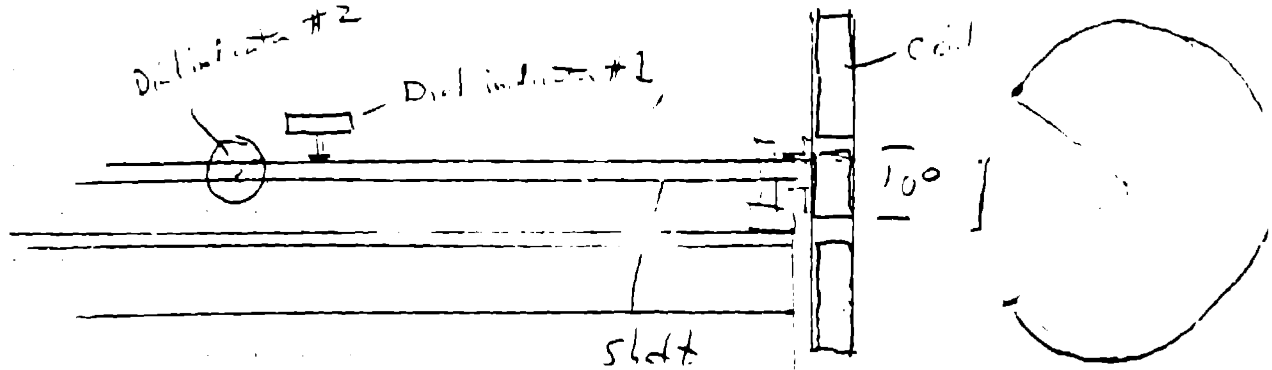

Fix dial indicator to mapper stand so that they measure x and y displacement of the shaft. Take readings, rotate shaft by 180° and read again. (do this as a function of z.) The center of rotation is given by the average of the two readings. (assuming the shaft is round and the diameter is constant)

2) Align z-axis parallel to quadrupole center

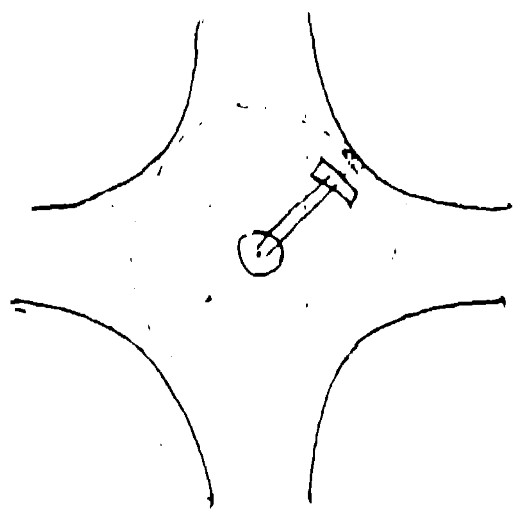

Coil resistances

Mixed { Mix $2.83610\ k\Omega$

120° $1.10330\ k\Omega$

Pot set at .4600

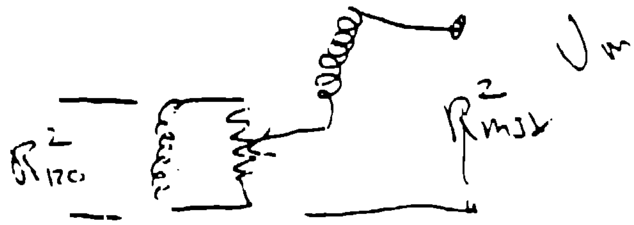

$R^2_{120} = 1.1403\ k\Omega - .0499$

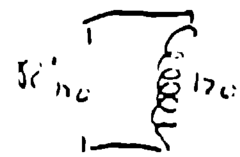

$R^2_{mix} = 2.8759 \quad - .0499$

$R'_{10} = 197.9 - .0499$

38563

$R'_{120} = 1.2745 - .0499$

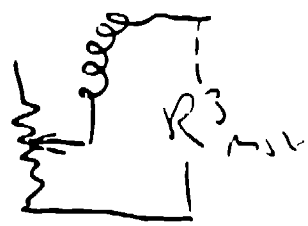

$R^3_{mix} = 4.6405 - .0499$

$R^3_{pot} = 10.0095 - .0499$

Just Pulse transform .0966

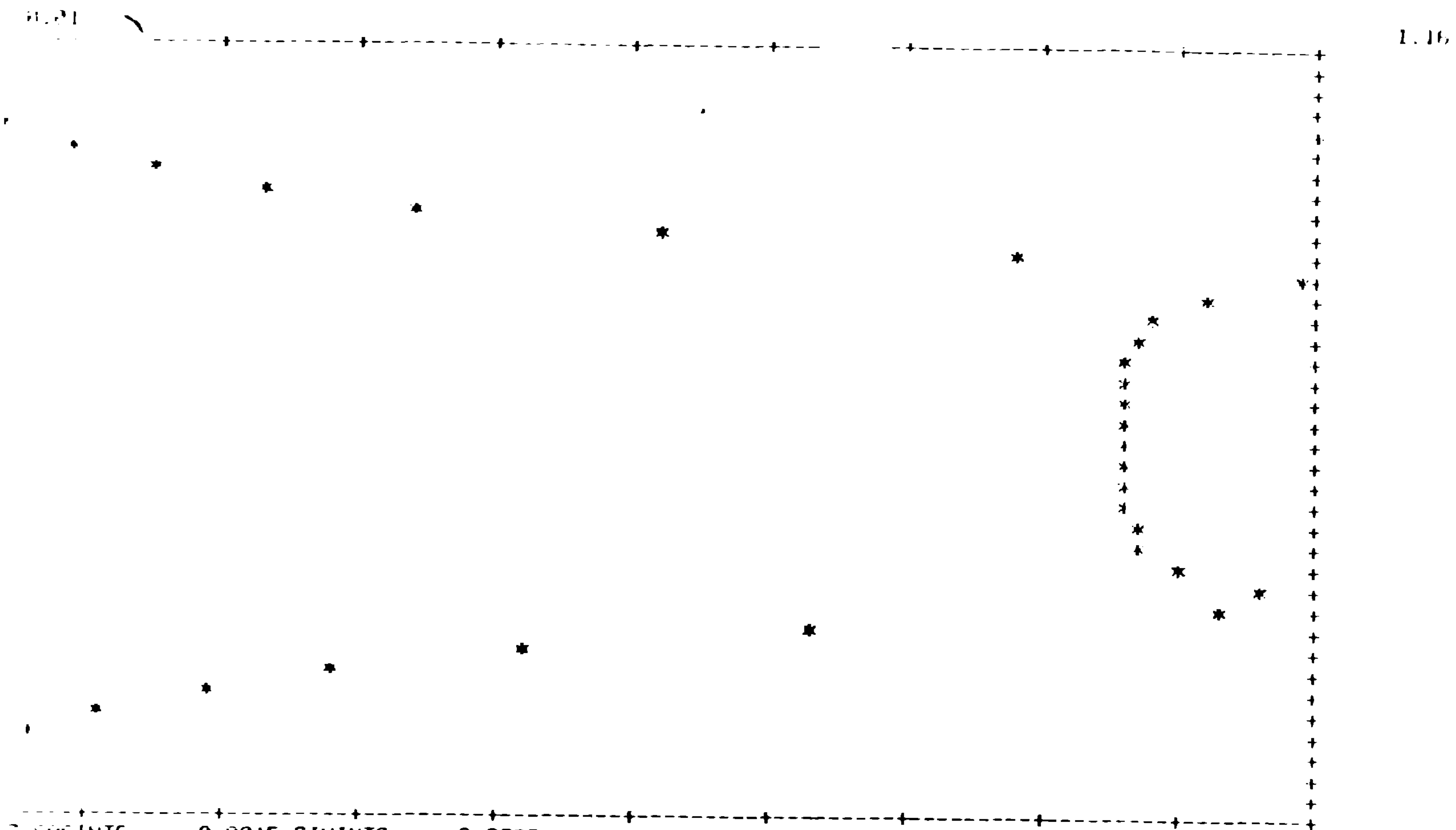

3 COSINTG= -0.0015 SININTG= 0.0008

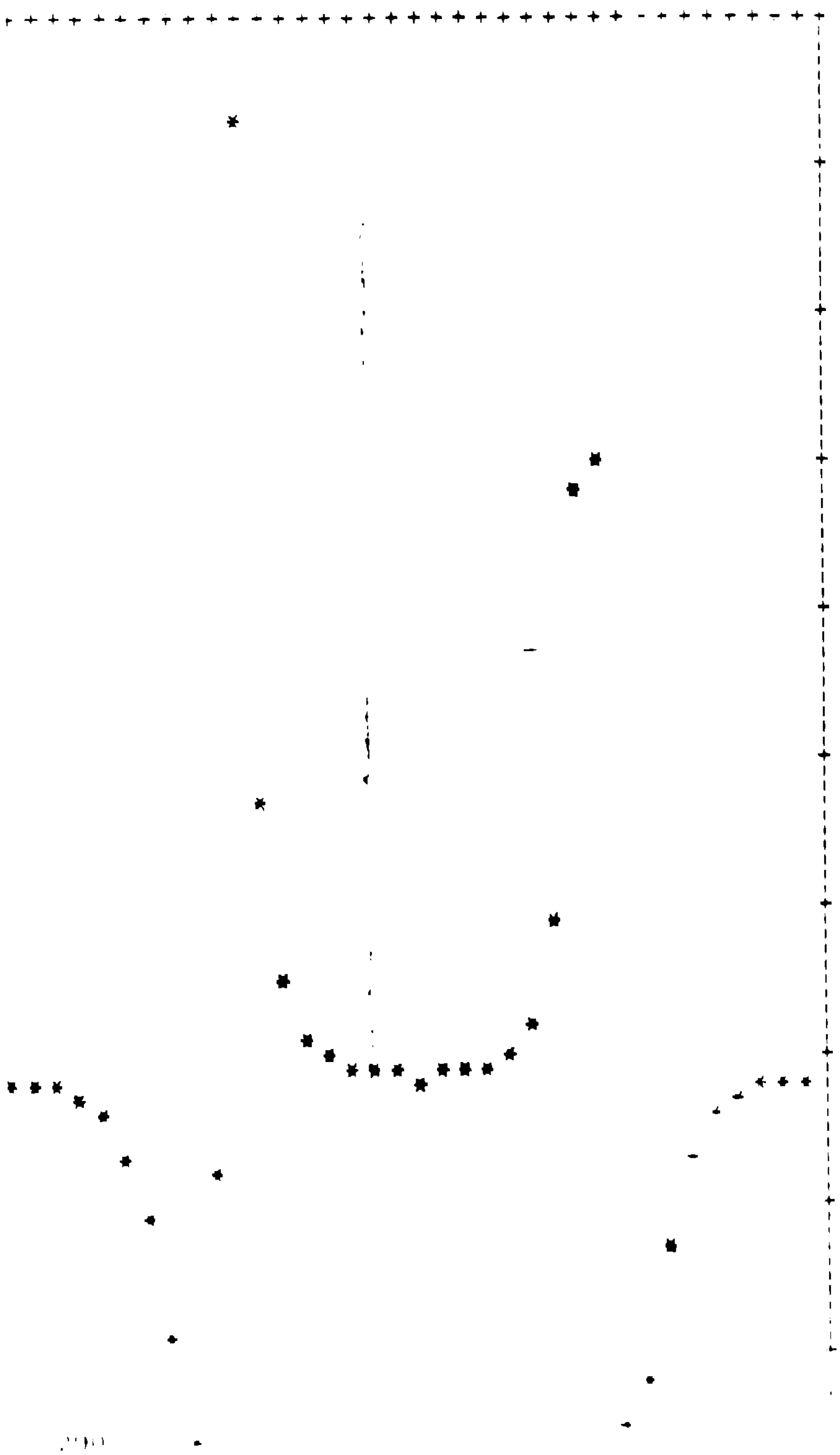

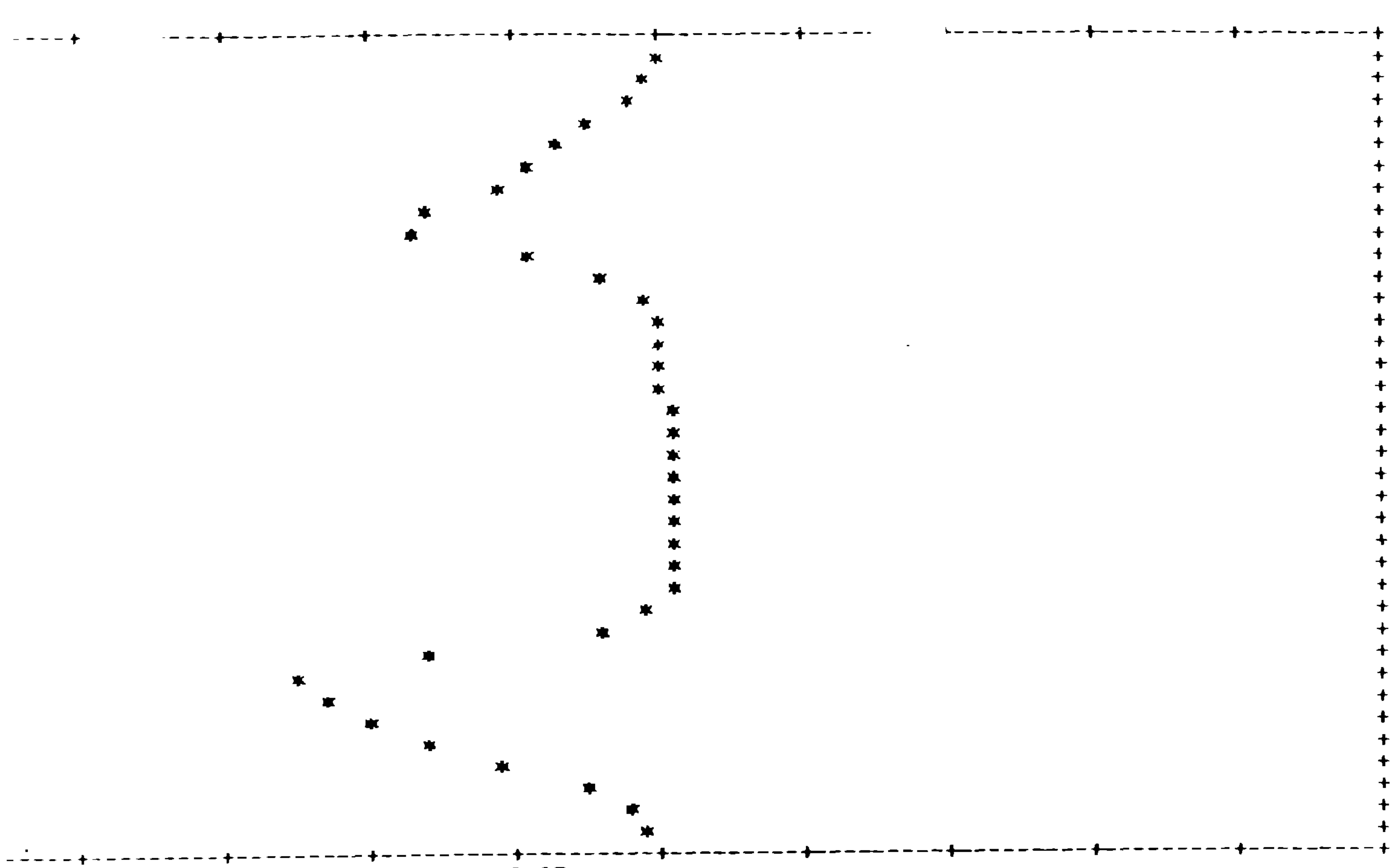

5 COSINTG=   0.0637 SININTG=   0.0027

QUADRUPOLE MEASUREMENTS AND ANALYSIS

12-Aug-1991

Measurements of Quadrupoles for The Bates SHR.

John Zumbro

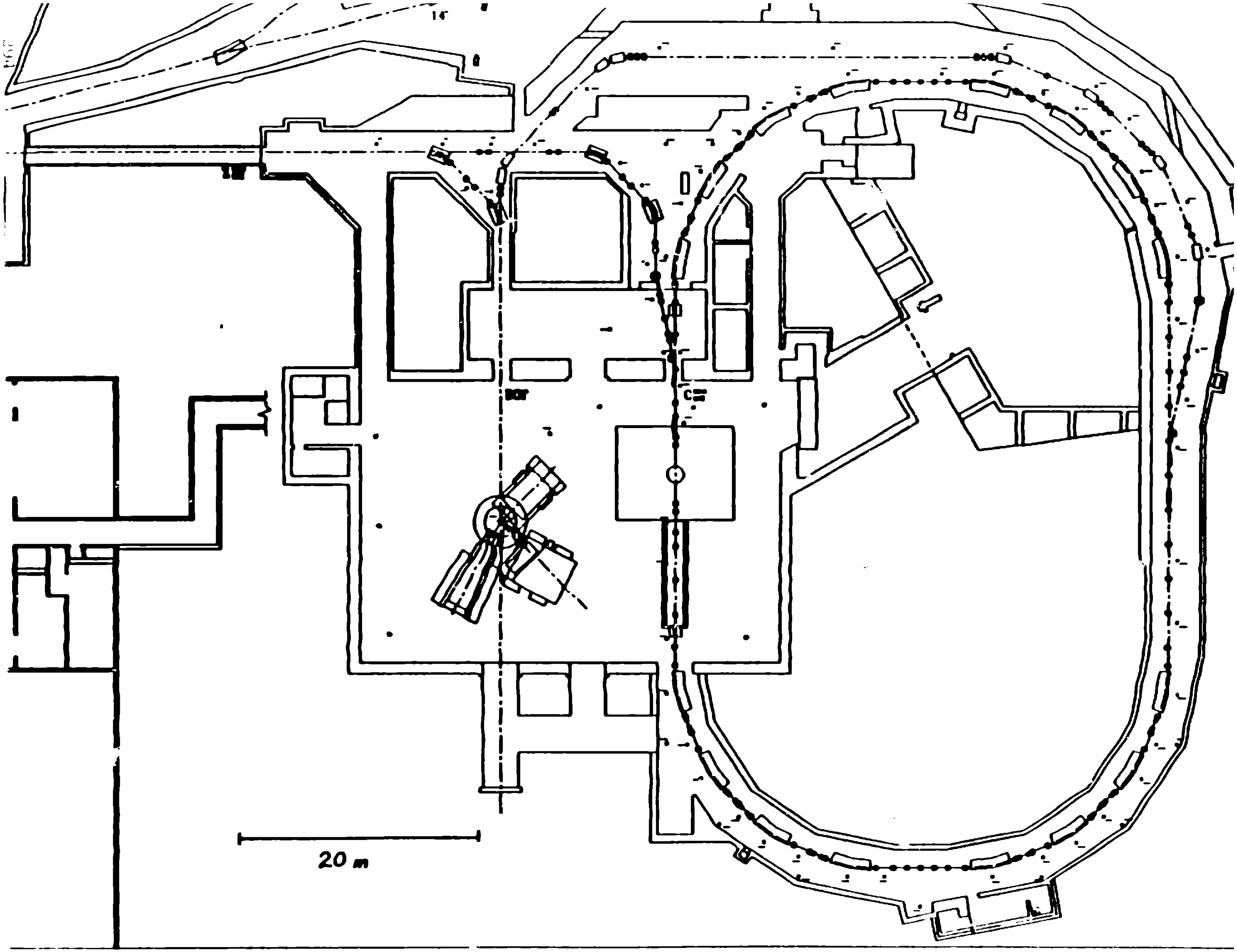
20 m

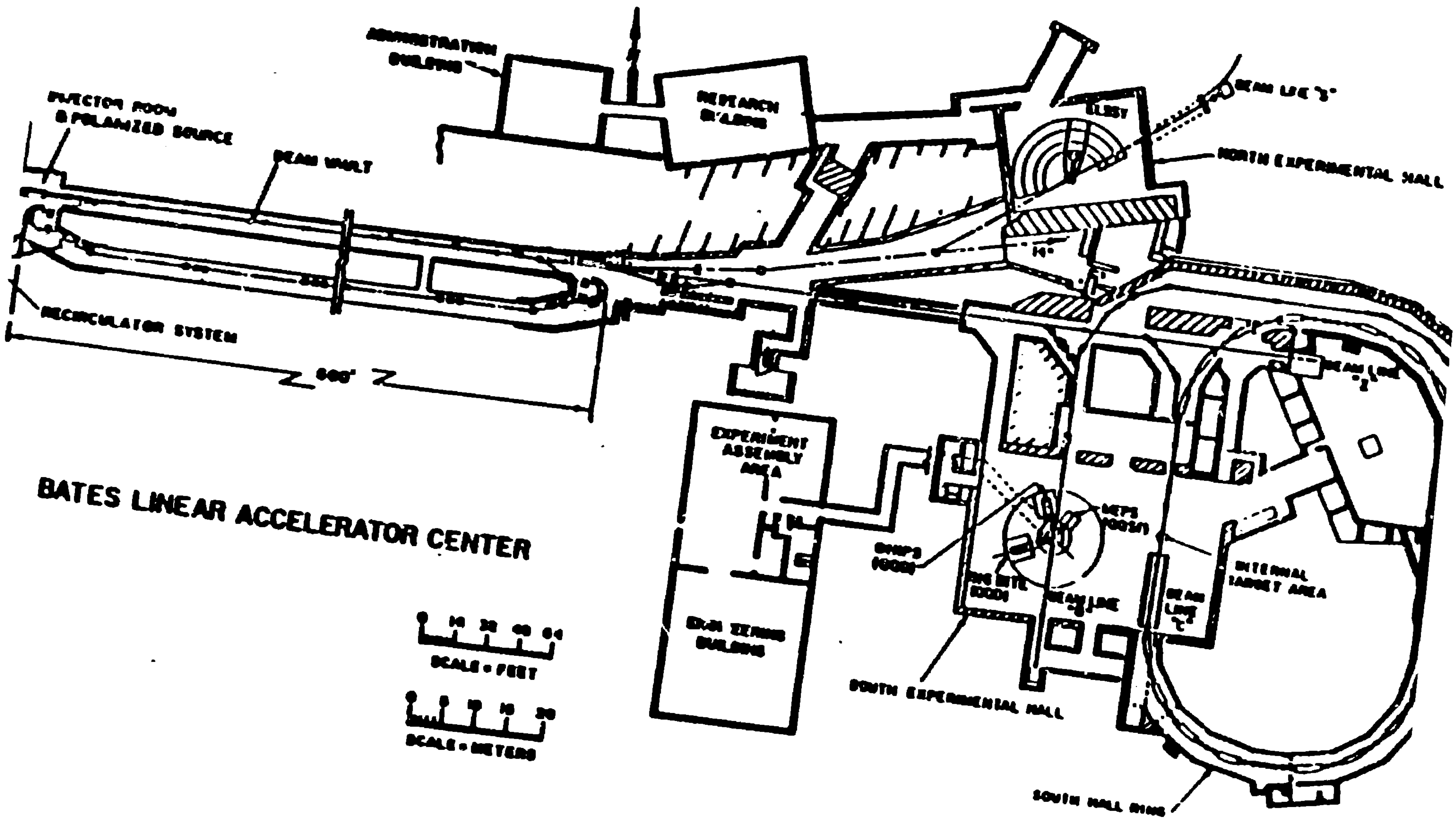

BATES LINEAR ACCELERATOR CENTER

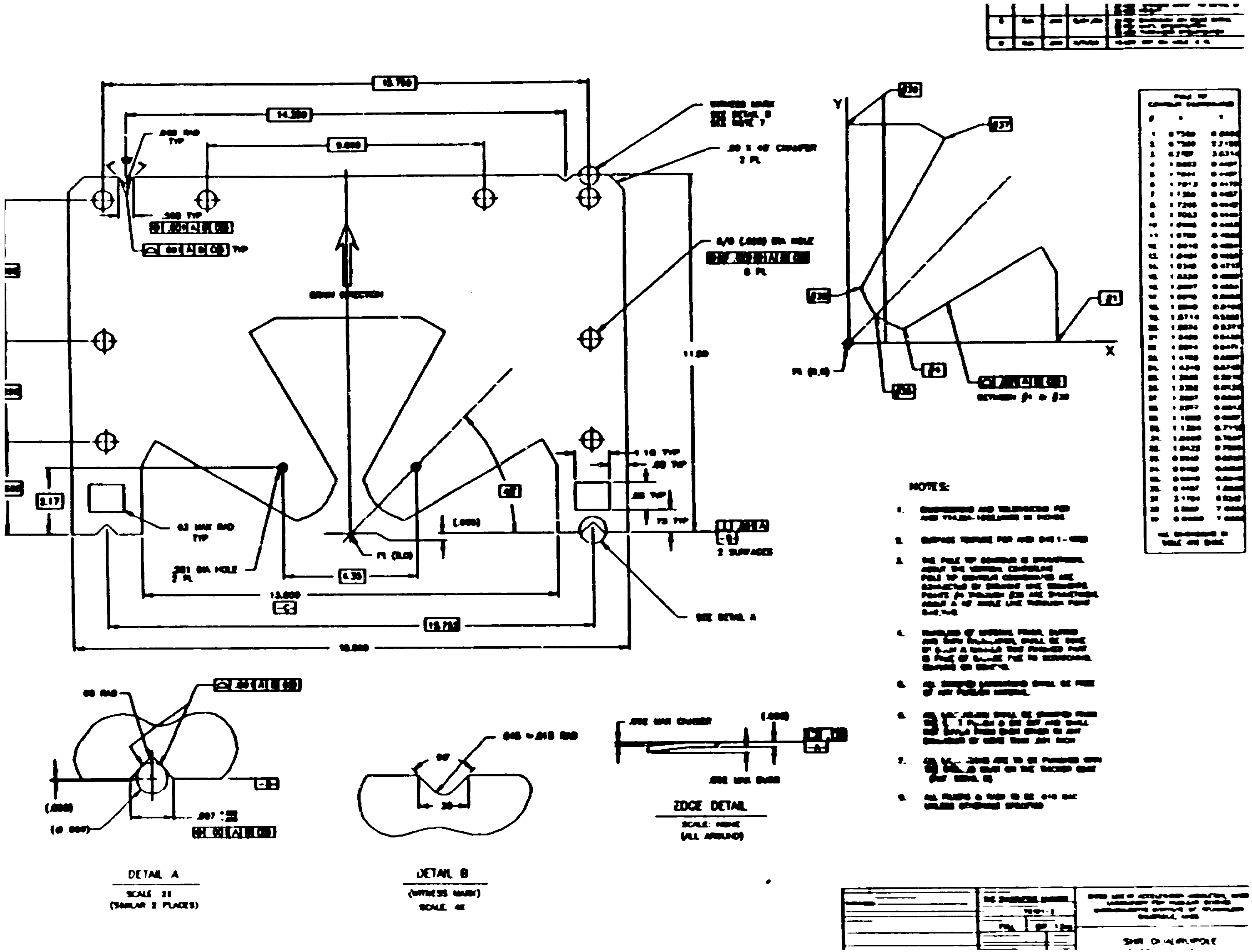

14.300
9.000
11.50
3.17
4.35
13.000
15.750
16.000
X
Y
SEE DETAIL A
2 SURFACES
NOTES:
EDGE DETAIL
SCALE: NONE
(ALL AROUND)
DETAIL A
SCALE 2X
(SIMILAR 2 PLACES)
DETAIL B
(WITNESS MARK)
SCALE 4X

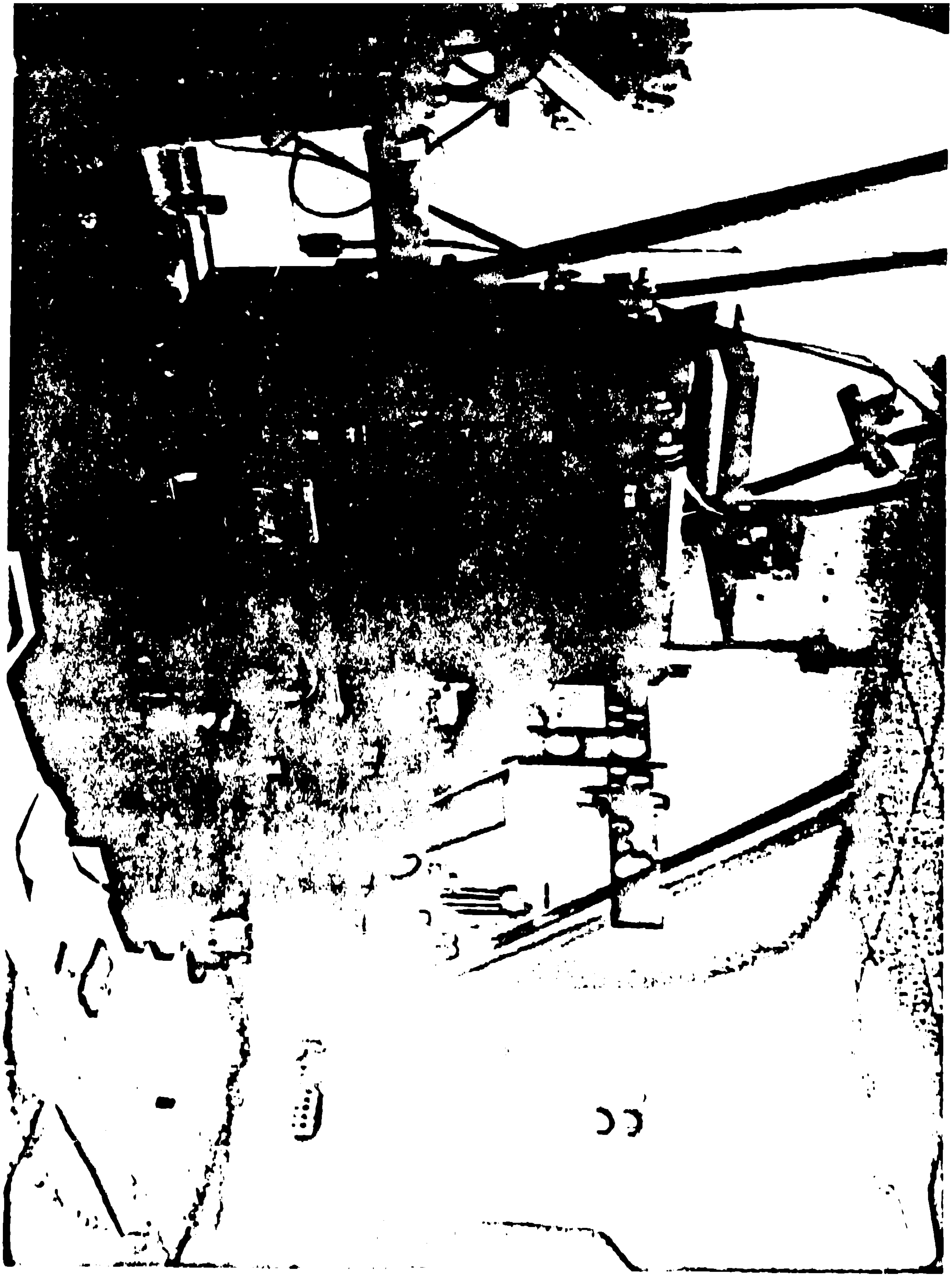

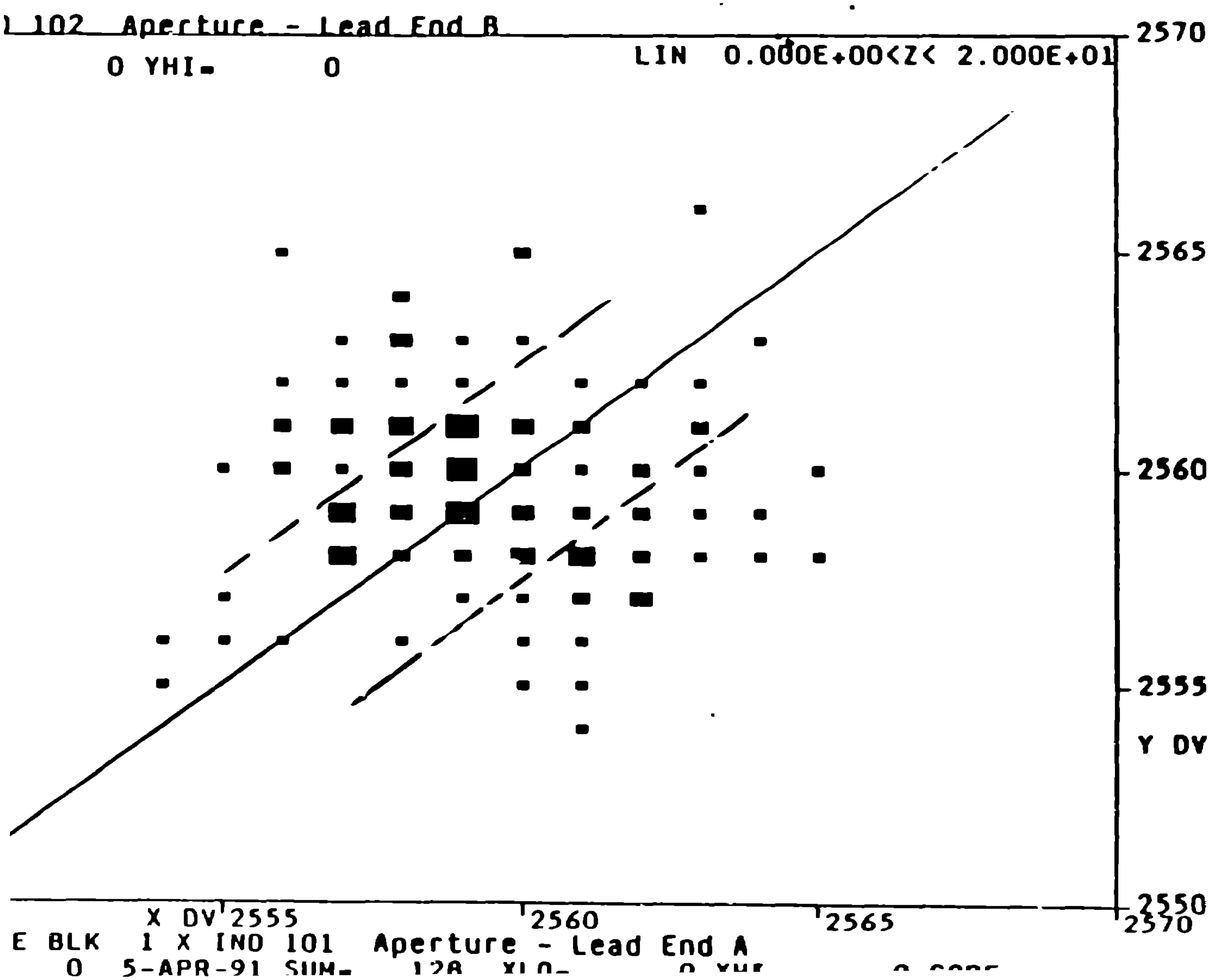
1 102 Aperture - Lead End B
0 YHI= 0
LIN 0.000E+00<Z< 2.000E+01
2570
2565
2560
2555
Y DV
2550
2570
X DV 2555
2560
2565
E BLK 1 X IND 101 Aperture - Lead End A
0 5-APR-91 SUM= 128 XLO=

FIG. 2b

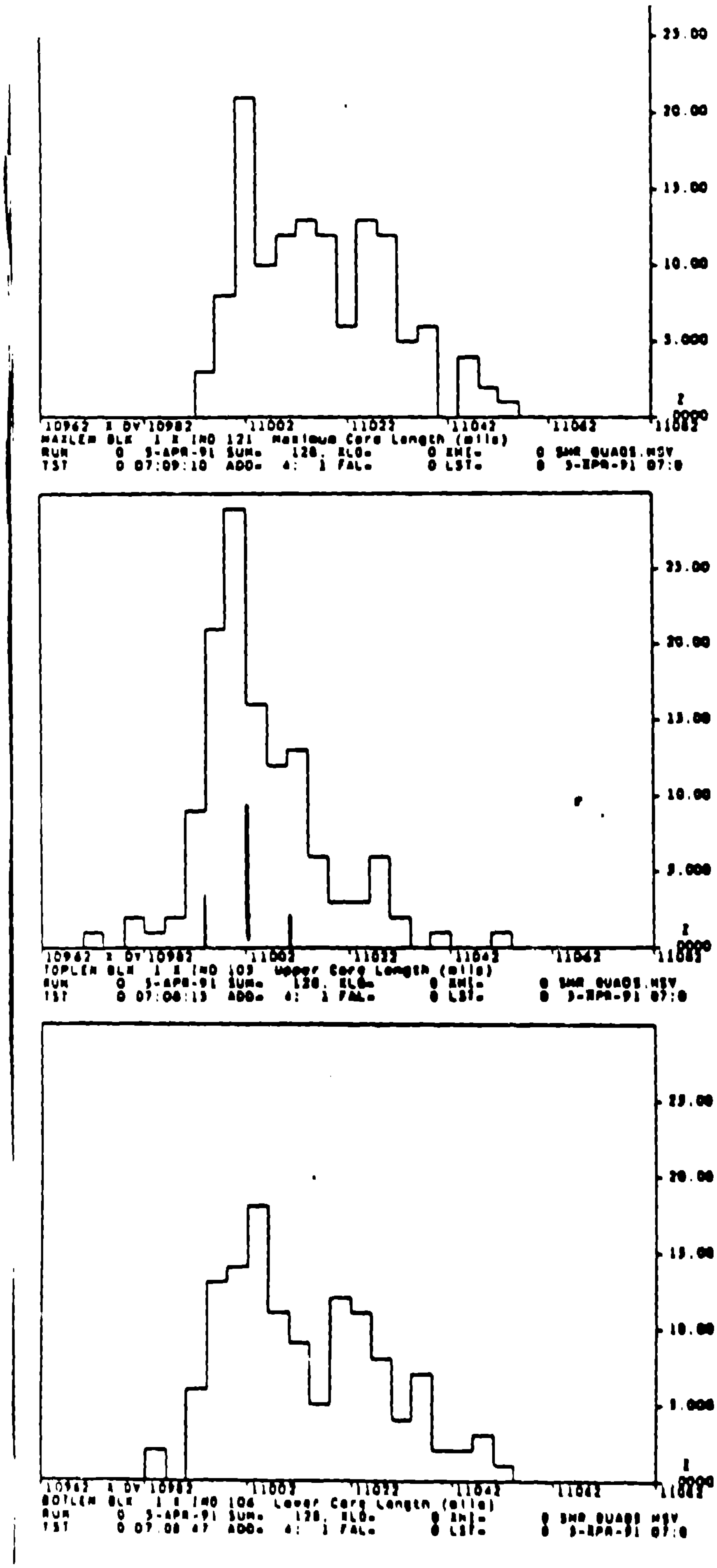
25.00
20.00
15.00
10.00
5.000
10962
10982
11002
11022
11042
11062
11082

FIG. 1

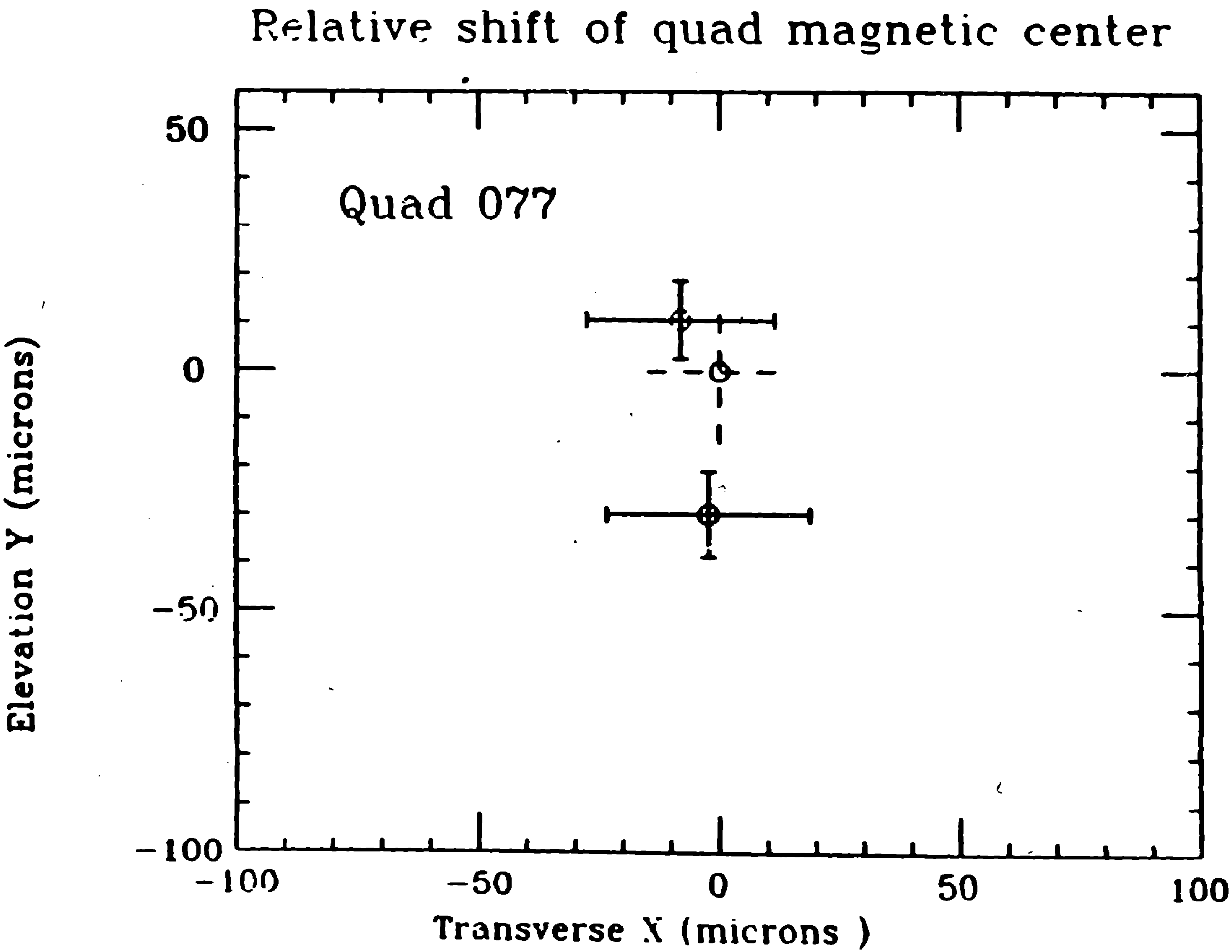

Relative shift of quad magnetic center
Quad 077
Elevation Y (microns)
Transverse X (microns)
50
0
−50
−100
−100
−50
0
50
100

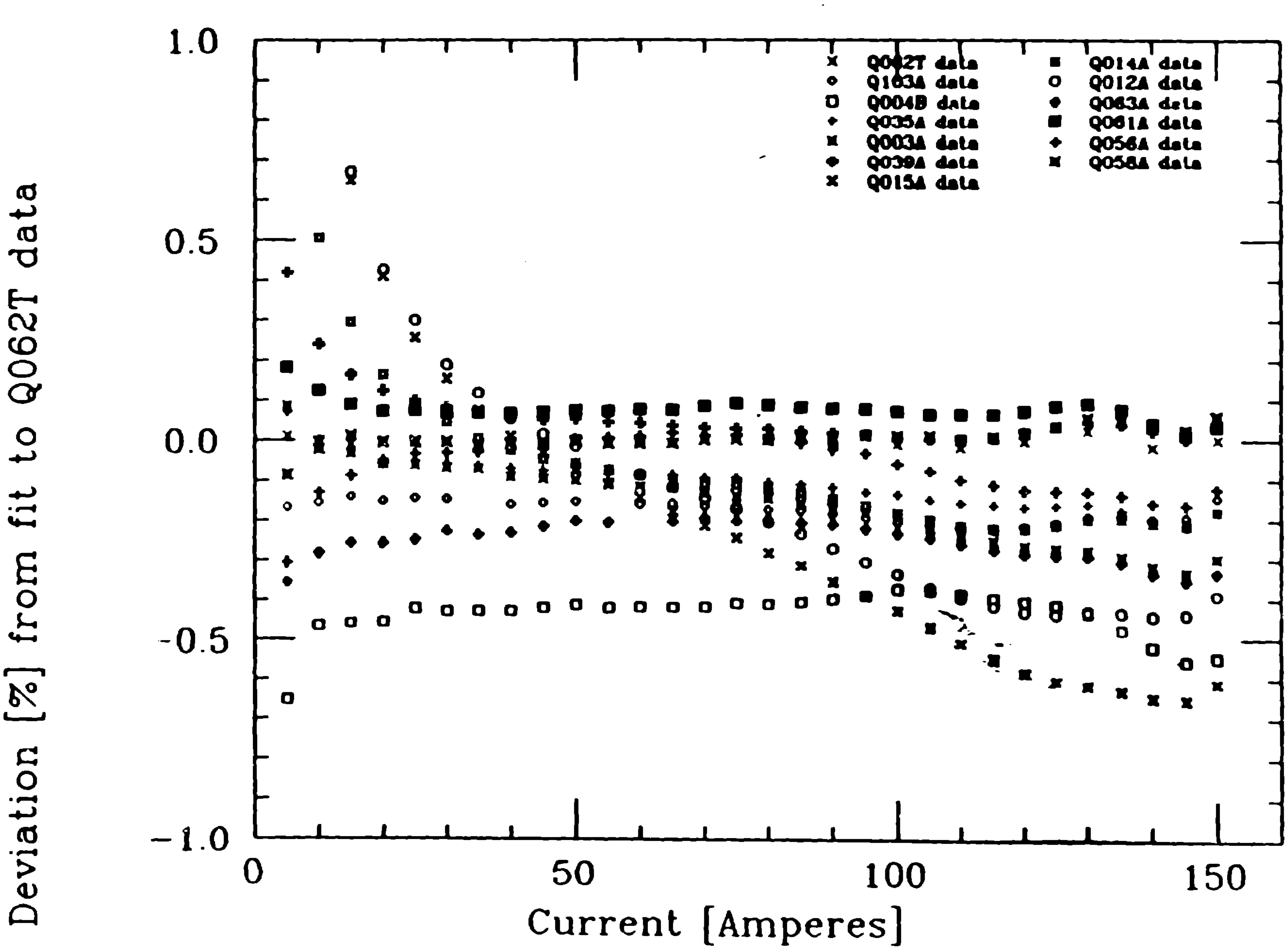
Q062T data
Q103A data
Q004B data
Q035A data
Q003A data
Q039A data
Q015A data
Q014A data
Q012A data
Q063A data
Q061A data
Q056A data
Q058A data
1.0
0.5
0.0
-0.5
-1.0
0
50
100
150
Deviation [%] from fit to Q062T data
Current [Amperes]

FIC

YLO= 0 YHI= 0 TH= 30 PHI= 45

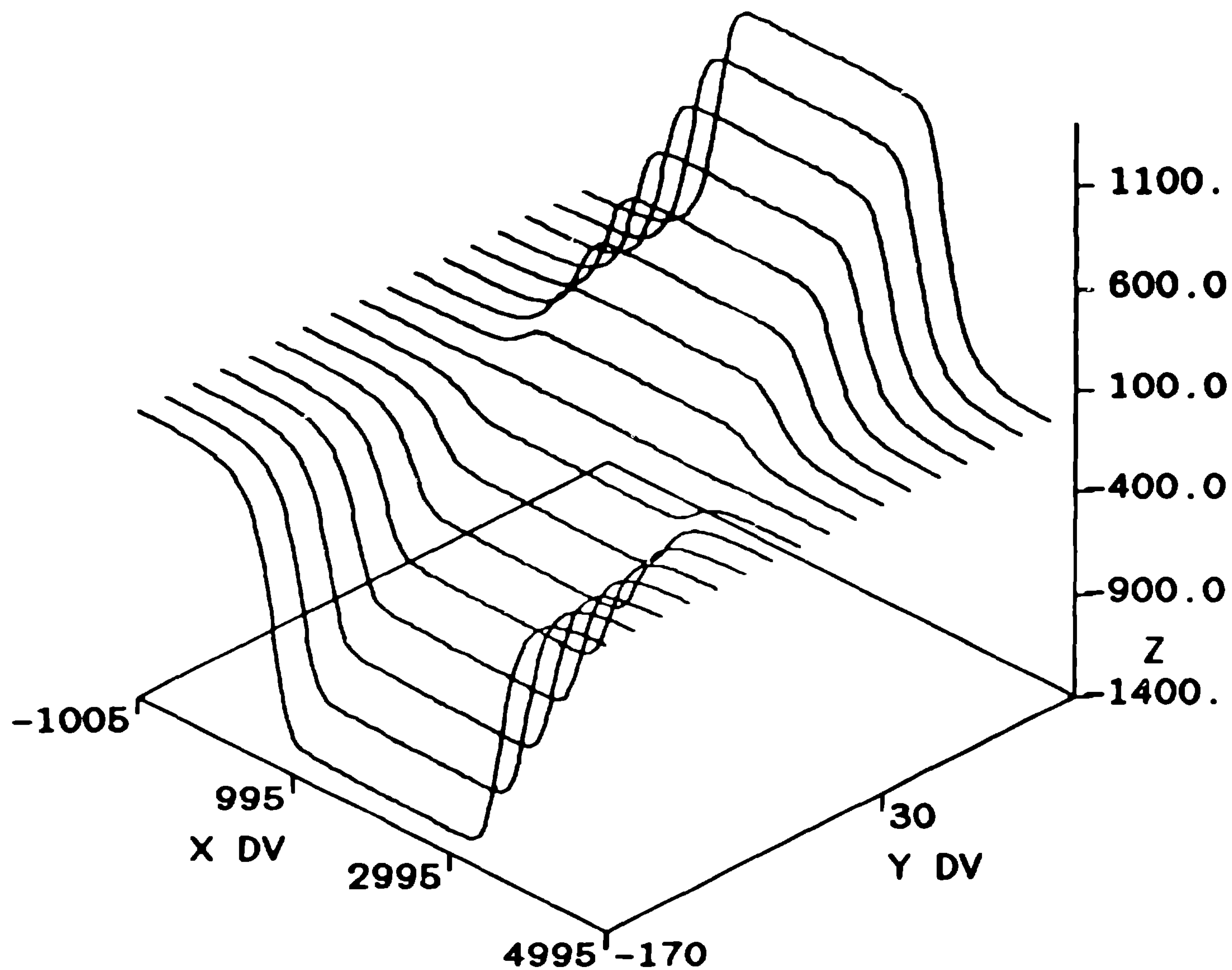

BYXZ BLK 3 X IND 227 Z-Cord (0.1 mm)
0 9-AUG-91 SUM=-12623. 0= 0 XHI= 0 17AUG9 151
0 10:43:52 ADD= 1: 1 = 0 LST= 0 30-JUL 1 1

Y IND 225 X-Cord (0.1 mm)

YLO= 0 YHI= 0

TH= 1 PHI= 0

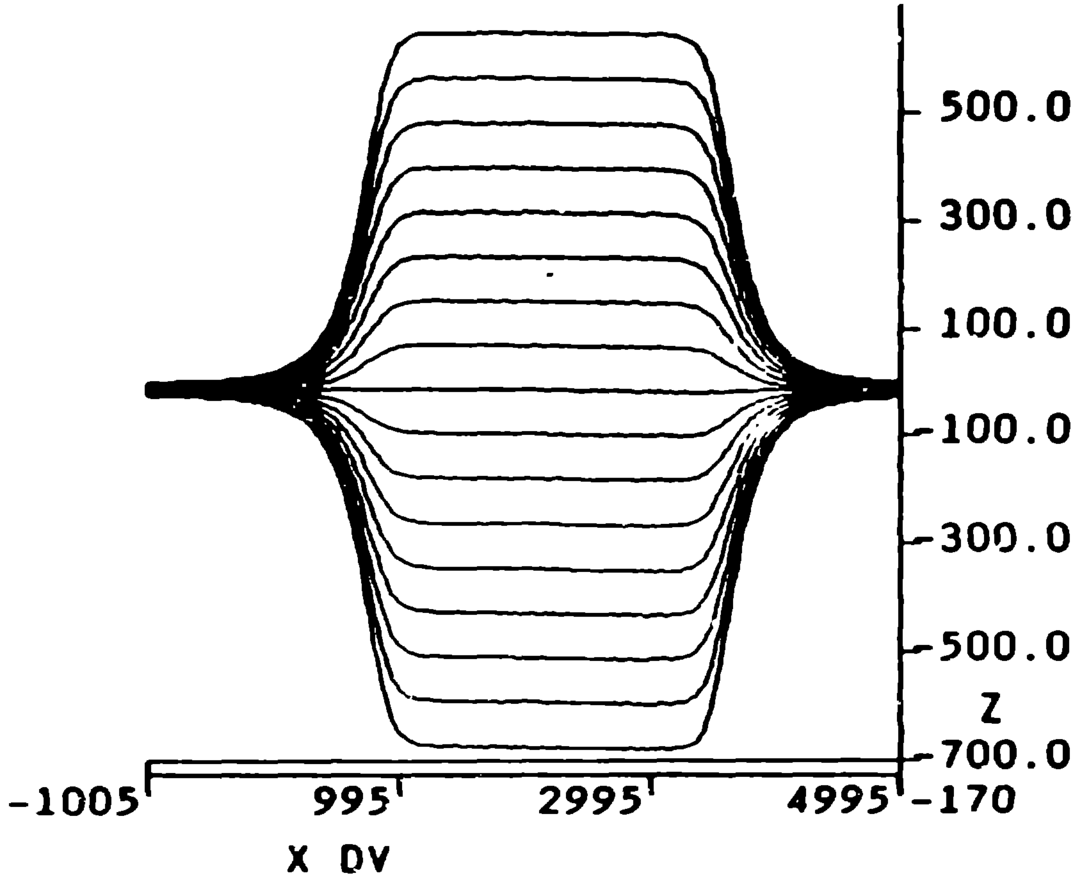

BYXZ BLK 3 X IND 227 Z-Cord (0.1 mm)

RU 0 9-AUG-91 SUM= -6056. X 0 XHI= 0 18AUG90 08.H

TS 0 12:57:20 ADD= 1: 1 F. 0 LST= 0 7-AUG-9 .6:2

YLO= 0 YHI= 0 TH= 1 PHI= 0

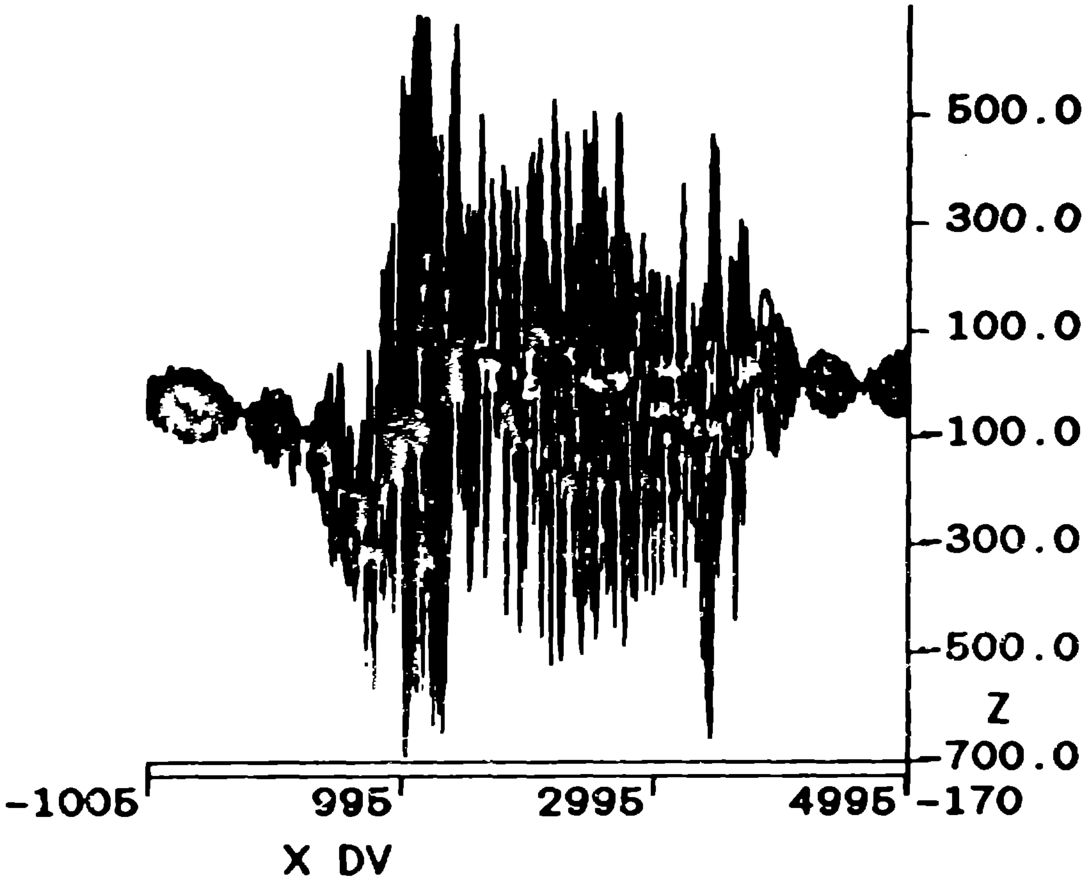

BYXZR BLK 4 X IND 227 Z-Cord (0.1 mm)
R' 0 9-AUG-91 SUM=-87949. Y = 0 XHI= 0 17AUG90 518
T 0 10:47:51 ADD= 1: 1 F = 0 LST= 0 30-JUL- 17

YLO= 0 YHI= 0 TH= 1 PHI= 0

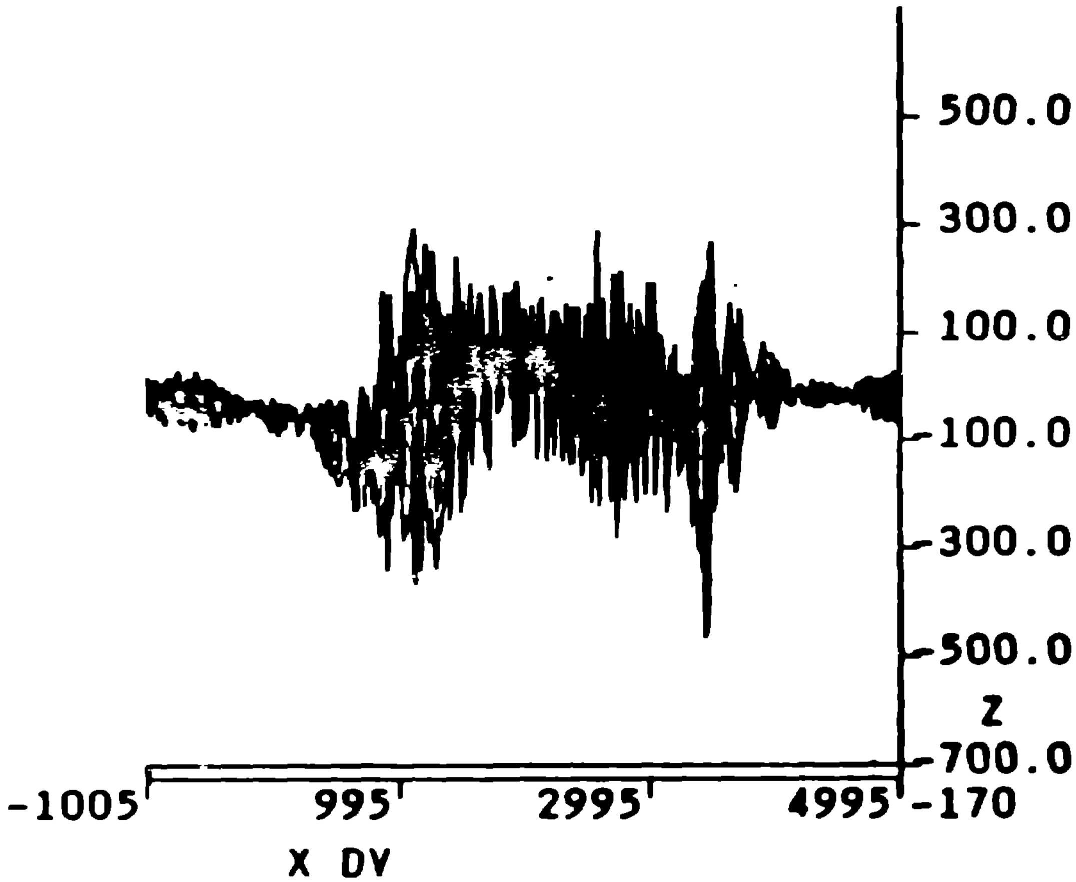

BYXZR BLK 4 X IND 227 Z-Cord (0.1 mm)
RUN 0 9-AUG-91 SUM=-60294. XLO= 0 XHI= 0 18AUG90 1608.H
TST 0 12:35:41 ADD= 1: 1 FAL 0 LST= 0 7-AUG-91 :2

Y IND 225 X-Cord (0.1 mm)
YLO= 0 YHI= 0 TH= 1 PHI= 0

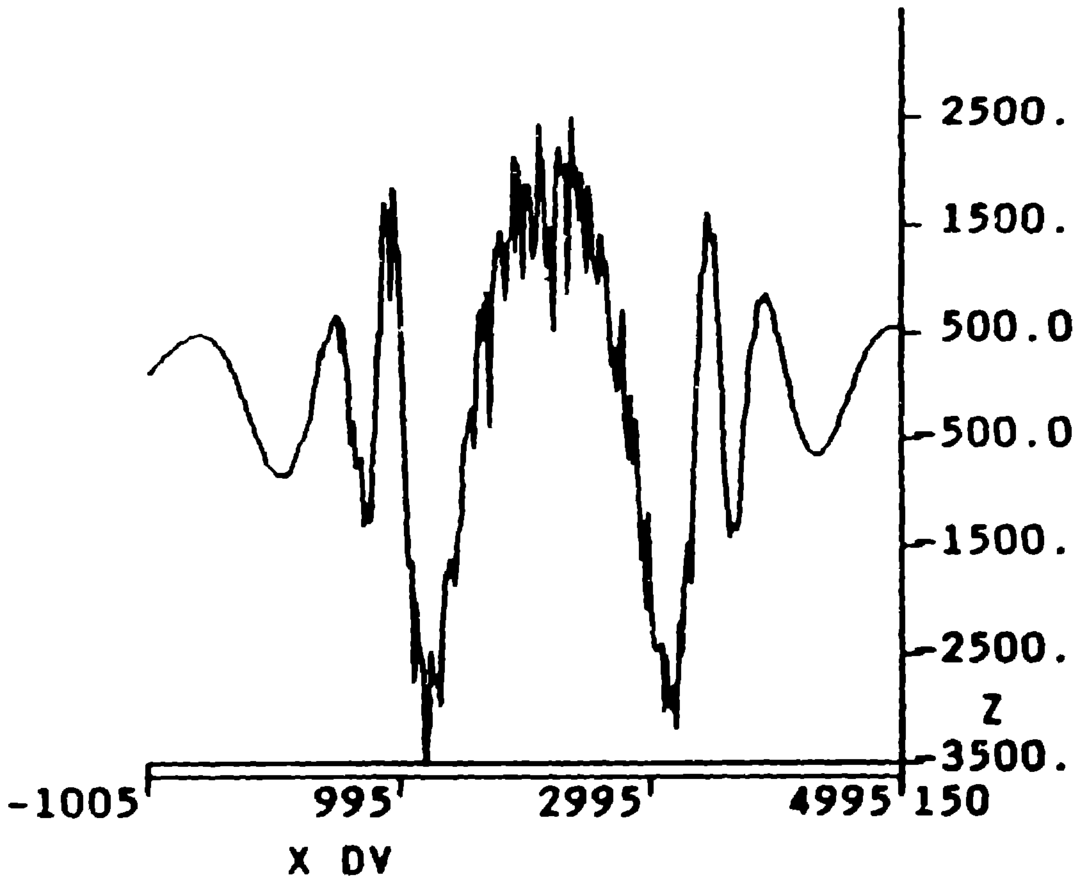

BYX7R BLK 4 X IND 227 Z-Cord (0.1 mm)
RU 0 9-AUG-91 SUM= 15147. XL 0 XHI= 0 26SEP90 8.
TS 0 13:05:28 ADD= 1: 1 FA 0 LST= 0 9-AUG-91 .4:

)= 0 YHI= 0 TH= 1 PHI= 0

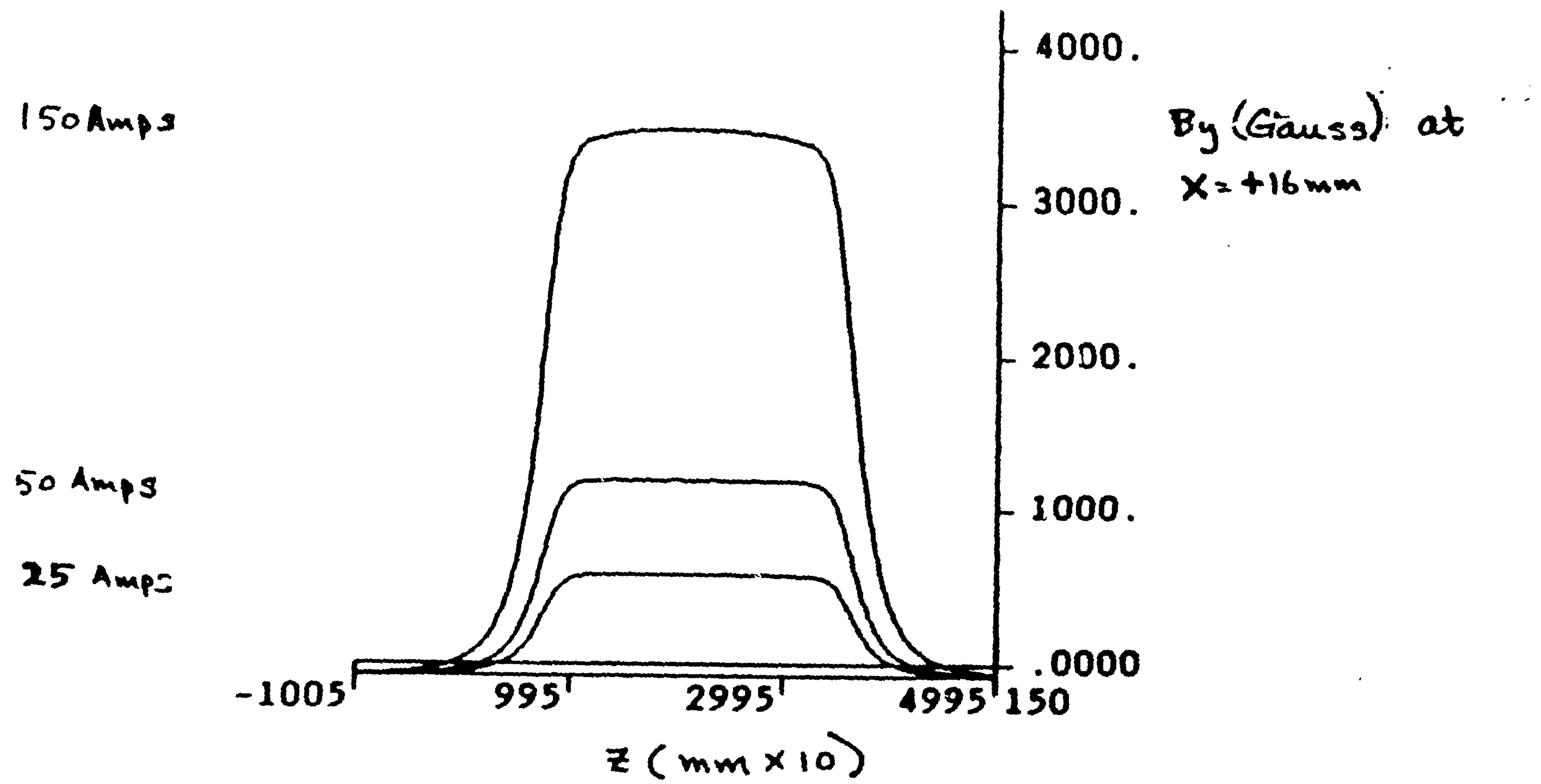

XZ BLK 3 X IND 227 Z-Cord (0.1 mm)
N 0 31-JUL-91 SUM=540348. XLO= 0 XHI= 0 26SEP90 1548.H
T 0 13:02:12 ADD= 1: 1 FAL= 0 LST= 0 31-JUL-91 12 4

YLO= 0 YHI= 0   ... 1 YHI= 0

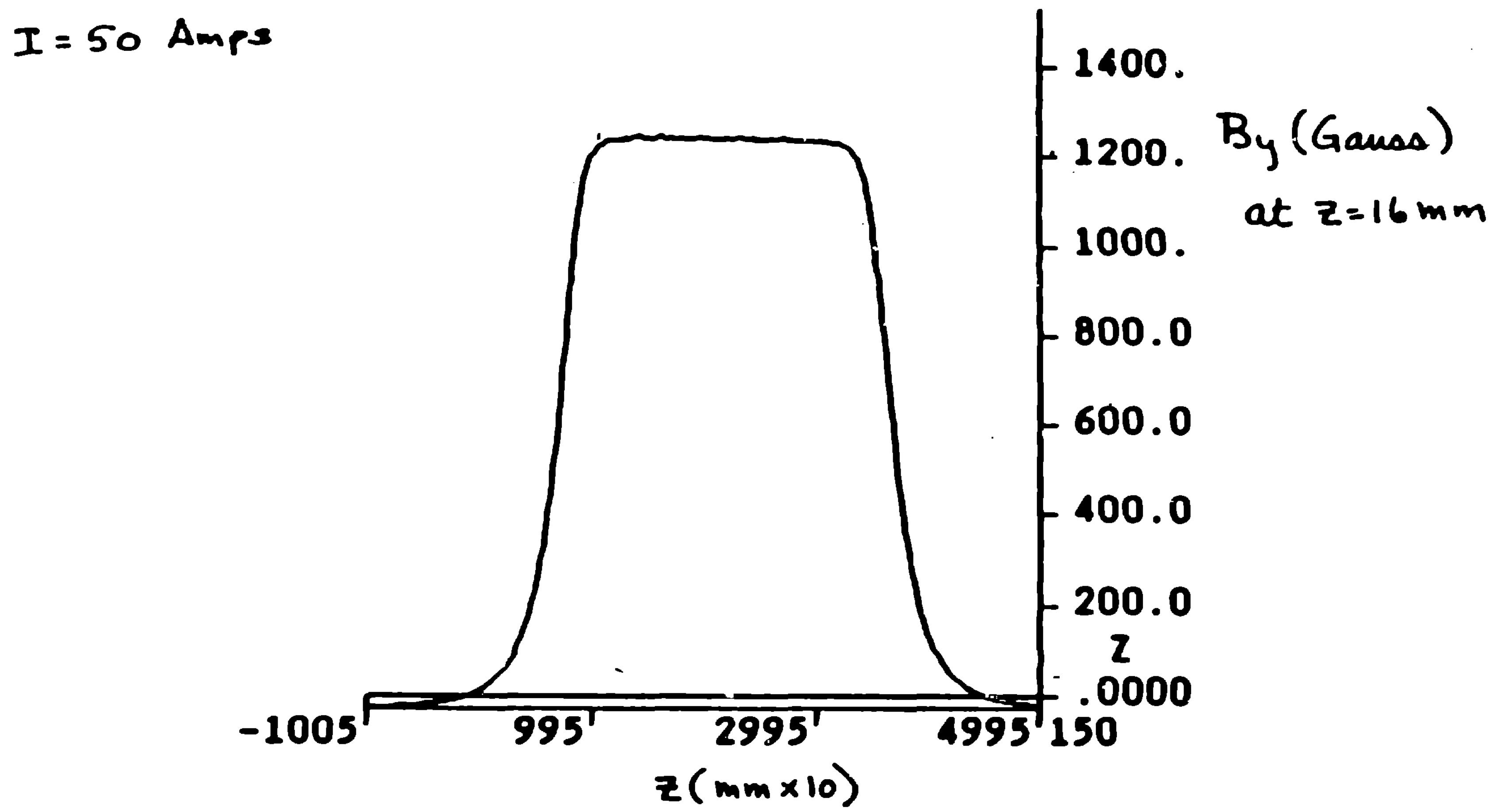

BYXZ BLK 3 X IND 227 Z-Cord (0.1 mm)
RUN 0 7-AUG-91 SUM=195373. XL 0 XHI= 0 17AUG90
TS 0 13:09:12 ADD= 1: 1 FA 0 LST= 0 30-JUL-91 1

ɪ IND 225 X-Cord (0.1 mm)
YLO= 0 YHI= 0 TH= 1 PHI= 0

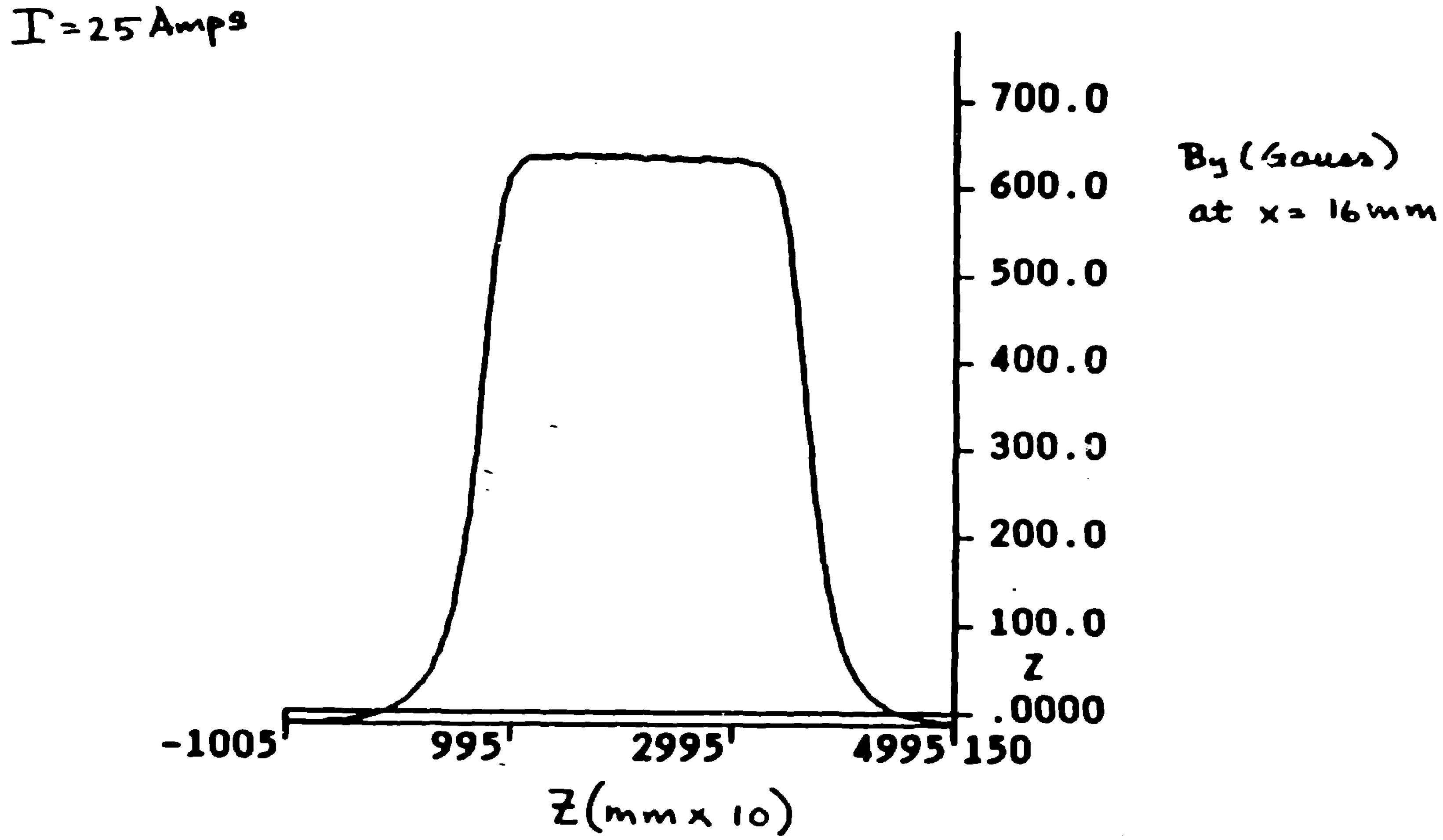

BYX7 BLK 3 X IND 227 Z-Cord (0.1 mm)
RU 0 7-AUG-91 SUM= 99861. X 0 XHI= 0 18AUG90 08

TH= 1 PHI= 0

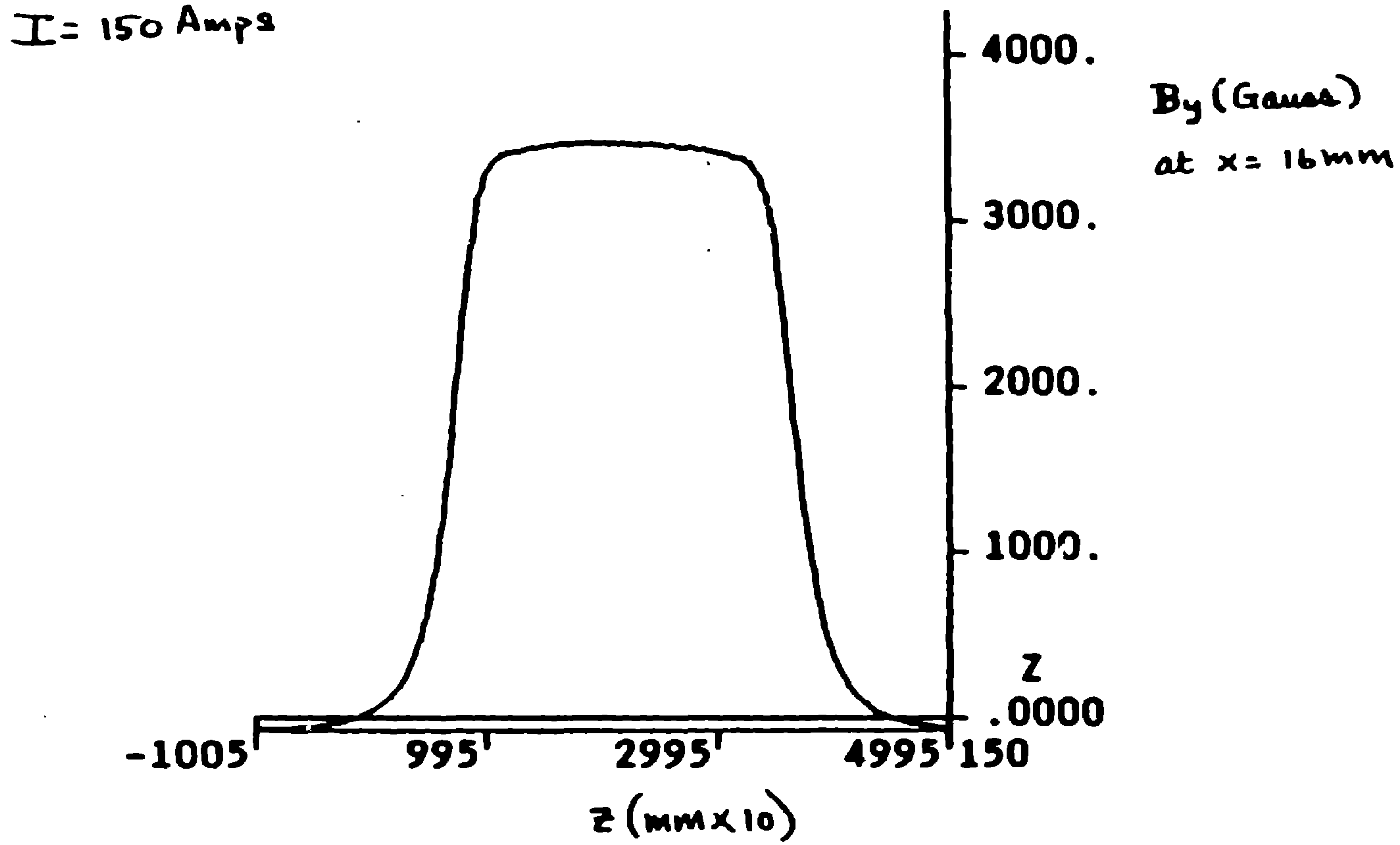

BYXZ BLK 3 X IND 227 Z-Cord (0.1 mm)
RUN 0 7-AUG-91 SUM=540348. X = 0 XHI= 0 26SEP90 48
TS 0 13:08:46 ADD= 1: 1 F = 0 LST= 0 31-JUL-91 12

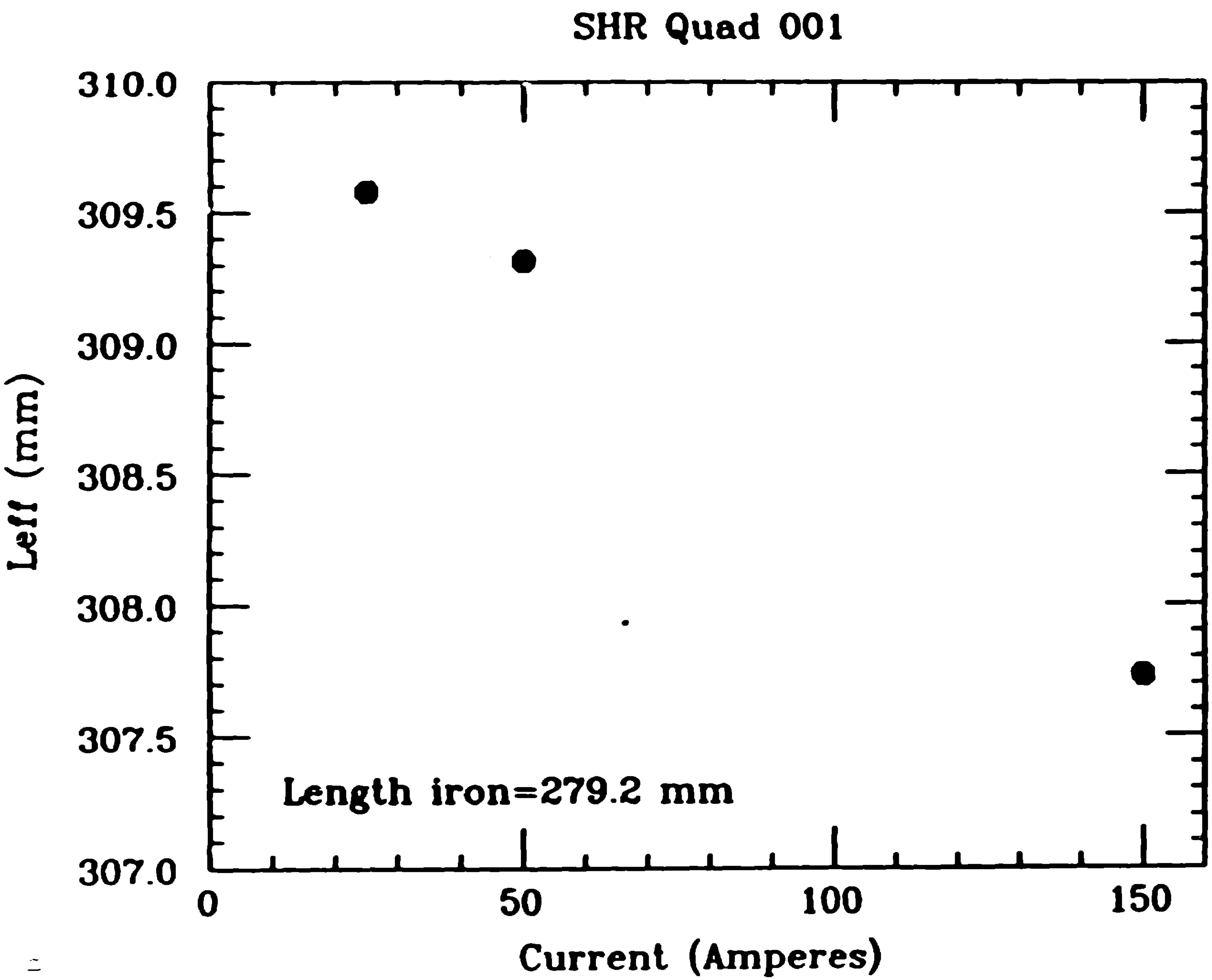

SHR Quad 001
310.0
309.5
309.0
308.5
308.0
307.5
307.0
Leff (mm)
Length iron=279.2 mm
0
50
100
150
Current (Amperes)

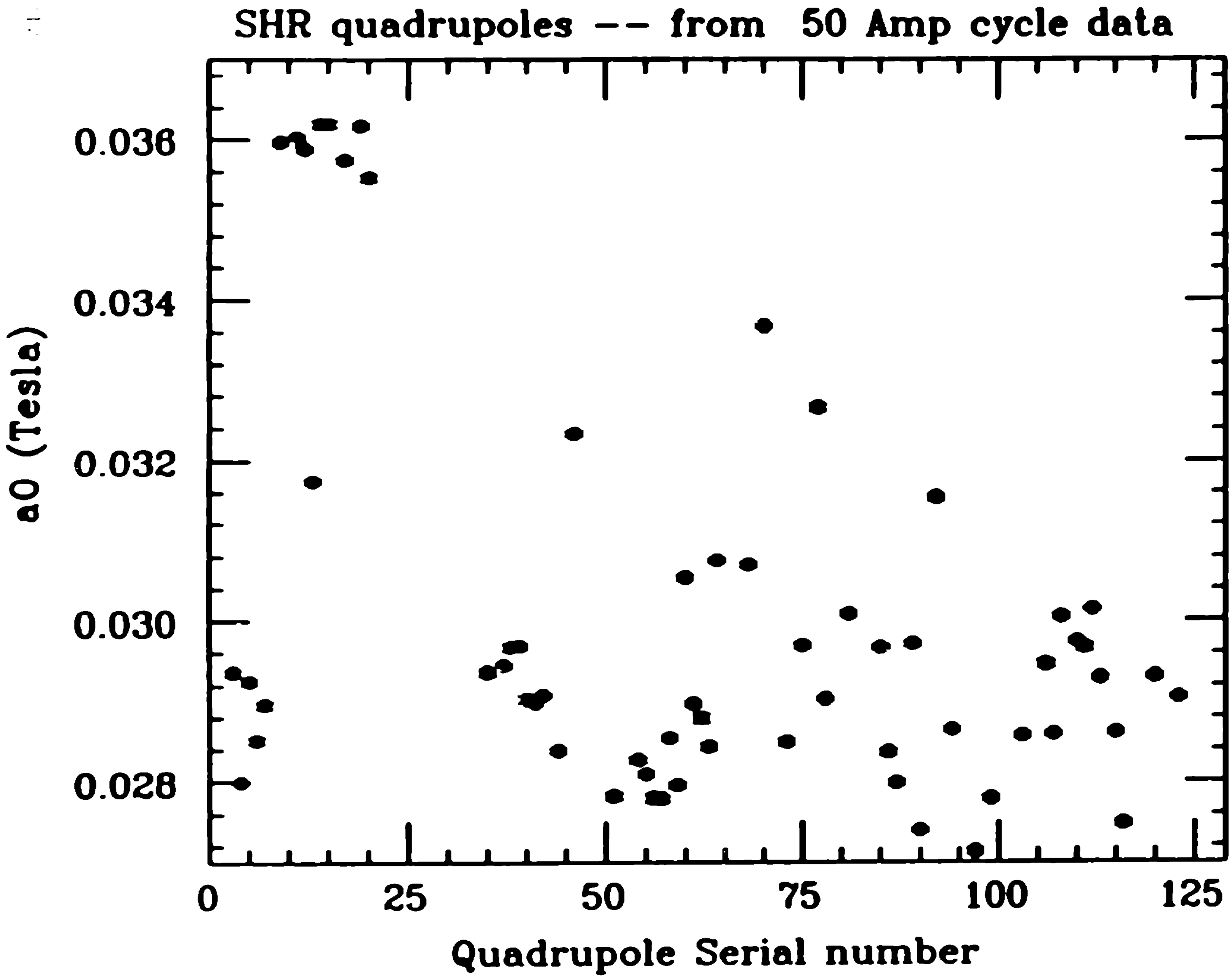
SHR quadrupoles -- from 50 Amp cycle data
0.036
0.034
0.032
0.030
0.028
a0 (Tesla)
0
25
50
75
100
125
Quadrupole Serial number

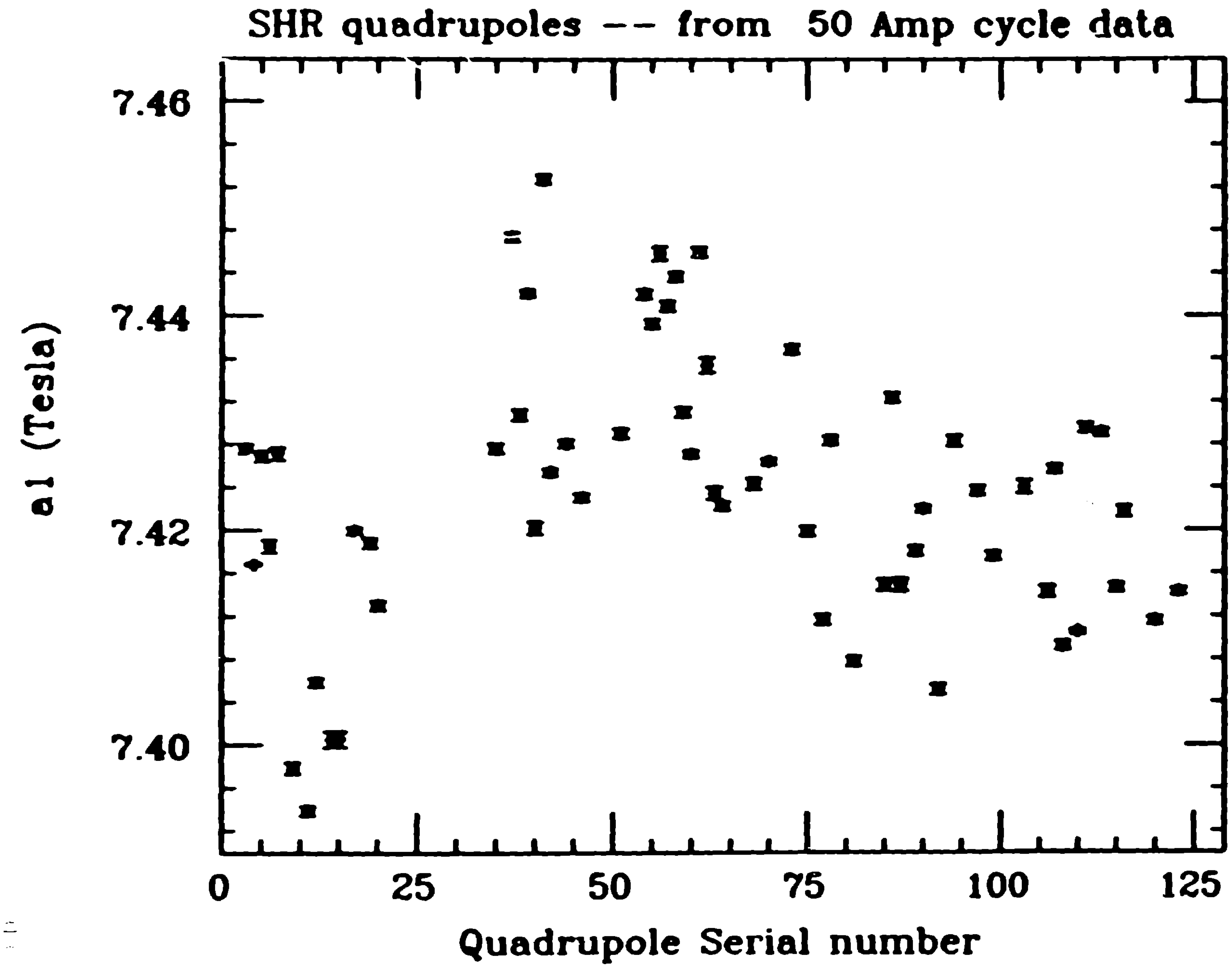

SHR quadrupoles -- from 50 Amp cycle data
7.46
7.44
7.42
7.40
a1 (Tesla)
0
25
50
75
100
125
Quadrupole Serial number

ANALYSIS OF 3D QUADRUPOLE DATA

Jeff Arrington

(Analysis of 3D data)
or
"Deciding What Counts"

Reference made to
"Calculations of Higher Multipole Components
in a Large Superconducting Quadrupole Magnet"
by
J. Napolitano and T. Hunter (CEBAF)

Goal: Comparison of B field model in RAYTRACE/MOTER to 3D (TOSCA) type results.

Problems generating reliable, comparable TOSCA data

↓

New question: How much detail (how many terms) should be included to represent <u>measured</u> data accurately

By way of review:

RAYTRACE calculates magnetic fields based on z derivatives of

$$\frac{1}{1+e^{S}} \qquad \text{(ENGE fcn)}$$

$$S = \sum_{n=0}^{5} C_n s^n \qquad s = \frac{z}{2R}$$

The C_n chosen so that ENGE fcn fits $m=0$ component of field.

Thus 1ST step in extending model in RAYTRACE might be to fit $N=6, m=0$ B component to exp. data.

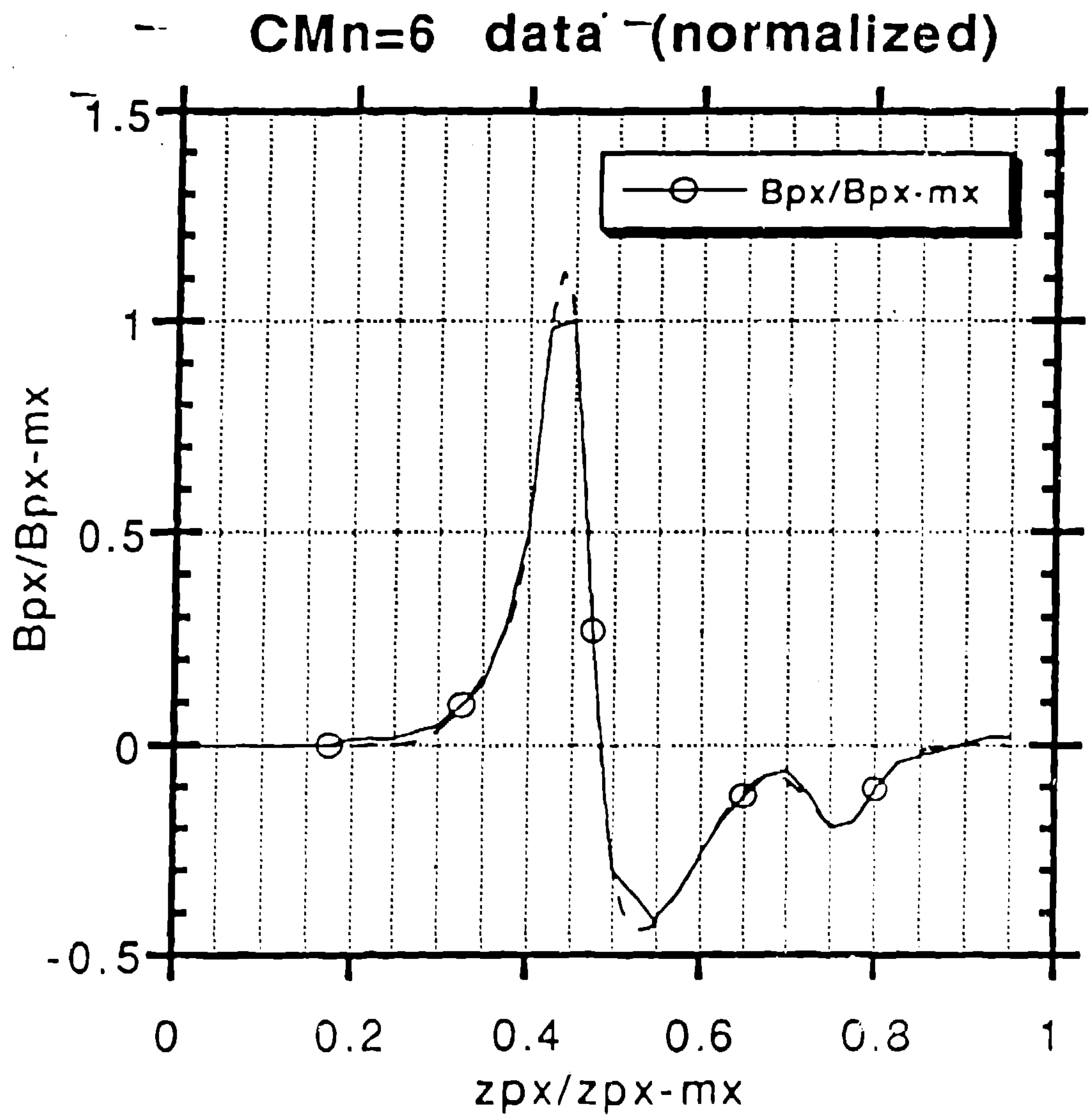
CMn=6 data (normalized)
Bpx/Bpx-mx
1.5
1
0.5
0
-0.5
0
0.2
0.4
0.6
0.8
1
zpx/zpx-mx
Bpx/Bpx-mx

$$B_{6r} = \cos(6\theta)\left(\frac{r}{r_0}\right)^5 \sum_{m=0}^{\infty}\left[b_{mn}(z)\left(r/r_0\right)^{2m}\right.$$

$$B_{6r} \sim F(\theta)\left(\frac{r}{r_0}\right)^5\left[b_{06} + b_{16}\left(r/r_0\right)^2 + b_{26}\left(r/r_0\right)^4 + \dots\right]$$

$$b_{m,n}(z) = C_{mn}\, r_0^2\, \frac{d^2 b_{m-1,n}}{dz^2} \qquad m \geq 1$$

$$B_{6r} \sim F(\theta)\left(\frac{r}{r_0}\right)^5\left[b_0 + C_{mn}\, r_0^2\, b_0''\right]$$

$$b_0'' \equiv \frac{d^2 b_0}{dz^2}$$

or

$$b_0 + C_{16}\, r_0^2\, b_0'' + C_{26}\, r_0^2\, r_0^2\, b_0^{(iv)} + \dots$$

1. Fit data w/ 4 Gaussians

$$g_i(x) = a_i \exp\left[\frac{-(x-x_{0i})^2}{s^2}\right]$$

2. MATHEMATICA $\rightarrow b_0'', b_0^{(iv)}$

3. MATHCAD $\rightarrow \frac{M=1}{M=0}, \frac{M=2}{M=0}$

(for $r/r_0 \sim 1$, $r_0 = 0.15m$)

4. N=6 conclusions + plans

- At LEAST m=1,2 needed
- 5,6 Gaussian fit needed.
- Mathematica $\exists\, \tau \Rightarrow$ as many as m=5

Plot of Ratio of m=1 term to m=0 term, N=6

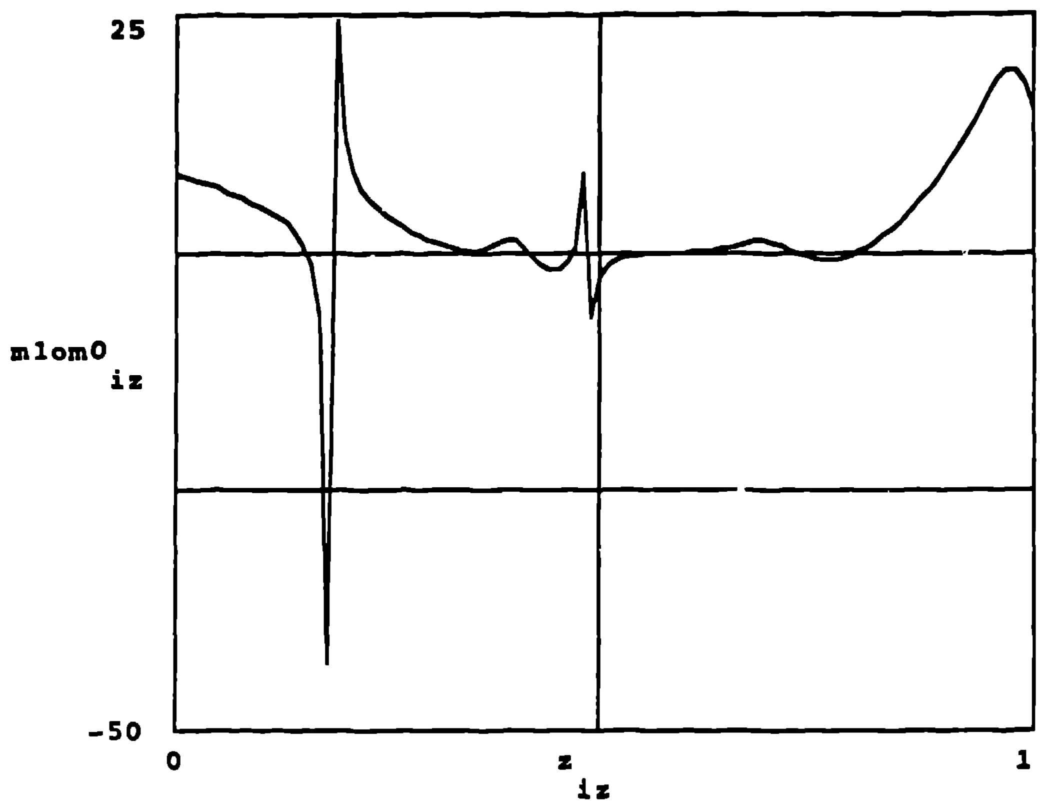

Plot of Ratio of m=2 term to m=0 term, N=6

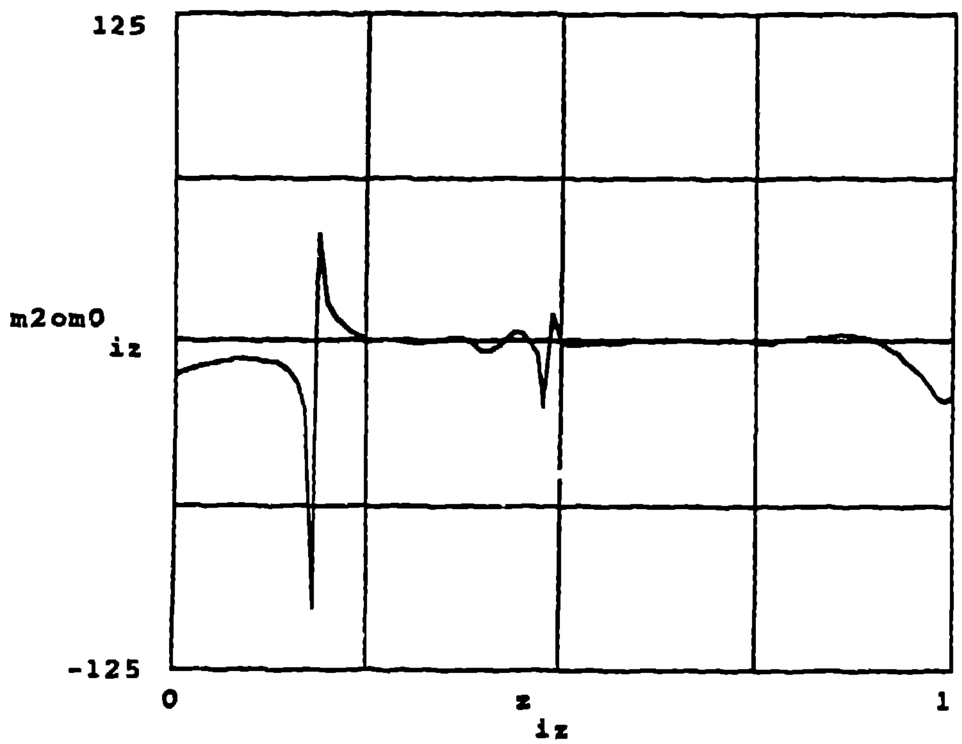

Similar analysis for $n=4$ data (NOT as significant as $n=6$) shows at least $m=1,2$ should be included.

Now for actual problem, we have (1st approx.)

$$b_0 + C_{mn} r_0^2 b_0'' = \sum_i a_i \exp\left[-\frac{(x-x_{0i})^2}{s^2}\right]$$

By hand, sol'n reduces to

$$\int e^{-\frac{(x-x_0)^2}{s^2}} \cos(qx)\, dx$$

Mathematica solution

$$\sim e^{(a+bi)} \operatorname{erf}(c+di)$$

Complex + hard to take derivatives

Numerical problem

Linear, 2nd order, DE

Very STIFF!

Suggestions ????

Plot of Ratio of m=1 term to m=0 term, N=4

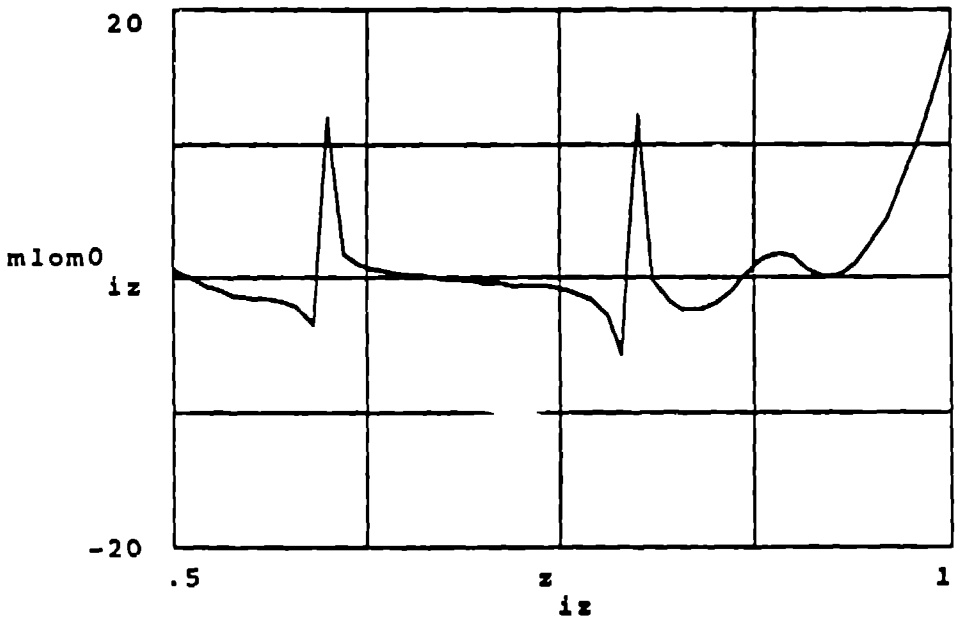

Ratio of m=2 term to m=0 term, N=4

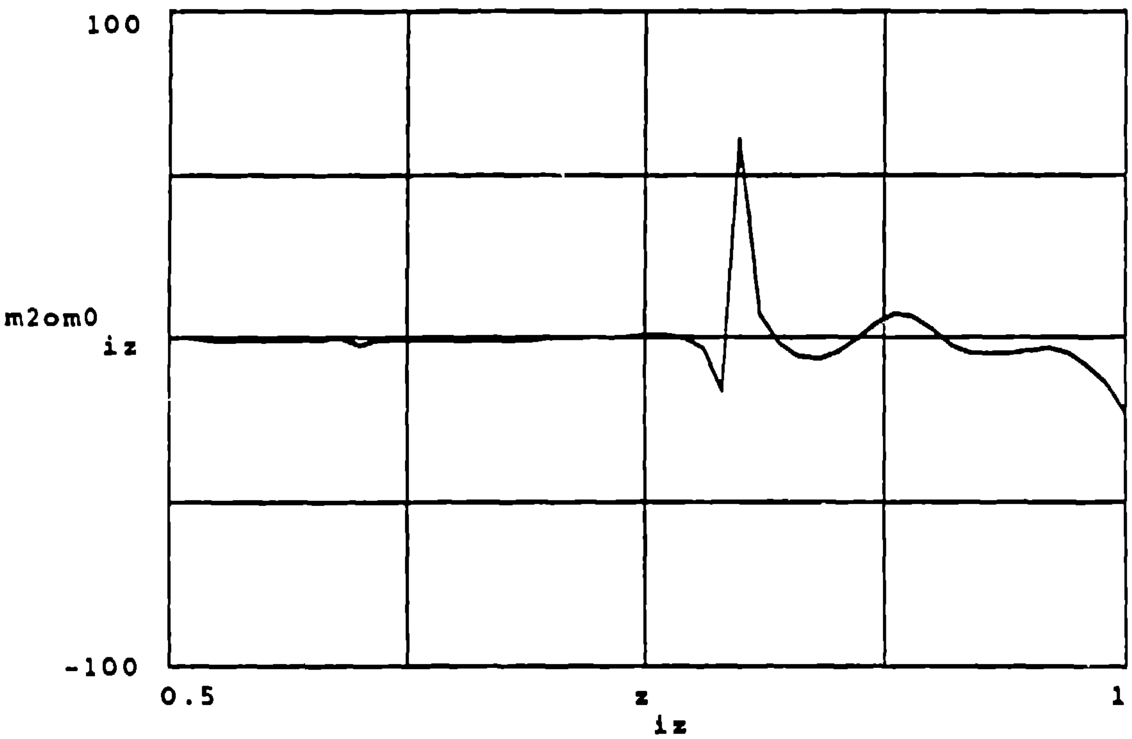

Conclusions

1. $N=6$ $m=1,2\ldots?$ needed

2. $N=4$ $m=1,2,\ldots?$ needed

3. $N=10,14$ unmeasured

   Test tentatively planned for fall/winter '91. (ARCH, TOM.)

4. Results from 3 to be used to add to RAYTRACE/MOTER field model

5. Current/new model to be compared to TOSCA ASAP.

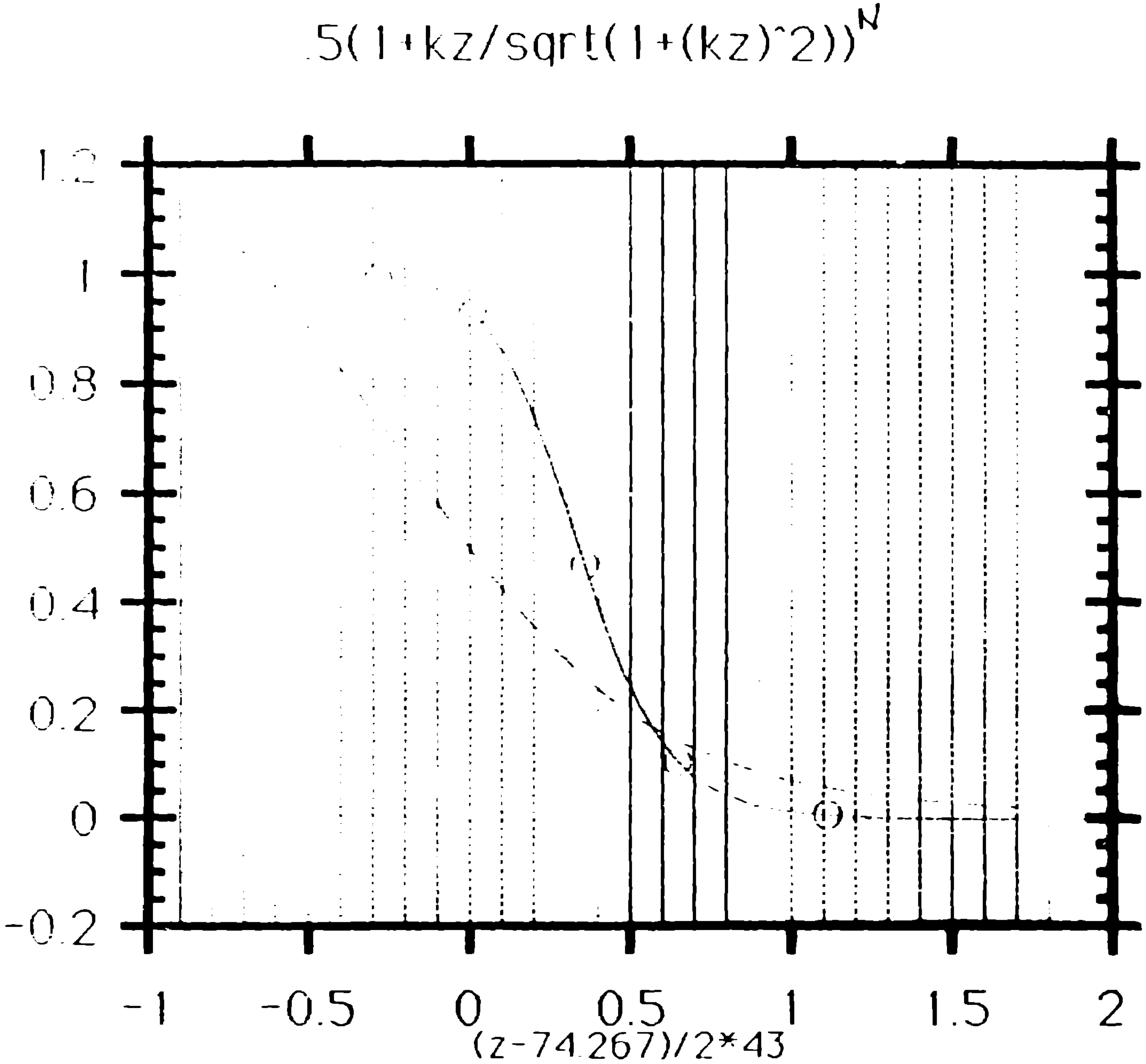
.5(1+kz/sqrt(1+(kz)^2))^N
1.2
1
0.8
0.6
0.4
0.2
0
-0.2
-1
-0.5
0
0.5
1
1.5
2
(z-74.267)/2*43

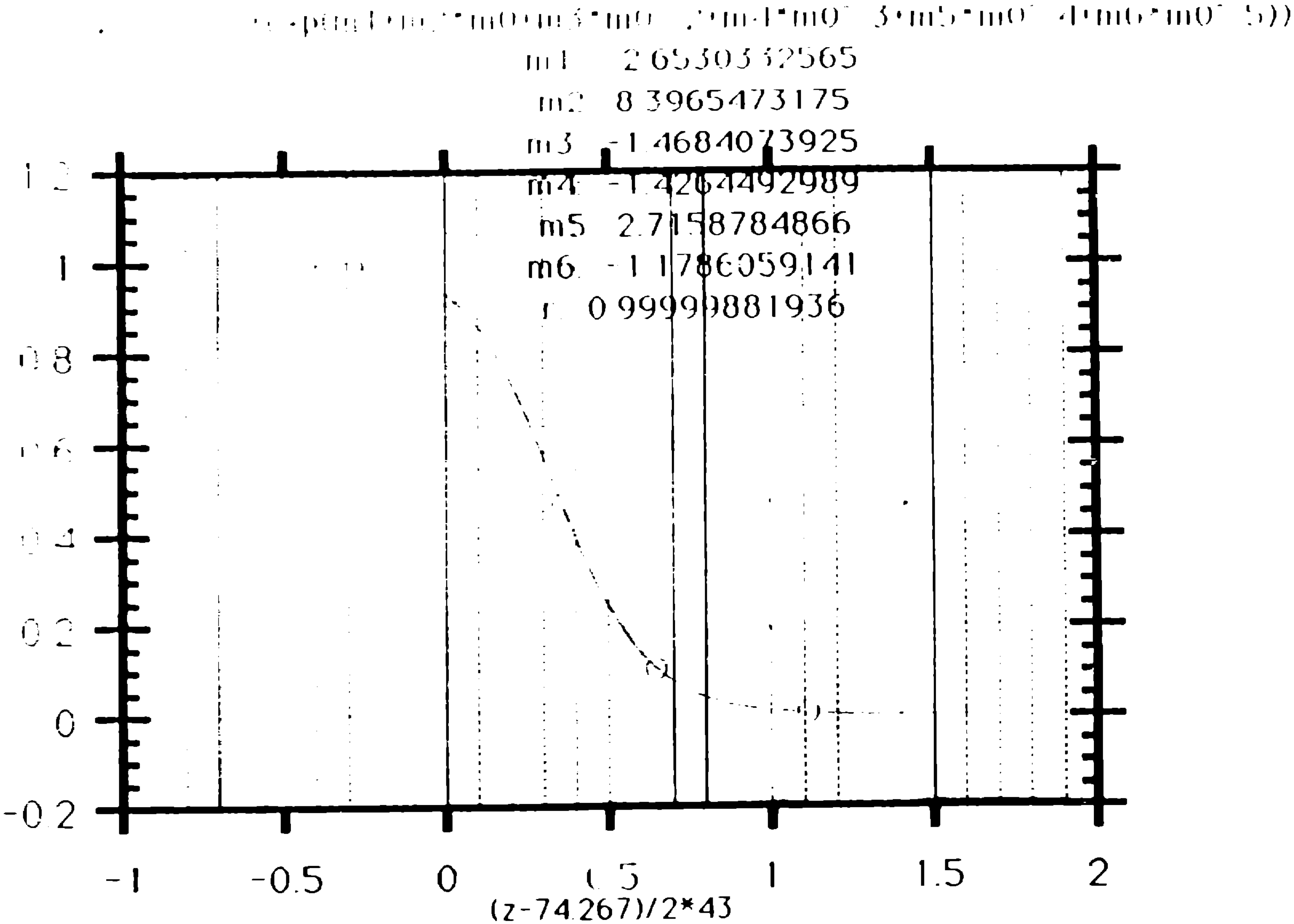
m1 2.6530332565
m2 8.3965473175
m3 -1.4684073925
m4 -1.4264492989
m5 2.7158784866
m6 -1.1786059141
r 0.99999881936
1.2
1
0.8
0.6
0.4
0.2
0
-0.2
-1
-0.5
0
0.5
1
1.5
2
(z-74.267)/2*43

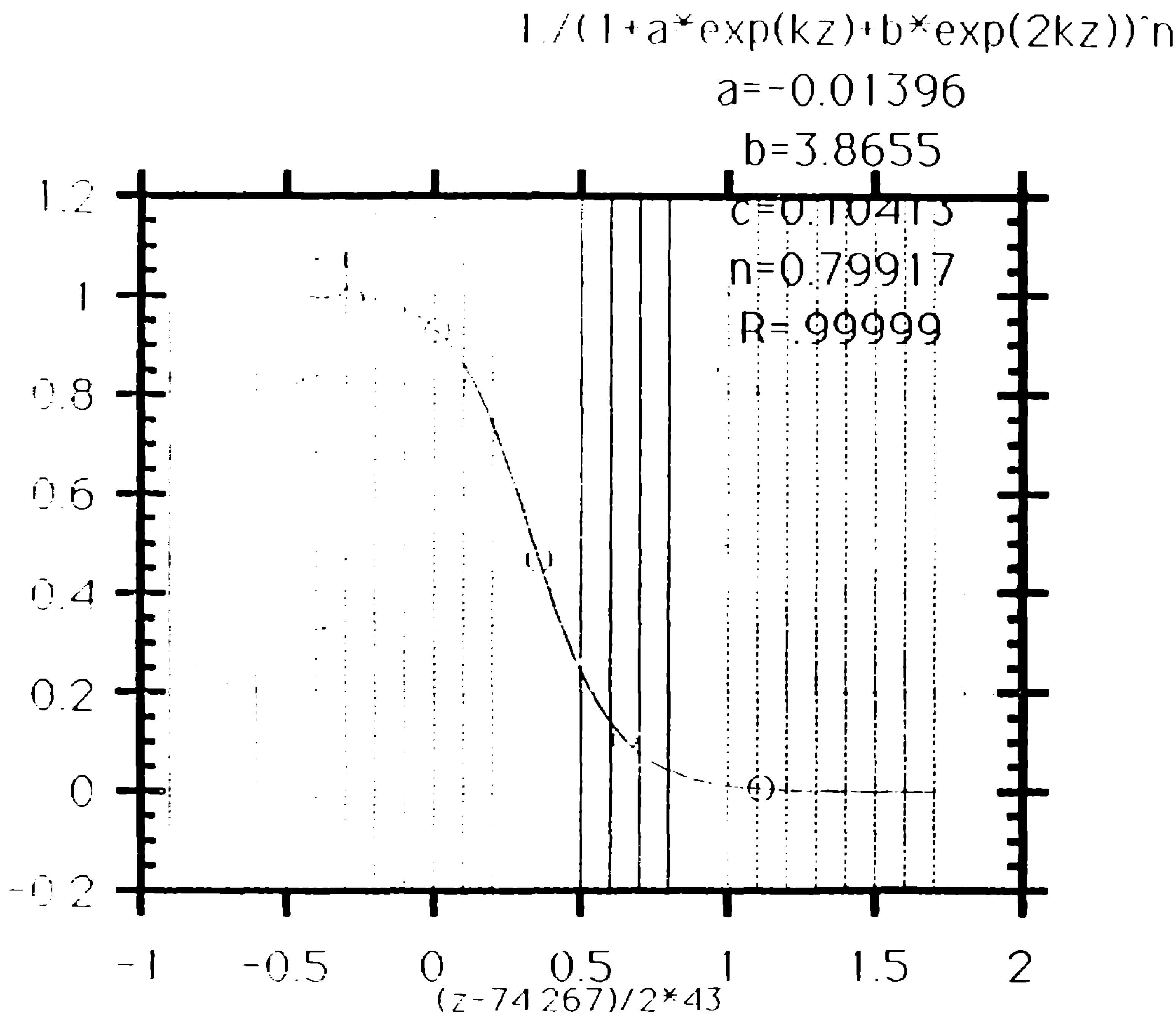

1./(1+a*exp(kz)+b*exp(2kz))^n
a=-0.01396
b=3.8655
c=0.10413
n=0.79917
R=.99999
1.2
1
0.8
0.6
0.4
0.2
0
-0.2
-1
-0.5
0
0.5
1
1.5
2
(z-74.267)/2*43

QUADRUPOLE 3D FRINGE FIELDS
THEORETICAL LECTURE

(C

Multipole 3D Fields in Vacuum

K. Halbach, LBL

PILAC Workshop, Aug. 91

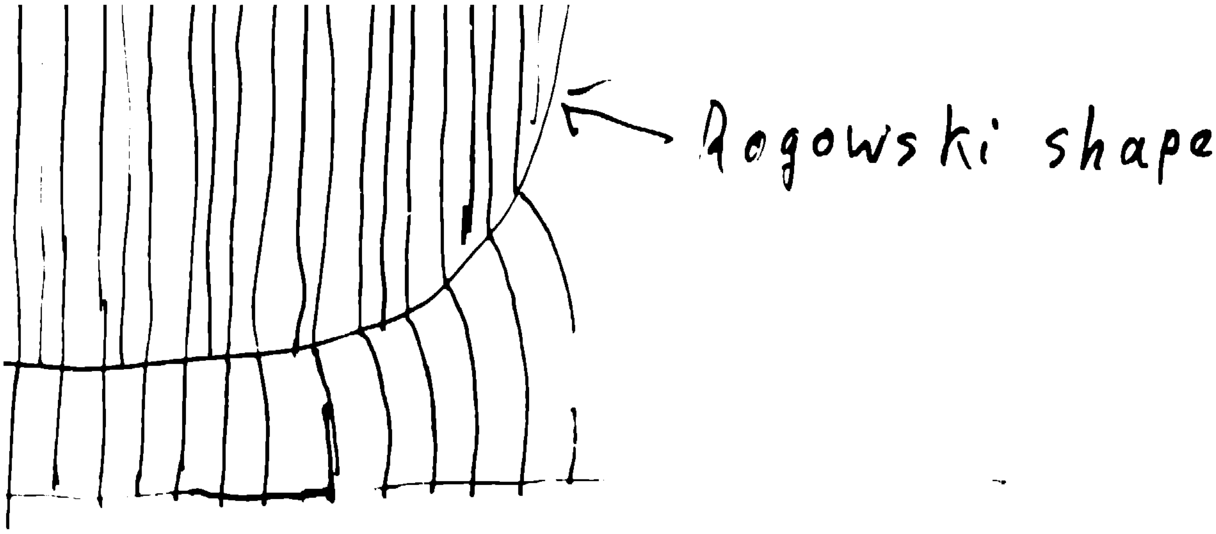

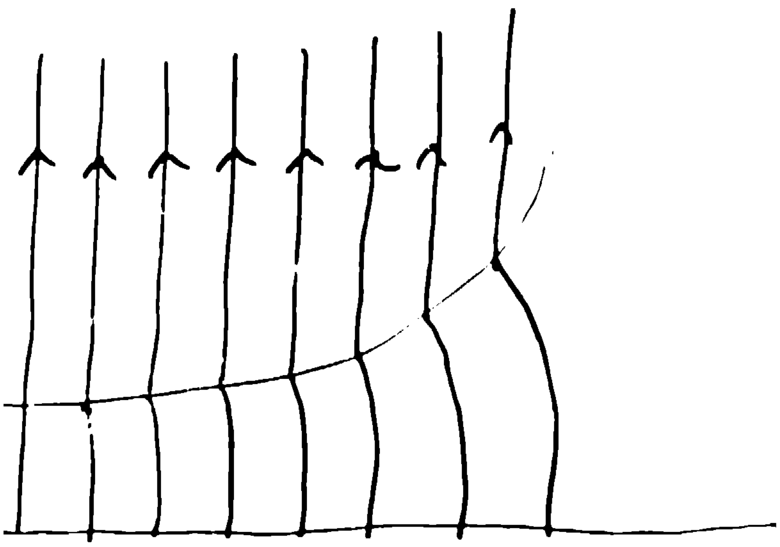

eff increses with increasing field

1)

1) Properties of straight line integrals over 3D fields

2) Utilization of $\nabla^2 H_{x,y,z}(x,y,z)=0$

3) $V, \vec{H}$ in cylindrical coordinatesystem

4) Use and exploitation of (3.9), (3.10), method #1: expansion in r^2

5) Magnetic field measurement/characterization priorities

6) Use and exploitation of (3.9), (3.10), method #2: direct use of $B_\varphi(r_0, \varphi, z)$ (r_0 = "large") to get 3D fields

7) Use and exploitation of (3.9), (3.10), method #3: Exact calculation of 3D fields from analytical function $G_n(0, z)$

8) Methods to determine $G_n(0,z)$

1) <u>Properties of straight line integrals over 3D fields</u>

$$\frac{1}{L}\int_{z_1}^{z_2} H_{x,y}(x,y,z)\,dz = \bar{H}_{x,y}(x,y)$$

$$\frac{\partial}{\partial x}H_y - \frac{\partial}{\partial y}H_x = 0 \longrightarrow \frac{\partial}{\partial x}\bar{H}_y - \frac{\partial}{\partial y}\bar{H}_x = 0$$

$$\frac{\partial}{\partial x}H_x + \frac{\partial}{\partial y}H_y + \frac{\partial}{\partial z}H_z = 0 \longrightarrow \frac{\partial}{\partial x}\bar{H}_x + \frac{\partial}{\partial y}\bar{H}_y = \frac{1}{L}\,H_z(x,y,z)\Big|_{z_2}^{z_1}$$

When $H_z(x,y,z_1) = H_z(x,y,z_2)$, then integrals over 3D <u>Cartesian</u> field components have same mathematical properties as 2D fields

$\rightarrow \bar{H}_x - i\bar{H}_y = \bar{H}^* =$ analytical function of complex variable $z = x+iy = re^{i\varphi}$

$\bar{H}^* = i\,dF/dZ$; $A + iV = F(z) = \sum a_n Z^n$

$V = \sum |a_n|\, r^n \sin(n\varphi + \alpha_n)$ $\qquad (a_n = |a_n| e^{i\alpha_n})$

$n=1$ = dipole, $n=2$ = quadrupole, etc.

$N = 2.$

n	$\frac{n}{N}\cdot j_n = \frac{n}{N}\cdot\frac{\Delta C_n(x)}{i\epsilon}$	$\frac{n}{N}\cdot b_n = \frac{n}{N}\cdot\frac{\Delta C_n(rd)}{i\epsilon}$	$\frac{n}{N}\cdot a_n = \frac{n}{N}\cdot\frac{\Delta C_n(ad)}{\epsilon}$	$\frac{n}{N}\cdot p_n = \frac{n}{N}\cdot\frac{\Delta C_n(r)}{\epsilon}$
1	1.99E-01	-4.25E-01	7.46E-02	1.76E-01
2	2.50E-01	-5.16E-01	2.14E-01	5.00E-01
3	1.57E-01	-2.88E-01	2.88E-01	6.60E-01
4	0.0	6.76E-02	2.31E-01	5.00E-01
5	-2.05E-02	1.08E-01	1.08E-01	1.91E-01
6	0.0	4.45E-02	2.87E-02	0.0
7	1.61E-02	-1.04E-02	1.04E-02	-3.06E-02
8	0.0	1.28E-02	1.56E-02	0.0
9	-1.90E-03	1.25E-02	1.25E-02	7.53E-03
10	0.0	6.37E-03	5.81E-03	0.0
11	3.15E-03	-2.44E-03	2.44E-03	-3.62E-03
12	0.0	2.66E-03	2.79E-03	0.0
13	-2.45E-04	2.27E-03	2.27E-03	9.28E-04
14	0.0	1.26E-03	1.23E-03	0.0
15	6.69E-04	-5.55E-04	5.55E-04	-6.66E-04
16	0.0	5.76E-04	5.82E-04	0.0

TABLE 2
$N = 3.$

n	$\frac{n}{N}\cdot j_n = \frac{n}{N}\cdot\frac{\Delta C_n(x)}{i\epsilon}$	$\frac{n}{N}\cdot b_n = \frac{n}{N}\cdot\frac{\Delta C_n(rd)}{i\epsilon}$	$\frac{n}{N}\cdot a_n = \frac{n}{N}\cdot\frac{\Delta C_n(ad)}{\epsilon}$	$\frac{n}{N}\cdot p_n = \frac{n}{N}\cdot\frac{\Delta C_n(r)}{\epsilon}$
1	9.79E-02	-3.14E-01	5.09E-02	8.47E-02
2	1.56E-01	-4.95E-01	1.71E-01	2.84E-01
3	1.67E-01	-5.15E-01	3.03E-01	5.00E-01
4	1.33E-01	-3.90E-01	3.90E-01	6.39E-01
5	7.09E-02	-1.73E-01	3.97E-01	6.43E-01
6	0.0	6.55E-02	3.18E-01	5.00E-01
7	-1.34E-02	1.08E-01	1.95E-01	2.88E-01
8	-1.07E-02	9.03E-02	9.03E-02	1.08E-01
9	0.0	4.16E-02	2.51E-02	0.0
10	9.13E-03	-1.90E-03	1.90E-03	-3.38E-02
11	9.73E-03	-1.45E-02	5.49E-03	-2.05E-02
12	0.0	1.05E-02	1.31E-02	0.0
13	-1.01E-03	1.07E-02	1.36E-02	7.34E-03
14	-1.18E-03	9.85E-03	9.85E-03	5.82E-03
15	0.0	5.06E-03	4.56E-03	0.0
16	1.63E-03	-1.26E-03	1.26E-03	-3.66E-03
17	2.07E-03	-3.77E-03	1.18E-03	-2.54E-03
18	0.0	2.02E-03	2.12E-03	0.0
19	-1.12E-04	1.82E-03	2.12E-03	8.13E-04
20	-1.70E-04	1.69E-03	1.69E-03	7.84E-04
21	0.0	9.30E-04	9.07E-04	0.0
22	3.25E-04	-3.02E-04	3.02E-04	-6.44E-04
23	4.65E-04	-9.34E-04	2.46E-04	-4.79E-04
24	0.0	4.13E-04	4.18E-04	0.0

uncorrectable field errors. Another possibility is their by δ about the origin of the magnet, and a displace-

2) Utilization of $\nabla^2 H_{x,y,z}(x,y,z)=0$

$$\vec{H} = -\operatorname{grad} V \longrightarrow \operatorname{curl} \vec{H} = 0$$

$$-\operatorname{div} \vec{H} = \nabla^2 V = 0$$

$$H_x = -\partial V/\partial x \longrightarrow \nabla^2 H_{x,y,z} = 0$$

If I measure a <u>Cartesian</u> component of $\vec{H}$ on the surface enclosing a volume, and if I calculate from that the field inside the volume with an algorithm that does not violate the Laplace equ., field errors will be smaller in the volume than on its surface.

3) V, $\vec{H}$, in cylindrical coordinate system

$$)\quad \nabla^2 V = \left(\frac{\partial^2}{\partial r^2} + \frac{1}{r}\frac{\partial}{\partial r} + \frac{1}{r^2}\frac{\partial^2}{\partial \varphi^2} + \frac{\partial^2}{\partial z^2} \right) V = 0$$

Fourier series in φ

$$)\quad V(r,\varphi,z) = \sum V_n(r,z)\sin(n\varphi + \alpha_n) \; ; \quad \alpha_n = \text{const}$$

Allowed / forbidden harmonics determined by rotational symmetry. Example: if

$V(r, \varphi + \pi/2, z) = -V(r,\varphi,z)$,

only $n = 2, 6, 10 \cdots$ are allowed, = allowed harmonics. All others (eg. $n=4$ = octupole) are forbidden harmonics and can appear only when rotational symmetry is violated.

(3.2) into (3.1)

$$3)\quad \left(\frac{\partial^2}{\partial r^2} + \frac{1}{r}\frac{\partial}{\partial r} - \frac{n^2}{r^2} + \frac{\partial^2}{\partial z^2} \right) V_n = 0$$

$$\mathcal{L}\, V_n(r,z) = v_n(r,k)$$

$$4)\quad \left(\frac{\partial^2}{\partial r^2} + \frac{1}{r}\frac{\partial}{\partial r} - \frac{n^2}{r^2} + k^2 \right) v_n(r,k) = 0$$

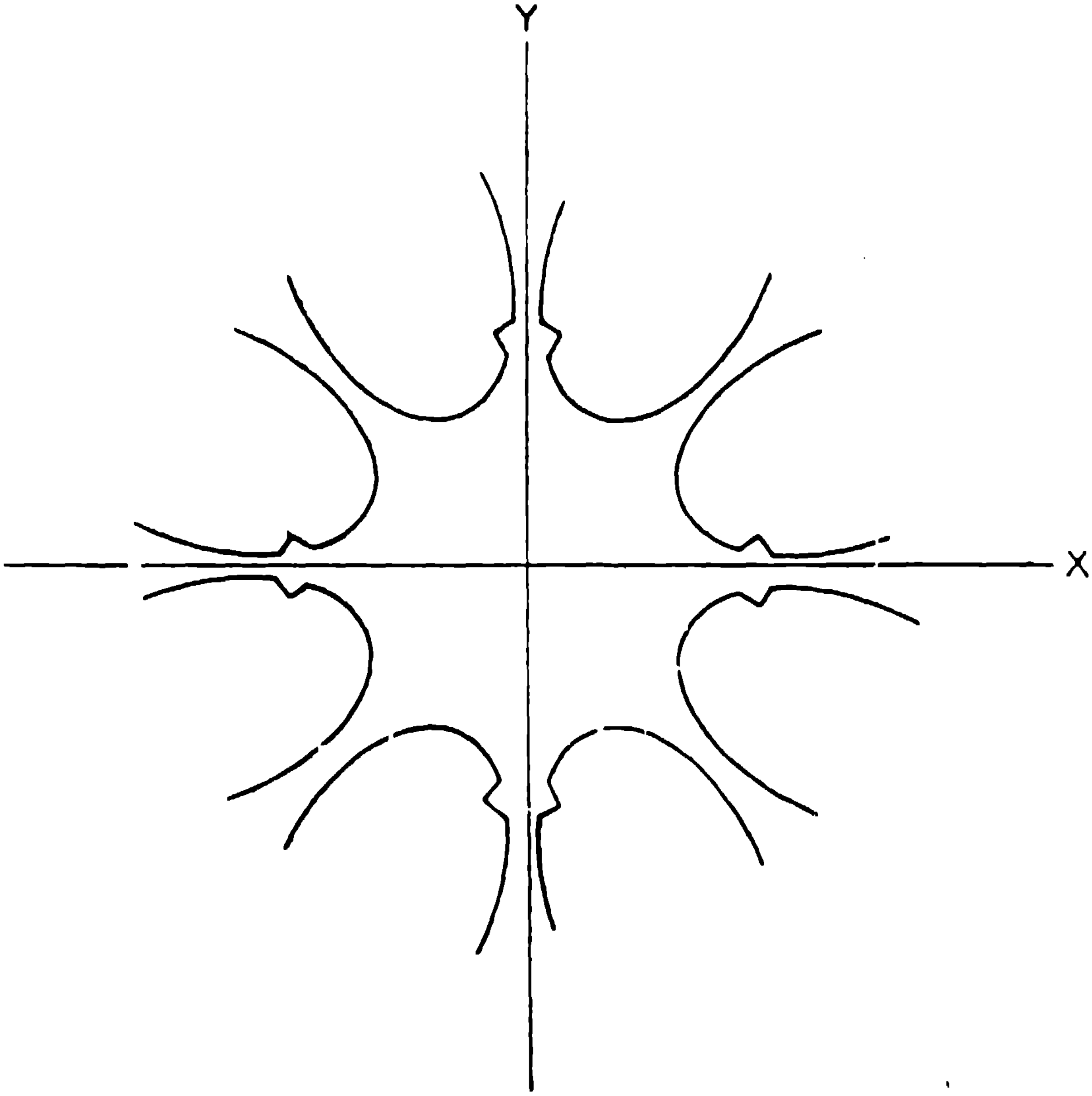

FIG. 3b

XBL 694 4825

4.U L

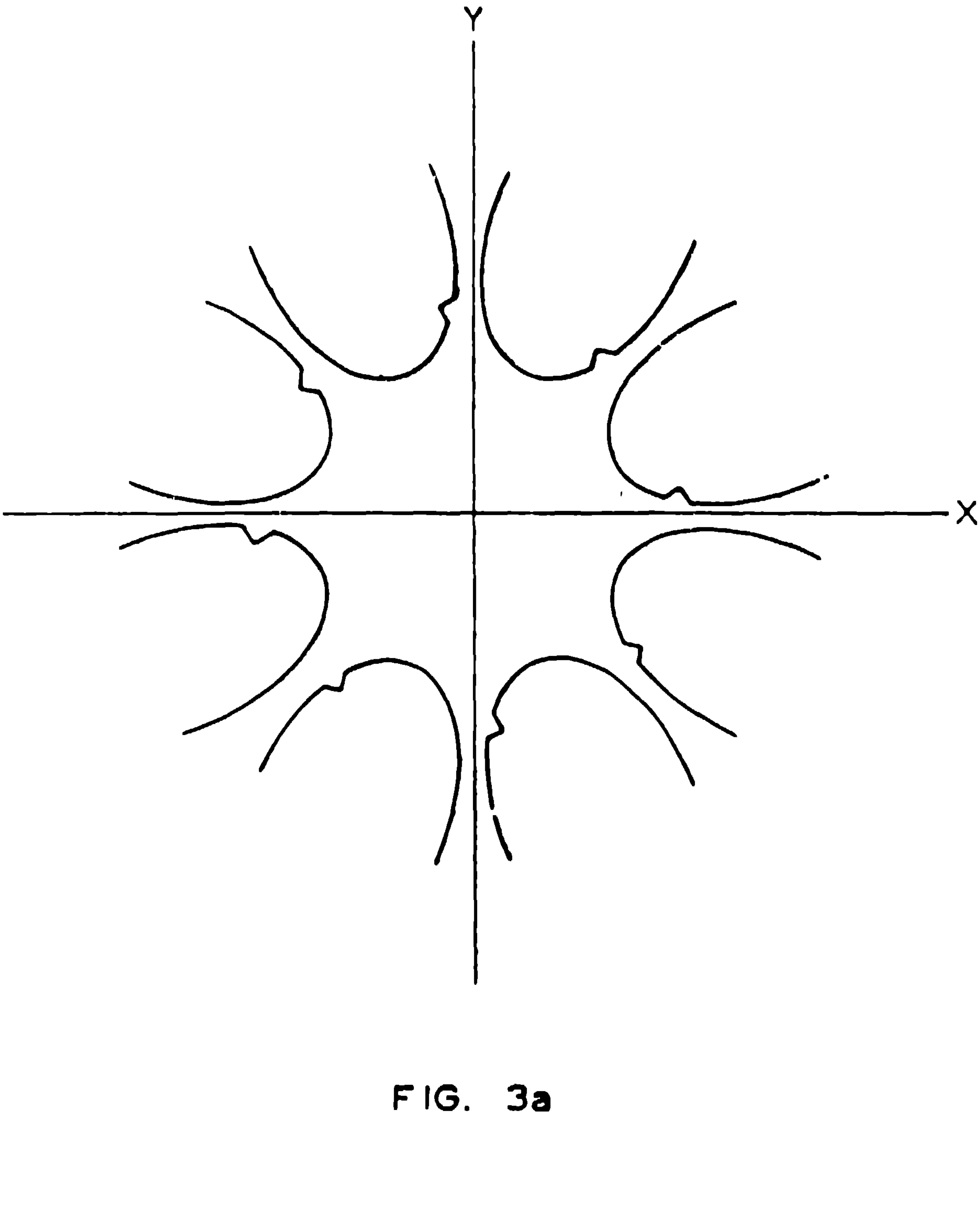

FIG. 3a

XBL 694 4824

This is NOT the
way to do it.

same cross sec-
length.

$= \frac{1}{2} \cdot \frac{\mu_0 I}{B\varrho}$

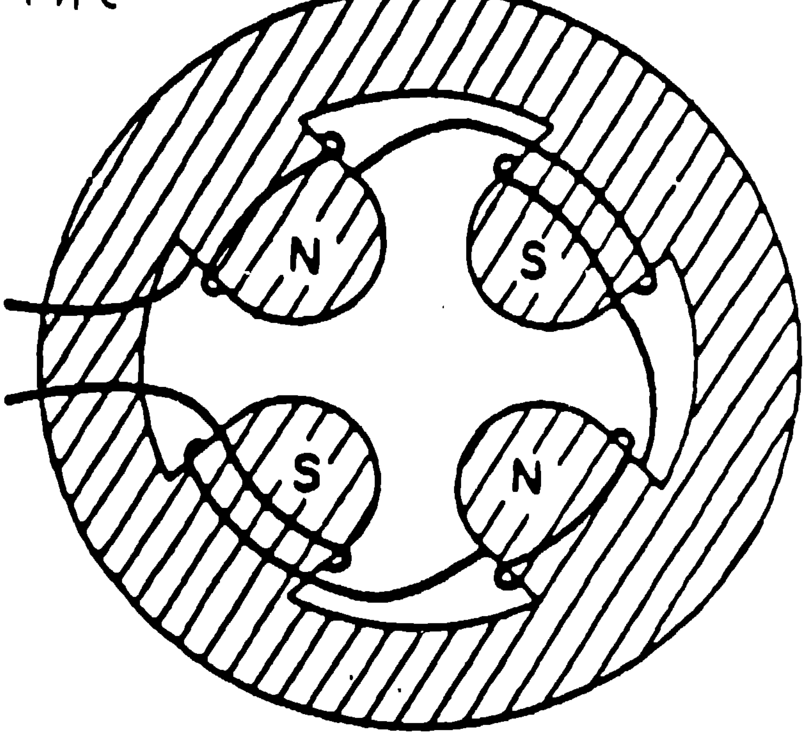

This is the correct
way to do it.

same cross sec-
length.

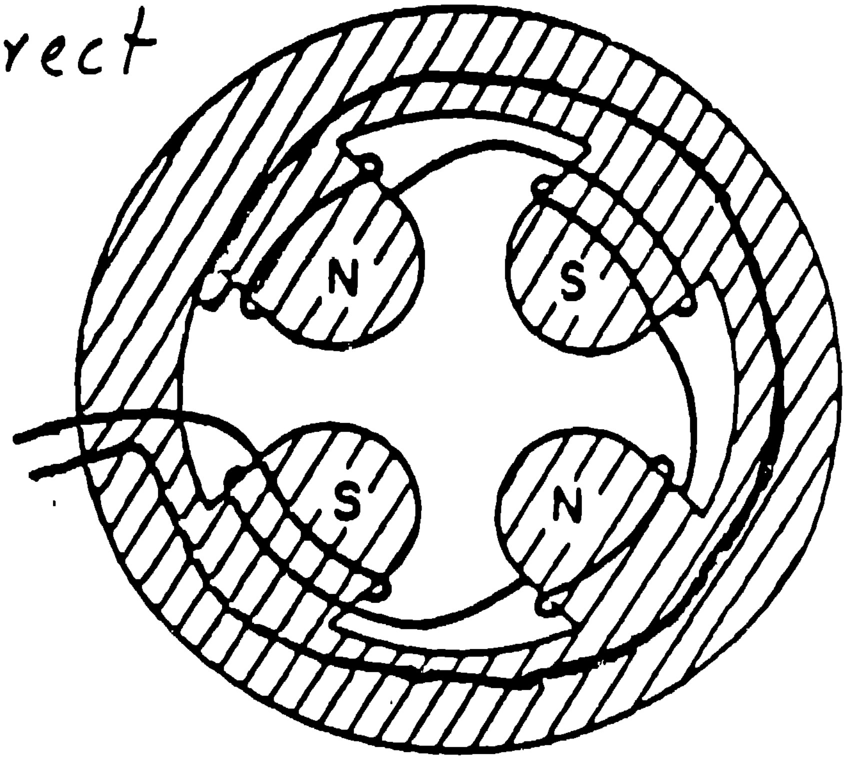

T.1)

Notation: $\mathcal{L}\,F(z) = \int_{-\infty}^{\infty} F(z)\, e^{-pz}\, dz = f(p)$

$$\mathcal{L}^{-1} f(p) = \int_{-i\infty+c}^{i\infty+c} f(p)\, e^{pz}\, dp/2\pi i = F(z)$$

Notice: $F^{(n)}(z) = \int f(p)\, p^n\, e^{pz}\, dp/2\pi i$

$$\mathcal{L}\, F^{(n)}(z) = p^n f(p) = p^n\, \mathcal{L} F(z)$$

Solution to (3.4)

) $v_n(r, k) = J_n(rk) \cdot C(k)$

coefficient for term $\sim I_n(rk)$ must be $=0$
since $I_n(x)$ blows up at origin.

) $J_n(x) = \frac{(x/2)^n}{n!} \Lambda_n(x)$ (Jahnke-Emde notation)

) $\Lambda_n(x) = 1 - \frac{x^2/4}{1!\,(n+1)} + \frac{(x^2/4)^2}{2!\,(n+1)(n+2)} - \frac{(x^2/4)^3}{3!\,(n+1)(n+2)(n+3)} + - + -$

"Absorb" $(k/2)^n/n!$ in $C(k) \longrightarrow g_n(k)$

) $v_n(r, k) = r^n \underbrace{\Lambda_n(rk)\, g_n(0, k)}_{g_n(r, k)}$

7) $v_n(r, k) = r^n g_n(r, k)$

0) $g_n(r, k) = \Lambda_n(rk)\, g_n(0, k)$

4) Use and exploitation of (3.9), (3.10), #1: expansion in r^2

Apply $\mathcal{L}^{-1}$ to (3.9), (3.10):

$$V_n = \mathcal{L}^{-1} v_n = r^n G_n(r,z) \tag{4.1}$$

$$G_n(r,z) = \left(1 - \frac{r^2 \partial^2/\partial z^2}{4(n+1)} + \frac{r^4 \partial^4/\partial z^4}{16 \cdot 2 \cdot (n+1)(n+2)} - + \right) G_n(0,z) \tag{4.2}$$

"gradient" on axis.

Comments to (4.2)

- (4.2) reflects again fact that z-integral over 3D fields satisfy 2D field equations.
- (4.2) should be used with caution, because calculating fields far from axis from gradient on axis <u>can</u> be dangerous. Degree of danger depends on how gradient on axis was determined.
- Semantic / technical point: I characterize multipolarity with n in $\sin(n\varphi + \alpha_n)$, <u>not</u> with power of r. Specific example:

in quad potential,

3) $V_2 \cos 2\varphi = \cos 2\varphi \left(r^2 G_2(0,z) - r^4 G_2''(0,z)/12 + - \right)$,

term $\sim r^4$ has nothing to do with octupole. This fact restricts possibility to correct this aberration with genuine octupole.

- To get feeling for consequences of 3. order aberration in fringe field of quad, ask simple question: what transverse kick is experienced by particle on straight trajectory through fringe field region?

Answer: in skew coordinate system,

1) $\Delta p_x / e = -\frac{B'}{2} \cdot y_0' \left(x_0^2 + (x_0'^2 R^2) \right)$ $\quad R^2 = \int G_2' z^2 dz$

2) $\Delta p_y / e = -\frac{B'}{2} x_0' \left(y_0^2 + (y_0'^2 R^2) \right)$

Trajectories: $x = x_0 + x_0' \cdot z$; $y = y_0 + y_0' \cdot z$

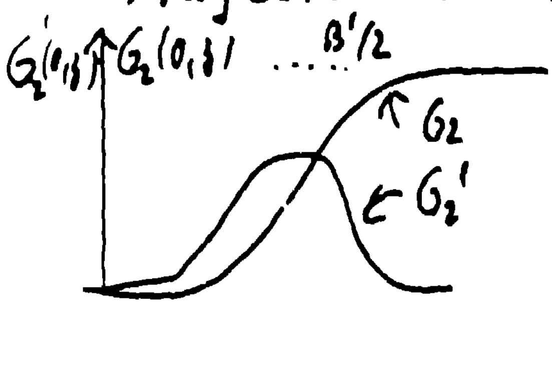

$z = 0$ chosen so that $\int z G_2' dz = 0$

for iron free CSEM quad: $R = \sqrt{r_1 r_2}/2$

$$\dot{\vec{p}} = e(\vec{v} \times \vec{B}) \; ; \quad x = x_0 + x_0' z \; ; \; y = y_0 + y_0' \cdot z$$

$$\Delta p_x / e = \int (\dot{y} B_z - \dot{z} B_y)\, dt = y_0' \cdot \int B_z \, dz - \int B_y \, dz$$

$\mu_0 V = r^2 \cos 2\varphi \, (G_2 - r^2 G_2''/12)$ in <u>skew</u> system!

$$\mu_0 V = (x^2 - y^2) G_2 - (x^4 - y^4) G_2''/12$$

To take only 3. order terms:

$$B_x = x^3 G_2''/3 \; ; \; B_y = - y^3 G_2''/3 \; ; \; B_z = (y^2 - x^2) G_2'$$

$$\Delta p_x / e = \underbrace{\int \frac{y^3}{3} G_2'' \, dz}_{} + y_0' \cdot \int (y^2 - x^2) G_2'$$

$$\underbrace{\frac{y^3}{3} G_2' \Big|}_{=0} - y_0' \cdot \int y^2 G_2' \, dz$$

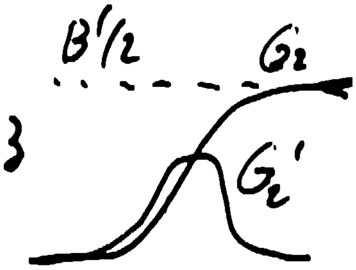

$$\Delta p_x / e = - y_0' \int (x_0^2 + 2 x_0 x_0' z + x_0'^2 z^2) G_2' \, dz$$

Chose $z = 0$ such that $\int G_2' \cdot z \, dz = 0$

$\int G_2' \cdot z^2 \, dz = B'/2 \cdot R^2$; R^2 of order r_{ap}^2

$$\Delta p_x / e = - \frac{B'}{2} \cdot y_0' (x_0^2 + x_0'^2 R^2)$$

$$\Delta p_y / e = - \frac{B'}{2} x_0' (y_0^2 + y_0'^2 R^2)$$

Comments and conclusions

- The largest contribution from $x_0'^2 R^2$ or $y_0'^2 R^2$ will always be much smaller than the largest contribution from x_0^2 or y_0^2, so for many cases, the term with R^2 can be ignored
- Total "damage" = sum from entrance and exit
- For quad of given integrated strength $B' \cdot L$, 3. order aberrations are $\sim 1/L$

5) Magnetic field measurement/characterization priorities

1) Allowed and forbidden harmonics inside
2) Allowed and forbidden harmonics integrated over whole length
3) Fundamental as function of z
4) Allowed harmonics as function of z

Comments

- Bearing and similar problems cause mainly contamination of $n =$ fundamental ± 1. Therefore: Null measurements for inside and length-integrated measurements
- Fringe field measurements are easy to "digest" when one measures $B_\varphi(r, \varphi, z)$, since that leads directly to V.

6) Use and exploitation of (3.9), (3.10), method #2: direct use of $B_\varphi(r_0, \varphi, z)$ (r_0 = "large") to get 3D fields

$$v_n(r, k) = \Lambda_n(rk) \cdot g_n(0, k)$$

$$V_n(r_0, k) = \Lambda_n(r_0 k)\, g_n(0, k)$$

$$(6.1) \quad g_n(0, k) = V_n(r_0, k) / \Lambda_n(r_0 k)$$

$$(6.2) \quad v_n(r, k) = V_n(r_0, k) \cdot \Lambda_n(rk) / \Lambda_n(r_0 k)$$

(6.2) can be used (FFT) to calculate 3D field for $r < r_0$ from measured $V_n(r_0, k)$, (6.1) = special case: gradient on axis

- Notice: if one likes to think in terms of convolution integrals, it is useful to notice that the zeroes of $\Lambda_n(x)$ are the same as those of $J_n(x)$
- This approach was implemented by Chris Morris in 197?

γ) Use and exploitation of (3.9),(3.10), method #3: Exact calculation of 3D fields from analytical function $G_n(0,z)$

Presented in some talks, but never published; never executed in detail, but looks very promising

.1 $$G_n(r,z) = \mathcal{L}^{-1}\, \Lambda_n(r p)\cdot g_n(0,p)$$

γ.1) $$G_n(r,z) = \frac{4^n (n!)^2}{(2n)!}\cdot\frac{2}{\pi}\int_0^{\pi/2} \mathrm{Re}\, G_n(0, z + i r\sin\varphi)\cdot\cos^{2n}\varphi\, d\varphi$$

γ.2) $$G_n(r,z) = \frac{4^{n+1}(n!)^2}{(2n)!\,\pi}\cdot\int_0^1 \mathrm{Re}\, G_n\left(0, z + i r\frac{2u}{1+u^2}\right)\left(\frac{1-u^2}{1+u^2}\right)^{2n}\frac{du}{1+u^2}$$

Form of expression shows clearly that $G_n(0,z)$ must be analytical, because how else could $G_n(0,z)$ be evaluated for complex argument; even piece-meal analytical expressions won't do.

(γ.2) can be used to design "ideal" multipole. To do it, one has to be clever/artful to invent appropriate $G_n(0,z)$

)

$$\mathcal{L}^{-1}\, \Lambda_n(r p)\, g_n(0,p) = G_n(r,z)$$

Use integral representation of $\Lambda_n(rp)$:

$$\Lambda_n(x) = 2 C_n \int_0^1 (1-\lambda^2)^{n-1/2} \cdot \cos(x\lambda)\, d\lambda$$

$\uparrow$ uninteresting numerical factor

$$G_n(r,z) = C_n \int_{-i\infty}^{i\infty} \int^1 (1-\lambda^2)^{n-1/2} \left(e^{irp\lambda} + e^{-irp\lambda}\right) e^{pz} g_n(0,p)\, d\lambda\, \frac{dp}{2\pi i}$$

integrate over p first:

$$G_n(r,z) = C_n \int_0^1 (1-\lambda^2)^{n-1/2} \Big(G_n(0, z+ir\lambda) + G_n(0, z-ir\lambda)\Big)\, d\lambda$$

$\lambda = \sin\varphi$

$$G_n(r,z) = 2 C_n \int_0^{\pi/2} \operatorname{Re} G_n(0, z+ir\sin\varphi) \cdot \cos^{2n}\varphi\, d\varphi$$

Determine C_n from condition $G_n(0,z) = G_n(0,z)$.

$$G_n(r,z) = \frac{4^n (n!)^2}{(2n)!} \frac{2}{\pi} \cdot \int_0^{\pi/2} \operatorname{Re} G_n(0, z+ir\sin\varphi) \cdot \cos^{2n}\varphi\, d\varphi$$

To actually evaluate fast, use $\tan\varphi/2 = u$:

$$G_n(r,z) = \frac{4^{n+1} (n!)^2}{(2n)! \cdot \pi} \cdot \int_0^1 \operatorname{Re} G_n\left(0, z + ir\frac{2u}{1+u^2}\right) \left(\frac{1-u^2}{1+u^2}\right)^{2n} \frac{du}{1+u^2}$$

8) Methods to determine $G_n(0,z)$

8.1) For R^2 in (4.4), measuring gradient "close" to axis is adequate

8.2) Feel less comfortable with 1) for actual ray tracing involving derivatives of $G_2(0,z)$

8.3) Measure $B_\varphi \to V$ at large r_0 and get from that gradient and derivatives on axis. o.k. for ray tracing with expansion in r^2 (if that approach is good enough)

8.4) "Invent" appropriately structured analytical functions for $G_n(0,z)$; calculate with (7.2) $G_n(r_0,z)$, and determine free parameters in $G_n(0,z)$ such that a good fit is obtained for the measured $G_n(r_0,z)$. For any magnet, this needs to be only done once. Calculation of fields should then be easy and fast with (7.2). I have some ideas of some suitable functions [eg. $1+\tanh(kz)$; $\left(1+\frac{kz}{\sqrt{1+k^2}}\right)^m$, etc.)], but have not done any "real"

8.5) Calculate $G_2(0, z)$ analytically.

Is "easy" to execute in some cases (e.g. iron-free CSEM dipole, quad) because one expands in r and needs to retain only lowest order term $\neq 0$. Can give useful ideas about choice of functions to be used for practical analytical expressions, and some models can give insight into properties of fringe fields.

$$B_y(x) = \cancel{f} f(x)$$

$\cancel{B_x}$ --

$$B_x(x,y) - i B_y(x,y) = -i f(x+iy)$$

$$\frac{1}{1+e^{\Sigma a_n x^n}}$$

$$\frac{1}{(1+a_1 e^{z} + a_2 e^{2z})^n}$$

ANALYSIS OF 3D FIELD DATA

MAGNETIC FIELD DATA

D. E. Lobb
TRIUMF/University of Victoria

---

1) Example system

---

2) Visual assessment of the accuracy of the results

---

3) Self-checking harmonic analysis

a) Comparision of radial and azimuthal field coefficients

b) Harmonic analysis at different radii

---

4) Discussion of properties of orthogonal functions

---

5) Introduction to Chebyshev polynomials

---

6) Chebyshev polynomial fits on the example system

a) Lines

b) Planes

c) Volumes

---

7) Summary

COMMENTS ON TOSCA MODELING

A maximum of 50000 nodes MAY be available.

When quadratic shape functions are used,
the number of non-zero elements in the
main matrix in TOSCA
may exceed memory capacity
for as few as 35000 nodes.

Two dimensional calculations
using PE2D or POISSON:
satisfactory precision may be obtained
using 5000, or 10000, or 15000 nodes.

For a three dimensional calculation,
the XY plane mesh is always coarser
than desired.

PRECISION

In the air gap region,

the field components divided by

some normalization value

can be precise to within 0.001 to 0.0001

THE EXAMPLE SYSTEM ON TOSCA

A boundary value quadrupole configuration.

No iron, no coils

The boundary is tangent to a circle,

centered at the origin,

radius 10 cm.

All nodes lie on or inside

the source surfaces

Total scalar potential values are

available in the region of interest.

(If coils and iron were used

this region would have reduced

scalar potential.)

UNITS: GAUSS, CENTIMETER

T7Q

$0 \leq z \leq 15$

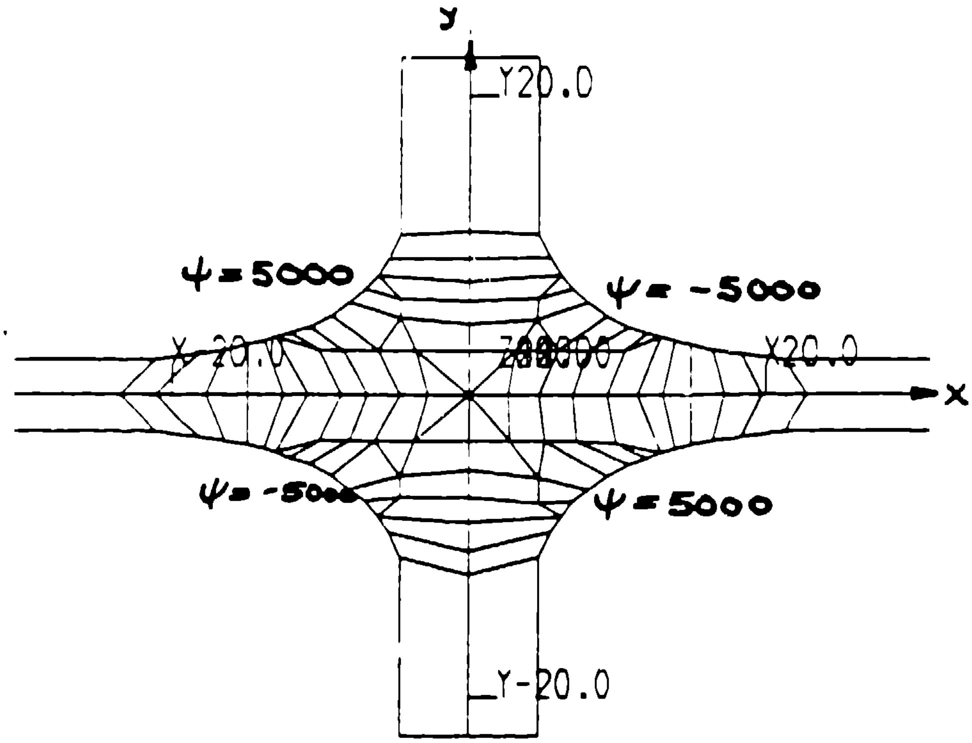

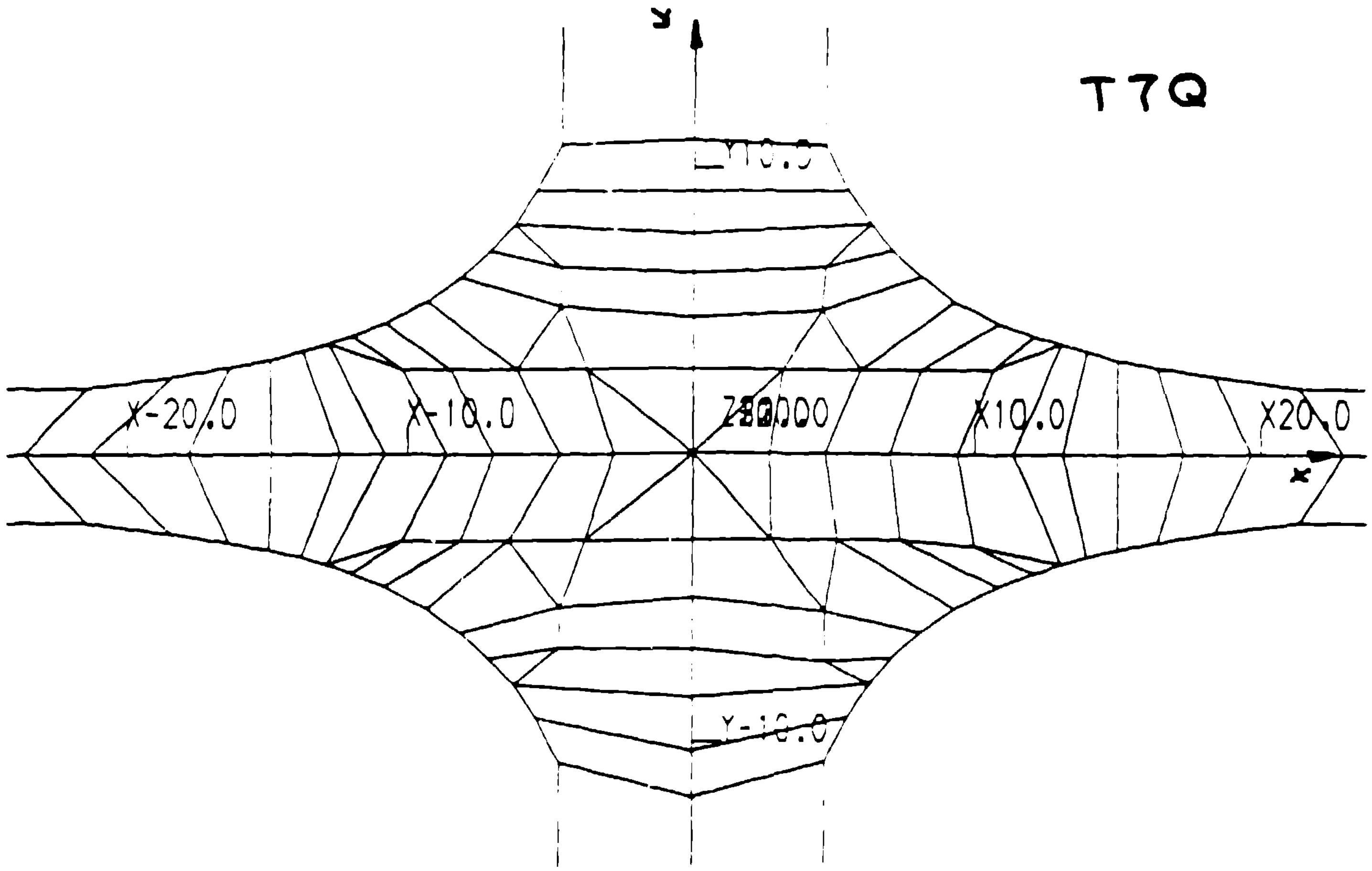
y
T7Q
Y10.0
X-20.0
X-10.0
X10.0
X20.0
x
Y-10.0

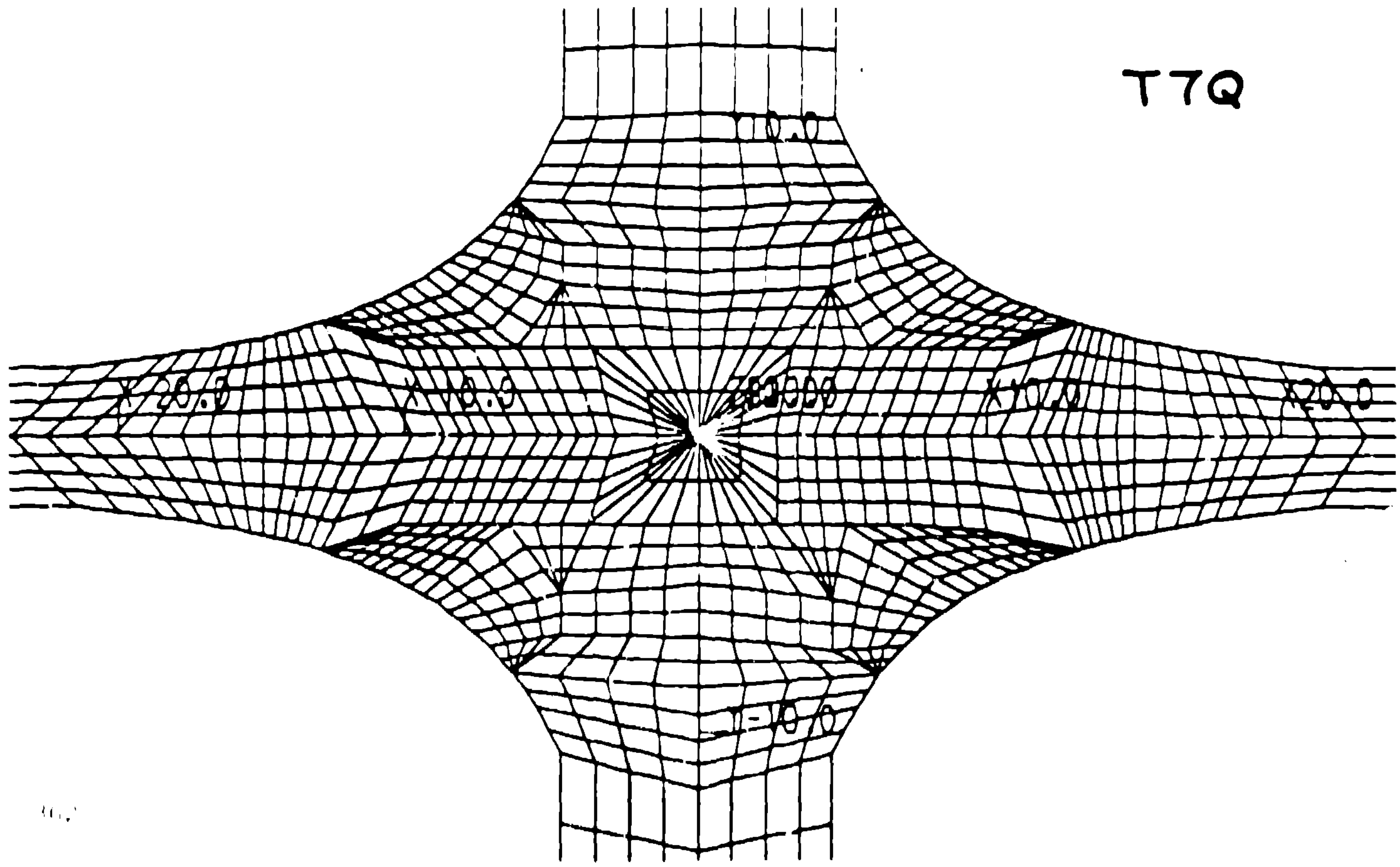
T7Q
Y10.0
X20.0
Y-10.0

VISUAL CHECKING OF CALCULATED FIELD RESULTS

Define a function

that would be constant

for a perfect magnet

Plot this function

For a quadrupole configuration,

a suitable function that tests

the XY plane components is

```
#GRAD=SQRT((HX*HX+HY*HY)/(X*X+Y*Y))
```

1000 segments per line were used

to eliminate any possible error

due to fitting by the plotting routines.

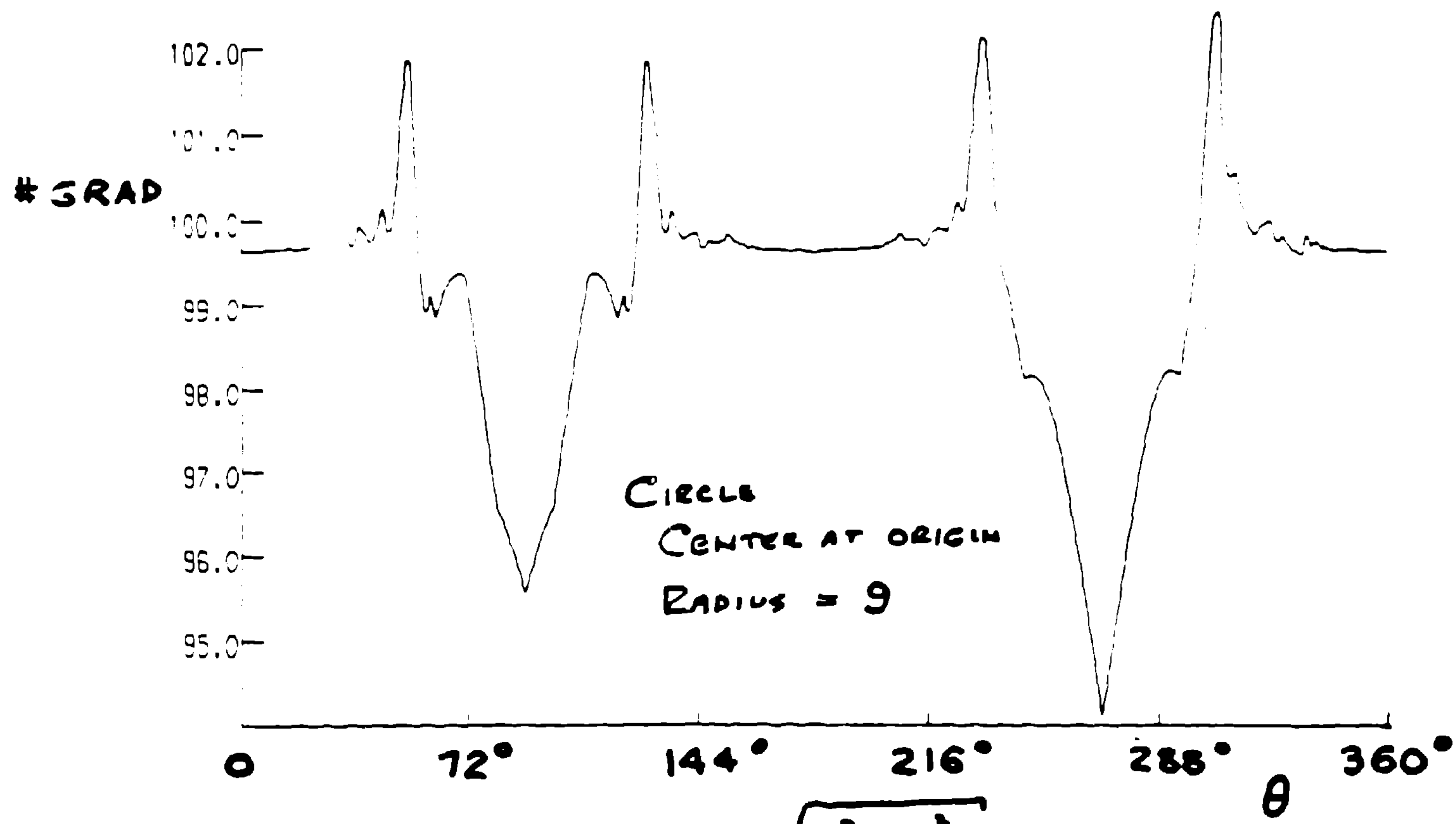

$$\# \text{GRAD} = \sqrt{\frac{H_x^2 + H_y^2}{x^2 + y^2}}$$

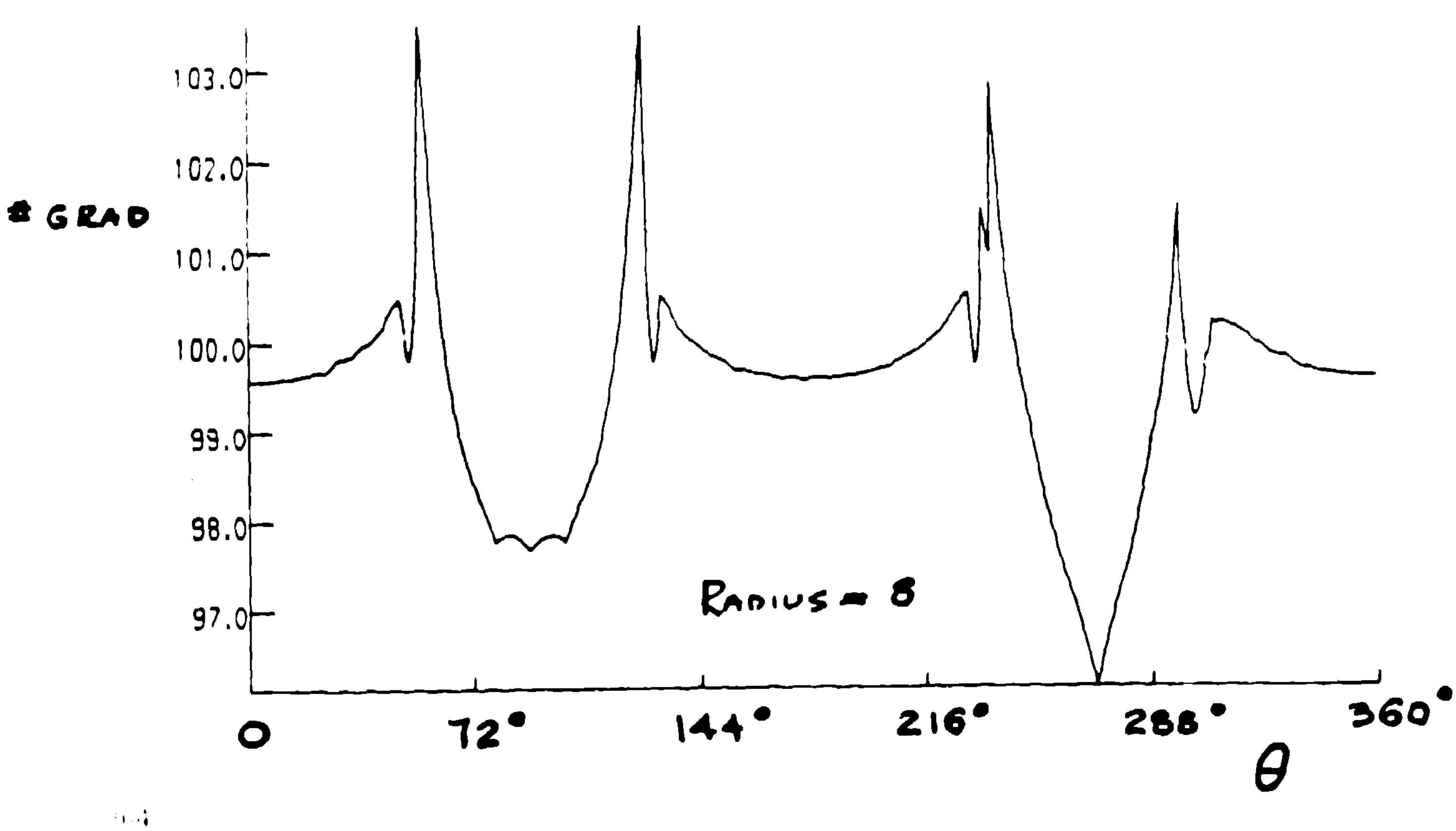

T7Q

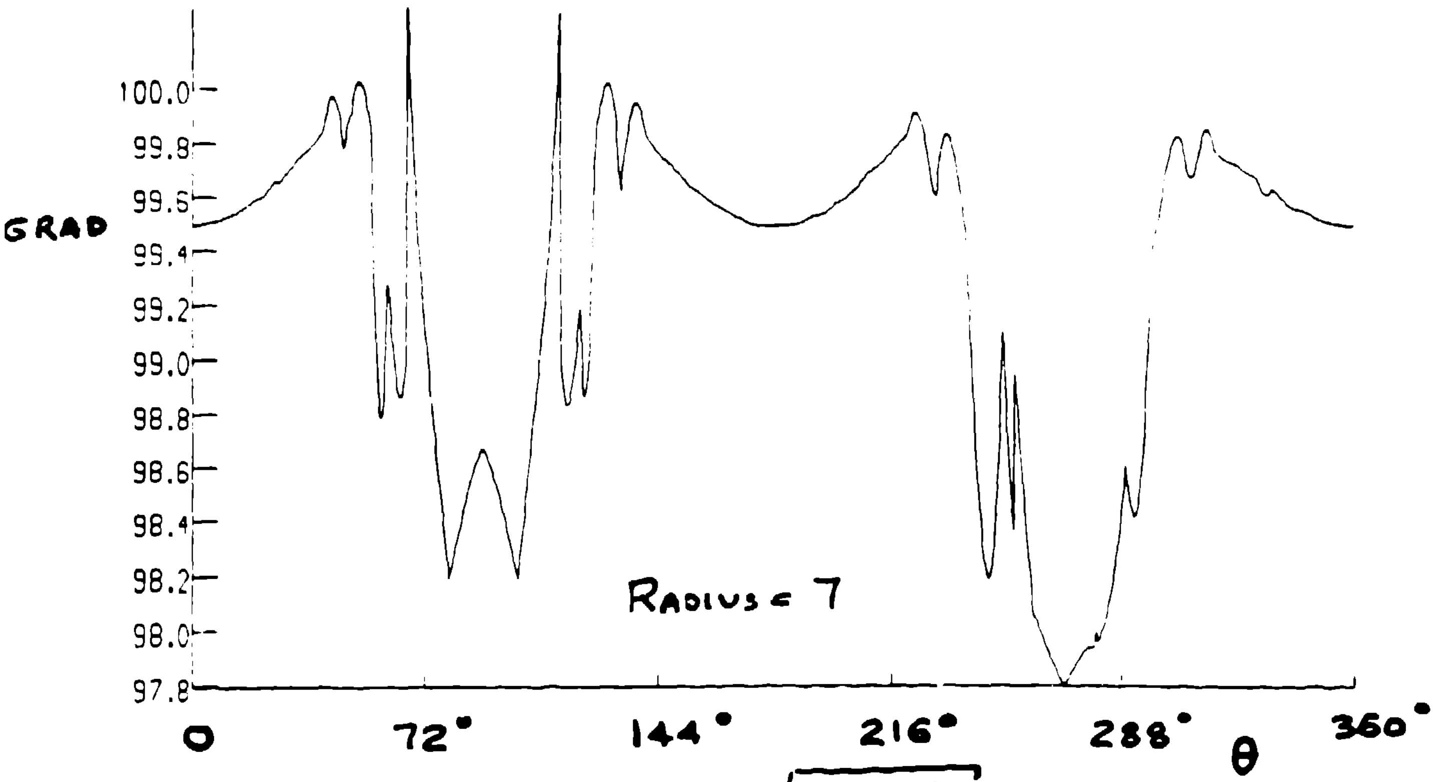

$$\# \text{ GRAD} = \sqrt{\frac{H_x^2 + H_y^2}{x^2 + y^2}}$$

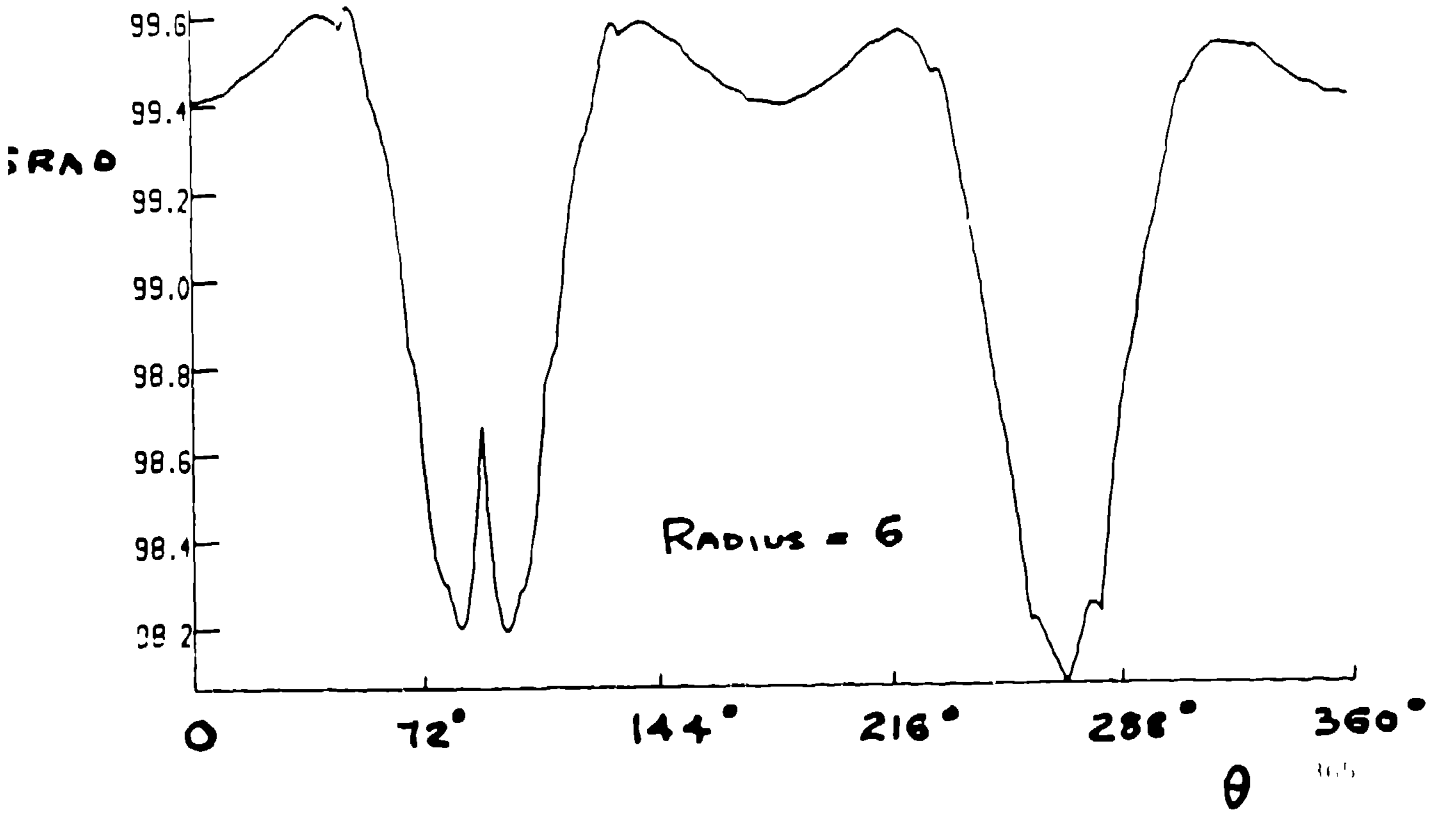

T7Q

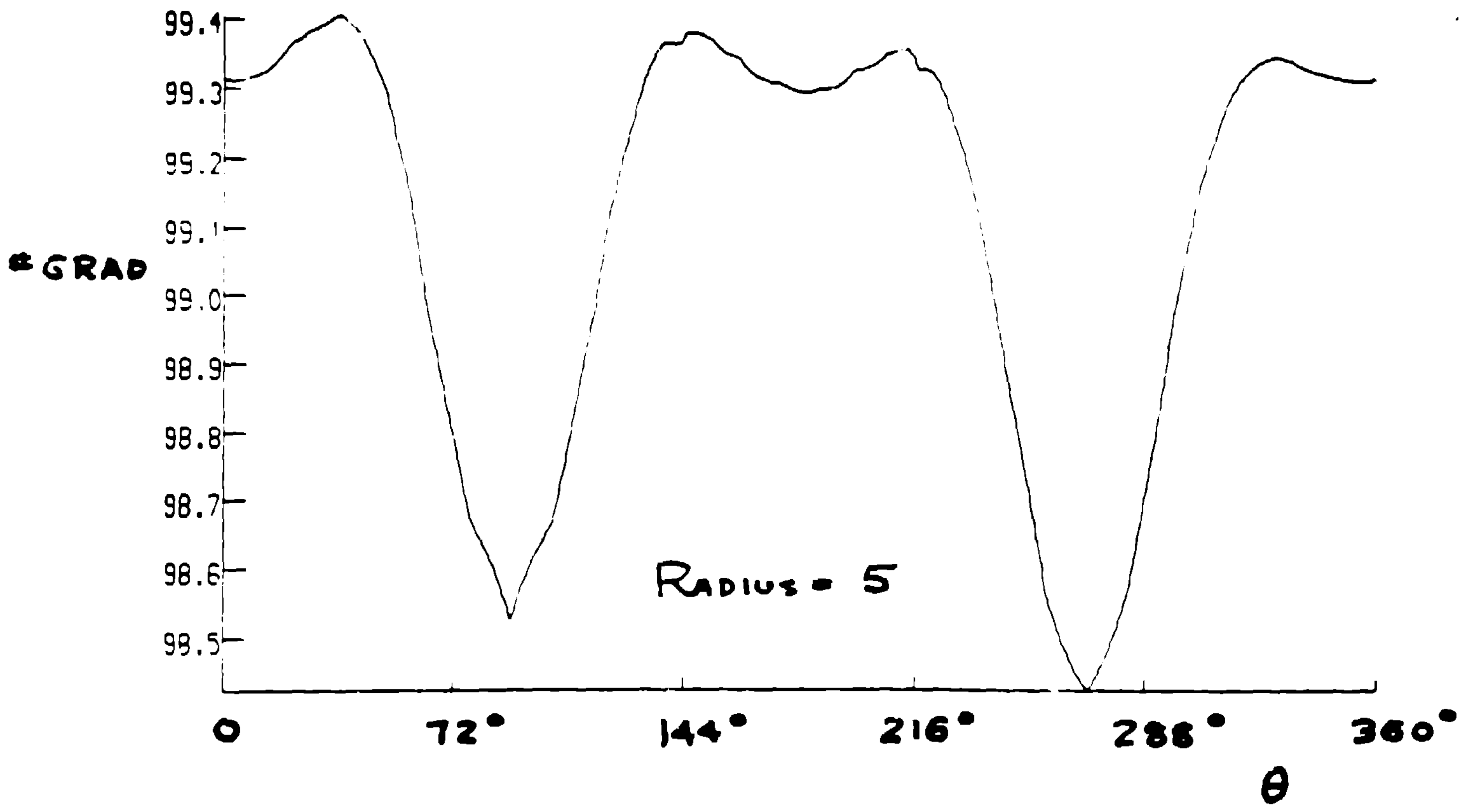
99.4
99.3
99.2
99.1
99.0
98.9
98.8
98.7
98.6
98.5
#GRAD
RADIUS = 5
0
72°
144°
216°
288°
360°
θ

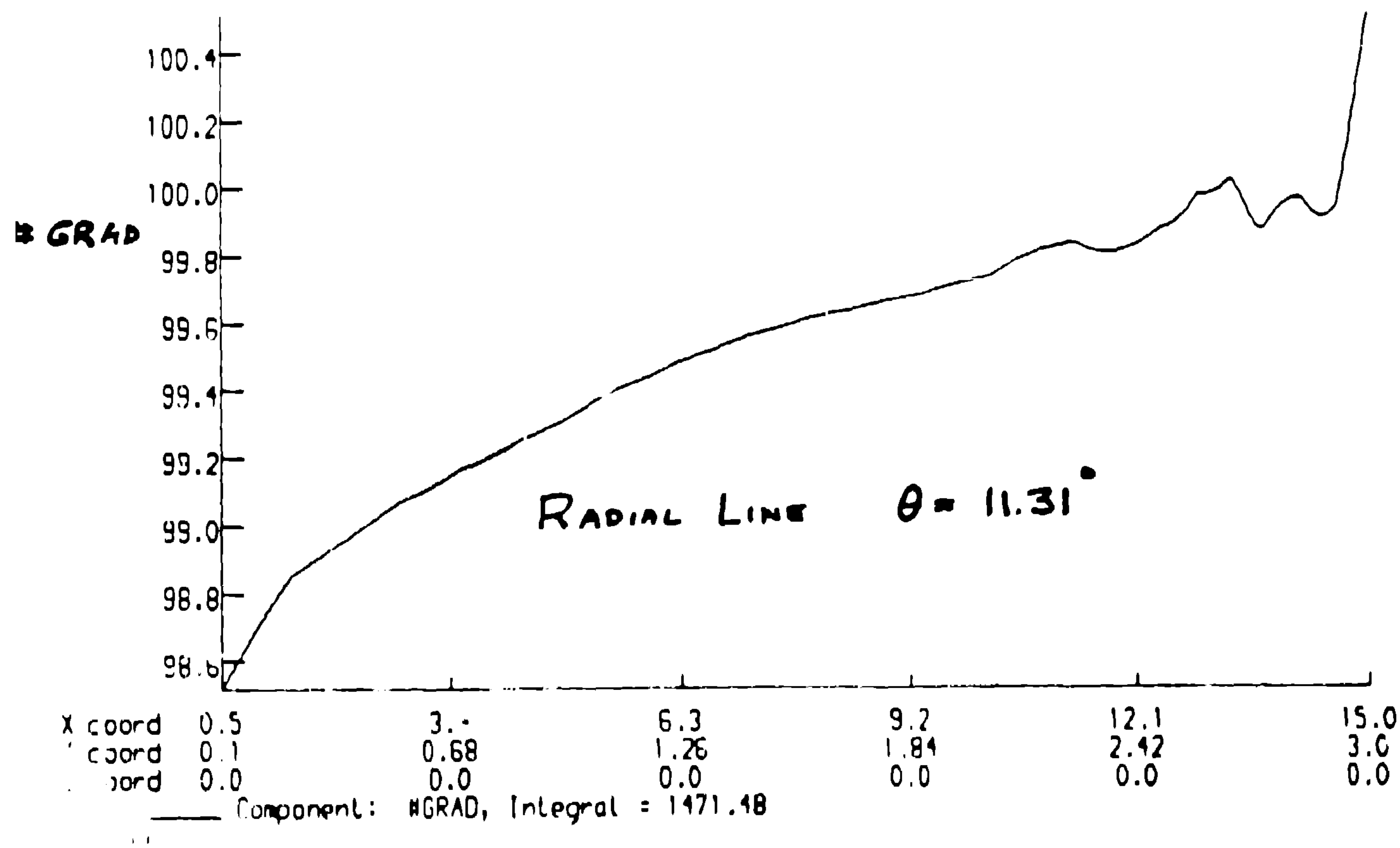
100.4
100.2
100.0
99.8
99.6
99.4
99.2
99.0
98.8
98.6
#GRAD
RADIAL LINE θ = 11.31°
X coord 0.5 3. 6.3 9.2 12.1 15.0
Y coord 0.1 0.68 1.26 1.84 2.42 3.0
Z coord 0.0 0.0 0.0 0.0 0.0 0.0
Component: #GRAD, Integral = 1471.48

HARMONIC ANALYSIS

AT A PARTICULAR VALUE OF Z

THE TERMS OF INTEREST HAVE THE FORM

SCALAR POTENTIAL:	$\left(\frac{r}{a}\right)^{n} \sin n\theta$
RADIAL FIELD:	$\left(\frac{r}{a}\right)^{n-1} \sin n\theta$
AZIMUTHAL FIELD:	$\left(\frac{r}{a}\right)^{n-1} \cos n\theta$

a : NORMALIZATION RADIUS

SELF-CHECKING HARMONIC COEFFICIENTS

The computational programs work in
Cartesian coordinates.

Convert Cartesian field components
into Cylindrical field components.

Calculate the harmonic coefficients
for the radial and azimuthal fields

The two sets of coefficients should
be the same.

Note that harmonic coefficients are obtained
by integration, which smooths data;
the harmonic coefficients are more precise than
the visual examination of #GRAD results
would indicate.

HARMONIC COEFFICIENTS FOR T7Q

100 segments

Calculation radius = Normalization radius = 5 cm

---

rmonic rder	THETA1=0 THETA2=90		THETA1=90 THETA2=180		THETA1=180 THETA2=270		THETA1=270 THETA2=360	
	Rad.	Azi.	Rad.	Azi.	Rad.	Azi.	Rad.	Azi.
2	496.0	495.4	495.9	495.4	495.7	495.0	495.7	495.2
4	1.784	1.783	1.777	1.763	2.027	2.154	1.913	1.934
6	-.718	-.741	-.773	-.756	-.791	-.903	-.800	-.768
8	0.114	0.128	0.137	0.118	0.174	0.282	0.195	0.211
	The coefficients below mainly represent error							
0	0.32	0.021	-.004	0.007	-.001	-.118	-.050	0.001
2	-.011	-.013	-.015	-.032	0.002	0.115	0.015	0.006
4	0.008	0.011	-.018	-.008	-.003	-.108	0.011	0.032
6	0.016	0.007	0.002	-.007	-.009	0.1221	-.020	-.008

We may estimate from above that the field values have a precision of about 3 parts in 5000 (0.06%)

THE MODEL T8QQ (30315 nodes)

The XY geometry defined in first quadrant only

Z = 0 is a symmetry plane

Fine subdivision in Z direction.

Quadratic XY elements

are used in the central region

out to Z = 35

Extrusion plane Z (cm)	Subdivision	Interval
0		
	8	1.875
15		
	6	1.667
25		
	4	2.500
35		
	7	5.714
75		

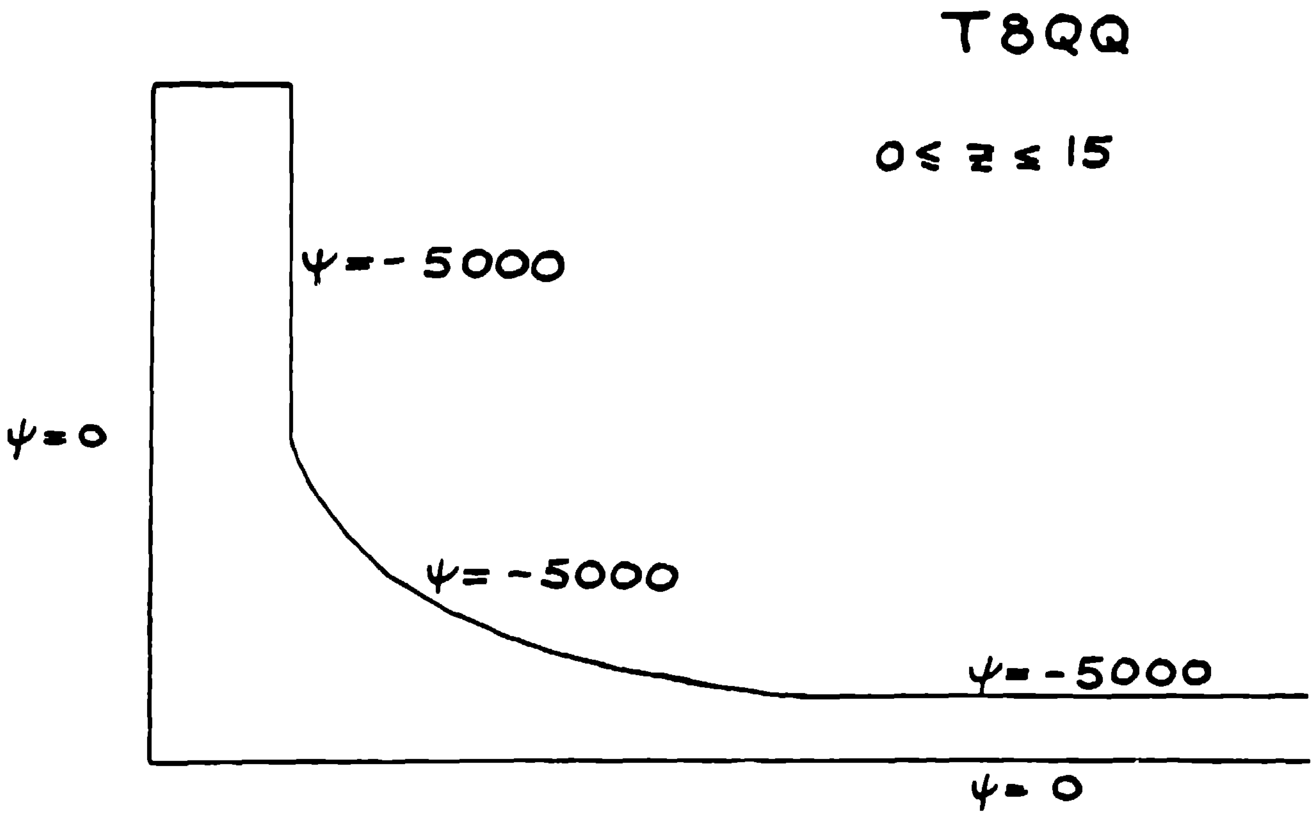
T8QQ
0 ≤ z ≤ 15
ψ = -5000
ψ = 0
ψ = -5000
ψ = -5000
ψ = 0

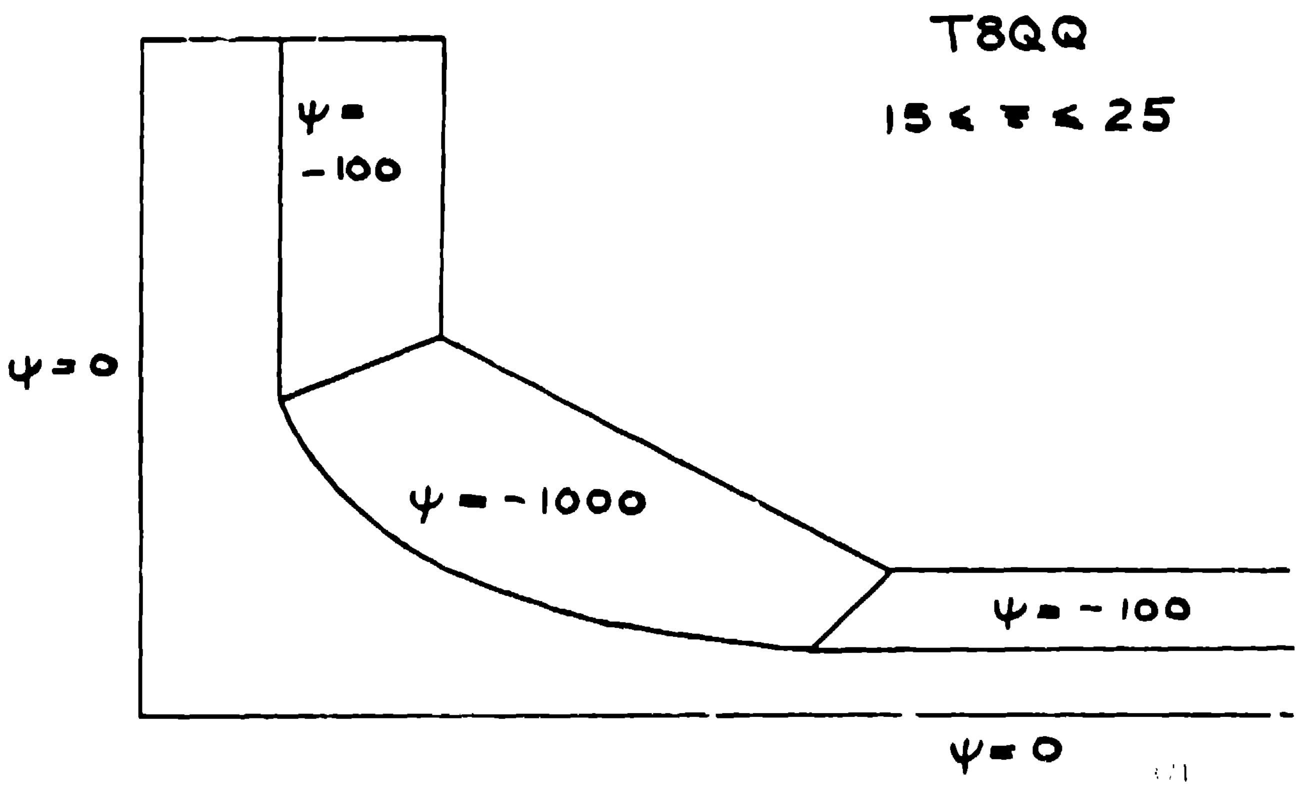
T8QQ
15 ≤ z ≤ 25
ψ =
-100
ψ = 0
ψ = -1000
ψ = -100
ψ = 0

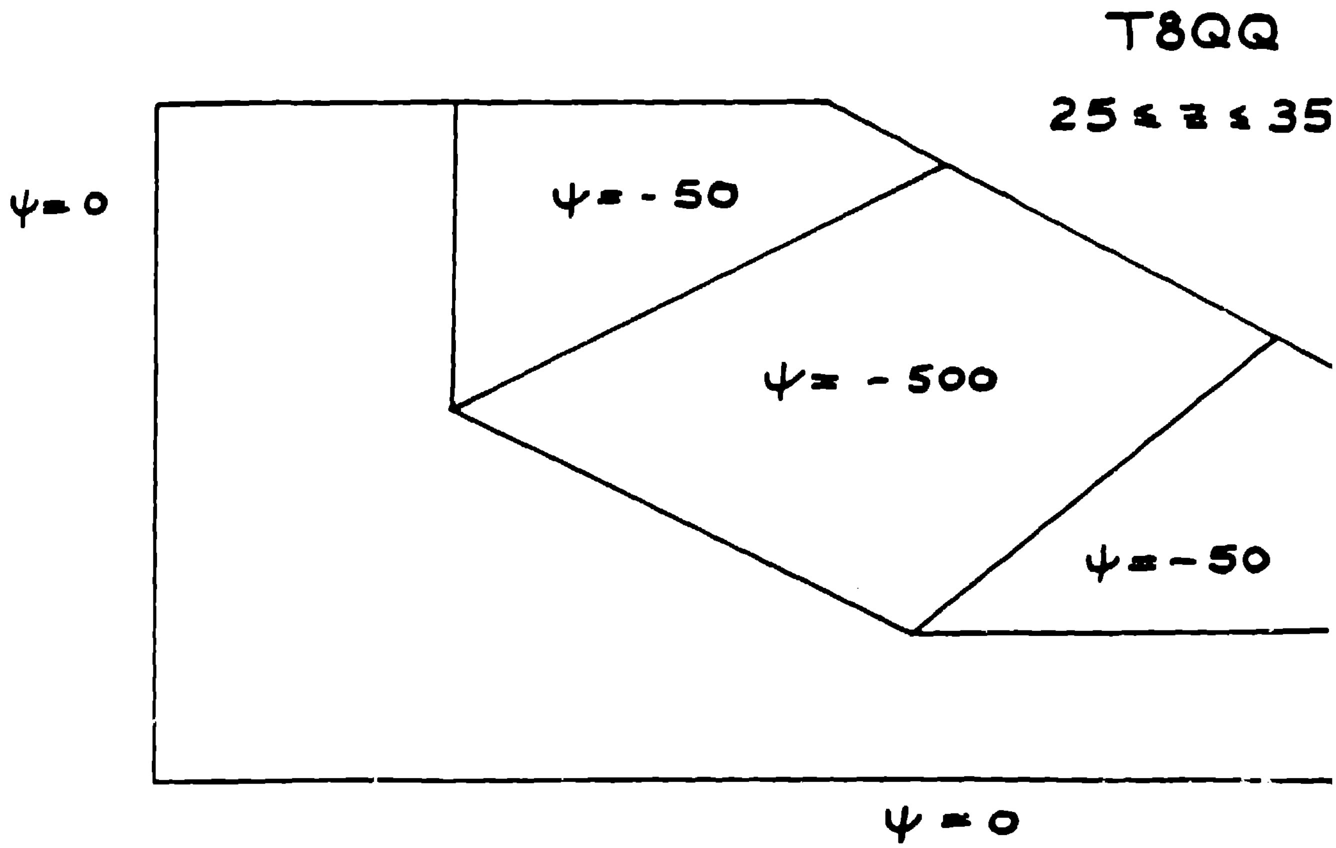
T8QQ
25 ≤ z ≤ 35
ψ = 0
ψ = -50
ψ = -500
ψ = -50
ψ = 0

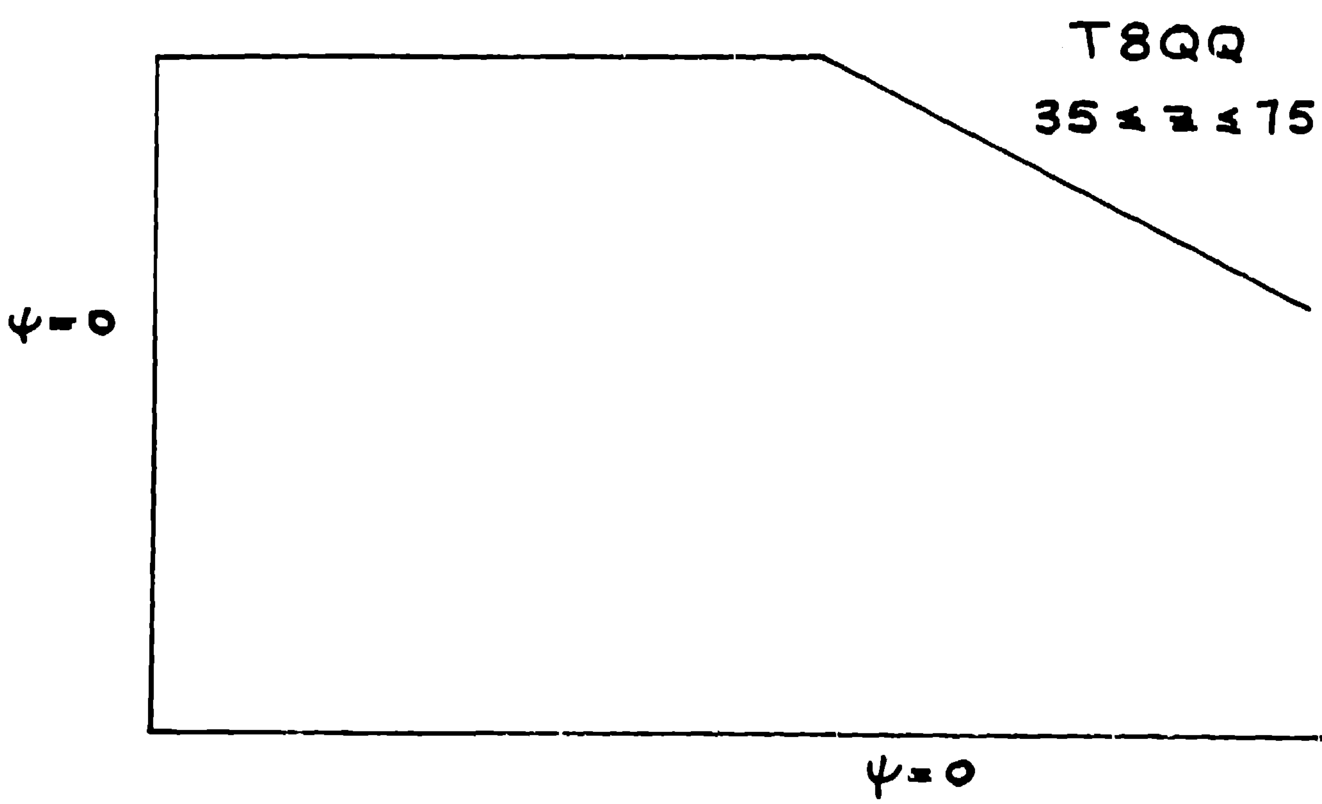
T8QQ
35 ≤ z ≤ 75
ψ = 0
ψ = 0

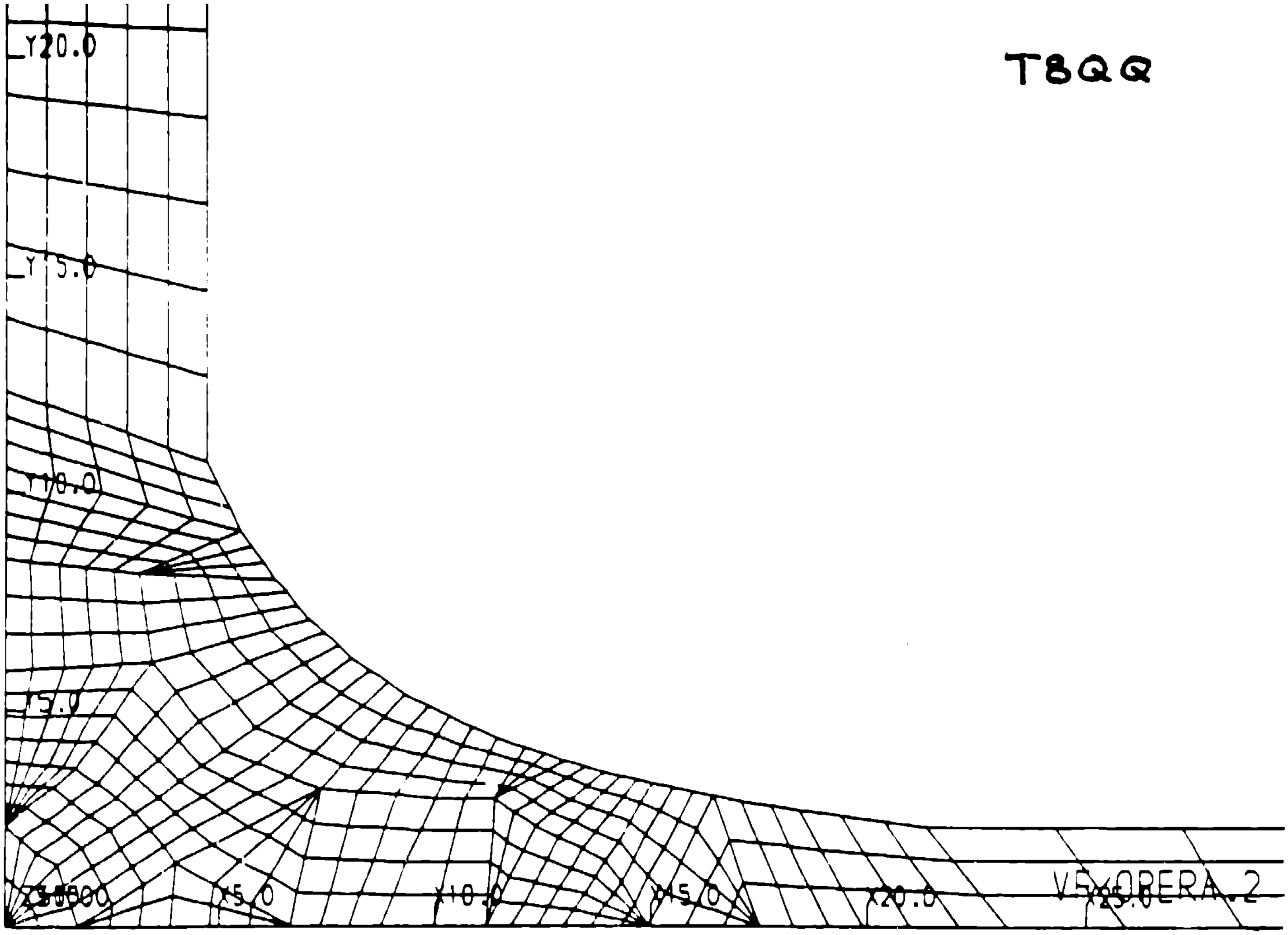
T8QQ
Y20.0
Y15.0
Y10.0
Y5.0
X5.0
X10.0
X15.0
X20.0
OPERA.2

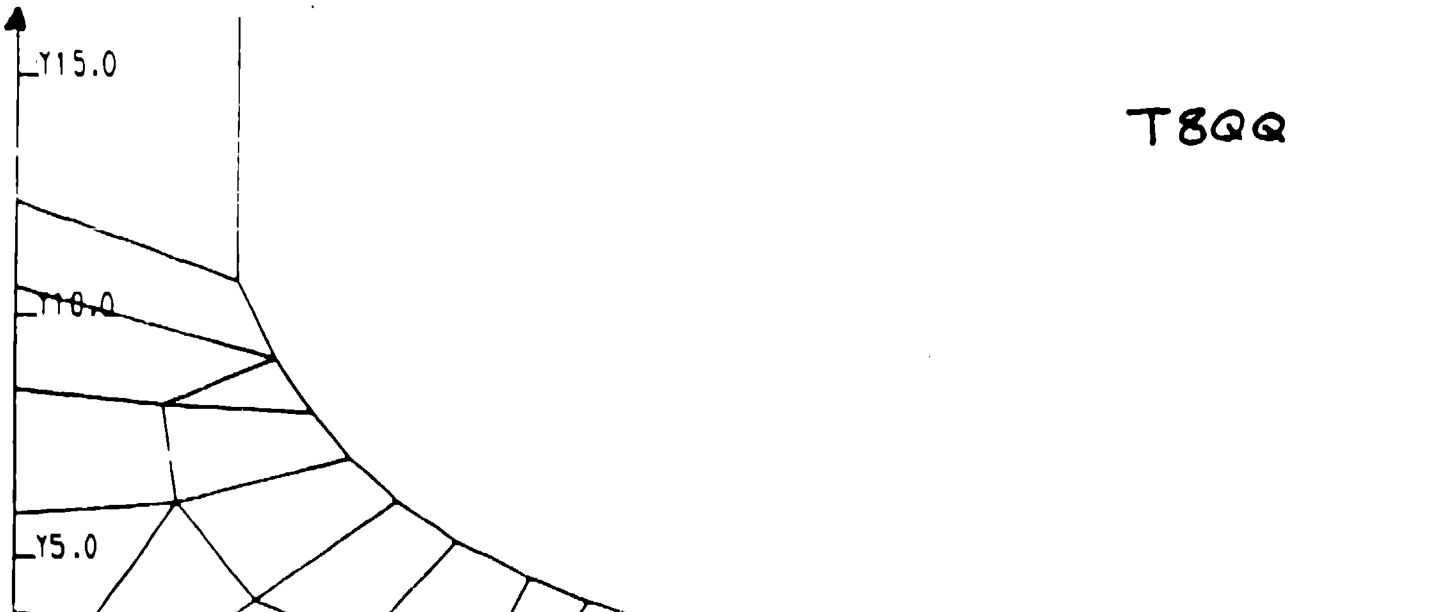
T8QQ
Y15.0
Y10.0
Y5.0
X5.0
X10.0
X15.0
X20.0
OPERA.2

CALCULATION OF HARMONIC COEFFICIENTS AT DIFFERENT RADII

To be done in a region in which the longitudinal

variation is small

Along arcs with radius such that

the arc stays at least one grid element

away from any source

The coefficients expressed in terms

of the same normalization radius

should be the same for small variations

in arc radius

(Small: less than, or about,
the size of a a grid element)

THETA1 = 0, THETA2 = 90 deg, 100 segments

Normalization radius = 5

Harmonic order	r = 4.5		r = 5		r = 5.5	
	Radial	Azimuthal	Radial	Azimuthal	Radial	Azimuthal
2	495.5	495.1	495.7	495.2	495.9	495.3
4	1.892	1.846	1.855	1.877	1.883	1.863
6	-0.6664	-0.7253	-0.7263	-0.6909	-0.6890	-0.7144
8	0.1446	0.0895	0.1135	0.1691	0.1847	0.1552
10	-0.0206	-0.0625	-0.0669	-0.0004	-0.0049	-0.0212
	The coefficients below mainly represent error					
12	-0.0579	-0.0277	-0.0311	-0.0037	0.0002	-0.0038
14	-0.0354	0.0185	0.0110	-0.0031	-0.0015	0.0021
16	-0.0140	0.0961	-0.0048	-0.0134	-0.0069	-0.0003

We may estimate from above that the field values have a precision of about 1 part in 5000 (0.02%) for locations near radius = 5

ORTHOGONAL FUNCTIONS

EXAMPLES:

NAME	SYMBOL	LOWER LIMIT (a)	UPPER LIMIT (b)	WEIGHTING FUNCTION r
SINUSOID	$e^{in\theta}$	0	2π	1
	$\sin n\theta$	0	2π	1
	$\cos n\theta$	0	2π	1
CHEBYSHEV POLYNOMIAL	$T_n(x)$	-1	$+1$	$\frac{1}{\sqrt{1-x^2}}$
	$U_{n-1}(x)$	-1	$+1$	$\sqrt{1-x^2}$

WRITE: $\phi_n(x)$ A MEMBER OF A FAMILY OF ORTHOGONAL FUNCTIONS

NORMALIZATION: $\|\phi_n\|_r = \int_a^b r(x)\,\phi_n^*(x)\,\phi_n(x)\,dx$

ORTHOGONALITY:

$$\int_a^b r(x)\,\phi_m^*(x)\,\phi_n(x)\,dx = \|\phi_n\|_r\,\delta_{mn}$$

For electric and magnetic fields in source-free space,
potential and field functions are continuous
with continuous derivatives to all orders.
(This is a property of Coulomb's Law and Biot-Savart Law;
actual fields are superpositions of Coulomb and/or
Biot-Savart fields.)

Therefore, we may write our functions of interest
as expansions in a particular family of
orthogonal functions.

$$f(x) = \sum_{n=0}^{\infty} C_n \, \phi_n(x)$$

($f(x)$ REAL, C_n MAY BE COMPLEX)

MULTIPLY BOTH SIDES BY $r(x)\ \phi_m^*(x)\,dx$,

INTEGRATE FROM a TO b:

$$\int_a^b r(x)\ \phi_m^*(x)\ f(x)\,dx = \sum_{n=0}^{\infty} c_n \int_a^b r(x)\ \phi_m^*(x)\ \phi_n(x)\,dx$$

$$= \sum_{n=0}^{\infty} c_n \|\phi_n\|_r\ \delta_{mn} = c_m \|\phi_m\|_r$$

$$\boxed{\begin{array}{l} c_m = \dfrac{1}{\|\phi_m\|_r} \displaystyle\int_a^b r(x)\ \phi_m^*(x)\ f(x)\,dx \\[2ex] \text{INDEPENDENT OF THE OTHER } c_n\text{'s} \end{array}}$$

$$c_m^* = \frac{1}{\|\phi_m\|_r} \int_a^b r(x)\ \phi_n(x)\ f(x)\,dx$$

WE <u>APPROXIMATE</u> A FUNCTION BY

A TRUNCATED SERIES:

$$\bar{f}(x) = \sum_{n=0}^{N} a_n\ \phi_n(x)$$

SHOULD $a_n = c_n \quad n = 0, 1, \cdots, N$??

Choose TO MINIMIZE THE WEIGHTED INTEGRATED SQUARED ERROR

$$\Delta_N = \int_a^b r(x)\left[f(x) - \bar{f}_N(x)\right]\left[f(x) - \bar{f}_N^*(x)\right] dx$$

$$= \int_a^b r(x)\, f^2(x)\, dx + \int_a^b r(x)\, f(x)\left[\bar{f}_N(x) + \bar{f}_N^*(x)\right] dx$$

$$+ \int_a^b r(x)\bar{f}_N(x)\, \bar{f}_N^*(x)\, dx$$

THIRD TERM:

$$\int_a^b r(x)\left[\sum_{n=0}^{N}{}' a_n \phi_n(x)\right]\left[\sum_{m=0}^{N}{}' a_m^* \phi_m^*(x)\right] dx$$

$$= \sum_{n=0}^{N} \sum_{m=0}^{N} a_n a_m^* \int_a^b r(x)\, \phi_n(x)\, \phi_m^*(x)\, dx$$

$$= \sum^{N} \sum^{N} a_n a_m^* \, \|\phi_m\|_r \, \delta_{mn}$$

$$= \left[\sum_{m=0}^{N} a_m a_m^*\right] \|\phi_m\|_r = \|\phi_m\|_r \sum_{m=0}^{N} |a_m|^2$$

SECOND TERM:

$$\int_a^b r(x) f(x) : \left\{ \sum_{n=0}^{N} \left[a_n \phi_n(x) + a_n^* \phi_n^*(x) \right] \right\} dx$$

$$= \sum_{n=0}^{N} a_n \int_a^b r(x) f(x) \phi_n(x) \, dx$$

$$+ \sum_{n=0}^{N} a_n^* \int_a^b r(x) f(x) \phi_n^* \, dx$$

$$= \sum_{n=0}^{N} \left\{ \left[a_n c_n^* + a_n^* c_n \right] \| \phi_n \|_r \right\}$$

$$= \sum_{m=0}^{N} \left\{ \left[a_m c_m^* + a_m^* c_n \right] \| \phi_m \|_r \right\}$$

THIRD TERM PLUS SECOND TERM

$$= \left\{ \sum_{m=0}^{N} \left[a_m c_m^* + a_m^* c_m + a_m a_m^* \right] \| \phi_m \|_r \right\}$$

$$= \left\{ \sum_{m=0}^{N} \left[\left(c_m c_m^* + a_m c_m^* + a_m^* c_m + a_m a_m^* \right) - c_m c_m^* \right] \| \phi_m \|_r \right.$$

$$= \sum_{m=0}^{N} (c_m - a_m)(c_m - a_m)^* \| \phi_m \|_r$$

$$- \sum_{m=0}^{N} c_m c_m^* \| \phi_m \|_r$$

So: $$\Delta_N = \left\{ \int_a^b r(x)\, f^2(x)\,dx - \sum_{m=0}^{N} |c_m|^2 \cdot \|\phi_m\|_r \right\}$$

$$+ \sum_{m=0}^{N} |c_m - a_m|^2 \|\phi_m\|_r$$

$$\boxed{\text{THE BEST FIT ACCORDING TO THE CHOSEN CRITERION IS } \Delta_N\Big]_{min} \text{ FOR } a_m = c_m \quad m = 0, 1, \cdots, N}$$

FOR $a_m = c_m \qquad m = 0, 1, \cdots, N$

$$\underbrace{\Delta_N}_{\geq 0} = \underbrace{\int_a^b r(x)\, f^2(x)\,dx}_{\text{NOT A FUNCTION OF } N} - \underbrace{\sum_{m=0}^{N} |c_m|^2 \cdot \|\phi_m\|_r}_{\text{ALL TERMS} \geq 0}$$

$$\lim_{N \to \infty} \sum_{m=0}^{N} |c_m|^2 \cdot \|\phi_m\|_r = \int_a^b r(x)\, f^2(x)\,dx$$

THEREFORE, SERIES ON L.H.S. ABOVE <u>CONVERGES</u>.

$$f(x) = \sum_{n=0}^{\infty} c_n \phi_n(x) = \sum_{m=0}^{\infty} c_m^* \phi_m^*(x)$$

(SINCE $f(x)$ IS REAL)

$$f^2(x) = \sum_{n=0}^{\infty} \sum_{m=0}^{\infty} C_n C_m^* \phi_n(x) \phi_m^*(x)$$

$$\int_a^b r(x) f^2(x)\,dx = \sum_{n=0}^{\infty} \sum_{m=0}^{\infty} C_n C_m^* \int_a^b r(x) \phi_n(x) \phi_m^*(x)\,dx$$

$$= \sum_{n=0}^{\infty} \sum_{m=0}^{\infty} C_n C_m^* \|\phi_m\|_r \delta_{nm}$$

$$= \sum_{m=0}^{\infty} C_m C_m^* \|\phi_m\|_r = \sum_{m=0}^{\infty} |C_m|^2 \cdot \|\phi_m\|$$

$$\Delta_N = \int_a^b r(x) f^2(x)\,dx - \sum_{m=0}^{N} |C_m|^2 \cdot \|\phi_m\|_r$$

$$= \sum_{m=0}^{\infty} |C_m|^2 \cdot \|\phi_m\|_r - \sum_{m=0}^{N} |C_m|^2 \cdot \|\phi_m\|_r$$

$$= \sum_{m=N+1}^{\infty} |C_m|^2 \cdot \|\phi_m\|_r$$

$$\boxed{\Delta_M = \sum_{m=N+1}^{\infty} |C_m|^2 \cdot \|\phi_m\|_r}$$

INCREASE N: Δ_m DECREASES.

Derivatives

Write $\quad g(x, p) \equiv \dfrac{d^p f(x)}{dx^p}$

$$f(x) = \sum_{n=0}^{\infty} c_n \phi_n(x) \longrightarrow g(x,p) = \sum_{n=0}^{\infty} c_n \phi_n^{(p)}(x)$$

Previous results apply to $g(x,p)$:

$\Delta_N]_{min}$ occurs for fitted coefficients equal to theoretical coefficients for $n = 0, 1, \ldots, N$.

Example: Sinusoid $\quad f(\theta) = \sum_{n=0}^{\infty} c_n e^{in\theta}$

$$g(\theta, p) = \sum_{n=0}^{\infty} \left[c_n (i)^p n^p \right] e^{in\theta}$$

Write $\quad b_n = c_n (i)^p n^p$

$$|b_n| = |c_n n^p|$$

FOR THE TRUNCATED FIT TO $g(x, p)$

$$\Delta_N \Big]_{min} = \sum_{m=N+1}^{\infty} |b_m|^2 \cdot \| \phi_m \|_p$$

$$= \sum_{m=N+1}^{\infty}{}' \, |c_m m^p| \cdot \| \phi_m \|_p$$

ALL TERMS IN THE SUM ARE POSITIVE.

$$|c_m m^p| > |c_m| \qquad m = N+1, \ldots, \infty$$

THE TRUNCATED FIT TO THE DERIVATIVE IS WORSE (OR MUCH WORSE) THAN THE SAME ORDER TRUNCATED FIT TO THE ORIGINAL FUNCTION.

RECTANGULAR APERTURE

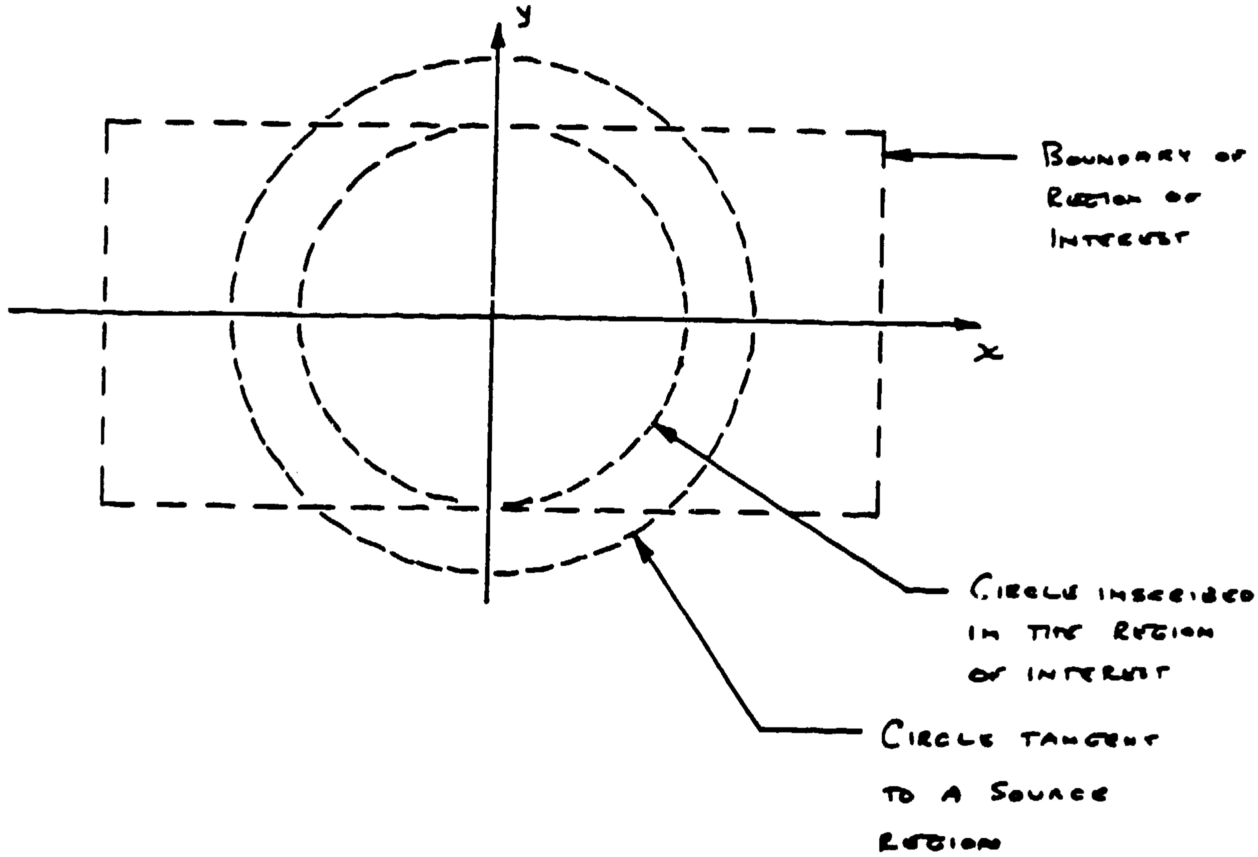

BECAUSE OF THE RADIAL BEHAVIOR $\left(\frac{r}{a}\right)^n$ AND $\left(\frac{r}{a}\right)^{n-1}$,

<u>EXTRAPOLATION</u> OF HARMONIC COEFFICIENTS

OBTAINED ON EITHER CIRCLE TO THE REGION

BEYOND THAT CIRCLE WILL RESULT IN A

GROWTH OF THE IMPRECISE HIGHER ORDER TERMS

RELATIVE TO THE MORE PRECISE LOWER ORDER TERMS

IN GENERAL 3D FORMULAE:

RADIAL DEPENDENCE : POWER LAWS

AZIMUTHAL DEPENDENCE : SINUSOIDS → EXPRESS AS TAYL
SERIES IN X, Y

AXIAL DEPENDENCE : EXPRESS AS TAYLOR SERIES

↓

3D FORMULAE COULD (IN THEORY) BE WRITTEN

WITH TERMS OF THE FORM $x^m y^n z^p$.

↓

INVERSION RESULTS FOR THE FAMILY OF ORTHOGONAL

POLYNOMIALS $\xi_m(x)$, $\xi_n(y)$, $\xi_p(z)$ ALLOW, IN

THEORY, THE FURTHER CHANGE IN REPRESENTATION

$$x^m y^n z^p \longrightarrow \xi_m(x)\, \xi_n(y)\, \xi_p(z)$$

390

FOLLOWING THIS LINE OF ARGUMENT, WE NOW WRITE

$$\psi(x,y,z) = \sum_{m=0}^{\infty} \sum_{n=0}^{\infty} \sum_{p=0}^{\infty} \alpha_{mnp}\, \xi_m(u)\, \xi_n(v)\, \xi_p(w)$$

$x_1 \le x \le x_2$	$y_1 \le y \le y_2$	$z_1 \le z \le z_2$
$\bar{x} = \dfrac{x_1 + x_2}{2}$	$\bar{y} = \dfrac{y_1 + y_2}{2}$	$\bar{z} = \dfrac{z_1 + z_2}{2}$
$a = \dfrac{x_2 - x_1}{2}$	$b = \dfrac{y_2 - y_1}{2}$	$c = \dfrac{z_2 - z_1}{2}$
$u = \dfrac{x - \bar{x}}{a}$	$v = \dfrac{y - \bar{y}}{b}$	$w = \dfrac{z - \bar{z}}{c}$
$-1 \le u \le +1$	$-1 \le v \le +1$	$-1 \le w \le +1$

SINUSOIDS: OSCILLATE BETWEEN LIMITS $-1, +1$

CAN TELL AT A GLANCE THE ROLE PLAYED BY ANY PARTICULAR COEFFICIENT.

CHEBYSHEV POLYNOMIALS OF THE FIRST KIND.

$T_n(u)$: n^{TH} ORDER POLYNOMIAL

$T_n(1) = 1 \qquad T_n(-1) = (-1)^n$

n EVEN : $T_n(u)$ EVEN : n ODD : $T_n(u)$ ODD

$T_n(u)$ HAS $(n-1)$ EXTREME VALUES IN $-1 < u < +1$

AT $\quad u_k = \cos \frac{k\pi}{n} \qquad k = 1, 2, \cdots, (n-1)$

$u = \cos \xi$

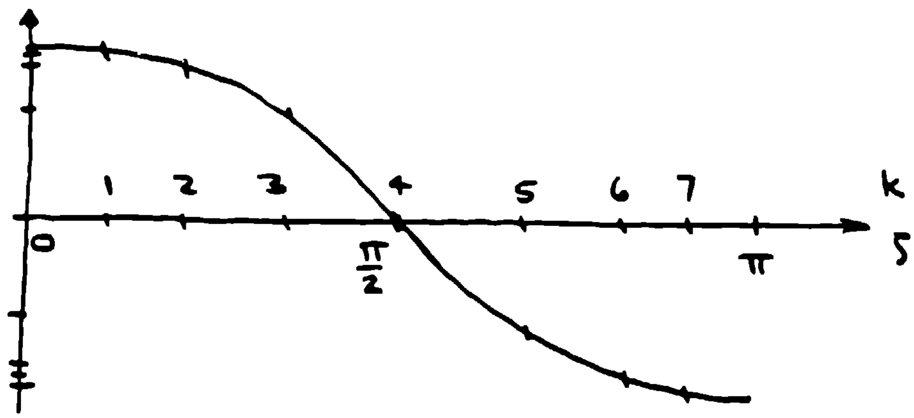

u_k VALUES BUNCHED NEAR $u = \pm 1$,
SPREAD OUT NEAR $u = 0$.

MONOTONIC BEHAVIOR FOR $|u| > 1$

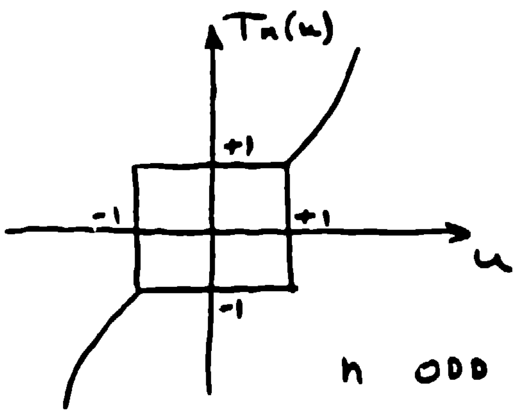

n ODD

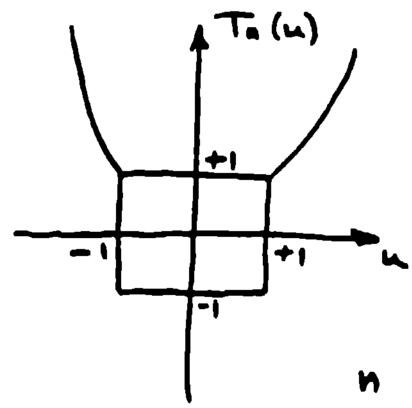

n EVEN

Handbook of Mathematical Functions

With Formulas, Graphs, and Mathematical Tables

Edited by

Milton Abramowitz and Irene A. Stegun

National Bureau of Standards Applied Mathematics Series • 55

Issued June, 1964

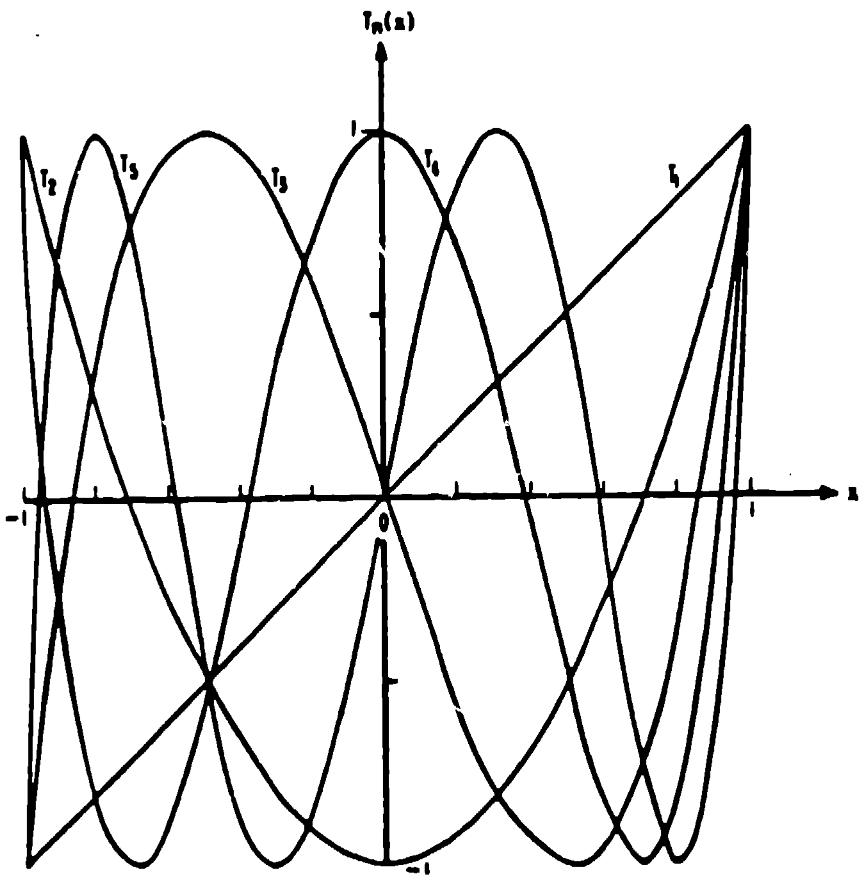

FIGURE 22.6. *Chebyshev Polynomials* $T_n(x)$.

CHEBYSHEV POLYNOMIAL OF SECOND KIND

$$\frac{dT_n}{du} = n\, U_{n-1}(u)$$

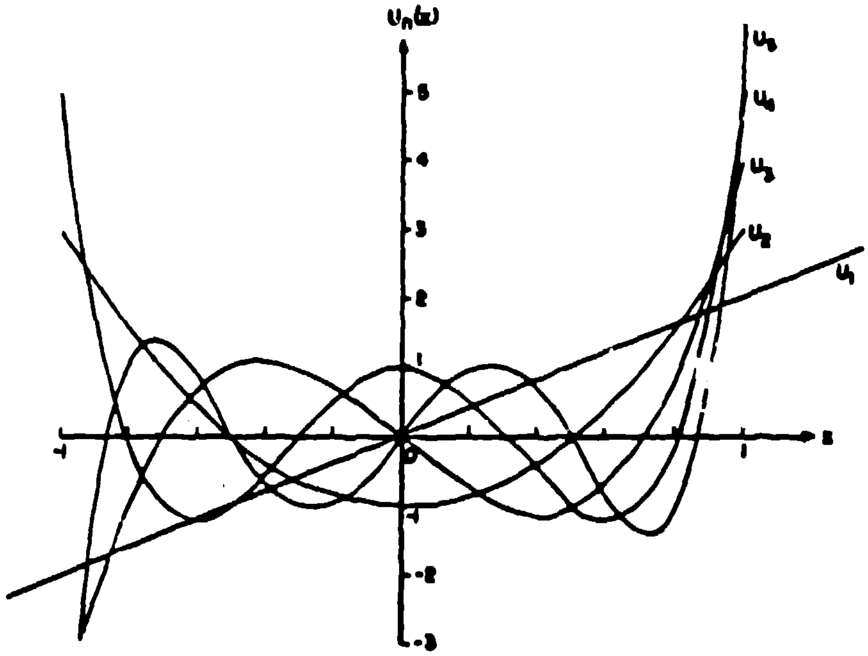

FIGURE 22.7. *Chebyshev Polynomials* $U_n(x)$,

ORTHOGONALITY INTEGRALS

$$\int_{-1}^{+1} T_m(u)\, T_n(u) \frac{du}{\sqrt{1-u^2}} = \begin{cases} \pi & m=n=0 \\ \frac{\pi}{2} & m=n\neq 0 \\ 0 & m\neq n \end{cases}$$

$$\int_{-1}^{+1} U_{m-1}(u)\, U_{n-1}(u) \sqrt{1-u^2}\, du = \frac{\pi}{2}\, \delta_{mn} \qquad \begin{matrix} m>1 \\ n>1 \end{matrix}$$

IN PRACTICE, THE ABOVE WOULD BE APPROXIMATED BY SUMMATIONS ACCORDING TO A PARTICULAR QUADRATURE RULE.

NOTATION : $\sum_{n=0}^{N}{}'' d_n \equiv \frac{d_0}{2} + d_1 + \cdots + d_{N-1} + \frac{d_N}{2}$

SUMMATION ORTHOGONALITY RESULTS

$$\sum_{r=0}^{M}{}'' T_j(u_r)\, T_k(u_r) = \begin{cases} 0 & j \neq k \\ \frac{M}{2} & j = k \neq 0 \text{ OR } j = k \neq M \\ M & j = k = 0 \text{ OR } j = k = M \end{cases}$$

$$\sum_{r=0}^{M}{}'' \left[\sin^2 \frac{\pi r}{M}\right] U_{j-1}(u_r)\, U_{k-1}(u_r) = \begin{cases} 0 & j = k \\ M & j = k \neq 0 \text{ OR } j = k \neq M \\ 0 & j = k = 0 \text{ OR } j = k = M \end{cases}$$

$u_r = \cos\left(\frac{\pi r}{M}\right)$ $\qquad v_s = \cos\left(\frac{\pi s}{N}\right)$ $\qquad w_t = \cos\left(\frac{\pi t}{P}\right)$

$0 \le r \le M$ $\qquad 0 \le s \le N$ $\qquad 0 \le t \le P$

NOTE : LOCATIONS ARE <u>SPECIFIED</u> AND ARE NOT EQUALLY SPACED.

THESE RELATIONSHIPS ARE USED IN THE MATERIAL PRESENTED SUBSEQUENTLY.

MATERIAL WRITTEN UP IN

D.E. LOBB, THE USE OF CHEBYSHEV POLYNOMIALS IN FITTING MAGNETIC FIELD DATA, UVIC TRIUMF REPORT, VPN-88-2, AUGUST 1988 (REVISED JULY 1991)

(A COPY IS AVAILABLE HERE FOR COPYING.)

$$\vec{B} = -\nabla\psi$$

$$B_x = -\partial\psi/\partial x\ , \quad B_y = -\partial\psi/\partial y\ , \quad B_z = -\partial\psi/\partial z$$

IF WE POSTULATE:

$$\psi(x,y,z) = \sum_{m=0}^{M''} \sum_{n=0}^{N''} \sum_{p=0}^{P''} \alpha_{mnp}\, T_m(u)\, T_n(v)\, T_p(w)$$

THEN:

$$B_x(x,y,z) = -\sum_{m=0}^{M''} \sum_{n=0}^{N''} \sum_{p=0}^{P''} \frac{m\, \alpha_{mnp}}{a}\, U_{m-1}(u)\, T_n(v)\, T_p(w)$$

$$B_y(x,y,z) = -\sum_{m=0}^{M''} \sum_{n=0}^{N''} \sum_{p=0}^{P''} \frac{n\, \alpha_{mnp}}{b}\, T_m(u)\, U_{n-1}(v)\, T_p(w)$$

$$B_z(x,y,z) = -\sum_{m=0}^{M''} \sum_{n=0}^{N''} \sum_{p=0}^{P''} \frac{p\, \alpha_{mnp}}{c}\, T_m(u)\, T_n(v)\, U_{p-1}(w)$$

THE COEFFICIENT $\alpha_{\mu\nu\rho}$ MAY BE OBTAINED, IN GENERAL, FROM FOUR <u>INDEPENDENT</u> CALCULATIONS:

$$\alpha_{\mu\nu\rho} = \frac{8}{MNP} \sum_{r=0}^{M}{}'' \sum_{s=0}^{N}{}'' \sum_{t=0}^{P}{}'' T_\mu(u_r)\, T_\nu(v_s)\, T_\rho(w_t)\, \psi(u_r, v_s, w_t)$$

$$\alpha_{\mu\nu\rho} =$$

$$- \frac{8a}{\mu MNP} \sum_{r=0}^{M}{}'' \sum_{s=0}^{N}{}'' \sum_{t=0}^{P}{}'' \sin^2\left(\frac{\pi r}{M}\right) U_{\mu-1}(u_r)\, T_\nu(v_s)\, T_\rho(w_t)\, B_x(u_r, v_s, w_t$$

$$\alpha_{\mu\nu\rho} =$$

$$- \frac{8b}{\nu MNP} \sum_{r=0}^{M}{}'' \sum_{s=0}^{N}{}'' \sum_{t=0}^{P}{}'' T_\mu(u_r) \sin^2\left(\frac{\pi s}{N}\right) U_{\nu-1}(v_s)\, T_\rho(w_t)\, B_y(u_r, v_s, w_t)$$

$$\alpha_{\mu\nu\rho} =$$

$$- \frac{8c}{\rho MNP} \sum_{r=0}^{M}{}'' \sum_{s=0}^{N}{}'' \sum_{t=0}^{P}{}'' T_\mu(u_r)\, T_\nu(v_s) \sin^2\left(\frac{\pi t}{P}\right) U_{\rho-1}(w_t)\, B_z(u_r, v_s, w_t)$$

These formulae can be reduced

to two dimensional formulae

for planes parallel to

XY, or YZ, or ZX coordinate planes

and to one dimensional formulae

for lines parallel to

X, or Y, or Z coordinate axes.

we do not have OPERA source code;

we cannot instruct OPERA to

calculate fields at the desired locations

of a "Chebyshev grid".

Temporary Solution

We generate OPERA data on a finely spaced

grid, we do local quadratic interpolation

of these values to obtain values at

the desired locations.

Another temporary problem

We need to use large values of M, N, and P

in the coefficient calculations so as to

adequately sample the field,

but we need to be able to set to zero

(i.e., not calculate, not use)

coefficients of order higher

than a specified order.

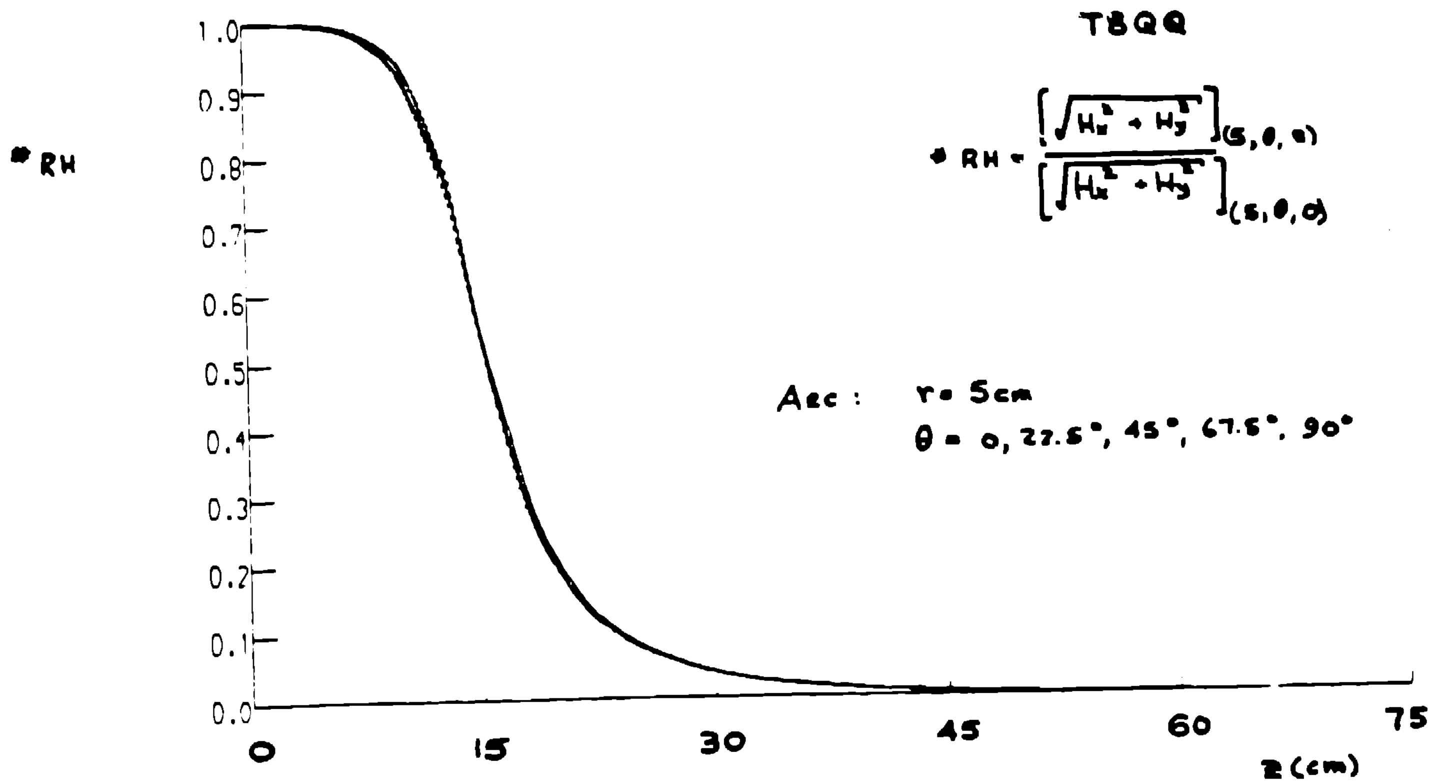
T8QQ
*RH
$$*RH = \frac{\left[\sqrt{H_x^2 + H_y^2}\right]_{(5,\theta,z)}}{\left[\sqrt{H_x^2 + H_y^2}\right]_{(5,\theta,0)}}$$
Arc: r= 5cm
θ = 0, 22.5°, 45°, 67.5°, 90°
1.0
0.9
0.8
0.7
0.6
0.5
0.4
0.3
0.2
0.1
0.0
0
15
30
45
60
75
z (cm)

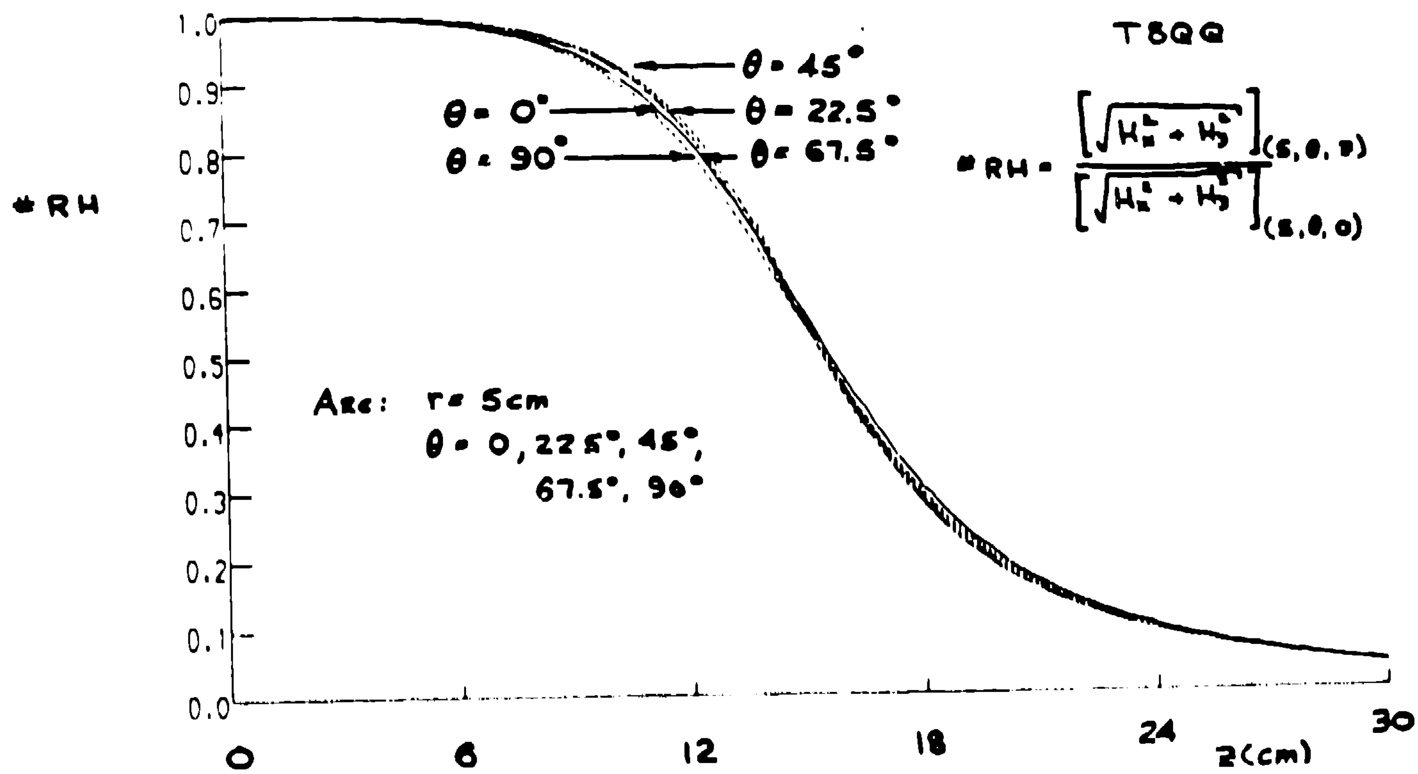
T8QQ
*RH
θ = 45°
θ = 0°
θ = 22.5°
θ = 90°
θ = 67.5°
$$*RH = \frac{\left[\sqrt{H_x^2 + H_y^2}\right]_{(5,\theta,z)}}{\left[\sqrt{H_x^2 + H_y^2}\right]_{(5,\theta,0)}}$$
Arc: r= 5cm
θ = 0, 22.5°, 45°,
67.5°, 90°
1.0
0.9
0.8
0.7
0.6
0.5
0.4
0.3
0.2
0.1
0.0
0
6
12
18
24
30
z(cm)

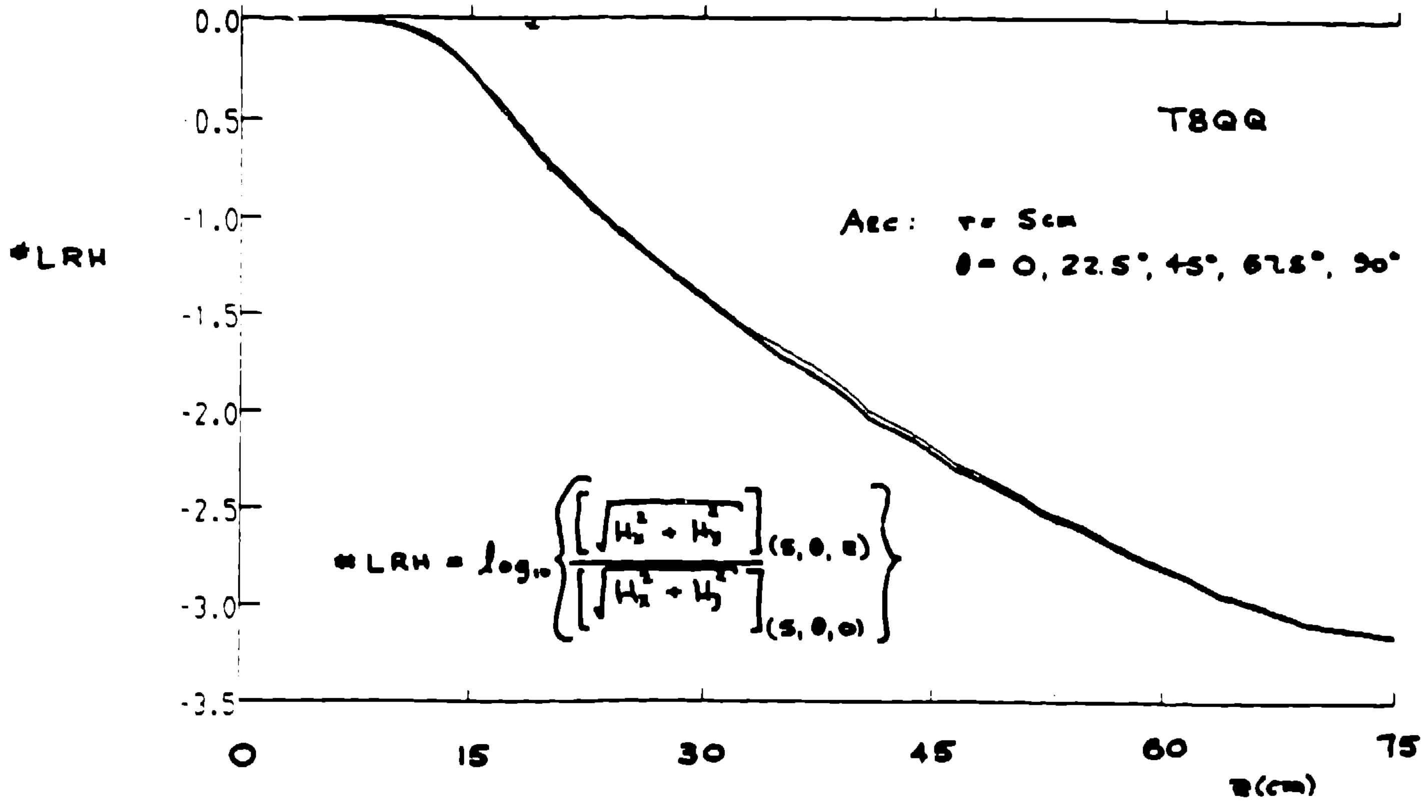
T8QQ
Arc: r = 5cm
θ = 0, 22.5°, 45°, 67.5°, 90°
*LRH
$*LRH = \log_{10}\left\{\dfrac{\left[\sqrt{H_x^2 + H_y^2}\right]_{(5,0,z)}}{\left[\sqrt{H_x^2 + H_y^2}\right]_{(5,0,0)}}\right\}$
0.0
-0.5
-1.0
-1.5
-2.0
-2.5
-3.0
-3.5
0
15
30
45
60
75
z(cm)

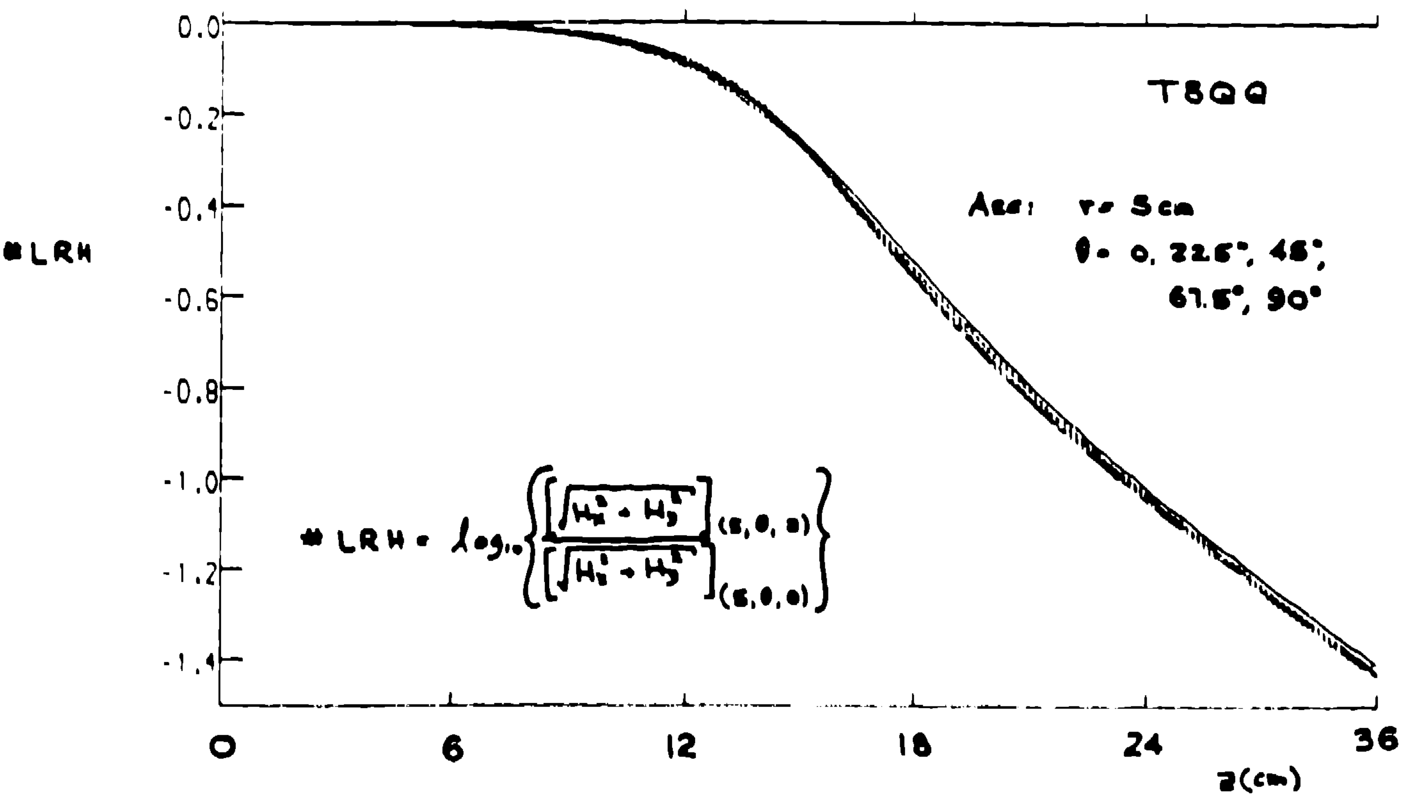
T8QQ
Arc: r = 5cm
θ = 0, 22.5°, 45°,
67.5°, 90°
*LRH
$*LRH = \log_{10}\left\{\dfrac{\left[\sqrt{H_x^2 + H_y^2}\right]_{(5,0,z)}}{\left[\sqrt{H_x^2 + H_y^2}\right]_{(5,0,0)}}\right\}$
0.0
-0.2
-0.4
-0.6
-0.8
-1.0
-1.2
-1.4
0
6
12
18
24
36
z(cm)

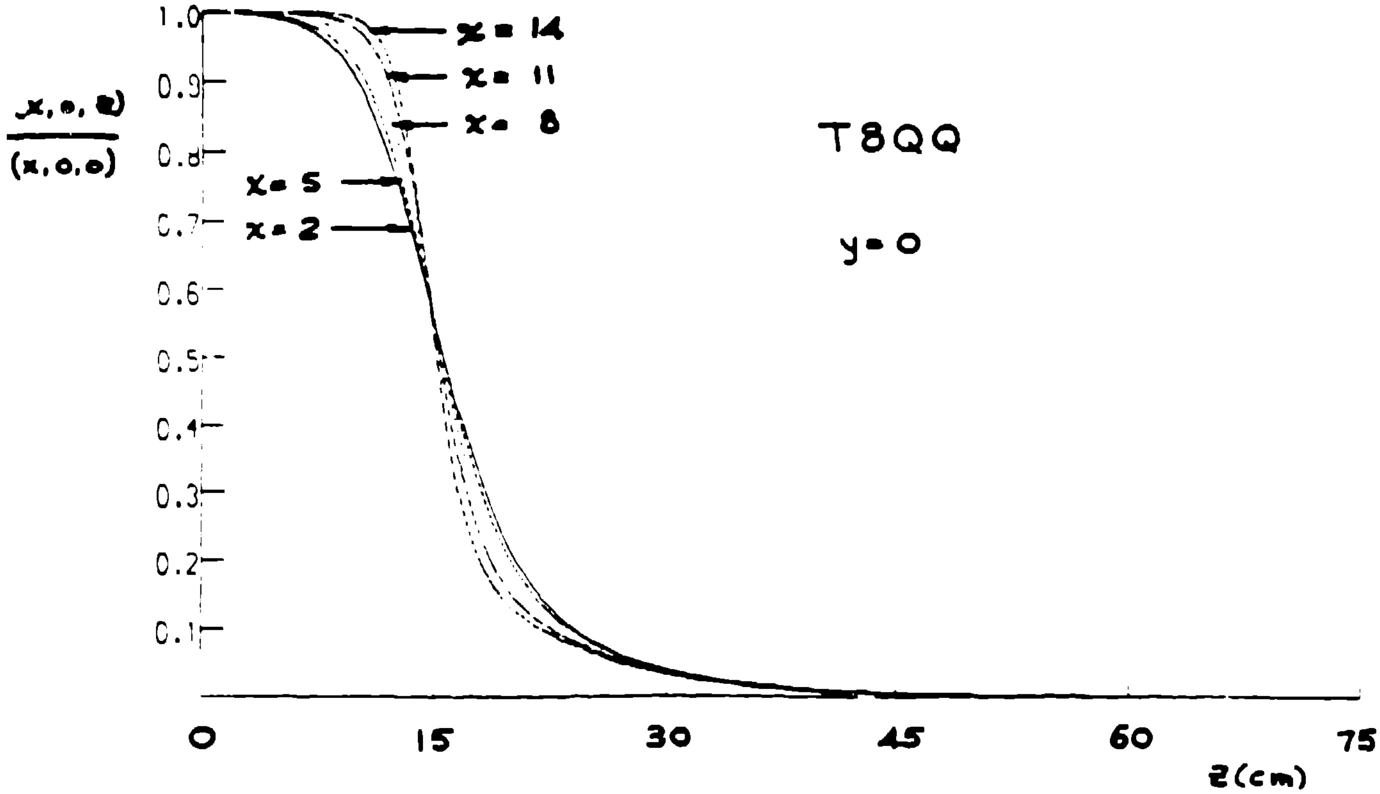
x = 14
x = 11
x = 8
x = 5
x = 2
T8QQ
y = 0
1.0
0.9
0.8
0.7
0.6
0.5
0.4
0.3
0.2
0.1
0
15
30
45
60
75
z (cm)

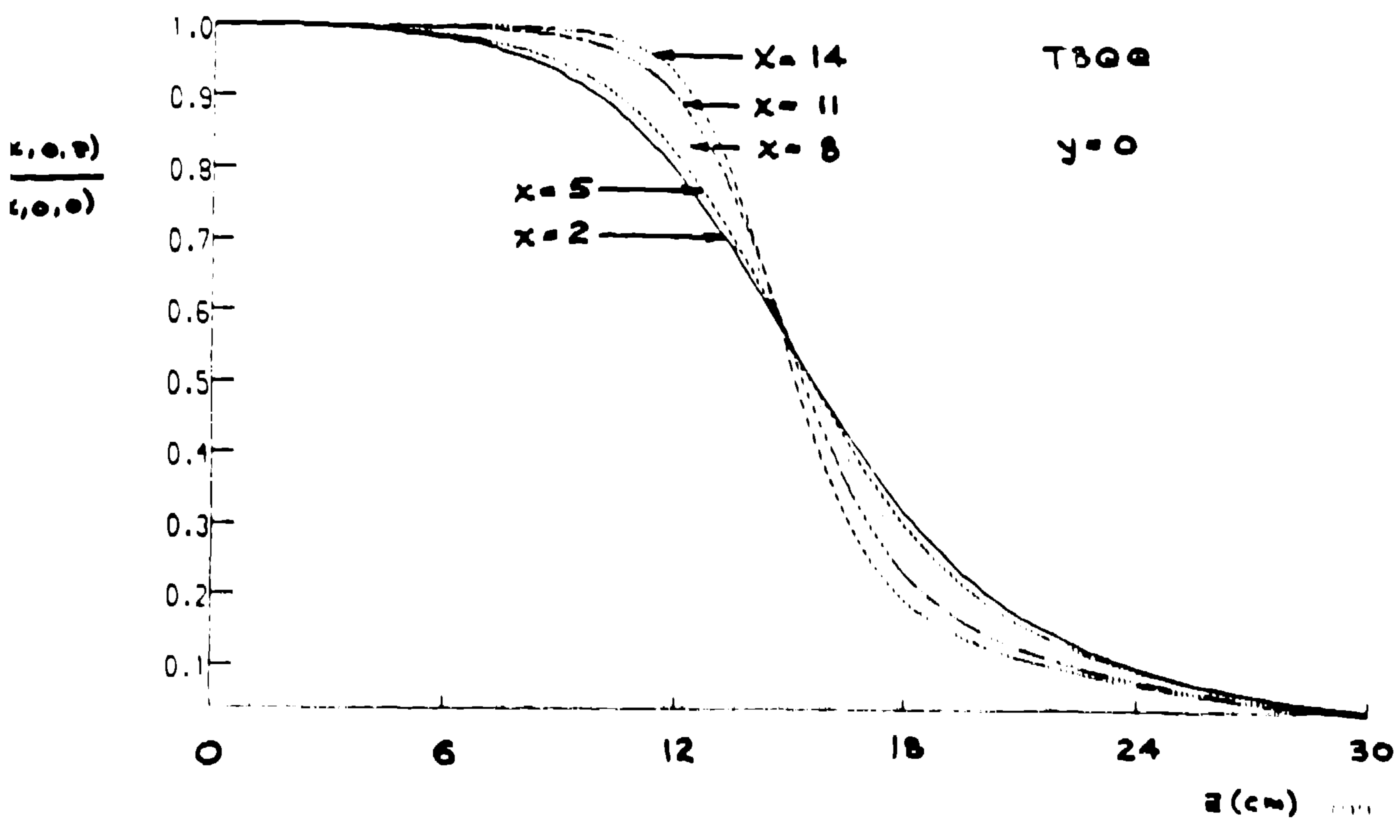
x = 14
x = 11
x = 8
x = 5
x = 2
T8QQ
y = 0
1.0
0.9
0.8
0.7
0.6
0.5
0.4
0.3
0.2
0.1
0
6
12
18
24
30
z (cm)

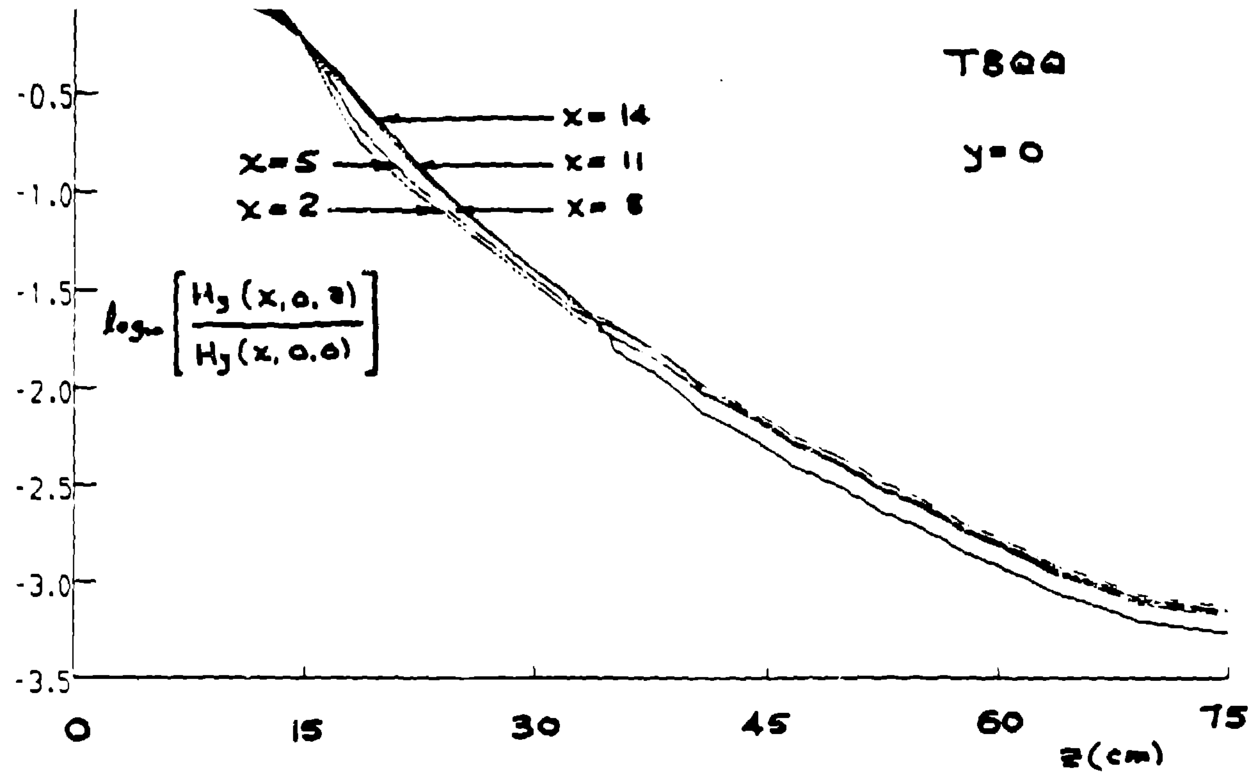
T8QQ
y = 0
x = 14
x = 5
x = 11
x = 2
x = 8
$\log_{10}\left[\frac{H_y(x,0,z)}{H_y(x,0,0)}\right]$
-0.5
-1.0
-1.5
-2.0
-2.5
-3.0
-3.5
0
15
30
45
60
75
z (cm)

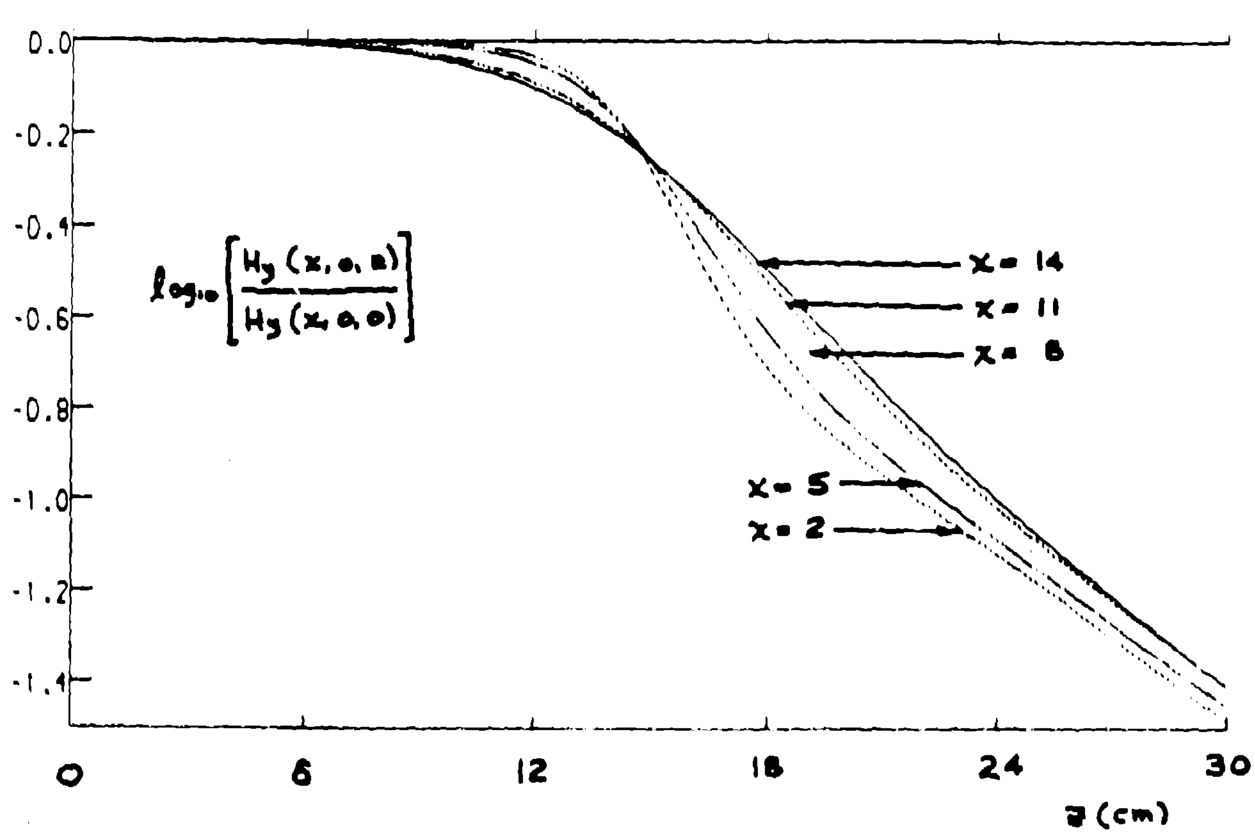
0.0
-0.2
-0.4
-0.6
-0.8
-1.0
-1.2
-1.4
$\log_{10}\left[\frac{H_y(x,0,z)}{H_y(x,0,0)}\right]$
x = 14
x = 11
x = 8
x = 5
x = 2
0
6
12
18
24
30
z (cm)

FRINGE FIELD

ONE REGION FIT : $X = 5$, $Y = 0$, $15 \le Z \le 75$

$$\log_{10}(HY) = -\sum_{n=0}^{20} a_n T_n(w) \qquad w = \frac{Z-45}{30}$$

n	a_n
0	1.463
1	-1.430
2	0.2399
3	-0.01986
4	0.03212
5	0.001219

FROM THIS FIT, CALCULATE $\log_{10}(HY)$, THEN HY; COMPARE TO OPERA VALUES OF HY.

Z	HY (OPERA)	HY (FIT TO $\log_{10}$ HY)	% DIFFERENCE
20.4	90.220	90.3233	0.11
32.4	13.715	14.1189	2.95
38.4	7.2661	6.9794	-3.95
56.4	1.1002	1.0994	-0.08
68.4	0.44022	0.4346	-1.23

Fringe Field

Three Regions: $X = 5$, $Y = 0$

n	$15 \le Z \le 30$ $W = \frac{Z - 22.5}{7.5}$	$30 \le Z \le 45$ $W = \frac{Z - 37.5}{7.5}$	$45 \le Z \le 75$ $W = \frac{Z - 60}{15}$
0	3.662	1.789	−0.06958
1	−0.5795	−0.3793	−0.4936
2	0.03889	0.004608	0.06554
3	0.0007247	−0.001557	0.01496
4	−0.006149	0.01062	0.003828
5	0.002780	−0.003590	−0.002693

Do the same comparison as on the previous page

Z	HY (OPERA)	HY (Fit to $\log_{10}$ HY)	% Difference
23	56.073	56.105	0.06
37	8.5814	8.5874	0.07
41	4.9429	4.9261	−0.34
57	1.0336	1.0270	−0.63

TRANSITION REGION

FIT TO HY: $$HY = -\sum_{n=0}^{20} b_n T_n(w)$$

TWO REGIONS

$X = 5, \quad Y = 0$

n	$0 \le Z \le 10$ $W = \frac{Z-5}{5}$	$10 \le Z \le 15$ $W = \frac{Z-12.5}{2.5}$
0	-969.8	-553.1
1	18.02	191.4
2	8.519	-0.3525
3	2.659	-14.08
4	0.6084	0.6172
5	0.07533	1.395

$0 \le Z \le 10$: WORST ERROR = 0.02 @ $Z = 8.25$
0.004 %

$10 \le Z \le 15$: WORST ERROR = 0.07 @ $Z = 11.25$
0.02 %

$\boxed{\text{GOOD FIT}}$

---------- T8QQ (4186 Points) ----------

XY plane at Z=0

X ranges from	0.00	to	9.00	NX =	91	DX =	0
Y	0.00		4.50	NY =	46	DY =	0

The fit was M=20, N=20.

---------- CHEBYSHEV COEFFICIENTS ----------

The BX, BY, PHI coefficients are grouped by values of m and n.

	n=0	n=1	n=2	n=3	n=4
m=0					
BX	0.0000E+00	0.0000E+00	0.0000E+00	0.0000E+00	0.0000E+00
BY	0.0000E+00	-.2014E+04	0.6082E-01	0.1192E-01	-.2044E-01
PHI	-.4028E+04	-.2014E+04	-.1370E-01	0.6335E-01	-.1243E+00
m=1					
BX	-.2019E+04	-.1009E+04	-.2317E+00	-.8256E-01	-.9094E-01
BY	0.0000E+00	-.1010E+04	-.2535E+00	-.9469E-01	-.2631E-01
PHI	-.2019E+04	-.1009E+04	-.2738E+00	0.2245E-01	-.1088E+00
m=2					
BX	-.4109E+01	-.2133E+01	-.5286E-01	-.5978E-01	-.4839E-01
BY	0.0000E+00	-.2133E+01	-.8714E-01	-.4489E-01	-.3379E-01
PHI	-.4153E+01	-.2133E+01	-.1043E+00	-.4728E-01	-.6731E-01
m=3					
BX	0.1136E+01	0.7872E+00	0.2404E+00	0.7454E-01	0.9264E-02
BY	0.0000E+00	0.7823E+00	0.2804E+00	0.5022E-01	-.1347E-01
PHI	0.1121E+01	0.7639E+00	0.2613E+00	0.438[illegible]E-01	-.3233E-01
m=4					
BX	0.2823E+00	0.1599E+00	0.3243E-01	0.2043E-02	0.5468E-02
BY	0.0000E+00	0.1874E+00	0.3501E-01	0.1393E-02	-.2168E-01
PHI	0.2608E+00	0.1468E+00	0.4147E-01	0.4977E-02	-.6741E-02

---------- T8QQ (4186 Points) ----------

XY plane at Z=15

X ranges from	0.00	to	9.00	NX =	91	DX =	0.10
Y	0.00		4.50	NY =	46	DY =	0.10

The fit was M=20, N=20.

---------- CHEBYSHEV COEFFICIENTS ----------

The BX, BY, PHI coefficients grouped by values of m and n.

	n=0	n=1	n=2	n=3	n=4
m=0					
BX	0.0000E+00	0.0000E+00	0.0000E+00	0.0000E+00	0.0000E+00
BY	0.0000E+00	-.1078E+04	0.2006E+02	0.7448E+01	0.2193E+01
PSI	-.2184E+04	-.1077E+04	0.2095E+02	0.8257E+01	0.2834E+01
m=1					
BX	-.1086E+04	-.5329E+03	0.1466E+02	0.5760E+01	0.1766E+01
BY	0.0000E+00	-.5325E+03	0.1500E+02	0.5997E+01	0.1881E+01
PSI	-.1085E+04	-.5315E+03	0.1588E+02	0.6778E+01	0.2495E+01
m=2					
BX	0.1571E+02	0.1346E+02	0.8186E+01	0.3529E+01	0.1195E+01
BY	0.0000E+00	0.1381E+02	0.8583E+01	0.3835E+01	0.1371E+01
PSI	0.1702E+02	0.1474E+02	0.9377E+01	0.4481E+01	0.1872E+01
m=3					
BX	0.1326E+02	0.1003E+02	0.4941E+01	0.2082E+01	0.7143E+00
BY	0.0000E+00	0.1037E+02	0.5336E+01	0.2433E+01	0.9301E+00
PSI	0.1439E+02	0.1115E+02	0.5960E+01	0.2896E+01	0.1277E+01
m=4					
BX	0.4664E+01	0.3672E+01	0.2021E+01	0.9505E+00	0.3918E+00
BY	0.0000E+00	0.4026E+01	0.2363E+01	0.1262E+01	0.5913E+00
PSI	0.5500E+01	0.4480E+01	0.2732E+01	0.1521E+01	0.7659E+00

---------- T8QQ_SWAP (2257 points) ----------

Compared to all other diagrams and examples,
the coordinate axes have been cyclically permuted:

	All other diagrams and examples	This exampl
Horizontal to the right	X	Y'
Vertical	Y	Z'
Beam axis	Z	X'

---------- T8QQ_SWAP (2257 points) ----------

Horizontal to the right: Y', Vertical: Z', Beam axis: X'.

X'Y' plane at Z'=4.5

X' ranges from	5.00	to	20.00	NX =	61	DX =	0.25
Y'	0.00		9.00	NY =	37	DY =	0.25

The fit was M = 20, N = 20.

---------- CHEBYSHEV COEFFICIENTS ----------

	n=0	n=1	n=2	n=3	n=4
m=0					
BX	0.0000E+00	0.0000E+00	0.0000E+00	0.0000E+00	0.0000E+00
BY	0.0000E+00	-.2691E+04	-.1259E+02	0.3219E+01	-.9844E+00
PHI	-.5348E+04	-.2687E+04	-.8712E+01	0.6452E+01	0.1415E+01
m=1					
BX	0.1944E+04	0.1029E+04	0.7521E+02	0.2428E+02	0.8712E+01
BY	0.0000E+00	0.9921E+03	0.4458E+02	0.3652E+01	-.1784E+01
PHI	0.1906E+04	0.9928E+03	0.4521E+02	0.4191E+01	-.1390E+01
m=2					
BX	0.5080E+03	0.2982E+03	0.5140E+02	0.6739E+01	-.2371E+00
BY	0.0000E+00	0.2952E+03	0.4993E+02	0.6845E+01	0.8770E+00
PHI	0.4998E+03	0.2908E+03	0.4602E+02	0.3595E+01	-.1518E+01
m=3					
BX	-.2606E+03	-.1587E+03	-.3735E+02	-.1116E+02	-.2712E+01
BY	0.0000E+00	-.1454E+03	-.2649E+02	-.3742E+01	0.1302E+01
PHI	-.2488E+03	-.1476E+03	-.2833E+02	-.5329E+01	0.2475E+00
m=4					
BX	-.2367E+03	-.1625E+03	-.5604E+02	-.1329E+02	-.1491E+01
BY	0.0000E+00	-.1585E+03	-.5391E+02	-.1291E+02	-.2195E+01
PHI	-.2273E+03	-.1542E+03	-.5036E+02	-.1018E+02	-.1481E+00

We now return to the usual coordinate system:

Horizontal to the right: X, Vertical: Y, Beam axis: Z

A Comparison of the results of an M = N = P = 7 Chebyshev fit

(higher order 3D fits cannot be done until a program bug is fixed)

to T800 (8788 points)

X ranges from	0.00	to	9.00	NX =	26	DX =	0.36
Y	0.00		4.50	NY =	13	DY =	0.375
Z	5.00		15.00	NZ =	26	DZ =	0.40

against the results of OPERA calculations at representative locations

(Since the YZ and ZX planes are zero equipotential surfaces we expect HX(X,0,Z) = HY(0,Y,Z) = POT(X,),Z) = POT(0,Y,Z))

CHEBYSHEV COEFFICIENTS

X	Y	Z		HX	HY	HZ	POT
0.0	1.5	13.0	OPERA	105.898	0.0072	-0.0015	0.0000
0.0	1.5	13.0	FIT	105.78	-0.4404	0.2451	3.5049
0.0	1.5	13.0	% DIFF.	-0.11	-	-	-
6.0	0.0	12.0	OPERA	0.0395	493.142	-0.0024	0.0000
6.0	0.0	12.0	FIT	-0.4974	494.770	-0.8834	-1.8509
6.0	0.0	12.0	% DIFF.	-	0.33	-	-
6.0	1.5	13.0	OPERA	124.185	456.316	-79.1127	-675.580
6.0	1.5	13.0	FIT	124.06	456.65	-79.162	-676.69
6.0	1.5	13.0	% DIFF.	-0.10	0.07	0.06	0.16
9.0	4.5	7.0	OPERA	452.770	902.702	-5.6201	-4026.93
9.0	4.5	7.0	FIT	456.38	905.71	-4.5854	-4017.3
9.0	4.5	7.0	% DIFF.	0.80	0.33	-18.41	-0.24
3.0	4.5	8.0	OPERA	438.958	291.416	-20.6492	-1292.7
3.0	4.5	8.0	FIT	439.09	291.75	-21.332	-1298.2
3.0	4.5	8.0	% DIFF.	0.03	0.11	3.31	0.43
0.0	3.0	14.0	OPERA	188.376	0.0045	-0.0019	0.0000
0.0	3.0	14.0	FIT	187.80	0.4182	-0.3517	3.5707
0.0	3.0	14.0	% DIFF.	-0.31	-	-	-
9.0	3.0	10.0	OPERA	316.890	898.786	-46.7594	-2613.93
9.0	3.0	10.0	FIT	314.52	890.01	-34.706	-2605.4
9.0	3.0	10.0	% DIFF.	-0.75	-0.98	-25.78	-0.33
6.0	0.0	7.0	OPERA	-0.0006	585.320	-0.0003	0.0000
6.0	0.0	7.0	FIT	0.0603	585.74	0.1246	-5.9809
6.0	0.0	7.0	% DIFF.	-	0.07	-	-
0.0	3.0	6.0	OPERA	291.383	0.0071	-0.0002	0.0000
0.0	3.0	6.0	FIT	291.05	0.0199	-0.0589	-3.8794
0.0	3.0	6.0	% DIFF.	-0.11	-	-	-

VPN-88-2
August 1988
Revised July 1991

The Use of Chebyshev Polynomials For Fitting Magnetic Field Data

D.E. Lobb

TRIUMF, Physics Department, University of Victoria
Victoria, B.C., Canada V8W 3P6

1. We are interested in the static magnetic field within a source-free rectangular cube specified by

$$x_1 \leq x \leq x_2, \; y_1 \leq y \leq y_2, \quad z_1 \leq z \leq z_2 \tag{1.1}$$

where x, y and z are local Cartesian coordinates. We are also interested in rectangular areas parallel to the Cartesian coordinate planes and in fields along lines parallel to the Cartesian coordinate axes.

Under some symmetry conditions, data need to be available only over a certain portion of this region; this is discussed in Section 10 below. We define

$$a = (x_2 - x_1)/2, \; b = (y_2 - y_1)/2, \; c = (z_2 - z_1)/2 \tag{1.2 a}$$

$$\bar{x} = (x_2 + x_1)/2, \quad \bar{y} = (y_2 + y_1)/2, \quad \bar{z} = (z_2 + z_1)/2 \tag{1.2 b}$$

$$u = (x - \bar{x})/a, \qquad v = (y - \bar{y})/b, \qquad w = (z - \bar{z})/c \tag{1.3}$$

so that

$$|u| \leq 1, \quad |v| \leq 1, \quad |w| \leq 1. \tag{1.4}$$

The magnetic field $\vec{B}(x,y,z)$ is characterized by a scalar potential $\psi(x,y,z)$ with

$$\vec{B} = -\nabla\psi \tag{1.5}$$

with

$$B_x = -\frac{\partial\psi}{\partial x}, \quad B_y = -\frac{\partial\psi}{\partial y}, \quad B_z = -\frac{\partial\psi}{\partial z}, \tag{1.6}$$

Data values are available either from a magnetic field calculating program or from measurement.

In the following section we iscuss some properties of orthogonal functions, of orthogonal polynomials, and of Chebyshev polynomials. We then show that various common methods of fitting magnetic field data are formally equivalent to a Chebyshev fit. An analytic form is postulated for the fitted field configuration and properties of this representation are presented.

2. Orthogonal functions, orthogonal polynomials and Chebyshev polynomials

Let us write $f(u)$, an arbitrary function of u, as an expansion in a family of orthogonal functions $g_n(u)$

$$f(u) = \sum_{j=0}^{\infty} a_j g_j(u) \; . \tag{2.1}$$

If the $g_j(u)$ form a complete set, the RHS has the value

$$\lim_{\epsilon \to 0} \frac{[f(u+\epsilon) + f(u-\epsilon)]}{2} \tag{2.2}$$

at all values of u. Since we are interested in $-1 \leq u \leq +1$, we introduce the intermediate variable ζ with

$$u = \cos\zeta \; , \quad -1 \leq u \leq +1 \; , \quad 0 \leq \zeta \leq \pi \; , \tag{2.3}$$

and write the Fourier cosine series

$$f(u) = \sum_{j=0}^{\infty}{}' d_j \cos j\zeta \equiv \sum_{j=0}^{\infty} d_j \cos j\zeta - d_0/2 \; . \tag{2.4}$$

This implies that $f(u)$ is an even function of ζ; this is of no interest in the present context since we are interested in $0 \leq \zeta \leq \pi$ and are not interested in $-\pi < \zeta < 0$. The coefficients are given by

$$d_j = 2/\pi \int_{\zeta=0}^{\pi} f(u) \cos j\zeta \, d\zeta \ . \tag{2.5}$$

The truncated series

$$f(u) \approx \sum_{j=0}^{J\,'} d_j \cos j\zeta \tag{2.6}$$

has the property that, for a given value of J, the squared error integrated over $0 \leq \zeta \leq \pi$ is a minimum compared to the integrated squared error resulting from any other choice of coefficients in the truncated series.

A further truncation is:

$$f_J(u) = \sum_{j=1}^{J\,''} d_j \cos j\zeta \equiv \sum_{j=1}^{J} d_j \cos j\zeta - 1/2[d_0 + d_J \cos J\zeta]. \tag{2.7}$$

This form allows the use of a particular summation orthogonality relationship (Eq. 6.8 below) to calculate the values of the coefficients.

General properties of Chebyshev polynomials of the first and second kind are presented in references [1]) and [2]). The Chebyshev polynomial of the first kind, $T_n(u)$, is an n^{th} order polynomial which is even if n is even and odd if u is odd and which is represented over the range $-1 \leq u \leq +1$, $0 \leq \zeta \leq \pi$, by

$$T_n(u) = \cos n\zeta = \cos[n(\cos^{-1}u)]. \tag{2.8}$$

It has its (n-1) extreme values of +1 and -1 located at

$$\zeta_k = \frac{k\pi}{n} \qquad u_k = \cos\left(\frac{k\pi}{n}\right) \qquad k = 1,2,\ldots,(n-1) \ . \tag{2.9}$$

Values at the ends of the range of interest are +1 at $u = +1$ and $(-1)^n$ at $u = -1$. The regular spacing of the values $\zeta_k = k\pi/n$ becomes a distorted spacing of values $\cos(k\pi/n)$ with points more closely spaced near $u = \pm1$ and more distantly spaced near $u = 0$.

Cheyshev polynomials of the second kind, $U_n(u)$, are obtained by differentiating $T_n(u)$:

$$\frac{dT_n}{du} = \frac{dT_n}{d\zeta}\frac{d\zeta}{du} = n\,\frac{\sin n\zeta}{\sin \zeta} \equiv nU_{n-1}(u) \qquad (2.10)$$

$$U_{n-1}(u) \equiv \frac{\sin n\zeta}{\sin \zeta} \qquad (2.11)$$

We may write powers of u and v as expansions in Chebyshev polynomials:

$$u^M = \sum_{m=0}^{M} \alpha_m\, T_m(u) \qquad (2.12)$$

$$v^N = \sum_{n=0}^{N} \beta_n\, T_n(v) \qquad (2.13)$$

The Chebyshev polynomials of the first and second kind are related by

$$T_n(u) = 1/2\left[U_n(u) - U_{n-2}(u)\right] \qquad n \geq 2 \qquad (2.14)$$

The coefficients in the inverse relationship

$$U_n(u) = \sum_{j=1}^{n} \varepsilon_j\, T_j(u) \qquad (2.15)$$

do not have a simple form.

For $n \geq 2$ and $|u| \leq 1$, it is convenient to calculate numerical values using the recursion relationships

$$T_k(u) = 2u\, T_{k-1}(u) - T_{k-2}(u) \qquad (2.16)$$

and

$$U_k(u) = 2u\, U_{k-1}(u) - U_{k-2}(u)\ . \qquad (2.17)$$

A few Chebyshev polynomials of low order are presented in Table 1, with the inverse results presented in Table 2.

Table 1.

n	$T_n(u)$	$U_n(u)$
0	1	1
1	u	$2u$
2	$-1 + 2u^2$	$-1 + 4u^2$
3	$-3u + 4u^3$	$-4u + 8u^3$
4	$1 - 8u^2 + 8u^4$	$1 - 12u^2 + 16u^4$

Table 2.

1	T_0	U_0
u	$T_1(u)$	$\frac{1}{2} U_1(u)$
u^2	$\frac{1}{2}\left[T_0 + T_2(u)\right]$	$\frac{1}{4}\left[U_0 + U_2(u)\right]$
u^3	$\frac{1}{4}\left[3T_1(u) + T_3(u)\right]$	$\frac{1}{8}\left[2U_1(u) + U_3(u)\right]$
u^4	$\frac{1}{8}\left[3T_0(u) + 4T_2(u) + T_4(u)\right]$	$\frac{1}{16}\left[2U_0 + 3U_2(u) + U_4(u)\right]$

3. The one-dimensional truncated Taylor series

It is very usual to represent the field component normal to the median plane (zx plane) along a $z = z_0$ line in the median plane ($y=0$) by

$$b_y(x) \equiv \frac{B_y(x,0,z_0)}{B_y(0,0,z_0)} = \sum_{j=0}^{N} \nu_j\, u^j \tag{3.1}$$

Substituting Eq. 2.12 above, we may write

$$b_y(x) = \sum_{j=0}^{N} \sum_{k=0}^{j} \nu_j\, \alpha_k\, T_k(u) = \sum_{k=0}^{N} \delta_k\, T_k(u) \tag{3.2}$$

so the one-dimensional Taylor series representative is formally equivalent to a Chebyshev expansion.

It should be noted that a Taylor series has poor properties for purposes of numerical fitting: for $j \geq 2$ the power u^j varies slowly near $u = 0$ and rapidly near $u = \pm 1$.

4. The two-dimensional truncated Taylor series

A common representation of a component of a two-dimensional field is

$$B_y(x,y) = \sum_{j=0}^{J} \sum_{k=0}^{K} c_{jk}\, u^j\, v^k \tag{4.1}$$

Substituting Eqs. 2.12 and 2.13 we may write

$$B_y(x,y) = \sum_{j=0}^{J} \sum_{k=0}^{K} c_{jk} \sum_{\ell=0}^{j} \sum_{m=0}^{k} \epsilon_{jk}\, \beta_m\, T_\ell(u)\, T_m(v) = \sum_{m=0}^{J} \sum_{n=0}^{K} \eta_{mn}\, T_\ell(u)\, T_m(v) \tag{4.2}$$

so the two-dimensional Taylor Series representation is formally equivalent to a Chebyshev expansion.

5. Two- and three-dimensional harmonic representations

For a two-dimensional field (functions of x and y with no variation along the z direction) it is convenient to use the complex independent variable

$$\xi = x + iy = re^{i\theta} \tag{5.1}$$

with the complex potential

$$W(\xi) = A(\xi) + i\psi(\xi) \tag{5.2}$$

where A and ψ are the vector and scalar potentials respectively. Truncated solutions of the two-dimensional Laplace's equation may be written in the form

$$W(\xi) = \sum_{n=0}^{N} \gamma_n \xi^n = \sum_{n=0}^{N} \gamma_n[\cos n\theta + i \sin n\theta] \tag{5.3}$$

with the fields given by

$$B_y + i B_x = -\frac{dW}{d\xi} = -\sum_{n=1}^{N} n \gamma_n \sum_{m=0}^{n-1} x^m (iy)^{n-1-m} \binom{n-1}{m} \tag{5.4}$$

Substituting Eqs. 2.12 and 2.13 above, we again obtain a Chebyshev series in the form

$$B_y + i B_x = \sum_{p=1}^{N} \sum_{q=1}^{N} \delta_{pq} T_p(u) T_q(v)$$

with $\delta_{pq} = 0$ for $p + q > N$.

The form of this result differs from the form of the result presented in Eq. 4.2 in that the latter result allowed for truncation at different orders of polynomials in u and v.

The harmonic representation of a magnetic field is practical only for a region that is a circular disc. Values obtained by extrapolation beyond the disc are prone to error since the n^{th} order harmonic is associated with a radial dependence of $(x^2 + y^2)^{n/2}$ for the potential and $(x^2 + y^2)^{(n-1)/2}$ for the field components. This suggests the desirability of another method of fitting that is appropriate to a rectangular area in a plane.

Three-dimensional fields within a cylindrical volume may be represented by harmonic series where coefficients are functions of z (reference [2]); however, this is practical only if the variation of the field with z is "slow" compared to the variation with x or y.

6. Three-dimensional Chebyshev fit

We wish to have a representation in which the x, y and z directions are treated in the same manner. We also want this representation of a three-dimensional field in three-dimensional space to reduce easily to forms appropriate to three-dimensional fields on planes parallel to coordinate planes and on lines parallel to coordinate axes. We postulate that the scalar potential $\psi(x,y,z)$ and the field components ($\vec{B} = -\nabla\psi$) may be represented by the following truncated Chebyshev series (the $\sum''$ notation is defined in Eq. 2.6 above):

$$\psi(x,y,z) = \sum_{m=0}^{M}{}'' \sum_{n=0}^{N}{}'' \sum_{p=0}^{P}{}'' \alpha_{mnp} \, T_m(u) \, T_n(v) \, T_p(w) \tag{6.1}$$

$$B_x(x,y,z) = - \sum_{m=0}^{M}{}'' \sum_{n=0}^{N}{}'' \sum_{p=0}^{P}{}'' \frac{m \, \alpha_{mnp}}{a} U_{m-1}(u) \, T_n(v) \, T_p(w) \tag{6.2}$$

$$B_y(x,y,z) = - \sum_{m=0}^{M}{}'' \sum_{n=0}^{N}{}'' \sum_{p=0}^{P}{}'' \frac{n \, \alpha_{mnp}}{b} T_m(u) \, U_{n-1}(v) \, T_p(w) \tag{6.3}$$

$$B_z(x,y,z) = - \sum_{m=0}^{M}{}'' \sum_{n=0}^{N}{}'' \sum_{p=0}^{P}{}'' \frac{p \, \alpha_{mnp}}{c} T_m(u) \, T_n(v) \, U_{p-1}(w) \tag{6.4}$$

The orthogonality result

$$\int_{-1}^{+1} T_m(u) \, T_n(u) \, (1-u^2)^{-0.5} \, du = \begin{cases} \pi & m=n=0 \\ \frac{\pi}{2} & m=n\neq 0 \\ 0 & m\neq n \end{cases}$$

is not in a convenient form for numerical integration due to the behavior of $(1-u^2)^{-0.5}$ as $u \to +1$ and $u \to -1$.

The orthogonality result

$$\int_{-1}^{+1} U_{m-1}(u)\, U_{n-1}(u)\, (1-u^2)^{0.5}\, du = \frac{\pi}{2}\, \delta_{mn} \qquad \begin{matrix} m>1 \\ n>1 \end{matrix} \tag{6.6}$$

could be integrated numerically.

More convenient forms for numerical computation are the following summation orthogonality results:

$$\sum_{r=0}^{M}{}'' T_j(u_r)\, T_k(u_r) = \begin{cases} 0 & j \neq k \\ \frac{M}{2} & j=k\neq 0 \text{ or } j=k\neq M \\ M & j=k=0 \text{ or } j=k=M \end{cases} \tag{6.7}$$

and

$$\sum_{r=0}^{M}{}'' \left(\sin^2 \frac{\pi r}{M}\right) U_{j-1}(u_r)\, U_{k-1}(u_r) = \begin{cases} 0 & j \neq k \\ M & j=k\neq 0 \text{ or } j=k\neq M \\ 0 & j=k=0 \text{ or } j=k=M \end{cases} \tag{6.8}$$

with

$$u_r = \cos \frac{\pi r}{M} \qquad (0 \leq r \leq M) \tag{6.9}$$

$$v_s = \cos \frac{\pi s}{N} \qquad (0 \leq s \leq N) \tag{6.10}$$

$$w_t = \cos \frac{\pi t}{P} \qquad (0 \leq t \leq P). \tag{6.11}$$

Eq. 6.7 is presented in many references (for example, [1]) and [2])); since Eq. 6.8 is not presented in many of the standard works, a proof is presented in Appendix I.

The coefficient $a_{\mu\nu\rho}$ is calculated from input data values of $\psi(u_r, v_s, w_t)$ by

$$a_{\mu\nu\rho} = \frac{8}{MNP} \sum_{r=0}^{M}{}'' \sum_{s=0}^{N}{}'' \sum_{t=0}^{P}{}'' T_\mu(u_r)\, T_\nu(v_s)\, T_\rho(w_t)\, \psi(u_r, v_s, w_t) \tag{6.12}$$

Once these coefficients have been calculated, Eqs. 6.1 to 6.4 may be used to calculate potential or field values at any desired location.

Since the ψ, B_x, B_y and B_z fits of the same field should, in theory, all yield the same set of coefficients, the lack of correspondence of coefficients calculated using different components of the same input field data will give a measure of the inconsistency in the input data and/or errors associated with the truncated fit. For example, coefficients calculated using ψ data may be used to calculate B_x, B_y and B_z values at the data points; these results may be compared to the input B_x, B_y, B_z data values. Coefficients may be obtained from input data values of $\vec{B}$ by

$$\alpha_{\mu\nu\rho} = - \frac{8a}{\mu MNP} \sum_{r=0}^{M}{}'' \sum_{s=0}^{N}{}'' \sum_{t=0}^{P}{}'' \sin^2\left(\frac{\pi r}{M}\right) U_{\mu-1}(u_r)\, T_\nu(v_s)\, T_\rho(w_t)\, B_x(u_r, v_s, w_t) \tag{6.13}$$

$$\alpha_{\mu\nu\rho} = - \frac{8b}{\nu MNP} \sum_{r=0}^{M}{}'' \sum_{s=0}^{N}{}'' \sum_{t=0}^{P}{}'' T_\mu(u_r) \sin^2\left(\frac{\pi s}{N}\right) U_{\nu-1}(v_s)\, T_\rho(w_t)\, B_y(u_r, v_s, w_t) \tag{6.14}$$

and

$$\alpha_{\mu\nu\rho} = - \frac{8c}{\rho MNP} \sum_{r=0}^{M}{}'' \sum_{s=0}^{N}{}'' \sum_{t=0}^{P}{}'' T_\mu(u_r)\, T_\nu(v_s) \sin^2\left(\frac{\pi t}{P}\right) U_{\rho-1}(w_t)\, B_z(u_r, v_s, w_t)\ . \tag{6.15}$$

In Eq. (6.13), $0 < \mu < M$; in Eq. (6.14), $0 < \nu < N$; and in Eq. (6.15), $0 < \rho < P$. The low order coefficients not calculated are those that play no role in the appropriate field expansion. The high order coefficients not calculated are those for which all terms in the summation are zero due to data values being located at zeros of the Chebyshev polynomials of the second kind.

It is important to note that, due to the terms $\sin^2(\frac{\pi r}{M})$, $\sin^2(\frac{\pi s}{N})$ and $\sin^2(\frac{\pi t}{P})$, the field components normal to the bounding surface of the region play no role in Eqs. (6.13) to (6.15). For this reason, it is prudent to have the region of input data somewhat larger than the region for which fitted values are desired.

7. The equations for the three-dimensional field in a plane parallel to a coordinate plane

Let us consider the case in which B_x, B_y and B_z field data are available over a rectangular area in an xy plane at $z = z_c$ $(w = w_c)$. If we write

$$\beta_{mn}(w_c) = \sum_{p=0}^{P}{}'' \alpha_{mnp} T_p(w_c) \tag{7.1}$$

$$\gamma_{mn}(w_c) = \sum_{p=0}^{P}{}'' \frac{p\alpha_{mnp}}{C} U_{p-1}(w_c) \tag{7.2}$$

then

$$\psi(x,y,z_c) = \sum_{m=0}^{M}{}'' \sum_{n=0}^{N}{}'' \beta_{mn}(w_c) T_m(u) T_n(v) \tag{7.3}$$

$$B_x(x,y,z_c) = -\sum_{m=0}^{M}{}'' \sum_{n=0}^{N}{}'' \frac{m\,\beta_{mn}(w_c)}{A} U_{m-1}(u) T_n(v) \tag{7.4}$$

$$B_y(x,y,z_c) = -\sum_{m=0}^{M}{}'' \sum_{n=0}^{N}{}'' \frac{n\,\beta_{mn}(w_c)}{B} T_m(u) U_{n-1}(v) \tag{7.5}$$

$$B_z(x,y,z_c) = -\sum_{m=0}^{M}{}'' \sum_{n=0}^{N}{}'' \gamma_{mn}(w_c) T_m(u) T_n(v) \tag{7.6}$$

The coefficients are obtained from input data values by

$$\beta_{\mu\nu}(w_c) = \frac{4}{MN} \sum_{r=0}^{M}{}'' \sum_{s=0}^{N}{}'' T_\mu(ur)\, T_\nu(v_s)\, \psi(u_r, v_s, w_c) \tag{7.7}$$

$$\beta_{\mu\nu}(w_c) = -\frac{4A}{MN\mu} \sum_{r=0}^{M}{}'' \sum_{s=0}^{N}{}'' \sin^2\left(\frac{\pi r}{M}\right) U_{\mu-1}(u_r)\, T_\nu(v_s)\, B_x(u_r, v_s, w_c) \tag{7.8}$$

$$\beta_{\mu\nu}(w_c) = -\frac{4B}{MN\nu} \sum_{r=0}^{M}{}'' \sum_{s=0}^{N}{}'' T_\mu(u_r) \sin^2\left(\frac{\pi s}{N}\right) U_{\nu-1}(v_s)\, B_y(u_r, v_s, w_c) \tag{7.9}$$

$$\gamma_{\mu\nu}(w_c) = -\frac{4}{MN} \sum_{r=0}^{M}{}'' \sum_{s=0}^{N}{}'' T_\mu(u_r)\, T_\nu(u_s)\, B_z(u_r, v_s, w_c) \tag{7.10}$$

In Eq. (7.8) $0 < \mu < M$, and in Eq. (7.9) $0 < \nu < N$.

Equations for the planes $x = x_c (u = u_c)$ and $y = y_c (\nu = \nu_c)$ are obtained by cyclic permutation of Eqs. (7.1) to (7.10).

8. The equations for the three-dimensional field along a line in a plane parallel to a coordinate axis

Let us consider the case in which B_x, B_y and B_z field data are available along the line parallel to the x axis with $y = y_c$ $(v = v_c)$ and $z = z_c$ $(w = w_c)$. If we write

$$\delta_m(v_c, w_c) = \sum_{n=0}^{N}{}'' T_n(v_c) \sum_{p=0}^{P}{}'' T_p(w_c)\, a_{mnp} \tag{8.1}$$

$$\varepsilon_m(v_c, w_c) = \sum_{n=0}^{N}{}'' \frac{n\, U_{n-1}(v_c)}{B} \sum_{p=0}^{P}{}'' T_p(w_c)\, a_{mnp} \tag{8.2}$$

$$\eta_m(v_c, w_c) = \sum_{n=0}^{N}{}'' T_n(u_c) \sum_{p=0}^{P}{}'' \frac{p\, a_{mnp}}{C} U_{p-1}(w_c) \tag{8.3}$$

then

$$\psi(x,y_c,z_c) = \sum_{m=0}^{M_n} \delta_m(v_c,w_c)\; T_m(u) \tag{8.4}$$

$$B_x(x,y_c,z_c) = -\sum_{m=0}^{M_n} \frac{m\;\delta_m(v_c,w_c)}{A}\; U_{m-1}(u) \tag{8.5}$$

$$B_y(x,y_c,z_c) = -\sum_{m=0}^{M_n} \varepsilon_m(v_c,w_c)\; T_m(u) \tag{8.6}$$

$$B_z(x,y_c,z_c) = -\sum_{m=0}^{M_n} \eta_m(v_c,w_c)\; T_m(u) \tag{8.7}$$

The coefficients are obtained from input data values by

$$\delta_\mu(v_c,w_c) = \frac{2}{M} \sum_{r=0}^{M_n} T_\mu(ur)\; \psi(u_r,v_c,w_c) \tag{8.8}$$

$$\delta_\mu(v_c,w_c) = -\frac{2A}{\mu M} \sum_{r=0}^{M_n} \sin^2\!\left(\frac{\pi r}{M}\right) U_{\mu-1}(u_r)\; B_x(u_r,v_c,w_c) \tag{8.9}$$

$$\varepsilon_\mu(v_c,w_c) = -\frac{2}{M} \sum_{r=0}^{M_n} T_\mu(u_r)\; B_y(u_r,v_c,w_c) \tag{8.10}$$

$$\eta_\mu(v_c,w_c) = -\frac{2}{M} \sum_{r=0}^{M_n} T_\mu(u_r)\; B_z(u_r,v_c,w_c) \tag{8.11}$$

In Eq. (8.9), $\mu > 0$.

Equations for the lines $z = z_c$, $x = x_c$ and $x = x_c$, $y = y_c$ are obtained by cyclic permutation of Eqs. (8.1) to (8.11).

9. A Chebyshev fit for a two-dimensional magnetic field derived from a vector potential

If we postulate
$$A_z(x,y) = \sum_{m=0}^{M''} \sum_{n=0}^{N''} \beta_{mn}\, T_m(u)\, T_n(u), \tag{9.1}$$

then
$$B_x = \frac{\partial A_z}{\partial y} = \sum_{m=0}^{M''} \sum_{n=0}^{N''} \left(\frac{n\beta_{mn}}{B}\right) T_m(u)\, U_{n-1}(v) \tag{9.2}$$

$$B_y = -\frac{\partial A_z}{\partial y} = \sum_{m=0}^{M''} \sum_{n=0}^{N''} \left(-\frac{m\beta_{mn}}{A}\right) U_{m-1}(u)\, T_u(v) \tag{9.3}$$

In theory, an expansion of the functions U_n in terms of functions T_m would allow Eqs. (7.4) and (9.2) for B_x, and Eqs. (7.5) and (9.3) for B_y to be brought to the same form; however, in practice this would not be worth the effort.

10. Symmetry Properties

We shall consider the consequences of particular functions being either even or odd function of u, or v, or w.

10.1 Midplane Symmetries and Antisymmetries

		ψ	Values of a_{mnp} that are constrained to be zero, for $\ell = 0,1,2,\ldots$
a)	B_x even in u	odd in u	$m = 2\ell$
b)	B_y even in v	odd in v	$n = 2\ell$
c)	B_z even in w	odd in w	$p = 2\ell$
d)	B_x odd in u	even in u	$m = 2\ell + 1$
e)	B_y odd in v	even in v	$n = 2\ell + 1$
f)	B_z odd in w	even in w	$p = 2\ell + 1$

10.2 Symmetric "Dipole"

	B_x	B_y	B_z	ψ	Values of a_{mnp} that are constrained to be zero for $k = 0,1,2,\ldots$ and $\ell = 0,1,2,\ldots$
a)	odd in u odd in v	even in u even in v	even in u odd in v	even in u odd in v	$m = 2k + 1$ $n = 2\ell$
b)	even in v odd in w	odd in v odd in w	even in v even in w	even in v odd in w	$n = 2k + 1$ $p = 2\ell$
c)	even in w even in u	even in w odd in u	odd in w odd in u	even in w odd in u	$p = 2k + 1$ $m = 2\ell$

10.3 Asymmetric "Quadrupole"

	B_x	B_y	B_z	ψ	Values of a_{mnp} that are constrained to be zero for $k = 0,1,2,\ldots$ and $\ell = 0,1,2,\ldots$
a)	even in u odd in v	odd in u even in v	odd in u odd in v	odd in u odd in v	$m = 2k$ $n = 2\ell$
b)	odd in v odd in w	even in v odd in w	odd in v even in w	odd in v odd in w	$n = 2k$ $p = 2\ell$
c)	odd in w even in u	odd in w odd in u	even in w odd in u	odd in w odd in u	$p = 2k$ $m = 2\ell$

10.4 "Quadrupole" Symmetry

In addition to the constraints

$$\psi(u,v,w) = -\psi(-u,v,w) \tag{10.1}$$

and

$$\psi(u,v,w) = -\psi(u,-v,w) \tag{10.2}$$

which results in

$$\alpha_{2k,2\ell,p} = 0 \qquad \begin{matrix} k = 0,1,2,\ldots \\ \ell = 0,1,2,\ldots \end{matrix} \tag{10.3}$$

We have for A = B the additional constraint

$$\psi(u,v,w) = \psi(v,u,w) \tag{10.4}$$

which results in

$$\alpha_{mnp} = \alpha_{nmp}. \tag{10.5}$$

Appendix I

A Proof of the Summation Orthogonality Relationship for Chebyshev Polynomials of the Second Kind.

Let us consider:

$$S = \sum_{r=0}^{n}{}'' \sin j\left(\frac{\pi r}{n}\right) \sin k\left(\frac{\pi r}{n}\right) = \sum_{r=0}^{n-1} \sin j\left(\frac{\pi r}{n}\right) \sin k\left(\frac{\pi r}{n}\right)$$

$$= \frac{1}{2} \sum_{r=0}^{n-1} \left[\cos(j-k)\frac{\pi r}{n} - \cos(j+k)\frac{\pi r}{n}\right]$$

$$= \frac{1}{2} \operatorname{Re} \sum_{r=0}^{n-1} \left[\exp[i(j-k)\frac{\pi r}{n}] - \exp[i(j+k)\frac{\pi r}{n}]\right]$$

$$= \frac{1}{2} \operatorname{Re}\left\{\frac{1-\exp[i(j-k)\pi]}{1-\exp[i(j-k)\frac{\pi}{n}]} - \frac{1-\exp[i(j+k)\pi]}{1-\exp[i(j+k)\frac{\pi}{n}]}\right\} \qquad (I.1)$$

For the case $j \neq k$ with both $(j+k)$ and $(j-k)$ odd, we have

$$\exp[i(j-k)\pi] = \exp[i(j+k)\pi] = -1 \qquad (I.2)$$

and

$$S = \frac{1}{2} \operatorname{Re}\left\{\frac{2}{1-\exp[i(j-k)\frac{\pi}{n}]} - \frac{2}{1-\exp[i(j+k)\frac{\pi}{n}]}\right\}$$

$$= \frac{1}{2} \operatorname{Re}\left\{\frac{-2i[i\exp[-i(j+k)\frac{\pi}{2n}]]}{\exp[-i(j-k)\frac{\pi}{2n}] - \exp[i(j-k)\frac{\pi}{2n}]} - \frac{-2i[i\exp[-i(j+k)\frac{\pi}{2n}]]}{\exp[-i(j+k)\frac{\pi}{2n}] - \exp[i(j+k)\frac{\pi}{2n}]}\right\}$$

$$= \frac{1}{2} \operatorname{Re}\left\{\frac{i\exp[-i(j-k)\frac{\pi}{2n}]}{\sin[(j-k)\frac{\pi}{2n}]} - \frac{i\exp[-i(j+k)\frac{\pi}{2n}]}{\sin[(j+k)\frac{\pi}{2n}]}\right\}$$

$$= \frac{1}{2}\,\mathrm{Re}\left\{\frac{i\cos[(j-k)\frac{\pi}{2n}] + \sin[(j-k)\frac{\pi}{2n}]}{\sin[(j+k)\frac{\pi}{2n}]} - \frac{i\cos[(j+k)\frac{\pi}{2n}] + \sin[(j+k)\frac{\pi}{2n}]}{\sin[(j+k)\frac{\pi}{2n}]}\right\}$$

$$= 0\ . \tag{I.3}$$

For the case $j=k$ with both $(j+k)$ and $(j-k)$ even, we have

$$\exp[i(j-k)\pi] = \exp[i(j+k)\pi] = +1$$

and

$$S = \frac{1}{2}\,\mathrm{Re}\left\{\frac{1-\exp[i(j-k)\pi]}{1-\exp[i(j-k)\frac{\pi}{n}]} - \frac{1-\exp[i(j+k)\pi]}{1-\exp[i(j+k)\frac{\pi}{n}]}\right\} = 0\ . \tag{I.4}$$

For $j=l=n$ or $j=k=0$ we have

$$S = \sum_{r=0}^{n-1}\sin^2\frac{j\pi r}{n} = \frac{1}{2}\sum_{r=0}^{n-1}\left[1-\cos\frac{2j\pi r}{n}\right] = \frac{n}{2} - \frac{1}{2}\,\mathrm{Re}\sum_{r=0}^{n-1}\exp\left[i\left(\frac{2j\pi r}{n}\right)\right]$$

$$= \frac{n}{2} - \frac{1}{2}\,\mathrm{Re}\left\{\frac{1-\exp[i\ 2j\pi r]}{1-\exp\left[i\ \frac{2j\pi r}{n}\right]}\right\} = \frac{n}{2}\ . \tag{I.5}$$

For $j=k=0$ we have

$$S = \sum_{r=0}^{n-1}\sin^2 0 = 0$$

and for $j=k=n$ we have

$$S = \sum_{r=0}^{n-1}\sin^2(r\pi) = 0\ . \tag{I.7}$$

In summary, we have

$$\sum_{r=0}^{n''}\sin j\left(\frac{\pi r}{n}\right)\sin k\left(\frac{\pi r}{n}\right) = \begin{cases} 0 & j\neq k \\ \frac{n}{2} & j=k\neq 0 \ \text{ or } \ j=k\neq n \\ 0 & j=k=0 \ \text{ or } \ j=k=n \end{cases} \tag{I.8}$$

Now, since the r=0 and r=n terms in the sum are both zero, we may write

$$\left.\begin{array}{l} \displaystyle\sum_{r=0}^{n}{}' \sin j\left(\frac{\pi r}{n}\right) \sin k\left(\frac{\pi r}{n}\right) \\[2ex] \displaystyle\sum_{r=0}^{n} \sin j\left(\frac{\pi r}{n}\right) \sin k\left(\frac{\pi r}{n}\right) \\[2ex] \displaystyle\sum_{r=1}^{n-1} \sin j\left(\frac{\pi r}{n}\right) \sin k\left(\frac{\pi r}{n}\right) \end{array}\right\} = \left\{\begin{array}{ll} 0 & j=k \\[2ex] \frac{n}{2} & j=k=0 \quad \text{or} \quad j=k=n \\[2ex] 0 & j=k=0 \quad \text{or} \quad j=k=n \end{array}\right. \tag{I.9}$$

Now, with

$$u_r = \cos\frac{\pi r}{n} \tag{6.9}$$

and

$$\sin j\left(\frac{\pi r}{n}\right) = \sin\left(\frac{\pi r}{n}\right) U_{j-1}(u_r) \tag{I.10}$$

(see Eq. (2.11)), the above relationships can be written

$$\left.\begin{array}{l} \displaystyle\sum_{r=0}^{n}{}'' \sin^2\frac{\pi r}{n}\, U_{j-1}(u_r)\, U_{k-1}(u_r) \\[2ex] \displaystyle\sum_{r=0}^{n}{}' \sin^2\frac{\pi r}{n}\, U_{j-1}(u_r)\, U_{k-1}(u_r) \\[2ex] \displaystyle\sum_{r=0}^{n} \sin^2\frac{\pi r}{n}\, U_{j-1}(u_r)\, U_{k-1}(u_r) \\[2ex] \displaystyle\sum_{r=1}^{n-1} \sin^2\frac{\pi r}{n}\, U_{j-1}(u_r)\, U_{k-1}(u_r) \end{array}\right\} = \left\{\begin{array}{ll} 0 & j=k \\[4ex] \frac{n}{2} & j=k=0 \text{ or } j=k=n \\[4ex] 0 & j=k=n \text{ or } j=k=0 \end{array}\right. \tag{I.11}$$

References

1) L. Fox and I.B. Parker (1968) **Chebyshev Polynomials in Numerical Analysis**, Oxford University Press.

2) M.A. Snyder (1966) **Chebyshev Methods in Numerical Approximation**, Prentice-Hall Inc.

3) D.E. Lobb (1973) Nucl. Instr. and Meth. 114, 609-614.

ANALYSIS OF DIPOLE FRINGE FIELDS

QUADRUPOLES WITH PERFECT N=2 SYMMETRY

Large Bore Magnet Optics.

Filippo Neri AT-3

Peter Walstrom Grumann/LANL

J. van Zeijts University of Maryland

HOOPLA

High Order Optics Program at Los Alamos

PILAC Workshop

Aug 13 1991

seal, *Cystophora cristata*, of northern seas, spotted coat and an *inflatable hoodlike* or in the region of the nose. Also called "blad-

ım, hŏŏd′-) *n.* 1. A gangster; thug. 2. A youth. [Origin unknown.]

n., *pl.* -doos. 1. Voodoo. 2. a. Bad luck. bad luck. —*tr.v.* hoodooed, -dooing, -doos. to. [Perhaps variant of VOODOO.] —hoo′-

ingk′) *tr.v.* -winked, -winking, -winks. 1. To in. 2. *Archaic.* To blindfold. 3. *Obsolete.* Synonyms at deceive. [HOOD + WINK.]

lang. Nonsense. [Origin unknown.]

pl. hoofs or hooves (hŏŏvz, hōōvz). 1. The ing the toes or lower part of the foot of a ers Perissodactyla and Artiodactyla, such as 2. The foot of such an animal, especially a e human foot. —on the hoof. Alive; not yet ecially of cattle. —*v.* hoofed, hoofing, hoofs. e with the hoofs. 2. *Informal.* To walk. dance. 2. To go on foot; walk. Often used *instead of taking a cab.* [Middle English ŏf. See kapho- in Appendix.*]

und′, hŏŏf′-) *adj.* Afflicted with drying and ool, resulting in lameness. Said of a horse.) *adj.* Having hoofs; ungulate.

′fər) *n. Slang.* A professional dancer; espe-

Also Hug-li. A branch of the Ganges, rising ublic of India, and flowing 160 miles south l.

curved or sharply bent device, usually of drag, suspend, or fasten something. 2. A ; snag. 4. Anything shaped like a hook, as: d plant or animal part. b. A short angled letter. c. *Surfing.* The lip of a breaking . The fixed part of a door hinge; the pin. . 7. *Boxing.* A short swinging blow de- d arm. 8. *Golf.* A stroke which sends the player. —by hook or (by) crook. By what- fair or unfair. —get the hook. *Slang.* To wn —hook, line, and sinker. *Slang.* en r; completely. —off the hook. n b or a vexatious obligation. 2. Left

433

often between unlikely associates or factors.

hook·worm (hŏŏk′wûrm′) *n.* Any of numerous small, parasitic nematode worms of the family Ancylostomatidae, having hooked mouth parts with which they fasten themselves to the intestinal walls of various hosts, including man, causing the disease ancylostomiasis.

hookworm disease. Ancylostomiasis (*see*).

hook·y¹ (hŏŏk′ē) *adj.* -ier, -iest. Resembling a hook; hook-shaped.

hook·y² (hŏŏk′ē) *n. Informal.* Absence without leave; truancy. Used in the phrase *play hooky.* [Perhaps from HOOK (to escape).]

hoo·li·gan (hōō′lĭ-gən) *n. Informal.* A young ruffian; hoodlum. [Origin obscure.] —hoo′li·gan·ism′ *n.*

hoop (hōōp, hŏŏp) *n.* 1. A circular band of metal or wood put around a cask or barrel to bind the staves together. 2. A large wooden, plastic, or metal ring used as a plaything. 3. One of the lightweight circular supports for a hoop skirt (*see*). 4. A circular, ringlike earring. 5. One of a pair of circular wooden or metal frames used to hold material taut for embroidery or similar needlework. 6. A croquet wicket. —*tr.v.* hooped, hooping, hoops. 1. To hold together or support with or as if with a hoop or hoops. 2. To encircle. [Middle English *hoop*, Old English *hōp*, from Germanic *hōpaz* (unattested).]

hoop·er (hōō′pər, hŏŏp′ər) *n.* A cooper (*see*).

hoop·la (hōōp′lä′, hŏŏp′-) *n. Slang.* 1. Boisterous jovial commotion or excitement. 2. Talk intended to mislead or confuse. [French *houp-là*!.]

hoo·poe (hōō′pōō, -pō) *n.* An Old World bird, *Upupa epops*, having distinctively patterned plumage, a fanlike crest, and a slender, downward-curving bill. [Variant of obsolete *hoop*, from Old French *huppe*, from Latin *upupa* (imitative).]

hoop-pet·ti·coat narcissus (hōōp′pĕt′ĭ-kōt′, hŏŏp′-). The petticoat narcissus (*see*).

hoop skirt. A long full skirt belled out with a series of connected hoops.

hoop snake. Any of several snakes, such as the mud snake (*see*), that supposedly grasp the tail in the mouth and move with a rolling, hooplike motion.

hoo·ray. Variant of hurrah.

Hoo·sac Mountains (hōō′sək). A section of the Green Range, in western Massachusetts. Highest elevation, Spruce Hill (2,588 feet).

hoose·gow (hōōs′gou′) *n. Slang.* A jail. [Spanish *juzgado*, courtroom, from the past participle of *juzgar*, to judge, from Latin *jūdicāre*, to JUDGE.]

hoop

hoop skirt
Illustration in *Punch*, August 1856

Fringe Fields (Dipole ?).

- Basic equations.
- The importance of being analytic.
- Maps versus particle tracking.
- Questions.

Midplane Symmetric Case.

Scalar potential: $\partial_{xz}^2 = \dfrac{\partial^2}{\partial x^2} + \dfrac{\partial^2}{\partial z^2}$

$$V = \sum_{l=0}^{\infty} \frac{(-1)^l}{(2\,l+1)!} \partial_{xz}^{2l} B_y(x,0,z)\, y^{2l+1}$$

Magnetic field:

$$B_y = \sum_{l=0}^{\infty} \frac{(-1)^l}{(2\,l)!} \partial_{xz}^{2l} B_y(x,0,z)\, y^{2l}$$

This expansion makes sense only if the derivatives of By exist.

...

Hamiltonian equations.

$$H = -\sqrt{P_\tau^2 - m^2 - \Pi_x^2 - \Pi_y^2} - A_z$$

$\Pi_x = P_x - A_x \qquad \Pi_y = P_y - A_y$

$$\dot{x} = \frac{\partial H}{\partial P_x} = \frac{\Pi_x}{\sqrt{P_\tau^2 - m^2 - \Pi_x^2 - \Pi_y^2}} \qquad \dot{P}_x = \frac{\frac{\partial A_x}{\partial x}\Pi_x + \frac{\partial A_y}{\partial x}\Pi_y}{\sqrt{P_\tau^2 - m^2 - \Pi_x^2 - \Pi_y^2}} + \frac{\partial A_z}{\partial x}$$

$$\dot{y} = \frac{\partial H}{\partial P_y} = \frac{\Pi_y}{\sqrt{P_\tau^2 - m^2 - \Pi_x^2 - \Pi_y^2}} \qquad \dot{P}_y = \frac{\frac{\partial A_x}{\partial y}\Pi_x + \frac{\partial A_y}{\partial y}\Pi_y}{\sqrt{P_\tau^2 - m^2 - \Pi_x^2 - \Pi_y^2}} + \frac{\partial A_z}{\partial y}$$

$$\dot{\tau} = \frac{\partial H}{\partial P_\tau} = \frac{-P_\tau}{\sqrt{P_\tau^2 - m^2 - \Pi_x^2 - \Pi_y^2}} \qquad \dot{P}_\tau = 0$$

We need the vector potentials.

Vector Potentials.

$$\beta(x,0,z) = \int_{-\infty}^{z} B_y(x,0,z')dz'$$

$$A_x = \sum_{l=0}^{\infty} \frac{(-1)^l}{(2l)!}\partial_{xz}^{2l}\beta(x,0,z)\,y^{2l}$$

$$A_y = \sum_{l=0}^{\infty} \frac{(-1)^l}{(2l+1)!}\partial_{xz}^{2l}\frac{\partial}{\partial x}\beta(x,0,z)\,y^{2l+1}$$

$$A_z = 0$$

This is just one possible choice of gauge.

Particularly convenient if no x dependence, but it can be used in the general case.

The Importance of being analytic.

- No matter what method is used, if one wants to expand final conditions as a polynomial of the initial conditions, one assumes the existence of a series expansion of the potentials.
- Maxwell equations force analytic solutions in current-free regions.
- There is no such thing as a "Maxwell Spline".
- The only way to interpolate measured data in a way consistent with Maxwell equations is to use a *single* analytic function.
- Analytic functions have the added advantage that one can usually take the derivatives exactly and program them.

Map Methods.

Rather than integrating particles and then deriving Taylor series coefficients, directly compute the coefficients.

In simple cases we can derive analytic results, in general we derive ordinary differential equations for the Taylor coefficients and then integrate them numerically.

Faster than integrating particles (?) and possibly more exact (?).

Not *necessarily* related to either Lie or Differential Algebras.

One possible algorithm (GENMAP) computes Lie coefficients, but one does not have to use them.

Equations for Maps.

The equation of motion for a particle can be written as.

$$\mathbf{z} = (\; x, \quad P_x, \quad y, \quad P_y, \quad \tau, \quad P_\tau \;)$$

$$\dot{\mathbf{z}} = \mathbf{J}\,\frac{\partial H}{\partial \mathbf{z}}$$

Dot denotes derivative with respect to independent variable *s*.

$$\mathbf{J} = \begin{pmatrix} 0 & 1 & 0 & 0 & 0 & 0 \\ -1 & 0 & 0 & 0 & 0 & 0 \\ 0 & 0 & 0 & 1 & 0 & 0 \\ 0 & 0 & -1 & 0 & 0 & 0 \\ 0 & 0 & 0 & 0 & 0 & 1 \\ 0 & 0 & 0 & 0 & -1 & 0 \end{pmatrix}$$

If we introduce a set of functions giving the initial coordinates in term of the final ones:

$$z_i(0) = T_i(s, \mathbf{z})$$

Then the following equations follow:

$$\dot{T}_i = \frac{\partial H}{\partial \mathbf{z}}\,\mathbf{J}\,\frac{\partial T_i}{\partial \mathbf{z}}$$

These are PDEs. They can be solved for the Taylor coefficients of *T*. Then, after inversion, we can obtain the coefficients of the map.

This method is actually used in HOOPLA.

Implementation.

The direct integration method has been up to now used only for Halbach (permanent) magnets or Walstrom (see next talk) magnets but it is generally applicable.

The field models used are analytic formulas derived by P. Walstrom.

The programming has mostly been done by J. van Zeijts.

For very high order one needs to be very careful, since the high order derivatives oscillate very fast.

We tend to prefer self-adjusting, variable step methods.

Alternatively, since the potentials *are* analytic, we can use very high order Adams methods, but still use brute force doubling of the number of steps until the results stop changing. Exact to 13 digits! Round-off?

Walstrom
Magnet
Winding

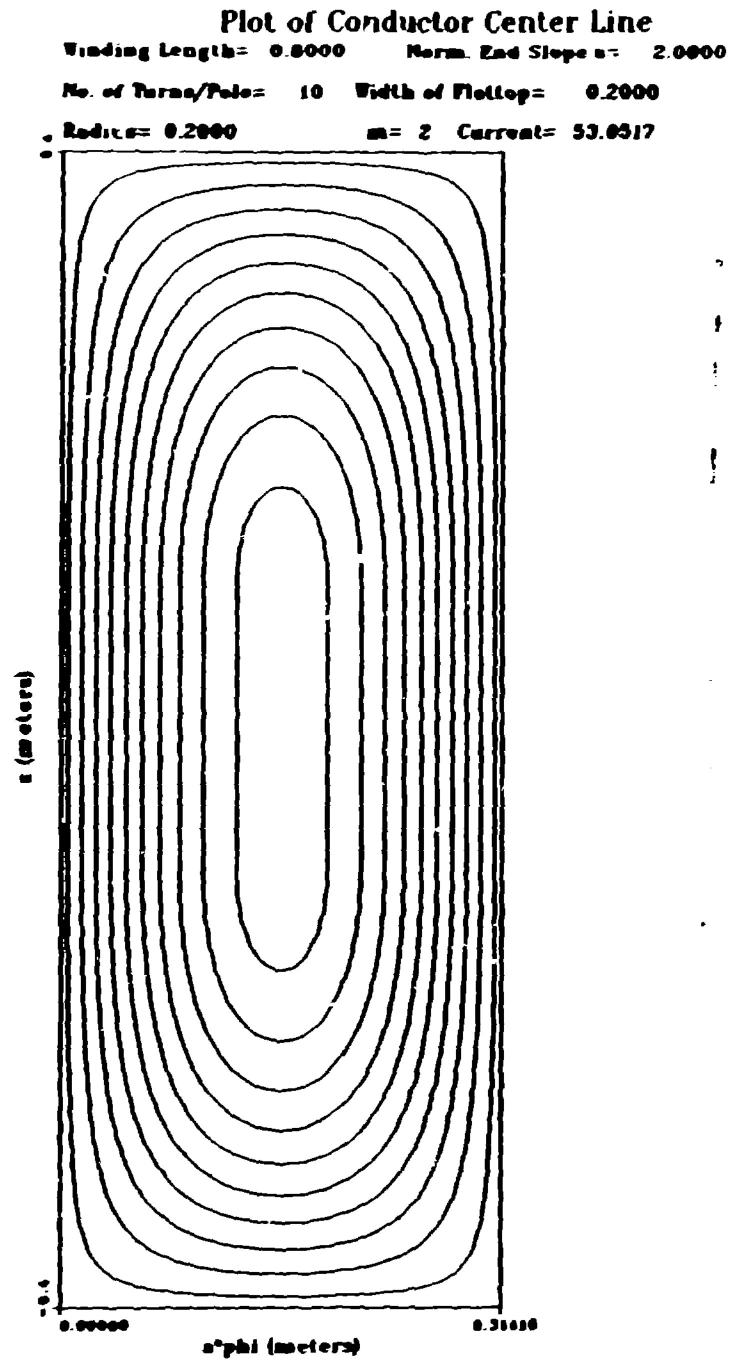

Application

Beam expanding telescope aberrations.

List of contributors:

A. Dragt, University of Maryland, A. Jason,LANL,

R. Kraus, LANL, C. T. Mottershead, LANL, P Walstrom, Grumann/LANL,

J. van Zeijts, University of Maryland.

Fifth Order Correction

Thanks to **Tlie**, it is now possible to fit fifth order (12-pole) correctors.

- Fifth order geometric aberrations are generated by –

$$f_6 = Ax^6 + Bx^4y^2 + Cx^2y^4 + Dy^6$$

- Therefore four duodecapole (m=6) trims are needed to cancel these four coefficients
- **Tlie** did it for thin shell REC multipoles in alternating 0.5 m sections of Quad A and all of Quad B:

	DDA1	DDA2	DDA3	DDB
Field (T/m^5)	2.70	-1.86	0.516	-0.028
Percent of quad	-5.44%	3.75%	-1.04%	-0.032%

- Multipole correctors increase the next higher geometric aberration in the corrected maps. These agree with tracking statistics in appropriate cases :

RMS kick amplitude at 10 cm

	Focused (C1)	Octupoles (C3)	Duodecapoles (5)
Order 3	93.94	0.0	0.0
Order 5	0.62	6.71	0.0
Order 7	0.031	0.035	1.283
Order 9	0.0036	0.0038	0.1016

- Computing to 2 orders higher than correction is required for accuracy.

AT DIVISION
Los Alamos

CEBAF SUPERCONDUCTING Cos (2θ) QUADRUPOLE

CEBAF HRS $\cos 2\theta$
SUPERCONDUCTING QUADRUPOLES

- CEBAF HRS
- Quads: Basic choice
- Design Parameters
- TOSCA 3D Field Analysis
- Lorentz Forces
- Tolerances
- Correctional Multipoles
- Remarks

J. Alcorn
A. Gavalya
J. Mougey
J. Simkin
T. Tortschanoff
N. Tuzel

PILAC workshop
Aug 12, 13, 1991
S. Nanda

HALL A EXPERIMENTAL EQUIPMENT CEB

- **High Resolution Spectrometer Pair HRS^2**
  - Two identical 4 GeV/c spectrometers, QQDQ configuration, with superconducting magnets
  - Focal plane instrumentation: Vertical drift chambers, scintillation and Cerenkov counters, shower detectors, focal plane proton polarimeter
- **High power solid and cryogenic targets**
- **Beam line equipment**
  - Including high power dump and beam polarimeter.
- **Data acquisition and counting house equipment**

HALL "A" ELEVATION VIEW

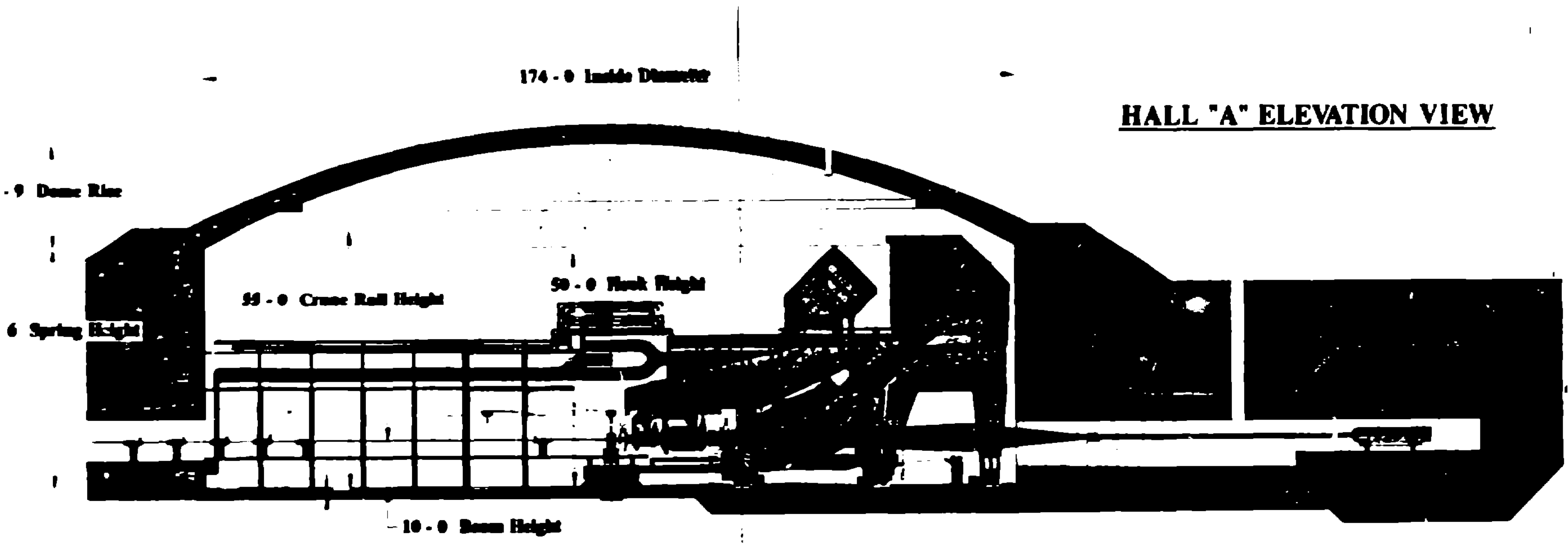

ensions are in "Feet - inches".

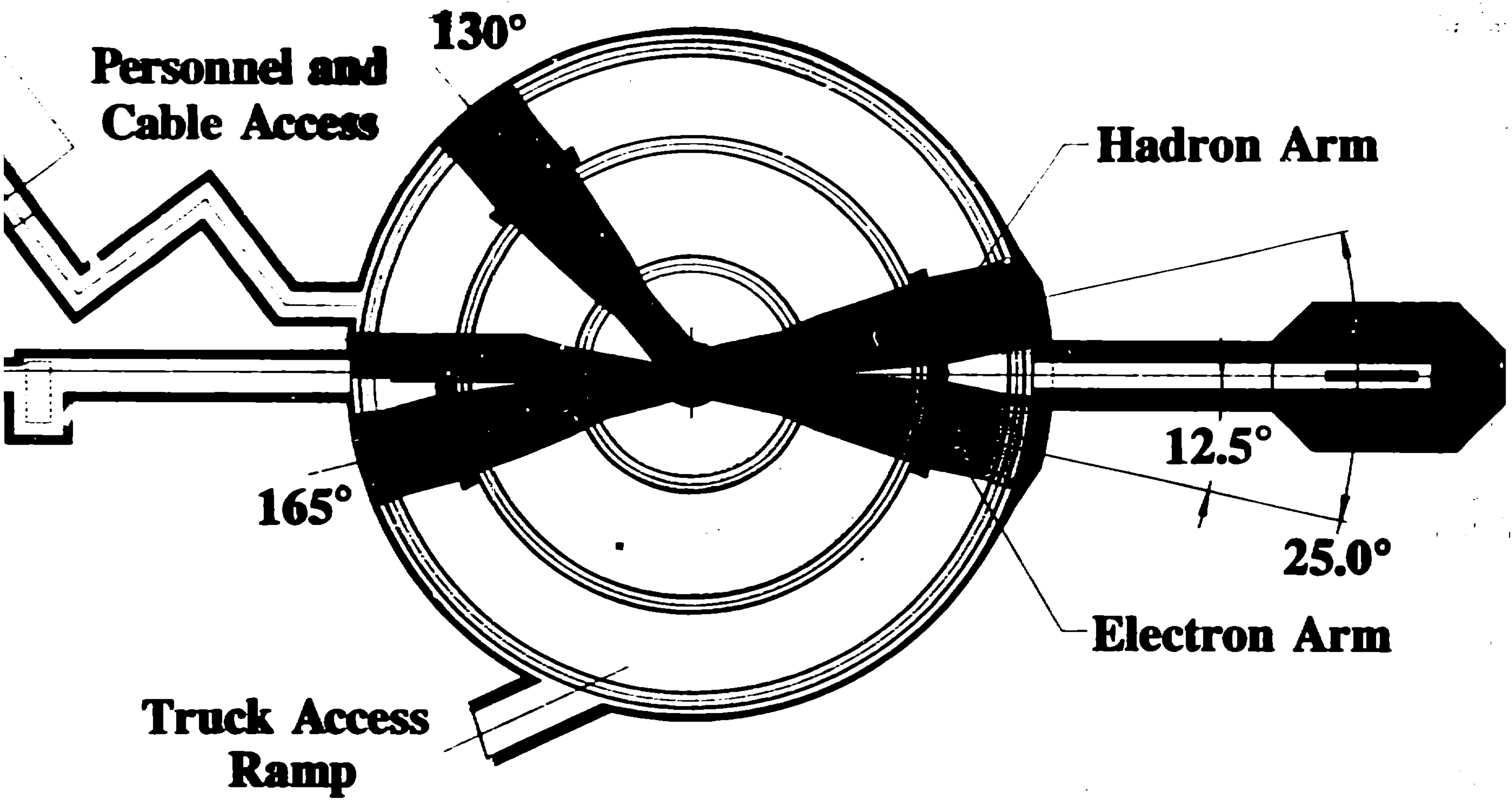

RANGE OF POSITIONS FOR HRS "ARMS"

CEBAF HRS SPECIFICATIONS

CONFIGURATION:

OPTICS	QQD_nQ
BEND	45° (vertical)
OPTICAL LENGTH	23.4 m
D/M	5.0
FOCAL PLANE ANGLE	38° (w.r.t O.A.)
DISP. MATCHING	NO
HARDWARE CORRECTION	4th Order

ACCEPTANCES:

P_{max}	4 GeV/c
$\Delta(\delta p/p)$	±5%
$\Delta\Omega$	7 msr
Δy_t	±5 cm

RESOLUTIONS* (FWHM)

$\delta(\delta p/p)$	momentum	$< 10^{-4}$	($\sim 4\times10^{-4}$ hw; $< 10^{-4}$ sw)
$\delta\theta$	scatt. angle	0.1 mr	
δy_t	vertex	1.0 mm	

* The following parameters are assumed

detector $\delta x \approx 250\,\mu m$
$\delta\theta \approx 0.5$ mr

beam $\delta p/p \leq 10^{-4}$
$\delta x \approx 100\,\mu$

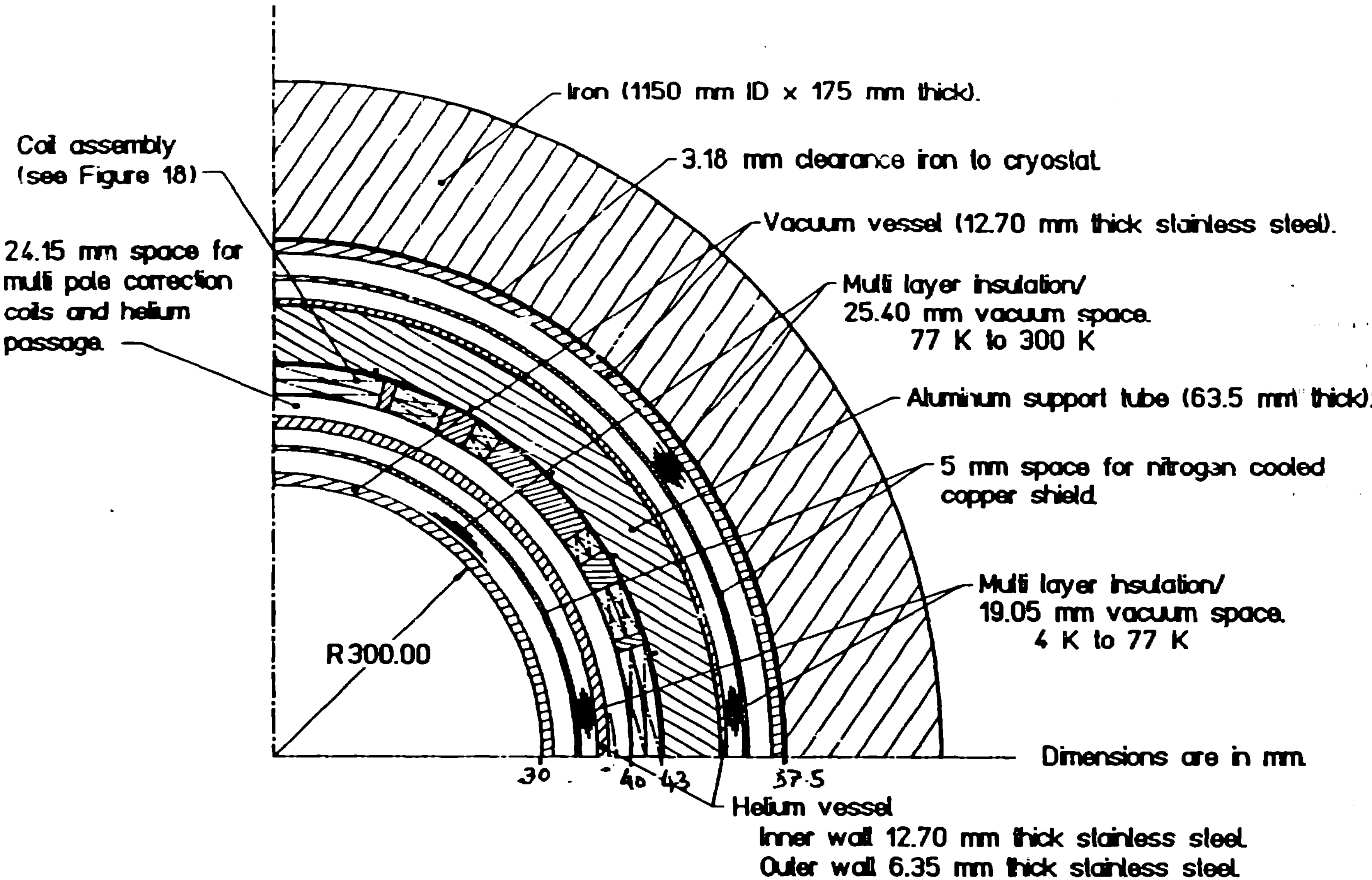

Cosine 2θ Quadrupole: Assembly Cross-Section

Figure Q.11

2/7/91

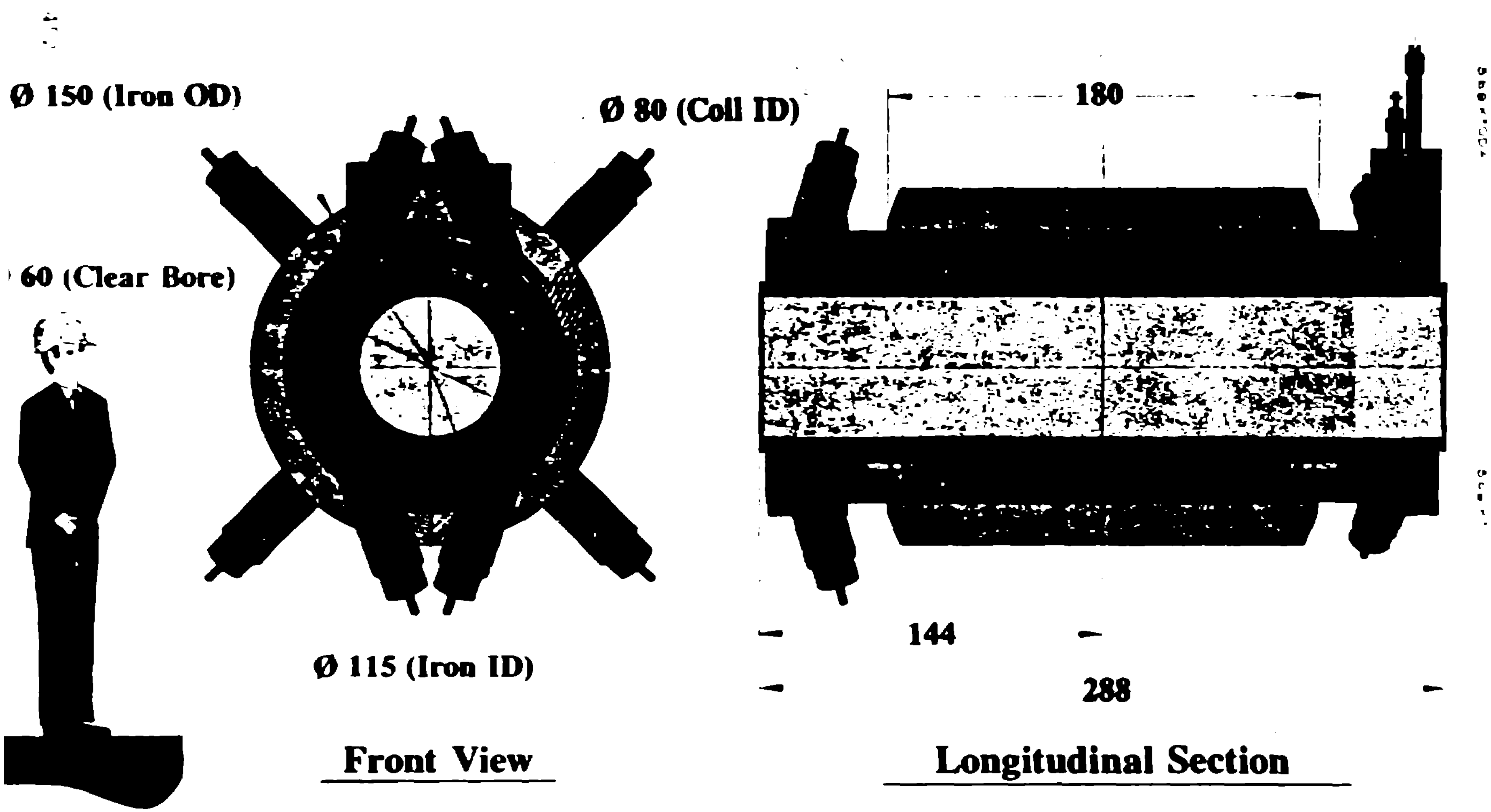

Dimensions are in cm.

Approx. Weight 40 Klbs.

COSINE 2θ QUADRUPOLE

Table I. Quadrupole Requirements				
		Q1	Q2	Q3
Magnetic Length	(m)	0.8	1.8	1.8
Useful Aperture	(m×m)	0.22×0.30	0.50×0.36	0.33×0.55
Useful Aperture Field	(T)	1.3	-0.88	-0.82
Quadrupole	(T/m)	8.650	-3.116	-2.946
Sextupole	(T/m^2)	0	0.123	1.000
Octupole	(T/m^3)	0	1.767	-1.037
Gradient Uniformity	$\Delta G/G$	10^{-3}	10^{-3}	10^{-3}
Distance from Target	(m)	2.2	4.75	18.96

Table II. Design Parameters			
	Q1	Q2	
Field Gradient	9.0	3.5	T/m
Magnetic Length	0.8	1.8	m
Useful Aperture	0.3	0.6	m
Gradient Uniformity	10^{-3}	10^{-3}	

Absolute Azimuthal Positioning	± 2 mr
Azimuthal Position Measurement	± 0.1 mr
Vertical Pointing	± 0.1 mr
Radial Position	± 0.5 cm
Azimuthal Traversing Rate	3°/min

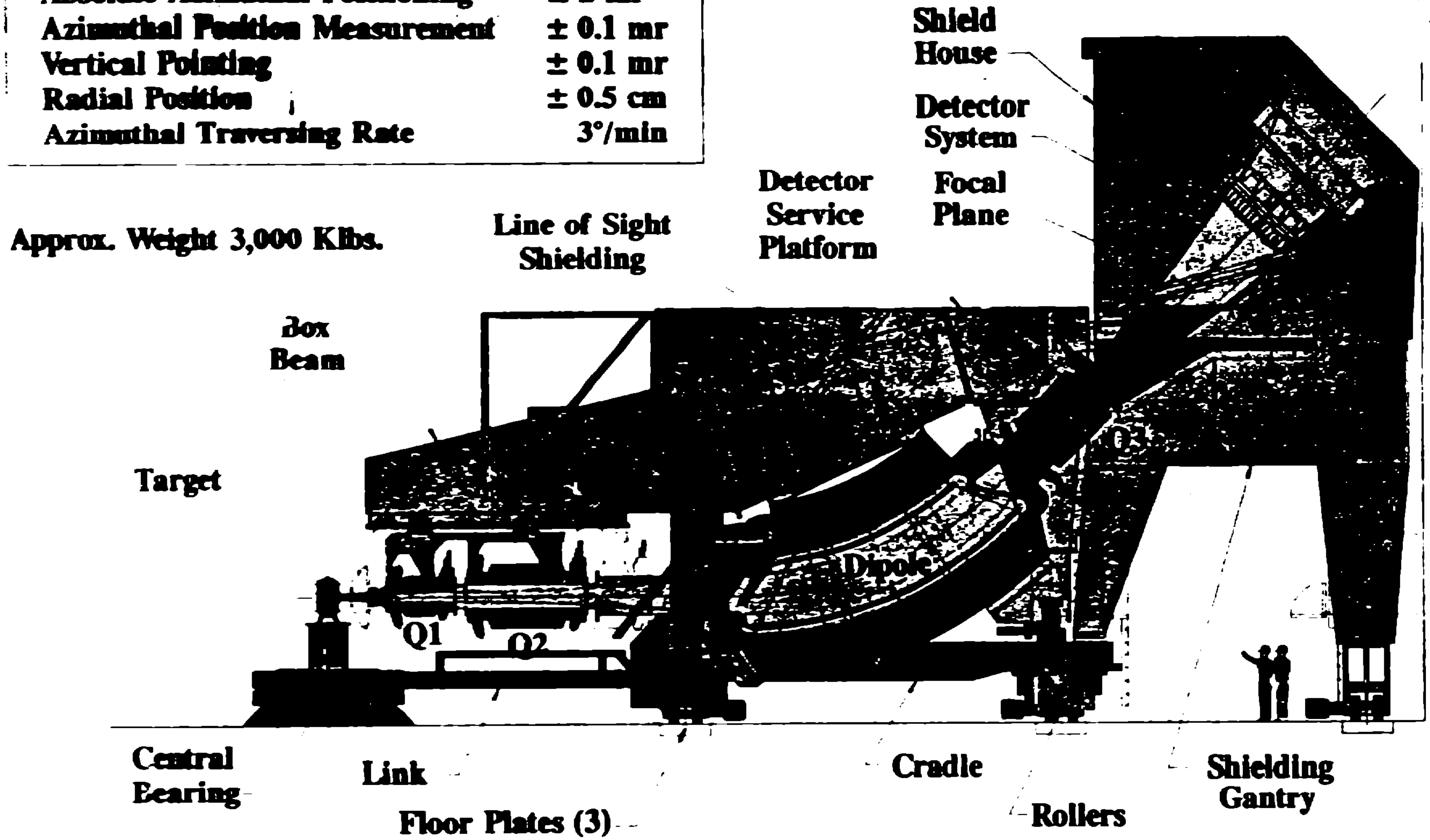

4 GEV SPECTROMETER/SUPPORT ASSEMBLY

Notes:

- Dimensions are in mm

Conductor:

- Maximum operating current: 1850 A
- Average current density: 67.5 A/mm^2 @ 1850 A
- Acceptance test current: 2000 A

NbTi:

- Jc = 3000 A/mm^2 @ 2.5 T , 4.5 K
- Jop = 1575 A/mm^2 @ 2.5 T , 4.5 K

Composite wire insert:

- Configuration: flattened (Rutherford) cable
- Number of wires: 18
- Wire diameter: 0.500 mm (19.7 mils)
- Cu:NbTi ratio = 2:1

Copper substrate:

- Area: 25.6 mm^2
- Average current density at operating current: 72.3 A/mm^2
- Material: Oxygen Free High Conductivity (OFHC) (CDA 102), fully annealed.

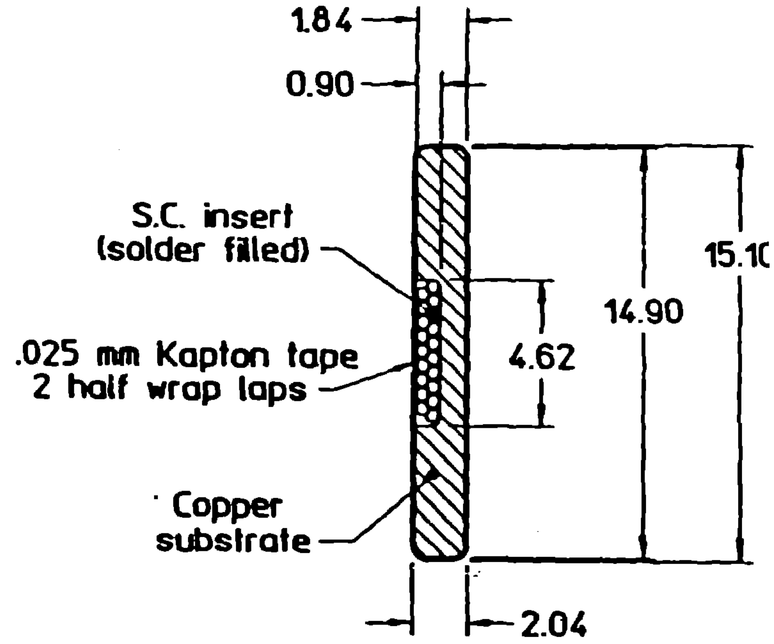

1.85 KA Conductor of Reference Design

Figure Q.15

2/4/91

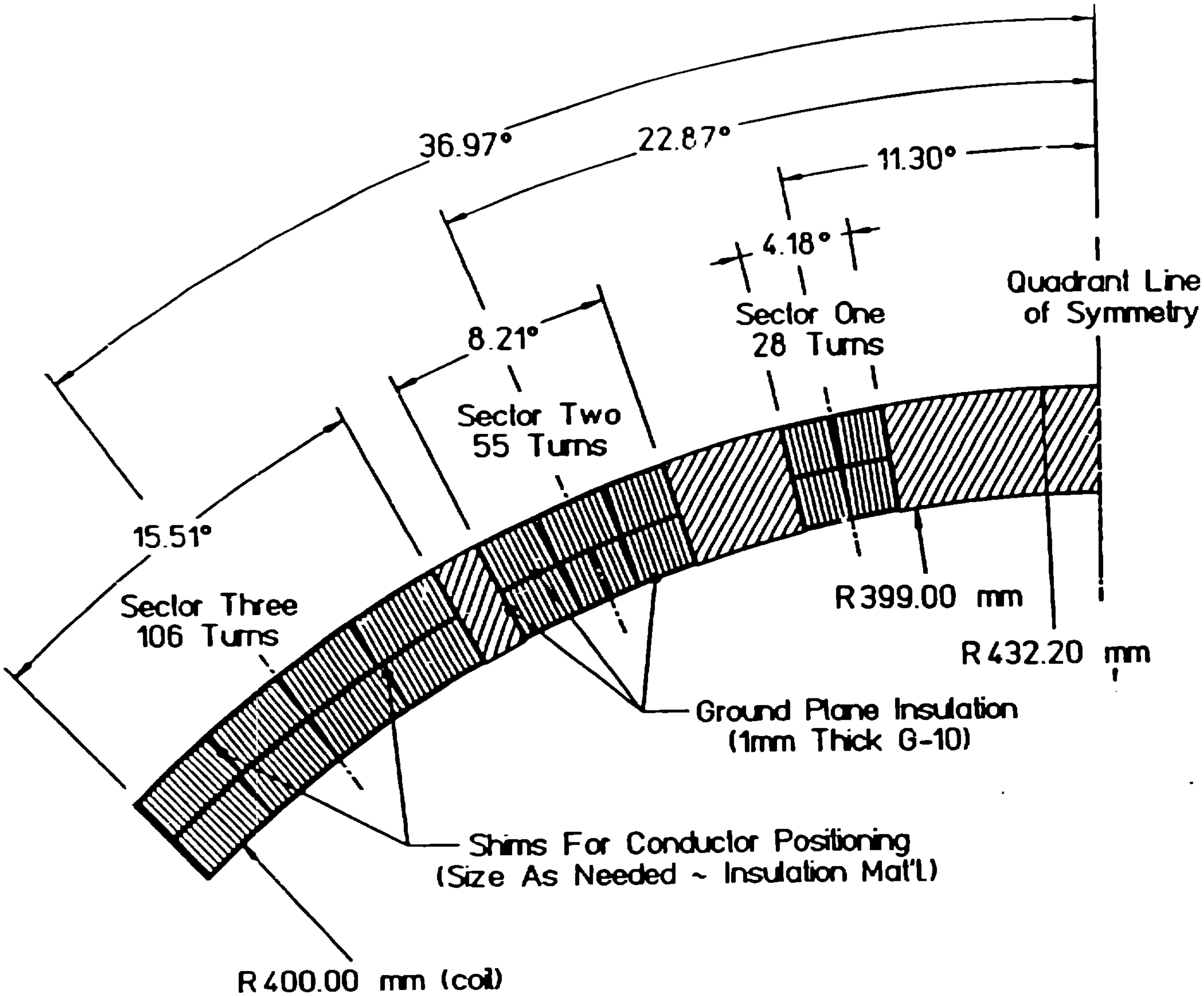

1/28/91

Coil Quadrant Cross-Section

Figure Q.12

Jun491 04:30:23 Page 2 : PLOT

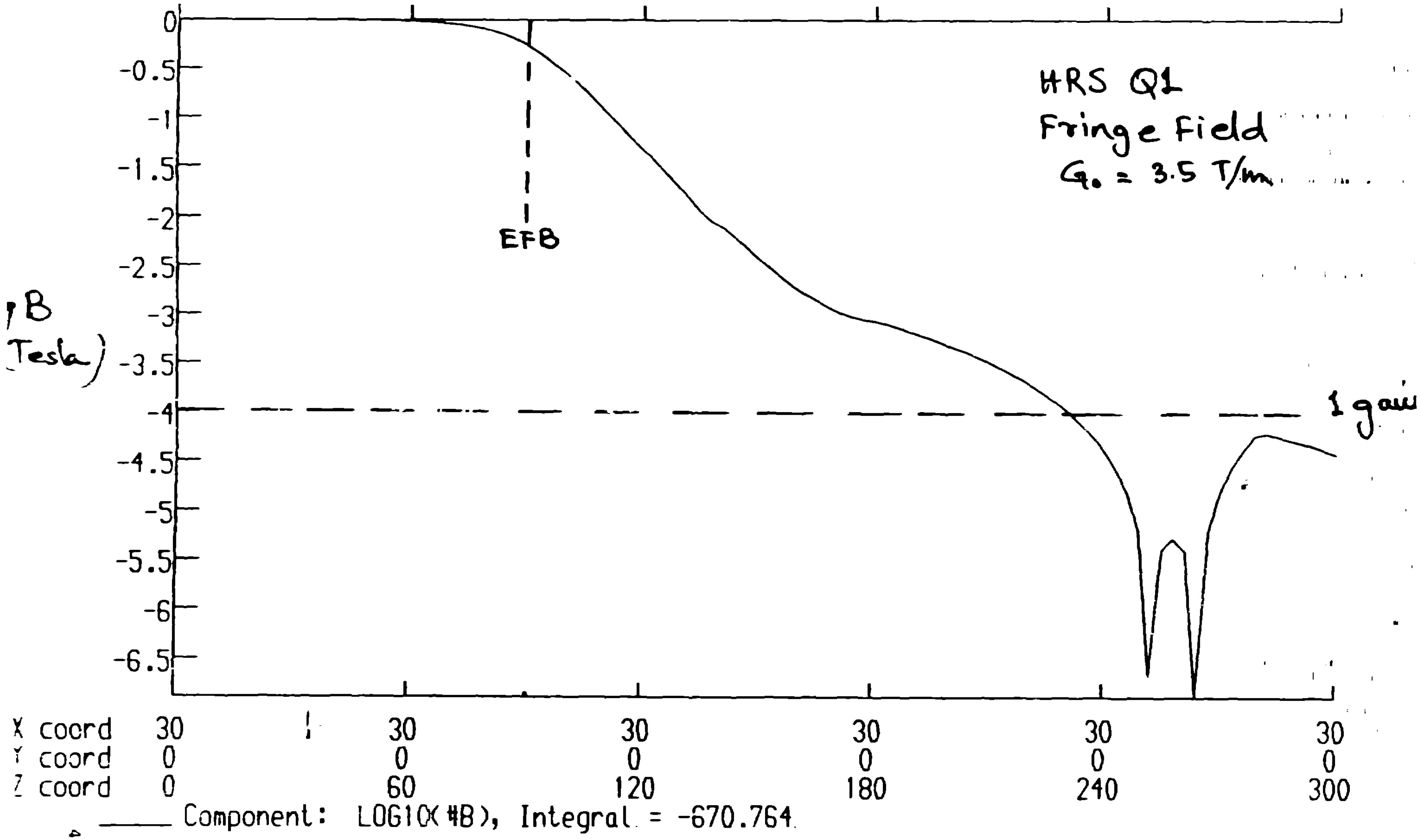

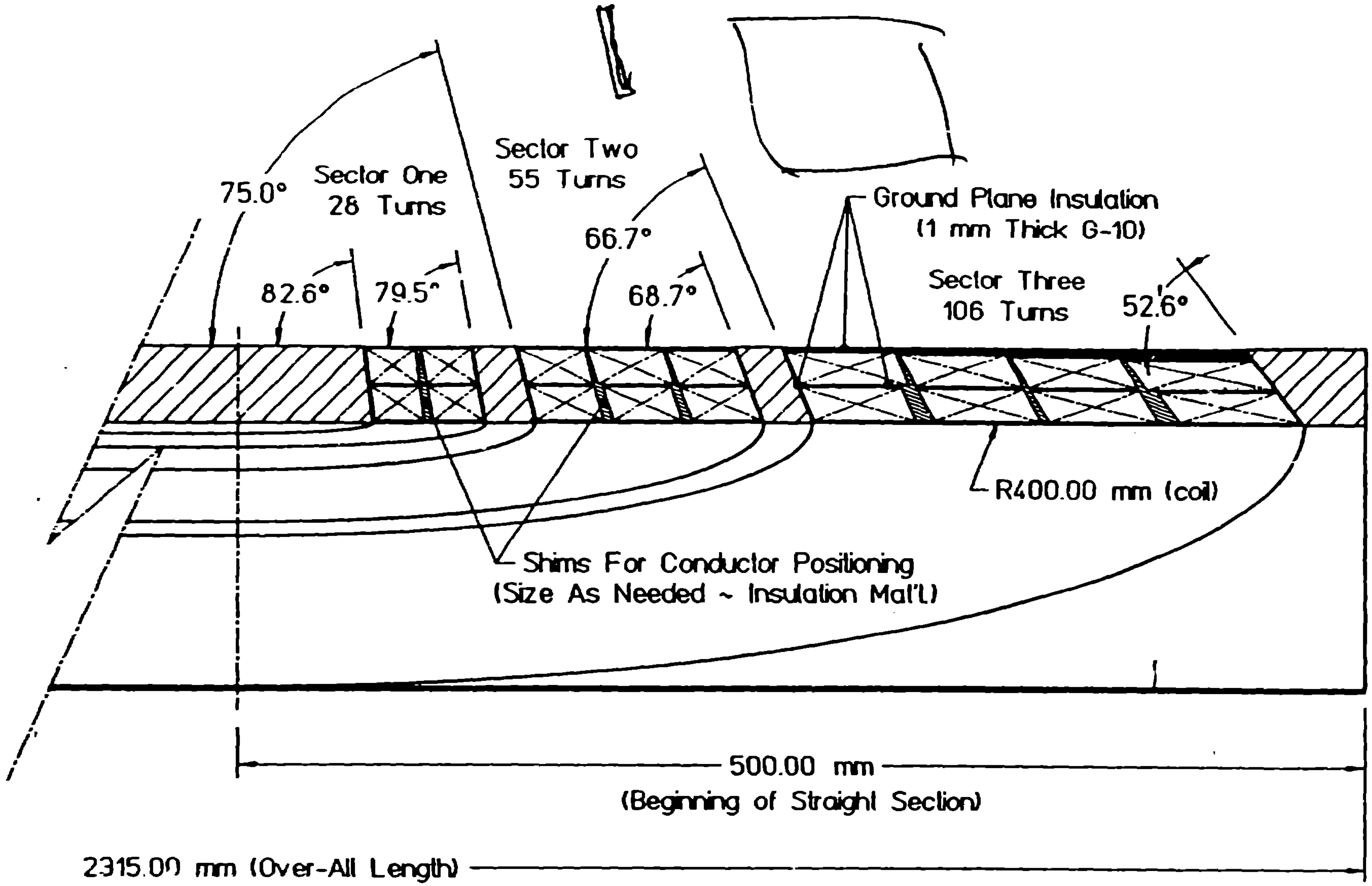

Coil Quadrant Longitudinal–Section

2/4/91

Figure Q.13

Why cos(2θ) design?

Iron dominated quadrupole

- Field shaped by iron pole faces
  Cannot reach gradient specification

Panofsky quadrupole

- Allows rectangular aperture
- Lower Amp-turns and stored energy
  Complicated end shapes.
  Difficult to obtain desired field quality.
  Auxiliary multipole windings
  difficult to incorporate.

cos(2θ) quadrupole

- cylindrical geometry
- Simple end shapes
- Easier mechanical design
- Auxiliary multipole windings easily implemented
- ISR/LEP proven technology
  Higher Amp-turns and stored energy

Cos2θ Current Distribution

Magnetic Field in 2D cylindrical geometry

$$B_\theta(r,\theta) = \sum_n a_n r^{n-1} \mathrm{Cos}\, n\theta$$

where n is an integer.

<u>Note that n gives rise to 2n poles</u>

n=2 is a QUADRUPOLE with Cos2θ current distribution

Perfect Cos2θ Practical Approximations

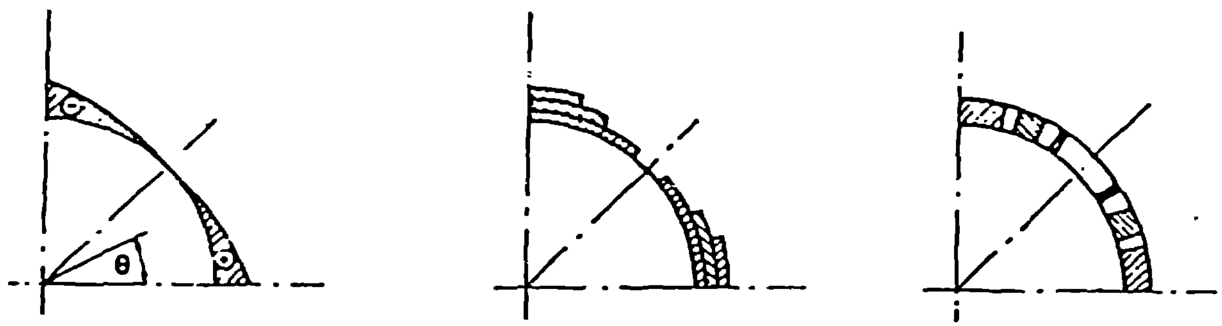

Departure from perfect Cos2θ distribution creates higher harmonics. However, due to 4-fold symmetry of the geometry, the allowed harmonics are

$$n = 2, 6, 10, 14\ldots$$

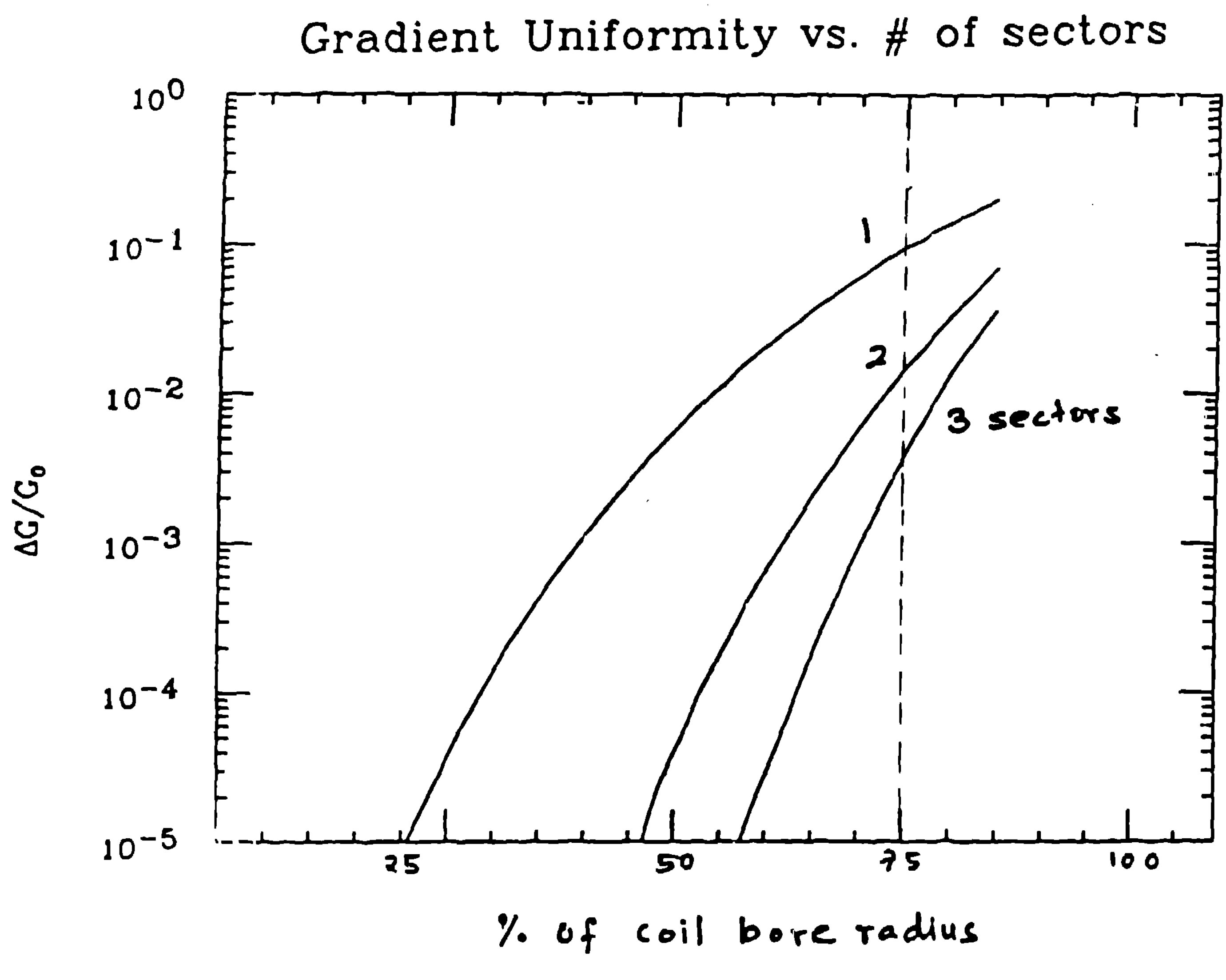

Figure 1. Gradient error as a function of percentange of the coil bore for one, two, and three sector Cos2θ approximations.

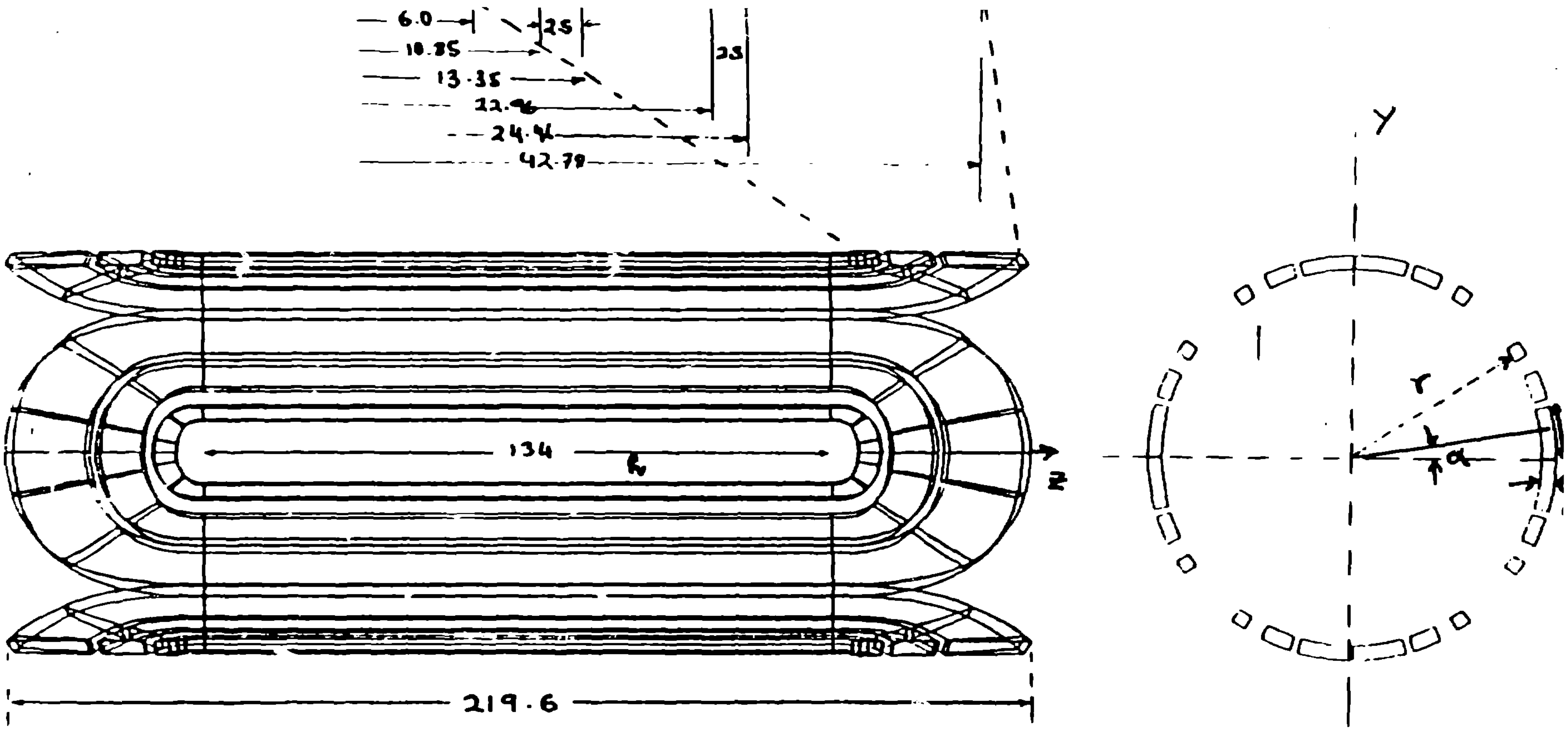

Figure 3. Full coil geometry for Q1.

VF/OPERA.

Previous Des
(5T/m, 80 cm g

Table VI. Operating characteristics

	Q1	Q2		
Current density (overall)	8.34	5.63	kA/cm^2	16.5
Total Amp-turns	0.97	1.4	MA	2.9
Operating current	2946	1989	A	
Stored Energy	116	592	kJ	3500
Peak coil field	2.10	1.83	T	4
Max. radial force	7.3	7.8	Ton/m	32
Max. tangential force	10.8	11.6	Ton/m	46
Max. axial force	11.4	13.1	Ton/m	4i

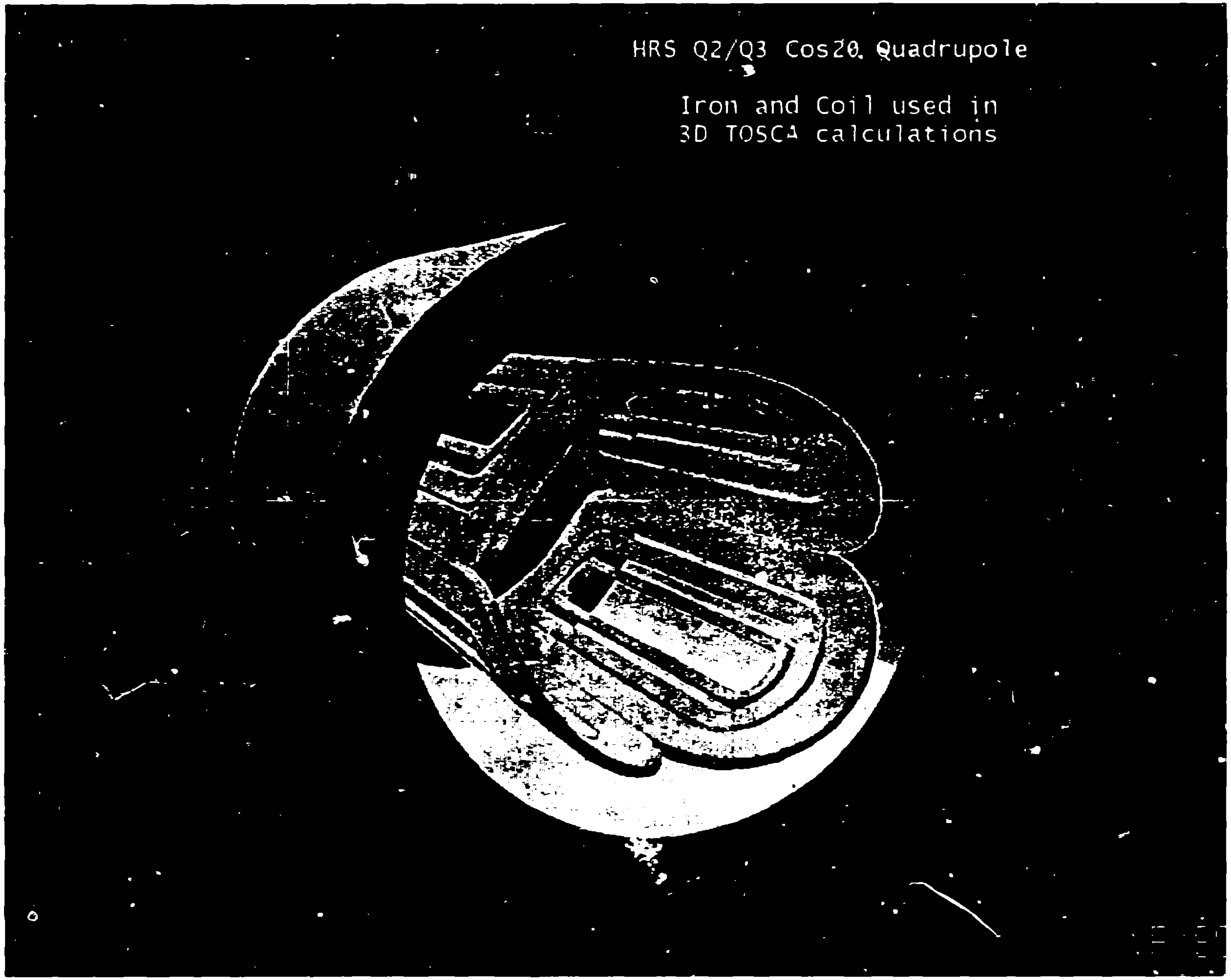
HRS Q2/Q3 Cos2θ Quadrupole
Iron and Coil used in
3D TOSCA calculations

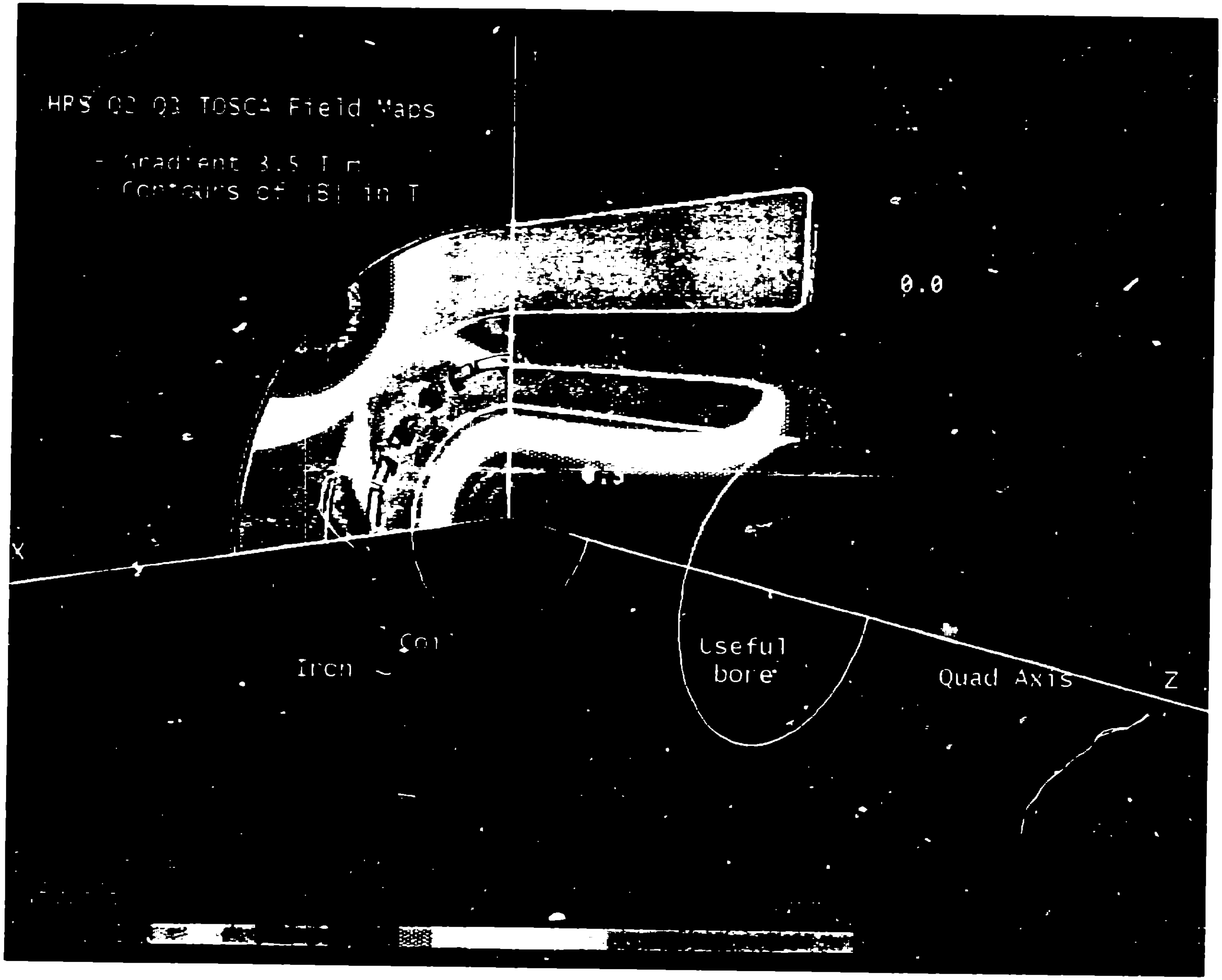
HRS Q2 Q3 TOSCA Field Maps
Gradient 3.5 T/m
Contours of |B| in T
0.0
X
Coil
Iron
Useful bore
Quad Axis
Z

2.3 Harmonic Analysis

The coefficients C_n's were evaluated by Fourier analysis of the TOSCA field maps evaluated at the useful bores in different transverse planes along the axis of the quadrupoles. The results of the harmonic analysis is summarized in Table 6 for the central straight section (z=0) and integrated along the axis of the quadrupole. It is evident from the results that in the central section of the quadrupole, contribution to the field from the high order harmonics are of the order of 1×10^{-4} or lower. In fact, the strongest contribution comes from the n=26. This comes as no surprise since with a three sector coil the optimization in the straight section minimizes only the first five harmonics. This situation is somewhat degraded in the integrated multipole strengths. The coil ends contribute significantly in the region of z=70 cm to about z=120 cm. In particular, the first harmonic, the dodecapole, exceeds 10^{-3} level. It might be necessary to add a correctional dodecapole element in the auxiliary multipolar windings. Shown in figure 6a is the axial distribution of the quadrupole term; the distribution of the first few multipoles along the axis of the quadrupole are shown in Figure 6b.

Table 6
Harmonic Analysis

n	C_n/C_2 at $z=0$	$\int C_n/C_2$
6	1.2704×10^{-4}	2.5154×10^{-3}
10	4.1271×10^{-5}	3.8197×10^{-4}
14	1.6440×10^{-5}	1.7551×10^{-4}
18	1.0091×10^{-7}	6.5316×10^{-5}
22	2.0450×10^{-5}	4.2844×10^{-5}
26	1.5062×10^{-4}	8.2971×10^{-5}
28	1.1772×10^{-9}	1.2377×10^{-9}

3. Energy and Forces

The field distribution on the inner surface of the coil was calculated with TOSCA. The peak field on the conductor was determined to be 1.83 T which occurs at the coil ends. The peak coil field in the straight section of Q2 is 1.5 T. These values are quite conservative for a cryomagnet. Stored energy and magnetic body forces along the coil were also evaluated with TOSCA. The magnetic forces in the transverse plane at the straight section of Q2 are shown in Figure 7a and forces at the end sections are plotted in Figure 7b. The forces in these figures are in metric Tons/m.

Quad – Harmonic Analysis

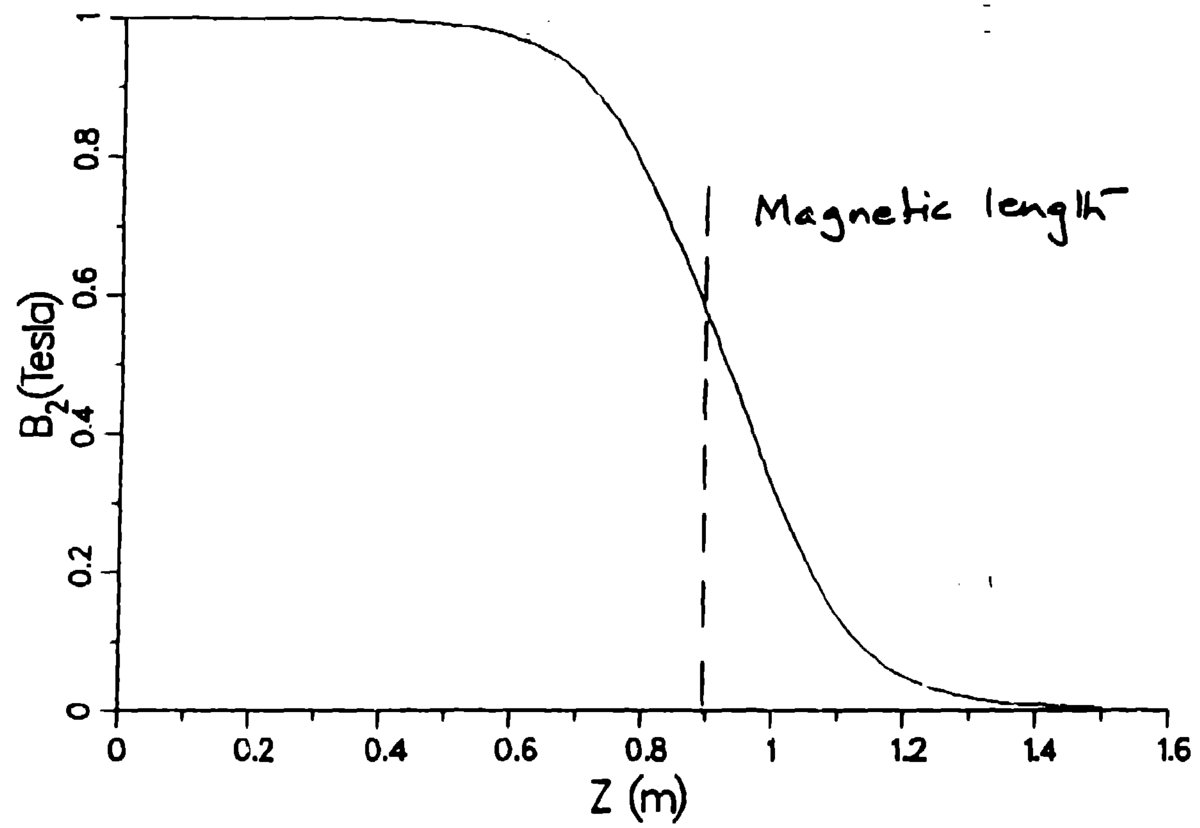

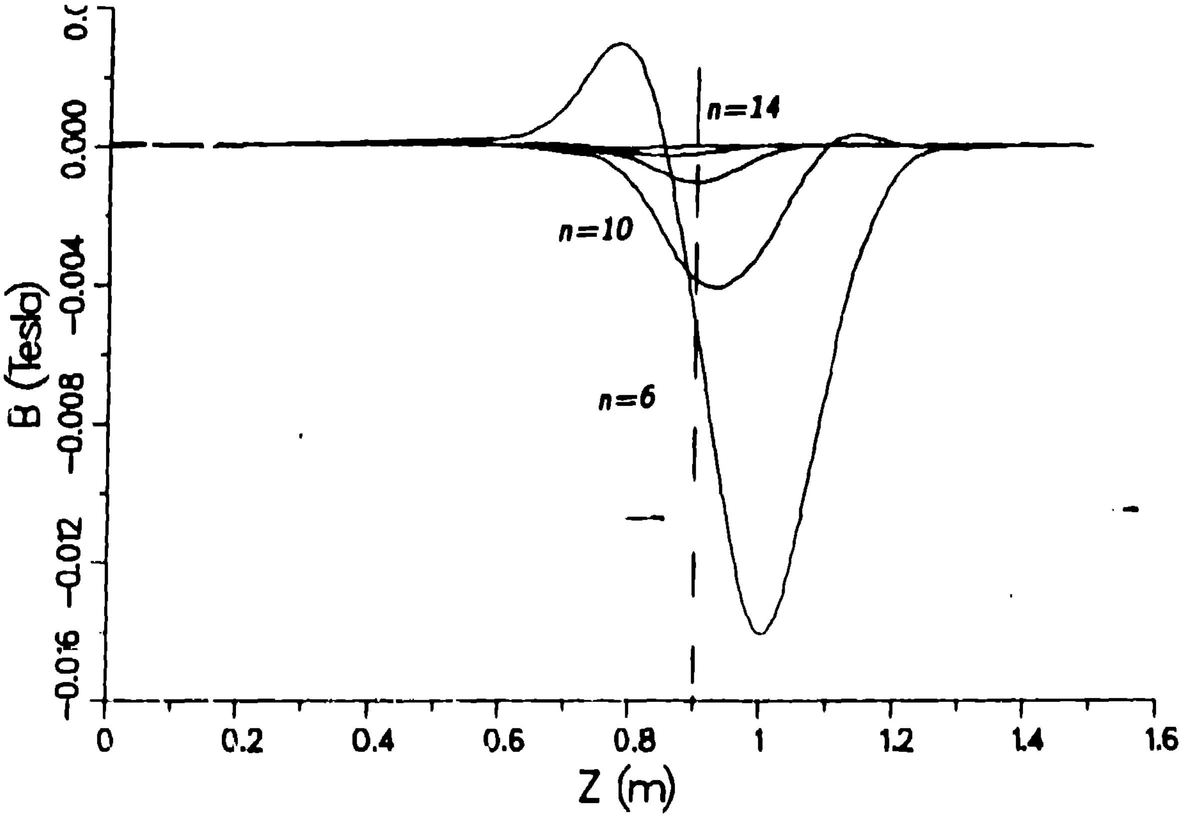

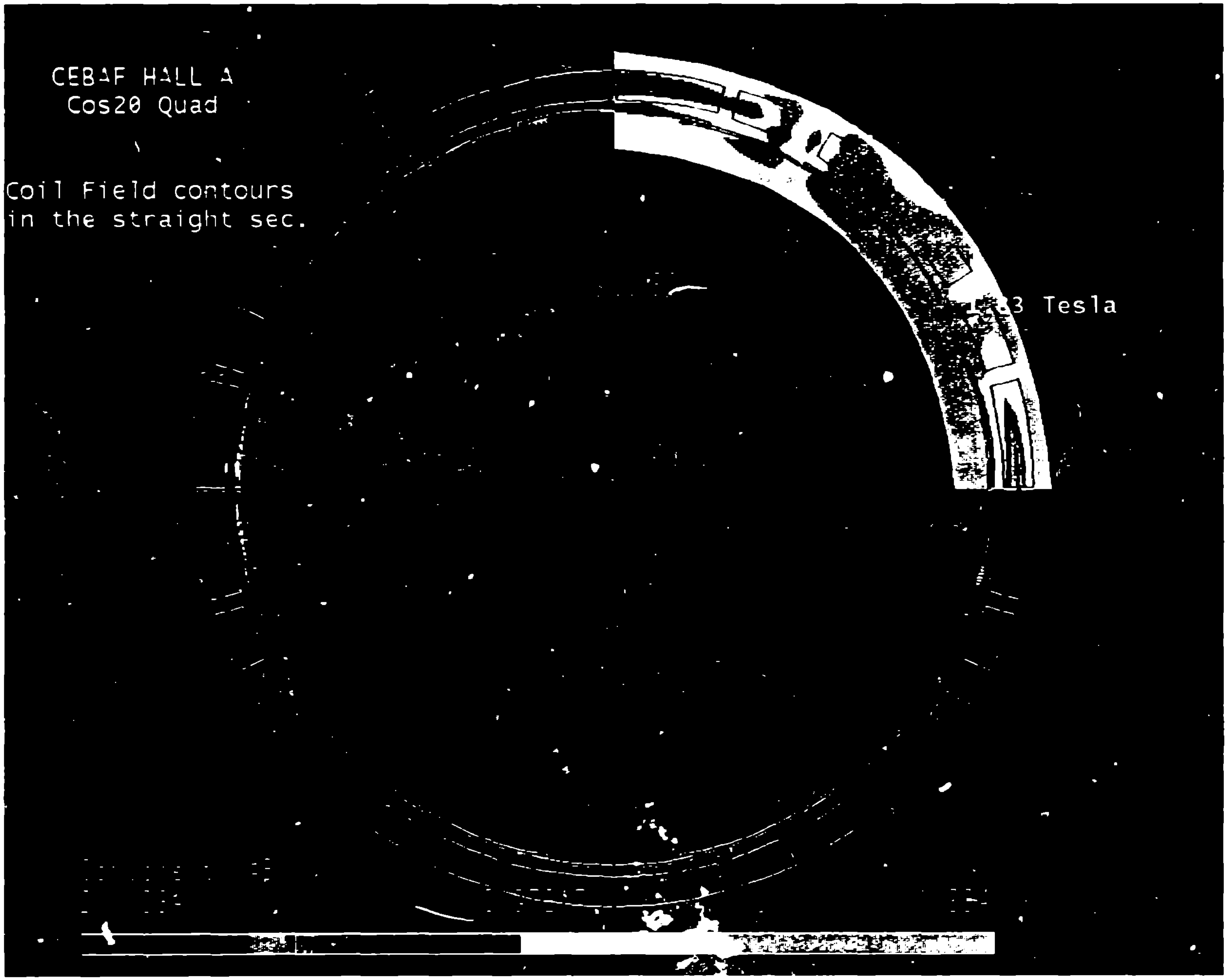
CEBAF HALL A
Cos2θ Quad
Coil Field contours
in the straight sec.
Tesla

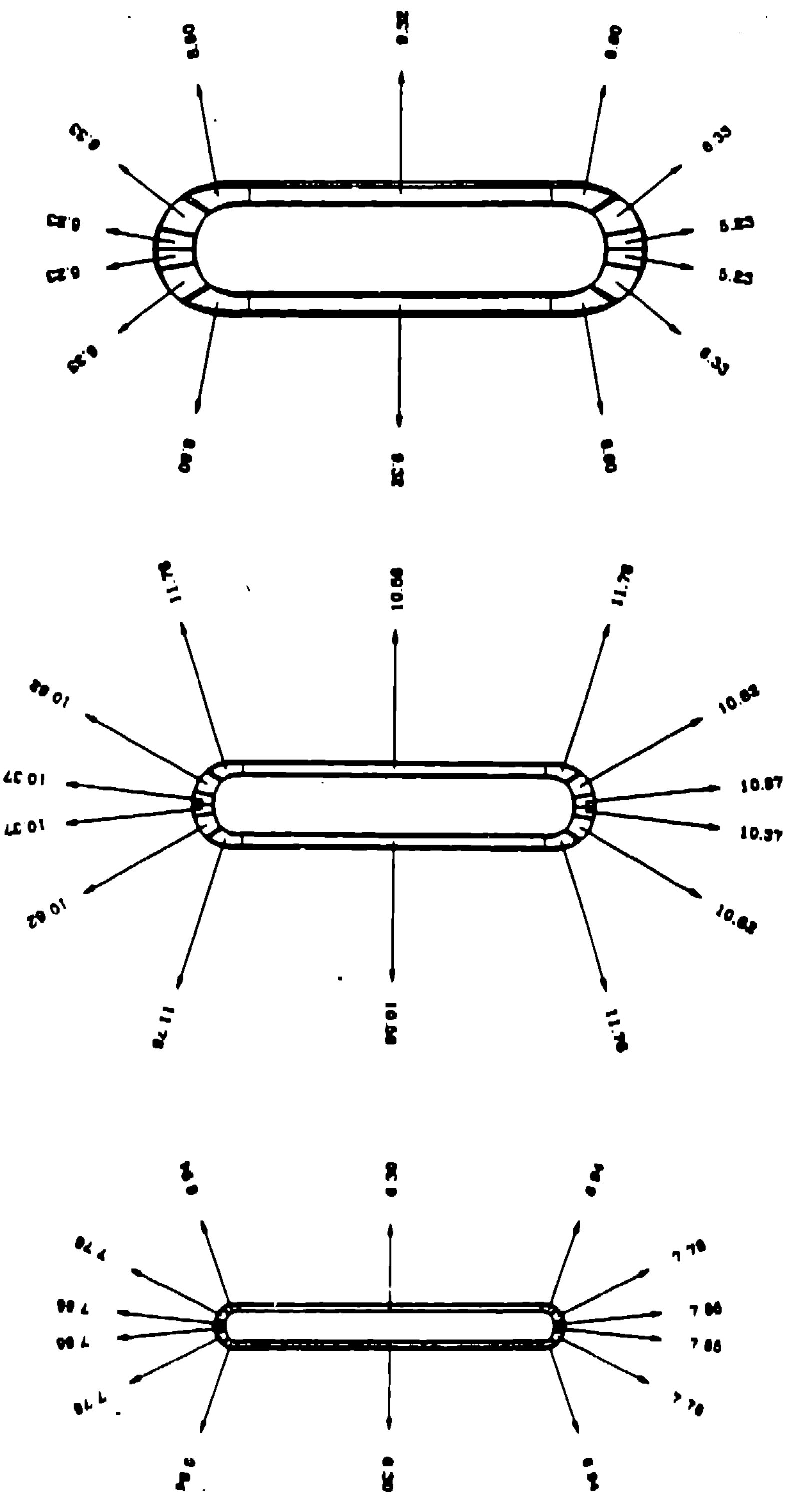
8.80
8.32
8.33
8.23
11.78
10.58
10.82
10.37
8.94
8.30
7.78
7.88

Q_2/Q_3

MAGNETIC FORCES (Ton/m)

$G_0 = 3.5$ T/m

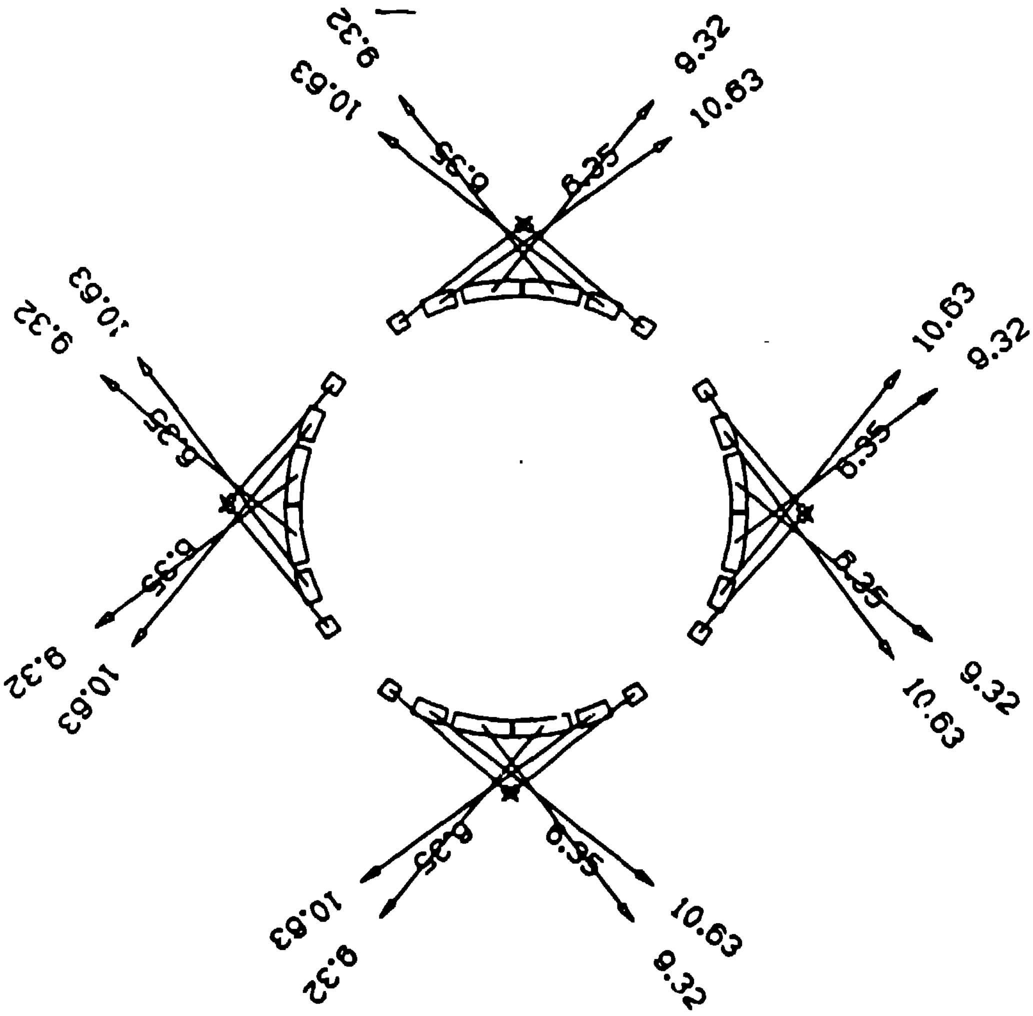

Sextupole Forces (Ton/m)

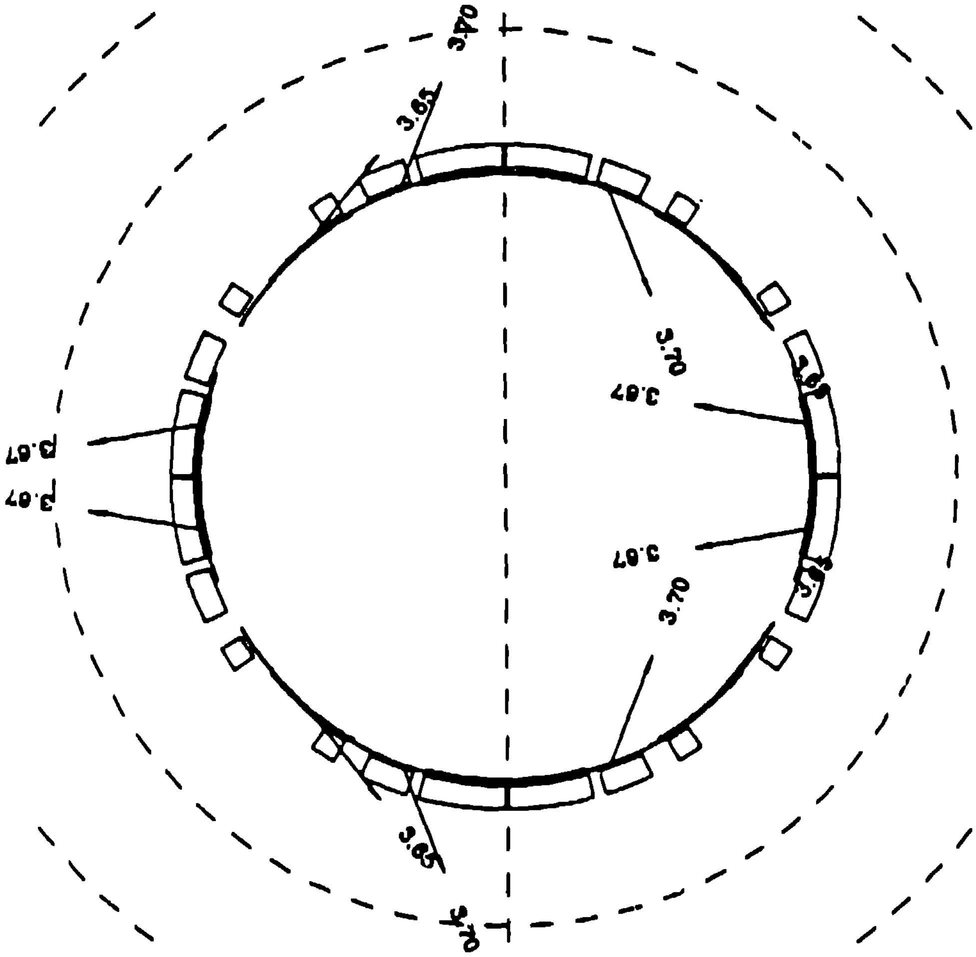

FIGURE Q.8 - SHEET 1

Conductor placement tolerances

- Studied in 2D with program CEM
  - compute fields in cylindrical geometry in the presence of a $\mu = \infty$ shield.
  - Analytic
- few cases cross checked with TOSCA and POISSON
  - good agreement.
- Both symmetry preserving and symmetry breaking type of mis placements were studied.
- 3D alignment issues studied with TOSCA.

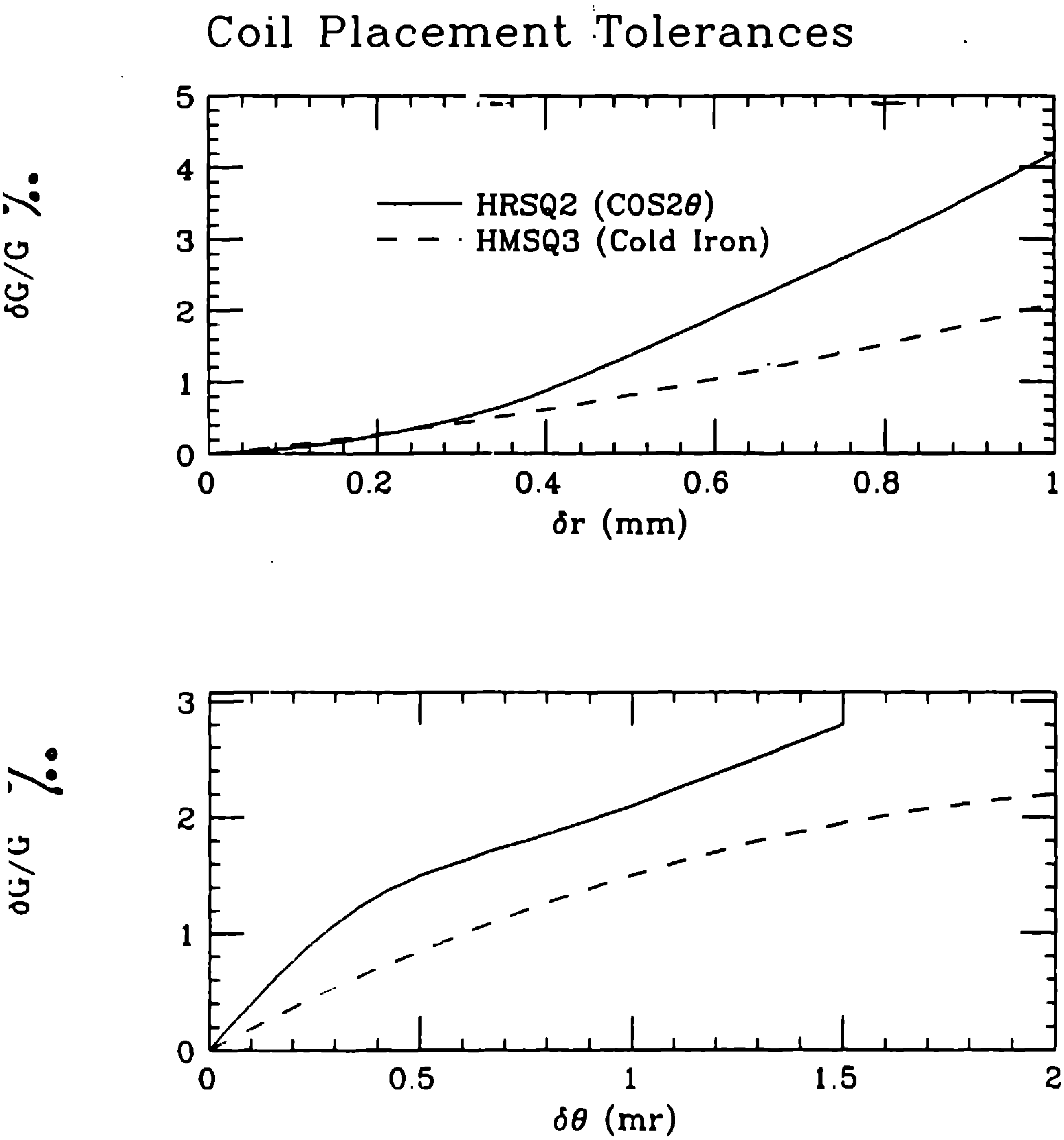

Coil Placement Tolerances
δG/G ‰
HRSQ2 (COS2θ)
HMSQ3 (Cold Iron)
0 0.2 0.4 0.6 0.8 1
δr (mm)
0 1 2 3 4 5
δG/G ‰
0 0.5 1 1.5 2
δθ (mr)
0 1 2 3

Fig. 6

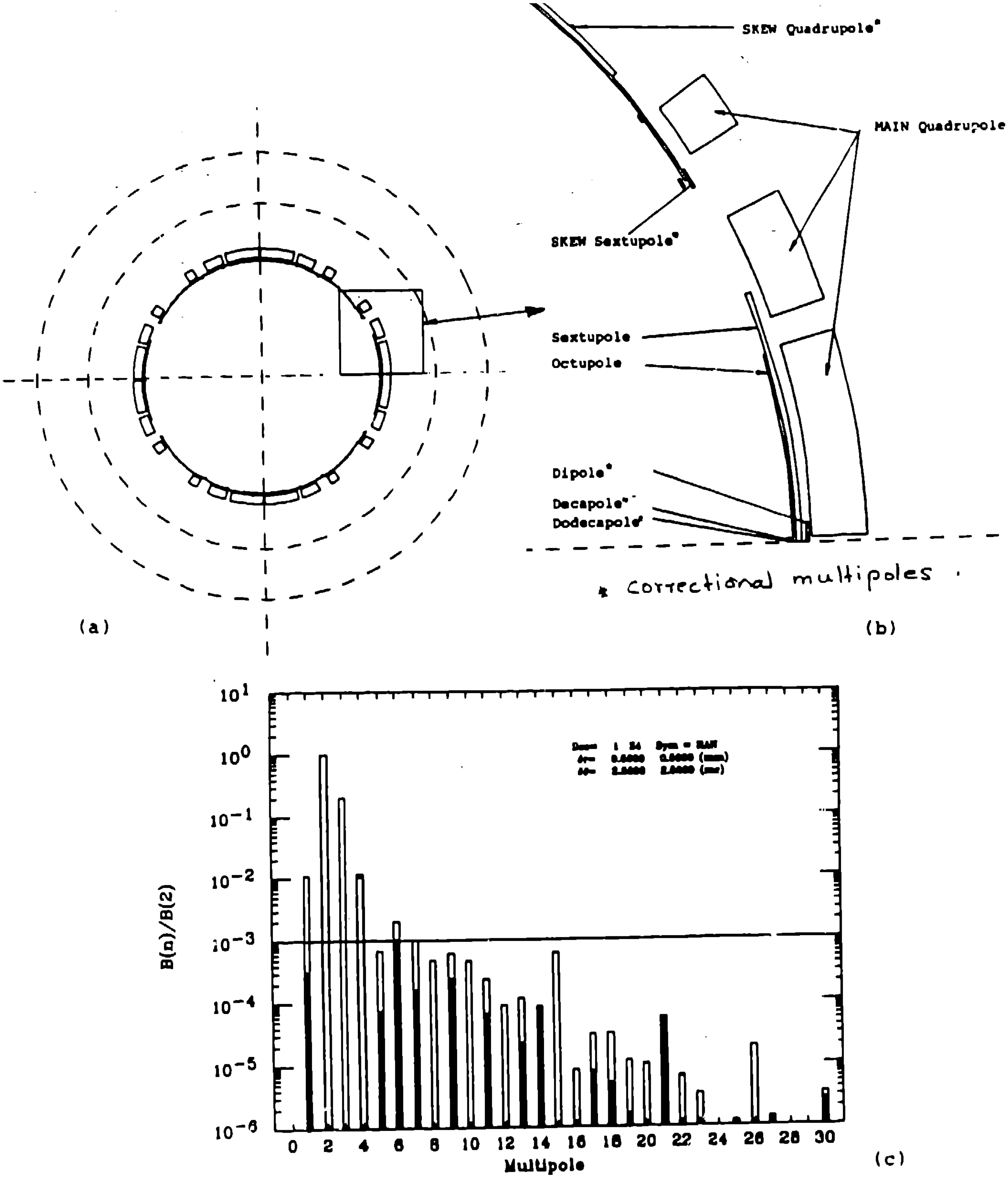

Figure 5.20 a) Schematic view of multipole windings. b) Blow up of the multipole layers; c) Harmonic strengths relative to the quadrupole term allowing for a random misalignment of ±0.5 mm. The solid(open) bars are with(without) correctional multipoles. Note that n=3,4 are required by optics.

Table 7
Multipole Elements

n	Type	Phase (deg)	Field (r=30cm) (Tesla)	Magnetic Length (cm)	Ampere Turns (kA)	Turns per pole	Coil Radius (cm)	Coil Length (cm)	Sector Angle (deg)
3	normal	0	0.10	207	183	305	38.45	224	20.0
4	normal	0	0.045	202	109	137	38.75	216	15.0
1*	normal	0	0.01	210	7.7	39	39.80	220	3.95
1*	skewed	90	0.01	210	7.6	39	39.65	220	3.92
2*	skewed	45	0.01	210	10.8	27	39.50	220	2.88
3*	skewed	30	0.01	210	15.5	26	39.35	220	2.78
5*	normal	0	0.01	210	33.3	33	39.20	220	3.51
6*	normal	0	0.01	210	50.0	42	39.05	220	4.32

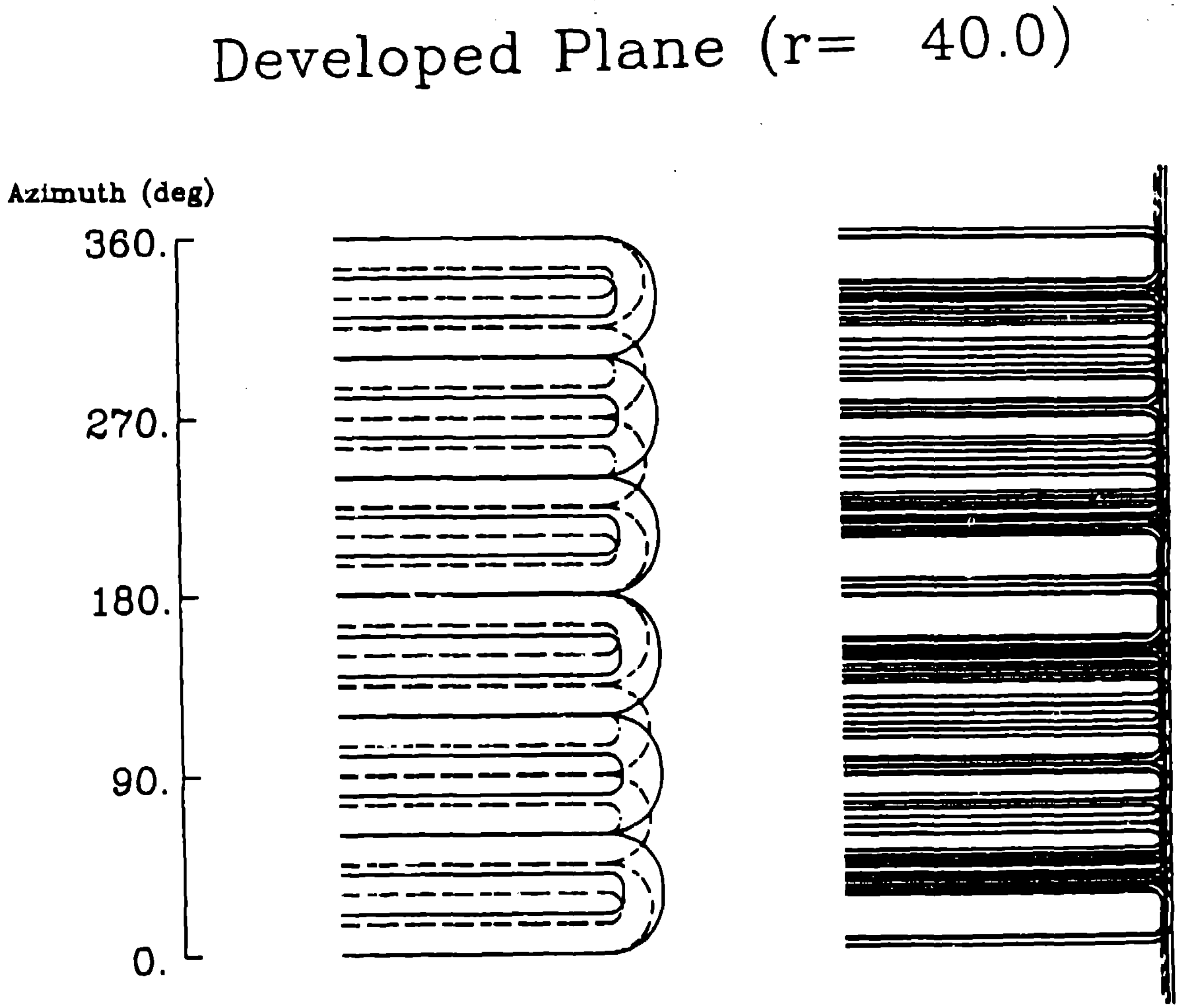

Figure 10 Schematic layout of the end sections of the multipole windings. a) Sextupole and octupole coils. b) All other correctional multipoles as described in the text.

Table I. **Basic Features**

COIL	$Cos2\theta$	Cold Iron
Ideal Current:	$Cos2\theta$ Current distribution	Hyperbolic Current sheet
Design Approximation:	Constant thickness 3-sector blocks	Single rectangular block
Goodness of Approx:	First five harmonics are eliminated	None of the harmonics are eliminated
Coil field Contribution:	Current dominated Typically 75%	Equal to iron Typically 50%
End shape:	Constant Perimeter	Saddle
Coil confinement:	Simple Essentially 2D	Complex 3D
Coil placement Tolerance:	high	high

IRON	$Cos2\theta$	Cold Iron
Function:	Shield	Field shaping
Geometry:	Simple cylinder No end shaping	Hyperbolic Pole Complex end profiles
Field Contribution:	25%	50%
Maximum Pole-tip Field:	None	1.3 Tesla*
Machining Tolerance:	low	high

It was suggested by the HMS team that the cold iron HMSQ3 may be a possible candidate for the two large HRS quadrupoles. The HMSQ3 has a 76 cm warm bore; for the HRS use only 60 cm of this will be used. One then expects the field quality to be better over this smaller useful bore. Furthermore, this allows room for placement of multipolar windings in the unused portion of the bore for HRS needs.

We have studied the HMSQ3 with 3D TOSCA analysis. The study is by no means complete, but already demonstrates some problem areas in meeting HRS requirements. Given in Table II are the parameters of the HMSQ3 with the HRS gradient requirement; the reference cos2θ design parameters are also shown for comparison.

Table II HRSQ2 and HMSQ3 magnetostatics			
	HRSQ2 (Cos2θ)	**HMSQ3** (Cold Iron)	
Excitation parameters			
Gradient	3.5	3.5	T/m
Amp-turns	1.4	0.9	MAT
Stored Energy	0.6	0.5	MJ
Coil Forces	13	17	Ton/m
Iron/Coil contribution	24/76	49/51	%
Field Quality (r=30 cm)			
$B_6/B_2(z=0)$	3.5×10^{-4}	2.5×10^{-3}	
$\int \Delta G/G$	1.3×10^{-3}	7.6×10^{-3}	
$\Delta L/L(.3 \leq G \leq 3.5T/m)$	1.4×10^{-3}	2.1×10^{-2}	
Peak fields			
Iron (straight)	1.4	2.1	Tesla
Iron (Ends)	1.2	3.5	Tesla
Coil (straight)	1.5	1.9	Tesla
Coil (Ends)	1.8	?	Tesla
Weights			
Total	11.8	11.4	Ton
Iron Mass	10.0	8.6	Ton
Cold Mass	1.4	10.0	Ton
Tolerances			
Coil Placement	±0.25	±0.30	mm
Iron Surface	±0.50	±0.05	mm

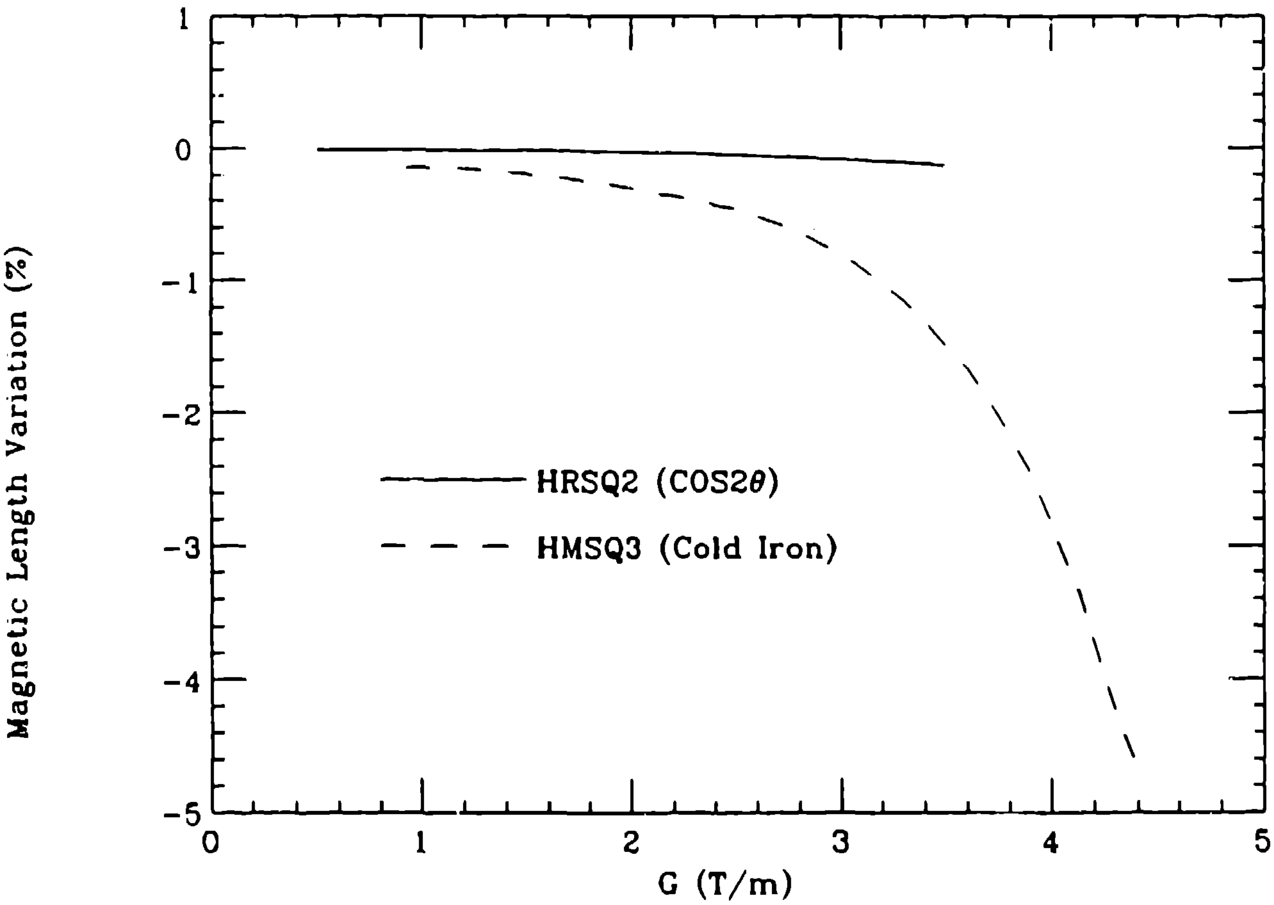

Magnetic Length Variation (%)
1
0
-1
-2
-3
-4
-5
0
1
2
3
4
5
G (T/m)
HRSQ2 (COS2θ)
HMSQ3 (Cold Iron)

Fig. 5

Remarks:

- Large bore, short length quads are true 3D beasts!
  - Good 3D finite element computations — are required for accurate analysis.

- For high resolution, high peak field, and wide dynamic range applications, avoid field shaping with iron.
  - Current dominated magnets exhibit better linearity; hence, better reproducibility.

- Avoid sharp bends in coil (particularly out-of-plane bends e.g. saddle ends)
  - If constraints dictate sharp bends, dilute current density in the region

- Applications where "good field" region is close to the coil, pay attention to the peculiarities of superconductors.
  - Persistent currents (Irreversible filament magnetization)
  - Meissner effect
  - Conductor microstructure..

- Most likely field error will be due to "non-allowed" harmonics e.g. dipole, sextupole octupole... because of 4-fold symm. breaking in manufacturing process.

  - Tighten tolerances (?)

- After all is said and done, buy some extra insurance

  - Auxiliary correctional low multipole windings

  - Multipoles may be cheaper than tighter tolerances!

Still, if the magnet turns out to be a lemon...

DON'T WORRY!

The guy who designed the HUBBLE telescope is looking for a roommate in his exiled South American home full of venomous snakes!

UPGRADES TO 'TRANSPORT' AND 'TURTLE'

transport

DRAMATIS PERSONAE

C. H. MOORE
S. K. HOWRY
H. S. BUTLER
B. K. KEAR
R. H. HELM
K. L. BROWN
S. KOWALSKI
D. C. CAREY
CH. ISELIN
F. ROTHACKER
R. PORDES

TURTLE

(Trace Unlimited Rays Through Lumped Elements)

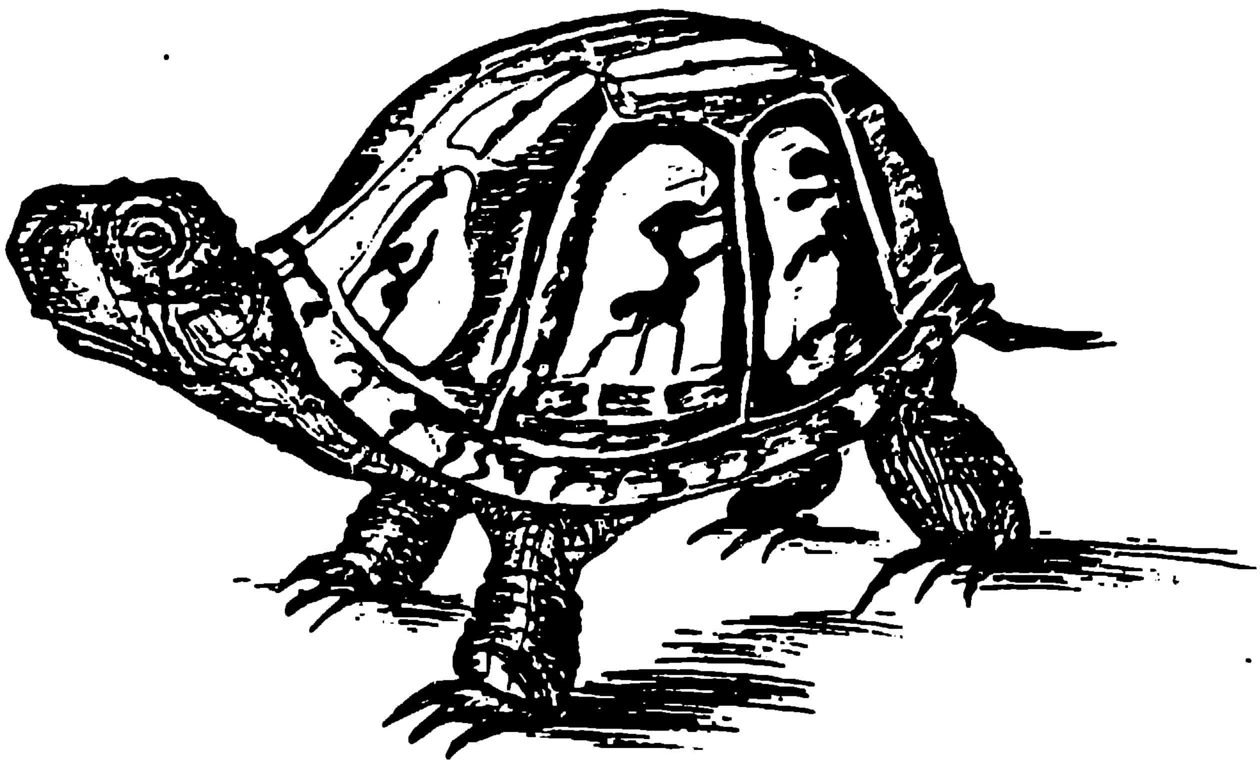

D. C. Carey

Particle decay inserted by: K. L. Brown

Ch. Iselin

Second-Order Equations

$$d\vec{T} = \hat{x}\,dx + \hat{y}\,dy + (1+hx)\,\hat{t}\,dt$$

$$\vec{T}'' - \frac{1}{2}\frac{\vec{T}'}{T'^2}\frac{d}{ds}T'^2 = \frac{q}{p}T'(\vec{T}' \times \vec{B})$$

Magnetic Field:

$$B_x = \frac{p_0}{q}\left[-nh^2 y + 2\beta h^3 xy\right]$$

$$B_y = \frac{p_0}{q}\left[h - nh^2 x + \beta h^3 x^2 + \frac{1}{2}(n-2\beta)h^3 y\right.$$

$n \rightarrow$ Quadrupole component

$\beta \rightarrow$ Sextupole component

Second-Order Equations of Motion

$$\frac{d^2x}{ds^2} + (1-n)h^2 x = h\delta + h^3(2n-\beta-1)x^2$$
$$+ \frac{1}{2}h^3(2\beta-n)y^2 + \frac{1}{2}hx'^2$$
$$- \frac{1}{2}hy'^2 + h^2(2-n)x\delta - h\delta^2$$

$$\frac{d^2y}{ds^2} + nh^2 y = 2h^3(\beta-n)xy + h^2 n y\delta$$
$$+ hx'y'$$

Third-order Equations of Motion

$$
\begin{aligned}
\frac{d^2x}{ds^2} + (1-n)h^2 x = \; & h\delta + h^3(2n-\beta-1)x^2 \\
& + \tfrac{1}{2}h^3(2\beta-n)y^2 + \tfrac{1}{2}hx'^2 \\
& - \tfrac{1}{2}hy'^2 + h^2(2-n)x\delta - h\delta^2 \\
& - h^4(\gamma+2\beta-n)x^3 \\
& + h^4(3\gamma+3\beta-\tfrac{1}{2}n)xy^2 \\
& - nh^2x'yy' + \tfrac{1}{2}nh^2xy^2 \\
& + h^2(\tfrac{3}{2}n-2)xx'^2 + h^3(\beta-2n-1)x^2\delta \\
& - h^3(\beta-\tfrac{1}{2}n)y^2\delta + \tfrac{3}{2}hx'^2\delta \\
& + \tfrac{1}{2}hy'^2\delta - h^2(2-n)x\delta^2 + h\delta^3
\end{aligned}
$$

$$\frac{d^2y}{ds^2} + nh^2 y = 2h^3(\beta - n)\, xy + h^2 n y \delta$$

$$+ h x' y' + h^4 (3\gamma + 4\beta - n)\, x' y$$

$$- h^4 \left(\gamma + \frac{1}{6} n + \frac{1}{3}\beta\right) y^3$$

$$- h^2 (2 - n)\, x x' y' - \frac{3}{2} n h^2 y y'^2$$

$$+ h x' y' \delta - 2h^3 (\beta - n)\, x y \delta$$

$$- \frac{1}{2} n h^2 x'^2 y - n h^2 y \delta^2$$

Third Order

$$x_i(1) = \sum_j R_{ij}\, x_j(0) + \sum_{j,k} T_{ijk}\, x_j(0)\, x_k(0)$$

$$+ \sum_{j,k,\ell} U_{ijk\ell}\, x_j(0)\, x_k(0)\, x_\ell(0)$$

Specification:

ORDER 3 ; (Type code 17.)

U matrix constraint:

FIT -i jkℓ. (desired value) (tolerance) ;

FIT NAME = Uijk , VALUE = (value), TOLER = (toler) ;

Octupole:

OCTUPOLE (length) (pole tip field) (aperture) ;

Third-Order Terms For

Central region of bending magnet (combined function)
Quadrupole with fringing fields
Sextupole
Octupole

$$x_1 = R x_0 + T x_0 x_0 + U x_0 x_0 x_0$$

Expand about trajectory x_0

x_{1c} image of x_{0c}, element by element

$$x = x_c + \Delta x$$

$$x_{1c} + \Delta x_1 = R(x_{0c} + \Delta x_0) + T(x_{0c} + \Delta x_0)(x_{0c} + \Delta x_0)$$

$$+ U(x_{0c} + \Delta x_0)(x_{0c} + \Delta x_0)(x_{0c} + \Delta x_0)$$

$$\Delta x_1 = (R + 2T x_{0c} + 3U x_{0c} x_{0c}) \Delta x_0$$

$$+ (T + 3U x_{0c}) \Delta x_0 \Delta x_0 + U \Delta x_0 \Delta x_0 \Delta x_0$$

$$R^* = R + 2T x_{0c} + 3U x_{0c} x_{0c}$$
$$T^* = T + 3U x_{0c}$$

Shifted matrices - not symplectic
Include higher-order terms, including chromatic

Off - axis beam caused by

Centroid shift
Misalignment
Excess horizontal bend field
Vertical bend field

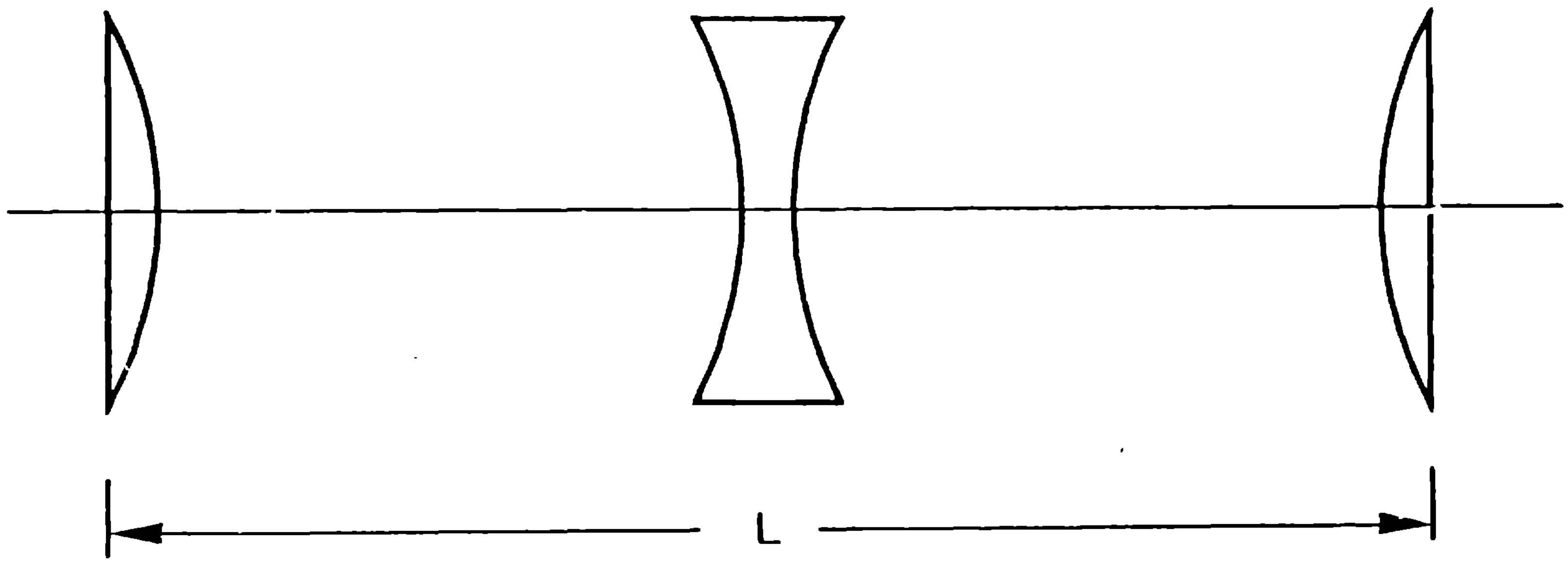
L

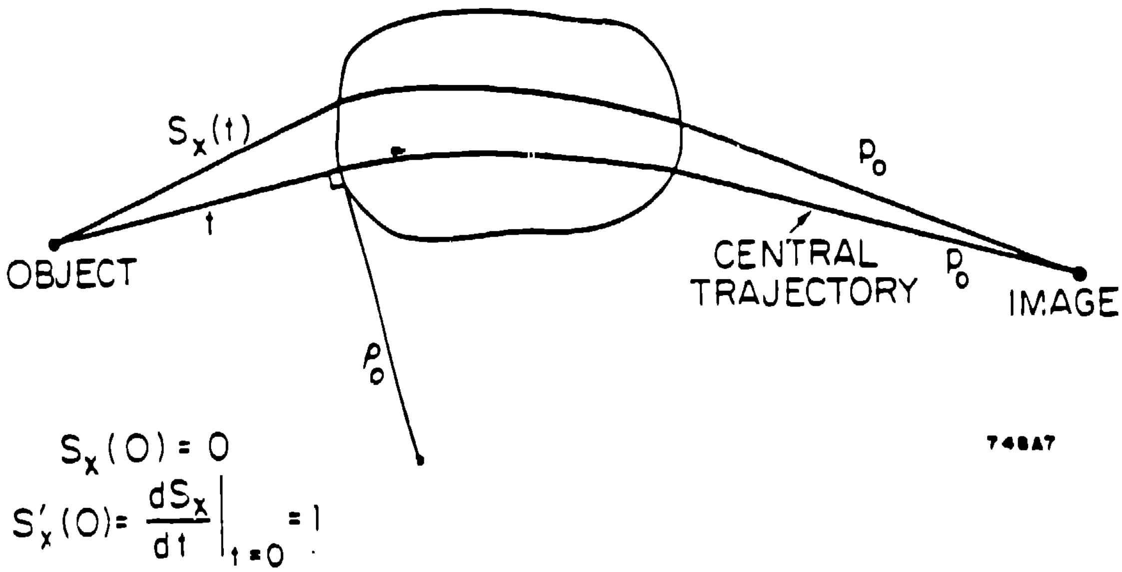
$S_x(t)$
p_o
t
OBJECT
CENTRAL
TRAJECTORY
p_o
IMAGE
ρ_o
$S_x(0) = 0$
$S'_x(0) = \left.\frac{dS_x}{dt}\right|_{t=0} = 1$
748A7

160 cell FODO

90° phase advance per cell

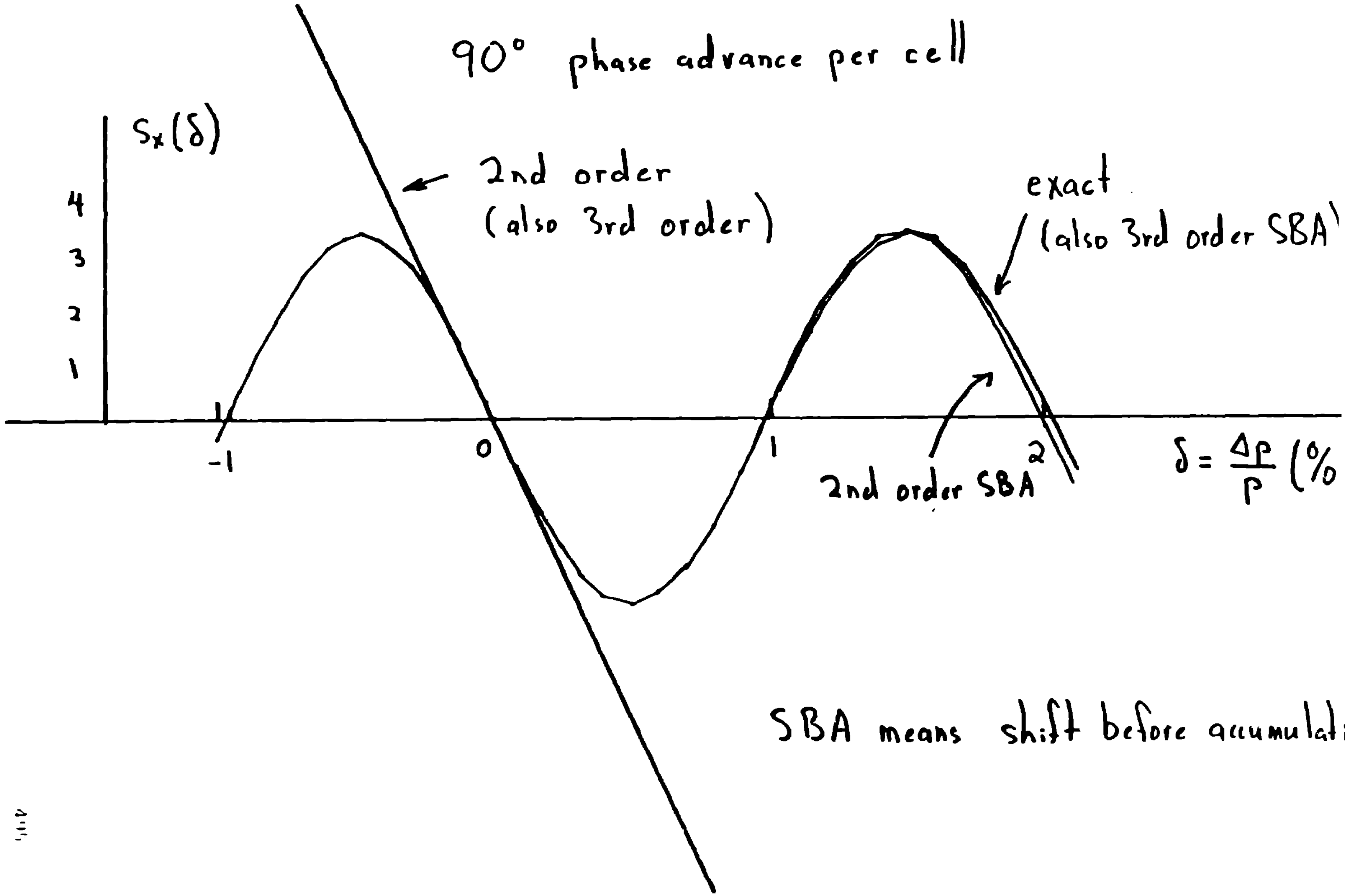

SBA means shift before accumulati

Bending Magnet with Excess Field

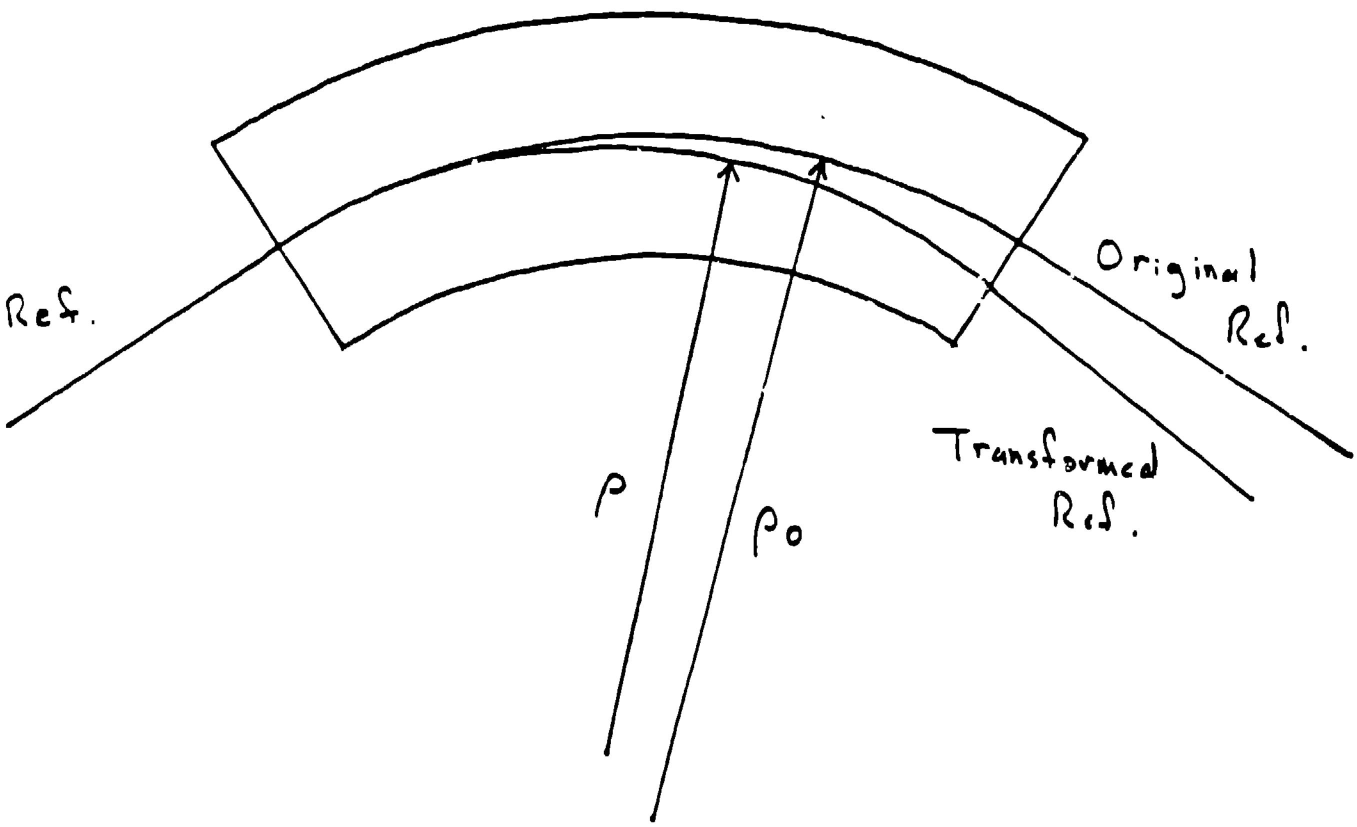

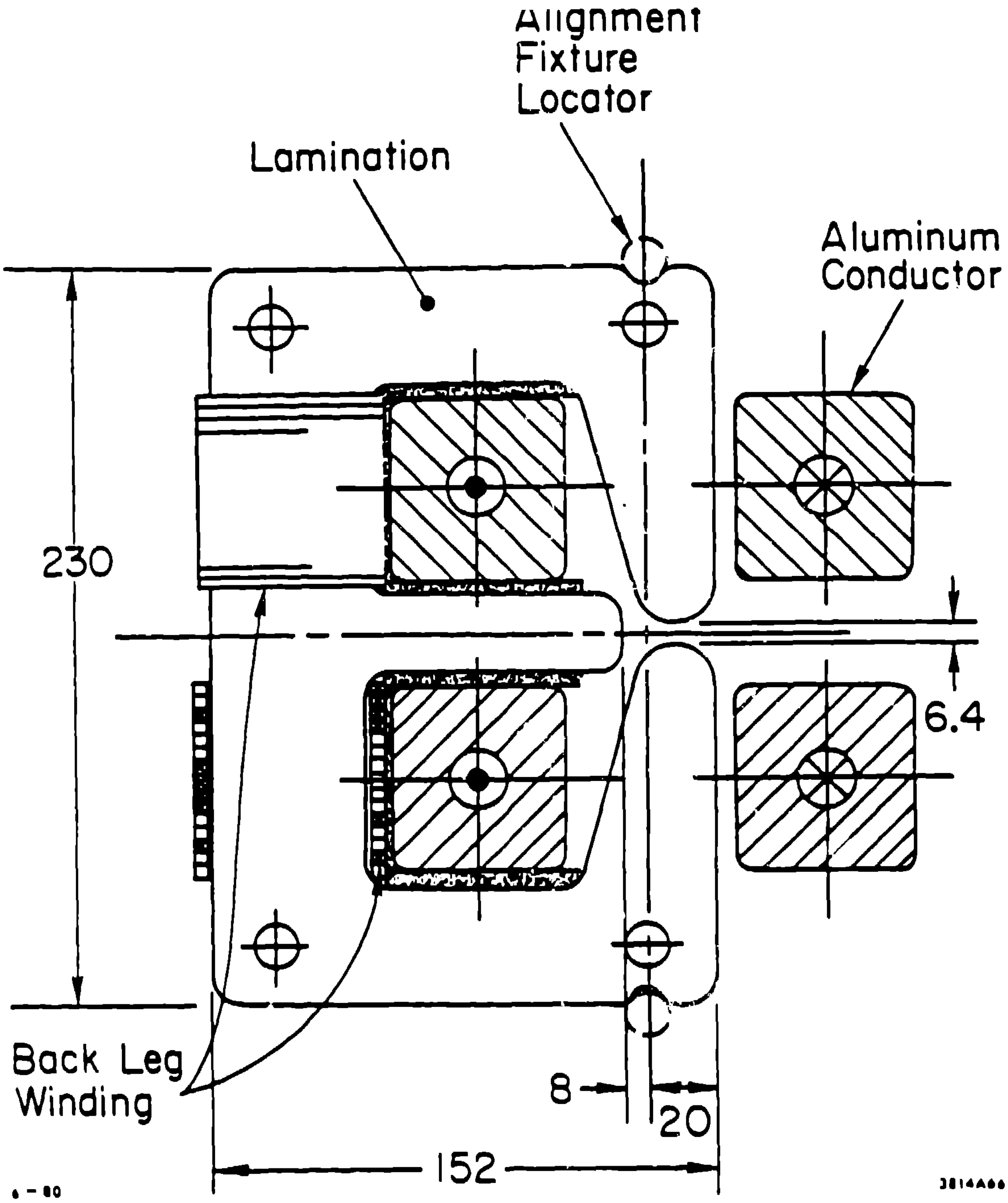

Fig. 7. Cross section of the SLC arc magnets. Dimensions are in millimeters.

Magnetic field expansion on magnetic midplane

<u>Midplane symmetry:</u>

$$B_x = 0$$

$$B_y = B_0(1 - nhx + \beta h^2 x^2)$$

<u>Midplane non-symmetric:</u>

$$B_x = B_0 r_a (v_a - n'hx + \beta' h^2 x^2)$$

$$B_y = B_0(1 + r_0)(1 - nhx + \beta h^2 x^2)$$

r_0 includes effect of horizontal beam steering

$$B_x = B_0\Big[v_R - n' h_0 x - n h y + \beta' h_0^2 x^2 + 2\beta h h_0 x y - \tfrac{1}{2}(2\beta' - n' - v_R) h_0^2 y^2\Big]$$

$$B_y = B_0\Big[(1+r_s) - n h x + (n' - v_R) h_0 y + \beta h h_0 x^2 - (2\beta' - n' - v_R) h_0^2 x y - \tfrac{1}{2}(2\beta - n) h h_0 y^2\Big]$$

Insert into equations of motion and solve

$$x_s = x_{as} + R x_0 + T x_0 x_0$$

x_{as} zeroth order arising from

1) Excess horizontally bending field

2) Vertically bending field

First-order equations of motion

$$\frac{d^2x}{ds^2} + (1-n)h^2 x = h\delta$$

$$\frac{d^2y}{ds^2} + nh^2 y = 0$$

Excess bend:

$$\frac{d^2x}{ds^2} + [1-n+r_s(2-n)]h_0^2 x = -r_s h_0 + h\delta$$

$$\frac{d^2y}{ds^2} + nhh_0 y = 0$$

Non midplane symmetric:

$$\frac{d^2x}{ds^2} + (1-n)h^2 x = h^2(v_R - n')y + h\delta$$

$$\frac{d^2y}{ds^2} + nh^2 y = h^2(2v_R - n')x + v_R h - v_R h\delta$$

First-order Midplane Symmetric Excess Bend

$$x_{1s} = - r_s \frac{h_o}{k_x^2}(1-c_x)$$

$$x'_{1s} = - r_s h_o s_x$$

$$(x|x_o) = c_x = \cos k_x t$$

$$(x|x'_o) = s_x = \frac{h}{k_x} \sin k_x t$$

$$(x|\delta) = d_x = \frac{h}{k_x^2}(1-c_x)$$

$$(x'|x_o) = c'_x = - k_x \cos k_x t$$

$$(x'|x'_o) = s'_x = \cos k_x t$$

$$(x'|\delta) = d'_x = h s'_x$$

$$(y|y_o) = c_y = \cos k_y t$$

$$(y|y'_o) = s_y = \frac{h}{k_y} \sin k_y t$$

$$(y'|y_o) = c'_y = - k_y \cos k_y t$$

$$(y'|y'_o) = s'_y = \cos k_y t$$

where now we have

$$k_x^2 = [(1-n)+r_s(2-n)]h_o^2$$

$$k_y^2 = nhh_o$$

D. Second-Order Terms

The midplane-symmetric equations of motion

$$\frac{d^2x}{ds^2} + [(1-n)+r_s(2-n)]h_o^2 x = - r_s + h\delta + hh_o^2(2n-\beta-1)x^2 \quad (14$$

$$+ \frac{1}{2} hh_o^2(2\beta-n)y^2 + \frac{1}{2} (2h_o-h)x'^2$$

$$- \frac{1}{2} hy'^2 + hh_o(2-n)x\delta - h\delta^2$$

$$\frac{d^2y}{ds^2} + nhh_o y = 2hh_o^2(\beta-n)xy + hh_o ny\delta + h_o x'y'$$

Non-midplane-symmetric First-Order Matrix Elements

$$y_{1s} = v_R \frac{1-c_y}{nh}$$

$$y'_{1s} = v_R h s_y$$

$$(x|y_0) = (v_R - n') \frac{c_y - c_x}{1-2n}$$

$$(y|x_0) = (n' - 2v_R) \frac{c_x - c_y}{1-2n}$$

$$(x|y_0') = (v_R - n') \frac{s_y - s_x}{1-2n}$$

$$(y|x_0') = (n' - 2v_R) \frac{s_x - s_y}{1-2n}$$

$$(x'|y_0) = (v_R - n') \frac{c_y' - c_x'}{1-2n}$$

$$(y|\delta) = -v_R d_y + (n' - 2v_R) \frac{d_x - d_y}{1-2n}$$

$$(x'|y_0') = (v_R - n') \frac{s_y' - s_x'}{1-2n}$$

$$(y'|x_0) = (n' - 2v_R) \frac{c_x' - c_y'}{1-2n}$$

$$(l|y_0) = (v_R - n') \frac{d_y' - d_x'}{1-2n}$$

$$(\lambda|y_0') = (v_R - n') \frac{d_y - d_x}{1-2n}$$

$$\frac{d^2x}{ds^2} + (1-n)h^2 x = h\delta + (v_R - n')h^2 y$$
$$+ (2n - \beta - 1)h^3 x^2 + (2\beta' - 3n' + v_R)h^3 xy$$
$$+ \tfrac{1}{2}(2\beta - n)h^3 y^2 + \tfrac{1}{2} h x'^2 - \tfrac{1}{2} h y'^2$$
$$+ (2-n)h^2 x\delta - (v_R - n')h^2 y\delta - h\delta^2$$

$$\frac{d^2y}{ds^2} + n h^2 y = v_R h - v_R h\delta + (2v_R - n')h^2 x$$
$$+ (\beta' - 2n' + v_R)h^3 x^2 + 2(\beta - n)h^3 xy$$
$$- \tfrac{1}{2}(2\beta' - n' - v_R)h^3 y^2 - h^2(2v_R - n')x\delta$$
$$+ n h^2 y\delta + \tfrac{1}{2} v_R h x'^2 + h x' y'$$
$$+ \tfrac{1}{2} v_R h y'^2 + v_R h\delta^2$$

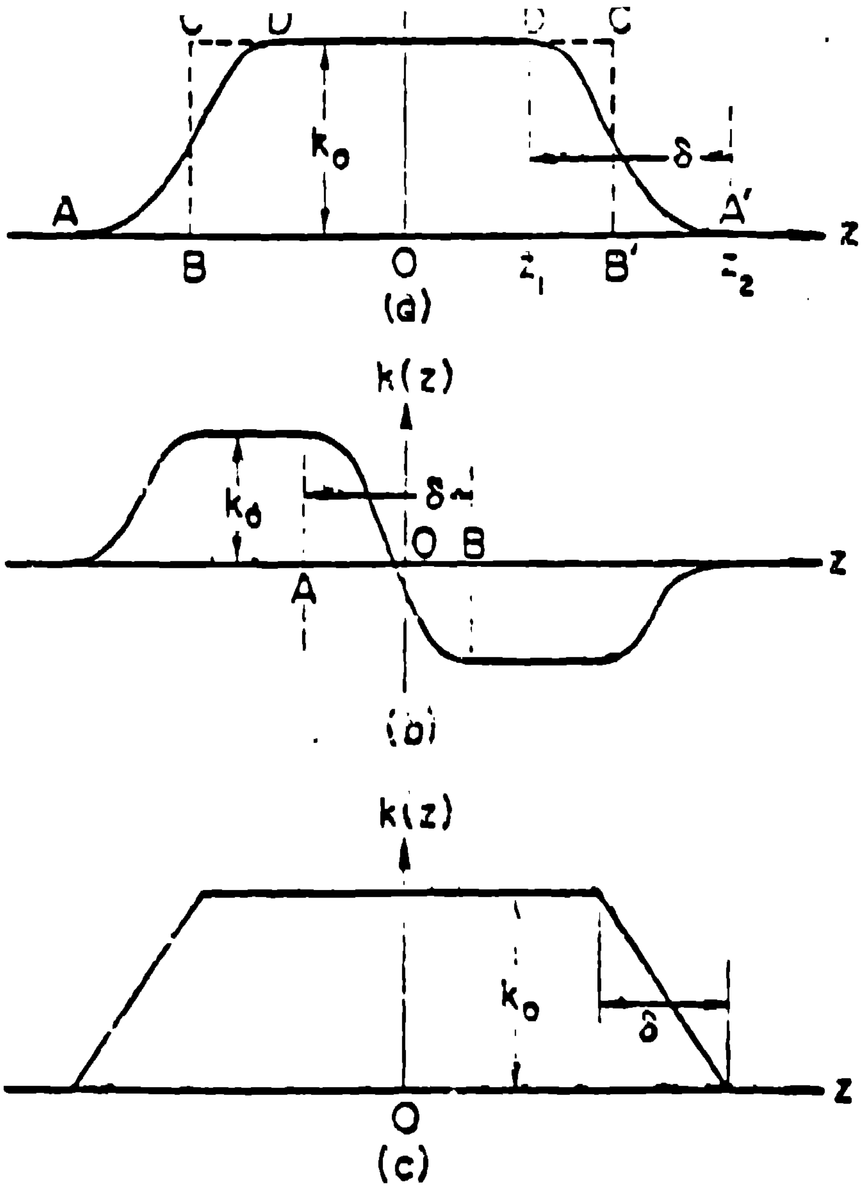

Fig. 1. Illustration of possible variations of the function $k(z)$ along the optic axis, showing the meaning of the parameters k_0 and δ. The rectangle BCC′B′ in (a) gives the rectangular model. Part (b) shows a region of rapidly varying $k(z)$ between the members of a doublet. The linear-ramp model is illustrated in part (c).

Third-Order Quadrupole

$$x'' + k^2 x = k^2\left(x'yy' - \frac{3}{2}xx'^2 - \frac{1}{2}xy'^2\right) + (k^2)'xyy' + \frac{1}{12}(k^2)''\left(3xy^2 + x^3\right)$$

Use Green's function

Integrate by parts

End up with integrals over entire length of quadrupole not involving derivatives of k^2.

Model fringe field as

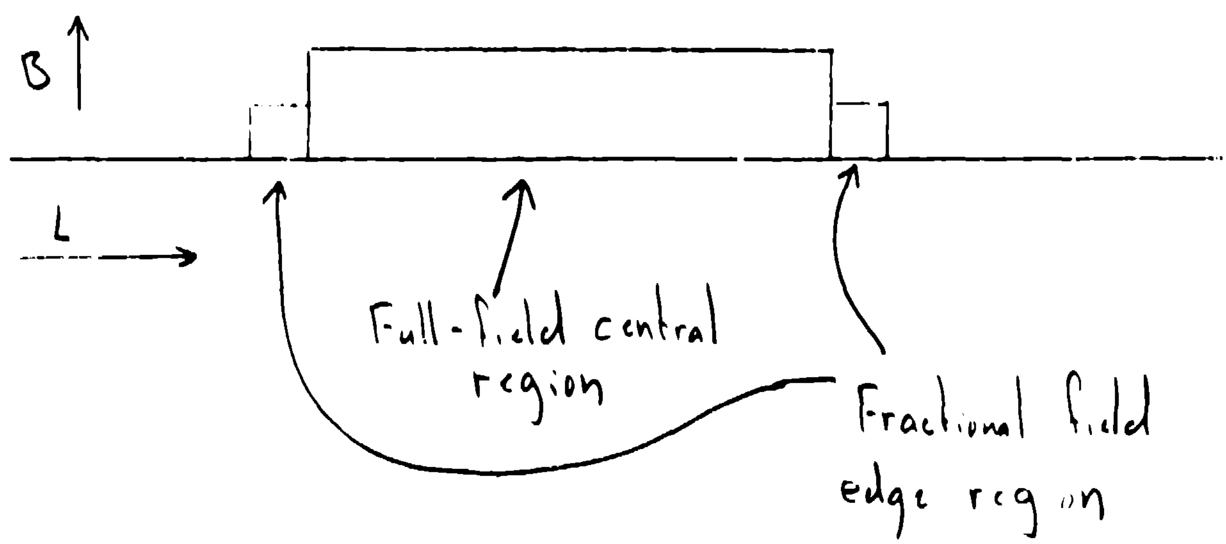

Use MAD notation

DIPOLE FRINGE FIELDS:

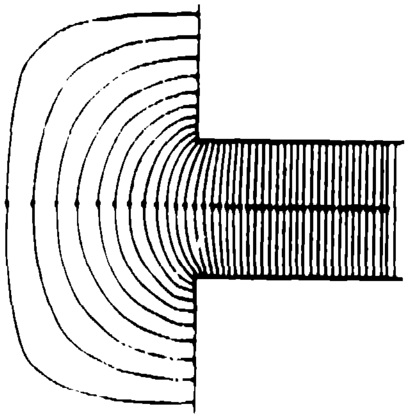

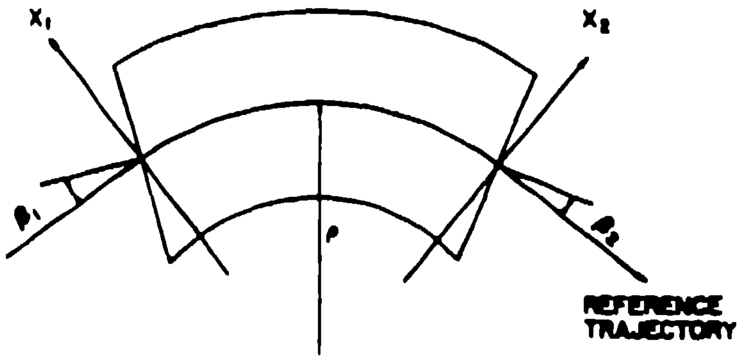

$$\frac{dh}{dt} \neq 0$$

Problems:

- True R. T. *not* a simple arc (0^{th} order shift)
- Power series expansions not well defined
- Need practical definition of fringing fields

(Note: not a problem for higher multipoles because of optical axis, R. T. does not change)

Impulse approximation (sharp cut-off):

- Gives no 0^{th} order shift
- Misses reduction in vertical focusing
- Leads to infinities in the third order

Approach:

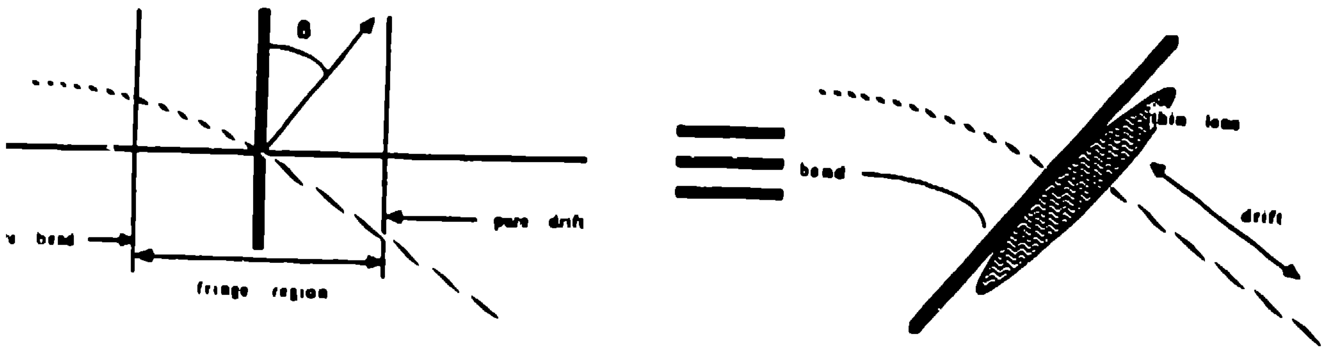

- Pole face rotation + Extended field $\Longleftrightarrow$ Normal boundary + Thin lens
- Field extent parametrized by gap size d

$$\epsilon = \frac{d}{\rho}$$

- Assume $\epsilon \ll 1$, get R_{ij}, T_{ijk}, U_{ijkl} as a power series in ϵ ($O(\epsilon)$ here)
- $\epsilon \to 0$: impulse approximation (see which U_{ijkl} causes ∞ in the 3rd order)

Mathematical Formulation:

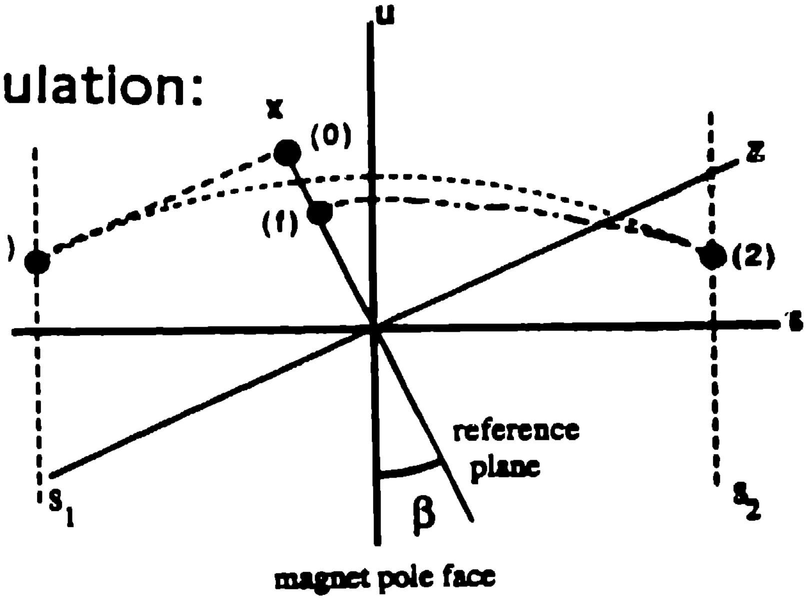

- $\mathcal{M}^{0\mapsto 1}$: drift $(z=0) \mapsto (s=s_1)$
- $\mathcal{M}^{1\mapsto 2}$: fringe $(s=s_1) \mapsto (s=s_2)$
- $\mathcal{M}^{2\mapsto f}$: bend $(s=s_2) \mapsto (z=0)$

- $\mathcal{M}^{0\mapsto f} = \mathcal{M}^{2\mapsto f}\mathcal{M}^{1\mapsto 2}\mathcal{M}^{0\mapsto 1}$

Field:

$$h(s) = \frac{B_y(y=0)}{B_0}$$

$h(s_1)=0,\ h(s_2)=1;\ \dot{h}(s_1)=\dot{h}(s_2)=\ddot{h}(s_1)=\ddot{h}(s_2)=0$

$$\int_{-\infty}^{s^*} h(s)ds = s^* \quad \text{for} \quad s^* \gg d$$

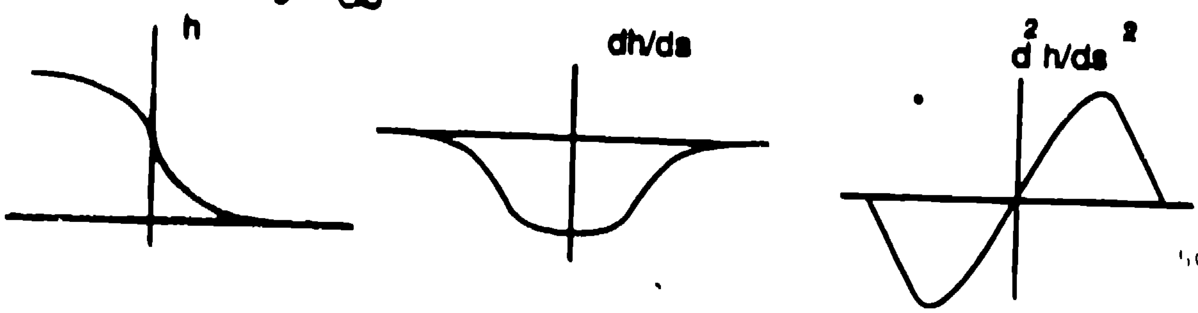

RESULTS : total fringe field map

$s_2 = -s_1 \to \infty$

$$\frac{s_2^2}{2} = \int_{s_1}^{s_2} ds \int_{s_1}^{s} h_0(s')ds'$$

$h_0(s)$: step-function centered at $s = 0$

- Zeroth Order: R. T. shift

$$\begin{aligned} \Delta x &= \epsilon^2 \sec^2 \beta I_1 \\ \Delta x' &= \epsilon^2 \sec^2 \tan \beta I_1 \end{aligned}$$

$$I_1 = \int_{-\infty}^{+\infty} ds \int_{-\infty}^{s} ds' \left[h_0(s') - h(s')\right]$$

- First Order:

$O(\epsilon)$:

$$I_2 = \int_{-\infty}^{+\infty} ds \, [1 - h(s)] \, h(s)$$

$O(\epsilon^2)$:

$$\begin{aligned} I_3 &= \int_{-\infty}^{+\infty} ds \, [1 - h(s)] \int_{-\infty}^{s} ds' h^2(s') \\ I_4 &= \int_{-\infty}^{+\infty} ds \left[1 - h^2(s)\right] \int_{-\infty}^{s} ds' h(s') \end{aligned}$$

Note: integrands go to zero at both limits

$$
\begin{aligned}
x_f &= \epsilon^2 \frac{I_1}{\cos^2\beta} + x_0 \left[1 - \epsilon^2 I_1 \frac{\sin^2\beta}{\cos^4\beta}\right] \\
&\quad + x_0' \epsilon^2 I_1 \frac{2\sin\beta}{\cos^3\beta} - \delta\epsilon^2 \frac{I_1}{\cos^2\beta} \\
x_f' &= \epsilon^2 I_1 \frac{\sin\beta}{\cos^3\beta} + x_0 \tan\beta \\
&\quad + x_0' \left[1 + \epsilon^2 I_1 \frac{3\sin^2\beta}{\cos^4\beta}\right] - \delta\epsilon^2 I_1 \frac{2\sin\beta}{\cos^3\beta} \\
y_f &= y_0 \left[1 - \frac{\epsilon^2}{\cos^4\beta}\Big(I_1 - (I_3 + I_4)(1 + \sin^2\beta)\Big)\right] \\
&\quad - y_0' \epsilon^2 I_1 \frac{2\sin\beta}{\cos^3\beta} \\
y_f' &= -y_0 \left[\tan\beta - \epsilon I_2 \frac{(1 + \sin^2\beta)}{\cos^3\beta}\right. \\
&\quad \left. + \epsilon^2 \frac{\sin\beta}{\cos^5\beta}\Big(2I_5(3 + \sin^2\beta) - I_3(1 + \sin^2\beta)\Big)\right] \\
&\quad + y_0' \left[1 + \frac{\epsilon^2}{\cos^4\beta}\Big(I_1 \sin^2\beta + (I_3 + I_5)(1 + \sin^2\beta)\Big)\right]
\end{aligned}
$$

where

$$
I_5 = I_1 + I_4
$$

Second Order Matrix Elements:

$$I_2 = \int_{-\infty}^{+\infty} ds[1-h(s)]h(s)$$
$$I_6 = \int_{-\infty}^{+\infty} ds[1-h(s)]h^2(s)$$

$$\begin{aligned}
T_{111} &= -\frac{\tan^2\beta}{2} + O(\epsilon^2) \\
T_{133} &= \frac{\sec^2\beta}{2} - \epsilon I_2 \frac{\sin\beta(5+\sin^2\beta)}{2\cos^4\beta} + O(\epsilon^2) \\
T_{212} &= \tan^2\beta + O(\epsilon^2) \\
T_{216} &= -\tan\beta + O(\epsilon^2) \\
T_{233} &= \frac{\sin\beta(1+\sin^2\beta)}{2\cos^3\beta} \\
&\quad -\epsilon\frac{\sin^2\beta}{\cos^5\beta}[I_2(5-\cos^4\beta) - I_6\frac{\cos^2\beta}{2}] + O(\epsilon^2) \\
T_{234} &= -\tan^2\beta - \epsilon I_2 \frac{\sin\beta(8+\cos^2\beta)}{\cos^4\beta} + O(\epsilon^2) \\
T_{313} &= \tan^2\beta - \epsilon I_2 \frac{\sin\beta(1+\sin^2\beta)}{\cos^4\beta} + O(\epsilon^2) \\
T_{414} &= -\tan^2\beta + \epsilon I_2 \frac{\sin\beta(1+\sin^2\beta)}{\cos^4\beta} + O(\epsilon^2) \\
T_{423} &= -\sec^2\beta + \epsilon I_2 \frac{\sin\beta(5+\sin^2\beta)}{\cos^4\beta} + O(\epsilon^2) \\
T_{436} &= \tan\beta - \epsilon I_2 \frac{2(1+\sin^2\beta)}{\cos^3\beta} + O(\epsilon^2)
\end{aligned}$$

$\epsilon = 0$: sharp cut-off ✓

Third Order Matrix Elements:

- Six additional integrals:

$$J_1 = \int_{-\infty}^{+\infty} ds \left[\frac{dh(s)}{ds}\right]^2 \rightsquigarrow \epsilon^{-1}$$
$$J_2 = \int_{-\infty}^{+\infty} ds \left[\frac{dh(s)}{ds}\right]^2 s \rightsquigarrow \epsilon^{0}$$
$$J_3 = \int_{-\infty}^{+\infty} ds \left[\frac{dh(s)}{ds}\right]^2 s^2 \rightsquigarrow \epsilon^{1}$$
$$J_4 = \int_{-\infty}^{+\infty} ds \left[\frac{dh(s)}{ds}\right]^2 \int_{-\infty}^{s} ds' h(s') \rightsquigarrow \epsilon^{0}$$
$$J_5 = \int_{-\infty}^{+\infty} ds \left[\frac{dh(s)}{ds}\right]^2 s \int_{-\infty}^{s} ds' h(s') \rightsquigarrow \epsilon^{1}$$
$$J_6 = \int_{-\infty}^{+\infty} ds \left[\frac{dh(s)}{ds}\right]^2 \int_{-\infty}^{s} ds' \int_{-\infty}^{s'} ds'' h(s'') \rightsquigarrow \epsilon^{1}$$

- Integrands go to zero at both limits
- J_n's appear in $U_{i,j,k,l}$ only when $i, j, k, l = 3, 4$
- Divergent term:

$$U_{4333} = -\frac{2}{3}\frac{(1+\sin^2\beta)}{\cos^4\beta}\frac{J_1}{\epsilon} + \cdots$$

e. g. , Chromatic Terms:

$$
\begin{aligned}
U_{1116} &= \frac{\tan^2\beta}{2} + O(\epsilon^2) \\
U_{1336} &= \frac{\sec^2\beta}{2} + \epsilon I_2 \frac{\sin\beta(5+\sin^2\beta)}{\cos^4\beta} + O(\epsilon^2) \\
U_{2126} &= -\tan^2\beta + O(\epsilon^2) \\
U_{2166} &= \tan\beta + O(\epsilon^2) \\
U_{2336} &= -\frac{\sin\beta(1+\sin^2\beta)}{\cos^3\beta} + O(\epsilon^2) \\
U_{2346} &= \tan^2\beta - \epsilon I_2 \frac{2\sin\beta(1+\sin^2\beta)}{\cos^4\beta} + O(\epsilon^2) \\
U_{3136} &= -\tan^2\beta + \epsilon I_2 \frac{2\sin\beta(1+\sin^2\beta)}{\cos^4\beta} + O(\epsilon^2) \\
U_{4146} &= \tan^2\beta - \epsilon I_2 \frac{2\sin\beta(1+\sin^2\beta)}{\cos^4\beta} + O(\epsilon^2) \\
U_{4236} &= \sec^2\beta - \epsilon I_2 \frac{2\sin\beta(5+\sin^2\beta)}{\cos^4\beta} + O(\epsilon^2) \\
U_{4366} &= -\tan\beta + \epsilon I_2 \frac{3(1+\sin^2\beta)}{\cos^3\beta} + O(\epsilon^2)
\end{aligned}
$$

GIOS

GIOS

and Fringing Fields

H. Wollnik

University Giessen, Germany

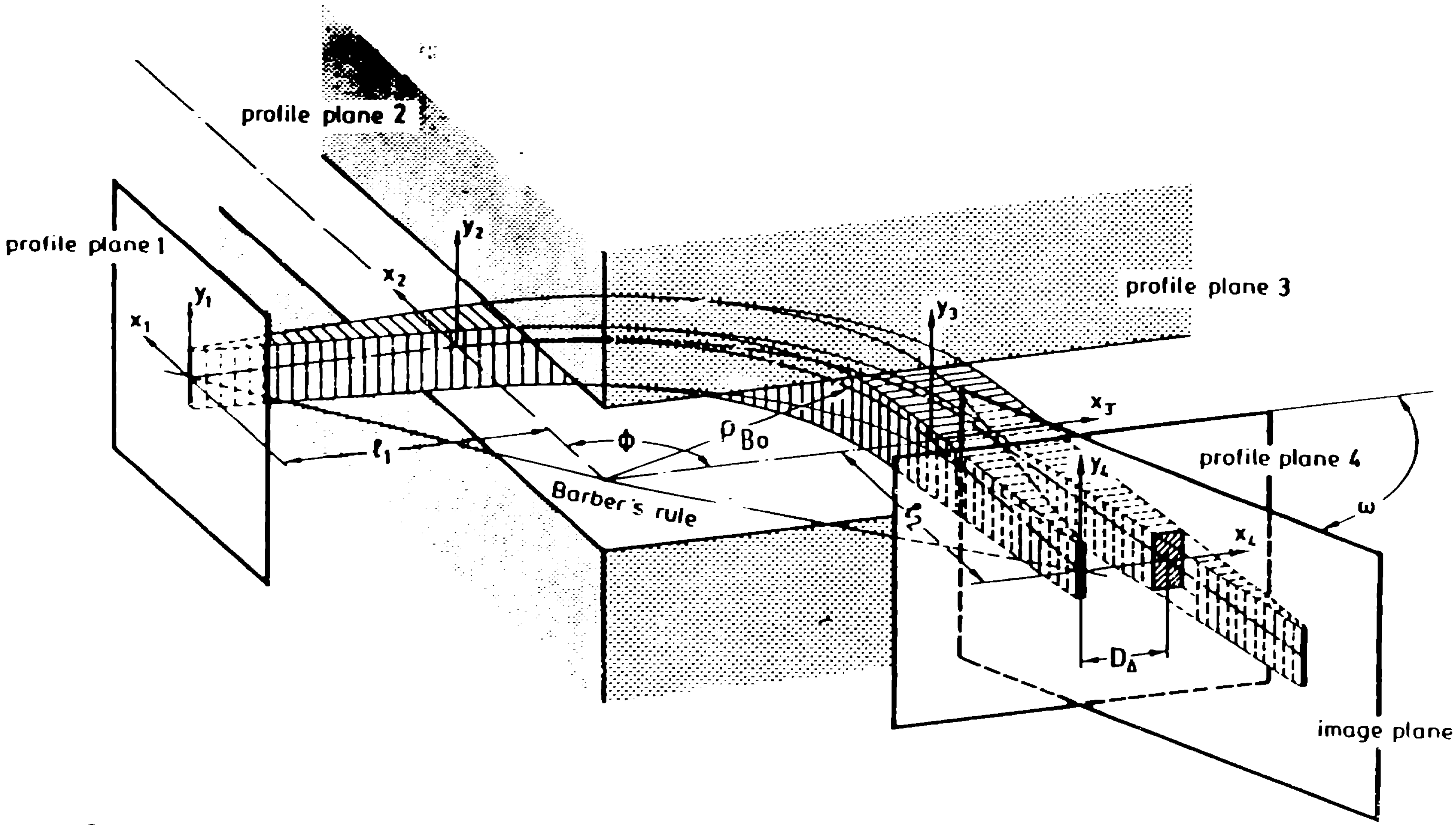

profile plane 2
profile plane 1
profile plane 3
profile plane 4
image plane
Barber's rule
y_1
x_1
y_2
x_2
y_3
x_3
y_4
x_4
ℓ_1
Φ
ρ_{Bo}
ω
D_Δ

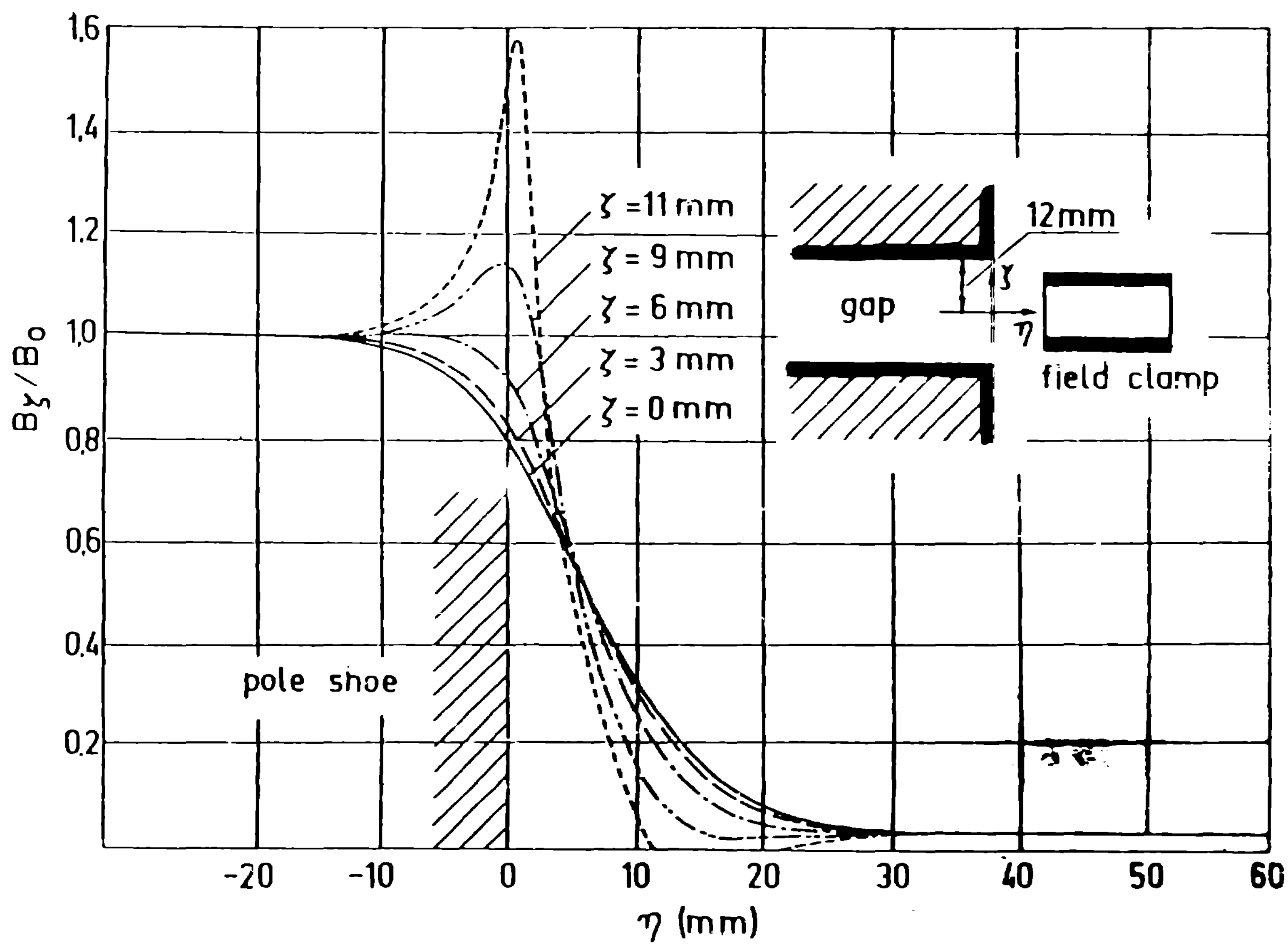

1,6
1,4
1,2
1,0
0,8
0,6
0,4
0,2
B_ζ/B_0
-20
-10
0
10
20
30
40
50
60
η (mm)
ζ = 11 mm
ζ = 9 mm
ζ = 6 mm
ζ = 3 mm
ζ = 0 mm
12mm
gap
ζ
η
field clamp
pole shoe

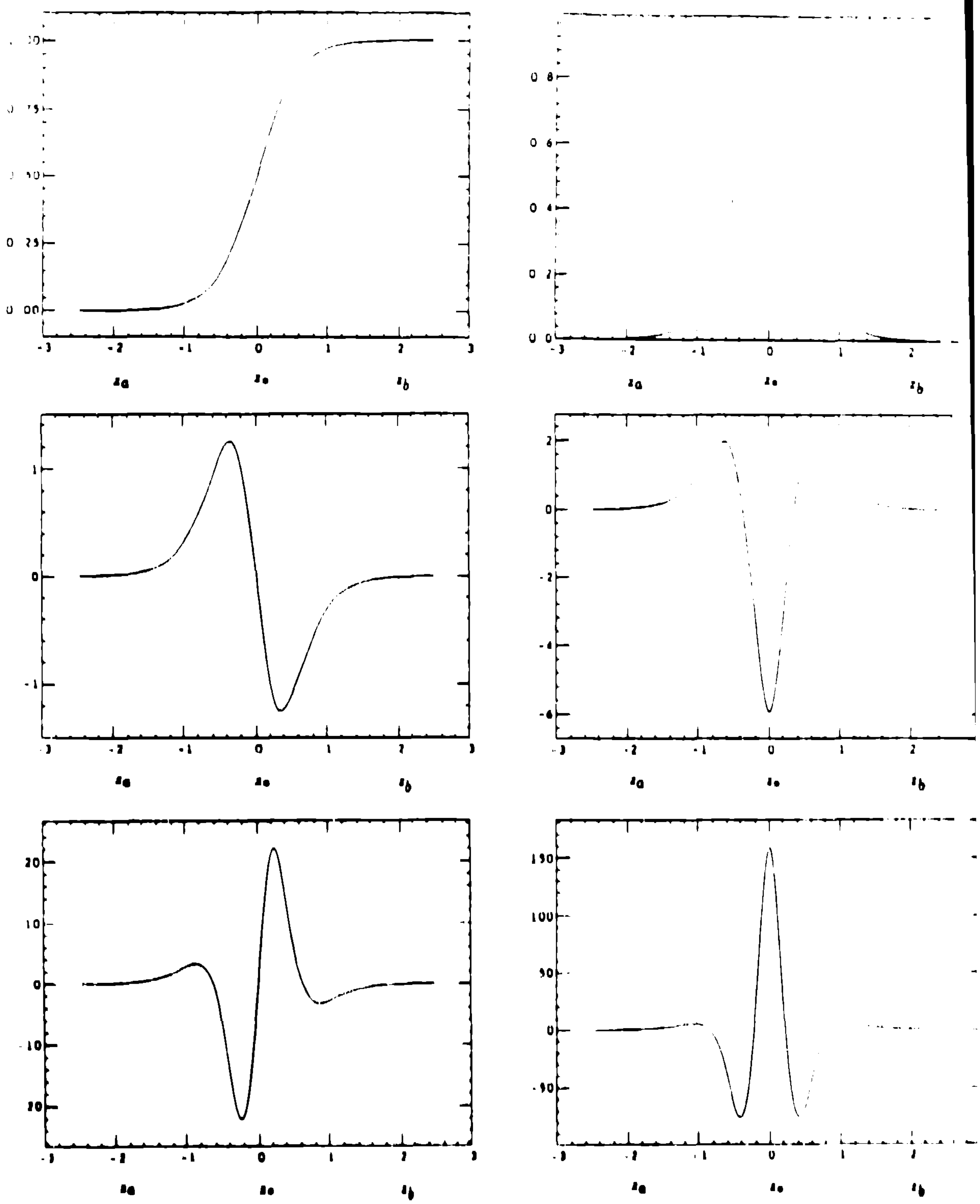

Fig. 1 The value and first five derivatives of the quadrupole strength as functions of the position on the optic axis. Note that a $z = z_a$ the value of $M_{1,1}$ is zero and has reached saturation at $z = z_b$. The curves shown were obtained by evaluating the function a different z values with fifth order DA. These results are required for eqs. (11) and (12).

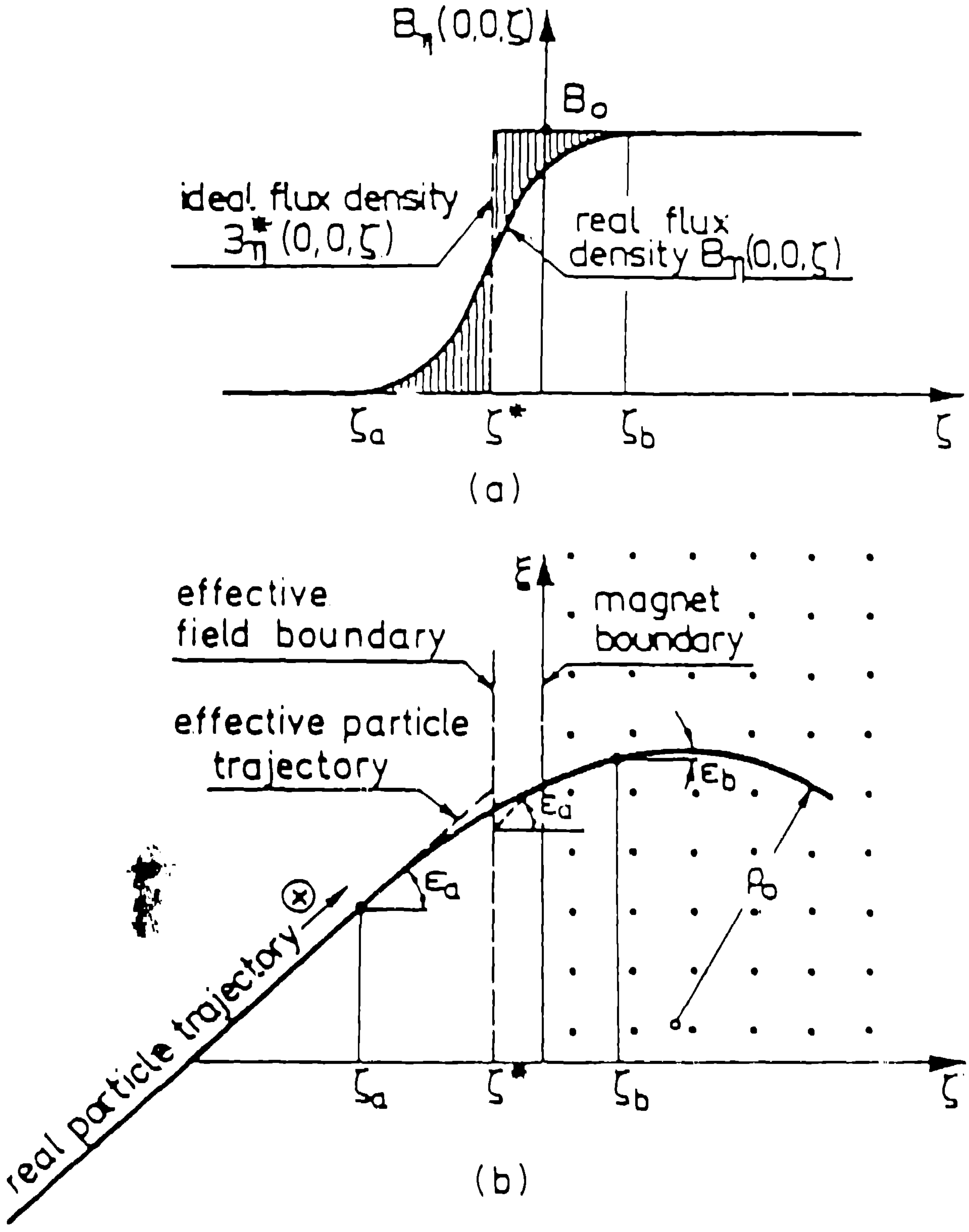

$B_\eta(0,0,\zeta)$
B_o
ideal flux density
$B^*_\eta(0,0,\zeta)$
real flux
density $B_\eta(0,0,\zeta)$
ζ_a
ζ^*
ζ_b
ζ
(a)
ξ
effective
field boundary
magnet
boundary
effective particle
trajectory
ε_a
ε_b
ρ_o
real particle trajectory
ζ_a
ζ^*
ζ_b
ζ
(b)

$$
\begin{aligned}
B_x\left(x,y,z\right) &= 0 \\
B_y\left(x,y,z\right) &= B_y\left(0,0,z\right) + \tfrac{y^2}{2}\left(\tfrac{\partial^2 B_y}{\partial y^2}\right)_{0,0,z} + \ldots \\
B_z\left(x,y,z\right) &= y\left(\tfrac{\partial B_y}{\partial y}\right)_{0,0,z} + \ldots
\end{aligned}
$$

$$
\begin{aligned}
curl\ \vec{B} &= \tfrac{\partial B_y}{\partial z} - \tfrac{\partial B_z}{\partial y} = 0 \\
div\ \ \vec{B} &= \tfrac{\partial^2 B_y}{\partial y^2} + \tfrac{\partial^2 B_y}{\partial z^2} = 0
\end{aligned}
$$

$$
\begin{aligned}
B_x\left(x,y,z\right) &= 0 \\
B_y\left(x,y,z\right) &= B_y\left(0,0,z\right) - \tfrac{y^2}{2}\left(\tfrac{\partial^2 B_y}{\partial z^2}\right)_{0,0,z} + \ldots \\
B_z\left(x,y,z\right) &= y\left(\tfrac{\partial B_y}{\partial z}\right)_{0,0,z} + \ldots
\end{aligned}
$$

$$
m\ddot{x} = qv_zB_y\left(x,y,z\right) - qv_yB_z\left(x,y,z\right)
$$

$$
\begin{aligned}
m\dot{x} = {} & q\int_{z_a}^{z_b} v_zB_y\left(0,0,z\right)\ dz - q\int_{z_a}^{z_b} yv_y\left(\frac{\partial B_y}{\partial z}\right)_{0,0,z}\ dz - \\
& q\int_{z_a}^{z_b} \frac{y^2v_z}{2}\left(\frac{\partial^2 B_y}{\partial z^2}\right)_{0,0,z}\ dz + \ldots
\end{aligned}
$$

fringing–field effects of a homogenous magnetic sector

$$\begin{pmatrix} x_f \\ a_f \\ y_f \\ b_f \end{pmatrix} = \begin{pmatrix} 1 & \ldots I1 & 0 & 0 \\ t & 1 - \ldots I1 & 0 & 0 \\ 0 & 0 & 1 - \ldots I_1 & \ldots I1 \\ 0 & 0 & 1 + \ldots I_8 & t - \ldots I_4 \end{pmatrix} \begin{pmatrix} x_i \\ a_i \\ y_i \\ b_i \end{pmatrix}$$

some higher order effects:

$$\begin{aligned}
(x, xx) &= -\tfrac{t^2}{2} \\
(x, xxa) &= -t^3 \\
(x, xyy) &= \tfrac{1}{2}t^2\left(1 + 2t^2\right) + \ldots I_{11} \\
(x, ayy) &= \tfrac{t}{c^2} + \ldots I_{12} \\
(a, xyy) &= \tfrac{t^3}{2} + \ldots I_7 \\
(y, yyy) &= \tfrac{1}{6c^3}\left(1 + 6t^2\right) + \ldots I_{11} \\
(b, yyy) &= \tfrac{t}{18} sf\left(8 + 11t^2 + 12t^4\right) + \ldots I_7 \\
(b, yyb) &= -\tfrac{1}{2}\left(1 + t^4\right) + \ldots I_{11}
\end{aligned}$$

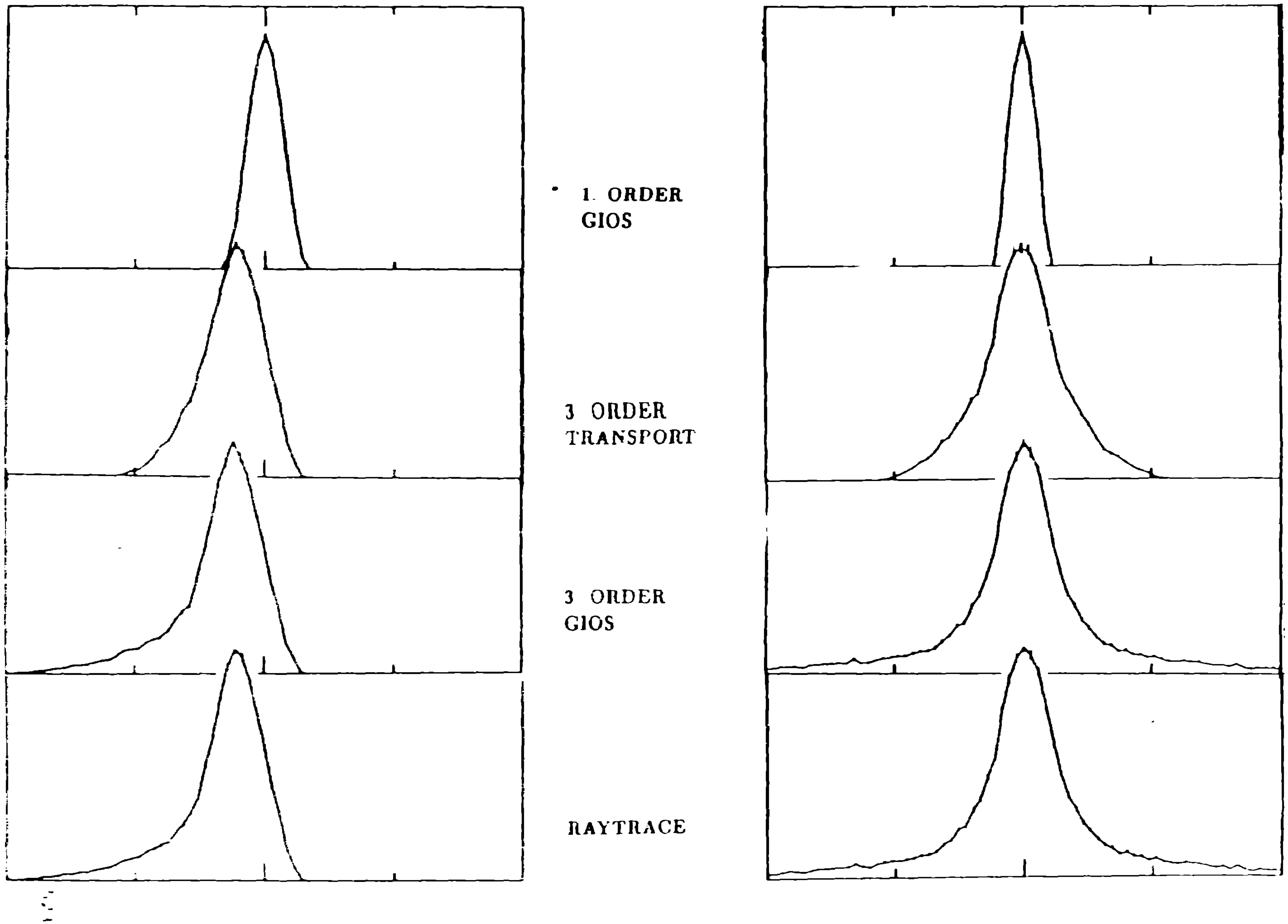
1. ORDER GIOS
3 ORDER TRANSPORT
3 ORDER GIOS
RAYTRACE

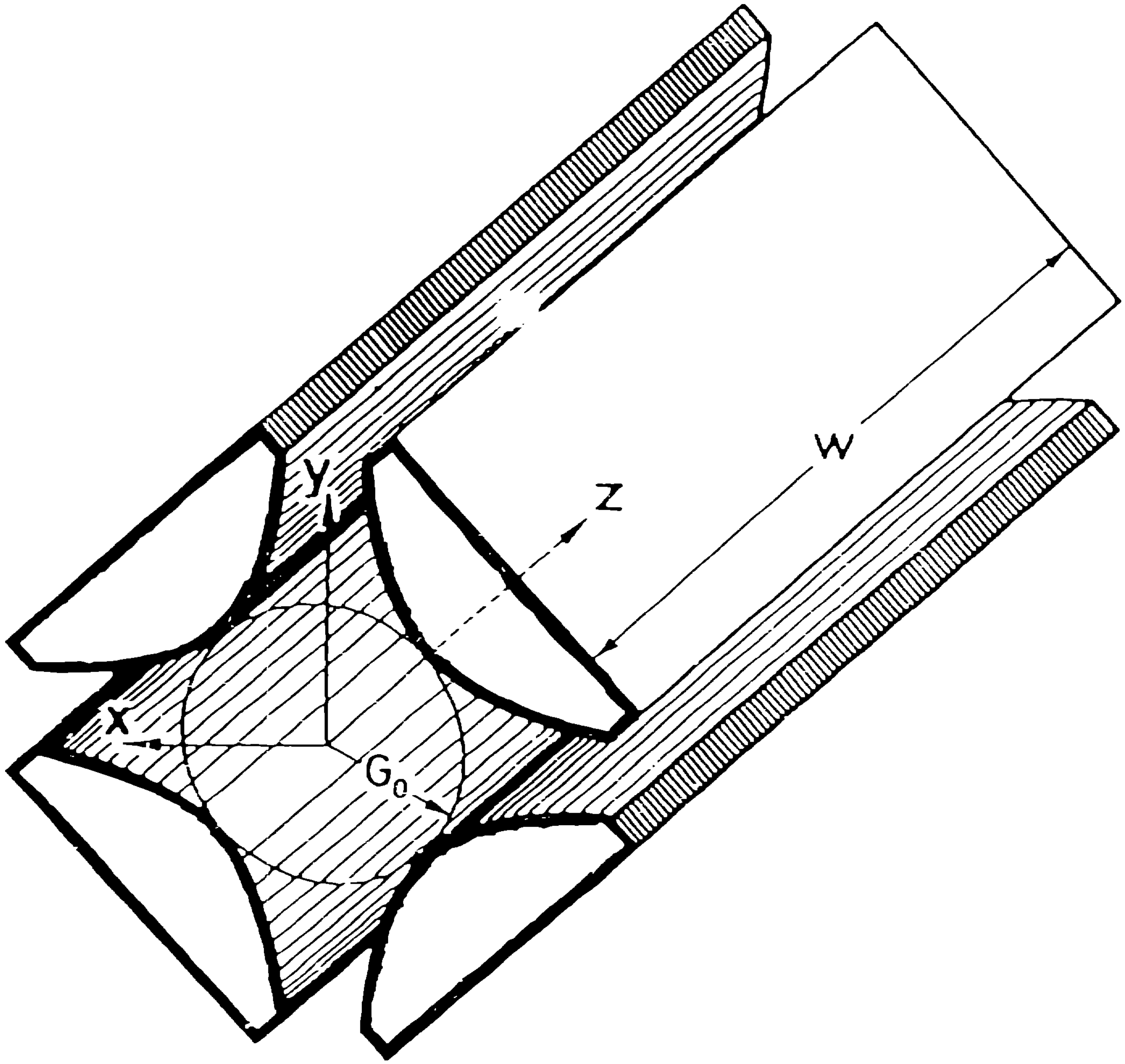
y
z
W
x
G_0

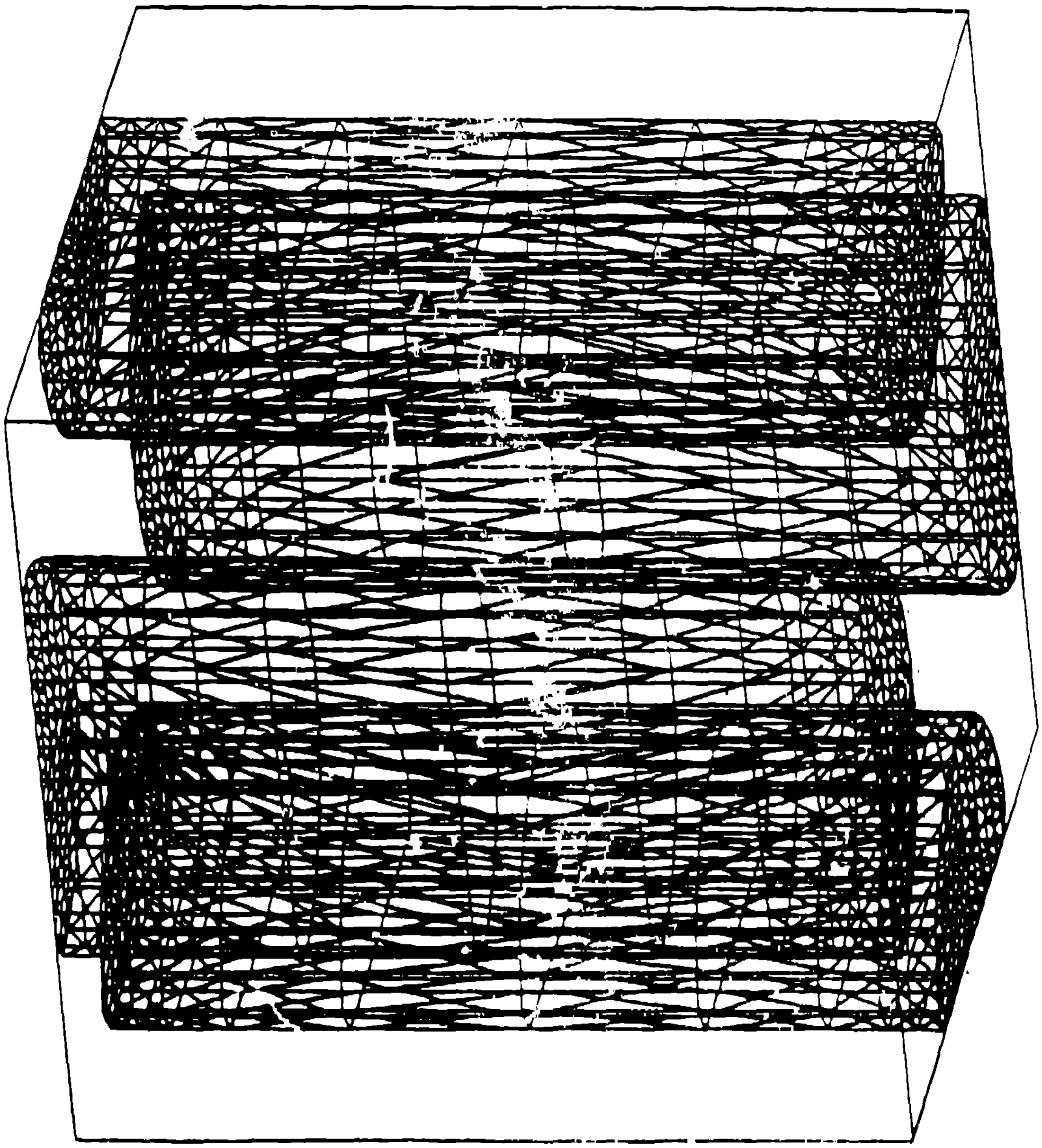

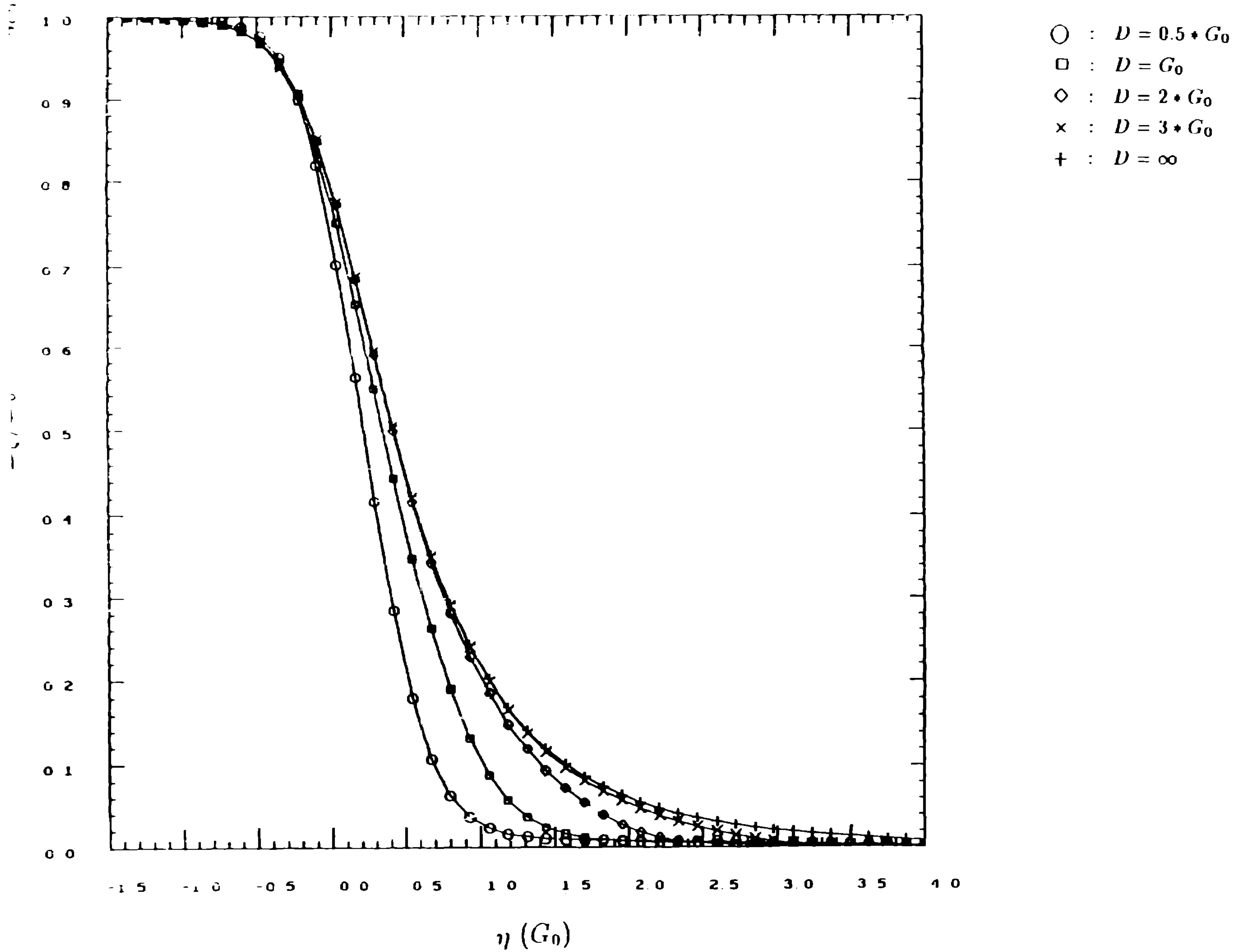

1.0
0.9
0.8
0.7
0.6
0.5
0.4
0.3
0.2
0.1
0.0
-1.5
-1.0
-0.5
0.0
0.5
1.0
1.5
2.0
2.5
3.0
3.5
4.0
$\eta\ (G_0)$
○ : $D = 0.5 * G_0$
□ : $D = G_0$
◇ : $D = 2 * G_0$
× : $D = 3 * G_0$
+ : $D = \infty$

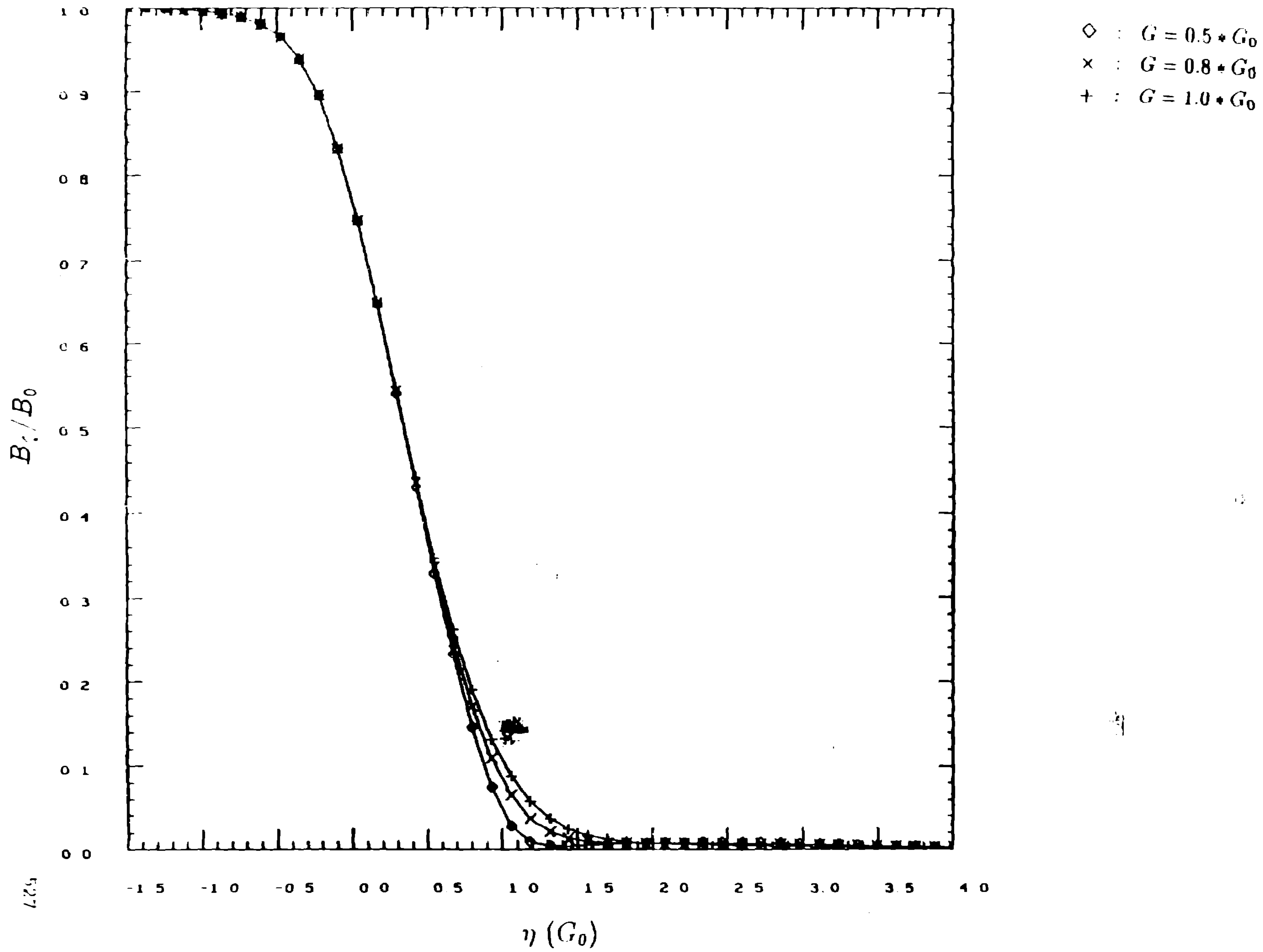

◇ : $G = 0.5 * G_0$
× : $G = 0.8 * G_0$
+ : $G = 1.0 * G_0$
1.0
0.9
0.8
0.7
0.6
0.5
0.4
0.3
0.2
0.1
0.0
-1.5
-1.0
-0.5
0.0
0.5
1.0
1.5
2.0
2.5
3.0
3.5
4.0
$\eta\ (G_0)$

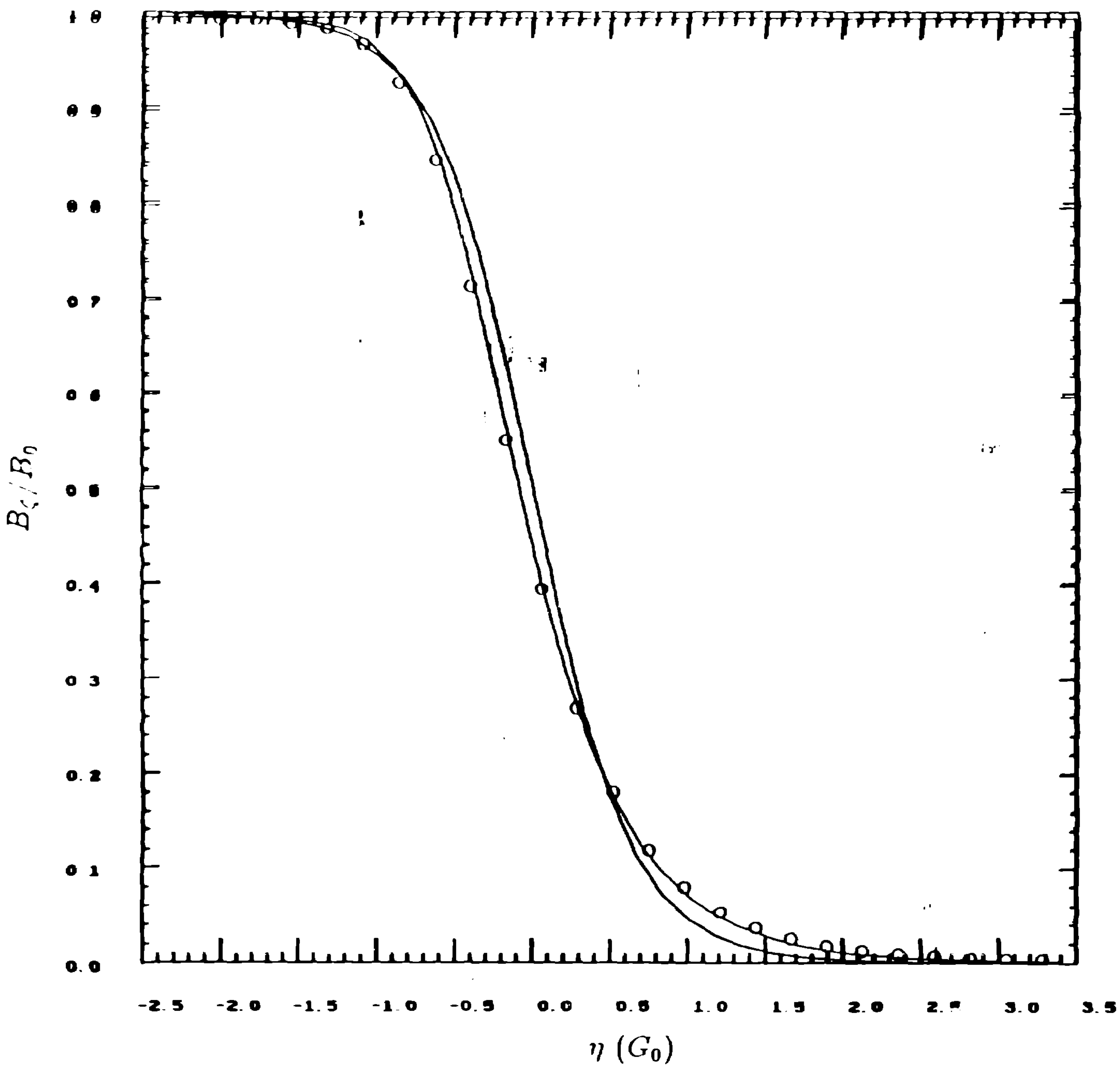

○ : *experimental values*

Ratio $R_2/R_1 = 1.5$

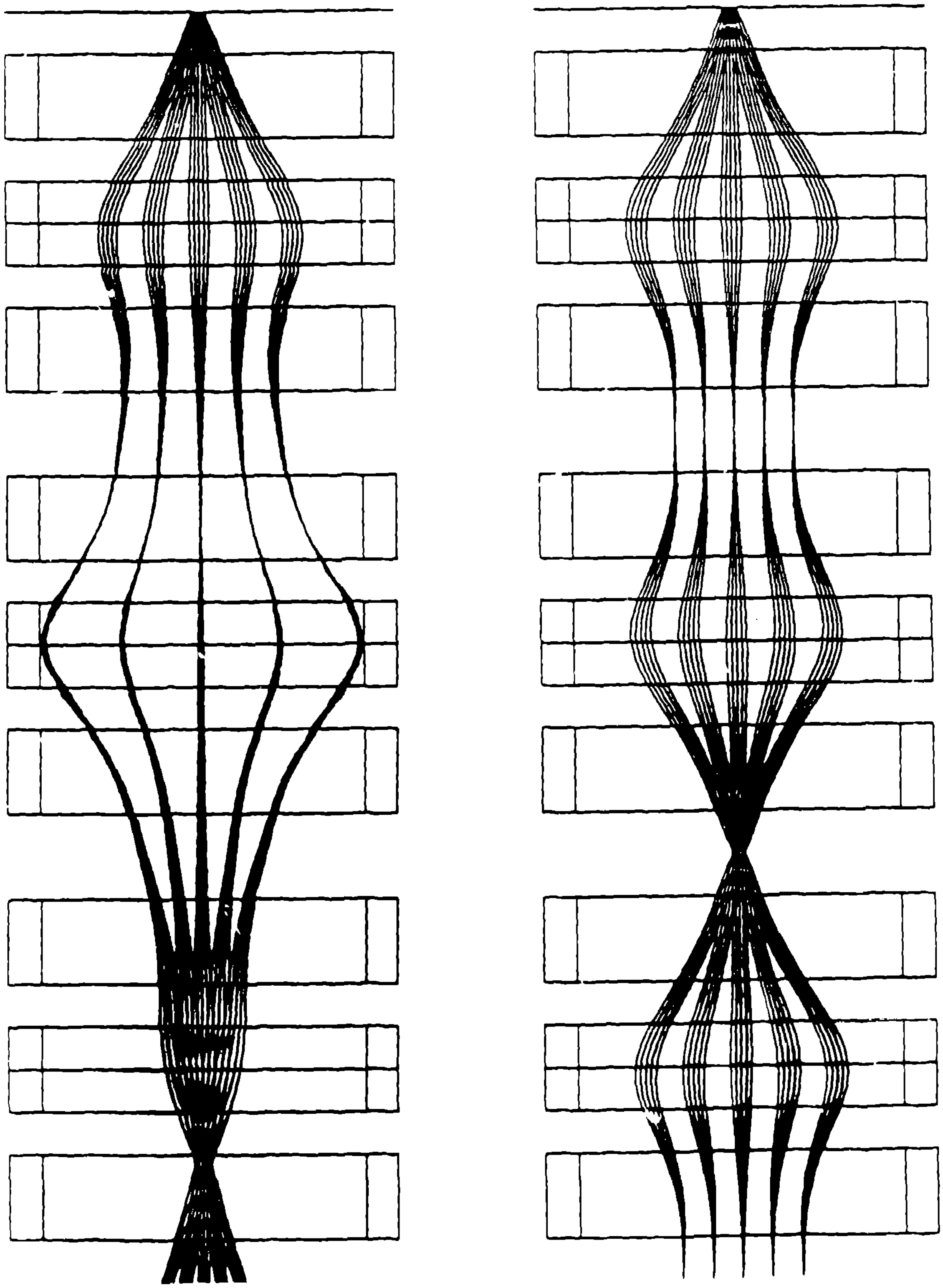

fringing–field effects of a quadrupole

$$\begin{pmatrix} x_f \\ a_f \\ y_f \\ b_f \end{pmatrix} = \begin{pmatrix} 1 - K_0^2 I_1 & -2K_0^2 I_2 & 0 & 0 \\ K_0^4 I_3 & 1 + K_0^2 I_1 & 0 & 0 \\ 0 & 0 & 1 + K_0^2 I_1 & 2K_0^2 I_2 \\ 0 & 0 & -K_0^4 I_3 & 1 - K_0^2 I_1 \end{pmatrix} \begin{pmatrix} x_i \\ a_i \\ y_i \\ b_i \end{pmatrix}$$

some third–order effects:

$$\begin{aligned} (x, xxx) &= +\tfrac{1}{12} K_0^2 \\ (x, xyy) &= +\tfrac{1}{4} K_0^2 \\ (a, xxx) &= -\tfrac{1}{3} K_0^4 \cdot I_4 \\ (a, xyy) &= -K_0^4 \cdot I_4 \\ (y, yyy) &= -\tfrac{1}{12} K_0^2 \\ (y, yxx) &= -\tfrac{1}{4} K_0^2 \\ (b, xxx) &= -\tfrac{1}{3} K_0^4 \cdot I_4 \\ (b, yxx) &= -K_0^4 \cdot I_4 \end{aligned}$$

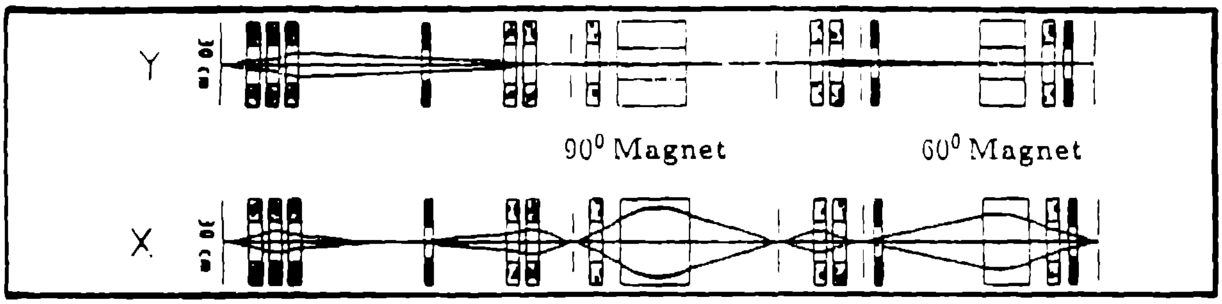
Y
X
90^0 Magnet
60^0 Magnet

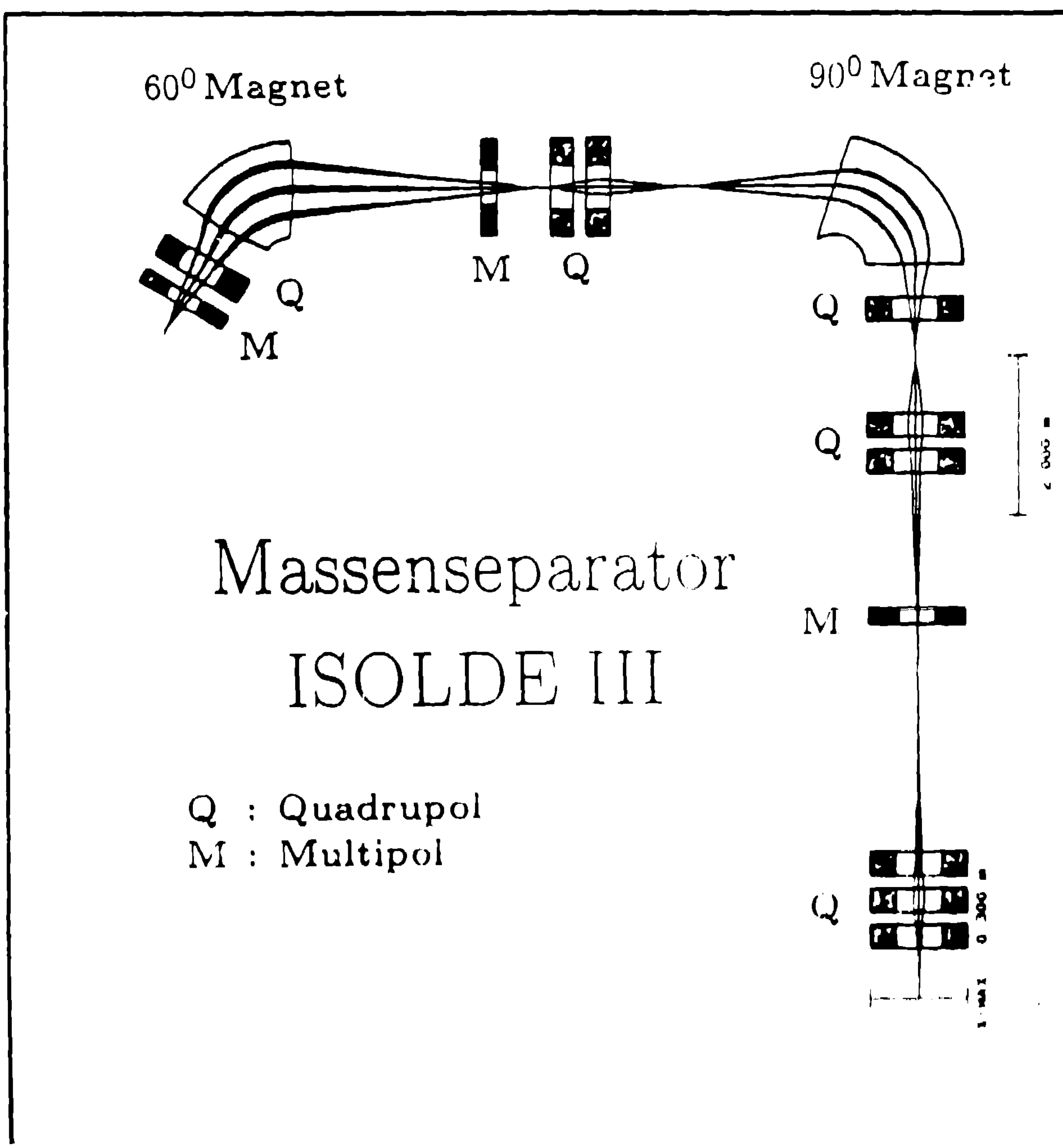
60^0 Magnet
90^0 Magnet
Q
M
Massenseparator
ISOLDE III
Q : Quadrupol
M : Multipol

$^{130,131,132}Xe$

ISOLDE 2
Endfokus

R ≈ 500 (70%)

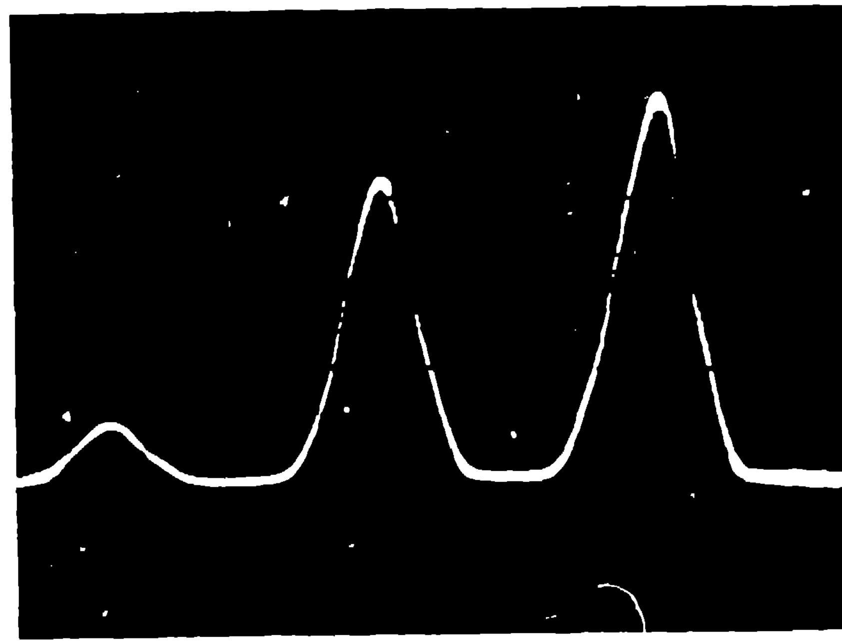

ISOLDE 3
1. Stufe

R ≈ 2700 (98%)

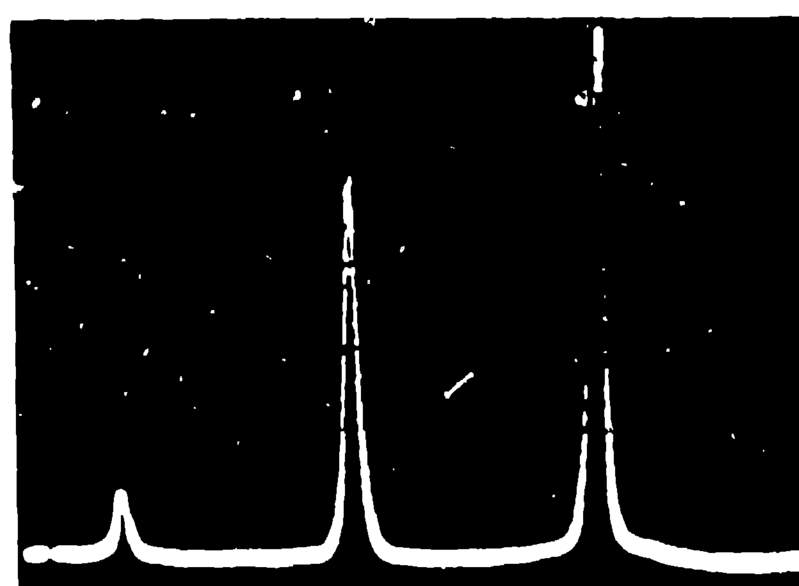

⊢ 13,9 mm ⊣

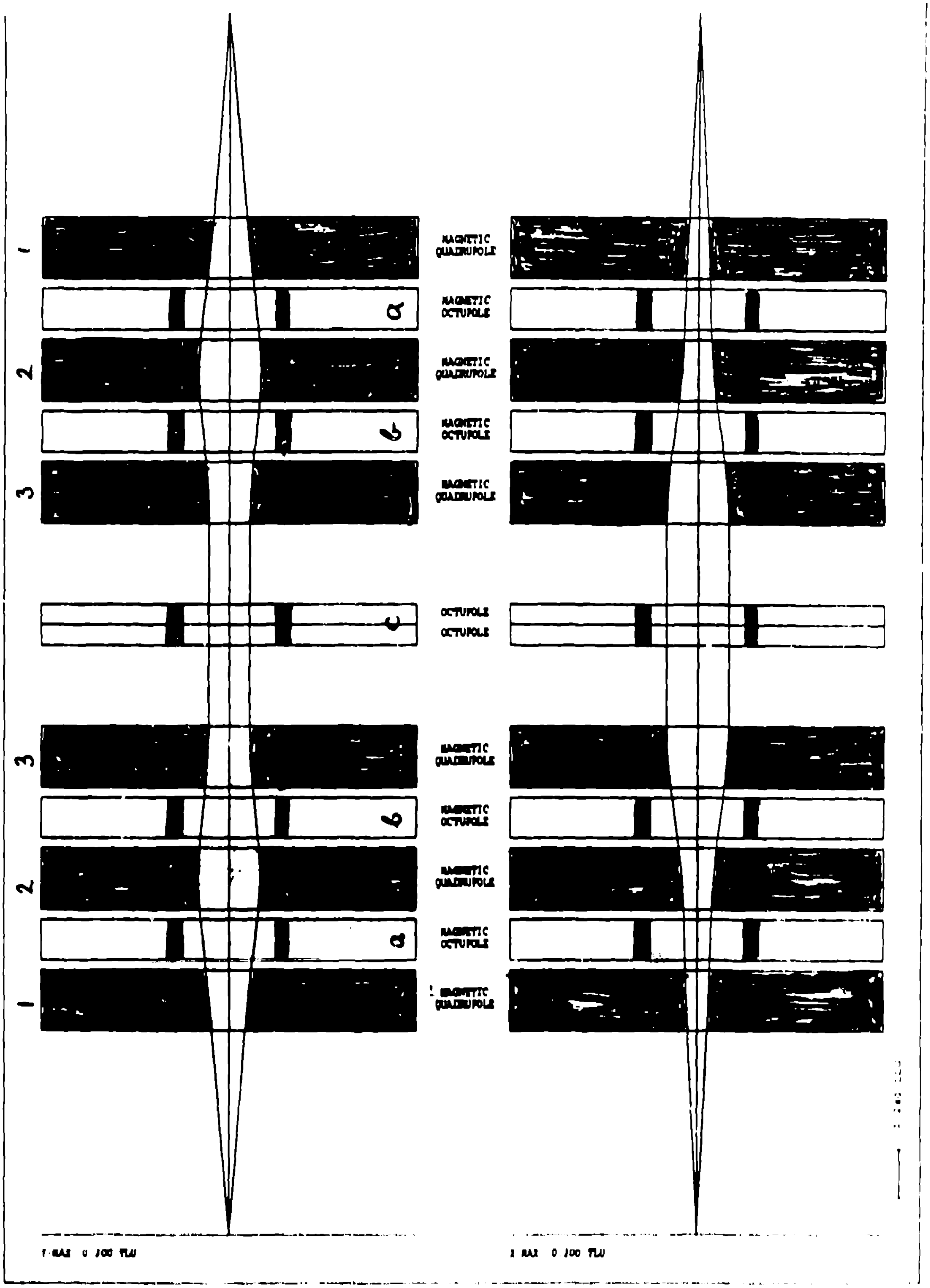

1
MAGNETIC QUADRUPOLE
a
MAGNETIC OCTUPOLE
2
MAGNETIC QUADRUPOLE
b
MAGNETIC OCTUPOLE
3
MAGNETIC QUADRUPOLE
c
OCTUPOLE
OCTUPOLE
3
MAGNETIC QUADRUPOLE
b
MAGNETIC OCTUPOLE
2
MAGNETIC QUADRUPOLE
a
MAGNETIC OCTUPOLE
1
MAGNETIC QUADRUPOLE

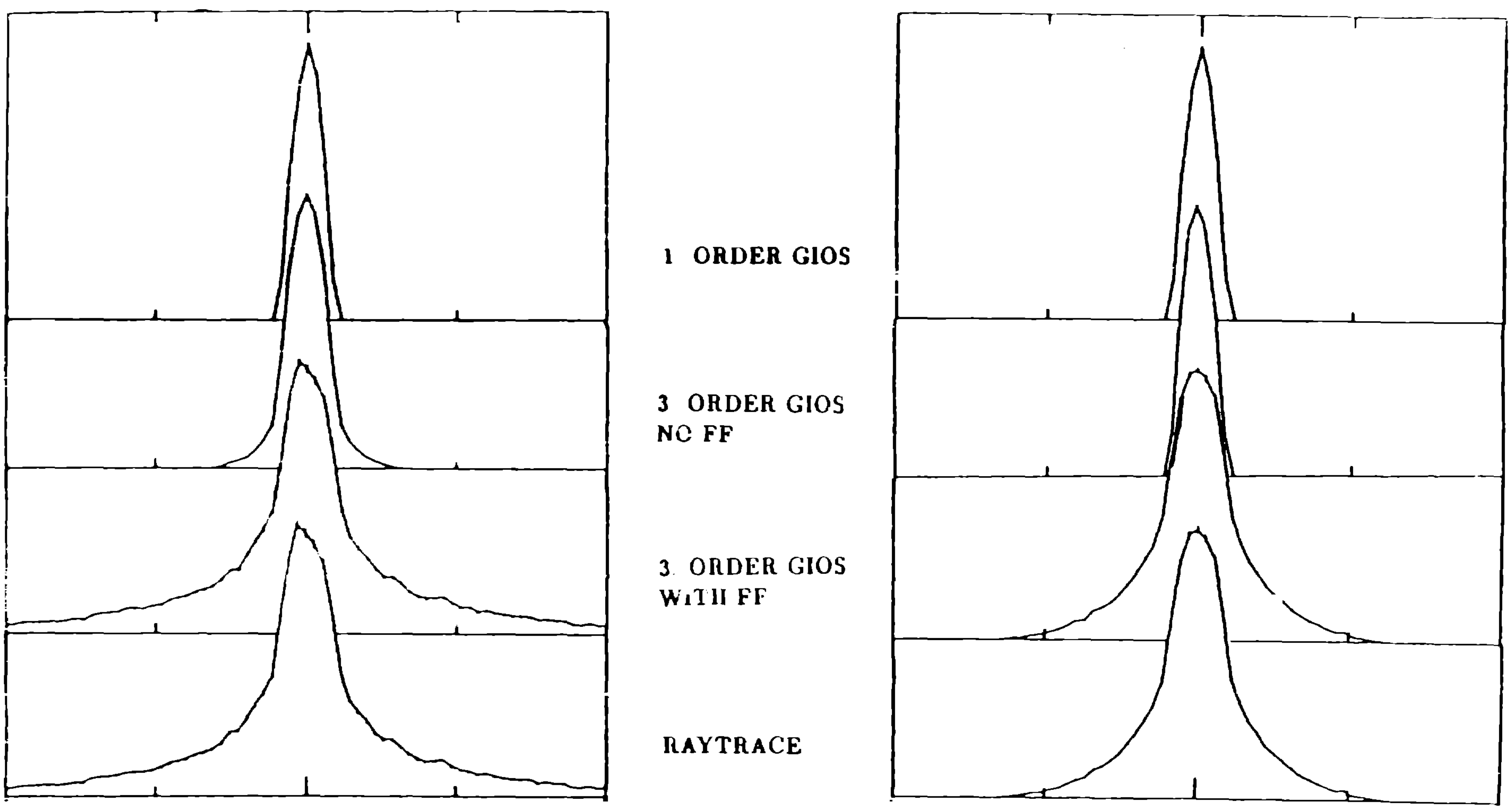

1 ORDER GIOS
3 ORDER GIOS
NO FF
3. ORDER GIOS
WITH FF
RAYTRACE

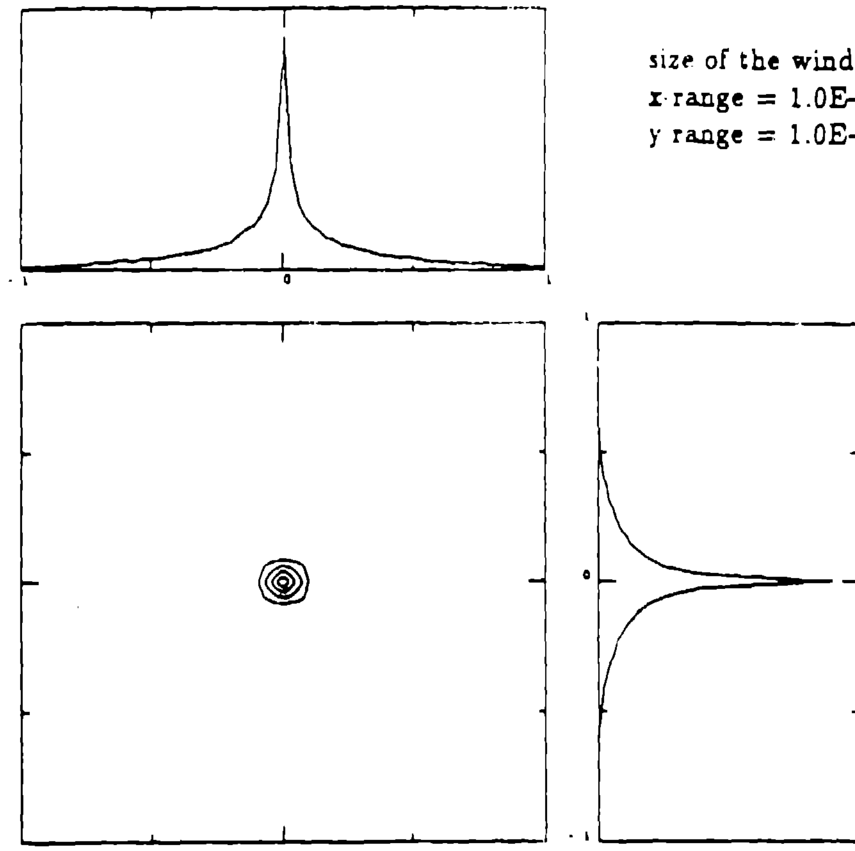

size of the window
x-range = 1.0E-3 m
y range = 1.0E-3 m

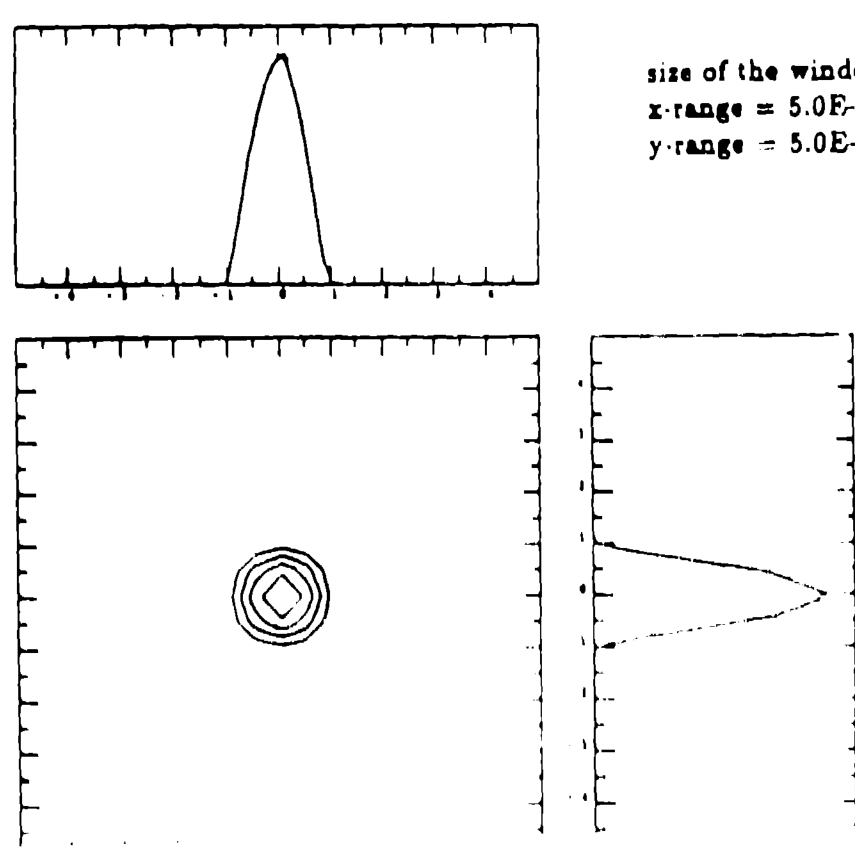

size of the window
x-range = 5.0E-5 m
y-range = 5.0E-5 m

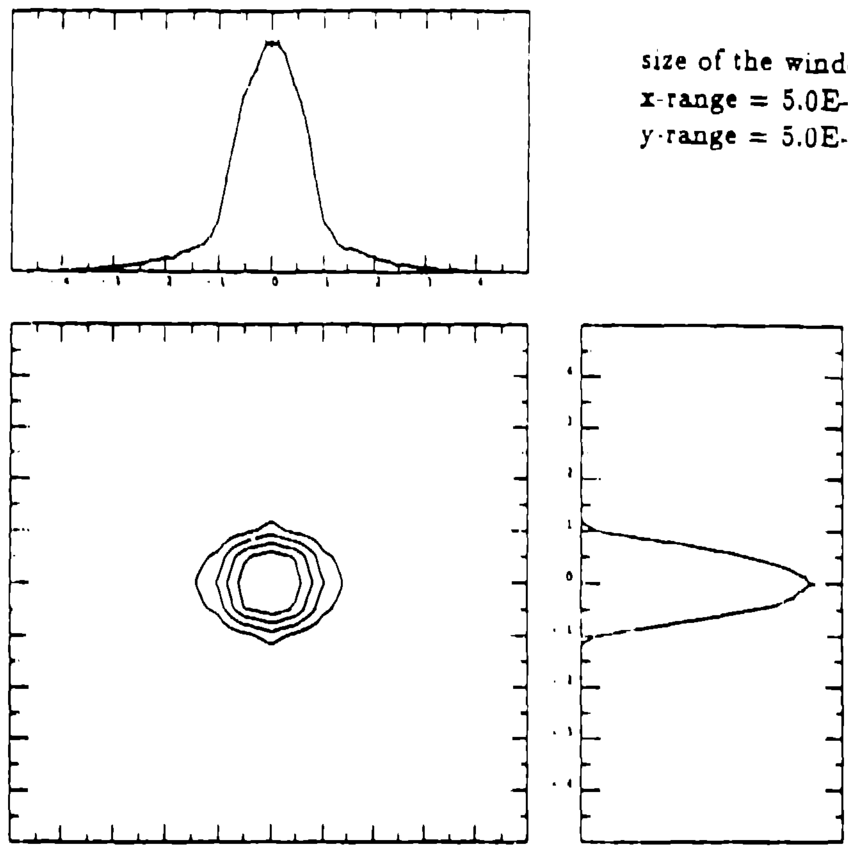

size of the window
x-range = 5.0E-5 m
y-range = 5.0E-5 m

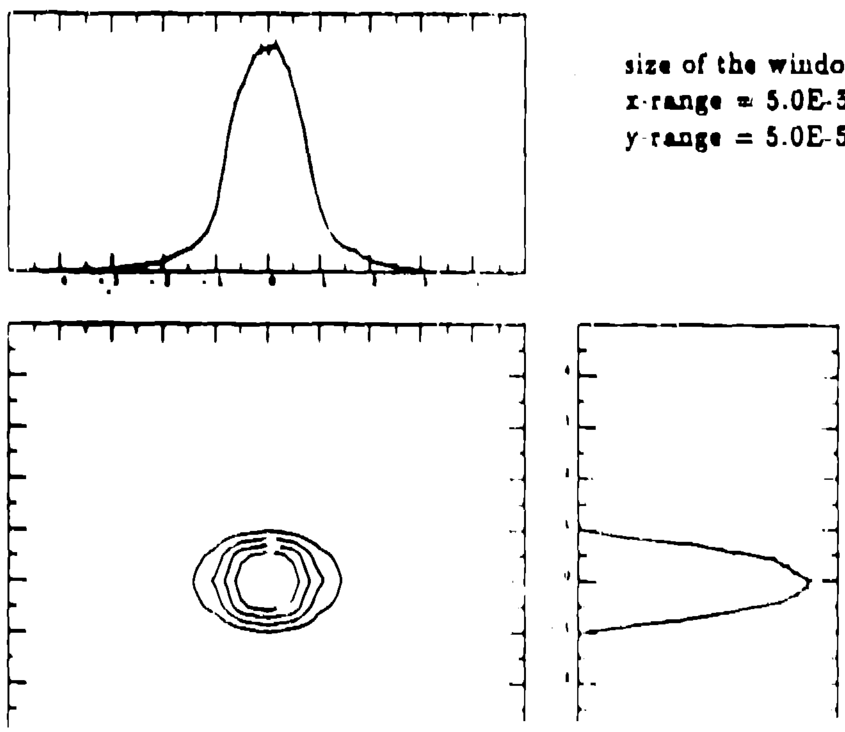

size of the window
x-range = 5.0E-3 m
y-range = 5.0E-5 m

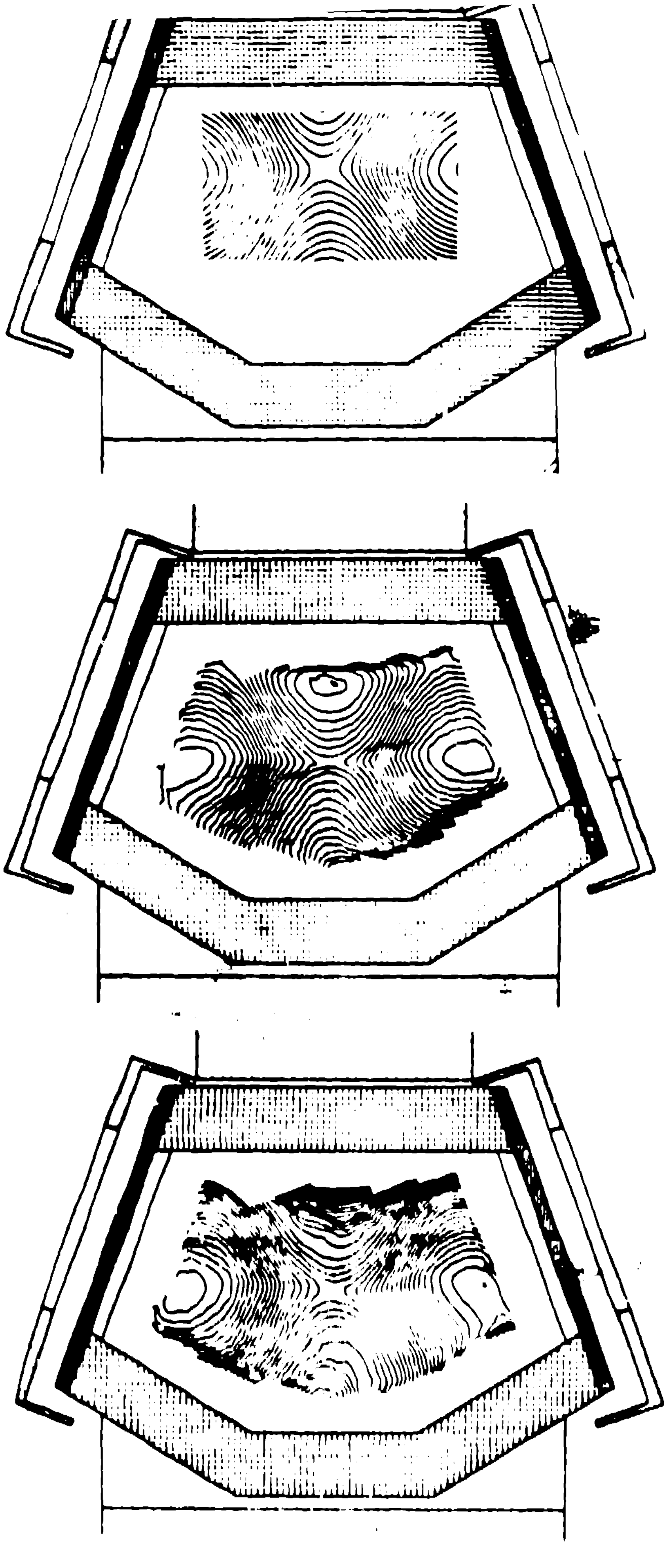

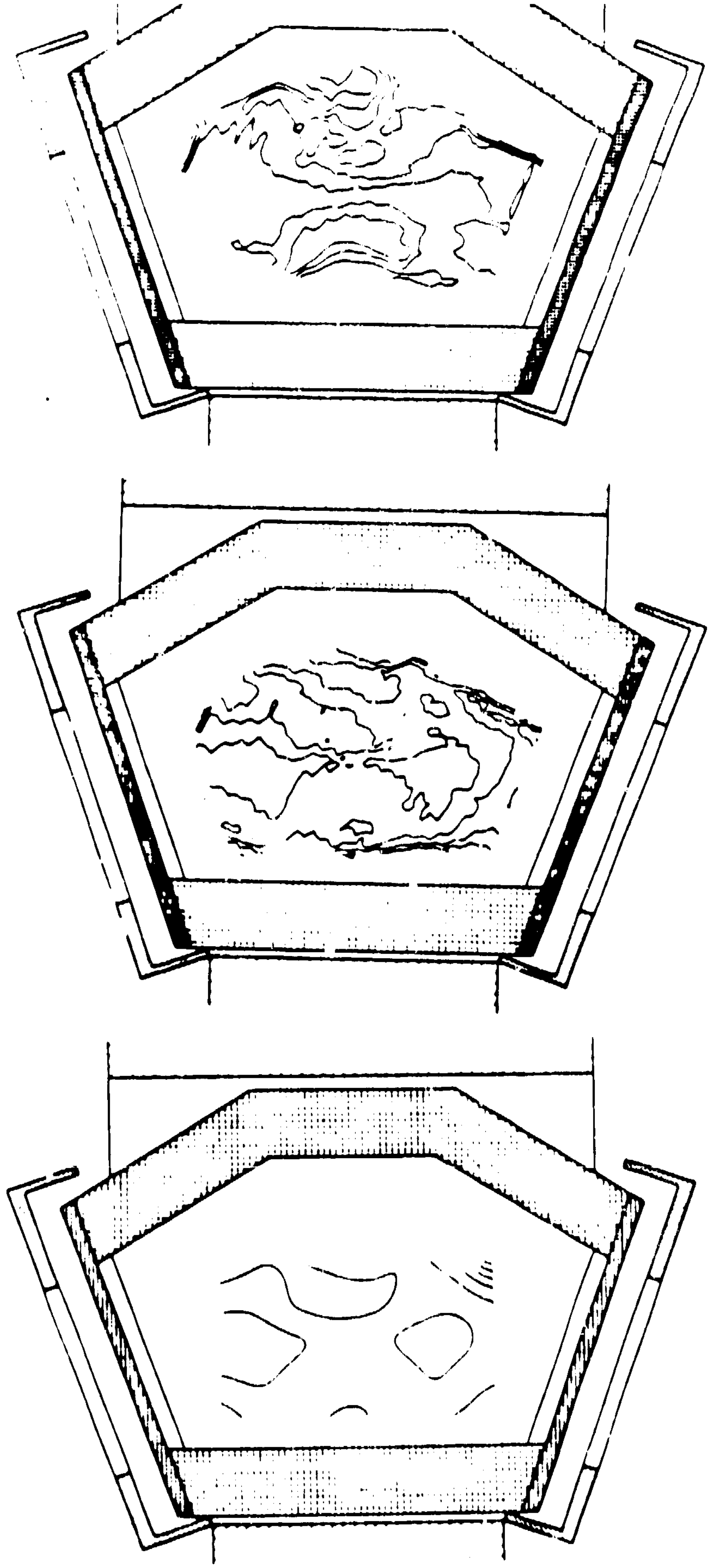

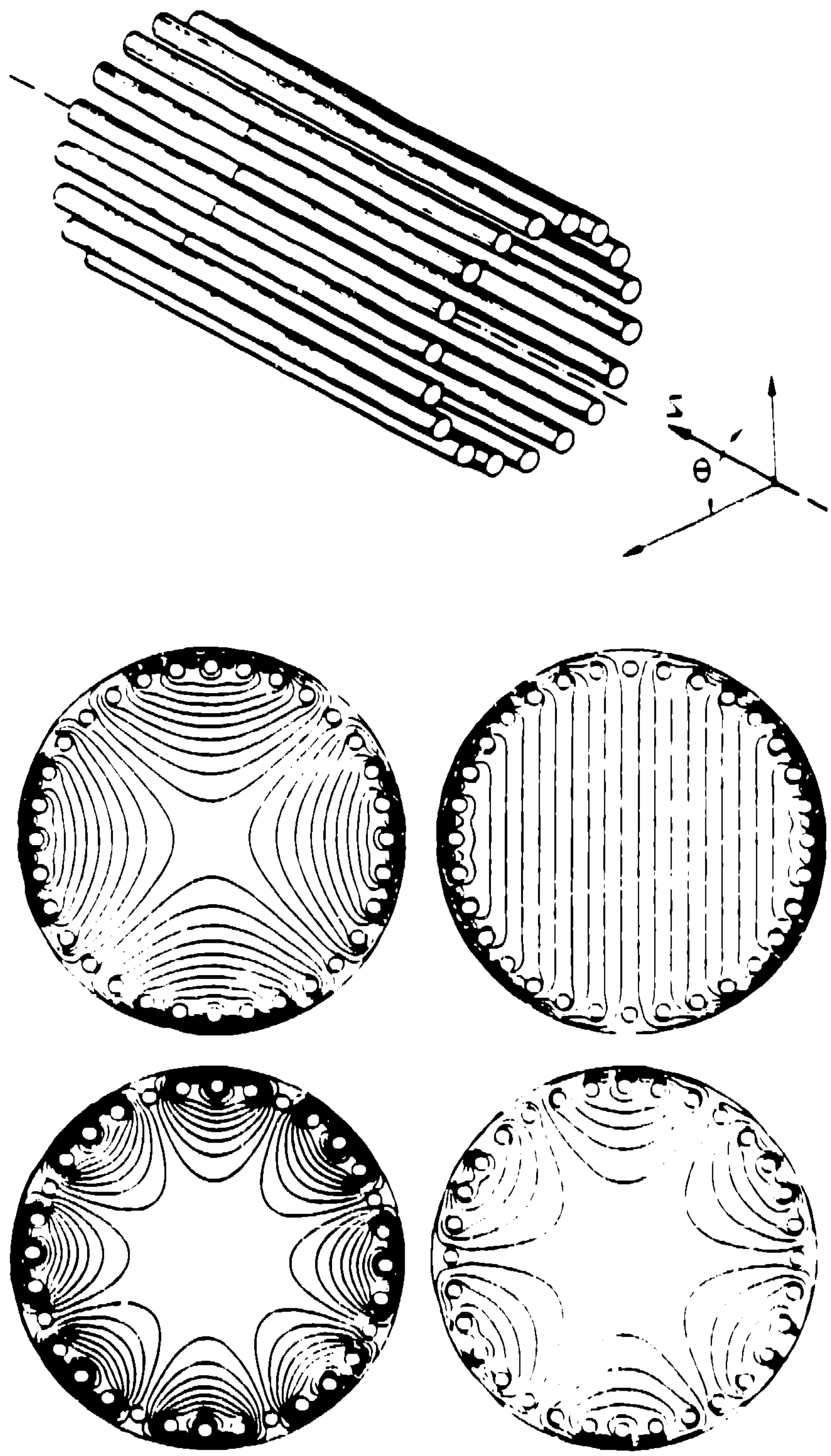
Θ

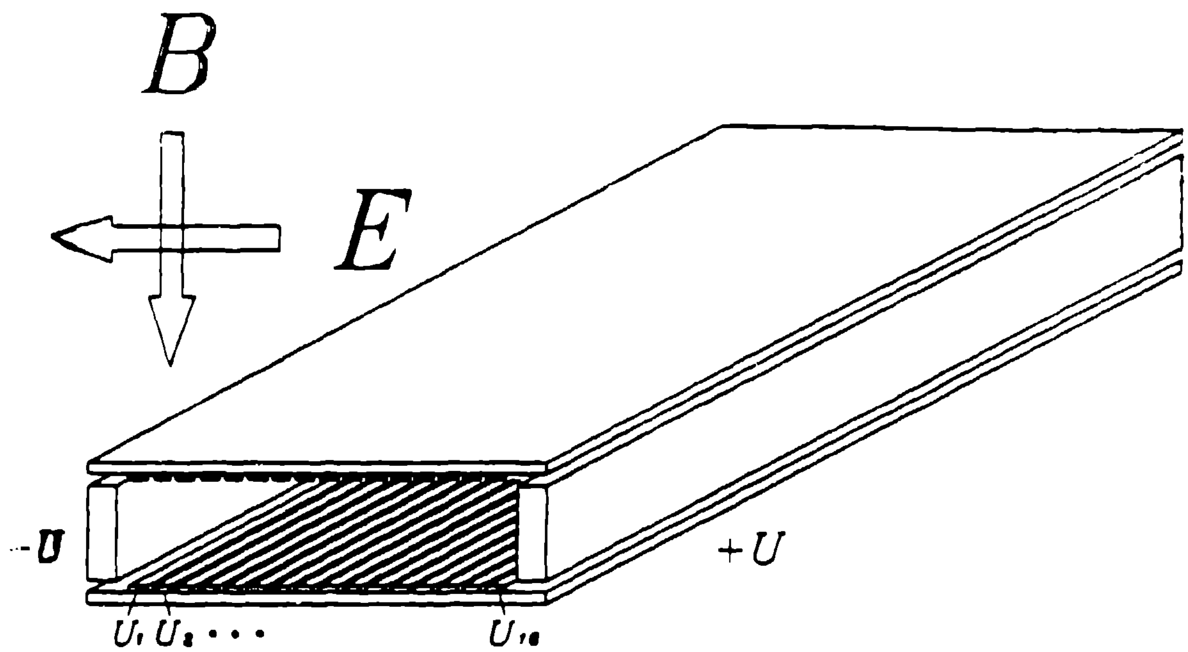
B
E
-U
+U
U_1 U_2 · · ·
U_{16}

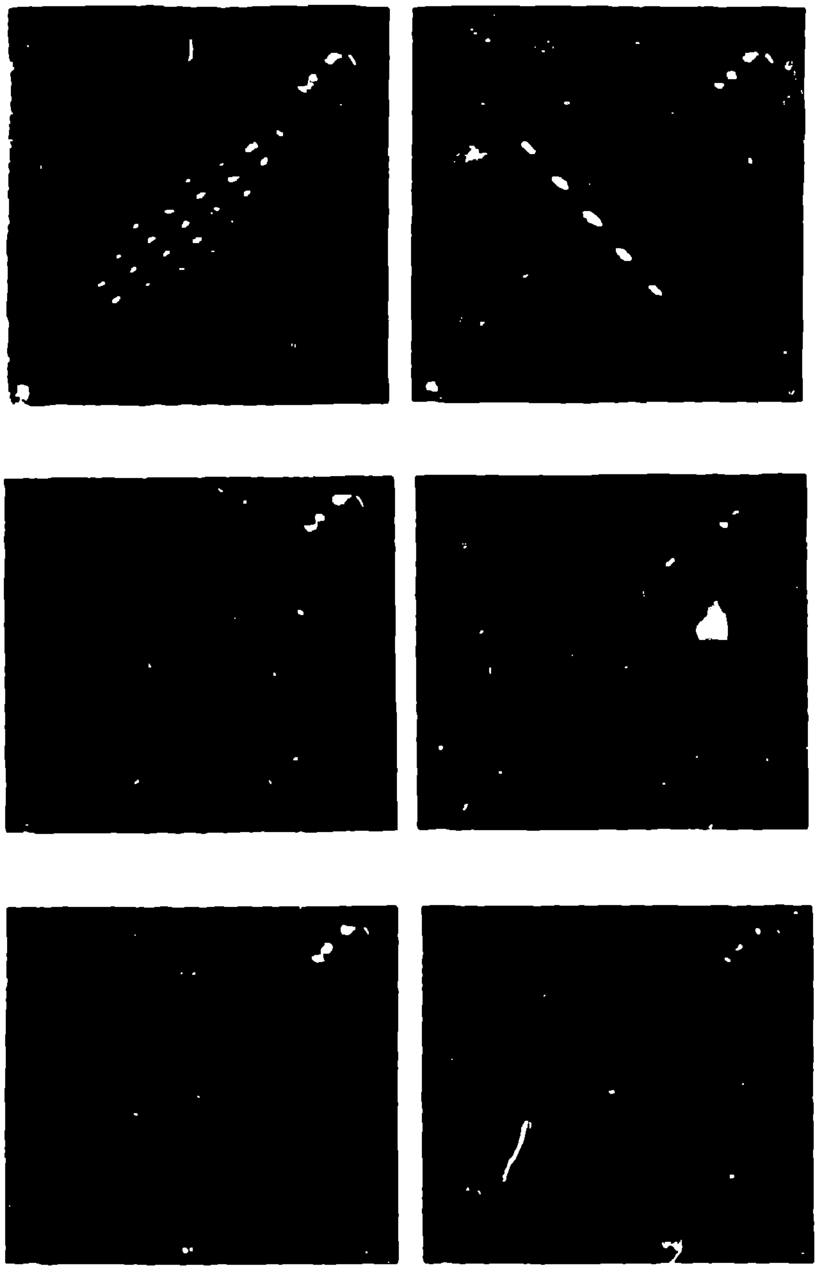

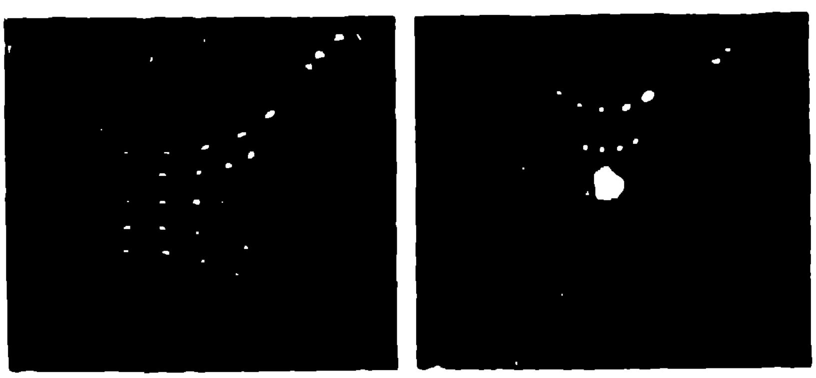

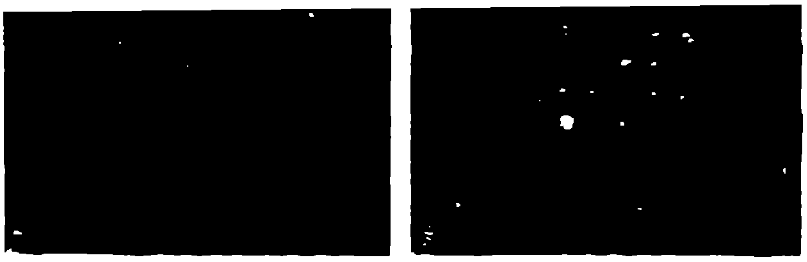

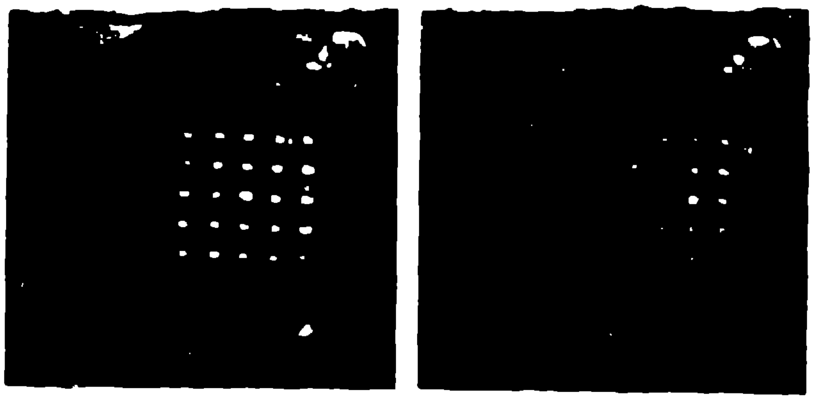

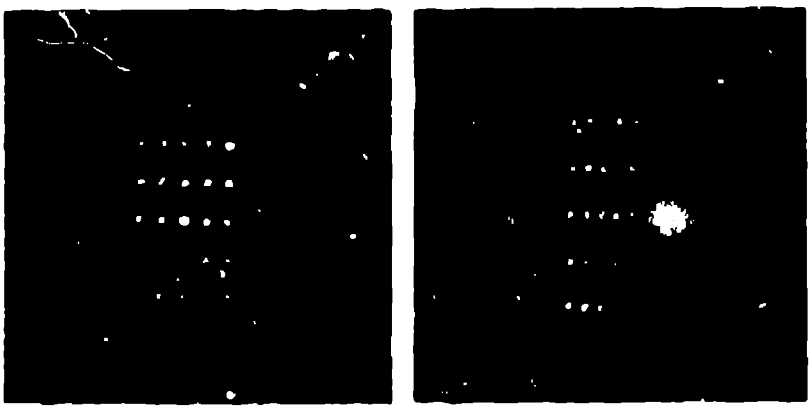

$$\frac{1}{\rho_0}\int_{z_a}^{z_b}\frac{B(0,0,z)}{B_0}dz \approx \frac{\Delta z}{\rho_0} \approx 0.05$$

$$\int_{z_a}^{z_b}\frac{B'(0,0,z)}{B_0}dz \approx 1$$

$$\int_{z_a}^{z_b} z\frac{B'^2(0,0,z)}{B_0^2}dz \approx 1$$

$$\rho_0\int_{z_a}^{z_b}\frac{B'^2(0,0,z)}{B_0^2}dz \approx \frac{\rho_0}{\Delta z} \approx 20$$

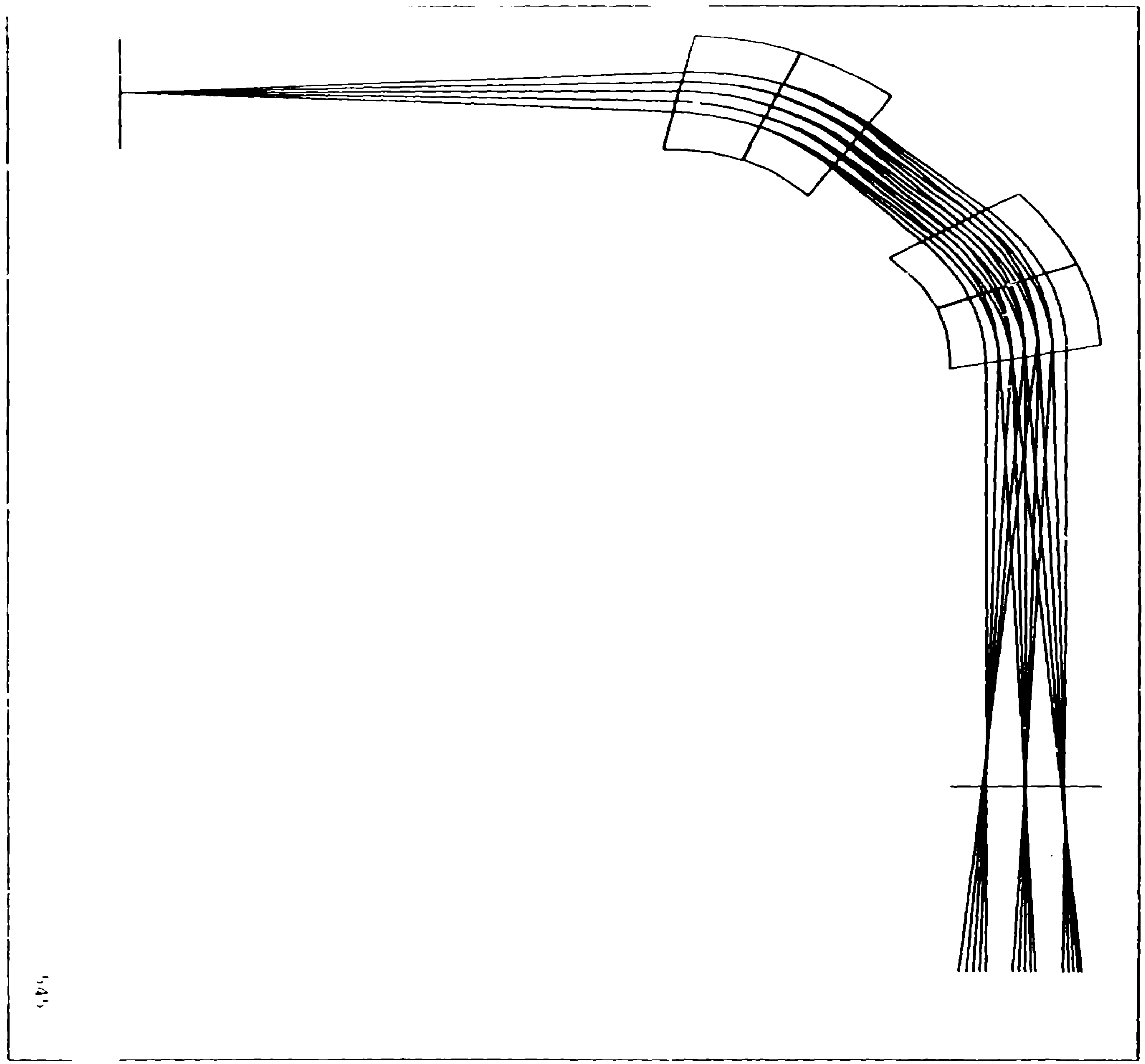

GIOS ..PFILE INTERPRETER (DECGKS) VERSION OF 24 07 91 BY J.T. , UNIVERSITY OF GIESSEN

MARYLIE

University of Maryland
Charged Particle Beam Codes

(In Collaboration with LANL)

- MARYLIE 3.0
  3rd Order
- MARYLIE 3.1
  3rd Order with Errors
- MARYLIE 5.0
  5th Order
- MARYLIE 5.1
  5th Order with Errors
- CHARLIE (R. Ryne)
  3rd Order with 2-d
  Nonlinear Space Charge
- TLIE (J. van Zeijts and F. Neri)
  Arbitrary Order with Errors

MARYLIE 3.0
User's Manual

A Program for Charged Particle Beam Transport Based on Lie Algebraic Methods *

Alex J. Dragt and Johannes van Zeijts

Center for Theoretical Physics
Department of Physics and Astronomy
University of Maryland
College Park, Maryland 20742

David R. Douglas

Continuous Electron Beam
Accelerator Facility
Newport News, Virginia 23606

Etienne Forest

Lawrence Berkeley Laboratory
Berkeley, California 94720

Robert D. Ryne

Lawrence Livermore Laboratory
Livermore, California 94550

Liam M. Healy

Naval Research Laboratory
Washington, DC 20375

Filippo Neri
C. Thomas Mottershead

Los Alamos National Laboratory
Los Alamos, New Mexico 87545

Petra Schüett

Technische Hochschule Darmstadt
6100 Darmstadt, West Germany

April 1991

*Work supported in part by U.S. Department of Energy Contract AS05-80ER10666

13.2 Element Type-Code Mnemonics (Functional Order)

The beam-line elements and their type code mnemonics, as currently available in MARYLIE 3.0, are listed below according to function along with the subsections that describe them in detail and/or give examples of their use.

Type Code	Element	Subsections
drft	Drift space	6.1
	dipole bend magnets	
nbnd	a) Normal entry bending magnet, with or without fringe fields.	6.2
pbnd	b) Parallel faced bending magnet, with fringe fields and equal entry and exit angles.	6.3
gbnd	c) General bending magnet.	6.4
prot	d) Used for leading and trailing pole face rotations.	6.5
gbdy	e) Used for the body of a general bending magnet.	6.6
frng	f) Used for hard-edge dipole fringe fields.	6.7
cfbd	g) Combined function bend.	6.8
cfrn	h) Change fringe fields of combined function dipoles.	6.29
sol	Solenoid.	6.23
quad	Magnetic quadrupole.	6.9
cfqd	Combined function magnetic quadrupole.	6.24
recm	REC quadrupole multiplet.	6.27
sext	Magnetic sextupole.	6.10
octm	Magnetic octupole.	6.11
octe	Electric octupole.	6.12

549

Type Code	Element	Subsections
srfc	Short RF cavity.	6.13
arot	Axial rotation.	6.14
thlm	"Thin lens" approximation to low order multipoles.	6.16
cplm	"Compressed" approximation to low order multipoles.	6.17
twsm	Linear matrix transformation specified in terms of twiss parameters.	6.15
dism	Dispersion matrix.	6.22
jmap	Map with matrix part J.	6.18
mark	Marker.	6.25
dp	Data point.	6.26
spce	Space for accounting purposes.	6.28
usr1 ⋮ **usr5**	User specified subroutines that act on phase space data.	6.20
usr6 ⋮ **usr9**	User specified subroutines that produce or act on maps.	6.21
r****	Random counterpart of the element with type-code mnemonic ****.	6.19

13.4 Simple Command Type-Code Mnemonics (Functional Order)

Simple commands and their type code mnemonics, as currently available in MARYLIE 3.0, are listed below according to function along with the subsections that describe them in detail and/or give examples of their use.

Type Code	Command	Subsections
end	Halt execution. Must be last entry of a lattice listing.	7.1
of	Open files.	7.24
cf	Close files.	7.23
rt	Perform a ray trace.	7.2
num	Number lines in a file.	7.27
circ	Set parameters and circulate.	7.3
wcl	Write contents of a loop.	7.33
rapt	Aperture the beam with a rectangular aperture.	7.18
eapt	Aperture the beam with an elliptic aperture.	7.19
wnd	Window a beam.	7.20
whst	Write history of beam loss.	7.21
pmif	Print contents of Master Input File (file 11).	7.4
ptm	Print transfer map.	7.7
tmi	Input matrix elements and polynomial coefficients from an external file.	7.5
tmo	Ouptut matrix elements and polynomial coefficients to an external file.	7.6
ps1 ⋮ ps9	Parameter set specification.	7.25
rps1 ⋮ rps9	Random parameter set specification.	7.26
wps	Write out parameters in a parameter set.	7.28
stm	Store the existing transfer map.	7.16

551

Type Code	Command	Subsections
gtm	Get a transfer map from storage.	7.17
mask	Mask off specified portions of existing transfer map.	7.13
ftm	Filter the existing transfer map.	7.22
sqr	Square the existing transfer map.	7.15
symp	Symplectify matrix portion of transfer map.	7.14
iden	Replace existing transfer map by the identity map.	7.8
inv	Replace existing transfer map by its inverse.	7.9
rev	Replace existing transfer map by its reversed map.	7.11
revf	Replace existing transfer map by reverse factorized form.	7.12
tran	Replace existing transfer map by its "transpose".	7.10
tpol	Twiss polynomial.	7.37
dpol	Dispersion polynomial.	7.38
time	Write out execution time.	7.29
cdf	Change drop file.	7.30
bell	Ring bell at terminal.	7.31
wmrt	Write out value of merit function.	7.32
paws	Pause.	7.34
inf	Change or write out values of infinities.	7.35
zer	Change or write out values of zeroes.	7.36
cbm	Change or write out beam parameters.	7.39

13.6 Advanced Command Type-Code Mnemonics (Functional Order)

Advanced commands and their type code mnemonics, as currently available in MARYLIE 3.0, are listed below according to function along with the subsections that describe them in detail and/or give examples of their use.

Type Code	Command	Subsection
cod	Compute off-momentum closed orbit data.	8.1
tasm	Twiss analyze static map.	8.2
tadm	Twiss analyze dynamic map.	8.3
ctr	Change tune range.	8.28
snor	Static normal form analysis.	8.8
dnor	Dynamic normal form analysis.	8.9
asni	Apply script $\mathcal{N}$ inverse.	8.29
rasm	Resonance analyze static map.	8.4
radm	Resonance analyze dynamic map.	8.5
sia	Static invariant analysis.	8.10
dia	Dynamic invariant analysis.	8.11
psnf	Compute power of static normal form.	8.12
pdnf	Compute power of dynamic normal form.	8.13
pnlp	Compute power of nonlinear part.	8.30
trsa	Transport static A.	8.24
trda	Transport dynamic A.	8.25

Type Code	Command	Subsections
fasm	Fourier analyze static map.	8.15
fadm	Fourier analyze dynamic map.	8.16
pold	Polar decomposition of a map.	8.22
tbas	Translate basis.	8.6
exp	Compute exponential.	8.7
gbuf	Get buffer contents.	8.14
amap	Apply map to a function or moments.	8.17
bgen	Generate beam.	8.34
tic	Translate initial conditions.	8.35
smul	Multiply a polynomial by a scalar.	8.18
padd	Add two polynomials.	8.19
pmul	Multiply two polynomials.	8.20
pb	Poisson bracket two polynomials.	8.21
mn	Compute matrix norm.	8.33
psp	Polynomial scalar product.	8.32
pval	Evaluate a polynomial.	8.23
sq	Select quantities.	8.26
wsq	Write selected quantities.	8.27
csym	Check symplectic condition.	8.31

13.8 Procedures and Fitting and Optimization Commands (Functional Order)

Procedures and fitting and optimization commands and their type code mnemonics, as currently availably in MaryLie 3.0, are listed below according to function along with the subsections that describe them in detail and/or give examples of their use.

Type Code	Procedure/Command	Subsection
bip	Begin inner procedure.	9.1
bop	Begin outer procedure.	9.2
tip	Terminate inner procedure.	9.3
top	Terminate outer procedure.	9.4
aim	Specify quantities to be fit or optimized and set target values.	9.5
vary	Specify quantities to be varied.	9.6
fit	Carry out fitting operation.	9.7
mrt0	Merit function (least squares).	9.10
mrt1 ⋮ mrt5	Merit functions (user written).	9.11
opt	Carry out optimization.	9.8
con1 ⋮ con5	Constraints.	9.9
grad	Compute gradient matrix.	9.15
scan	Scan parameter space.	9.18
rset	Reset menu entries.	9.16
flag	Change or write out values of flags and defaults.	9.17
cps1 ⋮ cps9	Capture parameter set.	9.12
fps	Free parameter set.	9.13
dapt	Compute dynamic aperture.	9.14

Bending a Beam without Breaking

Construction of a Complete Achromat through third order

Alex J. Dragt

University of Maryland

An Isochronous Achromat

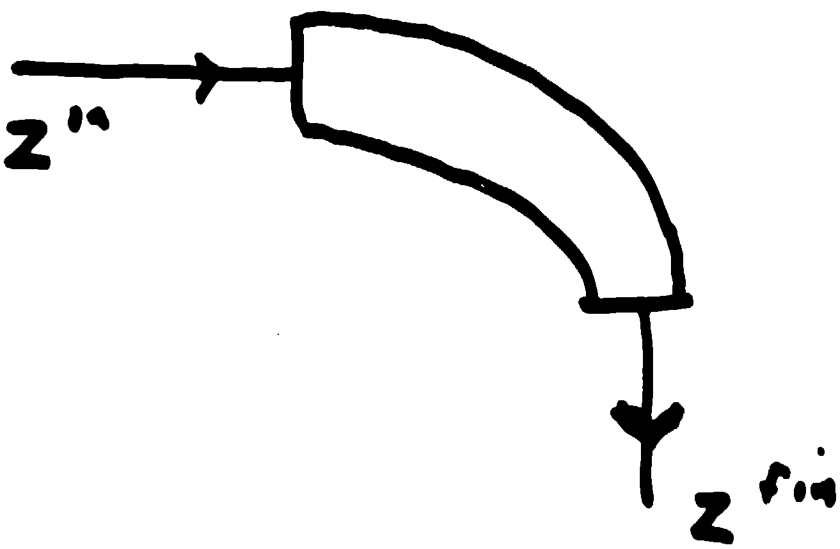

$$Z = (x, p_x, y, p_y, \tau, p_\tau)$$

τ = time of flight deviation

p_τ = − energy deviation

Generally have

$$z_a^{fin} = \sum_b R_{ab} z_b^{in}$$

$$+ \sum_{b,c} T_{abc} z_b^{in} z_c^{in}$$

$$+ \sum_{b,c,d} U_{abcd} z_b^{in} z_c^{in} z_d^{in}$$

$$+ \cdots$$

Want to have

$$z_a^{fin} = z_a^{in} + O(z^4) \Rightarrow$$

$$R_{ab} = \delta_{ab}, \quad T_{abc} = 0,$$

$$U_{abcd} = 0$$

How many conditions must be satisfied?

R_{ab}	36
T_{abc}	126
U_{abcd}	336
	498 conditions

Need 498 knobs?

Actually, can be done with

3 1st order knobs

3 2nd order knobs

8 (6) 3rd order knobs

---

14 knobs

Use three conditions:

a) Symplectic condition

b) Midplane symmetry

c) Periodicity

Outline

0. Introduction

1. Symplectic Maps
   - A. Definition
   - B. Importance

2. Production, Parameterization, Manipulation
   - A. Lie Operators
   - B. Lie Transformations
   - C. Production Theorem
   - D. Factorization Theorem
   - E. Multiplication
   - F. Truncation
   - G. Calculation

3. Applications

1. Symplectic Maps

Notation

$z = (q_1 \cdots q_n ; p_1 \cdots p_n).$

<u>Dynamical</u> <u>System</u>

$$z^{\text{initial}} \longrightarrow \boxed{\mathcal{M}} \longrightarrow z^{\text{final}}$$

Write relation between initial and final conditions

as

$$z^{\text{final}} = \mathcal{M} \, z^{\text{initial}}$$

$\mathcal{M}$ called a Transfer Map

Assume $\mathcal{M}$ comes from following Hamilton's equations of motion:

That is, there exists $H(\overbrace{q,p,t}^{z})$ such that

$$\boxed{\dot{q}_a = \partial H/\partial p_a \,, \quad \dot{p}_a = -\partial H/\partial q_a \,.}$$

<u>Capitalize</u> on <u>this</u> <u>assumption</u>.

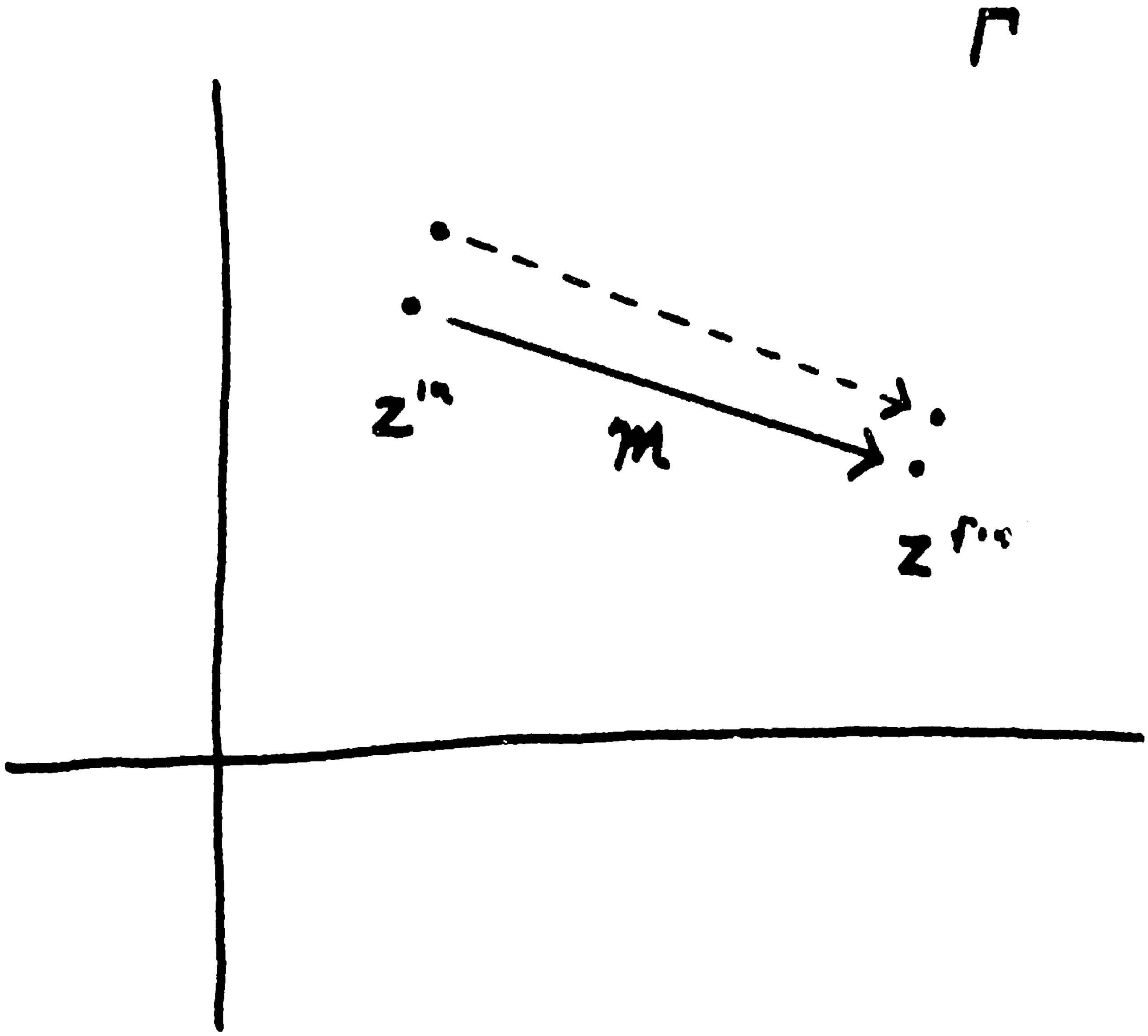

study effect of $\mathcal{M}$
on nearby points.

Form the Jacobian matrix M defined by

$$M_{ab}(z^{in}) = \partial z_a^{fin} / \partial z_b^{in}.$$

M describes small changes in z^{fin} produced by small changes in z^{in}.

Define the fundamental $2n \times 2n$ matrix J,

$$J = \left(\begin{array}{c|c} 0 & I \\ \hline -I & 0 \end{array}\right)$$

Then ....

Then $\mathcal{M}$ is a <u>symplectic</u> <u>map</u>

if

$$\boxed{\tilde{M}(z^{in})\, J\, M(z^{in}) = J \quad \text{for all } z^{in}}$$

Note that symplectic maps are severely restricted.

$\mathcal{M}$ comes from a Hamiltonian.

$$\Updownarrow$$

$$\tilde{M} J M = J \,, \quad \underline{\underline{\text{All } z\text{'s}}}$$

$$\Updownarrow$$

M is a <u>symplectic</u> matrix
and $\mathcal{M}$ is a symplectic map. } Strong restriction on $\mathcal{M}$

$$\Updownarrow$$

Liouville's Theorem, Conservation of All Poincare Invariants.

Symplectic Map = Canonical Transformation

Basic Problem

Produce

Parameterize

Manipulate

Symplectic Maps

The code

MARYLIE does this using

Lie algebraic methods

Taylor Series Expansion

write

$$z_a^{fin} = K_a + \sum_b R_{ab} z_b^{in}$$

$$+ \sum_{b,c} T_{abc} z_b^{in} z_c^{in}$$

$$+ \sum_{b,c,d} U_{abcd} z_b^{in} z_c^{in} z_d^{in}$$

$$+ \cdots .$$

a) Entries of R, T, U, $\cdots$, inter-related by symplectic condition. Coefficients far from being independent.

c) Expansion generally not symplectic if truncated. Example $\cdots$

a) Lie Operators

Let $f(z)$ be any function.

Define the associated (differential) Lie Operator $:f:$ by

$$\boxed{:f: \overset{\text{def}}{=} \sum_i \frac{\partial f}{\partial q_i}\frac{\partial}{\partial p_i} - \frac{\partial f}{\partial p_i}\frac{\partial}{\partial q_i}}.$$

Let $h(z)$ be any other function.

Then,

$$\boxed{:f:h = \sum_i \frac{\partial f}{\partial q_i}\frac{\partial h}{\partial p_i} - \frac{\partial f}{\partial p_i}\frac{\partial h}{\partial q_i} = [f,h]},$$

or $\boxed{:f:h = [f,h]}$. ⟵ Poisson Bracket

Thrm. $\{:f:, :g:\} \overset{\text{def}}{=}$

$$:f::g: - :g::f: = :[f,g]:$$

The commutator of 2 Lie operators

b) Lie Transformations

Define powers of $:f:$ by

$:f:^0 h = h$

$:f: h = [f, h]$

$:f:^2 h = [f, [f, h]]$, etc.

Define the operator $\exp(:f:)$ by

$$\boxed{\exp(:f:) \stackrel{\text{def}}{=} \sum_{n=0}^{\infty} :f:^n / n!}$$

Lie Transformation.

Explicitly, this gives

$$\exp(:f:)\, h = h + [f, h] + [f, [f, h]]/2! + \cdots .$$

<u>Notation:</u> Sometimes write

$$\exp(:f:) = e^{:f:} .$$

c) Production Theorem

Let $f = f(z^{in})$, and define

z^{fin} by

$$z_a^{fin} = \exp(:f:)\, z_a^{in}.$$

Write this as

$$z_a^{fin} = \mathcal{M}\, z_a^{in}.$$

Then,

$$\boxed{\mathcal{M} = \exp(:f:)}$$

is a Symplectic Map.

d) Factorization Theorem

Suppose $\mathcal{M}$ is an arbitrary symplectic map expanded in a Taylor Series. Then, one can write

$$\boxed{\mathcal{M} = e^{:f_1:}\, e^{:f_2:}\, e^{:f_3:}\, e^{:f_4:} \cdots}$$

where each f_n is a homogeneous polynomial in the z's of degree n.

<u>Correspondence to Taylor Series.</u>

$$\begin{tikzcd} \mathcal{M} = & e^{:f_1:} \arrow[d] & e^{:f_2:} \arrow[d] & e^{:f_3:} \arrow[d] \arrow[dr] & e^{:f_4:} \arrow[d] & \cdots \\ & K & R & T & U & \end{tikzcd}$$

$$\underbrace{K}_{\text{errors}} \quad \underbrace{R}_{\text{linear behavior}} \quad \underbrace{T \quad U}_{\text{nonlinear behavior}}$$

Aberrations

Normal Forms

Problem: Given m, find an a such that

$$n = a\, m\, a^{-1}$$

is as "nice" as possible.

When this is done, n is called a <u>normal form</u>.

Similar in spirit to diagonalizing a matrix. There one asks, "What is intrinsic to a matrix, and what depends on the choice of coordinate system?".

$$m = a^{-1}\, n\, a$$

Thm: Suppose $\mathcal{M}$ is static and has transverse tunes. (Transverse eigenvalues of R lie on the unit circle.)

Suppose the transverse tunes ν_x and ν_y are not resonant through order 4:

$$\ell \nu_x + m \nu_y \neq \text{integer}$$

$$|\ell| + |m| \leq 4.$$

Example: $\nu_x = 1/5$, $\nu_y = 1/6$

$$
\begin{aligned}
h_4 = \; & \star\, p_\tau^{2}\,(x^2 + p_x^2) \\
& + \star\, p_\tau^{2}\,(y^2 + p_y^2) \\
& + \star\, (x^2 + p_x^2)^2 \\
& + \star\, (y^2 + p_y^2)^2 \\
& + \star\, (x^2 + p_x^2)(y^2 + p_y^2) \\
& + \star\, p_\tau^{4}
\end{aligned}
$$

<u>Note</u>:

$h_2 : \quad \nu_x, \nu_y, \star \Rightarrow 3$ knobs

$h_3 : \quad 3\star \Rightarrow 3$ knobs

$h_4 : \quad 6\star \Rightarrow 6$ knobs

Observation

Can sometimes bring η to this form even when tunes are resonant providing the corresponding driving terms are absent.

Examples:

eri
$\nu_x = 1/7$, $\nu_y = 2/7$

$2\nu_x - \nu_y = 0$, $\nu_x + 3\nu_y = 1$

driving terms absent due to midplane ($x\,y$) symmetry

Then, there exists an $\mathcal{a}$ such that $\mathcal{N}$ takes the form

$$\mathcal{N} = e^{:h_2:} e^{:h_3:} e^{:h_4:}$$

where

$$h_2 = -2\pi\nu_x (x^2 + p_x^2)/2$$

$$-2\pi\nu_y (y^2 + p_y^2)/2$$

$$+ * p_\tau^2$$

$$h_3 = * p_\tau (x^2 + p_x^2)$$

$$+ * p_\tau (y^2 + p_y^2)$$

$$+ * p_\tau^3$$

$\nu_x = 1/5\,, \quad \nu_y = 1/5$

$\nu_x - \nu_y = 0$

absent due to midplane symmetry

$2\nu_x - 2\nu_y = 0$

present, but removable using 2 octopole correctors

$h_4:$ * Re $(x + i p_x)^2 (y - i p_y)^2$

* Im $(x + i p_y)^2 (y - i p_y)$

2 * $\Rightarrow$ 2 knobs

Application

Recipe for a Complete Third Order Achromat

Consider a simple FODO cell with bending and 8 corrector slots:

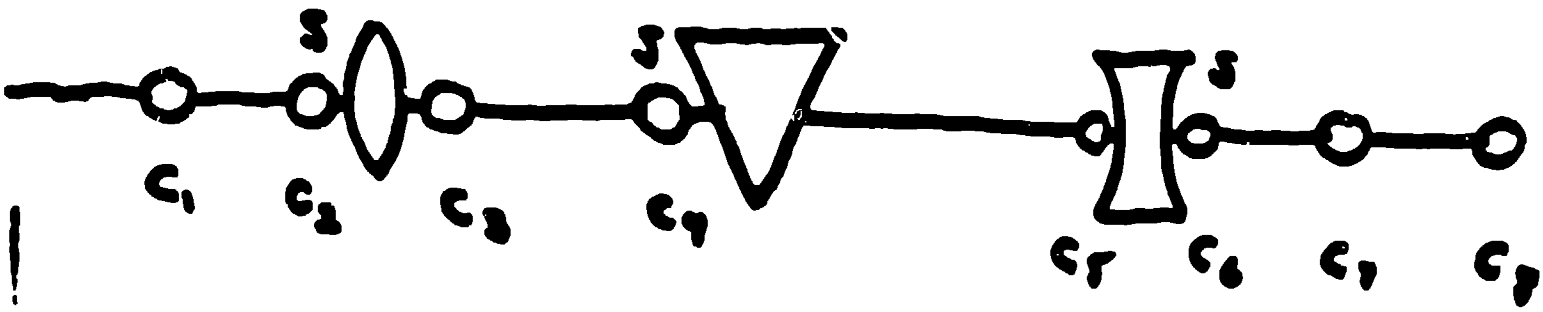

Follow Three Simple Steps:

1. Adjust the two quads and the cell length (or a third quad) so that

$$h_2 \begin{cases} \nu_x = 1/5, \quad \nu_y = 1/5 \\ \star = 0. \end{cases}$$

2. Adjust 3 sextupoles so that

$$h_3 \left\{ \; 3 \star = 0 \right.$$

3. Adjust 8 (6) octupoles so that

$$h_4 \left\{ \; 8\,(6) \star = 0 \right.$$

```
...elease Development Version 5/20/91
Copyright 1987 Alex J. Dragt
 l rights reserved

Data input complete; going into #labor.
#comment
 This is an example of a complete third order achromat.
#beam
  1.00000000000000
  2.86000000000000
  1.00000000000000
  1.00000000000000
#menu
 zer       zer
  0.000000000000000E+00  2.000000000000000E-08  0.000000000000000E+00
 fileout  pmif
   1.00000000000000       12.0000000000000       3.00000000000000
 c1        thlm
  0.000000000000000E+00  0.000000000000000E+00  0.000000000000000E+00
  0.000000000000000E+00   7.63061277477838      0.000000000000000E+00
 c2        thlm
  0.000000000000000E+00  0.000000000000000E+00  0.000000000000000E+00
  0.000000000000000E+00  -17.3118102946524      0.000000000000000E+00
 c3        thlm
  0.000000000000000E+00  0.000000000000000E+00  0.639630442258911
  0.000000000000000E+00   13.1778927562859      0.000000000000000E+00
 c4        thlm
  0.000000000000000E+00  0.000000000000000E+00 -0.956065374173185
  0.000000000000000E+00  -2.31070361422000      0.000000000000000E+00
 c5        thlm
  0.000000000000000E+00  0.000000000000000E+00  0.208442260336593
  .000000000000000E+00   13.9735586196307      0.000000000000000E+00
 c6        thlm
  0.000000000000000E+00  0.000000000000000E+00  0.000000000000000E+00
  0.000000000000000E+00  -15.9155072443971      0.000000000000000E+00
 c7        thlm
  0.000000000000000E+00  0.000000000000000E+00  0.000000000000000E+00
  0.000000000000000E+00   3.27606764258812      0.000000000000000E+00
 c8        thlm
  0.000000000000000E+00  0.000000000000000E+00  0.000000000000000E+00
  0.000000000000000E+00  -2.00314873971958      0.000000000000000E+00
 dr1       drft
   1.00000000000000
 dr.5      drft
  0.500000000000000
 dr2       drft
  0.519011603105030
 bend      nbnd
  18.0000000000000       0.000000000000000E+00  0.500000000000000
  0.200000000000000       1.00000000000000       1.00000000000000
 hfq       quad
  0.300000000000000      0.745388387071964       1.00000000000000
   1.00000000000000
 hdq       quad
  0.300000000000000     -0.842490808214709       1.00000000000000
   1.00000000000000
 cmapout  ptm
   3.00000000000000       3.00000000000000      0.000000000000000E+00
  0.000000000000000E+00   1.00000000000000
  nd       end
```

```
#lines
 whole
     1*dr1          1*dr2          1*c1           1*dr1          1*c2           &
     1*hfq          1*c3           1*dr1          1*c4           1*bend         &
     1*dr1          1*c5           1*hdq          1*c6           1*dr1          &
     1*c7           1*dr2          1*dr1          1*c8
 cachro
     5*lwhole
#lumps
 lwhole
     1*whole
#loops
#labor
    1*fileout
    1*zer
    1*cachro
    1*cmapout
    1*end
lump lwhole   constructed and stored.( 1)

matrix for map is :

 1.00000E+00 -6.20639E-11  0.00000E+00  0.00000E+00  0.00000E+00  3.50600E-12
 2.11028E-12  1.00000E+00  0.00000E+00  0.00000E+00  0.00000E+00  2.93529E-12
 0.00000E+00  0.00000E+00  1.00000E+00 -6.81257E-11  0.00000E+00  0.00000E+00
 0.00000E+00  0.00000E+00  2.27543E-12  1.00000E+00  0.00000E+00  0.00000E+00
-2.93519E-12  3.50539E-12  0.00000E+00  0.00000E+00  1.00000E+00 -1.60026E-11
 0.00000E+00  0.00000E+00  0.00000E+00  0.00000E+00  0.00000E+00  1.00000E+00

nonzero elements in generating polynomial are :


end of MARYLIE run
```

```
Copyright 1987 Alex J. Dragt
All rights reserved

Data input complete; going into #labor.
#comment
 This is an example of a complete third order achromat made of thick
 elements.  For ease of comparison with other codes, all fringe-
 field effects have been neglected.
#beam
  1.00000000000000
  2.86000000000000
  1.00000000000000
  1.00000000000000
#menu
 zer      zer
  0.000000000000000E+00  2.000000000000000E-08  0.000000000000000E+00
 fileout  pmif
   1.00000000000000       12.0000000000000       3.00000000000000
 c1       cfqd
  0.300000000000000       1.00000000000000      0.000000000000000E+00
  0.000000000000000E+00
 c2       cfqd
  0.300000000000000       2.00000000000000      0.000000000000000E+00
  0.000000000000000E+00
 c3       cfqd
  0.300000000000000       3.00000000000000      0.000000000000000E+00
  0.000000000000000E+00
 c4       cfqd
  0.300000000000000       4.00000000000000      0.000000000000000E+00
  0.000000000000000E+00
 c5       cfqd
  0.300000000000000       5.00000000000000      0.000000000000000E+00
  0.000000000000000E+00
 c6       cfqd
  0.300000000000000       6.00000000000000      0.000000000000000E+00
  0.000000000000000E+00
 c7       cfqd
  0.300000000000000       7.00000000000000      0.000000000000000E+00
  0.000000000000000E+00
 c8       cfqd
  0.300000000000000       8.00000000000000      0.000000000000000E+00
  0.000000000000000E+00
 cp1      ps1
  0.000000000000000E+00  0.000000000000000E+00  0.000000000000000E+00
  0.000000000000000E+00   25.1707502760476      0.000000000000000E+00
 cp2      ps2
  0.000000000000000E+00  0.000000000000000E+00  0.000000000000000E+00
  0.000000000000000E+00  -26.4409006724282      0.000000000000000E+00
 cp3      ps3
  0.000000000000000E+00  0.000000000000000E+00   3.24975783016200
  0.000000000000000E+00   13.8784804977115      0.000000000000000E+00
 cp4      ps4
  0.000000000000000E+00  0.000000000000000E+00  -4.33263796704460
  0.000000000000000E+00  -7.49095110399962      0.000000000000000E+00
 cp5      ps5
  0.000000000000000E+00  0.000000000000000E+00  0.734828919856963
  0.000000000000000E+00   31.5325612211653      0.000000000000000E+00
 cp6      ps6
  0.000000000000000E+00  0.000000000000000E+00  0.000000000000000E+00
  0.000000000000000E+00  -45.2313702861510      0.000000000000000E+00
 cp7      ps7
  0.000000000000000E+00  0.000000000000000E+00  0.000000000000000E+00
  0.000000000000000E+00   30.2884235117547      0.000000000000000E+00
```

```
  0.000000000000000E+00  0.000000000000000E+00  0.000000000000000E+00
  0.000000000000000E+00  -20.2121368506963      0.000000000000000E+00
 dr-.3     drft
 -0.300000000000000
 rl        drft
   1.00000000000000
 dr.5      drft
  0.500000000000000
 dr2       drft
  0.519011603105030
 bend      nbnd
   18.0000000000000      0.000000000000000E+00  0.500000000000000
  0.200000000000000      0.000000000000000E+00  0.000000000000000E+00
 hfq       quad
  0.300000000000000      0.745388387071964      0.000000000000000E+00
  0.000000000000000E+00
 hdq       quad
  0.300000000000000     -0.842490808214209      0.000000000000000E+00
  0.000000000000000E+00
 mapout    ptm
   3.00000000000000       3.00000000000000      0.000000000000000E+00
  0.000000000000000E+00   1.00000000000000
 end       end
#lines
 set
     1*cp1         1*cp2         1*cp3         1*cp4         1*cp5        &
     1*cp6         1*cp7         1*cp8
 whole
     1*set         1*dr1         1*dr2         1*dr-.3       1*c1         &
     1*dr1         1*dr-.3       1*c2          1*hfq         1*c3         &
     1*dr-.3       1*dr1         1*dr-.3       1*c4          1*bend       &
     1*dr1         1*dr-.3       1*c5          1*hdq         1*c6         &
     1*dr-.3       1*dr1         1*c7          1*dr-.3       1*dr2        &
     1*dr1         1*dr-.3       1*c8
 cachro
     5*lwhole
#lumps
 lwhole
     1*whole
#loops
#labor
    1*fileout
    1*zer
    1*cachro
    1*mapout
    1*end
lump lwhole   constructed and stored.( 1)

matrix for map is :

 1.00000E+00 -6.20639E-11  0.00000E+00  0.00000E+00  0.00000E+00  3.50597E-12
 2.11028E-12  1.00000E+00  0.00000E+00  0.00000E+00  0.00000E+00  2.93530E-12
 0.00000E+00  0.00000E+00  1.00000E+00 -6.81257E-11  0.00000E+00  0.00000E+00
 0.00000E+00  0.00000E+00  2.27543E-12  1.00000E+00  0.00000E+00  0.00000E+00
-2.93519E-12  3.50539E-12  0.00000E+00  0.00000E+00  1.00000E+00 -1.60025E-11
 0.00000E+00  0.00000E+00  0.00000E+00  0.00000E+00  0.00000E+00  1.00000E+00

nonzero elements in generating polynomial are :


end of MARYLIE run
```

Variations

1. Tune cell so that $\nu_x = 1/5$, $\nu_y = 1/6$ (or vice versa). Tune sextupoles as before, and tune 6 octupoles.

Then 30 such cells produce a complete achromat. <u>No</u> midplane symmetry is required.

2. Tune cells so that

$\nu_x = 1/7$, $\nu_y = 3/7$.

Tune sextupoles as before, and tune 6 octupoles.

Then 7 such cells produce a complete achromat. Midplane symmetry is required.

Then,

$$m = a^{-1}\, n\, a$$

with

$$n = e^{:h_2:} \, ,$$

$$h_2 = -2\pi/5\ (X^2 + P_x^2)/2$$

$$\quad -2\pi/5\ (Y^2 + P_y^2)/2 .$$

Consider

$$m^5 = a^{-1} n a \, a^{-1} n a \cdots$$

$$= a^{-1} n^5 a.$$

But $n^5 = I \Rightarrow$

$$\boxed{m^5 = a^{-1} I a = I}$$

Thus, 5 such cells placed in a row yield a

Complete Third Order

Achromat

Then,

$$m^s = a^{-1} n^s a$$

with $\quad n^s = e^{:h:}$

where $\quad h =$ [illegible] $P_s^2 +$ [illegible] $P_s^3 +$ [illegible] P_s^4.

In this case, n^s and a commute, so that

$$\begin{aligned} m^s &= a^{-1} n^s a \\ &= n^s a^{-1} a = n^s \\ &= \text{pseudo identity} \end{aligned}$$

In this case, one has a third order achromat except for energy dependent time of flight terms:

$$x^{fin} = x^{in}$$

$$P_x^{fin} = P_x^{in}$$

$$y^{fin} = y^{in}$$

$$P_y^{fin} = P_y^{in}$$

$$\tau^{fin} = \tau^{in} + a P_\tau^{in} + a {P_\tau^{in}}^2 + a {P_\tau^{in}}^3$$

$$P_\tau^{fin} = P_\tau^{in}$$

Incomplete Third Order Achromat

Give up isochrony.

Do not worry about coefficients of P_τ^2, P_τ^3, P_τ^4. Requires:

1. No fitting on length or 1 less quad/cell
2. One less sextupole/cell
3. One less octupole/cell

HOW TO REMEDY THE SITUATION – II

FORGET THE RIGHT BEND?

I think we have to have a good look at this option!

OPTICS USING DIFFERENTIAL ALGEBRA

COSY INFINITY

A Beam Optics and Accelerator Code

M. Berz
Michigan State University

```
      SUBROUTINE elmm(L,Z,K01,K02,K03,K04,K05,K27,K32,NORDER,NG,ND)
*     ************************************************************
*
*
      IMPLICIT DOUBLE PRECISION (A - Z)
*
      INTEGER NORDER, NG, ND
*
      DOUBLE PRECISION L(0:461,7)
*
*     K01    : QUADRUPOLE STRENGTH
*     K02    : HEXAPOLE STRENGTH
*     K03    : OCTUPOLE STRENGTH
*     K04    : DECAPOLE STRENGTH
*     K05    : DODECAPOLE STRENGTH
*     K27    : 1./(MAGNETIC RIGIDITY)
*     K32    : ENERGY/(M*C**2)
*
      K30    = 1./(1+K32)
      K31    = 1./(1+K32/2.)
*
      FX2 = -K01*K27
*
      FY2 = +K01*K27
*
      IF(FX2.LT.-1.D-8) THEN
         AFX = SQRT(-FX2)
         CX  = COS(AFX*Z)
         SX  = SIN(AFX*Z)/AFX
      ELSEIF(FX2.GT.1.D-8) THEN
         AFX = SQRT(FX2)
         EX  = EXP(AFX*Z)
         EEX = 1.D0/EX
         CX  = (EX + EEX)/2.D0
         SX  = (EX - EEX)/2.D0/AFX
      ELSE
         CX  = 1.D0
         SX  = Z
         FX2 = 1.D-8
      ENDIF
*
      IF(FY2.LT.-1.D-8) THEN
         AFY = SQRT(-FY2)
         CY  = COS(AFY*Z)
         SY  = SIN(AFY*Z)/AFY
      ELSEIF(FY2.GT.1.D-8) THEN
         AFY = SQRT(FY2)
         EY  = EXP(AFY*Z)
         EEY = 1.D0/EY
         CY  = (EY + EEY)/2.D0
         SY  = (EY - EEY)/2.D0/AFY
      ELSE
         CY  = 1.D0
         SY  = Z
         FY2 = 1.D-8
      ENDIF
*
*
      CS2 = CX
      CS3 = SX
      CS4 = CY
      CS5 = SY
      CS6 = Z
      KK2 = K31*K32
      KK3 = K30*K32
      FF2 = FX2
      TT2 = CS2
      TT3 = CS3
      TT4 = CS3*FF2
      TT5 = CS4
      TT6 = CS5
      TT7 = CS5*FF2
      TT8 = CS6
      TT9 = CS6*KK2
      TT10 = CS6*KK3
      L(1,1) = (+TT2)
      L(2,1) = (+TT3)
      L(1,2) = (+TT4)
      L(2,2) = (+TT2)
      L(3,3) = (+TT5)
      L(4,3) = (+TT6)
      L(3,4) = (-TT7)
      L(4,4) = (+TT5)
*
      IF(ND.EQ.0.AND.NG.EQ.0) GOTO 100
*
      L(6,6) = (+1)
      L(6,7) = (-0.5D+00*TT8-0.25D+00*TT9+TT10)
*
      IF(NG.EQ.0) GOTO 100
*
      L(5,5) = (+1)
      L(5,7) = (+0.5D+00*TT8+0.25D+00*TT9-TT10)
*
  100 IF(NORDER.EQ.1) GOTO 1000
*
      CS7 = CS3*CX
      CS8 = CS3*SX
      CS9 = CS4*CX
      CS10 = CS4*SX
      CS11 = CS5*CX
      CS12 = CS5*SX
      CS13 = CS5*CY
      CS14 = CS5*SY
      CS15 = CS6*CX
      CS16 = CS6*SX
      CS17 = CS6*CY
      CS18 = CS6*SY
      KK4 = KK2*K31*K32
      KK5 = KK3*K31*K32
      KK6 = K02*K27
      FF3 = 1/FX2/FX2
      FF4 = FF3*FX2
      TT11 = KK6*FF4
      TT12 = CS2*KK6*FF4
      TT13 = CS8*KK6
      TT14 = CS3*KK6*FF4
      TT15 = CS7*KK6*FF4
      TT16 = KK6*FF3
      TT17 = CS2*KK6*FF3
      TT18 = CS8*KK6*FF4
      TT19 = CS14*KK6
      TT20 = CS13*KK6*FF4
      TT21 = CS14*KK6*FF4
      TT22 = CS16*FF2
      TT23 = CS16*KK2*FF2
      TT24 = CS3*KK2
      TT25 = CS15
```

*

*   26.840 lines further...

*

```
L(433,7) = (+0.375D+00*(-TT1715-TT6913)+0.1875D+00*TT6912
  +0.75D+00*TT1716+0.1953125D+00*TT345-0.9765625D-01*TT346
  -0.392578125D+00*TT1717+0.196289062 5D+00*TT6914+0.15625D+00*TT
  1718+0.53125D+00*TT1719-0.3046875D+00*TT6915+0.859375D-01*(+TT
  1693+TT1721)-0.4296875D-01*TT1694+0.52734375D-01*(-TT1695-TT
  6916)+0.263671875D-01*TT6872+0.3125D-01*(+TT6873+TT6874-TT6920)
  -0.234375D-01*TT6875-0.171875D+00*TT1720+0.10546875D+00*TT1722
  +0.625D-01*(-TT6917-TT6918)+0.46875D-01*TT6919+0.15625D-01*TT
  6921+0.78125D-02*TT6922-0.390625D-02*TT6923)
L(448,7) = (-0.48828125D-01*TT59+0.244140625D-01*TT347
  +0.20564453125D+00*TT1723-0.14282226563D+00*TT6924-0.390625D-01
  *TT348-0.5078125D+00*TT1724+0.263671875D+00*TT6925
  -0.232421875D+00*TT8+0.1162109375D+00*TT9+0.53466796875D+00*TT
  60-0.26733398438D+00*TT351-0.1484375D+00*TT10-0.8046875D+00*TT
  61+0.439453125D+00*TT352+0.1015937 5D+00*TT349-0.91796875D-01*TT
  350-0.2490234375D+00*TT1725+0.12451171875D+00*TT6926
  +0.109375D+00*(+TT1726+TT1728)+0.296875D+00*TT1727
  -0.17578125D+00*TT6927-0.546875D-01*TT1729-0.5859375D-01*TT
  1730+0.29296875D-01*TT6928+0.3125D-01*(+TT6929+TT6930)
  -0.234375D-01*TT6931+0.78125D-02*(+TT6892+TT6933)+0.390625D-02*(
  -TT6893+TT6934)+0.1953125D-02*(-TT6894-TT6935)+0.9765625D-03*TT
  6895-0.15625D-01*TT6932)
L(457,7) = (+0.1953125D-01*TT8-0.29296875D-01*TT9+0.322265625D+00
  *TT60-0.46386718750+00*TT351+0.23071289063D+00*TT1731
  -0.38452148438D-01*TT6936+0.1171875D+00*TT10-0.859375D+00*TT61
  +0.111328125D+01*TT352-0.52734375D+00*TT1732+0.85449218750-01*TT
  6937)
L(264,7) = (+0.41015625D-01*(+TT53-TT54)+0.87890625D-02*(+TT325-TT
  327)+0.10253906250-01*(-TT1678+TT1680)+0.56396484375D-01*(+TT
  6850-TT6852)+0.234375D-01*(-TT326+TT1679+TT328-TT1681+TT1687+TT
  6856-TT6859)+0.123046875D+00*(-TT6851+TT6853)-0.8203125D-01*TT
  329-0.17578125D-01*TT330+0.205078125D-01*TT1682
  +0.7470703125D-01*TT6854+0.46875D-01*(+TT1683-TT1684)
  -0.12890625D+00*TT6855-0.9375D-01*TT1685+0.3125D-01*(-TT1686+TT
  6857-TT6858)+0.78125D-02*(-TT6860-TT6865)+0.390625D-02*(-TT
  6861+TT6866)+0.1953125D-02*(+TT6862+TT6867)+0.9765625D-03*TT
  6863-0.15625D-01*TT6864)
L(299,7) = (+0.1875D+00*TT6868-0.375D+00*TT6869-0.3515625D+00*TT
  333-0.9765625D-01*TT334+0.87890625D-01*TT1690+0.19628906250+00
  *TT6870+0.15625D+00*(+TT1691-TT1692)-0.3046875D+00*TT6871
  -0.1171875D+00*TT1693-0.4296875D-01*TT1694+0.29296875D-01*TT
  1695+0.263671875D-01*TT6872+0.3125D-01*(+TT6873-TT6874-TT6880)
  -0.234375D-01*TT6875-0.234375D+00*TT1696-0.859375D-01*TT1697
  +0.5859375D-01*TT1698+0.52734375D-01*TT6876+0.625D-01*(+TT6877
  -TT6878)-0.46875D-01*TT6879-0.15625D-01*TT6881+0.78125D-02*TT
  6882+0.390625D-02*TT6883)
L(369,7) = (-0.87890625D-01*TT56-0.244140625D-01*TT335
* +0.2197265625D-01*TT1699+0.14282226563D+00*TT6884+0.390625D-01*(
* +TT336-TT1700)-0.263671875D+00*TT6885-0.380859375D+00*TT8
* -0.1162109375D+00*TT9+0.9521484375D-01*TT60+0.26733398438D+00*TT
* 351+0.1484375D+00*(+TT10-TT61)-0.439453125D+00*TT352
* -0.29296875D+00*TT337-0.91796875D-01*TT338+0.732421875D-01*TT
* 1701+0.12451171875D+00*TT6886+0.109375D+00*(+TT1702-TT1703)
* -0.17578125D+00*TT6887-0.140625D+00*TT1704-0.546875D-01*TT1705
* +0.3515625D-01*TT1706+0.29296875D-01*TT6888+0.3125D-01*(+TT
* 6889-TT6890)-0.234375D-01*TT6891+0.78125D-02*(-TT6892-TT6897)
* +0.390625D-02*(-TT6893+TT6898)+0.1953125D-02*(+TT6894+TT6899)
* +0.9765625D-03*TT6895-0.15625D-01*TT6896)
 L(424,7) = (+0.41015625D-01*(-TT57+TT54)+0.87890625D-02*(-TT339+TT
* 327)+0.1025390625D-01*(+TT1707-TT1680)+0.56396484375D-01*(-TT
* 6900+TT6852)+0.234375D-01*(+TT340-TT1708-TT328+TT1681+TT1714+TT
* 6904-TT6907)+0.123046875D+00*(+TT6901-TT6853)-0.8203125D-01*TT
* 341-0.17578125D-01*TT342+0.205078125D-01*TT1709
* +0.7470703125D-01*TT6902+0.46875D-01*(+TT1710-TT1711)
* -0.12890625D+00*TT6903-0.9375D-01*TT1712+0.3125D-01*(-TT1713+TT
* 6905-TT6906)+0.78125D-02*(-TT6860+TT6909)+0.390625D-02*(-TT
* 6861-TT6910)+0.1953125D-02*(+TT6862-TT6911)+0.9765625D-03*TT
* 6863+0.15625D-01*TT6908)
 L(434,7) = (-0.1875D+00*TT6912+0.375D+00*TT6913+0.3515625D+00*TT
* 345+0.9765625D-01*TT346-0.87890625D-01*TT1717-0.19628906250+00
* *TT6914+0.15625D+00*(-TT1718+TT1719)+0.3046875D+00*TT6915
* +0.1171875D+00*TT1693+0.4296875D-01*TT1694-0.29296875D-01*TT
* 1695-0.263671875D-01*TT6872+0.3125D-01*(-TT6873+TT6874-TT6920)
* +0.234375D-01*TT6875-0.234375D+00*TT1720-0.859375D-01*TT1721
* +0.5859375D-01*TT1722+0.52734375D-01*TT6916+0.625D-01*(+TT6917
* -TT6918)-0.46875D-01*TT6919-0.15625D-01*TT6921+0.78125D-02*TT
* 6922+0.390625D-02*TT6923)
 L(449,7) = (-0.87890625D-01*TT59-0.244140625D-01*TT347
* +0.2197265625D-01*TT1723+0.14282226563D+00*TT6924+0.390625D-01*(
* +TT348-TT1724)-0.263671875D+00*TT6925-0.380859375D+00*TT8
* -0.1162109375D+00*TT9+0.9521484375D-01*TT60+0.26733398438D+00*TT
* 351+0.1484375D+00*(+TT10-TT61)-0.439453125D+00*TT352
* +0.29296875D+00*TT349+0.91796875D-01*TT350-0.732421875D-01*TT
* 1725-0.12451171875D+00*TT6926+0.109375D+00*(-TT1726+TT1727)
* +0.17578125D+00*TT6927+0.140625D+00*TT1728+0.546875D-01*TT1729
* -0.3515625D-01*TT1730-0.29296875D-01*TT6928+0.3125D-01*(-TT
* 6929+TT6930)+0.234375D-01*TT6931+0.78125D-02*(+TT6892-TT6933)
* +0.390625D-02*(+TT6893+TT6934)+0.1953125D-02*(-TT6894+TT6935)
* -0.9765625D-03*TT6895-0.15625D-01*TT6932)
 L(458,7) = (+0.234375D-01*TT8-0.390625D-02*TT9-0.8203125D-01*TT
* 60+0.380859375D+00*TT351-0.32470703125D+00*TT1731
* +0.76904296875D-01*TT6936+0.15625D-01*TT10+0.21875D+00*TT61
* -0.9140625D+00*TT352+0.7421875D+00*TT1732-0.17089843750+00*TT
* 6937)
 L(459,7) = (+0.390625D-01*TT8+0.390625D-02*TT9-0.1171875D-01*TT
* 60-0.683593750-01*TT351+0.10790820125D+00*TT1731
* -0.76904296875D-01*TT6936-0.15625D-01*TT10+0.3125D-01*TT61
* +0.1640625D+00*TT352-0.4296875D+00*TT1732+0.1708984375D+00*TT
* 6937)
 L(460,7) = (+0.13671875D+00*TT8+0.29296875D-01*TT9+0.5859375D-02
* *TT60-0.48828125D-02*TT351-0.25634765625D-01*TT1731
* +0.38452148438D-01*TT6936-0.1171875D+00*TT10-0.15625D-01*TT61
* +0.1171875D-01*TT352+0.5859375D-01*TT1732-0.85449218750-01*TT
* 6937)
*
  500 IF(NORDER.EQ.5) GOTO 1000
*
 1000 CONTINUE
*
      RETURN
      END
```

Differential Algebra

An **Algebra** (vector space with multiplication) with a **Derivation** ∂ that satisfies

$$\partial(a \cdot b) = (\partial a) \cdot b + a \cdot (\partial b)$$

In particular, we are using a differential algebra of equivalence classes of infinitely often differentiable functions. Two functions are called n-equivalent if their derivatives agree to order n.

The derivation is very useful for nonlinear dynamics problems; allows efficient computation of flow of differential equations (= Transfer Maps).

Any differential algebra with at least two derivations contains a Lie algebra. (Generalization of Lie algebra).

90 Degree homogeneous sector through 50th order; only dependence of final position x on initial angle Ai is shown.

	Coefficient $(x\|a^n)$	Exponent of Ai n
1	0.000000E+00	0
2	0.500000	1
3	-.625000E-01	4
4	-.312500E-01	6
5	-.954961E-02	8
6	-.438368E-02	10
7	-.175964E-02	12
8	-.494470E-03	14
9	-.120357E-03	16
10	-.303507E-04	18
11	-.748015E-05	20
12	-.166065E-05	22
13	-.340812E-06	24
14	-.682165E-07	26
15	-.133936E-07	28
16	-.252307E-08	30
17	-.454204E-09	32
18	-.792470E-10	34
19	-.135272E-10	36
20	-.225391E-11	38
21	-.365251E-12	40
22	-.576846E-13	42
23	-.891832E-14	44
24	-.135248E-14	46
25	-.201106E-15	48
26	-.293181E-16	50

Implementation of DA on a Computer

There is a DA package that works to arbitrary order and for arbitrarily many variables.

(In practice, on a VAX 8650 one encounters the following limitations because of space:)

$$v = 6 \Rightarrow o \leq 20$$

$$v = 10 \Rightarrow o \leq 10$$

Difficulties that had to be resolved:

- efficient multiplication
- storage (vectors are often very sparse)
- functions (at the moment, we have trig, hyperbolic, exp, ln, roots and all their inverses)
- precompiler to change existing code

DAFOR

Differential Algebra Precompiler Version 3

Reference Manual

M. Berz

Department of Physics and Astronomy
and National Superconducting
Cyclotron Laboratory
Michigan State University
East Lansing, Mi 48824

```
      CALL   DACSU(ISA 1A    ,ZS           ,ZL)
*DA *
*DA * Y(1)=Y(1)+EKK*(XL*XL-ZL*ZL)
      CALL   DAMUL(XL        ,XL        ,IS( 1)     )
      CALL   DAMUL(ZL        ,ZL        ,IS( 2)     )
      CALL   DASUB(IS( 1)    ,IS( 2)    ,IS( 3)     )
      ISA 4A = Y     (INT(.000001+ 0.100000D+01))
      CALL   DACMU(IS( 3)    ,EKK          ,IS( 5)  )
      CALL   DAADD(ISA 4A    ,IS( 5)    ,Y(1))
*DA *
*DA * Y(2)=Y(2)-2.D0*EKK*XL*ZL
      ISA 1A = Y     (INT(.000001+ 0.200000D+01))
      RS( 2) = 0.200000D+01 *  EKK
      CALL   DACMU(XL        ,RS( 2)       ,IS( 3)  )
      CALL   DAMUL(IS( 3)    ,ZL        ,IS( 4)     )
      CALL   DASUB(ISA 1A    ,IS( 4)    ,Y(2))
*DA *
      GOTO 2
C--NORMAL OCTUPOLE
   24 EKK=EKK*1D-6
*DA * XL=X(1)-XS
      ISA 1A = X     (INT(.000001+ 0.100000D+01))
      CALL   DACSU(ISA 1A    ,XS           ,XL)
*DA *
*DA * ZL=X(2)-ZS
      ISA 1A = X     (INT(.000001+ 0.200000D+01))
      CALL   DACSU(ISA 1A    ,ZS           ,ZL)
*DA *
*DA * XX=XL*XL
      CALL   DAMUL(XL        ,XL        ,XX)
*DA *
*DA * ZZ=ZL*ZL
      CALL   DAMUL(ZL        ,ZL        ,ZZ)
*DA *
*DA * Y(1)=Y(1)+EKK*XL*(XX-3D0*ZZ)
      CALL   DACMU(ZZ        ,0.300000D+01,IS( 1)   )
      CALL   DASUB(XX        ,IS( 1)    ,IS( 2)     )
      ISA 3A = Y     (INT(.000001+ 0.100000D+01))
      CALL   DACMU(XL        ,EKK          ,IS( 4)  )
      CALL   DAMUL(IS( 4)    ,IS( 2)    ,IS( 5)     )
      CALL   DAADD(ISA 3A    ,IS( 5)    ,Y(1))
*DA *
*DA * Y(2)=Y(2)-EKK*ZL*(3D0*XX-ZZ)
      CALL   DACMU(XX        ,0.300000D+01,IS( 1)   )
      CALL   DASUB(IS( 1)    ,ZZ        ,IS( 2)     )
      ISA 3A = Y     (INT(.000001+ 0.200000D+01))
      CALL   DACMU(ZL        ,EKK          ,IS( 4)  )
      CALL   DAMUL(IS( 4)    ,IS( 2)    ,IS( 5)     )
      CALL   DASUB(ISA 3A    ,IS( 5)    ,Y(2))
*DA *
      GOTO 2
C--NORMAL DECAPOLE
   25  EKK=EKK*1D-9
*DA * XL=X(1)-XS
      ISA 1A = X     (INT(.000001+ 0.100000D+01))
      CALL   DACSU(ISA 1A    ,XS           ,XL)
*DA *
*DA * ZL=X(2)-ZS
      ISA 1A = X     (INT(.000001+ 0.200000D+01))
      CALL   DACSU(ISA 1A    ,ZS           ,ZL)
*DA *
```

Numerical Integration using DA

Suppose motion is described by

$$\frac{d}{dt}\vec{r} = \vec{f}(\vec{r}, t)$$

Let $h(\vec{r}, t)$ be a function of phase space. Then we obtain

$$\begin{aligned} \frac{d}{dt}h(\vec{r}, t) &= \vec{\nabla} h \cdot \frac{d}{dt}\vec{r} + \frac{\partial h}{\partial t} \\ &= \vec{\nabla} h \cdot \vec{f} + \frac{\partial h}{\partial t} = L_f h \end{aligned}$$

$$\frac{d^2}{dt^2}h(\vec{r}, t) = L_f^2 h$$

$$\frac{d^3}{dt^3}h(\vec{r}, t) = L_f^3 h$$

etc. Thus, by applying L_f enough times, we obtain a high-order numerical integrator. In case $\vec{f}(\vec{0}) = \vec{0}$, the order is unlimited; otherwise, the order is limited by the order to which f is known.

COSY INFINITY

- Arbitrary order
- Maps depending on parameters (mass dependence!)
- No approximations in motion or field description
- Large library of elements
- Arbitrary Elements (you specify fields)
- Very flexible input language
- Powerful interactive graphics
- Errors: position, tilt, rotation
- Tracking through maps
- Normal Form Methods
- 80 page manual with index

COSY INFINITY
Version 4

User's Guide and Reference Manual [1]

M. Berz

Department of Physics and Astronomy
and National Superconducting
Cyclotron Laboratory
Michigan State University
East Lansing, Mi 48824

[1] Supported in Part by the U.S. National Science Foundation, Grant No. PHY 89-13815

The guts of COSY

Major parts:

- DA package (10,000 lines)
- Compiler/Executer for COSY language (4,000 lines)
- Optimizers (3,000 lines)
- Graphics interfaces (1,000 lines)

Altogether about 20,000 lines of standard FORTRAN 77.

Compilation/Execution is in one step, no linking.

Incremental compilation possible (Physics routines COSY.FOX are compiled only once)

Current COSY Implementations

Currently (July 1991) there are about 60 registered users of the code. Implementations exist at the following institutions:

Argonne National Laboratory
Atomic Energy of Canada Ltd., Chalk River
BESSY, Berlin
Brookhaven National Laboratory
CEBAF, Newport News
CERN, Geneva
California State University, Los Angeles
DESY, Hamburg
Fritz Haber Institut, Berlin
GANIL, Caen
GSI, Darmstadt
KFA, Juelich
Krasnojarsk Polytechnical Institute
Lawrence Berkeley Laboratory
Los Alamos National Laboratory
MIT Bates Laboratory, Boston

MPI Heidelberg
POSTECH, Korea
Paul Scherrer Institute, Villingen
Soviet Academy of Sciences, Leningrad
Soviet Academy of Sciences, Novosibirsk
Stanford Linear Accelerator Center
TRIUMF
Texas A+M, College Station
Texas Tech
Universite Laval
University of Beijing
University of Berlin
University of Bochum
University of Bonn
University of Frankfurt
University of Giessen
University of Groningen
University of Saskatchewan
University of Wisconsin
Wilson Laboratory, Cornell University

Currently processing about 20 more license registrations. The new institutions involved are

Boeing, Seattle
CEA, Saclay
Grumman Aerospace, Princeton
Indiana University Cyclotron Facility
Interatom, Bergisch Gladbach
SSC Laboratory, Dallas
University of California Los Angeles
Varian Associates, Palo Alto

Environments in which COSY currently runs

1. Systems
   - VAX VMS
   - SUN
   - HP
   - IBM Mainframes
   - IBM PC (Lahey F77)
   - Cray
2. Graphics
   - Direct Tektronix
   - Direct PostScript
   - LaTeX picture mode
   - GKS-based VAX VMS
   - GKS-based Tektronix
   - GKS-based PostScript
   - GKS-based HP7475 plotter
   - GKS-based HP Paintjet / DEC JL250
   - IBM PC VGA with Lahey F77
   - Low resolution ASCII

Elements in COSY

- Magnetic and electric multipoles
- Superimposed multipoles
- Combined function bending magnets with edge angles
- Electrostatic deflectors
- Wien filters
- Wigglers
- Solenoids
- Glaser round lens
- 3 tube electrostatic round lens
- Exact fringe fields to all of the above
- General electromagnetic element
- Glass lenses, mirrors, prisms with arbitrary surfaces
- Misalignments: position, angle, rotation

All can be computed to arbitrary order, and the dependence on any of their parameters can be computed.

Applications of COSY INFINITY

- Interactive design of spectrometers
- Interactive design of accelerator lattices
- High-order analysis
- Fringe field analysis
- Measured fields
- Error analysis, parameter dependences
- Closed orbit, lattice parameters, parameter dependence of these
- Normal Form, resonant and non-resonant, resonance driving terms

The COSY Language

- Structured Language with nesting of procedures
- Object oriented; allows direct DA and picture variables
- Flow control statements including optimization

```
BEGIN ;
   VARIABLE ;
   PROCEDURE ;      ENDPROCEDURE ;
   FUNCTION ;       ENDFUNCTION ;
      <assignments>
      <procedure calls>
      IF ;             ENDIF ;
      WHILE ;          ENDWHILE ;
      LOOP ;           ENDLOOP ;
      FIT ;            ENDFIT ;
END ;
```

MAGNET WITH ERRORS

```
PROCEDURE HOBEND ; {NINTH ORDER INHOMOGENEOUS
MAGNET WITH AXIS OFFSET, TILT AND ROTATION}
 OV 9 2 0 ; RP .1 4 1 ;
 UM ;
 RA .1 ;
 SA 1E-6 0 ;
 TA .02 0 ;                WRITE 6 ' BEGINNING WORK ' ;
 MS 2 45 .05 .1 .2 .3 .4 .5 ;
                           WRITE 6 ' WRITING MAP ' ;
 PM 7 ;                    WRITE 6 ' DONE ' ;
 ENDPROCEDURE ;
```

MAPS WITH KNOBS

```
PROCEDURE KNOBS ;
   OV 5 2 2 ; RP .1*PARA(1) 4 1 ;
   UM ;                          WRITE 6 ' BEGINNING WORK '
   MQ .1 .1*PARA(2) .1 ;  WRITE 6 ' WRITING MAP ' ;
   WRITE 6 MAP(1) ;
   PM 7 ;                        WRITE 6 ' DONE ' ;
   ENDPROCEDURE ;
```

The General Electromagnetic Element

Allows the computation of the map of any given arrangement of fields, especially measured data. Need to supply

- List of s-values (Position along optic axis)
- List of Curvatures
- List of magnetic multipole strengths
- List of electric multipole strengths

If known, the derivatives of the above quantities with respect to s can also be supplied; allows more coarse spacing / higher accuracy. Example:

GE 100 5 S H V W ;

Currently we are working on an interface routine that accepts measured data on a 3D cartesian grid (expected September 91).

Beamline Definition

```
PROCEDURE MAGIC_SYSTEM D L S01 S02 S03 ;
   DL 3.*D ;
   MQ L  .08 .05 ;
   DL D ;
   MQ L -.08 .05 ;
   DL D ;
   MO D S01 .05 ;
   DL D/2 ;
   MO D S02 .05 ;
   DL D/2 ;
   MO D S03 .05 ;
   DL D ;
   MQ L  .08 .05 ;
   DL D ;
   MQ L -.08 .05 ;
   DL 3.*D ;
   ENDPROCEDURE ;
```

Tuning the Magic System

```
PROCEDURE MAGIC1 ; VARIABLE L 1 ;
   OV 1 2 0 ; RP .1 4 1 ; L := .1 ;
   SB 0 .05 0 .05 0 0 ;
   WHILE L#0 ;
      WRITE 6 ' PLEASE GIVE L (.1 < L < 1) ' ;
      READ 5 L ;
      UM ; CR ; ER 1 4 1 4  1 1 1 1 ;
      BP ; MAGIC_SYSTEM .05 L 0 0 0 ; EP ;
      PM 6 ; PG -1 -51 ;
      ENDWHILE ;
   ENDPROCEDURE ;
```

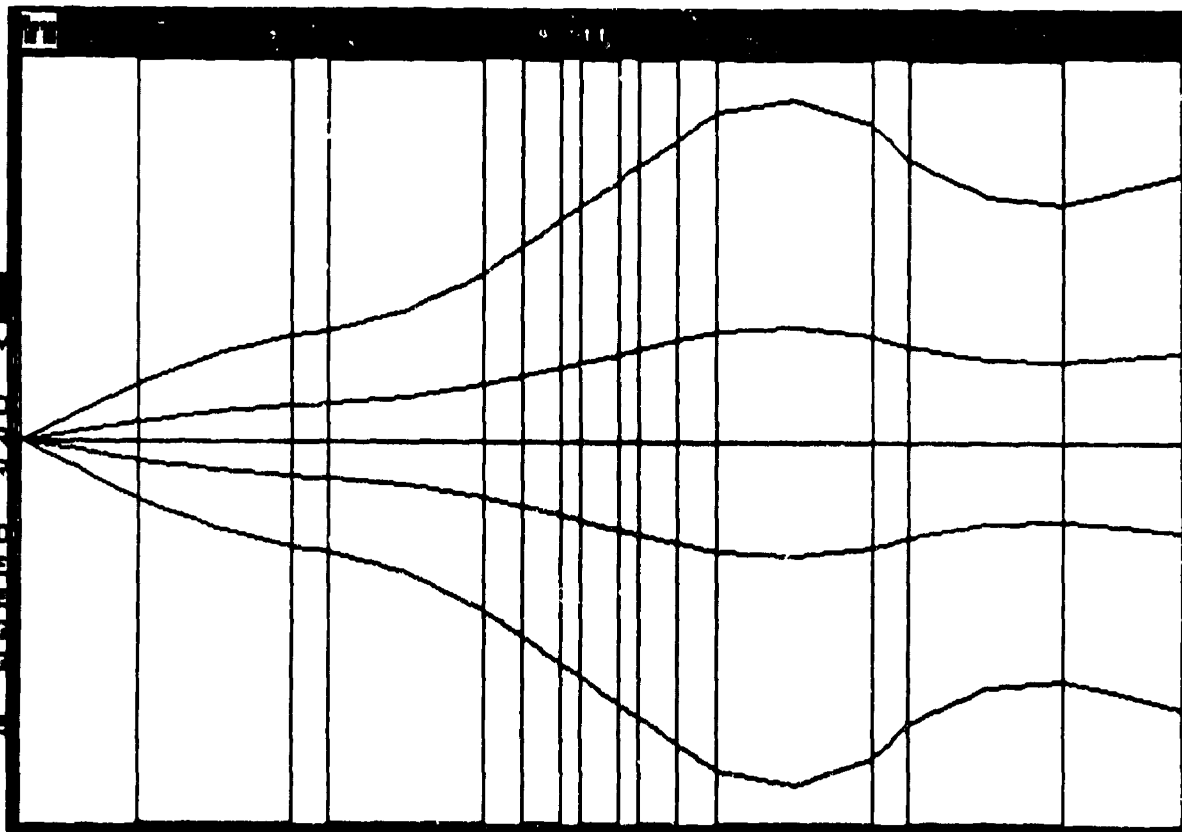

```
    DO YOU HAV
1
    PLEASE CHO
 1: HIGH ORDER
 2: HIGH ORDER
 3: MAPS WITH
 4: GRAPHICS D
 5: TUNING THE
 6: TUNING THE
 7: OPTIMIZING
 8: EVALUATING
 9: FITTING A
10: REPETITIVE
6
PLEASE GIVE L
.2
 -1.359119       -2.429142       0.0000000E+00  0.0000000E+00  0.0000000E+00  100000
 0.7012583        0.5175819      0.0000000E+00  0.0000000E+00  0.0000000E+00  010000
 0.0000000E+00  0.0000000E+00   0.5175819      -2.429142        0.0000000E+00  001000
 0.0000000E+00  0.0000000E+00   0.7012583      -1.359119        0.0000000E+00  000100
--------------
PLEASE GIVE L
```

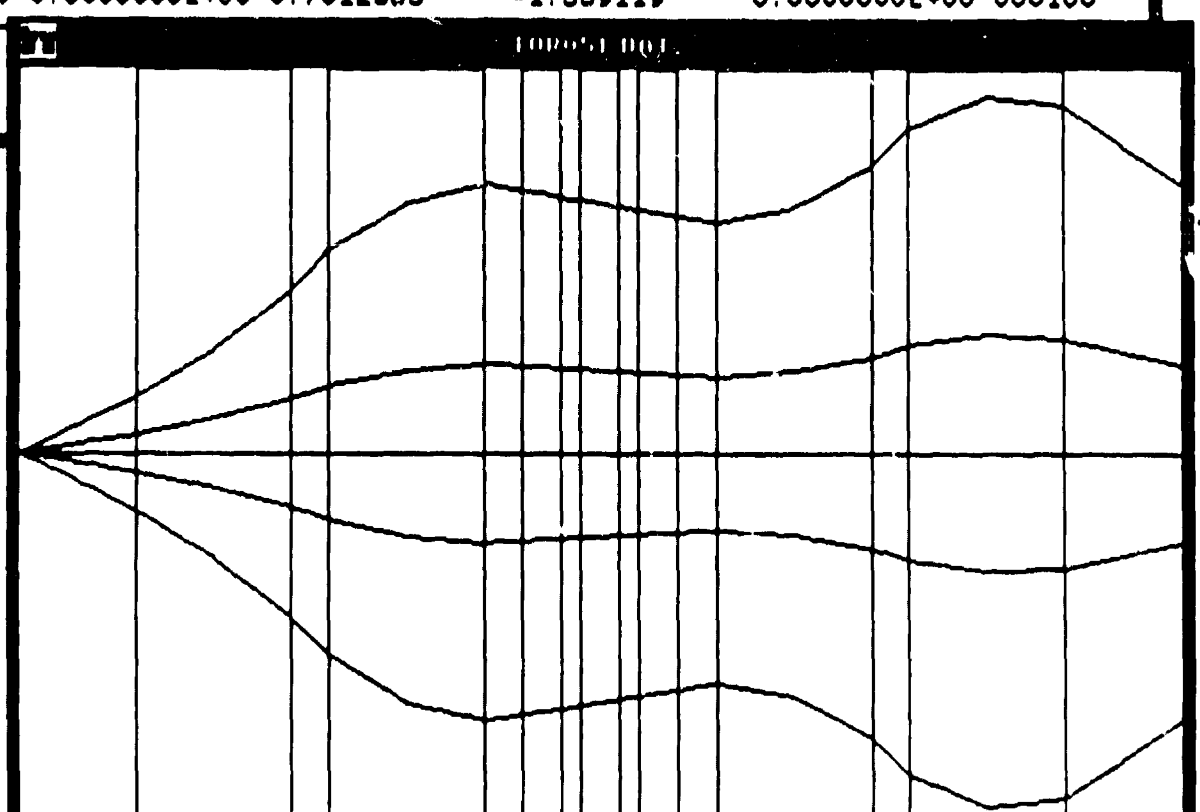

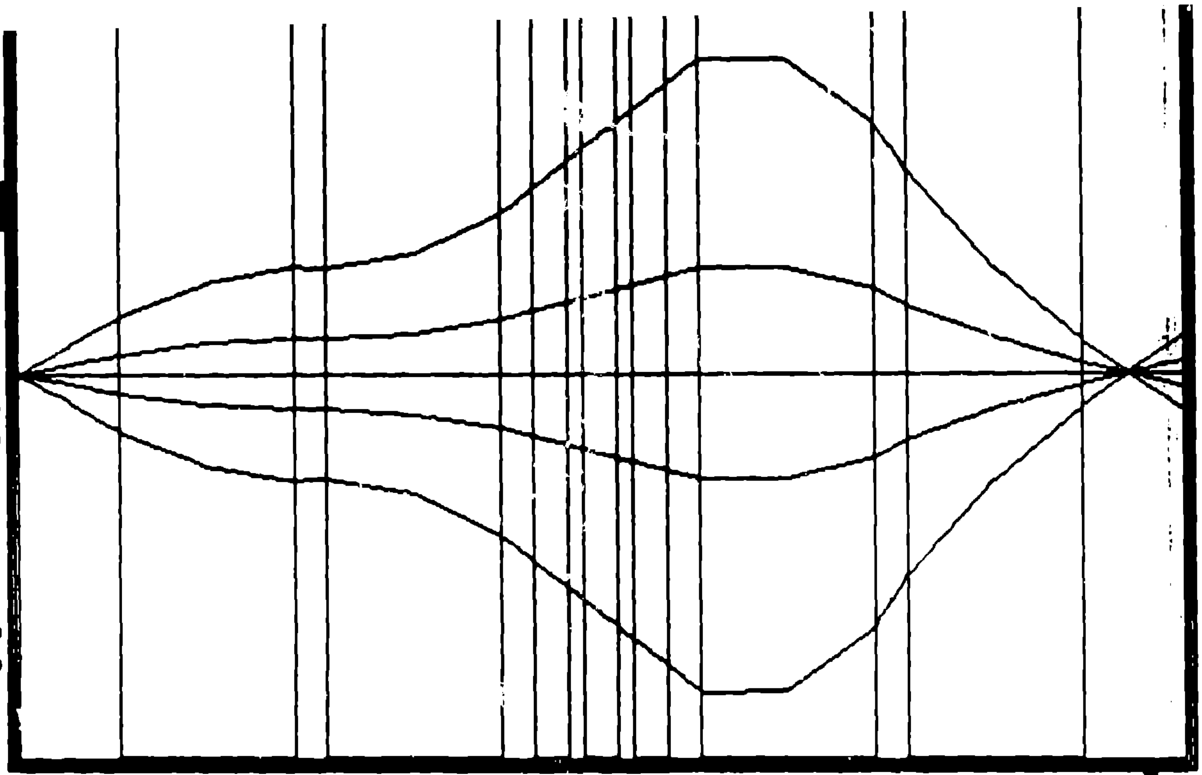

```
--------------
PLEASE GIVE L
.26
-0.9514268
-0.2188390E-01
 0.0000000E+00
 0.0000000E+00
--------------
PLEASE GIVE L
.27
-0.5402389
-0.1755053
 0.0000000E+00
 0.0000000E+00
--------------
PLEASE GIVE L
.265
-0.7635040      0.7613391      0.0000000E+00 0.0000000E+00 0.0000000E+00 100000
-0.9798769E-01 -1.212041       0.0000000E+00 0.0000000E+00 0.0000000E+00 010000
 0.0000000E+00  0.0000000E+00 -1.212041      0.7613391     0.0000000E+00 001000
 0.0000000E+00  0.0000000E+00-0.9798769E-01-0.7635040      0.0000000E+00 000100
--------------
PLEASE GIVE L
```

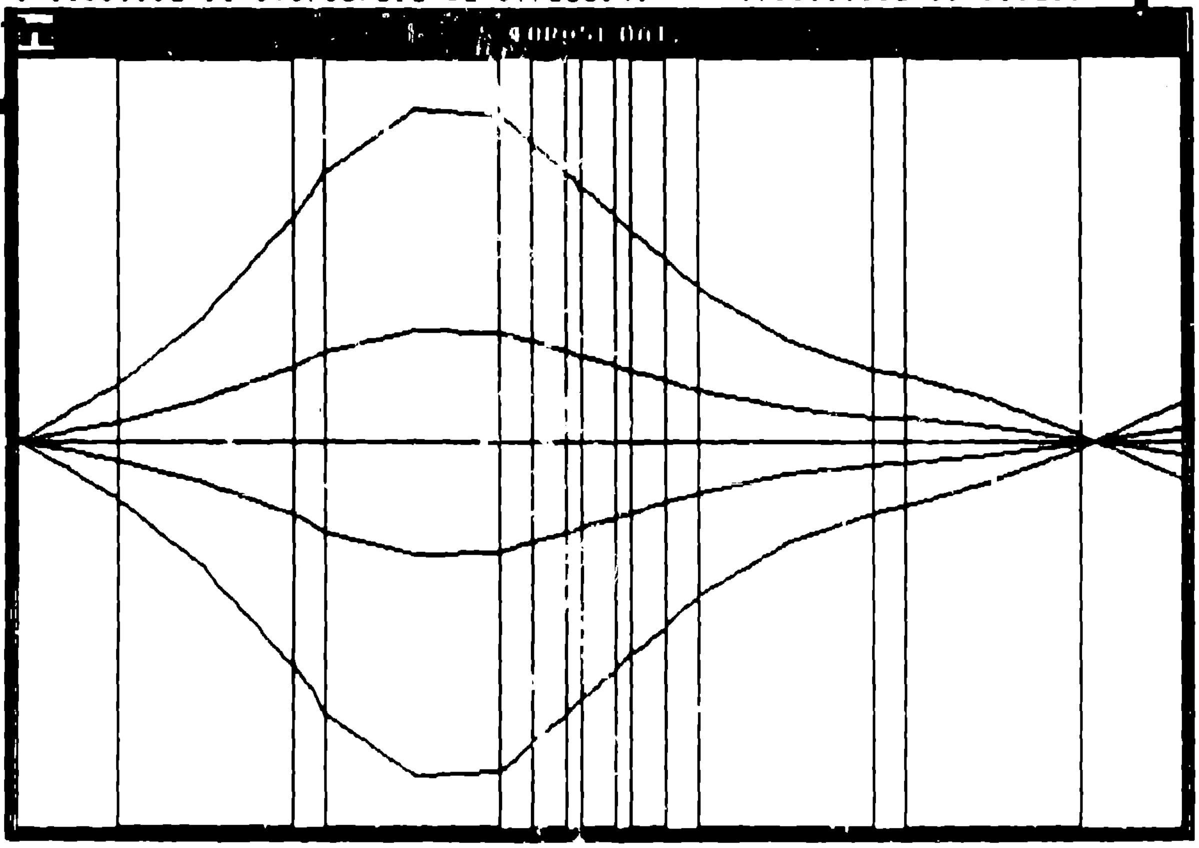

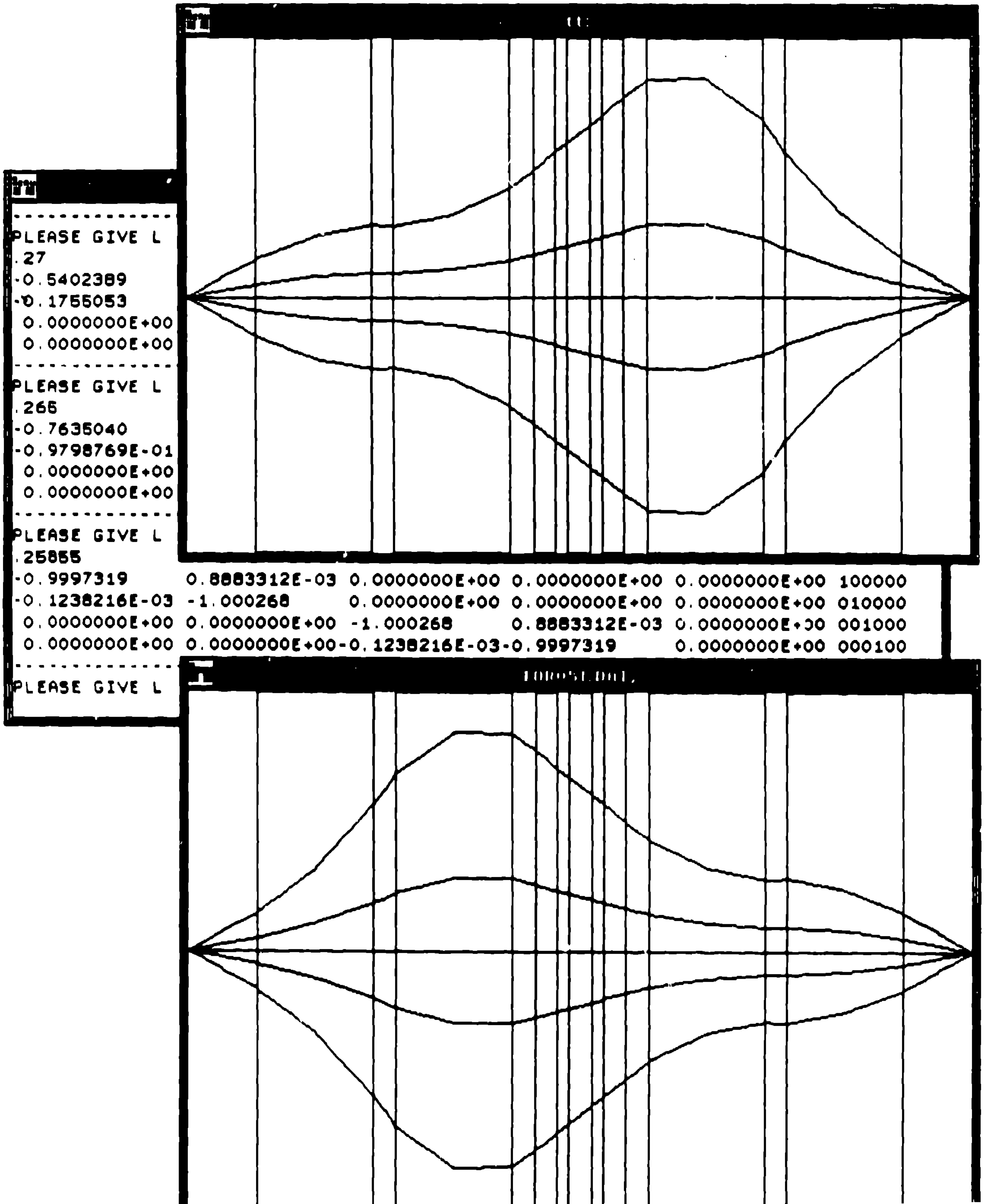
PLEASE GIVE L
.27
-0.5402389
-0.1755053
0.0000000E+00
0.0000000E+00
PLEASE GIVE L
.265
-0.7635040
-0.9798769E-01
0.0000000E+00
0.0000000E+00
PLEASE GIVE L
.25855
-0.9997319 0.8883312E-03 0.0000000E+00 0.0000000E+00 0.0000000E+00 100000
-0.1238216E-03 -1.000268 0.0000000E+00 0.0000000E+00 0.0000000E+00 010000
0.0000000E+00 0.0000000E+00 -1.000268 0.8883312E-03 0.0000000E+00 001000
0.0000000E+00 0.0000000E+00-0.1238216E-03-0.9997319 0.0000000E+00 000100
PLEASE GIVE L

Third Order Optimization

```
PROCEDURE MAGIC3 ;
   VARIABLE L  1 ; VARIABLE O1 1 ; VARIABLE O2 1 ;
   VARIABLE O3 1 ; VARIABLE OX 1 ; VARIABLE OY 1 ;
   OV 3 2 0 ; RP .1 4 1 ; L := .258538902555212 ;
   SB 0 .01 0 .01 0 0 ;
   O1 := -1E-2 ; O2 := 2E-2 ; O3 := -1E-2 ;
   FIT O1 O2 O3 ;
      UM ; CR ; ER 1 4 1 4  1 1 1 1 ;
      MAGIC_SYSTEM .05 L O1 O2 O3 ;
      BP ; DL 1E-3 ; EP ;
      OX := ABS(MA(1,222))+ABS(MA(1,233)) ;
      OY := ABS(MA(3,444))+ABS(MA(3,422)) ;
      WRITE 6 ' OCT. STR. O1, O2, O3: ' O1 O2 O3 ;
      WRITE 6 ' SUM OF THIRD ORDER ABERRATIONS
            (ANGSTROM): ' (OX+OY)*1E10 ;
      PG -1 -51 ;
      ENDFIT OX+OY 1E-12 1000 1 ;
   ENDPROCEDURE ;
```

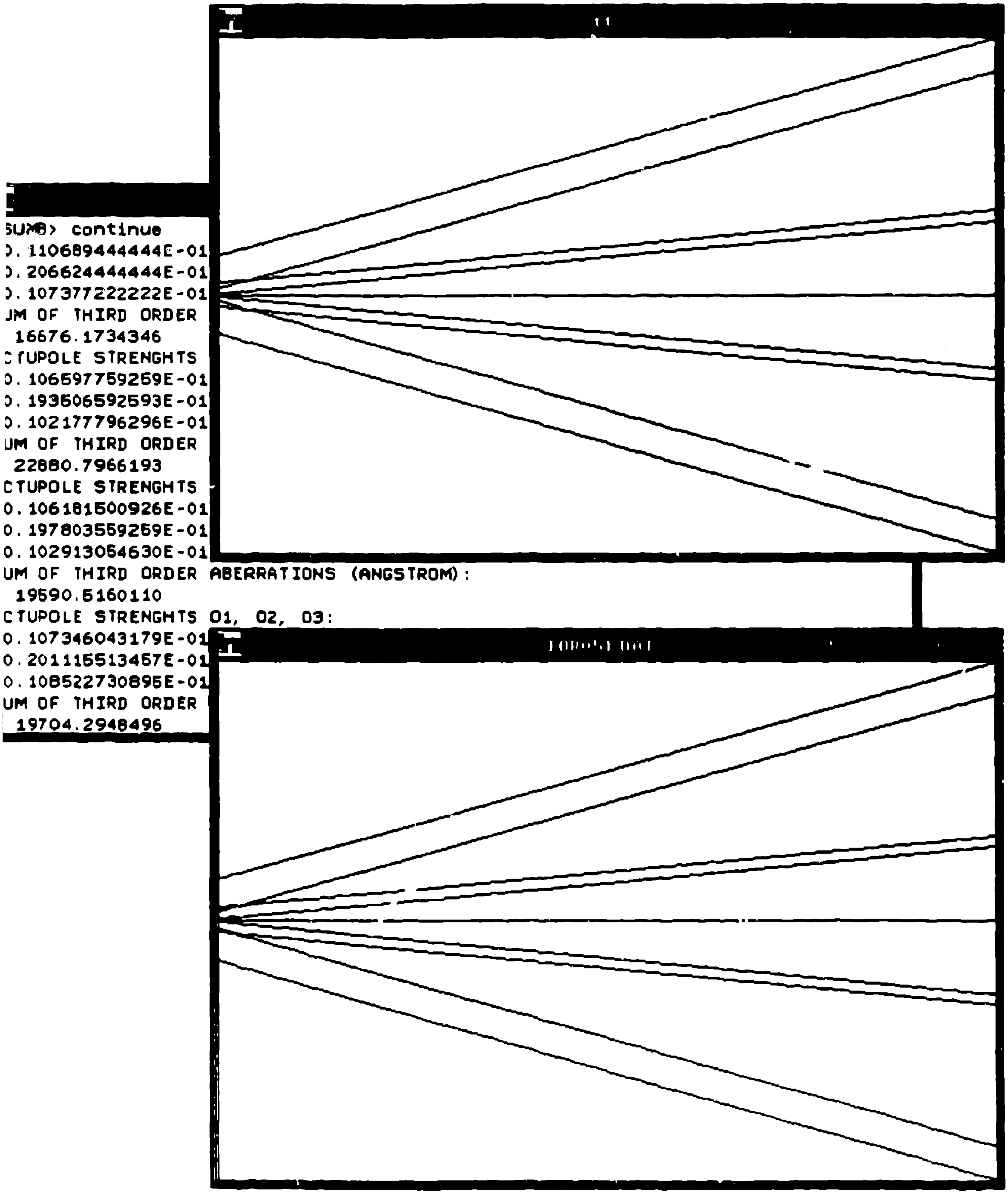
SUMB> continue
).110689444444E-01
).206624444444E-01
).107377222222E-01
JM OF THIRD ORDER
16676.1734346
CTUPOLE STRENGHTS
0.106597759259E-01
0.193606592593E-01
0.102177796296E-01
UM OF THIRD ORDER
22880.7966193
CTUPOLE STRENGHTS
0.106181500926E-01
0.197803559259E-01
0.102913054630E-01
UM OF THIRD ORDER ABERRATIONS (ANGSTROM):
19590.5160110
CTUPOLE STRENGHTS O1, O2, O3:
0.107346043179E-01
0.201116513457E-01
0.108522730895E-01
UM OF THIRD ORDER
19704.2948496

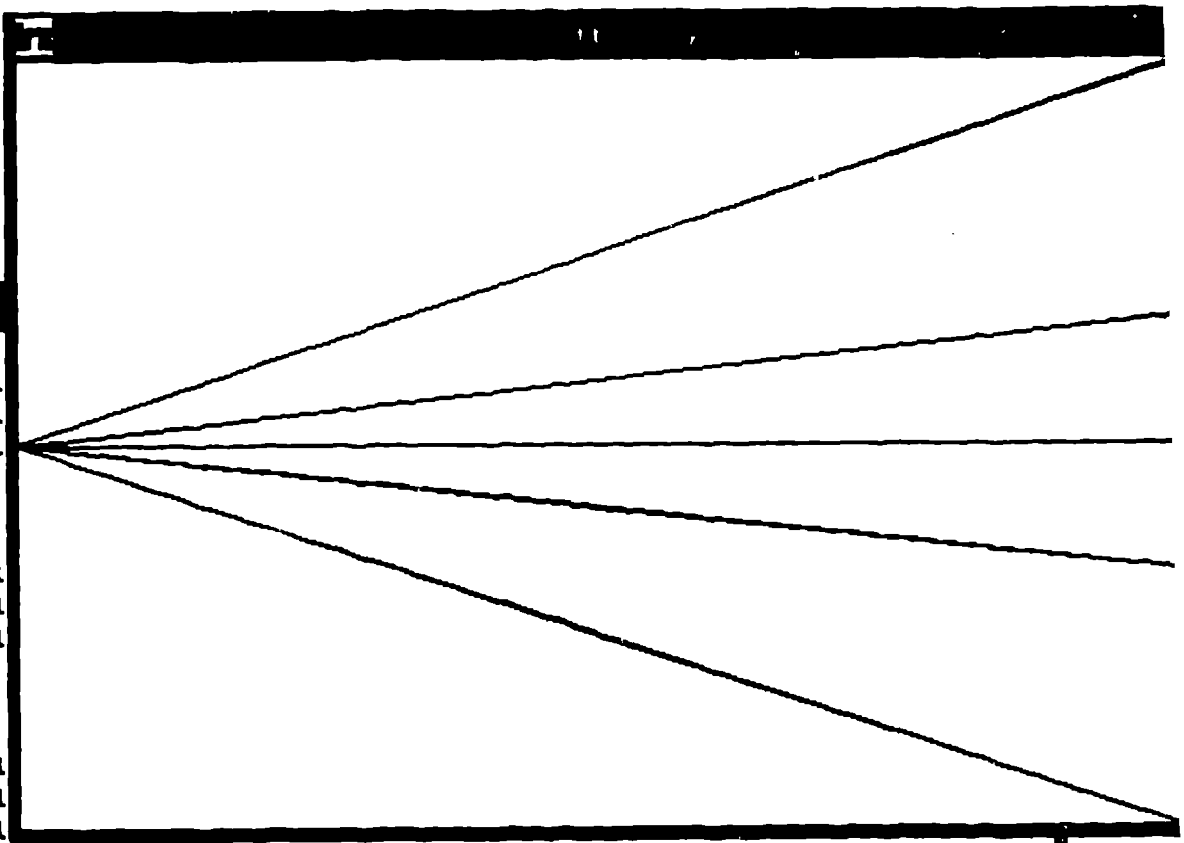

```
OCTUPOLE STRENGHTS
-0.131601491722E-01
 0.253877039823L 01
-0.131567772222E-01
SUM OF THIRD ORDER
 0.656947708874
OCTUPOLE STRENGHTS
-0.131602999240E-01
 0.253879091867E-01
-0.131568539193E-01
SUM OF THIRD ORDER
  1.13764362274
OCTUPOLE STRENGHTS
-0.131601789870E-01
 0.253878125194E-01
-0.131568695027E-01
SUM OF THIRD ORDER ABERRATIONS (ANGSTROM):
 0.505125313493
OCTUPOLE STRENGHTS 01, 02, 03:
-0.131601482653E-01
 0.253877005450E-01
-0.131567832656E-01
SUM OF THIRD ORDER
 0.414114231820
```

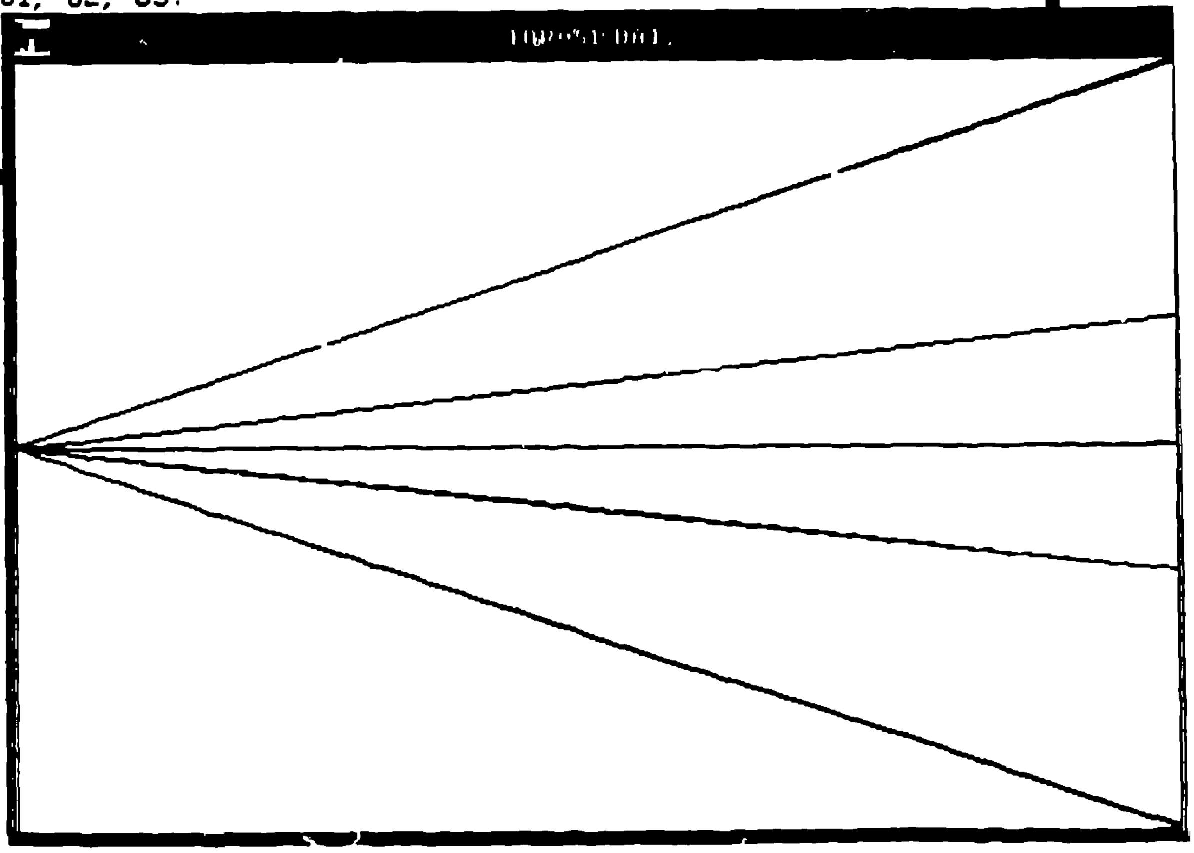

Fifth Order Aberrations

```
PROCEDURE MAGIC5 ; VARIABLE L 1 ;
   VARIABLE O1 1 ; VARIABLE O2 1 ; VARIABLE O3 1 ;
   VARIABLE OX 1 ; VARIABLE OY 1 ;
   OV 5 2 0 ; RP .1 4 1 ;  L := .258538902555212 ;
   SB 0 .01 0 .01 0 0 ;
   O1 := -1.3154806E-2 ; U2 := 2.5379889E-2 ;
   O3 := -1.3154772E-2 ;
      UM ; CR ; ER 1 4 1 4  1 1 1 1 ;
      MAGIC_SYSTEM .05 L O1 O2 O3 ;
      BP ; DL 1E-5 ; EP ;
      OX := ABS(MA(1,22222))+ABS(MA(1,22244))
           +ABS(MA(1,24444)) ;
      OY := ABS(MA(3,44444))+ABS(MA(3,44422))
           +ABS(MA(1,42222)) ;
      WRITE 6 ' SUM OF FIFTH ORDER ABERRATIONS
            (ANGSTROM): ' (OX+OY)*1E10 ; PG -1 -51 ;
      READ 5 L ;
   ENDPROCEDURE ;
```

Lissajoux Figures

```
PROCEDURE LISSA ;
   VARIABLE ISTOP 1 ;
   PROCEDURE FIGURE IU WX WY ;
      VARIABLE PICTURE 100000 ; VARIABLE T 1 ;
      PICTURE := MOVE (1,0,0) ;
      LOOP T 0 8*ATAN(1) .01 ;
         PICTURE := PICTURE&
            DRAW(COS(WX*T),SIN(WY*T),0) ;
         ENDLOOP ;
      WRITE IU PICTURE ;
      ENDPROCEDURE ;
   WRITE 6 ' DRAWING LISSAJOUX FIGURES ' ;
   FIGURE -1 11 12 ; FIGURE -51 12 13 ;
   READ 5 ISTOP ;
   ENDPROCEDURE ;
```

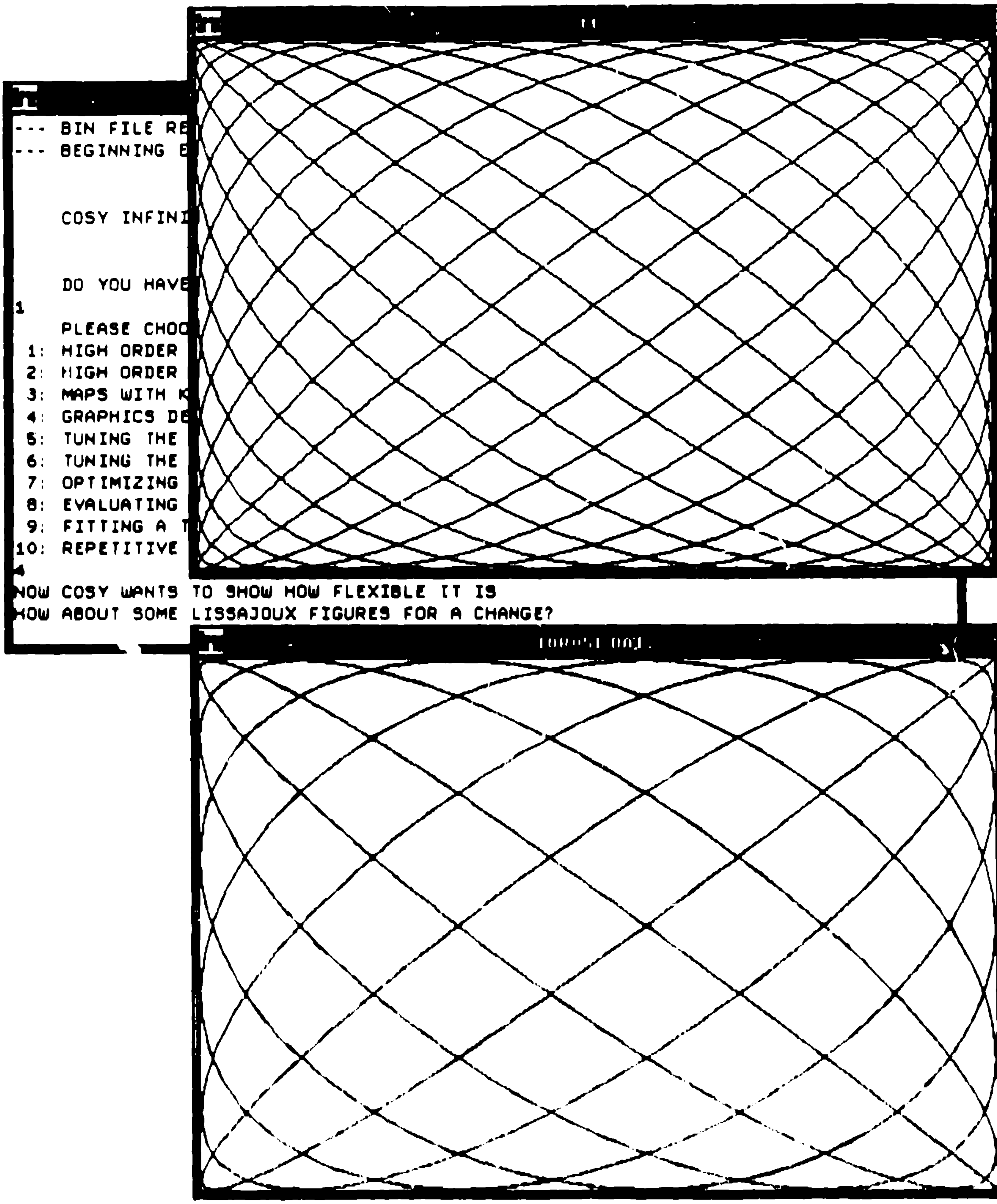
--- BIN FILE RE
--- BEGINNING B
COSY INFINI
DO YOU HAVE
1
PLEASE CHOO
1: HIGH ORDER
2: HIGH ORDER
3: MAPS WITH K
4: GRAPHICS DE
5: TUNING THE
6: TUNING THE
7: OPTIMIZING
8: EVALUATING
9: FITTING A T
10: REPETITIVE
4
NOW COSY WANTS TO SHOW HOW FLEXIBLE IT IS
HOW ABOUT SOME LISSAJOUX FIGURES FOR A CHANGE?

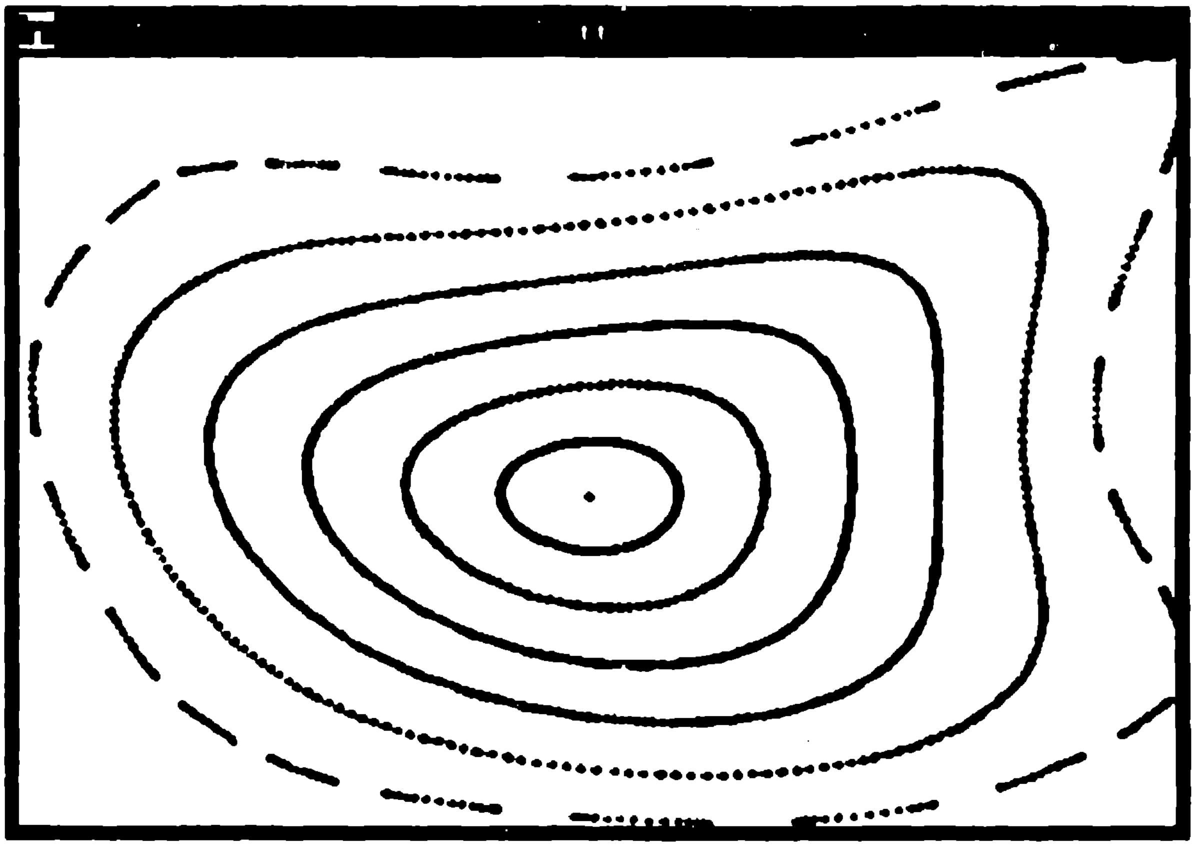

```
GIVE NUMBER OF TURNS
500
GIVE K
.276746
TRANSFER MAP
-0.1672602     -0.9859128      0.0000000E+00 0.0000000E+00 0.0000000E+00 100000
 0.9859128     -0.1672602      0.0000000E+00 0.0000000E+00 0.0000000E+00 010000
 0.0000000E+00 0.2797598E-01 0.0000000E+00 0.0000000E+00 0.0000000E+00 200000
 0.0000000E+00-0.3298080      0.0000000E+00 0.0000000E+00 0.0000000E+00 110000
 0.0000000E+00 0.9720240      0.0000000E+00 0.0000000E+00 0.0000000E+00 020000
--------------------------------------------------------------------------------
GIVE NUMBER OF TURNS
500
GIVE K
.28
TRANSFER MAP
-0.1873813     -0.9822873      0.0000000E+00 0.0000000E+00 0.0000000E+00 100000
 0.9822873     -0.1873813      0.0000000E+00 0.0000000E+00 0.0000000E+00 010000
 0.0000000E+00 0.3511176E-01 0.0000000E+00 0.0000000E+00 0.0000000E+00 200000
 0.0000000E+00-0.3681246      0.0000000E+00 0.0000000E+00 0.0000000E+00 110000
 0.0000000E+00 0.9648882      0.0000000E+00 0.0000000E+00 0.0000000E+00 020000
--------------------------------------------------------------------------------
GIVE NUMBER OF TURNS
```

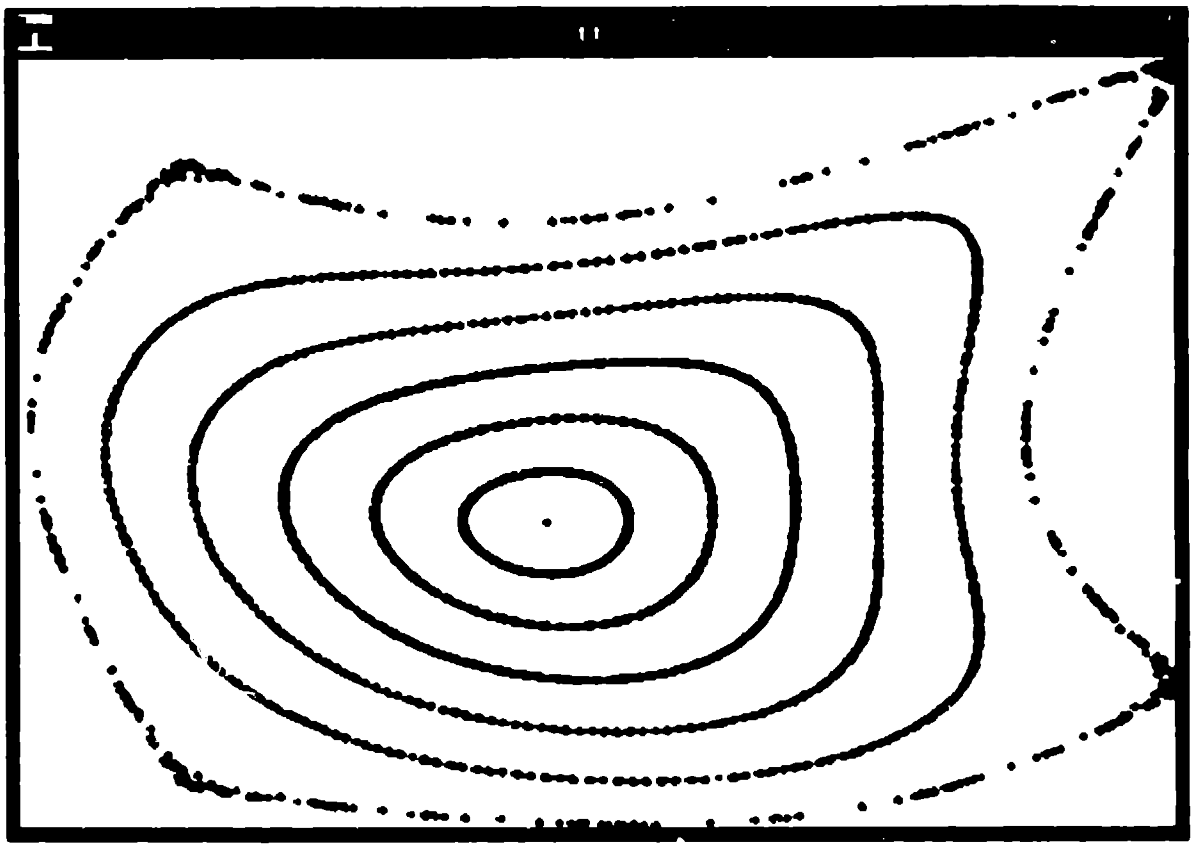

```
 1: HIGH ORDER QUAD
 2: HIGH ORDER COMBINED FUNCTION MAGNET WITH ERRORS
 3: MAPS WITH KNOBS
 4: GRAPHICS DEMO
 5: TUNING THE MAGIC SYSTEM - POOR MAN'S VERSION
 6: TUNING THE MAGIC SYSTEM - FIRST ORDER
 7: OPTIMIZING THE MAGIC SYSTEM - THIRD ORDER
 8: EVALUATING THE MAGIC SYSTEM - FIFTH ORDER
 9: FITTING A TRIPLET
10: REPETITIVE TRACKING
10
GIVE NUMBER OF TURNS
500
GIVE K
.276746
TRANSFER MAP
-0.1672602      -0.9859128      0.0000000E+00 0.0000000E+00 0.0000000E+00 100000
 0.9859128      -0.1672602      0.0000000E+00 0.0000000E+00 0.0000000E+00 010000
 0.0000000E+00 0.2797598E-01 0.0000000E+00 0.0000000E+00 0.0000000E+00 200000
 0.0000000E+00-0.3298080      0.0000000E+00 0.0000000E+00 0.0000000E+00 110000
 0.0000000E+00 0.9720240      0.0000000E+00 0.0000000E+00 0.0000000E+00 020000
--------------------------------------------------------------------------------
GIVE NUMBER OF TURNS
```

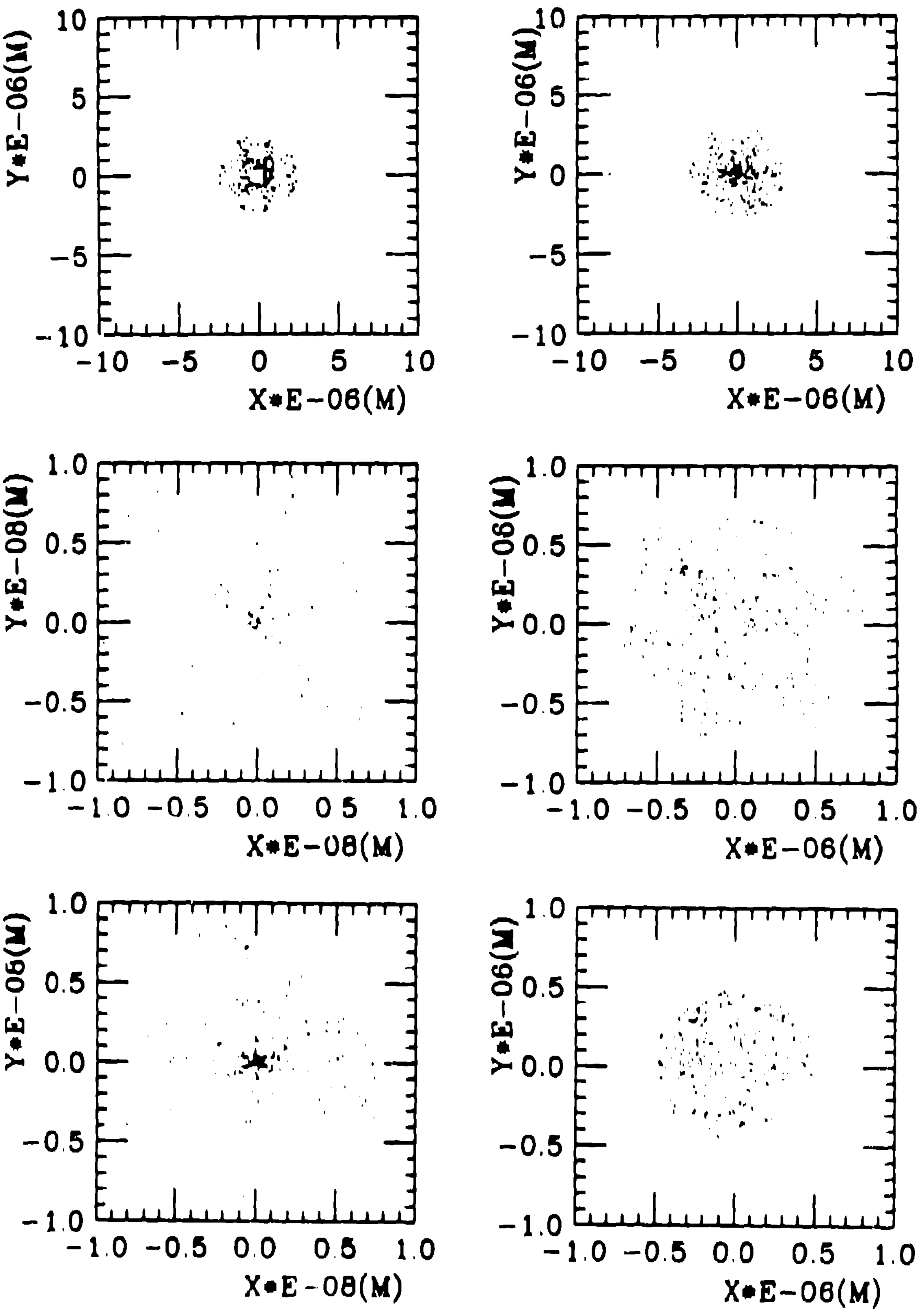

Figure 4: The beam spots for "uncorrected(top)", "sextupole corrected(middle)" and "octupole corrected(bottom)" systems up to 5th order calculations. The left side is for the point source i.e $x_0 = y_0 = 0$, $a_0 = b_0 = 0.001$ and the right side is for $x_0 = y_0 = 10\mu m$, $a_0 = b_0 = 0.001$ in the demagnification ratio of 20 to 1.

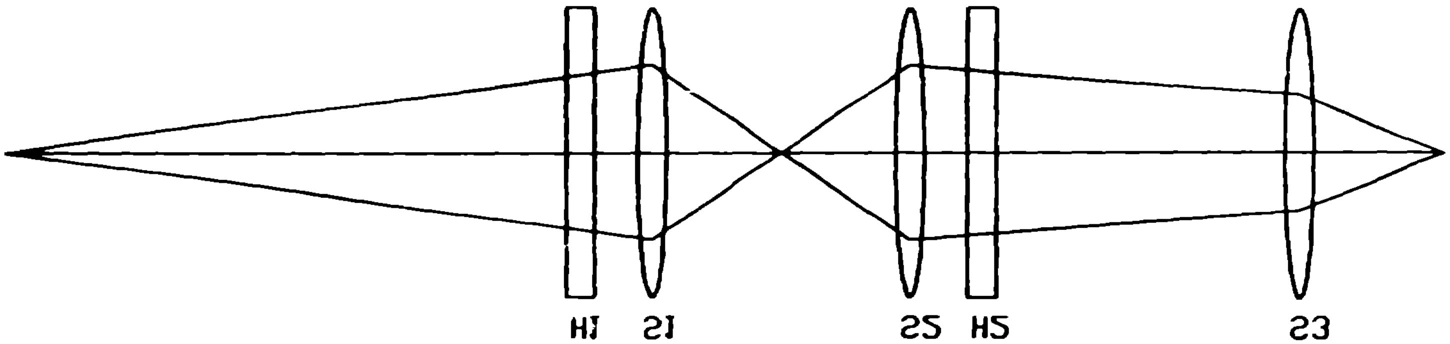
H1
S1
S2
H2
S3

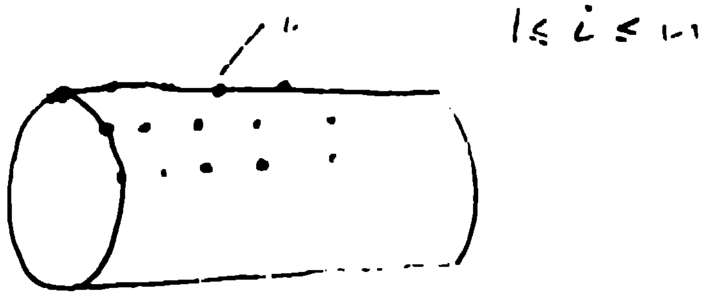

V_i determine V.

Solve n Potential Problems, where for the j-th problem $V_j = 1$, $V_i = 0$ $(i \neq j)$.
Call result $V^{(j)}$.

Then, in general,

$$V = \sum V_j \cdot V^{(j)} \qquad (*)$$

$V^{(j)}$ depends <u>only</u> on geometry (e.g. cylin. and have to be computed only once.
Additional simplification: cylindrical symm.

$\Rightarrow$ Doing a harmonic analysis <u>once</u> for the $V^{(j)}$ allows a harmonic analysis of any Potential.

Multipole terms: $\sum V_j \cdot m^{(j)}$

Normal Form Theory

Goal: perform a nonlinear change of variables such that the motion in the new variable pairs is rotationally invariant:

$$\mathcal{M} \circ \mathcal{R} = \mathcal{R} \circ \mathcal{M}$$

If the map is symplectic, this means circles. If the map is damped, we obtain logarithmic spirals.

Advantage: Tune with amplitude is trivial to compute, since each iteration of the map corresponds to the same angle advance.

Other Advantages: - Provides pseudo invariants the quality of which allows conclusions about the map; - sensitive to resonances, allows efficient study of resonances

History of Normal Form Theory

- Probably first studied by Birkhoff 1917
- Introduced to Accelerator Physics in Lie Algebra Picture by Dragt and Finn 1979
- Lie implementation to third and fifth order by Neri 1985
- Arbitrary order differential algebraic/Lie algebraic formulation 1938
- Arbitrary order purely differential algebraic formulation including damped systems M.B. 1991

The DA Normal Form Algorithm

Assume linear part of map has been diagonalized by a linear change of basis:

$$\mathcal{M} = \mathcal{R} + \mathcal{S}$$

where $\mathcal{R}$ has on its diagonal the values $r_j \cdot e^{\pm i\nu_j}$ (pair structure).

Now attempt to simplify the map by a nonlinear transformation. Choose transformation

$$\mathcal{A}_m = \mathcal{E} + \mathcal{T}_m$$

Up to order m, the inverse is $\mathcal{A}_m^{-1} =_m \mathcal{E} - \mathcal{T}_m$, and we obtain

$$\begin{aligned}
& \mathcal{A} \circ \mathcal{M} \circ \mathcal{A}^{-1} \\
=_m \; & (\mathcal{E} + \mathcal{T}_m) \circ (\mathcal{R} + \mathcal{S}_{m-1}) \circ (\mathcal{E} - \mathcal{T}_m) \\
=_m \; & (\mathcal{E} + \mathcal{T}_m) \circ (\mathcal{R} + \mathcal{S}_{m-1}) \circ (\mathcal{E} - \mathcal{T}_m) \\
=_m \; & \mathcal{R} + \mathcal{S}_{m-1} + (\mathcal{T}_m \circ \mathcal{R} - \mathcal{R} \circ \mathcal{T}_m)
\end{aligned}$$

Removing Terms in the Normal Form Step

We can use the commutator $\mathcal{C}$ of $\mathcal{T}_m$ and $\mathcal{R}$ to remove terms from $\mathcal{S}_{m-1}$. We write

$$\mathcal{T}^{\pm}_{mj} = \sum \; (\mathcal{T}^{\pm}_{mj}|k_1^+, k_1^-, \ldots, k_n^+, k_n^-) \cdot (v_1^+)^{k_1^+}(v_1^-)^{k_1^-} \cdot \ldots \cdot (v_n^+)^{k_n^+}(v_n^-)^{k_n^-}$$

$$\mathcal{C}^{\pm}_{mj} = \sum \; (\mathcal{C}^{\pm}_{mj}|k_1^+, k_1^-, \ldots, k_n^+, k_n^-) \cdot (v_1^+)^{k_1^+}(v_1^-)^{k_1^-} \cdot \ldots \cdot (v_n^+)^{k_n^+}(v_n^-)^{k_n^-}$$

Because of the simple form of $\mathcal{R}$, we obtain

$$\begin{aligned} &(\mathcal{C}^{\pm}_j|k_1, k_1^-, \ldots, k_n^+, k_n^-) \\ = \; &-C^{\pm}_j(\vec{k}^+, \vec{k}^-) \;\cdot\; (\mathcal{T}^{\pm}_j|k_1^+, k_1^-, \ldots, k_n^+, k_n^-) \end{aligned}$$

where

$$C^{\pm}_j(\vec{k}^+, \vec{k}^-) = r_j \cdot e^{\pm i\nu_j} - \left(\prod_{j=1}^{n} (r_j)^{k_j^+ + k_j^-}\right) \cdot e^{i\vec{\nu}\cdot(\vec{k}^+ - \vec{k}^-)}$$

So we can remove every term for which $C^{\pm}_j(\vec{k}^+, \vec{k}^-)$ is nonzero!

Removable Terms in the Symplectic Case

In the symplectic case, all r_j are one (no damping). Then everything is removable except

$$\vec{\nu} \cdot (\vec{k}^{+} - \vec{k}^{-}) = l \cdot 2\pi \pm i \cdot \nu \quad \forall l$$

This can occur in the following cases:

1. $\vec{n} \cdot \vec{nu} = 2\pi l$ has nontrivial solutions (we are on a resonance; physics case)
2. $k_l^{+} = k_l^{-} \;\; \forall\, l \neq j$, and $k_j^{+} = k_j^{-} \pm 1$ (unavoidable; mathematics case)

Removable Terms under Damping

In case there is damping (or blow up), some of the r_j are not 1. In this case, additional terms can be removed.

Of particular interest is the case of total damping in which all r_j are less than one. Then everything can be removed except

1. $k_l^+ = k_l^- = 0 \quad \forall\ l \neq j$, and $k_j^+ = k_j^- \pm 1$ (unavoidable; mathematics case)

But this is the identity!

This has important consequences:

- Damped systems are not susceptible to resonances
- There are no amplitude dependent tune shifts in damped systems

On-line Correction of Aberrations in Particle Spectrographs

M. Berz, K. Joh, J. A. Nolen
Department of Physics and Astronomy and
National Superconducting Cyclotron Laboratory,

B. M. Sherrill and A. F. Zeller
National Superconducting Cyclotron Laboratory,
Michigan State University, East Lansing, Mi 48824

Abstract

A new method is presented that allows the reconstruction of trajectories and the on-line correction of residual aberrations that limit the resolution of particle spectrographs. Using a computed or fitted high order transfer map that describes the uncorrected aberrations of the spectrograph under consideration, it is possible to determine a pseudo transfer map that allows the computation of the corrected data of interest as well as the reconstructed trajectories in terms of position measurements in two planes near the focal plane.

The technique is only limited by the accuracy of the position measurements and the accuracy of the transfer map. In practice the method can be expressed as an inversion of pseudo transfer map and implemented in the differential algebraic framework. The method will be used to correct residual high aberrations in the S800 spectrograph which is under construction at the National Superconducting Cyclotron Laboratory at Michigan State University.

1 Introduction

Efficient modern high-resolution mass spectrographs usually offer rather large phase space acceptances. One such spectrograph is the S800 currently under construction at Michigan State University's National Superconducting Cyclotron Laboratory [1, 2]. Such large acceptance high resolution spectrographs usually require a careful consideration and correction of aberrations. But because of the large phase space acceptance, effects of rather high orders contribute. This makes the correction process often considerably more difficult and complex, and sometimes even prevents a complete correction of aberrations in the conventional sense.

It is often possible to circumvent or at least alleviate these problems by using additional information about the particles. In particular, one often measures not only their final position but also their final angle by means of a second detector. With this additional information it is to some degree possible to retroactively construct the whole trajectory of the particle. This information can be used both for the numerical correction of the quantities of interest, but it also reveals additional properties like the initial angle, which is of course of interest in the study of many nuclear processes.

In the past such trajectory reconstruction techniques were quite involved, often requiring extensive ray tracing and the storage of large arrays of ray data and extensive interpolation. In this paper, we present a rather direct and efficient method based on differential algebraic (DA) techniques.

In recent years we have shown that maps of particle optical systems can be computed to much higher orders than previously possible using DA methods [3, 4, 5, 6]. Furthermore, the techniques also allow the accurate treatment of very complicated fields that can be treated only approximately otherwise. In our particular case, these include the fringe fields of the large aperture magnets required for such particle spectrographs. So for the first time there is now the possibility to really compute all the aberrations that comprise a modern high resolution spectrograph without having to rely on tedious ray tracing.

On the practical side this requires high order codes for the computation of highly accurate maps for realistic fields. The new code COSY INFINITY [7, 8, 9, 10] allows such computations in a very powerful language environment. It also has extensive and general optimization capabilities, supports interactive graphics and provides ample power for customized problems, and it provides all the necessary tools for efficient trajectory reconstruction.

In the next section, we will discuss an important algorithm for this task, the inversion of transfer maps. Section 3 outlines the use of map inversion techniques for the purposes of trajectory reconstruction. Section 4 provides an outlook for the practical application in connection with the S800 spectrograph.

2 Inversion of Transfer Maps

At the core of the operations that follow is the need to invert transfer maps in their DA representation. Though at first glance this appears like a very difficult problem, we will see that indeed there is a rather elegant and closed

*Supported in Part by the U.S. National Science Foundation, Grant Number PHY 89-13815

algorithm to perform this task.

We begin by splitting the map A_n into its linear and nonlinear parts:

$$A_n = A_{1n} + A_{2n}. \quad (1)$$

Furthermore, we write the sought for inverse as M_n.

$$A^{-1n} = M_n \quad (2)$$

Composing the functions, we obtain

$$\begin{aligned} (A_1 + A_{2n}) \circ M_n &= E_n \Rightarrow \\ A_1 \circ M_n &= E_n - A_{2n} \circ M_n \Rightarrow \\ M_n &= A_1^{-1} \circ (E_n - A_{2n} \circ M_{n-1}). \quad (3) \end{aligned}$$

Here "$\circ$" stands for the composition of maps. In the last step use has been made of the fact that knowing M_{n-1} allows us to compute $A_{2n} \circ M_n$. The necessary computation of A_1^{-1} is a linear matrix inversion.

Equation (3) can now be used in a recursive manner to compute the M_i order by order.

3 Trajectory Reconstruction

The result of the computation of the transfer map of the system allows us to relate final quantities to initial quantities and parameters. In our case, the relevant quantities are the positions in x and y directions as well as the measures of slopes p_x/p_0, p_y/p_0 and the energy of the particles under consideration. Usually the initial x, which is determined by the target thickness or a subsequent slit, is kept small to provide a minimal entrance width. So the final positions and slopes are primarily determined by the energy, and to higher orders also by the initial y position and the initial slopes.

In the full transfer map we now set x_i to zero and consider the following submap:

$$\begin{pmatrix} x_f \\ a_f \\ y_f \\ b_f \end{pmatrix} = S \begin{pmatrix} a_i \\ y_i \\ b_i \\ d \end{pmatrix} \quad (4)$$

This map relates the quantities which can be measured in the two planes to the quantities of interest. The map S is not a regular transfer map, and in particular its linear part does not have to be a priori invertible. In a well designed particle spectrograph, the linear part has the following form:

$$\begin{pmatrix} x_f \\ a_f \\ y_f \\ b_f \end{pmatrix} = \begin{pmatrix} 0 & 0 & 0 & * \\ * & 0 & 0 & * \\ 0 & * & * & 0 \\ 0 & * & * & 0 \end{pmatrix} \cdot \begin{pmatrix} a_i \\ y_i \\ b_i \\ d_i \end{pmatrix} \quad (5)$$

where a star denotes an entry that is not zero. Since the system is imaging, clearly (x,a) vanishes, and all the other

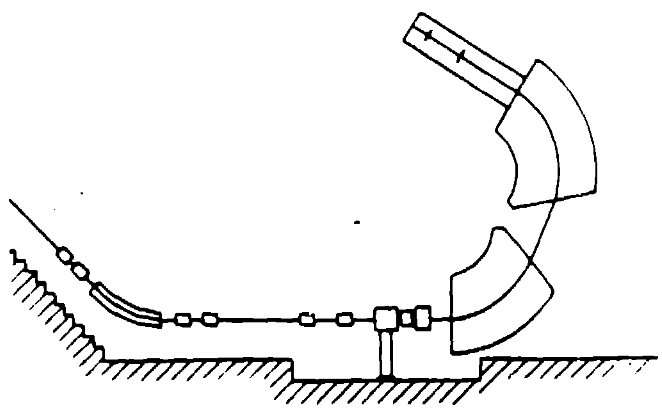

Figure 1: The vertical layout of the S800 spectrograph

zero terms vanish because of midplane symmetry. (x,d) is maximized in spectrograph design, and (a,a) cannot vanish in an imaging system because of symplecticity. In fact, to reduce the effect of the finite size entrance slit, (x,x) is minimized within the constraints, and so (a,a) = 1/(x,x) is also maximized.

Because of symplecticity, (y,y)(b,b)-(y,b)(b,y) = 1, and so we obtain for the total determinant of S:

$$|S| = (x,d) \cdot (a,a) \neq 0, \quad (6)$$

besides being nonzero, the size of the determinant is also a good measure of the quality of the spectrograph: the larger the better.

So certainly the linear matrix is invertible, and according to the last section, this entails that the whole nonlinear map S is invertible to arbitrary order, and thus it is possible to compute the initial quantities of interest to arbitrary order.

A closer inspection of the algorithm shows that in each iteration, the result is multiplied by the inverse of the linear matrix S. Since the determinant of this inverse is the inverse of the original determinant and is thus quite small, this entails that the originally large terms in the nonlinear part of the original map are more and more suppressed. So clearly even with trajectory construction, the original investment in the quality of the spectrograph, which is determined by its dispersion and its x demagnification, directly influences the quality of the trajectory reconstruction.

4 The Correction of Aberrations in Spectrographs

The proposed superconducting magnetic spectrograph, the S800 [1] shown in fig. 1, for the National Superconducting Cyclotron Laboratory will allow the study of heavy ion reactions with magnetic rigidities of up to 1.2 GeV/c. It will have an energy resolution of one part in 10000 with

Table 1: The S800 Spectrograph

Drift	l = 60 cm
Quad	l = 40 cm, G_{max} = 21 T/m , d = .01 m
Drift	l = 20 cm
Quad	l = 40 cm, G_{max} = 6.8 T/m, d = .02 m
Drift	l = 50 cm
Dipole	r = 2.6667 m, B_{max} = 1.5T, ϕ = 75 deg, ϵ_1 = 0 deg, ϵ_2 = 30 deg
Drift	l = 140 cm
Dipole	r = 2.6667 m, B_{max} = 1.5T, ϕ = 75 deg, ϵ_1 = 30 deg, ϵ_2 = 0 deg
Drift	l = 257.5 cm

large solid angle of about 20 msr and an energy acceptance of about 10 percent.

The spectrograph will be used in connection with the new K1200 Superconducting Cyclotron for beams of protons up to Uranium with energies of 2 to 200 MeV/u. It will provide unique opportunities for research in various areas, including the study of giant resonances, charge exchange, direct reaction studies and fundamental investigations of nuclear structure [11].

The S800 consists of two superconducting quadrupoles and two 75 degree dipoles with y-focusing edge angles. Table 1 lists the parameters of the system. The settings of the quadrupoles shown here correspond to particles of 193.04 MeV, mass 100 and charge 50. Standard optics notation is used.

After a careful measurement of the crucial fringe fields of the dipoles, we will be using COSY to determine the high order properties of the map of the spectrograph. The computation of the map S from the resulting transfer map can be performed directly within the COSY environment, and so can the inversion of the map S. Altogether, a correction map S is found, the nonlinearity of which is determined by the nonlinearity of the original map and the quality in the spectrograph measured by (x,d)/(x,x). It is anticipated that the correction map can be used for an on line determination of the relevant data without having to store the raw two plane position measurements.

In closing we would like to note that the method can also be employed for spectrographs for which no sufficient field measurements are known. To this end, one has to perform experimental ray tracing and fit the resulting data with a polynomial type transfer map. Also in this case, the inversion can be done in the map picture resulting in a rather compact representation of the data necessary for correction.

References

[1] J. Nolen, A.F. Zeller, B. Sherrill, J. C. DeKamp, and J. Yurkon. A proposal for construction of the S800 spectrograph. Technical Report MSUCL-694, National Superconducting Cyclotron Laboratory, 1989.

[2] L. H. Harwood A. F. Zeller, J. A. Nolen and E. Kashy. The MSU 1.2 GeV/c spectrograph. In *Workshop on High Resolution, Large Acceptance Spectrometers, ANL/PHY-81-2*. Argonne National Laboratory, 1982.

[3] M. Berz. Arbitrary order description of arbitrary particle optical systems. *Nuclear Instruments and Methods*, A298:426, 1990.

[4] M. Berz. Differential Algebraic description of beam dynamics to very high orders. *Particle Accelerators*, 24:109, 1989.

[5] M. Berz. Differential Algebraic treatment of beam dynamics to very high orders including applications to spacecharge. *AIP Conference Proceedings*, 177:275, 1988.

[6] M. Berz. Differential Algebraic description and analysis of trajectories in vacuum electronic devices including spacecharge effects. *IEEE Transactions on Electron Devices*, 35-11:2002, 1988.

[7] M. Berz. COSY INFINITY Version 3 reference manual. Technical Report MSUCL-751, National Superconducting Cyclotron Laboratory, Michigan State University, East Lansing, MI 48824, 1990.

[8] M. Berz. Computational aspects of design and simulation: COSY INFINITY. *Nuclear Instruments and Methods*, A298:473, 1990.

[9] M. Berz. COSY INFINITY, an arbitrary order general purpose optics code. *Computer Codes and the Linear Accelerator Community*, Los Alamos LA-11857-C:137, 1990.

[10] M. Berz. COSY INFINITY. In *Proceedings 1991 Particle Accelerator Conference*, San Francisco, CA, 1991.

[11] N. Anantaraman and B. Sherrill, Editors. Proceedings of the international conference on heavy ion research with magnetic spectrographs. Technical Report MSUCL-685, National Superconducting Cyclotron Laboratory, 1989.

A POSSIBLE TEST OF QUAD OPTICS USING EPICS

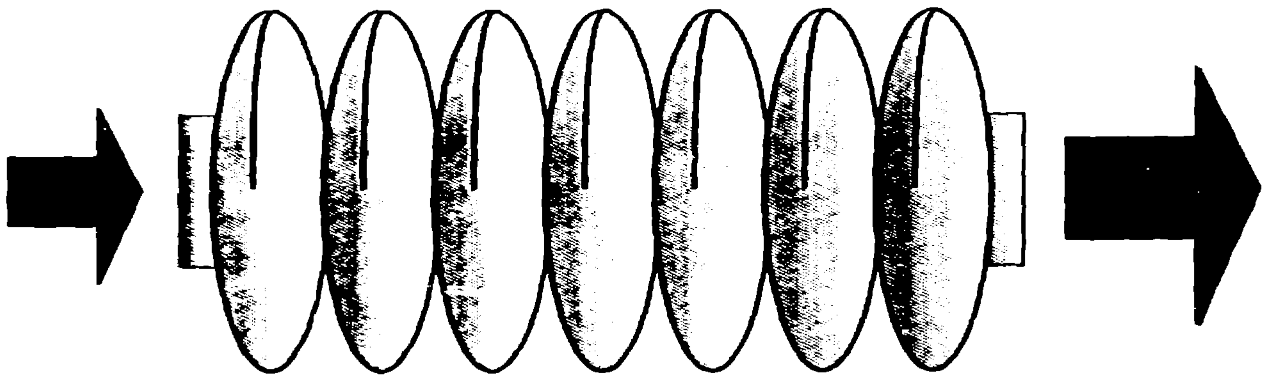

PILAC

Proposal to Test EPICS Quad Optics

• a Talk for
• PILAC Optics Meeting
• by
• Arch Thiessen
• 13 August, 1991

Los Alamos

EPICS Spectrometer Quad Triplet

- Installed and Operating
- Use Experimental Ray-Tracing Only
- Full 3rd Order Coefficients Available
-
- Try to Compute Coefficients
    - and Solid Angle

What I Have in Mind

- Compute 3-D Fringe Fields
  - Using TOSCA
  - Take Account of Adjacent Quad
- Measure 3-D Fringe Fields
  - Using Proposal of Klaus Halbach
  - Measure Bphi vs phi at large r
  - Analyze with Bessel Functions
  - In Presence of Adjacent Magnet
- Align Chambers, Targets, and Slits
  - And Measure Location of Vac Chbr
- Modify RAYTRACE/MOTER
  - Use TOSCA & Measurement Info
- Compute Coefficients and Solid Angle
  - Compare with Experiment

Personnel & Time Scale

- TOSCA
  - Barbara Weintraub - next 1-2 months
  - Including effects of Adjacent Quad
- Measurement Apparatus
  - Modify by Xmas
    * With Advice of Klaus Halbach
    * Measure in Place
      - Designed by
        - Barbara Weintraub
        - Steve Greene
        - John Zumbro
- Measurement Logistics
  - Measure Before Beam on (May?)
    * Barbara Weintraub - MP-8
    * Steve Greene - EPICS
    * John Zumbro - MP-14
- Bessel Function Analysis
  - Jeff Arrington - ACU
- MOTER/RAYTRACE Mods
  - Zumbro & Thiessen
  - U of Pa Student ?
- Comparison of Experiment and Theory
  - Zumbro & Greene

Los Alamos

Value of Experiment

- A Clear Goal
- Tests Concepts for PILAC Design
- Gives EPICS Confidence in Solid Angle

RAPPORTEUR

PILAC OPTICS WORKSHOP

AUGUST 12, 13, 1991

RAPPORTEUR

K. BROWN

1) PILAC in its present form is a highly optimized design. Many things have to work right at the same time. In this respect, PILAC resembles SLC at SLAC. It would be useful to make improvements to the design that provide a margin for error.

2) Optics programs are in good shape. With Lie-Algebra and calculations to very high order, in some cases to tenth order. This is an important achievement for the field. Many important problems can now be addressed that were impossible previously. Many papers can be written. But some of this work will be meaningless unless the magnetic field models in the codes are also improved to models. This workshop gave some clues as to how to begin.

EVALUATION OF ENVIRONMENTALLY SAFE CLEANING AGENTS FOR DIAMOND TURNED OPTICS

Lonnie A. Theye, Robert D. Day, Jeffrey Weinrach
Los Alamos National Laboratory
Los Alamos, NM 87545

Rudolf Schubert
Bell Communications Research
Red Bank, NJ 07701

Stephen Seiffert
Benchmark Environmental Corporation
Albuquerque, NM 87110

Background and Need:

Precision machining of metal surfaces using diamond turning has increased greatly in popularity at LANL in recent years. Similar techniques are used extensively to manufacture metal mirrors for use in laser applications. The diamond turned surfaces are easily damaged, making the selection of a cleaning agent very critical.

These surfaces have been traditionally cleaned using Trichloroethane (TCA) to remove residual oil remaining from the machining process. The TCA was then removed with an ethanol rinse, leaving a residue free surface. Recently, however, TCA was pronounced environmentally unsafe. Consequently, we are searching for an environmentally safe cleaning agent for these diamond turned metal optics.

The concern with using alternative solvents is the potential for residual surface films that produce reflectivity changes related to a combination of wavelength, surface coverage, film thickness and dielectric properties. Therefore, we have initiated a program for testing the effectiveness of a variety of environmentally safe solvents used to clean diamond turned optical surfaces.

Our basic test plan consists of comparing a number of environmentally safe solvents against the TCA/ethanol cleaning system. We have identified twelve candidate solvents, but have only been able to perform a partial test on one of them to date. This paper discusses the results obtained to date using this solvent known as P F [1].

Experimental Procedure:

Three different materials have been used for the tests. They are: Oxygen free high conductivity (OFHC) copper, electrolytic tough pitch (ETP) copper and 6061 aluminum. These materials were selected because they are currently used for many diamond machining applications. Test specimens were cut from a single piece of bar stock into blanks 3/4 inch in diameter and 1/8 inch thick.

The surfaces to be tested were finished using a single-point diamond tool with a tool nose radius of approximately 3mm. The machining conditions were adjusted so that a 1 um/rev feed was obtained.

A fixture was made to simultaneously machine nine blanks. Clean mineral oil was used as a cutting fluid. After removing the blanks from the machine they were stored in a mineral oil bath until they could be cleaned. The mineral oil plus any particulates generated by the machining process must be cleaned from the surface.

The cleaning procedure consisted of squirting cleaning solvent onto the oily surface and then air-drying with pressurized clean air. The fluid coming off of the surface during the cleaning process was collected for subsequent chemical analyses.

The following techniques are used to evaluate each solvent's effectiveness:

A. Bidirectional Reflectance Distribution Function (BRDF) scatter measurements
B. Ellipsometric analysis.
C. Observation of the surface using a Nomarski microscope.
D. Artificially aging for the equivalent of ten years using those solvents which provide the best surfaces based upon the three techniques listed above. After aging, an Auger analysis will be performed to determine surface contamination film thickness.

BRDF Measurements:
The BRDF is a measure of the amount of light scattered by a surface away from the normal angle of reflection. It is sensitive to both particulates and surface films and is a good measure of the surface performance in a typical application. For the purposes of this study, the BRDF measurements provide a functional criterion against which to evaluate the solvents. These measurements are made at a wavelength of 0.6328 mm and at off axis scattering angles between 0.5^{o} and 60^{o}. These correspond to a range of surface wavelengths between 0.73 µm and 73 µm.

Ellipsometry Measurements:
Ellipsometry is a sensitive technique used to measure surface film thicknesses of less than one monolayer. Therefore it is a very good quantitative method for determining how well a solvent removes surface oils. By using data obtained from the chemical analyses performed on the collected rinses along with a mathematical model, ellipsometric measurements can be used to determine the type and amount of surface contaminant. An advantage of this technique is that it works in air as opposed to vacuum.

Nomarski Microscope:
According to Bennett and Mattsson [2] the Nomarski (or Differential Interference Contrast) microscope is the most sensitive instrument for observing surface cleanliness next to the human eye. It is a good method for recording the surface condition on film, but since it produces a qualitative analysis it does not provide a numerical comparison of results

Artificial Aging and Auger Analysis:
Long term performance of an optic is often an important requirement. Since the cleaning solvent affects surface chemistry, it was decided to artificially age the specimens after cleaning them. The aging is performed in a chamber with an atmosphere containing high concentrations of corrosive chemicals normally present in our environment. For example, a typical corrosive atmospheric mixture will be 10-ppb hydrogen sulfide, 10-ppb chloride, and 200-ppb nitrogen dioxide with a relative humidity of 70%[3]. The Auger analyses performed after aging determines the surface contamination thickness as a function of the solvents used.

Data Analyses Obtained Thus Far:

To date BRDF measurements have been made on three cleaning systems:
1) trichloroethane with an ethanol rinse
2) PF with an ethanol rinse, and
3) PF with no rinse.

Figures 1 through 6 are plots of these data for ETP copper and 6061 aluminum. (The results for the OFHC copper were very similar to those obtained for the ETP copper and therefore are not presented.) An examination of these plots reveals that the amount of scatter produced from the surface cleaned with the PF/ethanol system was similar to that of the TCA/ethanol system for both copper and aluminum substrates. The surfaces that were cleaned using PF without the ethanol rinse produced much more scatter than the surfaces cleaned with the TCA/ethanol system. The peak observed at approximately 40 degrees on the copper data is caused by diffraction effects from the machining marks.

Aging and Auger Analyses Results:

The copper and aluminum were aged for 10 days in an Accelerated Aging Chamber. Auger analyses were performed on each sample after the tests to determine the elements present in the contamination layer and to determine the contamination layer thickness. Figure 7 shows a typical Auger Spectrum taken on one of the copper samples. Figures 8 through 10 are the depth profiling data for the ETP Copper samples with a sputtering rate of 100 angstroms per minute. Figures 11 through 13 are the depth profiling data for the 6061 Aluminum samples with a sputtering rate of 200 angstroms per minute. From these data it has been concluded that there is no significant differences between the cleaning procedures for either material with regard to future corrosion.

Ellipsometric measurements have been delayed because of instrument repair.

Summary:

We discussed the plan to test the cleaning capability of a number of environmentally safe solvents used on diamond turned metal optics. Partial results have been obtained on three cleaning systems, indicating that a suitable replacement for TCA can be found.

Acknowledgement:

This work was funded by the U.S. Department of Energy under contract W 7405 ENG 36, for the University of California.

The authors wish to express their appreciation to Sandia Systems, Albuquerque, NM for taking the BRDF data.

References:

1. P F is a registered trademark of P-T Technologies of Clearwater, Florida.

2. Bennett, Jean M. and Mattsson, Lars, Introduction to Surface Roughness and Scattering, Optical Society of America, Washington, DC, 1989, p. 30.

3. Schubert, R., "A Second Generation Accelerated Atmospheric Corrosion Chamber," American Society for Testing and Materials Special Technical Publication 965, pp. 374-384.

BRDF Measurements on ETP Copper

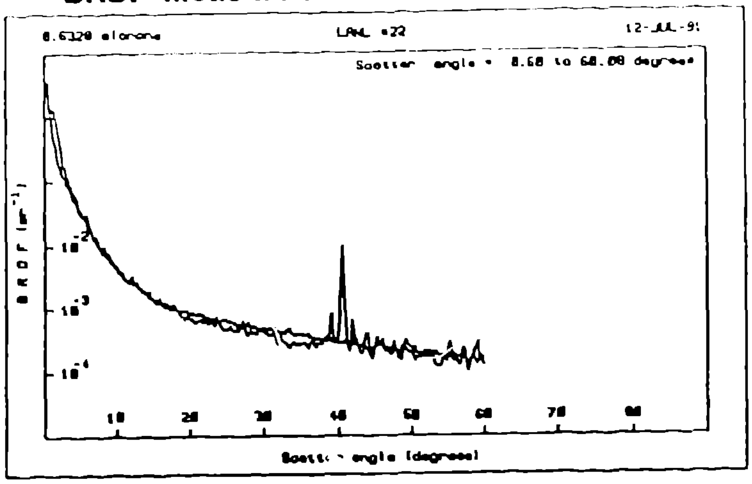

Fig. 1. ETP Copper with TCA and Ethanol Rinse

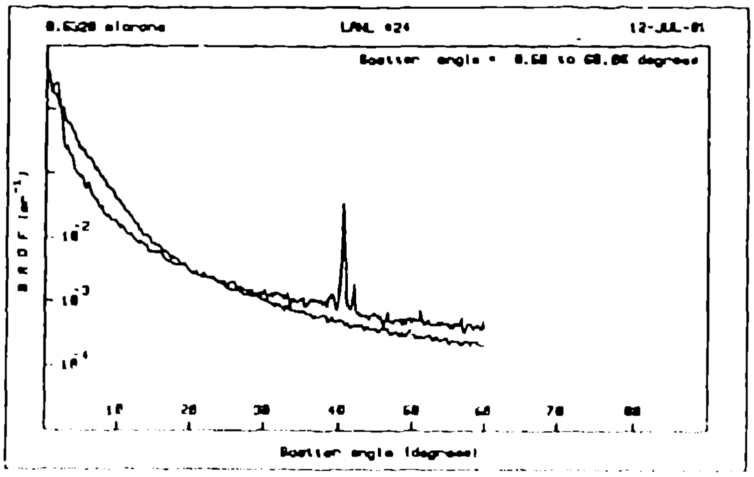

Fig. 2. ETP Copper with PF Rinse

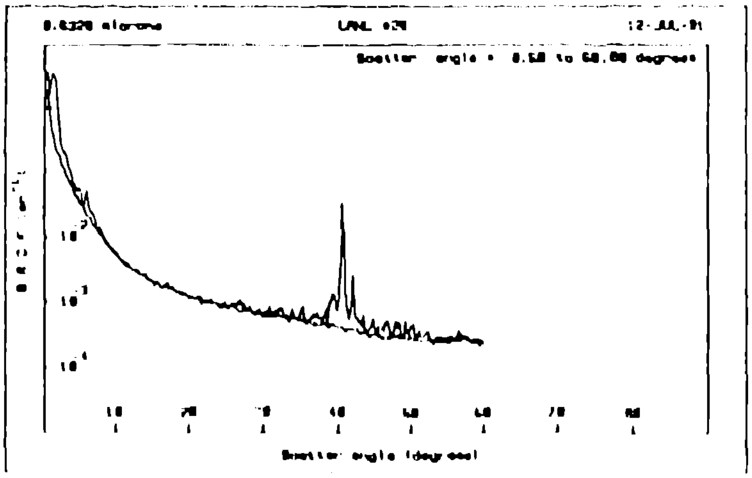

Fig. 3. ETP Copper with PF and Ethanol Rinse

BRDF Measurements on 6061 Aluminum

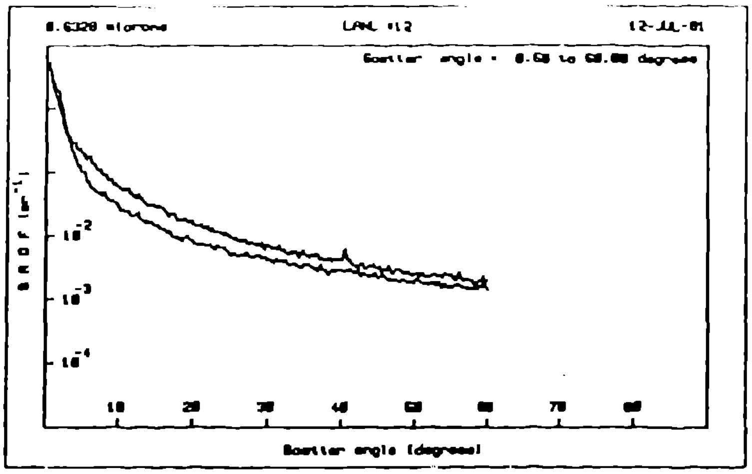

Fig. 4. 6061 Aluminum with TCA and Ethanol Rinse

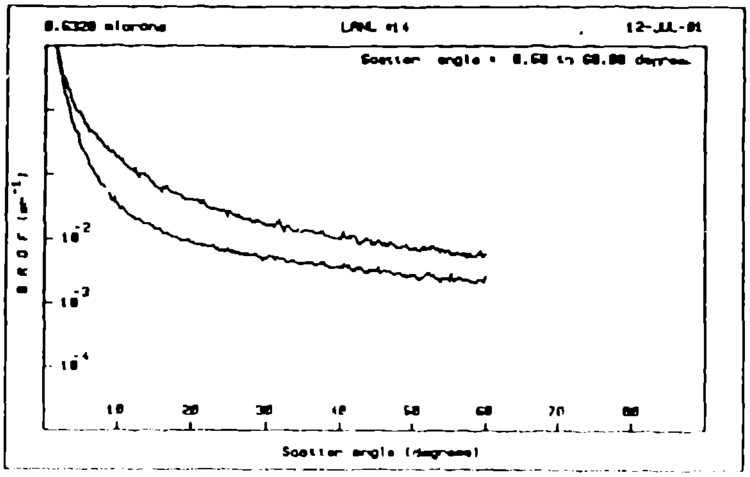

Fig. 5. 6061 Aluminum with PF Rinse

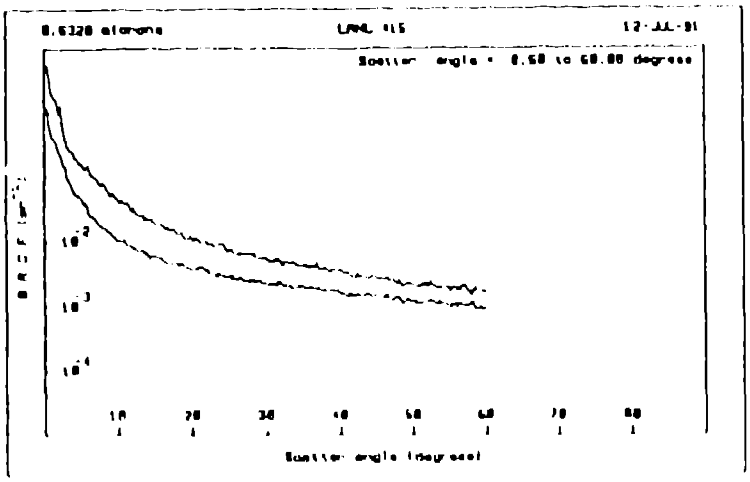

Fig. 6. 6061 Aluminum with PF and Ethanol Rinse

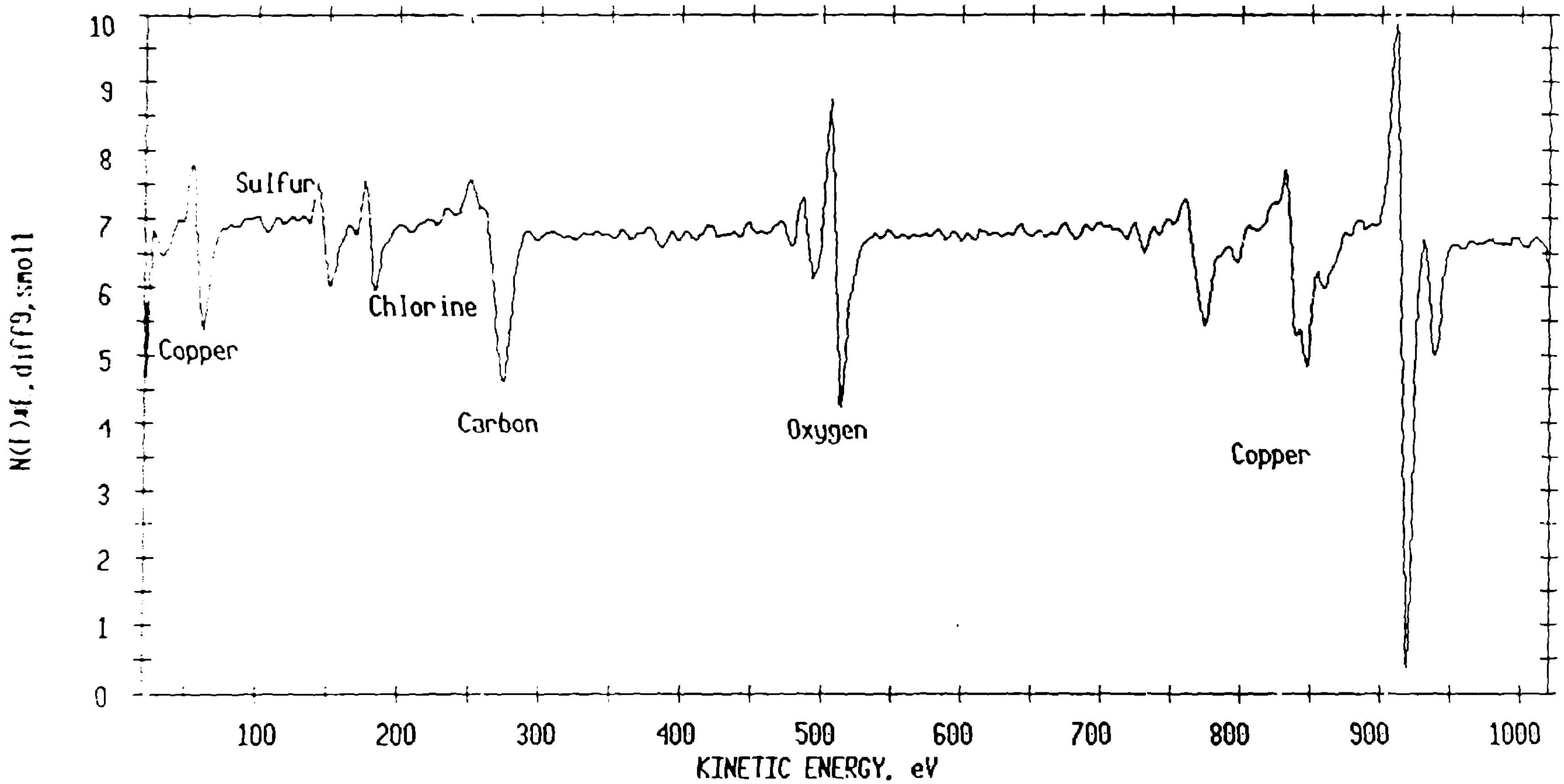

Fig. 7. Auger Spectrum for Artifically Aged ETP Copper

Depth Profiles for ETP Copper
Sputtering Rate is 100 A/Min

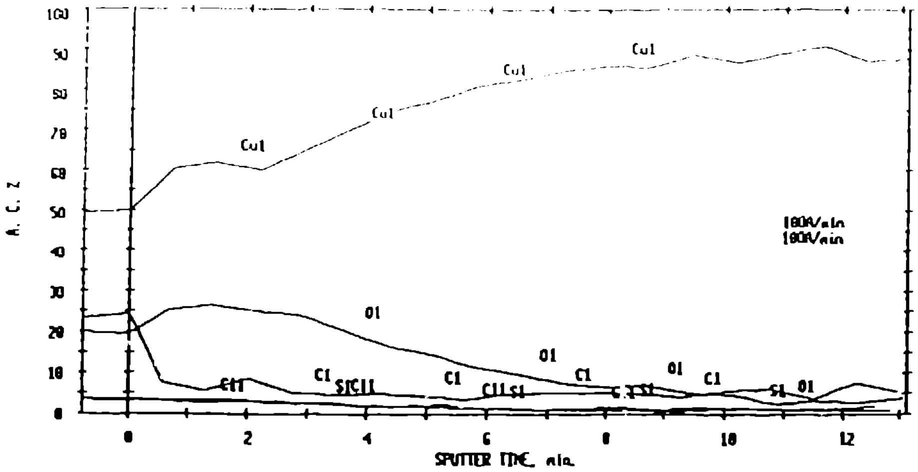

FIG. 8. TCA ETHANOL

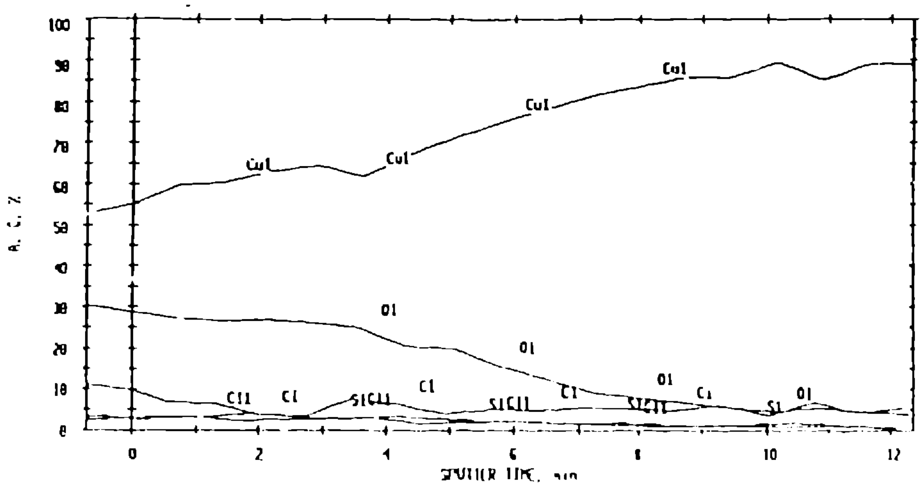

FIG. 9. PF/ETHANOL

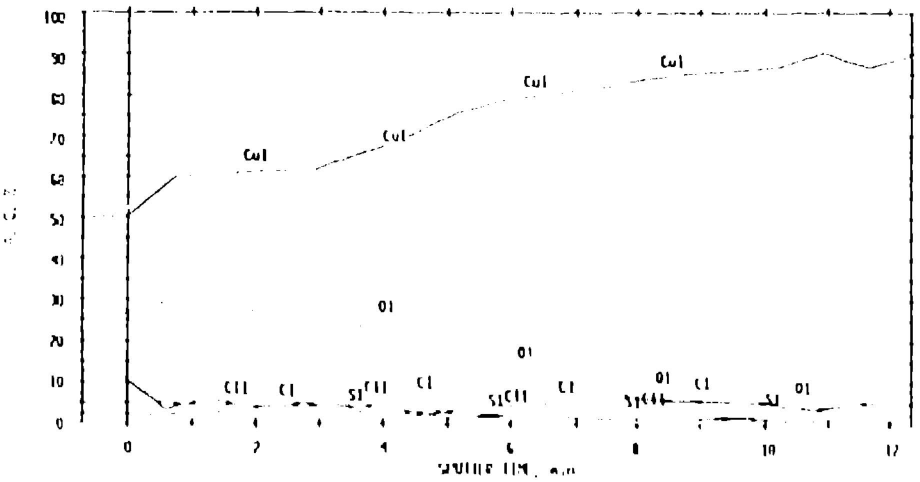

FIG. 10. PF/ONLY

Depth Profiles for 6061 Aluminum
Sputtering Rate Is 200 A/Min

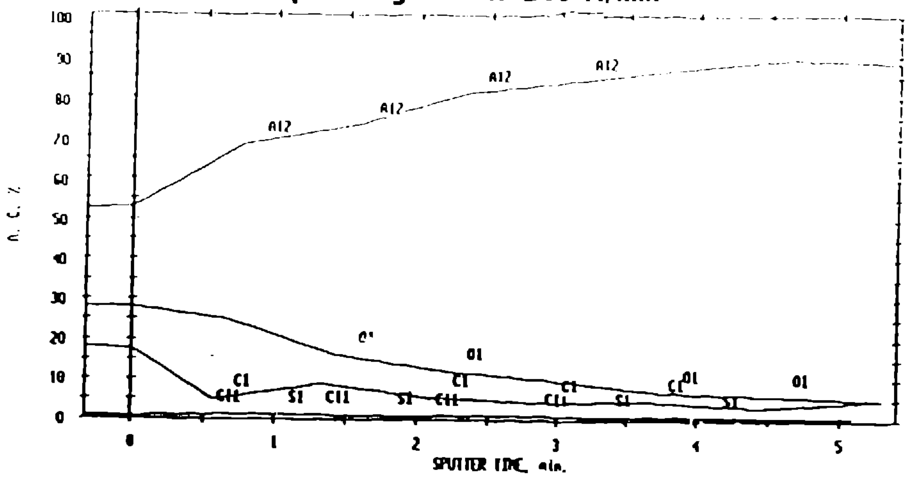

FIG. 11. TCA/ETHANOL

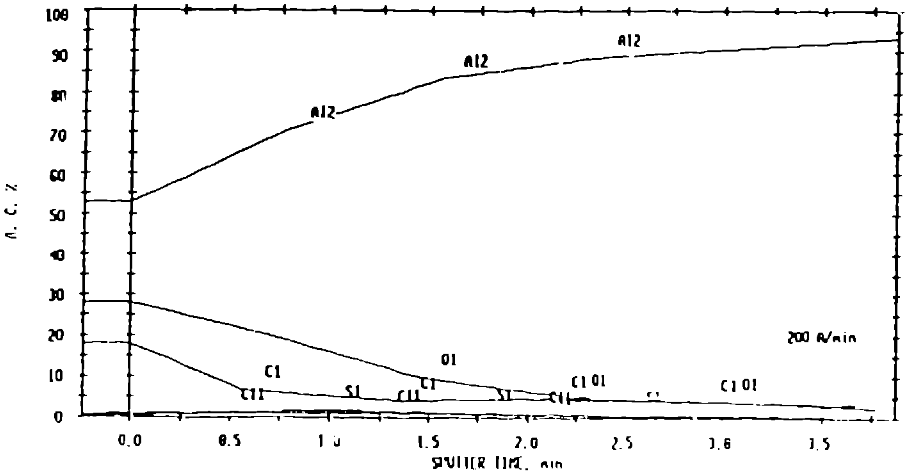

FIG. 12. PF/ETHANOL

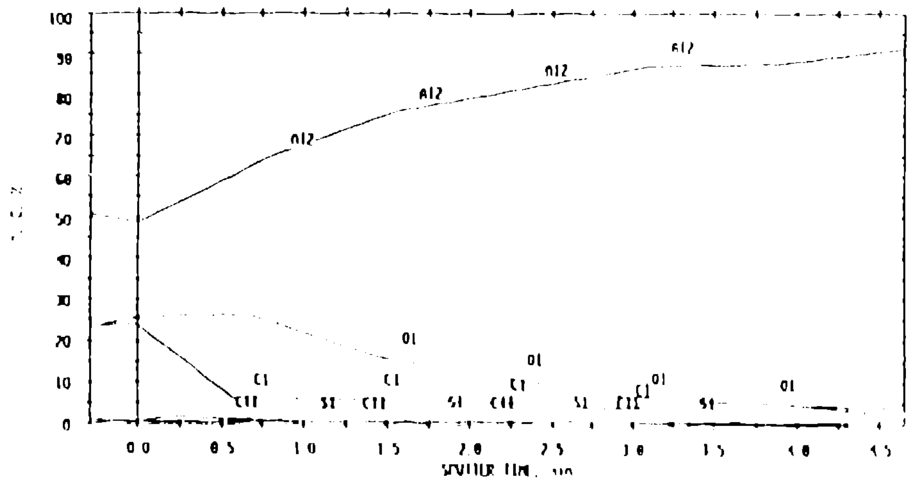

FIG. 13. PF/ONLY

LA-UR-91-3441

--24

LA-UR--91-3441

DE92 003801

TITLE Portable Radiation-Detection Instruments for Distinguishing Nuclear from Non-nuclear Munitions

AUTHOR(S) Paul E. Fehlau

SUBMITTED TO IEEE Nuclear Science Symposium
November 2-9, 1991
Santa Fe, New Mexico

Los Alamos Los Alamos National Laboratory
Los Alamos, New Mexico 87545

PORTABLE RADIATION-DETECTION INSTRUMENTS FOR DISTINGUISHING NUCLEAR FROM NON-NUCLEAR MUNITIONS

Paul E. Fehlau
Los Alamos National Laboratory, Los Alamos, New Mexico 87545

Abstract

The emission of gamma rays and fast neutrons by nuclear materials provides a simple means for distinguishing between real nuclear munitions and other assemblies that are non-nuclear, such as nuclear-explosive-like test assemblies (NELAs) and conventional munitions.

The presence or absence of significant numbers of neutrons and characteristic plutonium gamma rays are distinguishing attributes for plutonium munitions. The presence of energetic gamma rays from ^{232}U daughters, if present in sufficient number, is a distinguishing attribute for highly enriched uranium munitions. Some portable instruments are being developed for verifying that munitions are or are not nuclear, and others are already commercially available. The commercial ones have been evaluated for pre-flight non-nuclear verification of NELAs in Air Force flight tests.

I. INTRODUCTION

Radiation detection provides a convenient means to test one or more attributes of a nuclear munition to verify that it is consistent with expectations. For example, the emission of penetrating, characteristic gamma rays and neutrons from nuclear munitions containing low-burnup plutonium can be used to distinguish them from either conventional munitions or test munitions that are non-nuclear, nuclear- explosive-like assemblies (NELAs). Similarly, munitions containing highly enriched uranium (HEU[1]) may be distinguished from NELAs by measuring penetrating gamma rays, provided that sufficient amounts of the isotope ^{232}U and its daughters are present in the HEU. Some form of background may be present for any of these radiations, but the backgrounds are usually low.

II. NUCLEAR MATERIALS RADIATION

Almost all nuclear materials are radioactive and emit one or more types of radiation, including neutron, alpha, and beta particles and photon bremsstrahlung, x-rays, and gamma rays). The radioactive emissions penetrate nuclear or encapsulating materials with differing degrees of effectiveness. Alpha and beta particles and low-energy photons, for example, are readily attenuated, making them suitable only for verifying a material type, such as verifying that bare, depleted-uranium parts are not highly enriched. Neutrons and gamma rays from plutonium are more penetrating and are available as a verification signature outside of an assembled nuclear munition.

Low-burnup plutonium contains about 6% of the ^{240}Pu isotope and emits both penetrating fast neutrons and intense, penetrating, characteristic gamma rays in the energy region between 330 and 450 keV. HEU, however, emits few neutrons, and its 185-keV gamma rays have limited penetration. Other uranium isotopes that may be present in HEU do have decay chains that lead to emission of penetrating gamma rays; for example, ^{232}U at 0.86 and 2.6 MeV and ^{238}U at 766 and 1001 keV. However, for HEU, the intensity of these higher energy gamma rays may be relatively low, and large detectors and long counting times may be needed to detect them. Another factor for these radiations is that they are often present in natural backgrounds, hence, using them for non-nuclear verification may give less confidence in the result than would other methods.

III. PORTABLE INSTRUMENTS

Portable instruments for distinguishing munitions can be as basic as a simple alpha detector used to measure the surface alpha-emission rate of bare uranium, munition parts, or they can be as complex as a portable multichannel analyzer (MCA) and high-purity germanium (HPGe) detector used to measure high-energy uranium-daughter radiations from an assembled munition. The middle ground is a class of portable, hand-held instruments that often are small, battery-powered, and have internal radiation detectors for ruggedness and microprocessor control for versatility. These instruments can be readily specialized for verifying that plutonium is either present or absent in a munition.

The specialized instruments use either a neutron-specific radiation detector to detect plutonium neutrons or a gamma-ray detector and firmware to strip a characteristic plutonium region-of-interest (ROI) from a broad gamma-ray spectrum.

The sections that follow give examples of the following: (1) neutron verification instruments based on scintillation or proportional-counter fast-neutron detectors, and (2) gamma-ray verification instruments that use the 330- to 450-keV gamma-ray region as a signature for the presence of plutonium.

---

[1] Enriched uranium is a nuclear material that contains more than the natural amount of the isotope ^{235}U. HEU contains 93% of the isotope.

IV. NEUTRON INSTRUMENTS

A. *Thermal Neutron Detectors*

Thermal neutron detectors are used to discriminate between real and other munitions because they can predominantly measure the neutrons in a mixed (neutron and gamma-ray) radiation field. However, the neutrons emitted by plutonium are fast neutrons so a polyethylene detector moderator is used to provide thermalization.

The two types of thermal neutron detectors in use are scintillation detectors based on enriched lithium (^{6}Li), and ^{3}He proportional counters. In these detectors, the gamma-ray response can be suppressed by using pulse-height discrimination, as is illustrated (Fig. 1) by the pulse-height spectra for enriched-lithium scintillators. The moderated ^{6}LiI(Eu)-scintillator[2] response to a ^{252}Cf fast-neutron source in (Fig. 1a) has a distinct peak region at the right from thermal and epithermal neutron interactions and a low-energy continuum region at the left from gamma-ray interactions. The two regions can be separated at the threshold of the neutron region by a pulse-height discriminator that will exclude gamma-ray pulses from environmental sources and other materials (such as depleted uranium) that may be found in NELAs.

The second scintillator in Fig. 1 is BC 702[3], which comprises an enriched-lithium compound mixed with a ZnS(Ag) phosphor and encased in transparent plastic. Its pulse-height spectrum (Fig. 1b) is a less intrusive one that does not give spectral information in either the gamma-ray or neutron regions. The spectrum shows only a gamma-ray spike at very low energy and a diminishing continuum of neutron pulses over most of the range. A pulse-height discriminator set just above the gamma-ray spike effectively separates the gamma-ray response from the neutron response. The situation for ^{3}He is much the same [1], and a discriminator readily excludes any gamma-ray response.

Fig. 1 Neutron reactions in the ^{6}LiI(Eu) scintillator (a) produce a peak region at the right, and gamma-ray interactions lead to a continuum of decreasing pulse heights at the left. In BC 702 (b), neutrons give the broad continuum, and gamma rays simply produce a spike at the extreme left.

B. *Hand-Held Neutron Verification Instruments*

Two manufacturers have commercially produced a hand-held neutron verification instrument originally developed [2] at Los Alamos for non-nuclear verification of NELAs. The Jomar Systems[4] JHH-22 and the TSA Systems[5] NNV-470 both use a moderated ^{6}LiI(Eu) scintillator and pulse-height discrimination to detect fast neutrons. The detector is moderated by surrounding it with horseshoe-shaped polyethylene and an acrylic light pipe (Fig. 2). Because munitions may provide some moderation, the moderator is thin in the most likely source direction, below the instrument's base.

Both the Jomar and TSA instruments were originally developed as prototypes for last minute verification that NELAs do not contain plutonium. The NNV-470 was selected for further development and now includes features that address the human factors involved in prelaunch, non-nuclear verification of NELAs carried by aircraft. These features include a large folding handle, membrane switches, and display illumination to facilitate using the instrument in a cold, dark environment by a person wearing foul-weather gear. Figure 3 shows the instrument being used, under less rigorous circumstances, by an operator from Sandia National Laboratories, the lead laboratory for implementing routine military use of the instrument. Besides the munition measurement in progress in Fig. 3, both background measurements and before and after radioactive source checks of the instrument are included in the verification procedure.

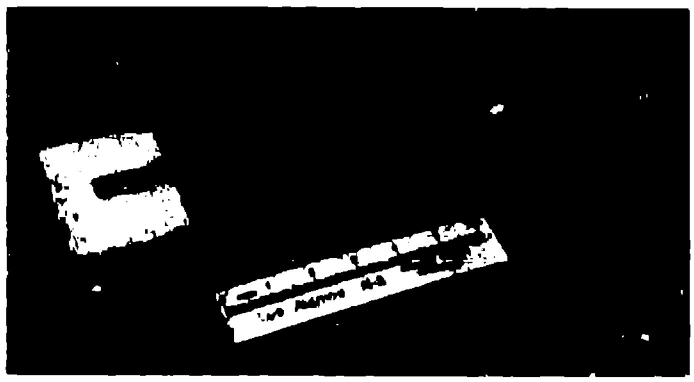

Fig. 2 The moderator and light pipe in the neutron verification instrument surround a ^{6}LiI(Eu) scintillator, which has an active volume that is 2.5 cm in diameter and 0.2 cm thick. The photomultiplier is a Hamamatsu type R1924 that is 2.5 cm in diameter and 7.5 cm long.

[2] Solon Technologies, Inc., Solon, Ohio 44139
[3] Bicron Corp., Newbury, Ohio 44065

[4] Jomar Systems, Inc., Los Alamos, NM 87544
[5] TSA Systems, Ltd., Longmont, CO 80501

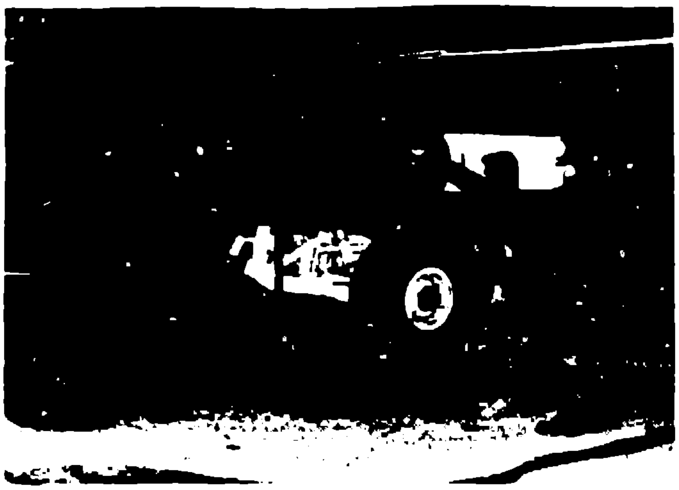

Fig. 3 Last minute, preflight verification of NELAs uses 20-s measurements and requires just a few minutes overall when carried out with the hand-held neutron verification instrument.

C. Field Experience with the Hand-Held Neutron Instruments

During one year of field use of the neutron verification instruments by Sandia operators, three 20-s measurements were used at each step in the verification procedure. After each 20-s measurement, the instruments sound a beeper, display the result, and begin a new measurement. Reference 3 reviews the measurement results obtained during the year, including reference measurement results for real munitions (Fig. 4). The real-munition results with the NNV-470 are proportional to similar measurement results from routine verifications carried out with a less portable MCA and shielded neutron-assay probe (SNAP) detector [4] at the Pantex plant. The approximately four-times-higher intrinsic efficiency of the SNAP detector, estimated at 10% in Ref. 4, allows the plant to shorten their measurement times to 10 s. The corresponding measurement results for NELAs during prelaunch, non-nuclear verification were all close to background and at least a factor of 10 below results for the real munition.

D. Prototype Instruments for Treaty Verification

Besides the standard NNV-470, two prototype hand-held instruments using the less intrusive, and somewhat less sensitive, BC 702 scintillator have been produced as prototypes for possible application to arms-control verification. These instruments achieve the same intrinsic detection efficiency as the NNV-470 for bare sources by using a larger (3.75-cm) diameter for the BC 702 scintillator to give it about twice the area of the original ^{6}LiI(Eu) scintillator. However, the BC

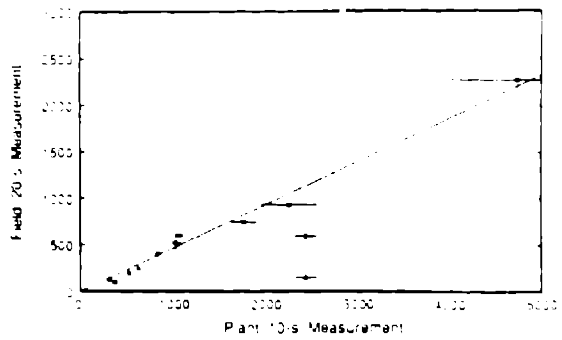

Fig. 4 The NNV-470 field results (y-axis, 20-s measurements) for real munitions show good proportionality with the corresponding Pantex confirmation results (x-axis, 10-s measurements). The outlying open-symbol points are for munitions in shipping containers or launch vehicles.

702-detector intrinsic efficiency for moderated sources is still expected to be somewhat lower than the original detector.

One of the prototype instruments appears identical to the original NNV-470, but is slightly heavier at 1.5 kg. The second prototype has a much different appearance because its detector assembly is mounted at the end of an extendable pole. The extended detector provides measurement access to munitions that, for whatever reason, are not within an arm's reach with the original instrument.

A much different prototype arms-control instrument for detecting neutrons from munitions more than an arms length away is a portable, self-contained, 10-kg, briefcase counting system that uses moderated ^{3}He proportional counters for its detector. The 5-cm-diam, 25-cm active length, proportional counters are mounted in hemi-cylindrical polyethylene moderators and have a high counter-gas pressure (10 A). These design features, described further in Ref. 5, provide good detector response to both bare and moderated neutron sources. The briefcase uses a Motorola 68HC11 microprocessor, a large LCD, and a 512-kbyte mass-storage RAM card to permit it to search for neutron sources, verify munitions, or monitor and display time-histories of neutron intensity.

V. GAMMA-RAY INSTRUMENTS

A. Hand-Held Gamma-Ray Verification Instruments

Gamma-ray verification instruments for plutonium munitions must reliably determine the energy of detected gamma rays and record their number for later analysis. The net intensity in a characteristic gamma-ray ROI can then be used to distinguish between real weapons and NELAs. To be effective, the radiation detector must be very stable. The Jomar JHH-01 verification instrument uses a NaI(Tl) scintillator that is stabilized by monitoring pulses from a light emitting-diode (LED) reference light source inside the detector

By gauging the LED pulse height, the instrument can determine the amount of gain adjustment that may be needed. This non-radioactive approach to stabilization makes the instrument more readily transportable than if a radioactive light pulser had been used. During tests of the first JHH-01 instruments, the LED stabilization maintained a 662-keV gamma-ray pulse within 2% of its mean pulse height over a temperature range of 8 to 40 °C [6]. This type of instrument is now commercially available from Jomar with the model number JHH-31.

The JHH-01 and JHH-31 instruments use a 330- to 450-keV plutonium ROI and two narrower regions centered on 330 and 450 keV for verification measurements (Fig. 5). The net peak intensity for the central region is obtained by using the two adjacent narrow regions to estimate the amount of underlying Compton-scattered radiation that must be subtracted. The instrument makes simultaneous 20-s-long measurements in each region, then calculates the net intensity in the central region and displays it. The net intensity for real munitions and NELAs can be markedly different; although, the differences are not always as great as with neutron detection. Hence, when gamma-ray verification is used for plutonium munitions, it is not unusual for neutron verification to be used as well.

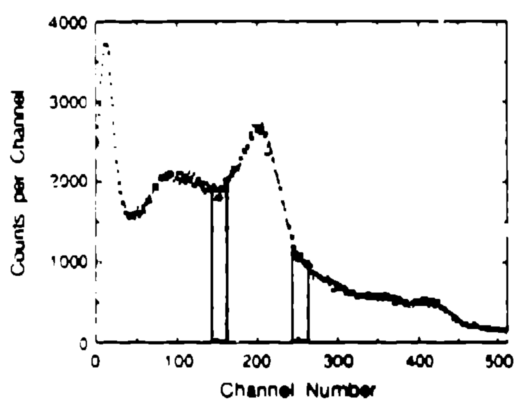

Fig. 5 The 330- to 450-keV peak region between the shaded regions is characteristic of plutonium. The shaded regions are used to estimate the underlying Compton scattered radiation, in this case from a 0.5-cm-thick depleted uranium plate shielding the plutonium.

B. Portable Gamma-Ray Verification Instruments

Portable MCAs and radiation detectors are the only choice, at present, for verifying that assembled munitions contain only HEU by measuring ^{232}U-daughter gamma rays. One of the small, commercial MCAs and a large NaI(Tl) or a HPGe detector are used. The more intense 0.86-MeV gamma ray usually penetrates well enough to offer shorter measurement times than for the 2.6-MeV gamma ray. Hower, the intensity of either one depends on ^{232}U being present in the HEU. For domestic applications, a representative sample of the real munition can be measured, and the average result is then available for determining decision thresholds for NELA verification. The arms-control application may not provide the same degree of assurance that these gamma rays are present in real munitions.

More portable, MCA-based instruments are being developed for verification applications. One commercial prototype is the TSA Systems MCA-465, just now appearing on the market. As yet, the MCA-465 is still being evaluated and any problems discovered will have to be corrected before it becomes a useful product. The concept behind the MCA-465 is a hand-portable, battery-operated MCA that uses either an internal or external NaI(Tl) detector for identifying gamma-ray emitting materials. Besides viewing spectra on an LCD, the operator can store up to 14 spectra for later transmission to a PC. Calibrating the detector is done by using a reference source and the calibrate mode to observe and move a selected gamma-ray peak to a desired channel by means of keyboard input. The nominal conversion gain is 8 keV/channel. ROIs can be set by the user, and the counts falling within each ROI can be displayed.

Another portable MCA instrument prototype is being developed for treaty verification applications where the operator needs very little information other than a simple yes or no. The instrument is the NAVI and is described elsewhere in these proceedings [7]. Its unique features include (1) its ability to identify either of two gamma-ray calibration sources and use three peaks from the spectrum to automatically calibrate the MCA, and (2) its ability to make its own determination of when it has sufficient data to make a decision about whether or not plutonium is present.

VI. CONCLUDING REMARKS

Portable radiation-detection instruments can be a useful and convenient means for distinguishing between nuclear and non-nuclear munitions. Their usefulness is best assured when close approach to the munition is allowed for verification and an opportunity is provided beforehand to establish decision thresholds from measurements of representative real munitions. Furthermore, easily and effectively using the instruments rests on the user being trained in their use and being given sufficient opportunity to maintain proficiency by practicing the verification procedures. Scheduled instrument maintenance is also necessary and should include calibration, measurements of standard sources to confirm normal operation, and a review of accumulated verification results for measurement control.

VII. ACKNOWLEDGMENTS

Many individuals in the Advanced Nuclear Technology Group at Los Alamos and present and past members of the Stockpile Evaluation organization at Sandia have provided valuable assistance in developing the instruments and procedures described here. The instrument manufacturers and DOE, Sandia, and many DoD representatives have also

provided valuable service toward achieving many of the goals involved in implementing a program of non-nuclear verification.

VIII. REFERENCES

[1] T. W. Crane and M. P. Baker, "Neutron Detectors," in "Passive Nondestructive Assay of Nuclear Material," T. D. Reilly, N. Ensslin, and H. A. Smith, Eds., U.S. Nuclear Regulatory Commission contractor report NUREG/CR-5550 (March 1991), p. 384.

[2] P. E. Fehlau, "Rugged, Lightweight, and Long-Operating Hand-Held Instruments for Neutron and Gamma-Ray Verification Measurements," *Proc. 22nd Midyear Topical Meeting of the Health Physics Society on Instrumentation*, San Antonio, Texas, December 4-8, 1988. Los Alamos National document LA-UR-88-2780 (November 1988).

[3] Paul E. Fehlau, "Field-Trial Results for Pre-Flight Non-Nuclear Verification in Air Force NELA Flight Tests," Los Alamos National Laboratory report LA-12006-MS (January 1991).

[4] R. B. Walton and T. L. Atwell, "Portable Neutron Probe, 'SNAP'," in "Nuclear Analysis Research and Development Program Status Report, January-April 1973," Los Alamos Scientific Laboratory report LA-5291-PR (May 1973), p. 14.

[5] P. E. Fehlau, W. S. Murray, K. B. Butterfield, and H. F. Atwater, "Hand-Held Verification Instruments for Intrinsic Radiation Detection," Los Alamos National Laboratory document LA-CP-89-332 (August 1991).

[6] P. E. Fehlau and G. Wiig, "Stabilized, Hand-Held, Gamma-Ray Verification Instrument for Special Nuclear Materials," *IEEE Trans. Nucl. Sci.* **NS-36**, 1160-1165 (February 1989).

[7] K. B. Butterfield, W. S. Murray, L. E. Ussery, and D. R. Millegan, "Portable Gamma-Radiation Analyzer for Treaty Verification," paper presented at the *IEEE 1991 Nuclear Science Symposium*, Santa Fe, NM, November 5-9, 1991.

LA-UR -91-3443

LA-UR--91-3443

DE92 003872

TITLE The Performance of a Single-Crystal BGO Annulus as a Compton-Suppression Detector

AUTHOR(S) Scott K. Matthews and Larry E. Ussery

SUBMITTED TO IEEE 1991 Nuclear Science Symposium
November 2-9, 1991
Santa Fe, New Mexico

Los Alamos National Laboratory
Los Alamos, New Mexico 87545

The Performance of a Single-Crystal BGO Annulus as a Compton-Suppression Detector

Larry E. Ussery
Los Alamos National Laboratory, Los Alamos, NM 87545

Scott K. Matthews
The George Washington University, Washington, D.C. 20052

Abstract

We have tested a single-crystal bismuth-germanate annulus in conjunction with a high-purity germanium detector as a Compton-suppression spectrometer, and have measured gamma-ray energies of up to 6.13 MeV.

I. Detector Description

We have tested a single-crystal BGO annulus (shown in Fig. 1) in conjunction with an Ortec high-purity germanium (HPGe) detector as a Compton-suppression spectrometer. Because the Compton cross section is forward peaked at higher energies, we have specified an annulus with most of the material in the forward scattering direction to maximize sensitivity at higher energies. A single phototube was chosen to enhance portability, although others have found that several phototubes improve the response[1]. The energy resolution measured with the annulus for 662-keV gamma rays from ^{137}Cs was about 40%.

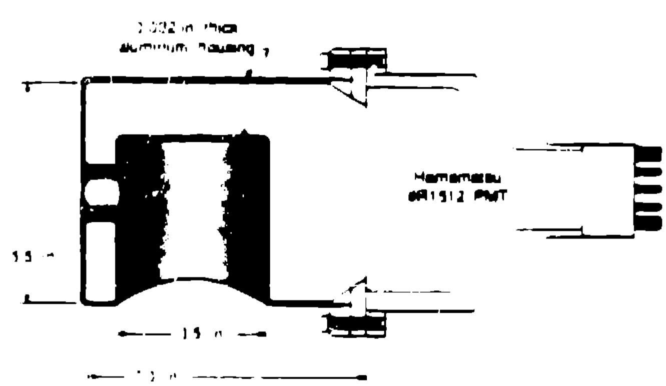

Fig. 1. Harshaw single-crystal BGO annulus and phototube

Figure 2 shows the counting circuit. Both sides of the veto circuit are identical and produce logical signals about 400 ns wide. A pre-amp is used with each detector, although it may not be necessary for the BGO. The final coincidence was made ~4 μs wide to accommodate the spectroscopy amplifier's pulse width. Data were collected with a multichannel buffer and a computer readout. The time resolution of the veto circuit was about 60 ns.

II. Detector Performance

In previous work with a BGO-based Compton-suppression system, Hildingsson et al.[1] found that a very low BGO threshold was necessary to accommodate multiply-scattered gammas. Figure 3 shows some of the suppression ratios (that is, the gated spectrum divided by the ungated spectrum) from Hildingsson's work[1] and the BGO thresholds for each ratio. We can see that a BGO threshold of 15 keV was necessary for the best suppression results. The present annulus is housed in a 0.032-in.-thick aluminum skin. The minimum transmission energy for this much aluminum is around 30 keV. Figure 4 shows the effect of BGO threshold on the suppression for the present detector. The top curve corresponds to about zero threshold (no lower threshold had any effect), so we expect that this is the limit imposed by the aluminum skin.

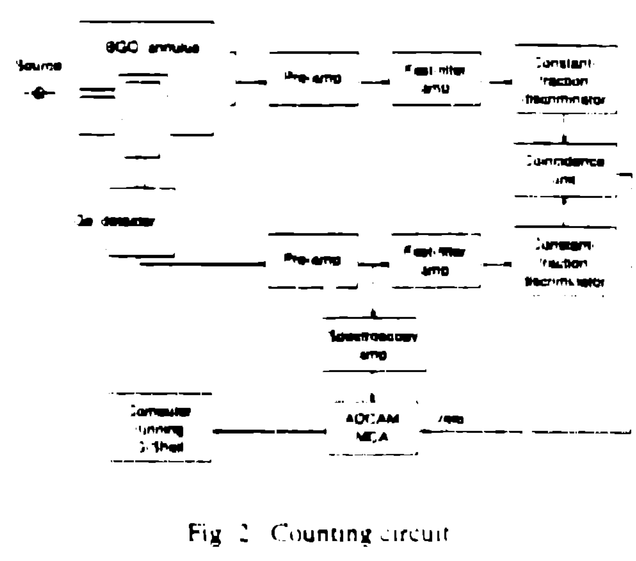

Fig. 2. Counting circuit

The very dense BGO should provide good shielding, which turns out to be the case. Although all other measurements were made with both detectors inside of a lead brick cave, we made two measurements outside of the cave for comparison. Fig. 5 shows these results. The lowest curve is an ungated spectrum with the detector inside the BGO and the lead cave in place. The middle curve is an ungated spectrum taken with the HPGe detector still inside the annulus, but with all of the lead removed. Finally, the upper curve is the spectrum taken with the HPGe detector ungated and unshielded. We can see that the BGO does a credible job as a shield for these kinds of measurements. Recall that there is a rather large hole in the BGO to admit the primary detector, and in the second curve, this constitutes a hole in the shielding. Furthermore, since this detector is designed primarily for use at higher energies where the background is negligible, it would be desirable to dispense with the lead if the "hole" could be plugged. For example, a secondary detector could be placed behind the HPGe (inside the detector case) to act both as a shield and as a detector, since the annulus loses a lot of counts in this direction.

A common way to characterize gamma spectroscopy systems is by measuring the peak-to-Compton ratio, which is defined as the ratio of the number of counts in the highest channel of the 1.33-MeV peak to the average number of counts between 1.040 MeV and 1.096 MeV in the ^{60}Co spectrum. Figure 6 shows gated and ungated ^{60}Co spectra. Table I shows the associated peak-to-Compton ratios (an improvement of about 200% for the gated results), as well as the ratio quoted by the detector manufacturer.

Table I
Peak-to-Compton ratio

Ge quoted	Ge measured	Ge plus BGO
70	54	152

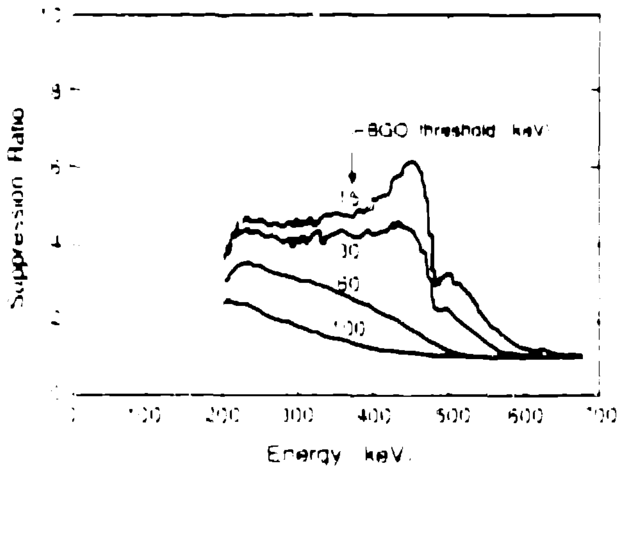

Fig. 3. Suppression ratio (ungated/gated) from Hildingsson et al. [?] shows the effect of threshold variation on gated spectra.

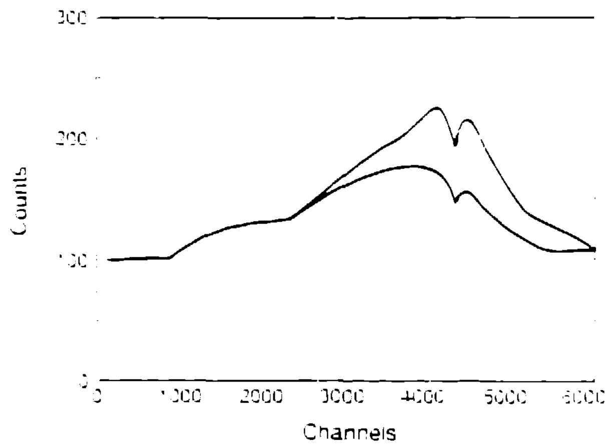

Fig. 4. Suppression ratios for our system.

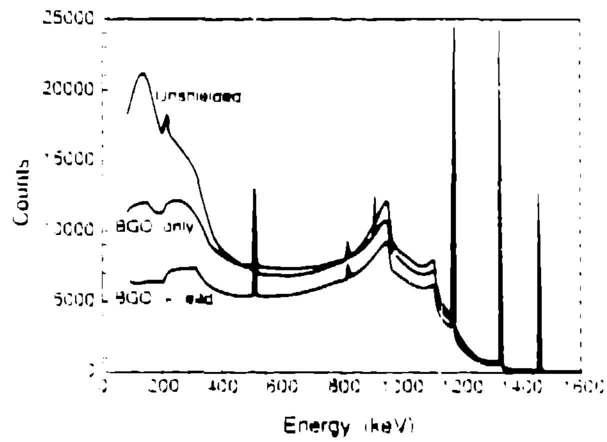

Fig. 5. Shielding effects.

Figure 7 shows spectra from an encapsulated ^{241}Am and ^{13}C source, which produces a gamma-ray spectrum with a primary gamma ray at 6.13 MeV and several prominent gammas above and below this peak. There is significant improvement in the high-energy spectrum: many peaks that are not prominent enough to be seen above the noise in the ungated spectrum become visible when the Compton veto is used. For example, Fig. 8 shows an expansion for the gated and ungated spectra of the area around 7915 keV. In the gated spectrum, we can see a peak from gamma rays produced by neutron capture on Cu (neutrons are produced in the source); this peak is not distinguishable in the ungated spectrum. Other peaks in this area are obviously much clearer as well.

The veto circuit is also valuable for eliminating counts from first and second escape peaks in the primary detector. Table II shows the ratios of counts in the 6130-keV photopeak to counts in the first and second escape peaks for the gated and ungated spectra. The ratio for the first escape peak is improved by a factor of 3 and the ratio for the second escape is improved by a factor of 7. Fig. 9 shows this spectra expanded around these peaks. Because the annihilation photons should be produced isotropically in the primary detector, the cave entrance subtracts significantly from the escape peak suppression [illegible]

Table II
Escape peak suppression

	Primary First Escape	Primary Second Escape
Ungated	1.16	2.18
Gated	2.97	14.4

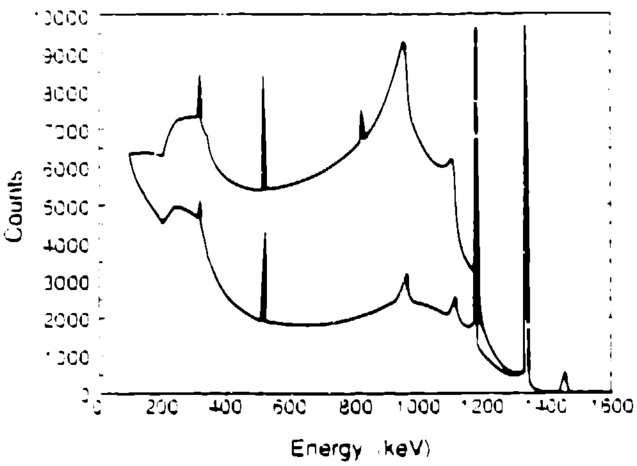

Fig. 6. ^{60}Co spectra, gated and ungated.

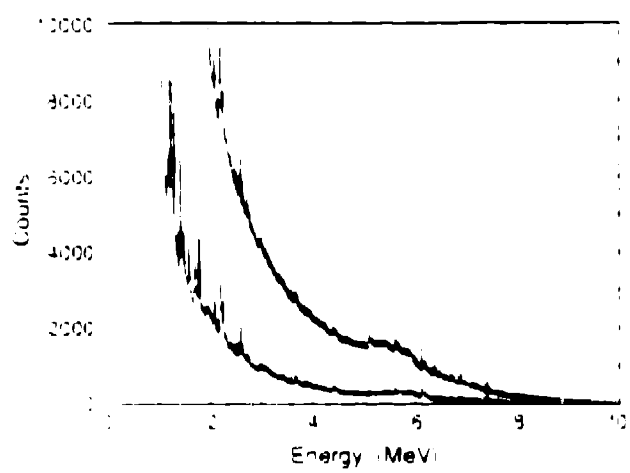

Fig. 7. Spectra from the ^{241}Am and ^{13}C source, gated and ungated.

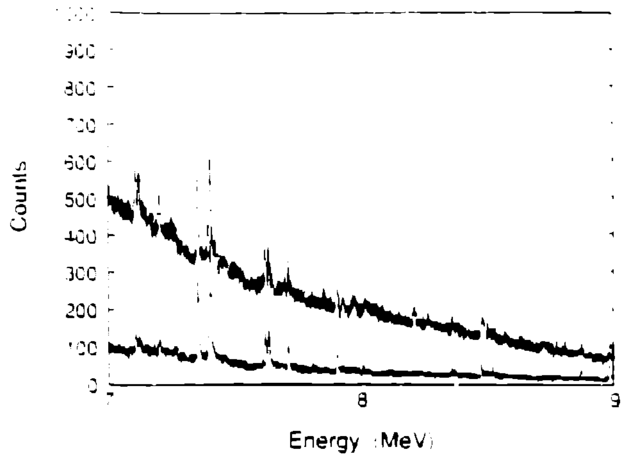

Fig. 8. ^{13}C/^{241}Am spectra, above 6130 keV.

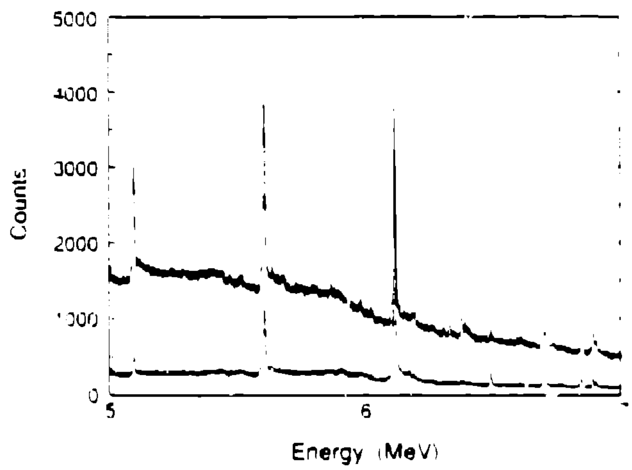

Fig. 9. 6130-keV γ, primary and escape peaks.

In conclusion, the veto circuit significantly improves the quality of spectra for gamma rays in the few MeV range. The main problems are the large sizes of the detector cave entrance, which could be plugged with an extra BGO detector in the HPGe housing, and the thickness of the aluminum skin, which could be replaced with something thinner or more transparent.

III. Reference

[1] L. Hildingsson et al., "Transverse BGO Compton Suppression Shield," *Nuclear Instruments and Methods*, **A252** (1986) pp. 91-94.

LA-UR -91-3446

LA-UR--91-3446

DE92 002523

TITLE MATERIALS AND SUPERCONDUCTING ELECTRONICS

AUTHOR(S) James L. Smith, ERDC

SUBMITTED TO Proceedings of the Superconducting Digital Circuits and Systems Conference ed. by E. Edelsack, George Washington Univ. Press (1991)

Los Alamos National Laboratory
Los Alamos, New Mexico 87545

MASTER

MATERIALS AND SUPERCONDUCTING ELECTRONICS

James L. Smith
Los Alamos National Laboratory

At Los Alamos we make things out of gold. I don't know why the TV has been on all morning. This is an example of what Keyworth says about consumer products, that it is okay if it is cold or hot inside, as long as the consumer doesn't know.

And remember that we must keep these things warmed up. That is why, if you want to save electricity, you unplug it. The consumer wants it on very fast.

I am not an electronics expert. Remember a few years ago that we all said that the real applications of the high T_c's will be those things that we can't think of yet, and it seems to me that in electronics, for the most part, that what has been done is unchanged from the low temperature materials.

In fact, the only difference with the high T_c materials is that you can't make a tunnel junction.

Bruce Murdock had asked me over a year ago about these materials. I mean, the question is, is there some thing that we can do with high T_c material that we can't do with low T_c materials, and I am going to talk about a couple of things today that we haven't tried. They are just ideas.

It seemed to me yesterday that it was very depressing when Paul Chu showed the roller coaster, with Chuck Byvik talking about all the gray men, the sort of graying national capability, and David Chaffee was very quiet at lunch yesterday.

He has "Superconductor Week," and I think he must have been wondering what kind of job he is going to have next. Let's not forget some of the glow we all felt a couple of years ago!

I mentioned M. K. Wu at National Tsing Hua University to David. He has this group of about 30 people, and they looked to me like they were all under 20. So there are other parts of the world where people are still trying to hustle, and I will try to give you a feeling for some of the things that we haven't done yet that we might do.

For making thin films for electronics, materials compatibility suggested the substrates for high T_c, Perovskite materials. We have been using things like strontium titanate, but funny thing, these are plagued by lattice transformations.

You cool the thing down from the temperature where you make the film, or you cool it down below room temperature, and there is a transformation. The thing twins, and it messes up your superconducting properties.

Incidently, the connection between the Perovskite-related high T_c materials and the real Perovskites, with all of their lattice transformations, in fact, tells you a little of the physics about why these things are superconducting. It is not some magnetic interaction.

The point is that this is a problem. Our substrates are no good. We need a cubic Perovskite which is something, in the low temperature limit, that is essentially impossible to find.

This is what I thought about after Bruce asked me what we could do. The point is, consider what these lattice changes can do for you, and I will remind you first about piezoelectrics because the guys who do ultrasonics are always impressive.

I mean, they understand that the oscillations they are getting in piezoelectrics are really tensor quantities. I mean, they can do transverse waves, longitudinal waves; they do shear waves. I don't even know all of these things that these guys do, but it is really impressive what you can do with a piezoelectric.

And the point is that rather than put a tiny little piezoelectric onto a big superconductor to check its properties, why not take a big piezoelectric and put a little superconducting film on and see what the properties of the film are. What kind of devices can we make out of this?

The same thing works with ferroelectrics. I mean, ferroelectrics give you a hysteretic device. I don't know how fast you can do these things. I looked up a little bit last week, and I found one old reference that said you could do a transformation that goes a half a meter in a microsecond, and that struck me as too fast. That is much faster than a shock wave. I don't know about the speed of these devices.

The point is, that this being a tensor quantity, there are all kinds of transformations available with your piezoelectrics. But it's not just piezoelectrics, with Perovskites you can get tetragonal, orthorhombic, and rhomboid -- that means it goes off of 90 degrees -- distortions.

And as far as I know, nobody has made these things yet.

Some of the atoms in these transformations will move more than an angstrom; that much I could find when I looked it up. So you have got big changes going on in the substrate, and this is something that you can't really do with low temperature superconductors. They are not intrinsically the same crystal structure as these substrates.

All of the high T_c superconductors bear a relationship to the Perovskite structures!

Now look at the extensive variables we have got for such devices. We had a problem with using Perovskites for the substrate because when you cooled it down it transformed. So the point is that we can control the temperature as an extensive parameter.

In the piezoelectrics you control with voltage. You control with stress, remember that is how people got the twins out of the Y-123 single crystals. You just squeeze it, and the things sweep out.

And in some materials you can make the changes with a magnetic field. So there is this huge variety of extensive variables that we can put on and get any kind of tensor transformations that we want.

The point is, we already know this works because when the substrates transform, they mess up the superconducting properties. The odds are we can, in fact, do critical field, do critical temperature, do J_c modifications by messing with the substrate.

Whatever will happen, there are going to be serious non-linear effects, and serious non-linear effects are what electrical engineers have known about since the heterodyne radio. Physicists have only understood non-linearities in the last ten years.

So the point is, this is where you get devices. I mean, it is amazing that you can make a circuit with that resistive phase transition in a JJ instead of having to have it hysteretic. I mean, I am still impressed by that kind of stuff. And this JJ stuff doesn't work as well with high T_c superconductors.

So another subject: Remember when we all wanted room temperature superconductors. That was the point four years ago, and it seems to me that everybody has fallen asleep. It seems strange to see Paul Chu now pushing Buckyballs into niobium tubes and heating them.

But a lot of people have seen higher temperature transitions in the Y-123. There are certain temperatures that keep reoccurring. Perhaps it is worth a little thought, and I saw something recently when I was in Taiwan that reminded me of all of this.

Two of the people who already pushed a little harder were Ken Taylor at the University of New South Wales and J.T. Chen at Wayne State University.

These are not guys who seek controversy. These are good solid physicists who are working, who found a phenomenon that was reasonably reproducible. They feel burned by the community because nobody would listen to them. The story and the evidence that they have is a lot better than room temperature fusion. It is more reproducible than that.

And it seems to me that I can begin to see what might be going on. Ken Taylor, early in 1987 found that if he kept his Y-123 ceramic below room temperature in gaseous nitrogen, that he could, during thermal cycling, get a resistive transition up to 141 Kelvin.[1]

J.T. Chen found by keeping the sample above room temperature in oxygen, and thermally cycling it, that he could get T_c's as high as 240 Kelvin. He started with an off stoichiometric ceramic, but from x-rays it was just made of the 1,2,3 material; the 2,1,1; and CuO phases.[2]

It is interesting that there is a symmetry here. I think nature might just be telling us something. If you keep it away from oxygen, below room temperature, or in oxygen above room temperature, there may be some subtle thing going on.

But perhaps there was something about their two materials that was different from other people's.

Chen will still say that, among his graduate students, some of them can always get to the high T_c and some of them can't, and that may sound like a lack of reproducibility. But any of us who have tried to make good Y-123, have noticed that for a few months it works and for a few months it doesn't, and eventually we figure out what we did wrong.

I think that there may be something going on here that is worth at least as much effort as we are putting into Buckyballs right now.

So what's new, Los Alamos has found some spiral growths, screw dislocations, in thin films.[3] But I was looking through old stuff and I saw that, in fact, Ken Taylor had seen those back in 1987 and published them in 1988, -- he had them in single crystals on a surface.[4]

With a scanning electron microscope, he could see the spirals, and as far as I could tell, this was the only published work before what Los Alamos and IBM did this spring on thin films.

But Chen has this new result! He has single crystals of Y-123 with thin platelets with the C-axis perpendicular to the thin direction, and he finds that on one side, 10 percent of the material is going superconducting at 240 Kelvin.

He says that under a microscope he can tell which side it is. Optically it is a little different, but these spiral things are optically flat, in case I forget to tell you again. The photo I will show you is optically flat material.

And anyway, they don't have good materials science at Wayne State, and Chen sent it to one of his friends at Bell Labs who took a look with a TEM. He thinned it, keeping track of which surface had the high T_c. Incidently, it wouldn't be superconducting at 240 K after you thinned it and put it in a vacuum system.

What it looked like were these layers. It looked like what the side view of a spiral thing should look like.

And I explained this to him, and let me show you what the spirals look like (Figure 1). This is a scanning tunneling microscope picture from Marilyn Hawley. This was stuff that Los Alamos submitted six weeks before IBM submitted theirs to NATURE, but our work from Los Alamos was published one day later because NATURE publishes on Thursday and SCIENCE on Friday.

Under the scanning-tunneling microscope, it appears four microns across and these steps are 12 angstroms high, so you have got about 1,000 times the magnification vertically as you do horizontally.

That is why Ken Taylor had trouble seeing with a scanning electron microscope, and why you tend not to notice what is going on with the surface of these things.

This is about a 2,000 angstrom film, but they all start growing this way.

It is easy to guess what might be going on to make a 240 Kelvin superconductor, and this is important. I mean, some of us have walked around in our winter coats at about 240 Kelvin. It's not that cold.

If the material is sensitive to the oxygen around room temperature and when you have spirals sweeping by each other -- the neighboring ones have the same sense -- you have all possible variations of two-layered structures coming together -- then it is easy to imagine that this modifies the mobility of oxygen or nitrogen within the substrate -- then you need a proximity effect that can give you enough of the material to see 10% of it superconducting.

At Wayne State it looks like with magnetic measurements on a polycrystal that you have got close to 50 percent of the material superconducting.

But why does the community reject this work? That is sort of the point. It may not work in thin films because of the epitaxial constraints of the substrates. I haven't tried any of these things. I haven't tried any of the stuff I've been talking about, but we will get on this.

So anyway, what I have talked about is, why don't we put some films down on some substrates and take advantage of what had been the problem with the substrates and, by the way, that might give us some new physics.

If we can, in an interesting way, modify the properties of these things, and I am unaware of anybody trying that, we might get a feeling of why the things are superconducting.

And it is also true: why don't we look a little harder for higher temperature superconductors instead of just picking on these two guys? Thank you.

DR. BIRNBACH: Can you explain what kind of Perovskites would do this for you?

DR. SMITH: They are all cubic at high enough temperatures. I can show you a generalized phase diagram [5], and the piezoelectrics are a very predictable material within this general class.

DR. GILMORE: How is Chen making his materials for his processing?

DR. SMITH: The stuff he gets -- he mixes up the powder -- the two oxides and the barium carbonate -- and does the heat treatment at 900 to 950C, not doing anything special.

But the fact that he has got extra phases tells you that the phase separation will tend to grow large grains. It is not unlike the way you grow single crystals.

My guess is that what he has done is that he has found a composition that tends to yield the spiral structure. He will have his friends do STM -- scanning tunneling microscopy -- start getting stuff looked at to see if this feature is present even in the polycrystal.

DR GILMORE: I was thinking about your spiral. They look like the sort of thing you get from vapor.

DR. SMITH: That is what we get, at Los Alamos, with heated substrates. That is a standard growth defect, and the point is that because of what Ken Taylor saw when he grew crystals, you can also get it out of a liquid transport.

So the point is that we already know that the single crystals will also have the same kind of growth structure. That is probably what Chen has with his off stoichiometric composition.

DR. GILMORE: I have a question about the micrograph that you showed.

DR. SMITH: That is a scanning tunneling microscope photo. That is off-axis sputtered, 2,000 angstroms thick onto a heated substrate. We will always see this. On films that we make that are c-axis vertical, we always see these structures on heated substrates. If you put the thing down and heat it later, it gives a different morphology.

DR. FLUSS: I have a question about those pictures. That is an STM picture which is telling us about electronic topology, tunneling topology. Has that been confirmed with the force microscope and do you see the same topology or can you actually distinguish insulating and conducting regions in the spirals?

DR. SMITH: Okay, the scanning tunneling microscope gives you the product of the electronic density of states and the morphology so that you are not necessarily seeing atoms.

You confirm the structure by also looking at atomic force microscopy which actually measures only the topology but has lower resolution. We have confirmed it with the atomic force microscope.

DR. BIRNBACH: Have you looked at a-axis films to see if you find the same kind of spirals?

DR. SMITH: a-axis: they look like little saucers up on end, just like you might think. That is recent work. It is all unpublished, but depending on the direction, it looks like little dishes sticking up on the surface.

PARTICIPANT: Have you looked at this done by other techniques? Do they have spiral structures?

DR. SMITH: I think that is what we get from the laser deposition but on a lot of our laser ablation films, we did a post heat treatment and then we get little lumps on it, but I am fairly sure that everything we do on a heated substrate will show this growth pattern. I am not 100 percent sure about the pulse laser. There is a different kind of sputtering to it.

REFERENCES

1. D.N. Matthews, A. Bailey, R.A. Vaile, G.J. Russell, and K.N.R. Taylor, Nature 328, 786 (1987).
2. J.T. Chen, L.E. Wenger, C.J. McEwan, and E.M. Logothetis, Phys. Rev. Lett. 58, 1972 (1987).
3. Marilyn Hawley, Ian D. Raistrick, Jerome G. Beery, and Robert J. Houlton, Science 251, 1587 (1991).
4. K.N.R. Taylor, P. Cook, T. Puzzer, D.N. Matthews, G.J. Russell, and P. Goodman, Physica C 153-155, 411 (1988).
5. F.S. Galasso, Structure, Properties and Preparation of Perovskite - Type Compounds (Pergammon, Oxford, 1969) p. 7 and p. 10; taken from R.S. Roth, J. Research NBS, RP 2736, 58 (1957).

Invited paper presented at the
Beijing International Symposium on Fast Neutron Physics,
Beijing, China (9-13 September 1991)

MECHANISM OF (n,γ) REACTION AT LOW NEUTRON ENERGIES

S. Raman
Oak Ridge National Laboratory, Oak Ridge, Tennessee 37831

and

J. E. Lynn
Los Alamos National Laboratory, Los Alamos, New Mexico 87545

MECHANISM OF (n,γ) REACTION AT LOW NEUTRON ENERGIES

S. Raman
Oak Ridge National Laboratory, Oak Ridge, Tennessee 37831

and

J. E. Lynn
Los Alamos National Laboratory, Los Alamos, New Mexico 87545

Abstract

We discuss the interplay between direct capture, valence capture, and compound-nuclear capture in attempting to explain the vast amount of capture data for light-mass nuclei.

1. Introduction

Information that has been accumulated in a vast range of nuclides on the radiative transitions that follow slow-neutron capture has been one of the main sources of knowledge on the detailed nuclear level structure of these nuclides. Most of this knowledge comes from γ-ray energies and level placements, the relative yields, branching ratios of secondary transitions between low-lying states, and angular correlations among successive secondary transitions. Spectroscopic information may also be contained in the *cross sections of the primary transitions* originating from the capturing state, and this fact is demonstrated by the success of "direct" theories of neutron capture for many nuclides, especially those of light and near closed-shell character.

2. $E1$ transitions

2.A. Direct capture

Although low-energy neutron capture can be regarded as the classical compound-nuclear process (the original experimental evidence for large neutron capture cross sections motivated Bohr in the creation of the compound-nucleus concept), it has also been known for a long time [1] that far away from resonances a *direct form of radiative capture* not involving the compound nucleus can exist. In this process, the neutron-target interaction is represented in zero order by a potential well, and the neutron that is initially in an s orbit simply falls into a p-wave orbit in the final nucleus resulting in the emission of a primary $E1$ transition. The theoretical analysis of this process requires a knowledge of the coherent scattering length and (d,p) spectroscopic factors.

This form of neutron capture is amenable to calculation because the major contribution to the radial factor of the $E1$ matrix element arises from a region outside the potential well where the wave functions are known. These wave functions depend only on the scattering length (for the initial state) and the binding energy plus single-particle spectroscopic factor (for the final state). Indeed, many partial $E1$ cross sections can be reproduced by a formalism that treats the potential with a sharp cutoff at the well radius and ignores all internal contributions to the matrix element. This version is known as *channel capture* (see Fig. 3 of Ref. [2]).

2.B. Channel capture

The channel-capture formula [1,3] is simple:

$$\sigma^{CH}_{\gamma(i\to f)} = \frac{0.0614}{R\sqrt{E_{lab}}}\left(\frac{Z}{A}\right)^2\left(\frac{M+m}{M}\right)^3 \sum_J g_J \frac{1}{|1-iP_0\mathcal{R}_J|^2}$$
$$\times \left| y^2\left(\frac{y+3}{y+1}\right)^2 + 2\,\mathrm{Re}\,\mathcal{R}_J \frac{y^3(y+1)(y+2)}{(y+1)^2} + |\mathcal{R}_J| y^2\left(\frac{y+2}{y+1}\right)^2 \right| \mathcal{W}_{J,jJ}\,\theta_f^2,$$

where

$$y = R\sqrt{\frac{M}{M+m}}\sqrt{\frac{2mE_f}{\hbar^2}},\ \mathrm{Re}\,\mathcal{R}_J = 1-(a_J/R),\ \ R = \left(1.16A^{1/3}+0.6\right)\mathrm{fm},$$

M – target mass, m – neutron mass, g_J – statistical weight factor, P_0 – penetration factor for s-wave neutrons, $\mathcal{R}_J$ – reduced $\mathcal{R}$ function, $\mathcal{W}$ – spin coupling factor, θ_f^2 – spectroscopic factor, E_f – binding energy of the final state, and a_J – scattering length. This simple analytical formula has been found to be very successful in estimating the cross sections of primary $E1$ transitions in many nuclides [3].

2.C. Potential capture

In the more detailed version of capture theory [4-8], called *potential capture*, the wave functions are computed numerically from a realistic optical model (such as Woods-Saxon) and the internal contributions are included. The optical-model parameters (well depth, diffuseness, and imaginary potential amplitude) are varied within physically reasonable limits to reproduce the measured scattering length (which may be affected by local compound-nuclear states). The depths of the real potential are then varied to reproduce the binding energies of final bound states of largely single-particle character. This is the *specialized optical-model* [S] procedure. This model works well even when (as in ^{9}Be) the scattering length (7.0 fm) is large compared to the potential radius (3.0 fm), resulting in large cancellations in the $E1$ matrix elements [5].

It can be argued that forced adjustment of the optical-model parameters is not the best way to proceed to explain thermal-neutron cross sections. Also, occasionally, certain optical-model parameters get pushed to values that are at the limits of physical acceptability. To circumvent this problem, the direct-capture amplitude can be written as a sum of two terms—a potential-capture amplitude (based on a global [G] potential such as Moldauer's) and a valence [*V*] correction due to the wave function of local resonance levels projected on the single-particle motion. The valence correction can be assessed from the difference between the calculated (from the optical model) potential scattering length and the measured scattering length of the target nucleus. We call this the *global optical model + valence correction* [*G+V*] procedure.

From the global optical-model calculations, a complex capture amplitude is obtained. The real part is the potential capture and the imaginary part gives a cross section that is the average of a resonance-resonance interference term (not a cross section averaged over resonances in the Hauser-Feshbach sense). From this, the valence radiation strength function can be obtained and hence the valence correction. The direct-capture cross section is given by

$$\sigma^{\mathrm{dir}}_{\gamma(i\to f)} = \sum_J g_J \left| \sqrt{4\pi} R \mathcal{R}^{\mathrm{loc}}_J \left[\frac{\overline{\Gamma}_{\lambda\gamma(i\to f)(\mathrm{val})}}{\Gamma_{\lambda n}} \right]^{1/2} + \sigma^{1/2}_{\mathrm{pot},\gamma} \right|^2 ,$$

where $\mathcal{R}^{\mathrm{loc}}_J$ is the contribution from local levels to the reduced $\mathcal{R}$ function

$$R\mathcal{R}^{\mathrm{loc}}_J = \left(a_{\mathrm{pot}} - a_J\right),$$

$\overline{\Gamma}_{\lambda\gamma(i\to f)(\mathrm{val})}$ is the average valency radiation width, and $\Gamma_{\lambda n}$ is the neutron width derived from the neutron strength function calculated from the optical-model scattering. In general, we find that the [*G+V*] and [*S*] methods give very similar results [6].

2.D. Compound-nuclear contributions

Differences between experimental and calculated cross sections are attributed to a *compound-nuclear radiative amplitude* due to the tails of nearby resonances. Compound nucleus (CN) is a generic term for mechanisms involving more general features of the wave functions than the simple picture of neutron motion in the field of the unexcited core of the target. It is uncorrelated with the single-particle content of the initial or final state. The experimental cross section $\sigma_\gamma(X)$ is

$$\sigma_\gamma(X) = \left(\sigma^{1/2}_{\mathrm{dir},\gamma} + \sigma^{1/2}_{\mathrm{CN},\gamma}\right)^2 .$$

The extracted CN cross section can be converted to a radiation width if it is assumed that the discrepancy between the potential and measured scattering lengths is due to a single capturing resonance level. Thus

$$\frac{k\left\langle \sigma_{\mathrm{CN},\gamma}/E^3_\gamma \right\rangle}{2\pi R\mathcal{R}^{\mathrm{loc}}} = \frac{\left\langle \Gamma_{\lambda\gamma,\mathrm{CN}}/E^3_\gamma \right\rangle}{E_\lambda} .$$

This radiation width can be compared with the *Cameron estimate*

$$\Gamma_{J,\gamma,CN}(\text{in eV}) \approx 0.33\times10^{-9}\, E_{\gamma}^{3}(\text{in MeV}) A^{2/3} D_{J}(\text{in eV}) \ ,$$

which usually underestimates the average strength of high-energy (~ 5 MeV) transitions. Alternatively, the compound-nuclear radiation width can be derived from the *Brink's model* of the damped giant resonance built on each final state, but it has been established that this model overestimates the widths for transitions in the 2 to 3 MeV range.

In general, the $\langle \Gamma_{\lambda\gamma,CN}/E_{\gamma}^{3}\rangle / E_{\lambda}$ deduced from experiment agrees (within an order of magnitude) with Cameron's $\langle \Gamma_{\lambda\gamma,CN}/E_{\gamma}^{3}\rangle / D_{J}$. By comparing them, we can suggest which bound or unbound level might be responsible for the CN contributions [9].

2.E. Generalized valence correction

For some nuclides the discrepancies between theory and experiment are not only greater than would be expected from the Cameron estimate, but also appear to be systematic. The softness of ^{44}Ca allows virtual excitation of quadrupole collective vibrations with sufficient amplitude to interfere with the direct-capture amplitude. The potential field that such a nucleus presents to an incoming neutron contains higher multipole terms that couple the initial configuration (target nucleus ⊗ single-particle motion within the spherical potential) to other configurations (target excited collective state ⊗ single-particle motion). The higher multipole terms have a similar mixing effect on the final states. This *generalized valence capture* model [9] leads to a systematic reduction (by a factor of 2) in the capture cross sections of transitions to the group of low-lying states in ^{45}Ca from the values computed in the direct-capture theory, thereby improving agreement with experiment. [There will also be a systematic enhancement for transitions to some higher-lying states but these have not been measured.]

2.F. Valence capture

The total (n,γ) capture cross sections discussed above are small (< 1 b) indicating that the influence of resonance wings is small. In some cases, nearby resonances clearly have a major influence and more complex capture mechanisms, such as the *valence mechanism*, have to be considered. We base our calculations on the $\mathcal{R}$-matrix theory of nuclear reactions and the assumption of a real potential. The fractionation of the modeled single-particle state into the actual resonance is known from the experimentally determined neutron width of the resonance. It is therefore unnecessary, in this approach, to model the expected average fractionation by the formulation of the imaginary part of the optical model. The valence-capture amplitude, while being closely related to the potential-capture amplitude, is now more sensitive to the components of the wave function in the internal region because the initial-state wave function has an antinode rather than a node close to the potential radius. This also allows significant valence capture by p-wave resonances (see Fig. 5 of Ref. [2]).

The valence contribution is proportional to $\Gamma^{1/2}_{\lambda(n)}\Gamma^{1/2}_{\lambda(\gamma,\mathrm{val})}/(E_\lambda - E)$. The valence γ width for resonance λ has the important property of $\Gamma^{1/2}_{\lambda(\gamma,\mathrm{val})} \propto \Gamma^{1/2}_{\lambda(n)}$. The valence term in the capture amplitude is constructive or destructive with respect to the potential-capture amplitude depending on whether the resonance level E_λ is above or below the thermal neutron energy E, respectively. In the case of ^{43}Ca (whose thermal capture cross section of 6.2 b is an order of magnitude greater than the direct capture cross section), the resonance influence is clearly dominant but not overwhelming. (Our analysis is approximate because the total scattering cross section and the parameters of the 1.48-keV resonance are poorly known.) Even though the resonance valence radiation width is small (~0.13 eV out of 1.9 eV), constructive interference yields an estimate of 3.7 b (a substantial fraction of the 6.2 b) for the direct component, indicating that even in this quasicompound nuclear situation, direct capture plays an important role.

At shown in the following table, direct-capture theory, at first sight, fails badly in the case of the ^{14}N(n,γ) reaction with thermal neutrons [10]. The deduced CN component is of similar magnitude to the direct component.

Final state E_f (keV)	Primary E_γ (keV)	$\sigma_{\gamma,\mathrm{dir}}$ (theory) (mb)	σ_γ(exp.) (mb)	σ_γ (CN) (mb)
0	10829	330	10	220 or 450
6324	4509	1	14	5 or 25
9152	1681	0.1	1	1

But a resonance at –24 keV is known from the ^{14}C(p,γ) reaction and we use its γ-ray spectrum and our calculated valence widths to deduce the compound-nuclear contributions. We then combine everything to estimate

Final state E_f (keV)	Primary E_γ (keV)	σ_γ (theory) (mb)	σ_γ(exp.) (mb)
0	10829	8	10
6324	4509	16	14
9152	1681	3	1

The agreement between theory and experiment is now satisfactory. The concept implicit in valence capture, namely that the neutron valence radiative width is of similar magnitude to the compound-nuclear radiative width, is shown explicitly here for the first time in a resonance formed by a non-neutron reaction.

We have applied the valence-capture theory to calculate (see table below) the expected total radiation width of the 153-keV resonance in ^{13}C [11]. The resulting width of ~ 0.2 eV disagrees strongly with the previous measured value of 2.4 ± 0.9 eV.

if $1p_{3/2}$	$\Gamma_{\gamma\to 6.1}$	$= 0.16$ eV	$\Gamma_{\gamma\to 6.7}$	$= 0.06$ eV
if $2p_{3/2}$		$= 0.14$ eV		$= 0.03$ eV

The partial radiation widths of the 6.1- and 6.7-MeV transitions have been remeasured at the Tokyo Institute of Technology [11].

$\Gamma_{\gamma\to 6.1} = 0.151^{+0.076}_{-0.033}$	$\Gamma_{\gamma\to 6.7} = 0.030^{+0.030}_{-0.013}$

These results offer a striking confirmation of the valence-capture theory. (Scattered-neutron sensitivity was probably underestimated previously.) Of the two possible scenarios for nucleosynthesis—red-giant He burning and nonstandard Big Bang—the new result has little significance for the former, but affects the latter in terms of a significant reduction in the production of $A \geq 14$ isotopes [11].

3. M1 transitions

Some tendency for the strong $M1$ transitions to be associated with high spectroscopic factors suggests the operation of a direct mechanism quite analogous to that for $E1$ transitions. In this case, the chances of arriving at a successful theory are slimmer for two reasons: (1) In the $E1$ case the matrix elements involve the electrostatic dipole moment, whereas in the $M1$ case, the operator depends on currents that may be described much more poorly by the wave functions of a simple direct-capture model. (2) The radial component of the $E1$ matrix element is more strongly weighted to the channel region—where the wave functions are well established by the energies of the initial and final states—than is the radial $M1$ element. In fact, in the $M1$ case, it is often stated that there can be no direct capture analogous to $E1$ because the radial wave functions are necessarily orthogonal in a simple potential well. However, because of the complexity of the nucleus, we usually find it necessary to generate the radial wave functions of the initial and final states with rather different mutual potentials (just as we usually do for $E1$ capture) and $M1$ transitions become possible. The $M1$ operator has the form [12]

$$H'_{M1,\mathfrak{M}} = \frac{e\hbar}{2mc}\left[\frac{3}{4\pi}\right]^{1/2}\left[\frac{\mu_l I_{\mathfrak{M}}}{I} + \frac{\mu_n \sigma_{n,\mathfrak{M}}}{\sigma}\right].$$

From this expression the reduced matrix element for the spin factor can be computed, while the radial matrix element is simply the integral of the product of the projection of the radial wave function of the initial state onto the entrance channel and the radial wave function of the single-particle component of the final state. Because there is no orbital contribution in the above $M1$ operator, the single-particle components of the initial and final states have zero orbital angular momentum in slow-neutron direct $M1$ capture.

In very light nuclei, direct $M1$ capture (with the $M1$ operator substituted in place of the $E1$ operator) appears to play a qualitatively important role.

Target	E_f (keV)	E_γ (keV)	σ_γ(theory) (mb)	σ_γ(exp.) (mb)
^9Be	6265	547	$37 \times \theta_f^2$	14
^{12}C	3089	1857	$25 \times \theta_f^2$	6
^{13}C	6094	2080	$24 \times \theta_f^2$	34
^{13}C	6900	1274	$68 \times \theta_f^2$	67

In ^{20}F, the direct-capture $M1$ model underestimates the cross sections to the two strongest $s_{1/2}$ states (at 3.488 and 3.526 MeV) by a factor of ~ 4 and to the state at 1.057 MeV by three orders of magnitude. In ^{21}Ne, the calculated cross section of the primary $M1$ transition to the 2.794-MeV state is an order of magnitude greater than experiment. In ^{23}Ne, the calculated and measured cross sections to the state at 1.02 MeV nearly agree (0.6 mb and 0,9 mb, respectively). In this region, the simple direct process has a substantial but not predominant role to play.

We have recently analyzed the $^7Li(n,\gamma)$ data in the 0 – 400 keV region [12]. We have (1) deduced the direct-capture cross section for thermal-neutron $E1$ capture as 39 mb, (2) analyzed the total cross section and angular distributions of scattered neutrons to deduce $\mathcal{R}$-matrix parameters, (3) showed that the potential-capture cross section behaves as $1/v$, and (4) calculated the valence $M1$ radiation width for the 255-keV resonance as 0.094 eV. The measured thermal-neutron capture cross section is 45.4 ± 3.0 mb. The capture data obtained at Lockheed (Palo Alto) are consistent with $1/v$, whereas those obtained at Karlsruhe are not. If we normalize the Karlsruhe data to thermal (and $1/v$), we infer a radiation width of 0.09 ± 0.02 eV (average of Lockheed and renormalized Karlsruhe data) which is now in agreement with theory. The Karlsruhe conclusion that the $^7Li(n,\gamma)$ reaction is not the predominant link to the primordial r process is not supported.

4. Conclusion

The nuclides that we have investigated till now are listed in the following table [13]. After more than half a century of study, we still do not have a fully quantitative or universally applicable theory of neutron radiative capture. What we have is a number of models that are applicable in different mass or energy regions and a certain amount of basic theory that explains, in principle, why some of these models work in certain situations. Fortunately, high-quality data continue to be produced in this area and this is leading to continued quantitative development and application of capture models.

Mechanism of (n,γ) reaction at low neutron energies

Mechanism	Explains[a]
*E*1 transitions	
Potential + valence correction + compound	^{7}Li, ^{9}Be, ^{12}C, ^{13}C, ^{19}F, ^{24}Mg, ^{25}Mg, ^{26}Mg, ^{28}Si, ^{29}Si, ^{30}Si, ^{32}S, ^{33}S, ^{34}S, ^{40}Ca, ^{42}Ca, ^{46}Ca, ^{48}Ca
Potential + generalized valence correction + compound	^{44}Ca
Valence + potential + compound	^{43}Ca
Compound + valence + potential	^{14}N
Valence	^{13}C (153 keV)
*M*1 transitions	
Potential	^{9}Be, ^{12}C, ^{13}C
Compound	^{14}N
Valence	^{7}Li (255 keV)

[a]Thermal-neutron capture unless stated otherwise.

5. Acknowledgments

This work was sponsored by the Department of Energy under Contract DE-AC05-84OR21400 with Martin Marietta Energy Systems, Inc. (Oak Ridge) and W-7405-eng-36 with the University of California (Los Alamos). We thank our colleagues who are listed in the references and especially Ed Jurney and Bill Starne; of Los Alamos.

[1] A. M. Lane and J. E. Lynn, Nucl. Phys. **17**(1960) 563; **17**(1960)586; See also J. E. Lynn, *Theory of Neutron Resonance Reactions*, Clarendon, Oxford (1968).

[2] S. Raman, in *Neutron Capture Gamma Ray Spectroscopy and Related Topics*, Proceedings of the Fourth International Conference at Grenoble, France, 1981 (Edited by T. von Egidy, F. Gönnenwein, and B. Maier), p. 357, Institute of Physics, Bristol (1982).

[3] S. Raman and J. E. Lynn, in *Neutron Induced Reactions*, Proceedings of the Fourth International Symposium at Smolenice, Czechoslovakia, 1985 (Edited by J. Kristiak and E. Betak), p. 253, VEDA, Bratislava (1986).

[4] S. Raman, R. F. Carlton, J. C. Wells, E. T. Jurney, and J. E. Lynn, Phys. Rev. C **32**(1985)18.

[5] J. E. Lynn, S. Kahane, and S. Raman, Phys. Rev. C **35**(1987)26.

[6] S. Kahane, J. E. Lynn, and S. Raman, Phys. Rev. C **36**(1987)533.

[7] S. Raman, S. Kahane, R. M. Moon, J. A. Fernandez-Baca, J. E. Lynn, and J. W. Richardson, Phys. Rev. C **39**(1989)1297.

[8] S. Raman, J. A. Fernandez-Baca, R. M. Moon, and J. E. Lynn, Phys. Rev. C **44**(1991)518.

[9] S. Raman, S. Kahane, and J. E. Lynn, in *Proceedings of the International Conference on Nuclear Data for Science and Technology, Mito, Japan, 1988* (Edited by S. Igarasi), p. 645, Saikon, Tokyo (1988).

[10] E. T. Jurney, J. E. Lynn, J. W. Starner, and S. Raman, to be publish.

[11] S. Raman, M. Igashira, Y. Dozono, H. Kitazawa, M. Mizumoto, and J. E. Lynn, Phys. Rev. C **41**(1990)458.

[12] J. E. Lynn, E. T. Jurney, and S. Raman, Phys. Rev. C **44**(1991)764.

[13] J. E. Lynn and S. Raman, in *Capture Gamma-Ray Spectroscopy*, Proceedings of the Seventh International Conference at Asilomar, California, 1990 (Edited by R. W. Hoff), p. 355, AIP, New York (1991).

LA-UR -91-3454

LA-UR--91-3454

DE92 002521

TITLE: CALCULATIONS OF LONG-LIVED ISOMER PRODUCTION IN NEUTRON REACTIONS

AUTHOR(S): M. B. Chadwick, T-2
P. G. Young, T-2

SUBMITTED TO: The Consultants' Meeting on Methods of Calculation of Fast Neutron Nuclear Data for Structural Materials, Int. Atomic Energy Agency, Nuclear Data Section meeting, 14-15 November 1991, Vienna, Austria

Los Alamos National Laboratory
Los Alamos, New Mexico 87545

Calculations of Long-Lived Isomer Production in Neutron Reactions

M.B. Chadwick and P.G. Young

Theoretical Division, Los Alamos National Laboratory, Los Alamos, New Mexico 87545

We present theoretical calculations for the production of the long-lived isomers: ^{121m}Sn (11/2-, 55 yr), ^{166m}Ho (7-, 1200 yr), ^{184m}Re (8+, 165 d), ^{186m}Re (8+, 2×10^5 yr), ^{178m}Hf (16+, 31 yr), ^{179m}Hf (25/2-, 25 d) ^{192m}Ir (9+, 241 yr), all which pose potential radiation activation problems in nuclear fusion reactors if produced in 14-MeV neutron-induced reactions. We consider mainly $(n, 2n)$ production modes, but also (n, n') and (n, γ) where necessary, and compare our results both with expermental data (where available) and systematics. We also investigate the dependence of the isomeric cross section ratio on incident neutron energy for the isomers under consideration. The statistical Hauser-Feshbach plus preequilibrium code GNASH was used for the calculations. Where discrete state experimental information was lacking, rotational band members above the isomeric state, which can be justified theoretically but have not been experimentally resolved, were reconstructed.

I. INTRODUCTION

Fusion systems operating on the deuterium-tritium reaction give rise to intense neutron fluxes that cause structural components to be activated. The first wall, in particular, is subjected to neutron damage that, in designs envisaged at present, could require its replacement every few years. Disposal or reuse of the material would be facilitated if the activation could be kept to low limits, and therefore there is a search for materials that will give rise to the minimum activation. The neutron fluxes in fusion systems are expected to be so high that multiple reactions will be possible in which a given nucleus interacts with a succession of neutrons. As a result, it is often important to have activation cross sections for unstable as well as stable nuclides. As there is often a lack of experimental data on activation cross sections of interest, it is important to be able to assess these cross sections theoretically. In this paper we shall present calculations of activation cross sections for a number of long-lived isomeric states which are considered important for fusion reactor design.

The isomeric state production cross sections that we have considered were calculated at the request of the United Kingdom and United States fusion programs, which are in the process of establishing nuclear data libraries and inventory code packages to enable activation in virtually any material to be estimated. In a recent paper [1] we presented theoretical calculations of the production cross sections of hafnium isomers in 14 MeV reactions, using the GNASH [2] code. These calculations were performed prior to the release of experimental measurements [3] of the cross sections for hafnium isomer production, and agreement to within a factor of 2-3 was found. Because the cross sections under consideration were rather small and the isomer spins very large, the agreement obtained was encouraging, and suggested that our theoretical approach can be extended for use in other isomer-production calculations. We have, therefore, now determined production cross sections for long-lived isomers in Sn, Ir, Ho and Re at 14 MeV. In addition, we have determined the variation of the production cross section with incident neutron energy, since neutron energies below 14 MeV are produced in fusion reactors in inelastic collisions. As the energy variation of the hafnium isomer production was not shown in Ref.1 we summarize our previous results for hafnium and give this variation.

The systematics of neutron-induced isomeric cross section ratios at 14.5 MeV have been been studied by Kopecky and Gruppelaar [4]. They used a simplified version of the GNASH code to determine the ratio of the cross section to the isomeric state and ground state in (n, n'), (n, p), (n, t), (n, α), and $(n, 2n)$ reactions, replacing the realistic nuclear level structure by two discrete states (the ground state and the isomeric state) plus a continuum of statistically described states. Their, approach is, therefore, considerably simpler than our calculations and so we have compared our results with the Kopecky systematics. We shall show that while such systematics are very useful, in many cases a full calculation (with a realistic description of the nuclear structure) is important in accurately determining isomer ratios. Also, Kopecky and Gruppelaar point out that their calculation is particularly sensitive to the simple model parameters that they adopt for the $(n, 2n)$ reaction. Our investigations into an analogous simple model confirm this, and indicate that for certain reactions one should be wary about using simple sytematic predictions. Finally, our calculations also include isomeric ratios for states formed in (n, γ) reactions, which are particularly resistant to simple systematics-based descriptions.

In Section II we give a brief description of the theoretical models that we use to describe the nuclear reactions, and in section III we show our results, and compare them with the Kopecky systematics and experimental data where available. We shall use the hafnium isomer calculations as a detailed example of our approach, and then indicate the isomer ratios, and their energy dependences, that we obtain for other nuclei. We give some conclusions concerning our general approach in Section IV.

II. DESCRIPTION OF THE CALCULATIONS

A. General Description

The GNASH nuclear theory code [2] is based on the Hauser-Feshbach statistical theory with full angular momentum conservation, and with width fluctuation corrections obtained from the COMNUC code [5] using the Moldauer approach. Preequilibrium emission processes, which are important for incident energies above about 10 MeV, are calculated using the exciton model of Kalbach [6]. Transmission coefficients for neutrons and charged particles are calculated using an optical model, and gamma-ray transmission coefficiens are obtained from giant dipole resonance approximations [7,8],making use of detailed balance. The level structure for each residual nucleus in a calculation is divided into discrete and continuum regions, with the former obtained from experimental complilations and the latter from phenomenological level density representations.

B. Optical Model

Both the Hauser-Feshbach theory and the exciton model require optical potentials to calculate transmission coefficients and inverse reaction cross sections. The coupled channels code ECIS [9] was used for deformed nuclei, and the code SCAT2 [10] for spherical nuclei. Before using an optical potential to generate transmission coefficients and reaction cross sections, the potentials were checked by comparing their predictions of elastic and total cross sections with experimental data, where available.

C. Gamma-Ray Transmission Coefficients

Transmission coefficients for gamma-ray emission coefficients were obtained using detailed balance, exploiting the inverse photoabsorption process. The Brink-Axel hypothesis is used, permitting the cross section for photoabsorption by an excited state to be equated with that of the ground state. The gamma-ray transmission coefficients were obtained from the expression

$$T^{X\ell}(\epsilon_\gamma) = 2\pi f_{X\ell}(\epsilon_\gamma)\epsilon_\gamma^{2\ell+1} \,, \tag{1}$$

where ϵ_γ denotes gamma-ray energy, $X\ell$ indicates the multipolarity of the gamma-ray, and $f_{X\ell}$ is the energy-dependent gamma-ray strength function. The strength functions for E1 decay were calculated either from standard Lorentzian expressions [7], given by

$$f_{E1}(\epsilon_\gamma) = K_{E1}\frac{\sigma_0\epsilon_\gamma\Gamma^2}{(\epsilon_\gamma^2 - E^2)^2 + \epsilon_\gamma^2\Gamma^2} \tag{2}$$

or from the generalized Lorentzian of Kopecky and Uhl [8]

$$f_{E1}(\epsilon_\gamma, T) = K_{E1}\left[\frac{\epsilon_\gamma \Gamma(\epsilon_\gamma)}{(\epsilon_\gamma^2 - E^2)^2 + \epsilon_\gamma^2 \Gamma(\epsilon_\gamma)^2} + \frac{0.7\,\Gamma\,4\pi^2 T^2}{E^5}\right]\sigma_0 \Gamma\,, \tag{3}$$

where

$$\Gamma(\epsilon_\gamma) = \Gamma\frac{\epsilon_\gamma^2 + 4\pi^2 T^2}{E^2} \tag{4}$$

$$T = \sqrt{\frac{B_n - \epsilon_\gamma}{a}}\,, \tag{5}$$

and $K_{E1} = 8.68 \times 10^{-8}\mathrm{mb}^{-1}\ \mathrm{MeV}^{-2}$ (nominally) but was usually determined empirically by matching the theoretical gamma-ray strength function for s-wave neutrons to experimental values compiled by Mughabghab [11]. The quantities B_n and a are the neutron binding energy and Fermi gas level density parameter, respectively. The Lorentzian parameters of the giant-dipole resonance, E and Γ, are taken from the tables of Dietrich and Berman [12].

In addition to E1 radiation, M1 and E2 components are also included. For M1, a standard Lorentzian expression was used for the gamma-ray strength function. When the Kopecky-Uhl formulation was employed, a giant resonance formulation was also used to calculate the E2 strength function [8]; otherwise, a Weisskopf expression (f_{E2} = constant) was incorporated.

D. Nuclear Structure and Level Densities

The level density model of Gilbert and Cameron [13] was used in the Hauser-Feshbach calculations. At high energies the Fermi gas model is used along with a constant temperature form for lower energies. A gaussian distribution of spin states is taken to describe the angular momenta of levels at a certain excitation energy

$$\rho(E, J, \pi) = \frac{(2J+1)}{2\sqrt{2\pi\sigma^2}}\exp\frac{-(J+\frac{1}{2})^2}{2\sigma^2}\rho(U) \tag{6}$$

where $U = E - \Delta$ (Δ is the pairing energy) and σ^2 is the spin cut-off parameter which is determined via $\sigma^2 = 0.146\sqrt{aU}A^{\frac{2}{3}}$ for the Fermi gas region. The spin cut-off factor is also determined from the spin distribution of observed low lying discrete levels and in the constant temperature region σ^2 is linearly interpolated between this value and the value of σ^2 where the Fermi gas region begins. In the high energy region the Fermi gas expression for $\rho(U)$ is

$$\rho(U) = \frac{\sqrt{\pi}}{12}\frac{1}{2\sqrt{\pi}\sigma}\frac{\exp 2\sqrt{aU}}{a^{\frac{1}{4}}U^{\frac{5}{4}}} \tag{7}$$

and at lower energies the constant temperature form is given by

$$\rho(E) = \frac{1}{T}\exp\frac{(E - E_o)}{T} \tag{8}$$

The pairing energy used to determine U is obtained from the Cook parameter set [14] and the level density parameters were calculated from the slow neutron resonance parameters of Mughabghab. The constant temperature $\rho(E)$ is chosen to match (both in value and in first derivative) the Fermi gas $\rho(U)$ at an energy E_{match} and to fit the known discrete levels at the lowest excitation energies. The parameters E_o, T and E_{match} are varied to achieve this.

The production cross section of a certain isomeric state is often particularly sensitive to the discrete nuclear level structure, since the gamma cascade of discrete states into the isomeric state will enhance its production. In many cases, the isomeric state of interest is a band-head, with a rotational band built upon it, though often the rotational band members have not been experimentally resolved and lie in a high-excitation energy region. Accordingly, the energies of the rotational levels were assessed theoretically (obtaining the moment of inertia from observed rotational bands at lower excitation energies) and GNASH was modified to allow these discrete levels to be embedded within the continuum of statistically described levels. In the case of our calculation of Hf isomers [1], this procedure was particularly important; we found that over 40% of the production of the ^{178}Hf(16+) in an $(n, 2n)$ reaction came from the decay of the 14- level and the inferred discrete rotational band states above the 14- and 16+ levels. In Fig. 1 we show schematically the combination of discrete and statistical levels for the case of the ^{178}Hf nucleus.

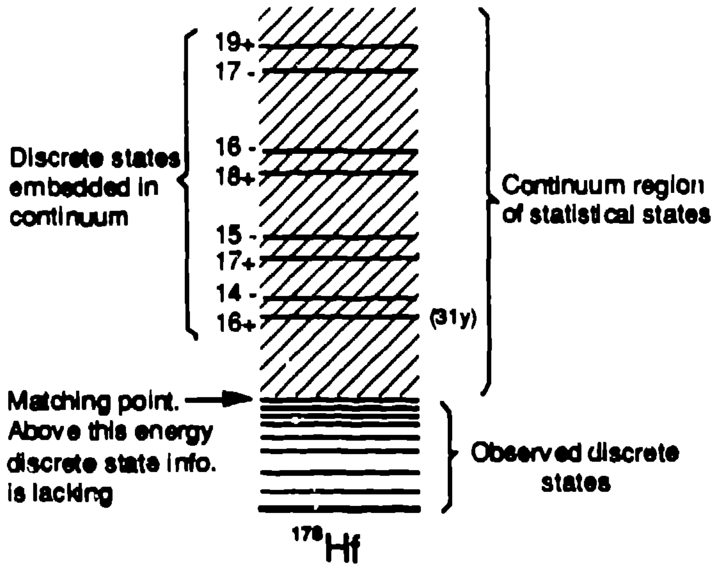

Fig. 1. A schematic representation of the combination of discrete, statistical and discrete levels embedded in the statistical continnum region used to describe the nuclear structure of ^{178}Hf.

III. RESULTS

A. The Hafnium Isomers: A Detailed Example

By way of example, in this subsection we shall give details of the calculations for the production of hafnium isomers. Full details can be found in Ref. [1]

The possibility of including small amounts of tungsten and tantalum in the first-wall material has been suggested, and after a few reactions on these nuclei hafnium could be produced. The presence of hafnium in a fusion reactor could pose serious activation problems due to the possible build-up of the isomeric state ^{178}Hf (J^{π} = 16+) with a 31-yr half life. This state, if produced in sufficient quantity, could lead to the first wall being active for a very long time after its removal from the reactor, and the high excitation energy of the state (2.447 MeV) results in harmful gamma radiation on its decay.

The ^{179}Hf$(n, 2n)$ and ^{178}Hf(n, n') reactions both give the ^{178}Hf(16+) isomer, with the (n,2n) reaction expected to be the dominant production mode. There is, however, also an isomeric state in ^{179}Hf(J^{π} = $\frac{25}{2}$−) with a 25-day half life that is sufficiently long-lived for subsequent neutron-induced reactions to occur. Once this ^{179m}Hf($\frac{25}{2}$−) isomer is produced, it would be expected that subsequent $(n, 2n)$ reactions could take place with a relatively large cross section leading to ^{178m}Hf(16+) as the spin difference between these isomers is small. Thus we calculate the ^{179m}Hf($\frac{25}{2}$−) $(n, 2n)^{178m}$Hf(16+)

reaction as well as those for the production of the ^{179m}Hf($\frac{25}{2}-$) state. Fig. 2 indicates the pathways that have been investigated.

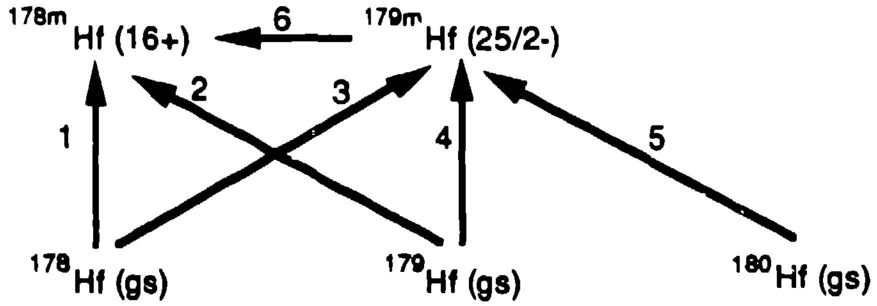

Fig. 2. Reaction pathways investigated fo the hafnium isomers. Pathways 2, 5 and 6 are $(n, 2n)$ reactions; pathways 1 and 4 are (n, n') reactions, and pathway 3 is a (n, γ) reaction.

Both the 16+ state and the $\frac{25}{2}-$ state are rotational band heads, though none of the other members of the rotational bands have been detected. In addition, there is a 14- band head state above the 16+ state that decays into the latter. Since a sizable fraction of the production cross section of these high-spin states comes from the gamma decay of higher-energy states, the rotational states were included explicitly into the calculation, their energies being estimated by determining the moment of inertia from low-lying rotational bands. These rotational levels were then embedded into the continuum of statistically described states (see Fig. 1 for a schematic illustration). Because the hafnium isotopes are highly deformed, the coupled channels code ECIS [9] was used to evaluate the transmission coefficents and the direct scattering cross sections to low-lying states. The optical potential that we used [15] described the total elastic and total cross sections fairly well.

In Table I below we show our theoretical results, along with experimental measurements where available. The experimental numbers of Patrick *et al.* [3] have been extracted from data assuming that the ratios of our theoretical results for production of the same isomeric state though different reactions are correct. In the experimental numbers that are quoted, the natural abundances of Hf have been taken into account. Reactions 1 through 6 are of importance for the determination of the production of the ^{178m}Hf(16+) state in fusion reactors, and are numbered according to the pathways in Fig. 2. Reactions 7,8 and 9 are also shown to allow further comparisons of our calculations with data.

TABLE I

Theoretical Cross Sections for the Production of Isomeric States in Hafnium Compared with Data Where Available*

Isomer Production Reaction	Theoretical Cross Section (mb)	Experimental Cross Section[a] (mb)
1. ^{178}Hf$(n,n')^{178m}$Hf(16+, 31 yr)	4.8×10^{-2}	
2. ^{179}Hf$(n,2n)^{178m}$Hf(16+, 31 yr)	2.9	5.91 ± 0.64
3. ^{178}Hf$(n,\gamma)^{179m}$Hf(25/2-, 25 days)	1.9×10^{-5}	
4. ^{179}Hf$(n,n')^{179m}$Hf(25/2-, 25 days)	5.7	12.8 ± 1.5
5. ^{180}Hf$(n,2n)^{179m}$Hf(25/2-, 25 days)	7.4	16.7 ± 1.9
6. ^{179m}Hf$(n,2n)^{178m}$Hf(16+, 31 yr)	158	
7. ^{180}Hf$(n,2n)^{179n}$Hf(1/2-, 18.7 s)	220	598 (Sothras) 690 (Rurarz) 570 (Prasad)
8. ^{180}Hf$(n,n')^{180n}$Hf(8-, 5.5 h)	19	12.4 (Hillman)
9. ^{179}Hf$(n,2n)^{178n}$Hf(8-, 4 s) + ^{178}Hf$(n,n')^{178n}$Hf(8-, 4 s)	1200	1452 ± 116 (Salaita) 749 ± 75 (Sothras)

*The reactions are numbered according to the pathways shown in Fig. 2.
[a]All Experimental Data are taken from the Brookhaven National Laboratory SCISRS file, except those of Patrick *et al.* [3][?].

B. The (n,2n) Isomeric Cross Section Ratios

We have concentrated on the $(n,2n)$ reaction mechanism for isomer production since, at 14 MeV, this is the dominant process through which most of the reaction flux goes. The following isomeric states, in addition to the hafnium states, have been considered in detail: ^{121m}Sn (11/2-, 55 yr) , ^{166m}Ho (7-, 1200 yr), ^{184m}Re (8+, 165 d), ^{186m}Re (8+, 2×10^5 yr), and ^{192m}Ir (9+, 241 yr). In all cases the experimentally measured discrete states have been examined and a matching point above which experimental data is missing has been determined. Rotational bands above the isomers were determined theoretically and included in the calculation, as discussed above. Optical potentials were found and checked against elastic and total scattering data, where available. In Table II below we show our results for the isomeric cross section ratio (the ratio of cross section to the isomeric state to the sum of the cross sections to ground state and isomeric state), for neutron energies between 8 and 14 MeV.

TABLE IIa

Isomeric Cross Section Ratios in (n,2n) Reactions

Neutron Energy (MeV)	^{122}Sn (n,2n) ^{121m}Sn (11/2-)	^{167}Ho (n,2n) ^{166m}Ho (7-)	^{179}Hf (n,2n) ^{178m}Hf (16+)	^{180}Hf (n,2n) ^{179m}Hf (25/2-)
8	0.	0.52	0.	0.
9	0.61	0.42	3.8×10^{-6}	5.1×10^{-6}
10	0.61	0.41	1.2×10^{-4}	1.6×10^{-4}
11	0.67	0.43	3.0×10^{-4}	5.3×10^{-4}
12	0.68	0.45	5.7×10^{-4}	1.1×10^{-3}
13	0.70	0.47	8.9×10^{-4}	2.4×10^{-3}
14	0.72	0.49	1.4×10^{-3}	3.6×10^{-3}

TABLE IIb

Isomeric Cross Section Ratios in (n,2n) Reactions

Neutron Energy (MeV)	^{185}Re (n,2n) ^{184m}Re (8+)	^{187}Re (n,2n) ^{186m}Re (8+)	^{193}Ir (n,2n) ^{192m}Ir (9+)
8	0.06	0.13	0.016
9	0.15	0.19	0.11
10	0.20	0.22	0.19
11	0.24	0.25	0.24
12	0.28	0.28	0.28
13	0.31	0.31	0.31
14	0.33	0.33	0.31

The isomer ratios above can be compared with the Kopecky systematics for $(n, 2n)$ reactions. Kopecky and Gruppelaar [4] showed that a simplified version of GNASH predicted 14- MeV isomer cross-section ratios that have a parabolic dependence on the isomer spin, with a peak at isomer spins between 3 and 5. Their calculated isomeric ratio described the library of experimental ratios reasonably well, though they commented that for the case of the $(n, 2n)$ calculation their results were particularly sensitive to the model parameters describing the simplified nuclear structure. In Fig. 3a, we show the 14 MeV isomer ratios from Tables IIa and IIb, compared with the Kopecky systematics. The differences between the line (the Kopecky prediction) and our theoretical results (triangles) can be understood as a measure of the need to perform full GNASH calculations with realistic nuclear structure and optical models. In the case of the hafnium isomers (25/2- and 16+) we have shown the experimental isomer ratio, from Patrick *et al.* In most cases the Kopecky systematics yield isomer ratios that are close to our detailed GNASH calculations. Our GNASH calculations for the isomer production cross section ratios of the 25/2- and 16+ levels in hafnium are seen to lie below the experimental numbers by about a factor of 2. The Kopecky sytematics overestimate the isomeric ratio for the 25/2- by about a factor of 4-5, and interpolating their curve to an isomer spin of 16 suggests that their systematics agree with the experimental measurement reasonably well.

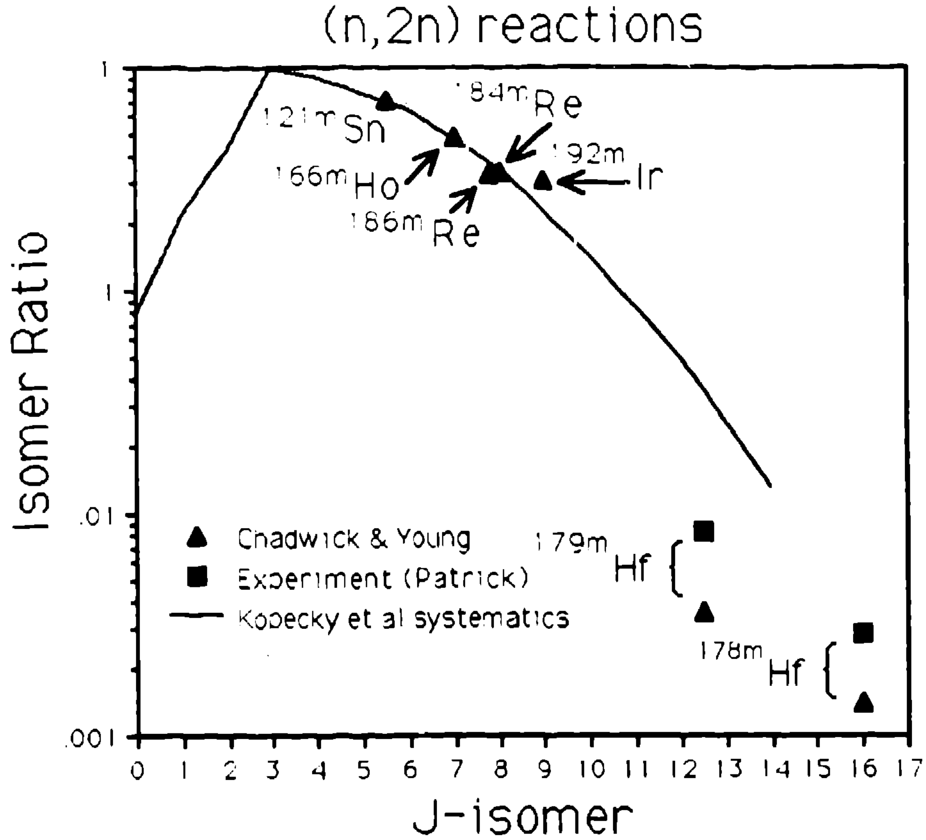

Fig. 3. The $(n, 2n)$ isomeric cross section ratio as a function of isomer spin, for 14 MeV incident neutrons. The Kopecky systematics calculation is compared with our GNASH calculations, and a comparison with data is made for the /2- and 16+ hafnium isomers.

As well as $(n, 2n)$isomeric cross section ratios for 14 MeV incident neutron energies, Table II contains the ratios for lower neutron energies, down to the threshold of about 8 MeV for $(n, 2n)$ reactions. The energy dependence of the isomeric ratio is of importance when assessing activation in a reactor induced by neutrons with degraded energies, after inelastic scattering processes have occurred. In Fig. 4. we show the variation of the isomer ratio with isomer spin for three different incident neutron energies: 14, 11 and 8 MeV.

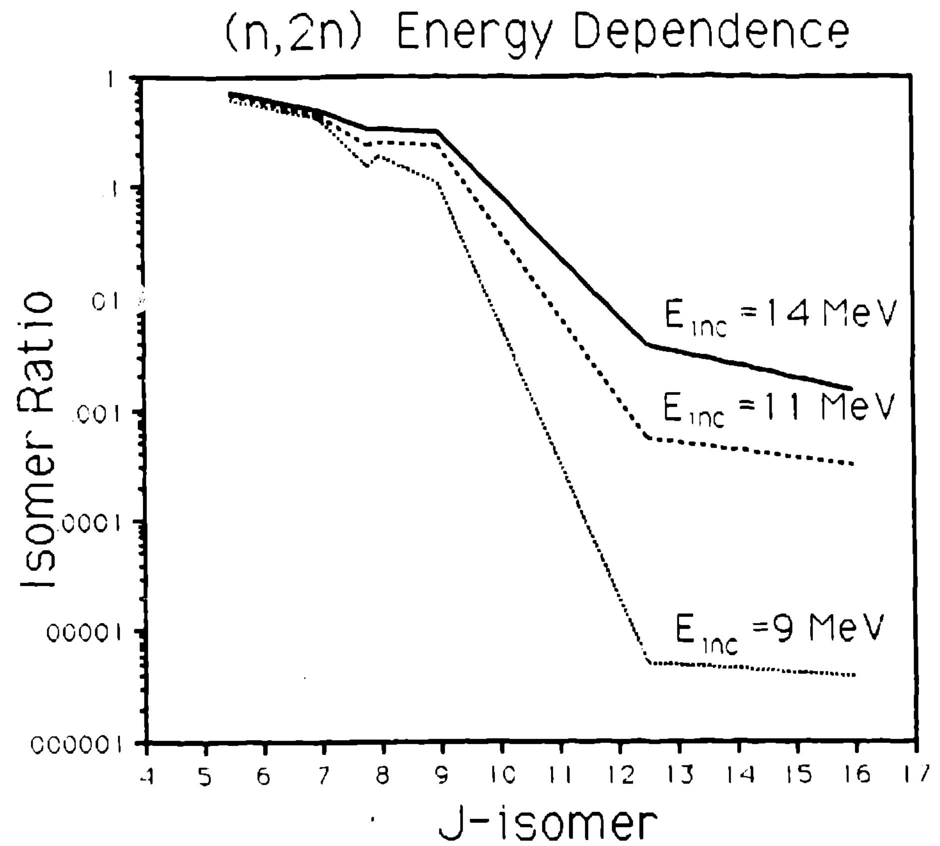

Fig. 4. The $(n,2n)$ isomeric cross section ratio as a function of isomer spin, for three different incident neutron energies. The lines connect GNASH calculations for the same isomers that are shown in Fig. 3.

It is seen that, for a given incident neutron energy, the $(n,2n)$ isomer ratio decreases with increasing isomer spin (at least for isomer spins above 4). This feature, which is also seen in experimental data and in the Kopecky calculations [4], can be simply understood in the following way. In $(n,2n)$ reactions both outgoing neutrons generally have low energies and are dominated by s-wave transitions. However, in order to produce a high-spin isomer, the intermediate nuclear states also have to be of high spin, and since the transmission coefficients at 14 MeV decrease with increasing l for large l, it would be expected that the isomer ratio would decrease strongly with increasing isomer spin. This same explanation accounts for another feature of our results. It is clear from our GNASH calculations that the variation of the isomer ratio with isomer spin is much stronger for lower incident neutron energies. At lower energies the decrease of the transmission coefficients with increasing l is even greater, resulting in a drastically reduced population of high-spin isomers in $(n,2n)$ reactions.

C. The (n, n') Isomeric Cross Section Ratios

The ground states of ^{178}Hf and ^{179}Hf are stable and are naturally occuring in hafnium, and natural niobium is monoisotopic in ^{93}Nb. Therefore we have considered the (n, n') reactions to the isomeric states for these nuclei. In addition we have also calculated the (n, n') reaction on ^{166}Ho to the isomeric state, the ground state of ^{166}Ho having a 1.1 day lifetime. We have determined the isomeric cross section ratio as a function of incident neutron energies between 1 and 14 MeV, and our results are shown in Table III.

TABLE III

Isomeric Cross Section Ratios in (n, n') Reactions

Neutron Energy (MeV)	^{93}Nb (n, n') ^{93m}Nb (1/2-)	^{166}Ho (n, n') ^{166m}Ho (7-)	^{178}Hf (n, n') ^{178m}Hf (16+)	^{179}Hf (n, n') ^{179m}Hf (25/2-)
1	$9.7^{-2} \times 10^{-2}$	8.3×10^{-3}	0.0	0.0
2	$8.9^{-2} \times 10^{-2}$	2.8×10^{-2}	0.0	4.5×10^{-5}
3	$8.5^{-2} \times 10^{-2}$	5.5×10^{-2}	2.2×10^{-15}	3.8×10^{-4}
4	8.8×10^{-2}	8.7×10^{-2}	4.4×10^{-11}	1.1×10^{-3}
5	8.9×10^{-2}	0.12	1.5×10^{-9}	2.8×10^{-3}
6	8.8×10^{-2}	0.15	1.5×10^{-8}	4.3×10^{-3}
7	8.7×10^{-2}	0.19	8.6×10^{-8}	7.1×10^{-3}
8	8.6×10^{-2}	0.24	3.9×10^{-7}	1.7×10^{-2}
9	8.6×10^{-2}	0.28	2.3×10^{-6}	3.2×10^{-2}
10	8.6×10^{-2}	0.30	1.2×10^{-4}	3.5×10^{-2}
11	8.6×10^{-2}	0.32	3.3×10^{-5}	3.4×10^{-2}
12	8.6×10^{-2}	0.34	7.2×10^{-5}	3.9×10^{-2}
13	8.7×10^{-2}	0.34	1.4×10^{-4}	3.7×10^{-2}
14	8.8×10^{-2}	0.36	2.8×10^{-4}	4.3×10^{-2}

For the high-spin isomers (all except ^{93m}Nb (1/2-)), the isomer ratio is seen to be a strongly-decreasing function of incident energy, and the higher isomer spins have the stronger the energy dependences. This is because the angular momentum brought in by the projectile neutron decreases with decreasing energy, and therefore results in a reduction in the high-spin isomer population. It is interesting to note that the energy dependence of the (n, n') isomer cross-section ratio is weaker than that of the $(n, 2n)$ reaction. If the two ratios are compared over the energy range 14-8 MeV, it is clear from Tables II and III that the isomer cross section ratio decreases less rapidly for the (n, n') reaction. This can be understood as follows: for an (n, n') reaction to occur at these energies, rather than an $(n, 2n)$ reaction, the primary-emitted neutron has to be emitted with a relatively high energy, so that gamma decay then occurs. A high-energy emitted neutron is able to carry off a large angular momentum, and hence can result in the population of high-spin residual nucleus states. $(n, 2n)$ processes, on the other hand, will be dominated by low-energy equilibrium-emission neutrons with small angular momenta, with a small probability of exciting the high-spin state. In the case of the (n, n') reaction on ^{93}Nb, the fact that the long-lived isomer is of low spin results in an isomeric cross section ratio which is approximately energy-independent.

The Kopecky-Gruppelaar systematic calculations for the (n, n') isomeric cross section ratio again show a peak at an isomer spin $J^m = 3 - 5$, and are compared in Fig. 3 with our calculations at 14 MeV. As well as showing our results from Table III in this figure, we include isomeric ratios at 14 MeV for the production of the ^{178m}Hf(8-), ^{179m}Hf(1/2-) and ^{180m}Hf(8-) states which we have also determined. In general the Kopecky-Gruppelaar systematics agree fairly well with our detailed GNASH calculations (to within a factor of 2-3). One notable exception is the isomer cross section ratio for the production of the ^{179m}Hf(25/2-), for which our calculation exceeds the systematics by more than an order of magnitude (and the experimental result of Patrick *et al* exceeds the systematics by an even greater factor). This is probably due to the fact that Kopecky *et al* adopt a ground-state spin of 0.5 in their model calculation, whereas in this case the ground-state spin is 4.5. Hence they overestimate the spin change in the reaction and consequently underestimate the isomeric cross section ratio.

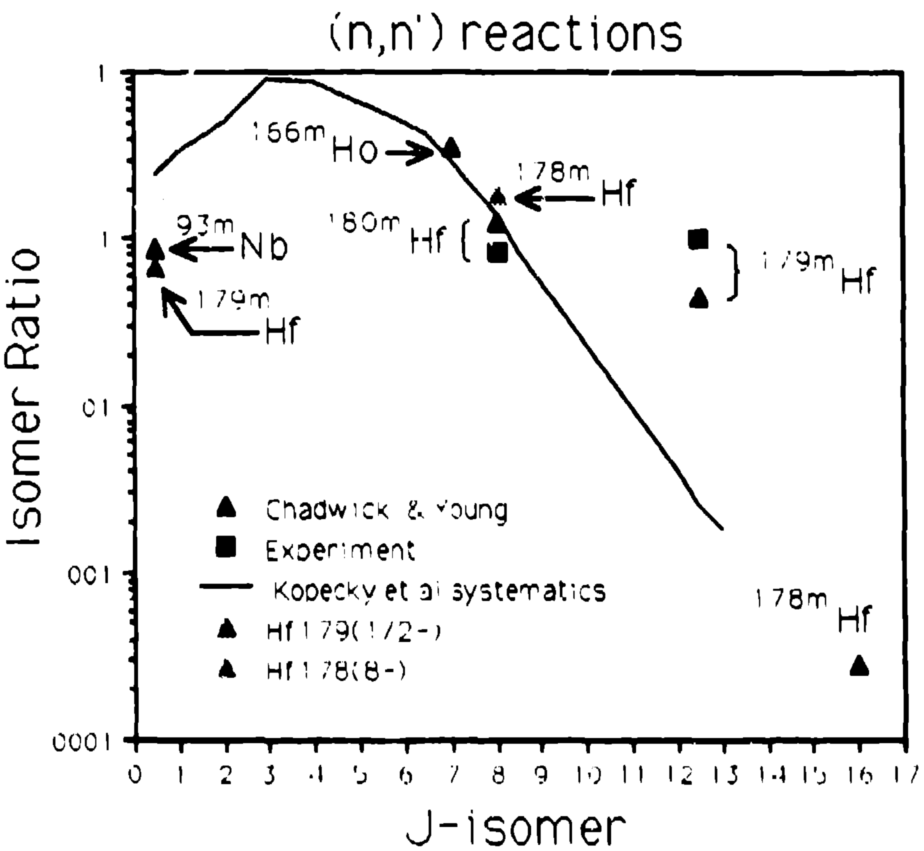

Fig. 5. The (n, n') isomeric cross-section ratio as a function of isomer spin for 14-MeV incident neutrons. The Kopecky systematics for one-step reactions are compared with

GNASH calculations and with experimental data.

D. Isomeric Cross Section Ratios for (n,γ) Reactions

A limited amount of cross-section data for total (n,γ) radiative capture reactions is available at neutron energies in the MeV region, and simple systematic behavior with atomic number A has been noted for 14-MeV neutrons [16]. In the case of (n,γ) reaction to isomeric states, however, experimental data are much more limited and consist mostly of data for thermal incident neutrons. Thermal (n,γ) isomer ratios for an assortment of heavy nuclei are plotted versus the spins of the isomeric states in Fig. 6. Clearly, simple systematic behavior is much less evident for thermal neutron capture data than for 14-MeV particle-production cross sections, especially for isomeric states with spins greater than 5. This situation, coupled with the almost complete lack of experimental data at higher energies, results in a pressing need for reliable theoretical estimates of (n,γ) isomer ratios.

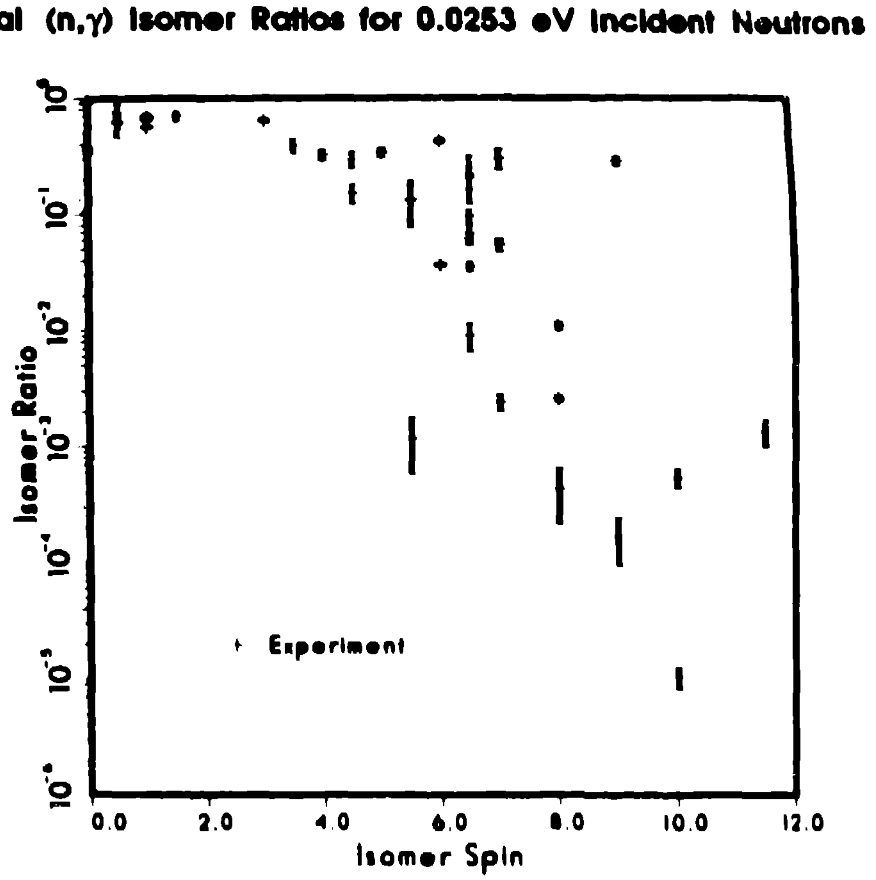

Fig. 6. Experimental isomer ratios for (n,γ) reactions with thermal neutrons, plotted as a function of spin of the isomeric states.

The GNASH code was used to calculate (n,γ) cross sections leading to isomeric states in ^{166}Ho(7^-, 1200 y), ^{178}Hf(16^+, 31 y; 8^-, 4 s), ^{179}Hf ($25/2^-$, 25.1 d; $1/2^-$, 18.7 s), ^{186}Re (8^+, 2 x 10^5 y), and ^{188}Re (6^-, 18.6 m). Except as noted below, the generalized Lorentzian form was utilized for the gamma-ray strength functions. The calculations were performed down to an incident energy of at least 1 keV in each case, at which energy the neutron transmission coefficients are completely dominated by s-waves, and it is possible to make a crude comparison with the thermal neutron experimental data. A selection of the isomeric ratios [relative to the total (n,γ) cross section] that results from the calculations for ^{105}Ho$(n,\gamma)^{166m}$Ho, ^{177}Hf$(n,\gamma)^{178m}$Hf, and ^{187}Re$(n,\gamma)^{188m}$Re reactions are shown in Fig. 7. The calculated isomer ratios are given explicitly in Table IV.

A feature of isomer ratios of Fig. 7 is a general trend of increasing ratio with increasing neutron energy. This behavior reflects the fact that more angular momentum is brought into the reactions as the neutron energy is increased thus increasing the population of higher spin states. For both the ^{165}Ho$(n,\gamma)^{166m}$Ho, and ^{187}Re$(n,\gamma)^{188m}$Re reactions, an anomaly is seen in the calculated isomer ratios near 300 keV that interrupts this general trend of increasing isomer ratios with neutron energy. This effect is thought to result from the fact that thresholds for one or more high spin states in the target nucleus opens in this energy region. The presence of these open channels to higher spin states permits neutron decays to occur more readily from higher spin states in the compound nucleus, thus reducing the high-spin population available for cascading to the isomeric state. As the incident neutron energy is further increased, more and more channels of all spins are opened, and the anomalous effect is overwhelmed by the increasing angular momentum brought into the reaction.

Calculated ^{177}Hf$(n,\gamma)^{178m}$Hf Isomer R

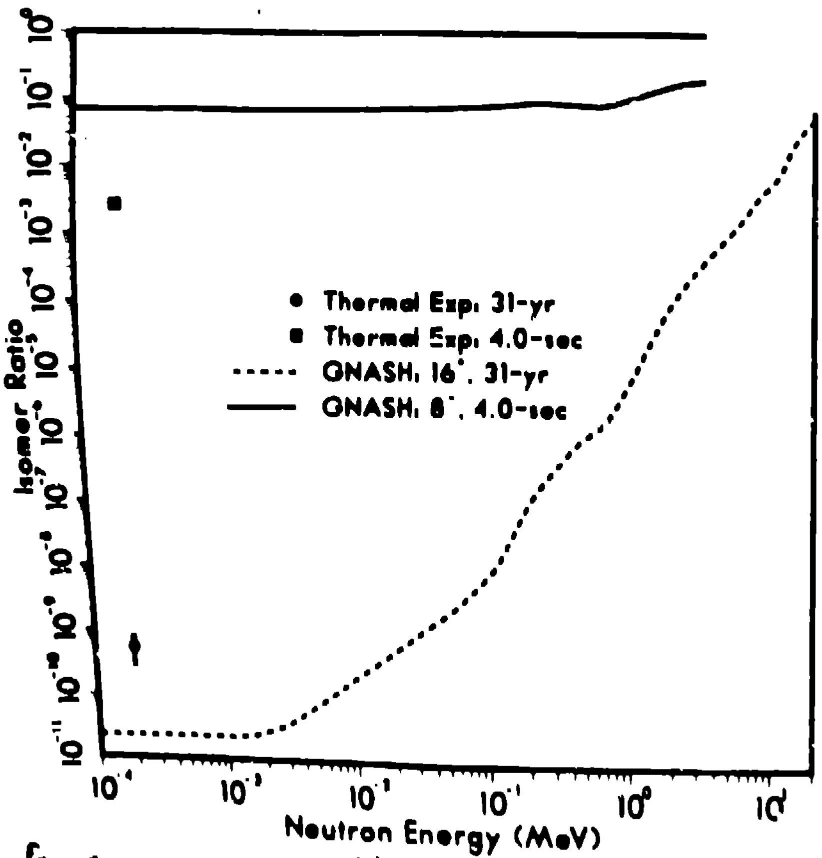

Fig 7.

Fig. 7. Calculated isomer ratios for $^{165}Ho(n,\gamma)^{166m}Ho$, $^{177}Hf(n,\gamma)^{178m}Hf$, and $^{187}Re(n,\gamma)^{188m}Re$ reactions from 0.1 keV to 20 MeV. Experimental data from thermal neutron measurements are included for comparison.

The agreement (or lack of agreement) between our calculated isomer ratios at lower energies and the thermal neutron measurements depends upon the extent to which the average properties (widths) embodied in our statistical model coincide with the very few channels involved in the thermal neutron measurements. Clearly, large differences between the calculations at $\sim$ 1 keV and the thermal measurements are possible, and such are seen in the case of the $^{177}Hf((n,\gamma)^{178m}Hf$ isomer ratios ($\sim$ factor of 20 differences). In the cases of the $^{165}Ho(n,\gamma)^{166m}Ho$ and $^{187}Re(n,\gamma)^{188m}Re$ reactions, however, the differences between the calculated ratios near 1 keV and the thermal experimental values are much smaller, of the order of 30%.

To investigate the behavior of isomer ratios with neutron energy and with isomer spin, a simple parametric study was performed using the $^{187}Re(n,\gamma)^{188m}Re$ reaction as a base case. In this study various values of spin between 0 and 16 were assumed for the isomeric state in ^{188}Re at $E_x = 172$ keV, and the isomer ratio was calculated as a function of incident neutron energy for each isomer spin. The $^{187}Re(n,\gamma)^{188m}Re$ reaction was chosen because the real isomer ($J^\pi = 6^-, E_x = 172$ keV) is not fed by any of the known discrete states, so all the isomer's excitation comes from decays from the continuum. Additionally, the calculated isomeric state branching ratio for the real isomer is consistent (within 30%) at the lowest energy of the calculation (0.1 keV) with the measured ratio for thermal neutrons. The results of these calculations, performed using a standard Lorentzian, are shown in Fig. 8 for incident neutron energies of 0.001, 1, and 14 MeV. The calculated isomer ratios show strong dependence on both incident neutron energy and on isomer spin. The calculations for the higher spin states are thought to depend strongly on details of the gamma-ray strength functions as well as on the level density in the compound nucleus, since populating the isomeric states occurs almost exclusively through multiple γ-ray cascades in the compound nucleus.

Theoretical Isomer Ratios as Functions of Isomer Spin Based on Fictitious $^{187}Re(n,\gamma)^{188m}Re$ Reactions

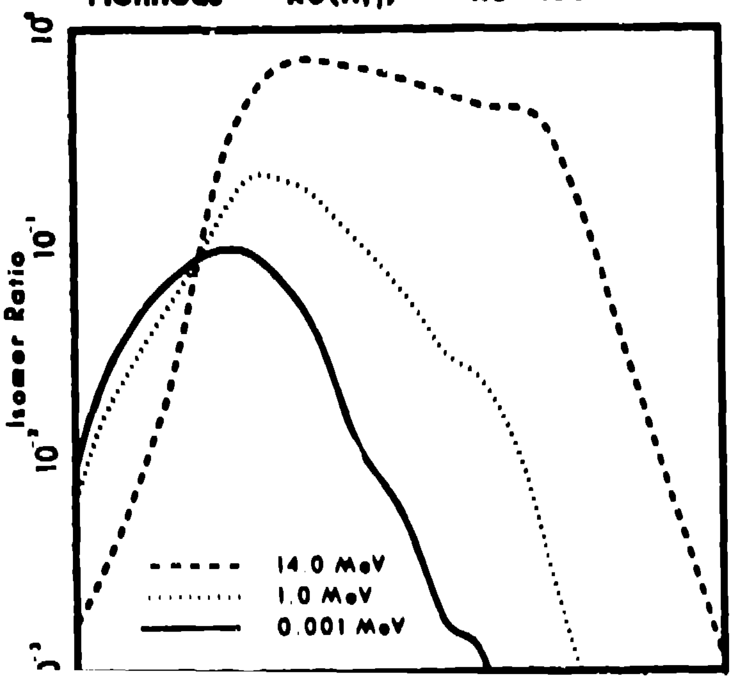

Fig. 8. Calculated isomer ratios as functions of incident neutron energy and isomer spin for the ^{187}Re$(n,\gamma)^{188m}$Re reaction. The calculations were performed by replacing the spin of the actual isomer in ^{188}Re$(j^{\pi} = 6^{-}, E_x = 172$ keV) by values from 0 to 20.

While it is attractive to consider using calculations such as those illustrated in Fig. 8 to search for systematic relationships that might be useful in making simple predictions of isomer ratios, we found that the calculated results for the various cases were strongly dependent on the properties of the nuclei in question. The (n,γ) reaction is specifically excluded from the "one-step reaction" systematics identified by Gruppelaar *et al.* [16], because the validity of those systematics was primarily established for (n,n'), (n,p), and (n,α) reactions and was doubtful for (n,γ). However, it was necessary for those authors to use the one-step reaction systematics for (n,γ) reactions in the REAC-ECN-3 library, due to the lack of other alternatives. A comparison between the one-step reaction systematics of Gruppelaar it et al. and our calculated (n,γ) isomer ratios at $E_n = 14$ MeV is given in Fig. 9. The calculated ratios are seen to differ significantly from the systematics, thus confirming the conclusion of Gruppelaar *et al.* that the one-step reaction systematics might not be valid for (n,γ) reactions. This further highlights the need for careful nuclear theory calculations for important reactions.

TABLE IVa

Isomeric Cross Section Ratios in (n,γ) Reactions

Neutron Energy (MeV)	^{165}Ho (n,γ) ^{166m}Ho (7-)	^{177}Hf (n,γ) ^{178m}Hf (8-)	^{178}Hf (n,γ) ^{178m}Hf (16+)
0.001	0.069	0.069	2.3×10^{-11}
0.01	0.078	0.071	2.0×10^{-10}
0.1	0.11	0.081	8.2×10^{-9}
0.2	0.13	0.092	1.1×10^{-7}
0.4	0.11	0.086	6.9×10^{-7}
0.6	0.14	0.087	1.3×10^{-6}
0.8	0.17	0.10	4.5×10^{-6}
1.0	0.19	0.11	7.1×10^{-6}
2.0	0.25	0.17	1.1×10^{-4}
4.0	0.32	0.21	6.3×10^{-4}
6.0	0.38	0.23	1.7×10^{-3}
8.0	0.43	0.25	3.9×10^{-3}
10.0	0.48	0.26	5.9×10^{-3}
12.0	0.57	0.28	1.1×10^{-2}
14.0	0.66	0.30	2.5×10^{-2}

TABLE IVb

Isomeric Cross Section Ratios in (n,γ) Reactions

Neutron Energy (MeV)	^{178}Hf (n,γ) ^{179}Hf (25/2-)	^{185}Re (n,γ) ^{186m}Hf (8+)	^{187}Re (n,γ) ^{188m}Re (6-)
0.001	1.9×10^{-13}	2.1×10^{-3}	0.048
0.01	2.7×10^{-12}	2.5×10^{-3}	0.051
0.1	1.4×10^{-10}	8.1×10^{-3}	0.088
0.2	1.5×10^{-9}	0.014	0.114
0.4	5.4×10^{-9}	0.016	0.099
0.6	2.8×10^{-8}	0.018	0.12
0.8	7.6×10^{-8}	0.022	0.14
1.0	1.6×10^{-7}	0.027	0.17
2.0	5.3×10^{-6}	0.061	0.24
4.0	9.8×10^{-5}	0.13	0.33
6.0	3.2×10^{-4}	0.18	0.40
8.0	1.8×10^{-3}	0.24	0.47
10.0	4.0×10^{-3}	0.29	0.52
12.0	9.3×10^{-3}	0.35	0.59
14.0	2.2×10^{-2}	0.45	0.69

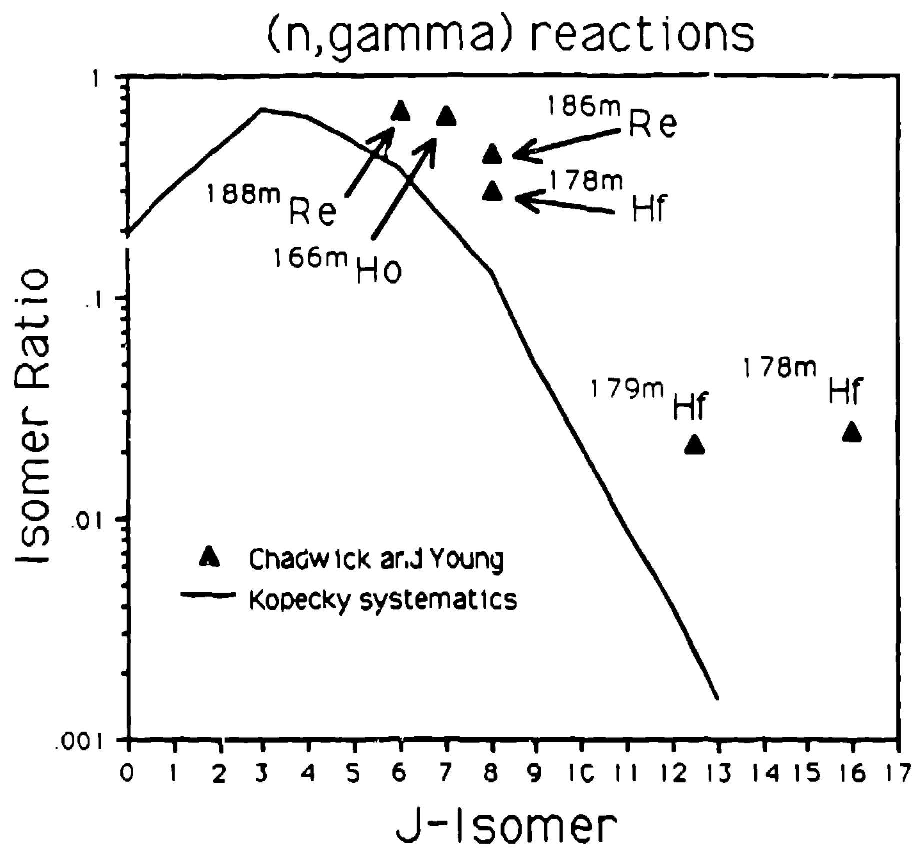

Fig. 9. The (n,γ) isomeric cross-section ratio as a function of isomer spin for 14-MeV incident neutrons. The Kopecky systematics for one-step reactions are compared with GNASH calculations.

IV. CONCLUDING REMARKS

We present calculations of the energy dependence of isomer ratios for long-lived metastable states in ^{93}Nb, ^{121}Sn, ^{166}Ho, ^{184}Re, ^{186}Re, ^{178}Hf, ^{179}Hf, and ^{192}Ir, populated by means of (n,n'), $(n,2n)$, and (n,γ) reactions. The calculated ratios for $(n,2n)$ reactions generally support predictions from systematics at 14 MeV except for isomer spins above $\sim$ 12. The agreement with systematics is not as good for (n,n') reactions as is the case for $(n,2n)$, but the systematics obviously are good enough to still be useful in developing large activation libraries. In the case of (n,γ) reactions, the theoretical values cannot be compared directly with the thermal neutron measurements but are roughly consistent at the lower energy range of the calculations.

Because of the limited amount of experimental data available on isomer ratios, nuclear theory codes such as GNASH provide a useful complement to the data base. The calculations are particularly important for (n,γ) reactions, as experimental data are extremely limited and systematics provide little guidance, as well as for determining the energy dependence of (n,n') and $(n,2n)$ isomer ratios, for which there is little experimental information. In general, we recommend that evaluations of important long-lived isomers be based on detailed theoretical analyses matched to the available experimental data. The use of systematics should be limited to providing data for less important reactions. In cases where systematics are used, particular care should be exercised with (n,γ) isomeric ratios, and the procedure, which is sometimes used, of setting the isomer ratio to 1/2 of the total (n,γ) cross sections should *never* be used at low energies, as it can lead to errors of many orders of magnitude.

A detailed description of the present work will be presented at the upcoming IAEA Research Coordination Meeting on "Activation Cross Sections for the Generation of Long-Lived Radionuclides of Importance in Fusion Reactor Technology," in Vienna, 11-12 November 1991.

V. REFERENCES

[1] M.B. Chadwick and P.G. Young, 'Calculations of the Production Cross Sections of High-Spin Isomeric States in Hafnium', Nucl. Sci. and Eng. **108**, 117 (1991).

[2] E.D. Arthur, 'The GNASH Preequilibrium-Statistical Model Code', Los Alamos National Laboratory report LA-UR-88-382 (1988); P.G. Young and E.D. Arthur, 'GNASH: A Preequilibrium, Statistical Nuclear-Model Code for Calculation of Cross Sections and Emission Spectra', Los Alamos Scientific Laboratory report LA-11753-MS (1990).

[3] B.H. Patrick, M.G. Sowerby, C.G. Wilkins and L.C. Russen, 'Measurements of 14-MeV Neutron Cross Sections for the Production of Isomeric States in Hafnium Isotopes,' presented at the Specialists' Mtg. Neutron Activation Cross Sections for Fission and Fusion energy Applications, Argonne, Illinois, September 13-15 1989.

[4] J. Kopecky and H.Gruppelaar, 'Systematics of Neutron-Induced Isomeric Cross Section Ratios at 14.5 MeV', ECN report ECN-200 (1987).

[5] C.L. Dunford, 'Compound Nucleus Reaction Programs COMNUC and CASCADE', AI-AEC-12931, Atomics Int. (1970).

[6] C. Kalbach,'The Griffin Model, Complex Particles and Direct Nuclear Reactions', Z. Phys. **A283**, 401 (1977).

[7] D.M. Brink, 'Some Aspects of the Interaction of Fields with Matter', D.Phil. The-

sis, Oxford (1955); P. Axel, 'Electric Dipole Ground State Transition Width Strength Function', Phys. Rev. **126**, 671 (1962).

[8] J. Kopecky and M. Uhl, 'Test of Gamma-Ray Strength Functions in Nuclear Reaction Model Calculations,' Phys. Rev. C **42**, 1941 (1990).

[9] J. Raynal, 'Optical Model and Coupled-Channel Calculations in Nuclear Physics', SMR-9/8, International Atomic Energy Agency (1972).

[10] O. Bersillon, 'SCAT2 - A Spherical Optical Model Code',in Progress Report of the Nuclear Physics Division, Bruyeres-le-Chatel (1977), CEA-N-2037, p. 111 (1978).

[11] S.F. Mughabghab, 'Neutron Resonance Parameters and Thermal Cross Sections', Parts A and B, in Neutron Cross Sections, V. 1, Academic Press Inc., New York, (1981) (part A) and (1984) (part B).

[12] S.S. Dietrich and B.L. Berman, 'Atlas of Photoabsorption Cross Sections Obtained with Monoenergetic Photons', Atomic and Nuclear Data Tables, 199 (1988).

[13] A. Gilbert and A.G.W. Cameron, 'A composite Nuclear-Level density formula with Shell Corrections', Can. J. Phys. **43**, 1446 (1965).

[14] J. L. Cook, H. Ferguson, and A. R. Musgrove, Aus. J. Phys. **20**, 477 (1967).

[15] E. D. Arthur, P. G. Young, A. B. Smith, and C. A. Philis, Trans. Am. Nucl. Soc. **39**, 793 (1981).

[16] H. Gruppelaar, H. A. J. van der Kamp, J. Kopecky, and D. Nierop, 'The REAC-ECN-3 Data Library with Neutron Activation and Transmutation Cross Sections for Use in Fusion Reactor Technology,' ECN report ECN-207 (1988).

State densities with linear momentum and their application to preequilibrium and photoabsorption reactions

M.B. Chadwick

Theoretical Division, Los Alamos National Laboratory, Los Alamos, New Mexico 87545

P. Obložinský

Institute of Physics, Slovak Academy of Sciences, 842 28 Bratislava, Czechoslovakia

We discuss the concept of state densities with linear momentum and describe their application to preequilibrium reaction theory as well as nuclear photoabsorption via the quasideuteron mechanism. An exciton model is presented for particle emission in nucleon-induced reactions in which linear momentum conservation is included. The nucleon emission contributions from the first two preequilibrium stages are calculated by determining exact particle-hole state densities with a specific energy and linear momentum in a Fermi-gas model of the nucleus. Angular distributions arise naturally from our treatment and do not have to be added in an *ad hoc* way. The angular distributions that we obtain from the first two preequilibrium stages are identical to those found using the Kikuchi-Kawai quasifree scattering kernel. Since many preequilibrium analyses are based upon an equidistant single-particle model of the nucleus, we also determine the state densities with linear momentum (and hence angular distributions) in such a model. A no-parameter quasideuteron model of photoabsorption is presented in which the Levinger parameter and Pauli-blocking function are determined theoretically, using state densities with linear momentum. Comparisons with data are shown, and the temperature dependence of the photoabsorption cross section is calculated.

I. INTRODUCTION

All theoretical descriptions of nuclear reactions in the continuum region make statistical assumptions concerning the complex multistep reaction process. In order to calculate cross sections for preequilibrium emission one simplifies the complicated nature of the different possible scattering processes by introducing averaged matrix elements of the various possible transitions and state densities for the different particle-hole preequilibrium configurations. Expressions for the state densities represent an integral part of any theoretical calculation, and a number of different approaches for obtaining such densities have been developed. Frequently an equidistant single-particle-state model is adopted, allowing a simple evaluation of the particle-hole state density. If there are no restrictions on the particle-hole excitations the formulae of Ericson [1] and Williams [2] result. Including finite well-depth restrictions leads to the slightly more complicated expressions in [3]. Partial state densities within an equidistant single particle model have been developed to describe the angular momentum [2], parity [4], and isospin [5] structure of the states. We have recently extended such ideas to obtain the linear-momentum structure of such particle-hole state densities [?,6].

The linear momentum structure of a state density is a useful concept since, for reasonably high excitation energies, a semiclassical description of the nucleus (where one pictures the individual nucleon states as eigenstates of linear momentum) becomes more realistic. By considering the variation of the accessible residual nucleus state density with nucleon emission angle, it is possible to obtain angular distributions of emitted particles in a consistent manner. We also describe how state densities with linear momentum can be used in a quasideuteron model of photoabsorption. We found such densities essential for a realistic description of the correlated nature of neutron-proton emission in photoabsorption processes above the giant resonance and below the pion threshold.

In section II we discuss state densities with linear momentum, and how they can be calculated both for a Fermi-gas and an equidistant single-particle-state model. In section III we describe two different applications of state densities with linear momentum. Section IIIA descibes how angular distributions can be obtained in an exciton model of preequilibrium reactions, and an account of this work is to appear in the November 1991 issue of Physical Review C - Rapid Communications. Section IIIB gives a description of out quasideuteron photoabsorption model (full details can be found in Ref.[?]) and we give some conclusions in section IV.

II. STATE DENSITIES WITH LINEAR MOMENTUM

We shall now show how state densities with linear momentum are calculated. We view the nucleus semiclassically, and wish to determine the number of $p-h$ states with an energy in the range $E \to E + dE$ and a total momentum in the range $\mathbf{K} \to \mathbf{K} + d^3\mathbf{K}$. This problem was first investigated by Madler and Reif [?] who used a partition-function approach. Unfortunately, their method is valid only for large numbers of excited particles and holes, and for most applications in nuclear reaction theories it is the simple particle-hole excitations that are most important. In addition, their approach suffers from some computational difficulties in making saddle-point approximations. Maddler and Reif's approach has been extended by Iwamoto [?] for use in heavy-ion calculations. Our approach, on the otherhand, is exact and leads to simple analytic expressions for the simplest $p-h$ state densities. The more complicated $p-h$ densities become harder to solve using our method due to the high-dimensionality of the integrations, though for many applications (including those shown in this paper) it is only densities for simple $p-h$ excitations that are needed.

In order to make our approach more transparent, we first indicate how state densities without linear momentum can be determined. The state density of a p-particle h-hole system can be obtained by convoluting single-particle and -hole densities with an energy-conserving delta-function. When linear momentum effects are not accounted for, this can be expressed as

$$\rho(p,h,E) = \frac{1}{p!h!}\int_{i=1}\cdots\int_{i=p}\int_{j=1}\cdots\int_{j=h}\delta(E-\sum_{i=1}^{p}\epsilon_i+\sum_{j=1}^{h}\epsilon_j)$$

$$\times\prod_{i=1}^{p}\rho(1p,\epsilon_i)\,\theta(\epsilon_i-\epsilon_F)\,d\epsilon_i\prod_{j=1}^{h}\rho(1h,\epsilon_j)\,\theta(\epsilon_F-\epsilon_j)\,d\epsilon_j, \tag{1}$$

where i labels the particles and j the holes. The theta functions are unity if their argument is greater than zero and zero otherwise, accounting for Pauli-blocking. The densities of single-particles and -holes in energy space are represented by $\rho(1p,\epsilon_i)$ and $\rho(1h,\epsilon_j)$, with the energies $\epsilon_{i,j}$ measured relative to the bottom of the nuclear well. The factorials $p!$ and $h!$ account for the indistinguishability of the particles and holes. If an equidistant single-particle model of the nucleus is used, the above expression would yield the Ericson state density expression, corrected to include finite nuclear well depth restrictions [?]. In a Fermi-gas model of the nucleus the single-particle and -hole densities in energy space are given by $\rho(1p,\epsilon_i) = 3A\sqrt{\epsilon_i}/2\epsilon_F^{3/2}$ and $\rho(1h,\epsilon_j) = 3A\sqrt{\epsilon_j}/2\epsilon_F^{3/2}$, where A is the nuclear mass number.

We now generalize the above expression to allow state densities with a specific linear momentum to be determined. The convolution of the single-particle and -hole states is now performed in momentum space, and a linear-momentum conserving delta function is included in the integration.

$$\rho(p,h,E,\mathbf{K}) = \frac{1}{p!h!}\int_{i=1}\cdots\int_{i=p}\int_{j=1}\cdots\int_{j=h}\delta(E-\sum_{i=1}^{p}\epsilon_i-\sum_{j=1}^{h}\epsilon_j)$$

$$\times\delta(\mathbf{K}-\sum_{i=1}^{p}\mathbf{k}_i-\sum_{j=1}^{h}\mathbf{k}_j)\ \prod_{i=1}^{p}\rho(1p,\mathbf{k}_i)\,\theta(k_i-k_F)\,d^3\mathbf{k}_i\ \prod_{j=1}^{h}\rho(1h,\mathbf{k}_j)\,\theta(k_F-k_j)\,d^3\mathbf{k}_j, \tag{2}$$

where $\mathbf{k}_i$ and $\mathbf{k}_j$ are the single-particle and -hole linear momenta, and k_F is the Fermi momentum. The density of single-particle and -hole states in momentum space are $\rho(1p,\mathbf{k}_i)$ and $\rho(1h,\mathbf{k}_j)$ respectively.

Neither Eq. (1) nor Eq. (2) include the possibility that some of the excited particles/holes can Pauli-block other particles/holes, though for the simple particle-hole configurations that we consider this effect can be safely ignored. As expected from symmetry, the density of states with linear momentum, $\rho(p,h,E,\mathbf{K})$, is independent of the direction of the total momentum $\mathbf{K}$ and depends only upon its magnitude. The dimensions of the state densities with linear momentum are $\mathrm{MeV}^{-1}(\mathrm{MeV}/c)^{-3}$, and they obey the relation

$$\rho(p,h,E) = \int \rho(p,h,E,\mathbf{K})\ 4\pi K^2 dK. \tag{3}$$

This equation also allows a useful check on analytic expressions that are derived for state densities with linear momenta. If they are integrated over all values of total momenta they must yield the 'conventional' state densities, which are only a function of energy.

A. The Fermi-gas model

In the Fermi-gas model the single-particle and -hole states are eigenstates of linear momentum, the density of such states in momentum-space being a constant which reproduces the number of nucleons,

$$\rho(1p,\mathbf{k}_i) = \rho(1h,\mathbf{k}_j) = \frac{A}{\frac{4}{3}\pi k_F^3} \equiv \kappa. \tag{4}$$

Below we give some analytic results for state densities with linear momentum for $p-h$ configurations which are important in preequilibrium reactions and will be used in the next section. We shall consider particle emission from only the first two preequilibrium stages since these dominate the preequilibrium spectrum for most nucleon-induced reactions. Thus we must evaluate the state densities for $1p1h$, $2p1h$, $2p2h$ and $3p2h$ excitations. The $\rho(1p,1h,E,\mathbf{K})$ density requires the solution of a six-dimensional integration, which can be solved analytically using the techniques shown in Ref. [7], giving

$$\rho(1p,1h,E,\mathbf{K}) = \frac{\pi m g^2}{K} \times \begin{cases} \left[k_F^2 - \left(\frac{mE}{K} - \frac{K}{2}\right)^2\right] & \text{if } K_{min} < K < K_1 \text{ or } K_2 < K < K_{max} \\ 2mE & \text{if } K_1 < K < K_2 \\ 0 & \text{otherwise.} \end{cases} \tag{5}$$

where

$$K_{\substack{min \\ max}} = \sqrt{2mE + k_F^2} \mp k_F, \tag{6}$$

$$K_{\substack{1 \\ 2}} = \sqrt{2(k_F^2 - mE) \mp 2k_F\sqrt{k_F^2 - 2mE}}. \tag{7}$$

The high-dimensionality of the integrations for the evaluation of the more complex state densities can be reduced by breaking up the integrals, making use of analytic solutions for simpler configurations. For instance, the $\rho(2p,2h,E,\mathbf{K})$ requires a twelve-dimensional integration, though it can be expressed as a convolution of two $1p1h$ state densities, each of which is known analytically, so that

$$\rho(2p,2h,E,\mathbf{K}) = \frac{1}{2!\,2!}\int\int \rho(1p,1h,E_1,\mathbf{K}_1)\;\rho(1p,1h,E-E_1,\mathbf{K}-\mathbf{K}_1)\;d^3\mathbf{K}_1\;dE_1, \tag{8}$$

which, by symmetry, can be reduced to a three-dimensional integral and can be solved numerically without any difficulties. We checked that when the state densities with linear momentum are integrated over all total momenta [using Eq. (3)] they yield the Fermi-gas state densities without linear momentum of Eq. (1).

In Fig. 1 the variation of the residual nucleus $1p1h$ and $2p2h$ state densities [Eqs. (5) and (8)] with emission angle is shown for the reaction ^{184}W(n,n') for an incident energy of 26 MeV and emission energies of 14.5 and 18.5 MeV. A Fermi energy of 35 MeV was adopted. These densities are strongly forward-peaked due to the variation of the state density with the linear momentum deposited in the residual nucleus. This forward peaking decreases with increasing exciton number as the linear momentum brought in by the projectile is shared among more particles and holes and the memory of the incident direction is lost. Since the angular distribution of emitted particles comes from the variation of the residual-nucleus phase space with emission angle, no preequilibrium emission from the $n = 3$ stage can occur for angles greater than about 110 degrees. This is a kinematical effect resulting from the restrictions of energy and momentum conservation and is also seen in Refs. [8, 10].

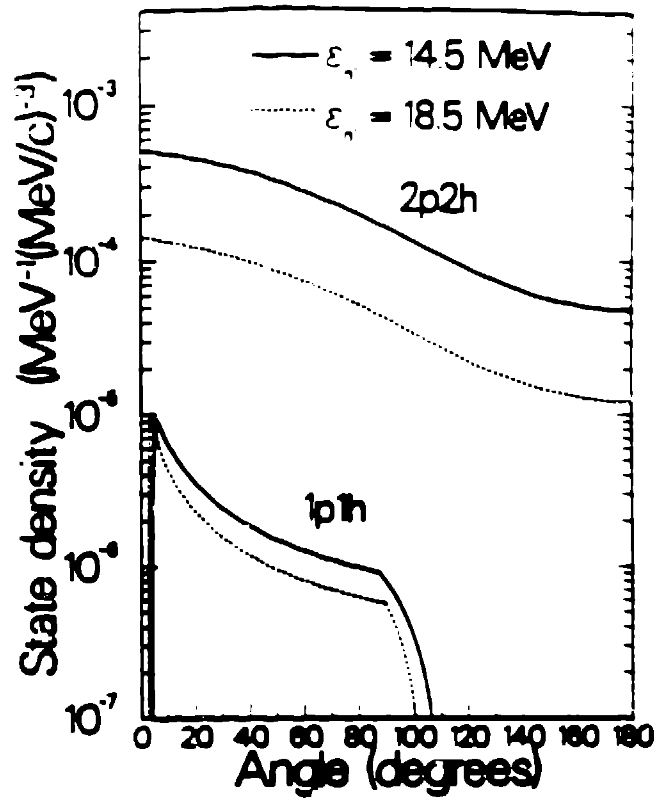

FIG. 1. The variation of the $1p1h$ and $2p2h$ state densities with emission angle for the residual nucleus in the reaction ^{184}W(n,n'). The incident energy is 26 MeV, and the emission energies are $\epsilon_{n'}$=14.5 and 18.5 MeV.

FIG. 1. The variation of the $1p1h$ and $2p2h$ state densities with emission angle for the residual nucleus in the reaction ^{184}W(n,n'), using a Fermi-gas model. The incident energy is 26 MeV, and the emission energies are $\epsilon_{n'}$=14.5 and 18.5 MeV.

B. Equidistant single-particle-state model

The above subsection contained expressions for state densities with linear momentum in a Fermi gas model of the nucleus. In such a model the single-particle states in energy space increase as the square-root of the excitation energy, and are constants in momentum space. In this section we shall indicate how state densities with linear momentum can be obtained for equidistant single-particle levels in energy space. This is of importance since preequilibrium reaction theories almost always use state densities which are based upon equidistant single-particle levels, due to their computational simplicity.

The particle-hole state density is determined using Eq. (2). We need, however, to determine the single-particle density in momentum space which yields equidistant levels in energy space. The number of single-particle states in momentum space with absolute momenta between k and $k + dk$ is

$$dN(k) = 4\pi k^2\, dk\, \rho_1(\mathbf{k}), \qquad (9)$$

where $\rho_1(\mathbf{k})$ denotes either $\rho(1p, \mathbf{k}_i)$ or $\rho(1h, \mathbf{k}_j)$, the single-particle (and -hole) density that we are determining. For equidistant levels in energy space, $dN(\epsilon) = g\, d\epsilon$, ϵ being the excitation energy and g the constant single-particle density. Since $\epsilon = k^2/2m$, this equation can be expressed as

$$dN(k) = \frac{gk}{m}\, dk. \tag{10}$$

Equations (??) yield the result for the single-particle density in momentum space.

$$\rho(1p, \mathbf{k}_i) = \rho(1h, \mathbf{k}_j) = \frac{g}{4\pi mk}. \tag{11}$$

In other words, the density of single-particle states in momentum space that yields equidistant states in energy space varies as $1/k$. Since the $1p1h$ state density determines the angular distribution from single-step scattering, we show below the $1p1h$ state density with linear momentum for an equidistant single-particle level nucleus, obtained by solving the six-dimensional integral (2) with Eq. (11),

$$\rho(1p, 1h, E, \mathbf{K}) = \frac{g^2}{8\pi mK} \ln\left[\frac{k_F + \sqrt{k_F^2 + 2mE}}{k' + \sqrt{k'^2 + 2mE}}\right] \tag{12}$$

where

$$\begin{aligned} k' &= \left|\frac{mE}{K} - \frac{K}{2}\right| \quad \text{if} \quad K_{\min} < K < K_1 \quad \text{or} \quad K_2 < K < K_{\max} \\ k' &= \sqrt{k_F^2 - 2mE} \quad \text{if} \quad K_1 < K < K_2 \\ \text{and } \rho(1p, 1h, E, \mathbf{K}) &= 0 \qquad\qquad \text{otherwise,} \end{aligned} \tag{13}$$

$K_{\min}, K_{\max}, K_1, K_2$ being given by Eqs. (6,7). As in the Fermi gas model, we again find an expression for the $1p1h$ density which has three different regions. The values of $K_{\min}, K_{\max}, K_1, K_2$ which define the boundaries of these regions are not sensitive to the particular single-particle densities adopted and are therefore identical for the Fermi-gas and equidistant models. Equation (3) must hold, indicating that if the above $1p1h$ state density is integrated over all momenta the Ericson density, with finite well-depth restrictions, results. We have checked that our Eq. (13) satisfies

$$\int \rho(1p, 1h, E, \mathbf{K}) 4\pi K^2 dK = \rho(1p, 1h, E) \equiv g^2 [E - (E - \epsilon_F)\theta(E - \epsilon_F)]. \tag{14}$$

Equation ([?]) can be compared with the analogous expression ([?]) for a Fermi-gas nucleus. While the functional form is clearly different, there are some close similarities. The angular distribution for a given emission energy arises from the dependence of the $1p1h$ state density on the momentum K, and it is seen that in the region $K_1 < K < K_2$ both Eqs. (5) and (13) show identical $1/K$ dependences.

The constant density of single-particle states in energy space is often taken as $g = A/14$, a value established from extensive data on slow neutron resonances. However, the Fermi-gas model as described in the previous section yields a density of states at the Fermi level of $3A/2\epsilon_F$, which for $\epsilon_F = 35$ MeV is a factor of 1.66 too small. This is a well known problem with the Fermi-gas model. On the otherhand, a value of $g = A/14$, while describing the density of states at the Fermi surface fairly well, overpredicts the number of nucleons by a factor of 2.5 in an equidistant model[?]. In order for a comparison to be made between the equidistant and Fermi-gas state densities, we have chosen a value of $g = 3A/2\epsilon_F$ so that the densities at the Fermi-level agree. This choice was motivated by the fact that for small excitation energies most excited particles and holes are close to the Fermi-level. In Fig. 2 the variation of the residual nucleus $1p1h$ state densities with emission angle is shown for the reaction $^{184}W(n,n')$ for an incident energy of 26 MeV and an emission energy of 18.5 MeV, for Fermi-gas and equidistant models. It is seen that the $1p1h$ state densities are very similar in the two models.

We again stress that our choice above for g was made solely to allow a comparison with our previous results for a Fermi-gas nucleus. Another approach might have been to use the commonly adopted value of $g = A/14$ for the equidistant model, but then use a Fermi-energy of 21 MeV in the Fermi-gas model in section IIa so that both models yield identical single-particle densities at the Fermi-level.

It is worth mentioning that Madler and Reif's method for determining state densities with linear momentum (which also uses an equidistant single-particle level model) fails completely for the important $1p1h$ state density with linear momentum. They show in Fig. 2 of Ref. [?] the variation of their $1p1h$ density with emission angle, which differs considerably in shape from our exact result in our Fig. 2. The shape of the $1p1h$ density is critically important in determining the angular distribution of emitted particles.

FIG. 2 the variation of the residual nucleus $1p1h$ state densities with emission angle. for the reaction ^{184}W(n,n') for an incident energy of 26 MeV and an emission energy of 18.5 MeV, for Fermi-gas and equidistant models.

III. APPLICATIONS OF STATE DENSITIES WITH LINEAR MOMENTUM

A. Angular distributions in the exciton preequilibrium model

It has been established that non-equilibrium processes play an important role in nuclear reactions induced by light projectiles with incident energies above about 10 MeV. The characteristic features of particle emission from the composite nucleus before equilibrium has been reached (preequilibrium emission) are an excess of high-energy particles, and a forward peaking in the observed angular distributions. The overabundance of high-energy particles is due to the nuclear excitation energy being shared among only a few degrees of freedom in the early stages of the reaction when preequilibrium emission occurs, and the forward peaking is indicative of the incident projectile's direction being partially preserved. Both quantum mechanical and semi-classical theories have been developed to account for preequilibrium emission. Quantum mechanical approaches such as that of Feshbach, Kerman, and Koonin (FKK) [12], Tamura *et al.* [13] and Koning and Akkermans [?] have been able to successfully describe the spectral shape and angular distribution of emitted particles, though the calculations are rather involved and their predictive power is limited [15]. The semiclassical exciton [16] and hybrid [17] preequilibrium models, on the other hand, are able to describe the angle-integrated spectral shapes successfully, though in their usual formulation they cannot yield angular distributions directly. In this section we shall show that by modifying the exciton model to include linear momentum effects it yields angular distributions in a natural and consistent way. We shall not explicitly discuss the hybrid model, though the modifications needed in it for the inclusion of linear momentum effects should be similar to those that we present for the exciton model.

In the exciton model the particle emission rates from the preequilibrium stages of the reaction are calculated by invoking microscopic reversibility and applying phase-space arguments. In its usual formulation it does not conserve linear momentum in the various intra-nuclear transitions and can not yield information concerning the angular distribution of emitted particles. In order to obtain such information, it has become commonplace to include in the model, in an *ad hoc* manner, a nucleon-nucleon scattering kernel obtained either from free nucleon-nucleon scattering [18, 19] or, more realistically, from quasifree scattering in nuclear matter using the Kikuchi-Kawai (KK) expression [10, 20–23], for reviews see Refs. [24, 25]. While the inclusion of a nucleon-nucleon scattering kernel within an exciton model is a physically plausible way to obtain angular distributions, no formal theoretical connection has been made between the exciton model and quasifree scattering descriptions. We shall show that by conserving linear momentum in the exciton model and by using the Fermi-gas state densities with linear momentum described in the previous section. the angular distributions obtained are identical to those found using KK quasifree scattering. We do not make use of the *fast particle* approximation, as in Ref. [18], but treat the excited particles and holes for a given preequilibrium stage statistically. The forward-peaked angular distributions that we obtain arise purely from phase-space factors, and possible dynamical effects are disregarded.

In the previous section we presented a method for exactly determining state densities with linear momentum. Since our approach involves convoluting single-particle and -hole states in a Fermi-gas nucleus, the complexity of the integrals increases rapidly for more complex preequilibrium stages. We are able, however, to determine the state densities with linear momentum needed for the calculation of first and second stage preequilibrium emission in nucleon-induced reactions. We assume, following Chiang and Hüfner [26], that preequilibrium emission beyond the second stage can be ignored before equilibrium emission occurs.

In the exciton model it is assumed that an incident nucleon interacts with the target nucleus to form a two-particle-one-hole ($2p1h$) state, and in subsequent two-body nucleon-nucleon interactions the excited system may pass through more complex particle-hole configurations towards equilibrium. Particle emission can occur from the early preequilibrium stages and these particles typically contribute to the high-energy part of the emission spectrum. The double-differential cross section for the emission of a particle with energy ϵ and direction Ω can be written as

$$\frac{d^2\sigma}{d\epsilon d\Omega} = \sigma_R \sum_{\substack{\Delta n=+2\\ n=3}} \frac{\lambda_n(\epsilon,\Omega)}{\Lambda_n^+ + \Lambda_n} D_n, \tag{15}$$

where the number of excitons is $n = p + h$. The reaction cross section of the incident particle on the target nucleus is σ_R, and D_n is the depletion factor, representing the probability that the system reaches the n-exciton configuration without preequilibrium decay. Λ_n^+ and Λ_n are the total rates for decay to more complex exciton configurations and for particle emission, respectively, and $\lambda_n(\epsilon,\Omega)$ is the ble-differential emission rate for a given type of particle. This is found from microscopic reversibility to be

$$\lambda_n(\epsilon,\Omega) = \frac{m\epsilon\,\sigma_{\text{inv}}(\epsilon)R(p)}{2\pi^3\hbar^3}\,\frac{\rho(p-1,h,E-\epsilon_\Omega,\mathbf{K}-\mathbf{k}_\Omega)}{\rho(p,h,E,\mathbf{K})}, \tag{16}$$

where the reaction cross section for the inverse process of nucleon absorption on the residual nucleus is $\sigma_{\text{inv}}(\epsilon)$. The composite system total energy and momentum before particle emission are E and $\mathbf{K}$ respectively, and the residual nucleus energy and momentum after emission are $E - \epsilon_\Omega$ and $\mathbf{K} - \mathbf{k}_\Omega$ respectively, all these quantities being measured relative to the bottom of the nuclear well. The energy and momentum of the emitted particle relative to the bottom of the nuclear well are $\epsilon_\Omega = \epsilon + B + \epsilon_F$ and $\mathbf{k}_\Omega$, where $|\mathbf{k}_\Omega| = \sqrt{2m(\epsilon + B + \epsilon_F)}$, B being the binding energy and ϵ_F the Fermi energy. $R(p)$ is a correction factor to account for neutron-proton distinguishability, and is discussed below. In the above expression state densities with linear momentum are shown, though the state densities that are used in the original exciton model are a function of energy only.

From Eq. (16) it is clear that the angular distribution of emitted particles from a preequilibrium stage arises from phase-space factors. For a given particle emission energy, the various emission directions result in different total momenta being transfered to the residual nucleus, with corresponding different accessible state densities. Thus the angular distribution of emitted particles from the $n = 3$ stage (i.e. single-step scattering) is given by the variation of $\rho(1p, 1h, E - \epsilon_\Omega, \mathbf{K} - \mathbf{k}_\Omega)$ with the emission angle. The angular distribution that we obtain using $1p1h$ state densities according to Eq. (5) is identical to that found by KK [10] for single-step quasifree scattering from a non-interacting Fermi-gas nucleus. An inspection of the physics involved suggests that this result is to be expected since our exciton model, and the quasifree scattering model of KK, both conserve linear momentum and energy in a Fermi-gas nucleus. Furthermore, the expression used by KK for single-step scattering uses a basic free-space nucleon-nucleon cross section which is isotropic, so that all the angular dependence arises implicitly from phase space factors, as done explicitly in our approach. The similarity of our exciton model with KK's approach can be most clearly seen in the work of Chiang and Hüfner [26], who use the KK scattering function to calculate single- and double-step quasifree scattering. Their expressions for the single- and double-step scattering use nuclear response functions [27] for a non-interacting Fermi-gas, which are directly proportional to our $1p1h$ and $2p2h$ state densities with linear momentum. It should be noted that from Eq. (8) it is clear that our model yields a convolution structure for the two-step scattering, which is common to most semiclassical scattering theories as well as the quantum mechanical FKK multistep direct theory.

For the calculation of nucleon emission cross sections we used Kalbach's parametrization [28] for the transition rates to more complex configurations, λ_n^+, which was originally determined without linear momentum considerations. This is reasonable since we found that λ_n, obtained by integrating Eq. (16) over all angles and energies for neutrons and protons, agreed to within 5% with the value obtained when linear momentum effects were not included. Also, this integral did not differ significantly from its value obtained using the traditional Ericson equidistant single-particle level state densities, corrected for a finite nuclear well depth. The neutron-proton distinguishability factor $R(p)$ [29] in Eq. (16) is consistent with the above parametrization [*]. The reaction cross sections in Eqs. (15,16) were determined using the Becchetti-Greenlees optical potential [30], and we took the Fermi energy to be 35 MeV.

Angular distributions for 14.5 and 18.5 MeV neutrons emitted in the reaction $^{184}W(n,n')$, induced by 26 MeV neutrons. At these emission energies the equilibrium emission contributions were found to be negligible. Shown for comparison are quantum mechanical FKK calculations and experimental data, taken from Marcinkowski *et al.* [15].

We have determined angular distributions for 14.5 and 18.5 MeV emitted neutrons in the reaction $^{184}W(n,n')$ induced by 26 MeV neutrons. Our results are shown in Fig. 2 and it is evident that the observed forward peaking in the data is accounted for in our model, though we underpredict the data at backward angles. Neutron emission from the $n = 3$ stage dominates scattering in the forward direction but does not contribute beyond 110 degrees, whereas $n = 5$ emission covers all directions but is too weak to account for the backward-angle data. This underprediction was also seen in Refs. [20–22] where the KK quasifree scattering kernel was used in semiclassical preequilibrium models, and results from the absence in our model of effects such as diffraction of the nucleons in the mean-field nuclear potential [21, 22]. It is beyond the scope of the present work to include such effects, which really require a quantum mechanical treatment. The dashed line shows a quantum mechanical calculation of the neutron scattering cross section using the FKK theory [15] which uses the distorted-wave Born expansion, and with single and double-step scattering the theory describes the angular distributions well. In Fig. 3 we show the proton emission spectra at five different angles for the reaction $^{54}Fe(p,p')$ induced by 62 MeV protons. For low emission energies we have included the equilibrium emission contribution (reduced due to the reaction flux lost through $n = 3$ and $n = 5$ preequilibrium emission), determined with the Hauser-Feshbach code GNASH [32]. The shapes of the spectra generally agree fairly well with experiment, but again we underpredict the backward-angle data. We also determined the angle-integrated spectrum and found that it describes the data well (since the backward-angle cross section is a minor fraction of the total preequilibrium cross section), and have compared it with an exciton model calculation using Fermi-gas state densities which do not include linear momentum, from Eq. (1). We found differences of less than 5% , indicating that it is not necessary to include linear momentum effects when determining angle-integrated spectra.

Spectra of protons emitted at a number of angles in the ^{54}Fe(p,p') reaction induced by 62 MeV protons compared with experimental data [31]. The full line shows the sum of $n=3$ and $n=5$ preequilibrium emission in our model, and the dash-dot line includes the equilibrium emission contribution.

The above results show that if a Fermi-gas model is used to evaluate state densities with linear momentum in an exciton model, angular distributions are obtained which are identical to those found using the KK scattering kernel. Therefore, if one used a preequilibrium model with Fermi-gas state densities which are only a function of energy (and not momentum), and in addition used a KK scattering kernel to obtain angular distributions, one would obtain identical results to those found using our above model. However, a number of authors [?,?] have adopted an inconsistent approach of using an equidistant single-particle-state model to determine state densities, with a KK scattering kernel for the angular distributions. A consistent approach would be to use the formalism shown in this section with the state densities with linear momentum from Section IIB/ Or, alternatively, use a preequilibrium model based on equidistant single-particle-states (without linear momentum considerations), in conjuction with a scattering kernel obtained from Eq. (13). Due to the close similarity between the $1p1h$ Fermi-gas and equidistant single-particle state densities seen in Fig. 2, the scattering kernel from Eq. (13) would be almost identical to that of KK.

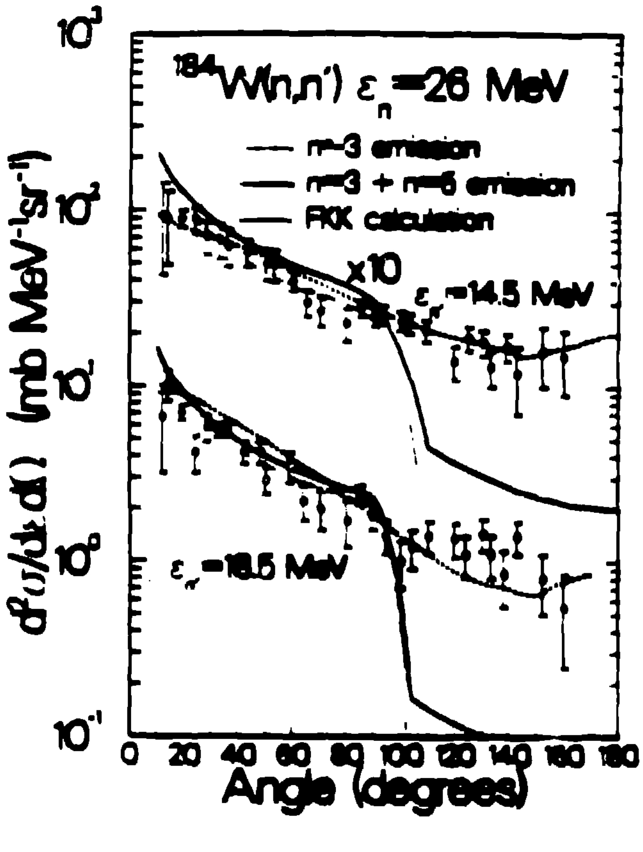

Fig 2

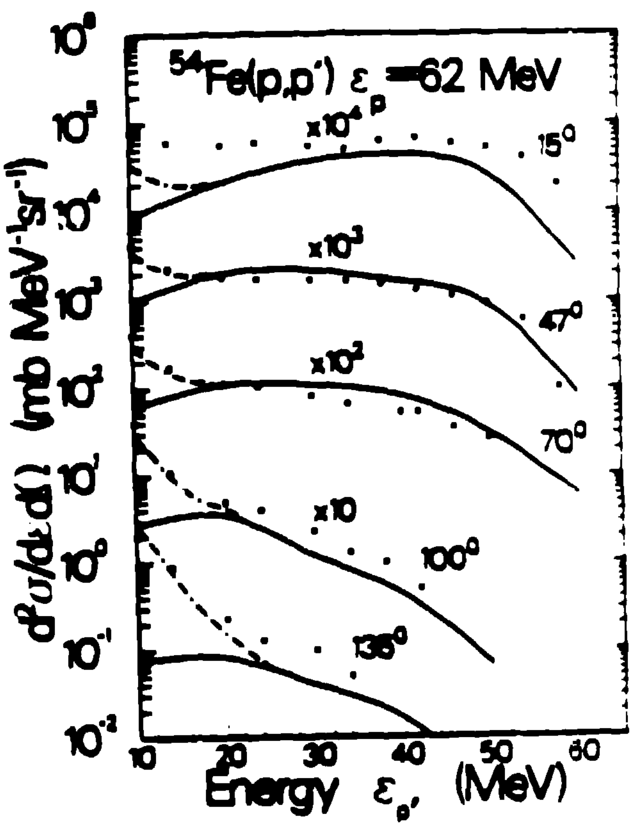

Fig 3

B. THE QUASIDEUTERON MODEL OF NUCLEAR PHOTOABSORPTION

In this section we shall discuss another application of state densities with linear momentum: nuclear photoabsorption on correlated neutron-proton pairs via the quasideuteron mechanism. A full discussion of this application can be found in our paper [?].

The quasideuteron model describes the dominant mechanism for nuclear photoabsorption for incident photon energies in the range 40 MeV $\lesssim \epsilon_\gamma \lesssim$ 140 MeV. This model was first proposed by Levinger [33–35] and has subsequently been applied extensively to analyze nuclear photoabsorption cross sections [36–39]. The model does, however, contain two free parameters and treats the effects of the Pauli exclusion principle in an entirely phenomenological manner. Here we present a quasideuteron model of photoabsorption which includes Pauli-blocking effects theoretically and does not contain any free parameters. In the quasideuteron model it is assumed that photoabsorption takes place on correlated neutron-proton pairs within a nucleus. The relatively small photon wavelengths ensure that the interaction takes place with a nucleon-nucleon pair, rather than with the nucleus as a whole, and the predominantly electric-dipole nature of the interaction implies photoabsorption only by neutron-proton pairs. Levinger showed [33, 35] that the nuclear photoabsorption cross section $\sigma_{qd}(\epsilon_\gamma)$ can be expressed in terms of the free deuteron photo-disintegration cross section $\sigma_d(\epsilon_\gamma)$,

$$\sigma_{qd}(\epsilon_\gamma) = \frac{L}{A} NZ\sigma_d(\epsilon_\gamma)f(\epsilon_\gamma), \tag{17}$$

where L is the Levinger parameter and $f(\epsilon_\gamma)$ is the Pauli-blocking function. The factor NZ is the total number of neutron-proton pairs inside the nucleus, which is multiplied by a reduction factor L/A to account for the fact that it is only correlated pairs that can be considered to be quasideuterons [40, 41]. In addition, the function $f(\epsilon_\gamma)$ accounts for those excitations of neutron-proton pairs that cannot occur since the Pauli-exclusion principle allows only final particle states which lie above the Fermi level. This effect is particularly important for low photon energies, and Levinger suggested that it can be represented by an exponential Pauli-blocking function [35]

$$f_{Lev}(\epsilon_\gamma) = e^{-D/\epsilon_\gamma}, \tag{18}$$

where D is a constant. Although a theoretical estimate for the Levinger parameter is well known [?], no theoretical derivation for the Pauli-blocking function has been given. In practice, L and D are treated as free parameters to fit the photoabsorption data. The difficulty in separating the effects of the Levinger parameter and the Pauli-blocking function in Eq. (1) has resulted in a substantial ambiguity in the L and D-values used by different groups; they range from $L = 4.9$ and $D = 60$ MeV (Ref. [42]) to $L = 10$ and $D = 80$ MeV (Ref. [43]). We shall describe below how we calculate L and $f(\epsilon_\gamma)$ theoretically.

Our starting point is an expression derived by Levinger [33] for the photoabsorption cross section on a neutron-proton pair, in the absence of Pauli-blocking

By using effective range theory Levinger was able to relate the photoabsorption on a quasideuteron inside the nucleus with relative momentum k, $\sigma_{qd}(k, \epsilon_\gamma)$, to that on a free deuteron, which is known experimentally,

$$\sigma_{qd}(k, \epsilon_\gamma) = \sigma_d(\epsilon_\gamma) \frac{2\pi(1 - \alpha r_0)}{V\alpha} \frac{1}{\alpha^2 + (k/\hbar)^2}, \tag{19}$$

where $k = |\frac{1}{2}(\mathbf{k}_\nu - \mathbf{k}_\pi)|$ is the initial relative momentum of a neutron-proton pair, $\alpha^{-1} = (\hbar/(2.23m)^{\frac{1}{2}})$ is related to the neutron-proton scattering length [†], m being the nucleon mass, and r_0 is the effective range. The nuclear volume in the above expression is $V = \frac{4}{3}\pi 1.2^3 A$ fm^3.

Following Levinger, we assume that if all the possible final neutron and proton states after photoabsorption are not Pauli-blocked, the photoabsorption cross section on a quasideuteron is given by Eq. (19). However, if the available phase space for the neutron and proton after photoabsorption is reduced by Pauli-blocking, we assume that the quasideuteron photoabsorption cross section is also reduced by the same amount. Thus we suppose that the cross section for photoabsorption is proportional to the available phase space. This is reasonable since Fermi's Golden Rule ought to be applicable as the electromagnetic perturbation is small compared to the nuclear interactions.

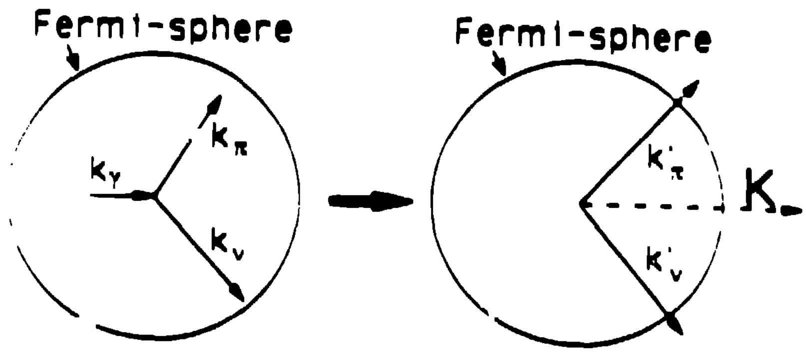

FIG. 5. Absorption of a hard photon by a quasideuteron in the nucleus. The initial linear momenta of the photon, neutron, and proton are $\mathbf{k}_\gamma$, $\mathbf{k}_\nu$, $\mathbf{k}_\pi$ respectively, and the final linear momenta are $\mathbf{k}'_\nu$, $\mathbf{k}'_\pi$. The total momentum is $\mathbf{K}$.

Figure 5 shows, in momentum space, the absorption of a hard photon upon a neutron-proton pair within the nucleus. The initial and final linear momenta, and the corresponding energies, are related by

$$\mathbf{k}_\nu + \mathbf{k}_\pi + \mathbf{k}_\gamma = \mathbf{K} = \mathbf{k}'_\nu + \mathbf{k}'_\pi$$

$$\epsilon_\nu + \epsilon_\pi + \epsilon_\gamma = E = \epsilon'_\nu + \epsilon'_\pi, \tag{20}$$

where primes refer to final states after photoabsorption, and $\mathbf{K}$ and E are the total linear momentum and total energy respectively. If the exclusion principle is obeyed the vectors $\mathbf{k}'$ and $\mathbf{k}'_-$ must extend beyond the Fermi-sphere as defined by the radius k_F. Considering all accessible final states that are consistent with the above constraints, one obtains the neutron-proton state density which depends on $\mathbf{K}$ and E only. This neutron-proton state density is written as $\rho(2p, E, \mathbf{K})$. The blocking factor $F(\mathbf{k}_\nu, \mathbf{k}_\pi, \mathbf{k}_\gamma)$ can then be expressed as the ratio of this two-particle state density to the one that is obtained when the Pauli exclusion principle is excluded.

$$F(\mathbf{k}_\nu, \mathbf{k}_\pi, \mathbf{k}_\gamma) = \frac{\rho(2p, E, \mathbf{K})}{\rho^{\text{NO PAULI}}(2p, E, \mathbf{K})}, \tag{21}$$

so that the photoabsorption on a particular quasideuteron pair with momenta $\mathbf{k}_\pi$, $\mathbf{k}_\nu$ is $\sigma_{qd}(k, \epsilon_\gamma) \times F(\mathbf{k}_\nu, \mathbf{k}_\pi, \mathbf{k}_\gamma)$ In order to determine the $2p$ state density with linear momentum, a 'two-component' version of Eq. (2) was used. Neutrons and protons are distinguished in this calculation, the neutron and proton single-particle densities in momentum space being given by $\kappa_\nu = N/(\frac{4}{3}\pi k_F^3)$ and $\kappa_\pi = Z/(\frac{4}{3}\pi k_F^3)$. The resulting state density has dimensions $((\text{MeV})^{-1}\ (\text{MeV}/c)^{-3})$ and is given by

$$\rho(2p, E, \mathbf{K}) =$$

$$\begin{array}{lll}
2\pi m\kappa_\nu\kappa_\pi\sqrt{mE - \frac{K^2}{4}} & \text{if} \left\{ \begin{array}{l} mE \geq k_F^2 + k_F K + \frac{1}{4}K^2 \\ \text{or } K \geq 2k_F \text{ and } \frac{1}{4}K^2 \leq mE \leq k_F^2 - k_F K + \frac{1}{2}K^2 \end{array} \right. \\
2\pi m\kappa_\nu\kappa_\pi\left[\frac{mE - k_F^2}{K}\right] & \text{if} \left\{ \begin{array}{l} K \geq 2k_F \text{ and } k_F^2 - k_F K + \frac{1}{2}K^2 \leq mE \leq k_F^2 + k_F K + \frac{1}{2}K^2 \\ \text{or } K \leq 2k_F \text{ and } mE \leq k_F^2 + k_F K + \frac{1}{2}K^2 \end{array} \right. \\
0 & \text{if} \left\{ \begin{array}{l} K \leq 2k_F \text{ and } mE \leq k_F^2 \\ \text{or } K \geq 2k_F \text{ and } mE \leq \frac{1}{4}K^2. \end{array} \right.
\end{array} \tag{22}$$

The two-particle state density that includes all transitions (including those that violate the Pauli principle) can be obtained from the results in Eq. (22) in the limit of $k_F \to 0$, yielding

$$\rho^{\text{NO PAULI}}(2p, E, \mathbf{K}) = \left\{ \begin{array}{ll} 2\pi m\kappa_\nu\kappa_\pi\sqrt{mE - \frac{K^2}{4}} & \text{if } mE \geq \frac{1}{4}K^2 \\ 0 & \text{otherwise.} \end{array} \right. \tag{23}$$

Equations (22) and (23) are used to evaluate the photoabsorption cross section on a specific quasideuteron in the nucleus. The nuclear photoabsorption cross section is then obtained by integrating $\sigma_{qd}(k, \epsilon_\gamma) \times F(\mathbf{k}_\nu, \mathbf{k}_\pi, \mathbf{k}_\gamma)$ over all possible neutron-proton pairs in a Fermi-gas nucleus. Such an integration yields a nuclear photoabsorption cross section of the form (17), with a Levinger parameter of $L = 6.5$ and a Pauli-blocking function as shown in Fig. 6 below. Fig. 6 also shows phenomenological exponential blocking functions with $D = 60$ and $D = 80$ MeV for comparison.

Our Pauli blocking function has the same general energy dependence as that of Levinger's *ad hoc* exponential function, i.e. at low incident energies it tends to zero and at high energies to unity, as it must, but the exact energy variation is rather different (see Fig. 6). We note that is not possible to reproduce the steep energy dependence of $f(\epsilon_\gamma)$ which we obtain with a phenomenological exponential function. Since the Pauli-blocking function calculation requires such a large amount of c.p.u. time, we have found a polynomial fit to our results to facilitate future uses of our Pauli-blocking function in nuclear reaction calculations and data evaluations. Our results can be well approximated in the photon energy range 20-140 MeV by the polynomial

$$f(\epsilon_\gamma) = 8.3714 \times 10^{-2} - 9.8343 \times 10^{-3}\epsilon_\gamma + 4.1222 \times 10^{-4}\epsilon_\gamma^2$$

$$-3.4762 \times 10^{-6}\epsilon_\gamma^3 + 9.3537 \times 10^{-9}\epsilon_\gamma^4. \qquad (24)$$

In Fig. 7 we show our calculated quasideuteron contribution to the nuclear photoabsorption cross section compared with data for the nuclei Pb, Ta, Sn and Ce. We also show the tails of the giant dipole resonances (GDR) which may contribute even at these high photon energies. The data as well as the GDR tails are taken from Ref. [36], and the photodisintegration cross section was taken from [44] It is seen that the sum of these two contributions describes the data fairly well. The comparison with data that we obtain seems to be better than that obained with a phenomenological exponential Pauli-blocking function (see, for instance, Leprètre *et al* [36]. If their quasideuteron component is added to the GDR component they significantly over-estimate the data below a photon energy of 40 MeV).

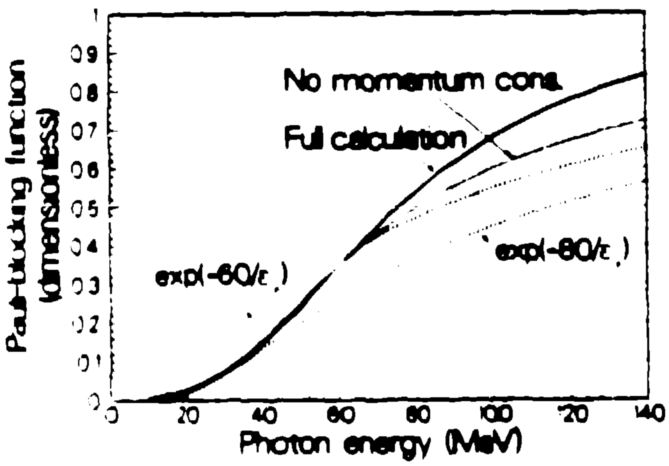

Fig 6

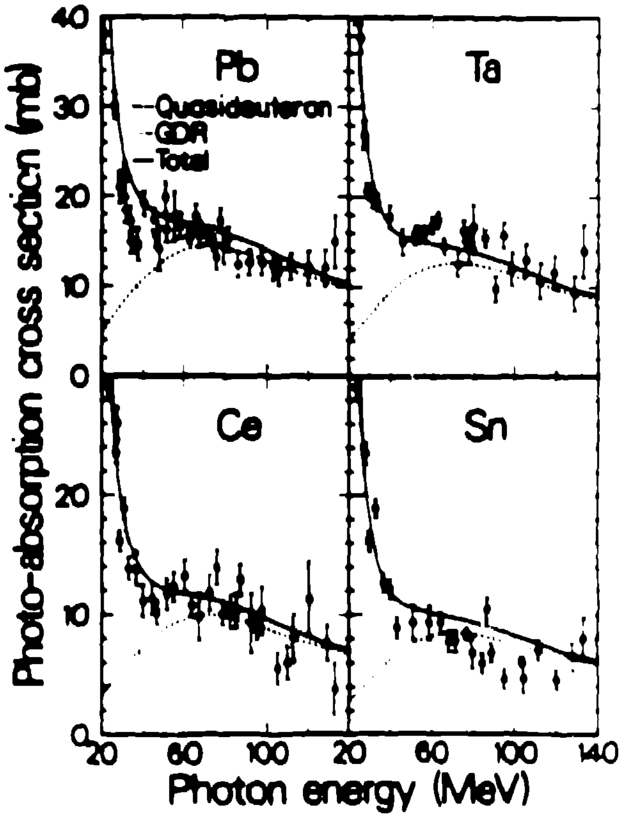

Fig 7

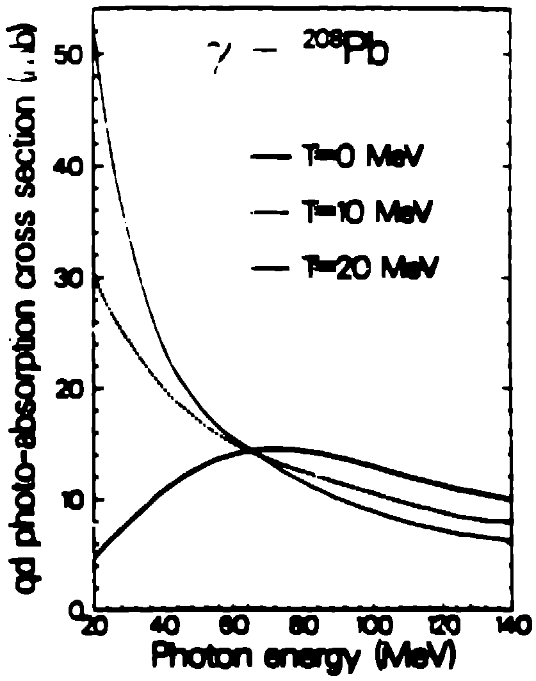

Fig 8

FIG. 6. The calculated quasideuteron component of the nuclear photoabsorption cross section as a function of photon energy is compared with experimental data for Pb, Ta, Sn and Ce. The full curve is the sum of the quasideuteron and GDR contributions. The tails of the GDR as well as experimental data are taken from Ref. [36].

We have also investigated the temperature dependence of the quasideuteron photoabsorption cross section. This is of interest since detailed balance can be applied to determine photon emission rates from hot nuclei produced in heavy-ion collisions via a quasideuteron mechanism [42, 45]. We assumed a Fermi-Dirac distribution of single-particle states and calculated state densities which are a function of energy, linear momentum, and temperature [?]. The photoabsorption cross section was found to be extremely sensitive to temperature, and an example of our results for photobasorption on ^{208}Pb is shown in Fig. 8.

IV. SUMMARY

We have introduced the concept of state densities with linear momentum, and have indicated an exact method for their determination. Our calculational procedure differs from that of Madler and Reif, and can be applied in the determination of state densities of simple particle-hole configurations. Simple analytic expressions can be found for such densities, facilitating their use in nuclear reaction theories. Two different applications for state densities with linear momentum have been presented.

The inclusion of linear momentum effects in an exciton model is able to explain the forward-peaked angular distributions observed in preequilibrium decay, and the angular distributions which they yield are identical to those seen in KK quasifree scattering. We have, therefore, provided a link between exciton model and quasifree scattering descriptions of nuclear reactions, and have provided further justification for the commonly adopted procedure of using a KK scattering kernel in an exciton model. We have also discussed state densities with linear momentum in an equidistant single-particle-state model, and have given expressions which allow angular distributions to be determined (though we also pointed out that the angular distributions would be almost identical to those of KK).

The quasideuteron model of photoabsorption that we have developed is based on phase space arguments and uses state densities with linear momentum. We have presented, for the first time, a theoretical basis for Pauli-blocking effects, and our no-parameter model is able to give a good description of the photoabsorption data for a wide range of nuclei. Our state densities, when generalised to include temperature dependence, were used to determine the quasideuteron photoabsorption cross section on an equilibrated hot nucleus. We found the cross section to be very sensitive to temperature.

These two applications have demonstrated the richness of state densities with linear momentum. They seem to have considerable versatility in their possible applications within nuclear reaction theories. We are presently investigating their application in hard-photon emission reactions and stopped pion-absorption processes.

We would like to thank Drs. M. Blann, P.E. Hodgson, D. Madland, G. Reffo, R. Smith and P.G. Young for helpful discussions, and one of us (M.B.C) acknowledges financial support from an SERC/NATO Fellowship.

REFERENCES

[1] T. E. Ericson, Adv. in Phys. **9**, 425 (1960).
[2] F. C. Williams, Nucl. Phys. **A163**, 231 (1971).
[3] P. Obložinský, Nucl. Phys. **A453**, 127 (1986); E. Betak and J. Dobes, Z. Phys. **A279**, 319 (1976).
[4] H. Gruppelaar, ECN report ECN-83-064.
[5] C. Kalbach, Phys. Rev. **C30**, 1310 (1984); Los Alamos Report LA-UR-91-2302.
[6] M.B. Chadwick and P. Oblozinsky, to be published in the November 1991 issue of Phys. Rev. C (Rapid Communications).
[7] M.B. Chadwick, P. Obložinský, P.E. Hodgson and G. Reffo, Phys. Rev. C. **44**, 814 (1991).
[8] P. Mädler and R. Reif, Nucl. Phys. **A337**, 445 (1980).
[9] A. Iwamoto, Phys. Rev. C **35**, 984 (1987).
[10] K. Kikuchi and M. Kawai, *Nuclear Matter and Nuclear Reactions*, (North-Holland, Amsterdam, 1968), p. 44; M.L. Goldberger, Phys. Rev. **74**, 1269 (1948).
[11] M. Chadwick and G. Reffo, Phys. Rev. C. **44**, 919 (1991)
[12] H. Feshbach, A. Kerman, and S. Koonin, Ann. Phys. **125**, 429 (1980); R. Bonetti, M.B. Chadwick, P.E. Hodgson, B.V. Carlson, and M.S. Hussein, Physics Reports **202(4)**, 171 (1991).
[13] T. Tamura, T. Udagawa, and H. Lenske, Phys. Rev. C **26**, 379 (1982).
[14] A.J. Koning and J.M. Akkermans, Ann. Phys. **208**, 216 (1991).
[15] A. Marcinkowski, R.W. Finlay, J. Rapaport, P.E. Hodgson, and M.B. Chadwick, Nucl. Phys. **A501**, 1 (1989).
[16] H. Gruppelaar, P. Nagel, and P.E. Hodgson, Riv. Nuovo Cimento **9**, 1 (1986).
[17] M. Blann, Ann. Rev. Nucl. Sci. **25**, 123 (1975).
[18] G. Mantzouranis, D. Agassi, and H.A. Weidenmüller, Phys. Lett. **57B**, 220 (1975); G. Mantzouranis, D. Agassi, and H.A. Weidenmüller, Z. Phys. **A 276**, 145 (1976)
[19] J.M. Akkermans, H. Gruppelaar and G. Reffo, Phys. Rev. C **22**, 73 (1980).
[20] Sun Ziyang, Wang Shunuan, Zhang Jingshang, Zguo Yihong and Han Huiyi, Z. Phys. **A 305**, 61 (1982).
[21] C. Costa, H. Gruppelaar and J.M. Akkermans, Phys. Rev. C **28**, 587 (1983).
[22] M. Blann, W. Scobel and E. Plechaty, Phys. Rev. C **30**, 1493 (1984).
[23] R.D. Smith and M. Bozoian, Phys. Rev. C **39**, 1751 (1989).
[24] H. Machner, Z. Phys. **A 327**, 175 (1987).
[25] E. Gadioli in *Proceedings of the International Conference on Nuclear Reaction Mechanisms*, Saha Institute of Nuclear Physics, Calcutta, Jan. 3-9 (1989), edited by S. Mukherjee (World Scientific, Singapore, 1989), p. 145.
[26] H C. Chiang and J. Hüfner, Nucl. Phys. **A349**, 466 (1980).

[27] A.L. Fetter and J.D. Walecka. *Quantum Theory of Many-Particle Systems*. (McGraw-Hill. New York, 1971). p. 161.
[28] C. Kalbach. Z. Phys. **A287**. 319 (1978).
[29] C.K. Cline. Nucl. Phys. **A193**. 417 (1972).
* In the recent preequilibrium calculations of F. Cvelbar, E. Betak and J. Merhar (J. Phys. **G17**. 113 (1991)) a value of K'=100 MeV^3 in the damping matrix element was adopted. Since our emission rates found using Fermi-gas levels are somewhat smaller than those obtained using equidistant levels, K' was increased to 135 MeV^3. The larger rates in our Fermi-gas calculation result from the normalization that we adopted for the single-particle states (Eq. (3)) which result in an underprediction of the density at the Fermi-level.
[30] F.D. Becchetti and G.W. Greenlees, Phys. Rev. **182**, 1190 (1969).
[31] F.E. Bertrand and R.W. Peelle. Phys. Rev. C **8**, 1045 (1973).
[32] P.G. Young and E.D. Arthur. Los Alamos National Laboratory Report LA-6947, Los Alamos National Laboratory (1977).
† Levinger's notation differs from the usual convention. The conventional inverse n-p scattering length is given by $\alpha - \frac{1}{2}\alpha^2 r_0$. Note also that in the literature there seems to be some confusion concerning r_0. It is the effective range, not the nuclear size parameter.
[33] J. S. Levinger. Phys. Rev. **84**, 43 (1951).
[34] J. S. Levinger. *Nuclear Photo-Disintegration* (Oxford University Press, Oxford, 1960). p.97.
[35] J. S. Levinger. Phys. Lett. **82B**, 181 (1979).
[36] A. Leprêtre, H. Beil, R. Bergère, P. Carlos, J. Fagot, A. De Miniac, and A. Veyssière, Nucl. Phys. **A367**, 237 (1981).
[37] R. Bergère. Nuovo Cim. A **76**, 147 (1983).
[38] J. Ahrens. H. Borchert, K.H. Czock, H.B. Eppler, H. Gimm, H. Gundrum, M. Kroning, P. Riehn, G. Sita Ram, A. Zieger and B. Ziegler, Nucl. Phys. **A251**, 479 (1975).
[39] M.L. Terranova, D.A. De Lima and J.D. Pinheiro Filho, Europhys. Lett. **9** (6), 523 (1989).
[40] F. Murgia and P. Quarati, Mod. Phys. Lett. **A4**, 1 (1989).
[41] P. C. Stein, A. C. Odian, A. Wattenberg, and R. Weinstein, Phys. Rev. **119**, 348 (1960).
[42] M. Prakash, P. Braun-Munzinger, J. Stachel, and N. Alamanos, Phys. Rev. C **37**, 1959 (1988).
[43] W. M. Alberico, M. Ericson, and A. Molinari, Ann. Phys. (N. Y.) **154**, 356 (1984).
[44] J. R. Wu and C. C. Chang, Phys. Rev C **16**, 1812 (1977).
[45] N. Herrmann *et al*, Phys. Rev. Lett. **60**, 1630 (1988).

Recent MCNP Developments

J. S. Hendricks and J. F. Briesmeister
Applied Theoretical Physics Division
Los Alamos National Laboratory
Los Alamos, NM 87545

Abstract

We report here both the status and recent developments in the MCNP Monte Carlo radiation transport computer code and also two items of more general interest to computational physics: the accuracy of modern physics computer codes and the performance of scientific workstations.

1 MCNP Introduction

MCNP is a Monte Carlo continuous-energy, three-dimensional neutron-photon-electron radiation transport computer code used in many industries, including nuclear well logging, medical imaging, and nuclear reactors. A general overview of MCNP was presented at the IEEE 1989 Nuclear Science Symposium[1]. Here we focus upon (1) a number of recent significant advances and new directions for MCNP, (2) the MCNP benchmark project that also provides insight into the reliability of modern computer codes and data libraries, and (3) a new timing study measuring the performance of MCNP on several computing platforms.

MCNP version 4 was released internationally in March 1991, featuring for the first time electron transport, a thick-target bremsstrahlung model, multitasking, pulse-height tallies, and other features. Several new Monte Carlo research programs are underway relating to MCNP and many new features are being prepared for the upcoming MCNP4A version of the code.

A program to benchmark the code against a wide variety of experimental measurements has reached a major milestone. Not only does this project document the accuracy of MCNP for neutron and photon transport problems, but it also provides insight into how well modern physics computer codes can model a variety of experiments.

As part of the evolution from being a Cray code to a UNIX code supported on many computer platforms, a timing study was made comparing performance of Sun, IBM, and HP workstations to the Cray. The results are reported here for the first time.

2 MCNP Overview and Status

MCNP is a general purpose Monte Carlo code for calculating the time-dependent continuous-energy transport of neutrons, photons, and/or electrons in three-dimensional geometries. Both fixed source and k_{eff} criticality problems can be solved and a number of output tally options are available. Data representations either can be fully or partially continuous or multigroup. The code is rich in variance reduction techniques that improve the efficiency of difficult calculations. The documentation for MCNP is a 600-page manual[2] describing the Monte Carlo theory, geometry, physics, cross sections, variance reduction techniques, tallies, errors, input, and output.

MCNP is used for many applications: reactor design (both fission and fusion), nuclear criticality safety, radiation shielding, nuclear safeguards, detector design and analysis, nuclear well logging, personnel dosimetry and health physics, accelerator target design, medical physics and radiotherapy, aerospace applications, defense applications, radiography, waste disposal, and decontamination and decommissioning. Recent major applications at Los Alamos include the space exploration initiative, general criticality safety, strategic nuclear materials safeguards, accelerator transmutation of nuclear waste, and safety analysis for the DOE New Production Reactor. Facilities designed with or having safety analysis performed by MCNP include the Dual Axis Radiographic Hydro Test facility (DARHT), the target area for the Manuel Lujan, Jr., Neutron Scattering Center (LANSCE), and the Materials Processing Laboratory radiological dose reduction studies.

MCNP is distributed for Los Alamos by the Radiation Shielding and Information Center (RSIC) in Oak Ridge, Tennessee. They receive requests for the code from about 50 institutions per year. MCNP also is distributed by the NEA Data Bank in France and can be accessed by anyone with an account on the Los Alamos Integrated Computing Network. We estimate that there are hundreds, perhaps more than a thousand, active users around the world at perhaps one hundred installations.

The Monte Carlo method was developed at Los Alamos during the Manhattan Project in the early 1940s. The current MCNP code is the heir to those early efforts. More than 350 person years have been invested into the research, development, programming, documentation, and data bases for MCNP. The first multipurpose code version was written in 1963. In the mid-70's, neutron and photon codes were merged to form MCNP, which has undergone major upgrades approximately every two to three years since. MCNP3 was released in 1983 and rewritten in standard Fortran. MCNP3A was released in 1985 and featured a very flexible generalized source. MCNP3B was released in 1988, featuring a repeated structures and/or lattice capability, a multigroup option, and tally output plotting.

MCNP4 was released in July 1990 at Los Alamos and in March 1991 to the Reactor Shielding and Information Center at Oak Ridge (version MCNP4.2). There are hundreds of minor improvements in addition to the following major new features:

- A continuous-energy electron transport package based on the Sandia National Laboratories Integrated Tiger Series (ITS)[3] has been incorporated into MCNP along with the associated data base.

- A thick-target bremsstrahlung approximation has been incorporated to model electron-induced photon production using the ITS electron data. The model includes much of the electron physics for photon generation at only a fraction of the cost of the fully-continuous-energy electron treatment.

- Shared memory multitasking has been added for multitasking workstations and the Cray multiprocessor mainframes. The clock turnaround for multitasked problems is reduced by approximately the number of processors used in the calculation.

- A pulse-height tally model is now available that records the energy deposited in a cell by each source particle and its secondary particles. Unlike other MCNP tallies, the pulse height tally models microscopic rather than macroscopic events.

- The criticality eigenvalue source can now use the full generality of other MCNP sources for the initial conditions in k_{eff} problems.

- MCNP can be interrupted interactively to request plots of tally quantities.

- Next-event estimators such as point detectors and the DXTRAN variance reduction scheme can now be used with $S(\alpha,\beta)$ thermal scattering [4,5].

- MCNP4 is the first MCNP version designed specifically for UNIX systems and has data paths built in and shell scripts distributed with the code, along with answer sets for specific systems.

3 MCNP4A

The next version of MCNP will be MCNP4A, scheduled for release in late 1992 or early 1993. The code will continue to evolve more towards a Unix workstation-based code. We believe that if massively parallel systems become widely available, they will have shared memory and be available with Unix and standard Fortran 77. Even workstations will become highly parallel. In the meantime, the current generation of workstations will become increasingly important as their performance approaches that of supercomputers. As shown in the timing studies presented later, some workstations already approach the Cray mainframes in performance.

Significant new features under active development for incorporation into MCNP4A are:

- ENDF/B-VI physics. The recent ENDF/B-VI data libraries include a number of new formats and formalisms such as correlated energy-angle scattering;

- Photons to 1 GeV. Although the MCNP4 electron/photon physics is based upon the Integrated Tiger Series, the present photon data only goes up to 100 MeV. MCNP is being given the capability to read multiple data sets with physics models appropriate to ranges up to 1 GeV;

- Improvements in the electron-photon transport package, including charge deposition tallies and variable electron substep sizes;

- A quasi-deterministic weight window generator developed [6,7] to more efficiently automatically estimate an optimum importance function for variance reduction than does the present scheme[8].

- The DXANG angle bias method[9] for particle collisions provides a numerically stable means of directionally biasing particles emerging from collisions.

- Expansion of the tallying capabilities for problems with lattices and repeated structures to permit tallying isolated components that are repeated.

- Periodic and white boundary conditions have been added.

- MCNP4A will write out history tapes for postprocessing either by the SABRINA color graphics code[10] to illustrate particle tracks or by the LAHET (high energy transport) code[11].

- The source model will include intrinsic radiation sources[12] to model radioactive decay.

Other major new features that we would like to put into MCNP if time and resources permit are:

- Upgrading the Integrated Tiger Series physics to ITS version 3.0 and incorporation of EGS4 [13] physics as appropriate.

- Probability table treatment for the unresolved range neutron cross section data;
- A generalized perturbation treatment.

A number of research projects are under way which will certainly have long-range effects upon MCNP, though perhaps not MCNP4A. These programs are funded by computer companies, oil services companies, the Department of Energy and some competitive Los Alamos National Laboratory discretionary research funding. They are:

- Variance-of-variance. A modified version of MCNP is available that scores the variance of the tally variance and produces a history score probability density function to provide more information on how reliable the MCNP estimated answers are.[14]
- Dataflow. A stripped-down version of MCNP has been written in the Id dataflow language, which is an advanced computer language designed for massively parallel MIMD (Multiple Instruction Multiple Data) computers.
- Oil and gas well logging (proprietary projects).
- Criticality problem eigenfunction stabilization. Although Monte Carlo can do an excellent job estimating eigenvalues (k_{eff}) of critical systems, the principal eigenfunction, such as the flux distribution across a reactor core, is sometimes estimated quite poorly with misleading error estimations.
- Variance reduction for collective multiparticle events. Some Monte Carlo estimates, for example, the pulse height tally, require detailed simulation of microscopic events. Current variance reduction techniques are correct for tallies determined by the behavior of individual particles, but not applicable when the tally is determined by the behavior of a collection of particles. The modeling of collective (or non-Boltzmann) transport is incompatible with normal variance reduction techniques, and new variance reduction methods must be developed.

MCNP is a sponsor- and user-driven computer code. Our sponsors determine what they want us to add to the code, and user feedback leads to many improvements. New features are incorporated into the code only after peer review, an extensive testing program, and residency in "patched versions," where algorithm robustness and sustained user interest and satisfaction must be demonstrated.

The large number of Monte Carlo research projects and MCNP4A development projects underway testifies to the continued vitality of the MCNP program.

4 MCNP Benchmarking

A major milestone has been reached in an ongoing program to formally benchmark MCNP. Two publications have just been released comparing MCNP calculations with a wide variety of analytic and photon benchmarks[15] and with three major classes of neutron experimental measurements[16]. These benchmarks not only serve to validate MCNP, but also indicate the high degree of reliability of modern computational methods and data.

In the first publication, LA-12196, analytic and photon benchmarks are considered. As would be expected, MCNP agrees with analytic problems to within the statistical uncertainty. Three families of photon experiments were also calculated: a gamma-ray skyshine experiment, a ^{60}Co air-over-ground experiment, and thermoluminescent dosimeter (TLD) experiments. These problems were deep penetration and streaming problems, and all required elaborate variance reduction. In all cases MCNP did well, agreeing to within statistical and measured uncertainties for all but the deepest penetrations. For penetrations on the order of ten mean free paths deep, MCNP usually was within a factor of two of the measurement, which often times was of questionable accuracy.

In the second publication, LA-12212, three families of neutron benchmarks are compared: the Livermore pulsed sphere measurements, the Oak Ridge fusion shielding benchmarks, and, finally, nine critical assemblies. The critical assemblies ranged from simple Godiva and Jezebel spheres to complicated arrays, and all converged sufficiently near $k_{eff} = 1$.

The Oak Ridge fusion shielding benchmarks involved streaming, deep penetration, and generation of neutron-induced photons. Fourteen-MeV neutrons were emitted isotropically and streamed down an iron pipe embedded in concrete before penetrating shields of 30.5 cm iron, or 45 cm iron and 10 cm of borated polyethylene. Neutrons and secondary photons then were measured at points on- and off-axis beyond the shield. Considering the deep penetration of up to 25 mean free paths, both neutron and photon results were excellent. Throughout the energy range, detailed-spectral results were always within a factor of two and integral results (the total flux at off-axis detectors) were never more than 25% off from the measurement. For shallower penetrations the calculations agreed with measurements within statistics.

The Livermore pulsed spheres used a 14-MeV neutron source and measure penetration of a wide variety of materials of various thicknesses at several angles. The results for 28 spheres indicate that the Monte Carlo results agree with the measurements except when the cross section data are poorly known. In the worst case, a liquid nitrogen sphere 7.7 mean free paths thick, MCNP differed from the experiment by 29% in the worst energy range and by 7% overall. By switching from ENDF/B-V cross sections to ENDF/B-VI data, the disagreement lessened to 13% and 3%, respectively.

From these benchmark calculations we conclude that modern computational methods, such as MCNP, are capable of accurately modeling neutron and photon physics in the applicable energy ranges to essentially the accuracy of the cross section data. For shallow penetrations we have full confidence in the calculational results. For deeper penetrations where small uncertainties in the physics data can build up to systematic deviations from measurement, we observe that even at 10 to 25 mean free paths the calculations are usually within a factor of two of measurements.

The two benchmark reports are available free to anyone contacting the authors. The E-mail address is MCNP@LANL.GOV.

These benchmarks are part of an ongoing project[17,18]. A cooperative program being carried out at General Electric, San Jose, consists of MCNP light water reactor benchmark problems[19,20]. A subsequent phase focusing on electron problems is planned.

5 Timing Study

We have recently completed a timing study comparing the performance of MCNP on the Cray-YMP264, Cray-XMP416, Sun Sparc 1, Sun Sparc 2, IBM RS/6000-550, and HP 9000/730. This paper is the first public disclosure of the results of this particular timing study, which has the following characteristics:

- It is limited to MCNP. We believe the results do not extrapolate to other computer codes. In particular, MCNP performs well on workstations relative to the Cray mainframes because MCNP does not vectorize well. For codes that vectorize, the Cray should perform much better than the workstations.
- The results we report are for the hardware and software available to us October 1991. The Fortran compilers used were the Sun 1.4, HP 8.05, IBM XLF2.2, and Cray CFT77 version 5.0.0.7 (UNICOS). Advances in both hardware and software, particularly compilers, will inevitably make our reported results obsolete.
- This timing study used a real production-version physics code.
- The problems used are the 25 MCNP test set problems available from RSIC. Our timing comparison is not limited to a single "typical" test problem.
- The results are reproducible. We report the MCNP performance (particle histories per minute) for each system. Anyone with a similar workstation and compiler can get the same test problem set and the same MCNP4.2 code from RSIC and replicate our results.

A typical set of performance data for the twenty-five MCNP test problems on the six machines is presented in Table 1. These data are normalized to the Cray YMP in Table 2, and to the IBM RS/6000-550 in Table 3. The average performance for the six systems relative to the YMP and based upon running the 25 problem set on each machine 3 - 7 times can be summarized as YMP = 100%, XMP = 86%, HP-730 = 91%, IBM-550 = 60%, Sun Sparc 1 = 12% and Sun Sparc 2 = 24%.

The highest level of optimization for each compiler was used to the best of our ability. All runs were done in 64-bit mode, although the workstations used 32-bit cross-section data. Timing results were obtained through the use of MCNP routines that return elapsed cpu plus system time as opposed to wallclock time or time in cycles. The performance for each problem on each machine rarely varied more than a few percent from trial to trial and was always within 10%.

We were surprised to see how strongly problem dependent our results were. For example, the IBM-550 consistently ranges from about 50% to 80% of the performance of the Cray YMP depending upon the problem. Therefore, we believe that studies comparing performance based upon a single "typical" problem can be very misleading.

We also found that performance was very sensitive to the compiler version used and the optimization level chosen. The performance of particular problems on the same machine with different optimization levels varied significantly. For example, on the Cray XMP problem 6 was the best performer with one optimization level and problem 11 was the best performer with another optimization level. On some machines we observed performance differences as much as 50% for different compilers and optimization levels.

We wish to repeat the caveats of one of our earlier published timing comparisons[21]. The performance of scientific workstation hardware and software is improving so rapidly that most measures are outdated by the time they are published. These performance figures give a relative comparison at one instant in time and are presented for information only.

One conclusion is clear from these timing studies. Scientific workstations today can approach the performance available only from mainframes a few years ago.

6 Summary

MCNP is a widely used and actively developed Monte Carlo radiation transport code. Many important features have recently been added and more are under development. Benchmark studies not only indicate that MCNP is accurate, but also that modern computer codes can give answers basically as accurate as the physics data that goes in them. Even deep penetration problems can be correct to within a factor of two after 10 to 25 mean free paths of penetration. And finally, Monte Carlo calculations, once thought to be too expensive to run routinely, can now be run effectively on desktop computers which compete with the supercomputers of yesteryear.

7 References

[1] R. A. Forster, R. C. Little, J. F. Briesmeister, and J. S. Hendricks, "MCNP Capabilities for Nuclear Well Logging Calculations," *IEEE Transactions on Nuclear Science*, **37**, (3) 1378 (June 1990)

[2] J. F. Briesmeister, Editor, "MCNP - A General Monte Carlo Code for Neutron and Photon Transport, Version 3A," Los Alamos National Laboratory report LA-7396-M, Rev. 2, (1986)

[3] J. A. Halbleib and T. A. Mehlhorn, "ITS: The Integrated TIGER Series of Coupled Electron/Photon Monte Carlo Transport Codes," Sandia National Laboratory report SAND84-0573 (1984)

[4] J. S. Hendricks and R. E. Prael, "Monte Carlo Next-Event Estimates from Thermal Collisions," *Nuclear Science and Engineering*, **109** (2) 150 - 157 (October 1991)

[5] J. S. Hendricks, R. E. Prael, "MCNP $S(\alpha,\beta)$ Detector Scheme," Los Alamos National Laboratory report, LA-11952 (October, 1990)

[6] T. E. Booth, "Intelligent Monte Carlo Phase-Space Division and Importance Estimation," *Trans. Am. Nucl. Soc.*, **60**, 358 (1989)

[7] T. E. Booth, "A Quasi-Deterministic Approximation of the Monte Carlo Importance Function," *Nuclear Science and Engineering*, **104** 374 - 384 (1990)

[8] T. E. Booth and J. S. Hendricks, "Importance Estimation in Forward Monte Carlo Calculations," *Nucl. Tech./Fusion*, **5** (1984)

[9] T. E. Booth, "A Weight Window/Importance Generator for Monte Carlo Streaming Problems," *Sixth International Conference on Radiation Shielding*, Tokyo, Japan (May 16-20, 1983)

[10] J. T. West III, "SABRINA: An Interactive Three-Dimensional Geometry-Modeling Program for MCNP," Los Alamos National Laboratory report LA-10688-M (1986)

[11] R. E. Prael and H. Lichtenstein, "User Guide to LCS: The LAHET Code System," Los Alamos National Laboratory report, LA-UR-89-3014 (1989)

[12] G. P. Estes, R. G. Schrandt, J. T. Kriese, "Automated MCNP Photon Source Generation for Arbitrary Configurations of Radioactive Materials and First Principles Calculations of Photon Detector Responses," Los Alamos National Laboratory report, LA-11153-MS (March 1988)

[13] W. R. Nelson, H. Hirayama, and D. W. O. Rogers, "The EGS4 Code System," Stanford Linear Accelerator Center report 265 (December 1985)

[14] T. A. Forster, "A New Method to Assess the Statistical Convergence of Monte Carlo Solutions," Accepted at the American Nuclear Society Winter Meeting (November 1991)

[15] D. J. Whalen, D. E. Hollowell, J. S. Hendricks, "MCNP: Photon Benchmark Problems," Los Alamos National Laboratory report, LA-12196 (September 1991)

[16] D. J. Whalen, D. A. Cardon, J. L. Uhle, J. S. Hendricks, "MCNP: Neutron Benchmark Problems," Los Alamos National Laboratory report, LA-122_2 (November 1991)

[17] D. J. Whalen, D. E. Hollowell, and J. S. Hendricks, "Monte Carlo Photon Benchmark Problems," *Proceedings of the International Topical Meeting on Advances in Mathematics, Computations, and Reactor Physics*, April 28 - May 2, 1991, **5**, 30.1 5-1 (April 1991)

[18] J. S. Hendricks, D. J. Whalen, D. A. Cardon, J. L. Uhle, "MCNP Neutron Benchmarks," Submitted to the American Nuclear Society Annual Meeting (June 1992)

[19] S. Sitaraman, "Benchmarking Study of the MCNP Code Against Cold Critical Experiments," *Trans. Am. Nucl. Soc.* **63** 426 (June 1991)

[20] S. Sitaraman, "Benchmarking Study of the Monte Carlo Code MCNP Against Light Water Reactor Critical Experiments," to be published as a General Electric Report.

[21] J. F. Briesmeister, F. W. Brinkley, B. A. Clark, J. T. West, "Los Alamos Radiation Transport Code System on Desktop Computing Platforms," *Trans. Am. Nucl. Soc.* **62** 455 (November 1990)

TABLE 1

MCNP PERFORMANCE (particle histories per minute)

Test Problem	YMP	XMP	Sun Sparc1	Sun Sparc2	IBM-550	HP-730
1.	7.1224E+4	5.9703E+4	7.3082E+3	1.5121E+4	3.7221E+4	5.8824E+4
2.	2.2188E+4	1.8704E+4	2.0580E+3	4.4248E+3	1.2058E+4	1.8270E+4
3.	1.8622E+4	1.6237E+4	2.6062E+3	5.9488E+3	1.3342E+4	2.0783E+4
4.	9.4285E+3	8.0183E+3	7.9256E+2	1.7386E+3	4.9727E+3	7.1908E+3
5.	2.0661E+3	1.7499E+3	1.5492E+2	3.6364E+2	1.0844E+3	1.5460E+3
6.	5.5836E+4	4.6859E+4	5.6022E+3	1.2010E+4	2.9499E+4	4.8780E+4
7.	1.8000E+4	1.5549E+4	2.2759E+3	4.8591E+3	1.1050E+4	1.8416E+4
8.	5.2182E+3	4.2544E+3	4.4183E+2	1.0714E+3	2.6923E+3	3.3281E+3
9.	3.4869E+4	3.0248E+4	5.3109E+3	1.1051E+4	2.5285E+4	4.0911E+4
10.	3.6352E+3	3.0767E+3	3.0525E+2	6.8259E+2	1.8029E+3	2.5751E+3
11	7.9454E+3	7.3203E+3	9.3985E+2	2.1572E+3	5.8575E+3	8.9109E+3
12.	4.0817E+3	3.5007E+3	3.7959E+2	8.3577E+2	2.1544E+3	3.0136E+3
13	2.6404E+4	2.3082E+4	3.6643E+3	8.3091E+3	2.1164E+4	3.4904E+4
14.	2.6560E+4	2.3252E+4	5.2306E+3	1.0648E+4	2.1490E+4	3.5993E+4
15.	2.1260E+4	1.8687E+4	3.2310E+3	6.4034E+3	1.3319E+4	2.4641E+4
16.	1.2064E+4	1.0332E+4	1.8328E+3	3.6729E+3	7.7781E+3	1.2976E+4
17.	1.4883E+4	1.2558E+4	1.6950E+3	3.6137E+3	9.3520E+3	1.3350E+4
18.	1.3017E+3	1.2104E+3	2.2095E+2	4.7372E+2	1.0808E+3	1.8551E+3
19	5.3358E+3	4.6138E+3	6.6262E+2	1.4055E+3	2.6490E+3	4.4280E+3
20.	2.1523E+4	1.7562E+4	1.7580E+3	4.3343E+3	1.2690E+4	1.2277E+4
21.	3.1801E+4	2.7927E+4	3.9481E+3	7.9734E+3	1.9036E+4	2.8289E+4
22	3.8328E+3	3.3800E+3	5.3422E+2	1.1577E+3	2.4343E+3	3.6923E+3
23.	5.6890E+3	4.6908E+3	4.6671E+2	1.1478E+3	3.2189E+3	3.4572E+3
24	1.8468E+3	1.6629E+3	2.9949E+2	6.3766E+2	1.3169E+3	2.0979E+3
25	3.7108E+4	3.2402E+4	6.0909E+3	1.2409E+4	2.6240E+4	4.4375E+4

TABLE 2

MCNP PERFORMANCE NORMALIZED TO CRAY-YMP

	YMP	XMP	Sun Sparc1	Sun Sparc2	IBM-550	HP-730
1.	100	84	10	21	52	83
2.	100	84	9	20	54	82
3.	100	87	14	32	72	112
4.	100	85	8	19	53	76
5.	100	85	7	18	52	75
6.	100	84	10	22	53	87
7.	100	86	13	27	61	102
8.	100	82	8	21	52	64
9.	100	87	15	32	73	117
10.	100	85	8	19	50	71
11.	100	92	12	27	74	112
12.	100	86	9	20	53	74
13.	100	87	14	31	80	132
14.	100	88	20	40	81	136
15.	100	88	15	30	63	116
16.	100	86	15	30	64	108
17.	100	84	11	24	63	90
18.	100	93	17	36	83	143
19.	100	86	12	26	50	83
20.	100	82	8	20	59	57
21.	100	88	12	25	60	89
22.	100	88	14	30	64	96
23.	100	82	8	20	57	61
24.	100	90	16	35	71	114
25.	100	87	16	33	71	120
Average:	100	86	12	26	63	96

TABLE 3

MCNP PERFORMANCE NORMALIZED TO IBM RS/6000-550

	IBM-550	YMP	XMP	Sun Sparc1	Sun Sparc2	HP-730
1.	100	191	160	20	41	158
2.	100	184	155	17	37	152
3.	100	140	122	20	45	156
4.	100	190	161	16	36	145
5.	100	191	161	14	34	143
6.	100	189	159	19	41	165
7.	100	163	141	21	44	167
8.	100	194	158	16	40	124
9.	100	138	120	21	44	162
10.	100	202	171	17	38	143
11.	100	136	125	16	37	152
12.	100	189	162	18	39	140
13.	100	125	109	17	39	165
14.	100	124	108	24	50	167
15.	100	160	140	24	48	185
16.	100	155	133	24	47	167
17.	100	159	134	18	39	143
18.	100	120	112	20	44	172
19.	100	201	174	25	53	167
20.	100	170	138	14	34	97
21.	100	167	147	21	42	149
22.	100	157	139	22	48	152
23.	100	177	146	14	36	107
24.	100	140	126	23	48	159
25.	100	141	123	23	47	169
Average	100	164	141	19	42	152

LA-UR -91-3461

Conf-9105xx1--x

LA-UR--91-3461

DE92 002519

TITLE THE NEUTRINOS IN MUON DECAY

AUTHOR(S) Peter Herczeg, T-5

SUBMITTED TO Invited talk presented at the symposium on "The Future of Muon Physics", Heidelberg, Germany, May 7-9, 1991. To Appear in the Proceedings (to be published in Zeitschrift für Physik C).

The neutrinos in muon decay

Peter Herczeg

Theoretical Division, Los Alamos National Laboratory
Los Alamos, New Mexico 87545

Submitted 21 October 1991

Abstract. We review the available information on the identity of the neutrino states emitted in muon decay, and discuss the exotic decay $\mu^+ \to e^+ \bar{\nu}_e \nu_\mu$.

---

1 Introduction

The main decay mode of the muon is the decay into two neutrinos [1]: $\mu^+ \to e^+ + n + n'$. In the standard model $n = \nu_{eL}$, $n' = \bar{\nu}_{\mu L}$, where ν_{eL} and $\nu_{\mu L}$ are massless left-handed neutrinos which accompany the corresponding left-handed charged leptons in doublets of $SU(2)_L$. The interaction responsible for this decay is due to W−exchange and has the V-A form

$$H^{(\mu)}_{V-A} = \frac{G_F}{\sqrt{2}} \bar{\mu}\gamma_\lambda(1-\gamma_5)\nu_\mu \bar{\nu}_e \gamma^\lambda (1-\gamma_5) e \; + \; H.c. \quad , (1)$$

where $G_F = (g^2/8m_W^2)(1+\Delta r)$; Δr represents radiative corrections [2].

In extensions of the standard model there may be new decay modes of the type $\mu^+ \to e^+ +$ *neutrinos*, and new decay interactions may be present. Among the decays $\mu^+ \to e^+ +$ *neutrinos* there could be some which violate the conservation of lepton family numbers and possibly also the conservation of the total lepton number. In the presence of the new interactions the neutrinos are expected to be massive, and the gauge group eigenstates are not expected to coincide with the mass-eigenstates. The mixing of the neutrinos may involve also heavy neutrino states, which cannot be emitted in the decays.

In this talk we shall review the existing information on the identity of the neutrinos in the main decay mode of the muon, and then discuss the particular exotic decay mode $\mu^+ \to e^+ \bar{\nu}_e \nu_\mu$.

2 The identity of the muon decay neutrinos

The most general local nonderivative four-fermion interaction that allows for lepton family number and total lepton number violation can be written in the helicity projection form [3] as [4]

$$\begin{aligned} H = 4 \sum_{i,j} \big[& (g^V_{LL})_{ij} \bar{e}_L \gamma^\lambda n_{iL} \bar{n}_{jL} \gamma_\lambda \mu_L \\ & + (g^V_{LR})_{ij} \bar{e}_L \gamma^\lambda n_{iL} \bar{n}^c_{jR} \gamma_\lambda \mu_R \\ & + (g^V_{RL})_{ij} \bar{e}_R \gamma^\lambda n^c_{iR} \bar{n}_{jL} \gamma_\lambda \mu_L \\ & + (g^V_{RR})_{ij} \bar{e}_R \gamma^\lambda n^c_{iR} \bar{n}^c_{jR} \gamma_\lambda \mu_R \\ & + (g^S_{LL})_{ij} \bar{e}_L n^c_{iR} \bar{n}^c_{jR} \mu_L \\ & + (g^S_{LR})_{ij} \bar{e}_L n^c_{iR} \bar{n}_{jL} \mu_R \\ & + (g^S_{RL})_{ij} \bar{e}_R n_{iL} \bar{n}^c_{jR} \mu_L \; + \; (g^S_{RR})_{ij} \bar{e}_R n_{iL} \bar{n}_{jL} \mu_R \\ & + (g^T_{LR})_{ij} \bar{e}_L t^{\alpha\beta} n^c_{iR} \bar{n}_{jL} t_{\alpha\beta} \mu_R \\ & + (g^T_{RL})_{ij} \bar{e}_R t^{\alpha\beta} n_{iL} \bar{n}^c_{jR} t_{\alpha\beta} \mu_L \big] + H.c. \end{aligned} \qquad (2)$$

The fermion fields in Eq. (2) are mass-eigenstates. The indices i, j run over all the neutrino states that can be emitted in the decay. For a fermion field (f) $f_L = \frac{1}{2}(1-\gamma_5)f$, $f_R = \frac{1}{2}(1+\gamma_5)f$; $t_{\alpha\beta} = \frac{i}{2\sqrt{2}}[\gamma_\alpha, \gamma_\beta]$. n_{iL} includes all the left-handed neutrino states ($n_{1L} \equiv \nu_{eL}$, $n_{2L} \equiv \nu^c_{eL}$, $n_{3L} = \nu_{\mu L}$ etc.), and the set n^c_{Ri} all the right-handed ones ($n^c_{1R} \equiv \nu^c_{eR}$, $n^c_{2R} \equiv \nu_{eR}$, $n^c_{3R} \equiv \nu^c_{\mu R}$, etc.).[1]

A special case of the Hamiltonian (2) is the one ($H^{(\mu)}_{LC}$), which contains all the possible interaction types (V,A,S,...), but allows only decay modes which conserve the individual lepton family numbers, and includes only ν_{eR} and $\nu_{\mu R}$ in addition to ν_{eL} and $\nu_{\mu L}$. $H^{(\mu)}_{LC}$ contains 10 coupling constants [$(g^V_{LL})_{13} \equiv g^V_{LL}$, $(g^V_{LR})_{14} \equiv g^V_{LR}$, $(g^V_{RL})_{23} \equiv g^V_{RL}$, $(g^V_{RR})_{24} \equiv g^V_{RR}$, $(g^S_{LL})_{24} \equiv g^S_{LL}$, $(g^S_{LR})_{23} \equiv g^S_{LR}$, $(g^S_{RL})_{14} \equiv g^S_{RL}$, $(g^S_{RR})_{13} \equiv$

[1] In Ref. [4] the constant $(g^V_{LL})_{ij}$ is denoted as $(G_0/\sqrt{2})g^{LL}_{ij}$; the correspondence between the notations for the other constants is analogous.

g^S_{RR}, $(g^T_{LR})_{23} \equiv g^T_{LR}$, and $(g^T_{RL})_{14} \equiv g^T_{RL}$]. In Ref. [5] limits have been set on all of these using the available experimental results on the muon lifetime, the positron energy spectrum and polarizations, and the inverse muon decay cross-section. One of the results of the analysis is the lower bound

$$Q_{LL} \equiv \left(\frac{1}{4} \mid g^S_{LL} \mid^2 + \mid g^V_{LL} \mid^2\right)(G_\mu/\sqrt{2})^{-2} > 0.949 \;\; (90\% \; c.l.), \tag{3}$$

obtained from muon-decay data alone on the quantity Q_{LL} which contains the standard model contribution. In Eq. (3) G_μ is the muon decay constant ($G_\mu = 1.16637(2) \times 10^{-5} GeV^{-2}$). For the contribution of the remaining coupling constants to the decay rate upper limits have been obtained (also from muon decay measurements), which are smaller than $(G_\mu/\sqrt{2})^2$ by factors of about 20 to 500. However, some of the coupling constants could still be quite large. For example the limit on $\mid g^S_{RL} \mid$ is $\mid g^S_{RL} \mid < 0.424(G_\mu/\sqrt{2})$ [5].

In the general case the muon decay parameters can be expressed through a set of quadratic functions of the coupling constants, which are generalizations of those for the lepton family number conserving case [4]. There is a one-to-one correspondence between the two sets [4], and consequently it is possible to use the results for the lepton family number conserving case to obtain constraints for the Hamiltonian (2). Thus, since [4]

$$\begin{aligned} \frac{1}{4} \mid g^S_{LL} \mid^2 &\longrightarrow \sum_{i>j} \mid (g^V_{LL})_{ij} + \frac{1}{2}(g^S_{LL})_{ji} \mid^2 , \\ \mid g^V_{LL} \mid^2 &\longrightarrow \sum_{i \le j} \mid (g^V_{LL})_{ij} + \frac{1}{2}(g^S_{LL})_{ji} \mid^2 , \end{aligned} \tag{4}$$

the constraint (3) becomes

$$Q_{LL} \equiv \sum_{i,j} \mid (g^V_{LL})_{ij} + \frac{1}{2}(g^S_{LL})_{ij} \mid^2 > 0.949(G_\mu/\sqrt{2})^2 . \tag{5}$$

In the analysis it has been assumed that the masses of the neutrinos that can be emitted in the decay are small enough that their effect on the positron spectrum can be neglected.

Information on one of the neutrino states in muon decay comes from the inverse muon decay process $\nu_\pi e^- \to \mu^- n_i$ where ν_π is the neutrino state emitted in $\pi^+ \to \mu^+ \nu_\pi$ decay, and n_i are some neutrino states. The cross-section for this reaction has been measured recently by the CHARM II collaboration [6] and by the CCFR collaboration [7], obtaining

$$S = 1.054 \pm 0.079 \qquad (CHARM\,II) , \tag{6}$$

$$S = 0.981 \pm 0.057 \qquad (CCFR) , \tag{7}$$

where S is the total cross-section for $(\nu_\pi e^- \to \mu^- n_1) + (\nu_\pi e^- \to \mu^- n_2) + \ldots$ relative to the cross-section predicted by the standard model. As ν_π is to an excellent approximation left-handed [8], S is given by (taking into account the limits on the coupling constants)

$$S \simeq \sum_i \mid (g^V_{LL})_{i3} + \frac{1}{2}(g^S_{LL})_{3i} \mid^2 (G_\mu/\sqrt{2})^{-2} , \tag{8}$$

where the neutrino state $\nu_\pi = \sum_j c_j n_{jL}$ has been denoted as n_{3L}. ($S \simeq \mid g^V_{LL} \mid^2 (G_\mu/\sqrt{2})^{-2}$ in the case of the Hamiltonian $H^{(\mu)}_{LC}$ [5]).

The experimental value of S enables one to set a lower bound on the term which includes the standard model contribution, and using $Q_{LL} \le 1$ an upper bound on the remaining part of Q_{LL} [5]. From (7) one obtains [7]

$$\sum_i \mid (g^V_{LL})_{i3} + \frac{1}{2}(g^S_{LL})_{3i} \mid^2 > 0.925(G_\mu/\sqrt{2})^2 \quad (90\% \; c.l.), \tag{9}$$

$$\sum_{\substack{i,j \\ j \ne 3}} \mid (g^V_{LL})_{ij} + \frac{1}{2}(g^S_{LL})_{ji} \mid^2 < 0.075(G_\mu/\sqrt{2})^2 \quad (90\% \; c.l.) \tag{10}$$

The limits from (6) are only slightly weaker.

The bound (9) implies that at least one of the μ^+−decay modes which involves the neutrino $\bar{\nu}_\pi$ produced in $\pi^- \to \mu^- \bar{\nu}_\pi$ decay dominates the μ^+−decay rate [4].

Regarding the nature of the state ν_π there is some experimental information from a search [9] for $e^\pm$−production by ν_π on nucleons. The experiment yielded $\Gamma(\pi^+ \to \mu^+ \bar{n}_e)/\Gamma(\pi^+ \to \text{all}) < 1.5 \times 10^{-3}$ (90% c.l.) and $\Gamma(\pi^+ \to \mu^+ n_e)/\Gamma(\pi^+ \to \text{all}) < 8 \times 10^{-3}$ (90% c.l.), where $\bar{n}_e$ and n_e are neutrino states capable of producing e^+ and e^-, respectively.[2] This indicates that ν_π is not the state which accompanies the positron or the electron in nuclear beta decay.

Information on the second neutrino in muon decay follows from the experiment of Ref. [10], where neutrinos (n_e) from μ^+−decay have been observed through the reaction $n_e D \to ppe^-$. The good agreement of the measured $n_e D \to ppe^-$ cross-section and the calculated one in the standard model indicates that the total muon decay rate contains a substantial contribution from muon decay into a final state in which one of the neutrinos is the one accompanying the positron in nuclear beta decay.

Experimental results [10,11,12,13] are available also on decays of the type $\mu^+ \to e^+ \bar{n}_e n_x$, where n_x is some neutrino state and n_e is a neutrino state capable of

[2] We remind the reader that we use the term "neutrino state" to refer to either a "neutrino" or an "antineutrino". Also, e.g. the state $n_e(\bar{n}_e)$ could be an antineutrino (neutrino) state. For Majorana neutrinos there is of course no distinction. On the other hand $\nu_e(\bar{\nu}_e)$ denotes the electron neutrino (electron antineutrino)

producing positrons on protons.[3] The best limit on the branching ratio

$$R \equiv \Gamma(\mu^+ \to e^+ \bar{n}_e n_x)/\Gamma(\mu^+ \to \text{ all}) \tag{11}$$

is

$$R < 0.018 \quad (90\% \; c.l.) \quad , \tag{12}$$

from the experiment of Ref. [13].[4]

It is evident from the above discussion that the experimental information regarding the muon decay interaction and the nature of the neutrinos involved is consistent with the standard model picture. Searches for non-standard contributions and non-standard decay modes continue to be of great importance. In the next section we shall consider the exotic decay $\mu^+ \to e^+ \bar{\nu}_e \nu_\mu$.

3 The decay $\mu^+ \to e^+ \bar{\nu}_e \; \nu_\mu$

The exotic decay mode $\mu^+ \to e^+ \bar{\nu}_e \nu_\mu$[5] was first considered [15] before the advent of gauge theories, in connection with the question regarding the nature of the suspected invariance principle which was supposed to account for the apparent absence of processes like $\mu \to e\gamma$, or $\mu^- N \to e^- N$. In the scheme of Ref. [15] the decay $\mu^+ \to e^+ \bar{\nu}_e \nu_\mu$ is one of the processes (muonium to antimuonium conversion is another) which would be allowed if the conservation of a multiplicative quantum number (muon parity) would be involved, but forbidden if the conservation law concerned additive quantum numbers (muon number and electron number). In the standard model the lepton family numbers are conserved and therefore $\mu^+ \to e^+ \bar{\nu}_e \nu_\mu$ (like $\mu \to e\gamma$, etc.) is forbidden. Beyond the standard model the presence of conserved lepton numbers (additive or multiplicative) is generally not expected.[6] We should note also that since the strength of the $\mu^+ \to e^+ \bar{\nu}_e \nu_\mu$ interaction is not related to the weak interactions, the existence of a conserved multiplicative quantum number cannot be ruled out by the absence of $\mu^+ \to e^+ \bar{\nu}_e \nu_\mu$ (or muonium to antimuonium conversion, etc.) at a certain level.

The decay $\mu^+ \to e^+ \bar{\nu}_e \nu_\mu$ could be mediated at the tree-level by non-standard Higgs bosons, or new gauge bosons. A simple extension of the standard model which allows $\mu^+ \to e^+ \bar{\nu}_e \nu_\mu$ can be obtained by adding to the Higgs doublet a singlet charged Higgs boson (h) and including singlet right-handed neutrinos. A coupling of the form[7]

$$L = g_{ee} \overline{\nu^c_{eR}} e_R h + g_{\mu\mu} \overline{\nu^c_{\mu R}} \mu_R h \; + \; H.c. \tag{13}$$

is then possible, which (if the right-handed neutrinos are sufficiently light) gives rise to $\mu^+ \to e^+ \bar{\nu}_e \nu_\mu$. The corresponding interaction after a Fierz transformation can be written in the form

$$H = \frac{g_{ee} g^*_{\mu\mu}}{8 m_h^2} \bar{\mu} \gamma_\lambda (1+\gamma_5) \nu_e \bar{\nu}_\mu \gamma^\lambda (1+\gamma_5) e \; + \; H.c. \tag{14}$$

Denoting $\overline{G} = \sqrt{2} g_{ee} g^*_{\mu\mu}/8m_h^2$, the branching ratio R (see (11), where now $\bar{n}_e = \bar{\nu}_e$, $n_x = \nu_\mu$) is given by $R = |\overline{G}|^2/(G_F^2 + |\overline{G}|^2) = |\overline{G}/G_\mu|^2$. The experimental limit (12) does not apply for this case, since the right-handed neutrinos do not couple to the W. There are however several indirect constraints on $\overline{G}$.

One constraint follows from the limits on the coupling constants of the general Hamiltonian (2). The Hamiltonian consisting of the standard model contribution and the interaction (14) is a special case of (2) with

$$(g^V_{LL})_{13} = G_F/\sqrt{2} \quad , (g^S_{RR})_{24} = 2\overline{G}^*/\sqrt{2} \quad , \tag{15}$$

and all the other coupling constants set to zero. From the analysis of muon decay data one has the limit $|g^S_{RR}| < 0.066 (90\% \; c.l.)$ [5] for $H^{(\mu)}_{LC}$, which translates in the general case to

$$\sum_{i>j} |(g^V_{RR})_{ij} \; + \; \frac{1}{2}(g^S_{RR})_{ji}|^2 < \; 0.0011 (G_\mu/\sqrt{2})^2 \tag{16}$$
$$(90\% \; c.l.) \quad .$$

Since the left-hand side of Eq. (16) is simply $|\frac{1}{2}(g^S_{RR})_{24}|^2$, we obtain from (15) and (16) the bound

$$|\overline{G}| < 0.032 \; |G_\mu| \quad (90\% \; c.l.) \quad . \tag{17}$$

Limits on $\overline{G}$ are implied also by the experimental value of the $W-$mass, and by charged current universality.

The muon decay constant in the presence of the interaction (14) is given by $G_\mu = G_F(1+$

[3] Further sources of positrons could be neutrinos from ordinary μ^+-decay due to oscillations, or even without oscillations if the weak eigenstate neutrinos contain heavy mass-eigenstates which cannot be produced in the decay[14]. A Majorana ν_{eL} can also produce a positron, but the amplitude is proportional to the neutrino mass.

[4] It should be noted that the limit (12) holds only for such decays $\mu^+ \to e^+ \bar{n}_e n_x$ where the spectrum of $\bar{n}_e$ (or the spectrum of n_x, if n_x can produce positrons) is the same as the spectrum of $\bar{\nu}_\mu$ in μ^+-decay. I am grateful to R. L. Burman for calling my attention to this aspect of the experiment. The experiment of Ref. [12], in which the reaction $\bar{\nu}_\pi + e^- \to \mu^- \bar{n}_e$ rather than muon decay was searched for, sets a limit only for the branching ratio of $\mu^+ \to e^+ \bar{n}_e \nu_\pi$.

[5] The $\bar{\nu}_e$ and ν_μ in this decay mode are by definition identical or nearly equal to the weak eigenstates $\bar{\nu}'_e$ and ν'_μ. If ν_e is a Majorana neutrino, then for left-handed (right-handed) couplings $\bar{\nu}_e$ is the right-handed (left-handed) component of ν_e.

[6] It is interesting to mention however the model of Ref. [16], where it was shown that the three-family standard model for the leptons can be extended in such a way that a multiplicative quantum number is conserved, while the conservation of the lepton family numbers is broken. This is achieved by requiring invariance of the unbroken theory under the permutation group S_3, and introducing three Higgs doublets, one for each lepton family. The decay $\mu^+ \to e^+ \bar{\nu}_e \nu_\mu$ is mediated by one of the new Higgs bosons. If the quarks are treated in this model in the same way as the leptons, the model runs into contradiction with experiment.

[7] This is analogous to the coupling of a doubly charged singlet Higgs boson to right-handed charged leptons, considered in Ref. [17].

$|\, \overline{G}/G_F\,|^2)^{1/2}$. Since G_μ is known experimentally and G_F can be evaluated using the experimental values of m_W, $\sin^2\theta_W$ and Δr, a constraint follows for $|\,\overline{G}/G_F\,|$. With $m_W = (79.91 \pm 0.39)$ GeV [18], $\sin^2\theta_W = 0.2291 \pm 0.0034$ [19], and $\Delta r = 0.056^{+0.006}_{-0.010}$ [19], we find

$$|\,\overline{G}/G_\mu\,| < 0.23 \quad (90\%\ c.l.)\ . \tag{18}$$

The experimental value of the ud-element U_{ud} of the Kobayashi-Maskawa matrix is defined as the ratio of the experimental value of the beta decay vector constant G_β and the muon decay constant G_μ. In the standard model $G_\beta = G_F\widehat{U}_{ud}$ (where $\widehat{U}_{ud}$ is the true KM matrix element), and $G_\mu = G_F$, so that $U_{ud} = G_\beta/G_\mu = \widehat{U}_{ud}$. In the presence of the interaction (14) we have $|\,U_{ud}\,|^2 = |\,\widehat{U}_{ud}\,|^2\,(1+|\,\overline{G}/G_F\,|^2)^{-1}$. Analogous relations hold for $|\,U_{us}\,|^2$ and $|\,U_{ub}\,|^2$, so that using the unitarity relation for the 3-family case one obtains

$$|\,U_{ud}\,|^2 + |\,U_{us}\,|^2 + |\,U_{ub}\,|^2 = (1+|\,\overline{G}/G_F\,|^2)^{-1}\ . \tag{19}$$

A recent analysis [20] yields $|\,U_{ud}\,|^2 + |\,U_{us}\,|^2 + |\,U_{ub}\,|^2 = 0.9989 \pm 0.0012$, implying

$$|\,\overline{G}/G_\mu\,| < 0.053 \quad (90\%\ c.l.) \tag{20}$$

The example (14) of an interaction that can give rise to $\mu^+ \to e^+\bar{\nu}_e\nu_\mu$ is just a possibility, without a particular motivation. Mohapatra and I have investigated [21] $\mu^+ \to e^+\bar{\nu}_e\nu_\mu$ and also muonium to antimuonium ($M \to \overline{M}$) conversion in the left-right symmetric $SU(2)_L \times SU(2)_R \times U(1)_{B-L}$ model of Ref. [22]. In this model $\mu^+ \to e^+\bar{\nu}_e\nu_\mu$ and $M \to \overline{M}$ conversion arise naturally, and moreover turn out to play a distinctive role. We have pointed out that with reasonable assumptions concerning some of the parameters of the model there is a lower bound in these models for the $\mu^+ \to e^+\bar{\nu}_e\nu_\mu$ rate and the $M \to \overline{M}$ conversion rate for the range of the muon neutrino mass m_{ν_μ} for which the constraint from cosmology requires ν_μ to be unstable. Below I shall give a brief sketch of this work, referring the reader to Ref. [21] for details and complete references.

The Higgs sector of the model contains the bidoublet field ϕ (2,2,0) and the triplet fields $\Delta_R(1,3,2)$ and Δ_L (3,1,2). Left-right symmetric models provide an attractive framework for understanding the origin of parity violation in the weak interactions. The class of $SU(2)_L \times SU(2)_R \times U(1)_{B-L}$ models with triplet Higgs bosons can also provide an explanation of the smallness of the masses of the observed neutrinos.

The observed energy density of the universe implies that neutrinos which are heavier than about 40 eV must be unstable, and that there is an upper bound on their lifetimes, which is a decreasing functin of their mass. For the muon neutrino the only decay mode that can satisfy the cosmological constraint is the decay $\nu_\mu \to \nu_e\nu_e\nu_e$ mediated by Δ_L^0-exchange. The cosmological constraint gives a lower bound (proportional to $m_{\nu_\mu}^{-3/2}$) on the strength $|\,G_0/\sqrt{2}\,|$ of the $\nu_\mu \to \nu_e\nu_e\nu_e$ interaction, which in turn implies an upper bound (proportional to $m_{\nu_\mu}^{3/4}$) on the mass m_o of the Δ_L^0. This bound combined with the lower bound $m_o \gtrsim 43$ GeV on m_o provided by the experimental value of the invisible width of the Z dictates that if ν_μ is unstable, its mass has to be larger than $\sim$ 36 keV. It follows that the model is viable for $m_{\nu_\mu} \lesssim$ 40 keV and for m_{ν_μ} in the range 36 keV $\lesssim m_{\nu_\mu} \lesssim$ 270 keV.

The decay is mediated by the exchange of the singly-charged Higgs boson Δ_L^+ [23]. The corresponding interaction can be written in the form

$$H = 2\frac{G_+}{\sqrt{2}}\bar{\mu}\gamma_\lambda(1-\gamma_5)\nu_e\bar{\nu}_\mu\gamma^\lambda(1-\gamma_5)e \quad + \text{H.c.}\ , \tag{21}$$

where $G_+ \simeq \sqrt{2}f_{ee}f_{\mu\mu}^*/8m_+^2$; m_+ is the mass of the Δ_L^+; f_{ee} and $f_{\mu\mu}$ are lepton$-\Delta_L$ Yukawa couplings.

The constant G_+ is related to G_o as

$$G_+^* = \frac{1}{2}G_oK_{e\mu}^{-1}\frac{f_{\mu\mu}}{f_{ee}-f_{\mu\mu}}\frac{m_o^2}{m_+^2}\ , \tag{22}$$

where $K_{e\mu}$ is the $e\mu$-element of the mixing matrix K in the charged-current interactions of the light neutrinos. Eq. (22) yields a lower bound on $|\,G_+\,|$, since it can be shown that not only $|\,G_o\,|$ but also $|\,f_{\mu\mu}\,|$ and m_o^2/m_+^2 are bounded from below.

Muonium to antimuonium conversion arises in the model at the tree level through Δ_L^{++}-exchange [24]. The resulting effective $M \to \overline{M}$ interaction is given by

$$H = \frac{G_{++}}{\sqrt{2}}\bar{\mu}\gamma^\lambda(1-\gamma_5)e\bar{\mu}\gamma_\lambda(1-\gamma_5)e \quad + \text{H.c.}\ , \tag{23}$$

where $G_{++} \simeq \sqrt{2}f_{ee}f_{\mu\mu}^*/8m_{++}^2$. G_{++}^* is related to G_o in the same way as G_+^* except for the replacement $m_+ \to m_{++}$ in Eq. (22). Since m_o^2/m_{++}^2 is, like m_o^2/m_+^2, bounded from below, a lower bound follows also for $|\,G_{++}\,|$.

We find $|\,G_+\,| \gtrsim 4 \times 10^{-4}G_F$ and $|\,G_{++}\,| \gtrsim 2 \times 10^{-4}G_F$ for 36 keV $\lesssim m_{\nu_\mu} \lesssim$ 270 keV [21]. The lower bounds increase with decreasing m_{ν_μ}. Thus, as the experimental limits on $|\,G_+\,|$ and/or $|\,G_{++}\,|$ become more and more stringent, the allowed range of m_{ν_μ} for which the model is viable becomes increasingly smaller. For $m_{\nu_\mu} \simeq$ 36 keV we obtain $|\,G_+\,| \gtrsim 2 \times 10^{-2}$ and $|\,G_{++}\,| \gtrsim 10^{-2}$.

The branching ratio R in Eq. (11) (with $n_e = \nu_e$, $n_x = \nu_\mu$) is given by

$$R = 4\,|\,G_+/G_\mu\,|^2\ . \tag{24}$$

The experimental limit (12) implies

$$|\,G_+\,| < 0.067G_\mu\ . \tag{25}$$

The Hamiltonian consisting of the interaction (21) and the standard model contribution corresponds to the general Hamiltonian (2) with

$$(g_{LL}^V)_{13} = G_F/\sqrt{2}\ ,\ (g_{LL}^S)_{13} = 4G_+^*/\sqrt{2} \tag{26}$$

and all the remaining constants absent. Eq. (10) in this case implies

$$| G_+ | < 0.14 G_\mu \quad (90\% \ c.l.) \tag{27}$$

From the experimental value of the W−mass and from charged current universality we obtain

$$| G_+ | < 0.12 \, G_\mu \quad (90\% \ c.l.) \tag{28}$$

and

$$| G_+ | < 0.026 \, G_\mu \quad (90\% \ c.l.) \ , \tag{29}$$

respectively. These are the same constraints as for $| \overline{G}/2 |$ before, since the muon decay constant is now given by $G_\mu = G_F(1 + 4 \mid G_+/G_F \mid^2)^{1/2}$. From the upper limits (25), (27), (28) and (29) the most stringent at present is the one from charged current universality. It should be noted however that this bound may be affected by theoretical uncertainties.

An experiment in preparation at LAMPF [25] plans to search for $\mu^+ \to e^+ \bar{\nu}_e \nu_\mu$ with a sensitivity corresponding to $| G_+ | \simeq 6 \times 10^{-3} G_F$. The LAMPF experiment will improve simultaneously the limit on $K_{e\mu}$ by a factor of ~ 3.5. This will increase the lower bound on $| G_+ |$ and $| G_{++} |$ by a factor of ~ 2.

The present experimental upper limit on $| G_{++} |$ is $| G_{++} | < 0.16 G_F$ (90% c.l.) [26]. The experiment under way at PSI [27] is expected to lower the upper limit to $10^{-3} G_F$.

4 Conclusions

In this talk we discussed two subjects in the field of muon decay: the status of our knowledge regarding the identity of the neutrinos emitted in muon decay, and the exotic decay mode $\mu^+ \to e^+ \bar{\nu}_e \nu_\mu$.

Concerning the identity of the muon decay neutrinos experiment indicates that among the decays $\mu^+ \to e^+ +$ *neutrinos* the decay mode which dominates the $\mu^+ \to e^+ +$ *neutrinos* rate involves the neutrino species of the standard model scenario: one of the neutrinos in this decay mode is the state $\bar{\nu}_\pi$ emitted in $\pi^- \to \mu^- \bar{\nu}_\pi$ decay, and the other the state n_e which accompanies the positron in nuclear beta decay; experiment indicates also that ν_π and n_e are not the same states. Muon decay and inverse muon decay data constrain the interaction that governs this decay mode to be the standard model interaction and/or a scalar type interaction. The experimental values of m_W and $\sin^2\theta_W$ indicate that the standard model contribution dominates.

The contribution of other decay interactions and decay modes to the $\mu^+ \to e^+ +$ *neutrinos* rate is constrained to be less than about 10%. Searches for non-standard contributions continue to be of great importance. From non-standard decay modes we discussed the exotic decay $\mu^+ \to e^+ \nu_e \nu_\mu$. More and more sensitive searches for this decay (as also searches for muonium to antimuonium conversion) will provide important information on an attractive class of left-right symmetric models.

Acknowledgement. I am grateful to R. L. Burman, V. W. Hughes, K. Jungmann, W. C. Louis, B. E. Matthias, R. N. Mohapatra and D. H. White for valuable conversations. I would also like to thank K. Jungmann and G. zu Putlitz for a most enjoyable symposium and wonderful hospitality. This work was supported by the United States Department of Energy.

References

1. Recent reviews of aspects of muon decay include R. Engfer, H. K. Walter: Ann. Rev. Nucl. Part. Sci. 36(1986)327; S. P. Rosen: Los Alamos National Laboratory preprint LA-UR-88-4013, invited talk at the Workshop on new directions in neutrino physics at Fermilab, Fermilab, Sept. 14-16, 1988; P. Herczeg: In: Rare Decay Symposium, eds. D. Bryman, J. Ng, T. Numao, J. Poutissou, p. 24. Singapore: World Scientific 1989
2. A. Sirlin: Phys. Rev. D22(1980)970
3. F. Scheck: Leptons, Hadrons and Nuclei. Amsterdam: North-Holland 1983; K. Mursula, F. Scheck: Nucl. Phys. B55(1985)189
4. P. Langacker, D. London: Phys. Rev. D39(1989)266
5. W. Fetscher, H.-J. Gerber, K. F. Johnson: Phys. Lett. 173B(1986)102; W. Fetscher, H.-J. Gerber, Note on muon decay parameters, In: Review of particle properties: Phys. Lett. 239B(1990)VI.11
6. D. Geiregat et al.: Phys. Lett. 247B(1990)131
7. S. R. Mishra et al.: Phys. Lett. 252B(1990)170
8. W. Fetscher: Phys. Lett. B140(1984)117
9. A. M. Cooper et al.: Phys. Lett. 112B(1982)97
10. S. E. Willis, et al.: Phys. Rev. Lett. 44(1980)522
11. T. Eichten et al.: Phys. Lett. 46B(1973)281; J. Blietschau et al.: Nucl. Phys. B133(1978)205
12. F. Bergsma et al.: Phys. Lett. 122B(1983)465
13. D. A. Krakauer et al.: Phys. Lett. 263B(1991)534
14. P. Langacker, D. London: Phys. Rev. D38(1988)907
15. G. Feinberg, S. Weinberg: Phys. Rev. Lett. 6(1961)381
16. E. Derman, D. R. T. Jones: Phys. Lett. 70B(1977)449; E. Derman: Phys. Lett. 78B(1978)497; E. Derman: Phys. Rev. D19(1979)317
17. R. N. Mohapatra: In: Eighth Workshop on Grand Unified Theory, Syracuse, ed. K. C. Wali, p. 200. Singapore: World Scientific 1987; D. Chang, W.-Y. Keung: Phys. Rev. Lett. 62(1989)2583
18. S. Lloyd: In: Proceedings of the 1991 Aspen Winter Conference in Elementary Particle Physics (unpublished)
19. P. Langacker, M. Luo: Phys. Rev. D44(1991)817
20. D. H. Wilkinson: Isospin and Quarks in Nuclear Beta-Decay, paper presented at the International Conference on Spin and Isospin in Nuclear Interactions, Telluride, Colorado, March 11-15, 1991, TRIUMF preprint TRI-PP-91-9
21. P. Herczeg, R. N. Mohapatra: Los Alamos National Laboratory preprint, Oct. 1991. A brief version of this paper is given in P. Herczeg, R. N. Mohapatra: Los Alamos National Laboratory preprint LA-UR-91-3038, to appear in the proceedings of the Particles and Fields '91 Conference of the APS, Vancouver, Canada, Aug. 18-22, 1991
22. R. N. Mohapatra, G. Senjanović: Phys. Rev. Lett. 44(1980)912; R. N. Mohapatra, G. Senjanović: Phys. Rev. D23(1981)165
23. P. Herczeg, R. N. Mohapatra (unpublished). Reported in P. Herczeg: In: Rare Decay Symposium, eds. D. Bryman, J. Ng, T. Numao, J. Poutissou, p. 24. Singapore: World Scientific 1989

24. A. Halprin: Phys. Rev. Let. 48(1982)1313

25. X.-Q. Lu et al.: A Proposal to Search for Neutrino Oscillations with High Sensitivity in the Appearance Channels $\nu_\mu \rightarrow \nu_e$ and $\bar{\nu}_\mu \rightarrow \bar{\nu}_e$, LAMPF Proposal LA-11842-P, Aug. 1990.

26, B. E. Matthias et al.: Phys. Rev. Lett. 66(1991)2716

27. K. Jungmann, W. Bertl et al.: Search for Spontaneous Conversion of Muonium to Antimuonium, PSI Experiment R-89-06.1

This article was processed using Springer-Verlag TEX Z.Physik C macro package 1991
and the AMS fonts, developed by the American Mathematical Society.

LASER DEPOSITION AND LASER MODIFICATION OF HIGH-TEMPERATURE SUPERCONDUCTING THIN FILMS

R. C. Dye, S.R. Foltyn and N. S. Nogar
Chemical and Laser Sciences Division

X. D. Wu and E.J. Peterson R. E. Muenchausen
Exploratory Research and Development Center
Los Alamos National Laboratory
Los Alamos, New Mexico 87545

ABSTRACT

Applications of high-temperature superconductors (HTSC) may require epitaxial thin films with $T_C \geq 77$ K, and $J_C \geq 10^6$ A/cm^2. *In-situ* pulsed laser deposition (PLD) is suitable for fabrication of such films. We report parametric studies on the effect of laser and processing parameters on the crystallinity, epitaxy and electrical properties of laser-deposited HTSC thin films.

In addition, several laser-based processes were used to modify the electrical properties (T_C and J_C) of PLD thin films. A direct-write laser heating (1.06 μm at ≈0.5 kW/cm^2 for ≈5 min) process in an oxygen atmosphere at ≈590 Torr was shown to selectively regenerate high-T_C material in microscopic domains from films that were partially deoxygenated. In separate work, electrical responses and crystallinity of HTSC films were measured as a function of excimer laser exposure using fluences in the rang 20-150 mJ/cm^2. The critical current and boundary layer could be modified with a high degree of accuracy.

1. INTRODUCTION

Many microelectronics, microwave and optoelectronics applications of the new metal-oxide based high-temperature superconductors (HTSC) will require epitaxial (high J_C) thin films with transition temperatures, $T_C \geq 77$ K. *In-situ* pulsed laser deposition (PLD) offers considerable promise for the fabrication of such films, even over large areas, in addition to buffer-layer and multilayer coatings [1-5].

Potential device structures for high-temperature superconducting (HTSC) thin films include interconnects, oscillators, switches, junctions, SQUIDs, filters and delay lines [6]. All applications will require the generation (and possible erasure) of superconducting structures in well-defined domains, preferably under gentle processing conditions. Critical current control may also be required for some applications. Mild processing conditions with an exceptionally clean interface between the superconducting and non-superconducting regions may be necessary to produce high quality HTSC thin-film devices. Several lithographic and direct-write patterning techniques, including ion-milling, plasma-etching, and wet chemical etching have been reported. These techniques may produce a damaged boundary or layer at the interface between the original high-T_c and modified materials that can severely degrade device performance.

We describe in this manuscript major characteristics of the laser deposition process for $YBa_2Cu_3O_{7-\delta}$ (YBCO) superconductors, including characteristics of the laser generated plume, and modifications occuring on the target surface. In addition, several methods for pattering of HTSC thin films, and for the modification of both T_c and J_c under relatively mild processing conditions, are described.

2. EXPERIMENTAL

The apparatus developed for PLD of YBCO thin films[7] consists of a modified six way 6" dia. stainless steel cross as shown in Figure 1. Load locks are provided for target and substrate introduction to minimize pumping times. The target can be rotated in conjunction with horizontal rastering of the laser beam while the substrate can be rotated to ensure uniform thickness (±10%) across the substrate diameter. The exposure (shots/site) was calculated by simply dividing the number of shots by a geometrical factor which is the area ratio of the annular ring of target material exposed divided by the laser beam area. Tilt flanges (±2°) allowed for precise alignment of target and substrate.

Provisions were made to heat the substrate, either indirectly on a Ni block or radiatively[8]. Deposition rates were measured by substituting a Inficon XTC, quartz microbalance (QCM) at the substrate position. Measured thickness values were calibrated by Rutherford backscattering (RBS) measurements. Processing gases were introduced into the deposition chamber using mass flow control to maintain a constant pressure. The excimer laser used in these experiments (Lambda Physik 203EMG) produced 200 mJ, 20 nsec pulses at 308 nm at repetition rates typically around 10 Hz.

Additionally, for some of the experiments described here, the plume optical emission was collected and analyzed[9]. One of two methods was used, depending on whether spatial or spectral resolution was required. In the former case, emission from the plume was passed through a narrow-band (~2 nm) interference filter, collected by a compound lens, and focussed onto a gated, intensified CCD detector. This allowed spatially resolved measurements, with a temporal resolution of ~25 nsec. In the latter case, light was collected by a 7.5 cm. diameter, 500 cm focal length quartz lens, and focussed onto the end of a (200 μm diameter) multi-mode fiber optic cable (FOC), 10 m in length. The distal end of the fiber optic cable was coupled to an 0.5 m monochromator equipped the CCD camera for spectrally resolved detection.

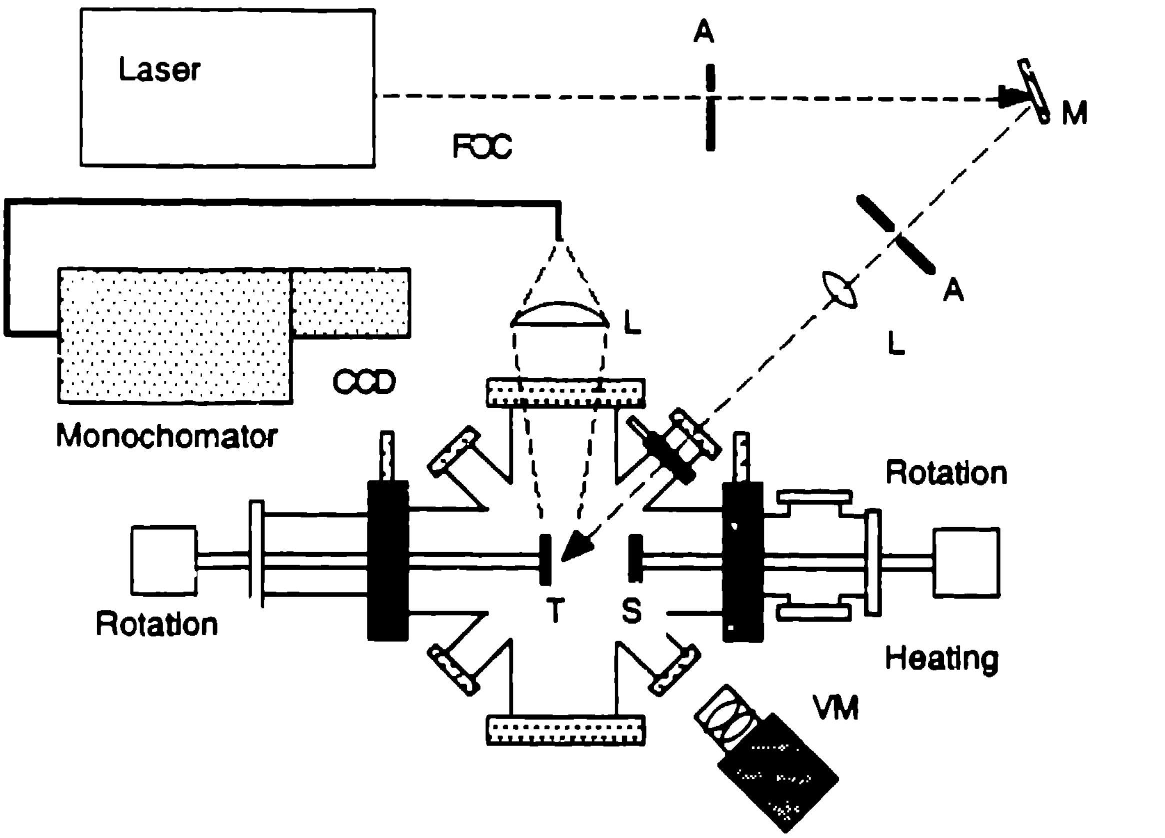

Figure 1. Experimental schematic: L=lens; M=mirror; A=aperture; FOC=fiberoptic cable; T=target; S=substrate; VM=video monitor.

For experiments in laser writing, the thin films, after thermally annealing the films in an argon atmosphere at a temperature of 400° C for 5-20 minutes, exhibited either no superconducting transition, or a transition temperature less than 60 K due to oxygen loss. Selected areas of the depleted film were then regenerated to 90 K by placing the sample in an oxygen chamber and radiating with 1.06 μm light from a Nd^{+3}:YAG laser operating at 80 MHz to produce 3.5 W of output. The beam was focused to approximately 0.5 mm^2. Patterns were established by having the sample in a windowed chamber which was mounted on a programmable, X-Y translational stage. The rate of travel of the stage was varied in the range near 0.1 mm/min. The patterns were then characterized by four-point probe and rf-eddy current measurements, as well as optical and electron spectroscopies.

The experiments on critical current modification used a simple contact mask design to pattern bridges for J_c measurements. The largest of three bridges was 200 μm by 2 mm and the other two bridges were 100 μm by 0.5 mm and 1 mm, respectively. The patterning laser output was homogenized and focused to a 7 mm by 12 mm spot size to overfill slightly the masked region. During patterning, the laser repetition rate was 10 Hz and an inert gas flow (Ar or N_2) was maintained across the mask to assist in cooling the mask and removing ablated particulates. Twelve 1 mm by 1 mm contact pads were deposited onto the three bridge structures by thermally evaporating silver. A five minute anneal under O_2 at 400 °C improved adhesion and lowered the contact resistance between the silver and the superconductor. The patterned film was wired into a 14 pin IC socket using a low melting indium solder. All I_c measurements were performed at a temperature of boiling liquid N_2 and zero applied magnetic field, using a 1 μV/cm criterion.

3. DISCUSSION AND RESULTS

A. Laser Deposition

The pulsed laser deposition technique was pursued as the physical vapor deposition technique of choice due to its unparalleled research and development versatility. The goals for this work were twofold. First, to develop an understanding of the basic physics and chemistry associated with the laser-target interaction, plume dynamics, and film growth. Second, to develop the technology to produce high-quality HTS ($YBa_2Cu_3O_{7-\delta}$) thin films over larger areas (> 1 sq. in.) which is essential for the development of passive microwave devices. This includes correlating the measured deposition rates and angular distributions, and the parametric dependence of film crystallinity and morphology with laser fluence and spatial profile, repetition rate, wavelength, target density and microstructure, ambient pressure and substrate temperature[10].

Parametric Studies. Radial variations in film thickness, fit to $\cos^n(\theta)$, and stoichiometry were investigated[7] as a function of laser fluence, spot size and number of shots (exposure time). Small spot sizes and long exposure times produced broad angular distributions (n=1.5), whereas large spot sizes at short exposure times produced highly forward directed angular distributions (n>8). Under typical spot size (2 mm) and exposure[7], plumes exhibited a $\cos^{3.5}(\theta)$ spread and the resulting films showed a Y deficiency for θ >20°. These results are consistent with a mechanism combining Knudsen layer formation[11],[12], resulting from collisional processes in the high density material within a few microns of the target surface, followed by unstable adiabatic expansion.

Deposition temperature and oxygen pressure were systematically varied between 600-800 °C and 1-20 Pa during film growth. A series of 200 nm

$YBa_2Cu_3O_{7-x}$ films were grown on (100) $Zr(Y)O_2$ substrates (YSZ) as a function of deposition temperatures between 550-800 °C. Dynamic impedance and XRD analysis showed that the best films could be grown at surface temperatures of 750 °C. A systematic variation in the magnitude and transition width of the dynamic impedance response suggests that the growth of epitaxial films is an activated process with an activation barrier of roughly 1.5 eV.

The deposition rate was found to decrease exponentially by up to an order of magnitude then level off at a **PD** product of 54 Pa-cm, where **P** is the static gas pressure and **D** is the target-substrate distance. A similar response has been observed for N_2 and O_2 which suggests that this behavior is not due to reactive scattering, however, Ar and He cause essentially no deposition rate decrease over the same **PD** range. Plume angular distributions and film stoichiometry were found to be independent of oxygen pressures out to 33 Pa, again consistent with Knudsen layer theory [11],[12]. Various post-deposition O_2 anneal protocols were also attempted. The simplest, an increase in the O_2 pressure to 27 kPa for a cool down time of 20 min., was effective to oxygenate the films.

Emission spectra were obtained as a function of pressure from the plume in the spectral region near 600 nm, where both atomic yttrium emission (Y^*) and yttrium monoxide emission (YO^*) could be observed. Figure 2 displays a spectrum obtained at an oxygen pressure of 7×10^{-2} torr. The two starred transitions correspond to Y^* while most of the remaining features are due to YO^*. The ratio of YO^* to Y^* emission was found to change dramatically with pressure of the ambient oxygen atmosphere. In general, it was observed that the ratio YO^*/Y^* increased linearly with pressure at low oxygen pressures, and approached a limiting value at pressures $\geq$ 0.4 torr.

In order to interpret these results, a kinetic model was developed: reaction of Y with O_2 was assumed to produce all observed YO^*, while the ablation process was assumed to produce Y and Y^*, and collisions were allowed to convert $Y \rightarrow Y^*$, and to quench the various excited states. Applying the steady-state approximation to the model results in the expression: $[YO^*]/[Y^*] = A[O_2]/(B + C[O_2])$, where the constants A,B, and C are sums of products of the rates and rate constants, and $[O_2]$ represents the oxygen pressure. This result obeys the same limiting forms at the experimental data.

These results indicate that collisions play a major role in the laser deposition process. This includes both intra-plume collisions, and plume-gas interactions, which will effect deposition rate and homogeneity. The latter can be seen by simple consideration of gas-kinetic effects. Under typical deposition conditions, the target-substrate distance will be $\approx$ several centimeters, and the pressure of processing gas will be a fraction of a Torr. Gas kinetic theory predicts that this will lead to 1-10 collisions for laser-ablated species between evolution form the target surface and deposition on the substrate. Since $\sim$10 collisions is typically sufficient to relax translationally excited atoms and small molecules, this means that at the upper end of the range for pressure-distance products that the deposition plume will be diffusing toward the substrate rather than being "sprayed" on as part of a well-directed plume. This places an upper limit on the pressure that can be used for efficient deposition. On the other hand, numerous measurements of chemical speciation in the plume, as well as our recent measurement of chemical reactivity with the processing gas, mandate that a reactive source of oxygen be present in the deposition atmosphere. This, in turn, places a lower limit on the oxygen pressure that can be used for the production of in-situ HTSC films.

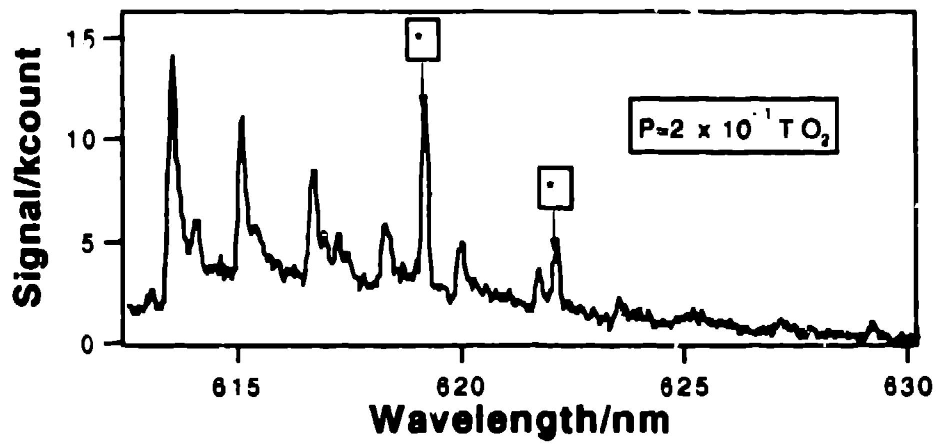

Figure 2. Emission spectrum from ablation of solid Y_2O_3 .

In separate experiments, the quality of superconducting thin films (200 nm thick) of $YBa_2Cu_3O_{7-x}$ on (100) $SrTiO_3$ were monitored as a function of deposition rate from 1 to 14.5 nm/s. The latter exceeded any previously reported deposition rates for epitaxially grown, laser deposited films [13]. Crystallinity of the films was examined by Rutherford backscattering in the channeling mode. The backscattering minimum yield (χ_{min}) was seen to increase monotonically with the deposition (laser repetition) rate. A χ_{min} of 3% was observed in the films deposited at the lowest deposition rate. Even at a deposition rate of 14.5 nm/s, the films show good crystallinity with χ_{min} of 15%, indicating epitaxial growth. Critical current densities $J_c(B=0)$ greater than 10^6 A/cm^2 at 75 K have been measured[5] for films grown on (100) $SrTiO_3$ at deposition rates up to 14.5 nm/sec.

Target modification effects. The deposition rate was always observed to decrease exponentially (by factor 2-10) as a function of laser exposure[14]; when this response is factored out the deposition rate is seen to increase linearly with laser fluence above an evaporation threshold at 0.1-0.5 J/cm^2 out to the highest fluence which we could obtain (30 J/cm^2). As expected, the deposition rate was found to increase linearly with laser irradiated area for a constant fluence and exposure.

The exposure dependent deposition rate decrease was usually accompanied by the gradual loss of proper stoichiometry (Cu/Y ratio increase) in the deposited films. Electron microprobe analysis of the resulting ablation track (no scanning) on the target showed significant Y enrichment with respect to Ba and Cu[15], as shown in Figure 3.

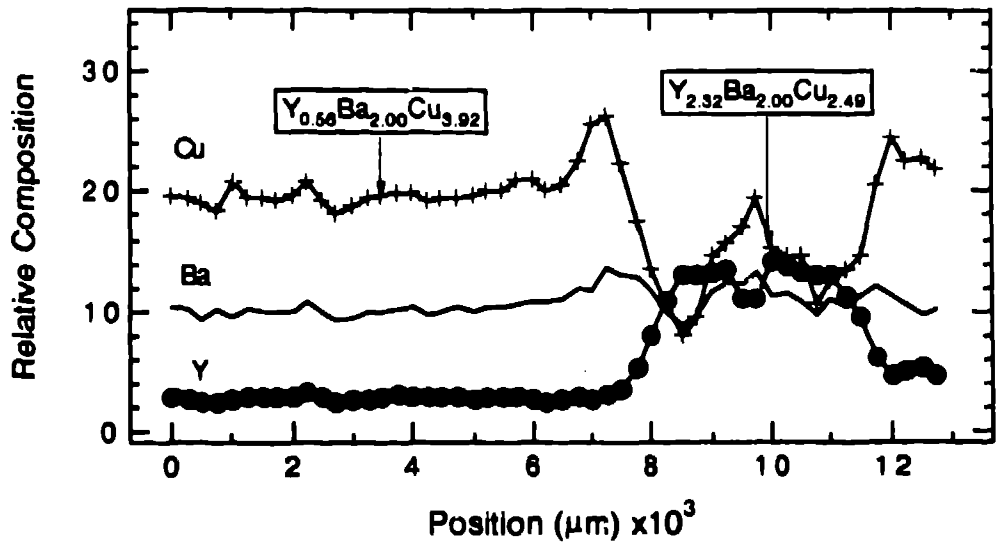

Figure 3. Electron microprobe measurements on exposed(right) and unexposed(left) regions of a YBCO target.

SEM showed adifference in target surface morphology for the laser irradiated (melted) region that in many cases exhibits a columnar regrowth structure. These results suggest that during the ablation process, the incongruently melted zone is larger than the congruently evaporated layer (etch depth). Additionally, microprobe analysis of the target surface unexposed by the laser also showed a relative Y deficiency. This is due to redeposition of Cu and Ba rich particulates from the ablation plume.

B. Laser Writing

We have demonstrated[16] a process for modification of a film's superconducting properties consisting of: 1) deposition of a high-quality HTSC thin film; 2) annealing the film in an Ar-atmosphere which lowers of eliminates T_C; and 3) local re-oxygenation by laser direct-write heating in an O_2 atmosphere. It is important to emphasize that this is a relatively gentle process; the laser heating is used to enhance oxygen diffusion and uptake in the material. The heating is substantially below levels that result in melting or other structural changes in the $YBa_2Cu_3O_{7-\delta}$ crystal structure[17]. There is no exposure of the HTSC to potential contaminates as is inherent in conventional lithographic and etching fabrication technologies.

The rf-eddy current response for an as-grown $YBa_2Cu_3O_{7-d}$ sample on $LaAlO_3$ showed an onset of the supercurrents in the sample at 92 K. The same type of onset was observed at 58 K after the thermal annealing. Four-point probe measurements confirmed these transitions. Because the annealing procedure was performed under such mild conditions (400° C) the drop in the transition temperature is due to the loss of oxygen in the lattice, rather than alteration of the crystal structure of the material. This allows for relatively easy migration of the oxygen back into the film. Similar responses were observed for the film deposited on $SrTiO_3$.

The rf-eddy current response of the film after the patterning clearly showed two different transitions. A large transition at 58 K was due to the response of the unpatterned material. Because the patterned lines are on the order of 0.4 X 3.0 mm^2, while the total detectable area is approximately 14 mm^2 the percentage of overall material converted to the higher transition temperature was less than 10%. This is consistent with the relatively small transition observed at 92 K. Furthermore, a 4-point measurement of the resistance, which measures only the first percolating pathway and not the amount of superconducting material, clearly showed a resistive transition at 92 K when the probes were on the patterned lines.

C. Laser Modification of Critical Current

In order to produce even simple devices from HTSC films, it may be necessary to control either the transition temperature or critical current with a high degree of precision. In few instances has reproducible modification of film transport properties been demonstrated. It is well established that changing the oxygen content of $YBa_2Cu_3O_{7-\delta}$ can affect the J_c [Singh, 1990 #24]. However, a change in the oxygen stoichiometry also changes T_c of the material[Gupta, 1990 #13].

Previous work involving laser processing of HTSC thin films has concentrated on laser etching [Inam, 1987 #26], patterning [Zheng, 1989 #17], or annealing [Otsubo, 1989 #18]. Recent work by Helvajian has suggested that atom and ion emission can be observed at fluences as low as 50 mJ/cm^2 at 308 nm [Wiedeman, 1990 #14]·[Wiedeman, 1991 #15]. The pronounced wavelength dependence of the threshold implies that the mechanism may include a photophysical component. We have examined the electrical and structural behavior of YBCO thin films as a function of 308 nm excimer laser exposure, at fluences below the ablation threshold. This method can lower the J_c of the film with a high degree of accuracy and reliability without significantly lowering T_c.

The superconducting properties of the irradiated films were monitored inductively by dynamic impedance (DI) to determine the effect exposure has on T_c. The dynamic impedance technique uses a single sense/drive coil 6 mm in diameter and placed 0.05 mm above the HTSC sample, and measures the out-of-phase (reactive) component at a set drive frequency. One obtains a direct measure of the impedance change in the coil caused by the coupling between the coil and the eddy-currents induced in the film[Libby, 1971 #23]. Using this monitor, the unirradiated film produced a sharp transition at 91 K with a width of only 1 degree. The inductive transition develops a tail in the curve after laser exposure; however, the onset transition temperature stays at 91 K past 2400 shots. Even after 6000 shots the onset T_c is only reduced by ≈ 4 °C. The inductive transition rapidly deteriorates beyond 6000 shots to 7200 shots; by 7000 shots the film does not show an induction transition.

To further investigate the electrical properties of the laser-irradiated film, I_c measurements were made. The critical current measurements as a function of laser shots and laser fluence are shown in Fig. 4. These measurements indicate that the critical current is a sensitive function of film exposure. At a laser fluence of 20 mJ/cm^2 the film did not indicate any degradation of I_c, while a shot dependent trend does begin at a fluence of 30 mJ/cm^2. This suggests that the modification process has a threshold of 25 ± 5 mJ/cm^2. This modification rate grows rapidly when the fluence is increased to 100 mJ/cm^2. At a constant J_c, I_c is proportional to the thickness of the remaining undamaged layer. The monotonic decrease in I_c can be explained by assuming that the measured critical current is proportional to the thickness of the unmodified layer.

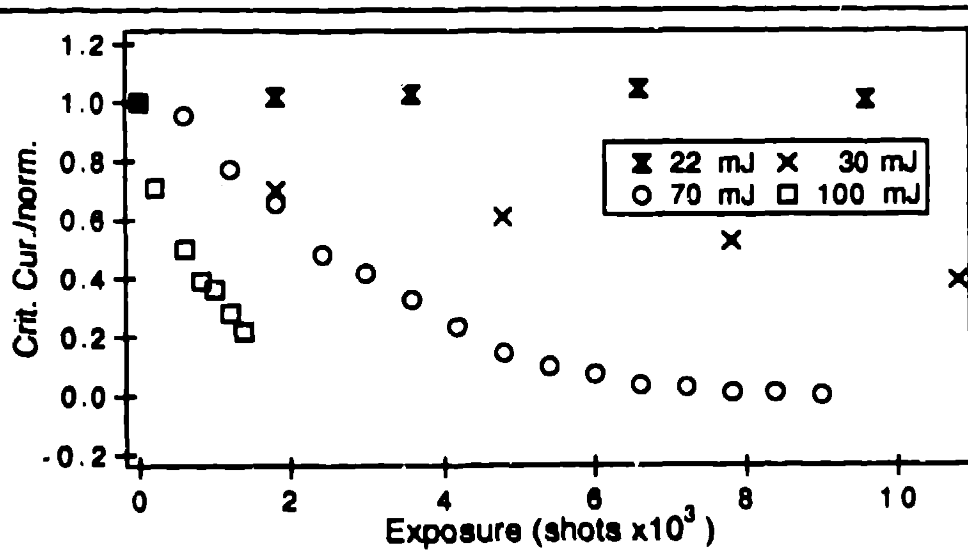

Figure 4. Normalized critical current measurements for laser (308 nm) irradiated films.

Rutherford backscattering (RBS) channeling data also taken on a film exposed to a laser fluence of 70 mJ/cm^2 further indicated that a disordered layer was being formed as a result of laser irradiation. Qualitatively, an increased channeling yield correlates with greater disorder in the film. Furthermore, the shape of the peaks indicated greater disorder at the surface: the surface. Within the error of the RBS measurement no material from the film is being removed, i.e., the film thickness (±10%) and stoichiometry (±3%) remain constant with this laser fluence. At a fluence of 70 mJ/cm^2, SEM showed no visible change in film morphology from that of the unexposed sample. Melting of the film was clearly observed when the fluence is increased to 150 mJ/cm^2. Optical micrographs revealed a slight color change in the film beginning at a fluence of 100 mJ/cm^2.

By adjusting the laser fluence and the number of laser shots the effective J_c in a thin film could thus be controlled to within 255 A/cm^2. The laser damage begins at a fluence of 25 ± 5 mJ/cm^2. Optical changes are observed at a fluence of 100 mJ/cm^2 and melting occurs at 150 mJ/cm^2.

ACKNOWLEDGEMENTS

This work was partially supported by the Superconductivity Pilot Center.

REFERENCES

[1] J. T. Cheung and H. Sankur. Crit. Rev. Solid State Mater. Sci., 15, 63-109 (1988).

[2] M. Leskela, J. K. Truman, C. H. Mueller and P. H. Holloway. . ac. Soc. A7, 3147-3171 (1989).

[3] J. Geerk, G. Linker and O. Meyer. Mat. Sci. Reps., 4, 193-260 (1989).

[4] T. Venkatesan, X.D. Wu, A. Inam, C. C. Chang, M. S. Hegde and B. Dutta. IEEE J. Quantum Electron, 25, 2388-93 (1989).

[5] X. D. Wu, R. E. Muenchausen, S. Foltyn, R. C. Estler, R. C. Dye, C. Flamme, N. S. Nogar, A. R. Garcia, J. Martin and J. Tesmer. Appl. Phys. Lett., 56, 1481-3 (1990).

[6] T. VanDuzer. IEEE Jour. of Quant. Electron., 25, 2365 (1989).

[7] R. E. Muenchausen, K. M. Hubbard, S. Foltyn, R. C. Estler, N. S. Nogar and C. Jenkins. Appl. Phys. Lett., 56, 578-80 (1990).

[8] R. C. Estler, N. S. Nogar, R. E. Muenchausen, X. D. Wu, S. Foltyn and A. R. Garcia. Rev. Sci. Inst., **62**, 437 (1991).

[9] R. C. Dye, N. S. Nogar and R. E. Muenchausen. Chem. Phys. Lett., **181**, 531 (1991).

[10] F. Heidelbach, R. E. Muenchausen, S. R. Foltyn, N. S. Nogar and A .D. Rollett., J. Mater. Res. submitted (1991).

[11] P W. Kelly and R.W. Dreyfus. Nucl. Instr. and Meth., **B32**, 321-348 (1988).

[12] Roger Kelly. J. Chem. Phys., **92**, 5047-56 (1990).

[13] X. D. Wu, R. E. Muenchausen, S. Foltyn, R. C. Estler, R. C. Dye, A. R. Garcia, N. S. Nogar, P. England, R. Ramesh and a. l. et. Appl. Phys. Lett., **57**, 523-5 (1990).

[14] R. E. Muenchausen, S. R. Foltyn, N. S. Nogar, R. C. Estler, E. J. Peterson and X. D. Wu. Nucl. Instrum. Methods Phys. Res., Sect. A, **A303**, (1991).

[15] S. R. Foltyn, R. C. Dye, K. C. Ott, E. Peterson, K. M. Hubbard, W. Hutchinson, R. E. Muenchausen, R. C. Estler and X. D. Wu. Appl. Phys. Lett., **59**, 594-6 (1991).

[16] R. C. Dye, R. E. Muenchausen, N. S. Nogar, A. Mukherjee and S. R. J. Brueck. Appl. Phys. Lett., **57**, 1149-51 (1990).

[17] R. J. Cava, A. W. Hewat, E. A. Hewat, B. Batlogg, M. Marezio, K. M. Rabe, J. J. Krajewski, Jr , W. F. Peck and L. W. Rupp. Physica C, **165**, 419-433 (1990).

LA-UR 91-3487

LA-UR--91-3487

DE92 003799

TITLE A NEW, LOW-PROFILE NEUTRON DETECTOR JUNCTION BOX

AUTHOR(S) B. G. Strait, H. R. Dye, and K. E. Kroncke

SUBMITTED TO 1991 IEEE Nuclear Science Symposium and Medical Imaging Conference
Santa Fe, New Mexico
November 2-9, 1991
(Full Paper)

Los Alamos

Los Alamos National Laboratory
Los Alamos, New Mexico 87545

A NEW, LOW-PROFILE NEUTRON DETECTOR JUNCTION BOX*

B. G. Strait, H. R. Dye, and K. E. Kroncke
Safeguards Assay Group, N-1
Los Alamos National Laboratory
Los Alamos, New Mexico

ABSTRACT

We have designed a new junction box for nondestructive assay instruments that is easier to build, maintain, and repair. Most high-voltage components are sealed from the atmosphere using potting material, therefore eliminating the maintenance requirement of replacing desiccators. The mechanical design cuts the cost of machining and makes it easy to remove and replace the ^{3}He tubes.

Neutron detectors in nondestructive assay instruments use junction boxes to distribute the high voltage to the ^{3}He tubes, to house the amplifier circuits, and to hold the ^{3}He tubes mechanically. The current design of a junction box is shown in Fig. 1. Operationally, this design has proven satisfactory although it does have several deficiencies, principally that it requires maintenance of desiccators to remove moisture from the high-voltage cavity of the junction box. As the desiccators become saturated with moisture, they must be replaced. Moisture in the high-voltage cavity causes high-voltage leakage or breakdown, which generates counts that are not related to neutrons. The new junction box design uses a potting material to seal out moisture from the high-voltage cavity and thus eliminates the maintenance problem of changing desiccators.

The current junction box design is 3-in. tall and 4-in. deep. The new design has a profile of only 1.5 in. and is 3.125 in. deep allowing 0.875 in. of polyethylene to be placed between the junction box and the instrument cavity if needed.

High-voltage distribution to the ^{3}He tubes in the conventional junction box is made by plugging a small-pin connector into the connector for the tube high-voltage interface for the ^{3}He tubes and soldering a bus wire between the tubes to this small-pin connector. This wiring procedure requires the tubes to be screwed in place in the junction box during the fabrication and remain in place during the junction box assembly. The problem with this design is that if the ^{3}He tubes need to be removed for replacement or removed because of detector space constraints during installation, the small-pin connectors must be removed from each tube and replaced during the reassembly. The high-voltage cavity of the conventional junction box is located below the amplifier cavity. To disassemble the high-voltage circuits, as just described, one must also disassemble the amplifier circuits to obtain access to the high-voltage cavity. Significant disassembly and rewiring are necessary to remove tubes from the conventional junction box. Simple removal and replacement of ^{3}He tubes was a design goal for the new junction box, as discussed later.

Manufacturing cost is always a concern in producing detectors. The new junction box design simplifies the mechanical fabrication of the junction box and reduces the wiring cost. The new junction box is less costly to build. It is machined from standard 1.5 in. by 1.5 in. aluminum stock with only simple drilling and milling. The adjacent junction boxes and the input connectors to the first amplifier card are connected with flat cables on which the connectors are easily installed.

Figure 2 is a drawing of the new low-profile junction box. Parts (A and C) of the drawing show the four cavities that the tubes screw into and the two cavities that contain the input/output printed circuit cards. The cross-sectional view of part (D) shows the insert for the interface with the ^{3}He-tube connector. It is machined out of KEL-F material, which provides high-voltage insulation between the high voltage on the pin and the junction box case. Bias voltage, usually about 1680 Vdc, is distributed to the four tubes using a bus wire soldered to the top of the four pins. A slot is machined in the ends of the pins to accommodate the bus wire. The KEL-F insert is press fitted into the cavity screw threads and epoxied to the junction box case at the top interface of the insert. The pin is also epoxied into the hole of the insert. The KEL-F insert and pin arrangement provides an interface that allows easy insertion and removal of the ^{3}He tube into and out of the junction box without having to rewire the junction box.

The ^{3}He tube output signal is a small current pulse produced as a result of neutrons interacting with the ^{3}He gas. The signal is coupled to an Amptek amplifier (see below for description) through a coupling capacitor. The coupling capacitor and a bleed resistor are mounted on a small-printed-circuit card and placed in the output cavity with an electrical connection to the bus wire. The output signal is transmitted to the Amptek amplifier by a small coax cable, RG174. Figure 3, part (B), is a schematic diagram of the output circuit. The

---

*This work was sponsored by the US Department of Energy, Office of Safeguards and Security.

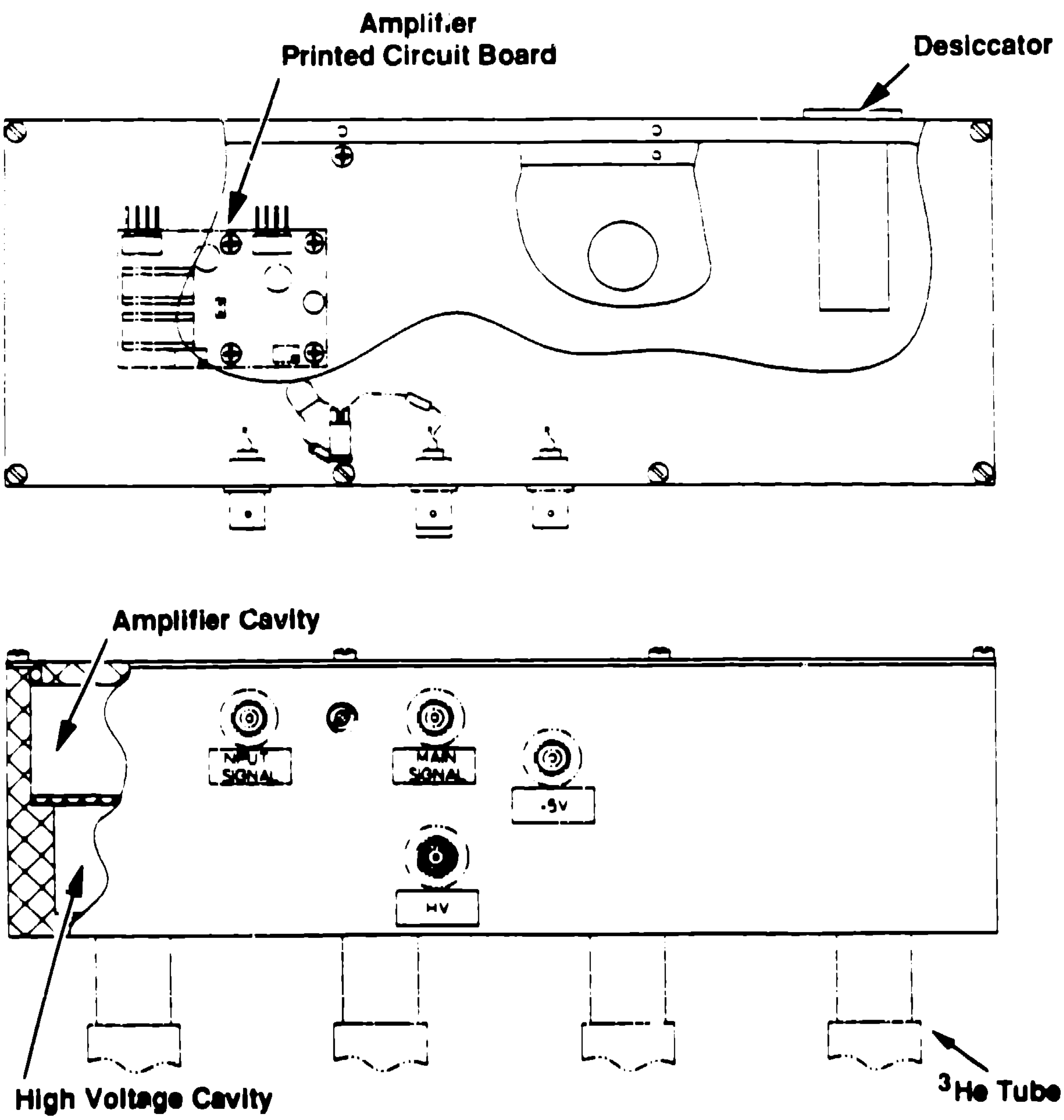

Fig. 1. Pass-through shuffler junction box, conventional design.

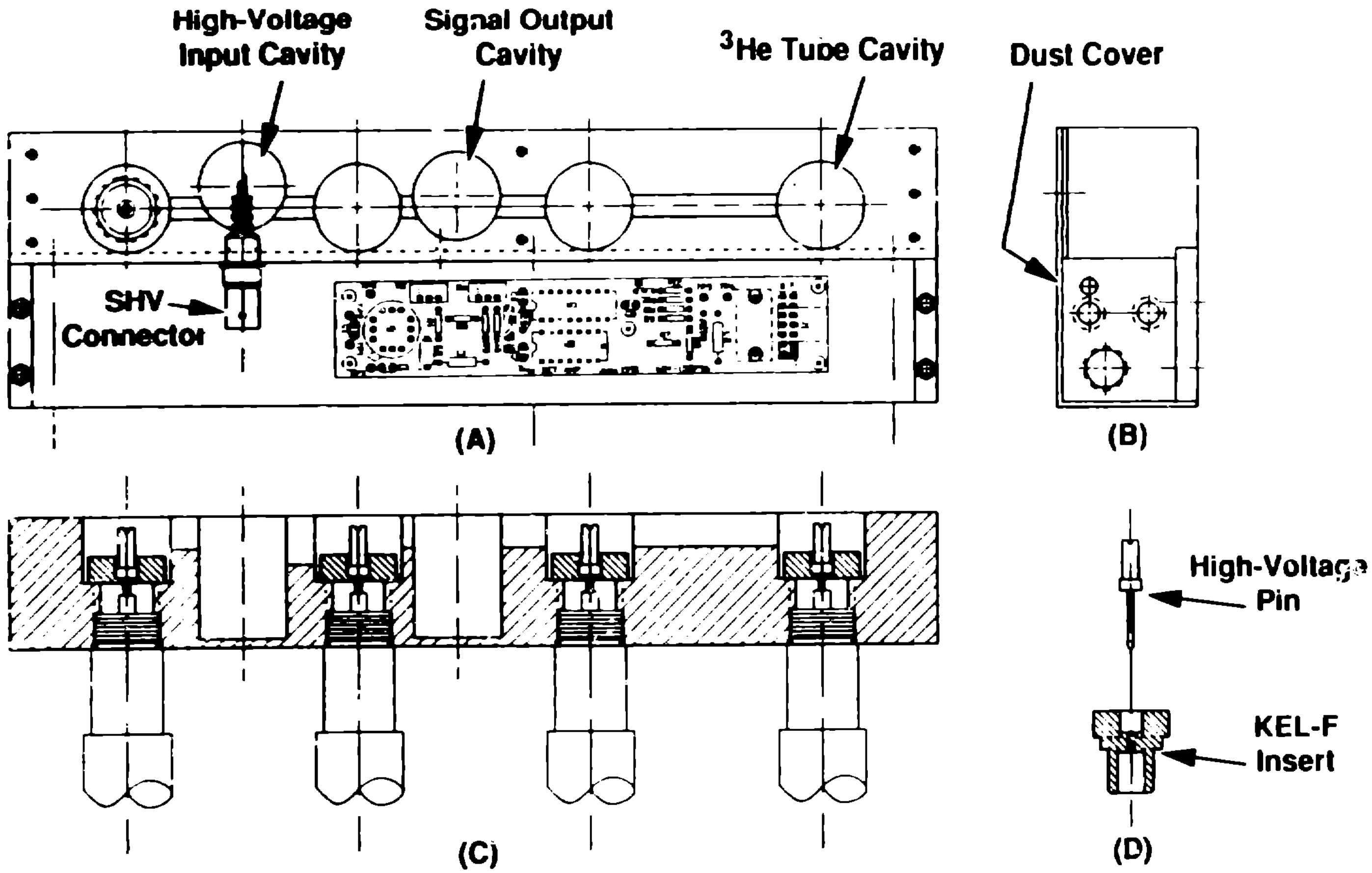

Fig. 2. New low-profile junction box.

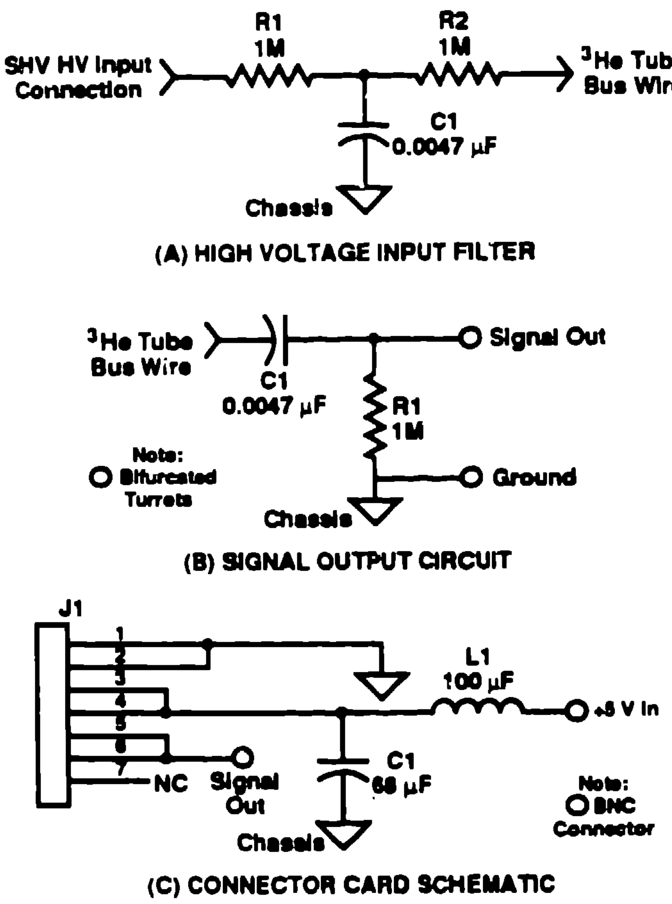

Fig. 3. Low-profile junction box circuit boards.

coupling capacitor is a ceramic disk made by TDK Corporation of America and was selected to withstand the high voltage and have a low-corona discharge, which can elicit superfluous counts from the detector.

After soldering the bus wire on the pins and installing the input/output printed-circuit cards, we filled the six cavities of the junction box with a potting material to seal moisture from the high-voltage components. An epoxy resin, STYCAST 2651 made by Emerson and Cuming, Inc., is used for the potting material. It was selected because it could be poured at room temperature and it had good high-voltage characteristics such as a dielectric strength of 450 V/0.001 in. and volume resistivity of 5×10^{16} Ω-cm. O-rings are used at the base of the ^{3}He tubes and the junction box to keep moisture from getting into the area where the tubes interface with the junction box.

Figure 2, part (B), shows a cross section from the end view of the junction box. This view shows the potted cavity cover and the dust cover of the junction box. The dust cover is a one-piece, right-angle cover, which fastens to the main junction box body with two screws on the top for easy removal of the cover. A separate cavity cover is used to contain the magnetic field in the area of the high-voltage components while adjustments are made on the amplifier card. This view also shows the connector interface panel; there is one for each bank of three junction boxes. Three cables are connected to each bank: the high-voltage cable, the +5 V power cable, and the output signal cable. Within the junction boxes, the high voltage is distributed to each junction box input cavity with coax cables and T-connectors. The +5 V and the detector output signals are distributed between amplifier cards using a seven-connector flat cable. A circuit diagram of the connector printed-circuit card is shown in Fig. 3, part (C).

The drawing in Fig. 4 illustrates a typical detector bank consisting of three modules, each with four ^{3}He tubes and one amplifier board. This figure also shows how the amplifiers in the three modules are connected by flat cables. The amplifier for the conventional junction box was repackaged to provide a more narrow printed-circuit card that better fits the new junction box layout. A schematic of the amplifier is shown in Fig. 5. The analog amplifier circuit and digital circuit are identical to the conventional junction box amplifier. The analog amplifier is a hybrid, charge-sensitive preamplifier discriminator made by Amptek, Inc. that has proven very reliable and is well suited for this application. Digital processing includes a single-shot that produces a 50-ns output pulse for each neutron event, a line driver, and a circuit to OR the signals from other amplifier cards. Light emitting diodes (LEDs) are used with the detectors to indicate visually when neutron events are being processed and are used during adjustment of the amplifier input threshold. In order to view the light from the LEDs after the detector module is assembled, a plastic fiber-optic cable conducts the LED light to a display panel at the electronics rack. The fiber optic interface to the LED uses a housing and fiber connectors made by AMP.

The new junction box was extensively tested to verify its performance and to determine if the potting material is successful in prohibiting moisture from entering the high-voltage area of the junction box. For comparison, identical tests were performed side-by-side with the conventional junction box because its performance is well established. Therefore, test data are presented for both junction boxes. Figure 6 shows the high-voltage-profile calibration plots for the junction boxes. The profile was taken using an AmLi source, the ^{3}He tubes were inserted in polyethylene, and the data were taken with a JSR-11 coincidence counter. As the plots indicate, the high-voltage profiles are almost identical.

Results of humidity tests on the new junction box before the potting material was added are shown in Fig. 7. The effects of humidity began to show at about 40% relative humidity. Above that amount, the counts of the unpotted new junction box increased considerably as shown in the graph. Increased humidity did not affect the counts for these tests on the conventional junction box because the desiccators were still effective in removing the small amount of moisture entering the junction box. The humidity tests were performed using an environmental chamber that can control both temperature and relative humidity. The temperature was set to 80° F for the unpotted humidity tests.

The moisture resistance of the potting material was tested by placing the potted junction box in the environmental

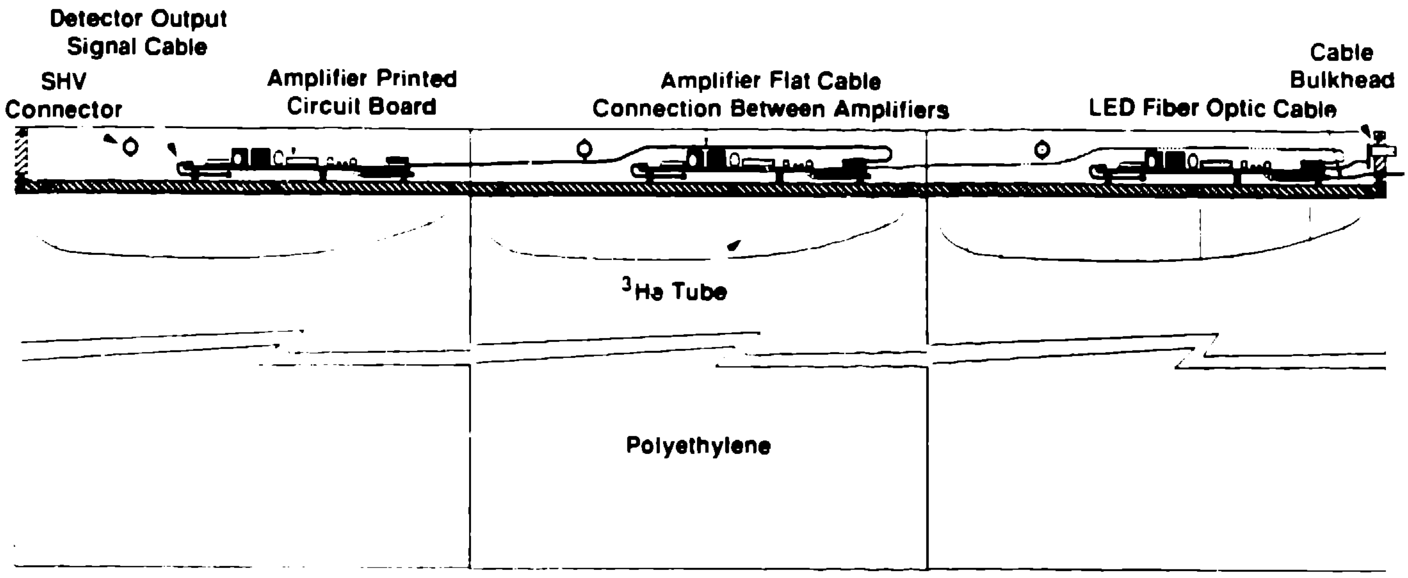

Fig. 4. Neutron detector bank.

chamber with high humidity at several different temperatures for a long time and measuring the background count rate. Tests were performed on the conventional junction box at the same time for comparison. Background tests were done with the ^{3}He tubes covered with sheets of cadmium but without using polyethylene. JSR-11 coincidence counters were used to collect the data and the results are shown in Fig. 8. The count rate shown is the counter's total counts accumulated over 1000 seconds and averaged over many hours, that is, 24 hours in many of the tests. The standard deviation of the count rates for the tests, which contained up to one hundred 1000-second runs ranged from 0.001 to 0.006 counts/s. The high voltage was set at 1680 V and the gate length of the JSR-11 was set to 128 µs. The background count rate for the new low-profile junction box shows a slight increase over the 40 days of testing. The same upward trend was also present in the conventional junction box. After about 30 days of continued exposure to the 90% relative humidity and the temperature of from 90°F to 120°F, the conventional junction box experienced some high-count rates for a couple of days, but then the count rates returned to normal. The desiccators had turned slightly pink by this time, indicating they were becoming saturated with moisture. Time did not permit testing beyond the 40 days. We believe that this was sufficient time at elevated humidity and temperatures to demonstrate the moisture resistance capability of the potting material.

In conclusion, we designed and tested a simple junction box that provides counting performance equal to that of the proven junction box design and has several significant improvements. This new junction box is cheaper to make, its design allows easy removal and replacement of ^{3}He tubes, and it is expected to require less maintenance.

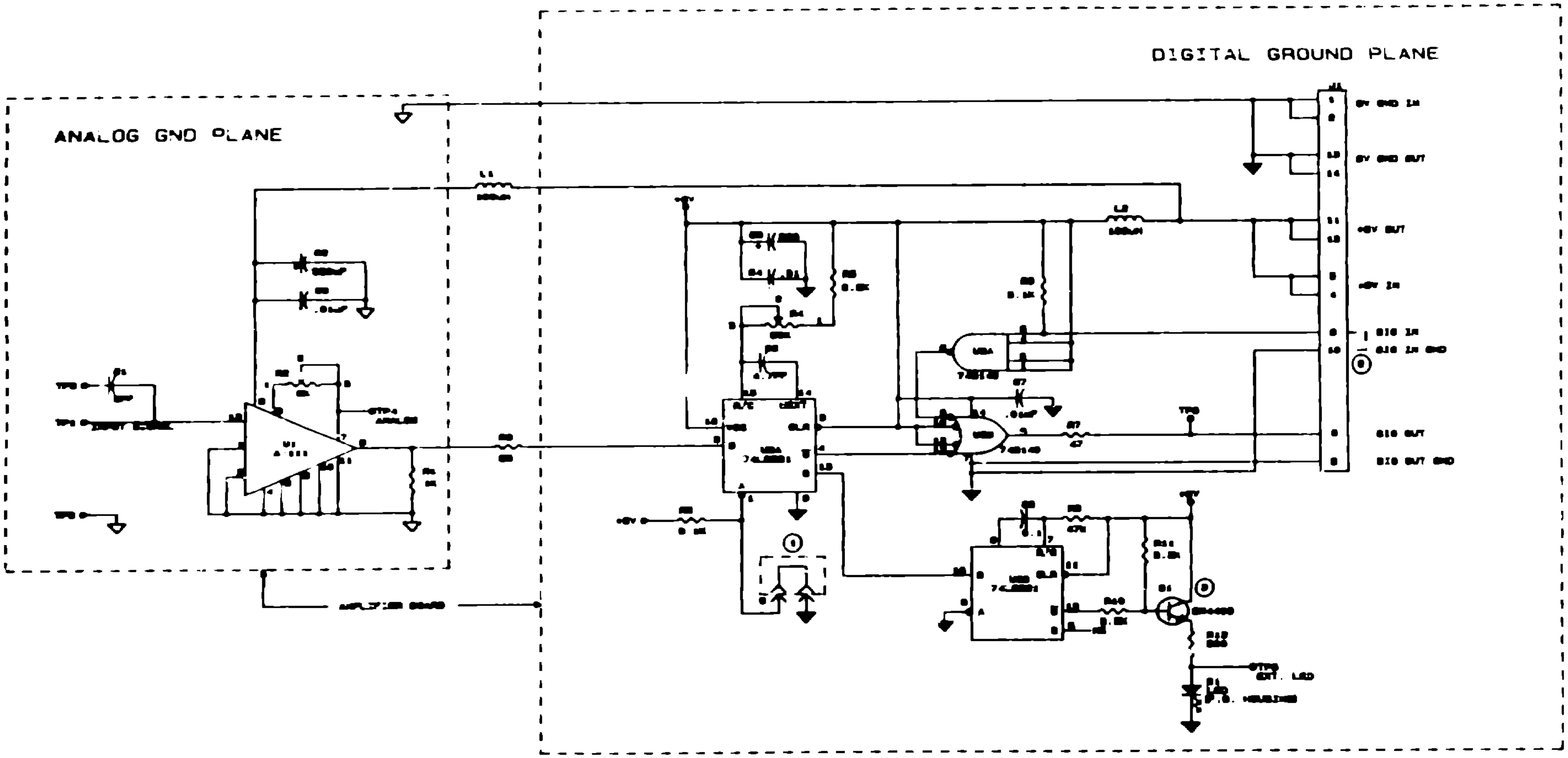

Fig. 5. Neutron detector amplifier schematic.

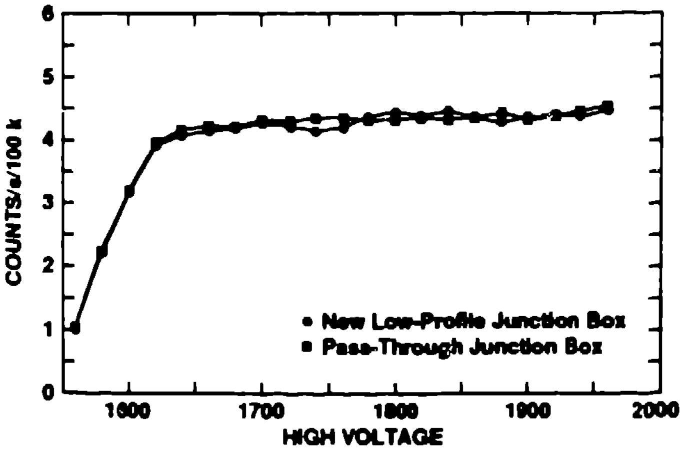

Fig. 6. High-voltage-profile calibration.

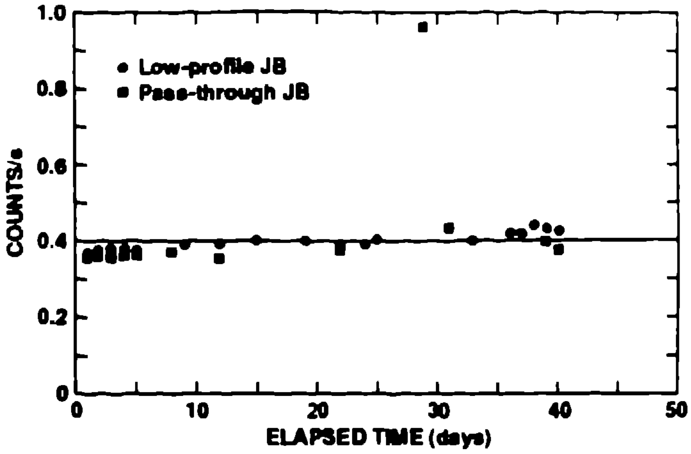

Fig. 8. Long-term humidity test results.

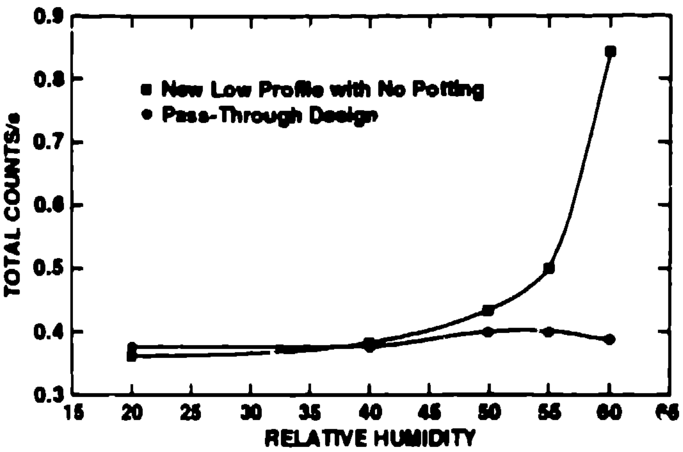

Fig. 7. Humidity test results on unpotted junction box.

18

LA-UR 91-3489

LA-UR--91-3489

DE92 003798

DEC 0 1991

TITLE Warhead Counting Using Neutron Scintillators: Detector Development, Testing and Demonstration

AUTHOR(S) R.C. Byrd, G.F. Auchampaugh, C.E. Moss, W.C. Feldman

SUBMITTED TO Conference Record and Proceedings 1991 IEEE Nuclear Science Symposium, 2-9 November 1991, Santa Fe, NM

Los Alamos

Los Alamos National Laboratory
Los Alamos, New Mexico 87545

MASTER

FORM NO 836 R4
ST NO 2629 5/81

Warhead Counting Using Neutron Scintillators: Detector Development, Testing, and Demonstration*

R. C. Byrd, G. F. Auchampaugh, C. E. Moss, and W. C. Feldman
Los Alamos National Laboratory, Los Alamos, NM 87545

Abstract

Although the number of warheads on a missile can be determined relatively simply by a scan of the emitted gamma radiation, this approach may be considered too intrusive because of the possibility of revealing high-resolution energy or position information. Neutron spectra are nearly featureless, and obtaining the position resolution needed to reveal warhead details would be very difficult. We describe the development of a fast-neutron detector based on a boron-loaded plastic scintillator used previously for space applications. The detector rejects gammas and scattered low-energy neutrons, and its segmentation allows narrow fan-shaped collimation within ±20° horizontally and ±50° vertically. Testing includes distinguishing between mock-ups with either two or three warheads and locating the ten warheads on a silo-based Peacekeeper missile.

I. INTRODUCTION

As a possible application of radiation-detection technology to treaty verification, we have developed a fast-neutron detector capable of resolving individual warheads on a missile deployed inside an underground silo. The system uses BC454 boron-loaded plastic scintillator, which was originally developed for space-based neutron detectors.[1] The present application takes advantage of the detector's ability to automatically correct for backgrounds from gammas and slow neutrons, and it introduces a similar technique that restricts the response to fast neutrons within a narrow forward-pointing collimator opening. This paper (1) explains the operating principles, (2) discusses the improvements in directionality, and (3) describes tests on missile mockups and a silo-based missile at F.E. Warren AFB. We conclude that the detector's neutron efficiency, background rejection, and directionality may be useful in treaty verification and other applications.

*This work was partially supported by the Office of Arms Control of the U.S. Department of Energy. The neutron detector and analysis programs were originally developed for the U. S. Army Strategic Defense Command.

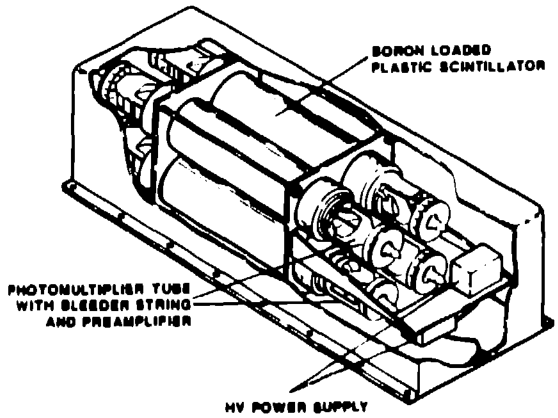

Figure 1: Cutaway View of the Neutron Detector

II. DETECTOR

The use of boron-loaded scintillators as fast-neutron detectors and their adaptation for space-based measurements have been described previously.[1] Figure 1 shows a cutaway view of the space instrument (the Army Background Experiment, or ABE); an identical unit was used for the current project. Four tightly-packed scintillator rods (7.6 cm in diameter and 20 cm in length) with phototubes at each end are enclosed in a light-tight housing that also contains the HV supplies and signal preamplifiers; a second package contains a CPU with a microprocessor and one megabyte of storage. Figure 2 shows the unit as deployed for warhead counting. The detector is completely surrounded by a 1-cm lead shield to reduce the gamma flux. A polyethylene neutron shield ($65 \times 42 \times 33$ cm^3) hangs from the silo wall and includes a narrow 5-cm × 20-cm aperture that faces inward toward the missile. By mounting the rod axes vertically and rotating the housing by 45°, the front rod (Rod 1) is shielded by the three rear rods (Rods 2,3,4). The total mass of the system is 165 kg: 8 kg for the hanger, 18 kg for the scintillators and CPU; 43 kg for the lead, and 96 kg for the CH_2.

The basic detector principle is illustrated schematically in Fig. 3, an incident fast neutron loses energy by a series of scatterings from the H, C, and B in the boron-loaded organic scintillators. Most of the incident energy is trans-

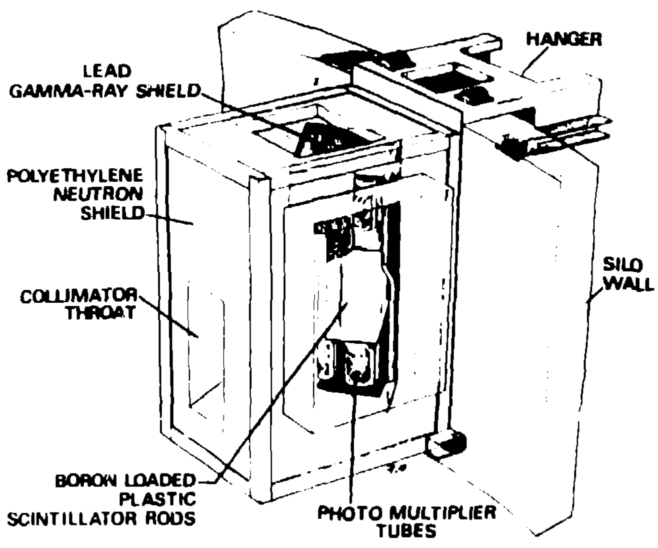

Figure 2: Detector and Shielding as Deployed in a Silo

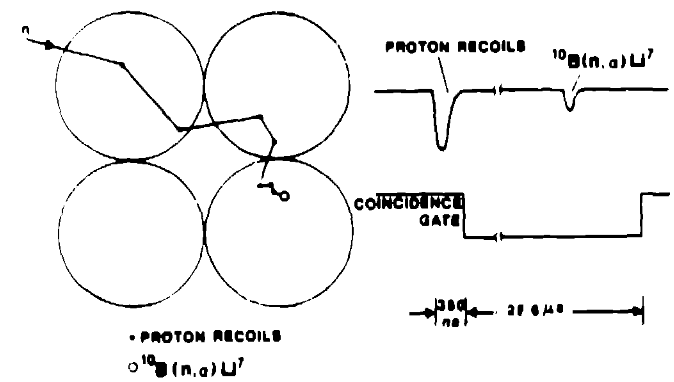

Figure 3: Schematic Operation of a Borated-Plastic Neutron Scintillation Detecter

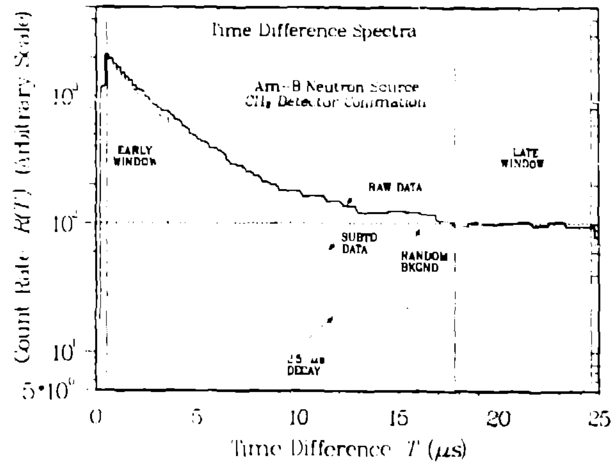

Figure 4: Time-Difference Spectrum with Windows for Neutron Capture and Random Coincidences

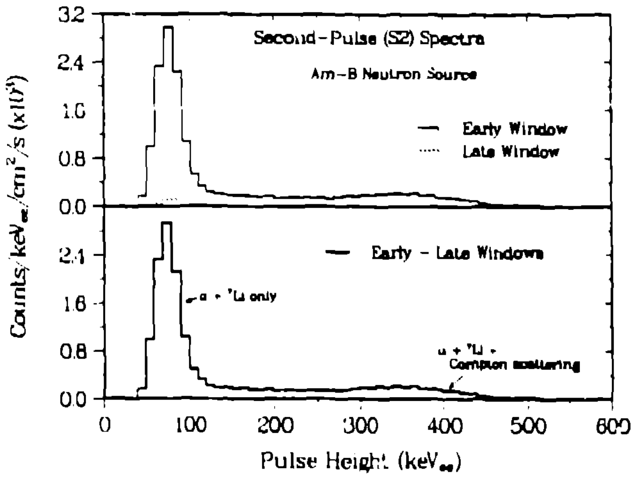

Figure 5: Light-Output Spectra for the Capture Pulse

ferred to recoil protons, which produce a detectable first light pulse for energy depositions above about 0.5 MeV. Neutrons that lose most of their energy are likely to be captured by the $^{10}B(n,\alpha)^7Li^*$ *reaction*, which provides a second pulse. For the standard boron density (5% by weight) of the BC454 scintillator, the capture time constant is 2.2–2.5 μs, depending on surrounding materials. After a 350 ns delay to exclude phototube after-pulsing, a coincidence gate opens to accept second pulses occurring within 25.6 μs. These events are stored to memory for off line analysis.

As shown in Fig. 4, in the off line analysis the neutron captures appears as an exponential fall off in the raw rate of time differences between the first *(S1)* and second *(S2)* pulses. At long times the coincidence rate reaches the constant value associated with uncorrelated events, as indicated by the "random bkgnd" level. In the two time windows shown, the data is associated primarily with either random coincidences (late window) or true scatter and capture coincidences (early window). Subtracting these two rates therefore provides a background corrected measurement of the incident fast-neutron flux. Alternatively, subtracting the constant random level from the raw data gives a spectrum ("subtd data") that is corrected for random coincidences. The agreement between this subtracted spectrum and the 2.5-μs decay curve shows this interpretation's validity for events in either of the two time windows. The intermediate times are contaminated by neutron rescattering and are excluded from further analysis.

Another requirement for the identification of capture events is shown in Fig. 5, which gives the light-output spectra for events with second *(S2)* pulses occurring in the early and late windows. The units of keV_{ee}, or "keV electron equivalent" normalize the light output in terms of electron energy; these units include the scintillator's saturation for the highly ionizing recoil ions.[1] The sharp peak corresponds to detection of only the recoil α and ^7Li particles, with complete escape of the 478 keV gamma from the $^7Li^*$ decay. The long shoulder results from events where additional energy is deposited by Compton scattering of the gamma. Subtracting the two upper spectra gives the background free spectrum in the lower panel, which confirms the detector's selectivity for fast-neutron capture events. The locations of the peak and the Compton edge (at 93 and 404 keV$_{ee}$) also provide the absolute calibration of the detector's light-output scale. Obtaining the spectrum in the lower panel therefore ensures that the detector is operating properly, that is, it is accepting only captured fast neutrons, correcting for accidental coincidences, and maintaining its absolute calibration.

A feature which is important in some applications[2] is the measurement of the energy of individual neutrons. Because the capture coincidence is obtained only for fast neutrons that scatter and moderate to essentially zero energy, the amplitude of the *S1* pulse is directly related to the incident neutron energy. Correcting for nonlinearities in detection efficiency and energy conversion[1] gives a normalized spectrum of incident neutron energies, as shown in Fig. 6 for 3.2-MeV Am-B isotopic neutron source. This spectrum is not obtained by unfolding a proton-recoil distribution, as for standard organic scintillators, but by simply histogramming the individual energy depositions.

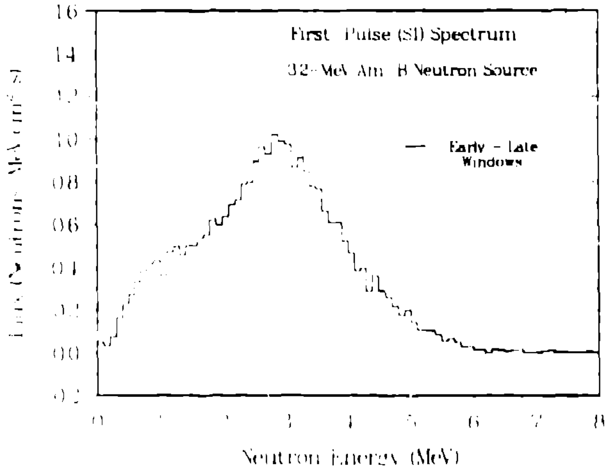

Figure 6: Am-B Energy Spectrum from the First Pulse

The subtraction of events in the two time windows also provides a different approach to gamma rejection. Because a single gamma cannot produce two pulses separated by the minimum time difference of 350 ns, all recorded gammas are random coincidences, as shown by the nearly flat time-difference spectrum in Fig. 7. The very slight falloff in rate is a dead-time effect; the line shows the calculated correction. Subtracting the corrected *S2* spectra for the early and late windows gives almost perfect cancellation; the small non zero result is in fact associated with the neutron background generated by cosmic ray interactions.

III. DIRECTIONALITY

The scatter and capture requirement ensures that the detector responds only to neutrons in the fission energy range of 0.5–15 MeV. For warhead counting, however, the detector must also have excellent directionality, that is, the

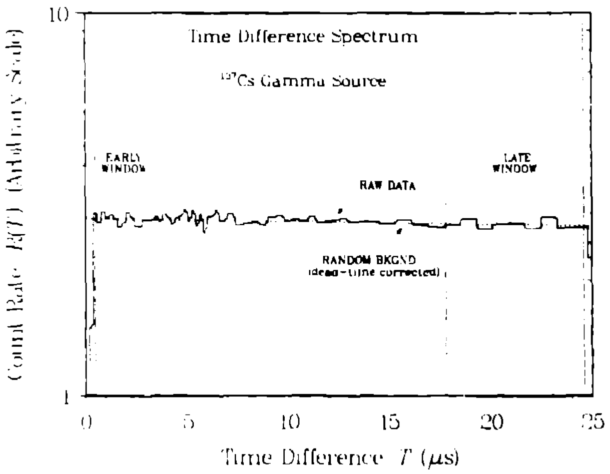

Figure 7: Time-Difference Spectrum for a Gamma Source

efficiency must be much higher for on-axis sources than for ones at the sides and rear. The use of a proton-recoil scintillator, which can reject neutrons that have scattered to energies below 0.5 MeV, increases the effectiveness of the CH_2 collimation (see Fig. 2), but much greater shielding would be needed to eliminate the count rate for off-axis fast neutrons from all directions. We have therefore devised a method to measure and then correct for the leakage of fast neutrons through the detector shielding.

Figure 8 illustrates the development of the technique. A ^{252}Cf fission source was moved around the detector in a horizontal plane. The curves show the measured count rates for the individual rods, normalized to the flux incident on a single rod to give a detection efficiency. Although the curve for the forward rod (Rod 1) peaks strongly at the collimator opening, it also has a 10–20% response to off-axis sources, especially at the thinner shielding on the enclosure's sides (±90°) and rear (180°). The other three rods—especially the rear Rod 4—further emphasize this transparency. For sources near the collimator opening, the three rear rods also show the effect of viewing the neutron source through slightly different apertures. Just as measurements made with the collimator open and closed could be subtracted, the count rates from different rods can be combined to cancel out the response to off-axis sources. The lower part of Fig. 8 shows the result of subtracting an empirical background given by $N_b = 0.4(N_2 + N_3) - 0.125N_4$. The subtracted efficiency for off-axis sources beyond ±20° is reduced drastically, and the subtraction of the offset contributions from the two side rods also slightly improves the detector's position resolution. The success of the weighting function may not be surprising for a horizontal scan, but Fig. 9 demonstrates that the same function also works for a vertical scan. This figure also shows the downward directed acceptance of the collimator, which was designed to look down on the warheads from above. Not shown here are the energy spectra for the calculated backgrounds, which have reasonable shapes at all energies.

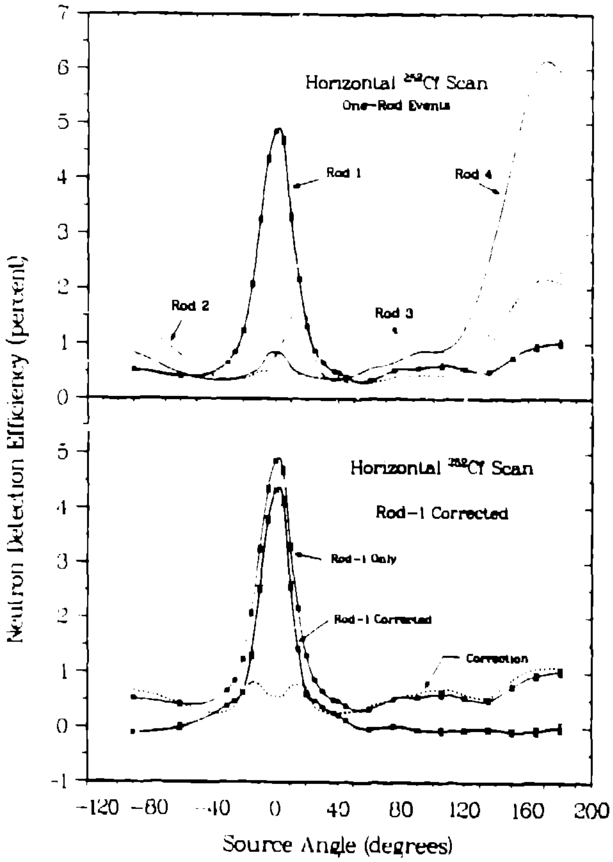

Figure 8: Development of Background Correction Using a Horizontal Angular Scan for a ^{252}Cf Fission Source

This discussion has not emphasized the significance of the "One-Rod" events in Figs. 8–9. Neutrons that pass through the shielding from the sides or rear are likely to fire a shielding rod before reaching the forward rod. Selecting only one-rod events improves the off-axis background rejection, but it reduces the on-axis efficiency because neutrons can scatter from Rod 1 into a rear rod. After applying the background corrections above, however, the added complexity of this anti-coincidence technique provides only a slight improvement in directionality.

IV. MOCKUP AND MISSILE TESTS

The detector testing relies on two sets of measurements, one on missile mockups and the other on a silo-based Peacekeeper missile. Figure 10 shows the layout for the mockup tests. The detector was located next to a large turntable that carried mockups made from either two or three distributed fission sources surrounded with simulated high explosive. Steel plates were placed in front of (2.5 cm) and behind (5.1 cm) the detector to represent scattering from the additional silo materials described below. By rotating the turntable, intensity scans could be measured as a function of source angle. Figure 11 compares the two and three source configurations and shows that the signature of the third source is the filled-in valley between the other two.

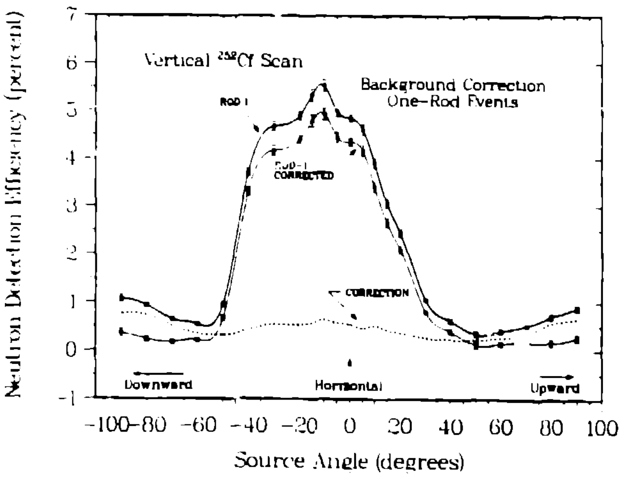

Figure 9: Background Correction for a Vertical Scan

Figure 12 shows a standard warhead arrangement for a Peacekeeper missile, with nine positions evenly spacing around the perimeter and a tenth located on a inner ring at the gap between positions 1 and 2. The figure also shows some important silo features. The outermost cylinder is the steel launch tube from the converted Minuteman silo; the next inner cylinder is the steel canister that contains the Peacekeeper missile. The detector is designed to fit in the 70-cm gap between the canister and launch tube and roll along the launch tube's upper rim as shown in Fig. 2. The large amount of scattering from the steel canister and launch tube explains the steel plates included in the mockup measurements.

The two- and three-source mockup scans can be used to predict the intensity pattern expected in the missile test. The three-source mockup represents the arrangement at the gap for the tenth warhead, and the two-source scan corresponds to the warheads at the empty gaps. To produce the nine-fold symmetry of the outer ring, the angle scale is simply compressed by factor of three and then repeated over 360 degrees. Based on this analogy, we would expect all ten Peacekeeper warheads to be readily identifiable. To illustrate, in Fig. 13 the two sets of mockup measurements are replaced by spline fits and shown as smooth curves. The angles for the measurements were selected to emphasize the differences between the peaks and valleys at the warheads and gaps. The 35 overlaid data points are the results of the silo measurements, with a slight scale adjustment that matches the two normalizations. The data generally favor the two-source pattern at all angles *except* at the gap between warheads 1 and 2, where the inner tenth warhead is located. Because of the large statistical errors, it is impossible to guarantee that further measurements would provide the unambiguous pattern predicted by the mockup test.

Finally, we return to the assertion that neutron measurements are inherently non intrusive. The only difference be-

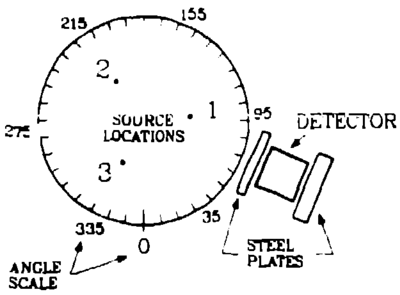

Figure 10: Layout for Mockup Scans

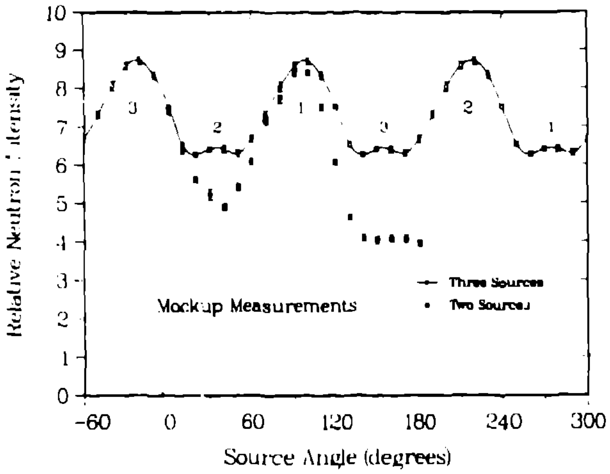

Figure 11: Mockup Scans for One or Two Sources

tween the measured energy spectrum for a warhead viewed through a missile canister and that for a warhead mockup viewed through a steel plate is a small increase in the number of low-energy scattered neutrons inside the closed silo. Furthermore, removing the steel plate in the mockup measurement provides an energy spectrum that is almost indistinguishable from a ^{252}Cf fission distribution. Thus, even spectral measurements reveal nothing more than the fact that a distributed fission source is being observed through a thick steel canister.

V. CONCLUSIONS

The boron-loaded scintillators used for these tests provide some advantages over the liquid scintillators and pulse-shape discrimination typically used in fast-neutron measurements. The ruggedness and ease of calibration that led to the detector's use in space instruments also supports its use for field operations such as the present silo measurements. The background correction technique developed to improve the detector's directionality complements the existing approach to eliminating backgrounds from gammas and low-energy neutrons. For other applications, it is important to note the restriction to relatively low-rate operation, because of the the low threshold needed to detect the second pulse, the high singles rate for low-energy neutron capture, and the instrumental dead time

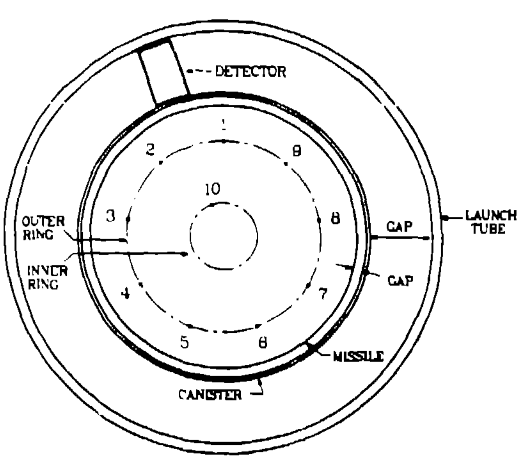

Figure 12: Silo Layout for a Peacekeeper Missile

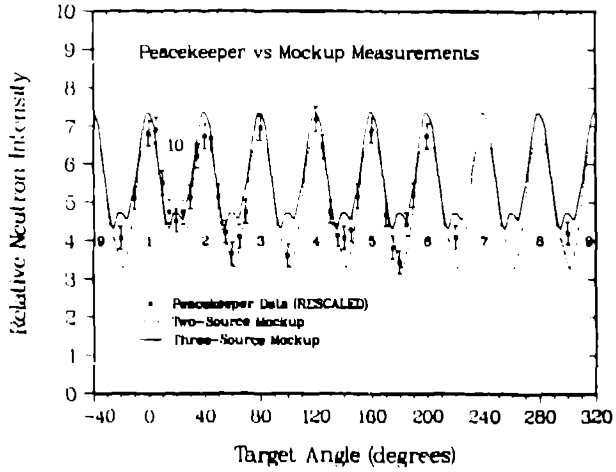

Figure 13: Missile Data versus Mockup Patterns

required for coincidence processing.

For warhead-counting applications, the results presented here indicate that collimated proton-recoil scintillators can, at least in some circumstances, provide the position resolution needed to resolve individual warheads without revealing intrusive information about their design. The actual utility of any radiation-detection approach, however, depends primarily on issues of treaty protocol, not on technical feasibility.

References

[1] D. M. Drake *et al.*, "New Electronically Black Neutron Detectors," *Nucl Inst and Meth*, A247:576–582, 1986; W. C. Feldman *et al.*, "A Novel Fast-Neutron Detector for Space Applications," *Nucl Inst and Meth*, A306:350–365, 1991.

[2] C. E. Moss *et al.*, "Detection of Uranium-Based Nuclear Weapons Using Neutron-Induced Fission," Paper 8B6.

LA-UR--91-3495

DE92 003797

Los Alamos National Laboratory is operated by the University of California for the United States Department of Energy under contract W-7405-ENG-36

TITLE: ON SIZE SCALING IN SHOCK HYDRODYNAMICS AND THE STRESS-STRAIN BEHAVIOR OF COPPER AT EXCEEDINGLY HIGH STRAIN RATES

AUTHOR(S): John M. Walsh, P-14
Gary L. Stradling, P-14
George C. Idzorek, P-14
Barry P. Shafer, WX-DO
Harold L. Curling Jr., SAIC, Albuquerque, NM 87106

SUBMITTED TO: Hypervelocity Impacts in Space

DISCLAIMER

Los Alamos National Laboratory
Los Alamos, New Mexico 87545

On Size Scaling in Shock Hydrodynamics and the Stress-Strain Behavior of Copper at Exceedingly High Strain Rates

John M. Walsh, Gary L. Stradling, George C. Idzorek, P-14
Barry P. Shafer, WX-DO
Harold L. Curling, Jr. SAIC

Summary

In recent years the Hypervelocity Microparticle Impact (HMI) project at Los Alamos has utilized electrostatically accelerated iron spheres of microscopic dimensions to extend the range of controlled hypervelocity impact experiments to about 100×10^5 cm/sec, well beyond the meteoroid velocity range and about an order of magnitude beyond the data range for precisely controlled impact tests with ordinary macroscopic particles. But the extreme smallness of the micro impact events brings into question whether the usual shock-hydrodynamic size scaling can be assumed. It is to this question of the validity of size scaling (and its refinement) that the present study is directed.

Hypervelocity impact craters are compared in which the two impact events are essentially identical except that the projectile masses and crater volumes differ by nearly 12 orders of magnitude---linear dimensions and times differing by 4 orders of magnitude. Strain rates at corresponding points increase 4 orders of magnitude in the size reduction.

Departures from exact scaling, by a factor of 3.7 in crater volume, are observed for copper targets--with the micro craters being smaller than scaling would predict.

This is attributed, using a well-established relation for the dependence of crater volume upon target yield stress, to a factor 4.7 higher effective yield stress occurring in the micro cratering flow. This, in turn, is because the strain rate there is about 10^8/sec as compared to a strain rate of only 10^4/sec in the macro impact. This pronounced strain rate effect in copper is compatible with recent theoretical models by Follansbee, Kocks, Rollett and others.

Aluminum targets are found to behave similarly, though primary emphasis has been placed on the copper data because the high strain rate properties of copper have been discussed more fully in recent literature.

Work in this area may be of interest for several reasons: The classical laws of shock-hydrodynamic size scaling, as applied to condensed media, are put to a much more stringent test than hitherto. The departure from strict size scaling is quantified and explained in terms of basic material properties. Also the measurement of impact craters for very small impact events leads to the determination of metal yield stresses at strain rates more than two orders of magnitude greater than have been obtained by other methods. The determination of material strengths at these exceedingly high strain rates is of obvious fundamental importance.

On Size Scaling in Shock Hydrodynamics and the Stress-Strain Behavior of Copper at Exceedingly High Strain Rates

John M. Walsh, Gary L. Stradling, George C. Idzorek, P-14
Barry P. Shafer, WX-DO,
Los Alamos National Laboratory
P. O. Box 1663, MS-D410
Los Alamos, New Mexico 87545

Harold L. Curling, Jr.
Science Applications International Corporation
2301 Yale S. E. Suite E, Albuquerque, NM 87106

Abstract

In recent years the Hypervelocity Microparticle Impact (HMI) project at Los Alamos has utilized electrostatically accelerated iron spheres of microscopic dimensions to generate hypervelocity impact experiments to about 100×10^5 cm/sec, about an order of magnitude beyond the data range for precisely controlled impact tests with ordinary macroscopic particles. But the extreme smallness of the micro impact events brings into question whether the usual shock-hydrodynamic size scaling can be assumed. It is to this question of the validity of size scaling (and its refinement) that the present study is directed.

Hypervelocity impact craters are compared in which the two impact events are essentially identical except that the projectile masses and crater volumes differ by nearly 12 orders of magnitude---linear dimensions and times differing by 4 orders of magnitude. Strain rates at corresponding points increase 4 orders of magnitude in the size reduction. Departures from exact scaling, by a factor of 3.7 in crater volume, are observed for copper targets--with the micro craters being smaller than scaling would predict. This is attributed to a factor 4.7 higher effective yield stress occurring in the micro cratering flow. This, in turn, is because the strain rate there is about 10^8/sec as compared to a strain rate of only 10^4/sec in the macro impact.

The measurement of impact craters for very small impact events leads to the determination of metal yield stresses at strain rates more than two orders of magnitude greater than have been obtained by other methods. The determination of material strengths at these exceedingly high strain rates is of obvious fundamental importance.

I. Introduction

The Hypervelocity Microparticle Impact (HMI) project,[1] has obtained impact data from microscopic iron spheres impacting targets at impact velocities from 1×10^5 cm/sec to 100×10^5 cm/sec. The iron spheres are charged and accelerated electrostatically[2] in a 6 MeV Van de Graaff accelerator. Each impact is characterized by simultaneous measurement of projectile charge and velocity using careful cross-correlation techniques[3]. Measurement of impact crater characteristics is performed using a scanning electron microscope. A typical crater in copper is shown in Fig. 1. Impact studies have been performed on a variety of materials relevant both to practical impacts in space and to the study of impact physics. In this discussion we focus on impacts in copper and aluminum in order to compare with existing libraries of data from macroscopic impact physics research.

II. Departure From Strict Size Scaling for Impact Craters in Soft Copper Targets

Micro impacts, when compared to the same impacts at ordinary sizes, make it possible to put classical shock-hydrodynamic size scaling to severe tests in which corresponding masses (and other extensive variables) are scaled down nearly 12 orders of magnitude---linear dimensions and times being scaled down 4 orders of magnitude. Strain rates increase four orders of magnitude in the size reduction.

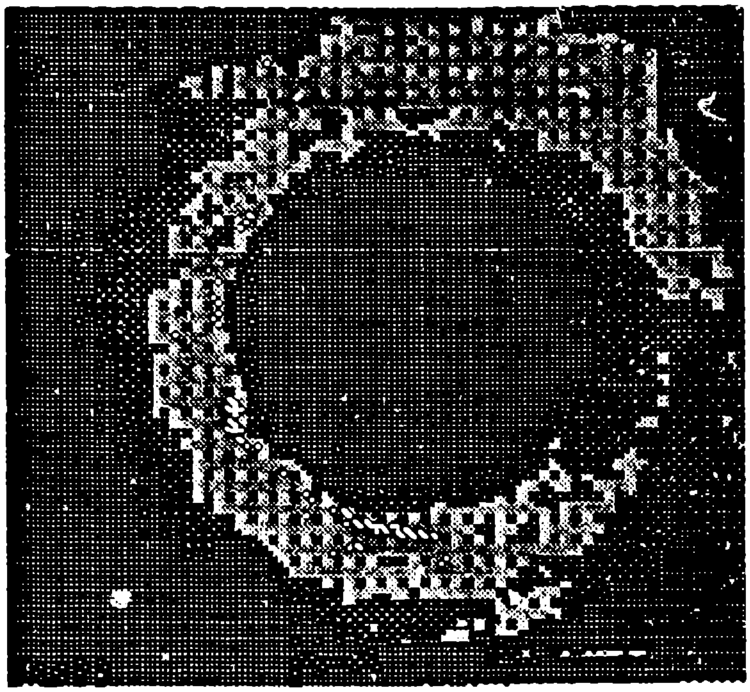

Fig. 1. A typical hypervelocity impact crater in copper produced by a microscopic iron sphere impacting at 12.5×10^5 cm/s. The craters produced by microscopic impacts are axisymmeteric and appear to be geometrically similar to the craters produced by macroscopic impacts.

As Fig. 2 we reproduce the pertinent data for copper, to call attention to the fact that the normalized target crater volume is a factor of 3.7 smaller for the IBF micro-impacts (projectile masses 0.25×10^{-12} gm and 1.5×10^{-12} gm) than for the large scale impacts (projectile masses 0.15 gm and 0.50 gm) at the same impact velocity (6×10^5 cm/sec). Exact size scaling would, of course, require that these normalized crater volumes be equal. Thus, the size reduction, by a factor[4] of about 0.3×10^{12} in the projectile mass (or, equivalently, by a factor of 0.7×10^4 in projectile diameter) has not only reduced the crater volume by a factor of 0.3×10^{12}, as it should in accord with strict scaling, but also by an additional factor of 3.7.

III. Strain-Rate Effect As a Reason for Scaling Failure

We believe that this failure to scale exactly is due to strain-rate effects within the copper. More fully, we develop here the notion that the higher strain rates in the smaller flows[5] cause a higher effective flow stress in the smaller flows and a correspondingly smaller crater.

In Fig. 3 we reproduce (in addition to impact data for copper) a well-known correlation formula due to Sorensen[6] for hypervelocity impact data. It shows, in particular, that crater volume V varies with target shear yield strength s as $s^{-0.845}$. This dependence of V on s is shown by Sorensen to fit a wide range of impact data for metal targets, encompassing a variation of s from 0.13 kilobars for lead to nearly 10 kilobars for a steel. See Ref. 6 for a detailed discussion. Similar dependences of V on s have been established in hydrocode studies. Thus, adopting Sorensen's correlation, we find that the observed 3.7-fold reduction in crater volume could be caused by a yield stress increase by a factor of 4.7.

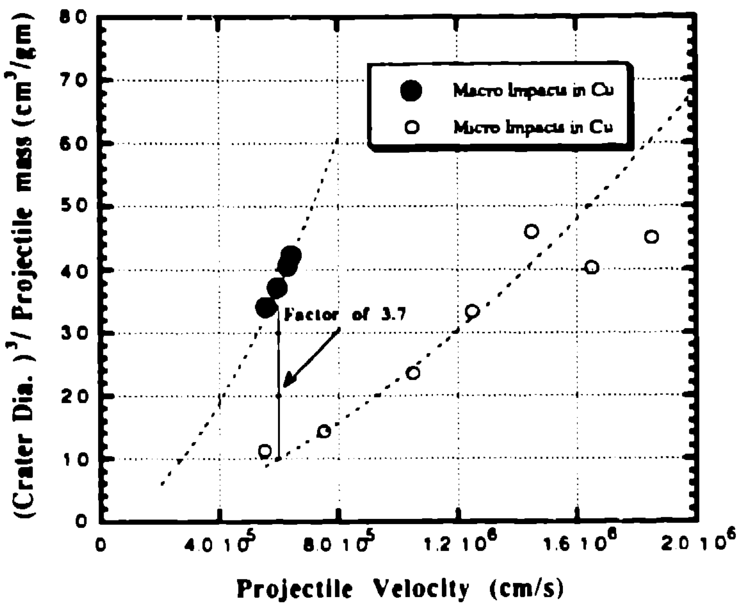

Fig. 2. Hypervelocity impact cratering data for copper. The upper curve, with four representative data points, is from Sorensen's empirical correlation of (macro) impact data for copper. See also Fig. 3 and Sorensen's paper (Ref. 6) for further information on Sorensen's work. The lower curve shows the (micro) impact data on copper. Of importance to the present discussion is the fact that the normalized crater volumes in the micro impacts are smaller by a factor of 3.7. The two curves would coincide if size scaling were exact.

IV. Strain Rates in Hypervelocity Impact

Next, we need a reasonably good estimate of the strain rates occurring in the cratering process. Specifically, it will suffice to estimate the average strain rate during the crater formation for the 0.3 gm (macro) impact at 6×10^5 cm/sec since we already know the ratio of the strain rates in the micro and macro events. Making this estimate is the object of the present Section.

It is useful to recall the prominent features of such a hypervelocity impact. The initial shock pressure is given by

$$P \approx \rho\, U_s\, U_p = 1.9 \times 10^{12}\ \text{dynes/cm}^2 = 1.9\ \text{megabars},$$

since the shock particle velocity U_p is 3×10^5 cm/sec from symmetry, the density ρ is 8.9 gm/cc and the shock wave velocity U_s associated with the given particle velocity is 7×10^5 cm/sec. This is more than three orders of magnitude greater than material strength, implying that the early phases of the impact are hydrodynamic with strength playing a negligible role. This shock front and the attached pressure pulse propagate almost hemispherically into the thick copper target, and serve to set the engulfed copper into nearly hemispherical motion. Were it not for the finite yield strength of the copper the (nearly hemispherical) crater would grow without limit. What happens instead is that the 1.385 kilobar copper yield strength limits the crater volume to about 83 times the volume of the impacting projectile, in accord with Sorensen's correlation formula as applied to this impact.

Two-dimensional finite difference hydrocode calculations (axisymmetric and time dependent, incorporating material compressibility and strength effects by utilizing available material property formulations) can provide us with a very detailed description of the impact process, and such calculations have been provided by a number of investigators over the past 30 years.

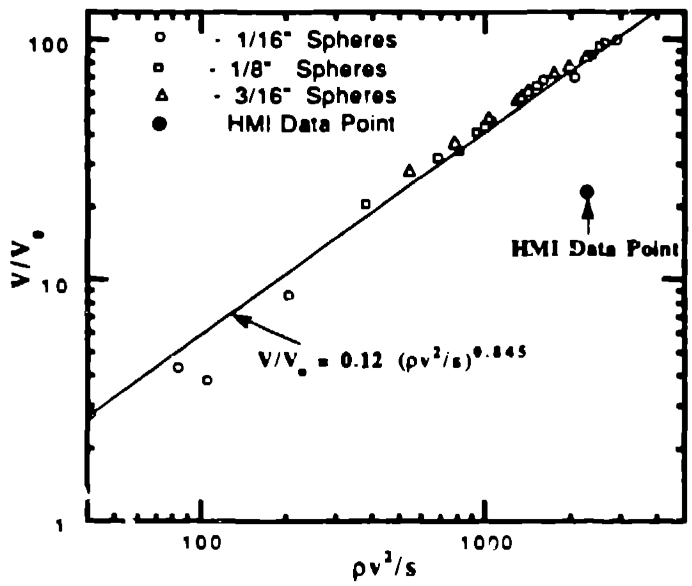

Fig. 3. Sorensen's data correlation for copper, from Ref. 6. The data extend to about 7.5×10^5 cm/sec. The analytical correlation is for several metals and therefore does not fit copper exactly, although quite well. It may be noted that the factor 3 variation in projectile diameters (27 in masses) does not cause an apparent size effect in the macro data points. The point at $v = 6 \times 10^5$ cm/sec on the micro curve (Fig. 2) has been transformed to this plot and is seen to be substantially below the macro data. (To transform this point the values $\rho = 8.9$ gm/cm^3 and $s = 1.385 \times 10^9$ dynes/cm^2 were used for the density and shear yield strength of annealed copper.) The projectile mass ratio between the micro and macro experiments is nearly twelve orders of magnitude, as explained in the fourth footnote.

While a specific computation has not yet been performed for our 0.3 gm, 6×10^5 cm/sec impact into copper, suitable computed results from other impacts have been reported in the literature and can be used to deduce (using only Sorensen's correlation formula and dimensional analysis) useful estimates of the effective strain rate in our impact. Dienes[7] has reported calculations for a spherical aluminum projectile (diameter 0.476 cm) impacting a hard aluminum target (shear yield strength 2.39 kilobars) of density 2.7 gm/cc at a velocity of 7.3×10^5 cm/sec. He finds for times of 2, 4, 8 and 16 microseconds that the crater depth is 0.4, 0.8, 0.9, an 1.0 of its final value. Hence for present purposes we can take this aluminum crater formation time to be 15 microseconds. Next we note that Sorensen's correlation formula:

$$V/V_0 = C_1(\rho v^2/s)^{.845}$$

is entirely equivalent to

$$T/T_0 = C_2(\rho v^2/s)^{\frac{.845}{3}} = C_2\,(\rho v^2/s)^{.282}$$

when re-expressed to give the time T for crater formation. Here T_0 is any suitable measure of the impacting projectile size (such as the time it takes the free flying projectile to move one diameter) that must, of course, be the same measure for the two impacts under consideration. Thus T_0 would be:

$T_0 = 0.476$ cm/(7.3×10^5 cm/sec) = .65 microseconds

for the aluminum problem and

$T_0 = 0.400$ cm/(6.0×10^5 cm/sec) = .67 microseconds

for our copper impact. Next for the two cases of aluminum and copper impacts, the quantities $(\rho v^2/s)$ and $(\rho v^2/s)^{.282}$ would be:

$(\rho v^2/s) = 602;$ $\qquad\qquad (\rho v^2/s)^{.282} = 6.08$

and for the copper impact;

$(\rho v^2/s) = 2313,$ $\qquad\qquad (\rho v^2/s)^{.282} = 8.88.$

Hence the 15 microsecond crater formation time for aluminum scales to

T=(8.88/6.08)(.67/.65)15 microseconds = 23 microseconds

for our copper impact.

In another problem from Ref. 7 a soft aluminum target (shear yield 0.75 kilobars) was used and total plastic work was reported instead of crater depth. (Other problem parameters were the same as in the hard aluminum impact.) At 4, 8 and 16 microseconds the total plastic work was 20%, 50%, and 95% of the final value when the flow was completely arrested. This again suggests a time like 15 microseconds for flow arrest. Scaling this over to our copper impact, by a calculation similar to that detailed for the hard aluminum, gives a time of 16 microseconds for the copper impact.

We need also to know the average strain occurring in the plastically deforming material when the crater is formed. Here both computational and experimental evidence (where targets thicker than about two crater depths react much the same as semi-infinite targets subjected to the same projectile impact) suggest that the target material within about one crater radius of the crater is effective in arresting the flow. For this material the strain field is a maximum, about 0.6 at the crater surface, dropping to essentially zero a crater depth into the material. A suitable average strain for this plastically deforming material is about 0.2. (This value may be reliable only to about a factor of two.) Dividing it by the above crater formation times of 23 microseconds and 16 microseconds implies average strain rates of 0.86×10^4/sec and 1.25×10^4/sec. Hence we adopt a value of 1.0×10^4/sec as an average strain rate in our 0.3 gm copper impact, recognizing that this value in uncertain by a factor of two. Surprisingly, perhaps, this uncertainty is tolerable in present considerations because of the weak dependence of yield stress on strain rate.

It may be noted that a more accurate determination of this average strain rate could be made as part of a hydrocode computation of our copper impact. For this purpose we suggest

$$\bar{\dot{\varepsilon}}_p = \frac{\sum_N \sum_K W_p(K,N)\, \dot{\varepsilon}_p(K,N)}{\sum_N \sum_K W_p(K,N)}$$

where K is the cell number and N is the time step number. The formula gives an average strain rate, averaged over all (Eulerian) cells and all time steps, with each $\dot{\varepsilon}_p(K,N)$ weighted in proportion to the amount of plastic work $W_p(K,N)$ occurring in the cell during the time step.

V. Comparison of Results With Recent Theoretical Expectations

In Section II we saw that when the projectile mass was reduced by a factor 0.3×10^{12}, the crater volume was reduced not only by this factor, as expected from size scaling, but by an additional factor of 3.7.

In Section III we found, using a well-established empirical correlation, that the factor 3.7 crater volume reduction would be caused by a yield stress increase by a factor of 4.7.

In Section IV we used published computational results for the crater formation process, together with the Sorensen correlation formula, to establish that the average strain rate in the macro impact was about 1.0×10^4/sec. This means that the average strain rate in our micro impact [which must be greater by a factor of $(0.3 \times 10^{12} \times 3.7)^{.333} = 1.03 \times 10^4$] is about 1.0×10^8/sec. So it remains to ask whether it is indeed reasonable to expect a factor 4.7 increase in the flow stress over this strain rate regime.

Any such estimates must be theoretical because measurements have been limited to strain rates below about 10^6/sec. Fortunately, the properties of copper at exceedingly high strain rates has been the subject of recent investigations by Follansbee, Kocks, Rollett and others. (See Refs 8 and 9 and literature cited there.) In Fig. 4 the theoretical stress *versus* strain rate curve is reproduced (from Fig. 2 of Ref. 9) for a constant strain of 0.1. This strain is taken to be an average strain during the cratering flow, corresponding to the estimate made in Section III that the average total strain is about 0.2. (Also the theoretical stresses were reduced by a factor of $\sqrt{3}$, , in accord with the von Mises yield condition, because longitudinal yield stresses were used, whereas shear yield stresses are used throughout the present paper.)

Plotted also in Fig. 4 are our two experimental points $\sigma = 1.385$ kilobars at $\dot{\varepsilon}_p = 10^4$ /sec and $\sigma = 6.5$ kilobars at $\dot{\varepsilon}_p = 10^8$ /sec

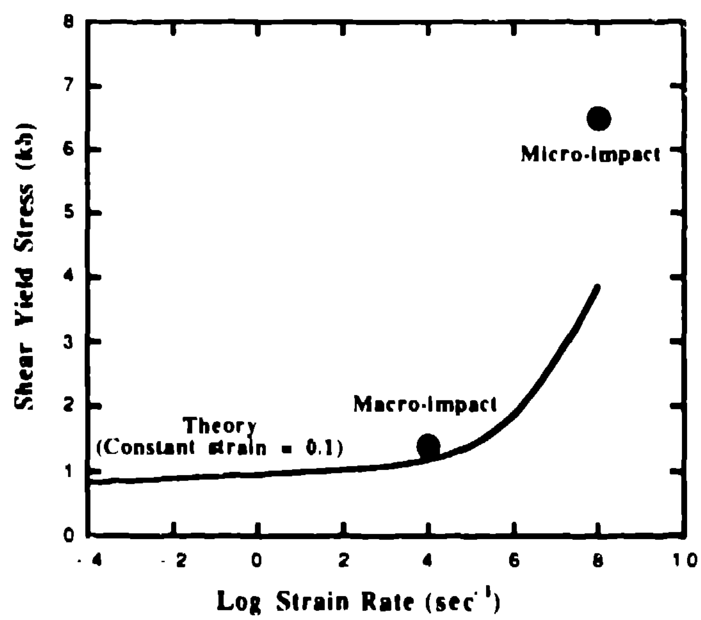

Fig. 4. Shear yield stress σ versus strain rate for copper strained to 0.1. The theoretical curve is from Ref. 9, the results from Fig. 2 of the reference being re-presented here in terms of shear yield stress at a constant strain of 0.1.

The most important conclusion to be drawn from the present comparison is that both the theory (Refs 8 and 9) and experiment are indicating a very substantial strain rate effect in copper in the 10^4/sec to 10^8/sec strain rate regime. The experimental effect is somewhat the larger, the yield stress increasing by a factor of 4.7 as compared to 2.8 for the theoretical curve. In the theoretical modelling[9] this strain rate effect has been attributed to a gradual transition, as the strain rate is increased, from thermally-activated to viscous-drag controlled deformation.

The experimental factor of 4.7 depends upon only the experimental volume ratio of 3.7 (Fig. 2) and the Sorensen correlation formula, and is estimated here to be reliable to 10% or less. Other aspects of the comparison are discussed in the next section.

VI. Comments on Sources of Error

It was remarked in Section IV that the estimate of the average strain rate in the macro impact was uncertain by a factor of about two. In the Fig. 4 data plot the experimental points are represented as circles with diameters spanning a factor of four in the strain rate. It is readily apparent that a lateral shift of the macro data point to either of the extreme positions (causing an equal lateral shift of the micro point) would have only a very small effect on the comparison.

In Section V we estimated an average strain in the cratering flow to be 0.1. This strain was used to select the appropriate constant-strain theoretical curve from Ref.(9). Had one used 0.05 or 0.2 instead of 0.1, the corresponding average-strain theoretical curve, in the two cases, would be below or above the macro experimental point and in somewhat poorer agreement with that point. Here, however, an alternative interpretation is useful: The properties of copper at strain rates around 10^4/sec and below, where test data and theoretical understanding have been in accord for years, can be assumed known. One then selects that particular constant-strain curve from Ref. (9) that causes agreement with the macro data point. This constant-strain curve is the one for an average strain in the cratering flow of about 0.13, instead of our estimated value of 0.1 given above. (This might, in the present situation, be a better way to estimate the average strain in the cratering flow). In any event, the theoretical strain rate enhancement factor (taken to be 2.8 in the last paragraph of Sec. V) is a weak function of which constant-strain curve one uses and would not be substantially affected.

Finally, we recall that the impacting spheres in the micro experiments are actually iron instead of copper. In our comparison of the micro- and macro-events these iron projectiles are assumed to be equivalent to copper projectiles of equal mass. This equal-mass assumption has been investigated extensively in test work and in computer studies[7] and is found to be accurate for sufficiently high velocities and/or density ratios sufficiently close to unity. For the present application at 6 x 10^5 cm/sec, with iron and copper projectiles, the cratering effects on thick copper targets are expected to be essentially identical.

VII. Extension to Aluminum

The IBF data for aluminum target impacts exhibits essentially the same behavior as copper, i. e. the micro crater volumes are small by about a factor of 4, corresponding to a strain rate enhancement of yield stress by a factor of 5.

Attention here has been focussed on copper because its constitutive modelling appears to be more advanced, but it seems likely that aluminum (another FCC metal) will exhibit similar behavior to copper at high strain rates[10].

VI. Conclusion

The classical laws of size scaling, as applied to the shock hydrodynamics of condensed media, have been put to severe test. The size reduction spans four orders of magnitude in length or time dimensions, or 12 orders of magnitude in extensive variables, such as corresponding masses or volumes. The observed departure from exact scaling is by a factor of 3.7 in extensive variables, or by 1.5 in corresponding lengths or times.

The departure is attributed to strain rate enhancement of the flow stress in the copper targets. This dramatic rise in flow stress at very high strain rates had already been anticipated in the theoretical literature.

Work in this area is of interest for several reasons:

1. It validates and/or refines classical shock-hydrodynamic size scaling, and thus pertains directly to the important engineering area of scale model experimentation.

2. For velocities above about 15 x 10^5 cm/sec, the only precisely controlled hypervelocity experiments have been performed, at Los Alamos and elsewhere, with electrostatically accelerated microparticles. Experimental data are available for velocities throughout the meteoroid velocity range (to about 70 x 10^5 cm/sec) and beyond. To understand this valuable data source, and to be able to scale it with confidence to larger impact events we need, as done here for copper, to quantify the departures from exact size scaling and attribute such departures to appropriate material properties.

3. Strain rates attainable in microparticle impacts extend the present day test range by more that two orders of magnitude. The determination of material strengths at these exceedingly high strain is of obvious fundamental importance.

REFERENCES

[1]P. W. Keaton, *et. al.*, "A hypervelocity-microparticle-impacts laboratory with 100 km/s projectiles," *Int. J. Impact Engng.* **10**, pp. 295-308, 1990; G. L. Stradling, *et. al.* , "Searching for momentum enhancement in hypervelocity impacts," *Int. J. Impact Engng.* **10**, pp. 555-570, 1990.

[2]Friichtenicht, J. F. (1962), "Two million volt electrostatic accelerator for hypervelocity research," Rev. Sci. Inst., **33**, 209. Friichtenicht, J. F. (1964), "Micrometeroid simulation using nuclear accelerator techniques," Nucl. Inst. Meth. **28**, 70. Lewis, A. R. and R. A. Walter (1970). Electrostatic acceleration system for hypervelocity microparticles with selected kinematic properties. NASA TN D-5780, Electronics Research Center, Cambridge, MA.

[3]Idzorek, G. C., P. W. Keaton, G. L. Stradling, M. T. Collopy, H. L. Curling Jr., and D. B. McColl (1989). "Data acquisition system for a hypervelocity-microparticle-impacts laboratory," *International Journal of Impact Engineering*, **10**, 1990.

[4] The average mass of the bigger impacts is $(0.5 + 0.15)/2 = 0.3$ gm. The average mass of the HMI impacts is $(0.25 + 1.5) \times 10^{-12}/2 = 0.9 \times 10^{-12}$ gm. Thus the reduction is by a factor of about 0.3×10^{12} on mass, or 0.7×10^{4} on linear dimensions and times.

[5] By the above factor of 0.7×10^{4} if the flows scaled exactly, and by an additional factor of $3.7^{0.333} = 1.5$ because of the smaller-than-expected craters--combining for a factor of 10^{4}.

[6]Neil R. Sorensen, "Systematic investigation of crater formation in metals," in *Proceedings of Seventh Hypervelocity Impact Symposium*. Martin Company, Orlando, 1965.

[7] J. K. Dienes and J. M. Walsh. "Theory of Hypervelocity Impact," S-Cubed Report 3SIR-676, May 1969. See also J. K. Dienes and J. M. Walsh. "Theory of Impact: Some general principles and the method of Eulerian codes," in *Hyper Velocity Impact Phenomena,* Edited by Ray Kinslow, Academic Press, 1970.

[8]P. S. Follansbee. "The rate dependence of structural evolution in copper and its influence on the stress-strain behavior at very high strain rates." *Impact Loading and Dynamic Behavior of Materials*, Edited by, C. Y. Chiem, H. D. Kunze, and L. W. Myer, Vol. 1, Informationsgesellschaft, Verlag 1988.

[9]P. S. Follansbee, "Shear prediction in shock loaded copper," In *Proceedings of 1991 APS Topical Conference on Shock Compression of Condensed Matter*. Also available as Los Alamos document, LA-UR 91-1994.

[10]Private communications with A. D. Rollett and P. S. Follansbee.

LA-UR 91-3497

LA-UR--91-3497

DE92 003796

TITLE: Exploration of the Neutron-Rich Mass Surface from ^{11}Li to ^{66}Fe

AUTHOR(S): D.J. Vieira, X.G. Zhou, X.L. Tu, J.M. Wouters, H.L. Siefert, K.E.G. Löbner, Z.Y. Zhou, V.G. Lind, and G.N. Butler

SUBMITTED TO: Proc. International Workshop on "Nuclear Shapes and Nuclear Structure at Low Excitation Energies", Cargese, Corsica, June 3-7, 1991

Los Alamos

Los Alamos National Laboratory
Los Alamos, New Mexico 87545

FORM NO 836 R4

Contribution to the Int'l. Workshop on "Nuclear Shapes and Nuclear Structure at Low Excitation Energies", Cargese, Corsica, June 3-7, 1991

EXPLORATION OF THE NEUTRON-RICH MASS SURFACE FROM ^{11}Li TO ^{66}Fe

D. J. Vieira[1], X. G. Zhou[2], X. L. Tu[2], J. M. Wouters[1], H. L. Seifert[1,3], K. E. G. Löbner[4], Z. Y. Zhou[1,5], V. G. Lind[2], and G. W. Butler[1]

[1]Isotope and Nuclear Chemistry Division, Los Alamos National Laboratory, Los Alamos, NM 87545, USA
[2]Department of Physics, Utah State University, Logan, UT, 84322 USA
[3]II. Physikalisches Institut, Universität Giessen, D-6300 Giessen, FRG
[4]Sektion Physik, Universität München, D-8046 Garching, FRG
[5]Department of Physics, Nanjing University, Nanjing, PRC

INTRODUCTION

A small revolution in our ability to perform mass measurements of light-mass, neutron-rich nuclei has occurred during the last five years with the extension of the direct, total mass measurement method to fast recoiling nuclei. To date the work of two groups, one using the SPEG spectrometer at GANIL and the other using the TOFI spectrometer at LAMPF, has yielded over 85 mass measurements of which 62 had not been reported previously. Extending from the neutron-halo nucleus ^{11}Li up to ^{66}Fe, a region relevant to the astrophysical r-process, these measurements have provided a valuable first glimpse into the interesting nuclear structure present in many of these exotic nuclei.

Herein we highlight the nuclear structure insight which has been gained from these measurements, especially that learned from a comparison to recent shell model calculations. Attention is given to: (1) the binding of loosely-bound neutron halo nuclei; (2) the N=14-16 region in the neutron-rich isotopes of O, F, and Ne where the strong two-body interaction plays an important role; (3) the deformed intruder state region around ^{31}Na of long standing interest; (4) the neutron-rich isotopes of sulfur and chlorine; and (5) the question of the isospin dependence (or independence) of neutron and proton pairing energies in the fp shell. Only the briefest account of this work can be given here; emphasis is place on the most recent results.

DIRECT MASS MEASUREMENTS OF FAST RECOILS

As mentioned above two separate groups have pioneered slightly different approaches for determining the total mass of fast recoiling nuclei. In the mass measurements using the Energy-Loss Spectrometer SPEG[1-3], a combined two-parameter determination of velocity and magnetic rigidity is carried out, while at TOFI[4-7] a single-parameter measurement of the ion's time-of-flight through the Time-Of-Flight Isochronous spectrometer serves to determine the mass-to-charge ratio of the ion. Z and Q identifications were obtained in both approaches from additional measurements of stopping power, velocity, total kinetic energy, and/or range. The SPEG experiments rely on the concentration of projectile fragmentation products at forward angles using 30-100 MeV/u hea , ion beams, while the TOFI measurements utilize fast (1-4 MeV/u) recoils produced in 800-MeV proton-induced target fragmentation and fission reactions. Given that a large variety of recoils are produced in these reactions and that both methods have reasonably large acceptances and are fast (with flight times typically of 1 μs or less), both groups have been able to make a wide range of systematic measurements which extend far from the valley of β-stability. Typical mass resolutions for both approaches are on the order of 3×10^{-4} with mass measurement accuracies ranging from 70 keV to 1.6 MeV depending on counting statistics. For the most part, good agreement between these two fast recoil methods has been found (see Fig. 1 caption for noteworthy exceptions).

A convenient way of displaying the nuclear mass surface without the complication of the odd–even staggering due to neutron pairing is to plot the masses in terms of two-neutron separation energies (S_{2n}) versus neutron number. Several interesting nuclear structure features can be gleamed from such a plot (see Fig. 1 and the discussion that follows).

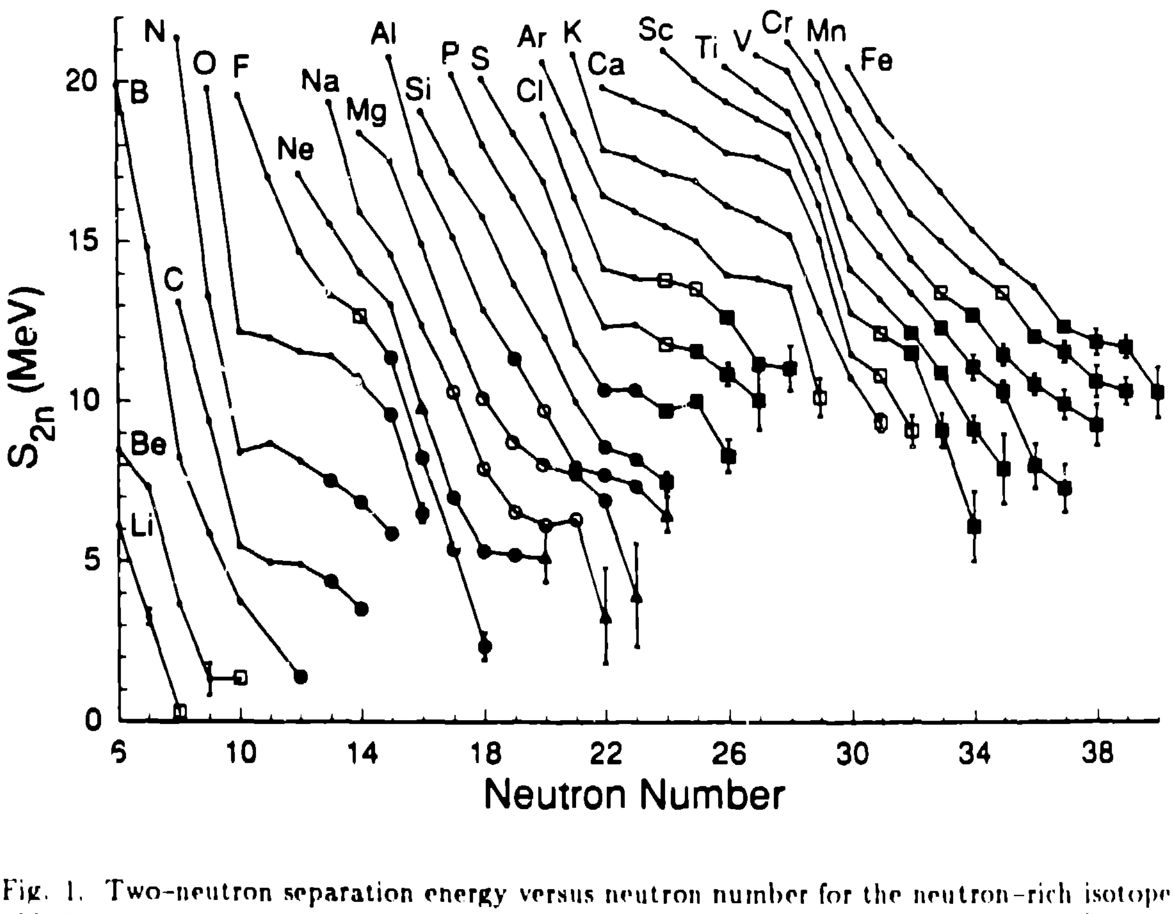

Fig. 1. Two-neutron separation energy versus neutron number for the neutron-rich isotopes of lithium to iron. Small data points (•) represent isotopes with well known masses[8]. Open symbols indicate those isotopes for which masses have been remeasured and the solid symbols are given for those nuclei where the first mass determination was reported by either the SPEG or TOFI groups[1-7]. ● = SPEG + TOFI overlapping measurements; ▲ = SPEG measurements and; ■ = TOFI measurements. A weighted average of all reported masses is plotted with the exclusion of ^{27}Ne and ^{30}Na from Ref.[7], ^{38}P from Ref.[2], $^{31-34}$Na from Ref.[9,10], and ^{31}Mg from Ref.[11]. Error bars are given where they exceed the symbol size.

Z=3 15 NEUTRON-RICH NUCLEI

Of current excitement are those nuclei which are very loosely two-neutron (or single neutron) bound, such as ^{11}Li, (^{11}Be), ^{14}Be, ^{17}B, where enhanced interaction (both total and electromagnetic dissociation) cross sections have been observed. These results are being interpreted in terms of an increased neutron radius, i.e., "a neutron halo", the extension of which is directly related to how weakly bound the last neutrons are. In the case of ^{11}Li, for example. the rms radius of the last two neutrons is calculated[12,13] to be anywhere from 5 to 12 fm (i.e., roughly 2 to 5 times the size of the proton rms radius) depending on which model is used. To date three mass measurements[9,6,14] have been performed for ^{11}Li yielding S_{2n} values of 190 (110), ?20 (120) and 340 (50) keV, respectively. The resulting weighted average is 315 (43) keV. Given that the size of the neutron halo is extremely sensitive to the S_{2n} value, additional higher precision measurements are needed to further constrain and test the validity of these models.

Other neutron-halo candidates worthy of attention are those of ^{19}B and ^{22}C which have been observed to be particle stable, but for which no mass determinations have been possible as yet due to their small production cross sections (roughly two orders of magnitude smaller than ^{17}B and ^{20}C). Using the latest SPEG and TOFI masses, the transverse Garvey-Kelson mass relationship[15] predicts S_{2n} values for ^{19}B and ^{22}C to be 360 and 110 keV, respectively. As such these nuclei should have neutron halos which are similar, if not larger, than that of ^{11}Li. Intensity and acceptance upgrades now being planned or built at several research facilities are likely to make the first measurement of such rare species possible.

Returning to Fig. 1, one prominent feature evident in this plot is the rapid S_{2n} falloff that occurs after N=8 which is then followed by a much slower decrease in S_{2n} values after N=10. This behavior is characteristic of a shell closure, in this case the completion of the p shell. Similar features, although less dramatic and not fully delineated here due to limitations in the vertical axis (i.e., several neutron-deficient isotopes have been excluded), are observed for the sd shell closure at N=20 and the completion of the $0f_{7/2}$ subshell at N=28. Analogous to the latter case, one might expect to see a sudden transition in the S_{2n} trend occurring at N=14 due to the completion of the $0d_{5/2}$ subshell. However, as is evident in the neutron-rich isotopes of O, F, and Ne, this transition occurs at N=15, not N=14. The explanation[6] of this effect came out of a detailed comparison to the shell model calculations of Wildenthal et al.[16] whose predictions, in contrast to most other mass models, were found to reproduce the observed S_{2n} trend in this region extremely well. In these calculations the single-particle energy spacing between the $0d_{5/2}$ and $1s_{1/2}$ levels is fairly small ($\sim$0.9 MeV), so the strong S_{2n} decrease observed in going from N=15 and N=16 results primarily from the interplay of two-body interactions, in this case the strongly attractive $[0d_{5/2}\text{-}0d_{5/2}]_{J=0}$ ($\sim$3 MeV) interaction is dominant. At N=14 and N=15 the contribution made by this $0d_{5/2}$ $0d_{5/2}$ interaction to the calculated S_{2n} value is sizable, while at N=16 its effect is minimal. In a strong sense this work has provided a challenging test of the shell model and verified the two-body interaction energies relevant to this region.

Moving up to the N=20 region one comes to the ^{31}Na region where enhanced binding energies relative to systematics and the predictions of most models has been noted for some time[9]. The SPEG and TOFI groups have now remeasured the masses of several Na isotopes and provided a number of new mass measurements for the adjoining Ne, Mg, and Al isotopes (see Fig. 1). The picture is now clear, given the good agreement between the SPEG and TOFI results, that the original[9] and subsequent[10] measurements of the Orsay group yielded masses which where consistently too bound with increasing deviations observed with increasing mass number, i.e., ^{31}Na (2.0 and 0.8 MeV, respectively), ^{32}Na (2.0 and 1 9 MeV), and ^{33}Na (and 4.0 MeV). Although the reported Orsay error bars are large (0.6 to 1.1 MeV), most of these deviations fall between 2 and 3 standard deviations.

After discussions[17] with the Orsay group, it appears that there where many possible sources of error in this early work, such as interference due to hydrocarbons, a bad divider network, and sagging high voltage during the accelerator beam pulses. Determining the true source of these errors now appears difficult and for the most part academic. However, the suggestion[4] that these errors may have arisen from boot strapping errors, analogous to those found[18] in the neutron-deficient Cs isotopes, is unfounded given that the different isotopic combinations used in the Na triplet (or double doublet) measurements never involved more than one unknown.

As can be seen in Fig. 1, an up-to-date view of the $^{31-32}$Na region no longer shows a dramatic S_{2n} upturn only a small increase, while the adjacent isotopes of Ne and Mg exhibit a slowly decreasing S_{2n} trend. However, evidence of enhanced binding in these nuclei is still indicated. These enhancements can be seen better in Fig. 2 where we contrast the experimental masses to recent shell model calculations. Concentrating on the solid line, i.e., the comparison to the normal $0\hbar\omega$ calculations of Wildenthal et al.[16] and Warburton et al.[19], a large deficiency in binding (2-3 MeV) is predicted in the N=20-21 isotones of Ne, Na, and Mg. By including two particle-two hole neutron excitations from the sd shell to the fp shell, so-called $2\hbar\omega$ excitations, Warburton et al.[19] has shown in the limit of weak coupling that increased binding in these nuclei occurs. In particular, a deformed intruder state which is dominated by neutron $(fp)^2$-$(sd)^{-2}$ configurations is found to be more bound (by 0.4 to 1.1 MeV) than the lowest $0\hbar\omega$ state in the localized Z=10-12, N=20-22 region. Moreover, Warburton et al. go on to show that the lowest $1\hbar\omega$ state in the odd neutron N=21,23 isotones competes with the lowest $2\hbar\omega$ state as being the most bound state.

Other shell model calculations have been performed by Poves and Retamosa[20] in the limit of $(0+2)\hbar\omega$ mixing. Even better agreement is noted in Fig. 2, however, there is considerable debate as to the validity of these calculations. For example, this calculation could suffer from the exclusion of $4\hbar\omega$ and higher order excitations which are known[21] to strongly mix with $0+2\hbar\omega$ configurations causing a binding energy shift in the ground state. None the less, both approaches result in the same basic finding - that a deformed intruder state is more bound than the lowest $0\hbar\omega$ state giving rise to enhanced binding of Z=10-12, N=20-22 nuclei. Given the very localized nature of this strongly prolate deformed region and the rich nuclear spectroscopy that these nuclei promise, additional investigations are clearly needed.

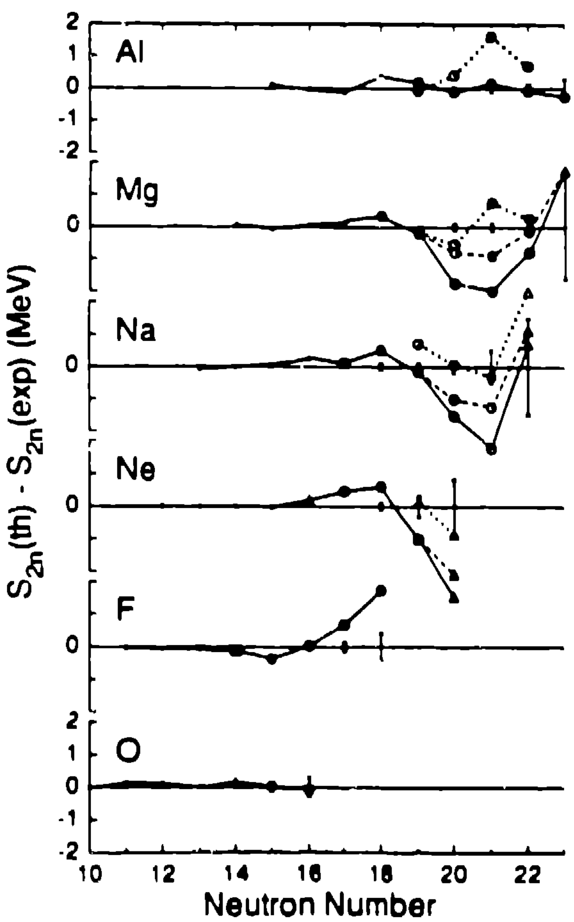

Fig. 2. A difference between the calculated two neutron separation energies and the experimental S_{2n} values is plotted versus neutron number for the neutron rich isotopes of Z=8-13. The symbols are as defined in Fig. 1. The solid line indicates the $0\hbar\omega$ shell model calculations of Wildenthal et al.[16] for N<18 or Warburton et al.[19] for N≥18. The dashed lines are for the $2\hbar\omega$ weak coupling calculations of Warburton et al.[19] and the dotted lines indicate the mixed $(0+2)\hbar\omega$ shell model calculations of Poves and Retamosa[20].

As is noted in Fig. 1 several new mass measurements have recently been reported in the heavier nuclei by the TOFI group[4,5]. Two major features are worth mentioning here – one is a shell model comparison to several neutron-rich S and Cl isotopes and the second is the neutron and proton pairing energies for several Z=21-26 isotopes. Concerning the first topic, remarkably good agreement (rms deviation=280 keV) between the experimental mass of $^{40-43}$S and $^{41-45}$Cl and those predicted by the relatively restrictive $\pi 0d_{3/2}$ $\nu 0f_{7/2}$ shell model calculations of Hsieh et al.[21] was found. This agreement confirms the general observation that in the middle of both proton and neutron shells the shell model works quite well even within a limited basis space, while near shell closures problems often develop if the basis space is not large enough to include important cross-shell contributions.

Finally, we would like to turn your attention to pairing energies and the question of their isospin dependence. An evaluation[22,23] of pairing energy systematics has revealed an apparent neutron-excess ($(N-Z)/A$) dependence in both neutron (Δ_n) and proton (Δ_p) pairing energies. However, we suspect that the observed dependence could arise from the natural correlation of pairing energy with mass number rather than with neutron-excess since the masses used in the evaluation covered a large mass range and that their fits where dominated by those nuclei lying along the valley of β-stability (i.e., the average neutron-excess and mass number are strongly correlated along stability). Moreover, the recent pairing energy study by Möller and Nix[24] finds that no inherent neutron-excess dependence in the pairing interaction itself is required. To experimentally answers this question a localized test of pairing energies in a limited A region which covers a wide range of neutron-excess is needed. Given the strong increase in binding energy per nucleon and the individual character of light nuclei, the first region where such a test could be made is in the fp shell. Thus we have applied our latest mass measurements of neutron-rich $0f_{7/2}$ subshell nuclei[5] to examining the neutron-excess dependence of pairing energies (see Fig. 3).

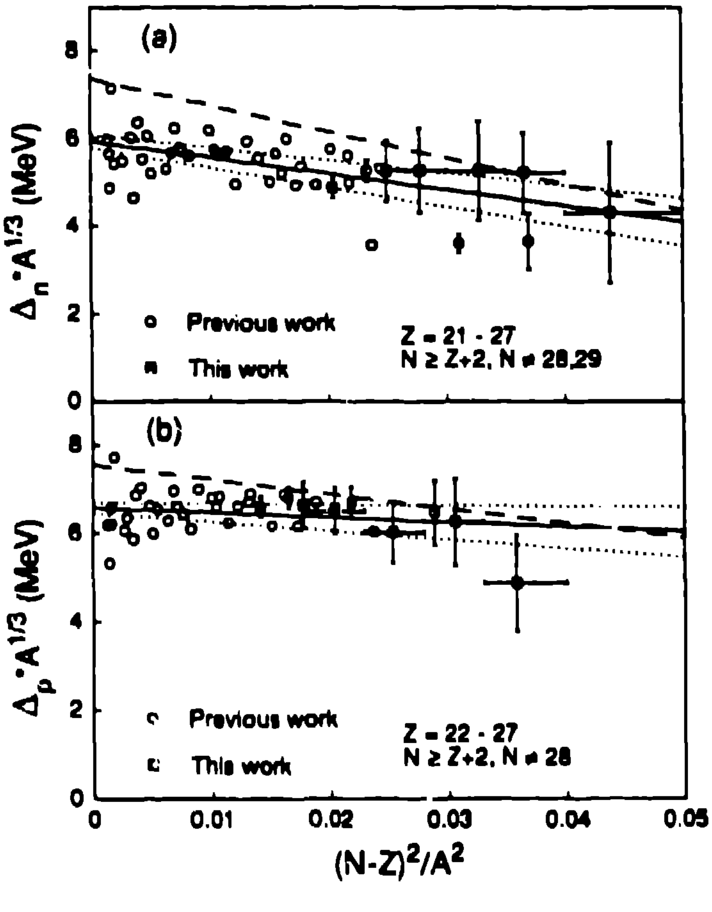

Fig. 3. A plot of (a) $\Delta_n A^{1/3}$ and (b) $\Delta_p A^{1/3}$ versus $(N-Z)^2/A^2$. The solid squares indicate the weighted average value of data points reported by Tu et al.[5] and the open circles indicate those data that were previously known[8]. The dashed lines are the global fits of Jensen et al.[23] while the solid lines are a fit to the data shown. The dotted lines indicate $\pm 1\sigma$ limits of the latter fit.

Although there is a considerable amount of scatter in the data and the latest measurements have larger error bars than are desired, the data show considerably less neutron excess dependence than that obtained by Jensen et al.[23]. (Note that we are not so concerned with the offset difference, but rather the slopes of these fits.) In particular, for the neutron pairing energies the neutron–excess dependence is roughly half as large as that of Jensen et al. while the proton pairing energies are one quarter as large. More to the point, in the case of proton pairing energies no neutron–excess dependence at all is indicated at the 1σ level. Clearly additional measurements of this type and further theoretical efforts are needed to elicit the underlying nature of nuclear pairing interactions and to show to which degree they are isospin dependent.

ACKNOWLEDGEMENTS

One of us (DJV) wishes to acknowledge support from the Alexander von Humboldt Foundation and the warm hospitality of the Gesellschaft für Schwerionenforschung mbH, Darmstadt, while on leave from Los Alamos National Laboratory. This work was performed under the auspices of the U.S. Department of Energy.

REFERENCES

1. N. A. Orr et al., Phys. Lett. B 258:29 (1991).
2. A. Gillibert et al., Phys. Lett. B 192:39 (1987).
3. A. Gillibert et al., Phys. Lett. B 176:317 (1986).
4. X. G. Zhou et al., Phys. Lett. B 260:285 (1991).
5. X. L. Tu et al., Z. Phys. A 337:361 (1990).
6. J. M. Wouters et al., Z. Phys. A 331:229 (1988).
7. D. J. Vieira et al., Phys. Rev. Lett. 57:3253 (1986).
8. G. Audi and A. H. Wapstra, Interim Atomic Mass Adjustment (June 1989), private communication.
9. C. Thibault et al., Phys. Rev. C 12:644 (1975).
10. C. Thibault et al., in: "Atomic Masses and Fundamental Constants 6", J. R. Nolen and W. Benenson, eds., Plenum, New York (1980) p.291; A. H. Wapstra and G. Audi, Nucl. Phys. A432:1 (1985).
11. C. Détraz et al., Nucl. Phys. A394:378 (1983).
12. W. R. Gibbs and A. C. Hayes, Phys. Rev. Lett. 67:1395 (1991), and references therein.
13. R. Anne et al., Phys. Lett. B 250:19 (1990).
14. T. Kobayashi et al., Spectroscopy of the Exotic Nucleus ^{11}Li via Pion-DCX Reaction $^{11}B(\pi^-,\pi^+)^{11}Li$, KEK Preprint 91-22 (1991), submitted to Phys. Rev. Lett..
15. G. T. Garvey and I. Kelson, Phys. Rev. Lett. 16:197 (1966); G. T. Garvey, W. J. Gerace, R. L. Jaffe, I. Talmi, Rev. Mod. Phys. 41:S1 (1969).
16. B. H. Wildenthal, Prog. Part. Nucl. Phys. 11:5 (1984); B. H. Wildenthal, M. S. Curtin, B. A. Brown, Phys. Rev. C 28:1343 (1983); B. H. Wildenthal, private communication.
17. G. Audi, private communication.
18. H. Stolzenberg et al., Phys. Rev. Lett. 65:3104 (1990).
19. E. K. Warburton, J. A. Becker, and B. A. Brown, Phys. Rev. C 41:1147 (1990).
20. A. Poves and J. Retamosa, "A Theoretical Study of the Very Neutron Rich Nuclei Around N=20", submitted to Nucl. Phys.; A. Poves and J. Retamosa, private communication.
21. S. T. Hsieh, X. Ji, R. Mooy, and B. H. Wildenthal, AIP Conf. Proc. 142:357 (1986).
22. P. Vogel, B. Jonson, and P. G. Hansen, Phys. Lett. B 139:227 (1984).
23. A. S. Jensen, P. G. Hansen, B. Jonson, Nucl. Phys. A431:393 (1984).
24. P. Möller and J. R. Nix, Nuclear Pairing Models, Los Alamos National Report LA-UR-90-1629 (1990), Nucl. Phys. A (in press).

LA-UR -91-3498

LA-UR--91-3498

DE92 003868

TITLE DIRECT SPECIATION OF METAL AND METALLOID IONS BY OPTICAL SPECTROSCOPIES

AUTHOR(S) P. R. Dixon, D. R. Janecky, J. A. Musgrave, C. D. Tait, D. L. Clark, and S. A. Ekberg

SUBMITTED TO DOE/BES Workshop in Sedimentary Basin/Fluid Rock Interaction, Norman, OK, November 1991

Los Alamos National Laboratory
Los Alamos, New Mexico 87545

DISTRIBUTION OF THIS DOCUMENT IS UNLIMITED

Direct Speciation of Metal and Metalloid Ions by Optical Spectroscopies

C. Drew Tait, David R. Janecky, David L. Clark, Scott A. Ekberg, Paul R. Dixon, John A. Musgrave; Isotope and Nuclear Chemistry Division, Los Alamos National Laboratory, Los Alamos, NM 87545
Philip C. Bennett; Department of Geological Sciences, University of Texas, Austin, TX 78713

Chemical interactions between dissolved organics and mineral surfaces have been increasingly the focus of investigations of diagenetic processes in sedimentary basins and in oil fields. These interactions can significantly influence the release, sequestering and transport of metals in low- to moderate-temperature hydrothermal ore systems such as the Mississippi Valley Type (MVT) deposits, and be a critical component of creation, destruction and reorganization of permeability through complex formation with the metalloids Si and Al. Our recent efforts have concentrated on organic-metalloid interactions because of their importance in rock alteration/weathering and in primary and enhanced oil recovery (EOR) processes.

Molecular level spectroscopic investigations of organic/inorganic interactions provide important new information on sedimentary geochemistry through the identification of interactions over moderate temperature and pH ranges. Although the official title of this project indicates the use of only optical spectroscopies, a combination of Uv/Vis/IR absoption, Raman scattering, and ^{29}Si and ^{13}C nuclear magnetic resonance (NMR) experiments are actually employed. A major advantage of integrating spectroscopic results with diagenesis studies is the ability to directly examine the mechanisms of interactions, even in complex matrices and with competing processes. Furthermore, we are extending these techniques to probe fluid inclusions with micro Raman and luminescence techniques to directly compare laboratory results with natural reservoir systems.

The mobility and transport of silica in natural waters has been a subject of debate for over a century (JULIEN, 1879; ILER, 1979). Field studies have found direct correlations between dissolved organic carbon (DOC) and dissolved silica in soil pore waters (CHESWORTH and MACIAS-VASQUEZ, 1985; WILLIAMS et al., 1985), lake and marine sediment pore waters (ASTON, 1983), shale pore waters (LERMAN, 1979), oil field formation waters (SURDAM et al., 1984), and oil-contaminated shallow groundwater (BENNETT and SIEGEL, 1987). This latter field study was especially important because it also correlated quartz etching under neutral pHs with DOC concentration. Therefore, matrix-destroying complexation of other rock-forming cationic constituents, especially Al, could not be invoked. The DOC's implicated in these correlations consist primarily of complex organic acids, including aromatic, keto- and hydroxy-acids, and other partially oxidized carbon species (AIKEN, 1987; BAEDECKER et al., 1987). Enhanced silicon mobility is thought to involve either an increase in proton availability from these acids or significant organo-silica interactions.

Decreased pH due to organic acids cannot account for the increased silicon mobility and quartz etching found in the near neutral (pH=6 to 7) oil-contaminated groundwater site near Bemidji, MN (BENNETT and SIEGEL, 1987), thereby implicating organo-silica interactions. These interactions may include hydrogen bonded charge transfer complexes as well as covalently bonded structures (ILER, 1979), although reliable direct evidence of these interactions is rare (FARMER, 1986; EVANS et al., 1990). Laboratory work by BENNETT et al. (1988) and BENNETT (1991) show that only poly-functional organic acids increase the dissolution rate of quartz and the final solubility of the mobilized silicon, so our studies have primarily focused on oxalate and citrate anions. Oxalate is the simplest difunctional acid anion and is also found naturally in concentrations of up to 3 mM in oil field brines (KHARAKA et al., 1984, 1987), while citrate is produced in significant quantities biologically and can exist in local environments, especially in soils near rock-weathering fungi. Furthermore, citrate is more active in mobilizing silica than oxalate (BENNETT et al., 1988). Other naturally occurring acids such as fulvic and humic acids are also implicated in silicon mobilization, but are too complex for these initial spectroscopic studies.

In a previous paper, Raman scattering and infrared absorption experiments purported to show spectroscopic evidence for a strong, covalently bonded silicon ester formed between oxalate and silicic acid (soluble silicon source) (MARLEY et al., 1989). As these experiments were only done at room temperature and at neutral pH, we decided to pursue them to examine the range of conditions in which this silicon ester could be expected to form. A diagnostic vibrational peak at 1305 cm^{-1}, both Raman and IR active and attributed to ν_{C-O-Si} (MARLEY et al., 1989), was used as the ester marker. This marker was observed in the IR when $4 < pH < 12$, and also showed no dissociation to at least 125°C. In fact, the spectrum was qualitatively unchanged to 175°C, but leakage from the cell precluded any quantitative conclusions. This temperature stability was considered especially important because organics in oil field brines and sedimentary basins in general exist between 85 and 200°C (i.e. between the temperatures at which organic-consuming bugs are significant and at which the organics decarboxylate - KHARAKA et al., 1984, 1987). Furthermore, this is also the temperature range of MVT deposit formation. However,

^{13}C NMR studies performed to corroborate the bidentate nature of the oxalate interaction with silicon did not revealed a ^{13}C chemical shift between pure oxalate and oxalate/silicic acid solutions (Figure 1), implying that any complexation must be below the NMR detection limit. Subsequent IR and Raman control experiments involving oxalate-only solutions also detected the 1305 cm^{-1} "marker" peak (Figure 1). Moreover, when we went back to the original paper (MARLEY et al., 1989), we discovered that the published control experiments involved oxalic acid rather than oxalate! Our experiments to determine the environment under which a silicon ester could exist instead turn into experiments that show where no detectable ester (or any other covalently bound Si-oxalate) is observed. Because silicon oxalate ester bond formation may be expected to strengthen at higher temperatures (see Al-oxalate data below), the negative findings from elevated temperature experiments are nonetheless a significant contribution.

In order to improve our detection limit to see if any significant organic-silicon interaction can occur, we have turned to ^{29}Si NMR experiments. These experiments probe the chemical environment of the Si atom rather than the organic carbons, and hence allow us to try to push the equilibrium toward complex formation by using excess organic species. Near-neutral solutions of ^{29}Si (introduced as enriched $^{29}SiO_2$ below the concentration that would result in dimerization / polymerization) and oxalate/citrate ligands were allowed to sit at room temperature for two months. Figure 2 shows the room temperature spectra for 2 mM Si alone and with 50 mM citrate or oxalate. No obvious new peak appears in the organic containing solutions, although a small hump possibly appears at ~-50 ppm in the oxalate spectrum. Therefore, no definitive evidence for a silicon ester is found, either because it is below the detection limit of the spectrometer, close to the detection limit (if the -50 ppm peak is real), or it is buried under the host Si peak at -116 ppm. However, these experiments are continuing, and, because they are new and an interpretational database has not yet been established, no final conclusions can yet be drawn from them . A striking feature of the spectra is the broadness of the parent Si peak (21 ppm or 1046 Hz), indicating exchange of the deuterium on $Si(OD)_4$ and D_2O solvent, where D_2O was used to provide an NMR signal "lock" to eliminate any signal drift problem. Because the broad signal implies either intermediate exchange kinetics or multiple species (dimers, trimers, etc.) with unresolved peaks, the temperature was both increased (52°C) and decreased in an effort to narrow the signal by entering the slow or fast exchange regimes. Furthermore, the $Si(OD)_4/D_2O$ sample has also been diluted by a factor of 10 with H_2O to try to eliminate the possibility that dimers/polymers contribute to the peak broadness. Not all of this data has been analyzed yet. However, the fact that 200 µM Si species can be observed with NMR is remarkable as it is a directly relevant environmental concentration. For example, [Si] in the Rio Grande reaches concentrations of 320 µM.

Besides silicon(IV), aluminum(III) is another major cationic constituent of rock and soil matrices. Aluminum is known to form multiligand complexes with oxalate at room temperature (BOTTARI and CIAVATTA, 1968; SJOBERG and OHMAN, 1985; THOMAS et al., 1991). In fact, oxalate solutions can leach aluminum from the relatively insoluble solid Al_2O_3 by stirring a slurrey with sodium oxalate at near neutral pH's (between 5 and 8). Aluminum-oxalate peaks are found in both IR and Raman spectra. Besides increasing the weathering of silicate minerals and consequently affecting geochemical cycles, biochemical cycles may also be affected by the simultaneous liberation of toxic Al and nutrients such as Fe, Ca, K, and Mg from mineral matrices (SJOBERG and OHMAN, 1985).

The effects of Al complexation by oxalate are easily followed spectroscopically, in contrast to the difficulty presented by Si complexation described above. Specifically, we have initiated experiments to determine the temperature dependence of Al-oxalate species, particularly to the moderate temperature regime relevant to sedimentary basins. As a pre-requisite, we first had to determine the spectroscopic signatures of the individual $Al(ox)_n^{3-2n}$ species. This process has been aided by previous room temperature speciation studies, mostly based on potentiometric results, which defined experimental conditions dominated by different complexes. Figure 3 shows the results of modifying the Al/oxalate ratio on the spectra. Since the log of the step-wise association constants for $Al(ox)^+$, $Al(ox)_2^-$, and $Al(ox)_3^{3-}$ are 6.0, 5.0, and 4.0 respectively (BOTTARI and CIAVATTA, 1968; SJOBERG and OHMAN, 1985), the 1428 cm^{-1} peak seen to dominate at oxalate/Al ratios ≥ 3 can be assigned to $Al(ox)_3^{3-}$, while the peak at 1408 cm^{-1} can be assigned to $Al(ox)_2^-$. A peak associated with $Al(ox)^+$ can not be definitely assigned, either because it is weak or buried beneath other peaks. The assigned peaks represent coordinated oxalate vibrations (major contributions from C-O and C-C stretches) with different force constants due to Al complexation. Peak assignments are also consistent with changes in oxalate availability as a function of pH (SJOBERG and OHMAN, 1985).

The major solution effect of increasing temperature is the decrease in solvent dielectric constant (BRIMHALL and CRERAR, 1987; SEWARD, 1984). Highly charged species are therefore destabilized relative to lower charged ones, and stability constants change to reflect this. Therefore, when conditions were set for equal concentrations of $Al(ox)_3^{3-}$ and $Al(ox)_2^-$ at room temperature, we expected an increase in temperature to lower the concentration of the highly charged $Al(ox)_3^{3-}$ species. However, Figure 4 shows no change in the populations of the two species, implying an increase in the association constant for $Al(ox)_3^{3-}$. This is even more remarkable when the lower availability of oxalate is taken into account in this pH=3 solution, as $\log k_2$ for oxalic acid increases from -4.29 at 25°C to -4.42 at 50°C and -4.69 at 80°C. Therefore, our emphasis has shifted to competition studies for oxalate as temperature is changed. For sedimentary basin geochemistry, a competing cation such as zinc, calcium, or iron could be tried. The oxalates of the first two, however, are not soluble enough for spectroscopic examination, so we will continue our experiments with Al(III) and Fe(III) competition for oxalate.

With enhanced understanding of rock matrix - organic interactions and spectral signatures of these interactions provided by the laboratory analogue studies, we intend to pursue investigations of organic species in fluid inclusions in sedimentary basins such as the oil-producing Austin Chalk. Geochemical issues of importance include thermal maturation and porosity of the surrounding rock matrix, petroleum migration history, and interactions of enhanced oil recovery (EOR) techniques. Fluid inclusions allow us to study these issues because they preserve the paleo-chemistry of the fluids that led to oil field development and contain the well-equilibrated fluid/mineral surface environment that is needed to predict the effects of EOR techniques. A range of temperatures is also readily accessible. Toward this end, we are acquiring a Raman microprobe accessory to allow examination of the vibrational fingerprints of organic species in inclusions down to 5 microns in size, and also the monochromator attachments for a UV adapted microscope to allow us to use synchronously scanned fluorescence. This latter technique has recently been used with macroscopic samples to add molecular specificity to sensitive luminescence measurements (PHARR et al. 1991; PHARR, 1991; CABANISS, 1991), and will be adapted here to microscopic measurements to probe the organics in fluid inclusions. The combined application of Raman microprobe and fluorescence will provide important cross checks. Demonstration of microscopic scale results will allow investigations of a diverse range of problems, including paleochemistry / paleoclimate of Yucca Mountain and ore-deposits in geothermal systems such as Carlin type gold deposits with organic-rich fluid inclusions (Jeff Hulen, Univ. of Utah, personal communication). Note that organics are unexpectedly present and largely ignored components in some geothermal systems such as the Valles Caldera drillcore fluid inclusions (MUSGRAVE and NORMAN, 1991; MUSGRAVE et al. 1991). Organic species are also often discussed but little quantified in many other systems, particularly with respect to potential coupled interactions with metals and metalloids which are direct applications of this work.

REFERENCES

Aiken, G.R.; Thorn, K.A.; Brooks, M.H. (1987) Nonvolatile organic acids in ground water contaminated with crude oil. U.S. Geol. Survey Open-File Rept. 87-109.

Aston, S.R. (1985) *Silicon Geochemistry and Biogeochemistry.* Academic Press, New York.

Baedecker, M.J.; Cossarelli, I.M.; Hopple, J.A. (1987) The composition and fate of hydrocarbons in a shallow glacial-outwash aquifer. *U.S. Geol. Survey Open-File Rept. 87-109.*

Bennett, P.C. and Siegel, D.I. (1987) Increased solubility of quartz in water due to complexation by dissolved organic compounds. *Nature* **326**, 684-687.

Bennett, P.C.; Melcher, M.E.; Siegel, D.I.; Hassett, J.P. (1988) The dissolution of quartz in dilute aqueous solutions of organic acids at 25°C. *Geochim. et Cosmochim. Acta* **52**, 1521-1530.

Bennett, P.C. (1991) *Geochim. et Cosmochim. Acta* **55**,

Bottari, E. and Ciavatta (1968) . *Gazz. Chim. Ital.* 1004.

Brimhall, G.H. and Crerar, D.A. (1987) Ore fluids: Magmatic to supergene. In *Thermodynamic Modeling of Geological Materials: Minerals, Fluids, and Melts;* (eds. I.S.E. Carmichael and H.P. Eugster); Review in Mineralogy **17** pp. 255-321.

Cabaniss, S.E. (1991) Synchronous fluorescence studies of metal-fulvic acid equilibria [abs]. Conference on Metal Speciation and Contamination of Soil, May 22-24, Jekyll Island, GA.

Chesworth, W. and Macias-Vasquez, F. (1985) pE, pH, and podzolization. *Amer. J. Sci.* **285**, 128-146.

Evans, D.F.; Parr, J.; Coker, E.N. (1990) Nuclear Magnetic Resonance studies of silicon(IV) complexes in aqueous solution - I. Tris-Catecholato complexes. *Polyhedron,* **9**, 813-823.

Farmer, V.C. (1986) Sources and speciation of aluminum and silicon in natural waters. In *Silicon Biochemistry* (eds. D. Evered and M. O'Connor). pp. 4-23. J. Wiley & Sons, New York.

Iler, R.K. (1979) *Chemistry of Silica.* Wiley-Interscience, New York.

Julien, A.A. (1879) On the geological action of the humus acids. *Amer. Assoc. Adv. Sci. Proc.* **28**, 311-410.

Kharaka, Y.K.; Law, L.M.; Carothers, W.W.; Goerlitz, D.F. (1984) Role of organic species dissolved in formation waters from sedimentary basins in mineral diagenesis. In *The Society of Econ. Paleontologists and Mineralogists Symposium on Relationship of Organic Matter and Mineral Diagenesis* (D.L. Gautier, Ed.) **38**, pp. 111-122.

Kharaka, Y.K.; Maist, A.S.; Carothers, W.W.; Law, L.M.; Lamothe, P.J.; Fries, T.L. (1987) Geochemistry of metal-rich brines from Central Mississippi Salt Dome Basin, USA. *Appl. Geochem.* **2**, 543-561.

Lerman, A. (1979) *Geochemical Processes, Water and Sediment Environments*. J. Wiley & Sons, Toronto.

Marley, N.A.; Bennett, P.; Janceky, D.R.; Gaffney, J.S. (1989) Spectroscopic evidence for organic diacid complexaton with dissolved silica in aqueous systems. I. Oxalic acid. *Org. Geochem.* **14**, 525-528.

Musgrave, J.A. and Norman, D.I. (1991) Fluid inclusion evidence for the evolution of the Sulphur Springs hydrothermal system, Valles caldera, New Mexico. *Econ. Geol.* submitted.

Musgrave, J.A.; Charles, R.W.; Goff, F.; Norman, D.I. (1991) Geochemistry of hydrothermal alteration and mineralization, Sulfur Springs, Valles caldera, New Mexico, in prep.

Pharr, D.Y. (1991) Analysis for groundwater petroleum contamination using synchronous scanning fluorescence [abs]. 21st International Symposium on Environmental Analytical Chemistry, May 20-22, Jekyll Island, GA.

Pharr, D.Y.; McKenzie, J.K.; Hickman, A.B. (1991) Fingerprinting petroleum contamination using synchronous scanning fluorescence spectroscopy. J. Groundwater, submitted.

Seward, T.M. (1984) The formation of lead(II) chloride complexes to 300oC: A spectrophotometric study. *Geochim. et Cosmochim. Acta* **48**, 121-134.

Sjoberg, S. and Ohman, L.-O. (1985) Equilibrium and structural studies of silicon(IV) and aluminium(III) in aqueous solution. Part 13. A Potentiometric and ^{27}Al nuclear magnetic resonance study of speciation and equilibria in the aluminium(III)-oxalic acid-hydroxide system. *J. Chem. Soc., Dalton Trans.* 2665-2669.

Surdam, R.C.; Boese, S.W.; Crossey, L.J. (1984) The chemistry of secondary porosity. In *Clastic Diagenesis* (eds. D.A. McDonald and R.C. Surdam); *AAPG Memoir 37*, pp. 127-150.

Thomas, F.; Masion, A.; Bottero, J.Y.; Rouiller, J.; Genevrier, F.; Boudot, D. (1991) Aluminum(III) speciation with acetate and oxalate. A potentiometric and ^{27}Al NMR study. *Environ. Sci. Technol.* **25**, 1553-1559.

Williams, L.A.; Parks, G.A.; Crerar, D.A. (1985) Silica diagenesis. I. Solubility controls. *J. Sediment. Petrol.* **55**, 301-311.

FIGURE CAPTIONS

1.(a) FTIR spectrum of a sodium oxalate / silicic acid mixture at neutral pH and the corresponding spectrum of sodium oxalate with no added silicon (inset, on different horizontal scale). The 1308 cm^{-1} peak is therefore not diagnostic of silicon ester formation as concluded by MARLEY et al. (1989). (b) Carbon-13 FT-NMR spectrum of a sodium oxalate / silicic acid mixture at neutral pD and the corresponding spectrum of sodium oxalate with no added silicon. (Because the spectra were obtained in D_2O to provide a frequency lock from deuterium to prevent frequency drift, pD is noted rather than pH). The identical chemical shifts argue for identical chemical environments for the oxalate carbons - namely, one not involved in a strong covalent bond with the silicon compound.

2. Room temperature ^{29}Si NMR spectra of (from bottom spectrum to top) 2 mM $^{29}Si(OD)_4$ (from an enriched 97% $^{29}SiO2$ silicon source) with no organic ligand (pD=6.7), 2 mM $^{29}Si(OD)_4$ / 50 mM sodium citrate (pD=7.4), and 2 mM $^{29}Si(OD)_4$ / 50 mM sodium oxalate (pD=7.4). Note that the spectra were taken in D_2O to provide a frequency lock to prevent signal drift, and that neutral D_2O has a pD of 7.5. For our 250 MHz spectrometer, we used a 10 µsec pulsewidth (180^o pulsewidth measurement for $Si(OD)_4$ was determined to be 43 µsec), a relaxation time of 90 seconds (T_1 for silicon is notoriously long), and an acquisition time of 0.82 sec. The lack of significant spectral change, despite the excess organic ligand, demonstrates the weakness (or extremely slow kinetics) of any chemical reaction between the silicic acid and organic bases.

3. Raman vibrational spectra from solutions of different Al^{3+} / $oxalate^{2-}$ concentration ratios at near neutral pH. Note that at near neutral pH, there is considerable precipitation for the (1:1) and (1:2) samples, as well as the presence of other Al-oxalate species such as $Al_2(OH)_2(Ox)_2$ and $Al_3(OH)_3(Ox)_3$ (SJOBERG and OHMAN, 1985). These additional species may be the cause of the 1449 cm^{-1}

peak observed only at these concentration ratios. The peaks at 1408 cm^{-1} and 1429 cm^{-1} are assigned to oxalate vibrations from $Al(Ox)_2^-$ and $Al(Ox)_3^{3-}$ respectively.

4. Temperature dependent Raman spectra for a solution of 20 mM Al^{3+} / 50 mM oxalate at pH=2.9. Under these conditions, the ratio of $Al(Ox)_2^-$ to $Al(Ox)_3^{3-}$ is 1 at 25°C (SJOBERG and OHMAN, 1985). Although the 1429 cm^{-1} peak from $Al(Ox)_3^{3-}$ was expected to lose intensity relative to the 1408 cm^{-1} peak of $Al(Ox)_2^-$ as the temperature was increased, the spectra show a lack of change with temperature, indicating that the third association constant ($Al(Ox)_2^- + Ox^{2-} \rightarrow Al(Ox)_3^{3-}$) actually increases with temperature, despite the high charge of $Al(Ox)_3^{3-}$ and the lower availability of oxalate at higher temperatures.

INFRARED ABSORPTION SPECTRA

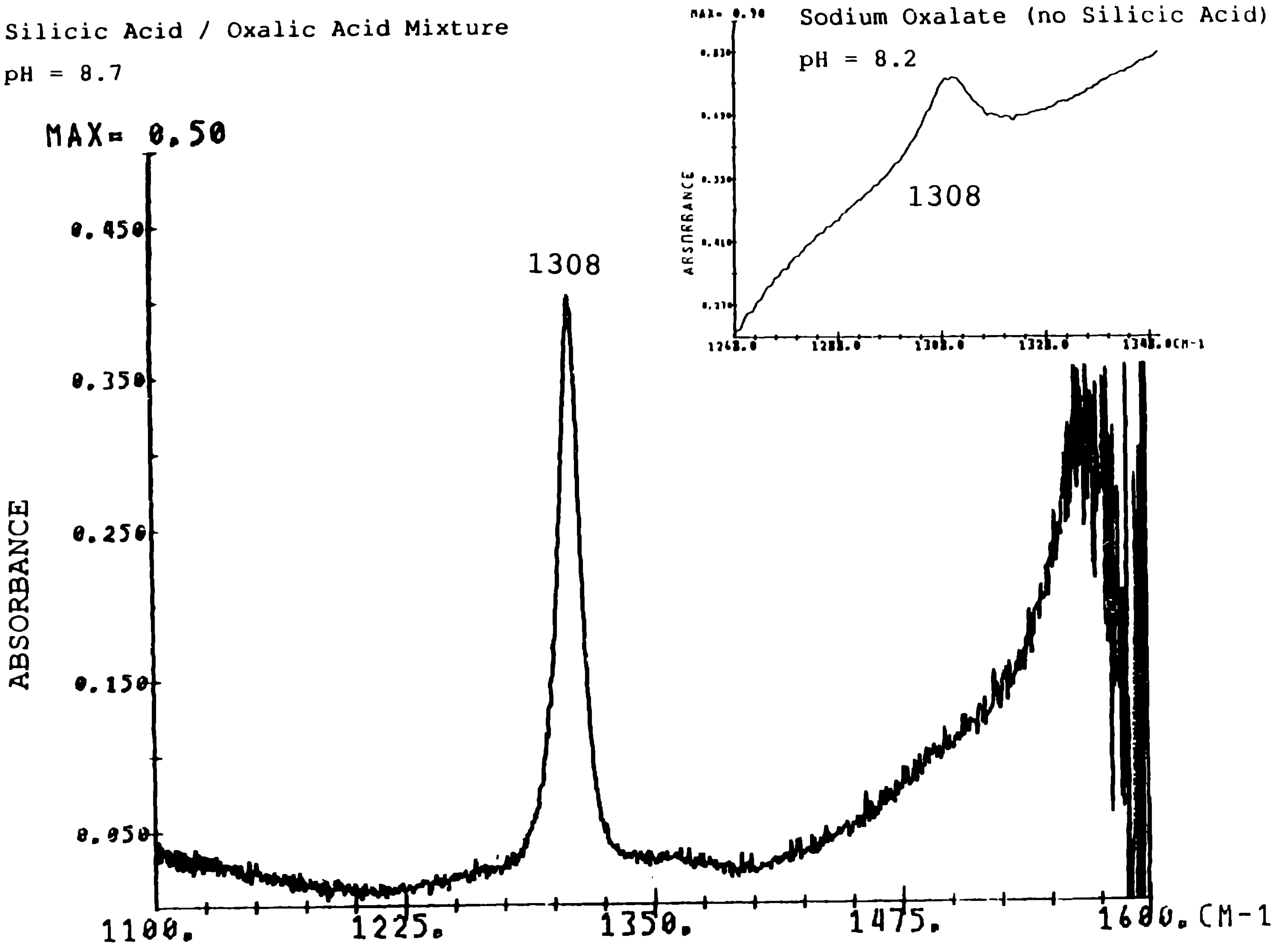

Figure 1a

NMR SPECTRA

Silicic Acid / Oxalic Acid Mixture
pD = 8

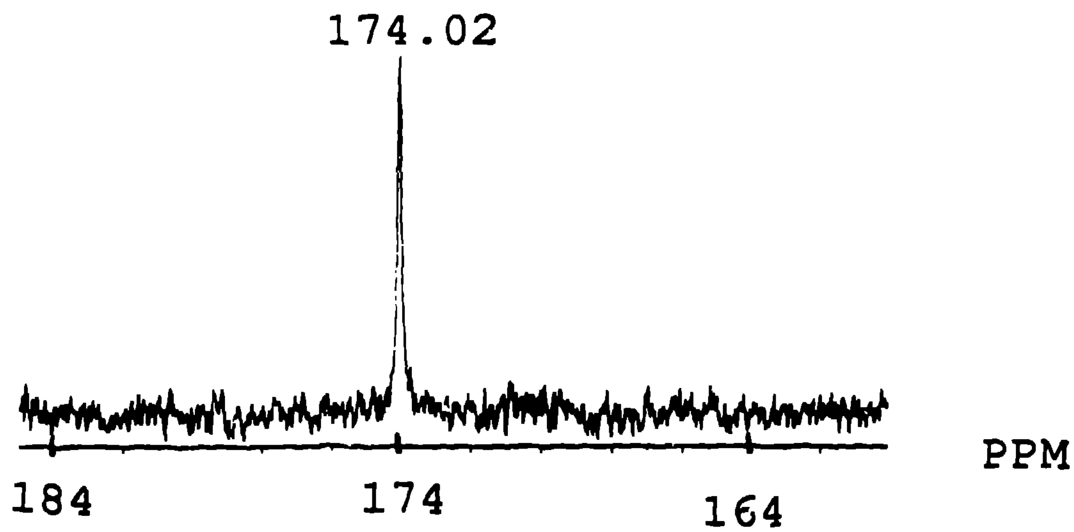

Sodium Oxalate (no Silicic Acid)
pD = 8

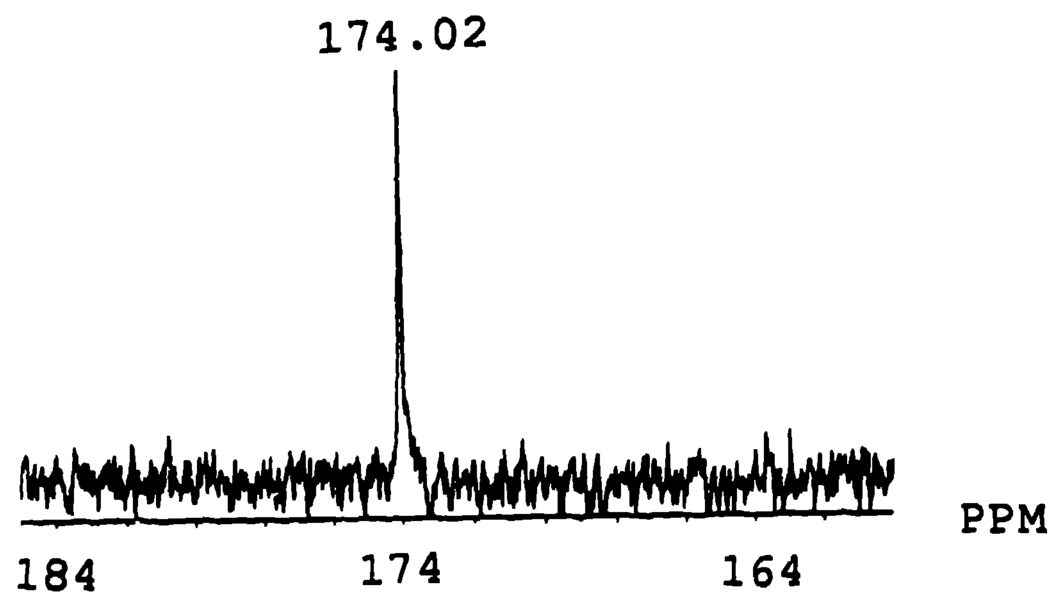

Figure 1b

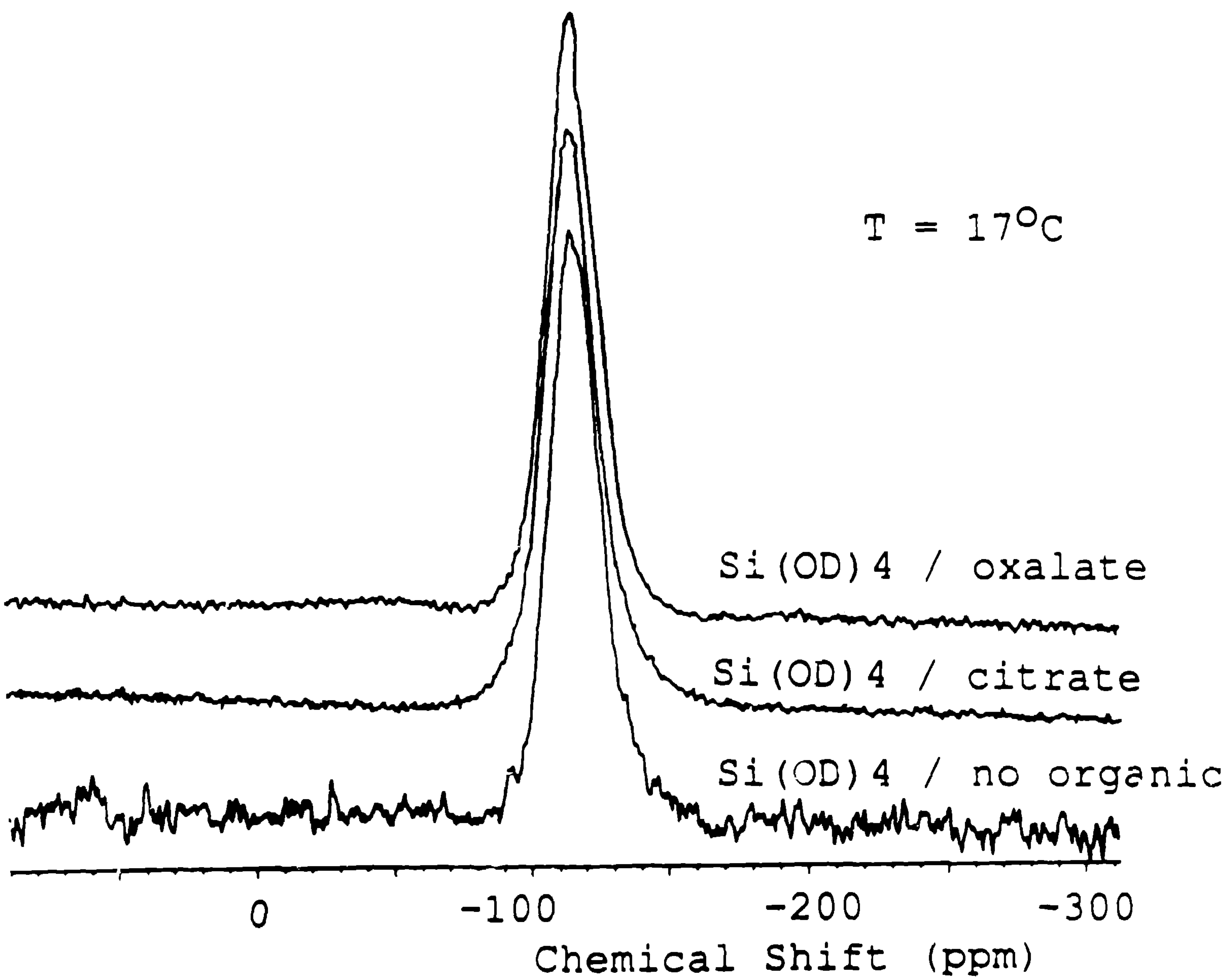

T = 17°C
Si(OD)4 / oxalate
Si(OD)4 / citrate
Si(OD)4 / no organic
0
-100
-200
-300
Chemical Shift (ppm)

Figure 2

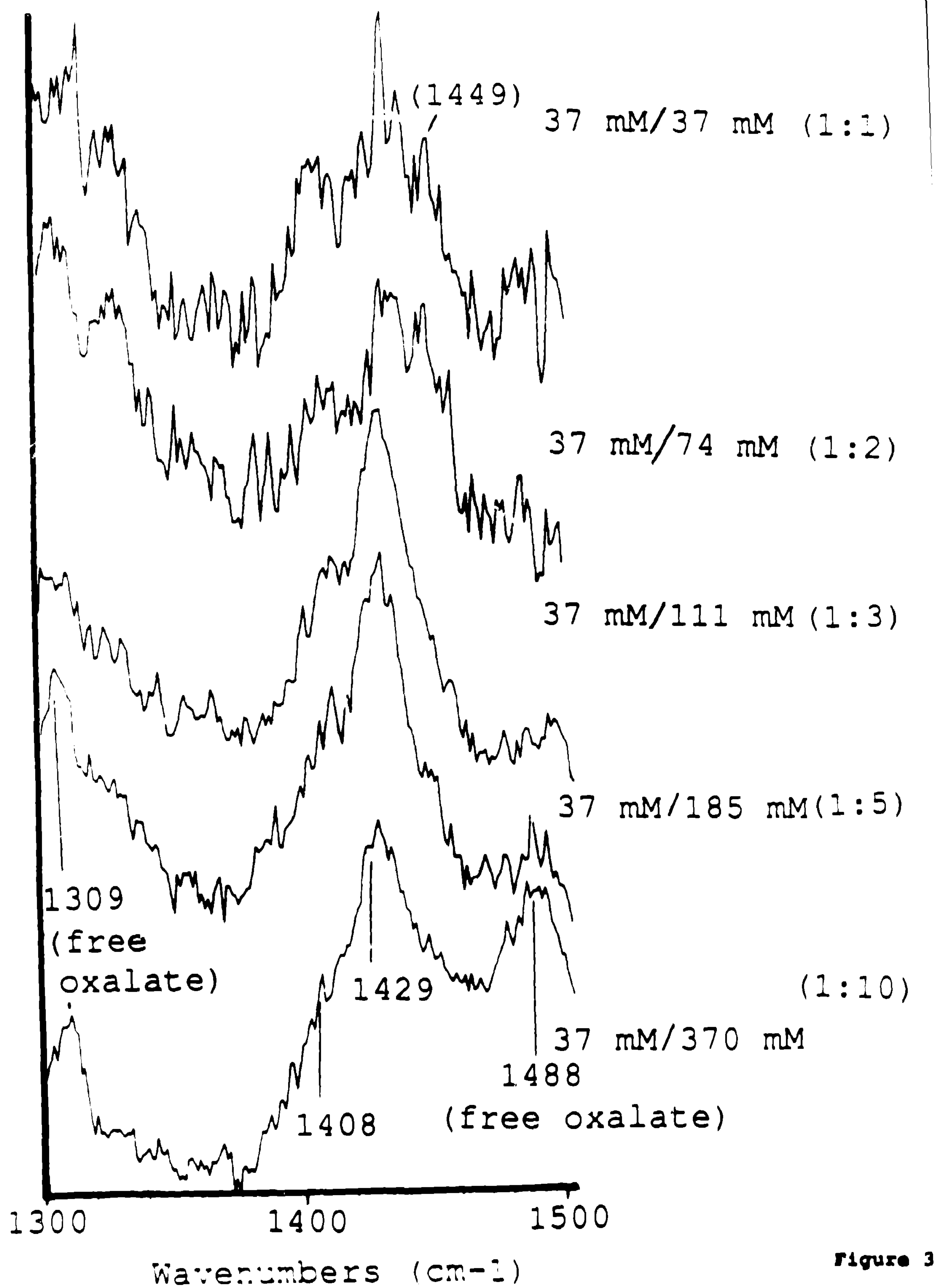

(1449)
37 mM/37 mM (1:1)
37 mM/74 mM (1:2)
37 mM/111 mM (1:3)
37 mM/185 mM(1:5)
1309
(free
oxalate)
1429
(1:10)
37 mM/370 mM
1488
1408
(free oxalate)
1300
1400
1500
Wavenumbers (cm-1)

Figure 3

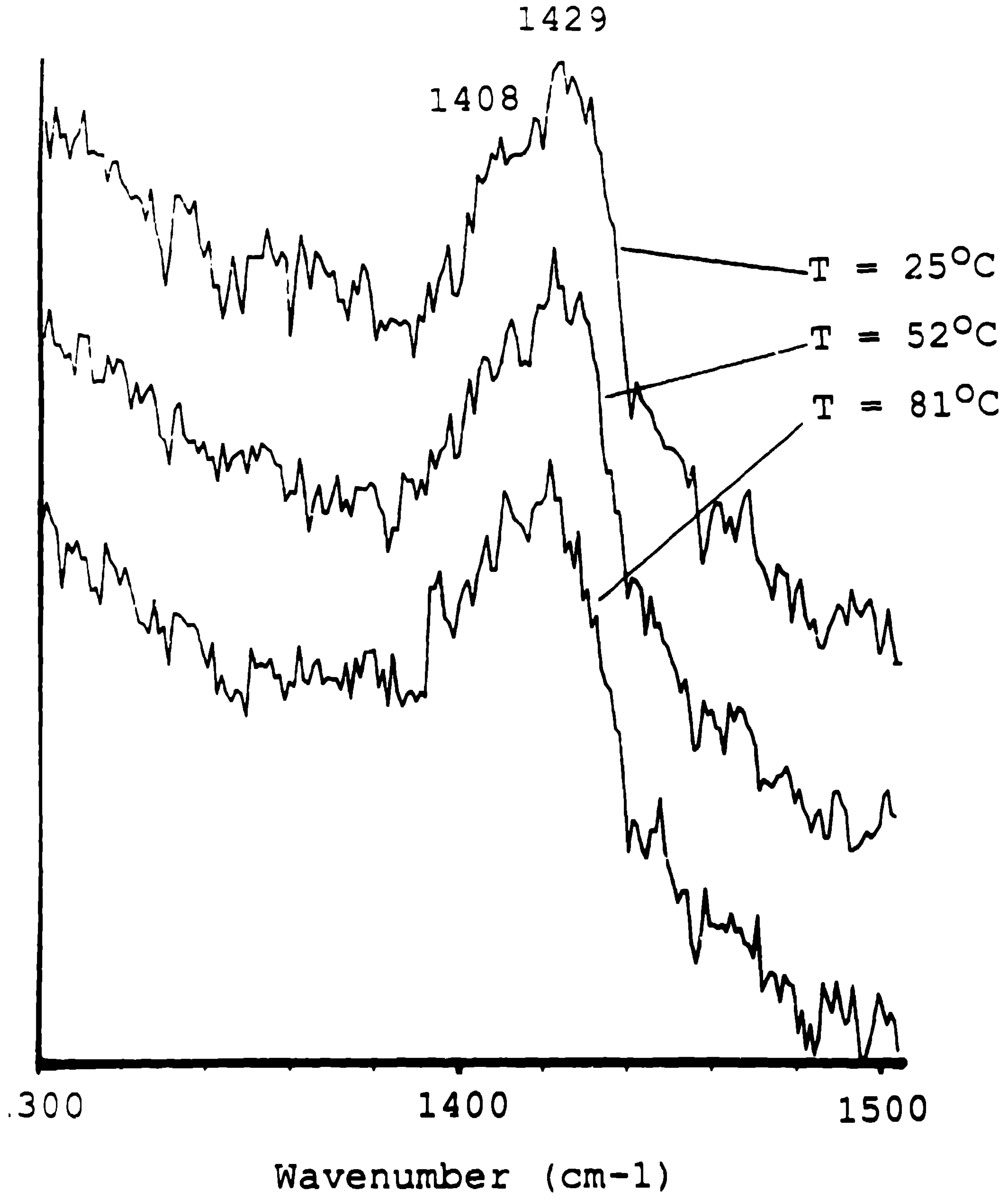

Figure 4

LA-UR -91-3501

LA-UR--91-3501

DE92 003867

Los Alamos National Laboratory is operated by the University of California for the United States Department of Energy under contract W-7405-ENG-36

TITLE STANDARDIZED RADIOLOGICAL HAZARD ANALYSIS FOR A BROAD BASED OPERATIONAL SAFETY PROGRAM

AUTHOR(S) WILLIAM W. WADMAN III
LARRY L. ANDREWS

SUBMITTED TO INTERNATIONAL RADIATION PROTECTION ASSOCIATION (IRPA8)

Los Alamos

Los Alamos National Laboratory
Los Alamos, New Mexico 87545

FORM NO. 836 R4

DISTRIBUTION OF THIS DOCUMENT IS UNLIMITED

STANDARDIZED RADIOLOGICAL HAZARD ANALYSIS FOR A BROAD BASED OPERATIONAL SAFETY PROGRAM

W. Wadman III[1] and L. Andrews[2]
Health and Safety Division
Los Alamos National Laboratory (LANL)
Los Alamos, New Mexico

ABSTRACT

The Radiological Hazard Analysis (RHA) Manual provides a methodology and detailed guidance for systematic analysis of radiological hazards over a broad spectrum of program functions, housed in a wide variety of facilities. Radiological programs at LANL include: research and experimentation; routine materials operations; production; non-destructive examination or testing; isotope and machine produced radiations; chemistry; and metallurgy. The RHA permits uniform evaluation of hazard types over a range of several orders of magnitude of hazard severity. The results are used to estimate risk, evaluate types and level of resource allocations, identify deficiencies, and plan corrective actions for safe working environments.

INTRODUCTION

Laboratories within the U.S. Department of Energy are undergoing significant changes in the manner by which they conduct operations. Operational Health Physics groups are not an exception. With budgetary constraints becoming more severe, staffing and resources strained or severely limited, methods had to be devised to provide equal or better service in spite of the hardships. Standardization of the methodology and consistency of evaluating the types and levels of radiological hazards involving several hundred projects in over 150 facilities, spread over 43 square miles, was essential for the operational Health Physics personnel. The Standardized Radiological Hazard Analysis Manual was determined to be one of several practical working tools for Health Physicists in the field. The 300 page manual starts with a detailed index from which an analysis plan is constructed. Once in the field, the use of the manual index provides ready access to guidance, assessment details, and forms for other hazards or issues that were either unexpected or not obvious during the initial assessment. The guidance contained in the manual is detailed, but allows for independent input by each Health physicist that uses it. The training on the use of the RHA Manual emphasizes that the guidance should be used as a tool to direct and focus analysis thought processes, but should not limit the RHA performance to merely a check list task.

Data from the detailed Radiological Hazard Analysis report sheets is subsequently input to a commercially available relational database which is both an analysis tool and the database for each and every facility for which a Radiological Hazard Analysis has been performed.

Blank pages of forms and reports are obtained from stock to replace those used from the binder to be ready for the next facility analysis.

DEVELOPMENT OF THE RHA MANUAL

There are existing methodologies for risk assessments of specific processes, and a few for multi-function facilities. The Nevada Operations Office of the DOE produced the 150 page "Radiological Safety Functional Appraisal and Program Review Guide," in 1990. (Do90) This has direct application to DOE/NVO facilities. It is based upon a radiological environmental program. A method for determining hazard classifications of DOE facilities was developed at Battelle PNL (Lu91). The hazard classification required a walkthrough by an inspection team of persons with considerable expertise in the various disciplines. More than one DOE Operations Office required the technique to be used by operating contractors of DOE facilities, to determine gross hazard classification values for their facilities. These determinations were not sufficiently in-depth to provide the level of detail LANL felt to be necessary for our operational hazard evaluations. The technique also did not provide useful data regarding operational hazards routinely faced by facility operations personnel, or health and safety support personnel.

The concept of the Standardized Radiological Hazard Analysis Manual was originated by one of the authors (LA). With access to a consultant with a broad spectrum of "hands-on" experience in the field of Health Physics, Industrial Hygiene, and Radiological Environmental Monitoring Programs, the project was undertaken.

The manual was conceived as a light-weight, notepad-sized document with outline formatted "reminders" for review while doing field facility walk-throughs. The document is now about 300 single side printed pages, maintained in a three inch thick binder, and requires training in its use to provide familiarity and a reasonable level of surety that it will be used uniformly by the trained staff.

Each type of radiological facility or operation was considered as an independent unit during the drafting of the RHA Manual. Details from observations, physical measurements, radiological measurements, locations of components, and similar pertinent data, are called out in the text of each hazard analysis section. In the initial draft, in both the manual and the software, each hazardous item was separate, as was each mitigation process, and was considered only for that room, building, or process. Subsequently, common items, such as glove boxes, filtrations, detection and alarm systems, were coded in the relational database software. This served to provide more rapid input, reduction in errors, and conservation of RAM and storage required by the computer program.

Hazard levels, risk assessments and hazard mitigating equipment or engineered features are analyzed in the software. All values obtained from the analytical results, relate to hazards present during normal operational circumstances. No attempt has been made to extend the analysis into accident scenarios. With the availability of information regarding radionuclides, inventory on hand, physical and/or chemical form, and details of the monitoring systems, and ventilation systems, assessing limited accident scenarios remains a possibility.

Each developmental iteration has only expanded the size of the overall program, both software and Manual. Some future consideration may be to purchase the relational database "engine", and write the specific RHA database applications program. Several advantages would be, easier commercial or public domain releases of the software component which could save 50% of the RAM occupied by features that are not used from the standard database product. Time savings could be realized by having direct page access to pertinent input requirements, rather than have to page through irrelevant subject matter to arrive at the appropriate page for the next input.

TYPES OF FACILITIES INCLUDED

The RHA Manual is designed to be used to evaluate radiological hazards associated with the following programmatic elements:

Research and Experimentation: explosion dynamics; armor, anti-armor; criticality; weapons enhancement; controlled thermonuclear reactions; free electron lasers,

Routine Operations: reactor operations; radioactive waste management; weapons production related operations; weapons testing operations; retirement storage operations,

Production: quality control; materials purity; lathe and milling shop operations; purification; enrichment; weapons related activities; medical aspects of LAMPF operations; X-ray crystallography confirmations,

Non-Destructive Examination or Testing: fixed X-Ray radiographic facilities; fixed facility Van de Graaf radiography; high speed x-ray of explosive events; portable radiographic unit safety; eddy current testing of radioactive materials; magnaflux testing of radioactive materials; betatron narrow beam, thick target radiography,

Isotope Produced Radiations: calibrations; sealed source radiography; activated accelerator component radiological protection; heat source radiological protection; incidental weapons component exposure control; weapons debris analysis; reactor fuel processing hot cell operations,

Machine Produced Radiations: Los Alamos Meson Physics Facility; IBF tandem Van de Graaf; single stage Van de Graaf; free electron laser; plasma focus devices; pulsed power conversion; health center x-rays; neutron generator facility; electron guns; ion implantation,

Chemistry: analytical; alloy; quality control; quality assurance; medical isotope purification hot cell operations,

Metallurgy: analytical; developmental; design improvement; stability improvement; yield improvement; induction heating; laser isotope separation,

Transportation: On-site, inter-area, intra-area, for safety and compliance with State and Federal shipping requirements on public roads,

Compliance Assessment: Confirm compliance with Health and Safety requirements imposed by all applicable State, Federal Agency requirements, laws, DOE Orders.

In the above 10 major areas, each of the 56 categories of operation, project, or facility has its own set of RHA forms. Each analysis must be independent in-so-far that it is not a component of a larger complex. If the latter is the case, the RHA forms are grouped into a facility package. The results of the full analysis of the units as a system will result in a different hazard rating because of the concurrent and dependent mode of operation.

CONCLUSIONS

Present operating facility inspections are performed with a perspective focused on the problem of immediate concern. The use of the RHA Manual will provide consistency for such evaluations. Performing full facility radiological hazards analyses will accomplish several objectives: Advance knowledge of the facility's or operation's hazards; provide a global perspective of concurrent but unrelated hazards of adjacent operations; consistent or uniform approach to evaluations and solutions; applications of "lessons learned"; greater confidence to younger professionals in the Health Physics Groups; a cross-training tool for professionals and technicians not familiar with areas outside of their duty areas; a computerized database with rapid access for rapid retrieval for the line organization, security, fire, and emergency response teams. Two peripheral uses of the RHA Manual may be:

1. The RHA may have use as a formal tool during the drafting of facility Safety Analysis Reports (SAR) and Updated Safety Analysis Reports (USAR).

2. There may be some value in training the facility supervision to use the system, to provide them with the capability to perform more frequent reviews of their facilities than can the limited staff of operational Health Physicists. This is beneficial for the Laboratory through the heightened awareness for radiological hazards in the workplace.

[1] Private Consultant to LANL. [2] LANL HS-12 Health Physicist

REFERENCES

Do90 U.S. Department of Energy, Nevada Operations Office, Environmental Compliance Branch, Environmental Protection Division, Las Vegas, Nevada. "Radiological Safety Functional Appraisal and Program Review Guide". (1990)

Lu91 Lucas, D.E., A Practical Approach to Hazard Classification, Rev 1., Battelle, Pacific Northwest Laboratories, Richland, Washington. March 1991.

This work was performed under the auspices of the University of California operated Los Alamos National Laboratory.